Characterization of Minerals, Metals, and Materials 2016

Edited by

Shadia Jamil Ikhmayies
Bowen Li
John S. Carpenter
Jiann-Yang Hwang
Sergio Neves Monteiro
Jian Li
Donato Firrao
Mingming Zhang
Zhiwei Peng
Juan P. Escobedo-Diaz
Chenguang Bai

TMS

Springer

Characterization of Minerals, Metals, and Materials 2016

Cover Image: SEM micrographic sample treated with water for 24h. From "Evaluation of White Bentonite Modified by Acid Attack," by C.G. Bastos Andrade, D.M. Fermino, M.G. Fernandes, and F.R. Valenzuela-Diaz, pp. 107-114.

TMS2016

145th Annual Meeting & Exhibition

FEBRUARY 14-18 DOWNTOWN NASHVILLE, TENNESSEE MUSIC CITY CENTER

New proceedings volumes from the TMS2016 Annual Meeting:

- 7th International Symposium on High-Temperature Metallurgical Processing
- CFD Modeling and Simulation in Materials Processing 2016
- Characterization of Minerals, Metals, and Materials 2016
- Energy Technology 2016: Carbon Dioxide Management and Other Technologies
- EPD Congress 2016
- Light Metals 2016
- Magnesium Technology 2016
- Rare Metal Technology 2016
- REWAS 2016
- Shape Casting: 6th International Symposium
- TMS 2016 Supplemental Proceedings

Characterization of Minerals, Metals, and Materials 2016

Proceedings of a symposium sponsored by
the Materials Characterization Committee of
the Extraction and Processing Division of
The Minerals, Metals & Materials Society (TMS)

held during

TMS2016
145th Annual Meeting & Exhibition

FEBRUARY 14-18 DOWNTOWN NASHVILLE,
TENNESSEE MUSIC CITY CENTER

Edited by:

Shadia Jamil Ikhmayies, Bowen Li, John S. Carpenter, Jiann-Yang Hwang, Sergio Neves Monteiro, Jian Li, Donato Firrao, Mingming Zhang, Zhiwei Peng, Juan P. Escobedo-Diaz, and Chenguang Bai

Editors
Shadia Jamil Ikhmayies
Bowen Li
John S. Carpenter
Jiann-Yang Hwang
Sergio Neves Monteiro
Jian Li
Donato Firrao
Mingming Zhang
Zhiwei Peng
Juan P. Escobedo-Diaz
Chenguang Bai

ISBN 978-3-319-48623-9 ISBN 978-3-319-48210-1 (eBook)
DOI 10.1007/978-3-319-48210-1

Chemistry and Materials Science: Professional

Published by Springer International Publishers, Switzerland, 2016
Reprint of the original edition published by John Wiley & Sons, Inc., 2016, 978-1-119-26439-2

Printed on acid-free paper

This Springer imprint is published by Springer Nature
The registered company is Springer International Publishing AG
The registered company address is: Gewerbestrasse 11, 6330 Cham, Switzerland

TABLE OF CONTENTS

Characterization of Minerals, Metals, and Materials 2016

Non-Ferrous

Method Development

Minerals

Processing and Corrosion

Ferrous

Clays & Ceramics

Composites

Extraction

Soft Materials

Electronic, Magnetic, Environmental, and Advanced Materials

Welding and Solidification

Poster Session

PREFACE

Characterization is a fundamental process in the field of materials science, without which no scientific understanding of engineering materials could be ascertained. It refers to the broad and general process by which the structure and properties of the material are probed and measured. While many characterization techniques have been practiced for centuries, new techniques and methodologies are constantly emerging. The Characterization symposium sponsored by the Materials Characterization Committee of TMS, focuses on all characterization techniques, developments in the techniques and their applications. Besides, the symposium focuses on material characterization from the bulk down to the nano-scale, on extraction and processing, and on understanding the performance of different characterization tests of materials.

The characterization symposium is a main symposium in the TMS annual meeting, which attracts scientists from academia and industry, experts, and students from the global community. In the TMS 2016 Annual Meeting & Exhibition held in Nashville, Tennessee, USA, the Characterization Symposium 2016 received 237 submissions, of which 110 are oral presentations, and 101 will be presented as posters. Of the presented papers, 100 are published in this book after being peer reviewed. These papers cover different fields which include: method development, ferrous and nonferrous metals, processing and corrosion, composites, extraction, minerals, clays and ceramics, welding and solidification, electronic, magnetic, environmental, advanced, and soft materials. The structures and microstructures of these materials are examined in terms of optical, electrical, electronic, mechanical, thermal, and functional properties.

This book provides the graduate students, scientists in academia, materials scientists and engineers, as well as the industry audience with up-to-date information on many types of materials and their characterization with an underlying theme of explaining the behavior of materials using novel approaches. The reader learns in this book about all types of characterization methods in general, and specifically about real-world applications in the minerals, metals, and materials areas. Bulk materials, thin films, joints and interfaces, powders, slags, micro- and nanostructures can be found in this book. Particular attention is paid to the relationship between production, extraction, processing, recycling, and loading of materials and alloys in practical use. The knowledge gained from this book can be used to assess quality, reliability, and safety, and to produce new materials with specific desired properties, and the need to characterize these materials throughout their life cycle has inspired innovations in methods and techniques.

The editors of this book express their sincere thanks and gratitude to TMS for giving the Materials Characterization Committee the opportunity to publish a stand-alone volume. The editors also thank the publisher, Wiley, who produced this wonderful book, and the authors, who are the basis of this scientific work. Finally the editors express their appreciation for the past chairs and members of the Materials Characterization

Committee, who are the builders of this great symposium, and they were keen to attract scientists and research groups from around the world to this symposium. These great past chairs and committee members gave young leaders, students, and beginners all care and attention, and make available to them the opportunity to excel, to highlight the skills, win prizes, and to take their place in the volunteer work of the Characterization of Minerals, Metals, and Materials Symposium and the Materials Characterization Committee.

Shadia Jamil Ikhmayies
Bowen Li
John S. Carpenter
Jiann-Yang Hwang
Sergio Neves Monteiro
Jian Li
Donato Firrao
Mingming Zhang
Zhiwei Peng
Juan P. Escobedo-Diaz
Chenguang Bai

EDITORS

Shadia Ikhmayies received a B.Sc. from the Physics Department in the University of Jordan in 1983, a M.Sc. in molecular physics from the same university in 1987 and the Ph.D. in producing and characterizing CdS/CdTe thin film solar cells from the same university in 2002. She worked in the Applied Science University from 2004 to 2009 as an assistant professor, and now works in Al Isra University in Jordan as an associate professor. Her research is focused on producing and characterizing semiconductor thin films such as SnO_2:F, ZnO, CdS, CdTe, $CuInS_2$, thin film bilayers such as SnO_2:F/CdS:In, and thin film CdS/CdTe solar cells. She also works in characterizing quartz in Jordan for the extraction of silicon for solar cells and characterizing different materials by computation. She has published 33 research papers in international scientific journals, three chapters in books, and 55 research papers in conference proceedings. She is the author of two books for Springer—*Silicon for Solar Cell Applications* and *Performance Optimization of CdS/CdTe Solar Cells*—which are in production.

Shadia is a member of the Jordanian Renewable Energy Society (JRES), The Minerals, Metals & Materials Society (TMS), and the World Renewable Energy Network (WREN), where she became a member of the steering committee in 2014. She is a member of the international organizing committee and the international scientific committee in the Third European Conference on Renewable Energy Systems (ECRES2015) which is usually held in Turkey. She was an associate editor for the *Journal of Physics Express* for Simplex Academic Publishers. She is an associate editor for the journal *Peak Journal of Physical and Environmental Science Research* (*PJPESR*) for Peak Journals. She is a member of the editorial board of the *International Journal of Materials and Chemistry* for Scientific & Academic Publishing, the editor in chief of the book *Advances in II-VI Compounds Suitable for Solar Cell Applications* for the Research Signpost, and the editor in chief of the book *Advances in Silicon Solar Cells* for Springer which is in production. She was the technical advisor/subject editor for *JOM* as a representative of the Materials Characterization Committee for the year 2014. She is a guest editor for a special issue in the *Journal of Electronic Materials* "S.I.: ECRES 2015". Shadia is a reviewer for 22 international journals and five international conferences and is now the chair of the Materials Characterization Committee of TMS.

Bowen Li is a Research Associate Professor in the Department of Materials Science and Engineering and Institute of Materials Processing at Michigan Technological University. His research interests include materials characterization, metals extraction, ceramic processing, antimicrobial additives, applied mineralogy, and solid waste reuse. He has over 90 publications, and 12 patents. Bowen Li received a Ph.D. degree in Mineralogy and Petrology from China University of Geosciences Beijing in 1998, and a Ph.D. degree in Materials Science and Engineering from Michigan Technological University in 2008. He has been an active member in TMS, SME, and China Ceramic Society. At TMS, he served as a member in Materials Characterization Committee, Powder Materials Committee, Biomaterials Committee, EPD Award Committee, and *JOM* Subject Advisor, as well as symposium co-organizer and session chair.

John S. Carpenter is a technical staff member in the Materials Science and Technology Division at the Los Alamos National Laboratory. Dr. Carpenter received his Ph.D. in Materials Science and Engineering from The Ohio State University in 2010 after performing his undergraduate studies at Virginia Tech.

His research interests include the characterization, processing, and mechanical testing of metallic nanocomposites fabricated via severe plastic deformation as well as additive manufacturing. Currently, his work focuses on understanding the relationship between plastic strain, texture, and the mechanical properties of bimetallic nanocomposites fabricated via accumulative roll bonding and joined using friction stir processing. This research involves the use of several characterization techniques including neutron scattering, x-ray synchrotron, PED, TEM, EBSD, and SEM. Mechanical testing for this work includes methods such as micropillar compression, microtension, and nanoindentation. He has more than 40 journal publications, one book chapter, and 19 invited technical talks to his credit.

With regard to TMS service, Dr. Carpenter currently serves as the past chair for the Materials Characterization Committee, a programming representative for the Extraction & Processing Division (EPD), and the vice chair for the Advanced Characterization, Testing & Simulation Committee. He is also a participating member of the Mechanical Behavior of Materials and the Nanomechanical Behavior committees. He serves as a Key Reader for *Metallurgical and Materials Transactions A* and has co-edited special sections in *JOM* related to neutron characterization,

coherent x-ray diffraction imaging methods, and modeling in additive manufacturing. He is the 2012 recipient of the Young Leader Professional Development Award for the EPD of TMS. Dr. Carpenter was also awarded an honorable mention for the 2012 Los Alamos National Laboratory Postdoctoral Distinguished Performance Award.

Jiann-Yang (Jim) Hwang is a professor in the Department of Materials Science and Engineering at Michigan Technological University. Wuhan Iron and Steel Group Company, a Fortune Global 500 company, has recruited him as its Chief Energy and Environment Advisor. He has been the Editor-in-Chief of the *Journal of Minerals and Materials Characterization and Engineering* since 2002. Dr. Hwang has started several enterprises in areas including water desalination and treatment equipment, microwave steel production, chemicals, flyash processing, antimicrobial materials, and plating wastes treatment. Several universities have honored him as a Guest Professor, including the Central South University, University of Science and Technology Beijing, Chongqing University, Kunming University of Science and Technology, etc.

Dr. Hwang received his B.S. degree from National Cheng Kung University 1974, M.S. in 1980 and Ph.D. in 1982, both from Purdue University. He joined Michigan Technological University in 1984 and has served as its director of the Institute of Materials Processing from 1992 to 2011. He has been a TMS member since 1985. His research interests include the characterization and processing of materials and their applications. He has been actively involved in the areas of separation technologies, pyrometallurgy, microwaves, hydrogen storages, ceramics, recycling, water treatment, environmental protection, biomaterials, and energy and fuels. He has more than 20 patents and has published more than 200 papers. He has chaired the Materials Characterization Committee and the Pyrometallurgy Committee in TMS and has organized several symposia.

Sergio Neves Monteiro received his Metallurgical Engineer diploma (1966) at the Federal University of Rio de Janeiro (UFRJ) an M.Sc. (1967) and Ph.D. (1972) from the University of Florida. He was named a full professor at UFRJ and head of department (1978), coordinator of the Post-Graduation Program in Engineering (1982) and Under-Rector for Research (1983). He became the Under-Secretary of Science for the State of Rio de Janeiro (1985) and Under-Secretary of Higher Education for the Federal Government (1989). He retired from UFRJ (1993), and joined the State University of North Rio de Janeiro. He went on to become a professor at the Military Institute of

Engineering, Rio de Janeiro (2012). He has published over 1200 articles in journals and proceedings; has been honored with awards including the ASM Fellowship; and is a top researcher of the Brazilian Council for Scientific and Technological Development and Top Scientist of State of Rio de Janeiro. He has been President of the Superior Council of the State of Rio de Janeiro Research Foundation (2012) and is currently Vice-President of the Brazilian Association of Metallurgy, Materials and Mining (ABM). Dr. Neves Monteiro is also a member of editorial board of five international journals, and editor of the *Journal of Materials Research and Technology*.

Jian Li is a senior research scientist at CanmetMATERIALS Natural Resources Canada. He obtained his B.Sc. in Mechanical Engineering from Beijing Polytechnique University, a M.Sc. in Metallurgical Engineering from Technical University of Nova Scotia (TUNS), and his Ph.D in Materials and Metallurgical Engineering from Queen's University, Kingston, Ontario. He has broad experience in materials processing and characterization including alloys deformation, recrystallization, and micro-texture development. Dr. Li has extensive experience in applying focused ion beam (FIB) microscope techniques in materials science. He is also an expert in various aspects of SEM-EDS and EPMA techniques. Dr. Li holds a patent, authored three book chapters and published more than 100 papers in scientific journals and conference proceedings.

Donato Firrao earned his Laurea in Chemical Engineering at the Politecnico di Torino, Turin, Italy, in 1968 and his M.Sc. in Metallurgical Engineering at The Ohio State University, Columbus, Ohio, USA, in 1970, on a Fulbright scholarship. Assistant Professor of Ferrous Extractive Metallurgy since 1968 and Lecturer of Chemistry at the Politecnico di Torino since 1971, Associate Professor of Technology of Metallic Materials there since 1983, he became Full Professor in the same subject – all at the same university in 1986. He was also a visiting fellow at the OSU MSE Dept. in 1978–1979. He was named Distinguished Alumnus of the OSU in 2003. He is the author of more than 225 papers primarily in the fields of physical and metallurgy and surface heat treatments; a member of AIM, ASTM, ESIS, TMS-AIME and of the Turin's Academy of Sciences; and a Fellow of ASM International. He is a Founding Partner of the Italian Fracture Group (IGF); its Secretary since its establishment in 1982; and was the Group's President between 1988 and 1994. He also served as Co-Chairman of the ESIS Technical Committee I (Elasto-Plastic Fracture Mechanics) from 1987 to 1996. He has been President of the Federation of

European Materials Societies (2000–2001), and since 1994 has been the President of the Board of Trustees of the Collegio Universitario di Torino (a private non profit university student housing Foundation) as well as being the Dean of the 1st College of Engineering at the Politecnico di Torino from 2005 to 2012. An expert in "failure analysis," he has acted as technical advisor to the judge in national and international relevant trials (such as, for instance, on the Ustica aircraft crash, on the Mattei affair, on the Sgrena/Calipari case, etc.).

Mingming Zhang is currently a senior research engineer at ArcelorMittal Global R&D in East Chicago, Indiana. His main responsibilities include raw material characterization and process efficiency improvement in mineral processing and ironmaking areas. He also leads a technical relationship and research consortium with university and independent laboratory members and manages a pilot pot-grate sintering test facility at ArcelorMittal Global R&D, East Chicago. Dr. Zhang has over 15 years of research experience in the field of mineral processing, metallurgical and materials engineering. He obtained his Ph.D. degree in Metallurgical Engineering from The University of Alabama and his Masters degree in mineral processing from General Research Institute for Non-ferrous Metals in China. Prior to joining ArcelorMittal, he worked with Nucor Steel, Tuscaloosa, Alabama where he was a metallurgical engineer leading the development of computer model for simulating slab solidification and secondary cooling process.

He has conducted a number of research projects sponsored by federal and private funding involving mineral beneficiation, thermodynamics and kinetics of metallurgical reactions, electrochemical processing of light metals, energy efficient and environmental cleaner technologies. He has published over 30 peer-reviewed research papers and he is the recipient of several U.S. and Chinese patents. Dr. Zhang also serves as editor and key reviewer for a number of prestigious journals. These include *Metallurgical and Materials Transactions B, Journal of Phase Equilibria and Diffusion, Mineral Processing and Extractive Metallurgy*, and *ASME Journal of Thermal Science and Engineering Applications*. Dr. Zhang has made more than 20 research presentations at national and international conferences including more than 10 keynote presentations. He is the recipient of 2015 TMS Young Leader Professional Development Award. He has been invited by a number of international professional associations to serve as conference symposium organizer and technical committee member. These associations include the Association for Iron & Steel Technology (AIST), The Minerals, Metals & Materials Society (TMS), and the Society for Mining, Metallurgy & Exploration (SME).

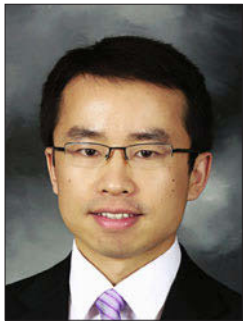

Zhiwei Peng is an Associate Professor in the School of Minerals Processing and Bioengineering at Central South University (China) and an Adjunct Assistant Professor in the Department of Materials Science and Engineering at Michigan Technological University. He received his B.E. and M.S. degrees from Central South University in 2005 and 2008, respectively, and his Ph.D. degree in Materials Science and Engineering from Michigan Technological University in 2012. His research interests include heat transfer in microwave heating, dielectric characterization of materials, non-thermal microwave effects, extractive metallurgy, computational electromagnetics, microwave absorbing materials, and biomaterials.

He has published over 50 papers, including 36 peer-reviewed articles in multiple journals such as *International Materials Reviews*, *Metallurgical and Materials Transactions A*, *JOM*, *Journal of Power Sources, Energy & Fuels*, *IEEE Transactions on Magnetics*, *IEEE Transactions on Instrumentation and Measurement*, *Ceramics International, ISIJ International, Applied Physics Express*, and *Annals of Medicine*. He has served as a key reviewer for a number of journals and been on the editorial board of the *Journal of Minerals and Materials Characterization and Engineering* since 2012. He received a TMS Travel Grant Award for the 141st TMS Annual Meeting & Exhibition, the Doctoral Finishing Fellowship and Dean's Award for Outstanding Scholarship of Michigan Technological University in 2012, and the Bhakta Rath Research Award of Michigan Technological University in 2013.

Dr. Peng is an active member of The Minerals, Metals & Materials Society (TMS). He co-organized four TMS symposia (Characterization of Minerals, Metals and Materials in 2013, 2014, 2015, and 2016) and co-chaired ten TMS symposia sessions since 2012. He is a member of the Pyrometallurgy and Materials Characterization committees, a *JOM* advisor for the Pyrometallurgy Committee, and a winner of the TMS EPD Young Leader Professional Development Award in 2014.

Juan Pablo Escobedo-Diaz is currently a Lecturer in the School of Engineering and Information Technology at UNSW Canberra at the Australian Defence Force Academy. He has been a TMS member since 2011 when he joined as a postdoctoral associate. To date he has co-organized 5 symposia at TMS meetings and in 2014 was a recipient of a Young Leader Award by TMS Structural Division.

His research interests center on the dynamic deformation of materials under extreme conditions, in particular high pressure and strain-rate. His efforts have been primarily focused on the use of several characterisation tools (OM, SEM, EBSD, TEM, x-Ray tomography, neutron diffraction, etc.) to provide a comprehensive explanation of dynamic fracture mechanisms.

Chenguang Bai has mainly engaged in ferrous metallurgy since he graduated from Chongqing University in 1982. From October 1995 to January 1997 he studied at the University of Toronto as a visiting scholar. During the past 33 years of his academic career, Professor Bai has trained 15 Ph.D. students and about 25 Ms.D. students, and published nearly 200 academic articles in international or domestic magazines. He has also received five fundings from NSFC. In 2011, the project 'Study and Application of Iron Ore Evaluation System in Ironmaking Process', finished by his team, was awarded the first grade prize of science and technology by the Ministry of Education, China. Prof. Bai was named as a 'National Outstanding Scientific and Technological Workers' in 2014, and was approved to receive the State Council special allowance in 2015.

SESSION CHAIRS

Non-Ferrous
Arnab Baksi
Evgeniya Skripnyak

Method Development
Andrew David Brown
Carl M. Cady

Minerals
Bowen Li
Zhiwei Peng

Processing and Corrosion
Jian Li
Prathmesh Joshi

Ferrous
Donato Firrao
Mingming Zhang

Clays & Ceramics
Jiann-Yang Hwang
Maria das Graças Silva-Valenzuela

Composites
Juan P. Escobedo-Diaz
Jeongguk Kim

Extraction
Li Qian
Mingming Zhang

Soft Materials
Sergio Monteiro
Zhiwei Peng

Electronic, Magnetic, Environmental, and Advanced Materials
Shadia Jamil Ikhmayies
Eren Yunus Kalay

Welding and Solidification
Yuanbo Zhang
Ece Canan Koşmaz

Characterization of Minerals, Metals, and Materials 2016

Non-Ferrous

Session Chairs:
Arnab Baksi
Evgeniya Skripnyak

Characterization of Minerals, Metals, and Materials 2016
Edited by: Shadia Jamil Ikhmayies, Bowen Li, John S. Carpenter, Jiann-Yang Hwang, Sergio Neves Monteiro, Jian Li, Donato Firrao, Mingming Zhang, Zhiwei Peng, Juan P. Escobedo-Diaz, and Chenguang Bai
TMS (The Minerals, Metals & Materials Society), 2016

EFFECT OF MICROSTRUCTURAL ANISOTROPY ON THE DYNAMIC MECHANICAL BEHAVIOUR OF ROLLED Ti-6Al-4V

A.C.H. Lock[1], A.D. Brown[1], R.A. Blessington[1], G. Appleby-Thomas[2], Md.Z. Quadir[3], P.J. Hazell[1], J.P. Escobedo[1]

[1]School of Engineering and Information Technology, UNSW Australia at the Australian Defence Force Academy, Canberra, ACT, 2600, Australia
[2]Centre for Defence Engineering, Cranfield University, Defence Academy of the United Kingdom, Shrivenham, SN6 8LA, UK

Keywords: Titanium, Microstructure, Compression, Tension

Abstract

The effect of microstructural anisotropy on the mechanical behavior of a hot rolled Ti-6Al-4V alloy has been investigated. Quasi-static and dynamic experiments in compression and tension were conducted on specimens with their deformation axis aligned along the rolling (RD), transverse (TD), and through thickness (TT) directions. Digital image correlation (DIC) was utilized to observe in-situ the development of deformation fields. Optical and electron backscatter diffraction (EBSD) microscopy were conducted on pristine and deformed specimens to examine the microstructural evolution for each loading profile. Initial characterization results show that the plate possesses a preferred orientation of the c-axis along the TD direction and about 40° from the TT. This resulted in the TD direction showing a tensile strength ~12% greater than RD and TT for all loading profiles. Post mortem characterization confirms these results as they reveal the presence of adiabatic shear bands with an accompanying localized re-orientation of the c-axes by ~90°, indicative of substantial tensile twinning.

Introduction

Ti-6Al-4V is a highly desirable material in the aerospace, automotive, and medical industries because of its good corrosion resistance, high strength-to-density ratio, environmental resistance, and fracture-related properties up to 600 ^{o}C [1]. Compared with the large body of literature available on the compression behavior at high strain rates [2-11], there are fewer studies that have investigated post-mortem EBSD imaging in dynamic compression [12], and tensile mechanical properties at high strain rates [13].

Cogue et al. [14] and Prakash et al. [15] explored the importance of twinning in static and dynamic compression of Ti-6Al-4V with an equiaxed microstructure. They found that when a cylinder is compressed along its axis, a tensile strain is induced perpendicularly to it, and grains having their c-axis close to perpendicular with the compression direction accommodate this deformation, at least partially by introducing a tensile twin. Galan et al. [16] analysed the dynamic and static tensile behavior of Ti-6Al-4V at different temperatures, but did not conduct any post-mortem microstructural analysis.

Initial Material Characterization

Figure 1 shows the EBSD micrographs of the as-received Ti-6Al-4V plate. The orientation map shows the crystallographic orientation with the normal aligned along TD and the normal of the texture plot aligned along TD, and the other two axes are as indicated.

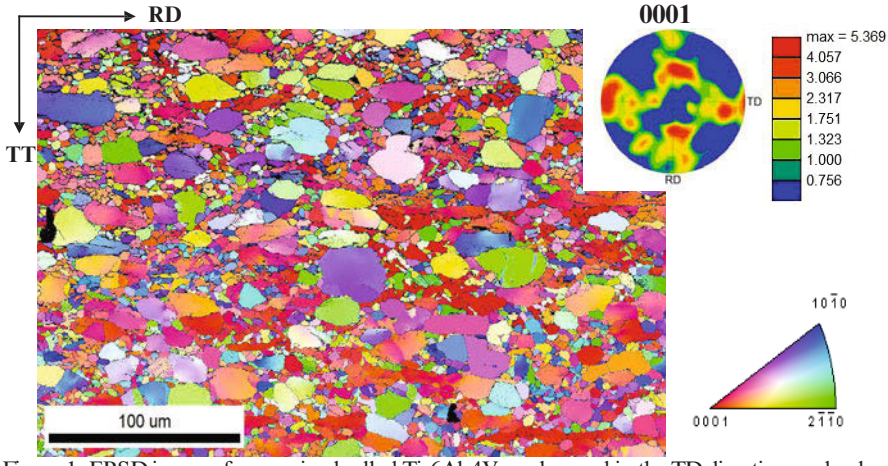

Figure 1. EBSD image of as-received rolled Ti-6Al-4V as observed in the TD direction, and pole figure.

A bimodal grain size distribution is readily observed with average grain sizes of 5 and 25 microns. For the case of the smaller grains, a strong split 0001 texture is observed along the TD direction and at 40° away from TT, whereas the larger grains show a fairly random crystallographic orientation. As observed by Cogue et al. [1], the hexagonal unit cells in dynamic compression tests will be expected to flip the 0001 unit cells approximately 90 degrees from the loading axis. This phenomenon occurs because the critical resolve shear stresses are so high to be accommodated by the slip systems and so twinning occurs.

Figure 2 shows the scanning electron microscopy image and energy dispersive spectroscopy phase maps of the same region as in Fig. 1. The high volume fraction of α phase grains indicate that the material was slowly cooled from the beta transus temperature so that the β phase transformed by nucleation and growth to a globular/lenticular colony microstructure comprised of α phase within a β matrix. A mixture of globular and lenticular α phase gives an indication of the working and heat treatment the material underwent, that being α/β working followed by a duplex anneal, just below the beta transus temperature to form some equiaxed primary alpha (α_p) grains and significantly below the beta transus temperature to form the separately nucleated lenticular secondary-alpha (α_s) between the α_p equiaxed regions. The heterogeneous shaped α phase also indicate mechanical working in the α/β phase thermal process. This morphology is typical of gas turbine applications where both creep and low cycle fatigue failure are required, and lenticular and globular α phase, respectively improve these mechanical properties [17].

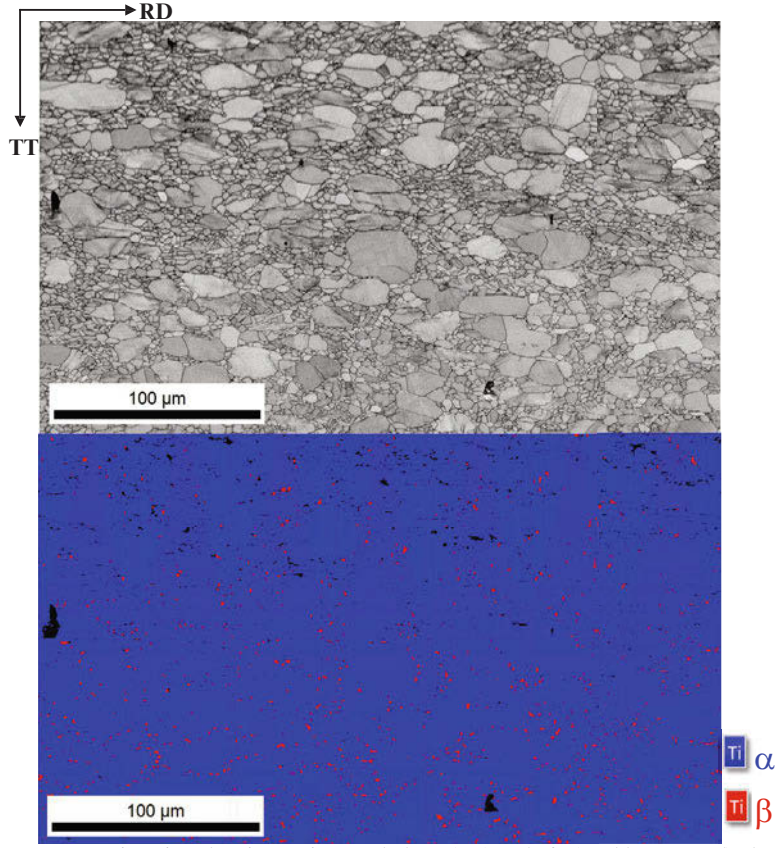

Figure 2. EBSD imaging showing grain morphology (top) and α/β (α – blue, β – red) phase (bottom).

Experimental Methods

Samples were machined with their deformation axes along the RD, TD, and TT directions of the plate. For compression experiments, specimens were machined with dimensions of 7.5 mm in diameter and height in all directions, whereas tensile samples with 10 x 6 x 3 mm gauge area were machined in the RD and TD directions.

In preparation for DIC measurements, all tensile specimens were given a white spray paint background with a black speckle pattern spray painted on top. Quasi-static tensile tests were conducted on the Shimadzu Autograph AGS-X 50 kN universal testing machine. Dynamic compression tests were conducted on a Split Hopkinson Pressure Bar (SHPB) at the following conditions: room temperature, maraging steel bar (12.7 mm diameter, 152.4 mm striker bar length for low strain rates, 76.2 mm striker bar length for high strain rates), 152.4 mm striker bar speed at 50 m/s, with momentum trap.

Results and Discussions

Figure 3 shows results from quasi-static tensile tests. The effect of anisotropy is clearly observed. Specimens along the RD direction exhibit an average ultimate tensile strength (UTS) of 1020 MPa, whereas in the TD the average UTS was 1150 MPa. While the UTS differed by 12% in the rolling and transverse directions, the strain at fracture was similar. The slightly stronger behaviour in the TD correlates with the strong basal texture along TD, as shown in Figure 1. The hexagonal unit cell has the lowest critical resolve shear stress (CRSS) on prismatic slip planes, and hence stronger behaviour can be expected in loading directions parallel to the c-axis.

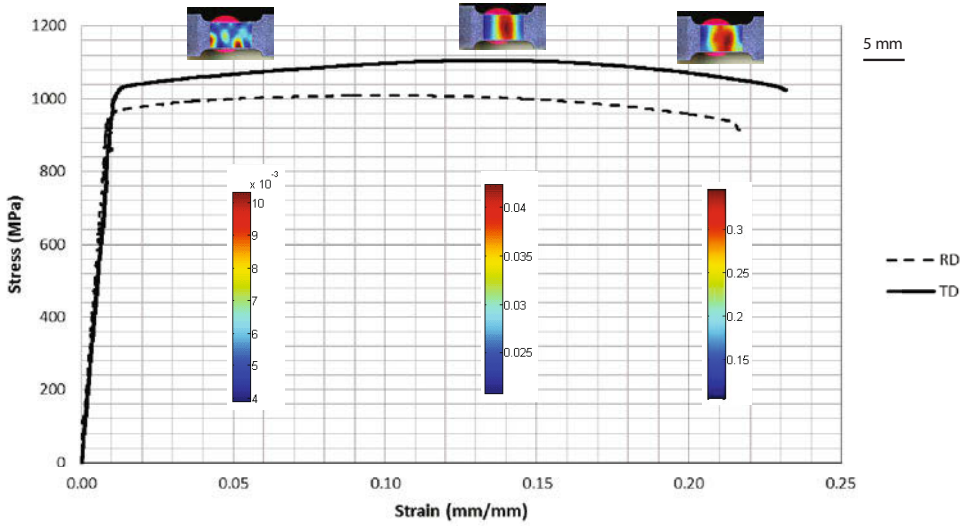

Figure 3. Tensile, quasi-static, stress-strain results of RD and TD directions. DIC images show the evolution of representative strain fields during testing.

Dynamic compression tests were conducted at room temperature utilizing a SHPB. Figure 4 shows the results at strain rates of approximately 1100 and 1700 s^{-1} for all directions. Similar to the quasi-static tensile testing, the dynamic compression tests indicate that the TD (yield strength (YS) = 1700 MPa) is stronger than both the RD and TT directions (YS = 1500 MPa). While the compression specimens plastically deformed to a strain between 0.04 and 0.08, they did not fracture.

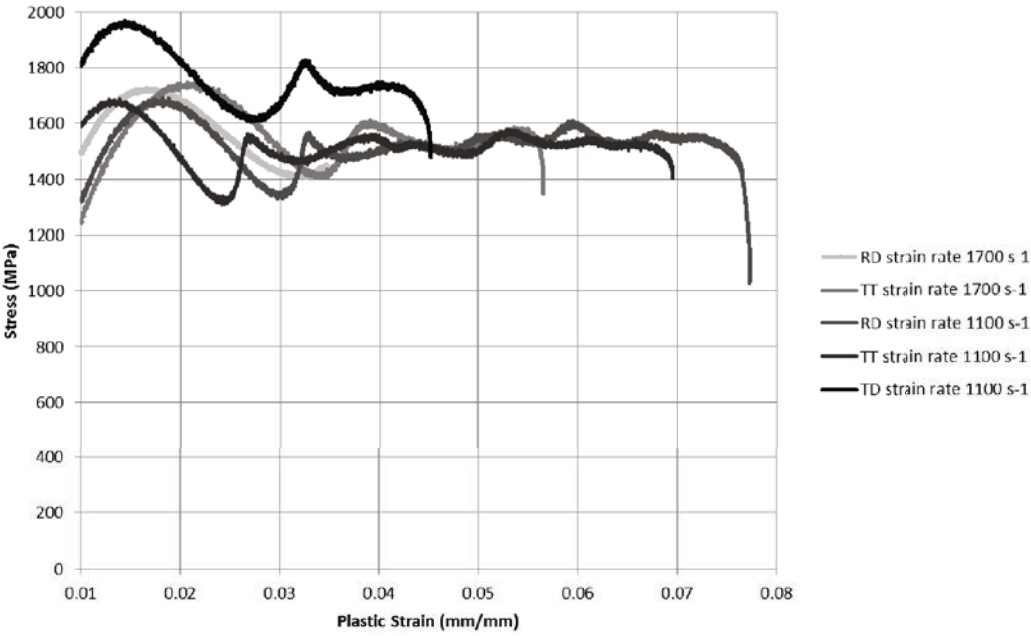

Figure 4. Dynamic compression stress-plastic strain curves at strain rates 1100 and 1700 s^{-1}.

Comparing the responses of the RD and TT samples at different dynamic strain rates in Figure 4, little effect is observed on the materials' stress-strain behaviour. There is however, a significant difference in strength in the TD direction. The as-received EBSD imaging in Figure 1 indicated c-axis alignment in the TD direction. Therefore, the increase in strength in the TD direction can be correlated to c-axis alignment in that loading direction. The data presented in Figure 4 has not undergone post processing and is obtained directly from the voltage-time history of the strain gauges on the incident and transmission bars.

The as received EBSD image in Figure 1 indicates that there is a preference for the c-axis in the hexagonal unit cells to align along the TD direction. The EBSD image of a compressed TD sample in Figure 5 shows that the original c-axis alignment in the TD direction has flipped 90 degrees towards 10-10. This is explained by the compression loading inducing a tensile load perpendicular to the compression loading axis. The stress is so high for the slip systems to accommodate deformation such that the c-axes flip in the direction of the tensile load and accommodates the stress via twinning and shear banding.

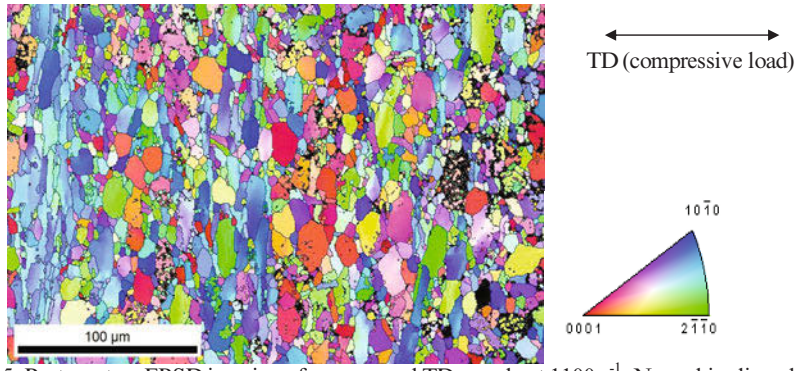

Figure 5. Post mortem EBSD imaging of compressed TD sample at 1100 s^{-1}. Normal is aligned along TD direction.

Figure 6 shows the results of a specimen compressed along the TT direction. A remarkable microstructural feature in this case is the of shear bands through the smaller grains whereas it appears that the larger grains hinder the formation of shear bands.

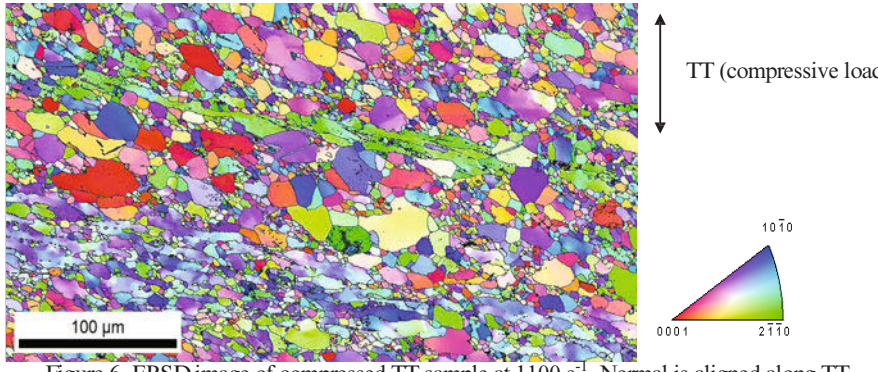

Figure 6. EBSD image of compressed TT sample at 1100 s^{-1}. Normal is aligned along TT direction.

Conclusions

Initial quasi-static tensile and dynamic compression tests indicate that the microstructure and texture of Ti-6Al-4V anisotropically affect its mechanical response. As-received EBSD imaging revealed a preferred c-axis alignment in the TD direction. Subsequent tensile and compression testing showed that the TD direction was stronger in both loading cases explained by the strong basal texture aligned along this direction. Post mortem EBSD analyses on compressed specimens show a re-orientation of grains towards 10-10 to accommodate tensile strains. Post mortem EBSD analysis on compressed TT samples presented the role α_p grains had in hindering the initial formation of adiabatic shear bands.

Further testing and analysis is currently underway including EBSD imaging and dynamic tensile experiments to further characterise the effect of anisotropy of this alloy on its mechanical behavior.

Acknowledgements

The authors would like to thank Cranfield University for providing the Ti-6Al-4V plate. Thomas d'Ews Thomson is thanked for assisting considerably in the manufacturing of specimens in a timely manner. Finally, David Sharp is also thanked for assisting with sample metallographic preparation.

References

1. F. Froes, Titanium: alloying, Encyclopedia of Materials: Science and Technology, (Elsevier Science Ltd., 2001), 9361-9364.
2. W. Lee and C. Lin, "High temperature deformation behavior of Ti6Al4V alloy evaluated by high strain-rate compression tests," *Journal of Materials Processing Technology,* (1998), pp. 127-136.
3. J. Millett, G. Whiteman, N. Bourne and G. Gray, "Role of anisotropy in response of Ti-6Al4V to shock loading," *Journal of Applied Physics,* (2008)
4. E. Wielewski, G. Appleby-Thomas, P. Hazell, and A. Hameed, "Micro-mechanics of spall initiation and propagation in Ti-6Al-4V during shock loading," *Materials Science and Engineering,* (2013), pp. 331-339.
5. J. Zhang, C. Tan, Y. Ren, X. Yu, H. Ma and H. Cai, "Adiabatic shear fracture in Ti-6Al-4V alloy," *Transactions of Nonferrous Metals Society of China,* (2011), pp. 2396-5401.
6. S. Osovski, D. Rittel, P. Landau and A. Venkert, "Microstructural effects on adiabatic shear band formation," *Scripta Materialia,* (2012), pp. 9-12.
7. D. Rittel, Z.G. Wang, "Thermo-mechanical aspects of adiabatic shear failure of AM50 and Ti6Al4V alloys," *Mechanics of Materials,* (2008), pp. 629-635.
8. S. Osovski, D. Rittel, A. Venkert, "The respective influence of microstructural and thermal softening on adiabatic shear localization," *Mechanics of Materials,* (2013), pp. 11-22.
9. A.S. Khan, Y.S. Suh, R. Kazmi, "Quasi-static and dynamic loading responses and constitutive modeling of titanium alloys," *International Journal of Plasticity,* (2004), pp. 2233-2248.
10. N. Biswas, J.L. Ding, V.K. Balla, D.P. Field and A. Bandyopadhyay, "Deformation and fracture behavior of laser processed dense and porous Ti6Al4V alloy under static and dynamic loading," *Materials Science and Engineering A,* (2012), pp. 213-221.
11. S. Nemat-Nasser, W. Guo, V.F. Nesterenko, S.S. Indrakanti, Y. Gu, "Dynamic response of conventional and hot isostatically pressed Ti-6Al-4V alloys: experiments and modeling," *Mechanics of Materials,* (2001), pp. 425-439.
12. E. Wielewski, C.R. Siviour and N. Petrinic, "On the correlation between macrozones and twinning in Ti-6Al-4V at very high strain rates," *Scripta Materialia,* (2012), pp. 229-232.
13. J. Peirs, P. Verleysen, J. Degrieck, "Experimental study of the influence of strain rate on fracture of Ti6Al4V," *Procedia Engineering*, (2011), pp. 2336-2341.
14. F. Cogue, W. Tirry, L. Rabet, D. Schryvers and P. Van Houtte, "Importance of twinning in static and dynamic compression of Ti-6Al-4V with an equiaxed microstructure," *Materials Science and Engineering,* (2012), pp. 1-10.
15. D. Leo Prakash, R. Ding, R. Moat, I. Jones, P. Withers, J. Quinta da Fonseca and M. Preuss, "Deformation twinning in Ti-6Al-4V during low strain rate deformation to moderate strains at room temperature," *Materials Science and Engineering A,* no. 527, (2010), pp. 5734-5744.
16. J. Galan, P. Verleysen and J. Degrieck, "Thermal effects during tensile deformation of Ti-6Al-4V at different strain rates," *Strain,* no. 49, (2013), pp. 354-365.
17. A.A. Salem et al., eds., Electron Backscatter Diffraction in Materials Science, (New York, NY: Springer Science+Business Media, 2009), 317.

Characterization of Minerals, Metals, and Materials 2016
Edited by: Shadia Jamil Ikhmayies, Bowen Li, John S. Carpenter, Jiann-Yang Hwang, Sergio Neves Monteiro, Jian Li, Donato Firrao, Mingming Zhang, Zhiwei Peng, Juan P. Escobedo-Diaz, and Chenguang Bai
TMS (The Minerals, Metals & Materials Society), 2016

MICROSTRUCTURE EVOLUTION DURING THERMAL AGING OF INCONEL 718

R. S. Devarapalli[1], E. Marin[2], J. Cormier[3], C. Le Gall[2] and J.-M. Franchet[4], and M. Jouiad[1*]
[1] Department of Mechanical and Materials Engineering, Masdar Institute of Science and Technology, PO Box 54224, Abu Dhabi, United Arab Emirates
[2] Snecma-Safran Group, Technical Department, 171 boulevard de Valmy - BP 31, 92702 Colombes Cedex, France
[3] Institut Pprime, CNRS – ENSMA – Université de Poitiers, UPR CNRS 3346, Department of Physics and Mechanics of Materials, ENSMA – Téléport 2, 1 avenue Clément Ader, BP 40109, 86961 Futuroscope Chasseneuil Cedex, France
[4] SAFRAN Center of R&T; Magny-les-Hameaux, 78114, France

Keywords: Inconel 718 Alloy, Thermal Treatment, HRTEM of 718 Alloy, Ledge Mechanism

Abstract

The Inconel 718 superalloy was subjected to isothermal and cyclic thermal annealing at 750^0C to assess its expected use at higher temperatures. Microstructure evaluation during isothermal annealing and thermal cycling was investigated by different imaging techniques. According to High Resolution Scanning and Transmission Electron Microscopy (HRSEM & HRTEM) results, all the annealed samples showed the coarsening of γ', γ" and δ precipitates, however, the total volume fraction of these precipitates remains the same for all heat treatment conditions. Using backscattered electrons images the size of γ', γ" and δ phases were measured and correlated with annealing time. The most striking result is the impact of thermal cycling which accelerates the growth inside the grains of γ" phase and at the vicinity of the grain-boundaries leading to its transformation to δ phase, which induces a fast decrease of the mechanical properties of thermally cycled specimens compared to isothermally aged ones. A close investigation showed that the γ" phase grows by ledge mechanism. Moreover, Electron backscattered diffraction analysis (EBSD) revealed no significant grain size change during all annealed times.

Introduction

Alloy 718 occupied an important place in components manufacturing for aerospace engines and high temperature applications. Indeed, Inconel 718 is widely used in aeronautic industries due to its ability to retain strength up to 650˚C for prolonged periods [1]. For instance, it is extensively used in turbine disks applications [2] due to its combination of excellent static and cyclic mechanical properties at high temperatures, good resistance to oxidation and corrosion. The low processing cost in comparison to several other cast and wrought and powder metallurgy (PM) processed superalloys made this alloy more successful [3, 4]. This alloy obtains its remarkable properties from two different hardening precipitates γ' and γ" [5]. These strengthening phases are coherent with the γ matrix and have respectively, an ordered faces centered cubic $L1_2$ and an order body-centered-tetragonal DO_{22} crystal structures [6, 7]**.** Many instances 718 alloy is directly used for engineering applications without prior solution heat treatment [4, 8, 9] resulting of increased strength, since improved static and cyclic properties are obtained by keeping a small

grain size and a residual hardening from the forging steps [9, 10]. The 718 superalloy is usually chosen for applications where maximum continuous operating temperatures are between 650°C-675°C [11]. One of the key question linked to the development of the new generation of civil aero-engines, where higher operating temperature are expected is to understand the impact of short peak temperature events in excess of 650°C-700°C on the durability of DA718 alloy, these peak temperatures are encountered during takeoff of aircrafts. More generally, the mechanical properties degradation upon thermal aging in 700°C – 800°C temperatures range has not been enough studied to assess the durability of this new class of engines [12] at higher temperature, one additional issue is to evaluate the impact of non-isothermal cycling on the microstructure evolution and on the mechanical properties degradation upon aging.

In this work, we report on DA 718 after different annealing conditions at 750^0C to understand the effect of aging temperature on different precipitates formation and growth and assess these evolutions on its mechanical behavior, namely micro-hardness and tensile properties

Experimental Procedure

The Specimen considered here is the DA 718 alloy with nominal composition is given in Table I. All the samples used in this study were supplied by SAFRAN-Snecma Genevilliers, which had received a DA heat treatment and standard precipitation heat treatment.

Table I. Nominal composition of Alloy 718

Element	Ni	Fe	Mo	Mn, Si	Cr	C	Nb	Ti	Al	Ta	Cu
Wt% min	Base	15.0	2.8	-	17.0	0.015	5.0	0.75	0.3	-	-
Wt% max	Base	21.0	3.3	0.35	21.0	0.040	5.5	1.15	0.7	0.1	0.3

Three different samples were considered for this investigation, namely DA718 annealed at 750˚C for 100 hours, DA718 annealed at 750˚C for 300 hours and DA718 thermally cycled at 750˚C for 100 hours as cumulative duration. Field Emission Gun Scanning Electron Microscope (FEGSEM) attached with Energy Dispersive X-ray microanalysis (EDX) was used for surface imaging and chemical composition analysis. Back-scattered electrons images (BSE) were used combined with high contrast detector (VcD, FEI™) to highlight different phases. Samples were first mirror polished then prepared using a electrolytic etching of 10% phosphoric acid in methanol. Specimens used for TEM analysis were prepared by cutting 3 mm disks from the bulk material using electro-discharge machine. These discs were mechanically thinned down to less than 100µm by using different grades of abrasive papers, the final electro polishing was performed by twin-jet electro polishing machine (Tenupol STRUERS™), using a solution of 10 vol. % perchloric acid in methanol at 5˚C and 20.5 V. FEI Tecnai operating at 200 kV and an aberration-corrected FEI Titan operating at 300 KV microscopes were used to examine the specimen foils. The same samples mentioned above were used for EBSD analyses. The EBSD analyses were carried out using FIB/SEM (Quanta 3D, FEI™). Mechanical tests are composed of hardness tests at room temperature and tensile tests at 650^0C after thermal annealing Brinell hardness measurements HRB 2.5/187.5 (i.e. indentation at 1.8 kN load and 2.5 mm in diameter of the indenter tip) were done for each sample, after mechanical polishing up to a mirror finish.

Five indentations at least were done on each sample. Tensile tests were performed using tensile specimens having a 13 mm gage length and a 4.3 mm gage diameter. Final sample's machining was done after thermal annealing has been done. The gage zone was polished up to a mirror finish, with the final polishing aligned with the stress axis. Tensile tests were performed at 650 +/- 1°C, using an electro-mechanic machine. These tensile tests were performed at 8.3 10^{-4} s^{-1} strain rate. Two to four tensile tests per aging conditions were performed and the results presented in the following of the article Yield stress (YS) at 0.2% of plastic deformation, Ultimate Tensile Stress (UTS) are averages over all the experiments performed after a given thermal annealing.

Results and Discussion

The samples annealed at different time intervals were observed under the SEM to reveal morphology of secondary phase precipitates and its composition. Figure 1 gives the distribution of large δ secondary phases in solid solution γ matrix at the vicinity of grain boundaries. The δ phase morphology look similar in thermally aged samples for 100 hours and thermally cycled ones with slab like structure (Fig. 1a &1c). However, for prolonged annealing time for instance 300 hours of aging, this δ phase tends to have disc like shape as it can be seen in figure 1(b).

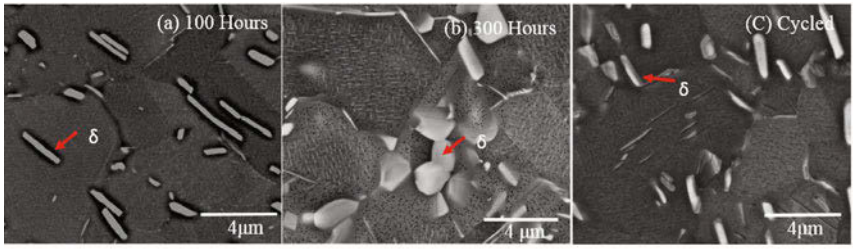

Figure 1. Microstructure of DA718 alloy after 3 different annealing conditions: a) 750˚C for 100 hours, b) 750˚C for 300 hours and c) Cycled at 750˚C for cumulative time of 100 hours.

Figure 2(a-c) shows the elemental analysis for the three different aged materials, namely isothermally annealed for 100 hours & 300 hours at 750˚C and thermally cycled at 750˚C respectively Fig. 2a, Fig .2b and Fig. 2c. One can clearly notice the change of δ precipitates feature at the vicinity of the grain boundaries. It seems to have discs like structure at 300 hours annealing time where it has slab like structure for 100 hours annealing time. In all cases, Energy Dispersive Spectroscopy (EDS) analysis shows the presence of Nb and small amount of Ti in these particles, which is consistent with the known composition if δ phase. The elemental composition in atomic % is given in Table II.

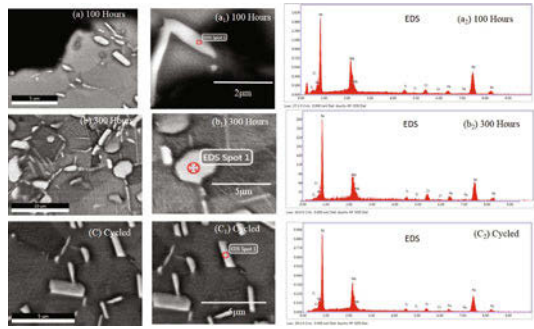

Figure 2. SEM images & the corresponding EDS spectra of δ phase of the considered samples

Table II. Chemical composition determined by EDS analysis.

Sample\Element at. %	Ni	Nb	Cr	Ti	Fe
100H annealed at 750˚C	71.54	14.96	5.1	3.33	5
300H annealed at 750˚C	67.53	12.73	9.23	2.78	7.7
Cycled at 750˚C	69.50	16.68	5.17	3.26	5.39

The Sigma Scan Pro scientific image analysis software developed by SYSTAT, San Jose, California was used to measure the area fraction of different phases present in the DA 718 alloy at different annealed conditions. Figure 3 shows the image-processed micrographs to measure the area fraction of total secondary phase particles from low magnification BSE images. The 100 hours annealed sample and cycled sample exhibit similar phase area fraction at the vicinity of grain boundaries however for the 300 hours annealed sample shows the heterogeneous distribution of δ phase mostly concentrated at the grain boundaries. The measured area fractions of different samples are given Table III. We found 5.52 %, 8.94 % and 7.54 % respectively for aged samples at 100 hours/750˚C, 300 hours/750˚C and cycled at 750˚C. This shows that the area fraction of δ phase is increasing with annealing time or cycling.

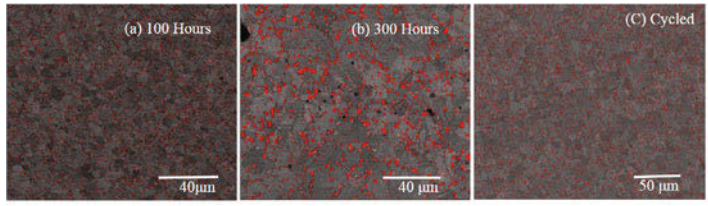

Figure 3. BSE micrographs: 100 hours /750˚C (a), 300 hours/750˚C (b), and cycled at 750˚C (c)

Table III. Area fraction of δ phase

Sample	Area fraction %
100H annealed at 750˚C	5.52
300H annealed at 750˚C	8.94
Cycled at 750˚C	7.54

Figure 4 illustrates high magnification BSE images obtained by high contrast BSE detector (VcD FEI™) along with image-processed micrographs for all three samples. Both γ', γ'' and δ were considered to calculate the total area fraction for both precipitates. The combined area fraction of all phases is given in Table IV. We found 9.11 %, 8.26 % and 8.23 % respectively for aged samples at 100 hours/750˚C, 300 hours/750˚C and cycled at 750˚C. This shows that the total area fraction of these phases remains unchanged with annealing time and conditions, however γ'' phase seems to transform to elongated structure in form of δ phase with increasing annealing time [13] and especially for cycled sample.

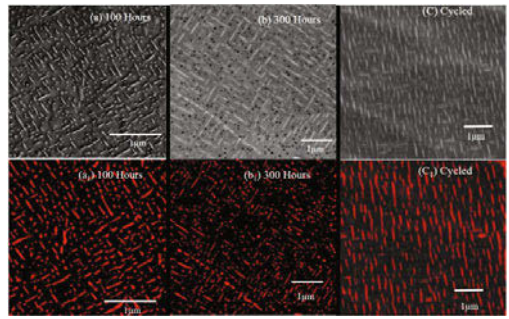

Figure 4. BSE images and image-processed micrographs: 100 hours /750˚C (a&a_1), 300 hours/750˚C (b&b_1), and cycled at 750˚C (c&c_1).

Table IV. Area fraction of γ' and γ''

Sample	Finer phase ($\gamma' + \gamma''$) %
100H annealed at 750˚C	9.11
300H annealed at 750˚C	8.265
Cycled at 750˚C	8.23

All aged samples were analyzed by EBSD (EDAX™ system) to screen the effect of annealing and thermal cycling on grain size and its orientation. The combined Image Quality (IQ) and Inverse Pole Figure (IPF) and grain size distribution are given in figure 5. The sample annealed for 100 hours/750˚C shows uniform grain size with average grain size observed at 4.7 μm^2 with no preferred orientation (see the standard triangle). The sample annealed at 300 hours/750˚C doesn't show any texture but a little increase in grain size from 4.7 μm^2 to 6.18 μm^2. The cycled sample at 750˚C also shows some a little increase in grain size from 4.7 μm^2 to 5.6 μm^2. Overall samples don't show any texture and no significant increase in grain size.

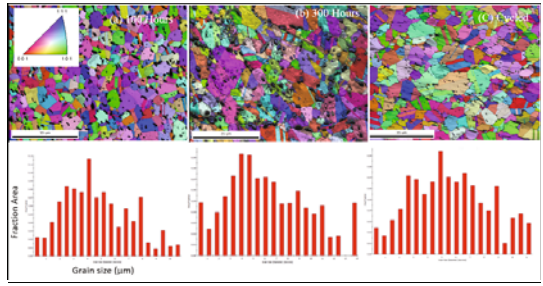

Figure 5. IQ+IPF maps and corresponding gain size distribution of 100 hours /750˚C (a), 300 hours/750˚C (b), and cycled at 750˚C (c).

The evolution of the micro-hardness of the three aged samples is plotted and given in figure 6. It is clear from the graph that up to 100 hours as isothermal annealing time at 750˚C no significant change was noticeable but beyond this time, we started to observe a rapid drop of the micro-hardness up and significant decrease was observed at 300 hours as isothermal annealing time at 750˚C. However, only for a cumulative time of 100 hours during thermal cycling, the micro hardness seems to be lower by factor of 10 %.

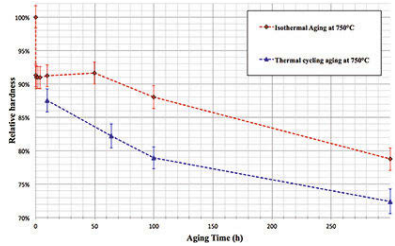

Figure 6. Relative hardness profiles of 100 hours /750˚C, 300 hours/750˚C, and cycled at 750˚C

Table V summarizes the different measured values of yield strength at 0.2 % and the ultimate tensile strength obtained for the three aged samples. It is noticeable from the Table V that the annealing time alters both yield strength and the ultimate strength of 718 alloy, however this degradation is accelerated by the thermal cycling.

Table V. Tensile properties of different aged samples considered.

Sample	YS (MPa)	UTS (MPa)
100H annealed at 750˚C	920	1060
300H annealed at 750˚C	660	898
Cycled at 750˚C	720	940

The degradation of mechanical properties of 718 alloy due to thermal aging is linked to the microstructure evolutions presented above. The most striking result from this study arises when comparing the impact of thermal cycling on the hardness evolutions. It is indeed observed a

faster decrease of the hardness under thermal cycling conditions compared to isothermal annealing at 750°C. Our results show significant degradation of properties in 100 hours (cumulative) cycled sample, but the total area fraction calculations shows major deviation observed in 300 hours annealed sample, this suggests little effect of δ phase growth on mechanical properties but rather the transformation of γ" to δ phase [13]. Figure 7 shows the BSE micrograph from sample cycled at 750^0C for 100 hours. The in-depth microstructural study reveals growth of δ phase and little presence of γ" (see markers). In addition, the same phenomena was observed inside the grains at finer scale but at this time we witness the growth and the transformation of γ" to δ phase. This result is similar to what was observed in different screened zones in cycled sample as seen in figure 4(c_1). Most likely, these transformation of γ" appears to be the reason behind the degradation of the mechanical properties of aged samples which is accelerated with thermal cycling.

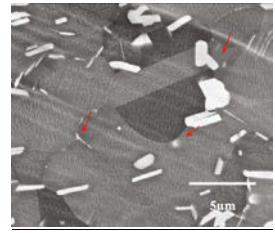

Figure 7. BSE image showing γ" precipitates free zone around δ phase (cycled sample at 750˚C for 100 hours as cumulative time).

In order to examine closely the growth of δ & γ" phases, further investigations were conducted by means of HRTEM. The main objective was to study the interface growth mechanism between γ" & δ phases and the matrix. A typical high-resolution image of thermally cycled specimen is given in figure 8 (a). Using Fast Fourier Transform (FFT), the orientations relationship between the matrix and the γ" phase were generated: areas A & C with [110] zone axis represent the matrix and the area B with [100] zone axis indicates the γ" phase. Both interfaces A/B & B/C reveal the same orientation relationship between γ matrix and the γ" phase $[110]_{\gamma}//[100]_{\gamma''}$.

(a) (b)

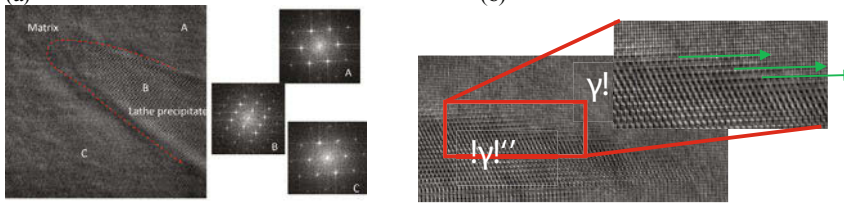

Figure 8. (a) HRTEM image and corresponding FFT patterns for different areas, (b) HRTEM image showing ledge mechanism observed along [110] direction in annealed sample.

Similar study conducted for 300 hours annealed sample suggests the growth of γ" precipitates by ledge mechanism as shown in figure 8(b). Indeed, at the γ & γ'' interface clear atomic steps are visible (green markers). The mechanism involved in thickening of the plate like γ" precipitate is

the motion of ledges across the broad face between γ and γ'' along [110] direction. The atomic attachment to ledges can occur at sites called kinks. The growth of the γ" precipitate is most likely taking place by terrace-ledge-kink mechanism. This is coherent with the fact that the total area fraction of γ', γ'' & δ phases remains the same for all the three samples. The overall growth mechanism, strongly suggest that is occurring according to Lifshitz, Slyozov & Wagner (LSW) theory as reported elsewhere [13], however the γ" and d size distribution may not be explained by sole LSW but rather modified LSW (LSM). This needs to be correlated to the ledge mechanism that occurs only in preferred directions.

Conclusion

The influence of the annealing and thermal cycling on mechanical properties of 718 alloy was investigated. Our findings show that there was a fast decrease in both micro-hardness and tensile properties with thermal and this effect was accelerated with thermal cycling. These mechanical properties degradation were attributed to γ" particles transformation to δ phase. It was also observed that both γ" & δ phases grow by ledge mechanism along [110] direction. This growth is well taken into account by LSW theory however the γ" & δ sizes can't be captured only by LSW theory but rather by modified LSM.

References

1. R. Cozar, and A. Pineau, "Morphology of γ' and γ" precipitates and thermal stability of inconel 718 type alloys," *Metall. Trans., 4* (1973), 47–59.
2. J. Zhao, J. H. Westbrook, and G. Editors, "Ultrahigh- Temperature Materials for Jet Engines," *MRS Bull.*, 2003, 28.
3. D. F. Paulonis, and J. J. Schirra, "Alloy 718 at Pratt & Whitney–Historical Perspective and Future Challenges," *Superalloys*, 2001**,** 13–23.
4. E. A. Loria, "The Status and Prospects of Alloy 718," J. of Metals, 40 (7) (1988), 36–41.
5. L. Renhof, et al., "Analysis of Microstructural Properties of IN 718 After High Speed Forging," *Superalloys 718, 625, 706 and Derivatives, TMS*, 2005, 261–270.
6. S. J. Hong, W. P. Chen, and T. W. A. Wang, "Diffraction study of the γ″ phase in Inconel 718 superalloy," *Metall. Mater. Trans. A,* 32 (2001), 1887–1901.
7. X. S. Xie, J. X. Dong, and M. C. Zhang, "Research and Development of Inconel 718 Type Superalloy," *Materials Science Forum,* 539-543 (2007), 262–269.
8. D. D. Krueger, "The development of direct aged 718 for gas turbine engine disk applications Superalloy 718," *Metallurgy and Applications, TMS*, (1989), 279-296.
9. Y. C. Fayman, "Microstructural characterization and elemental partitioning in a direct-aged superalloy DA 718," *Mater. Sci. Eng.*, 92 (1987), 159–171.
10. T. Matsui, "Dynamic Recrystallization Behavior of Waspaloy during Hot Working," *Mater. Trans.*, 55 (2014), 255–263.
11. S. Mannan, S. Patel, and J. De Barbadillo, "Long term Thermal stability of Inconel alloys 718, 706, 909, & Waspaloy at 593 °C and 704 °C," *www.specialmetals.com*, 2010, 10.
12. C. Slama, and M. Abdellaoui, "Structural characterization of the aged Inconel 718," *J. Alloys Compd.*, 306 (2000), 277–284.
13. Y. F. Han, P. Deb, and M. C. Chaturvedi, "Coarsening behaviour of γ'' & γ' particles in Inconel alloy 718," *Metal Science*, 16 (1982), 555.

Characterization of Minerals, Metals, and Materials 2016
Edited by: Shadia Jamil Ikhmayies, Bowen Li, John S. Carpenter, Jiann-Yang Hwang, Sergio Neves Monteiro, Jian Li, Donato Firrao, Mingming Zhang, Zhiwei Peng, Juan P. Escobedo-Diaz, and Chenguang Bai
TMS (The Minerals, Metals & Materials Society), 2016

Microstructure Characterization of Nickel Alloy 718 with Automated Optical Image Processing

Thomas A. Ivanoff[1], Trevor J. Watt[1], Eric M. Taleff[1]

[1]The University of Texas at Austin, Mechanical Engineering, Austin, TX 78712

Keywords: Superalloy, Nickel, 718, Optical imaging, Microstructure

Abstract

The microstructure of a vacuum arc remelted (VAR) nickel alloy 718 ingot was characterized using macro photography and studied with quantitative image analysis techniques. Microstructure quantification was used to produce information that may aid the determination of how melt parameters influence solidification microstructures. Such information is expected to eventually support new understandings of how solidification defects, such as freckle channels and white spots, form. Two slabs were sectioned from the center of a laboratory-scale alloy 718 VAR ingot. Each slab was ground and etched to reveal dendritic solidification microstructures. Custom automated instrumentation was used to acquire 454 digital images of these slabs at a 1:1 magnification. Images were subsequently stitched and blended to produce two mosaic images, one 562 and the other 579 megapixels in size. Digital image analysis techniques were used to identify primary and secondary dendrite arms. These image analysis techniques and the results they produced are presented.

Introduction

Nickel alloy 718 ingots are commonly produced using multiple casting processes. Initial casting processes, like vacuum induction melting (VIM), often produce ingots with undesirable qualities that are used as feedstock for secondary refining processes. Vacuum arc remelting (VAR) is one such method used to refine ingots produced by VIM. VAR uses a DC current to melt metal from an electrode that then re-solidifies in a water-cooled copper crucible. This process is performed under vacuum to reduce impurity content by removing volatile tramp elements and oxides [1-5]. Although VAR is capable of producing exceptionally clean ingots, it is susceptible to the formation of solidification defects such as freckle channels and white spots. These defects can result from a too shallow or too deep melt pool and are of concern because they reduce strength and low-cycle fatigue life [2]. Refinement and control of microstructure during VAR is essential to the production of a uniform defect-free ingot [6]. Quantitative characterization of microstructure in a VAR ingot, when correlated with processing parameters for that ingot, is expected to provide information that manufacturers can use to improve VAR processing and could provide validation data necessary to the development of improved process models that can predict defect formation [7]. This study uses macrophotography and quantitative digital image analysis techniques to characterize the dendritic solidification structure of an alloy 718 VAR ingot. The specific goal of this study is to identify the size, shape, and orientation of primary dendrite arms. Primary dendrite arm direction can provide a history of the melt pool during solidification, as the primary dendrite arms generally extend along the solidification direction [8].

Experimental Procedure

The material characterized in this study was sectioned from a laboratory-scale alloy 718 round ingot produced by VAR at Los Alamos National Laboratory [7]. The ingot, which was cut in half to facilitate easier handling, initially measured 210 mm in diameter and 400 mm in height. A 28-mm-thick slab offset by 2.5 mm from the ingot centerline was sectioned from each half of the ingot along the casting direction. Each smaller slab was then ground flat to reveal the ingot centerline and was etched using Canada etchant to reveal the segregation microstructure [9]. This procedure reveals the dendritic microstructure by preferentially removing material from the inter-dendritic regions. When appropriate side lighting is applied, the dendritic microstructure is clearly revealed and can be imaged by macrophotography. Mosaic images of the two slabs sectioned from the ingot are shown in Figure 1 after sectioning, grinding, and etching.

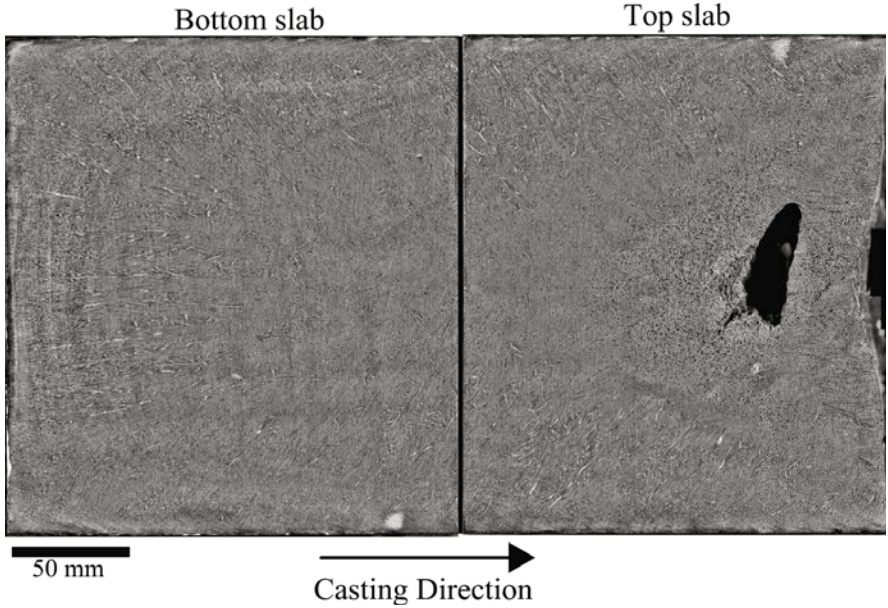

Figure 1. Mosaic images are shown of the sectioned, ground, and etched ingot slabs. Each slab was stitched from over 200 individual macrophotographs.

Individual macrophotographs were taken with a Canon EOS 60D DSLR camera equipped with a 22.3×14.9 mm, 18MP sensor and a Sigma 105-mm F2.8 EX DG OS HSM macro lens. Two studio strobe units were mounted 60 cm away and 29 cm high on either side of the slab to ensure even lighting across its entire surface. Additionally, a circular polarizing filter was mounted on

the lens to mitigate the effects of specular reflection off of the slab surface. After extensive optimization experiments, the best photography settings were determined be an *f*-stop of 8 and an exposure time of 1/250 seconds, the fastest possible with this camera for proper syncing to the strobes, at an ISO number of 100. These settings provided the depth of field necessary to adequately capture surface topography while providing the sharpest images possible. Phase detection auto focus functionality of the camera was used to focus prior to the acquisition of each image, a step necessary to account for small height variations across the slab surface. Because of the large number of images required to completely cover each slab surface, an automated image acquisition system was constructed. A robotic stage provides precise positioning of each image. This is important because maintaining a consistent overlap and camera orientation between images improves the image stitching procedure and the quality of the stitched image mosaics. Magnification varied from approximately 223 to 225 pixels/mm over the bottom slab and from 228 to 229 pixels/mm over the top slab. The individual components of the image acquisition system are:

- Vibration isolated mounting table
- An X-Y stage mounted on an optical breadboard
- Camera and camera mounting/adjustment equipment
- Computer and hardware used for image acquisition and X-Y stage control

The X-Y stage is secured to an optical breadboard fitted to a table with vibration isolating feet. The camera is mounted to the X-Y stage with a ball-head mount and a macro-focusing rail. The ball-head mount allows the user to level the camera lens relative to the slab surface. The macro-focusing rail is used to finely adjust the height of the camera when focusing on the slab at a set magnification. During imaging, the camera is traversed over the slab surface by two stepper motors. Both the motion of the X-Y stage and the operation of the camera are controlled by computer through a custom software program. In order to identify and analyze individual primary and secondary dendrite arms, each slab was imaged as a mosaic at approximately 1:1 magnification (228 pixels/mm for the camera system used). The completed image mosaics are presented in Figure 1 and referred to as the bottom and top slabs as shown. The top and bottom slab mosaic images are comprised of 250 and 204 individual macrophotographs, respectively, automatically positioned for approximately 20% linear overlap between adjacent images, in both the horizontal and vertical directions. Stitching of individual macrophotographs into a mosaic was completed with the Grid/Collection stitching plugin contained within the FIJI distribution of ImageJ, a free open-source image display and manipulation software [10, 11].

Data Analysis

Particle identification software was used to quantify the dendritic solidification microstructure from the stitched image mosaics. The principal objective is to identify primary dendrite arms and their orientations. However, the identification of secondary dendrite arms is also of interest. This was accomplished by using FIJI to identify image features that represent dendritic solidification structures. The key to using this approach effectively is to prepare the image in a manner that assists the software identification of features that represent actual dendritic structures by using select digital image processing and particle filtering techniques.

Prior to feature detection by software, the mosaics require rotating, cropping, scaling adjustments, conversion to a binary image format, and morphological operation adjustments. Rotation and cropping ensure that the mosaic images are properly aligned with respect to each other and remove the excess area around the edges of each image, which would confuse the analysis software. Each image was scaled to a consistent magnification of 110 pixels/mm, a magnification sufficient for software feature detection in this application. Next, a contrast limited adaptive histogram equalization (CLAHE) process was applied to each image mosaic. This creates a uniform histogram with intensity ranging from 0 to 255 over the entire 8-bit grayscale image. This step improves conversion to a binary image format by equalizing unevenly lighted areas. The CLAHE processed image was then converted to a binary image, wherein the valleys created during etching, which represent inter-dendritic regions, are processed into black pixels and the higher areas, which represent dendrite arms, are lighter and processed into white. This conversion is highly dependent upon the quality and depth of the surface etch. Thus, achieving a suitable etch is vital to the quality of the binary image. In this study images were thresholded at a value of 127, on an 8-bit scale, so that pixels below this intensity value were converted to black and those above were converted to white. The binary conversion is necessary to transform the image data into a form that the FIJI particle detection software is capable of handling. This software locates and identifies areas of continuous white pixels and labels those areas as individual particles, thus the term particle detection, and ignores regions of continuous black pixels. Because software detection of features, i.e. particles, from the as-converted binary image is poor, the binary image is further processed using morphological operations that grow and shrink regions of like-colored pixels prior to particle detection. Experiments determined that two erosion operations sufficiently separated the pixel regions that represent dendrites for software detection to operate adequately. An individual image taken from the upper left corner of the bottom slab, assuming the casting direction is up, is presented in Figure 2 to demonstrate each image processing step. Figure 2 shows (a) the original grayscale image, (b) that image after CLAHE processing, (c) after binary conversion, and (d) after two erosion steps.

Software particle detection was applied to the image mosaics processed as described above. The particle detection results produced by the FIJI software package were further filtered through software scripts. Filtering was used to remove irrelevant particles based on size and geometric characteristics. In this study, particles with lengths less than 22 pixels (200 µm) or greater than 5000 pixels (45,455 µm) were removed from the data set; this bound the particle sizes to those likely representative of dendritic features. Additional filtering removed particles with small aspect ratios or that were highly spherical. The results of these image analysis procedures and particle filtering steps are presented in Figure 3, where particles are shown as straight lines overlaid on the image from which they were identified. Figure 3 demonstrates the detection of both primary and secondary dendrite arms. Whether a line represents a primary or secondary dendrite arm can typically be determined from its length and orientation in the image. Although many primary dendrite arms were not identified, those that are appear to be quite consistent with the optical data. The correct identification of even a fraction of primary dendrite arms is significant because it provides a path to the fully automated quantification of dendritic microstructure in very large data sets that are resistant to manual characterization. As improved software analysis techniques are developed, the ability to correctly identify a larger fraction of dendritic features is expected to follow.

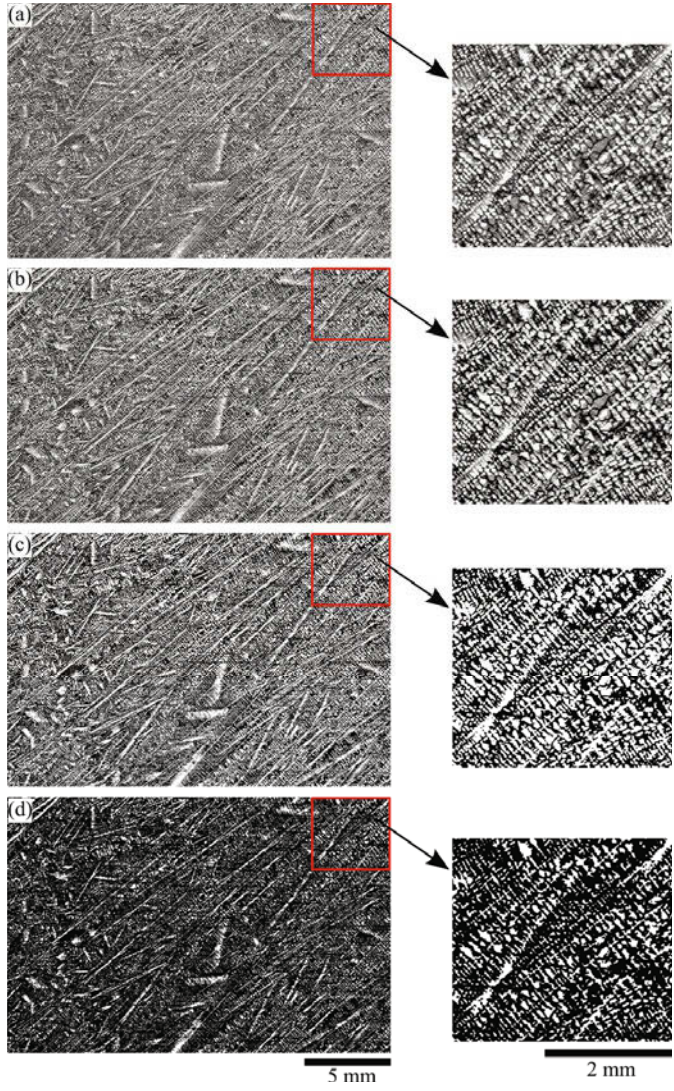

Figure 2. Presented is a single digital image at four stages of processing: (a) after conversion to 8-bit grayscale TIFF, (b) after contrast limited adaptive histogram equalization (CLAHE), (c) after binary conversion, and (d) after morphological processing.

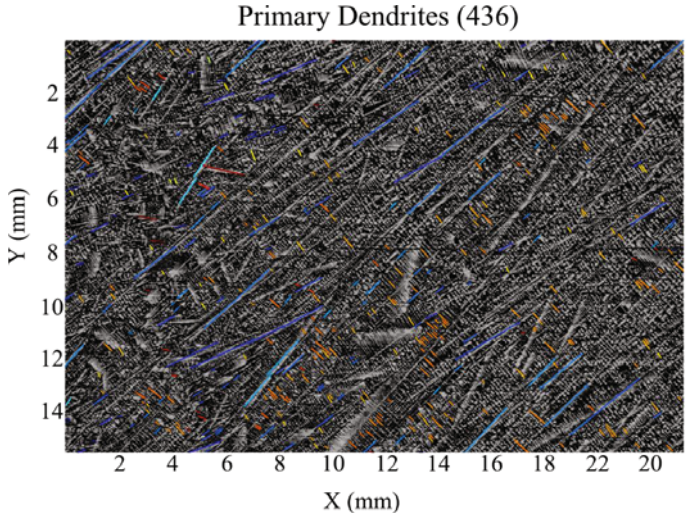

Figure 3. Particles identified using the FIJI particle analysis functionality are overlaid on the processed imaged from which they were identified.

Conclusions

The digital image analysis and particle identification procedures used in this study proved effective at identifying primary dendrite arms and their orientations. Although, there are a number of secondary dendrite arms that are also identified. Additional filtering to correct secondary dendrite arm identification and to remove outliers may further improve the accuracy of this technique. Once primary dendrite arms are identified, they can be used to calculate melt pool profiles and solidification directions based on their relative orientations within the ingot. Calculated melt pool profiles have the potential to provide new insights into how solidification defects form. Furthermore, automated measurements of secondary arm spacing in the regions immediately adjacent to primary dendrite arms have the potential to provide information on local solidification rates. It is hoped that manufacturers can use this information to predict defect formation, improve VAR processing, and validate process models.

References

1. John K. Tien and Thomas Caulfield, eds., *Superalloys, Supercomposites and Superceramics* (San Diego, CA: Academic Press Inc., 1989), 99-148.

2. J.M. Moyer et al., “Advances in Triple Melting Superalloys 718, 706 and 720,” *Superalloys 718, 625, 706 and Various Derivatives*, ed. E.A. Loria (Warrendale, PA: TMS, 1994), 39-48.
3. L.A. Jackman, G.E. Maurer, S. Widge, “White spots in Superalloys,” *Superalloys 718, 625, 706 and Various Derivatives*, ed. E.A. Loria (Warrendale, PA: TMS, 1994), 153-166.

4. J.A. Van Den Avyle, J.A. Brooks, A.C. Powell, “Reducing Defects in Remelting Processes for High-performance Alloys,” *JOM*, 50 (3) (1998), 22-25.

5. F.J. Zanner et al, “Vacuum Arc Remelting of Alloy 718,” *Superalloy 718 – Metallurgy and Applciations*, ed. E.A. Loria (Warrendale, PA: TMS, 1989), 17-32.

6. K.O Yu, J.A. Domingue, “Control of Solidification Structure in VAR and ESR Processed Alloy 718 Ingots,” *Superalloy 718 – Metallurgy and Applications*, ed. E.A. Loria (Warrendale, PA: TMS, 1989) 33-48.

7. T.J. Watt et al., “Solidification Mapping of a Nickel Alloy 718 Laboratory VAR Ingot,” *Proceedings of the 2013 International Symposium on Liquid Metal Processing and Casting*, ed. M.J.M Krane, A Jardy, R.L. Williamson, J.J. Beaman (Hoboken, NJ: John Wiley & Sons, Inc., 2013), 261-270.

8. W. Kurz and D. J. Fisher, *Fundamentals of Solidification* (Enfield, NH: Trans Tech Publications, 1998), 82-85.

9. T. Le Roux and D.A. Wells, “Assessment and Comparison of the Sensitivity of Various Macroetches for Alloy 718,” *Superalloy 718 – Metallurgy and Applications*, ed. E.A. Loria (Warrendale, PA: TMS, 1989), 109-118.

10. J. Schindelin et al., “Fiji: an open-source platform for biological-image analysis,” *Nature methods*, 9 (7) (2012), 676-682.

11. S. Preibisch, S. Saalfeld, P. Tomancak, “Globally Optimal Stitching of Tiled 3D Microscopic Image Acquisitions,” *Bioinformatics*, 25 (11) (2009), 1463-1465.

Characterization of Minerals, Metals, and Materials 2016
Edited by: Shadia Jamil Ikhmayies, Bowen Li, John S. Carpenter, Jiann-Yang Hwang, Sergio Neves Monteiro, Jian Li, Donato Firrao, Mingming Zhang, Zhiwei Peng, Juan P. Escobedo-Diaz, and Chenguang Bai
TMS (The Minerals, Metals & Materials Society), 2016

AN EMPIRICAL EQUATION TO PREDICT THE POROSITY OF TITANIUM FOAMS

Xiao Jian, Cui Hao, Qiu Guibao, YangYang

College of Materials Science & Engineering, Chongqing University, 400044, China

Keywords: Porous material; Titanium; Foam; Powder metallurgy; Porosity

Abstract

Structural control is an interesting but less studied subject in titanium foam production using space holder technique. In this paper, an empirical equation was reported to predict the porosity of pure titanium foams. The empirical equation is $P = 0.9S_c + 0.011$, where P and S_c represent porosity and spacer content, respectively. Results indicate that porosity is always lower than spacer content by approximately 10%. The porosities obtained from this method are also always lower than 90%.

Introduction

Titanium foams used as bone implants in biomedical applications have attracted increasing scientific and technological interest recently because of their ability to fuse together the advantages of porous structure and titanium[1]. However, processing and synthesizing this material have been a puzzling problem. The reason is that it needs a high vacuum (or high-purity protective atmosphere), high temperature processing equipment and low reactivity of mold materials with respect to liquid titanium when a mature melting process is applied[2]. With the development of powder metallurgy, the fabrication processes for titanium foams have focused on solid-state processing. Examples of such processes are loose sintering, investment casting, hollow powder sintering, metal injection molding, and space holder technique. In the last process, temporary materials, such as carbamide, ammonium bicarbonate, NaCl, starch, saccharose, and Mg[3-5], have been used as a space holder. Most of these materials completely

evaporate at low temperature, whereas others (e.g., NaCl) are removed through dissolution. This technique has become the most famous process for fabricating titanium foams because of its flexible designation of pore structure as porosity, pore size and its distribution, pore morphology, and the degree to which the cells are open or closed. In the Gibson and Ashby study[6], porosity was taken as the single most important structural feature of a cellular solid, and its value was determined by the spacer content in the space holder technique. Hence, studying the relationship between porosity and spacer content is important to help people obtain a better understanding of the structural control of titanium foams.

Therefore, the aim of this study is to test the feasibility of obtaining an empirical equation. A simple discussion is provided, as this work attempts to predict for the first time the porosity of titanium foams obtained by using the space holder technique. We do not include titanium-based alloys as NiTi and Ti-6Al-4V foams [7-9].

Results and discussion

Fig. 1 shows the porosity–spacer content data in the selected literature. Although other reports were also related to pure titanium foams obtained by using the space holder technique, these were eliminated to meet at least one of the following criteria: (1) Porosity was directly assumed to be equal to spacer content[10-12]; (2) Spacer content was included but without porosity[13]; (3) Porosity was included but without spacer content[14-18]; (4) Neither spacer content nor porosity was included[19]; and (5) Porosity and spacer content were both included, but the prepared foams were damaged in shape[5, 20, 21]. Some data were obtained from the figures in the literature[22-27]. For example, the symbol F9 in Fig. 1 of the current study stands for the data from ref. figure 9 in Laptev's work[24]. The spacer content is the same, but a different porosity was obtained in terms of different sintering temperatures and time, pressing pressure,

spacer size, and type. The influencing factors of porosity include parameters from both the space holder and synthesis process. Considering these parameters, an empirical equation is shown in Eq. 1, where P and S_c are dimensionless quantities.

$$P=0.9S_c+0.011,\ R^2=0.88175 \quad (1)$$

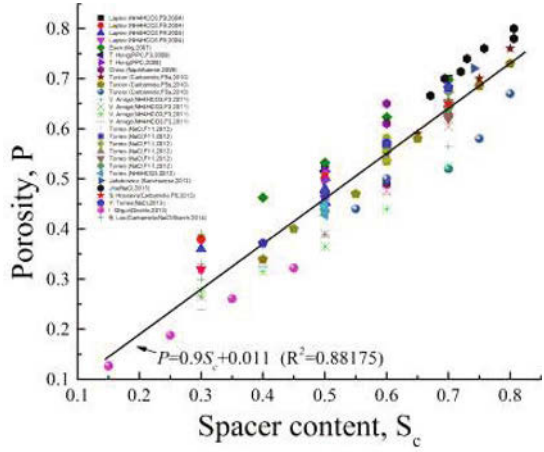

Fig. 1 The porosity of titanium foams plotted against spacer content in desired literatures[4, 22-34]. The solid line represents the fitting equation.

Fig. 2 shows the relationship between the ideal and empirical equations. When $S_c \approx 0$, $P \approx 0.011$ (point A in Fig. 2), the porosity remains even without any spacer particles. This case belongs to conventional powder metallurgy, and the porosity was generated from incomplete sintering of titanium powder. When $S_c \approx 1$, $P \approx 0.911$ (point B in Fig. 2), the porosity is <100%, although all are spacer particles. This result further proves that the volume of spacer holes shrink during sintering from the point of view of the equation. The finding also indicates that titanium foams with porosity over 90% fabricated by space holder technique presents a major challenge. When $P \leq S_c$, $S_c \geq 0.11$ (point C in Fig. 2), only when the spacer content is greater than a certain value can the porosity be less than it. This result confirms that porosity is not always less than

the spacer content even when the volume of spacer holes shrinks during sintering (i.e., porosity may be larger or equal). Given that the spacer content would not be too low with this technique (otherwise, using space holder technique would be unnecessary), the porosity can be assumed to be always less than the spacer content.

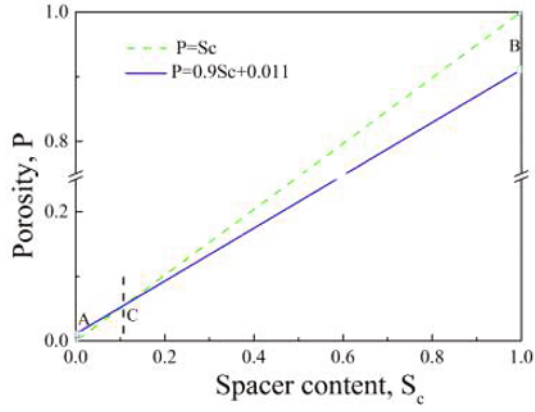

Fig.2 The relationship between the ideal (dash line) and empirical (solid line) equations.

In the author's previous work, pure titanium foams were prepared by using acicular carbamide as the space holder[35]. The spacer contents were 60%, 70% and 80%, respectively. The porosities were accordingly 50.2%, 62.8% and 71.4%, which was the average value of three parallel samples for each spacer content. According to the ideal equation ($P = S_c$), the porosities are 60%, 70% and 80%, and 55.1%, 64.1%, and 73.1% dependent on Eq. 1, as shown in Fig. 3. The porosities predicted by the empirical equation were closer to practical values when compared with those of the ideal equation. When the porosity exceeds 60% (The pore structure of the foam samples was changed from closed to open, as shown in Fig. 4), its value based on the empirical equation was quite consistent with that of practical. It seems that a better prediction

was obtained when the empirical equation for the porosity of pure titanium foams with an open structure.

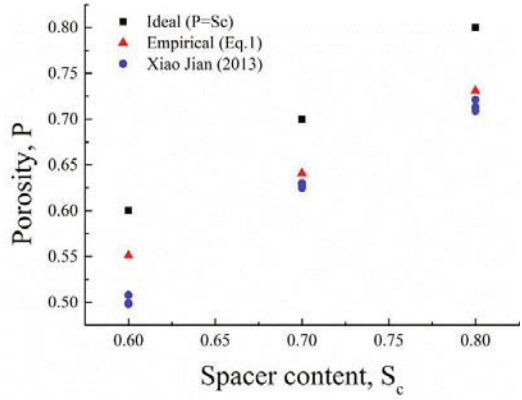

Fig. 3 Comparison of the ideal, empirical and practical porosities in author's previous work.

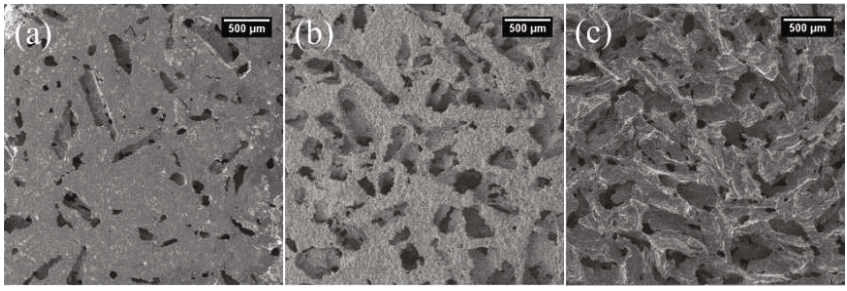

Fig. 4 The SEM images of foam samples with porosity: (a)50.2%, (b)62.8%, (c)71.4%[35].

Fig. 5 shows the comparison between the predicted porosities based on empirical equation and those of titanium alloy foams reported in literatures. In Aydoğmuş's work[7], the magnesium was used as the space holder. The spacer content and porosity were in the range of 50-80% and 59-81%, respectively. The porosity was larger than the spacer content. The predicted values were much more closer to actual ones with the porosity increased, though the predicted value was less than the actual. In Bansiddhi's work[8, 9], NaF and NaCl were taken as the space holders,

respectively. For NaF, the spacer content and porosity were 40.1% and 39.5%, respectively. The predicted porosity (37.2%) was less than that of actual. For NaCl, the spacer content and porosity were 40% and in the range of 32-36%, respectively. On the contrast, the predicted porosity (37.1%) was larger than the actual ones. It appears that a better prediction was obtained for closed-cell titanium alloy foams.

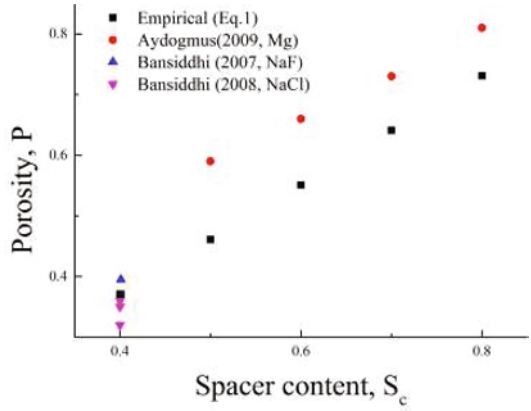

Fig. 5 A comparison between the predicted porosity based on empirical equation and actual ones of titanium alloy foams reported in literatures.

Conclusions

An empirical equation was obtained to predict the porosity of pure titanium foams prepared by space holder technique. The obtained equation shows a linear relation between the porosity and the spacer content. The porosity is always lower than the spacer content by approximately 10%. The porosities of titanium foams obtained from this technique are always lower than 90%. A better prediction was obtained for pure titanium foams with open structure in an author's work. For titanium alloy foams, closed-cell structure obtains a better prediction. It was found that the

decreased volume of spacer holes during sintering larger than the volume of micropores in cell-walls is a significant phenomenon for space holder technique.

Acknowledgements
This research is financially supported by the National Natural Science Foundation of China (Grant No. 51174243).

References

[1] Singh R, Lee PD, Dashwood RJ, Lindley TC. Titanium foams for biomedical applications: A review. Mater Tech. 2010;25:127-36.
[2] Dunand DC. Processing of titanium foams. Adv Eng Mater. 2004;6:369-76.
[3] Qiu GB, Xiao J, Zhu JY, Liao YL, Bai CG, Zhang J. Processing and mechanical properties of titanium foams enhanced by Er2O3 for biomedical applications. Mater Tech. 2014;29:118-23.
[4] Jakubowicz J, Adamek G, Dewidar M. Titanium foam made with saccharose as a space holder. J Por Mater. 2013;20:1-5.
[5] Mansourighasri A, Muhamad N, Sulong A. Processing titanium foams using tapioca starch as a space holder. J Mater Pro Tech. 2012;212:83-9.
[6] Gibson LJ, Ashby MF. Cellular solids: structure and properties. Cambridge, UK: Cambridge University Press; 1999.
[7] Aydoğmuş T, Bor Ş. Processing of porous TiNi alloys using magnesium as space holder. J All Com. 2009;478:705-10.
[8] Bansiddhi A, Dunand DC. Shape-memory NiTi foams produced by replication of NaCl space-holders. Acta Biomater. 2008;4:1996-2007.
[9] Bansiddhi A, Dunand DC. Shape-memory NiTi foams produced by solid-state replication with NaF. Intermetallics. 2007;15:1612-22.
[10] Smorygo O, Marukovich A, Mikutski V, Gokhale AA, Reddy GJ, Kumar JV. High-porosity titanium foams by powder coated space holder compaction method. Mater Lett. 2012;83:17-9.
[11] Bram M, Stiller C, Buchkremer HP, Stöver D, Baur H. High Porosity Titanium, Stainless Steel, and Superalloy Parts. Adv Eng Mater. 2000;2:196-9.
[12] Kim SW, Jung H-D, Kang M-H, Kim H-E, Koh Y-H, Estrin Y. Fabrication of porous titanium scaffold with controlled porous structure and net-shape using magnesium as spacer. Materials Science and Engineering: C. 2013;33:2808-15.
[13] Ye B, Dunand DC. Titanium foams produced by solid-state replication of NaCl powders. Mater Sci Eng A. 2010;528:691-7.
[14] Niu W, Bai C, Qiu G, Wang Q. Processing and properties of porous titanium using space holder technique. Mater Sci Eng A. 2009;506:148-51.
[15] Wen C, Yamada Y, Shimojima K, Chino Y, Asahina T, Mabuchi M. Processing and mechanical properties of autogenous titanium implant materials. J Mater Sci: Mater Medic. 2002;13:397-401.
[16] Imwinkelried T. Mechanical properties of open pore titanium foam. J Biome Mater Res A. 2007;81:964-70.
[17] Tuncer N, Arslan G. Designing compressive properties of titanium foams. J Mter Sci. 2009;44:1477-84.
[18] Wang X-h, Li J-s, Hu R, Kou H-c, Zhou L. Mechanical properties of porous titanium with different distributions of pore size. Transactions of Nonferrous Metals Society of China. 2013;23:2317-22.
[19] Kwok PJ, Oppenheimer SM, Dunand DC. Porous Titanium by Electro chemical Dissolution of Steel Space holders. Adv Eng Mater. 2008;10:820-5.
[20] Sharma M, Gupta G, Modi O, Prasad B. PM processed titanium foam: influence of morphology and content of space holder on microstructure and mechanical properties. Powder Metall. 2012;56:55-60.

[21] Sharma M, Gupta GK, Modi OP, Prasad BK, Gupta AK. Titanium foam through powder metallurgy route using acicular urea particles as space holder. Mater Lett. 2011;65:3199-201.
[22] Tuncer N, Arslan G, Maire E, Salvo L. Investigation of spacer size effect on architecture and mechanical properties of porous titanium. Mater Sci Eng A. 2011;530:633-42.
[23] Hong T, Guo Z, Yang R. Fabrication of porous titanium scaffold materials by a fugitive filler method. J Mater Sci: Mater Medic. 2008;19:3489-95.
[24] Laptev A, Bram M, Buchkremer H, Stöver D. Study of production route for titanium parts combining very high porosity and complex shape. Powder Metall. 2004;47:85-92.
[25] Amigó V, Reig L, Busquets D, Ortiz J, Calero J. Analysis of bending strength of porous titanium processed by space holder method. Powder Metall. 2011;54:67-70.
[26] Torres Y, Pavon JJ, Rodriguez JA. Processing and characterization of porous titanium for implants by using NaCl as space holder. J Mater Pro Tech. 2012;212:1061-9.
[27] Hosseini S, Yazdani-Rad R, Kazemzadeh A, Alizadeh M. A Comparative Study on the Mechanical Behavior of Porous Titanium and NiTi Produced by a Space Holder Technique. Journal of Materials Engineering and Performance. 2013:1-10.
[28] Jha N, Mondal D, Dutta Majumdar J, Badkul A, Jha A, Khare A. Highly porous open cell Ti-foam using NaCl as temporary space holder through powder metallurgy route. Mater Design. 2013;47:810-9.
[29] Torres Y, Rodriguez JA, Arias S, Echeverry M, Robledo S, Amigo V, et al. Processing, characterization and biological testing of porous titanium obtained by space-holder technique. J Mter Sci. 2012;47:6565-76.
[30] Chino Y, Dunand DC. Creating Aligned, Elongated Pores in Titanium Foams by Swaging of Preforms with Ductile Space Holder. Adv Eng Mater. 2009;11:52-5.
[31] Esen Z, Bor Ş. Processing of titanium foams using magnesium spacer particles. Scripta Mater. 2007;56:341-4.
[32] Lee B, Lee T, Lee Y, Lee DJ, Jeong J, Yuh J, et al. Space-Holder Effect on Designing Pore Structure and Determining Mechanical Properties in Porous Titanium. Mater Design. 2014.
[33] Torres Y, Lascano S, Bris J, Pavón J, Rodriguez-Ortiz JA. Development Of Porous Titanium For Biomedical Applications: A Comparison Between Loose Sintering And Space-Holder Techniques. Materials Science and Engineering: C. 2013.
[34] Gligor I, Soritau O, Todea M, Berce C, Vulpoi A, Marcu T, et al. Porous cp Titanium Using Dextrin as Space Holder for Endosseous Implants. Particulate Science and Technology. 2013;31:357-65.
[35] Xiao J, Qiu G, Liao Y, Bai C. Microstructure and Mechanical Properties of Titanium Foams Prepared with Carbamide as Space Holder. Rare Met Mater Eng. 2015;44:1724-9.

Characterization of Minerals, Metals, and Materials 2016
Edited by: Shadia Jamil Ikhmayies, Bowen Li, John S. Carpenter, Jiann-Yang Hwang, Sergio Neves Monteiro, Jian Li, Donato Firrao, Mingming Zhang, Zhiwei Peng, Juan P. Escobedo-Diaz, and Chenguang Bai
TMS (The Minerals, Metals & Materials Society), 2016

MICROSTRUCTURE OF METAL INJECTION MOLDED MIM418 USING MASTER ALLOY TECHNIQUE

Lin Zhang, Xiaowei Chen, Chi Chen, Xuanhui Qu

Institute of Advanced Materials and Technology, University of Science and Technology Beijing; Haidian District Xueyuan Road 30; Beijing, 100083, China

Keywords: Powder Metallurgy, Ni-based Superalloy, Master Alloy, Metal Injection Molded, MIM418.

Abstract

The MIM418 superalloy was prepared by metal injection molding using master alloy technique. The influence of heat treatment on microstructure of MIM418 alloy was discussed in this paper. The relative density of the sintered specimens reaches 96%. Homogenous microstructure is achieved after solution treatment at 1200°C for 4h. The sphere secondary γ′ phase is about 0.1 μm and distributes uniformly in the grain. The aging temperature of 750°C is suitable for the MIM418 superalloy due to the slow coarsening rate and non-significant morphology change of precipitated phases.

Introduction

The K418 superalloy developed in the 1970s in China is widely used as turbine wheel in automotive turbocharger [1], whose chemical compositions are similar to those of IN713C. The K418 superalloy is a precipitation hardened Ni-based superalloy, which has excellent high temperature mechanical properties, good fatigue property, prominent oxidation and corrosion resistance at elevated temperature [2]. However, the usual way of manufacturing K418 consists of vacuum induction melting, conventionally casting into different specifications of components and machining, which has limited the application in civilian high temperature components because of its high cost.

Metal injection molding (MIM) is a near-net shape technique by the introduction of plastic injection molding into powder metallurgy area, which is cost-effective for the mass production of complex shaped components [3]. Master alloy technique is the way to mix the base powder with a small quantity of so-called master alloys, which carry most of the alloying elements required in the final composition and aid the sintering process via liquid phase sintering [4]. Introducing the master alloy powders into MIM process can reduce the amount of pre-alloyed powders, and increases the sintering activity due to the transient liquid phase [5] and high compositional gradients between master alloy powders and the base powders [6].

Therefore, we designed a master alloy powder Cr-23Al-16.6Mo-8.3Nb-2.9Ti-0.5C-0.4Zr-0.05B to blend with carbonyl Ni and then the mixed powder was binded and injection molded to tensile test specimens. The influence of heat treatment to the microstructure is mainly discussed in this paper.

Experimental procedure

The ingot crushing method was used to produce the master alloy powder Cr-23Al-16.6Mo-8.3Nb-2.9Ti-0.5C-0.4Zr-0.05B. Then the master alloy powder was mesh screened to 300 mesh number. The master alloy powder and the carbonyl Ni powder with the size of 0.5 μm were blended with the blend ratio of 13: 37 (Master alloy: Ni) for 2h. And then the mixed powder was milled with the proprietary wax-based binder system. The powder loading of the feedstock was 65vol.%. The specimens were injected with a CJ-80E type molding machine at 150~170°C. Prior to sintering, the binders were removed by solvent debinding and thermal debinding under the atmosphere H_2. Subsequently, the debinded specimens were sintered at 1240°C for 2h in vacuum. The density of sintered specimens was measured by Archimedes method. And then the specimens were solution treated at 1000~1200°C for varied periods under protective atmosphere Ar. The specimens after solution treated at 1200°C were aged at 750~950°C for 16~24h. After etching the specimens, the microstructure was observed by hot field emission scanning electron microscope.

Results

The morphology and the particle distribution of the master alloy powder Cr-23Al-16.6Mo-8.3Nb-2.9Ti-0.5C-0.4Zr-0.05B is shown in Figure 1. The master alloy powder is polyhedral due to the mechanical crushing. Although the fine particle with the size around 8 μm is in major, there is a little coarse particle with the size more than 15 μm. According to the result of particle distribution analysis, D_{10}, D_{50}, D_{90} of the master alloy powder are respectively 3.1 μm, 7.7 μm and 17.6 μm The fine particle is benefit for the sintering because of the high specific surface area. However, the high specific surface area leads to the high oxygen content which is 0.2wt.% according to the chemical analysis. The XRD analysis result is shown in Figure 2. The main phases are Cr_2Nb, Al_3Nb and Al_9Cr_4. Other elements dissolve in the matrix and form the solid solution.

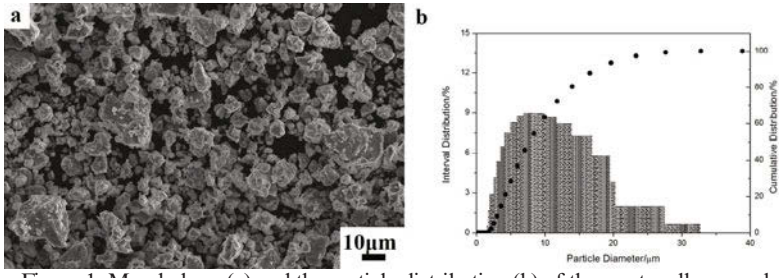

Figure 1. Morphology (a) and the particle distribution (b) of the master alloy powder

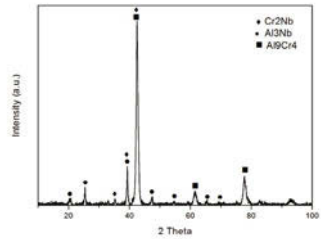

Figure 2. XRD spectrum of the master alloy powder

The microstructure of the sintered MIM418 is shown in Figure 3. The relative density of the sintered specimens is 96%. Therefore, Figure 3a shows that there are a few pores in the specimens with the size around 5 μm. However, the larger defects also appear in the red circle in Figure 3a, which are the secondary pores left after melting/dissolution and covered by sponge-like residues [7]. These defects are the powerful evidence of the appearance of the transient liquid phase during sintering process. The high magnification image (Fig.3b) shows that the primary γ′ phase is square after sintered. However, the arrange of the size of the γ′ phase is from 0.2 to 1.5 μm, which reduces the homogeneity of the microstructure. Therefore, further heat treatments are needed in order to improve the homogeneity of the microstructure.

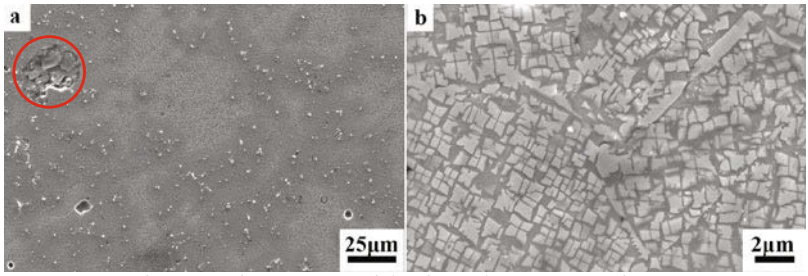

Figure 3. Microstructure of the sintered MIM418 specimens

Subsequently, we carried out the solution treatment to dissolve the elements to acquire more homogenous microstructure. According to Figure 4, it is indicated that at the temperature of 1000°C, the γ′ phase does not dissolve into the matrix so the γ′ phase becomes coarser to 1~2 μm. As for 1100°C, the temperature is approached to the dissolving temperature of the γ′ phase so that the average size changes to about 1 μm and the fine γ′ phase with the size about 0.5 μm is disappeared mostly in comparison to that of sintered specimens. Meanwhile, the morphology of the γ′ phase changes from square to sphere. With the temperature increased to 1200°C, the γ′ phase mostly dissolves to the matrix and precipitates during cooling to form the secondary γ′ phase with the size about 0.1 μm. The secondary γ′ phase is sphere and fine, which distributes homogenously in the grain. Also, along the grain boundary, the γ′ phase distributes like a necklace, which can hinder the movement of dislocation and grain boundary and can reduce the

possibility of intergranular fracture.

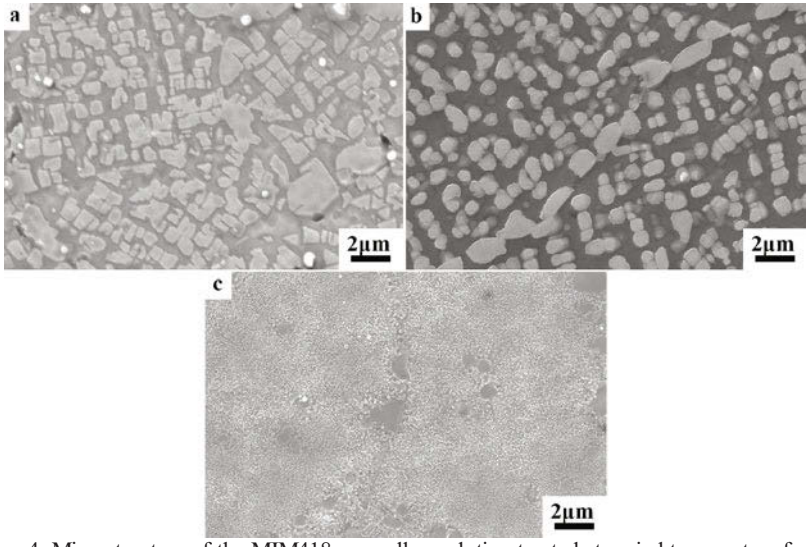

Figure 4. Microstructure of the MIM418 superalloy solution treated at varied temperature for 8 h: (a) 1000°C; (b) 1100°C; (c) 1200°C

The microstructure of MIM418 after solution treatment at 1200°C for varied period is shown in Figure 5. It is indicated that solution treating for 2h is too short for the γ′ phase to dissolve because there is still some square primary γ′ phase with the size about 1 μm in the grain as well as the sphere secondary γ′ phase with the size around 0.1 μm (Fig.5a). As for the sample solution treated for 4h, the primary γ′ phase disappears mostly and the secondary γ′ phase precipitates homogenously in the grain. When the solution treatment time increases up to 8h, the size of the secondary γ′ phase does not change and maintains at 0.1 μm. This is ascribed to the fast cooling rate in air and the secondary γ′ phase does not have enough time and temperature to get coarser. However, the γ′ phase along the grain boundary get coarser from 0.5 μm to 2 μm. Due to the γ′ phase containing high levers of Nb or Zr along the grain boundary (Table 1), the dissolve temperature for this γ′ phase is higher than the γ′ phase Ni_3(Al, Ti) in the grain. Therefore, the γ′ phase along the grain boundary gets coarser with the increasing of solution treatment time. In summary, the best solution treatment process is keeping the specimens at 1200°C for 4h, by which the primary γ′ phase dissolves mostly and the secondary γ′ phase distributes homogenously in the grain as well as that the γ′ phase along the grain boundary does not grow severely.

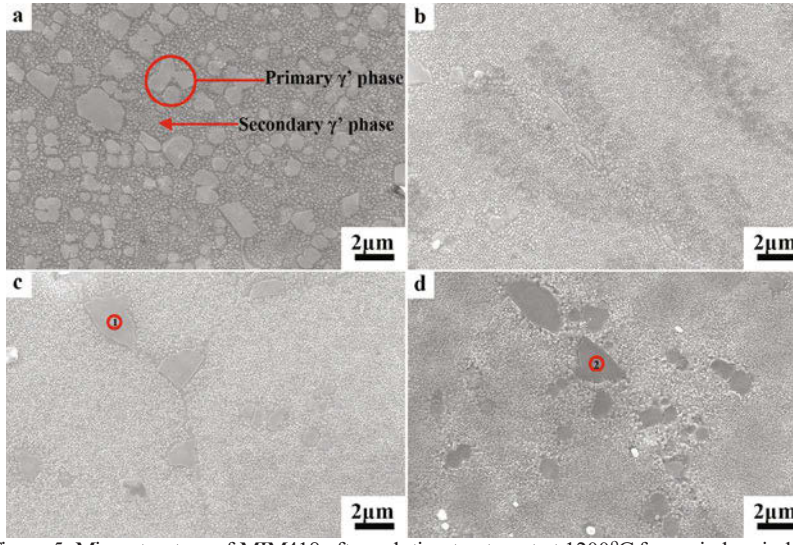

Figure 5. Microstructure of MIM418 after solution treatment at 1200°C for varied periods of time: (a) 2h; (b) 4h; (c) 6h; (d) 8h

Table Ⅰ. The EDS Spot Analysis of γ′ Phase in Figure 5 (wt.%)

	Ni	Cr	Al	Ti	Nb	Zr
Spot 1	48.34	9.42	4.34	11.30	23.23	3.37
Spot 2	31.38	6.41	1.92	0.03	-	46.43

The aging treatment was carried out after solution treatment at 1200°C for 4h to improve the microstructure of MIM418. Due to the aging temperature lower than that of dissolving temperature of γ′ phase, the third γ′ phase separates out from the supersaturated matrix, while the secondary γ′ phase gets coarser. According to Figure 6, at 750°C, the coarsening rate of the secondary γ′ phase is slow. After aging at 750°C for 16h, the size of the secondary γ′ phase even maintains at 0.1 μm so that the secondary γ′ phase and the third γ′ phase is hard to be distinguished from the SEM image (Fig.6a). As for the specimens aged at 750°C for 24h, the secondary γ′ phase slowly grows up to 0.8 μm, but the third γ′ phase does not change much and keeps about 0.1 μm. At the aging temperature of 930°C, the γ′ phase changes a lot in comparison to the 750°C aged specimens. Firstly, the morphology of the γ′ phase changed from sphere to triangle. Then the size of the secondary γ′ phase after aging at 930°C for 16h grows up to 0.6 μm and the size of the third γ′ phase also grows up to about 0.2 μm, while the secondary and third γ′ phase is still 0.1 μm at 750°C. In case of the aging time of 24h, the size of the secondary and third γ′ phase changes to 0.9 μm and 0.3 μm respectively. It is indicated that at the temperature of 930°C, the coarsening rate of precipitated phases is very fast. Due to the fast coarsening rate and severe change of morphology of the γ′ phase, the aging temperature of 930°C is not suitable for MIM418. The longer aging time at 750°C for MIM418 may improve microstructure, which

needs to be proved in future research.

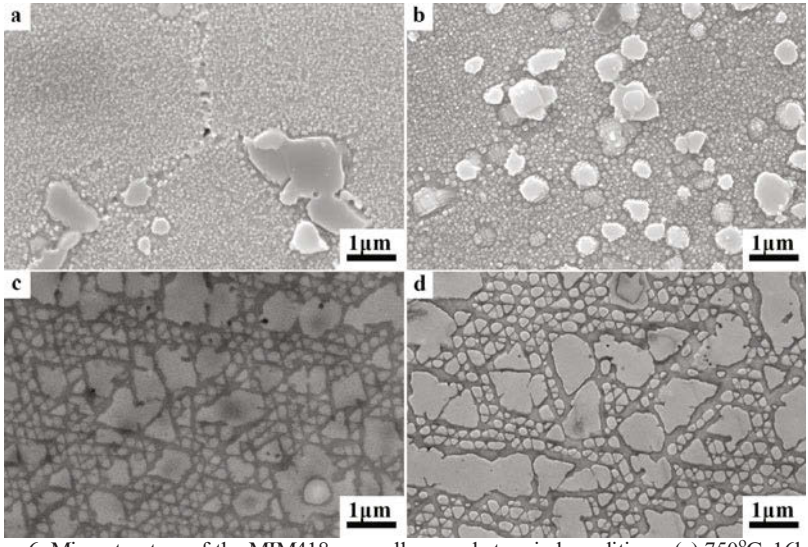

Figure 6. Microstructure of the MIM418 superalloy aged at varied conditions: (a) 750°C, 16h; (b) 750°C, 24h; (c) 930°C, 16h; (d) 930°C, 24h

Conclusion

The ingot crushing method was adopted to obtain the master alloy powder with fine particle distribution and the sintered specimens were acquired with relative density 96% by MIM. The best solution treatment process is keeping the specimens at 1200°C for 4h. After solution treatment at 1200°C for 4h, the sphere secondary γ′ phase is about 0.1 μm. Meanwhile, the distribution and morphology of the γ′ phase along the grain boundary becomes like necklace, which can hinder the movement of dislocation and grain boundary. After aging, the third γ′ phase separates out and the secondary γ′ phase gets coarser. The aging temperature of 750°C is suitable for the MIM418 superalloy due to the slow coarsening rate and non-significant morphology change of precipitated phases.

Acknowledgements

This work is financially supported by National Natural Science Foundation of China (51374027, 51174029) and National High Technology Research and Development Program of China (863 Program) (2012AA03A514).

References

1. Burghardt Klöden et al., "High-Temperature Properties of MIM-Processed Superalloys," *PIM*

International, 4(4)(2010), 63-67.
2. Zhaoxia Shi et al., "Solidification Characteristics and Segregation Behavior of Ni-based Superalloy K418 for Auto Turbocharger Turbine," *Journal of Alloys and Compounds*, 571(2013), 168-177.
3. Bernardo N. Nobrega, Jr Waldyr Ristow, Ricardo Machado, "MIM Processing and Plasma Sintering of Nickel Base Superalloys for Aerospace and Automotive Applications," *Powder Metallurgy*, 51(2)(2008), 107-110.
4. José Sicre Artalejo et al., "Quantification of Hardening in Fe–Mn Master Alloys Prepared by a Mechanical Alloying Process Via Nanoindentation Experiments," *Journal of Materials Research*, 26(14)(2011), 1726-1733.
5. R. Oro, M. Campos, J. M. Torralba, "Study of High Temperature Wetting and Infiltration for Optimising Liquid Phase Sintering in Low Alloy Steels," *Powder Metallurgy*, 55(3)(2012), 180-190.
6. P. A. Davies et al., "Development of Master Alloy Powders, Including Nickel-Based Superalloys, for Metal Injection Molding (MIM)," *Advances in Powder Metallurgy and Particulate Materials*, 8(2003), 8-1.
7. Raquel Oro et al., "Effect of Processing Conditions On Microstructural Features in Mn–Si Sintered Steels," *Materials Characterization*, 95(2014), 105-117.

Characterization of Minerals, Metals, and Materials 2016

Method Development

Session Chairs:
Andrew David Brown
Carl M. Cady

Characterization of Minerals, Metals, and Materials 2016
Edited by: Shadia Jamil Ikhmayies, Bowen Li, John S. Carpenter, Jiann-Yang Hwang, Sergio Neves Monteiro, Jian Li, Donato Firrao, Mingming Zhang, Zhiwei Peng, Juan P. Escobedo-Diaz, and Chenguang Bai
TMS (The Minerals, Metals & Materials Society), 2016

EFFECT OF POISSON'S RATIO ON STRESS/STRAIN CONCENTRATION AT CIRCULAR HOLES IN ELASTIC PLATES SUBJECTED TO BIAXIAL LOADING - THREE DIMENSIONAL FINITE ELEMENT ANALYSIS

Amr A. Abd-Elhady[*,**], *Hossam El-Din M. Sallam*[*,***]

[*]*Faculty of Engineering, Jazan University, Jazan, Jazan 45142, P.O.Box 706*,*Saudi Arabia*
[**]on sabbatical leave from Mechanical Design Department, Faculty of Engineering, Helwan University, Cairo 11718, Egypt
[***]On sabbatical leave from Faculty of Eng., Zagazig University, Zagazig, Egypt

Abstract

It is necessary to determine stress and strain concentration factors around the circular notch in order to determine the site of crack initiation. The through-thickness variations of stress and strain concentration factors for plate contains a central circular notch subjected to biaxial loading have been investigated by using three dimensional finite element method (3D FEM). To study the effect of Poisson's ratio (ν) on elastic stress/strain concentration factors around the circular notch, four different values of Poisson's ratio (ν), varied from 0.1 to 0.4, have been studied numerically.

It is found that the maximum stress and strain concentration factors increase with increasing the Poisson's ratio (ν). The stress and strain concentration factors increase with decrease the biaxial ratio. Furthermore, the effect of Poisson's ratio (ν) on stress and strain concentration factor decreases with increasing the biaxial ratio.

Keyword

Stress concentration factor, SCF; Strain concentration factor; Circular notch; biaxial load; Three dimension finite element.

1. Introduction

Structures with circular holes have been widely used in engineering designs. This circular notch will create stress or strain concentrations. When stress concentrations exist in a structure, its strength is often different from that measured using specimens under uniaxial loading. It is necessary to determine stress or strain concentrations around the circular notch in order to determine the site of crack initiation, which can severely reduce the overall strength of the structure.

The actual 3D stress fields in the neighborhood of the notch root or circular hole are very complex [1]. The SCF or strain concentration factor in the interior of a plate with a hole or notch is significantly higher than the value on the free surface or the corresponding planar solution [1–7]. On the other hand, in engineering practice, SCF and strain concentration factor measurement are always made on the free surfaces. This may

cause danger in engineering applications without proper consideration of the 3D stress distributions. She and Guo [8] show that through thickness variation of stress concentration factor, K_σ, for elliptic holes subjected to tensile stress is very slight in the thin plate and increases with increasing the plate thickness. The corresponding peak value (K_σ) max is located at the center of thickness for thinner plate but shifts to the free surface in thick plate. Recently, She and Guo [6, 8] have already demonstrated that the SCF changes along the hole front in the thickness direction. However, the influence of Poisson's ratio has not been considered in their works.

Kotousov and Wang [9] have studied the effect of thickness and Poisson's ratio on stress concentration based on some theoretical methods which showed that the 3D stress concentration is a function of thickness and Poisson's ratio. However, these existing theoretical methods often give the SCF as a mean value view, cannot solve the distribution of SCF along the notch front in the thickness direction and so cannot obtain the maximum SCF along the notch front. Furthermore, Peishi et al. [10] found that the thickness-dependent maximum of SCF, increases significantly with increasing the Poisson's ratio in the elliptic holes subjected to tensile loading. Tlilan [11] studied the influences of Poisson's ratio and the geometric configuration upon the strain concentration factor, defined under triaxial stress state, of notched bars with U-notch. Tlilan show that, the Poisson's ratio has a significant effect on the strain concentration factor, especially for deep and intermediate notch depths.

The main objective of the present work is to study the influence of Poisson's ratio (ν) and biaxial ratio on the stress and strain concentration factors and their relations of elastic finite thickness plate containing a circular subjected to far end uniform biaxial loading using 3D finite element method.

2. Numerical model

2.1. Definitions of the geometrical parameters

The plate containing a circular hole subjected to biaxial loading is illustrated in Fig. 1. The notch diameter is $2D$ and the radius of the notch is ρ. The thickness, width and the height of the plate are $2B$, $2W$ and $2H$, respectively. The plane x-y (plane $z = 0$) is the mid plane of plate and two plate surface are $z = B$ and $z = -B$, respectively. The geometrical parameters of specimens are chosen as follows:

$D = 1$ mm;
$B/D = 2.5$;
$\nu = 0.1$, 0.2, 0.3 and 0.4;
The biaxial ratio, λ, = -1, -0.5, 0, 0.5 and 1;
Young's modulus $E = 200$ GPa;
$W/D = H/D = 100$;

2.2. Definitions of the stress and strain concentration factor

In this paper, the stress and strain concentration factor is denoted as K_σ and K_ε respectively and the stress and strain concentration factor at the mid point of the plate is $K_{\sigma mp}$ and $K_{\varepsilon mp}$ respectively.

$$K_\sigma = \frac{\sigma_{NR}}{\sigma_{net}}; \qquad (1)$$

$K_{\sigma mp} = K_\sigma$ at z = 0

$$K_\varepsilon = \frac{\varepsilon_{NR}}{\varepsilon_{net}} \qquad (2)$$

$K_{\varepsilon mp} = K_\varepsilon$ at z = 0

Where:

$$\sigma_{net} = \frac{\sigma_y W}{W - D} \qquad (3)$$

$$\varepsilon_{net} = \frac{\sigma_y W}{E(W - D)} \qquad (4)$$

Here, σ_{NR} and ε_{NR} are the longitudinal stress and strain in Y direction of plate at the notch root; σ_{net} and ε_{net} are the mean stress and strain of net section on the ligament, respectively. The K is meaning stress or strain concentration factor.

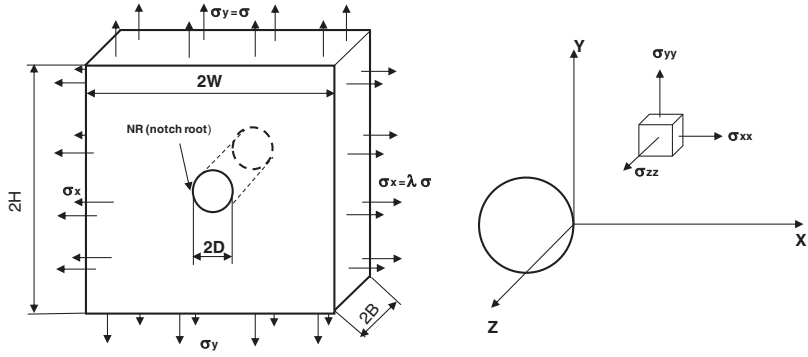

Fig. 1 The geometry of the plate with circular hole notch under biaxial loading.

2.3. Finite Element Analysis

ABAQUS [12] was selected to perform the numerical analysis owing to its powerful and comprehensive functions and precision. Therefore, a three-dimensional (3D) finite element model has been developed to account for geometric and material behavior of isotropic plate. A uniform, $\sigma_y = \sigma$, stress of 50 MPa is applied on the above and down boundary of the plate and $\sigma_x = \lambda\sigma$, in other hand side as shown if Fig. 1. The finite

element meshes constructed with hexagonal structural mesh, C3D8 (An 8-node linear brick) elements, are used for a plate under Standard/static analysis.

Around 30 planar layers are divided through the thickness of the plate. The mesh refinement process is carried out to assure that results are not dependent upon the element size. In order to accomplish that, the size of element decreases gradually with distance from the open hole decreasing (as shown in Fig. 2). This means that the finite element (FE) meshes in the neighborhood of the hole are much denser. The plate are modeled with around 45000 elements.

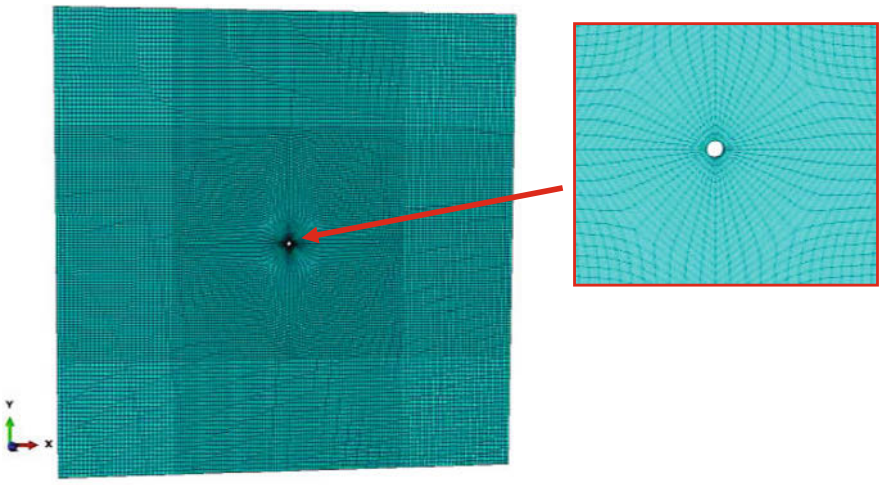

Fig. 2 Finite element model mesh.

2.4 Model Verification

To verify the accuracy of the present result, the values of normalized stress, $K_\sigma/K_{\sigma mp}$, and strain, $K_\varepsilon/K_{\varepsilon mp}$, concentration factor (normalized by each value of mid plane) for ν =0.3 and uniaxial loading , $\lambda = 0$ are compared with the previous numerical results using 3-D analysis found in the literature, $B/D = 2.5$, $W/D = 100$ and $H/D = 100$, [13], as shown in Figures 3. Figures 2 and 3 show an excellent agreement between present model result and data in literature [13].

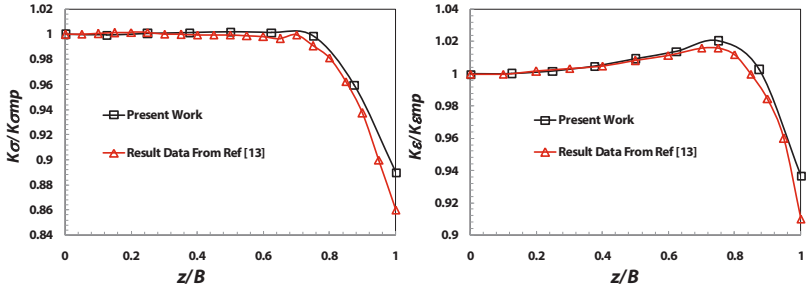

Fig. 3. The distributions of the stress and strain concentration factor through-thickness of notch root for present work and numerical result in literature [13].

3. Results and Discussion

Fig. 4 illustrates the variation of normalized stress concentration factor, $K_\sigma/K_{\sigma mp}$, (the stress is normalized by each value of mid plane) versus z/B for different ν and λ. The results in Fig. 4 may be divided into two regions. In the first region, for $z/B \leq 0.8$, the value of stress concentration factor through the plate thickness was almost constant. In the second region, for $z/B > 0.8$, the values of $K_\sigma/K_{\sigma mp}$ decreased by increasing the value of z/B. The obtained results for $D = 1$ mm, are compared with the result for $D = 0.5$ with the same ratio of B/D, W/D and H/D to validate the proposed value. The values of $K_\sigma/K_{\sigma mp}$ for $D = 1$ is identical to this obtained for $D = 0.5$ with the same ratio of B/D, W/D and H/D.

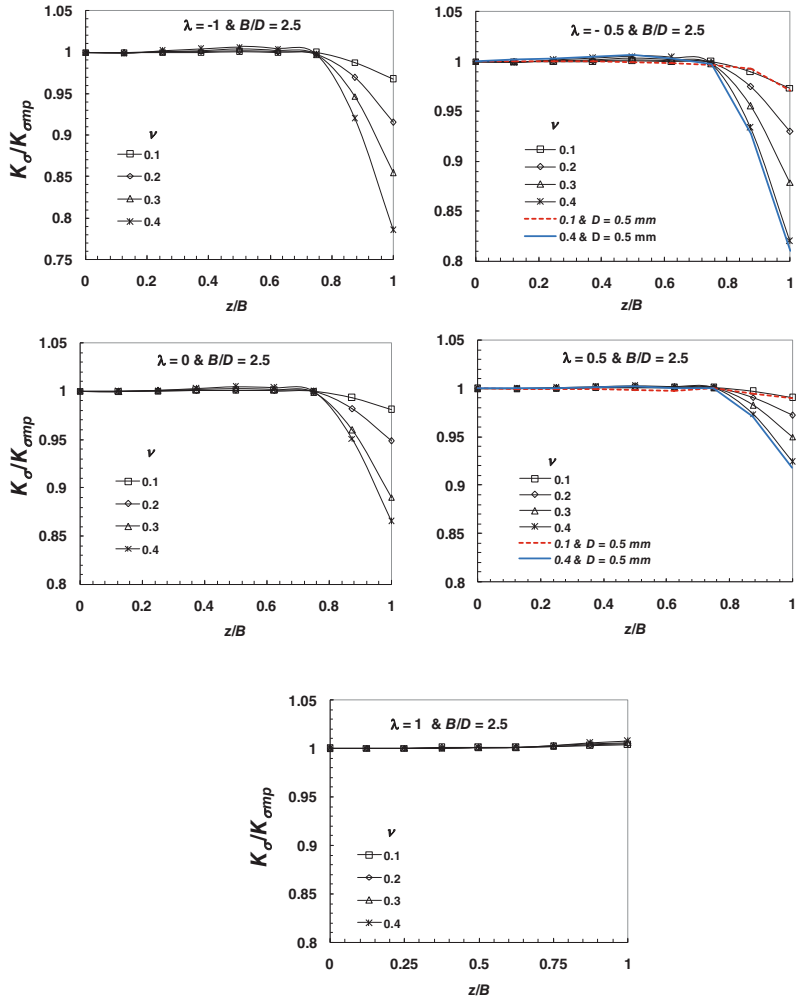

Fig. 4. The distributions of the stress concentration factor through-thickness of notch root for different biaxiality ratio (λ) and different Poisson's ratio (ν).

Fig. 5 represents the variation of normalized strain concentration factor, $K_\varepsilon/K_{\varepsilon mp}$, (also, the strain is normalized by each value of mid plane) versus z/B for different ν and λ. The

curve of, $K_\varepsilon/K_{\varepsilon mp}$, versus, z/B, almost is same trend of figure 2. At different value of λ the normalized stain concentration factor increase to reach to it's a peak value and then decrease by increasing the dimensionless z/B

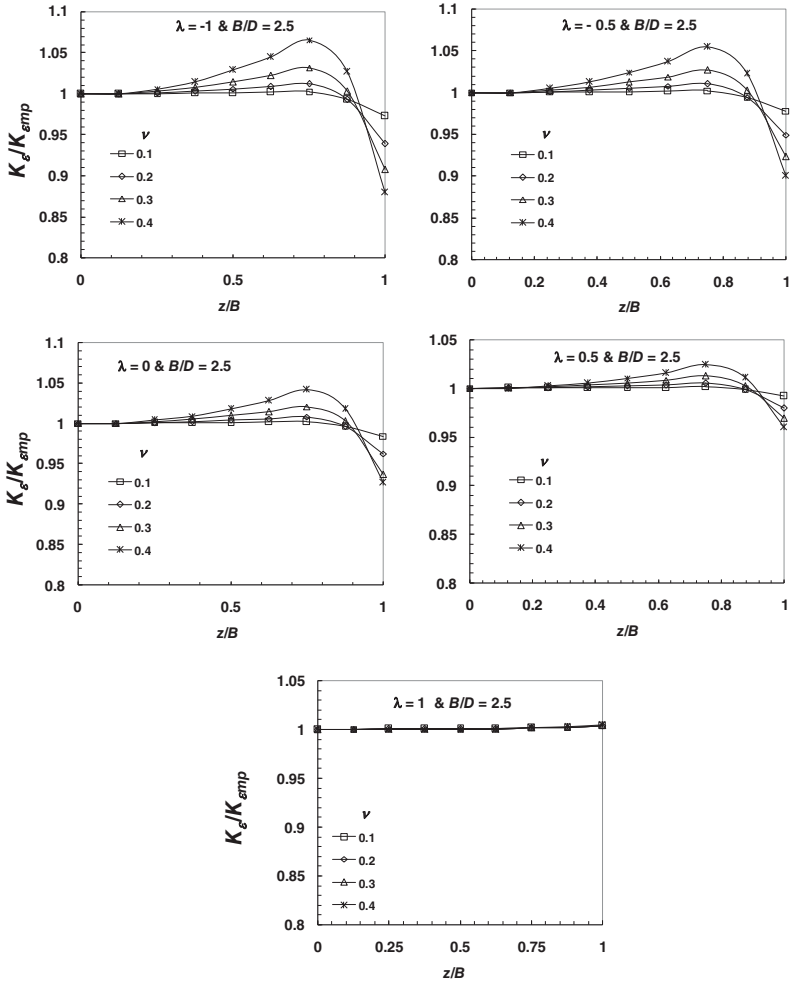

Fig. 5. The distributions of the strain concentration factor through-thickness of notch root for different biaxiality ratio (λ) and different Poisson's ratio (ν).

The previous curves represent the variation of either the normalized $K_\sigma/K_{\sigma mp}$ or $K_\varepsilon/K_{\varepsilon mp}$, for $\lambda \neq 1$, can be divided to three regions. In the first region $K_\sigma/K_{\sigma mp}$ or $K_\varepsilon/K_{\varepsilon mp}$ increased with increasing z/B to reach its peak value. In this region, the $K_\sigma/K_{\sigma mp}$ or $K_\varepsilon/K_{\varepsilon mp}$ increase with increasing ν for the same z/B. in the second region, all values of $K_\sigma/K_{\sigma mp}$ or $K_\varepsilon/K_{\varepsilon mp}$ decrease with increasing z/B by different values of decrement to intersect at one point ($z/B \approx 0.8$ in case of $K_\sigma/K_{\sigma mp}$ and $z/B \approx 0.9$ in case of $K_\varepsilon/K_{\varepsilon mp}$). In the third region ($K<K_{mp}$), the previous decrement continued to get opposite trend on the surfaces. The $K_\sigma/K_{\sigma mp}$ or $K_\varepsilon/K_{\varepsilon mp}$ decreases with increasing ν for the same z/B. Therefore, it can be concluded that the high value of $K_\sigma/K_{\sigma mp}$ or $K_\varepsilon/K_{\varepsilon mp}$ at the plate interior is for maximum Poisson's ratio, while, $K_\sigma/K_{\sigma mp}$ or $K_\varepsilon/K_{\varepsilon mp}$ at minimum Poisson's. But, for $\lambda = 1$, the normalized $K_\sigma/K_{\sigma mp}$ or $K_\varepsilon/K_{\varepsilon mp}$ are not changed by increasing the values of z/B and are equal 1.

'not affected by change the values' to 'not affected by changing the values'

Figure 6 presents the variation of mid plane stress and strain concentration factor with λ for different dimensionless ν. For $\lambda \neq 1$, the stress and strain concentration factor increase by increasing ν. $K_{\sigma mp}$ and $K_{\varepsilon mp}$ decrease with an increase in λ. This may be due to increasing the compression stress in the notch root by increasing the biaxial ratio, λ. It was found also that the $K_{\sigma mp}$ and $K_{\varepsilon mp}$ is close to that given by Peterson [16] when λ is equal to zero. Furthermore, the effect of Poisson's ratio (ν) on stress and strain concentration factor decreases with increasing the biaxial ratio. For $\lambda = 1$, the stress and strain concentration factor are not affected by changing the values of Poisson's ratio. Furthermore, the relation between stress or strain concentration factor and biaxial ration, λ is linear as shown in the figure 6 which is in agreement with derived by Peterson [14].

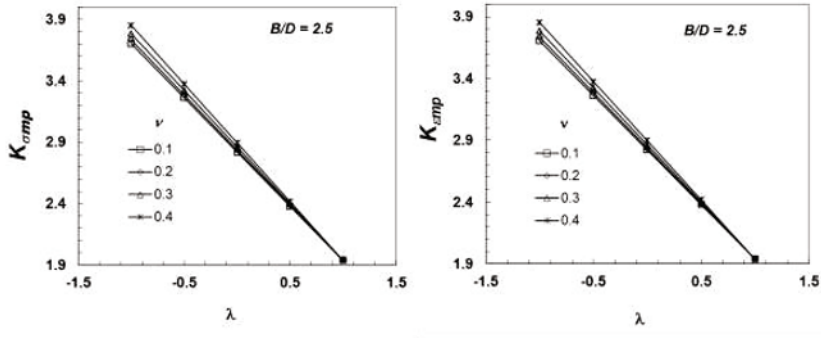

Fig. 6. The stress and, strain concentration factor at the mid point of the notch versus to biaxiality ratio λ for different ν.

Figures 7 and 8 show the contours of the resulted Von Mises stress and longitudinal stress (σ_{yy}) around the open hole. It is observed that, the values of Von Mises stress and σ_{yy} decrease by increasing the values of the biaxial ratio λ. the value of σ_{yy} around the second notch root at the upper and lower hole transform from the compression to tension by increasing the values of the biaxial ratio λ as shown in figure 8.

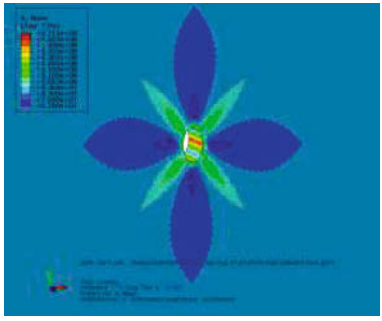

λ = -1

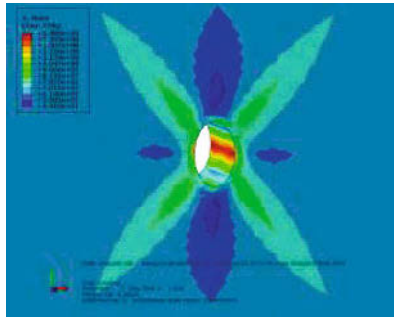

λ = -0.5

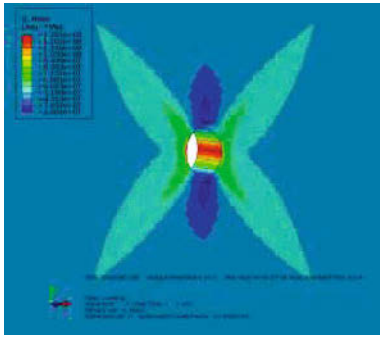

λ = 0

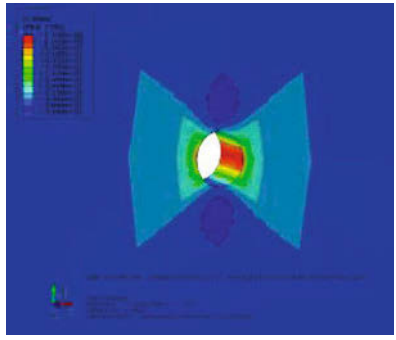

λ = 0.5

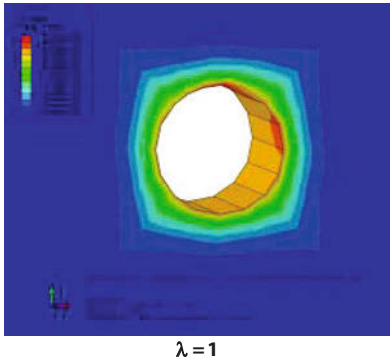

λ = 1

Fig. 7 Von Mises contours around the open hole

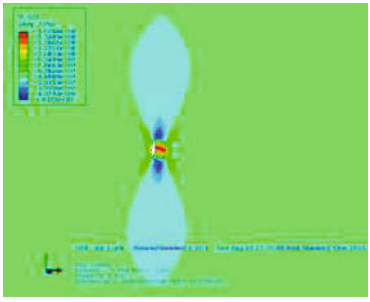

λ = -1

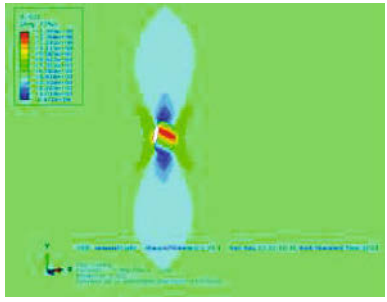

λ = -0.5

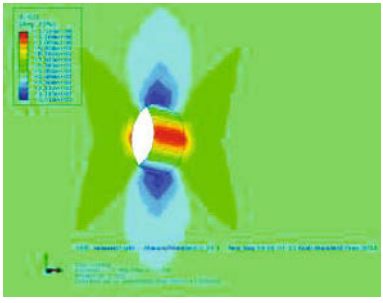

λ = 0

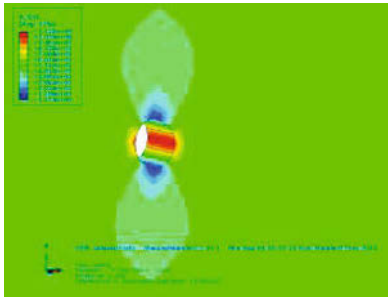

λ = 0.5

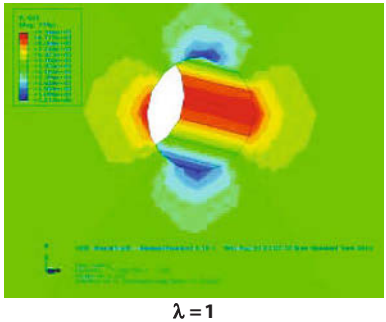

λ = 1

Fig. 8 Longitudinal stress (σ_{yy}) contours around the open hole

4. Conclusions

It can be concluded from the present numerical work that:

1. the maximum stress and strain concentration factors increase with increasing the Poisson's ratio (ν).
2. The stress and strain concentration factors increase with decreasing the biaxial ratio.
3. The effect of Poisson's ratio (ν) on stress and strain concentration factor decreases with increasing the biaxial ratio. Furthermore, For $\lambda = 1$, the stress and strain concentration factor are not affected by change the values of Poisson's ratio.

5. References

[1] Li ZH, Guo WL. Three-dimensional elastic stress fields ahead of blunt V-notches in finite thickness plates. Int J Fracture 2001;107: 53–71.

[2] Nakamura T, Parks DM. Three-dimensional crack front fields in a thin ductile plate. J Mech Phys Solids 1990;38:787–812.

[3] Wang X. Elastic T-stress solutions for semi-elliptical surface cracks in finite thickness plates. Eng Fract Mech 2003:731–56.

[4] Li ZH, Guo WL, Kuang ZB. Three-dimensional elastic stress fields near notches in finite thickness plates. Int J Solids Struct 2000;37: 7617–31.

[5] Yang Z, Guo WL, Xu X. Three-dimensional elastic stress fields near notches in finite thickness bimaterial plates. J Mech Strength 2003;25:90–4.

[6] She CM, Guo WL. Numerical investigations of maximum stress concentration at elliptic holes in finite thickness piezoelectric plates. Int J Fatigue 2006;28:438–45

[7] Amr A. Abd Elhady. Stress and strain concentration factors for plate with small notch subjected to biaxial loading – Three dimensional finite element analysis. Ain Shams Engineering Journal (2010) 1, 139–145

[8] She CM, Guo WL. Three-dimensional stress concentrations at elliptic holes in elastic isotropic plates subjected to tensile stress. Int J Fatigue 2007;29:330–335

[9] Kotousov A, Wang CH. Three-dimensional stress constraint in an elastic plate with a notch. Int J Solids Struct 2002;39:4311–26.

[10] Peishi Yu, Wanlin Guo, Chongmin She, Junhua Zhao The influence of Poisson's ratio on thickness-dependent stress concentration at elliptic holes in elastic plates International Journal of Fatigue 30 (2008) 165–171 (Peishi et al., 2008)

[11] Tlilan H. M. Effect of Poisson's Ratio on the Elastic Strain Concentration Factor of Notched Bars under Static Tension and under Pure Bending Jordan Journal of Mechanical and Industrial Engineering Volume 4, Number 6, December 2010 (Tlilan, 2010)

[12] ABAQUS user's manual version 6.3. Pawtucket, RI: Hibbitt, Karlsson and Sorensen Inc.; 2002.

[13] zheng Yang, Chang-Boo Kim, Chongdu Cho, Hyeon Gyu Beom "The concentration of stress and strain in finite thickness elastic plate containing a circular hole" International Journal of solid and Structures, 45 (2008) 713-731.

[14] Peterson RE. Stress concentration factors. New York: John Wiley and Sons; 1997.

Characterization of Minerals, Metals, and Materials 2016
Edited by: Shadia Jamil Ikhmayies, Bowen Li, John S. Carpenter, Jiann-Yang Hwang, Sergio Neves Monteiro, Jian Li, Donato Firrao, Mingming Zhang, Zhiwei Peng, Juan P. Escobedo-Diaz, and Chenguang Bai
TMS (The Minerals, Metals & Materials Society), 2016

Methodology for Determining Spall Damage Mode Preference in Shocked FCC Polycrystalline Metals from 3D X-Ray Tomography Data

A.D. Brown[1], Q. Pham[2], P. Peralta[2], B.M. Patterson[3], J.P. Escobedo-Diaz[1], S.N. Luo[4], D. Dennis-Koller[3], E.K. Cerreta[3], D. Byler[3], A. Koskelo[3], X. Xiao[5]

[1]SEIT, The University of New South Wales; Northcott Dr.; Canberra, ACT, 2610, Australia
[2]Arizona State University; 501 E. Tyler Mall; Tempe, AZ, 85287, USA
[3]Los Alamos National Laboratory; Los Alamos, NM, 87545, USA
[4]Peac Institute of Multiscale Sciences; 2nd Section Chuanda Rd.; Chengdu, 610207, China
[5]Argonne National Laboratory; 9700 S. Cass Ave.; Lemont, IL, 60439, USA

Keywords: X-ray tomography, spall, shock loading, microstructure, copper

Abstract

Three-dimensional X-ray tomography (XRT) provides a non-destructive technique to determine the location, size, and shape of spall damage within shock loaded metals. Polycrystalline copper samples of varying thermomechanical histories were shocked via plate impacts at low pressures to ensure incipient spall conditions. Additionally, samples of similar heat-treated microstructures were impacted at various loading rates. All 3D XRT volumetric void data underwent smoothing, thresholding, and volumetric sieves. The full inertia tensor was found for each void, which was used to create best fit ellipsoids correlating shape to damage modes. Density distributions were plotted for the best-fit ellipsoid semi-axes aspect ratios a/c and b/c, where, $a \leq b \leq c$. It was found that >60% of voids in heat-treated samples resembled transgranular damage, whereas >70% of voids in the rolled sample resembled intergranular damage. Preliminary analysis also clearly indicates an increase of void coalescence with decreasing tensile loading stress rates for impacted samples of similar microstructures.

Introduction

Dynamic damage formation in materials subjected to high stress and strain rate conditions resulting from the propagation of shock waves is a complex process affected by the microstructure, intrinsic and extrinsic defects, and the loading profile, or, shock wave shape [1-17]. Spall damage is the primary damage mode in metallic materials subject to shock loading and occurs when tensile release waves from an impact interact and exceed the tensile strength of the material, resulting in void nucleation, growth, and coalescence in the form of a spall plane [1-3]. Recent studies on shocked copper have made progress in linking the microstructure to damage development [8-16], however, determining the mechanisms governing the spall damage process also requires careful consideration of the loading profile for a complete analysis on damage development [17]. This mechanism interplay is the focus of the work presented here using 3D XRT analysis of spalled copper polycrystals (PCs) of varying thermomechanical histories and loading conditions.

Studies have shown statistical preference for spall damage being present at grain boundaries (GBs) with misorientation angles between 25° and 50° in incipiently spalled copper PCs of varying thermomechanical histories [9,13-15,17]. It has become widely accepted that

special Σ1 and Σ3 GBs are resistant to void nucleation [8-17]. Additionally, it has been shown that incoherent Σ3 boundaries, in the form of terminated twins at the tips of annealing twins, are susceptible to damage nucleation [8,9,14] and is consistent with molecular dynamics simulations [18,19]. The inclination of GBs with respect to the shock direction have been studied by Fensin et al. [16] and Krishnan et al. [15]; concluding that GBs oriented 67° to 90° from the shock direction in 2D and adjacent GBs with high Taylor factor mismatches along both the 3D crystallographic shock and GB normal direction are most likely to experience spall nucleation and growth, respectively. The preference between inter- and transgranular damage present within incipiently spalled copper PCs of varying thermomechanical histories using 3D XRT has been qualitatively investigated by Brown et al. [13,14], concluding that plastic pre-strain from cold rolling forces spall nucleation and growth to be dominant at the GBs, indicative of void shapes resembling flat sheets, whereas heat treated samples contained high concentrations of spherical and oblate ellipsoidal shapes, indicative of transgranular and coalesced damage, respectively. Escobedo et al. [17] varied the loading history of heat treated copper PCs and found that advanced stages of damage growth and coalescence from samples experiencing slower tensile stress rates. This work aims to provide a quantitative technique to determine damage mode preference and the level of damage growth and coalescence as functions of microstructure and loading histories from 3D XRT data collected from previous shock experiments [13,14,17].

Experimental Procedures

All target materials were prepared using Hitachi 99.995% pure copper or 99.999% pure, oxygen-free high-conductivity (OFHC) copper; additional information on the thermomechanical target manufacturing processes, microstructural analysis, impactor-target experimental procedures, and diagnostics tools for samples 1 and 2 and samples 3 and 4 may be found in Brown et al. [14] and Escobedo et al. [17], respectively. Table 1 contains relevant information on the target samples studied in this work and note that sample 1 contains pre-existing plasticity from as-received (AR) rolling conditions whereas samples 2-4 all underwent similar heat treatments (HT).

Table I: Impactor-target geometry and shock parameters for each sample.

Sample #	Impactor Velocity (m/s) / Thickness (mm)	Target Thickness (mm)	σ_{shock} (GPa)	σ_{spall} (GPa)	# of Voids	Av. Void Vol x 10^3 (μm^3)
1	205 / 0.5	1.0	4.11	1.22	457	182
2	155 / 0.5	1.0	3.07	1.56	533	5.19
3	91 / 1.5	3.0	1.60	1.24	409	71.1
4	92 / 2.5	6.0	1.62	1.03	185	192

Rectangular sections with a 1mm x 1mm cross-section were exhumed from the central spall zone in samples 1 and 2, whereas ~2mm diameter cylindrical cross-sections were exhumed from the central spall zone in samples 3 and 4 for 3D XRT analysis. X-ray tomography was performed on exhumed sections from samples 1, 3, and 4 at Los Alamos National Laboratory (LANL) with resolution of ~2.24 m per pixel, whereas sample 2 was scanned at the Advanced Photon Source (APS) at Argonne National Laboratory at beamline 2-BM with resolution of ~0.65 m per pixel. Beam conditions for LANL and the APS may be found in [20] and [14], respectively. It was determined by Patterson et al. [20] that a minimum 1,000 voxels (cubic pixels) are required for maintaining less than 10% absolute error for accurately rendering the shape of an object, thus all XRT datasets were sieved to a minimum of 1,000 voxels for the shape fitting analysis used in this work. All XRT datasets underwent careful smoothing and thresholding processes before applying the 1,000 voxel volumetric sieve. Voids appearing at the edges of the dataset were removed in the software using a "border kill" function, as these features cannot be properly characterized by volume or shape.

The moments of inertia are mathematical properties that are determined by the shape and volume distribution in 2D or 3D space with respect to a reference axis [20]. The Avizo® software package was used to obtain the full inertia tensor of each spall damage site of at least 1,000 voxels in volume for each dataset. Each inertia tensor may be used to fit individual voids to a best fit ellipsoid for damage mode analysis. Solving for the semi-axes governing these ellipsoid shapes requires the following steps using the full inertia tensors obtained from Avizo® [21], which are defined as; in this case the z-axis is taken as the reference direction:

$$M_{1z} = \frac{1}{A(X)} \int z dx dy dz, \tag{1}$$

$$M_{2z} = \frac{1}{A(X)} \int (z - M_{1z})^2 dx dy dz, \tag{2}$$

$$M_{xz} = \frac{1}{A(X)} \int (x - M_{1x})(z - M_{1z}) dx dy dz, \tag{3}$$

where, Eqs. (1), (2) and (3) are the first and second order moments of inertia, respectively. Classically the moments are defined using a combination of the other two reference axes [21], however, as seen in equations 1 and 2, Avizo® defines the inertia terms with respect to their own axis and uses a summation in the discrete case to approximate the integrals from the volumetric data. The eigenvalues of the full inertia tensor are taken for each void and the principal moments are taken as $M_{2x} \geq M_{2y} \geq M_{2z}$. To relate the principal moments of inertia to the semi-axes of a best fit ellipsoid, the principal moments of inertia are represented using the integral in Eq. 2 and transformed into spherical coordinates to map an ellipsoid into a unit sphere:

$$M_{2z} = \frac{1}{A(X)} \int (cz' - cM_{1z}')^2 |J| dx' dy' dz' \tag{4}$$

defining,

$$x' \equiv \frac{x}{a}, y' \equiv \frac{y}{b}, z' \equiv \frac{z}{c} \tag{5}$$

$$J = \left|\frac{\partial(x,y,z)}{\partial(x',y',z\prime)}\right| = abc \tag{6}$$

and substituting Eqs. 5 and 6 into Eq. 4 yields,

$$M_{2z} = abc\frac{1}{A(X)}\int_0^1\int_0^{2\pi}\int_0^{\pi} c^2 r^4 \cos^2\varphi \sin\varphi d\varphi d\vartheta dr \tag{7}$$

where a, b, and c are the corresponding semi-axes of an ellipsoid along the x, y, and z-axes, respectively, and J is the Jacobian. Solving the integral in Eq. 7 and substituting:

$$\frac{1}{A(X)} = \frac{M}{\frac{4}{3}\pi abc} \tag{8}$$

yields an expression relating the principal moment of inertia to an ellipsoid's semi-axis:

$$M_{2z} = \frac{1}{5}Mc^2 \tag{9}$$

where M is the volume of the object and cyclical substitution of x and y into Eq. 9 may be done to relate the principal moments M_{2x} to a and M_{2y} to b. For emphasis, typical relationships between the principal moments and ellipsoid semi-axes are proportional to the sum of the squares of the other two semi-axes terms as explained in Wang et al. [21], however, Eq. 9 is obtained by correctly solving the moments as defined by the software [22]. Following the previously prescribed convention relating the three principal moments the semi-axes of best fit ellipsoids will always be defined as $c \geq b \geq a$. The volume term, M, becomes irrelevant to the analysis process because the ratios of the semi-axes a/c and b/c will be used to quantify void shapes damage modes.

Results and Discussions

Inspection of the thresholded and sieved 3D XRT data enables preliminary qualitative analysis on the expected amount of inter- and transgranular damage present in the target samples, as well as the evolution of void growth and coalescence. Renderings for all datasets are shown in Fig. 1. Damage mode preference and the maturity of void coalescence clearly vary between samples. Sample 1 appears to have a large amount of thin, sheet-like voids that have experienced quite a bit of growth, indicative of intergranular damage mode preference. Samples 2 and 3 appear to have a large amount of spherical shaped voids, indicative of transgranular damage mode preference, and, finally, sample 4 contains long "string of pearls" voids, indicative of heavy damage coalescence.

Each void underwent the ellipsoid shape fitting process outlined in the previous section with their resulting semi-axes aspect ratios a/c and b/c plotted against one another. Figure 2 shows how differences in a/c and b/c change the characteristic shape of the fitted void. As a/c and b/c approach 1 the resulting spheroid is indicative of transgranular damage, as voids have been shown to open as octahedra in FCC single crystals [23]. As a/c approaches 0 for a constant b/c, the resulting shape fit becomes a flattened disk, indicative of a void following a GB interface through the thickness of the material. As each aspect ratio approaches intermediate values, coalescence of two or more voids is the primary representative damage mode.

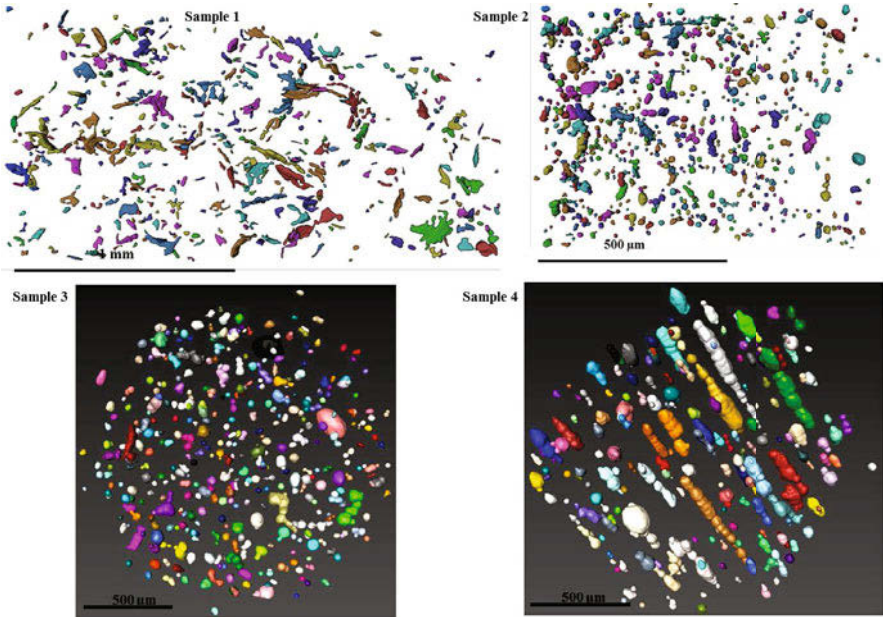

Figure 1. Spall damage renderings from 3D XRT data for target samples 1-4. The shock direction is out of the page and void colors are for visual aide only. Sample 1 and 2 renderings are from [14].

From Figure 2 it is clear that the inertial shape fitting process matches the preliminary visual inspection observations: sample 1 showing a distinct lack in spheroid voids and a cluster of sheet-like voids, samples 2 and 3 showing clusters toward the spheroid regime, and sample 4 showing a wide range in shapes of low to moderate aspect ratio combinations matching the "string of pearls" void shapes. Further quantification of the aspect ratio combinations is achieved by placing the values of *a*/*c* and *b*/*c* into 10 bins ranging from 0-1, as seen in Figure 3.

Sample 1, which contains plastic pre-strain in the grain bulk from the cold rolling process, has 93% of its voids with an *a*/*c* aspect ratio ≤0.5 with ~60% of voids falling into the 0.1-0.3 bin range, while also having 73% of its voids with an *b*/*c* aspect ratio ≤0.6. This clearly indicates that >70% of all damage within sample 1 is indicative of intergranular damage, explained by the strengthening of the grain bulk with respect to the GBs and corroborated by GB statistic studies [13,14]. Samples 2-4, HT material conditions, show a drastic increase in the amount of oblate and spheroid ellipsoids as indicated by the rightward shift in both the *a*/*c* and *b*/*c* aspect ratios in Fig. 3. Samples 2 and 3 contain 38% and 22% of voids with an *a*/*c* aspect ratio ≤0.5, respectively, while containing 80% and 90% of its voids with a *b*/*c* aspect ratio ≥0.6, respectively. There is a clear shift towards spheroid shaped voids indicative of ~60% and ~80% transgranular damage present for the HT samples 2 and 3.

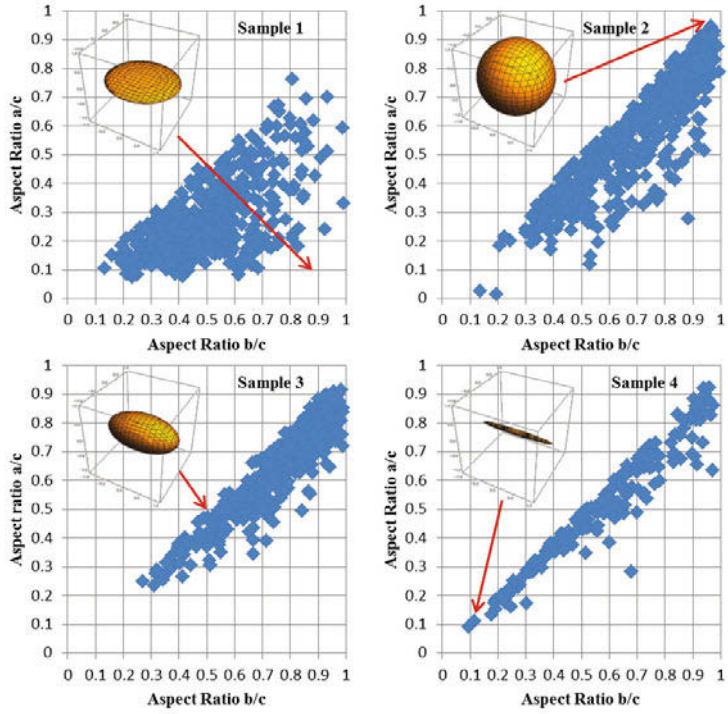

Figure 2. Best fit ellipsoid semi-axes ratio plots for samples 1-4. Arrows indicate the aspect ratio combinations resulting in their respective volumetric shapes for visual aide.

Lastly, sample 4 is most meaningfully compared to sample 3. They were manufactured to maintain the same amount of GB densities with respect to varying loading rates to probe the effect of a longer sustained stress pulse in shocked PC Cu [17]. Figure 3 illustrates that sample 4, which experienced the lowest stress rate and largest region under tension, has the most even, or, "Gaussian," distribution of void fractions for aspect ratios *a*/*c* and *b*/*c*. Sample 4 contains 48% of voids with an *a*/*c* aspect ratio ≤0.5 and 35% of voids with a *b*/*c* aspect ratio ≤0.5. This indicates that ~50% of the dataset is indicative of void coalescence, which is to be expected from the visual inspection of the spall plane in Fig 1.

It is clear that interplay between microstructure and loading rate exists for determining the preferential damage mode experienced by shocked FCC metals, in this instance PC Cu. Additional investigation between materials of differing thermomechanical histories coupled with varying loading profiles is imperative to gain a better understanding of damage kinetics in shocked materials, which aide the improvement of modeling efforts such as [15].

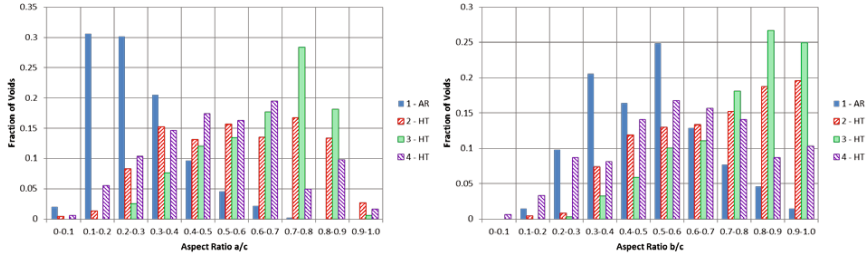

Figure 3. Void fraction distribution plots for aspect ratios *a*/*c* (left) and *b*/*c* (right) in each sample.

Conclusions

A methodology has been suggested for quantifying damage mode preference in shocked FCC metals using individual damage sites' inertia tensors obtained from 3D XRT. Since XRT is a nondestructive technique for acquiring data on the volumetric distribution of voids it becomes a simple exercise to locate specific sites of interest within the post mortem specimens for additional data acquisition such as electron backscattering diffraction. Preliminary conclusions drawn from this work in addition to providing an outline for a successful characterization method include: spall damage nucleation and growth is forced to the GBs when the sample contains pre-existing plasticity from cold rolling, damage nucleates throughout the spall plane with the removal of plasticity via annealing processes, and that decreasing the tensile loading rate / increasing the volume of material under tension greatly increases the maturity of void growth and coalescence in the spall process.

Acknowledgements

This research work was funded by LANL under LDRD #20060021DR, LDRD-DR #20100026 and by the Department of Energy, NNSA, under SSAA Grants #DE-FG52-06NA26169, DE-FG52-10NA29653, and DE-NA0002005 and APS General User Proposal 35561. Los Alamos National Laboratory is operated by LANS, LLC, for the NNSA of the US Department of Energy under contract DE-AC52-06NA25396. Eric Loomis, Pat Dickerson (LANL), Damian Swift (LLNL), David Wright, and Dallas Kingsbury (ASU) are thanked for their help during the various phases of the research work. Access to the TRIDENT Facility & Electron Microscopy Laboratory at LANL, Pavel Shevchenko at APS 2-BM, as well as the Center for High Resolution Electron Microscopy and the Mechanical Testing Laboratory at ASU is gratefully acknowledged.

References

[1] D.R. Curran, L. Seaman, D.A. Shockey, "Dynamic Failure of Solids," *Physics* Reports, 147 (5 & 6) (1987), 253-388.
[2] D.E. Grady, "The Spall Strength of Condensed Matter," *Journal of the Mechanics and Physics of Solids*, 36 (3) (1988), 353-384.
[3] M.A. Meyers, *Dynamic Behavior of Materials* (John Wiley & Sons, New York, 1994).

[4] R.W. Minich et al., "Effect of Microstructural Length Scales on Spall Behavior of Copper," *Metallurgical and Materials Transactions A*, 35 (A) (2004), 2263-2673.
[5] B.L. Henrie et al., "Investigating Inciepiently Spalled Tantalum through Multiple Planes and Serial Sectioning," *AIP Conference Proceedings*, 845 (2005), 627.
[6] Czarnota et al., "Modelling of Dynamic Ductile Fracture and Application to the Simulation of Plate Impact Tests on Tantalum," *Journal of the Mechanics and Physics of Solids*, 56 (2008), 1624-1650.
[8] P. Peralta et al., "Characterization of Incipient Spall Damage in Dhocked Copper Multicrystals," *International Journal of Damage* Mechanics, 18 (2009), 393-413.
[9] L. Wayne et al., "Statistics of Weak Grain Boundaries for Spall Damage in Polycrystalline Copper," *Scripta Materialia*, 63 (2010), 1065-1068.
[10] J.P. Escobedo-Diaz, "Effects of Grain Size and Boundary Structure on the Dynamic Tensile Response of Copper," *Journal of Applied Physics*, 110 (2011), 033513.
[11] E.K. Cerreta et al., "Early Stage Dynamic Damage and the Role of Grain Boundary Type," *Scripta Materialia*, 66 (2012), 638-641.
[12] J.P. Escobedo, E.K. Cerreta, D. Dennis-Koller, "Effect of Crystalline Structure on Intergranular Failure during Shock Loading," *JOM*, 66 (1) (2014), 156-164.
[13] A.D. Brown et al., "3-D Characterization of Global and Local Microstructural Effects on Spall Damage in Shock Loaded FCC Metals: Experimental and Modeling," *ASME Int., Mechanics of Solids, Structures and Fluids*, IMECE2013-65642 (2013), V009T10A033.
[14] A.D. Brown et al., "Microstructural Effects on Damage Nucleation in Shock-Loaded Polycrystalline Copper," *Metallurgical and Materials Transactions A*, 46 (10) (2015), 4539-4547.
[15] K. Krishnan et al., "Three-Dimensional Characterization and Modeling of Microstructural Weak Links for Spall Damage in FCC Metals," *Metallurgical and Materials Transactions A*, 46 (10), 4527-4538.
[16] S.J. Fensin et al., "Effect of Loading Direction on Grain Boundary Failure Under Shock Loading," *Acta Materialia*, 64 (2014), 113-122.
[17] J.P. Escobedo et al., "Influence of Shock Loading Kinetics on the Spall Response of Copper," *Journal of Physics: Conference* Series, 500 (11) (2014).
[18] W. Han et al., "Deformation and Spallation of Shocked Cu Bicrystals with Σ3 Coherent and Symmetric Incoherent Twin Boundaries," *Physical Review B*, 85 (2012), 024107.
[19] E.Q. Lin et al., "Shock Response of Copper Bicrystals with a Σ3 Axisymmetric Tilt Grain Boundary," *Computational materials Science*, 59 (2012), 94-100.
[20] B.M. Patterson et al., "Dimensional Quantification of Embedded Voids or Objects in Three Dimensions using X-ray Tomography," *Microscopy and Microanalysis*, 18 (2012), 390-398.
[21] L. Wang, Y.J. Park, Y. Fu, "Representation of Real Particles for DEM Simulation using X-ray Tomography," *Construction and Building Materials*, 21 (2007), 338-346.
[22] Avizo® 8 Reference Guide (2013).
[23] A.L. Stevens, L. Davison, W.E. Warren, "Spall Fracture in Aluminum Monocrystals: A Dislocation Dynamics Approach," *Journal of Applied Physics*, 43 (1972), 4922-4927.

Characterization of Minerals, Metals, and Materials 2016

Minerals

Session Chairs:
Bowen Li
Zhiwei Peng

Characterization of Minerals, Metals, and Materials 2016
Edited by: Shadia Jamil Ikhmayies, Bowen Li, John S. Carpenter, Jiann-Yang Hwang, Sergio Neves Monteiro, Jian Li, Donato Firrao, Mingming Zhang, Zhiwei Peng, Juan P. Escobedo-Diaz, and Chenguang Bai
TMS (The Minerals, Metals & Materials Society), 2016

MINERALOGICAL ANALYSIS OF NICKEL/COPPER POLYMETALLIC SULFIDE ORE BY X-RAY DIFFRACTION USING RIETVELD METHOD

Guangshi Li [1], Hongwei Cheng [1,2], Cong Xu [1], Changyuan Lu [1], Xionggang Lu [1,2], Xingli Zou [1,2], Qian Xu [1,2]

[1]School of Materials Science and Engineering, Shanghai University, 200072, Shanghai, People's Republic of China

[2]State Key Laboratory of Advanced Special Steel, Shanghai University, 200072, Shanghai, People's Republic of China

Keywords: polymetallic sulfide ore; X-ray Diffraction; Rietveld method; mineral.

Abstract

The analysis of mineralogical characteristics has important significance in comprehensive utilization of polymetallic sulfide mineral resources. The wavelength dispersive X-ray fluorescence (WDXRF) and X-ray diffraction were performed for the standardless quantitative analysis of Ni/Cu polymetallic sulfide ore. On the basis of fundamental parameter approach and Rietveld refinement Method, the validity of mineralogical identification and quantification was confirmed for analyzing this complex sulfide ore. The quantification results were in good agreement with elemental concentrations determined by XRF and ICP, which has explained the subtle differences among four samples in the range of different granularity (>10mm; 6-10mm; 1-6mm; <1mm;). In addition, the thermogravimetric curves and magnetic hysteresis curves, as well as element distribution map characterized by SEM-EDS, shown tiny differences among four samples. These results indicate that quantitative phase analysis using the Rietveld method represents a new powerful and fast tool in studies of the complex sulfide deposit.

Introduction

The polymetallic sulfide deposit is one of the most valuable and economically important nickel sources in the world. With continuously exploiting, the nickel resources are gradually exhausted. As it is of great urgent to seek a way of sustainable development of Ni/Cu polymetallic sulfide mineral, the wide application, strategic importance and industrial value of nickel. Many researches have studied the recovery of valuable metals from Ni/Cu polymetallic sulfide mineral in a laboratory scale [1-3]. Previous studies focused on the roasting/leaching process and phase transformation mechanism [4, 5]. However, recent efforts to develop the characterization of polymetallic sulfide minerals have been heavily addressed by several groups [6-8]. The Characterization of mineralogical properties is of crucial importance in the metallurgical process [9-11]. Currently, the XRD based Rietveld refinement method [12-15] has been carried out for the quantification phase analysis of various minerals and metallurgical processes [16-22]. Prandel has investigated the qualitative and quantitative composition of a hard-setting soil using the XRF, and Rietveld refinement based XRD techniques, and the XRD results shown a good agreement with XRF methods [23]. However, The Ni/Cu polymetallic sulfide mineral, which was collected from Sinkiang, has not previously been studied by the WDXRF and Rietveld based XRD method. In this paper, four different sizes range of Ni/Cu polymetallic sulfide mineral samples

were investigated using the XRD-Rietveld method based on the element concentrations obtained by WDXRF.

Experimental methods

A. Sample Preparation

The Ni/Cu sulfide ores, which were collected from Ca La Tonke (Sinkiang, China), were washed with deionized water three times, and then air-dried in the oven at 50ºC for 8 h. The dried ore was put through a series of graded sieves (S1: Φ>10mm; S2: 6mm<Φ<10mm; S3: 1mm<Φ<6mm; S4: Φ<1mm). Four samples were ground to fine powder (crushed in a wear resistant cast iron mortar, and then grinded in an agate mortar). 5g of four samples were respectively pressed into disks in a stainless steel module (8 mm i.d.) with the indication on the pressure gauge of 4.2 MPa using a hydraulic press. Then the specimens were treated by spray-gold.

B. Characterization Methods

Wavelength dispersive X-ray fluorescence (WDXRF) and inductively coupled plasma atomic emission spectrometry (ICP-AES)

The fine graded powder samples were randomly selected from the finely mineral powder and analyzed in X-ray fluorescence spectrometer (XRF-1800, SHIMADZU LIMITED) using sequential scanning (4º/min, 40kV-95mA-Rh source) and semi-quantitative mode. Meanwhile, the investigation was carried out for the precise determination of several important elements (such as Fe, Ni, Cu, etc.) of different sizes range samples by the ICP-AES (PERKINE 7300DV).

X-ray powder diffraction (XRD) and Quantitative phase analysis (QPA)

Four fine powder samples were grinded to mineral grain diameter under 200 mesh, and then examined in a Bruker-AXS D8 ADVANCE diffractometer, with Cu radiation (40 kV, 40 mA) ,with 0.02 º per step and 3s time per step(2 theta range from 10 º to 100 º). And the LynxEye detector were used to collect diffraction data covering 2.93 º(2 theta) of the pattern simultaneously.

Quantitative phase analysis was performed using the fundamental parameter approach (FPA) by the TOPAS 4.2 program (Bruker AXS). This software was based on the Rietveld full-pattern refining principle that first presented by Hill and Howard [24]. Bish and Howard [18] have applied the matrix flushing approach to the Rietveld refinement and presented that the weight fraction of phase A in an n phase mixture was given by the equation:

$$\omega_A = \frac{S_A(ZMV)_A}{\sum_{k=1}^{n} S_k(ZMV)_k}$$

In this context, S_A is the Rietveld scale factor, $(ZMV)_A$, which can be calculated from the known crystal structure information, is a constant for phase A. And the crystal structure files of all phases were obtained from the American Mineralogist Crystal Structure Database (http://www.minsocam.org/MSA/Crystal_Database.html) [25].

Other characterization method

Four gold-sprayed wafer specimens were characterized by SEM-EDS (FESEM; SU70, Hitachi, Japan). The elements distribution was revealed by the EDS mapping in SU70

within the TEAMTM EDS Analysis System. The thermogravimetric analysis (TGA) was adopted to evaluate the thermal stability of the powder samples (S_1, S_2, S_3 and S_4) using a Thermogravimetric analyzer (NETZSCH STA 449 F3 Jupiter) under air atmosphere with a flow rate of 20 ml min^{-1}, and heated to 1000 ºC (10 ºC min^{-1}). The magnetic hysteresis loops of S_1 and S_2 were obtained by a vibrating sample magnetometer (VSM, Lakeshore7407, CHINA TREND LIMITED).

Results and Discussion

A. element and phase Quantitative analysis of the Ni/Cu polymetallic sulfide mineral

Table 1. Elemental analysis of four samples (S_1, S_2, S_3 and S_4) by WDXRF and ICP-AES

	S_1 (wt%)		S_2 (wt%)		S_3(wt%)		S_4 (wt%)	
	XRF	ICP	XRF	ICP	XRF	ICP	XRF	ICP
Fe	37.16	44.63	29.05	37.43	32.59	42.05	28.71	38.47
Co	0.16	0.11	0.14	0.10	0.15	0.11	0.13	0.10
Ni	2.62	2.69	2.00	2.20	2.45	2.63	2.20	2.36
Cu	3.19	2.93	2.30	2.31	2.91	2.96	2.67	2.93
S	25.71	**	20.31	**	22.78	**	17.38	**
Na_2O	0.84	0.57	1.44	1.16	0.84	0.73	0.65	0.75
MgO	4.03	1.22	5.74	2.30	5.25	1.68	5.48	1.88
Al_2O_3	3.35	1.89	5.56	4.10	3.86	2.51	3.70	2.51
SiO_2	13.51	6.91	22.89	13.98	16.18	9.31	17.01	9.73
K_2O	0.49	0.23	0.82	0.52	0.62	0.31	0.58	0.31
CaO	1.62	0.83	2.29	1.11	2.33	1.16	1.12	1.75
Total	92.70	62.00	92.54	65.50	90.26	63.46	82.66	60.81

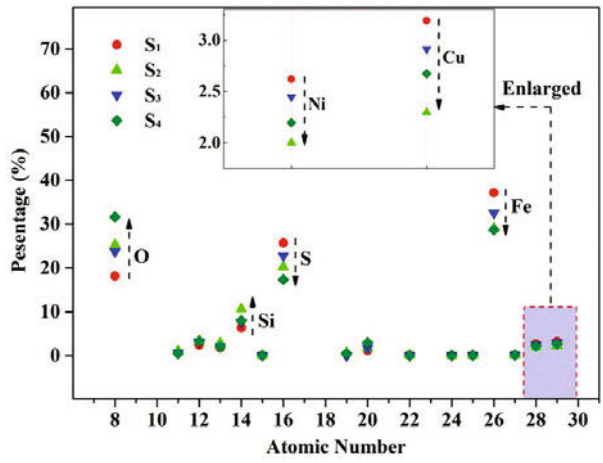

Figure 1. The comparison of main elements in different sizes range samples using WDXRF

The chemical composition of the Ni/Cu polymetallic sulfide mineral samples were shown in Table 1 by WDXRF and ICP-AES analyses. The results of four samples in the range of different granularity (S_1, S_2, S_3 and S_4) presented that the polymetallic sulfide deposit contained a high level of Fe, and the concentration of Ni or Cu was around 2-3% (the percentage of Cu is slight higher than that of Ni). There should be some minor differences between the results of WDXRF and ICP-AES, which might be

the result of fluorescent effect of iron by WDXRF. Figure 1 was clearly reflected the content and change trends of O, Si, S, Ni, Cu and Fe among four samples. As observed in Figure 2, the content of Ni and Cu followed similar trends: S_1>S_3>S_4>S_2, and were the same order of magnitude. While the trend of Fe and S (S_1>S_3>S_2>S_4) was slightly different from that of Ni and Cu. This indicated that sample S_2 and S_4 were with a lower concentration of Ni and Cu, and the contents of O (S_1<S_3<S_2<S_4) and Si (S_1<S_3<S_4<S_2) also revealed that sample S_2 was with maximum concentration of gangue, sample S_4 came the second. The analysis of the main elements indicated that the range of granularity had great effects on the concentration of elements.

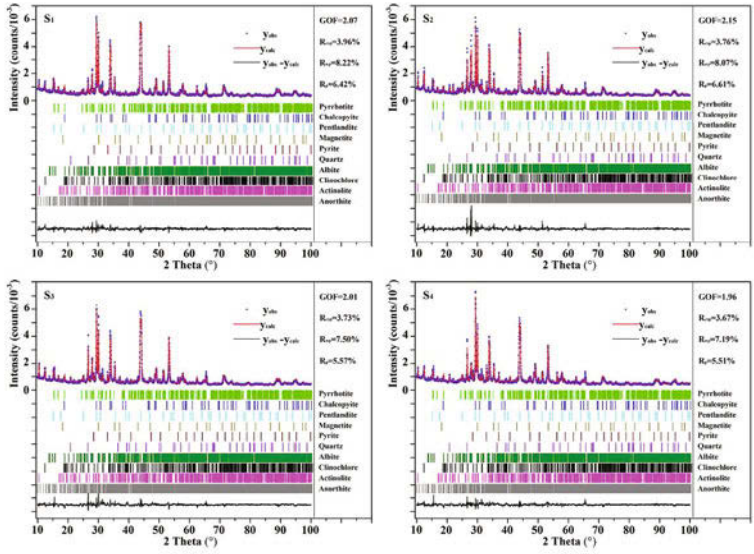

Figure 2. Refinements obtained using the Rietveld method based on the fundamental parameter approach with the TOPAS software.

Figure 2 presented the results of the Rietveld refinement of four mineral samples. In the figure, y_{obs} states for the observed pattern using X-ray diffractometer, y_{calc} states for the calculated pattern using TOPAS software, y_{obs}- y_{calc} states for the residual profile and the vertical lines of colors states for the Bragg peak positions of different phases. The R-factors, which are frequently used for the judgement of the refinement, is defined as[26]:

$$R_{wp} = \Sigma_{2\theta}\left(\frac{y_{obs(2\theta)} - y_{calc(2\theta)}}{\sigma_{2\theta}}\right)^2 / \Sigma_{2\theta}\left(\frac{y_{obs}}{\sigma_{2\theta}}\right)^2;$$

$$R_{exp} = (N - P) / \Sigma_{2\theta}\left(\frac{y_{obs}}{\sigma_{2\theta}}\right)^2 ;$$

$$\text{Gof} = R_{wp} / R_{exp}.$$

In the context, R_{wp} is the weighted profile R-factor, R_{exp} is the expected R-factor, N and P state for the number of points in the data set and parameters adjusted in the refinement respectively, and the "goodness of fit" can be abbreviated to "GOF".

Table 2. The QPA of the minerals in four samples (S_1, S_2, S_3 and S_4).

Mineral & Crystaline Structure Database	Weight (%) of four samples			
	S_1	S_2	S_3	S_4
Pyrrhotite COD#2104750	58.52	43.22	53.54	41.85
Pentlandite COD#90006125	6.81	4.70	6.50	6.30
Chalcopyite COD#2104753	10.83	7.00	10.61	10.31
Magnetite COD#1011084	3.71	4.00	3.78	3.71
Pyrite ICSD#10422	0.53	1.74	2.14	3.53
Quartz COD#9012600	3.96	6.21	5.61	7.46
Albite COD#9002197	4.57	12.73	4.21	8.06
Clinochlore COD#9008042	2.11	4.43	3.18	5.71
Actinolite ICSD#68319	2.00	4.67	2.13	3.82
Anorthite ICSD#86319	6.95	11.30	8.29	9.24

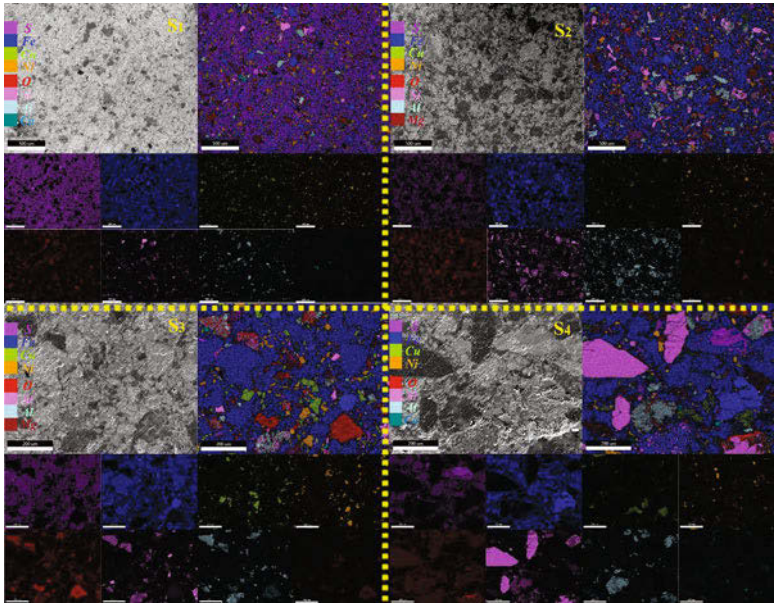

Figure 3. SEM backscattered electron micrographs (grayscale) and EDS mapping (color graphic) of the elements (S, Fe, Cu, Ni, O, Si, Al and Mg) over the whole wafer mineral samples.

The value of R-factors and GOF indicated that the minimization and the convergence of the refinement was authentic and convincible. And the quantification of minerals in the range of different granularity were shown in Table 2. It has been observed that high amounts of Pyrrhotite (around 40-58%) in all samples, and that of sample S_2 and S_4 were less than S_1 and S_3. The trend was consistent with the results of the XRF (Fe: S_1>S_3>S_2>S_4). The mass fractions of Pentlandite and Chalcopyite were also agree with the trend of Ni and Cu concentration by XRF (S_1>S_3>S_4>S_2).Thus, almost all Ni and Cu, shown in table 1, were in Pentlandite and Chalcopyite minerals respectively. And most Fe was in Pyrrhotite (Fe_7S_8), the remaining one was in Pentlandite ($(Fe,Ni)_9Fe_8$),

Chalcopyite ($CuFeS_2$) , Pyrite (FeS_2) and Magnetite (Fe_3O_4). The results suggested that the trends of the concentration of Ni, Cu and Fe were consistent with the mass percentage of Pentlandite, Pyrrhotite and Chalcopyite respectively. As shown in Figure 3, the element distribution of four samples were found no significant differences. And the result might be that the X-ray mapping could not really capture the difference of the element distribution in the range of different granularity.

B. other properties of the Ni/Cu polymetallic sulfide mineral

The TG measurements indicated that the reactions occurred between 420 ° C and 500 ° C (area A) with a total weight increase of around 2% in Figure 4.a. And this was mainly due to the sulfation of polymetallic sulfides and the O_2 consuming in the feeding gas correspondingly. In contrast, the mass change between 500 ° C and 640 ° C was result of the oxidation of sulfides in the samples and the SO_2 release. The decomposition of metallic sulfates might contribute the weight loss in Area C, D and E [2, 27]. As shown in Figure 4.b, S_1 and S_2 presented obviously wasp-waisted hysteresis loops. It was suggested that the main reason of "special shape" was that at least two magnetic phases with strongly contrasting coercivities must coexist [4]. And the percentage of magnetic components (Pentlandite, Pyrrhotite and Magnetite) were different between S_1 and S_2, which made the saturation intensity a slight difference.

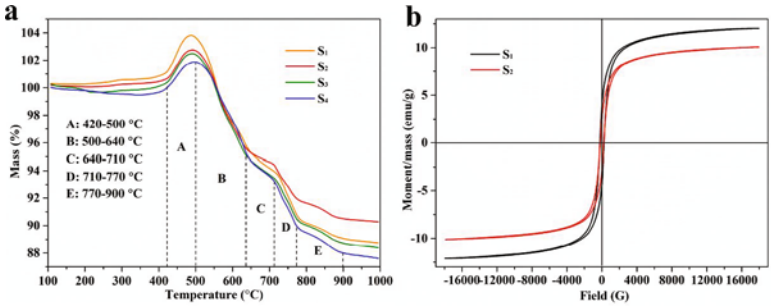

Figure 4. a. TG curves of four particle size ranges heated at 10 ° C per minute in air; b. magnetic hysteresis loops of S_1 and S_2 at room temperature obtained by vibrating sample magnetometer.

Conclusions

Those results shown that the WDXRF, ICP-AES, XRD-Rietveld refinement method, SEM-EDS, TG and magnetic hysteresis loop were efficient in investigating mineralogical properties of this Ni/Cu polymetallic sulfide mineral. The Rietveld refinement, a powerful tool for structure solution and phase quantitative analysis technique, was successfully applied to the mineral quantification of polymetallic sulfide deposit. The obtained quantification revealed that the range of different granularity obviously affected the concentration of the valuable minerals (such as Pentlandite, Pyrrhotite etc.). Nonetheless, the grain size distribution was related to the components in the mineral, the internal relations between them was unclear. Finally, the results of WDXRF were in conformity with that of the Rietveld based QPA method, which might be a new way to characterize the mineralogical properties of the Ni/Cu polymetallic sulfide mineral in the future.

Acknowledgments

This work was supported financially by Grant 2014CB643403 from the National Key Program for Basic Research of 973 Program.

References

[1]. Yu, D.W., Utigard, T.A.&Barati, M., "Fluidized Bed Selective Oxidation-Sulfation Roasting of Nickel Sulfide Concentrate: Part II. Sulfation Roasting". *Metallurgical and Materials Transactions B*,2013. 45(2): p. 662-674.

[2]. Yu, D.W., Utigard, T.A.&Barati, M., "Fluidized Bed Selective Oxidation-Sulfation Roasting of Nickel Sulfide Concentrate: Part I. Oxidation Roasting". *Metallurgical and Materials Transactions B*,2013. 45(2): p. 653-661.

[3]. Liu, X.W.*et al*, "Recovery of valuable metals from a low-grade nickel ore using an ammonium sulfate roasting-leaching process". *International Journal of Minerals, Metallurgy, and Materials*,2012. 19(5): p. 377-383.

[4]. Zhu, H.H.*et al*, "Oxidation Behavior and Mechanism of Pentlandite at 973 K (700 A degrees C) in Air". *Metallurgical and Materials Transactions B-Process Metallurgy and Materials Processing Science*,2012. 43(3): p. 494-502.

[5]. Živković, Z.i.D., Mitevska, N.&Savović, V., "Kinetics and mechanism of the chalcopyrite-pyrite concentrate oxidation process". *Thermochimica Acta*,1996. 282-283: p. 121-130.

[6]. Balić-Žunić, T., Katerinopoulou, A.&Edsberg, A., "Application of powder X-ray diffraction and the Rietveld method to the analysis of oxidation processes and products in sulphidic mine tailings". *Neues Jahrbuch für Mineralogie - Abhandlungen*,2011. 188(1): p. 31-47.

[7]. Monecke, T.*et al*, "Quantitative Phase-Analysis by the Rietveld Method Using X-Ray Powder-Diffraction Data: Application to the Study of Alteration Halos Associated with Volcanic-Rock-Hosted Massive Sulfide Deposits". *The Canadian Mineralogist*,2001. 39(6): p. 1617-1633.

[8]. Mumme, W.G., Tsambourakis, G.&Cranswick, L., "Improved petrological modal analyses from X-ray and neutron powder diffraction data by use of the Rietveld method .lll. Selected massive sulfide ores". *Neues Jahrbuch Fur Mineralogie-Abhandlungen*,1996. 170(3): p. 231-255.

[9]. Li, J.*et al*, "Applications of Rietveld-based QXRD analysis in mineral processing". *Powder Diffraction*,2014. 29(S1): p. S89-S95.

[10]. Wang, X.*et al*, "Quantitative X-ray diffraction phase analysis of poorly ordered nontronite clay in nickel laterites". *Journal of Applied Crystallography*,2011. 44(5): p. 902-910.

[11]. Li, G.S.*et al*. "Phase transformation and element migration in the oxidation process of nickel-copper sulfide ore". in *Characterization of Minerals, Metals, and Materials 2015 - TMS 2015 144th Annual Meeting and Exhibition, March 15, 2015 - March 19, 2015*. 2015. Orlando, FL, United states: Minerals, Metals and Materials Society.495-502.

[12]. Alves, M.E.*et al*, "Rietveld-based mineralogical quantitation of deferrified oxisol clays". *Australian Journal of Soil Research*,2007. 45(3): p. 224.

[13]. Rietveld, H.M., "The Rietveld method". *Physica Scripta*,2014. 89(9): p. 098002.

[14]. Rietveld, H.M., "Line profiles of neutron powder-diffraction peaks for structure refinement". *Acta Crystallographica*,1967. 22(1): p. 151-152.

[15]. Rietveld, H.M., "A profile refinement method for nuclear and magnetic structures". *Journal of Applied Crystallography*,1969. 2(2): p. 65-71.

[16]. Madsen, I.C., Scarlett, N.V.&Webster, N.A., "*Quantitative phase analysis*", in *Uniting Electron Crystallography and Powder Diffraction*. 2012, Springer. p. 207-218.
[17]. Webster, N.A.S.*et al*, "Fundamentals of Silico-Ferrite of Calcium and Aluminum (SFCA) and SFCA-I Iron Ore Sinter Bonding Phase Formation: Effects of CaO:SiO2 Ratio". *Metallurgical and Materials Transactions B*,2014. 45(6): p. 2097-2105.
[18]. Bish, D.L.&Howard, S.A., "Quantitative phase analysis using the Rietveld method". *Journal of Applied Crystallography*,1988. 21: p. 86-91.
[19]. Taylor, J.C.&Matulis, C.E., "A new method for Rietveld clay analysis. Part I. Use of a universal measured standard profile for Rietveld quantification of montmorillonites". *Powder Diffraction*,1994. 9(02): p. 119-123.
[20]. Ufer, K.*et al*, "Quantitative phase analysis of bentonites by the Rietveld method". *Clays and Clay Minerals*,2008. 56(2): p. 272-282.
[21]. Ward, C.R.&Taylor, J.C., "Quantitative mineralogical analysis of coals from the Callide Basin, Queensland, Australia using x-ray diffractometry and normative interpretation". *International Journal of Coal Geology*,1996. 30(3): p. 211-229.
[22]. Young, R.A.&Nederland, S.E.C., The rietveld method. Vol. 1. 1995*: Oxford University Press Oxford*
[23]. Prandel, L.V.*et al*, "Mineralogical analysis of clays in hardsetting soil horizons, by X-ray fluorescence and X-ray diffraction using Rietveld method". *Radiation Physics and Chemistry*,2014. 95: p. 65-68.
[24]. Hill, R.&Howard, C., "Quantitative phase analysis from neutron powder diffraction data using the Rietveld method". *Journal of Applied Crystallography*,1987. 20(6): p. 467-474.
[25]. Downs R T, H.-W.M., "The American mineralogist crystal structure database". *American Mineralogist*,2003. 88(1): p. 247-250.
[26]. Stephens, P.W., Uniting Electron Crystallography and Powder Diffraction: Chapter 2 Rietveld Refinement. NATO Science for Peace and Security Series B: Physics and Biophysics ed. Kolb U., Shankland K., Meshi L., Avilov A. &David W.I. Vol. 1. 2012*: Springer Science+ Business Media Dordrecht*
[27]. Yu, D.W.&Utigard, T.A., "TG/DTA study on the oxidation of nickel concentrate". *Thermochimica Acta*,2012. 533: p. 56-65.

Characterization of Minerals, Metals, and Materials 2016
Edited by: Shadia Jamil Ikhmayies, Bowen Li, John S. Carpenter, Jiann-Yang Hwang, Sergio Neves Monteiro, Jian Li, Donato Firrao, Mingming Zhang, Zhiwei Peng, Juan P. Escobedo-Diaz, and Chenguang Bai
TMS (The Minerals, Metals & Materials Society), 2016

STUDY ON COAL MINERALS PHASE TRANSFORMATIONS UNDER DIFFERENT COKING CONDITIONS

Shuxing Qiu, Shengfu Zhang*, Pengqi Zhang, Guibao Qiu, Qingyun Zhang
College of Materials Science and Engineering, Chongqing University, Chongqing 400044 China
*Corresponding author. Email: zhangsf@cqu.edu.cn (Shengfu Zhang)

Keywords: Minerals, Phase transformations, Coking conditions, Quantitative analysis

Abstract

The minerals in coals have a great influence on coke properties. Therefore, it is important to research the minerals phase transformations under different conditions in the coking process. X-Ray Diffraction and Mineral Quantitative Analysis Method were used to investigate blending coal minerals phase transformations under different coking conditions. The results show that with the increase of coking temperature, most of minerals contain clays and calcite changes in a certain degree. Kaolinite firstly transforms to metakaolin, then transforms to mullite, sillimanite, quartz, cristobalite and alumina. Anhydrite reacts with other minerals and makes content of itself decrease. Pyrite converts into mackinawite and iron carbon compounds, then transforms into pyrrhotite. With the increase of coking time, the species of main minerals decomposition products in blending coal coking process do not change. However, the content of quartz increases by 11.38%, the contents of cristobalite and mullite decrease by 1.52% and 8.52%, respectively.

Introduction

Minerals are a very important and complex part of coal. It is obvious that the species and content of the minerals are different between the different metamorphism degree coals. In the blast furnace process, minerals have a great impact on the coke degradation. They lead to the carbon consumption by the reduction of the oxides in the coke above 1400 ℃ and expansion of the meta-aluminosilicates in the lower zone [1,2]. Apart from that, part of minerals which contains metallic iron, pyrrhotite, iron oxides and calcium oxide can enhance the coke reactivity index(CRI), resulting in the increase of the gasification reaction rate[3-6]. Minerals in coke are usually decided by the minerals in raw coal and coking conditions. The types of minerals in the coals before and after coking are similar which mainly include clays, carbonates, minerals bearing sulfur and other minerals. Therefore, the coking condition is a key factor to the changes of minerals.

Since the coking conditions have significant influence on the minerals in coke, it is important to study coal minerals phase transformations under different coking conditions in the coking process. Mitchell researched the kinds of minerals of coals

which were heated progressively from 400 ℃ to 1400 ℃ at 100 ℃ intervals by X-ray diffraction (XRD) analyses and found that kaolinite, metakaolinite, mullite, anhydrite and anorthite were presented just in a limited temperature range [7]. Filippidis researched the minerals in two lignite samples under different temperature by using Scanning Electron Microscopy (SEM) and Energy Disperse Spectroscopy (EDS). The results showed that the calcite, quartz, kaolinite, illite and pyrite were found in the coal, and then decomposed to other minerals under a certain coking conditions [8]. Grigore researched minerals in coke which produced from carbonizing in three ovens of different capacity and carbonization parameters. It showed that the minerals in coal undergone complex reactions during the transformation of the coal to coke [9]. Although some researches about minerals transformation from coal to coke were studied, the effect of coking conditions on minerals transformations is still scarce.

The aim of this study is to identify the minerals phase transformations in coking process under different conditions deeply to observe the effect of coking conditions on minerals in coke, which will help to improve coke quality in coking process.

Experimental

Coke Preparation

The raw materials are Nantong coal (NT), Yonghun coal (YH) and Shoumei coal (SM). The proximate and ash analyses of the coke were shown in **Table Ⅰ**. The proportion of blending coal (BC) was 40%, 50% and 10% in sequence. The blending coal (<3 mm, the moisture content 10%) was charged into a coking reactor (100 mm diameter and 500 mm high) and bulk density was 0.9 kg/m^3. The coking oven was then placed in an electrically heated test oven and carbonized for 8 h by controlling the temperature of the electric heating elements so that the temperature rise curve in the coal was equivalent to that in an actual coke oven with the flue temperature of 1050 ℃. In this experimental, the coking temperature and time were studied for the effect on minerals transformations in coking process. The different coking conditions were shown in **Table Ⅱ**. The coking time was a constant value which was 8 h when the effects of coking temperature on minerals transformations were investigated. On the contrary, the coking temperature was a constant value which was 1050 ℃.

Table Ⅰ Proximate and elements analysis of NT, YH, SM coal (wt.%)

Coal	Proximate Analysis				Elements Analysis				
	M_{ad}	V_d	FC_d	A_d	C_d	H_d	O_d	N_d	S_d
NT	0.89	21.31	66.66	12.03	76.82	4.16	5.27	1.21	0.51
YH	2.38	26.90	62.77	10.33	75.01	4.52	6.38	1.76	2.01
SM	2.85	18.22	69.80	11.98	76.13	3.78	6.65	0.82	0.47

M: moisture, V: volatiles, FC: fixed carbon, A: ash, ad: air dry, d: dry.

Table Ⅱ The different coking conditions in coking process

Coking temperature /℃	650	850	1050
Coking time/h	6	7	8

Minerals Characterization

The crystalline phases of coal and cokes were identified and quantified by X-ray diffraction analysis. The XRD had a monochromator and a copper Kα X-ray source. The accelerating voltage and current were 40 kV and 150 mA, respectively. Apart from that, the coke samples were scanned with a scanning rate of $4°min^{-1}$ over the angular range of 10° to 90°, and the scanning interval was set in 0.02°/step [10].

Minerals quantitative analysis was carried out by Mineral Quantitative Analysis Method. This method was based on the theory of Rietveld refinement and usually used the mathematical models made up by Pseudo-Voigt, Lorentzian, Gaussian and Ikeda-Carpenter functions to simulate the XRD spectrum of the coal and cokes. In calculation, the relative content of crystalline phases which showed in the XRD spectrum and the suitable mathematical models of coal and coke were chosen to make sure the best match between the simulative and actual patterns. By this way, the relative content of crystalline phases was gained.

Results and discussion

Minerals transformations under different coking temperature in coking process

XRD spectrum of blending coal and cokes under the different coking temperature are shown as **Figure 1**. As shown in **Figure 1**, BCC-650 ℃,BCC-850 ℃ and BCC-1050 ℃ represent the cokes produced by the carbonization of blending coal under the coking temperature of 650 ℃,850 ℃and 1050 ℃, respectively. The main minerals in blending coal can be divided into clays, carbonates, minerals bearing sulfur and other minerals. The relative contents of the crystalline phases contain minerals and oxides in coal and cokes are quantified by Mineral Quantitative Analysis Method and shown in **Table Ⅲ**.

Clays, the most important part of blending coal, usually contains kaolinite and illite. Part of kaolinite converts to metakaolin at the coking temperature of 650℃. When the temperature reaches up to 450 ℃, kaolinite begins to lose crystal water [11,12]. With the increase of coking temperature, the content of kaolinite decomposition is increased by 19.88%. In this part, the most of kaolinite begin to converts to metakaolin. Wang Xuejing reported that the layered structure of kaolinite would be partly changed and produced the weak crystal phase to some degree when temperature reaches up to 650 ℃ [13]. When the coking temperature reaches up to 1050 ℃, kaolinite disappears completely and may mainly transforms into mullite, sillimanite, quartz, cristobalite and alumina [14,15]. In addition, M. Grigore gained the same result about the existence of alumina [9]. Illite in blending coal is very complex and

the kinds of decomposition product are difficult to identify, hence the further analysis is needed in the last research.

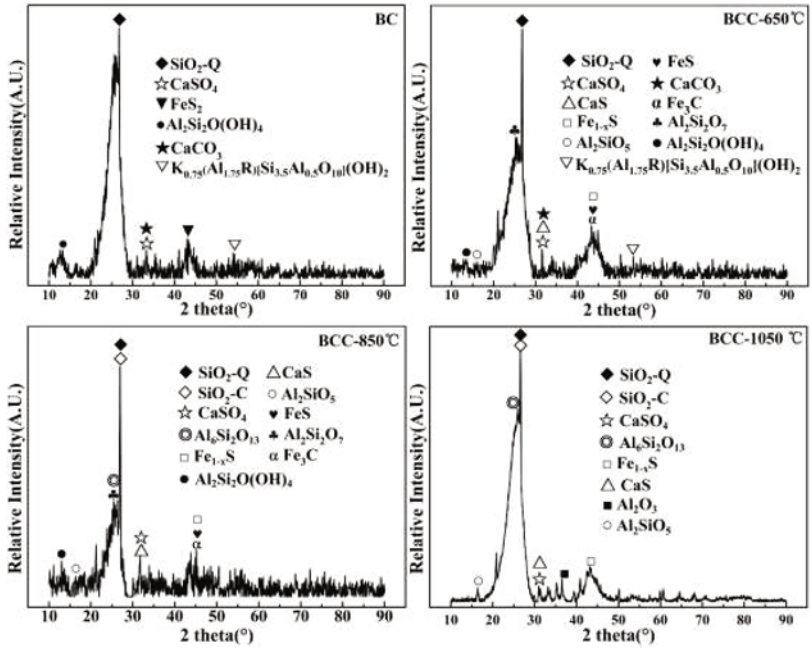

Figure 1 XRD spectrum of blending coal and cokes under different coking temperature

Carbonates is an important part of blending coal. The representative mineral is calcite achieved the content of 15.32%. When coking temperature reaches 650℃, Calcite partly decomposes and transforms to oldhamite. O. Kerkkonen reported that the calcite lost the carbon oxide to form calcium oxide, and then reacted with minerals bearing sulfur to form oldhamite. However, the phase of calcium oxide does not appear in the XRD spectrum of coke in this work. It may be that the calcite decomposes to amorphous calcium oxide which can not be identified by XRD, and then reacts with the minerals which bearing sulfur to forms oldhamite [1,16]. Calcite disappears completely in the coke when coking temperature reaches up to 850 ℃.

Minerals bearing sulfur in BC are pyrite and anhydrite, whose content are 5.80% and 9.78%, respectively. In the coke, the minerals bearing sulfur contain pyrrhotite, anhydrite and oldhamite. Mackinawite is just found in the BCC-650 ℃ and BCC-850 ℃. It is mainly because pyrite firstly transforms to mackinawite, then partly transforms into pyrrhotite [17, 18]. With increase of coking temperature, the content of mackinawite which comes from pyrite decreases. On the contrary, pyrrhotite increases. Apart from that, part of pyrrhotite decomposition products will react with minerals bearing calcium and produced oldhamite. The content of anhydrite changed

a little in the BCC-650 ℃ and BCC-850 ℃. Besides, the content of anhydrite makes a big change in the BCC-1050 ℃. It is mainly due to anhydrite decomposes to minerals bearing sulfur, reacts with other minerals and produces a trace of new minerals.

Table Ⅲ Minerals quantitative analysis of blending coal and cokes under different coking temperature (wt.%*)

Minerals	Molecular Formula	BC	BCC-650 ℃	BCC-850 ℃	BCC-1050 ℃
Quartz	SiO_2-Q	18.87	21.84	22.03	34.96
Cristobalite	SiO_2-C	-	-	8.01	11.68
Kaolinite	$Al_2Si_2O_5(OH)_4$	41.20	30.12	10.24	-
Anhydrite	$CaSO_4$	9.78	9.01	7.87	1.51
Pyrite	FeS_2	5.80	-	-	-
Calcite	$CaCO_3$	15.32	10.12	-	-
Illite	$K_{0.75}(Al_{1.75}R)[Si_{3.5}Al_{0.5}O_{10}](OH)_2$	9.03	8.63	-	-
Mackinawite	FeS	-	4.21	2.52	-
Metakaolin	Al_2SiO_7	-	4.08	22.85	-
Mullite	$Al_6Si_2O_{13}$	-	-	11.70	18.96
Sillimanite	Al_2SiO_5	-	5.11	4.32	15.50
Fe_3C	Fe_3C	-	3.56	2.56	-
Pyrrhotite	$Fe_{1-x}S$	-	1.27	2.66	2.56
Alumina	Al_2O_3	-	-	-	11.32
Oldhamite	CaS	-	2.05	5.24	3.51

* Analytical results of minerals were based on calculation of ash.

Another common mineral in coal is quartz. In the BC, the content of quartz is 18.87%. The content of quartz increases with the increase of coking temperature because of the decomposition of kaolinite, illite and other amorphous substance. The content of mullite, cristobalite and sillimanite will increase due to degree of the clays transformation deepens. Apart from that, sillimanite transforms to mullite under high temperature. Fe_3C is found in the BCC-650 ℃ and BCC-850 ℃. It may be due to minerals bearing Fe reacts with carbon under certain degree. And Fe_3C can react with other minerals and convert to pyrrhotite under high temperature.

Minerals transformations under different coking time in coking process

Figure 2 shows the XRD spectrum of blending coal and cokes under the different coking time. The cokes carbonized by blending coal under the coking time of 6 h, 7 h

and 8 h could be described as BCC-6 h, BCC-7 h and BCC-8 h. The relative contents of the crystalline phases contain minerals and oxides in coal and cokes are quantified by Mineral Quantitative Analysis Method and shown in **Table IV**.

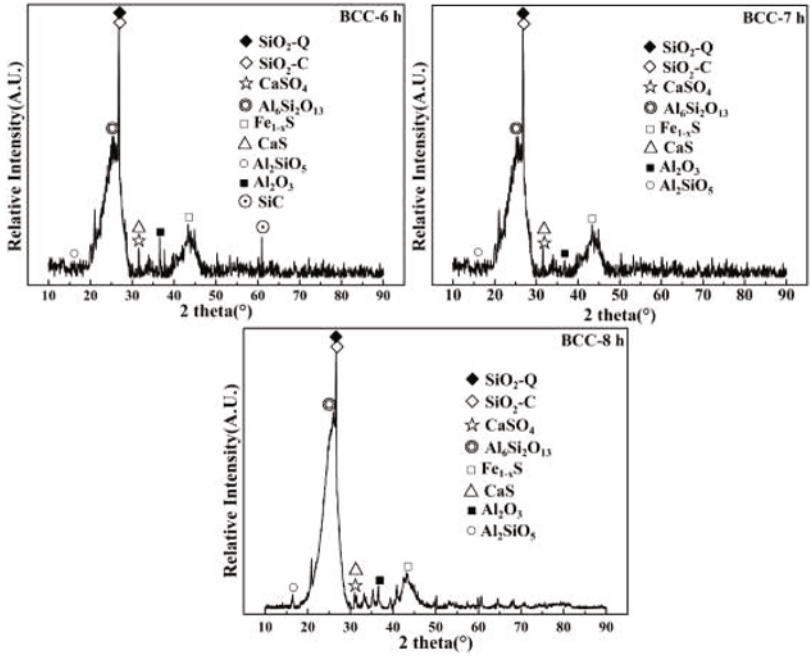

Figure 2 XRD spectrum of blending coal and cokes under different coking time

The main minerals in coke are quartz, cristobalite, mullite, sillimanite, pyrrhotite, alumina and oldhamite. The clays in BC completely disappears after coking process. Kaolinite may mainly transforms into mullite and partly transforms into quartz, cristobalite, sillimanite and alumina. Apart from that, a little part of kaolinite will react with organic carbon and produce silicon carbide which content is 3.67% when coking time is 6 h. With the increase of coking time, the contents of quartz and alumina increase. On the contrary, the contents of mullite and cristobalite decrease. The content of quartz increases by 11.38%, cristobalite decreases by 1.52% and mullite decreases by 8.52% under coking time of 8 h compared to 6 h, respectively. It is mainly because kaolinite in BC tends to convert to quartz and alumina rather than mullite and cristobalite. The content of pyrrhotite makes a slight decline when coking time reaches up to 8 h, because the content of pyrite which transforms to pyrrhotite may be affected by the coking time. When coking time increases, part of pyrite convert to other minerals bearing Fe. On the contrary, the content of oldhamite increases because of decomposition of anhydrite.

Table IV Minerals quantitative analysis of blending coal and cokes under different coking time (wt.%*)

Minerals	Molecular Formula	BC	BCC-6 h	BCC-7 h	BCC-8 h
Quartz	SiO_2-Q	18.87	23.61	27.26	34.99
Cristobalite	SiO_2-C	-	13.03	12.86	11.51
Kaolinite	$Al_2Si_2O_5(OH)_4$	41.20	-	-	-
Anhydrite	$CaSO_4$	9.78	6.21	6.54	1.51
Pyrite	FeS_2	5.80	-	-	-
Calcite	$CaCO_3$	15.32	-	-	-
Illite	$K_{0.75}(Al_{1.75}R)[Si_{3.5}Al_{0.5}O_{10}](OH)_2$	9.03	-	-	-
Mullite	$Al_6Si_2O_{13}$	-	28.12	27.99	19.60
Sillimanite	Al_2SiO_5	-	10.50	9.56	15.16
Pyrrhotite	$Fe_{1-x}S$	-	2.91	2.56	2.40
Alumina	Al_2O_3	-	9.30	10.55	11.32
Oldhamite	CaS	-	2.65	2.68	3.51
SiC	SiC	-	3.67	-	-

* Analytical results of minerals were based on calculation of ash.

Conclusions

The species and contents of minerals were analyzed in this study. Then minerals phase transformations under different coking time and temperature in coking process were obtained. From this study can be concluded the followings:

1. With the increase of coking temperature, the transformations of main minerals have a big change. Kaolinite firstly transforms to metakaolin, and then transforms to mullite, sillimanite, quartz, cristobalite and alumina. Calcite decomposes and partly transforms to oldhamite. Anhydrite reacts with other minerals and makes content of itself decrease. Pyrite converts into mackinawite and iron carbon compounds, then transforms into pyrrhotite.
2. Species of minerals have a little change between the different coking time in coking process. There are some differences for content of minerals under different coking time. The content of quartz increases by 11.38%, the contents of cristobalite and mullite decreases by 1.52% and 8.52%, respectively.

Acknowledgements

This work was supported by the National Natural Science Foundation of China (Grant No. 51474042) and the Fundamental Research Funds for the Central Universities (Grant No. CDJZR13130034).

References

[1] O. Kerkkonen. “Influence of Ash Reactions on Feed Coke Degradation in the Blast Furnace”. *Coke Making International (Germany)*, 9.2(1997): 34-41.

[2] W. W. Gill, et al. "The Influence of Ash on the Weakening of Coke."*Ironmaking Conference Proceedings*. 44. (1985):233-238.

[3] M. Grigore, R. Sakurovs, D. French, et al."Influence of Mineral Matter on Coke Reactivity with Carbon Dioxide."*ISIJ international* 46.4 (2006): 503-512.

[4] S. Nomura, H. Terashima, E. Sato, et al. “Some Fundamental Aspects of Highly Reactive Iron Coke Production.” *Journal of the Iron and Steel Institute of Japan*, 92.12 (2006): 849-856.

[5] A. Tomita. “Catalysis of Carbon–gas Reactions.” *Catalysis Surveys from Japan* 5.1(2001): 17-24.

[6] C.R. Ward. "Analysis and Significance of Mineral Matter in Coal Seams."*International Journal of Coal Geology*50.1 (2002): 135-168.

[7] R.S. Mitchell, H. J. Gluskoter. “Mineralogy of Ash of some American Coals-Variations with Temperature and Source.” *Fuel*, 55.2 (1976): 90-96.

[8] A. Filippidis, A. Georgakopoulos , A. Kassolifournaraki. "Mineralogical Components of some Thermally Decomposed Lignite and Lignite Ash from the Ptolemais Basin, Greece." *International Journal of Coal Geology* 30.4 (1996): 303-314.

[9] M. Grigore, R. Sakurovs, D. French, et al. "Effect of Carbonization Conditions on Mineral Matter in Coke."*ISIJ internationall*47.1 (2007): 62-66.

[10] S.F. Zhang, et al. "High Temperature Pyrolysis Behaviour and Kinetics of Lump Coal in COREX Melter Gasifier," *Ironmaking & Steelmaking*, 41.3 (2014): 219-228.

[11] D. M. Moore, R. C. Reynolds. *X-ray Diffraction and the Identification and Analysis of Clay Minerals*. Vol. 378. Oxford: Oxford university press, 1989.

[12] Cao Min, Gu Xiaohu, Fan Chong, et al. "Mineral Behavior in Coal Ash at High Temperature. " *Coal Conversion* 33.1 (2010): 12-15.

[13] Wang Xuejing, Zhang Jiamin, Li Xiaobo, et al. "Study on the Microstucture of Kaolin and Kaolin Fired." *China Non-Metallic Mining Industry Herald*, 5 (2007): 18-20

[14] Zheng Shuilin, Li Yang, Xu Xia. "Study of Effects of Temperature on the Physical and Chemical Properties of Calcined Kaolinite." *Journal of the Chinese Ceramic Society*, 31.4 (2003): 417-420

[15] J. V. O'Gorman, P. L. Walker. "Thermal Behavior of Mineral Fractions Separated from Selected American Coals." *Fuel* 52.1 (1973): 71-79.

[16] O. Kerkkonen, E.Mattila, R.Heiniemi. "The Correlation between Reactivity and Ash Mineralogy of Coke." *Iron and Steel Society*, Warrendale, PA (United States), 1996.

[17] J. C. Nankervis, R.B. Furlong. "Phase Changes in Mineral Matter of North Dakota Lignite Caused by Heating to 1200 ℃." *Fuel* 59.6 (1980): 425-430.

[18] C. M. Earnest. "Characterization of the Low-Temperature Ash Component of the Herrin 6 Coal Seam (Southwestern Illinois) by Thermal Methods of Analysis." *ThermochimicaActa* 121 (1987): 71-86.

Characterization of Minerals, Metals, and Materials 2016
Edited by: Shadia Jamil Ikhmayies, Bowen Li, John S. Carpenter, Jiann-Yang Hwang, Sergio Neves Monteiro, Jian Li, Donato Firrao, Mingming Zhang, Zhiwei Peng, Juan P. Escobedo-Diaz, and Chenguang Bai
TMS (The Minerals, Metals & Materials Society), 2016

ELECTRICAL EFFECT AND INFLUENCE FACTORS OF TOURMALINE

Qi Lu [1], Bowen Li [2], Feng Bai [1]

[1] China University of Geosciences, Beijing, 100083, China
[2] Michigan Technological University, Houghton, MI 49931, U.S.A

Keywords: Tourmaline, Piezoelectricity, Dielectricity, Pyroelectric property

Abstract

Tourmaline is a crystalline boron silicate mineral with special electrical and optical behaviors. In this study, electrical performances of crystalline tourmaline samples from various deposit sites in China were evaluated. The results show that the piezoelectric constants of tourmalines, in a fixed crystalline direction, depend on their mineral species and the specialty elements in the crystal. The piezoelectric constant of dravite is higher than that of elbaite. The variety of piezoelectricity is resulted from the element type in crystal structure. Dielectric properties tests show that tourmaline is a low dielectric constant material and the dielectric constant is from 4×10^{-12}pf/cm to 10×10^{-12}pf/cm. The dielectric constant along C axis is higher than that in any other directions. Under room temperature, pyroelectric property of a crystal is proportional to the dielectric properties, and negatively correlated to the ferric oxide ratio.

Introduction

Tourmaline has piezoelectric and pyroelectric property because of its polar structure. The special electrical properties of tourmaline have been found for a long time. According to Schmidt records, Dutch found that tourmaline can attract dusts when it was heated and discharge powder when it was cooled down. A Japanese researcher, Kubo confirmed the tourmaline with spontaneous polarity through an experiment in 1992. It can be used in many areas, such as infrared radiation, release of negative ions, adsorption and activating water [1]. Thus it becomes one of the most important materials in environmental protection. In order to improve its performance, the electrical properties of tourmaline were investigated in this study.

Experimental Procedure

1. Characteristics of Tourmaline Samples

Tourmaline samples used in the experiment were obtained from Nanyang (Henan province, HN), Gaoligong mountain (Yunnan province, YN) and Fuping (Hebei province, HB) in China. Samples of HN-1, YN-1, and HB-1 stand for the pure single crystals from Henan, Yunnan, and Hebei respectively. The chemical composition of samples was analyzed by X-ray fluorescence spectrometry (Instrument Philips PW2404).

The results in Table I show that the main compositions in the samples are SiO_2 and Al_2O_3 while containing a small amount of MnO and Na_2O. In addition, HN-1 contains only trace amounts of Fe and Fe_2O_3 (0.031%). The iron content of YN-1 is less than that in HB-1, which contains the

highest MgO content. These characteristics indicated that these samples belong to different categories of tourmalines. According to the classification of tourmaline, HB-1 is dravite, while HN-1 and YN-1 are classified as elbaite [2] [3].

Table I Chemical Components of Samples

Samples	HN-1	YN-1	HB-1
SiO_2	43.64	44.16	38.40
TiO_2	-	0.011	0.99
Fe_2O_3	0.031	1.68	6.31
FeO	-	1.75	-
MnO	0.43	0.14	-
MgO	-	0.029	10.08
CaO	0.72	0.47	0.66
Na_2O	2.17	2.55	2.13
K_2O	0.04	0.15	0.12
P_2O_5	0.05	0.16	-
F	4.09	-	0.01
loss	4.70	5.97	10.02
total	98.601	99.34	99.40

2. Piezoelectric Effect of Tourmalines

2.1 Conditions for the Generation of Piezoelectric Effect

Many crystal minerals such as tourmaline have polar structure. Under the action of pressure, electric charges can be produced due to crystal deformation. This phenomenon is called the piezoelectric effect. Variety of the piezoelectric effect depends on the external pressure and the polarization of the crystal minerals.

Structure of tourmaline belongs to trigonal system, with a symmetry class of $L^3 3P$ and space group of R3m. This is a necessary factor for producing piezoelectric effect. Under room temperature, tourmaline is not conductive. The electric charges of the crystal surface will be distributed unevenly when it is placed under external pressure. Even a small external pressure, it can show piezoelectric effect because of its low crystalline symmetry.
Any stress (tensile stress, compressive stress, or shear stress) applied to this kind of material can produce electric dipole. If the material is placed between two metals, the applied stress T and electric polarization P have a relationship as follows [4]:

$$P = d\,T \qquad (1)$$

Here, d is a constant, which is called piezoelectric modulus (Or piezoelectric strain coefficient), and its unit is $N^{-1} \cdot C$ (Coulomb / Newton). It represents the intensity of the electrodes produced by the unit stress.

2.2 Piezoelectric Properties of Different Species of Tourmalines

Piezoelectric coefficient of tourmaline crystal reflects the intensity of the piezoelectric property. The greater the piezoelectric constant, the stronger the piezoelectric effect is. By testing the piezoelectric constant of different tourmaline, we can analyze the variation of piezoelectric properties.

2.2.1 Test Methods and Conditions of the Piezoelectric Coefficient

The piezoelectric coefficients of samples named HN-3, YN-3, HB-3 and HB-4 were tested. HN-3 and YN-3 represent the sample from Henan and Yunnan. HB-3 and HB-4 represent the samples from Hebei province. The test temperature is 18℃. The samples were prepared by cutting an original tourmaline crystal into flakes in three different directions, ⊥C axis, // C axis, and Oblique to C axis.

2.2.2 Analysis of Test Results

2.2.2.1 Influence of Different Crystal Directions

From Table II and Figure I, it can be seen that the piezoelectric coefficient of HN-3 depends on its crystalline directions. The highest piezoelectric coefficient is occurred in the direction of perpendicular to C axis (2.3PC/N), while the lowest is showed in the direction parallel to C axis (0.1 PC/N), and a medium in the direction of oblique to C axis (1.7 PC/N).

Table II Piezoelectric Coefficients of Sample HN-3

sample	crystal direction	piezoelectric coefficient d(PC/N)
HN-P-1	// C axis	0.1
HN-X-1	Oblique to C axis	1.7
HN-U-1	⊥C axis	2.1
HN-U-2	⊥C axis	2.3

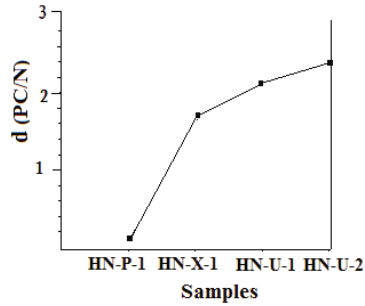

Figure I the piezoelectric coefficients from different direction of HN-3 sample

Sample YN-3 shows similar results of piezoelectric coefficient to HN-3 (Table III) and it also changes with different crystal directions.

Table III Piezoelectric Coefficient of Sample YN-3

samples	crystal direction	piezoelectric coefficient d(PC/N)
YN-P-1	// C axis	0.2
YN-X-1	Oblique to C axis	1.8
YN-U-1	⊥C axis	2.2

Table Ⅳ the Piezoelectric Coefficients of HB-3, HB-4 Samples

samples	crystal direction	piezoelectric coefficient d(PC/N)
HB-P-1	// C axis	0.5
HB-P-2	// C axis	0.7
HB-X-1	Oblique to C axis	1.9
HB-X-2	Oblique to C axis	2.1
HB-U-1	⊥C axis	2.2
HB-U-2	⊥C axis	2.3

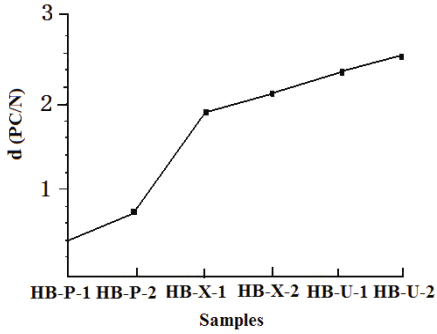

Figure II the piezoelectric coefficients from different direction of HB-3, HB-4 samples

The data of HB-P-1, HB-X-1 and HB-U-1come from the sample of HB-3, and the data of HB-P-2, HB-X-2 and HB-U-2 come from the sample of HB-4. In Table Ⅳ and Figure II, it can be seen that the piezoelectric coefficients of HB-3 and HB-4 also change with different crystal directions. This phenomenon was resulted from the structure of tourmaline crystal. Tourmaline has a complex tripartite ring-shaped of $[Si_6O_{18}]$ chain and six silicon-oxygen tetrahedron within its unit cell, where its horn points to the C axis direction. Under an external force or electric field, the direction perpendicular to the C axis has the strongest crystal deformation, which resulted in the strongest piezoelectric effect. In the direction parallel to C axis, it has the weakest deformation and the smallest piezoelectric effect.

2.2.2.2 Influence of Tourmaline Species and Chemical Composition

Tourmaline is not a single mineral, but a group of several closely related minerals. The three most well-known members are elbaite, schorl, and dravite. The formula of the tourmaline group is very complex, since it contains many elements and many combinations of elements. A simple generic formula for the tourmaline group is: $X_1Y_3Al_6(BO_3)_3Si_6O_{18}(OH)_4$. X = Na and/or Ca, Y = Mg, Li, Al, and/or Fe^{2+}. The formula of dravite is $NaMg_3Al_6(BO_3)_3Si_6O_{18}(OH)_4$ and the formula of elbaite is $NaMg_3Al_6(BO_3)_3Si_6O_{18}(OH)_4$.

The piezoelectric coefficients of elbaite (HN-3, YN-3) changed along with the crystalline directions is greater than that of dravite (HB-3) in the same direction. The difference is mainly caused by the atoms of Y position. Firstly, the ionic radius size of Y position is related to its dipole length. The larger the ionic radius, the higher the dipole (d) will be produced. The atomic radius and ionic radius of lithium, magnesium, iron, oxygen, and other elements are shown in Table Ⅴ. Secondly, the dipole moment is influenced by positive and negative ionic valence. Y position of lithium tourmaline is Li^+, and Y position of dravite is Mg^{2+} and Fe^{2+}. Dipole moment (u) relates to dipole length (d) and electric charge (q) as follows [5]:

$$u=q*d \qquad (2)$$

It can be concluded that the piezoelectric coefficient of elbaite is lower than that of dravite. Similarly, the piezoelectric coefficient of HN-3 is lower than YN-3 because the iron content of YN-3 is less than that in HN-3.

Table Ⅴ Atomic and Ionic Radii of Li, Mg, Fe, and O

atom	Atomic radius(pm)	ion	Ionic radius(pm)
Li	123	Li^+	60
Mg	136	Mg^{2+}	65
Fe	126	Fe^{2+}	76
O	73	O^{2-}	140

2.2.2.3 Influence of Crystallization

In order to study the influence of crystallization grade to dielectric coefficient, two samples with different grade of crystallization (HB-3, HB-4) were prepared and tested. The crystallization grade of HB-4 is better than HB-3. From Table 4, it can be seen that the piezoelectric coefficient of HB-4 is greater than that of HB-3 in the same direction. This indicates that higher crystallization grade will lead to a higher dielectric coefficient.

3. Dielectric Property of Tourmaline

Different species of tourmaline were selected to test the relationship of dielectric properties and spontaneous polarization. Curve of capacitance (C) variation was obtained under different frequencies. Dielectric constant was calculated according to the test results.

3.1 Preparation of Test Samples

Three large pure tourmaline crystals were selected, and cut into flakes from two different directions (⊥C axis and // C axis) respectively. Samples were named as HN-5, YN-5, and HB-5. The instruments used for this test was Agilent-4294A Impedance Analyzer. The test temperature was 20℃.

3.2 Influence of Different Crystal Directions

Table Ⅵ shows the test results of dielectric constant of tourmalines. It can be seen that in the ⊥C axis direction, the sample of elbaite (HN-U-5) has the highest dielectric constant, 6.9764×10^{-12}pf/cm. The sample of dravite (HB-U-5) has the lowest dielectric constant, 4.9282×10^{-12}pf/cm, while the dielectric constant of YN-U-5 is 6.583810^{-12}pf/cm, which is similar to that of HN-U-5.

Table Ⅵ Dielectric Constant from ⊥C Axis Direction of HN-5, YN-5 and HB-5 Samples

samples	species	crystal direction	dielectric constant ε_0 ($\times10^{-12}$pf/cm)
HN-U-5	elbaite	⊥C	6. 9764
YN-U-5	elbaite	⊥C	6. 5838
HB-U-5	dravite	⊥C	4.9282

Table Ⅶ shows the test results of dielectric constant of tourmalines along C axis direction. The sample of elbaite (HN-P-5) has the highest dielectric constant, 9.9585×10^{-12}pf/cm, while dravite (HB-P-5) has the lowest dielectric constant, 7.1813×10^{-12}pf/cm. The dielectric constant of YN-P-5 is 7.3226×10^{-12} pf/cm, which is similar to the sample of YN-P-5.

Table Ⅶ Dielectric Constant along C Axis Direction of the HN-5, YN-5, HB-5 Samples

samples	species	crystal direction	dielectric constant ε_0 ($\times10^{-12}$pf/cm)
HN-P-5	elbaite	// C	9.9585
YN-P-5	elbaite	// C	7.3226
HB-P-5	dravite	// C	7.1813

3.3 Effect of Different Tourmaline Species

Test results showed that different species of tourmaline crystals have different dielectric constant. Among three kinds of samples, elbaite species has the highest dielectric constant, in which HN-P-5 has the highest one, while the sample of dravite (HB-P-5) has the lowest dielectric constant. Since the dielectric constants of samples are between 4×10^{-12}pf/cm and 10×10^{-12}pf/cm, tourmaline is a kind of the materials with low dielectric constants. It can be applied to apparatus ceramic or porcelain electric vacuum connection, which requires a low dielectric constant in order to obtain a higher signal transmission speed[6].

4. The Pyroelectric Property of Tourmaline

Polar Crystals can produce electric charges when environmental temperature changes. This phenomenon is known as pyroelectric effect. The charge of pyroelectric effect is generated due to temperature change, while the charge of piezoelectric effect is produced by external force or electric field.

Among 32 crystallographic point groups of crystallography, there are 21 point groups which have no symmetry center. Only the crystals which have polar structure and no symmetry center can produce piezoelectric effect. Moreover, only 10 kinds of crystals were found to have pyroelectric effect among the crystals having piezoelectric effect. Pyroelectric coefficient (P_i) indicates the strength of pyroelectric effect. The spontaneous polarization (Ps) of crystals can be expressed as follow formula [7]:

$$\triangle P_s = P_i \triangle T \qquad (3)$$

P is a vector, generally have three components, that is, Pi (i=1, 2, 3), and its unit is $C/(m^2K)$. Under room temperature, pyroelectric property of a crystal is proportional to the dielectric properties. Dielectric test results showed that the order of dielectric properties is: HN-5> YN-5> HB-5. From Table Ⅷ it can be seen that pyroelectric property is negatively correlated to the ferric oxide ratio. If the crystal of tourmaline contains low ferric oxide, the pyroelectric effect will be better. According to dielectric test results and ferric oxide ratio, it can be concluded that the order of pyroelectric properties is: HN-5> YN-5> HB-5.

Table Ⅷ average dielectric coefficient of the samples with different ferric oxide ratio

sample	ε_0 ($\times 10^{-12}$pf/cm)	ferric oxide ratio
HN-5	8.26745	0.031
YN-5	7.1532	3.43
HB-5	6.05475	6.31

Conclusion

In this study, tourmaline samples produced from Henan, Yunnan, and Hebei provinces of China were selected and their electrical performances were investigated. The piezoelectric constants of tourmalines, in a fixed crystalline direction, depend on their mineral species and the elements in the crystal. The piezoelectric constant of dravite is higher than that of lithium tourmaline. Dielectric properties tests showed that tourmaline is a low dielectric constant material. The range of its dielectric constant is between 4×10^{-12}pf/cm and 10×10^{-12}pf/cm. The dielectric constant along C axis is higher than that in any other direction. Under room temperature, pyroelectric property of a crystal is proportional to the dielectric properties, and negatively correlated to the ferric oxide ratio. According to dielectric test results and ferric oxide ratio, the order of pyroelectric properties is: HN-5> YN-5> HB-5.

Acknowledgements

This project is supported by "the Fundamental Research funds for the Central Universities" under Grant No.2011YYL138.

References

1. T.Kubo and T.Nakamura, " Tourmaline group crystals reaction with water, " Ferroelectrics, 137(1992), 13-31.
2. Frank C. Hawthorne and Darrell J. Henry, "Classification of the minerals of the tourmaline group," Europe .J. Mineral, 11(1999), 201-215.
3. Fuat Yavuz, Vural Yavuz and Ahmet Sasmaz, "Win Clastour–a Visual Basic program for tourmaline formula calculation and classification," Computers Geosciences, 32 (2006), 1156-1168.
4. Cristiane Castaneda, Sigrid G. Eeckhout, Geraldo Magela da Costa, et al., "Effect of heat treatment on tourmaline from Brazil," Phys Chem Minerals, 33(2006), 207-216.
5. Donnay.G, "Structural mechenism of pyroelectricity in tourmaline," Acta Crystal Lographica, A33(1977), 927-932.
6. Zhang Chen and Shen Nengjue, "Status and development of electronic packaging materials," New Material Industry, 3 (2003), 5-12.
7. Wencheng Hu, "study on the Thermoluminescence motor management and BST Thin Films," (Ph.D. thesis, University of Electronic Science and Technology of China, 2008), 29-35.

Characterization of Minerals, Metals, and Materials 2016
Edited by: Shadia Jamil Ikhmayies, Bowen Li, John S. Carpenter, Jiann-Yang Hwang, Sergio Neves Monteiro, Jian Li, Donato Firrao, Mingming Zhang, Zhiwei Peng, Juan P. Escobedo-Diaz, and Chenguang Bai
TMS (The Minerals, Metals & Materials Society), 2016

WETTABILITY OF PYROLYTIC GRAPHITE BY MOLTEN BLAST FURNACE SLAG BEARING TiO_2

Yanhui Liu, Xuewei Lv, Chenguang Bai, Baohua Li

School of Materials Science and Engineering, Chongqing University, Chongqing, 400044, China

Keywords: Wettability, Contact angle, Interfacial tension, Interfacial reaction

Abstract

The wettability of graphite by the molten TiO_2-CaO-SiO_2-Al_2O_3-MgO (in mass%) Blast Furnace slag has been investigated using the dispensed drop method at 1673 K under the Argon atmosphere (Pressure≈ 1.10 atm). With the increase of TiO_2 content in the slag, the contact angle rises from 127° up to 147°, meaning that the TiO_2 worses the wettability between the molten slag and the graphite. On the contrary, the CaO/SiO_2 mass ratio can promote the wettability. Interfacial tensions between the slag and the graphite were also evaluated by using the Young's Equation. Thermodynamics calculations were also carried out to study the interfacial reactions, showing that the reaction sequence agree with the following: reduction of MgO, SiO_2, TiO_2, boudouard reaction and formation of 2CaO Ti_2O_3.

Introduction

In the process of iron-making in the blast furnace with pure Vanadic Titanomagnetite in Panzhihua Iron & Steel Corporation (Pan-steel), the mass percent of TiO_2 can reach 30%, causing several critical problems, such as foaming slag, viscous slag and high metal loss. There have been a number of studies aimed at the foaming slag, proving that the crucial influencing factor is the surface properties of the blast furnace slag [1-4]. When the bubbles are formed in the melts, the interfacial area between gas and melts will obviously increase. The lower of the surface tension of melts, the easier the bubbles are to form. Wettability and interfacial reactions have a great effect on formation, transition and attenuation of the bubbles in the melts, which greatly affects the formation of foaming slag [5-7].

There have been some studies on the wettability of graphite by molten slag. It was found that slags don't wet graphite. Shen *et al.* [8] investigated the wettability of graphite by molten SiO_2-MnO-TiO_2-FeO_x slag in the temperature range 1473-1673 K in an Ar atmosphere. They showed that a temperature-dependent reaction leads to a decrease in the contact angle as well as a foaming behavior of the sessile drop. Siddiqi *et al.* [9] investigated the wettability of graphite by CaO-SiO_2-Al_2O_3-MgO-FeO_x slag in the temperature range 1673-1873 K. In addition, experimental studies [10] showed that the change in the wetting is affected by the Gibbs free energy of the reactions and the wettability could be improved by increasing the iron oxide content and temperature. Moreover, the height of the foam was reported to increase with decreasing the O/Si in the slag [11].

In this study, the wettability of graphite by molten TiO_2-CaO-SiO_2-Al_2O_3-MgO blast furnace slag is investigated. Interfacial tensions between the slag and the graphite were also evaluated by using the Young's Equation. Thermodynamics calculations by the FactSage were also carried out to study the interfacial reactions.

Experimental

Sample preparation

Samples for surface tension measurement were prepared from pure chemical reagents, SiO_2, Al_2O_3, MgO, TiO_2 and CaO powders. These reagents were precisely weighed to form given compositions (shown in **Table I**), and mixed in an alumina mortar thoroughly. All the samples were premelted in a resistance furnace using the alumina crucible for one hour and air-cooled. The chemical composition analysis was conducted by XRF. By pre-melting the samples in the alumina crucible, there is some change in the slag compositions, in particular the Al_2O_3 mass fraction will increase by 0.6-1.5%, resulting in the slight reduce of the other oxides, such as CaO, SiO_2, MgO and TiO_2.Then, the sample was prepared to a cube with 3×3×3 mm^3 and used for measurement.

Table I. Chemical Composition of the slag samples

Sample	TiO_2	Al_2O_3	MgO	CaO	SiO_2	Basicity（CaO/SiO_2）
1#	8.00	14.00	8.00	36.67	33.33	1.10
2#	13.00	14.00	8.00	34.05	30.95	1.10
3#	18.00	14.00	8.00	31.43	28.57	1.10
4#	23.00	14.00	8.00	28.81	26.19	1.10
5#	28.00	14.00	8.00	26.19	23.81	1.10
6#	33.00	14.00	8.00	23.57	21.43	1.10
7#	23.00	14.00	8.00	26.05	28.95	0.90
8#	23.00	14.00	8.00	27.50	27.50	1.00
9#	23.00	14.00	8.00	30.00	25.00	1.20

Substrate preparation

For the measurement, pyrolytic graphite (99.9% purity) was used to be the solid substrate. The graphite was in plate shape with the surface dimensions of 20 mm × 20 mm and the height of 4 mm. Its surface was mechanically ground and carefully polished using different sizes of diamond pastes to get an average roughness (Ra) of < 400 nm.

Contact angle measurement

The experimental equipment schematic has been introduced in details somewhere else [12, 13]. The modified sessile drop technique, which is improved by the traditional sessile drop method, was adopted. The apparatus includes the following six parts: the furnace, image-forming system, the vacuum-made system, the heating-control system, the cooling system and data processing system. Both the slag and the substrate were cleaned in acetone with ultrasonic for three times before measurement, and the cleaning time is 5 minutes for each time. The sample and substrate were then put into a tube made of stainless steel outside the chamber and placed on top of a short piece of alumina rod respectively. The chamber of the furnace was first evacuated to about 5×10^{-4} Pa at the room temperature and then backfilled with high-purity (99.9999%) argon. Then, the furnace was heated at a rate of 20 $K\cdot min^{-1}$. When the temperature of the chamber reached the desired value, it should be kept for 30 minutes. Then the slag sample, initially placed in a tube made of stainless steel outside the chamber, was dropped through an open alumina tube into the chamber and then rested on the substrate surface. Because of the high testing temperature, the slag instantly melted after it was dropped. As soon as the drop was observed, the drop profile

was recorded by a high resolution camera and the time was defined as the start point for the wetting. After the wetting experiment, the samples was furnace-cooled at a rate of 30 K·min^{-1}.

Results and discussion

Wetting phenomena and contact angle

Figure 1 shows the images used to calculate the contact angle, indicating that the slag does not wet the graphite and the contact angle is above 90°. The contact angle data concerning the TiO_2 content obtained from the study are shown in **Figure 2**. With the increase of TiO_2 content, the contact angle rises from 127° up to 147°, meaning that the increase of TiO_2 within the slag worses the wettability of the graphite by the molten slag.

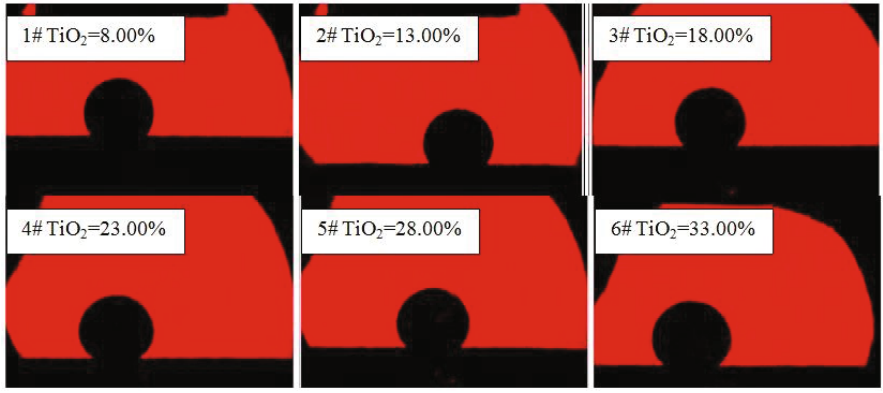

Figure 1. Images used to measure the contact angle of blast furnace slag bearing TiO_2 at 1673 K

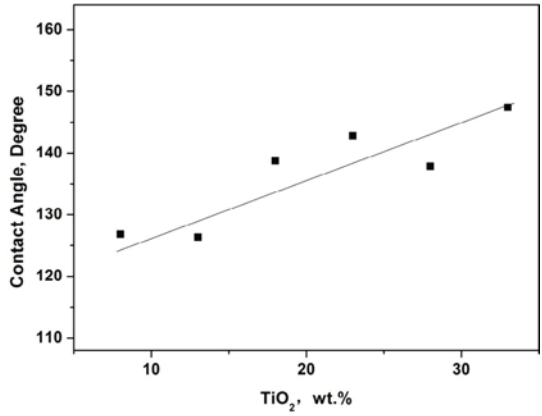

Figure 2. Variation of contact angle as a function of TiO_2 at 1673 K

Figure 3 and **Figure 4** shows that he contact angle goes down along with the increase of the CaO/SiO_2 ratio, indicating that increasing the basicity results in promoting the wettability.

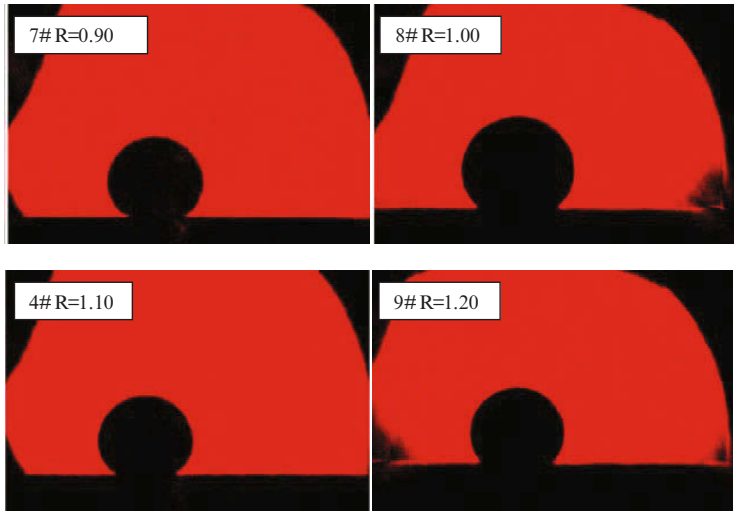

Figure 3. Images used to calculate the contact angle at 1673 K

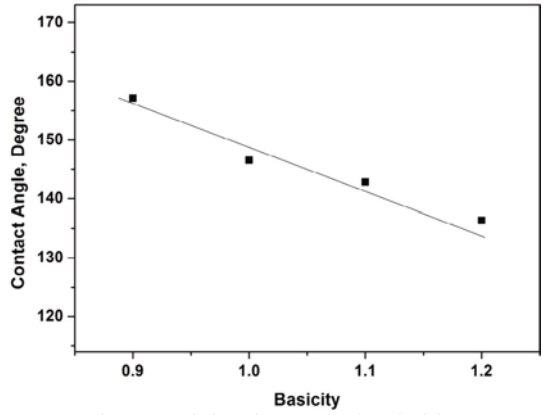

Figure 4. Variation of contact angle *vs* basicity

Evaluation for the interfacial tension

It is well known that the wettability can be described by the following Young's Equation [14]:

$$cos\theta = \frac{\sigma_{sg} - \sigma_{sl}}{\sigma_{lg}} \quad (1)$$

Here, the recognized value of the surface tension, σ_{sg}, for graphite is 45 mN/m. As for the surface tension, σ_{lg}, it can be well found by both the experimental values and the evaluation model. Therefore, the interfacial tension, σ_{sl}, can be calculated by the Eq. (1), which is shown in Eq. (2):

$$\sigma_{sl} = \sigma_{sg} - \sigma_{lg}\cos\theta \quad (2)$$

The calculated interfacial tensions were plotted in **Figure 5** and **Figure 6**, respectively. With the increase of TiO_2 within the slag, the interfacial tension between the slag and graphite goes up slowly. The interfacial tension was at the highest level when the TiO_2 content was between 18% and 25%, and the second higher level was from 26% to 33%. It is well known that the interfacial tension is closely related to the separation of the carbon particles from the molten slag in the blast furnace. The higher interfacial tension means that it is much harder to separate the carbon from the slag. **Figure 5** shows that the increase of TiO_2 is not good for the separation of the carbon particles from the slag. On the contrary, the increase of basicity results in the decrease of the interfacial tension, indicating that the increase of basicity is good for the separation of the carbon particles from the slag.

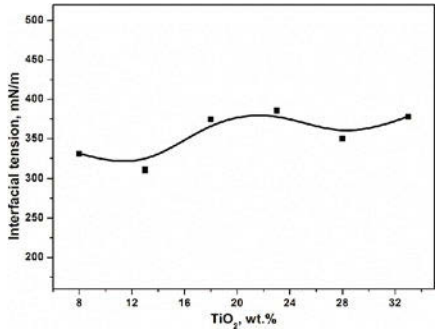

Figure 5. Calculated interfacial tensions as a function of TiO_2 within the slag at 1673 K

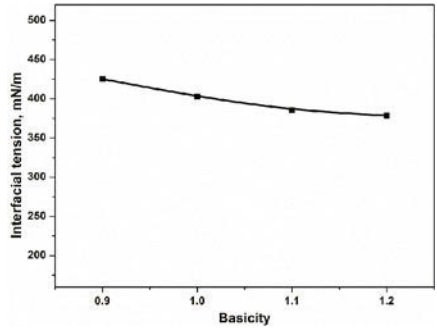

Figure 6. Calculated interfacial tensions as a function of TiO_2 within the slag at 1673 K

3.3 Interfacial reactions

Interfacial reactions between the molten slag and the graphite are easy to find in **Figure 1** and **Figure 3**. For convenience, a volatility index, V_t/V_0, is defined to evaluate chemical reactivity, which is shown in **Figure 7** and **Figure 8**. Where, V_0 is the volume of the first image since the drop initially melted, and V_t represents the variation of the volume as a function of time. The interfacial reactions were not violent at the first three pictures, meaning that these three pictures can be used to calculate the surface tension and the contact angle without considering the influence of interfacial reactions.

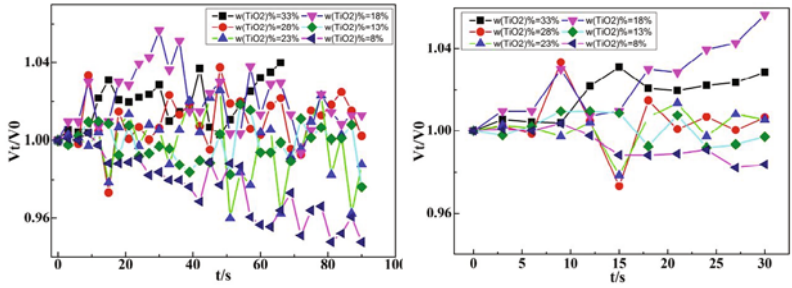

Figure 7. The volatility index as a function of TiO_2 at 1673 K (a, b shows the different time)

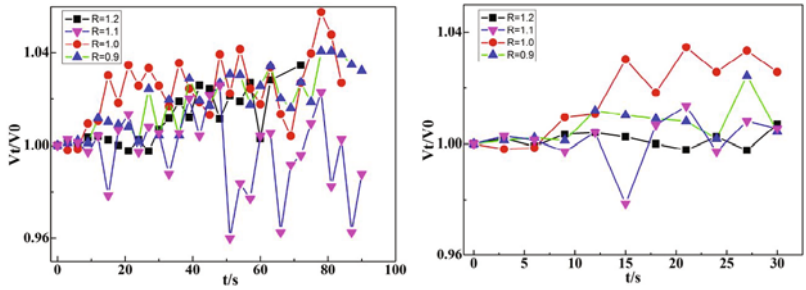

Figure 8. The volatility index *vs* Basicity at 1673 K (a, b shows the different time)

An "open" simulation of the reduction of the slag sample NO. 4 shown in **Table I** by carbon was calculated with FactSage. The effective pressure was assumed not to be the pressure in the chamber of the furnace. The pressure in the bubble was related with the surface tension and the radius of the bubble, which gives $P = 2\sigma/r$ (Laplace's Equation). Where, σ is the surface tension of the slag and r is the radius of the bubble. If we assume that the radius of the bubbles is around 0.5 mm and the surface tension is 432 mN/m, then P≈ 0.017 atm (close to 0.01 atm). In this study, the effective pressure used in FactSage was 0.01 atm.

Results are shown in **Figure 9**. The mole fraction of main gas, CO, is about 8%. The mole fraction of CO_2 starts at around 2.7% (except in the very early stages) and drops to 0.02% at the end. And the sum of the mole fraction of CO and CO_2 keeps constant. SiO(g) and Mg(g) actually become more important than CO_2 at the end, but only CO_2 can gasify the carbon to CO for

further reaction. Thermodynamics calculation shows that the reactive sequence is as follows: reduction of MgO, SiO_2, TiO_2, boudouard reaction and production of 2CaO Ti_2O_3.

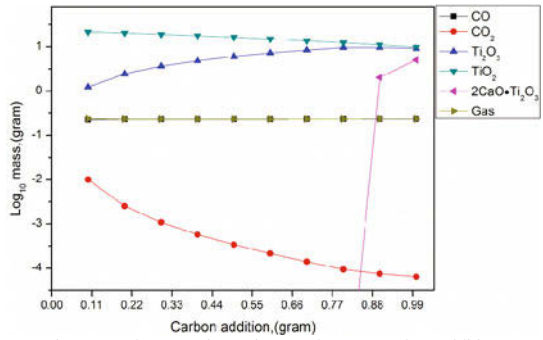

Figure 9. Changes of reaction products *vs* carbon addition

Graphite surface microstructure after grinding and polishing presents a " bumpy" sidewall morphology, shown in **Figure 10**. Its interfacial microstructure is shown in **Figure 10**. Reactions may happen both in the holes and the connecting region. Reactions can be divided into two two-phase reactions: gas/slag and gas/solid substrate. Reactions in the connecting region can be regarded as a three-phase reaction. Compared with three-phase reaction, two-phase reaction is easier to happen. Thermodynamics calculation shows that the formation of high melting phase, 2CaO Ti_2O_3 is in the final stage. Slag/graphite reactions are as follows:

(1) gas /slag interface:

$$2TiO_2 + CO = Ti_2O_3 + CO_2$$

(2) gas/graphite interface:

$$CO_2 + C_{(s)} = 2CO$$

(3) Production of Mg(g) and SiO(g)

$$MgO + CO = Mg_{(g)} + CO_2$$

$$SiO_2 + CO = SiO_{(g)} + CO_2$$

(4) Production of 2CaO Ti_2O_3

$$CaO+Ti_2O_3=2CaO\ Ti_2O_3$$

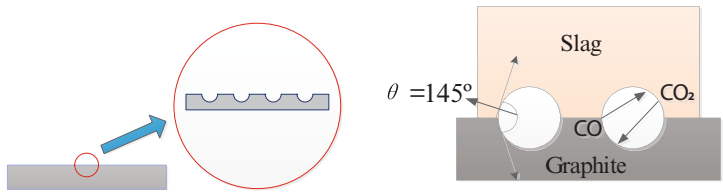

Figure 10. Schematic diagram of surface microstructure of Graphite after polished

Conclusions

The wettability of graphite by the molten TiO_2-CaO-SiO_2-Al_2O_3-MgO (in mass%) Blast Furnace slag has been investigated using the dispensed drop method at 1673 K under the Argon atmosphere. The main conclusions are as follows:

(1) With the increase of TiO_2, the contact angle rises from 127° up to 147°, meaning that the TiO_2 worses the wettability between the molten slag and the graphite. On the contrary, the CaO/SiO_2 mass ratio can promote the wettability.

(2) The increase of TiO_2 results in the increase of the interfacial tension, which is not good for the separation of the carbon particles from the slag. On the contrary, the increase of basicity has an opposite effect.

(3) Thermodynamics calculations were also carried out to study the interfacial reactions, showing that the reaction sequence agree with the following: reduction of MgO, SiO_2, TiO_2, boudouard reaction and formation of 2CaO Ti_2O_3.

Acknowledgement

The authors are especially grateful to the National Natural Science Foundation of China (NSFC) (Grant No. 51234010) and Chongqing University Graduate Students Scientific Research Innovation Project (No. CYB14026).

References

[1] H.F. Xu, F.X. Peng and R.S. Diao, "Behaviours of TiO_2 in the blast furnace smelting," *Ironmaking*, 8 (4) (1989), 1-6.

[2] J.M. Liu and X.Q. Jia, "Mechanism and Influence Factors of the Formation of Foaming Slag during the Smleting of High Titania Slag in Blast Furnace," *Iron Steel Vanadium Titanium*, 12 (2) (1991), 33-39.

[3] H.G. Du, *Theory of Smleting Vanadium and Titanium-Magnetite in Blast Furnace* (Beijing, China Science Press, 1996), 145-175.

[4] C.G., Bai, "Study on Some Physical Chemistry Problems of Blast Furnace Slag Bearing Titania", (Ph.D. thesis, Chongqing University, 2003), 3-8.

[5] K. Mukai, *Interfacial Physical Chemistry of High Temperatures Melts* (Beijing, China Science Press, 1996), 133-158.

[6] K. Wu, *Fundamental Theory on Melts of Bubble Metallurgy* (Beijing, China Metallurgical Industry Press, 2000), 65-71.

[7] N. Eustathopoulos, M.G. Nicholas, B. Drevet, *Wettability at High Temperatures* (Oxford, Pergamon Press Ltd., 1999): 330-347.

[8] P. Shen, H. Fujii, and K. Nogi, "Wettability of Some Refractory Materials by Molten SiO_2-MnO-TiO_2-FeO_x Slag," *Materials Chemistry and Physics*, 114 (2-3) (2009), 681-686.

[9] N. Siddiqi et al., "Wettability of Graphite by CaO-SiO_2-Al_2O_3-FeO-MgO Slag," *High Temperature Materials and Processes*, 16 (4) (1997), 213-225.

[10] N. Siddiqi et al., "Slag-Graphite Wettability and Reaction Kinetics Part 2 Wettability Influenced by Reduction Kinetics, " *Ironmaking and Steelmaking*, 27 (6) (2000), 437-441.

[11] H. Shigeta and I. Masahisa, "Foaming of molten slags containing iron oxide," *Iron & Steel*, 9 (1983), 6.

[12] Y.H. Liu et al., "Density of the Blast Furnace Slag Bearing TiO_2 at 1 673 K," *ISIJ International*, 54 (9) (2014), 2017-2024.

[13] Y.H. Liu et al., "Surface Tension of the Molten Blast Furnace Slag Bearing TiO_2: Measurement and Evaluation," *ISIJ International*, 54 (10) (2014), 2154-2161.

[14] T. Young, "An Essay on the Cohesion of Fluids," *Philosophical Transactions of the Royal Society of London*, 95 (1805), 65-87.

Characterization of Minerals, Metals, and Materials 2016
Edited by: Shadia Jamil Ikhmayies, Bowen Li, John S. Carpenter, Jiann-Yang Hwang, Sergio Neves Monteiro, Jian Li, Donato Firrao, Mingming Zhang, Zhiwei Peng, Juan P. Escobedo-Diaz, and Chenguang Bai
TMS (The Minerals, Metals & Materials Society), 2016

REMOVING SILICA AND ALUMINA FROM LIMONITE USING WET HIGH GRADIENT MAGNETIC SEPARATOR

Deqing Zhu, Hao Wang, Jian Pan

School of Minerals Processing and Bioengineering, Central South University, Changsha, Hunan 410083, China

Keywords: limonite, mineralogy, vertical ring pulsating high gradient magnetic separator, removing silica and alumina

Abstract

Removing alumina and silica from the limonite by wet high gradient magnetic separator was conducted to elevate iron grade of limonite which is based on the investigation of mineralogy of the ore. The results show that alumina exists mainly in the form of kaolinite and silica exists mainly in silicate, which mainly occurs with a size below 0.074 mm. The vertical ring pulsating high gradient magnetic separator was adopted to upgrade the limonite less than 0.074mm, under the conditions of pulp concentration of 20%, swivel rotational speed of 2r/min, pulsating speed of 300 times per min, roughing magnetic field intensity of 7000Gs and scavenging magnetic field intensity of 5000Gs, the iron grade was up to 57.98% from 52.20%, content of SiO_2 and Al_2O_3 was reduced to 5.15% and 3.11% from 8.51% and 4.48%respectively. The total iron recovery of limonite was 90.80%, removal rate of silica and alumina was 21.69% and 21.59% respectively.

Introduction

High gradient magnetic separation is a powerful and useful technique for the recovery of fine weakly magnetic particles. In the recent decades, high gradient magnetic separation has undergone significant advancements and its applications has expanded with the beneficiation of hematite, limonite, ilmenite and rare earth minerals, and the purification of quartz, feldspar, fluorite and kaolin[1]. Limonite is mostly composed of the states of earthy, jelly, non crystalline and cryptocrystalline, which usually develops in cracks between hematite and goethite[2], with weak magnetism[3]. With the rapid development of the iron and steel industry, the contradiction supply and demand of iron ore is becoming more prominent. Therefore, the utilization of low-cost limonite is one of the effective measures for reducing the costs of iron and steel enterprises. But the high contents of alumina and silica in limonite will lead to the decline of desulphurizing ability, the increase of coke rate and the operation of deteriorating blast furnace when it was used as raw materials of iron making[4-5]. At present, the main beneficiation processes of limonite are gravity separation process, flotation process, wet high gradient magnetic separation technology, magnetization roasting-magnetic

separation, etc. the change of limonite density would cause low iron recovery rate, causing the serious waste of resources by gravity separation process[6]. In addition, Flotation process is now faced with serious problems such as a lot of chemical sewage, which will cause serious pollution, as well as difficulties in solving the pollution problem of fine-grained mud[7]. Magnetization roasting-magnetic separation process would produce a lot of volatile and high energy consumption[8]. Limonite belongs to the weak magnetic minerals, which exists magnetic difference with other material particles and it can be used for high gradient magnetic separation in views of environmental protection, economic benefit and mineral properties. Only water and electricity were used in the whole process of high gradient magnetic separation and water can be recycled[9-10]. Therefore, it has the advantages of good economic efficiency and good environmental protection benefit at the same time.

Experimental

Research Method

The experiment mainly includes the process mineralogy of limonite and wet high gradient magnetic separation. In the Study of process mineralogy of limonite, A D/Max2500X X-ray diffraction was used to determine the main mineral composition of limonite. A Leica DMRXE light microscope and SIRION200 scanning electron microscope (SEM) with EDS were applied to investigate the occurrence of silica and alumina and its inlay relationship with iron. The chemical phase analysis was used to determine the phase composition of silica and alumina respectively. In the process of wet high gradient magnetic separation, firstly, limonite was blended and divided. After that, it was screened into fractions of 8-5mm, 5-3mm, 3-1mm, 1-0.5mm, 0.5-0.15mm, 0.15-0.074mm and -0.074mm. The content of SiO_2 and Al_2O_3 in each fractions of limonite was determined by chemical analysis and the fine limonite was used to magnetic separation by LHGC-500 forced oil cooling vertical ring high gradient magnetic separator (the highest magnetic field strength is 1.4T). After the high gradient magnetic separation, the iron grade, the content of SiO_2 and Al_2O_3 in concentrate and tailings was analyzed respectively.

The iron recovery rate and the removal rate of silica and alumina acted as evaluation index and the calculation method showed as follow:

$$R_{Fe} = \frac{m_2 \times TFe_2}{m_1 \times TFe_1} \times 100\% \quad (1)$$

$$\eta = (1 - \frac{m_2 \times n_2}{m_1 \times n_1}) \times 100\% \quad (2)$$

Where: R_{Fe}-Iron recovery rate (%);

η- Removal rate of silica or alumina;

m_1-The mass of limonite before high gradient magnetic (g);

m_2-The mass of concentrate after high gradient magnetic (g);

n_1-The content of silica or alumina before high gradient magnetic (%);

n_2-The content of silica or alumina after high gradient magnetic (%);

TFe_1-Iron grade of limonite before high gradient magnetic (%);

TFe_2-Iron grade of concentrate after high gradient magnetic (%).

Study on Process Mineralogy of Limonite

The chemical composition of limonite is listed in Table I. As shown in Table I, the iron grade is 55.21%, the loss of ignition is up to 9.69% and higher content of SiO_2, Al_2O_3 is 5.49% and 2.75%, respectively. Therefore, if it can be further reduced the content of silica and alumina, which will be able to serve as high quality raw materials for iron making.

Table I. Chemical composition of iron ore (%)

Fe	FeO	Fe_2O_3	SiO_2	Al_2O_3	CaO	MgO	K_2O	Na_2O	MnO	S	P	LOI*
55.21	0.30	78.60	5.49	2.75	0.16	0.089	0.067	0.055	1.88	0.036	0.098	9.69

LOI*-loss on ignition

The X-ray diffraction was used to study the mineral composition of limonite, and the results are shown in Figure 1. The XRD results show that the main material in the ore is goethite, hematite, quartz, kaolinite, etc.

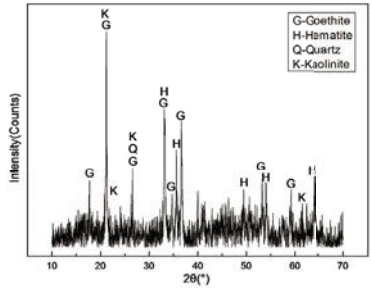

Figure 1 The X-ray diffraction analysis pattern of limonite

To determine the distribution of silica and alumina and its inlay relationship with iron in limonite, the process mineralogy of limonite was studied (Figure 2, Figure 3).

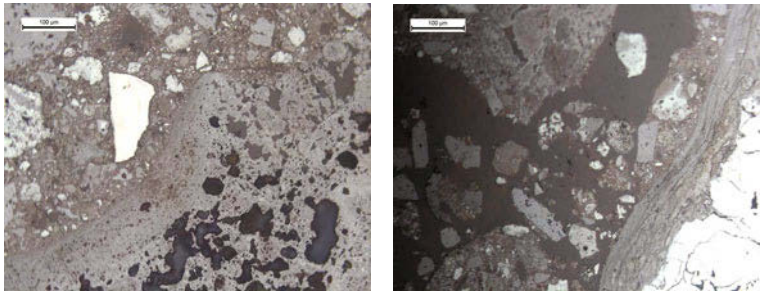

Figure 2 The optical microscope images of limonite

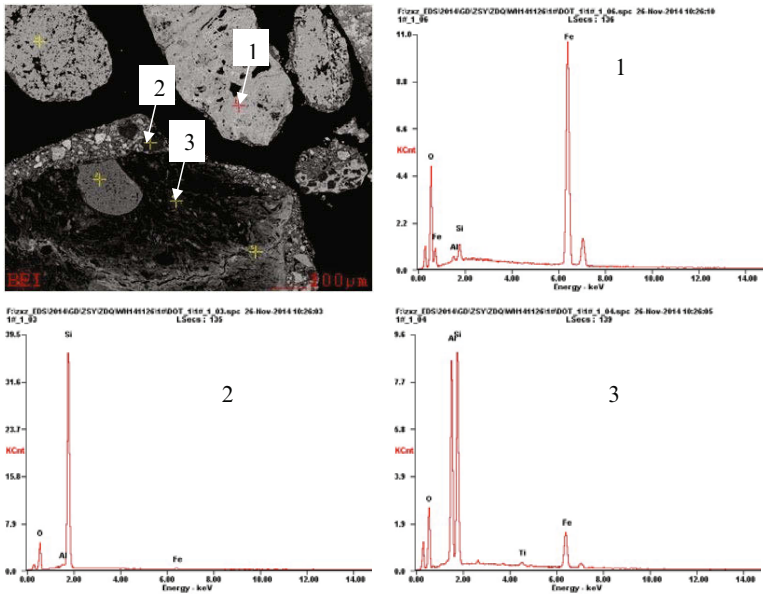

Figure 3 SEM images and EDS of point 1, 2 and 3 in limonite

As shown in Figure 2 and Figure 3, silica mainly exists in the form of silicate and the content of SiO_2 is 3.35%. The remaining silica exists in the form of quartz. Quartz mainly exists in two kinds of forms, one is assuming fine particle inclusions disseminated in limonite with embedded granularities of 20 m to 180 m. The other is forming bars with 5 m in width with other clay minerals disseminated in limonite. Alumina mainly exists in diaspore and kaolinite and the content of $A1_2O_3$ in the two kinds of minerals is 1.55% and 0.96% respectively. Alumina mineral mainly exists in two forms, one is assuming fine particle inclusions disseminated in limonite or inlayed at the edge of limonite. The kaolinite and diaspore filled in the limonite as cement. The other existential form is dispersing in iron minerals and assuming the structure of isomorphism. It is adverse for the separation of iron and alumina because of the mutual dissemination. A small amount of kaolinite adheres on the surface of massive limonite and forms bars with 20 m in thickness so it is easy to be removed in the high gradient magnetic separation process.

Wet High Gradient Magnetic Separation

The iron ore was screened into the fractions of 8-5mm, 5-3mm, 3-1mm, 1-0.5mm, 0.5-0.15mm, 0.15-0.074mm and -0.074mm. Distribution rate of iron, silica and alumina in each grade is shown in Table Ⅱ.

Table Ⅱ. The distribution of particle size and the content of iron, silica, alumina of each fraction in limonite

Fraction /mm	Yield /%	TFe /%	SiO_2 /%	Al_2O_3 /%	Distribution ratio of iron /%	Distribution ratio of silica /%	Distribution ratio of alumina/%
+8	5.11	56.10	2.83	2.39	5.20	2.63	4.41
-8+5	9.79	57.00	4.01	1.65	10.11	7.15	5.83
-5+3	22.98	57.10	4.07	2.28	23.31	17.04	18.92
-3+1	14.45	56.10	5.85	2.48	14.69	15.40	12.94
-1+0.5	12.18	55.20	5.33	2.54	12.19	11.83	11.17
-0.5+0.15	11.82	54.90	5.33	2.66	11.76	11.48	11.35
-0.15+0.074	4.63	56.40	5.79	2.72	4.73	4.88	4.54
-0.074	19.04	52.20	8.51	4.48	18.01	29.59	30.84
Total	100.0	55.43	5.49	2.75	100.00	100.00	100.00

As shown in Table Ⅱ, the content of silica and alumina less than 0.074mm are significantly higher and is up to 8.51% and 4.48% respectively, meanwhile, the fraction less than 0.074mm accounted for a higher proportion in the sample. Therefore, it is possible to achieve the goal of decreasing the content of silica and alumina in fine grade and improving the grade of iron ore by using high gradient magnetic separation in this experiment.

Rough Magnetic Separation of the Fraction Less than 0.074mm The vertical ring pulsating high gradient magnetic separator was adopted to upgrade the limonite less than 0.074mm under the conditions of pulp concentration of 20%, feeding capacity about 120Kg/h, swivel rotational speed of 2r/min, pulsating speed of 300 times per min, roughing magnetic field intensity of 7000Gs and the results are shown in Table III.

Table III. rough magnetic separation of the fraction less than 0.074mm

Feeding	Yield /%	TFe /%	Recovery rate of iron/%	SiO_2 /%	Removal rate of silica/%	Al_2O_3 /%	Removal rate of alumina/%
Raw ore	100.00	52.20	100.00	8.51		4.48	
Concentrate1	59.02	56.40	63.77	6.12	57.56	3.65	51.92
Tailing 1	40.98	46.15	36.23	11.95		5.68	

Scavenging Magnetic Separation of the Fraction Less than 0.074mm The vertical ring pulsating high gradient magnetic separator was adopted to upgrade the limonite less than 0.074mm under the conditions of pulp concentration of 20%, feeding capacity about 120Kg/h, swivel rotational speed of 2r/min, pulsating speed of 300 times per min, scavenging magnetic field intensity of 5000Gs and the results are shown in Table IV.

Table IV. scavenging magnetic separation of the fraction less than 0.074mm

Feeding	Yield /%	TFe /%	Recovery rate of iron/%	SiO_2 /%	Removal rate of silica/%	Al_2O_3 /%	Removal rate of alumina/%
Concentrate1	100.00	56.40	100.00	6.12		3.65	
Concentrate2	74.23	57.98	76.31	5.15	37.54	3.11	36.75
Tailing 2	25.77	51.85	23.69	8.91		5.21	

As seen in Table III and Table IV, the iron grade of fraction less than 0.074mm increases from 52.20% to 57.98% under the condition of roughing magnetic field intensity of 7000Gs and scavenging magnetic field intensity of 5000Gs and the content of SiO_2 and Al_2O_3 reduces to 5.15% and 3.11% from 8.51% and 4.48%, respectively. The total iron recovery of fraction less than 0.074mm is 48.66% and the removal rate of silica and alumina is up to 73.49% and 69.59% respectively.

The Comparison of Limonite Products before and after the Wet High Gradient Magnetic Separation

The vertical ring pulsating high gradient magnetic separator was adopted to upgrade the limonite less than 0.074mm under the conditions of pulp concentration of 20%, swivel rotational speed of 2r/min, pulsating speed of 300 times per min, roughing magnetic field intensity of 7000Gs and scavenging magnetic field intensity of 5000Gs. The content of Fe, SiO_2, Al_2O_3, the recovery rate of Fe and removal rate of silica and alumina of the new limonite obtained by mixing the concentrate less than 0.074mm and the other fraction limonite as shown in Table V and Table VI.

Table V. Product analysis of limonite after the wet high gradient magnetic separation on the fraction less than 0.074mm

Iron ore	Yield /%	TFe /%	Recovery rate of iron/%	SiO_2 /%	Removal rate of silica /%	Al_2O_3 /%	Removal rate of alumina/%
Original limonite	100.00	55.43	100.00	5.49		2.75	
New limonite	89.30	56.36	90.80	4.81	21.69	2.41	21.59

Table VI. Grain size composition comparison

Fraction/mm	+8	8-5	5-3	3-1	1-0.5	0.5-0.15	0.15-0.074	-0.074
Original limonite/%	5.11	9.79	22.98	14.45	12.18	11.82	4.63	19.04
New limonite/%	5.72	10.96	25.73	16.19	13.64	13.24	5.18	9.34

According to the results of Table V and Table VI, the iron grade of new limonite obtained by mixing the concentrate less than 0.074mm and the other fraction limonite is up to 56.36%

from 55.43% and the content of SiO_2 and Al_2O_3 reduces from 5.49% and 2.75% to 4.81% and 2.41%, respectively. The total iron recovery of ore is 90.80% and the removal rate of silica and alumina is 21.69% and 21.59%, respectively. Meanwhile, the limonite fraction less than 0.074mm reduces from 19.34% to 9.34%.

Conclusion

1. The analysis of process mineralogy demonstrates that alumina and silica minerals mainly exist in kaolinite, diaspore and silicate, which mainly occurs with a size below 0.074 mm.

2. The vertical ring pulsating high gradient magnetic separator was adopted to upgrade the limonite fraction less than 0.074mm under the condition of roughing magnetic field intensity of 7000Gs and scavenging magnetic field intensity of 5000Gs and the iron grade is up to 57.98% from 52.20% and the content of SiO_2 and Al_2O_3 reduces to 5.15% and 3.11% from 8.51% and 4.48%, respectively. The total iron recovery of fraction less than 0.074mm is 48.66% and the removal rate of silica and alumina is 73.49% and 69.59%, respectively.

3. The iron grade of new limonite obtained by mixing the concentrate less than 0.074mm and the other fraction limonite is up to 56.36% from 55.43% and the content of SiO_2 and Al_2O_3 reduces to 4.81% and 2.41% from 5.49% and 2.75%, respectively. Meanwhile, the total iron recovery of ore is 90.80% and the removal rate of silica and alumina is 21.69% and 21.59%, respectively.

References

1. J. Svoboda, “A realistic description of the process of high-gradient magnetic separation,” *Minerals Engineering*, 14(11) (2001), 1493-1503.

2. G.H. Li, et al. “Novel process and mechanisms of aluminum-iron separation of high-aluminum limonite ore,” *The Chinese Journal of Nonferrous Metals,* 18(11) (2008), 2087-2093. (In Chinese)

3. F.O. Connor, W.H. Cheung, and M.Valix, “Reduction roasting of limonite ores: effect of dehydroxylation,” *International journal of mineral processing,* 80(2) (2006), 88-99.

4. Y.C Hong, “Study on fundamental properties of limonite in sinter process,” *Journal of iron and steel research*, 22(9) (2011), 9-12. (In Chinese)

5. Z.Q Huang et al. “Phenomenon of reduction and volatilization of MgO at high temperatures,” *Journal of northeastern university: natural science*, 23(4) (2002), 355-358. (In Chinese)

6. G.Y Wang. *Mineralogy* (Beijing: China University of Geosciences press, 1991). (In Chinese)

7. L.O. Filippov, V.V.Severov, I.V. Fillppova, "An overview of the beneficiation of iron ores via reverse cationic flotation," *International journal of mineral processing,* 127(2014), 62-69.

8. K.O. Jang et al. "Chemical and mineral transformation of a low grade goethite ore by dehydroxylation, reduction roasting and magnetic separation," *Minerals engineering*, 60(2014), 14-22. (In Chinese)

9. Dahe Xiong, Shuyi Liu, and Jin Chen, "New technology of pulsating high gradient magnetic separation," *International journal of mineral processing*, 54(2) (1998), 111-127.

10. P.F Garcia et al. "High-gradient magnetic separation for technical scale protein recovery using low cost magnetic nanoparticles," *Separation and purification technology*, 150(2015), 29-36.

Characterization of Minerals, Metals, and Materials 2016
Edited by: Shadia Jamil Ikhmayies, Bowen Li, John S. Carpenter, Jiann-Yang Hwang, Sergio Neves Monteiro, Jian Li, Donato Firrao, Mingming Zhang, Zhiwei Peng, Juan P. Escobedo-Diaz, and Chenguang Bai
TMS (The Minerals, Metals & Materials Society), 2016

EVALUATION OF WHITE BENTONITE MODIFIED BY ACID ATTACK

[1*]C.G. Bastos Andrade; [1]D.M. Fermino; [1]M.G. Fernandes; [1]F.R. Valenzuela-Diaz

[1]Department of Metallurgical and Materials Engineering
EPUSP Escola Politécnica Universidade São Paulo
Postal Code 05508-900 – São Paulo - SP – Brazil
gianesic@usp.br

Keywords: clay, bentonite, acid attack, industrial use

Abstract

For industrial use, the smectite clays must be cleared of impurities, usually obtained by acid modification, using a high concentration solution of inorganic acid at temperatures under boiling point. In the present paper, a sample of white bentonite from Paraiba, Brazil, was modified by hydrochloric acid under moderate conditions (90°C, reaction times of 1, 6, 12, 18 and 24hours in close reactor, concentration of the aqueous solution of hydrochloric acid 1.5 M, acid solution/clay ratio of 1g/10mL). The purpose of these attacks is to reduce the concentration of impurities with minimal change in the clay minerals structure. The modified samples were characterized by X-ray diffraction (XRD), X-ray fluorescence (XRF), Cation Exchange Capacity (CEC), Stereomicroscopy, Scanning Electron Microscopy (SEM) and Energy Dispersive X-ray Detector (EDS). Thus, this modified bentonite tends to be a good economic and environmental alternative in manufacturing of products with high added value such as cosmetics and polymer/clay nanocomposites.

Introduction

The brazilian white bentonite from Paraiba is a smectite clay with non-preponderate interlayer cation and low iron concentration [1].
The classification of bentonites is determinate according the geologic origin of clay, but if the smectite clays presents the same properties of traditional bentonites and/or is commercialized to the same use, those clays, by a common agreement, can be classified as bentonites, which presents similar properties such as colloidal material, absolving capacity and activation capacity with high grades [2-5].
Among the bentonites for industrial use, exist those with highly water absorption and non-water absorption. The sodium interlayer is responsible for the capacity of bentonites absorption instead those not, have calcium as a preponderate cation [6,7].
The industrial application of bentonites is vast, mostly used in oil industry as drilling fluids, in pharmaceutic and cosmetics as dissecant, in the food industry as oil bleaching, among others applications. For those applications, bentonites needs to be clean of mineral impurities. Acid attack is a common method that provides a specific area increased by structure disorganization, mesopores and mineral impurities cleaning. Other benefit of acid attack is improving of acid sites with more porosity, excellent properties when apply in catalysis [8-13].

Modified clays with organic acid with high concentrations have being studied by several groups, aiming clays bleaching e purifying, for posterior use mostly in bleaching process or oil, grease and organic, minerals and animals fat. The industrial use for clays is also based on exchangeable cations and clay minerals properties [14-16].
The economic advantages over imported clays used in processes to obtain products with high value as cosmetics and nanocomposites justify the studies aiming to demonstrate that the white bentonite modified by moderated acid attack tends to be a good alternative to material raw.

Materials and Methods

Start Materials

The white bentonite, in its natural form, was from Paraíba´s State, Brazil was submitted to mild acid attack using a concentration of the aqueous solution of hydrochloric acid 1.5 M, clay/acid solution ratio of 1g/10mL, at 90°C under bellow boiling temperature and at short times of reaction 1, 6, 12, 18 and 24 hours in close reactor.
The attacked clay was washed, by filtration, with distilled water until pH 7-8, and then subjected to drying at 60°C for 24 hours.
After drying, the clay was grounded using a manual mortar and vibratory ball mill until completely pass through #200 mesh sieve.

Materials Characterization

The modified samples were characterized by X-ray diffraction (XRD), X-ray fluorescence (XRF), Cation Exchange Capacity (CEC), Stereomicroscopy, Scanning Electron Microscopy (SEM) and Energy Dispersive X-ray Detector (EDS).
The XRD was performed on diffractometer model X'Pert Pro MPD (Panalytical) with Cu anodes; scan from 5° to 90° 2Θ; 40kV and 40mA.
The scanning electron microscopy (SEM) and energy dispersive X-ray detector (EDS) were performed on scanning electron microscopy, Philips - EDAX INSPECT 50 with energy dispersive x-ray detector (EDS).
To observe the clay was used a stereomicroscopy Zeiss, model Stemi 2000C.
CEC was performed using the ammonium acetate method.
The XRF was performed on X-ray fluorescence spectrometer Panalytical model Axios Advenced with loss on ignition.

Results and Discussion

The intensity of the smectitic $d_{(001)}$ peak tend to diminish its intensity with the time of attack as the acid have more time to destroy the octahedral sheet of the clay mineral. The increase of the quartz peak with the time of acid attack is a possible indicative of the dissolution of part of the clay minerals. It was verified that the clays submitted to mild acid attack during long times presented more bleaching than others.
Table 1 presents the interplanar distance of the $d_{(001)}$ smectite peaks for white bentonite samples attacked for different times and its intensities. The table shows also the intensities of the quartz peaks at 3,33Å.

Table 1- $d_{(001)}$ smectitic peaks, smectitic peaks intensities, and intensities of the quartz peaks.

Sample	Smectitic peak $d_{(001)}$ (Å)	Smectitic peak intensity (counts)	Quartz peak at 3.33 Å intensity (counts)
24h in water	15.28	144	n/a
1h attack	15.45	140	50
6h attack	14.73	122	77
12h attack	15.16	104	58
18h attack	15.12	80	50
24h attack	15.86	64	80

The figures 1 and 2 presents the EDS results for samples treated with water for 24h and HCl for 24h at 90°C. Is possible to observe the peak reduction of metals, that indicates a good result of purification at sample treated with HCl for 24h.

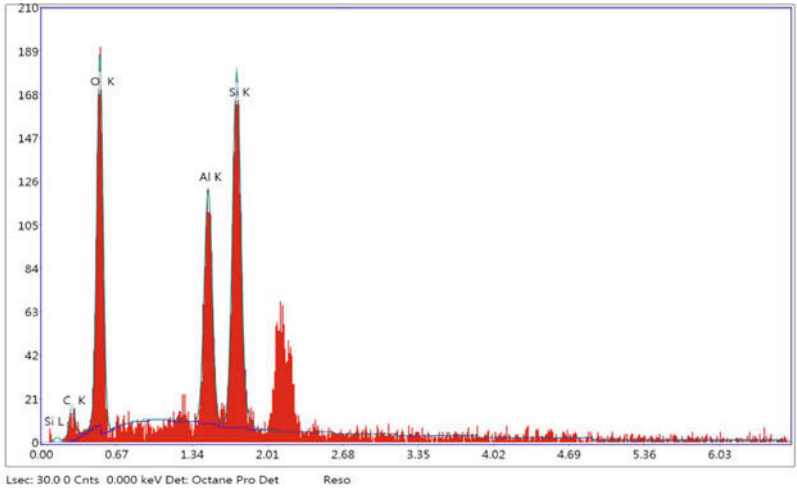

Figure 1 – EDS area / results white bentonite treated with H_2O for 24h

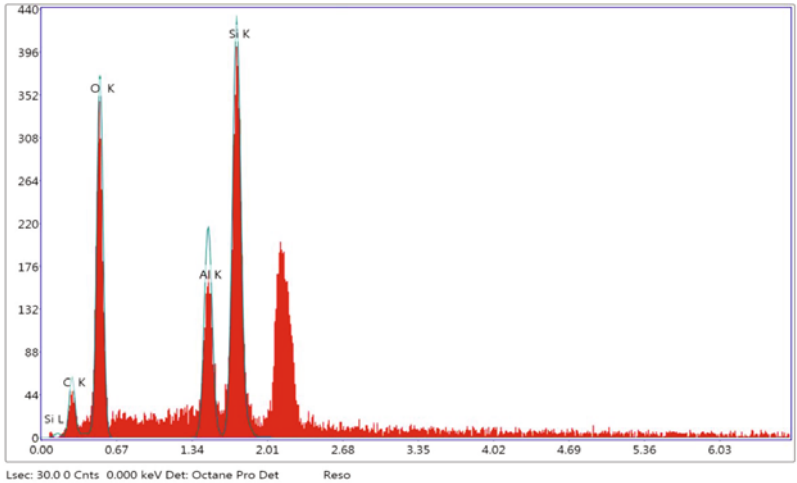

Figure 2 – EDS area / results white bentonite treated with HCl for 24h

Table 2 presents the XRF values where is possible to observe the oxides percentage diminishing after acid treatment.

Table 2 – XRF white bentonite, quantitative analysis, values in percentage of oxides.

Sample	SiO_2	Al_2O_3	Fe_2O_3	MnO	MgO	CaO	Na_2O	K_2O	TiO_2	P_2O_5	LI
H_2O	45.1	22.0	3.86	< 0.10	1.77	4.03	0.17	0.38	0.94	< 0.10	21.9
HCl 1h	49.5	24.1	4.09	< 0.10	1.17	0.31	< 0.10	0.40	1.04	< 0.10	19.4
HCl 6h	50.7	23.9	3.57	< 0.10	1.01	0.19	< 0.10	0.40	1.05	< 0.10	19.8
HCl 12h	52.3	22.0	3.01	< 0.10	0.78	0.11	< 0.10	0.40	1.10	< 0.10	20.4
HCl 18h	54.0	21.8	2.95	< 0.10	0.77	< 0.10	< 0.10	0.40	1.13	< 0.10	19.6
HCl 24h	55.5	20,.1	2.48	< 0.10	0.68	< 0.10	< 0.10	0.41	1.17	< 0.10	20.3

Table 3 presents the CEC values, that tends to diminish after treatment, with the time of attack with the 24 hours attacked sample having only 70% of the original value.

Table 3 - CEC results of white bentonite treated.

Sample	CEC (meq/100g)	% of the no attacked sample
24h in water	41.30	100
1h attack	38.29	92.72
6h attack	37.63	91.11
12h attack	33.27	80.55
18h attack	31.33	75.86
24h attack	28.99	70.20

At the stereomicroscopy image 1 is possible observe the impurity particles into the sample treated with water for 24h.

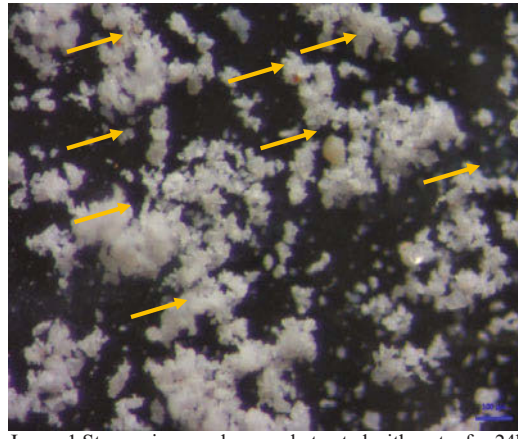

Image 1 Stereomicrography sample treated with water for 24h

At the stereomicroscopy image 2 the sample, treated with HCl for 6h, is possible to observe that sample is clean of impurity particles.

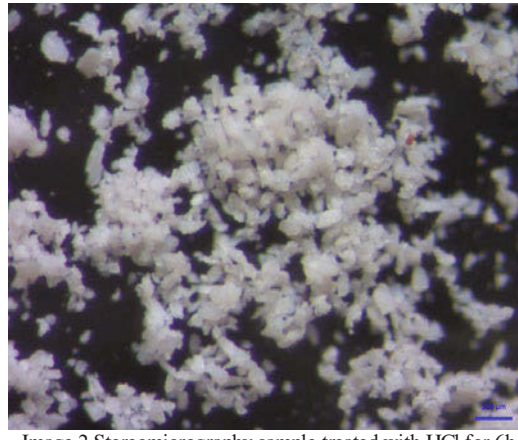

Image 2 Stereomicrography sample treated with HCl for 6h

The image 3 shows the SEM micrographic of the sample treated with water for 24h at 90°C.

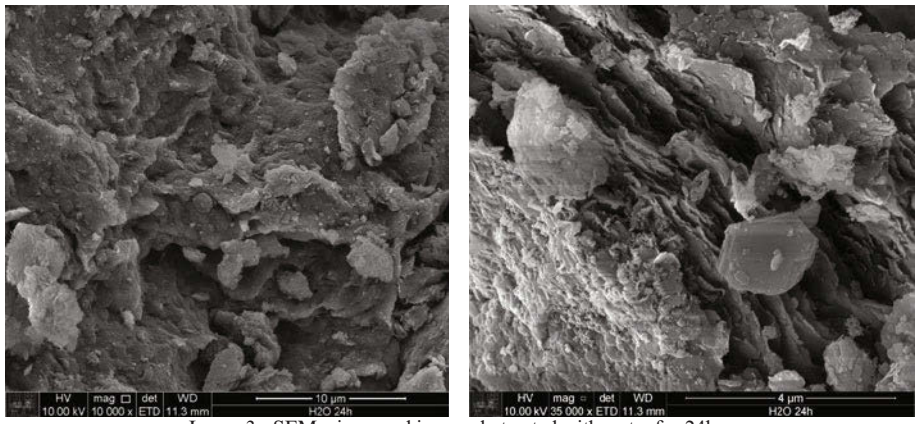

Image 3 - SEM micrographic sample treated with water for 24h

The image 4 shows the SEM micrographic of the sample treated with HCl for 24h at 90°C.

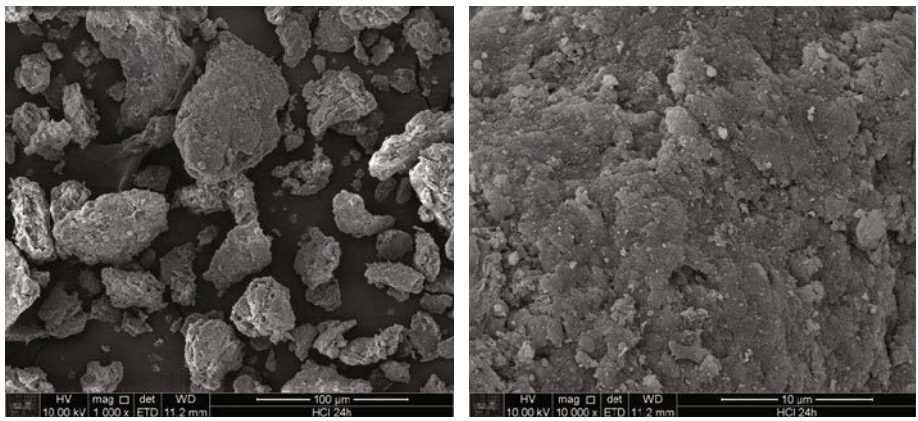

Image 4 - SEM micrographic sample treated with HCl for 24h

The lamellar structure of the samples is agglomerated in layers, mostly in same size. This is a possible indication that crystal structures of smectite do not present a complete destruction.

Conclusions

The white bentonite sample submitted to mild attack acid demonstrated a good response to the bleaching and purification at reaction time of 6 hours with a good preservation of crystalline structure and a good bleaching which was observed in Stereomicroscopy and SEM images.
At same time of treatment, was obtained a good quartz and other elements purification, observed in XRF.
The most evident modifications in decolorizing and CEC occurred in the first 12 hours of acid treatment.
In accordance with the methodology presented and from the results acquired, decrease the concentration of impurities, with no significant change in the clay minerals structure, aiming at use in products of high value such as cosmetics and polymer/clay nanocomposites revealed an economical and environment efficient alternative.

References

[1]Valenzuela-Diaz, F.R. Preparação a nível de laboratório de algumas argilas esmectíticas organofílicas. Tese (Doutorado). Departamento de Engenharia Química da Escola Politécnica da Universidade de São Paulo, SP, 1994.
[2]Souza Santos, P. Ciência e Tecnologia de Argilas, vol. 1, 2a Ed., Edgar Blücher, S. Paulo, SP, 1992.
[3]Grim, R.E.; Clay Mineralogy, 2nd Ed., McGraw-Hill Book, New York, EUA, 1968.
[4]Valenzuela-Díaz, R.F.; Souza Santos, P.; Souza Santos,H.: A Importência das argilas industriais brasileiras. Química Industrial V.42 p.33-37, 1992.
[5]Abreu, S.F. Recursos minerais do Brasil, Ed. Edgard Blucher, 2ª. Ed., V.1, SãoPaulo, SP, 1973.
[6]Pereira, K.R.O. Ativação ácida e preparação de argilas organofílicas partindo-se de argila esmectítica proveniente do Estado da Paraíba. Dissertação (Mestrado), Orientadora: Meiry Gláucia Freire Rodrigues, Campina Grande – PB, 2003.
[7]Pereira, K.R.O.; Ramos Vianna, M.M.G; Rodrigues, M.G; Valenzuela-Diaz, F.R. Argila de alguns poluentes orgânicos em argilas organofílicas. Anais do XVI Congresso Brasileiro de Ciência e Engenharia dos Materiais, CD. Porto Alegre, RS 2004.
[8]Gomes,C.F.Argilas: o que são e para que servem, 1a Ed., Fundação Calouste Gulbenkian, Lisboa, Portugal Ed., Fundação Calouste Gulbenkian, Lisboa, Portugal, 1988.
[9]Murray, H.H, Appl. Clay Sci. 17, 2000.
[10]Ferreira, H.S,; Menezes, R.R; Ferreira, H. S. ; Martins, A. B. ; Neves, G. A. ; Ferreira, H. C.; Cerâmica 54 (2008) 77.
[11]Amorim, L. V. ; Farias, K. V. ; Viana, J. D. ; Barbosa, M. I. R. ; Pereira, E. ; França, K. B.; Lira, H. L. ; Ferreira, H. C. Cerâmica 51 (2005) 128.
[12]Pereira, K.R.O.; Hanna, R.A.; Ramos Vianna, M.M.G; Pinto, C.A.; Rodrigues, M.G; Valenzuela-Diaz, F.R. Brasilian organoclays as nanostructure sorbents of petroleum-derived hydrocarbons. Materials Research, v.8, n.1, p.77-80, 2005.
[13]Vaccari, A.; Applied Clay Science 14, 1999.

[14]Souza Santos, P. Ciência e Tecnologia de Argilas, 2a com a colaboração de Soza Santos H., V.3Ed., Edgar Blücher, S. Paulo, SP (1989)vol.1 e 1992 vol.2e3 1ed. Tecnologia das Argilas – vol.2 Edgar Blücher e EDUSP, São Paulo, SP, 1974.
[15]Valenzuela-Diaz, F.R.; Souza Santos, P. Studies on the acid ativation of Brasilian smetctitic clays. Química Nova, v.24, n.3, 2001.
[16]Grim, R.E. Bentonites – Elsevier, Amsterdam, 1978.

Characterization of Minerals, Metals, and Materials 2016

Processing and Corrosion

Session Chairs:
Jian Li
Prathmesh Joshi

Characterization of Minerals, Metals, and Materials 2016
Edited by: Shadia Jamil Ikhmayies, Bowen Li, John S. Carpenter, Jiann-Yang Hwang, Sergio Neves Monteiro, Jian Li, Donato Firrao, Mingming Zhang, Zhiwei Peng, Juan P. Escobedo-Diaz, and Chenguang Bai
TMS (The Minerals, Metals & Materials Society), 2016

CHARACTERIZATION OF IRON OXIDE SCALE FORMED IN NAPHTHENIC ACID CORROSION

Peng Jin, Winston Robbins, Gheorghe Bota, Srdjan Nesic

Institute for Corrosion and Multiphase Technology,
Department of Chemical & Biomolecular Engineering, Ohio University,
342 West State Street, Athens, OH 45701

Keywords: Naphthenic acids, Magnetite, Iron oxide, High temperature corrosion, Crude fractions, Model sulfur compounds

Abstract

Naphthenic acid corrosion (NAC) is one of the major concerns for corrosion engineers in refineries. Iron sulfide (FeS) scales, formed from sulfur compound corrosion, are traditionally considered to be semi-protective and lower NAC. However, no relationship has been found between protectiveness and the characteristics of FeS scale. In this study, the corrosive processes of refineries have been probed with laboratory experiments using a model sulfur compound and petroleum-derived naphthenic acids. The morphology and composition of scales were analyzed with a combination of scanning electron microscopy (SEM), transmission electron microscopy (TEM), energy dispersive X-ray spectroscopy (EDS), and convergent beam electron diffraction (CBED). These high resolution microscopy techniques revealed the presence of an iron oxide (Fe_3O_4 or magnetite) layer on metal surfaces under a FeS layer in the scale. The presence of an oxide scale was correlated with the NAP acid activity during the experiments. It is postulated that the formation of the Fe_3O_4 layer resulted from the decomposition of iron naphthenates at high temperatures.

Introduction

Naphthenic acid corrosion (NAC) is one of the major concerns for corrosion engineers in refineries [1]. With the decreasing supply of light sweet crude oil the increasing prevalence of the heavy crude oil with high naphthenic acid content may lead to severe corrosion of facilities. However, sulfur compounds in crude oils are also corrosive while forming a quasi-protective iron sulfide scale so that interactions between the two components are difficult to predict. Combined sulfur and naphthenic acid (SNAP) corrosion is generally described by the following reactions: [2]

$$Fe + 2RCOOH \rightarrow Fe(RCOO)_2 + H_2 \quad \text{(Reaction 1)}$$
$$Fe + H_2S \rightarrow FeS + H_2 \quad \text{(Reaction 2)}$$
$$Fe(RCOO)_2 + H_2S \leftrightarrow FeS + 2RCOOH \quad \text{(Reaction 3)}$$

In NAC, naphthenic acid (RCOOH) attacks iron and generates oil-soluble iron naphthenate ($Fe(RCOO)_2$) as shown in Reaction 1. Reactive sulfur compounds in the crude oil also attack the iron (possibly by H_2S as an intermediate) and form an insoluble iron sulfide (FeS) scale,

Reaction 2. However, in solution, H_2S reacts rapidly with iron naphthenate and regenerates the naphthenic acid while excess naphthenic acid can, in a slower process, dissolve an iron sulfide scale, Reaction 3. The porous iron sulfide scale can be quasi-protective by limiting diffusion of the reactive species to the surface. However, conditions that promote this protection are ill-defined [3].

Our group has previously reported that NAC not only forms iron naphthenate but also could lead to the formation of a protective scale of magnetite (Fe_3O_4) [5]. This scale was hypothesized to be the product of iron naphthenate decomposition on the surface at high temperatures. To determine the effect of temperature on this magnetite formation, we have extended our pretreatment/challenge protocol to cover a range of temperatures with a model reactive sulfur compound and a petroleum-derived naphthenic acid mixture. To that end, steel rings were subjected to the pretreatment protocol at 450˚F, 600˚F, or 650˚F in an autoclave and then challenged for protectiveness at 650˚F in a rotating cylinder flow through reactor. After each corrosion experiment, corrosion rates were determined and surfaces examined by scanning electron microscopy (SEM), focused ion beam/transmission electron microscopy (FIB/TEM), energy dispersive X-ray spectroscopy (EDS), and convergent beam electron diffraction (CBED).

Experimental

Materials

Two commonly utilized refinery steels, A106 carbon steel (CS) and A182-F5 chrome steel (5Cr), were used in the shape of rings with inner diameter 70.43 mm, outer diameter 81.76 mm, and thickness 5 mm. Before experiments, each ring was polished with 400 and 600-grit silicon-carbide paper (SiC) in succession. Isopropanol was used to flush specimens during polishing to prevent oxidation and overheating. After polishing, specimens were wiped with a paper towel, rinsed with toluene and acetone, dried with N_2, and weighed.

After each experiment, rings were rinsed with toluene and acetone, gently rubbed with a soft plastic brush, treated with “Clarke” solution (ASTM G1 - 03) and reweighed. Corrosion rates were calculated by weight loss.

Test Solutions

Recrystallized dodecylsulfide (DDS) and a commercial naphthenic acid mixture (NAP) were used to represent reactive sulfur compounds and naphthenic acids. The DDS and NAP were dissolved in a technical grade white mineral oil to prepare three experimental solutions:

- "NAP only": NAP in mineral oil (TAN = 1.75, S = 0 wt.%),
- "DDS only": DDS in mineral oil (TAN = 0, S = 0.25 wt.%), and
- "DDS + NAP": DDS and NAP in mineral oil (TAN = 1.75, S = 0.25 wt.%).

Procedures

Pretreatment – A set of six rings (three of each alloy) were used in each experiment. They were immersed in a stirred one-liter autoclave filled with 0.7 liter of test solution. The autoclave was purged with N_2 and pressurized to 100 psig before the temperature was raised to a preset value (450˚F, 600˚F, or 650˚F). Pretreatment started when the autoclave reached the experiment temperature and continued for 24 hours. After cooling to room temperature, the autoclave was opened and rings were removed for weight loss measurement (two rings) and surface examination (the third ring).

Challenge - A parallel set of rings was prepared under the same pretreatment conditions in a stirred autoclave, but at the end of the pretreatment the entire set was transferred (unwashed with intact scales) onto a cylinder that was mounted in a High Velocity Rig (HVR) [5]. After the HVR had been brought to 650˚F with 7.5 ml/min flow of mineral oil alone, the rings were challenged with a mineral oil solution of NAP at TAN 3.5 and 650˚F for 24 h. When the HVR had cooled to room temperature the rings were removed for weight loss and surface examination by the same methods used after the pretreatment step.

Evaluation of Corrosion Rates

Corrosion rates of specimens were calculated based on their weight loss during the experiment. For the *pretreatment* experiment conducted in the autoclave, the corrosion rate was calculated using Equation (1).

$$CR_{Pretreatment} = \frac{(IW - FW)}{\rho_{steel} \times A_{s,Pretreatment} \times t_{Pretreatment}} \times 10 \times 24 \times 365 \qquad 1$$

where:
$CR_{Pretreatment}$ – Pretreatment corrosion rate, [mm/y]
IW – Initial weight of fresh polished ring, [g]
FW – Final weight of ring after treatment with Clarke solution, [g]
ρ_{steel} – Density of ring, [g/cm^3]
$A_{s,\ Pretreatment}$ – Area of ring exposed to corrosive fluid during pretreatment, [cm^2]
$t_{Pretreatment}$ – Duration of experimentation in the stirred autoclave (in each case 24 h), [h]

In a combined *pretreatment-challenge* experiment, freshly polished specimens were pretreated in the autoclave followed by challenging them in the HVR. While the corrosion rate in the *pretreatment* step could be calculated according to Equation (1), the challenge corrosion was assessed using Equation (2).

$$CR_{Challenge} = \frac{(IW - FW - WL_{Pretreatment})}{\rho_{steel} \times A_{s,Challenge} \times t_{Challenge}} \times 10 \times 24 \times 365 \qquad (2)$$

$CR_{Challenge}$ – Net corrosion rate from the challenge phase (excluding the autoclave phase), [mm/y]
IW – Initial weight of fresh polished ring, [g]
FW – Final weight of ring after treatment with Clarke solution, [g]
$WL_{Pretreatment}$ – Weight loss of ring in the pretreatment phase, [g]
ρ_{steel} – Density of ring, [g/cm^3]
$A_{s,\ Challenge}$ – Area of ring exposed to corrosive fluid during challenge, [cm^2]
$t_{Challenge}$ – Duration of experimentation in the HVR (in each case 24 h), [h]

Results

Pretreatment results

Figure 1 compares the corrosion rates for CS and 5Cr rings pretreated at 450˚F, 600˚F, and 650˚F with the three test solutions. Both steels showed similar *pretreatment* corrosion rate behavior. Corrosion rates increase with temperature in all cases as expected. The "DDS only" corrosion rates appear to increase more rapidly than "NAP only". Differences between CS & 5Cr in each solution were close to experimental error. In "DDS + NAP", the CS and 5Cr corrosion rates appear closer to the "NAP only" rates except at the highest temperature. Unexpectedly, in "DDS + NAP", the NAP appears to have suppressed the DDS contribution on CS while it has no effect on the 5Cr. This is consistent with the convention that the Cr provides protection against reactive sulfur compounds.

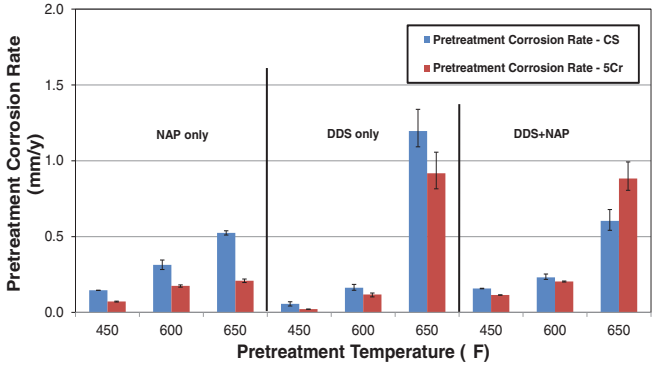

Figure 1. Pretreatment corrosion rates of CS and 5Cr at 450˚F, 600˚F, and 650˚F.

Challenge results

Figure 2 compares the CS and 5Cr *challenge* corrosion rates for pretreated rings with the baseline corrosion rates for freshly polished rings. Obviously, the metallurgy had more impact on corrosion resistance than pretreatment, *i.e.*, in all cases pretreated CS was more severely corroded than 5Cr. While "NAP only" pretreatment had a negligible effect on CS corrosion rates at all temperatures, "DDS only" pretreatment only afforded protection at 650˚F. The most protective scale for CS was generated in pretreatment with "DDS + NAP" at 600˚F. These results are consistent with expectations based on other SNAP corrosion studies.

The response of 5Cr to pretreatments was strikingly different. Pretreatment with "DDS only" on 5Cr was not protective at all temperatures while pretreatment with "NAP only" at 600˚F and 650˚F gave challenge corrosion rates close to zero. A similar pattern is seen for the pretreatments with both corrosive components, *i.e.,* challenge corrosion rates for rings after pretreatment at 600˚F and 650˚F with "DDS + NAP" were significantly lower than baseline. These results contradicted traditional SNAP corrosion theory that would anticipate a larger dependence on reactive sulfur. Therefore advanced surface analysis techniques were used to examine 5Cr ring surfaces.

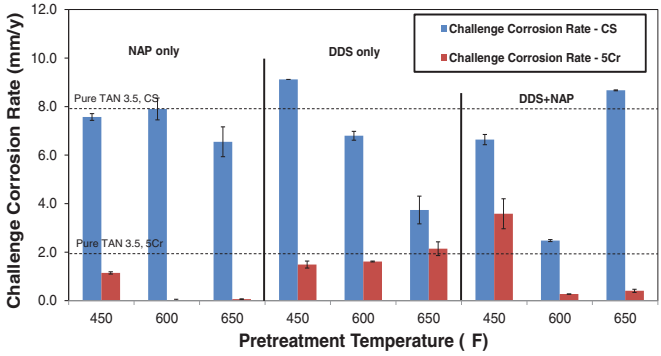

Figure 2. Challenge corrosion rates for CS and 5Cr pretreated with three solutions. Dotted lines indicate pure TAN 3.5 corrosion rates for CS and 5Cr, respectively.

5Cr Surface Analyses

There is no obvious corrosion product scale on the surface in the cross-section SEM and EDS analysis of 5Cr rings after *pretreatment* in "NAP only" at all three temperatures (Figure 3). However, rings corresponding to those shown in Figure 3b and c were the most resistant to the more severe challenge conditions with the same acid at higher TAN (Figure 2).

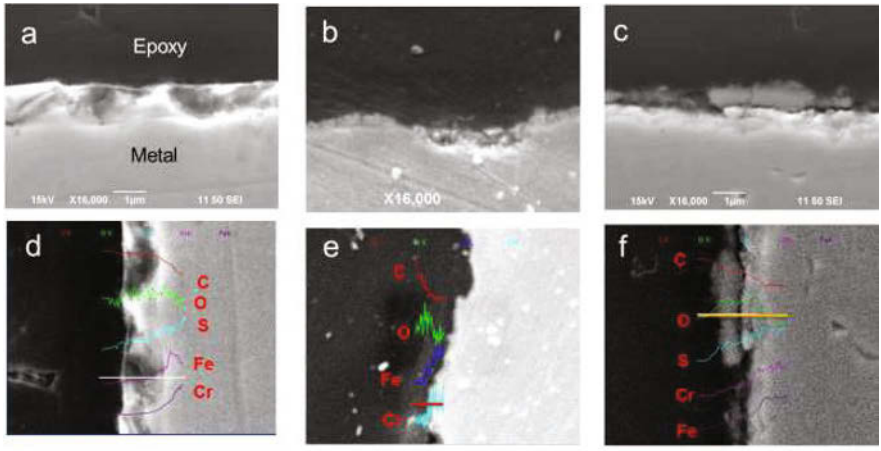

Figure 3. Cross-section SEM images of 5Cr rings pretreated in "NAP only" at 450°F (a), 600°F (b), and 650°F (c). Images (d), (e), and (f) show corresponding EDS analyses along the lines shown on images.

Combined FIB/TEM/EDS analyses were conducted on a 5Cr ring pretreated in "NAP only" at 450°F and 600°F to find the explanation for the resistance to the challenge. The TEM cross section for the 5Cr ring after 450°F pretreatment found no scale on the metal surface (Figure 4). This is consistent with the high *challenge* corrosion rate (Figure 2). On the other hand, after the pretreatment at 600°F a very thin (165 nm) scale is detected by TEM (Figure 5). EDS cross-section analyses detected no oxide scale for the 400°F pretreatment but did find evidence of iron and oxygen with traces of chromium and sulfur in the scale left by the 600°F pretreatment. The trace elements are attributed to the chromium in the alloy and sulfur content in NAP. Analysis of this scale by CBED shows magnetite (Fe_3O_4) as its major component (Figure 6) [5].

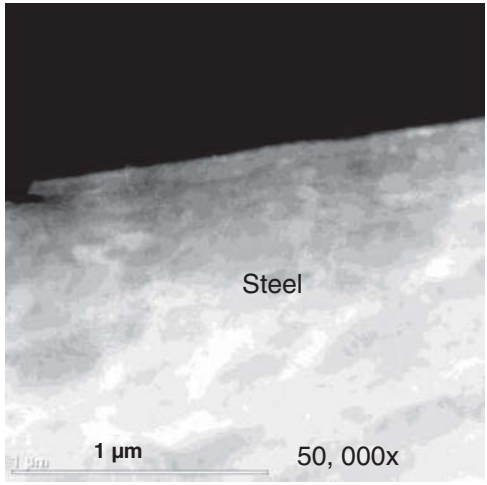

Figure 4. TEM image of 5Cr ring pretreated in "NAP only" at 450°F.

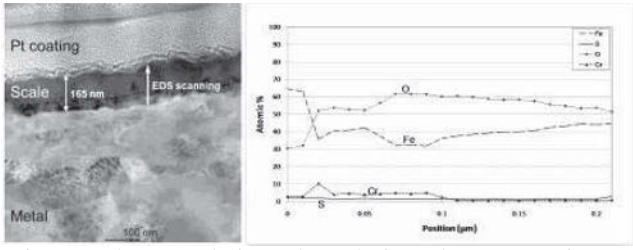

Figure 5. TEM image and EDS analysis on the scale formed on 5Cr specimen pretreated with "NAP only" solution at 600°F. The elemental data were collected along the white arrow from the bottom to the top.

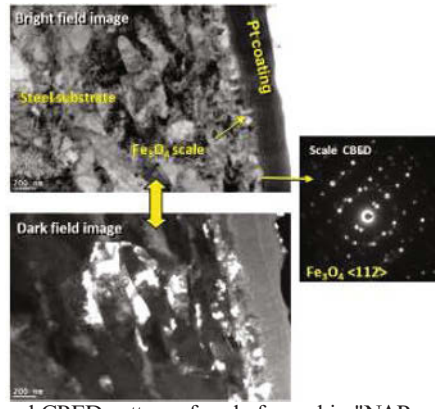

Figure 6. TEM images and CBED pattern of scale formed in "NAP only" solution at 600°F for 5Cr specimen (TEM image shown in Figure 5).

Discussion and Conclusion

In our prior research, a protective scale of magnetite was found on 5Cr after the pretreatment in "NAP only" at 600°F. The magnetite was proposed to be formed by the following mechanism [5]:

$Fe(RCOO)_2 \rightarrow FeO + CO_2 + RCOR$ (Reaction 4)
$4FeO \rightarrow Fe_3O_4 + \alpha\text{-}Fe$ (Reaction 5)

It is known that the magnetite (Fe_3O_4) and α-Fe can be formed by disproportionation of wurtzite (FeO) at temperatures above 572°F (300°C) [6,7]. In this work, the pretreatment temperature was lowered to 450°F and the magnetite scale was not formed. At 600°F and 650°F, a very thin, protective scale of magnetite did form on the 5Cr surface. In contrast, the pretreatment of CS at all three temperatures with "NAP only" provided no protection. Comparison between alloys with "NAP only" pretreatment suggests that Cr affects the surface formation of magnetite. Thus, NAC of CS in the pretreatment is high because it forms iron naphthenate that is solubilized into the bulk liquid during the 24 h in the autoclave, whereas with 5Cr some of the iron naphthenate decomposes to insoluble magnetite on the surface. This phenomenon appears to increase with temperature and also in the presence of the sulfur compound (compare the corrosion rates of "DDS only" with "DDS+NAP"). Furthermore, it provides a rationale for the lower baseline corrosion rate for 5Cr relative to CS in the challenge. The net result is that understanding the conditions that facilitate formation of magnetite during corrosion experiments is of crucial importance to the protectiveness of corrosion product scales. Additional experiments are in progress to better define the role of the sulfur compounds and naphthenic acids involved.

Acknowledgements

Authors would like to thank sponsors of the NAP JIP project in Ohio University.

References

1. S.D. Kapusta, A. Ooms, A. Smith, F. Van den Berg, and W. Fort, "Safe Processing of Acid Crudes," *CORROSION/2004*, paper no. 04637 (Houston, TX: NACE, 2004), 1-19.
2. E. Slavcheva, B. Shone, and A. Turnbull, "Review of Naphthenic Acid Corrosion in Oil Refining," *Brit. Corros. J.* 34 (2) (1999), 125-131.
3. G.M. Bota and S. Nesic, "Naphthenic Acid Challenges of Iron Sulfide Scales from Model Oil on Mild Steel at High Temperature," *CORROSION/2013*, paper no. 2512 (Orlando, FL: NACE 2013), 1-13.
4. D.G. Stroppa, L.F. Zagonel, L.A. Montoro, E.R. Leite, A.J. Ramirez, "High-Resolution Scanning Transmission Electron Microscopy (HRSTEM) Techniques: High-Resolution Imaging and Spectroscopy Side by Side," *ChemPhysChem,* 13(2) (2012), 437-443.
5. P. Jin, H.A. Wolf, and S. Nesic, "Analysis of Corrosion Scales Formed on Steel at High Temperatures in Hydrocarbons Containing Model Naphthenic Acids and Sulfur Compounds," *Surface and Interface Analysis,* 47 (2015), 454-465.
6. F.X. Redl, C.T. Black, G.C. Papaefthymiou, R.L. Sandstrom, M. Yin, H. Zeng, C.B. Murray, and S.P. O'Brien, "Magnetic, Electronic, and Structural Characterization of Nonstoichiometric Iron Oxides at the Nanolayer," *Journal of the American Chemical Society,* 126 (44) (2004), 14583-14599.
7. S. Stolen, R. Gloeckner, and F. Gronvold, "Nearly Stoichiometric Iron Monoxide Formed as a Metastable Intermediate in a Two-Stage Disproportionation of Quenched Wüstite. Thermodynamic and Kinetic Aspects," *Thermochim. Acta,* 256 (1995), 91-106.

Characterization of Minerals, Metals, and Materials 2016
Edited by: Shadia Jamil Ikhmayies, Bowen Li, John S. Carpenter, Jiann-Yang Hwang, Sergio Neves Monteiro, Jian Li, Donato Firrao, Mingming Zhang, Zhiwei Peng, Juan P. Escobedo-Diaz, and Chenguang Bai
TMS (The Minerals, Metals & Materials Society), 2016

EFFECT OF COLD WORK ON THE CORROSION RESISTANCE OF AN AUSTENITIC STAINLESS STEEL

Jian Li, W. Zheng, P. Liu and M. Podlesny

CanmetMATERIALS, Natural Resources Canada, 183 Longwood Road South, Hamilton, Ontario, Canada L8P 0A5

Keywords: stainless steel, cold rolling, microstructure, SCW

Abstract

Corrosion of candidate fuel cladding alloys has been a major concern in fuel cladding materials selection in the Canadian Gen-IV Supercritical Water-cooled Reactor (SCWR) conceptual design. In this study, austenitic stainless steel 310S was cold rolled in small steps in order to create severe shear deformation near the surface. Surface characteristics of the cold rolled specimen and the "as-received" specimens were compared. Their supercritical water (SCW) corrosion resistance was studied in a static autoclave, and evaluated using a FIB microscope. Although weight changes after corrosion test were similar for both samples, their subsurface microstructure has shown marked differences, which could affect their long terms corrosion and stress corrosion cracking susceptibility. The findings are consistent with the increased stress corrosion cracking (SCC) susceptibility of austenitic stainless steels in supercritical water when pre-strained.

Introduction

Austenitic stainless steel 310S is selected as one of the prime candidate fuel cladding material for the Canadian Gen-IV supercritical water-cooled reactor (SCWR) conceptual design due to its overall properties in corrosion and SCC resistance, high temperature mechanical properties and creep resistance [1]. Aside from substrate chemical composition, surface condition can play an important role in corrosion resistance of austenitic stainless steels under SCW condition. Sami [2] reported significant improvement of corrosion resistance of 316L alloy in their SCW corrosion test with severely deformed surface (as opposed to polished surface).

There have been reports on cold deformation on the pitting corrosion resistance of stainless steels [3-5]. Most of these studies suggest that cold work produces a harmful effect on the corrosion resistance of stainless steels. It is commonly accepted that cold work introduced to the material by deformation decreases the resistance of the material to localized corrosion [4]. Corrosion susceptibility was also attributed to material microstructure and specific surface texture formation [6,7].

Our previous work has shown that the introduction of cold work can in fact improve corrosion resistance of 316L under certain supercritical condition [8]. This benefit is attributed to the enhanced outward Cr diffusion via finely recrystallized grain boundaries near the surface that contributes to the maintenance of a continuous passive chromia layer during SCW exposure. However, aside from the benefit to improved corrosion resistance, cold work increases the SCC susceptibility of stainless steels as evident in our recent findings [1]. The mechanism of increased SCC susceptibility by pre-straining the samples has not been well understood.

The Canadian SCWR Concept aims to operate at higher temperature and pressure. Stainless steel 310S is one of the prime candidate materials, and the Canadian SCWR materials research team has focused their effort to evaluate this alloy for its mechanical properties, creep resistance,

corrosion resistance, SCC resistance and degradation by thermal neutron irradiation. The aim of this study includes the followings: 1) to investigate if increased surface deformation improves the SCW corrosion resistance of this alloy; 2) to investigate microstructure details of deformed 310S after extended SCW exposure and identify microscopy details that could attribute to the increased SCC susceptibility when cold work is imposed prior to SCC experiment under supercritical water condition.

Experiment and Method of Analyses

Stainless steel 310S strips used in this experiment were purchased from Metal Samples. These samples were annealed and have standard milled surface. The "as-received" samples are strips of 125.0 x 25.0 x 1.3 mm in size. One of the samples was rolled using a Stanet rolling mill with a set of polished roller (in order to achieve good surface finish). A total of 25% thickness reduction was achieved with 21 steps by reverse rolling. Small step rolling was used to increase the intensity of surface shear deformation.

Small test coupons of 20.0 x 10.0 x 1.0 mm in size were cut out from the both "as-received" and the rolled strips. Corrosion test was performed in a static autoclave. During the early stage of the corrosion experiment, the test was briefly interrupted due to problems with leaking autoclave seal. The test was then stabilized at 625 ºC, 24 MPa for 350 hours. Weight changes of test coupons were recorded.

A FEI Nova NanoSEM 650 was used to obtain images of deformed surface before and after the corrosion test, and EBSD was used to characterize the subsurface deformation structure. A FEI Helios NanoLab-650 focused ion beam (FIB) microscope was used to assess corrosion film thickness and the subsurface microstructure features. Details of FIB techniques can be found elsewhere [9].

Results and Discussion

As shown in Figure 1a, the "as-received" sample surface shows quite significant machining marks.

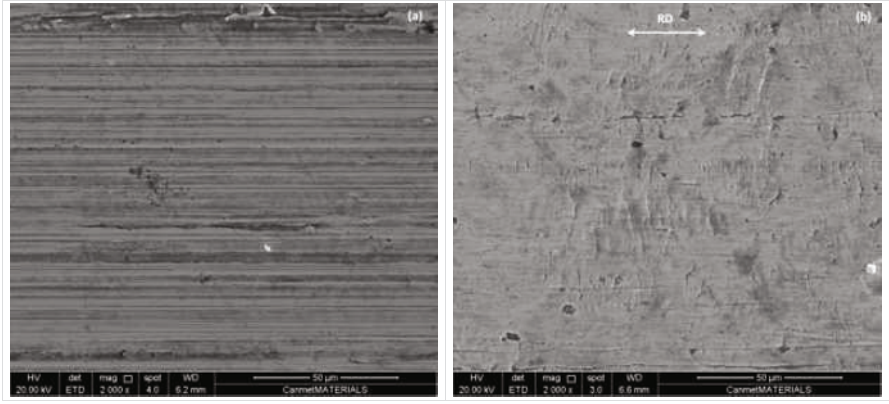

Figure 1 SEM images taken from surfaces of 310S sheets (a) as-received specimen, (b) after rolling

The rolling created visible deformation marks perpendicular to the rolling direction on the surface (Figure 1b). The rolling with small reductions steps can create severe plastic flow near the surface that the appearance of these surface deformation marks are expected. The pre-existed machining marks parallel to the rolling direction are flattened and become less significant after the rolling process.

Weight gains after SCW experiment are listed in Table-1. The ”as-received” specimen appeared to show higher weight gain.

Table 1. Weight gains after SCW test (mg/cm^2)

As-received	0.590
Cold Rolled	0.511

After the SCW test, both surfaces appeared to be very dull in color. SEM images in Figure 2 show surface oxidation typically found in high Cr austenitic steels. Although the surface morphology of the two oxidized surfaces are very similar, their chemical compositions are quite different based on the EDS spectra collected for the two surfaces. The oxide formed on the rolled surface contains only Cr and O, which is an indication of dense and protective Cr_2O_3 layer. In contrast, the oxide formed from the “as-received” specimen contains other elements that include Fe and Ni. This could either be a spinel phase or a relatively thin magnetite layer. The formation of different types of oxides on the two test specimens is consistent with the minor differences in weight gain shown in Table 1.

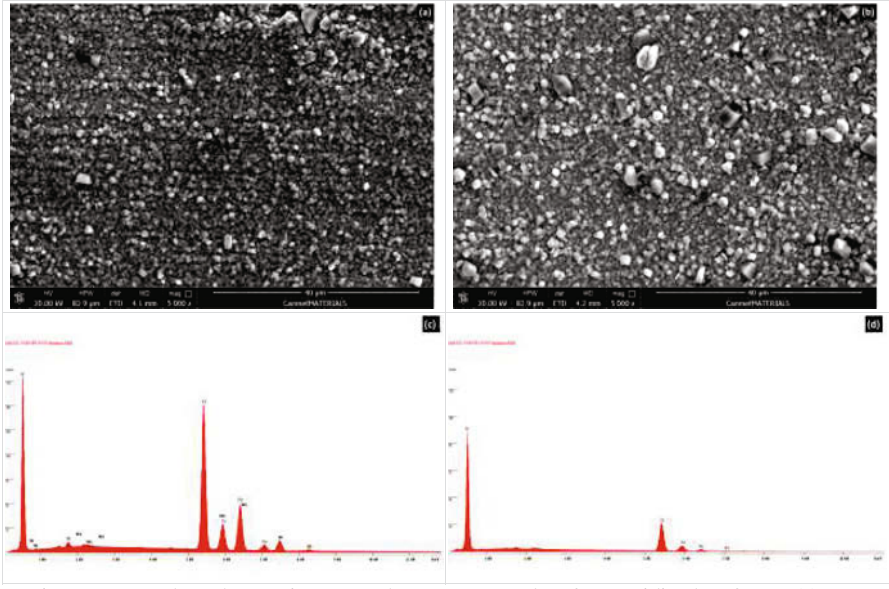

Figure 2 Secondary electron images and EDS spectra taken from oxidized surfaces. (a) post SCW tested “as-received” sample; (b) post SCW tested “rolled” sample; (c) EDS spectrum from the surface of (a); (d) EDS spectrum from the surface of (b).

FIB cross sections on these two specimens were performed in order to compare not only the surface corrosion film thickness, but also the subsurface microstructure. As shown in Figure 3, the oxide films formed on the two specimens are quite similar in terms of morphology and thickness (on the order of 800 nm). From the plan view EDS spectra (Figures 2c and 2d), the compositions are different. The oxide formed on the "as-received" specimen should be either a spinel phase or magnetite that are less protective compared to that of oxide on the rolled sample (chromia). However, the short term SCW test did not result in significant weight change differences.

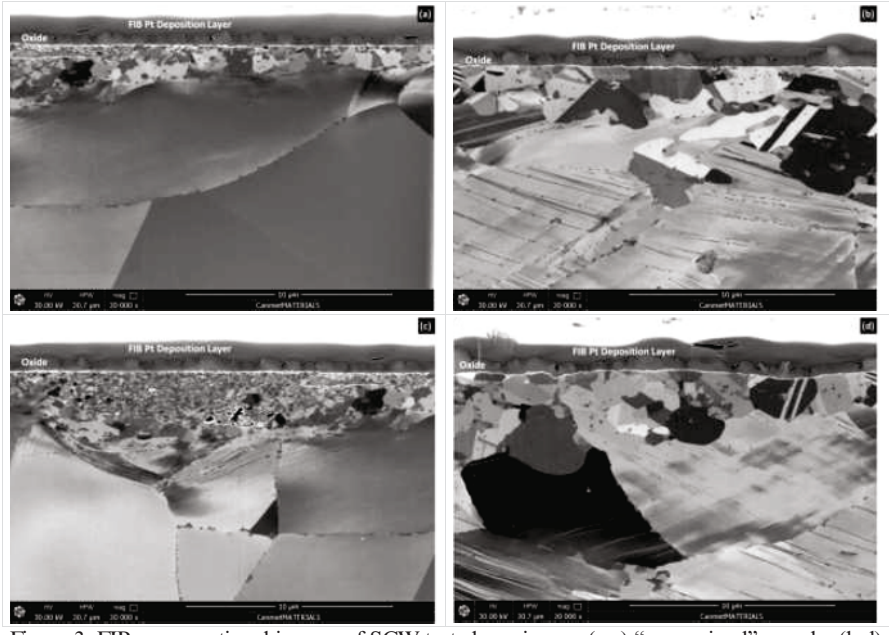

Figure 3. FIB cross sectional images of SCW tested specimens. (a,c) "as-received" sample; (b,d) rolled sample

There are marked differences in subsurface microstructures in the two samples after the SCW test. Immediately beneath the surface corrosion film, the "as-received" specimen formed a layer of extremely fine-grained structure, while the "rolled" sample has relatively larger grains. The rolling in small steps added significantly more subsurface deformation compared to that of the "as-received" specimen. Upon SCW test at elevated temperature (625 °C), recrystallization occurred in both samples. The rolled sample which has higher stored energy (in the subsurface area) recrystallized much earlier compared to the "as-received" specimen. This resulted in a larger grain size in the rolled specimen compared to that of the "as-received" specimen. For stainless steel 316L, the fine-grained subsurface layer can act as a diffusion short circuit that supplies sufficient Cr to the outer surface, and contributes to maintain a continuous Cr_2O_3 protective layer [2,8]. However, for stainless steels that have higher Cr content such as 310S, there should be enough Cr available to maintain the Cr_2O_3 protective film during SCW exposure. Thus the benefit of fine-grained subsurface layer is not as obvious as that of 316L. On the other hand, beneath the fine-grained zones, the "rolled" sample formed significant shear bands, while

the “as-received” sample has nearly stain-free microstructure. During the SCW test, precipitation (most likely σ phase [10]) occurs. For the “as-received” specimen, the precipitations are mostly on grain boundaries, whereas for the “rolled” specimen, they also appear on shear bands. In general, σ phase precipitation reduces local Cr content and compromise corrosion resistance. However, for high Cr stainless steels like 310S, the precipitation of σ phase has not shown negative effect to its SCW corrosion resistance at least in short terms experiments [10].

The two samples were also mounted and polished. EBSD maps collected from both samples further confirmed the formation of shear bands in the “rolled” specimen (Figure 4).

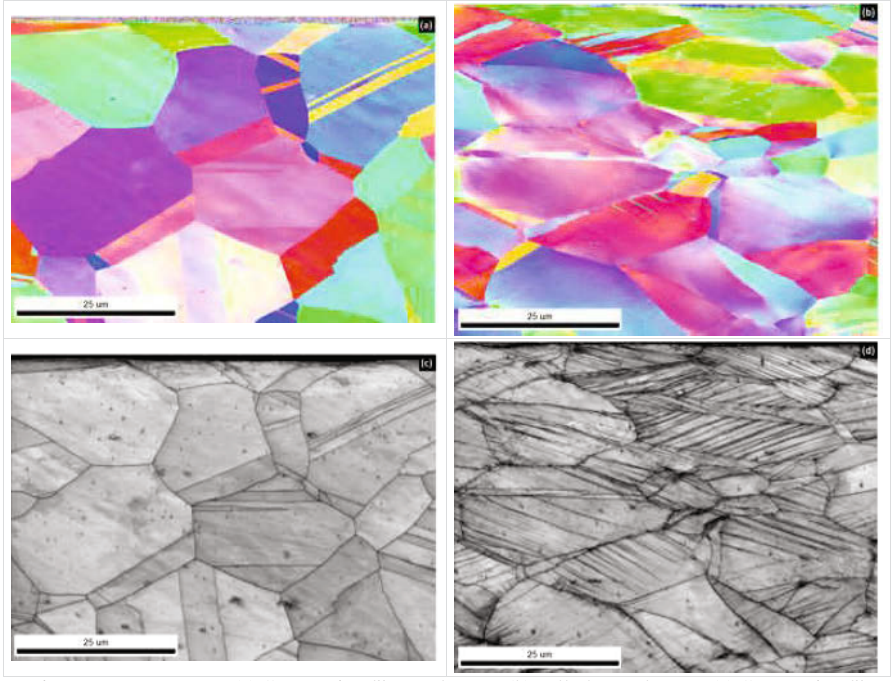

Figure 4. EBSD maps (a) “as-received” sample IPF; (b) rolled sample IPF; (c) “as-received” sample GB map; (d) rolled sample GB map

During the SCW test, these shear bands could assist inwards diffusion of oxygen. In the static autoclave corrosion test, the formation of continuous Cr_2O_3 protective film hinders the penetration of oxygen from SCW fluid into the stainless steels’ substrate. However, in slow strain rate tests (SSRT) for SCC susceptibility, the protective Cr_2O_3 film could continuously crack due to its low ductility and it will fail to conform to the substrate deformation. As illustrated in the schematic diagram in Figure 5, diffusion of oxygen into the stainless substrate can be greatly enhanced through the shear bands should they exist. Internal oxidation can occur either at these shear bands or along grain boundaries. With stress, SCC can occur much easier. This explains that the 310S and other high Cr stainless steels are prone to SCC cracking if they are subjected to cold work before the SSRT test in SCW. SCC was not observed for samples without pre-existing cold work [1].

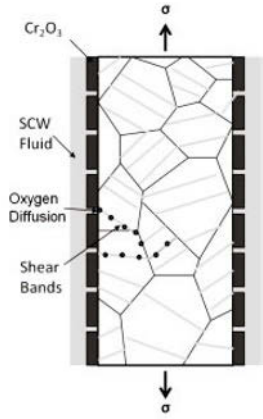

Figure 5. Schematic diagram of oxygen diffusion via shear bands in SCW SCC test by SSRT

Summary

Unlike stainless steel 316L, cold work has little advantage to SCW corrosion resistance for 310S. Upon SCW exposure at 625 ºC, the severely deformed subsurface recrystallized and formed a fine-grained microstructure just beneath the top surface. Rolling deformation resulted in significant shear band formation in the substrate. This contributes to the formation of σ phase by enhanced Cr diffusion. The implication of σ phase precipitation is not clear at this stage of the work. The increased susceptibility of SCC in 310S by pre-existing cold work can be attributed by the enhanced oxygen diffusion via shear bands into the substrate during SSRT test under SCW condition.

Acknowledgement

The authors would like to thank financial support from Her Majesty the Queen in Right of Canada, as represented by the Minister of Natural Resources.

References

[1] Guzonas, D., Zheng, W., and Li, Jian, Fuel Cladding Materials Selection for Canadian SCWR Concept, AECL-217-127100-ASD-001, 2014.
[2] Penttilä, S., Toivonen, A., Li, Jian, Zheng, W., and Novotny, R., Effect of surface modification on the corrosion resistance of austenitic stainless steel 316l in supercritical water conditions, Journal of Supercritical Fluids, vol.81, 157-163, 2013.
[3] B. Surowska; A. Weronski, Proceedings of the 14th International Scientific Conference "Advanced Materials and Technologies", Gliwice Zakopane, p. 425-428, 1995.
[4] S. Zor; M. Soncu; L. Capan, Journal of Alloys and Compounds, 480, 885, 2009.
[5] L. Peguet, B. Malki, B. Baroux, Corrosion Science, 49 (2007) 1933.
[6] Ramirez, A.H., Ramirex, C.H. and Costa, I., Int. J. Electrochem. Sci., 8, 2013, 12801-12815.
[7] Li, H., Jiang, Z., Ma, Q., and Li, Z., Advanced Materials Research , 217-218, 1180-1184, 2011.

[8] Li, Jian, Zeng, Y., Woo, O., Zheng, W., Liu, P., and Bibby, C., Proceedings of 143rd Annual Meeting and Exhibition, February 16-20, 2014, San Diego, CA, USA, ed. John S. Carpenter, 105-112, 2014
[9] Li, Jian, Advances in Materials Engineering Using State-of-the-art Microstructural Characterization Tools, in "New Material Science Research", Nova Science Publishers Inc., Invited. Ed. Lawrence V. Olivante, Nova Science Publisher, ISBN-13: 978-1-60021-654-1, 2008.
[10] Li, Jian, Zheng, W., Penttila, S., Liu, P., Woo. O.T., and Guzonas, D. (2014) Microstructure Stability of Candidate Stainless Steels for Gen-IV SCWR Fuel Cladding Application, Journal of Nuclear Materials, vol.454, 7-11, 2014.

Characterization of Minerals, Metals, and Materials 2016
Edited by: Shadia Jamil Ikhmayies, Bowen Li, John S. Carpenter, Jiann-Yang Hwang, Sergio Neves Monteiro, Jian Li, Donato Firrao, Mingming Zhang, Zhiwei Peng, Juan P. Escobedo-Diaz, and Chenguang Bai
TMS (The Minerals, Metals & Materials Society), 2016

PYROLYSIS OF ACTIVE FRACTION OF HUMIC SUBSTANCES-BASED BINDER FOR IRON ORE PELLETIZING

Guihong Han[1], Duo Zhang[1], Yanfang Huang[1*], Lulu Liu[1], Wencui Chai[1], Tao Jiang[2]

1. School of Chemical Engineering and Energy, Zhengzhou University, 450001, Zhengzhou, P.R. China.

2. School of Minerals Processing & Bioengineering, Central South University, Changsha, Hunan 410083, PR. China

Keywords: Humic substances, Pyrolysis, Organic binder, Gaseous product

Abstract

The authors have developed a series of humic substances-based binders for iron ore pelletizing. This work was to gather information for the further industry application of humic substances-based binders in the field of iron ore oxidized pellets production. Pyrolysis of humic substances as the active fraction in the binders and its effects on fired hematite pellets was investigated in this study. Pyrolysis product of humic substances was focusing on four main gases (CO_2, CO, $H_2$and C_xH_y). The results demonstrated that effect of O_2/N_2atmosphere on weight loss of humic substances is obvious above 600 °C. Instantaneous concentration of gas products is increased with increasing pyrolysis temperature. Weight percentage of CO_2 is increased obviously with increasing O_2 concentration, while those of CO and H_2 decreasing.

1. Introduction

Humic substances mainly exist in coals, soils, water and sediment, which consist of many active functional groups such as phenyl, carboxyl and alcohol hydroxyl[1-2]. Humic substances are also referred to as high molecular weight matter, with molecular weight estimated above ten thousands[3]. Since humic substances can be easily obtained and interact with other matter, they are generally used in modern industry, agriculture and health care[4-7].

Humic substances have been used as flotation chemicals in the mineral processing industry because of their typical molecular properties. Recently, humic substances are employed as the organic active fractions of a MHA binder for iron ore pelletizing and briquetting[8-9]. Interaction between humic substances with iron ore particles was reported in former investigations. The results revealed that adsorption of humic

Foundation item: National Science Fund for Young Scholars of China (Project (51404213andProject (51404214)) and the Development Fund for Outstanding Young Teachers
Corresponding author: Yanfang Huang; Email address: huangyf@zzu.edu.cn

substances onto iron ore particle surface can modify the interfacial characteristics and enhance the mechanical strength of green pellets[10,11].

The heating process with temperature changing from 200 ºC to 1000 ºC in air or weak oxidizing atmosphere is required for iron ore oxidized pellets production[8,12]. The binder becomes more fragile at a high temperature during drying, preheating and roasting process because of its occurring chemical oxidation, degradation and decomposition. The changing of binder in heating consequently leads to the decrease of mechanical strengths of pellets. Therefore, thermal stability becomes an important index for a pelletizing binder. As a good binder for iron ore pellets, an organic polymer should have exceptional thermal and oxidative stability[13]. The oxidizing roasting results of magnetite pellets have shown that the MHA binder is characterized by good thermal stability during high-temperature heating process. For example, the addition of the MHA binder has no obvious negative effect on the mechanical strength of final products[14]. This feature finally prompts the successful application of the MHA binder in magnetite oxidization pellets production. However, the intrinsic thermal characteristics of humic substances as the organic active fraction of a MHA binder are still not very clear. Thermal behaviors of humic substances during high-temperature process, therefore, is worthy of in-depth study.

Lots of gases will be produced during pyrolysis process of humic substances[15,16]. In this paper, pyrolysis behavior of humic substances in different O_2/N_2atmosphere is investigated. Infrared flue gas analyzer was used to simultaneously detect and measure four main gases including H_2, CO, CO_2 and C_xH_y.

2. Material and Methods

2.1 Materials

The humic substances in this research were isolated from a typical kind of Chinese lignite. The characteristics of lignite have been already revealed. And the extraction and separation procedures of humic substances have been described in former literatures[17,18]. The main chemical composition of humic substances obtained by Model PE2400 CHN Hydrocarbon Elemental Analyzer is shown in **Table I**.

Table I. Elemental Analysis of Humic Substances

wt.%, as analysed					Mole ratio	
C	H	O	N	S	C/H	O/C
67.89	4.35	25.60	1.24	0.93	1.30	0.28

As seen from **Table I**, the mole ratio of C/H and O/Cis 1.30 and 0.28, respectively, whileE4/E6 value is 3.76. The results shown in **Table I** indicate that the unsaturation degree of humic substances is quite high[2].

2.2 Pyrolysis Procedure

The pyrolysis experimental setup is shown in **Figure 1**. This devices mainly consisted of a controlled vertical furnace as heating system, a quartz reaction container as reactor, an inside thermocouple, an analytical balance, flow meters, and inlet and outlet values.

Thermo gravimetric experiments were used to determine weight change of humic substances once heated in different atmosphere. The experimental procedure can be described as following. A sample of around 15 g was weighted and heated in nitrogen or air (20%O_2 and 80%N_2) at a flow rate of 1 L/min when temperature is increased from room temperature to 1200°C with a heating rate of 10 ºC/min. Total weight of container and sample was instantaneously recorded by the analytical balance.

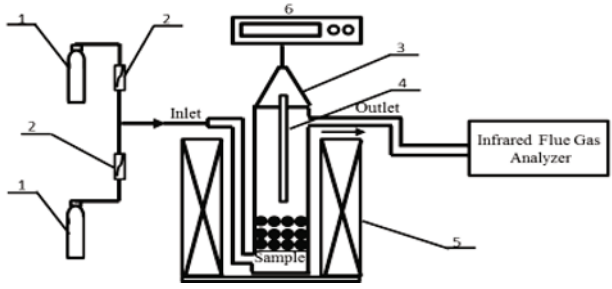

1-Gas cylinder 2-Flowmeter 3-Quartz reaction container
4-Thermalcouple 5-Vertical tube furnace 6-Analytical balance

Fig. 1. Experimental setup for humic substances during N_2/O_2pyrolysis process

Gas product contents were obtained by a model MRU MGA 5Infrared Gas Analyzer (IGA) during isothermal process. In this experiment, a sample of 15 g was weighted and heated in different atmosphere at a flow rate of 1 L/min under the scheduled pyrolysis temperatures with a hold time of 10 min. Then the gas products were collected and measured by a model Infrared Gas Analyzer (IGA).The Infrared Gas Analyzer in this research was mainly used to analyze CO, CO_2, H_2,O_2 and C_xHy ($1 \le x \le 3$) in the gas products.

3. Results and Discussion

3.1 Weight Loss of Humic Substances during Pyrolysis Process

When heating temperature was increased from 200 °C to 1200 °C during the nonisothermal pyrolysis process, weight loss of humic substances in different atmosphere was recorded as a function of temperature and the experimental results are depicted in **Figure 2**.

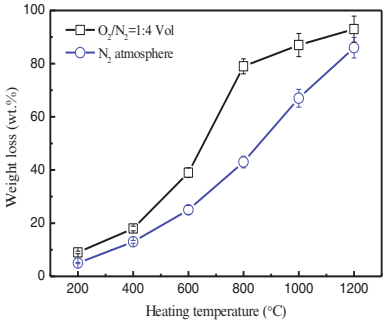

Fig. 2. Weight change curves of humic substances during nonisothermal process

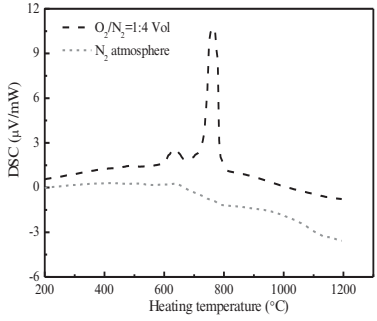

Fig. 3. DSC profiles of humic substances heated in different atmospheres

As seen from **Figure 2**, weight loss of humic substances in O_2/N_2 or N_2 atmosphere keeps increasing with the heating temperature increased. The results in **Figure 2** also show that weight loss rate of humic substances in O_2/N_2atmosphereis much faster than that in pure N_2. Noteworthy is that the effect of atmosphere on weight loss of humic substances is more obvious from 600 °C to 1000 °C.

Differential scanning calorimetry (DSC) was also used to study the effect of atmosphere on pyrolysis of humic substances from room temperature to 1200 °C with increasing rate of 10 °C/min.DSC profiles of humic substances heated in different atmosphere are presented in **Figure 3**.

It can be seen from **Figure 3**, there are obvious exothermic peaks in the DSC curve of humic substances heated in O_2/N_2compared to N_2 atmosphere. The former study has demonstrated that thermal decomposition of humic substances includes oxidation, combustion, dehydroxylation and/or decarboxylation during pyrolysis[9,19]. Appearance of exothermic peaks at 615 °C and 750 °C demonstrated that there happens intense oxidation-combustion reaction in 20% O_2 by volume atmosphere. The results in **Figure 3** reveal that, a series of rapid weight loss of humic substances from 600 °C to 800 °C with O_2/N_2pyrolysis in **Figure 2** is mainly caused by carbon burning.

3.2 Gaseous Products of Humic Substances during Pyrolysis Process

More than 30 pyrolysates have been successfully identified by various spectroscopic techniques in former reports, although their appearance is dependent on pyrolysis method and temperature. Gaseous products identified with infrared gas analyzer (IGA)under different pyrolysis temperatures in this study are listed in **Table II**.

As seen in **Table II**, taking the restrictions of infrared gas analyzer into account, CO, CO_2, H_2 and C_xH_y ($1 \leq x \leq 3$) are mainly included in the gas phase products during pyrolysis process of humic substances. Compared to spectroscopic techniques,

other small organic products including acetaldehyde, acetone and methanol etc al, could not be detected by IGA technique[15].

Table II. The Main Pyrolysates Identified with Infrared Gas Analyzer (IGA)

	Gas phase products	Pyrolysis temperature (°C)						
		358	480	510	610	770	800	1000
a	CO, CO_2, CH_4	X	X	X	X	X		
b	CO, CO_2, C_xH_y, H_2	X	X	X	X	X	X	X

Note: [a], reference; [b], experimental results in this study.

In addition, the content of gaseous products at 800 °C is mainly investigated in this research. The results concerning instantaneous concentration of gaseous products are given in **Figure 4** with oxygen concentration of 0%, 4%, 10% and 20% by volume.

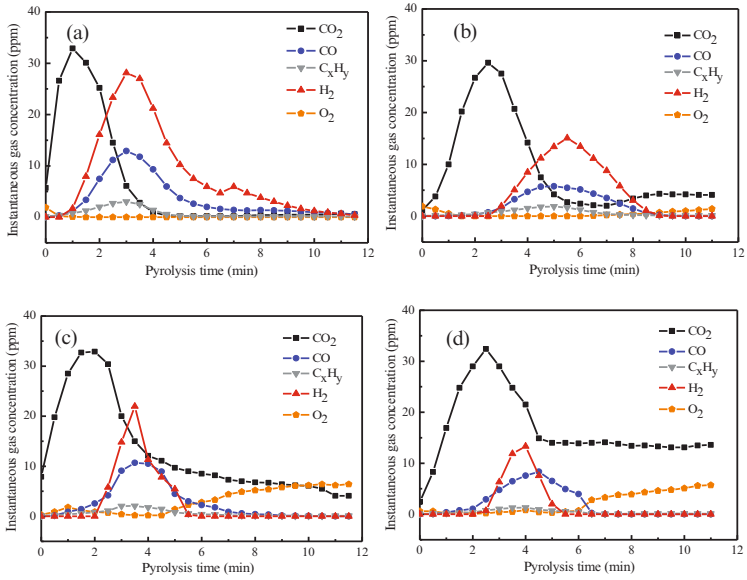

Fig. 4. Instantaneous concentration changing curves of gas phase products of humic substances heated at 800 °C in different atmospheres (a) pure N_2, and (b) 4% O_2, (c) 10% O_2, (d) 20% O_2 by volume

As shown in **Figure 4(a)**, instantaneous concentration of CO_2 is increased rapidly in the beginning and arrives to 32.90ppm after heated for 1 min. With a bit of a lag, the peak value of instantaneous concentration of CO,$H_2$and C_xH_y appears at about the 3rd min when heated in N_2atmosphere. **Figure 4(a)**also shows the peak value of instantaneous concentration of H_2, CO and C_xH_y is respectively 27.60ppm,13.20ppm and 7.15ppm. **Figure 4(b, c and d)** reflects that the peak value of instantaneous

concentration of H_2, CO and $C_xH_y$atpureO_2/N_2 atmosphere is respectively lower than that at pure N_2atmosphere. When oxygen content is about 20%, **Figure 4(d)** shows that the peak value of instantaneous concentration of H_2, CO and C_xH_y is respectively 13.00ppm,8.00ppm and 1.10ppm..

Based on IGA result, the required time for peak concentration of gas phase products at 800 ºC with oxygen concentration 0%, 4%, 10% and 20% by volume are given in **Figure 5**. Meanwhile, weight percentage of gas products with increasing O_2 concentration is obtained and plotted in **Figure 6**.

It can be seen from **Figure 5** that the required time for peak concentration of CO_2, H_2, CO and C_xH_y varies with O_2 concentration. Noteworthy is that the required time for peak concentration of all gas products in pure N_2 atmosphere appears the lowest value. Contrariwise, the required time for peak concentration of gas product with5% Vol O_2 concentration presents the maximum value.

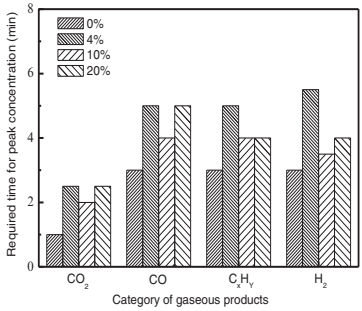

Fig. 5. Times for peak concentration of products

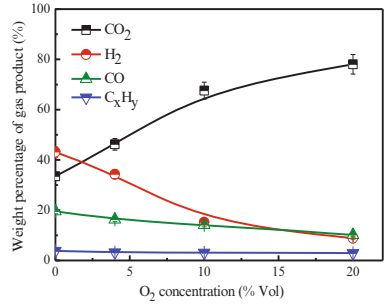

Fig. 6. Products Weight percentage

Figure 6 shows that weight percentage of CO_2 increases obviously with the increase of O_2 concentration. Contrariwise, weight percentage of CO and H_2decreases obviously with increasing O_2 concentration. As shown in **Figure 6**, the weight percentage of CO_2, CO and H_2 is respectively 33.51%, 19.55% and 43.13% when humic substances is heated at 800 ºC in pure N_2 atmosphere. The weight percentage of CO_2 is 78.04% when O_2 concentration comes to 20% O_2 by volume. And the weight percentage of CO and $H_2$is respectively 8.17 %and 10.85 % under the condition of 20% O_2 atmosphere.

4. Conclusions

Understanding and quantifying the pyrolysis product of humic substances is important in accelerating industry application of humic substances-based binder in the field of iron ore oxidized pellets production. The changing of gaseous products from humic substances was studied.

(1) Thermal stability of humic substances is quite well even in oxidation ambient at

high temperature. The weight loss of humic substances is relatively obvious from 600 °C to 1000 °C in whatever atmosphere.

(2) Instantaneous concentration of CO_2, CO, C_xH_y and H_2 is increased with increasing of pyrolysis temperature, with the peak value of their instantaneous concentration being respectively 32.90 ppm, 13.20 ppm, 7.15ppm and 27.6 ppm at 800°C when O_2 content is 0% by volume. The weight percentage of CO_2 in gas products is increased obviously with the increase of O_2 concentration, while the weight percentage of CO and H_2 decreasing.

Acknowledgement

The financial supports from the National Science Fund for Young Scholars of China (No.51404213and No.51404214) and the Development Fund for Outstanding Young Teachers (No.1421324065) are gratefully acknowledged.

References

[1] M.Schnitzer, and S. U.Khan, Humic Substances in the Environment, Marcel Dekker Inc, New York,(1972),1.

[2] W. J. Weber, J. X.Tang, Q. G.Huang: Environ. Sci. Technol, 40(2006), pp.1650.

[3] E. M.Thurman, R. L.Wersha, R. L.Malcolm, D. J.Pinckney: Organic Geochemistry, 4(1982), 27.

[4] N.Senesi, G.Sposito, J. P.Martin: Total Environ, 55 (1986), 351.

[5] J. J.Pignatello: Adv. Colloid Interface, 77(1998), 445.

[6] M.Trckova,L.Matlova,H.Hudcova,M.Faldyna, Z.Zraly, L.Dvorska, V.Beran, I. N.Pavlik:Vet. Med. Czech, 50(2005), 361.

[7] M.Kuhnert, K. P.Bartels, S.Kroll, N.Lange:Monatsh. Veterin¨armed, 46 (1991), 4–8. (In German)

[8] G.H. Han, Y. F. Huang, G. H. Li, Y. B. Zhang, Y. L. Zhou, T. Jiang, *ISIJ International*, 52(2012), 378.

[9] G.H. Han, T. Jiang, Y. F. Huang, Y.Zhang, G.Li, *Journal of Engineering Materials and Technology—Transactions of The ASME*, 134 (2012), 1.

[10] T. Jiang, G. H. Han, Y. B. Zhang, Y. F. Huang, G. H. Li, *International Journal of Mineral Processing*, 100 (2011), 172.

[11] G.H. Han, Y. F. Huang, G. H. Li, T. Jiang, *Mineral Processing and ExtractiveMetallurgy Review: An International Journal*, 35 (2014), 1.

[12] Y. F. Huang,G.H. Han,T. Jiang,Y. B. Zhang,G. H. Li:Mineral Processing and Extractive Metallurgy Review: An International Journal,34(2013), 42.

[13] G. Z.Qiu, T. Jiang, H. X Li, D. Z. Wang: Colloids and Surfaces A: Physicochemical and Engineering Aspects, 224(2003), 11.

[14] Y. F. Huang,G.H. Han,T. Jiang,G. H. Li, Y. B. Zhang, D. Wang: 3nd International Symposium on High-Temperature Metallurgical Processing, TMS2012.

[15] Gudrun Abbt-Braun, Fritz H. Frimmel, Hans-Rolf Schulten:Water Research DOI:10.1016/0043-1354(89)90124–3.
[16] C. Kolokassidou, I. Pashalidis, C.N. Costa, A.M. Efstathiou, G. Buckau:ThermochimicaActa, 454 (2007), 78.
[17] T.Jiang, G. H.Han, Y. B.Zhang, , Y. F.Huang, G. H.Li, Y. F. Huang: Journal of Central South University of Technology, 18 (2011), 68.
[18] Andre Henrique Rosa´, Luciana Camargo de Oliveira, Iramaia Correa Bellinˆ,Julio Cesar Rocha,LucianePimenta Cruz Romao˜, Newton Luiz Dias Filhod:ThermochimicaActa, 433 (2005), 77.
[19] M. E.Brown, Introduction to Thermal Analysis Techniques and Applications, Chapman & Hall, London,(1988), 1.

Characterization of Minerals, Metals, and Materials 2016
Edited by: Shadia Jamil Ikhmayies, Bowen Li, John S. Carpenter, Jiann-Yang Hwang, Sergio Neves Monteiro, Jian Li, Donato Firrao, Mingming Zhang, Zhiwei Peng, Juan P. Escobedo-Diaz, and Chenguang Bai
TMS (The Minerals, Metals & Materials Society), 2016

FERRONICKEL PREPARATION FROM NICKELIFEROUS LATERITE BY ROTARY KILN-ELECTRIC FURNACE PROCESS

Guanghui Li, Hao Jia, Jun Luo[1], Zhiwei Peng, Yuanbo Zhang, Tao Jiang

(School of Minerals Processing & Bioengineering, Central South University, Changsha, Hunan 410083, China)

Keywords: Nickeliferous laterite; Ferronickel; Smelting; RKEF

Abstract

Nickel is an important strategic metal, which is mainly used for stainless steel production. In the recent years, ferronickel has been used as a substitute for electrolytic nickel for alleviating the cost of stainless steel production. Rotary kiln-electric furnace (RKEF) smelting is currently the world-wide mainstreaming process for ferronickel production from nickeliferous laterite ore, in spite of the high power consumption. In this study, aiming to provide some meaningful guidance for ferronickel production of RKEF smelting, reductive roasting followed by smelting process was carried out. The conditions including reducing parameters (roasting temperature and time) and smelting parameters (coke dosage, CaO dosage, melting temperature and time) were ascertained. The metal recovery ratios, as well as Ni, Fe, S and P content of ferronickel were considered. The results showed that a ferronickel containing 10.32 wt. % Ni was obtained from a laterite with 1.85 wt. % Ni, the nickel recovery ratio was about 99%.

Introduction

Stainless steel has a widespread application in military, industrial and civilian for its high strength and ductility as well as excellent corrosion resistance. Nickel is the essential component for stainless steel production, which accounts for nearly two-thirds of total nickel consumption of the world [1-3]. In recent years, the annual output of stainless steel keeps the sustained growth in the world, especially in China. It is the main driving force of nickel demand increased dramatically [2].

Aiming to reduce the production cost of stainless steel, ferronickel produced from nickeliferous laterite ore by pyrometallurgy process has been used as a substitute for electrolytic nickel in recent years [4, 5]. Rotary kiln-electric furnace (RKEF) smelting is a successful process for disposing nickeliferous laterite ore to produce ferronickel, it has the advantages of raw material adaptability, good product quality and high production efficiency etc [6]. However, the RKEF process is considered to be energy intensive for producing ferronickel from laterite ores due to the low content of nickel and high contents of magnesia and silica in nickeliferous laterite ore [7].
Considering that smelting process of laterite ores will produce large amounts of slag, therefore,

[1]Corresponding author: Jun Luo, Email: luojuncsu@163.com, Tel.: (+86) 731 88830542

it is significant to reduce the production cost and increase economic efficiency by optimizing the process system to lower melting temperature. In this paper, it focused on the ferronickel production of RKEF smelting, which studied the properties of nickeliferous laterite ore, reductive roasting and smelting conditions optimization by theoretical and experimental research.

Experimental

Materials

Nickeliferous laterite ore. The nickeliferous laterite ore sample used in this study was taken from Sulawesi Island, Indonesia. Its chemical composition is shown in Table I, the sample is characterized by high magnesia and silica contents. According to the XRD results, the nickeliferous laterite mainly consists of lizardite ($(Mg,Fe)_3Si_2O_5(OH)_4$), goethite and hematite, indicating that it is a typical saprolitic laterite ore. Besides, the results of TG-DSC analysis (see Figure 1) shows that the mass change of the ore sample kept approximately constant with the temperature above 800 °C.

Table I. The main chemical compositions of the nickeliferous laterite ore/wt. %

TFe	TNi	SiO_2	MgO	Al_2O_3	CaO	Cr_2O_3	LOI
23.15	1.85	30.56	15.25	3.43	1.29	1.02	11.45

LOI*—loss on ignition

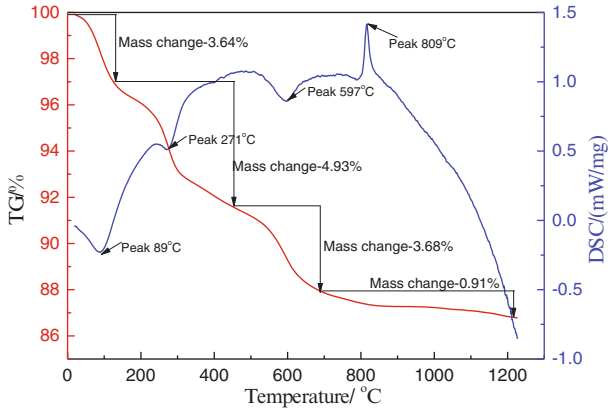

Fig. 1 TG-DSC curves of the nickeliferous laterite ore sample

Pulverized Coke. The size of pulverized coke was ground to 100wt. % passing 0.074 mm standard sieve, and the proximate analysis and chemical composition of its ash were listed in Table II. It can be seen that the content of fixed carbon is about 80%, indicating that the coke is a good reductant for smelting.

Table II. Proximate analysis of coke and chemical composition of its ash /%

Proximate analysis*			Main chemical composition of ash						
V_{daf}	FC_{ad}	A_d	TFe	SiO_2	CaO	Al_2O_3	MgO	P	S
2.85	79.20	17.95	3.60	6.52	1.69	3.83	0.21	0.0063	0.050

* V_{daf}: volatile matter content; FC_{ad}: fixed carbon content; A_d: ash content.

Methods

Experimental flowsheet. The laterite sample was ground to 90wt. % passing 0.074 mm standard sieve. The ground sample was mixed with a certain amount of pulverized coke, and then the mixture was granulated to the green pellets with 10-12 mm in diameter. The pellets were dried at 105 °C for 4 h.

The reductive roasting experiments were performed in a vertical resistance furnace with inner diameter of 70 mm. Firstly, the dried pellets were put into a pot, and then the pot was placed into the vertical resistance furnace with the fixed temperature for reduction. When the roasting finished, the reduced pellets were taken out from the furnace and cooled down with the protection of the coal. A small part of reduced pellets were prepared for analyzing the nickel and iron metallization.

The reductive smelting experiments were conducted in other high-temperature resistance furnace. Once the given temperature was attained, the pre-reduced pellets were loaded into a cylindrical heat-resistant corundum crucible. Then, the crucible was subjected to a vertical resistance furnace and smelted isothermally for a given period. After smelting, the smelting products were cooled to room temperature in the crucible isolated from atmospheric oxygen by covering the coal. The ferronickel and slag were separated from the cooled smelting products, respectively. The chemical composition of ferronickel was determined by X-ray fluorescence analysis (XRF, PANalytical, Axios mAX, Netherlands). The recovery ratios of nickel and iron were calculated and taken as evaluation indexes, as well as Ni, Fe, S and P content of ferronickel were also considered.

Results and Discussion

Effects of Reducing Roasting on the Nickel and Iron Metallization

Effect of pulverized coke dosage. As seen from Figure 3, the metallization of nickel and iron increased with the pulverized coke dosage below 9.5%, and kept nearly invariable with the pulverized coke dosage above 9.5%. The result showed that the reduction advantage of nickel reflected more obvious at relatively lower pulverized coke dosage under suitable reducing temperature and time. It is suitable for subsequent smelting that the nickel metallization is about 65% in reducing roasting process based on production experience. In fact, the nickel metallization reached 67.72% at coke dosage of 7.5% as shown in Figure 3, and the amount of remaining coke in pellets which roasted at 900 °C for 30 min was 6.6% in the meanwhile.

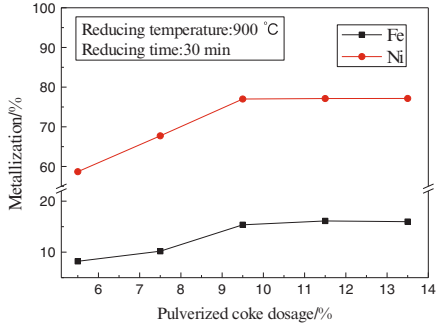

Fig. 3 Effect of pulverized coke dosage on the nickel and iron metallization

Effects of reducing temperature and time. The effects of reducing temperature and time on the metallization of nickel and iron were shown in Figure 4. It can be seen from Figure 4(a) that the metallization of nickel increased remarkably with the increasing reducing temperature from 800 to 900 °C, the metallization of nickel reached 77.00% at 900 °C and kept approximately constant with the temperature above 900 °C, and the iron metallization increased continuously with increasing reducing temperature. As to the reducing time, the iron metallization also increased significantly with the time below 30 min shown in Figure 4(b). However, with the prolonged reducing time, the metallization of nickel and iron changed little.

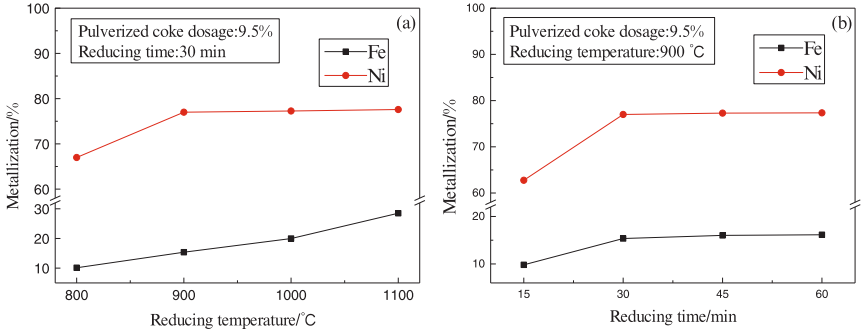

Fig. 4 Effects of reducing temperature and time on the nickel and iron metallization

Effect of Smelting on Ferronickel Product

Effect of pulverized coke dosage. The effect of pulverized coke dosage on ferronickel product quality including Ni recovery ratio, Fe recovery ratio, Ni, Fe, S and P content of ferronickel as shown in Figure 5 were studied. The coke here is the remaining coke of the pellets which roasted at 900 °C for 30 min. As can be seen from Figure 5(a) that Ni grade and Ni recovery ratio were 13.01% and 95.97% respectively at coke dosage of 4.9%. Obviously, the less coke dosage, and the less reduced metal, therefore there were high nickel grade in ferronickel for that nickel has a priority on reduction of iron. With the increasing coke dosage, more and more

nickel, iron, chromium oxide were reduced, especially Fe recovery ratio increased rapidly, and Ni grade in ferronickel correspondingly decreased. Figure 5(a) presents that Ni recovery ratio reached 99.03% at coke dosage of 6.6%, Ni grade was 10.32% in the meanwhile, it had little effect on improving Ni recovery ratio with increasing coke dosage, or even slightly decreased owing to decreasing FeO content in slag which affected slag melting temperature and viscosity. Since FeO content determined oxygen potential of slag, it is difficult for slag-making if FeO content were too low, and also the reaction ability of slag was insufficient. Figure 5(b) presented that S content of ferronickel gradually decreased and P content kept approximately constant with coke dosage increased from 4.9% to 9%, S and P content of ferronickel were 0.218% and 0.019% at coke dosage of 6.6%, respectively.

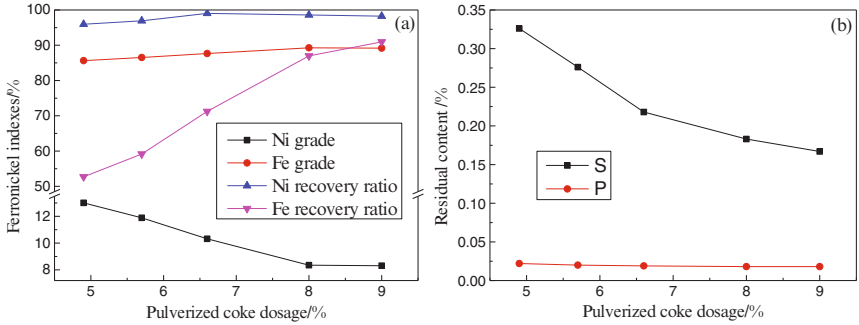

Fig. 5 Effect of pulverized coke dosage on ferronickel product quality
(CaO dosage: 10.6%; smelting temperature: 1500 °C; smelting time:30 min)

Effect of CaO dosage. Figure 6 showed effect of CaO dosage in the range of 8.3% to 17.3% on ferronickel product quality. The results of Figure 6(a) showed that Ni grade and Ni recovery ratio gradually increased with the CaO dosage below 10.6%, when CaO dosage further increased beyond 12%, Ni grade decreased slightly and Ni recovery ratio leveled off with the further increase of CaO dosage from 12% to 17.3%. By contrast, Fe grade and Fe recovery ratio decreased as CaO dosage increased from 8.3% to 10.6% and then increased slightly. As can be seen from Figure 6(a) that Ni grade and Ni recovery ratio exceeded 10% and 99% respectively with CaO dosage in the range of 10.6% to 12%. It can be concluded that a suitable range of CaO dosage can optimize the performance of slag, and then promote Ni grade and Ni recovery ratio by lowering the slag viscosity and density. The results of Figure 6(b) showed S content of ferronickel gradually decreased from 0.267% to 0.138%, and P content kept approximately constant with the CaO dosage increased from 4.9% to 9%.

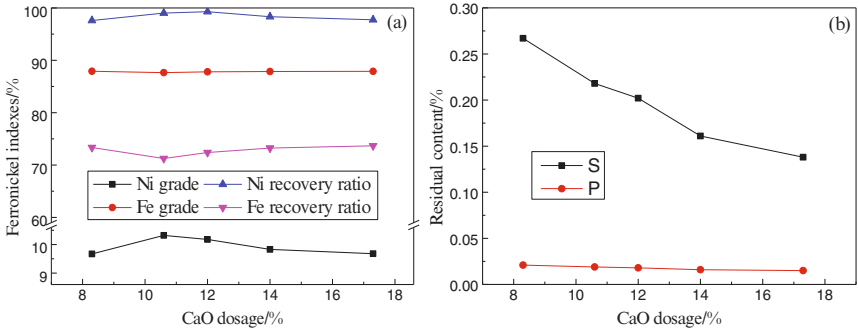

Fig. 6 Effect of CaO dosage on ferronickel product quality
(pulverized coke dosage: 6.6%; smelting temperature: 1500 °C; smelting time:30 min)

Effects of Smelting temperature and time. The effects of smelting temperature and time on ferronickel product quality were shown in Figure 7 and Figure 8. As shown in Figure 7(a) and Figure 8(a), Ni grade and Fe grade kept nearly invariable with the increasing smelting temperature from 1450 to 1600 °C and smelting time from 20 to 50 min. The results of Figure 7(a) showed Ni recovery ratio increased and then leveled off with the increasing smelting temperature, and Fe recovery ratio gradually increased in the meanwhile. It can be seen that Ni recovery ratio reached 99.03% and 99.21% at 1500 and 1550 °C, respectively. Figure 7(b) showed that S content of ferronickel gradually increased from 0.135% to 0.369% and P content of ferronickel changed little with smelting temperature in the range of 1450 to 1600 °C. With regard to smelting time, it is necessary to choose a suitable smelting time for ensuring the full settlement and separation of slag and iron in the process of smelting. When smelting time exceeded 30min, Ni recovery ratio kept nearly 99% shown in Figure 8(a), and Fe recovery ratio slightly increased with smelting time increased from 20 to 50 min. The results of Figure 8(b) presented smelting time from 20 to 50 min had little effect on desulfurization and dephosphorization. In the viewpoint of energy consumption, smelting temperature of 1500 °C and smelting time of 30 min were recommended, and a ferronickel containing 10.32% Ni with Ni recovery ratio of 99.03% and 87.65% Fe with Fe recovery ratio 71.25% was obtained.

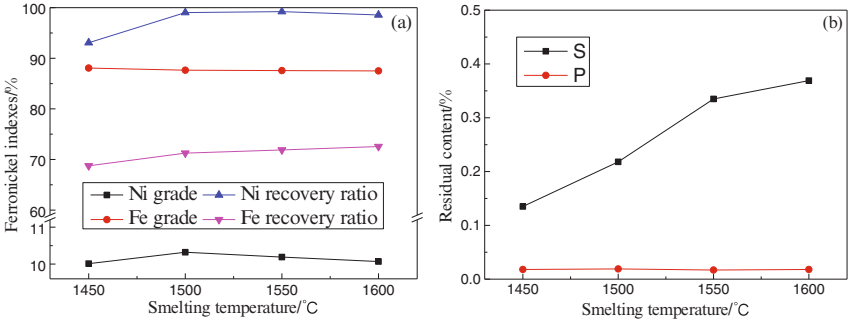

Fig. 7 Effect of smelting temperature on ferronickel product quality
(pulverized coke dosage: 6.6%;CaO dosage: 10.6%; smelting time:30 min)

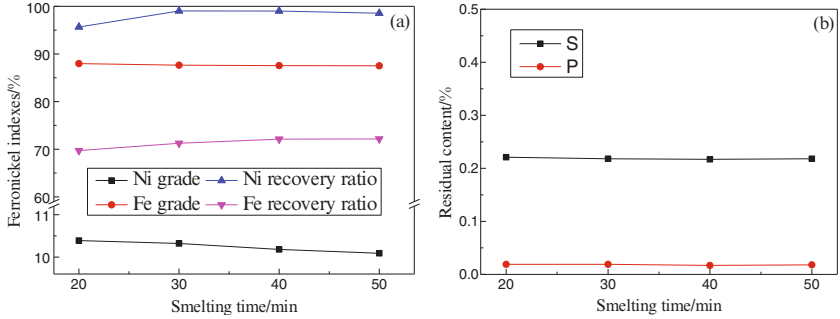

Fig. 8 Effect of smelting time on ferronickel product quality
(pulverized coke dosage: 6.6%;CaO dosage: 10.6%; smelting temperature: 1500 °C)

Conclusions

(1) The optimal reductive roasting conditions: roasting temperature of 900 °C, roasting time of 30 min and pulverized coke dosage of 9.5%. Under the optimal conditions, the Ni and Fe metallization reached 77.00% and 15.36%, respectively. However, it is more suitable for subsequent smelting at coke dosage of 7.5% while the Ni metallization was 67.72%, and the amount of remaining coke in pellets which roasted at 900 °C for 30 min was 6.6% in the meanwhile.

(2) The optimal smelting conditions: pulverized coke dosage of 6.6%, CaO dosage of 10.6%, smelting temperature of 1500 °C and smelting time of 30 min. Under the optimal conditions, a ferronickel containing 10.32% Ni with Ni recovery ratio of 99.03% and 87.65% Fe with Fe recovery ratio 71.25% was obtained from a nickeliferous laterite with 1.85 wt. % Ni and 23.15 wt. % Fe. Besides, S and P content of ferronickel were 0.218% and 0.019%. The results showed that a good smelting effect can be achieved at a relatively lower smelting temperature, by means of adding a suitable CaO dosage in the range of 10.6% to 12% to adjust the slag basicity.

References

[1]. R.R.Moskalyk and A.M.Alfantazi, "Nickel Laterite Processing and Electrowinning Practice," *Minerals Engineering*, 15 (8) (2002), 593-605.

[2]. M.J. Rao et al., "Carbothermic Reduction of Nickeliferous Laterite Ores for Nickel Pig Iron Production in China: A Review," *JOM*, 65 (11) (2013), 1573-1583.

[3] B.K. Reck, V.S. Rotter, "Comparing growth rates of nickel and stainless steel use in the early 2000s," *J. Ind. Ecol*, 16 (2012), 518–528.

[4]. M.J. Eckelman, "Facility-level energy and greenhouse gas life-cycle assessment of the global nickel industry," *Resour. Conserv. Recycl*, 54 (4) (2010), 256–266.

[5]. T. Norgate, S. Jahanshahi, "Assessing the energy and greenhouse gas footprints of nickel laterite processing," *Minerals Engineering*, 24 (7) (2011), 698–707.

[6]. C. Walker et al. "Future of Rotary Kiln-Electric Furnace (RKEF) Processing of Nickel Laterites," (Paper presented at the Proceedings of the European Metallurgical Conference, 2009).

[7]. Oxley A, Barcza N. "Hydro–pyro integration in the processing of nickel laterites," *Minerals Engineering*, 54 (2013), 2-13.

Characterization of Minerals, Metals, and Materials 2016
Edited by: Shadia Jamil Ikhmayies, Bowen Li, John S. Carpenter, Jiann-Yang Hwang, Sergio Neves Monteiro, Jian Li, Donato Firrao, Mingming Zhang, Zhiwei Peng, Juan P. Escobedo-Diaz, and Chenguang Bai
TMS (The Minerals, Metals & Materials Society), 2016

CHARACTERIZATION OF COPPER-MANGANESE-ALUMINUM-MAGNESIUM MIXED OXYHYDROXIDE AND OXIDE CATALYSTS FOR REDOX REACTIONS

Arnab Baksi[1], David L. Cocke[1], Andrew Gomes[1], John Gossage[1], Mark Riggs[2], Gary Beall[2,4] and Hylton McWhinney[3]

[1]Departments of Chemical Engineering, Lamar University, Beaumont, Texas 77710;
[2]Department of Chemistry, Texas State University, San Marcos, Texas 78666;
[3]Department of Chemistry, Prairie View A&M University, Prairie View, Texas 77446
[4]King Abdulaziz University, Faculty of Science, Department of Physics, Jeddah, Saudi Arabia

Keywords: Layered Double Hydroxides, Mixed catalyst, TGA-MS characterization, Hopcalite

Abstract

Complex multi-metal catalysts require several stages in their preparation. These are: co-mixing, co-precipitation, milling and sol-gel, drying, dehydroxylation, and calcination and sometimes regeneration of the hydroxide by rehydration. These processes require thermal analysis (DTA, TGA, DSC) and accompanying off gas analysis, plus one or more of these: XRD, XPS, SEM-EDS, FTIR and UV-VIS. In this study, hydrotalcite, hopcalite and mixed systems were prepared and guided by the above characterization techniques. The systems were initiated by mixing the chlorides or nitrates followed by hydrothermal treatments to produce the hydroxides which were further treated by washing, drying, and calcination. The thermal analysis was critical to guide the preparation through these stages and when combined with structural determination methods considerable understanding of their chemical and physical changes was obtained. The correlations between preparation and characterization will be discussed.

Introduction

The purpose of this work is to design and characterize a novel mixed catalyst material that can be used for redox reactions to remove toxic components from gas mixtures. Automobile exhaust is one of the major sources of toxics in the atmosphere. In this study, hydrotalcite based novel material is designed to prepare suitable catalyst that can be used in atmospheric toxic removal process. Layered Double Hydroxide (LDH) is one of the most promising materials families, widely used as catalyst, catalyst support, adsorbent and favorable catalysts support with large anion adsorption capacity [1-5]. They can be considered as anti-types of 2:1 (three-layer) clay minerals. The general chemical formula is written as $[M^{II}_{1-x}M^{III}_{x}(OH)_2]^{x+}[A^{n-}_{x/n}]^{x-}.yH_2O$, where M^{II} is a divalent cation (Mg^{2+} Zn^{2+}, Mn^{2+}, Mo^{2+}, Ni^{2+}, Cd^{2+}), M^{III} is a trivalent cation (Al^{3+}, Fe^{3+}, Cr^{3+}, Ga^{3+}), and A^{n-} is an anion, such as carbonate, chloride, sulfate, or phosphate. The trivalent cations (*e.g.*, Al^{3+}) generate positive charges on the layers, which are compensated by anions located in the interlayer region. Water molecules are also found in the interlayer space [6]. In a brucite layer, each Mg^{2+} ion is octahedral, surrounded by six OH^- ions and each octahedron shares edges to form an infinite two-dimensional layer. The brucite crystals are then formed when the 2-D layers are stacked one on the top of another via O–H···O hydrogen bonding between the adjacent layers (see Fig. 1). Partial replacement of Mg^{2+} ions by Al^{3+} gives

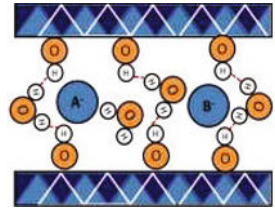

Figure 1: Schematic of layered double hydroxide structure where blue layers are brucite like positively charged layers and A and B are anions balancing the overall charge along with the water molecules present in the interlayer.

the brucite-like layers a positive charge, which in hydrotalcite itself is balanced by carbonate anions, located in the interlayer region (gallery) between the two brucite-like layers. This gallery also contains water molecules, hydrogen bonded to layer OH^- ions and/or to the interlayer anions. The electrostatic interactions and hydrogen bonds between the brucite-like layers and the gallery species hold the layers together, forming the three-dimensional structure [7].

The major techniques that are available to prepare LDH materials are shown in the Figure 2. The present report follows co-precipitation technique at elevated pressure and temperature and simultaneous doping of Cu-Mn oxide to design a modified structure.

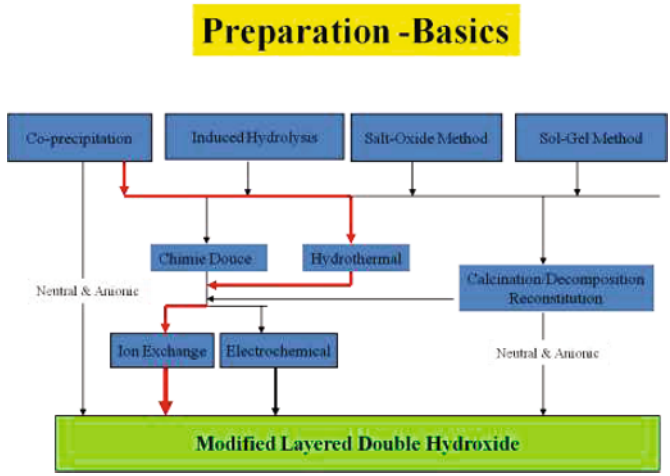

Figure 2: Different paths to prepare LDH. The red highlighted path indicates the process that was followed in the current work to prepare mixed hydroxides.

In this work, we have doped Cu-Mn based highly reactive catalyst inside the complex LDH structure to enhance the property of their mixed analog by selectivity and availability of active sites in redox reactions.

Experimental

Magnesium chloride, aluminum chloride, manganese chloride, cupric chloride and cupric nitrate were purchased from Fischer Scientific. Magnesium nitrate, aluminum nitrate, and manganese nitrate were purchased from Sigma Aldrich USA. Sodium hydroxide beads were purchased from Sigma (USA).

DI water was heated to 50°C. Salts of magnesium, aluminum, copper and manganese are mixed in 300 mL of DI water. The relative ratios of the salts were maintained as Machej *et al.* 2014 [8]. The solution kept in glass beaker and stirred for 10 minutes to ensure that the salts are completely dissolved. After that, the solution was transferred to a Teflon jacket and set the stirrer speed to 1000 rpm. The pH was monitored throughout the process. NaOH solution was slowly added to adjust the pH to 11. At pH 11, the solution became viscous, and its color was changed to brown. The Teflon jacket was placed inside the autoclave reactor and aged for 5 hrs at 170°C and at 12 bar after a 5-minute stirring. The product slurry was collected and a series of washing and centrifugation stages were performed. The resulting thick material was collected in a watch glass and placed in the oven for 24 hr at 50°C. After drying the sample was crushed to make fine powder. The fine powder was then calcined at 300°C to remove any crystal water. It is important to mention that the XRD, SEM and EDS analysis were performed on the product after calcination. However, for TGA-MS experiment the intermediate product was collected after the initial; drying at 50°C.

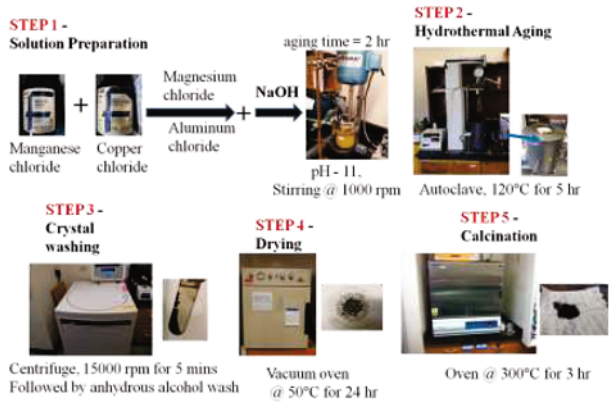

Figure 3: A detailed stepwise process shown to prepare chloride based mixed catalyst. For nitrate mixed catalyst the process was repeated with nitrate salts.

There were two types of mixed catalyst synthesized. The chloride based catalyst was prepared to compare the structural difference with that of nitrate. The procedure that describes in Figure 3 was followed for both chloride and nitrates.

Results

XRD data of the chloride and nitrate based mixed catalysts are shown in Figure 4. There were different phases that were identified in the chloride mixed product. Predominantly the hydrotalcite phase is mixed with copper oxide, and manganese oxide. There was a small amount of rhodochrosite ($MnCO_3$) phase identified that formed due to carbon dioxide incorporation from the atmosphere. An overlay data shows common hydrotalcite phase in both the samples. An overall comparison between chloride and nitrates reveals that the crystal formation was comparatively higher in case of chlorides.

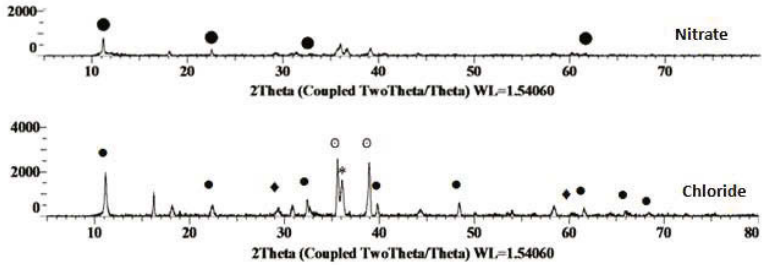

Figure 4: X-ray diffraction pattern of nitrate and chloride based mixed catalysts. The aging time was maintained as 5 hr and pH=10 was controlled for each sample. The hydrotalcite phases were identified for nitrate sample. For chloride sample, the symbols are representing ● hydrotalcite, Θ Cu_xO, ♦ MnO_x, * rhodochrosite ($MnCO_3$).

Figure 5 shows an overall comparison in TGA-MS plots between chloride and nitrate mixed catalysts. Figure 5 suggests that the thermal behavior of chloride mixed catalyst is complicated at higher temperature compared to that for the nitrate compound. The MS scan in chloride catalyst identifies evolved gases during the steps of weight loss at different temperatures. The dehydration reaction takes place around 100-150 °C. A CO_2 release at 200°C confirms the presence of carbonate in the structure and its degradation to CO_2. Further analysis on the peak details depicts a major dehydroxylation (loss of OH and H_2O) that takes place around 350-400 °C. In the off gas data, some HCl formation was noticed mostly at lower temperature range that comes from chloride that is present in the structure. There is a second large weight loss observed between 500-600°C in the TG plot, but no evolved gas was identified with the MS data analysis.

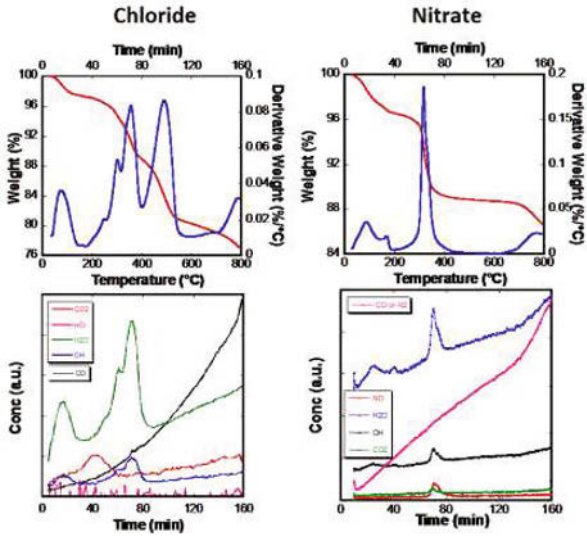

Figure 5: The thermal data for mixed catalysts and their off gas mass spectrometry analysis for chloride and nitrate mixed catalysts.

Figure 6 shows the difference between crystal morphologies by SEM analysis and EDS spectra for chloride and nitrate catalysts. The chloride crystals are more crystalline in nature and nitrates are amorphous. The same conclusion was drawn from the XRD results. The nitrogen was difficult to see and quantify in the EDS experiments. We suspect that the nitrate is decomposing in the electron beam to volatile products as it is well known in electron beam metal deposition from their nitrates [9].

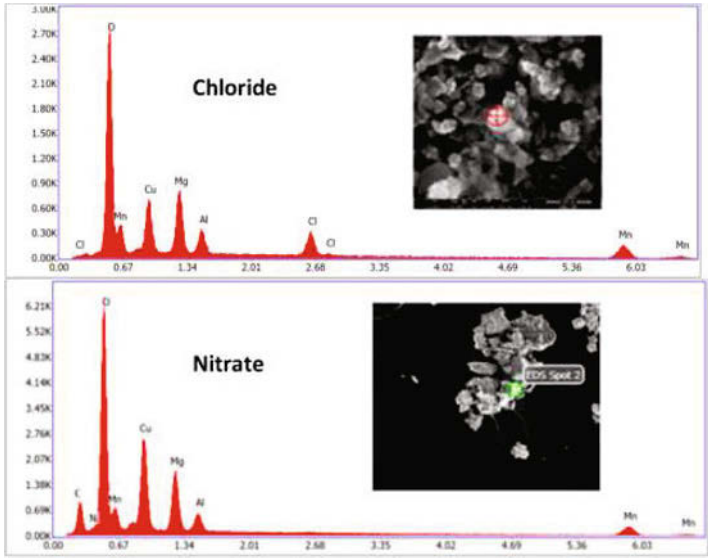

Figure 6: SEM and EDS results for chloride and nitrate samples. The EDS analysis spots are shown on the SEM image area. The nitrogen was difficult to see and quantify in the EDS experiments due to its probable decomposing in the electron beam to volatile products.

Discussion

Simultaneous thermal analysis and off gas mass spectrometry (MS) has proven to be exceptionally useful in the synthesis of mixed oxide doped hydrotalcite catalysts. Figure 5, a comparison between chloride and nitrate based mixed catalyst characterization shows that the mixed chloride catalyst behavior during dihydroxylation is complicated at the higher temperature range compared to the nitrate mixed oxide doped hydrotalcite. Fig. 4 also shows a TGA peak between 500-600°C that could not be identified through MS off-gas analysis. According to Figure 7 [10] $CuCl_2$, a major component used in the mixed catalyst synthesis, copper, can decompose at 500°C to form CuCl phase. Further increase in temperature drives a phase change of CuCl liquid to vaporize to a highly condensable gas (see Figure 7).

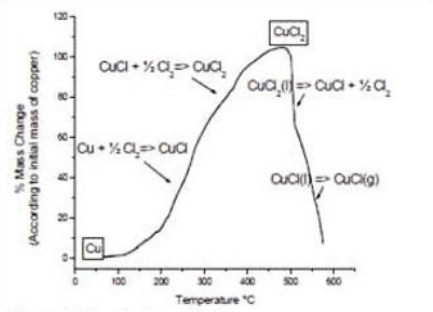

Figure 2: Non-Isothermal TG curve

Cu ions react with Cl^- to produce CuCl

$$CuCl \xrightarrow{500C} CuCl(Gas)$$

Figure 7: Explanation of the mystery peak in the chloride compound.[10]

In general, CuCl is a very stable compound and condensed in the transfer line from TG to MS at a lower temperature than the TG furnace. Thus, CuCl never reached the MS detector and deposited in the TGA- MS instrument connection system. Since the CuCl was in gas phase at above 500°C, there was a significant mass loss from this chloride mixed catalyst.

Nitrate based mixed catalyst off gas analysis in combination with TGA data are shown in Figure 5. The characteristic peaks in TGA plot were identified in the MS scan result. A dehydration peak at 100-150°C followed by dehydroxylation and decarbonization near 400°C is observed. The decarbonization reaction close to 400°C suggests that the nitrate based catalyst can clean the surface around that temperature range. In other words, carbon can be released easily in form of CO_2 from nitrate based self activating high oxidation catalysts. This discussion lead to an application of nitrate based catalyst at a higher temperature range compared to the similar chloride based catalyst system. It is also important to note that unlike the chloride based system, the nitrate catalysts do not release copper compounds at higher temperature ranges. This identifies nitrate catalyst as more suitable agent at higher temperature applications.

Conclusion

Copper-manganese-aluminum-magnesium mixed LDH based catalysts were prepared by hydro-thermal process, and characterized by the state-of-the-art instrumentation. Simultaneous thermal analysis and off gas mass spectrometry (MS) has proven to be exceptionally useful in confirming the composition and the structure of the mixed catalysts. The mystery peak in TGA of chloride mixed catalyst was identified as CuCl. The off-gas study of nitrate mixed catalyst shows its ability to clean the carbon contaminated surface at higher temperature.

Acknowledgement

We would like to thank Lamar University Research Enhancement Grant, 2014-15 and Department of Chemistry and Biochemistry Texas State University for funding this research.

References

1. Chen, D., et al., *Efficient removal of dyes by a novel magnetic Fe3O4/ZnCr-layered double hydroxide adsorbent from heavy metal wastewater.* J Hazard Mater, 2012. **243**: p. 152-60.

2. Lee, J., S. Rhee, and D.Y. Jung, *Orientation-controlled assembly and solvothermal ion-exchange of layered double hydroxide nanocrystals.* Chem Commun (Camb), 2003(21): p. 2740-1.

3. Liu, Y.L., et al., *Using Zn/Al layered double hydroxide as a novel solid-phase extraction adsorbent to extract polycyclic aromatic hydrocarbons at trace levels in water samples prior to the determination of gas chromatography-mass spectrometry.* Anal Bioanal Chem, 2012. **404**(5): p. 1603-10.

4. Sasai, R., W. Norimatsu, and Y. Matsumoto, *Nitrate-ion-selective exchange ability of layered double hydroxide consisting of MgII and FeIII.* J Hazard Mater, 2012. **215-216**: p. 311-4.

5. Zhang, M., et al., *Layered double hydroxide-carbon dot composite: high-performance adsorbent for removal of anionic organic dye.* ACS Appl Mater Interfaces, 2014. **6**(22): p. 20225-33.

6. Wan, D., et al., *Role of the Mg/Al atomic ratio in hydrotalcite-supported Pd/Sn catalysts for nitrate adsorption and hydrogenation reduction.* J Colloid Interface Sci, 2009. **332**(1): p. 151-7.

7. Braterman, P.S., Z.P. Xu, and F. Yarberry, *Layered Double Hydroxides (LDHs).* Handbook of Layered Materials, 2004: p. 373-474.

8. Machej, T., et al., *Cu/Mn-based mixed oxides derived from hydrotalcite-like precursors as catalysts for methane combustion.* Applied Catalysis A: General, 2014. **474**(0): p. 87-94.

9. Wickleder, M.S., et al., *Synthesis, Characterization and Electron Beam Assisted Decomposition of $(NO_2)[Au(NO_3)_4]$.* Chemistry of Materials, 2008. **20**(16): p. 5181-5185.

10. De Micco, G., A. Bohé, and D. Pasquevich, *A thermogravimetric study of copper chlorination.* Journal of alloys and compounds, 2007. **437**(1): p. 351-359.

Characterization of Minerals, Metals, and Materials 2016

Ferrous

Session Chairs:
Donato Firrao
Mingming Zhang

Characterization of Minerals, Metals, and Materials 2016
Edited by: Shadia Jamil Ikhmayies, Bowen Li, John S. Carpenter, Jiann-Yang Hwang, Sergio Neves Monteiro, Jian Li, Donato Firrao, Mingming Zhang, Zhiwei Peng, Juan P. Escobedo-Diaz, and Chenguang Bai
TMS (The Minerals, Metals & Materials Society), 2016

DISCUSSION ON COKING WASTEWATER TREATMENT AND CONTROL MEASURES IN IRON AND STEEL ENTERPRISES

Lei ZHANG[1], Jiannyang HWANG[2], Ting LENG[3], Gaifeng XUE[1], Gaoming WU[1]

[1] R&D center of WISCO, Wuhan, 430080, China;
[2] Michigan Technological University, Michigan, MI 49931, USA
[3] Manufacturing department of WISCO, Wuhan, 430050, China

Keywords: Iron and steel enterprise; coking wastewater; disposal methods; control measures; discussion

Abstract

According to the water quality characteristics of coking wastewater and the environmental protection requirements, the status of coking wastewater treatment technologies at home and abroad was described. Several methods and control measures of coking wastewater treatment were discussed in the effluent from iron and steel enterprises. It is an effective way to makes use of cleaner production technologies to reduce the amount of coking phenol cyanide wastewater produced from the source, and then adopt water supply for different water quality or series classification in-house according to the demand of water characters. It is necessary though looking for the available disposal way to reduce the coking wastewater effluent, which can provide a reference for process selection and research on treatment of coking wastewater in iron and steel enterprise.

Introduction

Coking wastewater is generated from coal coking, coal gas purification, and by-product recovery processes of coking, which is composed of phenolic compounds, heterocyclic compounds, polycyclic aromatic hydrocarbons, ammonia, cyanide, polycyclic nitrogen-containing aromatics, acyclic compounds, etc. Most of these constituents are refractory, poor biodegradability, toxicity and carcinogenic[1-3]. Biochemical treatment process of coking wastewater is easy to be affected by these factors, such as water quality (such as phenol, cyanide, etc.), water quantity fluctuation, higher temperature, etc, which can result in activated sludge poisoning, sludge aging and other phenomena, then affecting the effluent quality. At present, coking wastewater is generally treated by the A/O process (anaerobic/aerobic) combined with advanced oxidation process at home. According to the "Coking Chemical Industrial Pollutants Emission Standards in China"(GB16171-2012), the existing enterprises will implement more stringent emissions standards for wastewater discharge, such as, COD (chemical oxygen demand) is not more than 80mg/L, TN (total nitrogen) ≤ 20mg/L, NH_3 (ammonia nitrogen) ≤ 10 mg/L, polycyclic aromatic hydrocarbons (PAHs) ≤ 0.05 mg/L, benzo (a) pyrene ≤ 0.03ug/L and so on. Coking wastewater effluent discharge standards will bring about a serious challenge. One problem is that the typical indicators such as COD, NH_3-N, TN, cyanide in most of the current domestic coking companies cannot meet emission standards(GB16171-2012); and the other one is that some indicators cannot be monitored, like Polycyclic aromatic hydrocarbons (PAHs), benzene and (a) pyrene, five days of biochemical oxygen demand (BOD5). According to the existing national

standards, tons of coke unit product basic drainage volume is 0.4 m^3, and extra limited value is 0.3 m^3 in special region in China. Due to higher volume wastewater discharge, the conversion of pollutants concentration is more difficult to meet the requirements of emission standards(GB16171-2012). Therefore, with the implementation of the new national "environmental protection law" and the more stringent emission standards, more work should be focused on decreasing coking wastewater discharge and reuse in the existing company without delay.

Research status of treatment technology of coking wastewater at home and abroad

Few literatures reported on the advanced treatment and reuse technology of coking wastewater in Europe and the United States[4]. maybe there are small number of coking enterprises, what's more, these enterprises pay more attention to water conservation. Coking plant in U.S. Steel company first collected coking wastewater, and then diluted with equal amounts of water. Coking wastewater was first treated by the biochemical treatment and then advanced treatment using activated sludge process in Japan. More researches of deep treatment and reuse of coking wastewater are studied and explored in China [1,2]. There are two main technical routes: one is to focus on water quality stable, and the other one is focused on water quality. At present, reuse technology of coking wastewater were carried out through wet coke quenching, blast furnace slag washing, coal dust suppressant and sinter feed water etc[5].Wet quenching coke, blast furnace slag washing are still widely used in many iron and steel enterprises in China, but there are some problems to be solved, such as, pollutants transferring from water into air, site operation environment poor, corrosion problems of equipment and pipeline and other issues, which does not meet the requirements of sustainable development. According to the requirements of Chinese government, coking enterprises must construct wastewater treatment facilities, and wastewater efflux is prohibited; pollutant emissions of coking enterprises should reach the national and local emission standards and meet the requirements of the total discharge of major pollutants. Due to coking wastewater containing inorganic salts as well as some other organic pollutants, cost of wastewater treatment and reuse is about 20~30 Yuan/t, which is undoubtedly worse for low profit situation of iron and steel enterprises. Therefore, it is particularly necessary though looking for the available ways to meet the existing environmental laws, regulations and national standard requirements for iron and steel joint enterprise.

Proposals for the treatment of coking wastewater in iron and steel joint enterprises

Blast furnace slag washing

Blast furnace (BF) slag washing is one of the best choice for zero discharge and reuse of waste water, but the premise is that the coking wastewater must be treated in depth avoiding pollutes transferring or resulting in secondary pollution. According to the characteristics of high temperature decomposition of COD, ammonia nitrogen and other harmful substances in coking wastewater, the coking phenol cyanide wastewater can be recycled and utilized to realize the zero discharge in the BF INBA system. Water consumption in BF INBA system is mainly composed of granulation pump water, accident water, and seal cooling water, etc. Each BF INBA system has a closed circulating water system. Slag water ratio is 1:6 and slag washing

water can be recycled. Because of the water evaporation and slag carrying, the BF INBA system needs to add new industrial water. The amount of the new industrial water is about 0.5 ~ 1.0m3 per ton slag. According to the experience of domestic iron and steel company, drum washing water can be directly replaced by coking wastewater, but cost is high for the corrosion problems. To avoiding the corrosion problems of drum filter, coking wastewater, blast furnace drum washing water, granulation pump water should first mix and then is used for BF slag washing. Practice has proved that it is feasible [6].

Sintering ingredients water

The water content of sintering ingredient is generally 8~10%, the diameter of the impurity particles in water is less than 1mm. Experiments in the early stage of the sintering cup with coking waste water were carried out (See Table 1, Table 2). The results showed sintering time was slightly longer than that of tap water as sintering ingredients water. Sintering speed, finished product ratio and the coefficient were lower, while the drum strength was higher than adding tap water. From the sintering ore particle size composition, we draw conclusions that sintering ore segregation was higher using coking wastewater than that of tap water. Overall speaking, these side effects on the quality of sintering ore can be ignored.

Table 1 sintering test index

Sample	Sintering time min	Sintering speed mm/min	Finished product rate %	Utilization coefficient $t/(m^2h)$	Drum strength %	Max temperature ℃
Tap water	29.0	24.14	77.19	1.917	63.60	357
1#wastewater	31.0	22.58	72.51	1.707	67.20	359
2#wastewater	31.0	22.58	75.52	1.787	66.67	340

Table 2 Sinter granularity composition /(mm)

Sample	+40	25～40	15～25	10～15	5～10	-5
Tap water	16.71	13.26	10.61	10.88	25.73	22.81
1#wastewater	11.26	15.97	9.42	8.90	26.96	27.49
2#wastewater	12.24	15.89	10.68	8.85	27.86	24.48

Converter dedusting water

The thermal energy of high temperature flue gas generated during the process of converter smelting process can be used to crack the organic components of coking wastewater. Literatures reported that pollutant concentration in the effluent, such as ammonia, phenols, cyanide, COD and so on can be decreased dramatically, which can meet the requirements of the water quality of converter dedusting water[7]. What's more, the system was running in good condition, and venturi nozzles and water pipelines were not corroded or blocked. There were little adverse effects to the smelting process, metallurgic product as well as working environment [8].

"Zero discharge" technology in Coking Plant Wastewater

Coking wastewater "zero discharge" technology not only require water quality of coking waster treated to meet emission standards, but also to meet the national standard requirements of industrial cooling water in China (GB50500-2007). Biochemical treatment + advanced treatment + desalination technology(membrane separation technology) was widely used in China for coking wastewater "zero discharge", such as, China Baosteel company, China Kunming Iron and steel and China Taiyun Iron and steel, and so on [9]. But treatment cost is about 5~10 times higher than that of the comprehensive utilization of coking wastewater in the iron and steel enterprise.

Conclusions

The problem how to reach the discharge standards and reuse of coking wastewater is difficult to solve. In order to eliminate the risk of environmental protection and achieve the goal of zero discharge, the following several aspects should be considered:

1. Cleaner production should be implemented to reduce the amount of waste water from the source. Coal moisture control technology can be adopted to decrease the content of water into the furnace. Cross-tube primary cooling can reduce water pollution during the coking oven gas (COG) purification processes. Desulfurization wastewater from COG purification processes need to be pretreated and then piped wastewater into the wastewater treatment unit.

2. From the management point of view, technologies of serial reuse and segregated pretreatment should be widely used for coking wastewater "zero" emissions. According to the characteristics of the iron and steel enterprises, it is feasible to achieve zero discharge of coking wastewater from the overall situation. Coking wastewater can be used as cooling water for BF slag washing and steel slag quenching to compensate the evaporation loss.

3. Estimating from the environmental and economic benefits, the treatment cost of existing coking wastewater treatment process (biochemical treatment process + advanced oxidation process + desalination process) is about 5~10 times higher than that of the comprehensive utilization of coking wastewater in the iron and steel enterprise.

Therefore, focusing on technological progress, conducting cleaner production technology and reducing the wastewater amount from the source will become one of the best ways to treat the coking wastewater. Maybe it is the inevitable choice for iron and steel enterprises to enhance the ability of sustainable development.

References

[1]Zhu X. et al., "Optimization of Fenton and electro-Fenton oxidation of biologically treated coking wastewater using response surface methodology," *Separation and Purification Technology*, 81(3)(2011),444-450.

[2]Kim Y.M. et al., "Inhibitory effects of toxic compounds on nitrification process for cokes wastewater treatment," *Journal of Hazardous Materials*, 152(3)(2008),915-921.

[3] Zhou H. et al.," Profile and pollution characteristics of polycyclic aromatic hydrocarbons

in coking wastewater, "*Environmental Monitoring in China,* 30 (2) (2014),58-61.(in Chinese)

[4] M L.S . et al., "New approach to optimize operational conditions for the biological treatment of a high-strength thiocyanate and ammonium waste: pH as key factor, *"Water Resarch,* 42(3) (2008):774-80.

[5]Kong X, "Discussion on advanced treatment and reuse technology of coking wastewater ,*" China Environmental Protection Industry,* (5)(2010): 44-47. (in Chinese)

[6]TONG J., "Comprehensive utilization of coking phenol cyanogen wastewater in the Ironmaking and Sintering System," *Gansu metallurgy in China,* 36 (3)(2014), 57-60. (in Chinese)

[7] Zhang J, et al., "Feasibility studies on coking wastewater reuse for converter gas washing water systems," *Industrial Water Treatment,* 27 (9)(2007),56-59. (in Chinese)

[8] Cao W., et al., "Novel approach to the treatment of coking effluent by utilizing converter flue gas," *Industrial Water Treatment,* 25 (11)(2005),74-76. (in Chinese)

[9]Jin., et al., "Practical research on advanced treatment of coking wastewater by membrane process,*" Environmental pollution and control,* 35(1l) (2013),77-82. (in Chinese)

Characterization of Minerals, Metals, and Materials 2016
Edited by: Shadia Jamil Ikhmayies, Bowen Li, John S. Carpenter, Jiann-Yang Hwang, Sergio Neves Monteiro, Jian Li, Donato Firrao, Mingming Zhang, Zhiwei Peng, Juan P. Escobedo-Diaz, and Chenguang Bai
TMS (The Minerals, Metals & Materials Society), 2016

EFFECT OF MgO AND BASICITY ON MICROSTRUCTURE AND METALLURGICAL PROPERTIES OF IRON ORE SINTER

Mingming Zhang[1] and Marcelo W. Andrade[2]

[1]Sr. Research Engineer, ArcelorMittal Global R&D, East Chicago, IN 46312, USA
[2]Manager, ArcelorMittal Global R&D, East Chicago, IN 46312, USA

Keywords: Sinter, Pot-grate sintering, Microstructure, Mineral phase, Metallurgical properties

Abstract

The metallurgical properties of iron ore sinter mainly depends on sinter mineralogy and microstructure, which in turn depends on the chemical composition of the sinter mix. In order to meet blast furnace requirement on sinter quality, it is essential to optimize the MgO in sinter mix and sinter basicity to get desired properties. Laboratory pot grate sintering experiments and quantitative analysis of sinter mineralogical phases have been carried out to investigate the influence of MgO addition on microstructure and properties of low basicity and high basicity sinter. MgO addition has been varied from 2.2 to 4.5% for low basicity (2.1), and high basicity (3.5) sinter mixes. Mineralogical examination indicated that Magnetite-Mg phases increases when MgO content in sinter increases. To achieve balanced sinter quality to meet blast furnace specifications, high basicity with medium range of MgO sinter was recommended to sinter plant.

Introduction

Iron ore concentrates or fines cannot be charged into blast furnace directly because they are detrimental to the permeability of the furnace. These iron ore fines are therefore required to be agglomerated into larger pieces [1, 2]. Sintering is one of the most economic and widely used agglomeration process for preparing iron ore fines for blast furnace use. Many reactions may take place during the sintering process. Macroscopically iron sinter has a non-uniform structure with large irregular pores. Microscopically it consists of bonding phases, relict ore particles, remaining glassy phases and very small non-uniform pores and cracks. Depending on different parameters such as temperature, composition, oxygen partial pressure, time and atmosphere, different phases form in different proportions, while different morphologies develop. The morphology essentially reflects the mode of formation and is related to a particular chemical composition, heating and cooling rate of the sinter. Some of the common minerals and phases present in iron ore sinter are hematite (Fe_2O_3), magnetite (Fe_3O_4), magnesioferrite ($MgFe_2O_4$), silicoferrite of calcium and alumina (SFCA), with stoichiometries $M_{14}O_{20}$ (M= Ca, Fe, Al, Si), anorthite ($CaAl_2Si_2O_8$), calcium diferrite ($CaFe_4O_7$), dicalcium ferrite ($Ca_2Fe_2O_5$), dicalcium silicate (Ca_2SiO_4), SiO_2-rich glass, free lime, periclase (MgO) and olivine $(Mg, Fe)_2SiO_4$ [3, 4].

To obtain desired sinter mineralogy and meet blast furnace requirement on sinter quality, sinter plant usually need to adjust raw material blend composition and process parameters. For instance, increasing MgO concentrations in the sinter increases the amounts of the spinel (magnesium aluminum oxides) and glassy phases. The amount of sinter breakdown under low temperature and partially reduced conditions is commonly measured by the Low Temperature Degradation

(LTD) test and the sinter LTD is strongly dependent on the level of MgO. The presence of MgO in the sinter can improve its LTD, because MgO stabilizes magnetite and this decreases the hematite content, causing a lower stress in the sinter during the hematite to magnetite reduction in the blast furnace ironmaking process. Increasing sinter basicity (CaO/SiO_2) decreases the amount of total SFCA, and increases the acicular/columnar SFCA ratio and glassy phase content [6]. MgO and SiO_2 contents of iron sinter seem to have an interrelated effect on its physical and chemical properties. Therefore, there is a need to optimize sinter basicity and MgO content for each individual sinter plant operation. In this paper MgO effects on microstructure and properties of low basicity and high basicity sinter were investigated and a multiple regression analysis was performed based on pot-grate test results to predict sinter properties based on sinter chemistry and process variables.

Experimental

Materials

Raw materials used in this study consisted of iron ore blend (concentrates or pellet fines), sinter blend (in-plant recycled materials), fluxes (limestone and dolomite), and solid fuel (flue dust) as well as return fines as shown in Table I. The MgO content of the sinter was varied through the addition of dolomite. The sinter basicities (mass per cent CaO/mass per cent SiO_2) of the sinters ranged between 2.1 and 3.5, with a FeO content that ranged between 8.0 and 11.0 mass per cent.

Table I. Chemical analyses of raw materials used for sintering tests

Raw Materials	Total Fe	FeO	SiO_2	CaO	Al_2O_3	MgO	C	LOI
Sinter Blend	44.51	23.1	6.61	17.32	3.00	4.50	4.26	/
Iron Ore Blend	60.03	1.50	4.94	6.03	0.41	1.72	/	/
Return Fines	52.84	6.86	4.67	14	1.62	3.27	/	0
Limestone Flux	0.53	/	2.09	55.11	0.58	1.81	/	42.66
Dolomite Flux	0.13	/	1.25	39.23	0.37	13.34	/	45.36
Solid Fuel (Flue Dust)	9.92	/	4.3	2.66	2.65	0.76	68.31	72.8

Methods

The sinter experiments were performed in a laboratory sinter pot-grate test station at ArcelorMittal Global R&D (East Chicago, IN). The sintering tests were intended to simulate industrial sintering process with capability of high vacuum (up to 4,800 mm W.G., or 47 kiloPascal) and high temperature ignition (up to 1,350 ^oC).

The sintering tests include proportioning, mixing, ignition, sintering, cooling and conditioning. The raw materials were weighed into the required proportions and mixed in a cement mixer. Then the raw mix was loaded into the sinter pot, which is 400 mm in diameter and 500 mm in height. The finished sinter cake was conditioned and screened to simulate the actual condition in a typical industrial sinter plant. The sinter above ¼ inch (6.35 mm) was considered as finished sinter product and that of minus ¼ inch was used as return fines for next test.

Determination of Chemical and Metallurgical Properties

The chemistry of sinter samples was determined by X-ray fluorescence spectrometry (XRF). The FeO content was determined separately by a wet chemical procedure in which a portion of finely

ground sinter was dissolved in hydrochloric acid in non-oxidizing conditions and the resulting iron (II) in solution was determined by redox titration with potassium dichromate. ASTM E279-97, ISO 4696-1 and ISO 11258 testing methods were followed for the Tumble Index (TI), Low Temperature Degradation (LTD) and Reducibility (RI) tests, respectively.

Mineralogical Examination
For each specific sinter sample, at least five sinter pieces in the granulometric fraction of 10 to 15 mm were examined. A reflected light metallurgical microscope was used for the mineralogical examination. A JEOL-JXA 50 scanning electron microscope (SEM) with energy dispersive spectrometer was used to obtain additional information on various phases.

X-ray Diffraction (XRD) Analysis
The samples for XRD analyses were prepared by grinding the sinter samples down to 100% passing 100 mesh. The powdered samples were then spread over a flat sample holder. The diffraction patterns were obtained employing an X'pert Pro Diffractometer by PANalytical using Ni filtered Cu Kα radiation at 35kV and 50 mA. The samples were scanned at room temperature from 20 to 130 degrees at a step size of 0.10°, with a recording time of 4 seconds for each step.

Results and Discussion

Table II shows the average operating parameters used and/or determined during the sinter pot test program along with average chemical analysis and their measured or calculated quality and productivity indices. The test results with increasing basicity (Blend 3 to 6) demonstrate that as the sinter basicity increases the strength of the sinter also increases. These results are consistent with the reported theory that calcium ferrite compounds are the primary contributor to sinter strength and reported earlier results [6]. The needlelike shape of the ferrite precipitates allows for good binding of the different phases as shown in Figure 2b. It is expected that as the concentration of CaO increases, the quantity of glassy silicates slag formed will decrease. Also likely would be a decrease in fayalites due to increased calcium ferrite formation and a reduction in both the required sintering temperature and the fuel consumption. The test results confirmed the decrease in the maximum sintering temperature with increasing basicity.

The overall reducibility of the sinter is affected primarily by three factors in fluxed sinter with CaO/SiO_2 greater than 1.5: the highly reducible calcium ferrites, the less reducible magnesioferrites and poorly reducible fayalite compounds. Increases in the sinter basicity at constant MgO level should allow calcium ferrites to displace the weaker and less reducible magnesioferrite phases, resulting in a stronger more reducible sinter. The reduction in the amount of fayalite present due to the increase in CaO, and the decrease in both fuel rate and sintering temperature, should also lead to higher reducibility.

If the positive effect which increasing CaO/SiO_2 has on strength is indeed partially attributed to a reduction in the amount of magnesio-wustite phase present, then a relationship should exist between the strength and the MgO content of the sinter. This is indeed the case as demonstrated in Table II and Figure 1. This observation is consistent with literature report that there is a clear trends between the AI (abrasion index) which increases with increasing MgO content. As indicated in Abrasion Index comparison, the effect of MgO on the fraction of minus 30 mesh (-

0.6 mm) material generated is significant. Obviously the percentage of minus 30 mesh sinter generated can be decreased through a reduction in the MgO content. Increasing the ratio of Limestone and Dolomite in the sinter flux blend has the potential to increase the sinter strength and reduce the very fine fraction generated. Overall finer fraction of sinter (minus ¼'' or 6.35 mm) increases when MgO in sinter increases as shown in Figure 1. Based on the different levels of MgO sinter test results, it is recommended to keep sinter MgO at 2.7% would give relative higher sinter LTD and Tumbler index while still not resulting too much fines.

Table II. Laboratory pot-grate sintering test results with increasing MgO (Blend 1 to 4) and increasing basicity (Blend 3 to 6)

Materials (% wt wet)		**Baseline**	**Blend 1**	**Blend 2**	**Blend 3**	**Blend 4**	**Blend 5**	**Blend 6**
Mix Moisture, %		6.33	6.04	5.87	6.33	5.85	6.94	6.58
Average Sintering Temp., ºC		1142.95	1204.70	1169.18	1165.03	1193.58	1189.38	1181.00
Max. Windbox Flue Gas Temp.,ºC		330.90	322.54	320.60	312.00	381.60	283.90	251.20
Total Carbon, kg/Mg Usable Sinter		41.11	44.19	48.01	49.50	57.83	40.66	49.86
Sinter Chemistry	Fe	54.58	53.65	54.29	54.40	52.74	53.83	51.48
	CaO/SiO_2	2.31	2.52	2.20	2.10	2.40	3.20	3.50
	FeO	10.82	8.86	10.00	10.77	10.00	7.91	8.60
	CaO	12.12	12.98	11.58	11.22	12.58	14.18	16.77
	MgO	2.24	2.70	3.21	3.51	4.46	2.39	2.64
	Al_2O_3	1.05	1.23	1.29	1.04	1.28	1.03	1.50
Quality& Productivity	Tumble (%+6.35 mm)	78.47	78.40	72.75	75.70	77.91	79.57	80.51
	Abrasion Index(%-0.6mm)	4.22	4.40	4.91	4.42	4.82	4.02	4.12
	LTD (%+6.35 mm)	75.39	79.89	78.46	84.75	84.57	78.44	80.52
	Reducibility (R40)	1.31	1.23	1.14	0.95	0.87	1.09	1.11
	Productivity (ton/m^2-day)	65.54	60.62	59.23	55.16	53.91	65.70	66.04

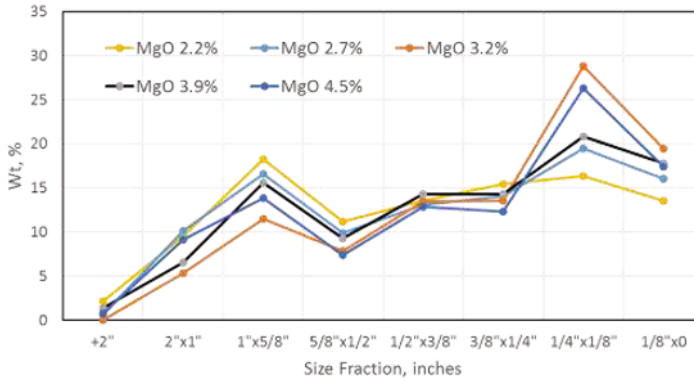

Figure 1. Sinter product size distribution.

Not only does the level of MgO in the sinter adversely affect the cold strength, it also decreases the reducibility of the sinter. Table II shows the detrimental effect that increasing the MgO content has on the reducibility of the sinter. It is clear that the effect of MgO holds over a wide range of sinter mixes and chemistries. It is important to notice that the negative effect which MgO has on reducibility and Tumble index when determining a method to increase the sinter strength through increasing sinter basicity (CaO/SiO_2). If an increase in the basicity of the sinter is made by increasing the sinter flux consumption at a constant limestone to dolomite ratio, then the beneficial effect of increased strength will be partially offset by a decrease in the reducibility resulting from the additional MgO.

There is one potential drawback to the high-strength and high-reducibility sinter obtained through increased basicity. The reduction at low temperatures of the highly oxidized calcium ferrites results in a volume change during the phase change to the lower oxidation state of iron. This volume change can cause micro-fracturing within the sinter, which could increase the surface area available for reduction. This process results in a highly reducible sinter with high cold strength, but one which could degrade rapidly in the upper regions of the blast furnace. Increasing the MgO content increases the amount of magnesioferrite (MF) phase as shown in Figure 2d. While the MF are weaker binders than calcium ferrites at very low temperatures and non-reducing conditions, their resistance to reduction gives superior strength under reducing conditions and temperatures of approximately 500°C. This is demonstrated in Table II which shows the inverse proportional relationship between sinter LTD and MgO content. Further correlation analysis of the test data show that the sinter MgO, FeO and basicity (CaO/SiO_2) have statistical significant effects on the LTD among all the considered factors as shown in Table III. The correlation coefficients of MgO, FeO and basicity with sinter LTD are 0.55, 0.38 and 0.24, respectively.

Table III. Pearson correlation coefficients between sinter chemistry and sinter LTD

	SiO_2	*CAO*	*CaO/SiO_2*	*MgO*	*Fe*	*FeO*	*Slag*	*LTD*
SiO_2	1.00							
CaO	0.52	1.00						
CaO/SiO_2	-0.75	0.17	1.00					
MgO	-0.69	-0.39	0.54	1.00				
Fe	0.24	-0.16	-0.44	-0.61	1.00			
FeO	0.17	0.09	-0.16	-0.23	0.26	1.00		
Slag	0.05	0.54	0.40	0.49	-0.79	-0.12	1.00	
LTD	-0.36	-0.26	**0.24**	**0.55**	-0.20	**0.38**	0.26	1.00

Increasing MgO content of sinter by using more dolomite can result in higher solid fuel consumption as indicated by total carbon consumption per kg of usable sinter in Table II. It should be noted that the temperature of dissociation of $MgCO_3$ is less than that of $CaCO_3$, 500 vs. 900°C respectively. In addition the thermal energy requirement for the calcination of Dolomite is lower than that of Limestone, 24.2 vs. 42.7 kcal/kg-mole, respectively. One would expect that the sintering with the higher percentage of dolomite would require less solid fuel than sintering with higher percentage of limestone. However, this was not the case. There are several contributing factors which explains this phenomenon. First, the laboratory sinter pot tests maintain a constant return fines level, independent of materials used or the resulted sinter chemistry, this practice has the effect of standardizing the base fuel consumption and allowing a reasonable means of comparing the expected fuel rate trends in actual sinter plant operations. Secondly, the constraints under which the test burdens were developed lead to an increase in the total flux percentage in the sinter mix as the dolomite fraction was increased. Both the higher silica content of dolomite and the specific combination of basicity chosen contributed to the increased flux consumption. The result was a change in the gangue content between each of the different mixes. Gangue content appears to have an effect on both sinter strength and fuel consumption.

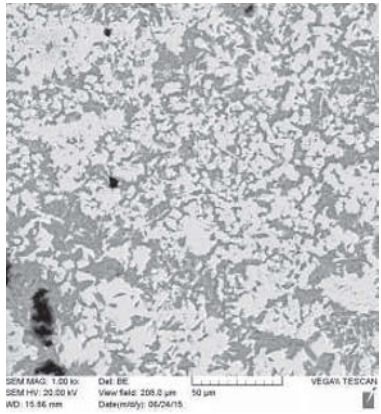

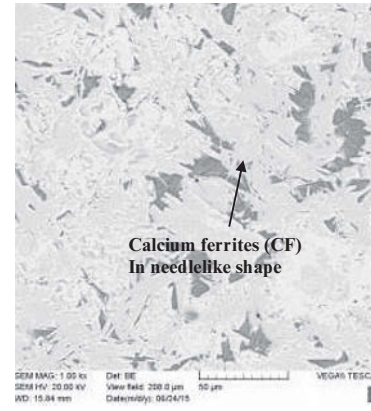

a). Sinter Basicity (CaO/SiO_2: 2.6)

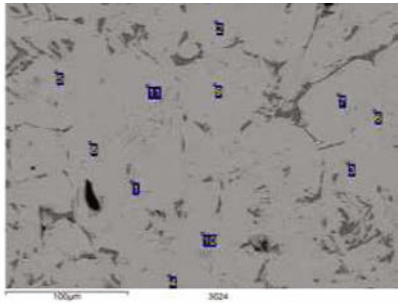

b). Sinter Basicity (CaO/SiO_2: 3.5)

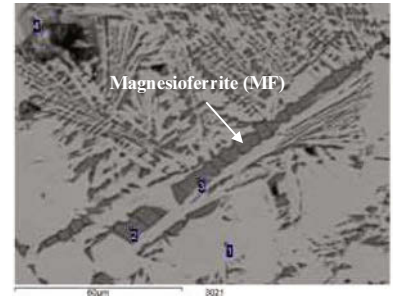

c). Sinter MgO 2.2 wt %

d). Sinter MgO 3.5 wt%

Figure 2. SEM micrographs of sinter samples

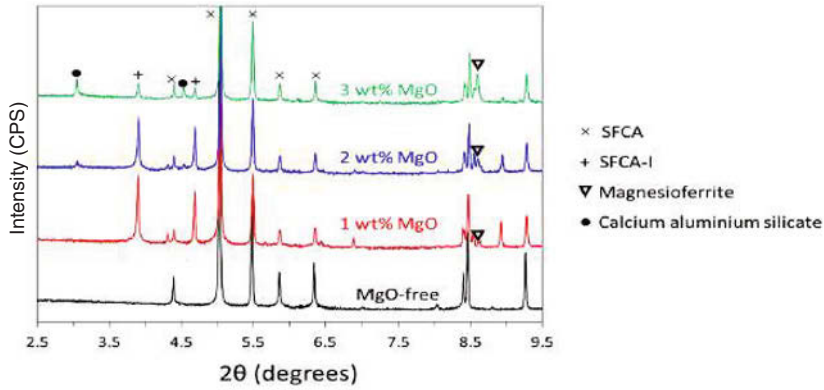

Figure 3. X-ray diffraction patterns of sinter samples with varying MgO contents

XRD analysis of the sinter samples revealed (Figure 3) that major mineral phases present in the sinter samples were calcium aluminum silicates (CAS), calcium ferrites (CF), magnesioferrite (MF), silico-ferrite of calcium and alumina (SFCA). Minor phases were wustite, silicates, calcium silicates and iron silicates. It is clear that magnesioferrite phases increase when MgO content increases in sinter. Also SFCA phases were identified in all sinter samples with different MgO, their peaks were obviously stronger in higher MgO sinter sample comparing to lower MgO sinter sample. CF and SFCA are desirable phases for sinter because they are beneficial to form bonding matrix in sinter and also easily reducible. They are typically formed by a solid-liquid reaction between hematite and Fe_2O_3 CaO melt, with the subsequent assimilation of SiO_2 and Al_2O_3 in the melt during sintering. It has been reported that SFCA could only be present in iron ore sinter if the temperature remained below 1,300°C, or the residence time at higher temperature was extremely short. If the temperature exceeded 1,300°C, then SFCA would transform to Fe_2O_3 (at high pO2) or Fe_3O_4 (at low pO2) in a calcium silicate-rich melt [4]. Also

acicular ferrite (<10 micron) formed at low temperature (<1,300ºC) is more reducible, whereas columnar ferrite (>10 micron) formed at high temperature (>1,300ºC, possibly coated with glass) is less reducible [5].

Conclusions

To achieve desired sinter properties for blast furnace operation, effects of sinter MgO and basicity on sinter microstructure and metallurgical properties were investigated by laboratory pot-grate sintering tests. The following conclusions were obtained:

1). MgO has positive effects on sinter LTD, however the sinter RI decreased with increasing MgO content of the sinter. The TI was uncertain while the AI increased with increasing MgO content. The cold strength of sinter can be increased by increasing the sinter basicity at a constant level of MgO.

2). The positive effect which MgO has on LTD continues up to a level of 3.5%; above this it no longer is beneficial to increase MgO considering its negative impacts on fine generations and reducibility.

3). XRD analysis of sinter samples with low MgO and high MgO content showed that magnesioferrite phase increases and more of the SFCA and SFCA-I phases were produced when MgO content in sinter increases.

Acknowledgements

The authors would like to thank ArcelorMittal Global R&D management for permission to submit this paper for publication and the support of local sinter plant for supplying raw materials for the laboratory test work.

References

[1]. Julius H. Strassburger, *Blast Furnace – Theory and Practice*, (Gordon and Breach Science Publishers, 1969), 211-215.

[2]. D. F. Ball, J. Dartnell, J. Davison, A. Grieve, and R. Wild, *Agglomeration of Iron Ores*, (Heinemann Educational Books Limited, London, 1973), 136-139.

[3]. N. S. Webster, M. I. Pownceby, I. C. Madsen, and J. A. Kimpton, Silico-ferrite of Calcium and Aluminum (SFCA) Iron Ore Sinter Bonding Phases: New Insights into Their Formation during Heating and Cooling, Metallurgical and Materials Transactions B, Vol. 43B, 2012, pp. 1344-1357.

[4]. Y.-C. Wang, J.-L. Zhang, F. Zhang, and G.-P. Luo, Formation Characteristics of Calcium Ferrite in Low Silicon Sinter, Journal of Iron and Steel Research, International, 2011, 18(10): 01-07.

[5]. S. C. Panigrahy, P. Verstraeten, J. Dilewijns, Influence of MgO addition on mineralogy of iron ore sinter, Metallurgical Transactions B, January 1984, Volume 15, Issue 1, pp 23-32.

[6]. M. Zhang, M. Coe, M. Andrade "Effect of Sinter Basicity on Sinter Productivity and Quality with High Rate of Recycled Materials," Drying, Roasting, and Calcining of Minerals, Eds: T. P. Battle, J. P. Downey, L. D. May, B. Davis, N. R. Neelameggham, S. Sanchez-Segado, and P. C. Pistorius, TMS (The Mineral, Metals and Materials Society), 2015.

Characterization of Minerals, Metals, and Materials 2016
Edited by: Shadia Jamil Ikhmayies, Bowen Li, John S. Carpenter, Jiann-Yang Hwang, Sergio Neves Monteiro, Jian Li, Donato Firrao, Mingming Zhang, Zhiwei Peng, Juan P. Escobedo-Diaz, and Chenguang Bai
TMS (The Minerals, Metals & Materials Society), 2016

MATERIAL CHARACTERIZATION OF POWER PLANT STEEL IN THE VIRGIN AND ARTIFICIALLY-AGED CONDITIONS

Magdy M. El Rayes, Ehab A. El-Danaf

Mechanical Engineering Department, College of Engineering, King Saud University, P.O.Box 800, 11421, Riyadh, Saudi Arabia.

Keywords: Martensitic-Ferritic steel, High Temperature Tensile Test, Microstructure, Mechanical Properties

Abstract

In the present study the microstructural and mechanical properties including high-temperature tensile test of martensitic-ferritic steel 9-12% Cr were assessed. This steel, which is usually used in gas turbine power plants serving as shroud, was tested in the as-received (virgin) and artificially-aged condition for 1344hrs (8 weeks) at 700 °C and the results were compared and analyzed. The high-temperature service of this steel suggested investigating the high temperature tensile behavior and the deformation mechanism occurring at different testing temperature and strain rates which were 540, 580 and 620 °C and 10^{-3}, 10^{-4} and 10^{-5} s^{-1}, respectively. The results showed that the microstructural features such as phases and carbides are factors which influence the high temperature mechanical properties. The stress- strain rate curves showed a large stress exponent of ≈ 15, indicating that the materials behavior lie in the power law breakdown regime. Based on stress vs. the reciprocal of temperature, the apparent activation energy was calculated as 443 kJ/ Mole. Plotting Zener Holloman parameter versus true stress made it possible to mathematically model all test results into a unified model.

Introduction

Components operating in the power generating plants normally suffer from deterioration of their properties due to their long operation at high temperature. This implies to know the potential mechanisms of material deterioration and their accumulation during high temperature service. De Cooman et al. [1] studied the hot deformation properties of austenitic binary Fe-Mn alloys with different Mn content. It was found that the activation energy for hot working increased with increasing Mn content and the dynamic recrystallization was observed for all the Fe-Mn alloys. They concluded that the activation energy of the Fe-Mn alloys was lower than that of the austenitic stainless steels. This is referred to the presence of other alloying elements in stainless steels, which increase the activation energy more than Mn. Li and Liu [2] investigated the high temperature tensile behavior of 6.5 wt % Si steel in the range from 300°C to 800°C. They reported that as the deforming temperature increases, the stress level continually decreases, whereas the elongation gradually increases. The elongation of 2 % at 300°C increases to 16.4 % at 350 °C. Chen et al. [3] conducted high temperature deformation experiment on HSLA steel using thermal/physical simulator. They concluded that the dynamic recrystallization softening and deformation hardening are two factors that influence the trend of the stress–strain curve. At the beginning of the deformation, strain hardening plays a role, making stress rise constantly, then the dynamic recrystallization softening reduces the stress. Nagasaka et al. [4] investigated

tensile properties of F82H steel after aging at 400-650°C for 100,000 h. and discussed the mechanisms of change in tensile properties due to long-term aging. They reported that the degradation of YS and UTS was 50 MPa or less at 550 °C and below at both room and high temperature tests. Above 550 °C, YS and UTS decreased with increasing aging temperature. Since the shroud under investigation is mainly intended to serve for long periods in high temperature atmospheres, therefore, the aim of this work is to characterize and compare the microstructural and mechanical properties of the as-received and artificially-aged conditions at room temperature, as well as to investigate the response of the aged material to high temperature deformation.

Materials and Methods

The material used in this work is 9-12 % Cr- martensitic- ferritic steel with the following chemical composition in wt.%: C: 0.328; Cr: 11.55; Ni: 0.196; Mn: 0.256; Si: 0.505; V: 0.0831; Ti: 0.012. This steel took two forms; one is in the as-received condition (virgin) whereas the second was in the artificially-aged condition which was heated for 1344 hrs. at 700 °C. The virgin (as-received) and the aged shrouds were wire EDM'd in the form of rods with 100 mm length and 11 mm diameter for extracting microstructural, hardness and tensile test samples. The microstructure was examined by using SEM, and EBSD. For SEM the samples were prepared according to standard metallographic sample preparation and etched with Vilella. The microstructure for both materials was, also, studied by EBSD using Oxford HKL system incorporated on FESEM- 7600 JEOL. These samples were polished with colloidal silica as a final step prior to imaging. 5 Vickers macro-hardness tests were performed each time using 1 kg and averaged. In order to evaluate the mechanical behavior of heat treated steels, tensile specimens were extracted from the center of the bar along its axis and were cut according to ASTM E-08. Tensile tests were conducted at room temperature as well as at different testing temperature of 540, 580 and 620 °C and strain rates of 10^{-3}, 10^{-4} and 10^{-5} s^{-1} using a computer equipped Instron 3385 H model machine; load-elongation data as well as furnace temperature were recorded.

Results and Discussion

Microstructural characterization

The microstructure of both conditions was found to be tempered martensite originated from large prior austenite grains (shown by white solid arrows) containing martensite laths (dark) having different orientations at which block boundaries exist (white dotted arrows) as shown in Fig. 1. The prior austenite grain size was almost constant of around 50 m for both material conditions due to the presence of thermally stable carbides at the austenite grain boundaries which inhibited the growth of austenite grains as reported by Thomas Paul et al. [5]. Fig. 2 shows a closer look at the carbide distribution and morphology of both conditions. In general, these carbides precipitated within the martensite laths, at lath boundaries and along prior austenite grain boundaries (PAGBs) forming a continuous network, which is identical to that found in [6, 7].

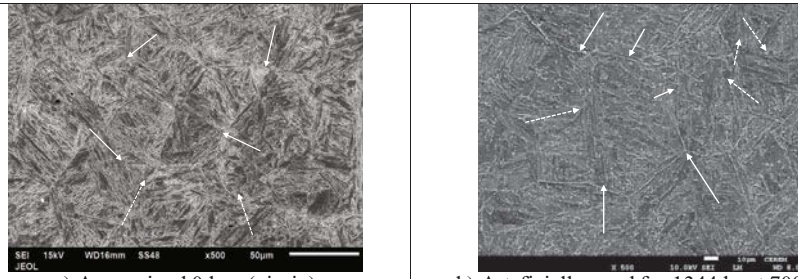

a) As-received 0 hrs. (virgin) b) Arteficially-aged for 1344 hr at 700 °C

Fig. 1 Martesitic-ferrtic microstructure showing the PAGBs for different conditions

In addition, Fig. 2 also shows that carbides/ precipitates (white) were heavily dispersed and eventually coagulated forming clusters within the entire microstructure.

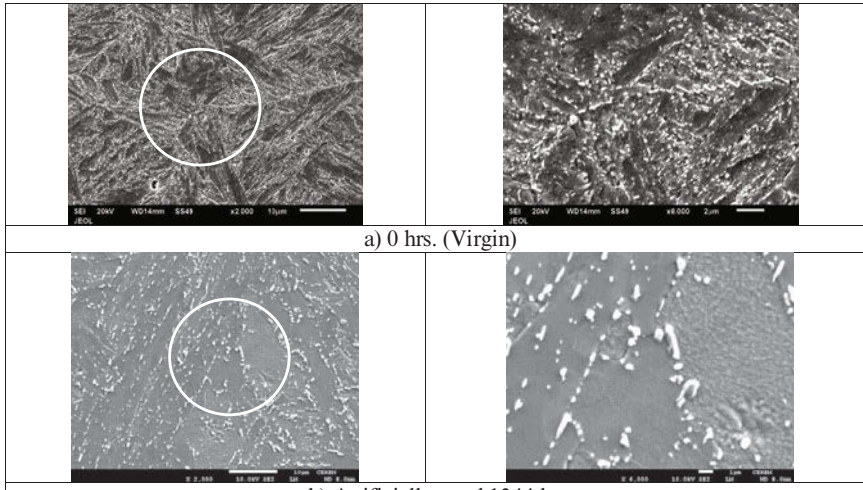

a) 0 hrs. (Virgin)

b) Artificially-aged 1344 hrs.

Fig. 2 Carbides and precipitates morphology at different magnifications. Left column: locations taken at x 2000 with white circle magnified at x 6000 shown in the right column.

Increased magnification was applied in order to visualize carbide morphologies and measure their size as well as to assist in differentiating between martensite laths and ferrite islands as shown in Fig. 3. Golanski and Slania [7] and Krauss [8] found the same phases of martensite and ferrite in the same type of steel used in the present work. In the virgin condition; Fig. 3 a), most carbides were spread within the whole microstructure and had either rod or spherical shape, having separate rods between 500 ~ 300 nm long and diameters of around 300 ~ 200 nm, respectively. This result was in line with that obtained in work [7]. With the artificially-aged

condition; Fig. 3 b), the carbides along the PAGB had rod-like shape of around 2.0 ~ 1.1 m long and started to coarsen and disintegrate.

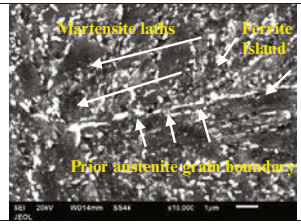

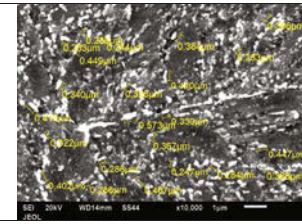

a) 0 hrs. (virgin)

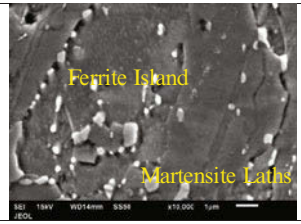

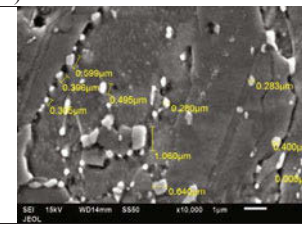

b) 1344 hrs. (Artificially-aged)

Fig. 3 Carbide morphologies and their dimensions; **Left column:** the microstructure at which carbide measurements were taken; **right column:** duplicate with carbide dimensions.

Ferrite islands were affected by aging as in Fig. 4, in which they evolved and coarsened on the expense of martensite laths. This result was also reported in [8, 9, 10, 11 and 12]. The reason is that the boundaries of the martensite crystals are associated with interfacial energy which provides a driving force for the coarsening of the ferrite that evolve from martensitic crystals [8].

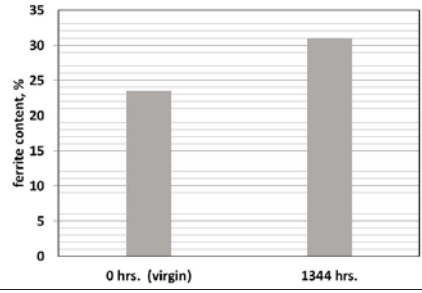

Fig. 4 Ferrite content with both material conditions.

Energy dispersive X-ray diffraction (EDS) The main carbide type found at the PAGBs and within the ferrite and martensite with both was $M_{23}C_6$ type as in Fig. 5. This carbide type is Cr-rich but may also contain W, Mo, V, Fe and B as agreed upon in publications [7, 12 and 13].

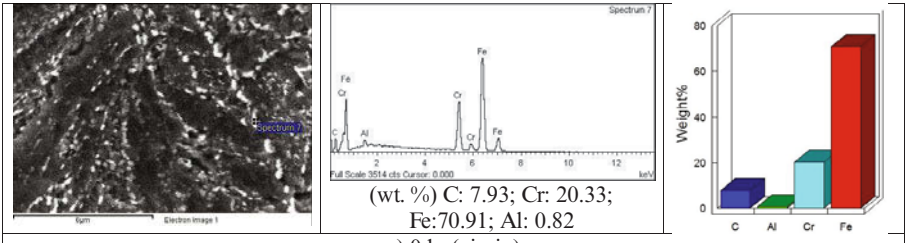

(wt. %) C: 7.93; Cr: 20.33; Fe:70.91; Al: 0.82

a) 0 hr (virgin)

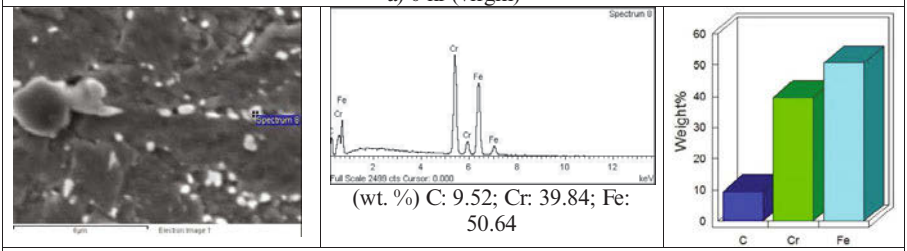

(wt. %) C: 9.52; Cr: 39.84; Fe: 50.64

b) Artificially aged- 1344 hrs

Fig. 5 EDS analysis of Cr- rich carbides ($Cr_{23}C_6$) at PAGBs for different treatments.

Electron backscattered diffraction (EBSD)

EBSD investigation indicated that the LAGBs (sub-grain boundaries) were reduced from the virgin to the artificially-aged condition, as shown in Fig. 6 a), due to their recovery under the effect of prolonged elevated temperature exposure. This result is confirmed in earlier publications [8, 12] where they reported same findings. In addition, the average misorientation angle increased; Fig. 6 b), because of the high temperature exposure leading to static recrystallization.

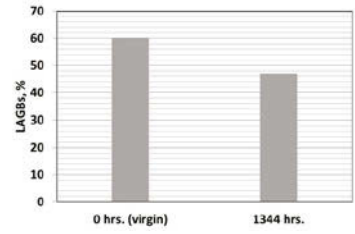

a)

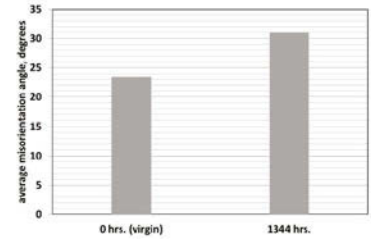

b)

Fig. 6 Comparison between virgin and artificially-aged materials with respect to: a) Low angle grain boundaries and b) Average misorientation angle.

Room temperature mechanical properties

The hardness and mechanical properties results were in line with microstructural ones where aging caused softening the material and also reduces the ultimate and yield strengths as shown in Fig. 7 a) and b) respectively. The high hardness and strength corresponding to the virgin condition is referred to the presence of martensite with high dislocation density as well as carbides and precipitates which are dispersed heavily within the martensite laths and along their boundaries. These carbides can pin the movement of dislocations and retard the migration of lath boundaries thus providing precipitation strengthening during deformation (tensile testing) [14].

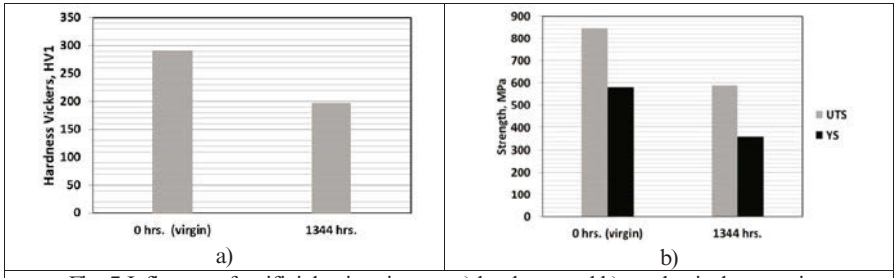

Fig. 7 Influence of artificial aging time on a) hardness and b) mechanical properties.

High Temperature Tensile Tests

Fig. 8 shows an example of true-stress vs. true-strain plots of 1344 hrs.-artificially aged samples tested at 620 ºC.

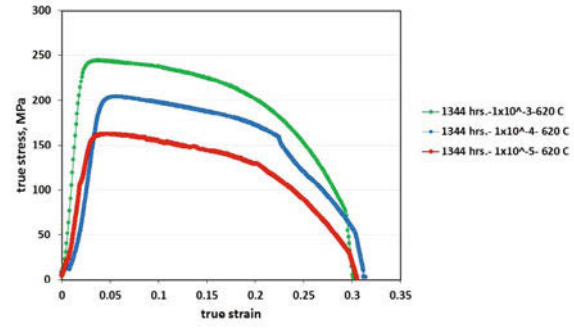

Fig. 8 True-stress vs. true strain plots for 3 strain rates at 620 ◦C.

Fig. 9 a) presents the stress dependence on strain rate at different temperatures. The plot was made to a semi logarithmic plot according to the exponential equation that is suitable for modeling the behavior for high stresses and low temperature which is stated as follows:

$$\dot{\varepsilon} = A' \exp \beta\sigma \quad (1)$$

$$\ln \dot{\varepsilon} = \ln A' + \beta\sigma \quad (2)$$

the β value inferred from the figure is 0.05. The reason behind using the exponential equation is that by plotting the data as strain rate versus stress on double logarithmic plot revealed a large stress exponent of ~15, which points that the data lies in the power law breakdown regime (PLB). Fig. 9 b) presents a double linear plot of stress versus the reciprocal of temperature for the three constant strain rates used in this study.

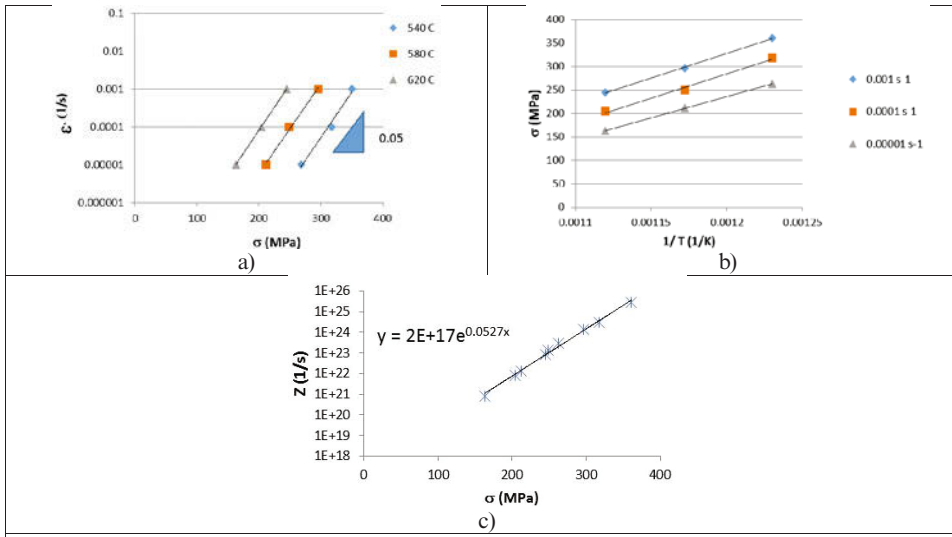

Fig. 9 Characteristics of high temperature behavior at 3 temperatures and 3 strain rates.

The slope of these fitted lines indicates the apparent activation energy as follows:

$$\sigma = - \ln A'' + (Q/\beta R)(1/T) \quad (3)$$

The activation energy calçulated was about 443 kJ/Mole. Fig. 9 c) presents the Zener Holloman parameter defined as $Z = \dot{\varepsilon} \exp(Q/RT)$ versus the true stress on a semi-logarithmic plot, to mathematically model all data points into a unified model. The model is stated as follows:

$$Z = \dot{\varepsilon} \exp(Q/RT) = A \exp \beta\sigma = 2E+17 \exp(0.052\ \sigma) \quad (4)$$

Acknowledgement

This project was funded by the National Plan for Science, Technology and Innovation (MARRIFAH), King Abdulaziz City for Science and Technology, Kingdom of Saudi Arabia, Award Project Number (08-ADV-209-02)

References

1. N. Caban˜ as, N. Akdut, J. Penning, and B.C. De COOMAN, *High-Temperature Deformation Properties of Austenitic Fe-Mn Alloys*, METALL MATER TRANS A, Volume 37 A, November 2006, 3305.
2. Hao-Ze Li, Zhen-YuLiu, *Tensile properties of strip casting 6.5 wt% Si steel at elevated temperatures*, MAT SCI ENG A-STRUCT, 639, (2015), 412-416.
3. Xizhang Chen, Yuming Huang, Yucheng Lei, *Microstructure and properties of 700 MPa grade HSLA steel during high temperature deformation*, J ALLOY COMPD 631, (2015), 225-231.
4. Takuya Nagasaka, Hideo Sakasegawa, Hiroyasu Tanigawa, Masami Ando,Teruya Tanaka, Takeo Muroga, Akio Sagara, *Tensile properties of F82H steel after aging at 400–650◦C for100,000 h,* FUSION ENG DES, (2015), Article in Press.
5. V. Thomas Paul, S. Saroja, M. Vijayalakshmi, *Microstructural stability of modified 9Cr–1Mo steel during long term exposures at elevated temperatures*, J NUCL MATER 378 (2008) 273–281.
6. Ján Michel, Marián Buršák, Marek Vojtko, *Microstructure and mechanical properties degradation of CrMo creep resistant steel operating under creep conditions,* MATER ENG - Materiálové inžinierstvo *18* (2011) 57-62.
7. G. Golanski, J. Slania, *Effect of different heat treatments on microstructure and mechanical properties of Martensitic GX12CrMoVNbN9-1 CAST STEEL*, ARCH METALL MATER., Volume 58 2013 Issue 1, DOI: 10.2478/v10172-012-0145-x.
8. Krauss G. 1990 Steels: *Heat Treatment and Processing Principles*, ASM INT, Materials Park, OH.
9. Cheng-Hsun Hsu, Hwei-Yuan Teng and Sheng-Chien Chiu, *Ultrasonic Evaluation of Temper-Embrittlement for Martensitic Stainless Steel*, MATER. TRANS., Vol. 44, No. 11 (2003) pp. 2363 to 2368.
10. Hilmar Kjartansson Danielsen, *Z-phase in 9-12%Cr Steels*, Ph.D. thesis, Department of Manufacturing Eng. and Management, Tech. University of Denmark, DK-2800 Kgs. Lyngby, Denmark, February 2007.
11. Cheng-Hsun Hsu, Hwei-Yuan Teng, and Yeong-Jern Chen, *Relationship Between Ultrasonic Characteristics and Mechanical Properties of Tempered Martensitic Stainless Steel*, JMEPEG (2004) 13:593-599, ASM INT, DOI: 10.1361/15477020420828.
12. G. Golañski, *Effect of the heat treatment on the structure and properties of GX12CrMoVNbN9-1 cast steel*, ARCH MATER SCI ENG, Volume 46, Issue 2, December 2010, Pages 88-97.
13. David Rojas Jara, Ph. D. Dissertation Thesis, *9-12 % Cr heat resistant steels: alloy design, TEM characterization of microstructure evolution and creep response at 650 °C*, Fakultaet fuer Maschinenbau der Ruhr Universitaet Bochum- Bochum 2011.
14. Kouichi MARUYAMA, Kota SAWADA and Jun-ichi KOIKE, *Strengthening Mechanisms of Creep Resistant Tempered Martensitic Steel*, ISIJ INT, Vol. 41 (2001), No. 6, pp. 641–653.

Characterization of Minerals, Metals, and Materials 2016
Edited by: Shadia Jamil Ikhmayies, Bowen Li, John S. Carpenter, Jiann-Yang Hwang, Sergio Neves Monteiro, Jian Li, Donato Firrao, Mingming Zhang, Zhiwei Peng, Juan P. Escobedo-Diaz, and Chenguang Bai
TMS (The Minerals, Metals & Materials Society), 2016

SITE-SPECIFIC STUDIES ON THE INTERFACIAL STRUCTURES OF GALVANIZED DUAL PHASE STEELS

Imran Aslam[1,2], Bin Li[4], Rich Martens[3], Johnny Goodwin[3], Hongjoo Rhee[1,2], Mark Horstemeyer[1,2], Frank Goodwin[5].

[1]Center for Advanced Vehicular Systems, Mississippi State University, Starkville, MS 39759
[2]Department of Mechanical Engineering, Mississippi State University, Mississippi State, MS, 39762, USA
[3]Central Analytical Facility, the University of Alabama, Tuscaloosa, AL 35487
[4]Department of Chemical and Materials Engineering, University of Nevada, Reno, NV 89557, USA
[5]International Lead Zinc Research Organization (ILZRO), Durham, NC 27713, USA

Keywords: Galvanized, Inhibition Layer, Selective Oxidation, TEM, FIB, Dual Phase Steel.

Abstract

Focused ion beam and transmission electron microscopy were employed as site-specific techniques to study the interfacial structures of galvanized steel. Four samples, processed under varying fuel-to-air ratio in the annealing chamber prior to hot-dipping, were analyzed. The specimen with the highest fuel-to-air ratio had a discontinuous external oxide layer only, which comprised of manganese and silicon oxides. As the fuel-to-air ratio decreased, the amount of internal oxides increased. For the specimen with the lowest fuel-to-air ratio, the internal oxides were observed approximately 500 nm in the steel subsurface. Due to the increasing amount of oxygen potential as the fuel-to-air ratio is decreased, the amount and depth of internal oxides increased since oxygen could diffuse deeper into the steel subsurface. The external oxides in two samples were found entrapped between the inhibition layer and the Zn coating, which indicates the inhibition layer is undercutting the oxides by dissolution of iron.

Introduction

Steel grades are becoming increasingly complex, especially with the development of third generation advanced high strength steels (AHSSs), in order to reduce vehicular weight and achieve the US Environmental Protection Agency fuel economy and emissions goals for 2025. The complexity of these steel grades is owed to the addition of alloying elements such as Mn, Si, Cr, V, etc, and heat treatments that cause an increase in strength and ductility [1,2]. The steel grades are then coated with metallic Zn in order to provide galvanic corrosion protection [3,4]. The steel strip is initially passed through an annealing furnace which comprises of N_2 and H_2 in order to reduce any Fe oxides at the steel strip surface. However, the addition of alloying elements introduce a whole set of complications. The primary obstacle that needs to be overcome is that the alloying elements diffuse to the surface of the steel during annealing of the steel strip, prior to hot-dipping in the Zn bath, and preferentially oxidize. These oxides negatively influence the wettability of the Zn to the substrate by hindering the reaction between Fe and the dissolved Al in the Zn bath. Al is added in very small percentages in the Zn bath such that Fe and Al preferentially react first to form a thin layer of Fe_2Al_5 [5], which is on the order of approximately 100 nm. This layer is

also called the inhibition layer as it inhibits the premature interaction between Fe and Zn and the formation of unfavorable Fe-Zn phases at the interface [3]. Once the Zn adheres to the substrate, its thickness is regulated using air knives. At this point in time, if the steel requires no further processing in order to preserve the luster of the coating, then it is called a galvanized steel.
Different techniques have been utilized in the past two decades to capture the nanoscale features at the interface, such as Scanning electron microscope (SEM), energy dispersive spectrometry (EDS), X-ray photoelectron spectrometry (XPS) [6] and Glow discharge optical emission microscope (GDEOS) [7]. However, the resolution provided by these techniques is limited. In order to resolve the nanoscale features at the interface, site specific techniques such as Focused Ion Beam (FIB) and Transmission Electron Microscope (TEM) are used. Literature shows promising results obtained using these techniques [8,9,10,11,12,13,14]. The oxides produced can be of different types, and each type has a certain morphology associated with it, e.g. granular or film-like, binary, ternary or higher order. The oxides are dependent upon the processing conditions and the composition of the steel substrate. Recent studies have shown that the type and morphology of the oxides on the strip surface change as the dew point decreases. Specifically, the morphology of the oxides changes from relatively loose granules to dense and smooth films with a decrease in the dew point [15]. The oxides that form at the surface of the steel are external oxides, but internal oxidation can also occur in the subsurface of the steel. In this research, the influence of annealing atmosphere composition on the type and morphology of the oxides will be evaluated by characterizing the interface using advanced techniques.

Experimental Methods

The AHSSs utilized in the current research were provided by AK Steel. Four steel sheets were studied which had a nomenclature from 1 till 4. These steel sheets were subjected to varying amounts of fuel-to-air ratios in the annealing chamber prior to zinc dip. Steel sheet 1 was processed at the highest fuel-to-air ratio and steel sheet 4 was processed at the lowest fuel-to-air ratio. The chemical composition of the hot-rolled steels are provided in Table I.

Table I. Chemical composition of the Dual Phase (DP) steels

Sample	Al	B	C	Ca	Cr	Cu	Mn	Mo
1, 2, 3 &4	0.049	0.0004	0.076	<0.0003	0.035	0.037	1.72	0.16

Sample	N	Nb	Ni	P	S	Si	Sn	Ti	V
1, 2, 3 &4	0.0031	<0.003	0.015	0.011	0.0055	0.17	<0.003	0.011	0.037

Small samples were cut from the bulk specimen and mechanically polished on one side to reveal a smooth zinc coating on the steel surface while ensuring minimal damage to the interface between Fe and Al. The samples were further fabricated using a TESCAN Lyra focused ion beam (FIB-FESEM), equipped with a gallium ion source, to extract 1 µm thin samples that were welded on a copper grid. A final thinning of the sample was performed to produce electron transparent samples that were less than a 100 nm thick. The samples were extracted such that the interfacial region between the Fe and Zn was captured for evaluation using advanced imaging techniques.

To image the samples at high magnification and resolution, a FEI Tecnai F-20 Transmission Electron Microscope (TEM) equipped with a field emission gun was utilized and operated at an acceleration voltage of 200 keV. The microscope was equipped with a CCD camera for Scanning transmission electron microscopy (STEM), high angle annular dark field (HAADF) detector, and EDS.

Results and Discussion

The interfacial layers present between the steel substrate and zinc coating were resolved by viewing the steel grades using HAADF in STEM mode which allows for atomic number contrast. Figure 1 illustrates the interfacial layer of sample 1, processed at the highest fuel-to-air ratio. The thickness of the inhibition layer, as pointed out by arrows in Figure 1, was measured using greyscale variation in ImageJ at a multitude of points, and the average thickness was evaluated to be approximately 52.2 nm with a standard deviation of 28.8 nm. The inhibition layer appears continuous but highly irregular, as evident by a high standard deviation. The Zn coating adjacent to the inhibition layer seems to be very brittle and flaky.

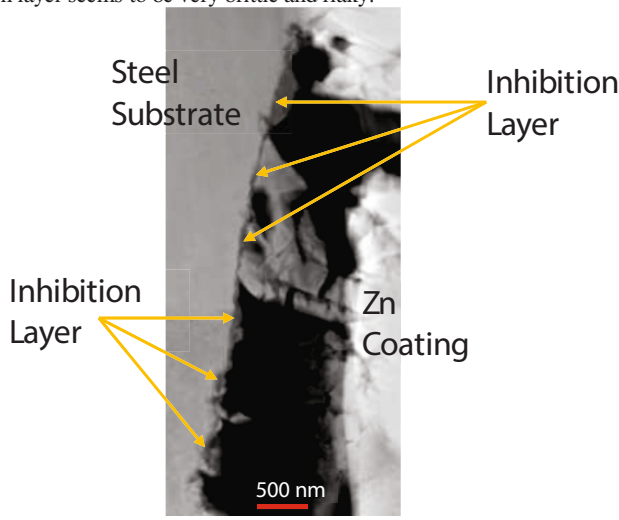

Figure 1. Interface for sample 1 captured at low resolution.

In order to determine the composition of interfacial layers across the interface, EDS line scans were conducted at various locations. Figure 2a demonstrates the line scan result across an interface and the results indicate the presence of an inhibition layer, as indicated by a spike in Al content that occurs across the interface, a simultaneous drop in Fe content, and an increase in the quantity of Zn. However, the intensity for Mn and Si were not observed at this location. The yellow box in Figure 2a represents a region of reference to adjust for drifting of the electron beam during the line scan. Figure 2b demonstrates another line scan across the interface at a different location and the results show a spike in content of Mn and Si that occurred at the region where the transition from steel substrate to inhibition layer occurs. This indicates the presence of external (surface) oxides

of Mn and Si. Figure 2c depicts another line scan across another region and the results show that a spike in Mn dominant oxide occurs between the inhibition layer and Zn coating.

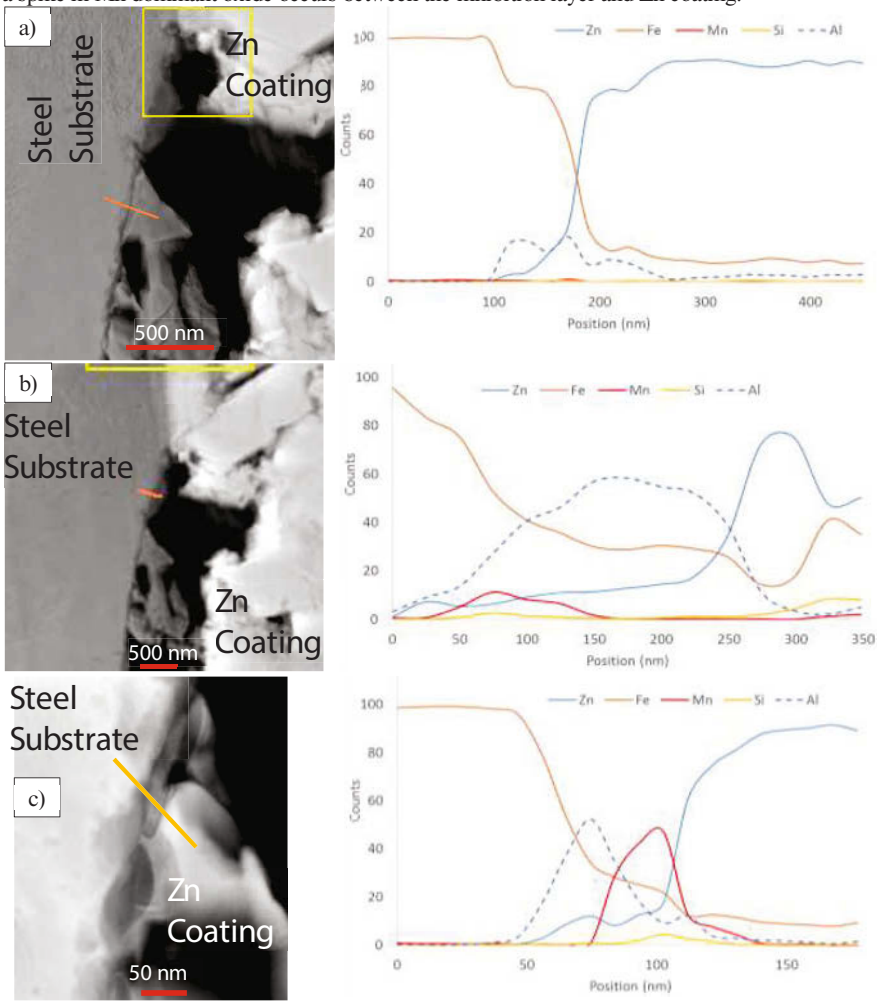

Figure 2. EDS line scans performed across the interfaces. a) No external oxides found, b) external oxide between Fe and Fe_2Al_5 layer, c) external oxides between Fe_2Al_5 and Zn coating.

Sample 2 was analyzed in a manner similar to Sample 1. A low resolution image of the inhibition layer is shown in Figure 3. The inhibition layer has an average thickness of 106 nm and appears discontinuous. However, the discontinuity is quite possibly caused due to the ion milling process.

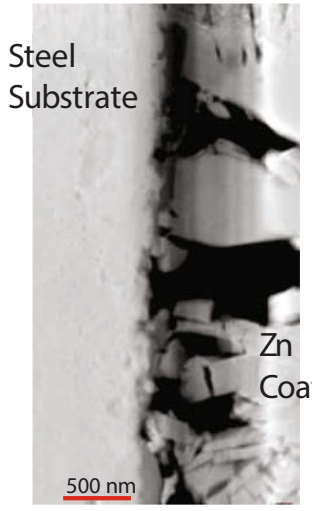

Figure 3. Interface for sample 2 captured at low resolution.

Figure 4 shows an EDS line scan conducted across the inhibition layer. The results indicate the presence of a Mn oxide at the surface of the steel substrate. The oxide layer is followed by the inhibition layer and finally the Zn coating. The EDS line scans were conducted at a multitude of locations, and the same trend was observed across all interfaces.

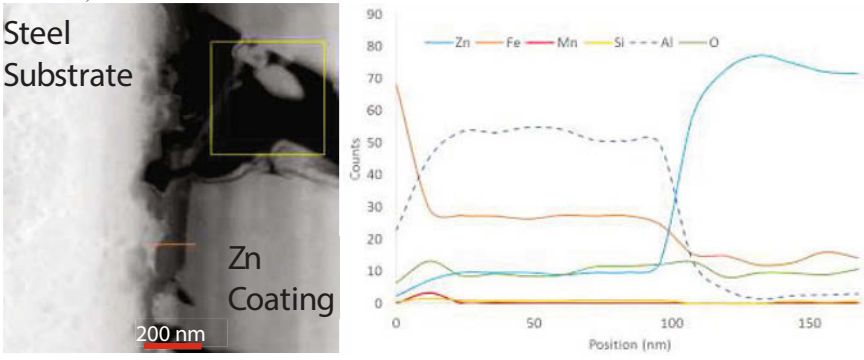

Figure 4. EDS line scans performed across the interfaces. External oxides found to occur between substrate and Fe_2Al_5 layer

At the subsurface of the steel substrate, a few dark spots were evident. An EDS point scan was conducted on these locations in order to determine the chemical composition of the region. The results of the point scan are depicted in Figure 5, which indicates the presence of Mn and Si oxides. Surprisingly, the second point scan picked up phosphorus as well. The oxides present at the subsurface of the steel substrate are categorized as internal oxides.

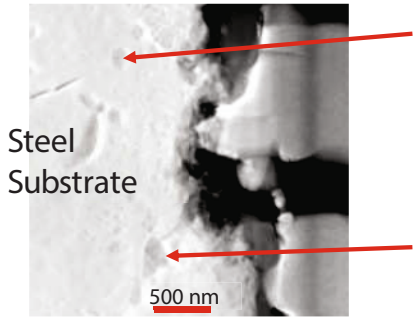

Element	Weight %	Atomic %
O	1.56	5.20
Al	0.05	0.11
Si	0.6	1.15
Mn	6.55	6.36
Fe	91.20	87.12
Zn	0	0
P	0.02	0.03

Element	Weight %	Atomic %
O	6.13	18.16
Al	0.31	0.54
Si	1.07	1.81
Mn	7.77	6.70
Fe	77.19	65.52
Zn	5.29	3.83
P	2.22	3.40

Figure 5. EDS point scans performed over dark regions in the steel substrate. Results show the spots comprise of Mn and Si oxides.

The inhibition layer in sample 3 is depicted in Figure 6. The average thickness of the layer is approximately 59 nm and appears to be continuous in nature. Figure 7a illustrates a line scan across the interface and exhibits the presence of an inhibition layer, as evident by an increase in intensity of Al. However, the Al intensity soon starts fading away as a spike in Mn and O occurs, indicating the existence of external oxides. As soon as the intensity in Mn diminishes, a subsequence increase in Al occurs once more which points towards the presence of the inhibition layer. Therefore, one can conclude that the oxide particle is embedded inside the inhibition layer. Figure 7b depicts another line scan and a point scan at two different locations. Both the results show the existence of external oxides comprising of Mn and Si oxides that are present between the inhibition layer and the Zn coating. In Figure 8, the internal oxides can be visualized to be distributed approximately 200 nm under the subsurface of the steel sheet.

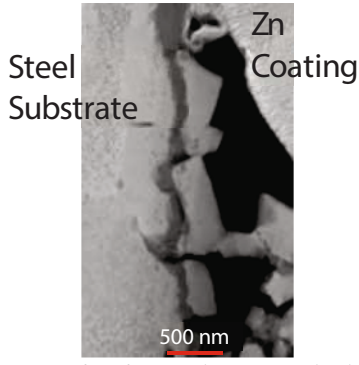

Figure 6. Interface for sample 3 captured at low resolution.

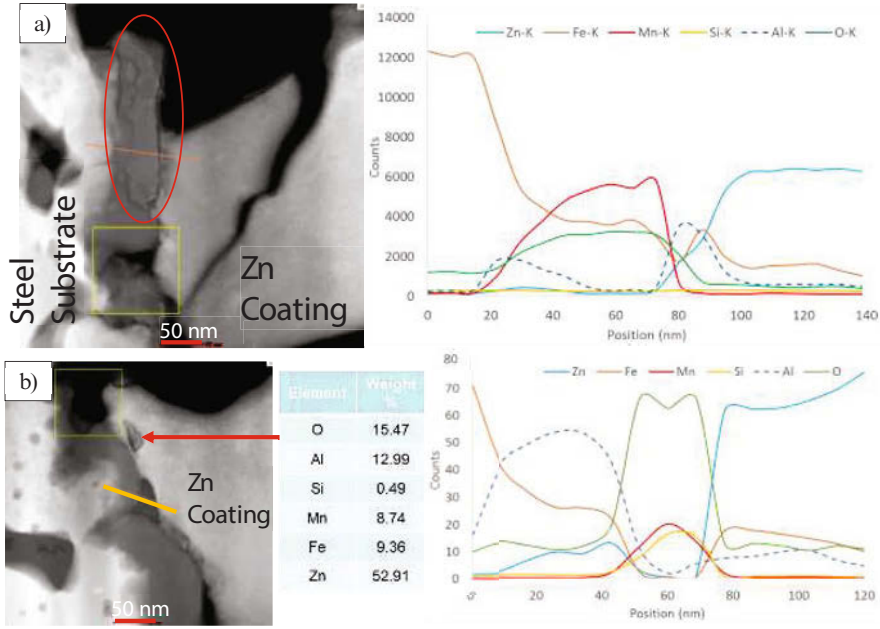

Figure 7. a) EDS line scan performed across the interface; oxide of Mn found entrapped in the inhibition layer. b) A line scan and a point scan indicate the presence of Mn and Si oxides between Fe_2Al_5 layer and Zn coating.

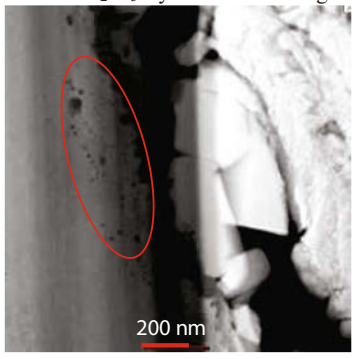

Figure 8. Internal oxides distributed approximately 200 nm in the subsurface of the steel substrate.

Sample 4 was annealed with the annealing chamber having the lowest fuel-to-air ratio amongst the four steel grades. The inhibition layer depicted in Figure 9a shows the inhibition layer to be continuous and has an average thickness of approximately 61 nm. Figure 9b illustrates a well-

defined layer of internal oxides which are present at a depth of approximately 500 nm in the subsurface of the substrate. These oxides are not distributed in the substrate and are almost arranged in a straight line. Figure 10 depicts an EDS line scan and a point scan at two different locations across the internal oxides, and both the instances identify these oxides to be comprising of Mn and Si. An EDS line scan was also conducted across the interface to identify interfacial structures, as seen in Figure 11. The results of the line scan show an increase in intensity of Mn with a simultaneous decrease in intensity of Fe. The spike in Mn is followed by an increase in intensity of Al, indicating the presence of the $Fe_2Al_{5-x}Zn_x$, inhibition layer.

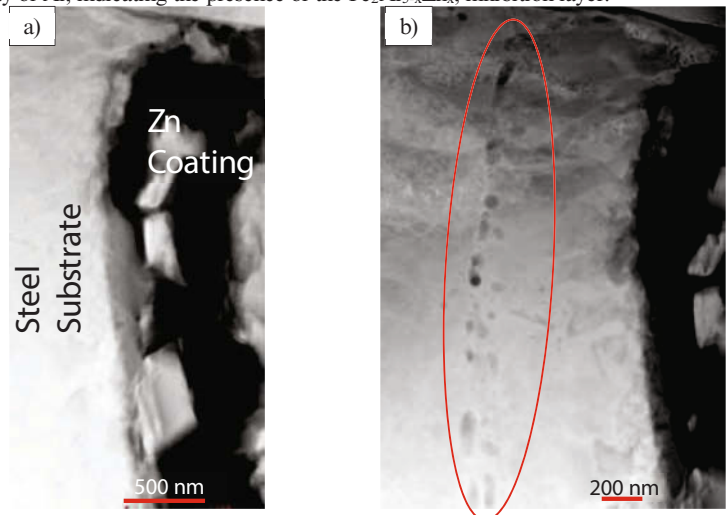

Figure 9. a) Interface for sample 4 captured at low resolution. b) The internal oxides are captured approximately 500 nm in the subsurface of the steel substrate.

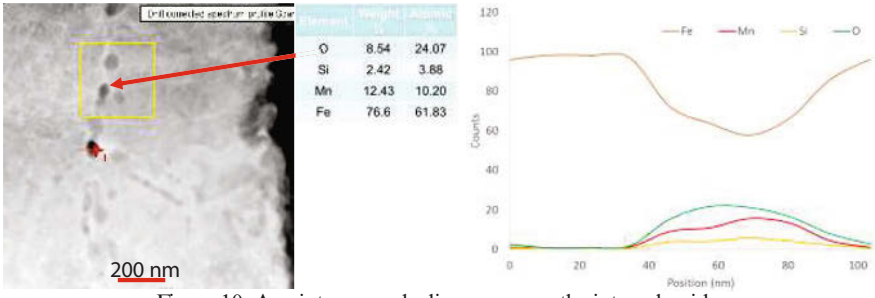

Figure 10. A point scan and a line scan over the internal oxides. Results show the oxides comprise of Mn and Si.

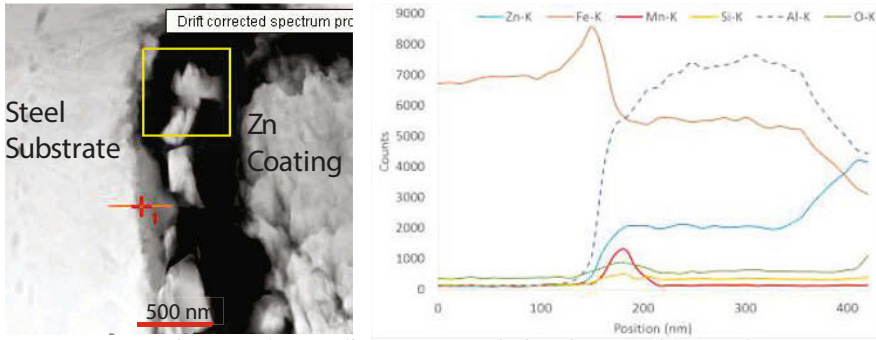

Figure 11. An EDS line scan across the interface reveals external Mn oxides present at the surface of the substrate.

A change in the types of oxides observed in each specimen can be clearly related to the amount of fuel-to-air ratio used in the annealing chamber. Sample 1 uses the highest fuel-to-air ratio, and as a result, the oxygen potential in the annealing atmosphere is the lowest which enables only the alloying elements at the surface of the substrate to be oxidized. As a result, we only observe an external, discontinuous Mn oxide layer with slight traces of Si. The low amount of Si observed here can be owed to the high Mn to Si ratio in the steel substrate. In sample 2, the fuel-to-air ratio is slightly lower than the one used in sample 1 and thus, the oxygen potential is slightly higher. As a consequence, the oxygen in the annealing chamber can penetrate deeper into the steel substrate and react with the alloying elements at the subsurface of the steel. However, oxidation is still dominant at the surface of the steel to produce external oxides. The trend was evident as internal oxides were scarcely found in the subsurface of the substrate. In sample 3, at an even lower fuel-to-air ratio used in the annealing chamber, the oxygen potential is high enough to allow increased penetration of oxygen into the subsurface of the steel. As a result, abundance of internal oxides increased, as depicted in Figure 8. At the lowest fuel-to-air ratio, used in sample 4, the oxygen potential was high enough such that the oxygen molecules penetrated up to 500 nm into the subsurface of the steel. This enabled for internal oxides to appear in a layer-like fashion.

Furthermore, the external oxides in sample 1 and 3 were found to be entrapped in between the inhibition layer and the zinc coating. These oxides are on the surface of the steel prior to zinc hot-dip and for the oxides to be separated from the surface would be possible if the inhibition layer is undercutting the oxides due to Fe dissolution [16]. Mn dominant oxides, which were found in sample 1 and 3, are known for being granular/porous in nature [13,17]. Therefore, the Al from the zinc bath can penetrate through the oxides and interact with the Fe in the substrate to form the inhibition layer in between the substrate and the oxide.

Conclusion

Four steel sheet samples were processed under varying fuel-to-air ratios in the annealing chamber prior to zinc dip. FIB was used to fabricate samples comprising of the interface between the steel substrate and Zn coating. Sample 1, processed at the highest fuel-to-air ratio, comprised of external oxides only due to the low oxygen potential in the annealing chamber. As the oxygen potential increased, the oxygen could penetrate further into the subsurface of the substrate. As a consequence, sample 4, processed at the lowest fuel-to-air ratio, comprised of internal oxides at

approximately 500 nm in the subsurface of the steel sheet. The external oxides in sample 1 and 3 were found to be entrapped between the inhibition layer and the Zn coating. A possible explanation for this phenomenon is the undercutting of oxides due to Fe dissolution and the formation of inhibition layer as a consequence. Furthermore, due to the granular nature of these oxides, which were Mn dominant, allow for Al to pass through them and interact with Fe.

References

1 B. Mintz, *Int. Mater. Rev*. 46 (2001) 169–197.
2 R. Bode, M. Meurer, T.W. Schaumann, W. Warnecke, *Proceedings of the Galvatech'04 Conference*, Association for Iron and Steel Technology, Chicago, USA, 2004, pp. 107–118.
3 A. Marder, "The metallurgy of zinc-coated steel," *Progress in Materials Science*, vol. 45, pp. 191-271, 2000.
4 J. Mackowiak and N. Short, "Metallurgy of galvanized coatings," *International Metals Reviews,* vol. 24, pp. 1-19, 1979.
5 S. Alibeigi, R. Kavitha, R.J. Meguerian, J.R. McDermid, *Acta Materialia*, 59 (2011) 3537-3549.
6 K.K.Wang, C.W. Hsu, L. Chang, D. Gan, K.C. Yang, *Applied Surface Science*, 285P (2013) 458-468.
7 M. Blumenau, M. Norden, F. Friedel, K. Peters, *Surface and Coatings Technology*, 205 (2011) 3319-3327.
8 Y. Adachi, K. Kamei, *Acta metallurgica Et Materialia*, 43 (1995) 3189-3197.
9 K. Kuroda, M. Takahashi, T. Kato, H. Saka, S. Tsuji, *Thin Solid Films*, 319 (1998) 92-96.
10 T. Kato, M.H. Hong, K. Nunome, K. Sasaki, K. Kuroda, H. Saka, *Thin Solid Films*, 319 (1998) 132-139.
11 L.A. Giannuzzi, J.L. Drown, S.R. Brown, R.B. Irwin, F.A. Stevie, *Microscopy Research and Technique*, 41 (1998) 285-290.
12 T. Kato, K. Nunome, K. Kaneko, H. Saka, *Acta Materialia*, 48 (2000) 2257-2262.
13 M.S. Kim, J.H. Kwak, J.S. Kim, Y.H. Liu, N. Gao, N.-Y. Tang, *Metallurgical and Materials Transactions*, A 40A (2009) 1903-1910.
14 R. Kavitha, J.R. McDermid, *Surface and Coatings Technology*, 212 (2012) 152-158.
15 M. Kim, J. Kwak, J. Kim, Y. Liu, N. Gao, and N. Y. Tang, "Galvanizability of Advanced High-Strength Steels 1180TRIP and 1180CP," *Metallurgical and Materials Transactions A*, vol. 40, pp. 1903-1910, 2009.
16 Z. Jiang, J. McGuffin-Cawley, J. McDermid, F. Goodwin, *Galvanizers Association Proceedings*, 2013.
17 R.Sagl, A.Jarosik, D.Stifter, G.Angeli, *Corros. Sci.*, 70 (2013) 268.

Characterization of Minerals, Metals, and Materials 2016
Edited by: Shadia Jamil Ikhmayies, Bowen Li, John S. Carpenter, Jiann-Yang Hwang, Sergio Neves Monteiro, Jian Li, Donato Firrao, Mingming Zhang, Zhiwei Peng, Juan P. Escobedo-Diaz, and Chenguang Bai
TMS (The Minerals, Metals & Materials Society), 2016

METALLURGY AND CREEP BEHAVIOR OF TYPE 310S STAINLESS STEEL AT HIGH TEMPERATURE IN DIFFERENT ATMOSPHERES AND LOADING CONDITIONS

Coralie Parrens[1]; Benoit Malard[1]; Jean-Luc Dupain[2]; Dominique Poquillon[1]

[1]CIRIMAT, Université de Toulouse, INP-ENSIACET, 4 allée Emile Monso - BP44362, 31030 Toulouse, France
[2]Messier-Bugatti-Dowty, Site de Bidos, 9 Rue Guynemer, 64400 Bidos, France

Keywords: 310S Stainless Steel, Microstructure, Creep, Ageing, Hydrogen, High Temperature

Abstract

Some large loading fixtures and furnaces intern parts are used for the heat treatment of aeronautical components. These reusable fixtures endure a succession of thermal cycles including quenching. Due to the loading and to the temperature, these devices are submitted to creep under complex atmosphere with low oxygen partial pressure content. Unusual damages and high creep strain rates have been reported on components made of 310S Stainless Steel. Therefore, the mechanical behavior at high temperature of this alloy was investigated. Many data are available in the literature about isothermal creep but few take into account the effects of atmosphere, thermo-mechanical cycles and microstructure evolution due to ageing. In addition to metallurgical characterization, **in situ** creep tests and conventional mechanical tests were performed to study the influence of the following parameters: temperature, stress level, thermo-mechanical cycles and atmosphere.

Introduction

Large aeronautical components up to 2 meters long and 500 kg are heat treated in order to obtain their optimal mechanical properties. This step requires the creation of specific loading fixture able to hang those components up and to avoid their deformations during heat treatment cycles. The intern parts of heat treatment furnaces are also specialized devices. The ageing and the mechanical properties of those components made of 310S stainless steel was studied. The influence of the specific atmosphere and loading conditions was also considered.

Heat treatment cycles are operated during 2 hours at 1143K. The high temperature and the cyclic aspect of thermal and mechanical solicitations affect the ageing and the mechanical properties of 310S stainless steel. A controlled atmosphere is required to avoid oxidation and carburation of production parts in the furnaces. This atmosphere contains hydrogen which may affect the mechanical behavior of many stainless steels [1-3].

Data are available about isothermal creep of 310S stainless steel. However, for this application we have to take into account the coupled effects of atmosphere, thermal and mechanical cycles, and microstructure evolution due to ageing. In addition to a microstructural characterization, mechanical tests have been performed. The influence of the different parameters was investigated through a comparison between **in situ** and conventional results.

Microstructure

Austenitic stainless steels are the most important class of corrosion resistant metallic materials. Their properties rely on a high chromium content allowing the formation of a protective oxide film layer, and a high nickel content chosen to have a stable austenitic structure. The composition of the studied 310S stainless steel is given below in Table I.

Table I : Composition in weight % of the studied 310S Stainless Steel

C	*Cr*	*Ni*	*Mn*	*Si*	*P*	*S*	*N*	*Co*
0.050	24.8	19.5	1.5	0.5	0.02	0.001	0.024	0.169

The observed microstructure is mainly austenitic. The presence of intergranular carbides and the undesirable σ phase was also observed. Ageing promotes phase transformation from austenite to sigma phase, which has a detrimental effect on the corrosion and the mechanical properties. The Schaeffler diagram (Figure 1) is used to predict the phases present in steels as a function of their composition. The identification of the different phases was done using Transmission Electron Microscopy coupled with local EDS analysis.

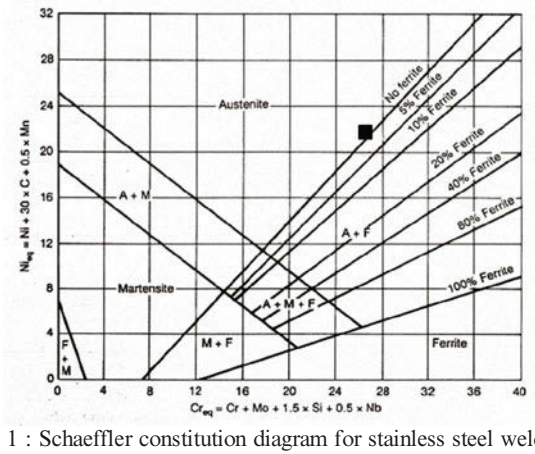

Figure 1 : Schaeffler constitution diagram for stainless steel weld metal, 310S composition is marked by the black square.

Carbides

Carbon solubility in austenite decreases rapidly as the temperature decreases. Nickel content also decreases the carbon solubility [4]. Depending on addition elements, MC, M_6C and M_7C_3 carbides could precipitate in austenitic stainless. In the studied 310S, we observed M_7C_3 primary carbides formed from the melt (Figure 2-A). Those carbides show high chromium contents as shown in Table II. These primary carbides are observed at austenitic grain boundaries

Table II: Composition of observed phases

at%	M_7C_3	$M_{23}C_6$	σ phase
Fe	10-15	22	50
Cr	80-82	72	41
Ni	3	4	6

Samples aged during 257 cycles **in service** showed an important amount of $M_{23}C_6$ carbides. These carbides precipitated both at grain boundaries (Figure 2-B) and inside grains (Figure 2-C). The measured chemical composition is shown in Table II.

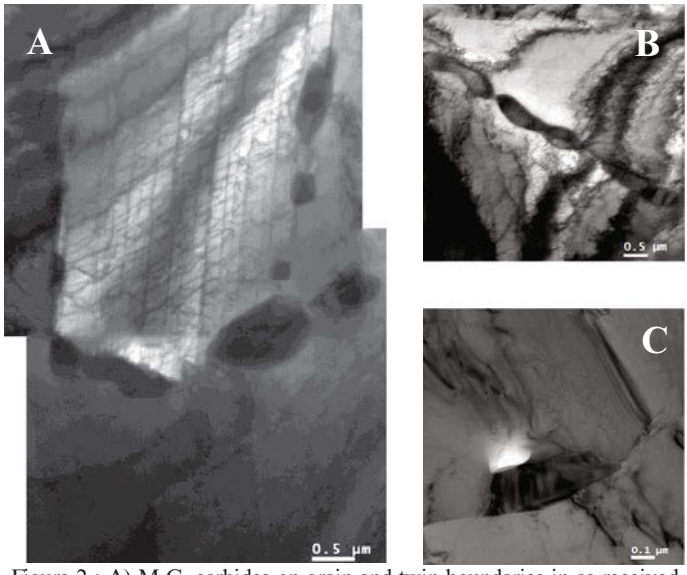

Figure 2 : A) M_7C_3 carbides on grain and twin boundaries in as-received material, B) $M_{23}C_6$ intergranular carbides in aged sample, C) $M_{23}C_6$ intragranular carbide in aged sample.

Sigma phase (σ)

The σ phase is one of the most frequently observed intermetallic compounds. Its precipitation is promoted by alloying elements such as chromium and manganese. The σ phase formation induces a local depletion in alloying elements inducing a ductility loss and a decrease in corrosion resistance. This intermetallic phase belong to Topologically Close Packed phases (TCP phases). TCP phases are characterized by close-packed layers of atoms that are separated from one another by large interatomic distances.

For the materiel of this study, the formation of σ phase occurs between 500 and 900°C. The composition of σ phase has been measured (using EDX). The results are presented in Table II. Sigma phase precipitation is mainly located on grain boundaries, especially on triple points. Some precipitates also grow on twin boundaries and near carbides. A second mode of precipitation was observed: long bands of σ phase are formed from initial bands of ferrite. The kinetics of this precipitation is about 100 times faster than for the σ phase growing from austenite [5]. These two types of precipitation are illustrated on Figure 3.

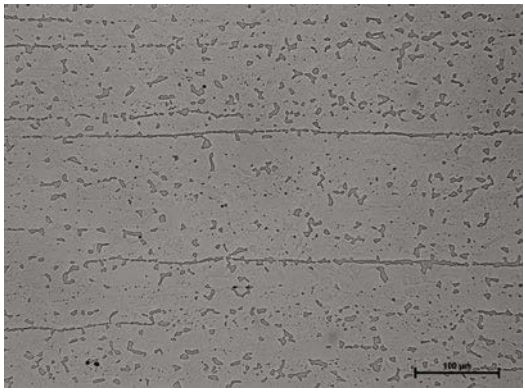

Figure 3 : Optical microscopy showing the two types of precipitation of σ phase in 310S stainless steel.

Sigma phase precipitates in austenite with a very slow kinetics. Isothermal heat treatments under air have been conducted to quantify this kinetics. The σ phase rate was measured by X-Ray Diffraction using the Rietveld method. The precipitation kinetics is plotted on Figure 4. The Johnson-Mehl-Avrami model [6] gave a good fit with experimental data. Furthermore, on this graph, the σ phase content of two samples taken from fixtures of the production line after 159 and 257 cycles is added to Figure 4 for comparison.

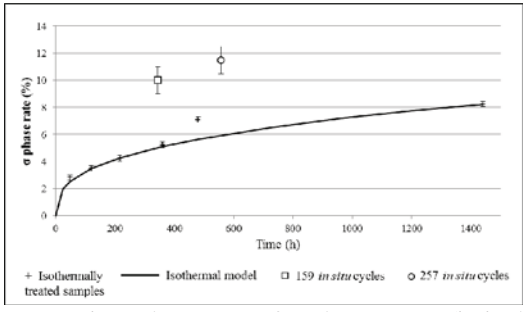

Figure 4 : Experimental measures of σ phase content (in isothermally treated and **in situ** treated samples) and precipitation kinetics model.

In-service stress and the succession of thermal cycles enhance chromium diffusion rate in the matrix. Furthermore, the growth of σ phase precipitate is a diffusion controlled mechanism [7]. So that **in situ** thermo-mechanical cycles could accelerate σ phase growth kinetics. Moreover, the effect of hydrogen on dislocations and cavities in the austenitic matrix may also affect the kinetics of formation of σ phase.

Samples extracted from real component after 257 in-service cycles have been submitted to EDX analysis. These specimens have 11.5% of brittle σ phase. We observed large chromium depletion in the austenite. The value decreases from 25 wt% to 21 wt% due to sigma phase formation. The austenite composition may affect the mechanical behavior. Thus, the ageing effect has to be considered as a key parameter for the characterization of mechanical properties.

Mechanical behavior

In addition to a general embrittlement due to ageing, accelerated strain rates are observed on **in service** devices. Embrittlement and creep properties are studied as a function of the different parameters previously identified: thermal and mechanical cycles, high temperature, hydrogen, ageing.

Thermal cycling within the production conditions induces residual stresses due to rapid cooling during oil quenching. These cycles impact the mechanical behavior when compared to isothermal solicitations. Moreover, hydrogen is known to accelerate creep strain rates [8]. Thus, the effect of atmosphere on the mechanical behavior has also to be quantified.

Embrittlement

First of all, the σ phase precipitation increases the hardness and decreases the toughness as well as the fracture strain. Vickers and Knoop hardness tests were used to measure the embrittlement due to ageing.

Firstly, we show that the as-received material hardness was 160HV whereas the value increased to 210HV after ageing 257 **in service** cycles. The precipitation due to ageing promotes the material hardening.

To evaluate the matrix evolution and σ phase hardness, Knoop indentations with low charges of 25 g were performed. Data available in the literature give 940HV for the σ phase hardness [9]. We measured 890HV for the σ phase stripes. This value is lower than literature's because the precipitates are too small to uncorrelate σ phase and matrix hardness: the matrix around precipitates shows plastic deformations during the tests. We also measured austenite hardness. Ageing generate hardening of the austenite that reaches 200HV.

Thus, σ phase formation generates embrittlement being a TCP brittle phase and modifying the austenite hardness. Figure 5 represents two Knoop indentations revealing the huge difference in hardness between both austenite and σ phase.

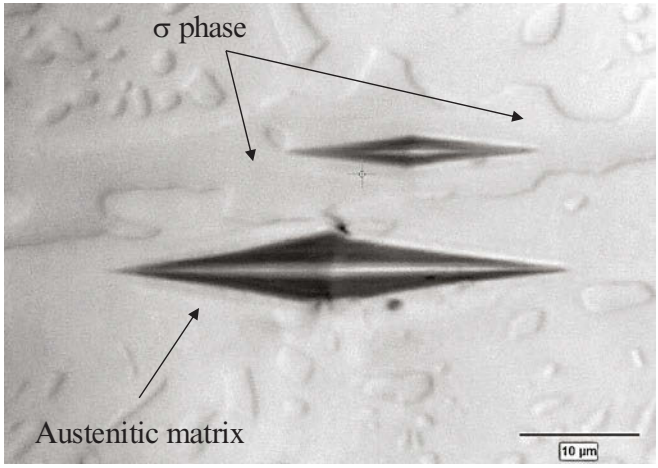

Figure 5 : Knoop indentations in a σ phase stripe and in the austenite matrix (25 g load)

In situ creep test

Unusual strain rates are observed during in-service conditions. An elastic model of the beams used for hanging production components allows us to identify the maximal stress level in the fixture (7.8 MPa). This stress level has been used to design **in situ** creep tests. A specific model of creep sample, adapted to the production line has been developed in order to perform **in situ** creep tests. These tests allowed us to evaluate uniaxial creep strain rates for two stress levels: σ = 5.0 MPa and 7.8 MPa, and to compare longitudinal and transversal behavior. As the fixtures are made from cold rolled beams, properties in the rolling direction may differ from those in transverse direction.

During **in situ** creep test, samples are periodically measured. These successive measurements allow us to get creep curves for these anisothermal cyclic solicitations. Good measurements and reliable results were obtained, even if it is difficult to perform **in situ** creep tests on a production line. The strain rate is constant for both stresses. These tests are original as they take into account the real thermal cycling and gas composition linked to **in service** conditions.

Usual creep tests

In the same time, classical isothermal creep tests were carried out in the laboratory at 1143K under air, argon, and hydrogenated argon. This technique allows us to determinate the stress/strain rate relation for different environment conditions. We performed these creep tests on as-received material and on aged material heat treated at 1143K for 60 days. The aged samples had a σ phase volume fraction of 8.3%. This value was measured by XRD using the Rietveld method.

In the same conditions, the aged material had a larger strain rate than the as-received material as shown in Figure 6. As only minor changes were observed on grain size, the acceleration of creep is probably due to the σ phase precipitation and the correlated chromium depletion in the austenitic matrix (decrease from 25% to 20%).

Mechanical behavior for higher stress levels: Isothermal creep tests under air have also been performed for larger stress levels: 50, 82 and 100 MPa. Primary creep is negligible and secondary creep was carefully analyzed. The strain rates are plotted in Figure 6 in a Norton diagram. Data are coherent with the previous results obtained on the as-received material for smaller stress levels. The measured creep strain rates show a linear relation. This constant Norton coefficient indicates that creep rates are controlled by the same mechanism for this range of stress at 1143K.

All the data plotted on figure 6 highlight that both ageing and in-situ conditions increase strain rate. However further tests are ongoing to separate cyclic effect from environment effect.

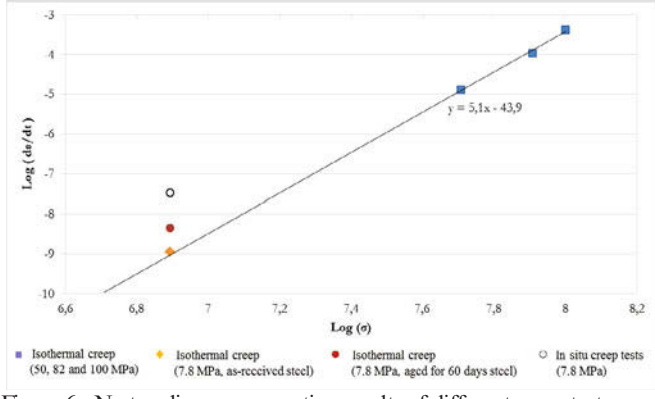

Figure 6 : Norton diagram presenting results of different creep tests

Conclusion

The specific use of 310S Stainless Steel as material for tools in heat treatment devices highlights an unusual creep behavior and an accelerated ageing. Mechanical and thermal stresses applied during thermal cycling influence diffusion kinetics of addition elements, especially chromium. Then, σ phase growth is enhanced inducing an acceleration of creep. This larger creep strain rates was quantified during **in situ** experiments and compared to the value obtained during isothermal creep tests. In the specific in-service conditions, for the stress level of fixture, we showed that 310S Stainless Steel creep strain rate increases by a factor 33 compared to isothermal creep under air. The influence of microstructural ageing was quantified.

Acknowledgement

The authors gratefully acknowledge Ronan Mainguy, Alexandre Freulon, Marie-Christine Lafont and Yannick Thebault for their help during mechanical tests and material characterizations.

References

1. Tien, C.W. and C.J. Altstetter, *Hydrogen-enhanced plasticity of 310S stainless steel.* Materials chemistry and physics, 1993. **35**(58-63).
2. Matsunaga, H. and H. Noda, *Visualization of Hydrogen Diffusion in a Hydrogen-Enhanced Fatigue Crack Growth in Type 304 Stainless Steel.* Metallurgical and Materials Transactions A, 2011. **42A**: p. 2696-2705.
3. Marchi, C.S., et al., *On the physical differences between tensile testing of type 304 and 316 austenitic stainless steels with internal hydrogen and in external hydrogen.* International Journal of Hydrogen Energy, 2010. **35**: p. 9736-9745.
4. Padilha, A.F. and P.R. Rios, *Decomposition of austenite in austenitic stainless steels.* ISIJ International, 2002. **42**(4): p. 325-337.
5. Barcik, J., *The kinetics of σ-phase precipitation in AISI 310 and AISI 316 steels.* Metallurgical Transactions A, 1983. **14**(4): p. 635-641.
6. Magnabosco, R., *Kinetics of sigma phase formation in a Duplex Stainless Steel.* Materials Research, 2009. **12**(3): p. 321-327.
7. Vitek, J.M. and S.A. David, *The Sigma Phase Transformation in austenitic Stainless steels.* Welding Research Supplement, 1986: p. 106-114.
8. Ferreira, P.J., I.M. Robertson, and H.K. Birnbaum, *Hydrogen effects on the interaction between dislocations.* Acta Materiala, 1998. **46**(5): p. 1749-1757.
9. Hall, E.O. and S.H. Algie, *The sigma Phase.* Metall. Rev., 1966. **11**: p. 61-88.

Characterization of Minerals, Metals, and Materials 2016
Edited by: Shadia Jamil Ikhmayies, Bowen Li, John S. Carpenter, Jiann-Yang Hwang, Sergio Neves Monteiro, Jian Li, Donato Firrao, Mingming Zhang, Zhiwei Peng, Juan P. Escobedo-Diaz, and Chenguang Bai
TMS (The Minerals, Metals & Materials Society), 2016

CHARACTERIZATION OF HUMIC ACID MODIFIED BENTONITE BINDER FOR IRON ORE PELLETIZATION

Yang Sun, Bin Xu, Yuanbo Zhang*, Bingbing Liu, Youlian Zhou, Zijian Su

School of Minerals Processing & Bioengineering, Central South University, Changsha, Hunan 410083, China

Keywords: HA, modified bentonite, characterization, iron ore, pelletization

Abstract

A new kind of iron ore pellet binder named humic acid modifying bentonite (HA-MB) has been developed by the author's group, which has the advantages of both organic HA and inorganic bentonite. The green pellet strength can be obviously improved by using the HA-MB binder. In this study, the detection of the characterization of HA-MB was conducted by zeta-potential, TG-DSC, FTIR, XRD, etc. The addition of HA was able to change the zeta-potential of bentonite. And HA-MB had more weight loss than that of bentonite according to TG-DSC analysis. Some functional groups of HA were also found in the FTIR spectrum of HA-MB. XRD result indicated that d(001) of crystal layer of bentonite had apparently altered due to the addition of HA.

Introduction

Bentonite is commonly used as the binder of iron ore pellet. It can improve the ballability of iron concentrates, the strength of wet green pellets and that of the dried pellets [1, 2]. However, the high silica and alumina contents in bentonite increase the gangue content of iron ore pellet and lead to an increase of coke breeze consumption during the blast furnace ironmaking.

HA binder that mainly comprise functional organic polymers is characterized by low ash content. And the adsorption of HA binder onto the surface of iron ore particles is able to change the interfacial characteristics of iron ores and improve the ballability of iron ore concentrates [3].

Extensive studies have been carried out on the modification of bentonite by adsorption of HA. It's found that the presence of strong interaction between HA and bentonite can change the zeta potential dramatically [4, 5]. *Aiguo Liu et al*. [6] reported that the connection bridge of the metal ions between bentonite and HA is the dominant adsorption mechanism.

*Corresponding author: Yuanbo Zhang, email:zybcsu@126.com

The authors' group has developed a new kind of iron ore pellet binder, humic acid modifying bentonite (HA-MB). The results have demonstrated that HA-MB binder was able to reduce the binder dosage and also provided a considerable strength of green and indurated pellet. In this work, comparative study on the characterization of bentonite, HA and HA-MB binders was conducted by the techniques of FTIR, Zeta potential, TG-DSC, XRD and SEM.

Experiment

Raw Materials

The raw Ca-bentonite is taken from Xinyang of China. The main chemical compositions of the sample bentonite are shown in Table I. And the Ca-montmorillonite is the main mineral composition and a small quantity of quartz exists in the bentonite. The basic physical indexes of the bentonite are presented in Table II. The BET surface area of the bentonite is 4865 cm^2/g. The elementary analysis of the HA was tested with a Model PE2400 CHN Hydrocarbon Elemental Analyzer and the results are listed in Table III. It can be seen that the HA contains 68.36 wt% organic substances and 32.64 wt% inorganic component.

Table I. Chemical compositions of the sample Ca-bentonite (wt%)

SiO_2	Al_2O_3	Fe_2O_3	CaO	MgO	K_2O	Na_2O	P	S	LOI*
73.26	9.64	3.19	2.23	1.83	1.39	0.70	0.03	0.05	10.41

LOI*: Loss on ignition.

Table II. Basic physical indexes of the sample Ca-bentonite

Ca-bentonite (%)	2HWA* (%)	Dilation ($mL \cdot g^{-1}$)	Colloid index ($mL \cdot (3\ g)^{-1}$)	BET surface area ($cm^2 \cdot g^{-1}$)
76.24	158	8.75	9.6	4865

2HWA* : Water absorption content in 2 hours.

Table III. Organic elementary analysis of the HA binder (wt. %)

Elementary composition*					Ash content
C	H	O	N	S	/
60.54	2.20	35.79	1.10	0.34	32.64

Elementary composition*: Calculated after deducting the ash content.

Methods

Characterizations of HA-MB were examined by FTIR, zeta-potential, TG–DSC, XRD

analyses,SEM, etc.

Infrared adsorption spectra of bentonite, HA and HA-MB were recorded using a USA Thermo Nicolet Nexus 670 FTIR spectrometer. The samples were dried at 80 ℃ and then put into a desiccator for FTIR analysis. The dried sample (about 1 mg) was mixed gently with 100 mg KBr powder and analyzed by FTIR. The KBr powder was used as background and theFTIR spectra were recorded in the range of 400−4000 cm^{-1}.

Zeta potential measurements of HA, bentonite and HA-MB were conducted by using a Malvern ZEN3600 Zeta potential analyzer. The concentrations of HA solution, bentonite suspension and HA-MB suspension were 1g/L. The variations of Zeta potentials under different pH values were evaluated at 25 ℃.

The thermal behaviors were studied using a Thermal Analyzer (NETZSCHSTA 449 C, Germany) at a heating rate of 20 ℃/min from the room temperature to 1000 ℃ in the air, and the gas flow rate was 150 mL/min. Approximately 10 mg sample was put into a calcined alumina crucible.

X-ray patterns were obtained on powdered samples with a Bruker D8 Advance (40 kV, 40mA), powder diffractometer using Cu Kα radiation. XRD patterns were achieved in step-scan mode from 3° to 70°. Crystalline phases were identified by comparison with the PDF standards (Powder Diffraction Files) from ICDD (International Centre for Diffraction Data).

Scanning electron microscope observations of the samples were performed under an acceleration voltage between 10 and 30 kV using a Quanta 200 ESEM(Environment Scanning Electron Microscope, FEI Corporation, Holland). The bentonite and HA-MB samples were added into distilled water at 25 ℃ and shaken for 1h. After that, the suspension was placed into a desiccator, dried naturally and then used for ESEM imaging.

Results and Discussion

FTIR Analysis

The FTIR spectra can indicate the physisorption and chemisorption of the HA onto the bentonite due to the existence, shift or absence of the peaks of functional groups. Fig. 1 showed the FTIR spectra of bentonite, HA and HA-MB.The peak at 3625 cm^{-1} was due to -OH band stretch within Al-OH. The characteristic band in the range of 3100-3500 cm^{-1} was assigned to stretching frequency of -OH group of hydrate water [7]. The overlaid absorption peak in the region of 1637 cm^{-1} in the FTIR spectrum

was attributed to -OH bending model of water (adsorbed water). IR peak at 915 cm^{-1} was attributed to Al-OH deformation peak [8]. The bentonite spectrum contains peaks 1090, 794, and 625 cm^{-1} result from the Si-O-Si stretching vibration of quartz in bentonite. The peaks at 1794 and 1740 cm^{-1} of HA-MB can be the C=O stretching vibration which came from the HA. Significant shift of the -COOH peaks from 1577 and 1387 cm^{-1} of HA to 1574 and 1395 cm^{-1} of HA-MB was a result of strong interactions of -COOH with bentonite. Interactions of HA with bentonite have occurred due to the disapperance of the peak 1193,1107, and 1033 cm^{-1} which were the C-O stretching vibration. The Si-O-Si linkage stretching vibration of HA-MB surface was observed at 1042 cm^{-1}, while the Si-O-Si linkage stretching vibration of bentonite was at 1030 cm^{-1}. This shifting of band clearly indicated that the interaction happened between Si-O-Si of bentonite with HA [9]. The FTIR results obviously showed that HA-MB was not a sample mixture of bentonite with HA because of the chemical interaction.

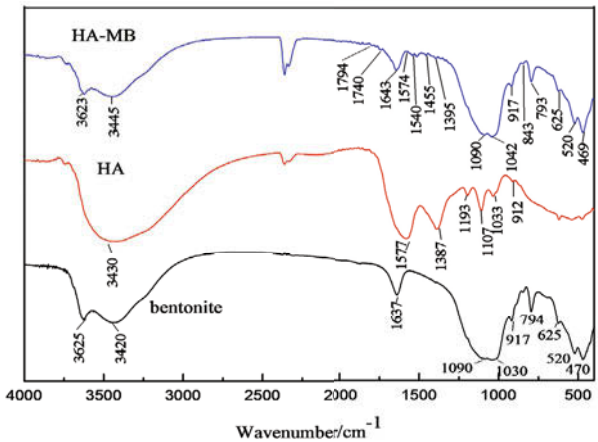

Fig. 1. FTIR of bentonite, HA and HA-MB.

Zeta potential analysis

Usually zeta potential can be used to estimate the possible effect of adsorbates on the properties of minerals. The curves of zeta potential versus pH value of HA, bentonite and HA-MB were shown in Fig. 2. Zeta potential values of HA and bentonite in the investigated pH range were negative and decreased with increasing pH values. So, electrostatic attraction was not applied to explain the interaction between bentonite and HA. What's more , the FTIR spectra had proved chemical adsorption of HA and MB. When pH<5.0, the zeta potential of the HA-MB was close to the HA. It may be attributed to that HA was bound to the Al-OH sites of surfaces via complexation. Moreover, the higher the pH value was, the greater the electrostatic repulsion force

was. But the Zeta potential of HA-MB was still lower than that of bentonite owing to chemical interactions such as ligand exchanges or hydrogen bond effect of the negative potential HA rather than electrostatic attraction.

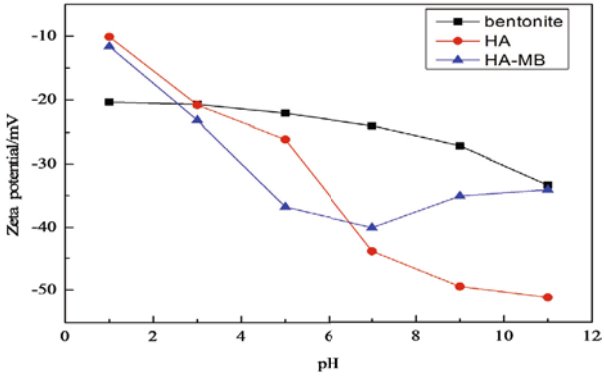

Fig. 2. The zeta potential of bentonite, HA and HA-MB.

TG-DSC analysis

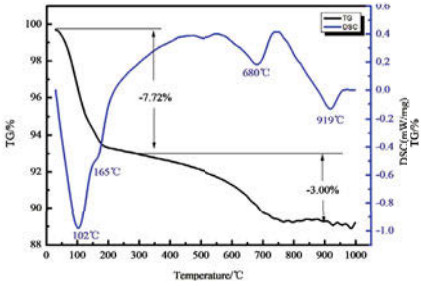

Fig. 3. TG-DSC of bentonite.

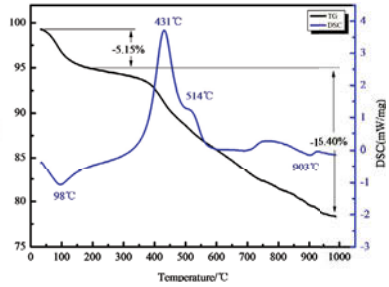

Fig. 4. TG-DSC of HA-MB.

The thermal analysis of natural bentonite was shown in Fig. 3. The first dominant mass loss of natural bentonite was due to the dehydration of interparticle water, adsorbed water and interlayer water. The DSC endothermic peaks corresponding to this change was observed at around 102 ℃ and 165 ℃ (Fig. 3). The first peak in the thermal decomposition of HA-MB linked with the loss of adsorbed water at 98 ℃ (Fig. 4). The mass loss of adsorbed water from TGA thermograms was 7.72% and 5.15% for the bentonite and HA-MB, respectively. The difference may result from that HA reacted with active sites of the bentonite that can form hydrogen bonds with water, which made HA-MB a less mass loss and lower dehydration temperature of water. The exothermic peaks of HA-MB at around 431 ℃ and 514 ℃ on DSC curve was attributed to the combustion and decomposition of HA in HA-MB [9]. And it

caused the total mass loss of HA-MB higer than that of bentonite. The phase transformation of bentonite and HA-MB were at 919 ℃ and 903 ℃, respectively, which showed a thermal instability of HA-MB [9]. The results may indicate stucture changes of bentonite result from the interaction between HA and bentonite.

XRD analysis

The X-ray diffraction analysis of natural bentonite confirmed montmorillonite (B) as dominant mineral phase (Fig.5 (a)). The main impurity mineral was quartz (S). The HA caused structural change in the bentonite (Fig.5 (b)) which can be seen from the mainly (001) reflection of montmorillonite. The intensities of (001) reflection of montmorillonite decreased significantly in the XRD patterns of HA-MB. Moreover, the (003) reflection of montmorillonite in the HA-MB patterns disappeared. The XRD peaks weaken and disappeared suggested the chemical intercation between the two phases and caused montmorillonite crystalline structure tansformation [10].

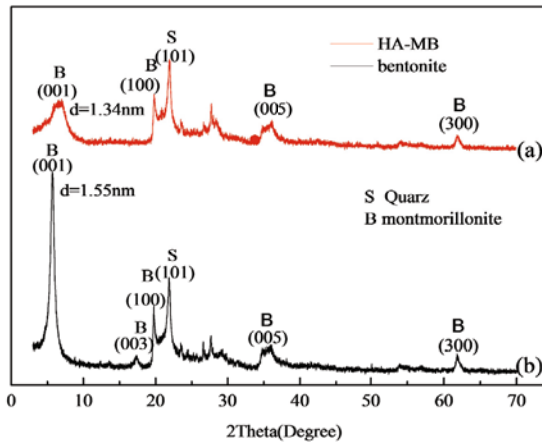

Fig. 5. XRD patterns of bentonite and HA-MB.

SEM analysis

Figs. 6 (a-d) showed the microstructure of bentonite and HA-MB. The micrograph of the bentonite can be clearly observed from Fig. 6 (a, c) which showed that the paticles diameter of bentonite was between 20 m and 100 m. The micrographs of HA-MB indicated the disaggregation decreased in size of bentonite particles by Fig. 6 (b, d). The diameter of particles HA-MB was less than 10 m, and the edges of the sheets were opened and separated forming small layers. So the separation of layers were explained by the phenomenon of HA adsorption and interaction with the surface and the transformation of their crystal lattice (Fig. 6 d). This further verified the XRD

analysis that HA had changed the crystal structure of bentonite.

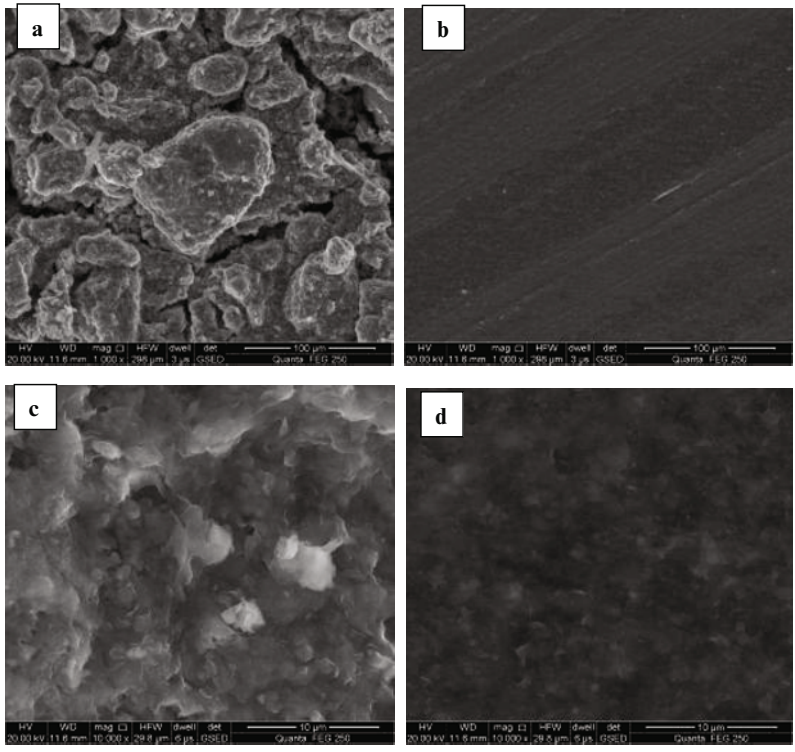

Fig. 6. SEM images of bentonite (a, c) and HA-MB (b, d).

Conclusions

The modification of bentonite by HA showed that HA had changed the structure of the montmorillonite and separated the sheet of bentonite. FTIR and Zeta potential results had pointed out that there were chemical adsorption between the bentonite and HA. TG-DSC results indicated that HA could interact with bentonite and reduce the thermal stability of bentonite. XRD results showed that the adsorption of HA was able to change the main d(001) and d(003)(basal) planes due to the structure alter of the bentonite. SEM images indicated that bentonite had dispersed into small particles and their crystal lattice been changed by HA. So the conclusions can be draw that HA-MB was formed owing to chemical interaction between HA , and HA caused the crystal structure transition. Perhaps it was for this reason that HA-MB as binder for iron ore pelletization can help improve the strength of green pellets.

References

[1] S.P.E. Forsmo et al., "Binding mechanisms in wet iron ore green pellets with a bentonite binder," *Powder Technology*, 169 (2006), 147–158.

[2] G.Z. Qiu et al., "Effects of binders on balling behaviors of iron ore concentrates," *Scandinavian Journal of Metallurgy*, 33 (2004), 39–46.

[3] Y.L. ZHOU et al., "Effect of modified humic acid binder on pelletisation of specularite concentrates," *Journal of Central South University,* 22 (2015), 1247–1255.

[4] D.J. Greenland, "Interactions between humic and fulvic acids and clays," *Soil Science*, 111 (1971), 34-41.

[5] M. Schnitzer, H. Kodama. "Montmorillonite: Effect of pH on its adsorption of a soil humic compound," *Science*, 153 (1966), 274-277.

[6] A.G. Liu, R.D. Gonzalez. "Adsorption/Desorption in a system congsisting of Humic Acid, heavy metals, and clay minerals," *Journal of Colloid and Interface Science*, 218 (1999), 225-232.

[7] J. Madejová, "FTIR techniques in clay mineral studies," *Vibrational Spectroscopy*, 31 (2003), 1–10.

[8] B. Caglar et al., "Characterization of the cation-exchanged bentonites by XRPD, ATR, DTA/TG analyses and BET measurement," *Chemical Engineering Journal*, 149 (2009), 242–248.

[9] K.H. Tan, "Complex formation between humic acid and clays as revealed by gel filtration and infrared spectroscopy," *Soil Biology and Biochemistry*, 8 (1976), 235–239.

[9] G.H. HAN et al., "Characteristic of humin fractions associated with inorganic minerals obtained by NaOH, and NaOH assisted with anthraquinone extraction procedures," *Journal of Central South University*, 19 (2012), 2286–2290.

[10] Tomáš Schütz , Silvia Dolinská, Annamária Mockovčiaková, "Characterization of Bentonite Modified by Manganese Oxides," *Universal Journal of Geoscience*, 1 (2013), 114-119.

Characterization of Minerals, Metals, and Materials 2016
Edited by: Shadia Jamil Ikhmayies, Bowen Li, John S. Carpenter, Jiann-Yang Hwang, Sergio Neves Monteiro, Jian Li, Donato Firrao, Mingming Zhang, Zhiwei Peng, Juan P. Escobedo-Diaz, and Chenguang Bai
TMS (The Minerals, Metals & Materials Society), 2016

Optimization of Material Properties of High Strength Multiphase Steels via Microstructure and Phase Transformation Adjustment

Annette Bäumer[1], Eva Zimmermann[1]

[1]ThyssenKrupp Steel Europe AG, Dept. of Technology and Innovation (TIS)
Kaiser-Wilhelm Strasse 100, 47161 Duisburg, Germany

Keywords: Dual Phase Steel, TRIP Steel, Annealing process

Abstract

For high strength multiphase steels for structural components in automotive applications many different material properties are required. Consequently, a diverse range of tests are performed to characterize the material properties during development as well as optimization of multiphase steels. These tests include classical tensile tests as well as formability tests which characterize bendability, edge crack sensitivity and deep drawability. All these properties are greatly dependent on the microstructure of the material. In the case of high strength multiphase steels, microstructure characterization involves evaluation of the volume fraction, stability, grain size as well as the distribution of the different phases present. Microstructural modifications - with the aim of obtaining the required material properties - may be achieved by variation of annealing parameters. In this paper it is shown how microstructural modification for high strength TRIP and Dual Phase steels resulted in better formability properties and different strength levels.

Introduction

For the application of materials in practical use, various material properties have to be combined and optimized. In the case of steels for automotive applications the primary focus is increasing strength whilst maintaining constant or improving formability. Targets set by the automotive industry have led to the development of various multiphase high strength steels at different strength levels. While ferritic steels make use of strengthening mechanisms such as grain refinement, solid solution hardening and precipitation hardening, multiphase high strength steels in addition to that also make use of strengthening and formability mechanisms that are related to the different microstructure phases present and to their size, stability and distribution. The strong correlation between microstructure and mechanical properties is, therefore, even more important as the microstructural phases develop during annealing of the cold rolled strip. In the case of multiphase steels, the aim of the annealing process is not only recrystallization of the deformed ferritic grains but also the formation of the different microstructure phases. During continuous annealing dual phase steels are first heated to a temperature between ac1 and ac3 to produce a certain proportion of austenite. This austenite will transform into ferrite and martensite upon cooling, such that the hard martensitic phase is embedded in a soft ferritic matrix. TRIP (transformation induced plasticity) steels make use of metastable retained austenite that transforms into martensite during deformation, thereby enabling a high level of deformation at high strength levels. This requires stabilization of the retained austenite during the annealing process. First, again the cold rolled strip is annealed in the intercritical ferritic-austenitic

temperature region. During cooling, part of the austenite will transform to ferrite. In a second holding step at lower temperatures, which is commonly called overaging step, carbide-free bainite is formed. Consequently, the austenite is enriched with carbon so that it is stable at ambient temperature unless deformed. Figure 1 illustrates the phase transformations during annealing process of Dual Phase and TRIP steels.

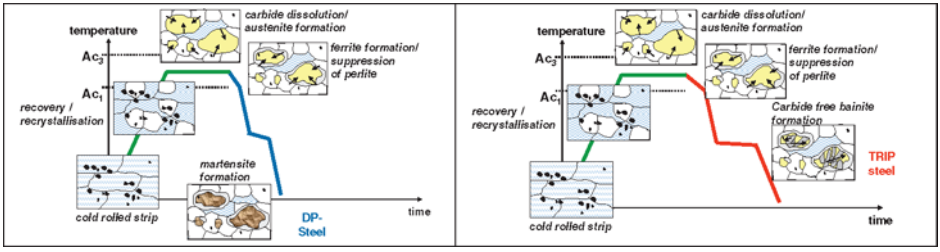

Figure 1: Phase transformations during annealing of Dual Phase (left) and TRIP steels (right) [1]

Development of microstructure during production processes is therefore a function of production parameters while mechanical and formability properties are directly correlated with the microstructure. Therefore, by optimization of, for example, annealing parameters it is possible to adjust microstructure and, consequently, material properties.

Experimental

Annealing parameter variation in annealing simulator

For testing annealing parameter variation on a lab scale, 165 mm x 450 mm samples of cold rolled strip were annealed with industrial annealing cycles. The samples were heated inductively and cooled with gas jet cooling so that defined annealing cycles could be reproduced. Tensile test samples as well as samples for microstructural analysis were taken of the middle part of the sample.

Characterization of mechanical properties

For characterization of the mechanical, formability and joining properties various tests are performed during product development and optimization. The results presented in this paper were taken from tensile tests, bending tests and hole expansion tests.
Tensile tests were performed according to DIN EN ISO 6892-1. For samples taken from industrially-produced material, sample form 2 was used (80 mm gage length), whereas for the materials prepared using the lab-scale annealing simulator sample form 1 was used (50 mm gage length). In case of determination of flow curves the tests were performed at a constant strain rate of 0.004 1/s.
Bending properties were evaluated using three point bending tests performed according to VDA 238-100. A rectangular shaped 60 mm × 60 mm sample was bent over a 2 mm bending mandrel until the first crack appeared. Thus, the bending properties of the materials were characterized in terms of the maximum bending angle. For evaluating the edge crack sensitivity, hole expansion

tests were performed according to ISO 16630. During this test a hole with a diameter of 10 mm was punched into the sample sheet. The hole was then extended from one side of the sample with a mandrel until first crack appeared. The maximum hole expansion ratio was determined by dividing the maximum diameter by the initial diameter.

Microstructure Analysis

First step for Microstructural analysis was light microscopy on samples prepared longitudinal to the rolling direction and etched with Nital and/or Klemm reagent. This enabled the visualization of the different phases and grains of microstructure. Automated image analysis was used for quantitative microstructure analysis. X-ray diffraction (XRD) was used to determine the volume fraction of retained austenite. In the case of high-strength multiphase steels, the microstructure is often too fine to visualize with the resolution of light microscopes. Thus, in a second step Field Emission Scanning Electron Microscopy (FE-SEM) was also used. This enabled small microstructure components with a grain size of less than 1 µm to be distinguished. Samples for XRD and FE-SEM analysis were prepared by etching with Nital reagent.
Further analysis of the microstructure was performed using Electron Back Scattered Diffraction method (EBSD). This enabled evaluation of the grain orientation as well as grain sizes. Furthermore, lattice distortion and misorientation was measured for single phases or for the entire microstructure via analysis of the Kernel Average Misorientation (KAM) [2-4].

Microstructure and mechanical property optimization

Determination of optimum temperature for bainitic transformation and stabilization of retained austenite during annealing of a new TRIP steel

The mechanical properties of TRIP steels are greatly dependent on the amount of retained austenite. During development of a TRIP steel with a tensile strength of 1000 MPa the optimum temperature for bainitic transformation during annealing had to be determined. As a first step, industrially-produced cold rolled sheet with a new chemical composition was annealed using a lab-scale annealing simulator. Overaging temperatures of the industrial annealing cycles were varied between 350 and 475 °C. After annealing, tensile and metallographic samples were taken from the annealed sheet and analyzed. The results are shown in Figure 2 with respect to the overaging temperature. On the left-hand side the volume fraction and lattice constant of retained austenite are plotted against the overaging temperature. A maximum retained austenite volume fraction of 14 % was obtained by overaging at temperatures between 425 and 475 °C. The lattice constant of retained austenite can be used to calculate the amount of carbon which is in interstitial solution in the retained austenite as the lattice will be strained and the lattice constant grows in correlation to the amount of carbon in interstitial solution. This value may also be used to characterize the stability of the austenite [5].
In this investigation the maximum lattice constant is reached in samples overaged at 425 and 450 °C. Figure 2 (right) shows that the highest fracture elongation is obtained through overaging at 425 °C with the corresponding ultimate tensile strength still in the required range. Thus, 425 °C was considered the optimum overaging temperature. This was later confirmed in a production trial with overaging temperatures varied between 420 and 470°C over the strip length.

Material formability tests were also performed using samples from this trial. As an example the results of bending tests are shown in Figure 3.

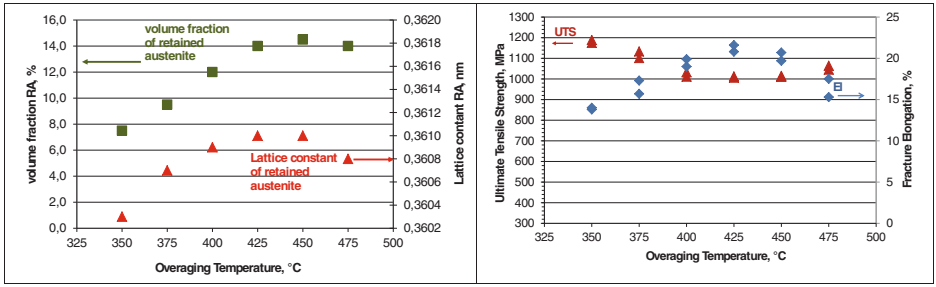

Figure 2: (left) volume fraction and lattice constant of retained austenite (both determined via XRD) , and (right) tensile strength and fracture elongation transverse to rolling direction with respect to the overaging temperature

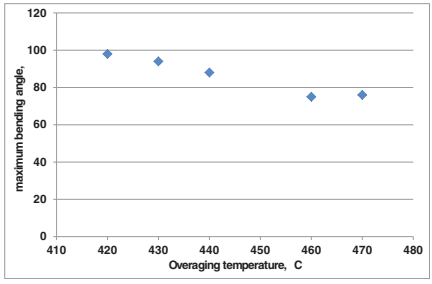

Figure 3: Maximum bending angle versus overaging temperature determined on industrially-produced material

Optimization of transformation behavior of retained austenite during deformation via optimization of matrix microstructure

Stabilization of retained austenite is a decisive step during the annealing process of TRIP steels. However, it is not the only factor that plays a decisive role. During development of a TRIP steel with a tensile strength of 800 MPa, mechanical properties determined via tensile tests were in the required range but deformation tests showed that the deformability was not typical for a TRIP steel despite a retained austenite concentration of 13 %. Figure 4 shows the results of light microscopy of the industrially-produced material etched using Nital and Klemm reagent. The Nital etching revealed an inhomogeneous ferrite grain structure with relatively large ferrite grains. In addition, Klemm etching showed that most of the ferrite grains belonged to primary ferrite. Furthermore, the bainitic phase fraction was relatively small. This led to the assumption that the intercritical annealing temperature might not be sufficiently high.

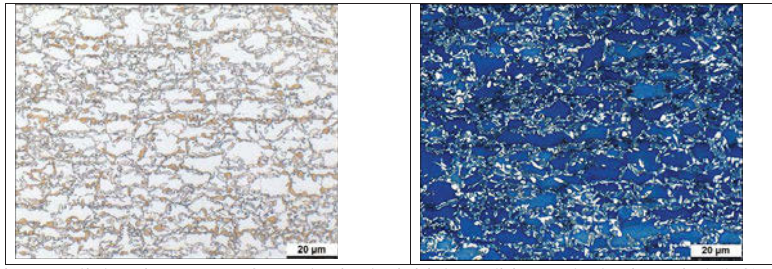

Figure 4: light microscopy of samples in the initial condition etched using Nital (left) and Klemm reagent (right).

Lab-scale tests were subsequently performed at various annealing temperatures. Optimum results were obtained by annealing at a temperature of 40 °C higher than the initial condition (Figure 5). Although the volume fraction of retained austenite (RA) determined via XRD was almost constant, the matrix microstructure was more homogeneous and was comprised of finer ferrite grains.

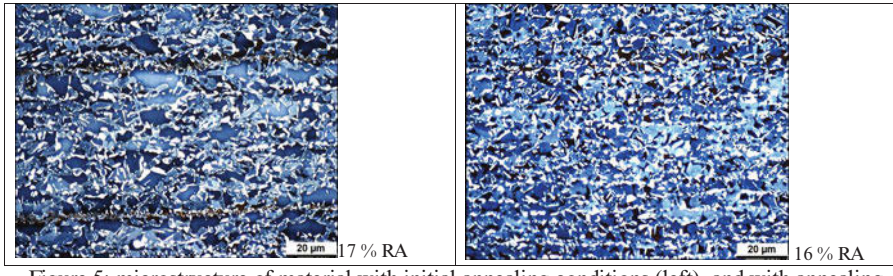

Figure 5: microstructure of material with initial annealing conditions (left) and with annealing temperature (lab scale trial) increased by 40°C (right). In both cases the sample was etched using Klemm reagent.

Industrial-scale material produced with increased annealing temperature was then investigated with respect to deformation properties. Figure 6 shows as an example the improvement in strain hardening behavior by comparison of the flow curves. With the new annealing parameters strain hardening is continuous and high until high deformations, thereby resulting in better deformability. This is due to the slower transformation rate of retained austenite, which is shown in the diagram on the right hand side.
Optimization of the microstructure also resulted in an increase in the average hole expansion ratio from 22 to 28%.

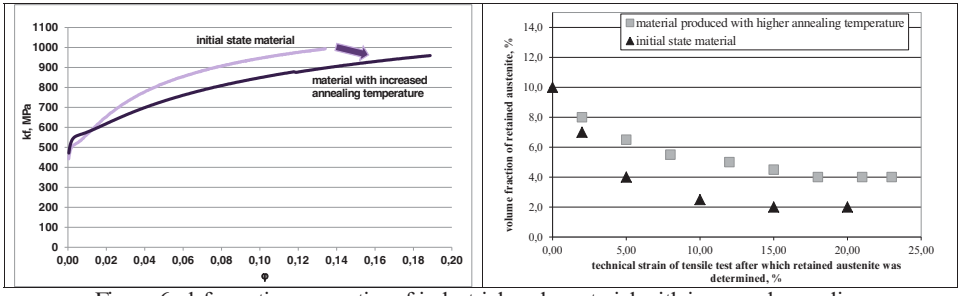

Figure 6: deformation properties of industrial-scale material with increased annealing temperature showing comparison of flow curves (left) and rate of transformation of retained austenite determined via interrupted tensile tests (right)

Variation of annealing parameters resulting in different strength levels of a Dual Phase steel

Many publications discussing different strength levels of Dual Phase steels focus on the volume fraction of martensite as the primary determiner of strength. In this case, higher intercritical annealing temperatures usually lead to higher volume fractions of martensite [6]. Nevertheless, the ferritic phase also plays a key role in determining the strength of dual phase steels. For example, it is possible to increase strength via variation of annealing parameters even if volume fractions of phases and grain sizes are kept constant.
During development of a Dual Phase steel with a tensile strength of 1000 MPa the annealing temperature was varied while maintaining a constant chemical composition. This resulted in ultimate tensile strengths in the range from 930 to >1200 MPa (Figure 7).

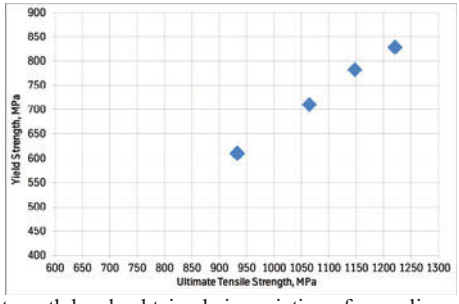

Figure 7: Different strength levels obtained via variation of annealing parameters during the development of a Dual Phase steel with a tensile strength of 1000 MPa.

The microstructures of all samples were investigated. Since the grain sizes of the materials were between 1-2 µm, the resolution of light microscopy was too low for adequate analysis. Thus, FE-SEM analysis was performed. For determination of the martensite volume fraction and grain size from FE-SEM images martensite grains were marked manually and then analyzed via automated

image analyzing software. The volume fraction of retained austenite was determined via XRD. EBSD analysis was performed for the ferritic phase. As an example, two samples are shown in Figure 8. The determined values for microstructure analysis are also given. Although the volume fraction of martensite in the two materials is almost identical and the grain sizes of martensite and ferrite differ only slightly, there is a difference in the tensile strengths of more than 200 MPa. Texture analysis using EBSD showed no cold rolling texture components so it may be concluded that the materials were fully recrystallized.
For further characterization of the ferritic phase the Kernel Average Misorientation (KAM) was evaluated using EBSD. Figure 9 shows the same samples as Figure 8 and it is clearly visible that the misorientation of the ferritic phase increases with increasing strength. Figure 10 shows the average KAM value for the different samples and confirms the statement quantitatively. This means that due to the different annealing parameters ferrite was formed at different temperatures. The ferrite that was formed at lower temperatures shows a higher degree of misorientation. This corresponds with an increase in the yield and ultimate tensile strength of the material.

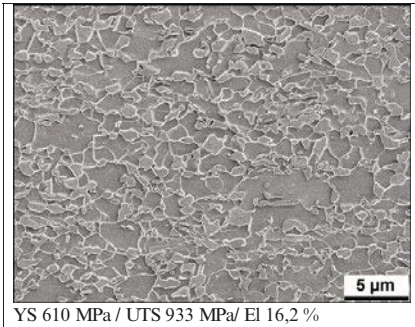

YS 610 MPa / UTS 933 MPa/ El 16,2 %
20,2 % Martensite, 6 % Retained Austenite (XRD)
Martensite grain size: 0,71 µm
Ferrite grain size (EBSD): 1,92 µm

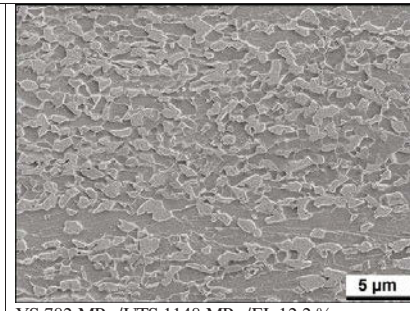

YS 782 MPa /UTS 1148 MPa /EL 12,2 %
21,5 % Martensite, 2 % Retained Austenite (XRD)
Martensite grain size: 0,78 µm
Ferrite grain size (EBSD): 1,67 µm

Figure 8: FE-REM images of dual phase microstructure with UTS of 930MPa (left) and 1150 MPa (right)

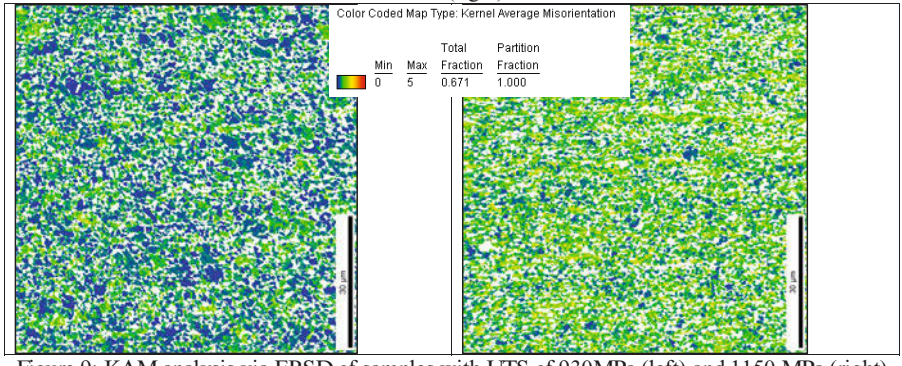

Figure 9: KAM analysis via EBSD of samples with UTS of 930MPa (left) and 1150 MPa (right)

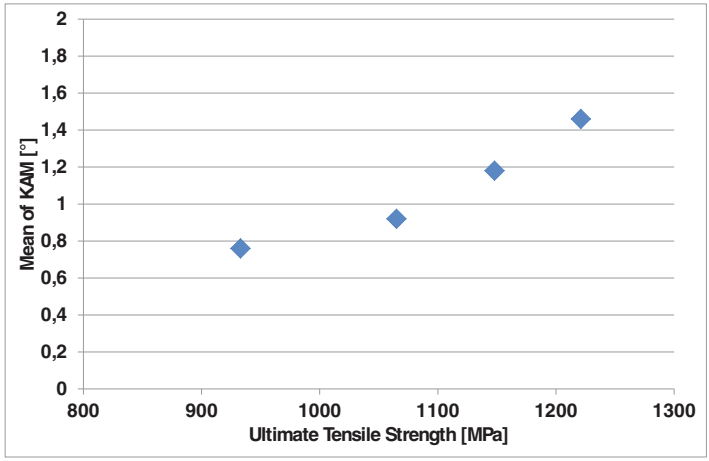

Figure 10: Mean of KAM value versus UTS of the test materials.

Conclusions

Three examples of steel developments of multiphase high-strength steels illustrated the strong correlation between production process, microstructure and material properties. For TRIP steels the importance of stabilization of retained austenite and its dependence on overaging temperature during annealing was shown. Furthermore, it was demonstrated that, in addition to the stabilization of retained austenite, the microstructure matrix plays a decisive role for material properties. Finally, for a Dual Phase steel with a tensile strength of 1000 MPa the importance of the ferritic phase was emphasized as well as its relevance concerning its contribution to the material strength.

References

1. H. Berndsen, F. Friedel, U. Etzold, E. Zimmermann, T.W. Schaumann: Sonderband Praktische Metallografie 34 (2003) S. 211
2. F. Friedel, U. Winkler, B. Holtz, R. Seyrich and H.-J. Ullrich: Crystal Research and Technology 2005 January, Volume 40 Issue 1-2, 182-187
3. Zaefferer S., Romano P., Friedel F.: J. of Microscopy 2008 Jun; 230(Pt 3):499
4. Angeli, J.; Füreder, E.; Panholzer, M.; Kneißl, A.: Praktische Metallographie, Band 43, 2006, S. 489-504
5. A. Zarei Hanzaki, P. D. Hodson, S. Yue, ISIJ Int. Vol. 35, No. 3, 1995, pp. 324-331
6. S. Yu et al. : Mat. Sci. Forum Vol 788 (2014), pp.351-356

Characterization of Minerals, Metals, and Materials 2016

Clays & Ceramics

Session Chairs:

Jiann-Yang Hwang

Maria das Graças Silva-Valenzuela

Characterization of Minerals, Metals, and Materials 2016
Edited by: Shadia Jamil Ikhmayies, Bowen Li, John S. Carpenter, Jiann-Yang Hwang, Sergio Neves Monteiro, Jian Li, Donato Firrao, Mingming Zhang, Zhiwei Peng, Juan P. Escobedo-Diaz, and Chenguang Bai
TMS (The Minerals, Metals & Materials Society), 2016

FORMULATION OF CERAMIC BODY TO PRODUCE ROOFING TILES USING WINKLER DIAGRAM

LF Amaral[1,a], CMF Vieira[1,b], SN Monteiro[2,c]
[1]UENF (State University of the North Fluminense Darcy Ribeiro);
Av. Alberto Lamego 2000, Campos dos Goytacazes, Rio de Janeiro, 28013-602, Brazil
[2]IME (Military Institute of Engineering);
Praça General Tibúrcio 80, Praia Vermelha, Urca, Rio de Janeiro, RJ, 22290-270, Brazil
[a]lfamaral28@gmail.com; [b]vieira@uenf.br; [c]snevesmonteiro@gmail.com.br

Keywords: Clay, heavy ceramic, body formulation

Abstract

Winkler diagram was the tool used to formulate roofing tiles ceramic bodies using three different clays. The objective was to obtain a ceramic product with good technological properties using local clay that has deficiencies in its chemical-mineralogical composition. Specimens were made by uniaxial press-molding at 35MPa and then fired at 850 ºC. The technological properties determined were flexural rupture strength, water absorption and linear shrinkage. The results showed that local clay has excessive coarse particles that impossibility its roofing tiles production and confirming the need to make a blend with other plastic raw materials. The Winkler Diagram was effective in the formulation of ceramic bodies due to the improvement of the observed properties.

Introduction

Campos dos Goytacazes has a traditional pole producer of heavy clay ceramic products in the Rio de Janeiro state, Brazil. The abundance of clays in this region is due by the quaternary sediments carried by the River Paraíba which forms the delta-alluvium plain [1]. However, the industries in this region have difficulties to produce roof tiles and blocks, and some cases, even the bricks, that attends the specifications required by the Brazilian standards. Thus, for the production of traditional ceramics, local clays have deficiencies in their composition that are related with the excessive water absorption and low mechanical strength of the products. Therefore, the process is not the just that could be responsible for the low performance of the ceramic products, but also the raw materials contribute to this [2,3].

The Winkler diagram is a helpful tool developed to formulate or reformulate ceramic body compositions. This a ternary diagram that is based on the particle size distribution, wherein it is assumes that particles having sizes smaller than 2 μm interact as plasticizers raw materials, being composed mainly of clay minerals, and the other particles, denominated coarse particles, act as unplasticizers raw materials. Thus, to produce heavy clay ceramics, it is necessary to dose the particles size distribution to achieve the adequate properties of ceramic body, as plasticity and dry bulk density [5-7].

To prove that these deficiencies of local clays can be overcome by the mixture of some raw materials, this work is based on the utilization of a methodology to rationally formulate a ceramic body to produce tiles.

Methodology

Two different clays, from Itaboraí – RJ (**I**) and Muriaé – MG (**M**) were used in a formulation ceramic body to produce roofing tiles in order to improve the properties of local clay from Campos dos Goytacazes (**C**), known as weak clay. All clayey samples were dried at 110 ºC for 24h and manually disaggregated through a 20 mesh sieving to provide the basic test material.

The particle size distribution of clays, determined by both wet sieving and the sedimentation method, was used to position them in Winkler Diagram. To formulate the ceramic bodies the B boundary area was chosen (**Figure 1**) that is intended for the production of roof tiles, designated in this diagram.

Rectangular specimens of the dimensions 11,5 cm x 2,5 cm with 8% moisture, molded in a steel matrix submitted to 35 MPa pressure, were used to investigated the technological properties. The specimens were dried at 110 ºC until the achievement of constant weight. The dried specimens were then fire at 850 ºC in an electric muffle furnace at a controlled heating rate of 2 ºC/min. Cooling occurred by natural convection after turning off the kiln and leaving the specimens inside.

The chemical composition of the raw materials was evaluated by X-ray Fluorescence in Unicam Solar 969 equipment The technological properties investigated by specific tests performed on the ceramic specimens were: water absorption, linear shrinkage and flexural strength by applying a three-points bend test.

Results and Discussion

As can be observed in **Table 1**, the predominant constituent of all clays is SiO_2, indicating the possibility to have quartz predominance in its composition. But these values are considered to be relatively low for clays [8].Normally, SiO_2 occurs as quartz, or combined to form the clay mineral structure [2].

The second most abundant component is Al_2O_3, however, when compared with other clays its values are considered relatively high [8]. This oxide together with SiO_2 participates almost completely in the formation of the clay mineral, but it may be present at hydroxides forms, as gibbsite ($Al(OH)_3$) [2,5].

The theoretical kaolinite have the value of 1,18 for theSiO_2/Al_2O_3 relation, so for the samples that have the presence of this clay mineral the closer this value the greater the amount of its. Comparing with other clays that produce singular ceramic products, the value of this relation for the clays studied is substantially low [8].

The alkaline oxides Na_2O and K_2O are considered as active fluxes, which contribute to the formation of liquid phase at around 700 ºC. They may occur in the crystalline lattice of certain clay minerals, in soluble salts or in compounds such as feldspar and mica. They can decrease the porosity of the fired products. However, for these clays, the content of these oxides is relatively low. Which contributes to the difficult that the local ceramic industries has to obtain products with low porosity [2,5].

Table 1. Chemical composition of clays (*wt. %*).

Composition	Clays		
	C	M	I
SiO_2	57.60	60.70	56.85
Al_2O_3	21.40	22.91	24.29
Fe_2O_3	7.37	4.31	6.36
TiO_2	1.07	1.19	1.02
K_2O	2.42	1.11	1.69
Na_2O	0.59	0.79	<0.05
CaO	0.40	0.69	0.12
MgO	1.17	0.34	0.97
L.o.I (%)*	7.69	7.72	8.54

*Loss on ignition

The particle size distribution has fundamental importance in the characterization of clays for traditional ceramic products. It can indicate the plastic behavior of ceramic bodies and some properties of fired products. The International Society of Soil Science (ISSS) classifies the soil particles according to its dimension, and fractionated it as clay minerals (< 2 μm), silt (2 – 20 μm) and sand (> 20 μm) fraction.

The fields in Winkler Diagram **(Figure 1**) correspond to the respective particle size distribution to process heavy clay ceramic products. It reveals that all the clays are situated as far as the proper region for roof tiles ceramic fabrication.

the low amount of clay mineral fraction of the **C** clay, confirming the necessity to make a blend of clays to produce roof tiles. This kind of product, localized in B area, needs a ceramic body with 30 – 50 wt.% of particles < 2 μm because it needs high plasticity to be shaped due to its curved form. Elevated percentage of clay minerals induces a high value of plasticity limit. Thus, on the shaping step, this leads to high content of water, and if the drying stage is not very well conducted it may cause drying cracks [7].

The **M** and **I** clay was chosen to be part of formulated ceramic bodies because it elevates the quantity of clay mineral fraction of formulated bodies. Inside of delimited triangle in **Figure 1** has all possible formulations that can be made. The chosen formulations are indicated in **Table 2**.

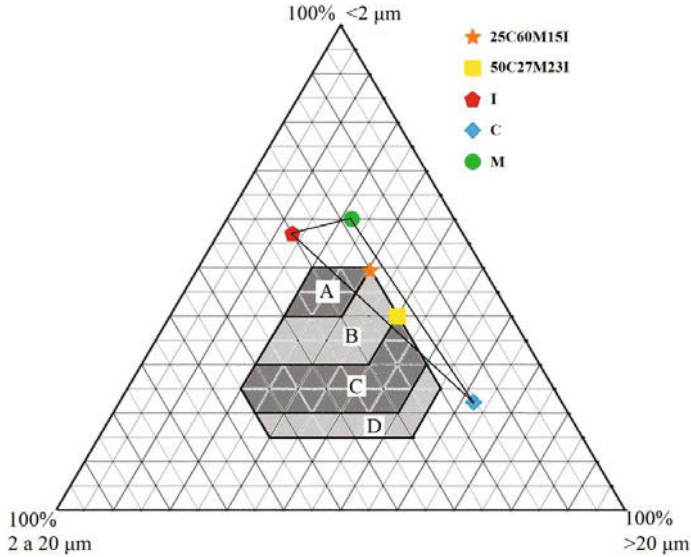

Figure 1. Particle size distribution (wt.%) in Winkler Diagram.

Table 2. Formulated ceramic bodies

Formulation composition	Clay (wt.%)		
	C	**M**	**I**
C	100	0	0
M	0	100	0
I	0	0	100
25C60M15I	25	60	15
50C27M23I	50	27	23

The mechanical strength of specimens fired at 850 ºC of the clays and formulations by flexural strength three-points bend test is shows in **Figure 2**. The **C** clay has a tendency to have the lowest values of mechanical strength of all clays, indicating that the 63 wt.% of particle size >20 µm, which correspond a sand fraction and it is rich in quartz mineral, may caused the reduction in mechanical strength. This can be explained by the allotropic transformation of quartz, which causes microcracks on the fired product [2,5]. Also in **Figure 2** can be observed that the formulation using 25% of **C** clay improved the mechanical strength of the pure **C** clay.

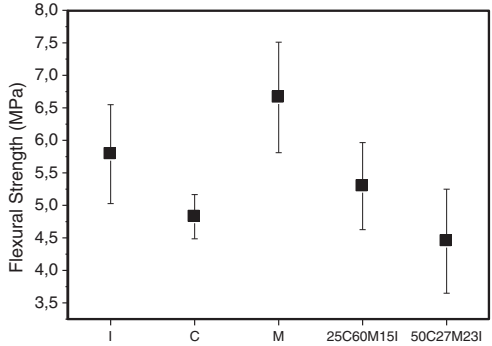

Figure 2. Flexural strength of the clays and the formulations of fired specimens at 850 ºC.

The water absorption of specimens fired at 850 ºC of the clays and the formulations is shown in **Figure 3**. In relation to the clays, it can be observed that **C** clay presented the highest value of water absorption of all clays and formulations too. Moreover, its the only clay that do not comply to a maximum of 20% water absorption required by the norm [10]. This behavior may be explained by the greater amount of quartz that is the main constituent of >20 µm fraction, indicated in Winkler Diagram. The principal sintering mechanism in traditional ceramic is by liquid phase formation. So as quartz acts as an inert material in this temperature range there will be less liquid phase formation and as consequence there will be more porosity [3]. Furthermore, it can be seen that the increment of the **C** clay in the formulations increases the water absorption.

The **I** clay presented the lowest value for this property, indicating that the liquid phase formation was more pronounced in this clay. Corroborating with other authors, this parameter suggest that clay minerals considered as fluxes minerals may contain in its composition [9]. With reference to the formulated bodies, it is notice that the both formulations, **25C60M15I** and **50C27M23I** presents a water absorption lower than the **C** clay. However, the first one presents the minor value, due to the major quantity of **C** clay.

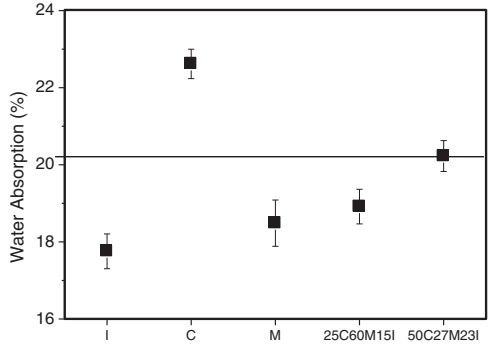

Figure 3. Water absorption of the clays and the formulations of fired specimens at 850 ºC.

The liquid phase formation on the sintering process is the responsible mechanism for closing the pores that is accompanied by dimensional retraction. The linear shrinkage is a parameter that indicates how much was the effectiveness in the sintering process and should be controlled to guarantee dimensional stability of the product [2]. The linear shrinkage of specimens fired at 850 ºC of the clays and the formulations is shows in **Figure 4**. It can be observed that M clay presents de highest value in comparison of all clays and also the formulations. Indicating that de sintering process was more effective in this case. As predict, the **C** clay did not have too much retraction due to the lower liquid phase formation, and also, the presence of quartz may cloak this value by its capacity to push the particles due its allotropic transformation accompanied by the dimensional variation.

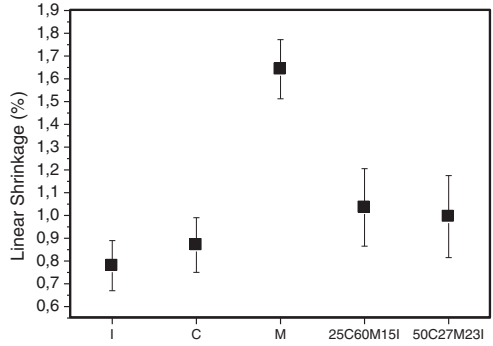

Figure 4. Linear Shrinkage of the clays and the formulations of fired specimens at 850 ºC

Conclusions

The local clay (**C**) presented excessive >20 µm particle size, confirm the need to be blended with plastic clays for the fabrication of roofing tiles according to the Winkler Diagram. The **I** and **M** clay has the necessary characteristics to make this blend due its excessive <2 µm particle size.

The viability of Winkler Diagram was confirmed in this study due to the improvement of mechanical strength and water absorption of the local clay (**C**) by using the mixture of raw materials.

The formulation that used the lower quantity of **C** clay and higher quantity of **M** clay showed better properties as mechanical strength and water absorption of all formulations.

The linear shrinkage showed that this temperature range could active the sintering mechanism by liquid phase formation, most evident in **M** clay.

Acknowledgement

The authors thank the Brazilian agencies CNPq, proc. n. 302930/2014-0 and FAPERJ, proc. n. E-26/201.192/2014 for supporting this research work.

References

1. A. R. Lamego, *O homem e o Brejo* (Rio de Janeiro, RJ: Editora LidadorLtda, 1974), 3-30.

2. S.N. Monteiro and C.M.F. Vieira, "Characterization of clays from Campos dos Goytacazes, north Rio de Janeiro State," *Tile &Brick Int*., 18 (2002), 152-157.

3. C.M.F. Vieira and S.N. Monteiro, "Reformulation of a kaolinitic clay ceramic body with sand and flux clay for roofing tiles production," *Materials Science Forum*, 727-728 (2012), 965-970.

4. C.M.F. Vieira,"Caracterização das argilas de Campos dos Goytacazes visando à fabricação de revestimento cerâmico semiporoso" (Doctor thesis, State University of the North Fluminense Darcy Ribeiro, 2001), 126.

5. P.S. Santos, *Ciência e tecnologia das Argilas* (São Paulo, SP: Edgard Blücher, 1989), 408.

6. S. Pracidelliand F.G. Melchiades, "A importância da composição granulométrica de massas para a cerâmica vermelha," *Ceram. Ind*., 2 (1/2) (1997),31- 35.

7. C.M.F. Vieira, H.S. Feitosa and S.N. Monteiro, "Avaliação da secagem de cerâmica vermelha através da curva de Bigot," *Ceram. Ind.*,8(1) (2003), 42-46.

8. C.M.F. Vieira, T.M. Soares and S.N. Monteiro, "Ceramic bodies for roofing tiles: characteristics and firing behavior," *Cerâmica*, 49 (2003), 245-250.

9. R. Gaidzinski, "Estudo do sazonamento de argilas para a utilização na indústria cerâmica" (Doctor thesis, Federal University of Rio de Janeiro, 2006), 179.

10. Associação Brasileira de Normas Técnicas - ABNT, Componentes Cerâmicos - telhas - terminologia, requisitos e métodos de ensaio, NBR 15310, Rio de Janeiro (2005).

Characterization of Minerals, Metals, and Materials 2016
Edited by: Shadia Jamil Ikhmayies, Bowen Li, John S. Carpenter, Jiann-Yang Hwang, Sergio Neves Monteiro, Jian Li, Donato Firrao, Mingming Zhang, Zhiwei Peng, Juan P. Escobedo-Diaz, and Chenguang Bai
TMS (The Minerals, Metals & Materials Society), 2016

FTIR SPECTROSCOPY OF SOME BRAZILIAN CLAYS

Maria das Graças da Silva-Valenzuela[1,2], Wang Shu Hui [1], Francisco Rolando Valenzuela-Díaz[1]

1) Polytechnic School, University of Sao Paulo, Sao Paulo, CEP 05508-030, Brazil.
2) Federal University of ABC, Santo André, Sao Paulo, CEP 09210-580, Brazil

Keywords: Montmorillonite FTIR, Kaolin FTIR, Clay minerals infrared.

Abstract

This work describes the FTIR spectroscopy of 05 bentonites and 03 kaolins from Brazil. All clay were previously dried at 60°C and sieved through the screens 200 and 325 mesh, before characterization by XRD and FTIR. Bentonite samples showed characteristic well-resolved peaks around 3620-3616 cm^{-1}, attributed to the OH stretching of structural hydroxyl groups. Kaolin samples showed characteristic peaks near 3690 cm^{-1} and 3675 cm^{-1}, assigned to the OH-stretching of the inner surface. A characteristic peak at 908 cm^{-1} has been previously linked to the presence of kaolinite, whose relative intensity in the spectra suggested differences in the kaolinite content in the clays. Peak around 780 cm^{-1} revealed the predominance of Fe^{3+}MgOH over Fe^{3+}AlOH and MgAlOH. Polycationic character of both bentonites and kaolins were clearly distinguished. Differences among the clay samples were linked to their chemical constitution, the amount of accessory minerals and the presence of structural substitutional cation(s).

Introduction

Clay minerals are important raw materials for several branch of the industry worldwide. These materials exhibit a ranging of physical and chemical properties, which may vary according to its origin and production batch. Properties such as swelling capacity, cation exchange capacity, color, chemical composition, adsorptivity, among others, are important variables in that materials, especially when intended for technological applications and may influence the characteristics of a particular finished product. The use of natural clays as raw material demands special control and depends of strict characterization to guarantee the reproduction of their properties. Smectites and kaolins are two kinds of clays, of sedimentary origin, available commercially in raw form at several deposits located in Brazil. The Brazilian smectites are usually polycationics and, as kaolins, often are composed of more than one clay minerals [2, 3] In this context, X ray diffraction and infrared spectroscopy techniques complement each other, allowing the access to the type of clay mineral structure and modifications caused in the structure through interaction with cations or any chemical substances [3 - 6].

In the present work, we investigate the use of X ray diffraction and infrared spectroscopy for characterization of eight natural Brazilian clays, in order to contribute for the improvement of these two techniques in the characterization of Brazilian clays.

Methodology

Clays

We studied 08 clays from deposits localized in three regions of Brazil: 03 polycationic bentonites (AM01-AM04) from northeastern, 01 bentonite (AM05) from south northeast, 01 kaolin (AM06) from northeastern, and 02 kaolins (AM07 and AM08) from north region. All clays were previously dried at 60°C and sieved through the screen 325 mesh before use.

X-ray diffraction

Diffractograms of the samples were collected using the powder method by a Philips X'Pert MPD diffractometer with CuK_{α} radiation, operating at 40 kV and 20 mA, at 2θ step scan of 0.1°/s.

ATR-FTIR spectroscopy

Infrared spectra of the samples were obtained using the Attenuated Total Reflectance-Fourier Transformed Infrared (ATR-FTIR) technique, by a Thermo Nicolet iS5 spectrometer, in the range of 4000-400 cm^{-1}. The powder of sample were analyzed without prior treatment.

Results and discussion

Diffraction patterns of the samples are shown in Figure 1. Analyzing the diffractograms of the five samples of smectite were observed peaks between $d_{(001)}$ = 5.71-5.87° which have been attributed to montmorillonite (MMT). These diffractograms also shown peaks between $d_{(001)}$ = 12.09-12.41° what is characteristic of kaolinite (K), which are present in this samples as accessory mineral. Meanwhile, the diffractograms of the three kaolin samples exhibited peaks of kaolinite in the range $d_{(001)}$=11.04-12.47°.

The diffractograms of AM01, AM02, AM03, AM04, AM06, and AM07 samples also revealed peaks in $d_{(001)}$=27.23° which were attributed to quartz. Other clay minerals, such as illite, feldspar and cristobalite are probably in the composition of some samples. Table 1 lists main peaks observed in the diffractograms of analyzed samples.

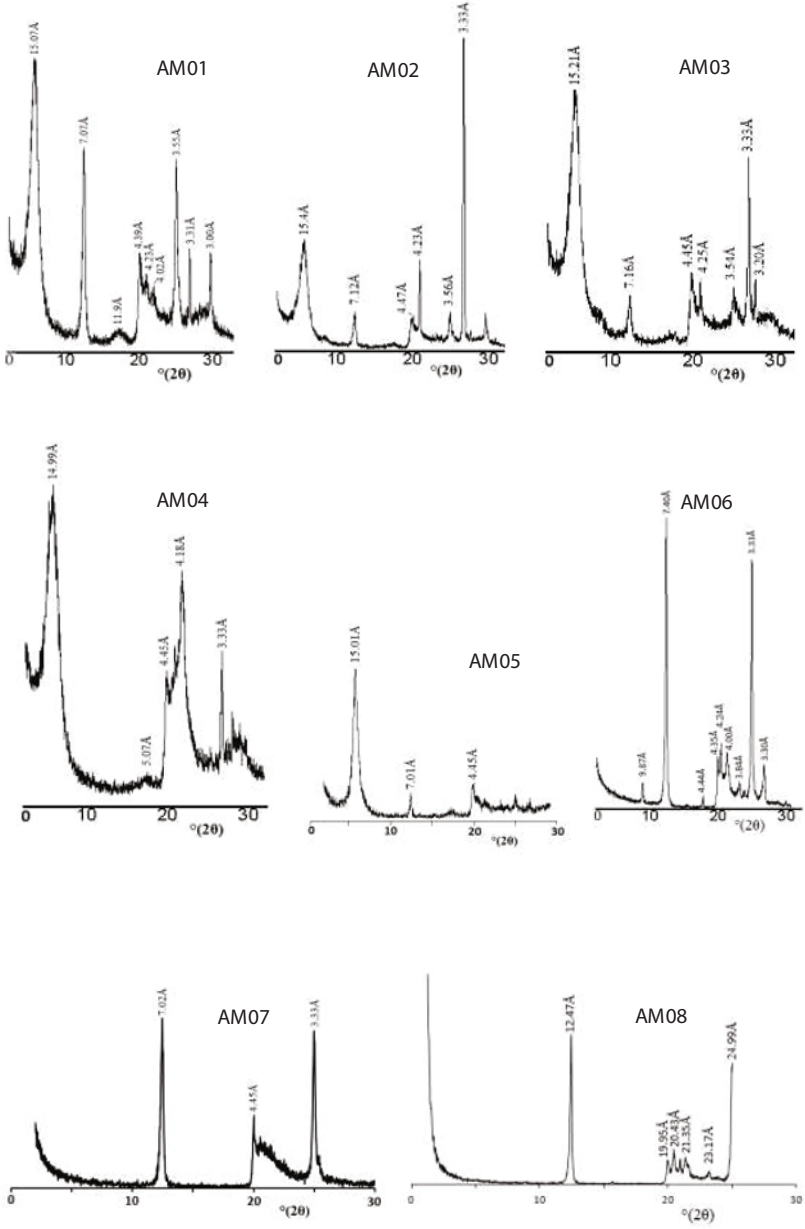

Figure 1. XRD of AM01-AM08 samples.

Table 1. Main peaks (Å) observed in the diffractograms of the samples.

Samples	AM01	AM02	AM03	AM04	AM05	AM06	AM07	AM08
Montmorillonite	15.07 3.00	15.4	15.21 4.45	14.99 4.45	15.01			
Kaolinite	7.07 4.39 3.55 2.54 2.46	7.12 4.47	7.16 3.54		7.02 4.45	7.40 4.44 4.35 3.84 3.56	7.02 4.45	7.08 4.46 4.35 4.02 4.17 3.83 3.56
Quartz	3.31	3.33	4.25 3.33	4.23 3.33		3.33	3.33	
Illite	5.07	9.98 5.01 3.56	4.98 3.20	5.07		4.35 4.24 3.30		
Cristobalite				4.18				
Feldspar	4.02							

FTIR spectra of layer silicates can be investigated by the OH stretching and OH bending vibrations absorbing near 3400-3750 cm^{-1} and 600-950 cm^{-1}, respectively [3]. Spectra of smectite samples are shown in Figure 2. The 1:1 structure of layer silicates such as kaolinite present three high frequency bands concerning to OH stretching of surface hydroxyl groups in 3697, 3669, and 3652 cm^{-1}, besides one band in 3620 cm^{-}1 attributed to OH stretching of inner group [3]. Table 2 lists all assigned peaks of the analyzed samples. At high frequency, the FTIR spectra of the five smectite samples analyzed in this work, showed some interesting differences in comparison with themselves. The samples AM01, AM02, AM03, and AM05 presented peaks near 3690 and 3650 cm^{-1} attributed to OH stretching of kaolinite, besides a peak in approximately 3620 cm^{-1}, which might be assigned to OH stretching of montmorillonite, typically occurring near 3629 cm^{-1}, or also might be attributed to OH inner group of kaolinite, what occur around 3620 cm^{-1} [3, 7]. This is an indication that these samples are a mixed of smectite and kaolinite. On the other hand, the AM04 spectra revealed only a band, in high frequency, next 3620 cm^{-1} assigned to montmorillonite [3].

The differences among spectra of the analyzed samples reinforce the results obtained by XRD diffractograms, and confirm that AM01, AM02, AM03, and AM05 samples are a mixture of montmorillonite and kaolinite, with this last clay mineral absent in the AM04 sample. The large band exhibited near 3400 cm^{-1} was attributed to adsorbed water [3]. The region among 700-950 cm^{-1}, in the FTIR spectra of the smectites, indicates the cation composition in the octahedral sheet [3]. For AM04 sample the peak near 791 cm^{-1} assigned to Fe(III)OHMg mode appear increased related the other smectite samples.

AM01 and AM05 samples exhibited increased peaks around 912 cm^{-1} what were attributed to AlAlOH mode for smectite samples, and to OH inner hydroxyl groups for kaolinite samples. This behavior seems to be related to the concentration of kaolinite in that samples, which is absent for AM04 and higher for AM01 and AM05. Other peaks attributed to the samples are shown in Table 2.

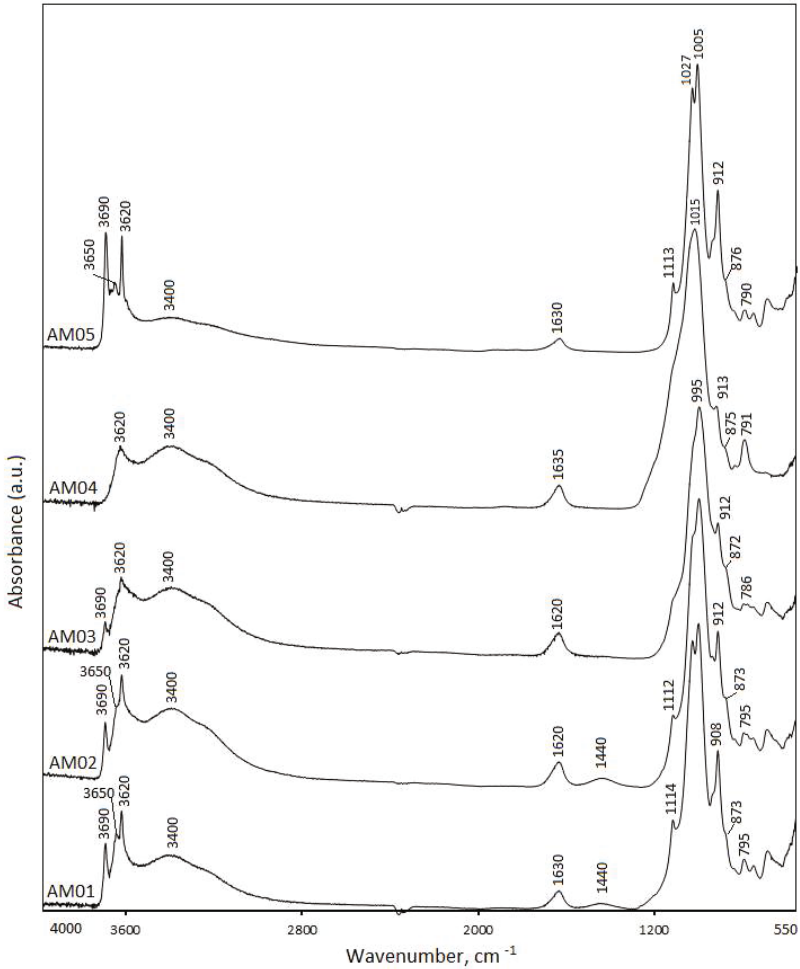

Figure 2. Infrared spectra of smectite samples (AM01-AM05).

Spectra of kaolinite samples are shown in Figure 3. The three FTIR spectra of the samples are very similar, presenting in high frequency peaks near 3690, 3670, and 3650 cm^{-1} attributed to OH stretching vibrations, and in 3620 cm^{-1} assigned to inner OH groups. Table 3 lists the attributed peaks to the FTIR spectra of AM06-AM08.

For all infrared spectra, the peak in approximately 2350 cm^{-1} was attributed to CO_2 of the room.

Table 2. List attributed peaks in the FTIR spectra of the smectite samples.

MMT	AM01	AM02	AM03	AM04	AM05
OH stretching	3690	3690	3690		3690
OH stretching	3650	3650	3650		3650
OH inner group	3620	3620	3620	3620	3620
	3400	3400	3400	3400	3400
	1630	1620	1620	1635	1630
	1440	1440			
	1114	1112			1113
	1030				
	1000	997	997	1005	1000
AlAlOH	908	912	912	913	912
Fe^{3+}AlOH	873	873	872	875	876
MgAlOH	836	836		836	839
Fe^{3+}OHMg	795	797	786	791	790

Table 3. Peaks assigned in FTIR of the kaolin samples

K	AM06	AM07	AM08
OH stretching	3690	3690	3690
OH stretching	3677	3677	3677
OH stretching	3653	3653	3653
OH inner group	3620	3620	3620
	1120	1115	1115
	1030	1029	1028
	1005	1004	1005
OH bending	938	936	938
OH inner group	912	912	912
	791	789	790
Surface OH	751	751	754

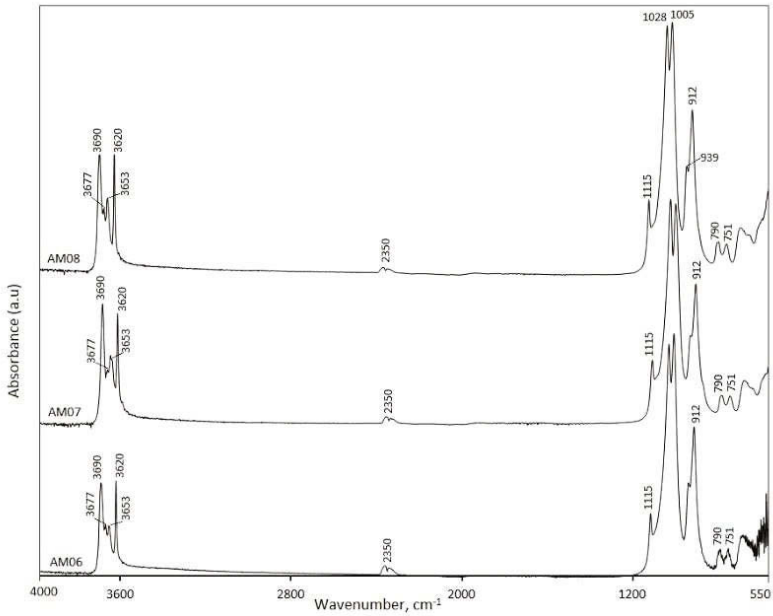

Figure 3. Infrared spectra of kaolin samples (AM06-AM08).

Conclusion

The study of the eight Brazilian clays by XRD and infrared spectra provided important informations about these materials. For the five analyzed smectites was possible to identify that four samples were constituted by two clay minerals, identified in the spectra as montmorillonite and kaolinite, and to estimate qualitatively their probable concentration by comparison of the spectra. For example, the large band of water near 3400 cm^{-1}, characteristic of smectites, appear wider for AM04, which is constituted mainly by smectite, and less wide for AM05, composed by montmorillonite and kaolinite probably with both of that clay minerals in similar concentration.

Acknowledgment

We are grateful to FAPESP for financial support.

References

[1] A. A. Cutrim, G. R. Marin-Cortés, F. R. Valenzuela-Díaz. Bentonitas da Paraíba. Ed. Interciencia. Rio de Janeiro. 2015.

[2] P. Souza-Santos. Tecnologia de argilas, aplicada às argilas brasileiras. Ed. Edgar Blucher. São Paulo. 1975.
[3] V. C. Farmer, The layers silicates: the infrared spectra of minerals. Mineralogical Society, London. pp 331-363. 1974.
[4] J. Bishop, J. Madejová, P. Komadel, H. Fro¨ Schl. The Influence of structural Fe, Al and Mg on the infrared OH bands in spectra of dioctahedral smectites. Clay minerals, 37 (2002) 607-616.
[5] J. Madejová and P. Komadel. Baseline studies of the clay minerals society source clays: Infrared methods. Clays and Clay Minerals, 49 (2001) 410-432.
[6] G. Sposito, R. Prost, J. P. Gaultier. Infrared spectroscopic study of adsorbed water on reduced-charge Na/Li-montmorillonites. Clays and clay minerals, 31-1 (1983) 9-16.
[7] P. Djomgoue and D. Npjopwouo. FTIR spectroscopy applied for surface clays characterization. Journal of Surface Engineered Materials and Advanced Technology, 3 (2013) 275-282.

Characterization of Minerals, Metals, and Materials 2016
Edited by: Shadia Jamil Ikhmayies, Bowen Li, John S. Carpenter, Jiann-Yang Hwang, Sergio Neves Monteiro, Jian Li, Donato Firrao, Mingming Zhang, Zhiwei Peng, Juan P. Escobedo-Diaz, and Chenguang Bai
TMS (The Minerals, Metals & Materials Society), 2016

PREPARATION AND CHARACTERIZATION OF MICROCAPSULES FROM PBSL/VMF2 NANOCOMPOSITE

Maria das Graças da Silva-Valenzuela[1,2], Guilherme Augusto Fabozzi[1], Felipe Cebukin[1], Helio Wiebeck[1], Francisco Rolando Valenzuela-Díaz[1], Shu Hui Wang[1]

[1]Polytechnic School, University of Sao Paulo, CEP 05508-030, Brazil.
[2]Federal University of ABC, Santo Andre, Sao Paulo, CEP 09210-580, Brazil

Keywords: Microcapsules, PBSL, Smectite, Nanocomposite

Abstract

In this work, nanocomposite films and microcapsules were prepared from a dispersion of poly(butylene succinate-co-lactate) (PBSL) and Brazilian clay (VMF2). A nanocomposite precursor solution was prepared by adding, under mechanic stirring, a solution of PBSL-5% to a dispersion of VMF2-0.8% in chloroform. Nanocomposite films were prepared by casting 10 mL of the nanocomposite precursor onto glass Petri dishes, then left overnight for solvent evaporation before drying in a vacuum oven. Microcapsules were obtained from the nanocomposite precursor by solvent diffusion method. PBSL and PBSL/VMF2 films and microcapsules thus prepared were characterized by optical microscopy, XRD, and SEM. XRD of VMF2 showed that this clay contains montmorillonite and kaolinite. XRD of the PSB/VMF2 nanocomposite showed intercalation of the montmorillonite, indicating that both clay minerals are finely dispersed within the polymer matrix. SEM of the microcapsules showed homogeneous spheres with particle sizes in the range 50-150 μm.

Introduction

Microcapsules made from biodegradable polymers constituting an auspicious way as possible delivery systems for many kinds of hydrophobics and hydrophilics substances, such as chemical and biochemical compounds. Composites and nanocomposites of several biopolymers has been studied with the aim of improving some of their properties. Poly(butylene succinate) (PBS) and its copolymers are materials candidate for application in delivery systems presenting good biodegradability and mechanical properties [1, 2]. The poly(butylene succinate-co-L-lactate) (PBSL) is a synthetic co-polymer of PBS produced by polycondensation of succinic acid, lactic acid, and butanediol [2]. Shibata et al. (2006) described some mechanical properties of blends of poly(L-lactide) (PLLA) with PBSL and PBS, concluding that such blends showed improvement in their properties relate pure PLLA, PBSL, and PBS [3]. Another way to improve properties of polymeric matrices is through nanocomposite formations, such as nanoclays, which are nanoparticles used as fillers or additives in polymers for various desired effects [4]. Smectites and kaolins are the most known Brazilian clays, which can be used as nanoclays presenting interesting properties for technological applications. In this study, we investigate the potential of PBSL in the preparation of microcapsule nanocomposites using a Brazilian clay as nanometric charge.

Methodology

Materials

We use the poly(butylene succinate-co-lactate) (PBSL) and a montmorillonite (MMT) tagged VMF2, as polymeric matrix and nanometric charge, respectively. PBSL was obtained from Mitsubishi Chemical Company, and VMF2 is a red clay from Bahia, Brazil. Chloroform P.A. and deionized water were utilized as solvents.

Preparation of PBSL/VMF2 nanocomposite

A nanocomposite precursor solution was prepared by adding, under magnetic stirring, a solution of PBSL-5% to a dispersion of VMF2-0.8% in chloroform.

Preparation of films and PBSL/VMF2 microcapsules

Nanocomposite films were prepared by casting 10 mL of the nanocomposite precursor onto glass Petri dishes, then left overnight for solvent evaporation before drying in a vacuum oven. Microcapsules were prepared based on emulsification-diffusion technique by addition of the nanocomposite solution to 0.5% polyvinyl alcohol solution (1/2, v/v) in a beaker, at mechanic stirring (1500 rpm) during 20 minutes [5, 6]. After, the mixture was left to rest for one hour for deposition of microcapsules obtained in the bottom of the beaker. The supernatant was retired and the microcapsules were washed with 300 mL of water, gently, for 5 minutes. Next, the supernatant was retired and the wash was repeated twice more. After wash, microcapsules were transferred to glass Petri dish, and dried in the oven at 30 °C, overnight.

X-ray diffractograms (XRD)

The analysis of VMF2, PBSL, and PBSL/VMF2 samples were performed by powder X-ray diffraction, using a Philips X'Pert MPD diffractometer with CuKα radiation, operating at 40 kV and 20 mA, at 2θ step scan of 0.1 °/s.

Optical microscopy and scanning electron microscopy (SEM)

We use a Zeiss stereomicroscope apparatus to observe form and homogeneity of microcapsules, and an Inspect F50 microscope equipment to analyze their structure, morphology and size average diameter.

Results and discussion

The X-ray curve patterns of VMF2 clay, PBSL co-polymer, and PBSL/VMF2 nanocomposite are shown in Figure 1. VMF2 sample presented two kinds of clay minerals, evidenced for the peaks in $d_{(001)}$=15.31 Å and $d_{(001)}$=7.14 Å attributed to montmorillonite and kaolin, respectively. The diffraction pattern of PBSL co-polymer was typical of an amorphous substance. The diffractogram of PBSL/VMF2 nanocomposite revealed a peak in $d_{(001)}$=16.53 Å assigned probably to montmorillonite, indicating that the polymer got into the clay sheets, forming a nanocomposite where the clay is intercalated. The kaolinite present in the VMF2 clay, and revealed in the diffractogram of this material, did not appear in the diffractogram of the nanocomposite. This could be due to exfoliation or small quantity of kaolinite.

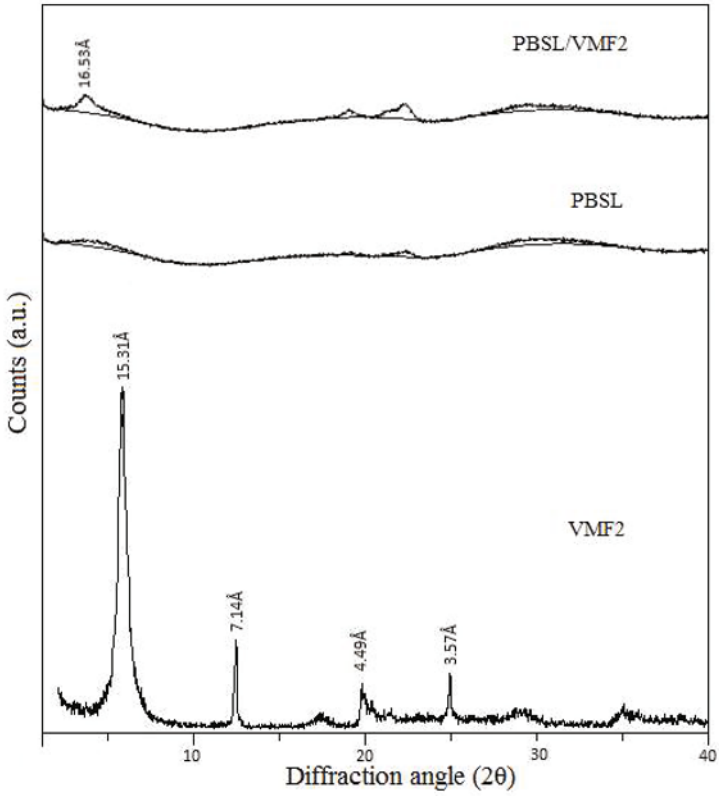

Figure 1. XRD curve patterns for VMF2, PBSL, and PBSL/VMF2.

The films obtained for PBSL polymer and PBSL/VMF2 nanocomposite were analyzed by SEM recording marked differences. The PBSL film showed a smooth surface but with several flaws due to little gaps, probably consequence of the rapid evaporation of the solvent during drying. The PBSL/VMF2 film presented a roughened surface, what was attributed to reinforcement of the clay in the polymeric matrix (data not shown). Figure 2 shows results obtained through optical microscopy. We observe that microcapsules exhibited spherical and homogeneous form (Figure 2a). Scanning electron microscopy revealed microcapsules with roughened surface and size diameter ranging 50-150 μm (Figure 2b).

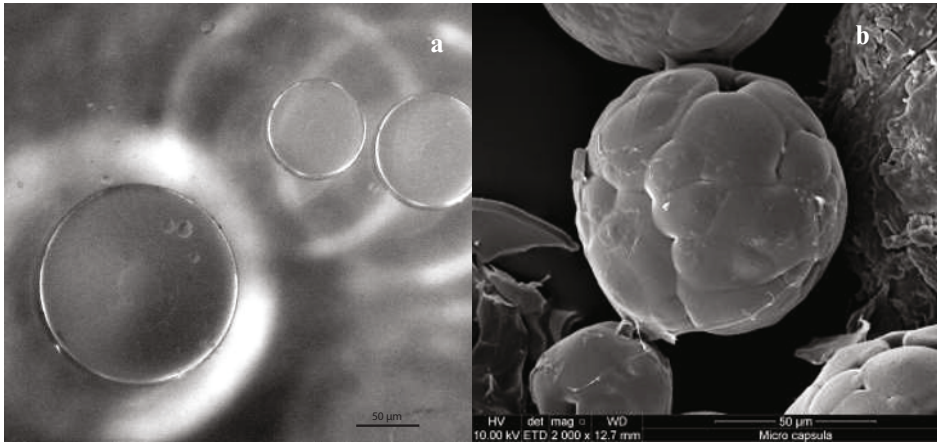

Figure 2. a) Image by optical microscopy, and b) micrograph by SEM of PBSL/VMF2 microcapsules.

Conclusions

The PBSL/VMF2 nanocomposite were used to prepare microcapsules aiming their application as delivery systems. The microcapsules presented a spherical and homogeneous form, a good average diameter range, and a roughened surface. Results showed that the nanocomposite was formed by the intercalation of montmorillonite clay mineral. The participation of kaolinite nanoclay in the nanocomposite formation must be better studied. The results described in this study indicated that the nanocomposite formed by PBSL and a Brazilian nanoclay has potential to be used as delivery systems.

Acknowledgment

We are grateful to FAPESP for financial support.

References

1. C. T. Brunner et al., "Performance of Biodegradable Microcapsules of Poly (butylene succinate), Poly (butylene succinate-co-adipate) and Poly (butylene terephthalate-co-adipate) as Dug Encapsulation Systems," *Colloids and Surfaces B: Biointerfaces*, 84 (2011), 498-507.
J. Xu and B. –H. Guo, "Microbial Succinic Acid, its Polymer poly(butylene succinate), and Applications," Plastics from Bacteria: Natural Functions and Application, ed. G. –Q. Chen (Berlin Heidelberg:©Springer Verlag, 2010), 347-388.
3. M. Shibata, Y. Inoue, and M. Miyoshi, "Mechanical Properties, Morphology, and Crystalization Behavior of Blends of Poly(L-lactase) with Poly(butylene succinate-co-L-lactate) and Poly(butylene succinate)," *Polymer*, 47 (2006), 3557-3564.
4. F. Uddin, "Clays, Nanoclays, and Montmorillonite Minerals*, Metallurgical and Materials Transactions A, 39A* (2008), 2804-2808.

5. D. Quintanar-Guerrero et al., “Influence of Stabilizing Agents and Preparative Variables on the Formation of Poly(D,L-lactic acid) Nanoparticles by an Emulsification-Diffusion Technique,” *International Journal of Pharmaceutics,* 143 (1996), 133-141.
6. M.G. Silva-Valenzuela et al., “Nanocomposite Microcapsules from Powders of Polyhydroxybutyrate (PHB), and smectite clays,” *Materials Science Forum,* 66 (2010), 794-798.

Characterization of Minerals, Metals, and Materials 2016
Edited by: Shadia Jamil Ikhmayies, Bowen Li, John S. Carpenter, Jiann-Yang Hwang, Sergio Neves Monteiro, Jian Li, Donato Firrao, Mingming Zhang, Zhiwei Peng, Juan P. Escobedo-Diaz, and Chenguang Bai
TMS (The Minerals, Metals & Materials Society), 2016

THERMAL PROPERTIES OF POLYPROPYLENE NANOCOMPOSITES WITH ORGANOCLAY AND DISCARDED BOND PAPER

Danilo Marin Fermino[1], Christiano Gianesi Bastos Andrade[1], Duclerc Fernandes Parra[2], Ademar Benevolo Lugão[2], Francisco R. Valenzuela Diaz[1]

[1]Department of Metallurgical and Materials Engineering - EPUSP (Escola Politécnica, Universidade de São Paulo)
Av. Prof. Mello Moraes, 2463, Cidade Universitária, CEP 05508-030, São Paulo, SP, Brazil;

[2]IPEN/CNEN (Nuclear and Energy Research Institute) Av. Prof. Lineu Prestes 2242, Cidade Universitária, Postal Code 05508-000, São Paulo, SP, Brazil.

Keywords: Polypropylene nanocomposites, Organophilic clay, Bentonite, Cellulose

Abstract

This work concerns the study of the effect of discarded bond paper on the thermal behavior of the polypropylene/organophilic clay nanocomposite. A brown polycationic bentonite from state of Paraíba, Brazil, was treated industrially with sodium carbonate to transform it into a bentonite which swells in water and then treated with ammonium chloride hexadecyltrimethylammonium to turn it into a swellable organoclay in organic liquids. Polypropylene with 3 % polypropylene graft compatibilizer (PP-g-AM) was mixed with 1 % and 2 % by weight of discarded bond paper and with 1% , 2% e 5 % by weight of organophilic clay using a twin-screw extruder. The specimens were prepared by the injection process. The nanocomposite specimens were characterized by XRD, SEM, and thermal analysis (ATG and DSC). The nanocomposites showed improved thermal properties compared with the polymer without filler.

Introduction

There has been increasing interest in preservation of the environment and sustainability of resources. So, the use of natural fibers is receiving renewed attention as an alternative to inorganic counterparts in materials technology. Particular consideration has been paid to cellulose fibers, which are the most abundant biomass resource on Earth [1].

The utilize of natural cellulosic fibers in composites have attracted the attention of researchers, manufactures and user agencies due to the consequence of exploitation of non-renewable resources and management of agro-industrial wastes leading to environmental and ecological balances. Certainly, natural cellulosic fibers are rapidly emerging as novel low cost materials for several industrial applications [2].

Natural fiber reinforced polymer composites have various applications, such as use in automotive industry, furniture, packaging and building construction fields. The main constituent of natural fiber is cellulose, which contains a huge number of polar hydroxyl groups that would lead to a highly hydrophilic property of fiber and a very poor interface between the natural fiber and polymer matrix. Compared with synthetic fibers, the advantages of using natural fiber in

composites are their low specific gravity, cheaper, renewability, biodegradability, and environmentally friendly [3-4].

Polymeric nanocomposites have attracted substantial scientific interest and developments over the last two decades with an enormous market opportunity especially for the automotives and packaging industries. It was based on layered silicates, principally montmorillonites (nanoclays), are the most commonly utilized reinforcing additives in thermoplastic polymers due to their nanoscale features giving rise to unique and superior combination of properties achievable at low loading, normally 1-5 %, compared to around 30-40 % in conventional polymer composites [5].

Polymer nanocomposites are polymers that have been reinforced with little quantities of nano-sized particles (nanofillers). These materials represent a radical alternative to conventional filled polymers. In contrast to conventional composites, where the reinforcement is on the order of micrometres, polymer nanocomposites are exemplified by discrete constituents on the order of a few nanometres. An important class of nanofillers involves nanoclays belonging to the smectite group, such as montmorillonite. Montmorillonite belongs to the family of 2:1 layered silicates. Its structure involves layers about one nanometer thick, each of which consists of two tetrahedral silica sheets fused to an edge-shared octahedral sheet of aluminium/magnesium oxide/hydroxide. To produce nanocomposite materials with best properties and performance, these nanoclays must be intercalated with the polymer matrix and also totally exfoliated [6].

The study of polymer organoclay nanocomposite due to its superior properties compared with pristine polymer has attracted main research and commercial interests. The inclusion of small concentrations of nanoparticles in polymers (< 5 wt. %) can have a significant impact on material properties.The increase in mechanical properties such as tensile strength and modulus, solvent resistance barrier properties and flame retardant are a couple of selected examples of the advantages provided by this new class of materials. But, to fully use this increase, it is necessary to achieve a relatively uniform dispersion of the clay nanoparticles within the polymeric host matrix [7-8].

During nanocomposites preparation by melt compounding initially an intercalation process of the polymer macromolecules into the interlayer spaces occurs and finally clay mineral exfoliation in the polymer matrix. This process is diffused control and requires a balance between shear rate and residence time to reach complete exfoliation. However, these requirements have some drawbacks, since polymer degradation can also take place [9].

Polypropylene/montmorillonite (PP–MMT) is one of the most frequently utilized nanocomposites to obtain property improvements produced in different forms and applications by means of a range of manufacturing processes at a relatively low cost. There is ample evidence that PP–MMT formed by melting processing is the most preferred method to produce nanocomposites for commercial use. The improvement on final properties usually depends on the degree of exfoliation, delamination, and clay dispersion [10].

A great extent of exfoliation is even more difficult to achieve in polypropylene (PP) than in other, more polar polymers. Nanocomposites cannot be prepared successfully from PP and an organophilic silicate (OMMT), a compatibilizer agent, usually a functionalized polymer like

maleated PP (MAPP), must also be added to the composite. The structure of PP/silicate composites is complicated even in the presence of a compatibilizer agent containing several structural entities in varying amounts [11-12].

Polypropylene clay nanocomposites are usually prepared by melt-blending, with organoclays and compatibilizers such as maleic anhydride (PP-g-MA). Compatibilizers are really required due to the huge polarity difference between the polyolefin matrix and the clay. PP-g-MA allows wetting of the clay surface by hydrogen-bond interactions between the anhydride functions and the oxygen atoms at the surface of the silicate layers. Normally, the morphology of clay/PP nanocomposite is a mixed intercalated/exfoliated structure [13-15]. The objective of this work is to obtain a polypropylene nanocomposite with using Brazilian clay and used bond paper for increasing thermal properties of this nanocomposite.

Materials and Methods

Isotactic polypropylene (iPP) with a melt flow index of 2.2 dg min^{-1} (230 ºC/2.16 Kg), was purchased from Braskem S.A., Brazil. An organophilic bentonite prepared with a commercial sodium bentonite (Chocolate Clay) from the state of Paraiba, Brazil, was used in this work. Four kilograms of discarded bond paper were collected and fragmented and placed in a plastic container with 40 liters of water. After 24 hours, this material was stirred with a mixer for 30 minutes at maximum speed of 2.800 rpm. After stirring the pulp was placed in a fabric bag and placed in a centrifuge to 2.300 rpm to facilitate drying. After centrifugation the paper pulp was passed on a 50 mesh sieve to reduce the size of the paper and then dried at 60 ºC for 72 hours. The organophilic clay and the paper with Irganox B215 FF (a blend of 0.2% of antioxidant and 0.4%, a thermal stabilizer) were manually mixed with coupling agent maleic anhydride (PP-g-MA), in a 3 wt % concentration to improve the clay adhesion to the polymer matrix.

A Mapplan Coperion twin screw extruder was used with a temperature range of 180 to 205 ºC and 800 rpm rotation. A Battenfeld TM 750/210 injection was used to manufacture the specimens for tensile strength. The temperature injection was 190ºC, and the mold temperature was 60ºC. For X-ray diffraction (XRD) was used the Diffractometer PANalytical X'Pert PRO, using Cu Kα radiation. Scanning electron microscopy was performed with an FEG FEI Inspect F50 instrument. The Balzers SCD 050 Sputter Coater was used to cover the samples with Au.

The melt and crystallization characteristics of the nanocomposites were studied with a Mettler Toledo DSC822^e differential scanning calorimeter (DSC). The specimens were subjected to temperatures of 25-280 ºC at a heating rate of 10 ºC min^{-1} in a nitrogen atmosphere. Melting enthalpy value for 100% crystalline PP is 209 kJ kg^{-1}. To study the nanocomposite mass loss, the Mettler Toledo SDTA851^e thermogravimetric analysis was used. The specimens were submitted to temperatures of 25 to 650 ºC at a heating rate of 10 ºC min^{-1} in an inert nitrogen atmosphere (N_2 flow 50 mL min^{-1}) and an oxygen atmosphere (O_2 flow 50 mL min^{-1}).
The nanocomposites identification is presented in Table I.

Table I. Identification specimens

Specimen	Identification
PP	Polypropylene, pristine
PP AM	Polypropylene with PP-g-MA
PPA 1%	Polypropylene with 1 % in weight of organophilic clay
PPA 2 %	Polypropylene with 2 % in weight of organophilic clay
PPC 1%	Polypropylene with 1 % in weight of cellulose
PPC 2%	Polypropylene with 2 % in weight of cellulose
PPAC 1%	Polypropylene with 1 % in weight of organophilic clay and 1 % in weight of cellulose
PPAC 2%	Polypropylene with 2 % in weight of organophilic clay and 2 % in weight of cellulose

Results and Discussion

Figure 1 shows the X-ray diffraction patterns of the nanocomposites with "organophilic clay". Table II presents the basal spacing values that were obtained for the "chocolate" clay and the nanocomposites.

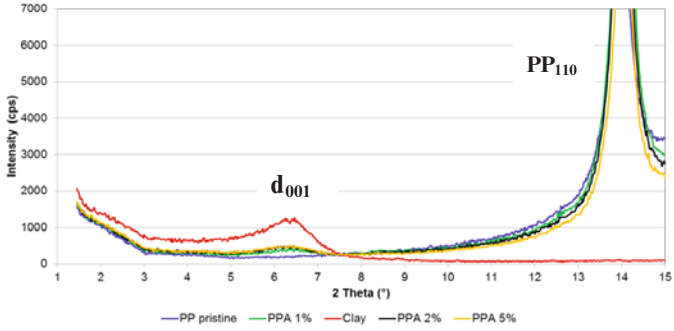

Figure 1. X-ray diffraction patterns of nanocomposite with organophilic clay.

Table II. Values of basal spacing obtained from the curves in the Figure 1

Specimens	d_{001} (Å)
Organophilic clay	13.70
PPA 1 %	13.87
PPA 2 %	14.28
PPA 5 %	14.11

Samples of the nanocomposites (PPA 1 %, PPA 2 % and PPA 5 %) clay peaks have suffered slight increase in the values of the interplanar distances. It was observed that there was an accentuated decrease in peak intensity for the organophilic clay nanocomposites because these peaks practically disappeared. This reduction in intensity of the main peak clay in relation to

nanocomposites suggest a disorganization of the clay lamellae, indicating a probably formation of exfoliated nanocomposites structures.

According Yadong et al. (2014) [16] intensity and the reduction in peak broadening indicate that the stacked plates becomes more disordered and partial exfoliation of the clay occurs. These results suggest that the dispersion of the clay plates within the polypropylene matrix is significantly increased in the presence of PP-g-MA.

Figures 2 and 3 show two micrographs of nanocomposite PPA 1 % and PPAC 1%, respectively. With SEM it was possible to observe the homogeneous distribution of the clay and cellulose fibers added to the polymer matrix.

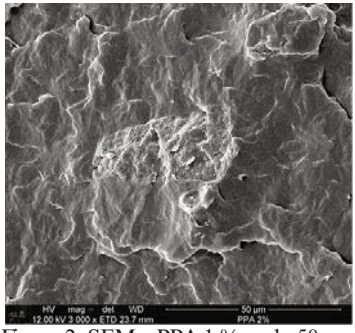

Figure 2. SEM – PPA 1 % scale 50 m

Figure 3. SEM – PPAC 1 % scale 50 m

Table III shows the small changes in the crystallization temperature of PP pristine in relation to the nanocomposites with organoclay clay and cellulose; the difference of temperature in 3 °C in the nanocomposites is not significant. Table IV shows small changes in the melting temperatures of the nanocomposites of organophilic clay and cellulose. There was a temperature change of 2 °C in the nanocomposites in relation PP Pristine. Table V are presented the crystallinity values for the nanocomposites from DSC curves. The additions of nanoparticles in semi-crystalline polymers, in general, not affect significantly the crystallinity of the nanocomposite materials. It has been proposed, however, that these particles produce a large number of nucleating sites and in turn reduce the size of resulting spherulites [17].

Table III. Crystallization temperatures for the nanocomposites from DSC curves.

Sample	*Temperature (°C)*
PP pristine	125
PPAM	126
PPA 1 %	128
PPA 2 %	128
PPA 5 %	128
PPC 1 %	127
PPC 2 %	128
PPAC 1 %	128
PPAC 2 %	128

Table IV. Melt temperatures for the nanocomposites from DSC curves.

Sample	*Temperature* (ºC)
PP pristine	175
PPAM	176
PPA 1 %	178
PPA 2 %	176
PPA 5 %	176
PPC 1 %	177
PPC 2 %	175
PPAC 1 %	176
PPAC 2 %	176

Table V. Crystallinity values (%) for the nanocomposites from DSC curves.

Sample	*Crystallinity (%)*
PP pristine	45
PPAM	48
PPA 1 %	44
PPA 2 %	44
PPA 5 %	44
PPC 1 %	46
PPC 2 %	47
PPAC 1 %	47
PPAC 2 %	46

Figure 4 shows the TG decomposition curves in an inert atmosphere (N_2) for the hybrid nanocomposites with organoclay and cellulose. The thermal stability is the same for the nanocomposites with clay. For PP pristine and PPAM, the decomposition temperature was smaller in relation to nanocomposites, demonstrating that the clay and cellulose promoted enhanced, improving the thermal stability of the hybrid nanocomposites.

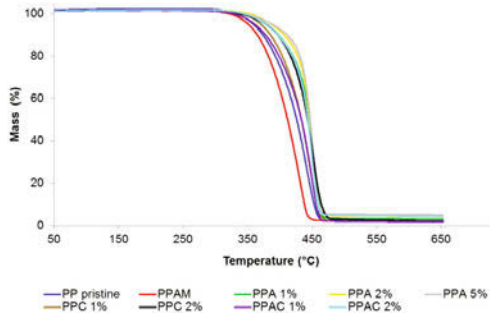

Figure 4. TG curves in a nitrogen atmosphere at a heating rate of 10 ºC min^{-1}.

Figure 5 show the TG decomposition curves are presented in a reactive atmosphere (O_2) for the hybrid nanocomposites with organoclay and cellulose. In an oxidizing atmosphere, the samples with PP pristine, PPAM, hybrid nanocomposites with clay and cellulose decompose into similar profiles.

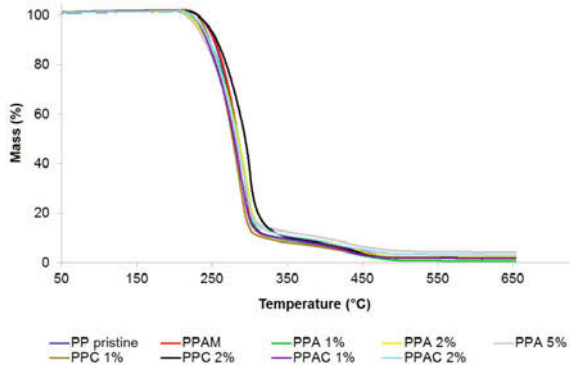

Figure 5. TG curves in a oxygen atmosphere at a heating rate of 10 ºC min^{-1}.

Conclusions

There was probably formation of nanocomposites exfoliated clay as demonstrated in the test X-ray diffraction. The SEM showed homogeneous distribution of the clay added to the polymer matrix. There were no significant changes in the thermal analysis by DSC for the hybrid nanocomposites of clay and cellulose. TG analysis the clay and cellulose promoted enhanced, improving the thermal stability of the hybrid nanocomposites in relation PP pristine.

Acknowledgments

The authors acknowledge CNPQ and CAPES for financial support and the Reimax Polymers Company.

References

[1] S. Ifuku and H. Yano, “Effect of a silane coupling agent on the mechanical properties of a microfibrillated cellulose composite”, *International Journal of Biological Macromolecules,* 74 (2015), 428-432.
[2] A. Pappua, V. Patil, S. Jain, A. Mahindrakar, R. Haque and V. K. Thakur, “Advances in industrial prospective of cellulosic macromolecules enriched banana biofibre resources: A review”, *International Journal of Biological Macromolecules*, 79 (2015), 449-458.
[3] L. He, W. Li, D. Chen, D. Zhou, G. Lu and J. Yuan, “Effects of amino silicone oil modification on properties of ramie fiber and ramie fiber/polypropylene composites”, *Materials and Design*, 77 (2015), 142-148.

[4] V. Khoshkava, H. Ghasemi and M. R. Kamal, "Effect of cellulose nanocrystals (CNC) on isothermal crystallization kinetics of polypropylene", *Thermochimica Acta*, 608 (2015), 30-39.
[5] S. Al-Malaika, H. Sheena , D. Fischer and E. Masarati, "Influence of processing and clay type on nanostructure and stability of polypropylene clay nanocomposites", *Polymer Degradation and Stability*, 98 (2013), 2400-2410.
[6] A. Ladhari, H. B. Daly, H. Belhadjsala , K. C. Cole and J. Denault, "Investigation of water absorption in clay-reinforced polypropylene nanocomposites", *Polymer Degradation and Stability*, 95 (2010), 429-439.
[7] M. Ataeefard and Siamak Moradian, "Surface properties of polypropylene/organoclay nanocomposites", *Applied Surface Science*, 257 (2011), 2320-2326.
[8] T. Koukoulas, W. R. Broughton and P. Woolliams, "Assessment of nanoparticle loading and dispersion in polymeric materials using optical wavefront correlation", *Polymer Testing*, 44 (2015), 57-65.
[9] A. S. Abreu, M. Oliveira and A.V. Machado, "Effect of clay mineral addition on properties of bio-based polymer blends". *Applied Clay Science*, 104 (2015), 277-285.
[10] L. G. Furlan, C. I. Ferreira, C. Dal Castel, K. S. Santos, A. C. E. Mello, S. A. Liberman, M. A. S. Oviedo and R. S. Mauler, "Effect of processing conditions on the mechanical and thermal properties of high-impact polypropylene nanocomposites", *Materials Science and Engineering A*, 528 (2011), 6715-6718.
[11] Z. Dominkovics, J. Hári, E. Fekete and B. Pukánszky, "Thermo-oxidative stability of polypropylene/layered silicate nanocomposites", *Polymer Degradation and Stability*, 96 (2011), 581-587.
[12] D. D. J. Rousseaux, M. Sclavons, P. Godard and J. Marchand-Brynaert, "Tuning the functionalization chemistry of polypropylene for polypropylene/clay nanocomposites", *Reactive & Functional Polymers*,72 (2012), 17-24.
[13] S. Zhu, J. Chen, Y. Zuo, H. Li and Y. Cao, "Montmorillonite/polypropylene nanocomposites: Mechanical properties, crystallization and rheological behaviors", *Applied Clay Science*, 52 (2011), 171-178.
[14] M. R. Abadchi and A. Jalali-Arani, "Crystallization and melting behavior of polypropylene (PP) in (vulcanized nanoscale polybutadiene rubber powder/PP) polymer-nanocomposites", *Thermochimica Acta*, 617 (2015), 120-128.
[15] M. Ataeefard and S. Moradian, "Surface properties of polypropylene/organoclay nanocomposites", *Applied Surface Science*, 257 (2011), 2320-2326.
[16] LV. Yadong, Y. Huang, M. Kong, J. Yang, Qi. Yang and G. Li, "Creep Lifetime Prediction of Polypropylene/Clay Nanocomposites Based on a Critical Failure Strain Criterion", *Composites Science and Technology*, 96 (2014), 71-79.
[17] W. Xu, G. Liang, H. Zhai, S. Tang, G. Hang and E. P. PAN, "Preparation and Crystallization Behavior of PP/PP-g-MAH/Org-MMT Nanocomposite", *European Polymer Journal,* 39 (7) (2003), 1467-1474.

Characterization of Minerals, Metals, and Materials 2016
Edited by: Shadia Jamil Ikhmayies, Bowen Li, John S. Carpenter, Jiann-Yang Hwang, Sergio Neves Monteiro, Jian Li, Donato Firrao, Mingming Zhang, Zhiwei Peng, Juan P. Escobedo-Diaz, and Chenguang Bai
TMS (The Minerals, Metals & Materials Society), 2016

INCORPORATION OF WASTE CERAMIC BLOCKS IN STRUCTURAL CERAMICS

Orley Magalhães de Oliveira[1,2], Maria das Graças da Silva-Valenzuela[1, 3], Christiano Gianesi Bastos Andrade[1], Antonio Hortêncio Munhoz Junior[4], Francisco Rolando Valenzuela-Díaz[1]

1) Polythecnic School, University of Sao Paulo, Sao Paulo, CEP 05508-030, Brazil.
2) IFBA - Federal Institute of Education , Science and Technology of Bahia - Campus Vitória da Conquista
3) Federal University of ABC, Santo André, Sao Paulo, CEP 09210-580, Brazil
4) Mackenzie Presbiterian University

Keywords: Structural Ceramics, manufacturing, waste, Industry.

Abstract

In Brazil, Ceramics Industries produce bricks and ceramic tiles in practically all the country. In the southwestern region of Bahia are located some of these industries. A considerable proportion of the material produced do not pass the quality control for not having a uniform visual appearance or have cracks. These burned pieces are generally discarded, resulting in a big quantity of waste. The objective of this work is the characterization of this industrial waste and thus consign them to other industrial applications. Our results demonstrate that the burned waste have potential to be used for incorporation in common clay for structural ceramics, thereby avoiding its disposal in nature and reducing this environmental liability. Experimental bodies were tested with different quantities of waste. The common clay and the burned waste were characterized by XRD, TG/DTA, and SEM. The burned specimens were tested for mechanical strength, water absorption, bulk density, and apparent porosity. An incorporation of 10% of waste furnished the best results.

Introduction

Many of the buildings in Brazil, mainly from homes construction, involves the use of bricks and tiles made from common clay [Cabral, et al. 1992]. The production systems of bricks and tiles in Brazil does not usually involve modern production systems and that result in a great quantity of broken burned products. The objective of this study is to evaluate the potential use of such kind of discarded burned material in the production of bricks and tiles by their incorporation in common clay. The common clay and the burned waste material comes from a brick and tile factory located near the city of Vitoria da Conquista, Bahia State, Brazil.

Methodology

Samples of common clay and of the burned waste were collected in a ceramic facility in the city of Encruzilhada, 90 km from the city of Vitória da Conquista, Bahia's State, Brazil. The common clay was dried at 100 ° C and then dry grinded in a ball mill until passing Taylor 80 sieve (0.18 mm). The burned waste was also dry grinded in a ball mill until passing Taylor 80 sieve.

X-ray diffraction

Diffractograms of the samples were collected using the powder method by a Philips X'Pert MPD diffractometer with CuK_{α} radiation, operating at 40 kV and 20 mA, at 2θ step scan of 0.1°/s.

Thermal analysis:

Differential Thermal analysis and Thermal Gravimetric Analysis were performed by a DTA/TGA STA409C NETZSCH. The heating rate was 10 °C / min in a nitrogen atmosphere. The initial and final temperatures of the analysis were 20 °C and 1300 ° C respectively.

Samples preparation:

Test samples were prepared with addition of 0.0 %; 5.0 %; 10.0 %; 20 %; and 30 % in weight of burned waste. The mixtures were homogenized manually, humidified up to 7.0% humidity and pressed in steel mold at 25 MPa. The dimensions of the samples were 6.0 cm x 2.0 cm x 0.5cm. Twenty specimens were pressed for each proportion of incorporation. After pressing, the specimens were dried at room temperature for 24 h and at 110 °C, also for 24h. Ten dried specimens were tested for flexural mechanical strength and ten were burned at 950 °C (10 °C/min). After cooling the samples were tested for flexural strength and ceramic properties.

Ceramic properties

Water absorption, apparent porosity and apparent density were obtained by measuring the dry, humid and immerse weight of the samples Souza Santos, 1992]. Three points flexural strength was performed using a Qtest DXL 022 896/039.testing machine.

Results and discussion

Diffraction pattern of the common clay is shown in Figure 1, and of the burned waste in Figure 2.

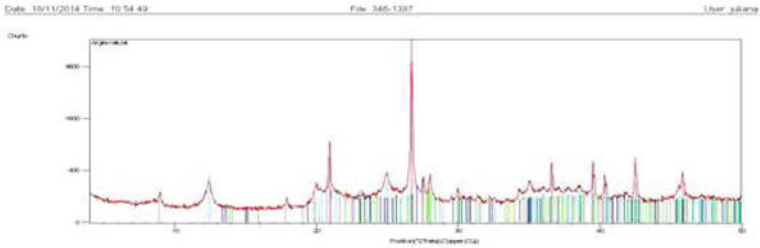

Figure 1. Diffratogram of the common clay.

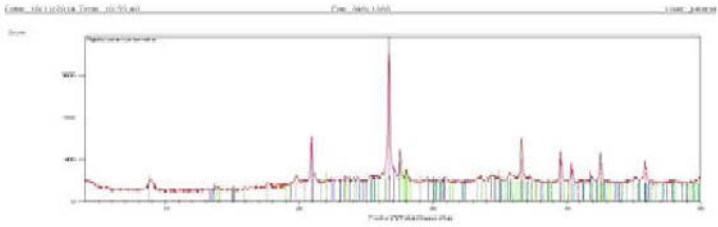

Figure 2. Diffratogram of the burned waste.

The common clay and the burned waste presented quartz, albite, muscovite and microcline. Only the common clay presented kaolinite. After common clay's burn, the kaolinite transforms into amorphous metakaolin and so, not appears in the diffractogram of the burned waste.
DTA/TG curves of the common clay are shown in Figure 3, and of the burned waste in Figure 4.

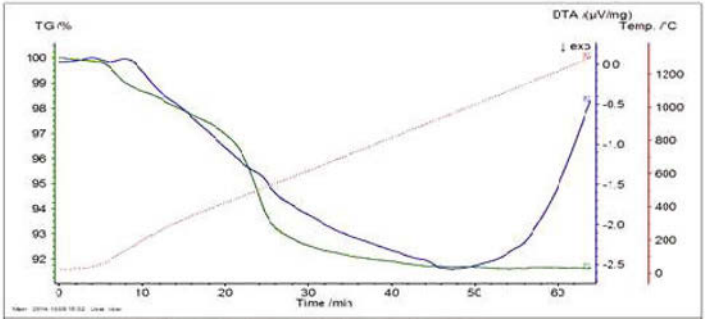

Figure 3. DTA/TG curves of the common clay.

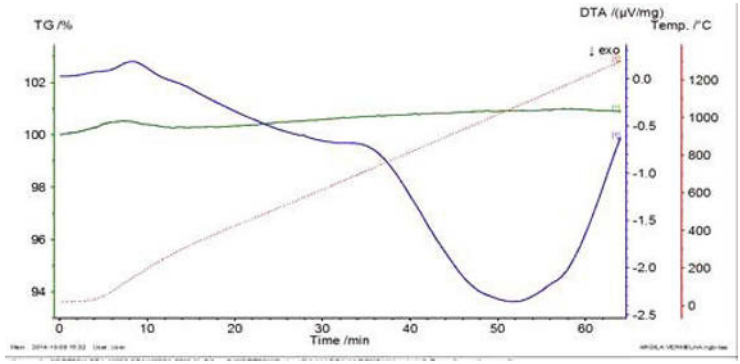

Figure 4. DTA/TG curves of the burned waste.

The common clay presents a weight loss of near 9% while de burned clay, as expected, practically not presents weight loss. At the common clay's DTA curve the kaolinite dehydroxilation is not well defined indicating no predominance of kaolin in the common clay.

In Table I are presented the flexural strength (after drying and after burning), water absorption, apparent porosity and apparent density of the burned specimens

Table 1. Ceramic properties.

% waste incorporations	**0.0**	**5.0**	**10.0**	**20.0**	**30.0**
Flexural strength after drying (MPA)	2.1	1.3	1.1	1.1	0.3
Flexural strength after burning (MPa)	4.6	1.9	2.4	1.4	0.4
Water absorption (%)	13.5	15.1	13.8	15.3	16.4
Apparent Porosity (%)	26.6	28.7	26.9	28.9	30.5
Apparent density (g/cm^3)	1.97	1.90	1.96	1.91	1.86

The dried specimens with 5.0 to 20.0% incorporation of waste presented similar flexural strengths, with values between 1.1 MPa and 1.3 MPa. Those values are lower than the value of the clay without waste but within the limits presented by Souza Santos [1992] for use in structural ceramics. The specimens with 30.0 % incorporation presented a very low value of 0.3 MPa. The specimens, with waste, with the highest value for flexural strength after burning was those with 10.0% of waste incorporation (2.4 MPa). Value lower than the value of the specimens without waste but within the limits presented by Souza Santos [1992] for use in structural ceramics. The water absorption of all the specimens were lower than the maximum of 20.0% recommended by Souza Santos for use in structural ceramics. The apparent porosity was not much affected by

the waste content, varying from 26.6 % for the specimens without waste to 30.5 % for the specimens with 30 % of waste incorporation. The apparent density was not much affected by the waste content, varying from 1.90 g/cm^3 for the specimens with 5.0 % of waste incorporation to 1.97 g/cm^3 for the specimens without waste incorporation.
The proportion that presented the best ceramic properties was 10%, by weight, as it has the highest flexural strength after burning.

Conclusion

It was founded a percentage of 10 % by weight of incorporation for the reuse of structural ceramic waste for the composition of a new ceramic product obtained from these mixtures. The "green" products will provide savings for clay used, avoiding the disposition of burned fragments of discarded products in land fields. .

Acknowledgment

We are grateful to FAPESP for financial support.

References

Marsis Cabral Junior, Anselmo Ortega Boschi,José Francisco Marciano Motta, Luiz Carlos Tanno, Ayrton Sintoni, José Mário Coelho, Marcelo Caridade; Panorama e Perspectivas da Indústria de Revestimentos Cerâmicos no Brasil, **Cerâmica Industrial**, Volume 15 - Número 3 - Maio/Junho – 2010

SOUZA SANTOS, P. de S. **Ciência e Tecnologia de Argilas**. Edgard Blucher: São Paulo, 1992.

Characterization of Minerals, Metals, and Materials 2016
Edited by: Shadia Jamil Ikhmayies, Bowen Li, John S. Carpenter, Jiann-Yang Hwang, Sergio Neves Monteiro, Jian Li, Donato Firrao, Mingming Zhang, Zhiwei Peng, Juan P. Escobedo-Diaz, and Chenguang Bai
TMS (The Minerals, Metals & Materials Society), 2016

SOLIDIFICATION OF DREDGED SLUDGE BY HYDRAULIC ASH-SLAG CEMENTITIOUS MATERIALS

Shu-Jing ZHU[1,3], Ying Qin[2], Jiann-Yang Hwang[1,3]

[1]Department of Resource and Environment Science, R&D Center of Wisco, Wuhan, 430080, P. R. China;
[2]School of Science, Wuhan University of Technology, 430070, Wuhan, China;
[3]Department of Materials Science and Engineering, Michigan Technological University Houghton, Michigan 49931-1295

Keywords: Solidified treatment, California Bearing Ratio (CBR), Cementitious, Dredged sludge

Abstract

Solidification treatment is used to treat hazardous wastes for disposal and to remediate the contaminated land. It is an increasingly popular technology for redevelopment of brown fields since treated wastes can often be left on-site, which can improve the site's soil for subsequent construction. In order to find home for the dredged sludge from the Pearl River Estuary Channel in China, the potential uses of treated dredged sludge by solidification treatment as valuable structural fill was investigated. Structure fills were prepared under various formula and curing conditions. Modulus of elasticity was detemined at 7 days, 14 days and 28 days with different types of load application. Atterberg limit, compactibility and CBR values are reported. The relationship between the microstructure and engineering properties of treated sludge are examined. The results clearly show the technical benefits by stabilizing soft soils with Hydraulic ash-slag cementitious materials. XRD and DTA-TG tests were carried out on certain samples to characterize the hydraulic compounds formed.

Introduction

The Pearl River estuary is the land that housed the Port of Guangzhou City, one of the largest ports on the South China. There are 2-3 million cubic meters of the sludge in the estuary which has to be removed annually to satisfy the primary navigation and to prevent or control the flood. The disposal of the sludge has been a problem.

Materials are required for the marine construction and environmental clean up in the area. Stabilized materials are required to improve sub-grades, capping layers or sub-bases for road projects and others [1]. Conventional materials such as cement, aggregates fibers and bricks are lacking locally. They have to be imported and are quite expensive. There is a

need to find alternative low cost blend materials which do not require special skills and equipment for their fabrication.

In this work the possibility of solidified dredged sludge was investigated. Soil based construction blocks have been used in North Africa for centuries, especially in rural regions and the desert [2]. This provides a direction for the study.

Strength tests in uniaxial compression, in indirect (splitting) tension and flexure were carried out on samples to which various percentages of hydraulic ash-slag cementitious material were added. Flexure strength was tested at 7 days, 14 days and 28 days and the California Bearing Ratio (CBR) values at the same curing time were also reported. In addition, X-ray diffraction (XRD) and Differential Thermal Analyzer–Thermogravimetric (DTA-TG) tests were carried out for the three kinds of soil stabilized with 9.2% binder added in order to study the characteristics of the various hydraulic compounds formed.

Materials

Dredged Sludge

The properties of dredged sludge used for this study are given in Table 1. The XRD analysis of it was also carried out and the results are presented in Fig.1. The main mineralogical constituents of the soils are quartz, calcite ($CaCO_3$) and montmorillonite ($Al_2O_34SiO_2 \cdot H_2O$) with small amounts of muscovite ($KAl_2Si_2Al_2O_3\text{-}10(OH)_2$) and plagioclase [2].

Hydraulic Ash-Slag Cementitious Material

The hydraulic ash-slag cementitious material used in the investigation is a patented chemical activator made by Wuhan University. It is a kind of hydraulic ash-slag cement material which was made up of some pozzolanic concrete dust, some byproduct of alkali industry, high blast furnace slag, some chemical agent and nearly 80% fly ash. The main mineralogical constituents are 1:$CaMgSi_2O_7$; 2: $CaAl_2Si_2O_3$; 3: $CaAl_2SiO_7$; 4: $CaAlSiAlO_7$; 5: $Ca(OH)_2$; 6: $CaSiO_3$; 7: $CaAl_4O_7$. It can be seen that the mineralogical constituents are very complex in which we can see AFm or AFt included .

Table 1. Properties of Perl River dredged sludge.

L_L (%)	P_L (%)	P_I (%)	Moisture (%)	dry density (g/cm^3)	density (g/cm^3)	G_s	C_c	q_u (kPa)	e_0
54	28	26	61.5	1.9	1.19	2.72	0.98	2.0	1.85

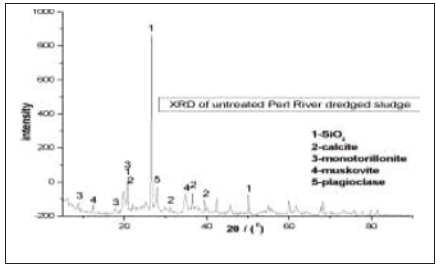

Fig. 1. XRD results of Perl River dredged sludge.

Experimental Procedure

All index property tests were performed in accordance with the standard for soil test method (GB/T 50123-1999). Preliminary tests such as compressive strength in the dry state and after 24h immersion in water were first conducted on the soil blocks without stabilization. Chemical stabilization was investigated by adding 7.6%, 8.4% and 9.2% of binder by weight of soil and its effect on compressive and splitting strength at different curing times was analyzed.

Samples for testing are prepared by first drying the soil in an oven, and a homogeneous mixture obtained by blending the required amount of Binder with the dry soil in a mechanical mixer before adding water and further mixing. The mixture is put in a normalized Proctor mould, covered with a plastic sheet for 24h before being demoulded and then left in the air laboratory until the age of testing.

The test specimens were prepared in two different batches. The first batch was used for microscopic test. The mix was cast into a 70.7×70.7×70.7 mm mold by hand for the strength test and cylindrical specimens (Ø=150mm, H=120mm) were used to get the CBR values, the strength test specimens were prepared with the static compaction (GB177-86) and the CBR specimens were prepared based on the standard of China Road (JTJ051-93).

After molding, test specimens were cured in a moisture chamber with a temperature of 20± 1°C and RH>96%. After a certain period of curing in the above- mentioned trial environments, the specimens was tested for compressive strength and CBR values. At the same time the paste specimens of the was analyzed by X-ray diffraction analysis (XRD) and sdifferential scaning construe–thermogravimetric（DTA-TG) , and a composition and structure for new formations of the cementing matter was determined.

Results and Discussion

Strength Tests

Fig.2 shows that the development of the unconfined compressive strength in relation to curing time. It can be seen that the increase of the Binder content increases the compressive strength because the hydration products of the Binder fill in the pores of the matrix and enhance the rigidity of its structure by forming a large number of rigid bonds connecting sand particles. And the effect of the age of curing on the compressive strength is shown on Fig.2. It can be clearly seen that the relative compressive strength obtained after 7 days of curing was about 70% of that obtained after 14 or 28 days of curing for up to 9.2% of Binder content. However, the relative compressive strength at 14 and 28 days for 7.6%, and 8.4% of Binder content as compared to that at 7 days was only about 65%. This shows that higher Binder content than 9.2% need a period of curing of 14–28 days for the complete strength to be developed. The higher content of binder is, in certain cases, the more effective it is. But the problems associated with the use on sullage would need to be addressed. Some of these problems may be: immersion time, practical problems of spreading and mixing these large quantities of sullage and decreased water demand. There are soils (sullage) yielding less satisfactorily stabilized results with high percentages of Binder.

CBR Tests

Table 2 shows the 28-day old (24-h soaked) CBR values in relation to Binder content. It can be seen that the CBR value usually increased by the increased of the binder content. The relation of compressive strength vs CBR is shown in Fig.2. It can be seen that a linear relationship between CBR and strength exists although this applies strictly to the soils examined. Similar relationships have been found for cement-stabilised soils by Maclean as referred to in Ref and S. Kolias. [5-8].

Table 2. CBR tests results.

Samples	Atterberg Limits		dry density (g/cm^3)	Water Contents (%)	CBR values(%) (each BINDER content)		
	ωL (%)	ωp (%)			7.6%	8.4%	9.2%
Sullage	46.5	23.4	1.18	32.9	104	141	141

XRD Investigation

In Fig.3, representative X-ray diagrams are presented for 7-day and 28-days old specimens stabilized with 9.2% Binder. The possible hydraulic compounds that have appeared are products of the Binder and/or soils hydration reaction. These include various types of tobermorites, calcium aluminium silicate hydrates like gismodine ($CaAl_2Si_2O_8$-$4H_2O$), etc., as well as the products resulted from the reaction of the SiO_2 in clay with the portlandite released during the hydration of Binder. In Fig.3 it is

observed that after curing for 28 days the sample containing 9.2% Binder appears to have decreased amount of tobermorites, but increased amounts of C_3AH_6 ($3CaO\text{-}Al_2O_3\text{-}6H_2O$) and C_2AH_8 ($2CaO\text{-}Al_2O_3\text{-}8H_2O$)). This is attributed to the effect of the addition of Binder, offering easy production of hydraulic compounds, like tobermorites especially at the early ages and made some other hydraulic compounds at the later curing ages. A comparison between XRD diagrams of samples cured for 7 days and 28 days (Fig.3) shows that there is a remarkable increase of the compounds corresponding to tobermorite while the SiO_2 decrease.

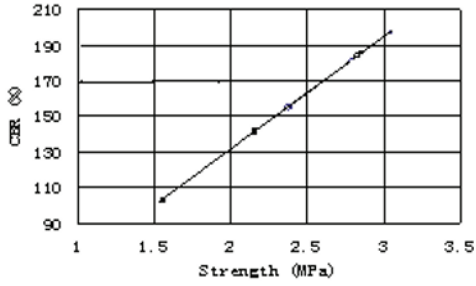

Fig. 2. Relation between strength and CBR in uniaxial compression

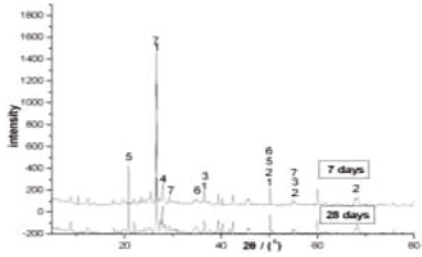

Fig.3. XRD-diagram of the solidified soils samples.

DTA-TG Study

The thermal profile of the samples, the weight loss at various stages of thermal reactions, and the 1st derivative of the weight loss are presented in Fig.4a. In the figure the temperature changes concerning the various compounds are shown. It can be observed that due to the high percentage of sullage, various thermal peaks attributed to the hydraulic products formed are almost overlapped by the peaks for soil minerals. For this reason a quantitative calculation of tobermorite was performed at the temperature range 60–140ºC, taking into account the corresponding amount of clay constituents in this range [9-10]. The weight loss corresponding the dehydroxylation of tobermorite in the temperature range 60–800 ºC is shown in the Figure. From this Figure it may be concluded that a continuous formation of

tobermorite takes place up to the 28 days hydration. The tobermorite formation rate seems to be higher than that of the reported values at 28 days curing period [11-12]. The phenomenon is more intense in the samples containing Binder at the early ages of curing. This means that the Binder addition offers the benefit of better setting and hardening behavior at the early ages. In Fig.4b, it can be seen that a continuous formation of hydration products occurs due to more and more reactions with the soil minerals. The tobermorite formation rate seems to be lower after the 28 days curing period.

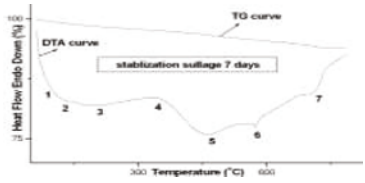

Fig. 4a. TG–DTA curves for the mixture of soil and 9.2% Binder content after 7 days curing.

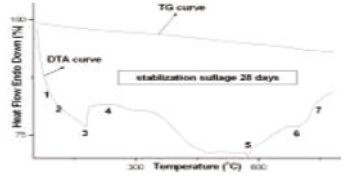

Fig. 4b. TG–DTA curves for the mixture of soil and 9.2% Binder content after 28 days curing.

Conclusions

This study shown that the sludge dredged from the Pearl River estuary can be safely solidified/stabilized with binder addition. The compressive strength of the samples were found to be increased wirh the binder contents increased. The study of the formation of the hydraulic products during the curing of clay containing as a stabilizing agent binder shows that a significant amount of hydration products were formed leading to a denser and more stable structure of the samples. A further curing time provides better setting and hardening and the combination of the binders can increase the early as well the final strength of the stabilised material. The binder reacts with the soil constituents (SiO_2 and the other aluminium silicates) leading to the formation of tobermorites and calcium aluminium silicate hydrates as well. And these results were consisted with the XRD and DTA -TG test.The mechanical properties such as strength, the water content, Compactibility CBR are considerably enhanced. If suitable measures are taken in order to avoid or minimise cracking of the stabilised layer and maintain the high modulus values, substantial reductions of non-structural

fill (i.e. embankment fill or general fill, etc.) in transportation related construction may be achieved. However, the above pavement analysis is based on laboratory values and in situ tests are needed in order to find more realistic values of the mechanical properties of the stabilised layer.

References

[1] R. Bahar, M. Benazzoug, S. Kenai, Performance of compacted cement-stabilised soil, Cement & Concrete Composites 26 (2004) 811–820

[2] Asavapisit, Suwimol; Naksrichum, Siripat; Harnwajanawong, Naraporn. Strength, leachability and microstructure characteristics of cement-based solidified plating sludge; Cement and Concrete Research. 2005, 6, 1042-1049.

[3] Baxter, Christopher D P.; King, John W.; Silva, Armand J.; Page, Matthew; Calabretta, Victor V. Site characterization of dredged sediments and evaluation of beneficial uses; Geotechnical Special Publication, n 127; Recycled Materials in Geotechnics; Proceedings of Sessions of the ASCE Civil Engineering Conference and Exposition: 2005, 150-161.

[4] Chew, S H.; Kamruzzaman, A H M.; Lee, F H. Physicochemical and engineering behavior of cement treated clays; Journal of Geotechnical and Geoenvironmental Engineering. 2004, 7, 96-706.

[5] Sherwood P. Soil stabilization with cement and lime. State of the art review, Transport Research Laboratory, 1993.

[6] S. Kolias , V. Kasselouri-Rigopoulou , A. Karahalios , Stabilisation of clayey soils with high calcium fly ash and cement, Cement & Concrete Composites 27 (2005) 301–313

[7] Tsonis P, Christoulas S, Kolias S. Soil improvement with coal ash in road construction. In: Proceedings of the 8th European Conference on Soil Mechanics and Foundation Engineering, Helsinki, 23–26 May 1983, pp. 961–4.

[8] Dawson AR, Elliot RC, Rowe RC, Williams GM. Assessment of suitability of some industrial by-products for use in pavement bases in the United Kingdom. Transportation Research Record 1486, pp. 114–23.

[9] Croney D. The design and performance of road pavements. HMSO 1977.

[10] Little DN. Handbook for stabilization of pavement subgrades and base courses with lime. Dubuque, IA, US: Kendall/Hunt publication Company; 1995.

[11] Borderick GP, Daniel DE. Stabilizing compacted clay against chemical attack. J Geotech Eng 1990;116(10):1549–67.

[12] Bouhicha M, Aouissi F, Kenai S. Performance of composite soil reinforced with barely straw. Int J Cem Concr ompos, special theme issue, natural fibre reinforced cement composites, in press.

Characterization of Minerals, Metals, and Materials 2016
Edited by: Shadia Jamil Ikhmayies, Bowen Li, John S. Carpenter, Jiann-Yang Hwang, Sergio Neves Monteiro, Jian Li, Donato Firrao, Mingming Zhang, Zhiwei Peng, Juan P. Escobedo-Diaz, and Chenguang Bai
TMS (The Minerals, Metals & Materials Society), 2016

SYNTHESIS AND CHARACTERISTICS OF ANORTHITE CERAMICS FROM STEELMAKING SLAG

Bowen Li[1,2], Mingsheng He[1], Jiann-Yang Hwang[1,2], Wangui Gan[3]

1-Advanced Materials R&D Center of WISCO, Beijing 102211, China
2-Department of Materials Science and Engineering, Michigan Technological University
1400 Townsend Dr., Houghton, MI 49931, USA
3-Metallic Resources Inc. of WISCO, Wuhan 430083, China

Keywords: Anorthite Ceramic, Steelmaking Slag, Synthesis

Abstract

Steelmaking slag is an alkaline solid waste consisting mainly oxides of calcium, iron, silicon, magnesium, and aluminum. Its large quantity and chemical property makes it challenging for recycling the material in various industrial applications. In this study, hot-poured steelmaking slag was used to prepare ceramics. After mixing with kaolin and quartz, ceramic products were synthesized via sintering. The appropriate sintering temperature is 1200°C. XRD analysis showed the major mineral phases were anorthite and pyroxene. SEM images showed that the new crystal particles were uniformly formed and distributed. Reaction mechanisms were discussed.

Introduction

Steelmaking slag is an alkaline solid waste consisting mainly oxides of calcium, iron, silicon, magnesium, and aluminum. It is produced by a Basic Oxygen Furnace (BOF) or an Electric Arc Furnace (EAF) during steel refinery [1]. Since lime and/or dolomite is applied as a fluxing agent in the process, the lime or dolomite combines with silicates, aluminum oxides, magnesium oxides, and ferrites during iron reduction, which forms steelmaking slag (Or steel furnace slag). After pouring from the furnace and cooling from its molten state, steelmaking slag is processed to remove all free metallics and sized into byproducts.

As a byproduct, steelmaking slag has a large volume production as 10%-13% of steel production [2, 3]. Steelmaking slag has been used as aggregates, fertilizer, and cementitious additive in concretes, etc. However, its large quantity and chemical property makes it challenging for recycling the material in various industrial applications [4].

Anorthite is the calcium-rich end member of the plagioclase feldspar solid solution series. The formula of pure anorthite is $CaAl_2Si_2O_8$. It can be synthesized by added alumina and silica in steelmaking slag in an appropriate amount. Since anorthite ceramics has many advantages for manufacturing and applications, such as appropriate strength, low electricity conductivity, low sintering temperature, broad materials supply, and low cost, it has greatly attracted research

attentions for synthesis with various minerals [5-10]. This study was to prepare anorthite ceramics by using hot-poured steelmaking slag.

Materials and Methods

The raw materials used for this study included steelmaking slag, kaolin, and quartz. Steelmaking slag was taken from Wuhan Iron & Steel Co. Group. The original slag was hot-poured with water, naturally cooled down to ambient temperature, then crushed into granules. After evenly mixing, the granules were ground into -325 mesh powder by a Raymond mill (Produced by WISCO Metallic Resources Ltd.). Both the kaolin and quartz were pulverized with dry process into powder below 325 mesh.

To determine the appropriate sintering temperature, melting point of the slag powder was measured by a high temperature melting point microscope. The slag sample was mixed with water to form a ϕ2mm cylinder, placed onto an aluminum sample stage, put in a tubular furnace and to be heated to desired temperature (temperature control at $\pm$0.3ºC).

The anorthite ceramic was prepared by mixing hot-poured steelmaking slag with quartz and kaolin in certain ratio in a blender, then placed the mixed powder in a rotating mill, spraying water while rotating the powder sample to form green ceramic beads. The green ceramic beads were transferred in a box furnace, heated to designed temperature, maintained the temperature for 2 hours, then naturally cooled to room temperature for characterization. The formula of ceramic was designed based on Cao-Al_2O_3-SiO_2 trinary phase diagram.

All the raw materials were analyzed by titration and energy dispersion spectrometer (EDS) to determine chemical compositions. Particle size and distributions were analyzed by a laser particle size analyzer with aqueous dispersing medium. X-ray diffraction (XRD) was used to determine mineral components of the materials, and scanning electron microscopy (SEM, JEOL 6400, accelerate voltage 20kV) was employed for microstructure analysis.

Results and Discussions

Characteristics of Steelmaking Slag

By titration analysis, the typical chemical composition of the slag are (wt%): SiO_2 10.93, Al_2O_3 1.38, CaO 42.36, MgO 8.83, TFe_2O_3 16.51, MnO 2.04, TiO_2 0.57, P_2O_5 1.27, and LOI 8.64. It showed a high content of CaO, and low concentrations of Al_2O_3 and MnO.

By XRD analysis, the major mineral components of the slag is calcium ferrite ($2CaO•Fe_2O_3$), calcium hydroxide ($Ca(OH)_2$), wustite (FeO), belite ($2CaO•SiO_2$), quartz (SiO_2), while containing less alite ($3CaO•SiO_2$) (Figure 1). To synthesize anorthite ceramics, appropriate amounts of alumina and silica were necessary to be added into the chemical system.

$$CaO + 2SiO_2 + Al_2O_3 \text{ ------- } CaO•Al_2O_3•2SiO_2 \quad (1)$$

$$(2CaO•SiO_2) + 3SiO_2 + 2Al_2O_3 \text{ ------- } 2(CaO•Al_2O_3•2SiO_2) \quad (2)$$

$$(3CaO•SiO_2) + 5SiO_2 + 3Al_2O_3 \text{ ------- } 3(CaO•Al_2O_3•2SiO_2) \quad (3)$$

Meanwhile, Fe^{2+} and Fe^{3+} can be in anorthite as a substitute of Ca^{2+} or Al^{3+}, or become component of pyroxene.

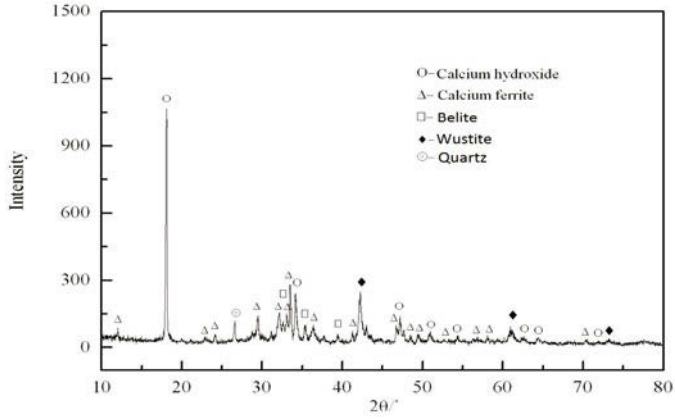

Figure 1. XRD Pattern of Steelmaking Slag

Figure 2 showed the particle size and distribution of the slag. The slag powder has a median size of 30 micron. The maximum particle size is smaller than 100 micron. The distribution curve has twin peaks: one is 20-50 micron; another is less than 10 micron.

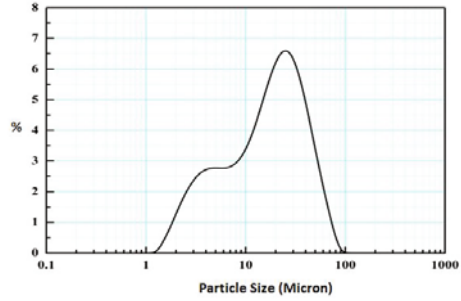

Figure 2. Particle Size Distribution of Steelmaking Slag

Under SEM, the slag particles showed irregular shapes with sharp edges and tips (Figure 3). The particle feature is corresponded to the results from laser analyzer.

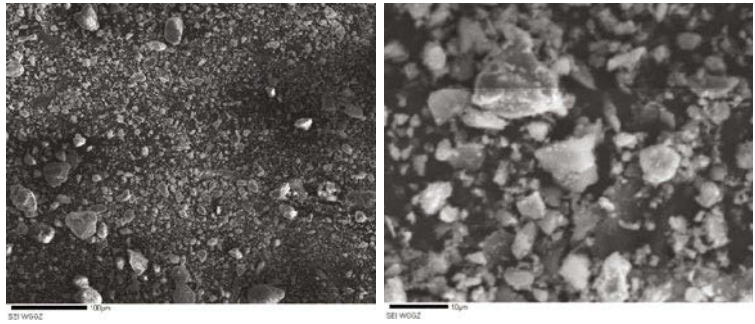

Figure 3. SEM Images of Steelmaking Slag

By heating in the melting point furnace, the slag showed its soft temperature at 1327ºC, semi-sphere temperature at 1368ºC, and flow temperature at 1399ºC (Figure 4).

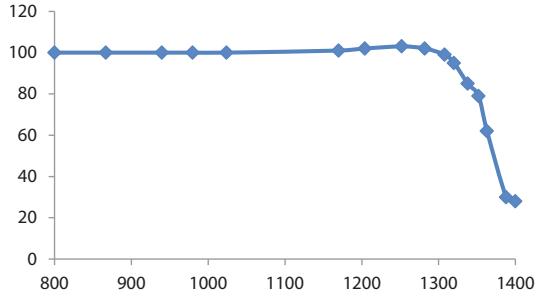

Figure 4. Melting Curve of Steelmaking Slag

Characteristics of Anorthite Ceramics

The green ceramic beads were sintered at 1100 ºC, 1150 ºC, 1200 ºC, 1250 ºC, and 1300 ºC for 2 hours, respectively. Sintered at 1100 ºC, the green beads still kept softly without liquid generated and color change. At 1150 ºC, the particles in green beads were ceramically bonded, though the mechanical strength was low. However, when the beads were heated to at 1300 ºC, liquid phase become the majority component of the ceramic, which indicated an over-burned state. Comparing with strength and surface appearances of ceramic beads, it can be determined that the best sintering temperature was 1200 ºC.

The synthesized ceramic is yellow-brown in color, with a porous microstructure (Figure 5). After sintering, the ceramic was well-recrystallized. The crystal grains showed plate-like, rod-like, or irregular shapes, and randomly orientations, with a uniform distribution. The interlock structure of the crystal grains provided mechanical strength of the ceramic body. The grain sizes mostly fell in a narrow range of 5-10 microns.

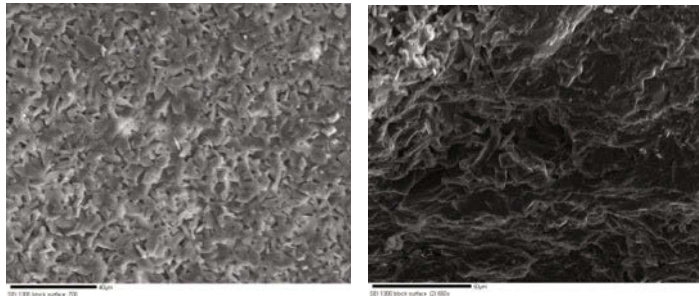

Figure 5. Topography of Anorthite Ceramic by SEM
(Surface)

On the cross-section of ceramic bead, SEM images indicated that the ceramic was well-sintered at 1200ºC (Figure 6).

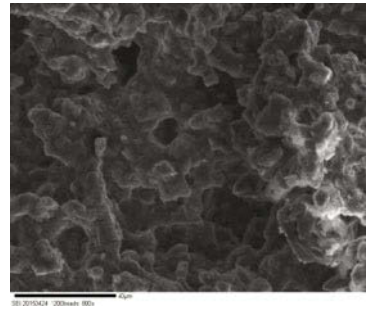

Figure 6. Topography of Anorthite Ceramic by SEM
(Cross Section)

Figure 7 showed the XRD pattern of the sintered ceramic. The major mineral components of the ceramic are anorthite ($CaO\text{-}Al_2O_3\text{-}2SiO_2$) and pyroxene. The characteristic peaks of belite, alite, kaolinite, and quartz disappeared. This indicated that the calcium silicates have entirely reacted

with the added alumina and silica. Kaolin was used as a binding agent to improve the strength of green beads while it also was a reaction substance as the supply of alumina for anorthite.

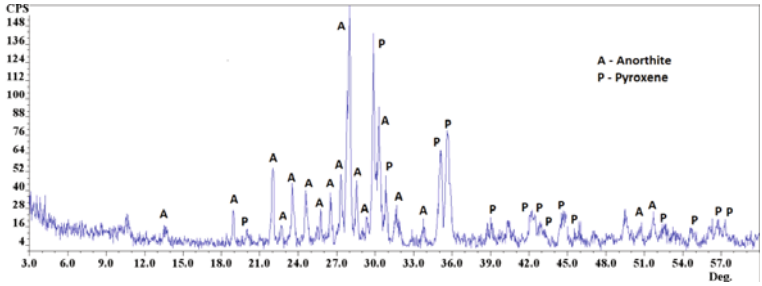

Figure 7. XRD Pattern of Anorthite Ceramic (Sintered at 1200ºC)

EDS analysis showed that the chemical composition of a typical anorthite ceramic are CaO 34.25%, SiO2 29.95%, Al2O3 25.78%, FeO 10.03% (Figure 8).

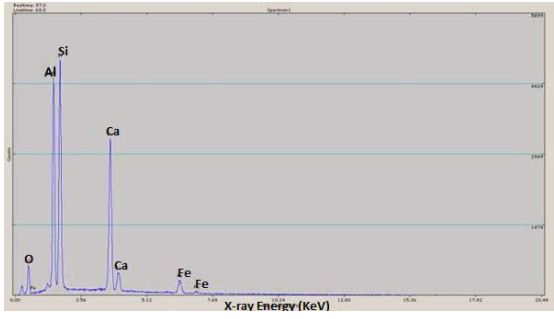

Figure 8. Chemical Composition of Anorthite Ceramic

Conclusions

By means of sintering, anorthite ceramic was prepared with hot-poured steelmaking slag, kaolin, and quartz. The ceramic products can be well sintered by heating at 1200°C. XRD analysis showed the major mineral phases were anorthite and pyroxene. The characteristic peaks of belite, alite, and quartz disappeared. SEM images showed that the new crystal grains were uniformly formed and distributed.

References

1. K. Horii, et al. “Processing and Reusing Technologies for Steelmaking Slag”, *Nippon Steel Technical Report*, No.104, August 2013.
2. Hao Bai, Pu Liu, Xian Bin Ai, Li Hua Zhao, Qi Tang, Shu Long Zheng. Analysis on the Microstructure Characteristics of Steel-Slag Based Ceramics. Advanced Materials Research, 2010, 150-151: 133-138.
3. A. R. Siddiqui, et al. “Iron and steel slag: An alternative source of raw materials for porcelain ceramics”, *Global NEST Journal*, (2014),16.
4. L.-H. Zhao, et al. “Synthesis of steel slag ceramics: chemical composition and crystalline phases of raw materials”, *International Journal of Minerals, Metallurgy and Materials*, (2015), 22(3): 325-333.
5. X. Cheng, et al. “Anze Shui, Pingan Liu. Fabrication and characterization of anorthite-based ceramic using mineral raw materials”, *Ceramics International*, (2012), 38(4): 3227–3235.
6. A. Mergen and Z. Aslanoğlu, “Low-temperature fabrication of anorthite ceramics from kaolinite and calcium carbonate with boron oxide addition”, *Ceramics International*, (2003), 29(6): 667–670.
7. M. R. Boudchicha, et al. “Crystallization and sintering of cordierite and anorthite based binary ceramics”, *Journal of Materials Science Letters*, (2001), 20(3): 215-217.
8. E. Y. Medvedovskii, and F. Y. Kharitonov, “Anorthite ceramic materials”, *Glass and Ceramics*, (1990), 47(12): 462-465.
9. Y. Han, et al., “Porous anorthite ceramics with ultra-low thermal conductivity”, *Journal of the European Ceramic Society*, (2013), 33(13–14): 2573–2578.
10. Y. Kobayashi and E. Kato, “Low-Temperature Fabrication of Anorthite Ceramics”, *Journal of the American Ceramic Society*, (1994), 77(3): 833–834.

Characterization of Minerals, Metals, and Materials 2016

Composites

Session Chairs:
Juan P. Escobedo-Diaz
Jeongguk Kim

Characterization of Minerals, Metals, and Materials 2016
Edited by: Shadia Jamil Ikhmayies, Bowen Li, John S. Carpenter, Jiann-Yang Hwang, Sergio Neves Monteiro, Jian Li, Donato Firrao, Mingming Zhang, Zhiwei Peng, Juan P. Escobedo-Diaz, and Chenguang Bai
TMS (The Minerals, Metals & Materials Society), 2016

TENSILE STRENGTH TESTS IN EPOXY COMPOSITES WITH HIGH INCORPORATION OF MALVA FIBERS

Ygor Macabú de Moraes[1], Carolina Gomes Dias Ribeiro[1], Frederico Muylaert Margem[1], Sergio Neves Monteiro[2], Jean Igor Margem[3]

[1] State University of the Northern Rio de Janeiro, UENF, , LAMAV; Av. Alberto Lamego, 2000, 28013-602, Campos dos Goytacazes, Brazil.
[2] Instituto Militar de Engenharia , IME, Praça Gen. Tibúrcio, nº80 Urca, Rio de Janeiro - RJ, 22290-270
[3] Instituto de Ensino Superiores do Censa, ISECENSA, Rua Salvador Correa, 139, 28035-310, Campos dos Goytacazes, Rio de Janeiro , Brazil.

Keywords: Malva fibers, epoxy matrix, tensile strength.

ABSTRACT

The natural fiber extracted from the leaves of malva plant, Urena lobata L., are currently among the most studied natural fibers, mostly because of its mechanical performance associated with high tensile strength and flexural strength. It is known that with the increase of fibers volume fraction the composite significant increases its tensile strength. This was obtained with amounts up to 30% in volume of malva. Thus the present work aims to study the influence of higher volumes of fiber on the tensile strength of specimens prepared under 5 tons of pressure. The fibers were previously washed and dried in an oven at 60ºC, after that poured together with the epoxy resin and catalyst mixture in the metal molds bone-shaped, and pressured to ensure specimens quality. The tensile strength increased significantly with higher amounts of malva fiber incorporated in the epoxy matrix. This better performance can be directly related to the fracture obstacle imposed by the fibers as well as the type of cracks resulting from the fiber/matrix interaction.

Introduction

The modern composite materials, especially those reinforced with synthetic fibers such as glass and carbon, have been used since last century to attend the demands required by most technological fields, from home appliances to aerospace [1]. In fact, fiber composites offer significant advantages over monolitic materials, such as common metallic alloys, plastic and ceramics. One of the most important is the ratio between the ultimate stress and the density, known as the specific strength. For example, in common glass fiber polymer composites, the so called “fiberglass”, the specific strength of around 400 MPa.cm3/g is higher than any conventional monolitic material. However, drawbacks exist. The energy required to fabricate “fiberglass” generates large emissions of CO2, which are responsible for global warming. Moreover, “fiberglass” is not recyclable and cannot be incinerated [2]. As a result, most synthetic fiber composites end up in landfills or contribute to rivers and oceans pollution.

Another alternative for synthetic composites is to apply natural lignocellulosic fibers as reinforcement of conventional polymer matrices. This has been the subject of many published papers [4-9] and already used in the automobile industry [10-12]. In addition to the environmental and societal advantages of the green composites [3], the lignocellulosic fiber reinforced conventional polymer composite also has economical and technical advantages [9]. In the case of a fiber collected as a waste [13], the price of the composite can be considerably lower than "fiberglass". Furthermore, with high strength lignocellulosic fibers such as sisal, ramie and malva [14] the specific strength of a composite may approach that of "fiberglass".

Therefore the objective of the present work is to investigate the mechanical behavior of polymer matrix composites reinforced with high volumes of natural malva fibers subjected to tensile stresses. The main difficulty of this type of analysis is the preparation of specimens which require time and especial attention.

Experimental procedure

The materials used in this work were malva fibers which was donated by a producer, Companhia Castanhal do Pará, from the North region of Brazil and commercial epoxy resin with phr13, in figure 1 it can be seen the malva plant and the as-received bundle of fibers.

Figure 1: malva plantation (a) and the fiber extracted (b).

The malva fibers had already presented a tensile of 1000MPa and have a diameter distribution of 0.020 – 0.100 mm with an average of 0.065 mm [15].

The fibers were placed aligned in a steel bone-shaped mold, the volume fraction of fiber used in this work was increased from 0 up to 40%. Into the fibers the still fluid polyester resin was poured into the mold. During this process particular care was taken to avoid air bubbles in the samples. Then the system was subjected to gradual increase of pressure from 0.5 to 5 tons which was relieved only after 24 hours at room temperature to make sure that the samples was not uncured. Then the samples were to post cured in at room temperature.

Than the samples were buffed to improve the surface quality. The dimensions of the samples were measured and catalogued to make possible further analysis. After that the samples was submitted to a tensile test in a Instron machine model 5582, with a strain rate of $4{,}2x10\text{-}4s^{-1}$ in controlled temperature environmental at 25ºC.

The fractural of samples was fragile and from the results recorded on the machine it was possible to obtain the values of tensile strength of these samples. Figure 2 represent a characteristic curve load versus extension of traction of this kind of test. The data of these tests also were recorded and used to find the values of tensile strength at break.

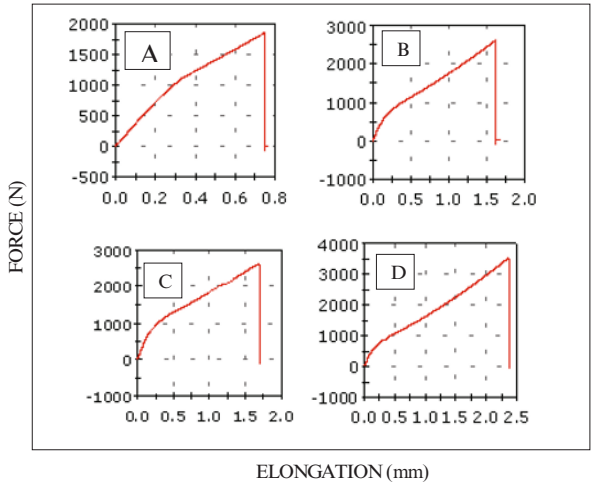

Figure 2: Curve Load versus Extension of traction for a sample with (a) 10%, (b) 20% and (c) 30% and (d) 40% of malva fiber incorporated.

Results and discussion

The table 1 shown the results of tensile strength for the composites incorporate with the corresponding volume of fiber incorporated. Also, the figure 3 contains the plotted curve based on these results.

Table 1: Tensile strength of the corresponding sample volume fraction of fiber.

Volume fraction of fiber (%)	Tensile strength (MPa)
0	32,92 ± 10,97
10	69.7 ±6,41
20	72,89 ± 4,78
30	86.7 ± 6,83
40	90,94 ± 19.9

Table 1 and figure 5 shown that occur a very high enhance when the volume fraction of fiber is increased. It can be seen especially when compared the results of pure epoxy (0% of volume fraction of fiber) and the high volume of fiber incorporated (40%).

The figure 3 illustrates the macro aspect of tensile ruptured specimens corresponding to the different volume fraction of malva fibers. In this figure, the fracture of neat epoxy specimens tends to be transversal to the tensile axis but with the increase of malva amount the evidence of malva fiber participation could be detected. This fact indicates that the fracture mechanism for the pure epoxy matrix was mainly associated with the propagation of transversal cracks although for the composites the non transversal crack indicate a low interface relation between the malva fiber and the epoxy matrix.

Figure 3. Typical tensile ruptured specimens volume fraction of malva reinforced polyester composites.

However is wise to notice that the deviations of some of these results are significant. It can be explained by the difficult of prepare samples uniformly. Also it can be explained by the irregular surface of the natural fibers which causes irregularities on the interface between the fiber and polymer.

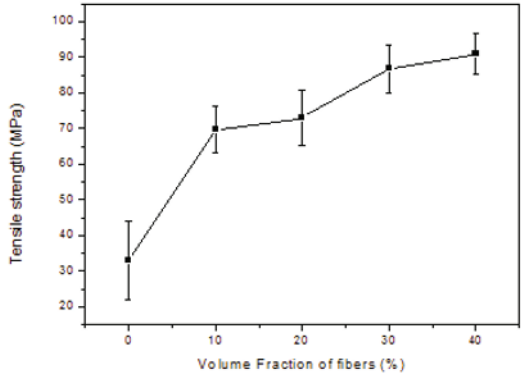

Figure 4: Tensile strength against the malva volume fraction in polyester composites

Another explanation of the low interface is because of the natural fibers are hydrophilic and the polymer matrix is hydrophobic. Therefore, even after drying in the oven, these fibers always have residual surface moisture which difficult the adhesion between fiber and matrix [16].

This kind of deficiency can be solved improving the techniques of preparation of the samples by taking extra care with the process of putting fibers and resin on the mold. Also the pressure it the system was submitted improve the interface between fiber and matrix which leads to superior materials.

Conclusions

- The increase amount of fibers have directly influence of the mechanical behavior of composites reinforced with natural fibers. An increase of the mechanical property occurs in higher volume of fibers incorporated.
- The samples studied in this work had they properties improved with the pressure which these were submitted.
- The high pressure fabrication process in a steel mold enabled the high volume specimens fabrication what can explain the superior result of the material because of its brittle interface fiber and matrix.

References

1. K.K. Chawla *Composite Materials Science and Engineering*, 2nd edition, Springer-Verlag, New York, 1998.
2. P. Wambua, I. Ivens and I.Verpoest, "Natural fibers: can they replace glass and fibre reinforced plastics?", *Composites Science and Technology*, 63 (2003) 1259-1264.
3. S. Nam, A.N. Netravali "Green Composites II. Environment-friendly, biodegradable composites using ramie fibers and soy protein concentrate (SPC) resin", *Fibers and Polym.* 7(4) (2006), pp. 380-388.
4. A .K. Bledzki, and J. Gassan, "Composites Reinforced With Cellulose-Based Fibers". *Prog. Polym. Sci*, 4 (1999) 221-274
5. D. Nabi Sahed and J.P. Jog, "Natural fiber polymer composites: a review", *Advances in Polymer Technol.,* 18 (1999), 221-274
6. A.K. Mohanty, M. Misra and G. Hinrichsen, "Biofibers, biodegradable polymers and biocomposites: an overview", *Macromolecular Mat. And Engineering*, 276/277 (2000), 1-24
7. S.J. Eichhorn, C.A. Baillie, N. Zafeiropoulos, L.Y. Mwakambo, M.P. Ansell, A. Dufresne, "Review of current international research into cellulosic fibres and composites", *J. Mater. Science*, 36 (2001) 2107-2113
8. A.K. Mohanty, M. Misra and L.T. Drzal, "Sustainable biocomposites from renewable resources: opportunities and challenges in the green material world", *J. Polym. Environ*., 10 (2002), 19-26
9. S.N. Monteiro, F.P.D. Lopes, A.S. Ferreira and D.C.O. Nascimento, "Natural fiber polymer matrix composites: cheaper, tougher and environmentally friendly". *JOM*, 61(1) (2009) 17-22.
10. S. Hill, "Cars that grow on trees". *New Scientists*, 153(2067) (1997) 36-39.
11. G. Marsh, "Next step for automotive materials". *Mater. Today*, 6(4) (2003) 36-43.
12. S.N. Monteiro, K.G. Satyanarayana, F.P.D. Lopes. "High strength natural fibers for improved polymer matrix", *Mat. Sci. Forum* 638-642, 2010, 961-966.
13. C.Y. Yue, H.C. Looi and M.Y. Quek, "Assessment of Fiber-Matrix Adhesion and Interfacial Properties Using the Pullout Test". Int. J. of Adhesion and Adhesives, 15 (1995), 73-80.

Characterization of Minerals, Metals, and Materials 2016
Edited by: Shadia Jamil Ikhmayies, Bowen Li, John S. Carpenter, Jiann-Yang Hwang, Sergio Neves Monteiro, Jian Li, Donato Firrao, Mingming Zhang, Zhiwei Peng, Juan P. Escobedo-Diaz, and Chenguang Bai
TMS (The Minerals, Metals & Materials Society), 2016

MICROSTRUCTURAL CHARACTERISTICS OF REACTION-BONDED B_4C/SiC COMPOSITE

Tianshi Wang[1], Chaoying Ni[1*], Prashant Karandikar[1,2]

[1]Department of Materials Science and Engineering, University of Delaware, Newark, DE 19716, USA
[2]M-Cubed Technologies, Inc., 1 Tralee Industrial park, Newark, DE 19711, USA

Keywords: Reaction-bond, Boron Carbide, B_4C, SiC, Microstructural Characterization

Abstract

A detailed microstructural investigation was performed to understand structural characteristics of a reaction-bonded B_4C/SiC ceramic composite. The state-of-the-art focused ion beam & scanning electron microscopy (FIB/SEM) and transmission electron microscopy (TEM) revealed that the as-fabricated product consisted of core-rim structures with α-SiC and B_4C cores surrounded by β-SiC and B_4C, respectively. In addition, plate-like β-SiC was detected within the B_4C rim. A phase formation mechanism was proposed and the analytical elucidation is anticipated to shed light on potential fabrication optimization and the property improvement of ceramic composites.

* Corresponding author. Tel 1 302 831 3569; Fax 1 302 831 4545

Introduction

Reaction-bonded B_4C/SiC ceramic composites were fabricated by infiltrating molten Si into a preheated preform consisting of B_4C, α-SiC and C to form a composite of near theoretical density [1]. The 10-15 vol% residual Si, together with other newly formed phases, bond the preexisting B_4C and α-SiC to produce a cohesive solid of advanced properties, including light weight (~2.8 g/cm^3), high thermal stability, and corrosion resistance, in addition to high mechanical properties such as Young's modulus (~420 GPa) [2,3], resulting in applications for armor, thermal management, wear, and precision equipment.

Due to different processing conditions and parameters, varied phase evolution and microstructures of B_4C/SiC ceramic composites were reported. Ness studied reaction-bonded SiC and found that the newly formed β-SiC grew epitaxially on original α-SiC [4]. To explain the structural evolution, Ness proposed a dissolution-precipitation mechanism for newly formed β-SiC. To understand B_4C-Si reaction, Teller sintered B-rich corner in the phase diagram of B-C-Si system to determine equilibrium phases and developed a theory for the formation of Si dissolved B_4C expressed as $B_{12}(Si,B,C)_3$ [5]. Hayun studied the microstructure of reaction-bonded B_4C (RBBC) and observed plate-like β-SiC as well as a core-rim microstructure consisting of B_4C grains surrounded by secondary $B_{12}(Si,B,C)_3$ which he assumed was formed by a dissolution-precipitation mechanism [6,7]. In a study by Karandikar, however, jagged B_4C microstructures were observed in RBBC which he suggested that a diffusion mechanism was more plausible to explain the rim formation of Si containing B_4C [8]. Due to the complexity of high temperature chemical reactions, phase

transformation, and the resulting phase structures, there are still significant gaps to bridge between the macrostructural characterization, phase evolution, and microscopic mechanisms.

In this study, a reaction-bonded B_4C/SiC composite was characterized by utilizing the cutting-edge FIB/SEM and TEM to precisely determine the composite constituents. An assessment was made based on the reaction bonding thermodynamics to elucidate in detail the diffusion, interactions, and phase transformations.

Experimental Procedure

The reaction-bonded B_4C/SiC composites were fabricated by infiltrating a preform of B_4C, α-SiC, residual C and 20-25 vol.% pores with molten Si at about 1500°C. Both the C and the porosity were left from preheating an organic binder used to form the green body of B_4C and α-SiC [9,10]. The reactions between the infiltrating liquid Si and the preform led to a dense product with desired near-net shape and dimension.

The microstructure of the samples was studied using a FIB/SEM (Zeiss Auriga 60) with an X-ray energy-dispersive spectrometer (EDS, Oxford Instruments X-Max 80) and a transmission electron microscope (TEM, JOEL JEM-2010F). SEM samples were prepared using a standard metallographic procedure that included a final polish with 1 m diamond suspension (Buehler MetaDi). An X-ray diffractometer (Bruker D8) was used to determine phases with a position sensitive detector (LynxEye).

TEM samples were prepared using the FIB/SEM. Two trapezoids along each side of selected areas were first milled to obtain a lamella of about 1 m thick, and the lamella was then further tilted to mill the cross-section. The lamella was thinned to a thickness of less than 100 nm by Ga ion beam of adequate energy. After that, the lamella was mounted to an OmniProbe (Oxford Instruments) by Pt deposition and then transferred to a copper grid.

Results and discussion

Phase Structures

Fig 1(a) is a typical SEM image of the composite microstructure. Four phases are identified based on grain morphology and contrast, together with the EDS mapping in Fig. 1(c)-(e), and these phases are B_4C (dark regions), SiC (grey grains), residual Si (bright regions), and the plate-like SiC which usually appears inside B_4C. The image contrast here is primarily from the average atomic number variation of phase constituents. No pores were detected by SEM as anticipated based on the process parameters.

Further analysis with an in-lens detector, which offers better topographic contrast, revealed the core-rim structures associated with most of B_4C grains and also with a considerable number of SiC grains, as shown in Fig. 1(b). Fig. 2 shows the XRD pattern of the sample and the peaks are indexed as α-SiC, β-SiC, B_4C, Si, and $B_{12}(Si,B,C)_3$.

To identify the formation mechanisms of the β-SiC, rim structures surrounding the original α-SiC and B_4C core grains, we proceeded with additional SEM and TEM investigations.

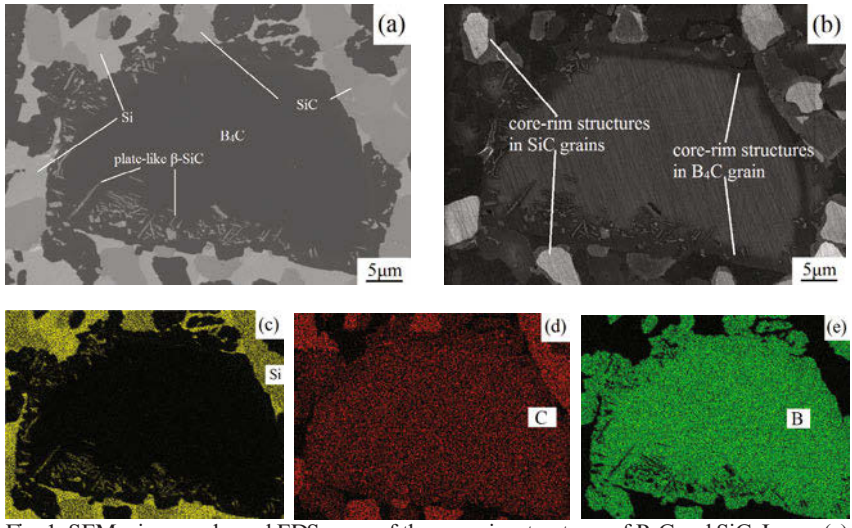

Fig. 1. SEM micrographs and EDS maps of the core-rim structures of B_4C and SiC. Image (a) and (b) were captured by a chamber secondary electron detector (SESI) and an in-lens detector respectively. Images (c-e) were EDS elemental maps of Si, C, and B respectively. The in-lens image (b) shows additional structural contrast within the grains, while the SESI image (a) and EDS mapping (c-e) do not.

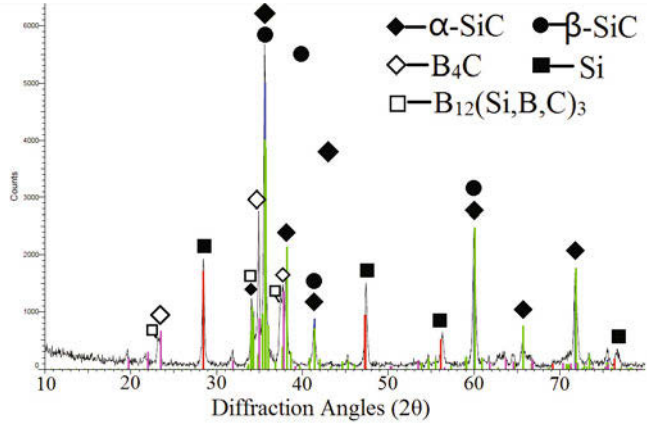

Fig. 2. X-ray diffraction pattern of the reaction-bonded SiC and B_4C composite. Five phases are identified.

Core-rim Structure of SiC

A core-rim structure of SiC is shown in Fig. 3(a). The rectangular inset is an image from a section polished by FIB while the rest of the image field of view is from a sample mechanically polished in a conventional way. It is noticed that the 4 original α-SiC grains are interconnected by the rim structure to form a cluster of SiC grains. The secondary electron image collected from SESI and the EDS mapping indicate negligible contrast difference between the newly formed β-SiC and the original α-SiC (Fig. 3b-c), suggesting a minimal compositional difference between the two types of SiC grains.

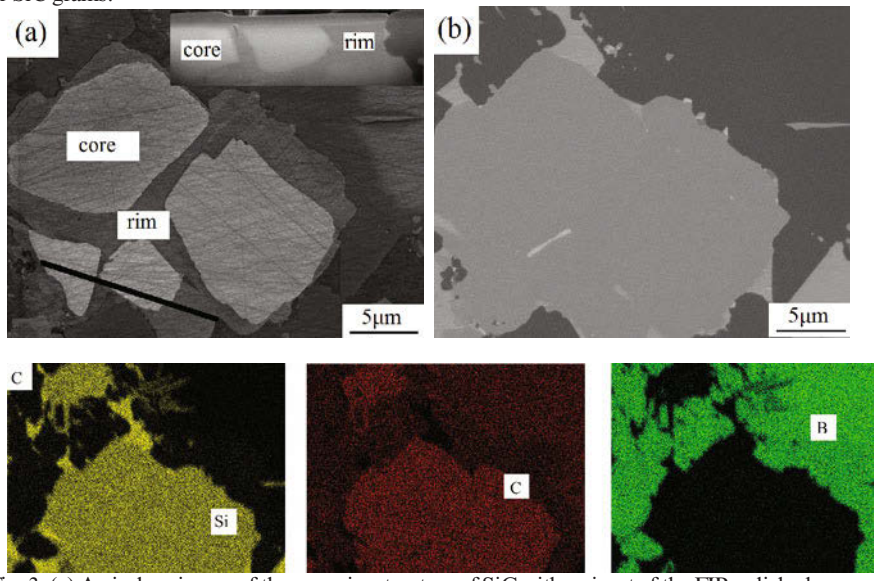

Fig. 3. (a) An in-lens image of the core-rim structure of SiC with an inset of the FIB polished cross-section; (b) chamber detector (SESI) image of the same area; (c) EDS mapping for C, Si and B, respectively. Both Si and C distribute evenly inside SiC grains, the original as well as the newly formed.

To further understand the SiC core-rim structure, we performed TEM. The upper-left area in Fig. 4 is in the SiC core while the lower-right area is in the SiC rim. TEM suggests that no obvious faults are detectable in the core area. However, the β-SiC rim is filled with faults and crystal defects, which also explains the topographical difference after the polishing that in turn contributes to the contrast of the in-lens image.

It is plausible that the β-SiC rim surrounding α-SiC grows based on the α-SiC core through a solidification process of the molten Si[C]. At the beginning, some residual carbon would dissolve

in the molten Si and generate a great amount of heat as dictated by the reaction thermodynamics. The heat further increases the dissolution of C in Si; therefore, the local temperature and C concentration in the reaction region are high. With a high diffusion coefficient at such high temperature, C should spontaneously diffuse to the vicinity of α-SiC where the temperature and C solubility are lower and the resulting supersaturated liquid Si[C] therefore heterogeneously crystalizes to form β-SiC attached to the original α-SiC grains, a preferred process due to relatively lower energy in contrast to the homogeneous nucleation in liquid phase. The newly formed β-SiC grows fast under a much lower temperature than that of the original α-SiC [11]. Such a mechanism of fast growth promotes a large number of faults inside the newly formed SiC grains.

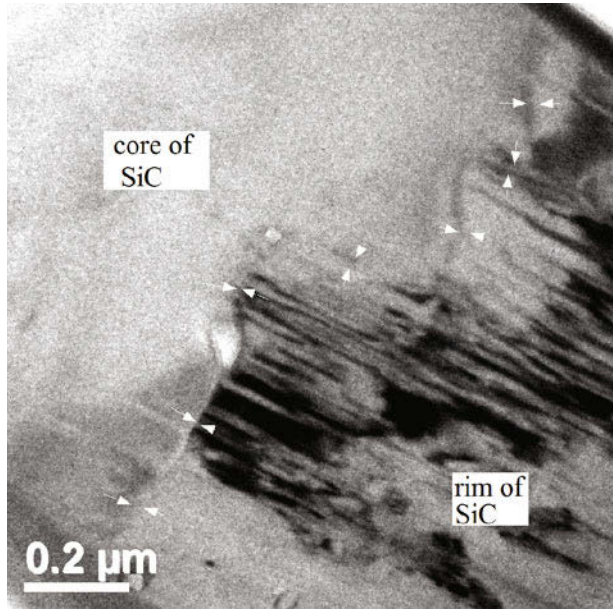

Fig. 4. TEM image of core-rim structure of SiC. Upper-left is the original α-SiC core area appearing free of crystal defects while the lower-right is the newly formed β-SiC, in which severe twinning and lattice distortion are visible. Arrows indicate the grain boundary of the two distinct areas.

Plate-like β-SiC

The plate-like β-SiC commonly appears in the rim of B_4C as shown in Fig. 1(a-c). Both of the plate-like and the occasional needle-like morphologies were observed by SEM after FIB milling of the β-SiC cross sections. A bright field TEM image of two β-SiC grains inside B_4C are shown in Fig. 5(a). Defects, especially stacking faults, are easily noticeable in the β-SiC. Fig. 5(b) is a bright field image of a grain boundary between β-SiC and B_4C.

Based on the SEM and TME observation and analysis, the formation mechanism of β-SiC is proposed as follows:

As the infiltrating Si meets the residual C in the green body, the molten Si dissolves C to form liquid Si[C], which is a highly exothermic process. Since solid SiC is more stable than B_4C at around 1600°C according to Si-C-B diagram [12] and the original B_4C, α-SiC and their surroundings are relatively away from the heat source of residual C, the β-SiC heterogeneously crystalizes on or in the vicinity of α-SiC and B_4C and grows into liquid Si[C] especially during the cooling process. While the formation of β-SiC surrounding B_4C occurs at a relatively higher temperature and the limiting factor of β-SiC growth is C concentration, the β-SiC grains tend to grow toward the C supersaturated liquid as plates with significant growth defects such as twinning and stacking faults. Defects are also observed in the β-SiC rim surrounding α-SiC presumably due to similar fast growth and thermal fluctuation.

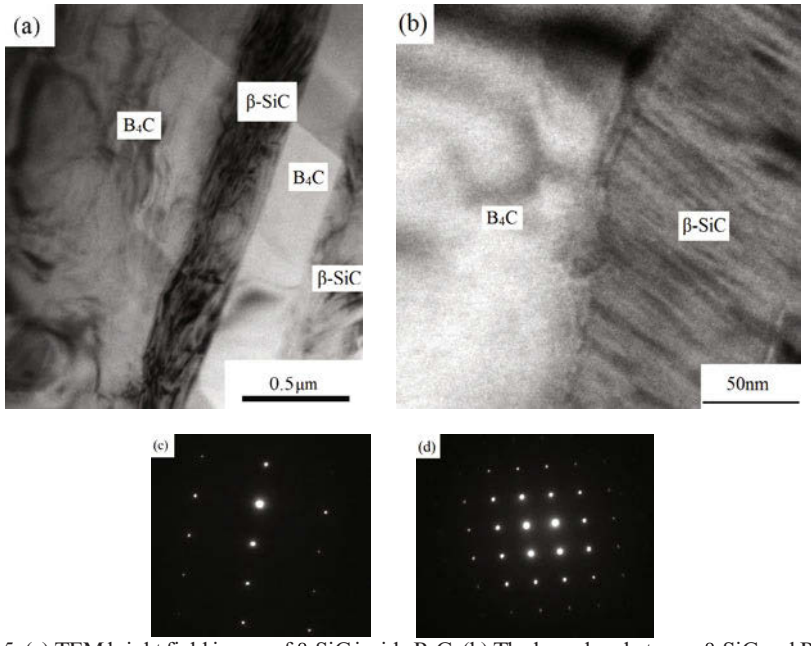

Fig. 5. (a) TEM bright field image of β-SiC inside B_4C; (b) The boundary between β-SiC and B_4C; (c) Diffraction pattern of β-SiC; (d) Diffraction pattern of B_4C.

Core-rim Structure of B_4C

Boron carbide rims were frequently observed around B_4C with relatively lower brightness in the secondary electron contrast. In addition, the β-SiC plates usually exist inside the rim and some of them also appear in the original B_4C.

An EDS line-scan along the black line in Fig. 6(a) shows that in this B_4C rim, Si maintains a very low concentration of around 2 at.% in the rim to form $B_{12}(Si,B,C)_3$ as also identified by XRD. It was suggested that the rim phase was formed by Si diffusion from liquid [8]. While the Si inward diffusion in B_4C indeed appears to be a plausible mechanism, additional investigation is necessary to fully exclude the possibility of $B_{12}(Si,B,C)_3$ re-precipitation following the B_4C dissolution as was suggested in literature [6,7]. It is believed also possible that the B_4C rim structure is formed by a process of simultaneous Si inward diffusion and limited $B_{12}(Si,B,C)_3$ growth within and towards the liquid Si[B,C] formed through an earlier dissolution of C and B_4C into the liquid Si. The plate-like β-SiC contained in the $B_{12}(Si,B,C)_3$ rim and the original B_4C could be secondary precipitates formed during the cooling process and these plates also appear to preferentially distribute along specific crystal planes of the B_4C and $B_{12}(Si,B,C)_3$ matrixes.

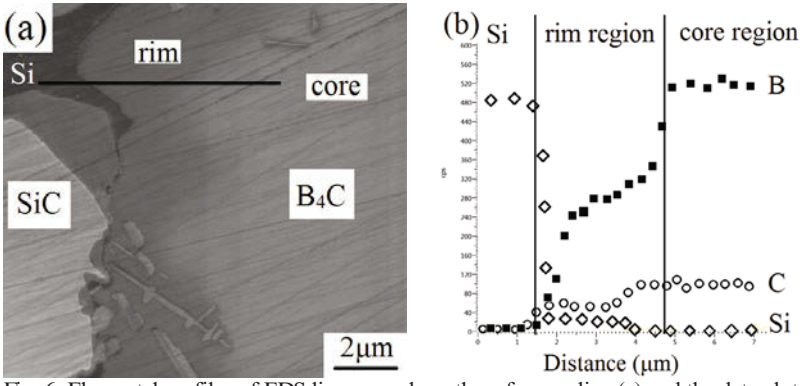

Fig. 6. Elemental profiles of EDS line-scan along the reference line (a) and the data plot (b).

Conclusion

The microstructural characteristics of a reaction bonded B_4C/SiC CMC were investigated. Apart from B_4C, α-SiC, and Si, we observed plate-like β-SiC and core-rim structures surrounding both SiC and B_4C grains. With TEM, we discovered significant faults and defects inside β-SiC plates and also in the β-SiC rim surrounding α-SiC. Based the morphology and thermodynamics, we propose that the rim of α-SiC is formed by precipitation of supersaturated Si[C] and the $B_{12}(Si,B,C)_3$ rim surrounding original B_4C is generated by means of a dominant Si diffusion. The β-SiC plates in B_4C and $B_{12}(Si,B,C)_3$ appear to precipitate during cooling and to distribute along certain crystal planes. The results are anticipated to help make potential improvements of the fabrication process and composite properties.

Acknowledgement

This work is supported by the II-VI Foundation. Instrumentation and staff supports from the W. M. Keck Center for Advanced Microscopy and Microanalysis at the University of Delaware are greatly appreciated.

References

[1] P. Karandikar et al., "Diamond-Reinforced Composite Materials and Articles, and methods for making same," US 8,474,362 (2013) 1-20.

[2] S.M. Salamone et al., "Effect of SiC:B_4C ratio on properties of Si-Cu/SiC/B_4C composites," Mech. Prop. Perform. Eng. Ceram. Compos. IX. (2014) 83–90.

[3] S.M. Salamone et al., "Macroscopic assessment of high pressure failure of B_4C and B_4C/SiC composites," Adv. Ceram. Aror IX Ceram. Eng. (2013) 25–30.

[4] J.N. Ness, T.F. Page, "Microstructural Evolution in Reaction-bonded Silicon Carbide," J. Mat. Sci. 21 (1986) 1377–1397.

[5] R.Telle, "STRUCTURE AND PROPERTIES OF SI - DOPED BORON CARBIDE," Phys. Chem. Carbides, Nitrides Borides, Springer Netherlands, 1990: pp. 249–267.

[6] S. Hayun et al, "Rim region growth and its composition in reaction bonded boron carbide composites with core-rim structure," J. Phys. Conf. Ser. 176 (2009) 012009.

[7] S. Hayun et al., "Microstructural evolution during the infiltration of boron carbide with molten silicon," J. Eur. Ceram. Soc. 30 (2010) 1007–1014.

[8] P.G. Karandikar et al., "Microstructural Development and Phase Changes in Reaction Bonded Boron Carbide," Adv. Ceram. ARMOR VI Ceram. Eng. Sci. Proc. 31 (2010) 251–259.

[9] M. Aghajanian, A. McCormick, "Composite Materials and Articles, and methods for making same," US 8,128,861 B1, 2012.

[10] M. Aghajanian et al., "Boron carbide composite bodies, and methods for making same," US 6,862,970 B2, 2005.

[11] A.S. BAKIN, "SiC HOMOEPITAXY AND HETEROEPITAXY," Int. J. High Speed Electron. Syst. 15 (2005) 747–780.

[12] E. Gugel et al., "Investigations in the ternary system boron--carbon--silicon," Solid State Chem. Proc. 5th Mater. Res. Symp., National Bureau of Standards, 1972: pp. 505–513.

Characterization of Minerals, Metals, and Materials 2016
Edited by: Shadia Jamil Ikhmayies, Bowen Li, John S. Carpenter, Jiann-Yang Hwang, Sergio Neves Monteiro, Jian Li, Donato Firrao, Mingming Zhang, Zhiwei Peng, Juan P. Escobedo-Diaz, and Chenguang Bai
TMS (The Minerals, Metals & Materials Society), 2016

ANALYSIS OF METHANOL SENSITIVITY ON SnO_2-ZnO NANOCOMPOSITE

Enobong E. Bassey[1,2*], Philip Sallis[2] and Krishnamachar Prasad[3]

[1]School of Energy, Construction and Environment, Faculty of Engineering, Environment and Computing, Coventry University, Coventry, United Kingdom
[2]Geoinformatics Research Centre, Faculty of Design and Creative Technologies, Auckland University of Technology, Auckland, New Zealand
[3]Department of Electrical and Electronic Engineering, Faculty of Design and Creative Technologies, Auckland University of Technology, Auckland, New Zealand

Keywords: SnO_2, ZnO, Nanocomposite, Methanol, Gas, Sensor

Abstract

This research reports on the sensing behavior of a nanocomposite of tin dioxide (SnO_2) and zinc oxide (ZnO). SnO_2-ZnO nanocomposites were fabricated into sensor devices by the radio frequency sputtering method, and used for the characterization of the sensitivity behavior of methanol vapor. The sensor devices were subjected to methanol concentration of 200 ppm at operating temperatures of 150, 250 and 350 °C. A fractional difference model was used to normalize the sensor response, and determine the sensitivity of methanol on the sensor. Response analysis of the SnO_2-ZnO sensors to the methanol was most sensitive at 350 °C, followed by 250 and 150 °C. Supported by the morphology (FE-SEM, AFM) analyses of the thin films, the sensitivity behavior confirmed that the nanoparticles of coupled SnO_2 and ZnO nanocomposites can promote the charge transportation, and be used to fine-tune the sensitivity of methanol and sensor selectivity to a desired target gas.

Introduction

This research paper presents the sensing behavior of a nanocomposite of tin dioxide (SnO_2) and zinc oxide (ZnO) in a 1:1 molar composition. Individual metal oxides have been used to analyze the sensitivity of various gases in different environmental conditions. In recent times, there has been significant interests in the application of nanocomposites of metal oxides as gas sensors [1, 2]. With increasing applicability of the differences in the effects of surface area and defect structures on higher reactivity, there is increased interests in applications of metal oxide nanostructures for gas sensing [3]. In this research, nanocomposites of SnO_2 and ZnO were fabricated into sensor devices by the radio frequency (RF) sputtering method, and used for the characterization of the sensitivity behavior of methanol vapor. The sensitivity behavior due to operating temperature difference is presented.

Experiment

Gas sensor thin films of SnO_2 and ZnO were prepared by mixing the SnO_2 and ZnO powders (99.9% purity) in 1:1 molar concentration. The mixed metal oxides were pressed to form the pellets, and sintered at 1100 °C for 5 hours in air ambient to form the target. Then the targets

were used to deposit films for 30 min on oxidized *p*-type silicon substrate <100> by RF sputtering. Using interdigital capacitor (IDC) structure pattern, contacts were made on the thin film by Ti/Pt. Field emission - scanning electron microscope (FE-SEM) and atomic force microscope (AFM) were used for the nanocharacterization of the thin films.

The sensor devices were subjected to methanol concentrations of 200 ppm at operating temperatures of 150, 250 and 350 °C. A fractional difference model was used to normalize the sensor response, and determine the sensitivity of the target gas by the sensor [4]:

$$S(\%) = \left(\frac{R_a - R_g}{R_a}\right) \times 100 \quad (1)$$

where Ra is the sensor resistance in synthetic air, and Rg is the sensor resistance in the presence of the test gas.

Results and Discussion

The FE-SEM exhibited significant structural heterogeneity and crystallinity of the films, with high particle size and large conglomerates (Figure 1). In comparison with pure SnO_2 and pure ZnO thin films [2], image analysis of the pure metal oxides films were slightly smoother than the SnO_2-ZnO devices.

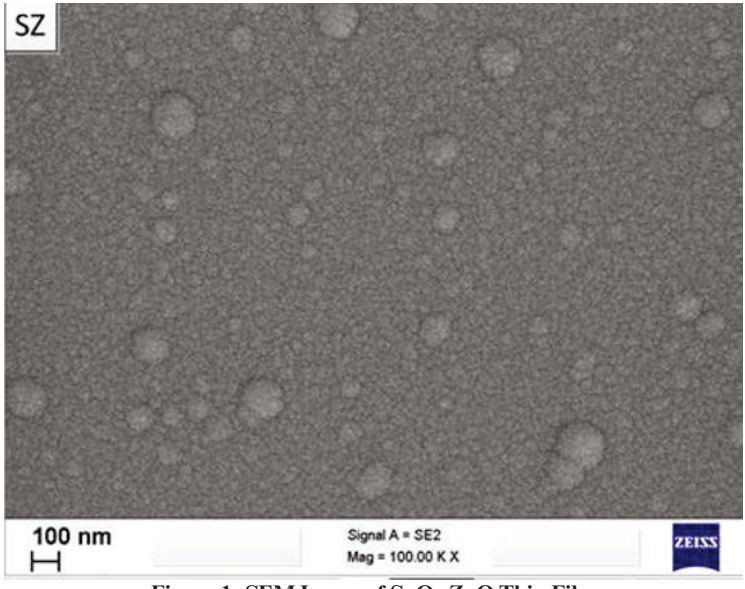

Figure 1: SEM Image of SnO_2-ZnO Thin Film

Although large conglomerates are not assumed to be taking part in the light-trapping process [5], we infer that this could have some effect on the sensitivity recorded by the SnO_2-ZnO sensor devices.

The AFM images of the SnO_2-ZnO thin films indicated minor hillocks on a relatively dense film surface (Figure 2). This AFM images collaborate the morphology of the thin films as obtained by the FE-SEM. From AFM image analysis, the average thin film particle height for SnO_2-ZnO was 6.042nm; but the thin film particle heights for SnO_2 and ZnO were 10.755 and 13.494 nm, respectively [6]. For ZnO–SnO_2 films fabricated by the filtered vacuum arc, the average surface roughness and the grain size observed by Çetinörgü [7] were in the range 0.3–1.5 nm and 19–24 nm, respectively.

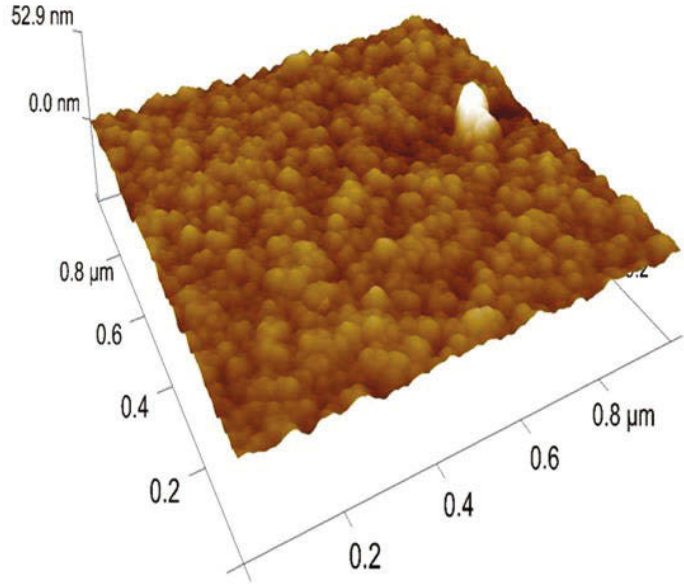

Figure 2: AFM Image of SnO_2-ZnO Thin Film

The normalized response presented by equation 1, the sensitivity behavior was observed to gradually increase with time once the methanol vapor was introduced (Figure 3). It reached a maximum value, and stabilized there as long as the target gas was flowing. Once the target gas was removed, the sensitivity gradually began to decrease and eventually reached zero. The highest sensitivity was recorded at the temperature of 350 °C, while the lowest was at 150 °C.

The sensitivity behavior by SnO_2-ZnO sensors confirmed the temperature dependence of the devices. The increase in sensitivity as the temperature was increased can be attributed to the energy activation by the external heat source to overcome the energy barrier of the reaction [8].

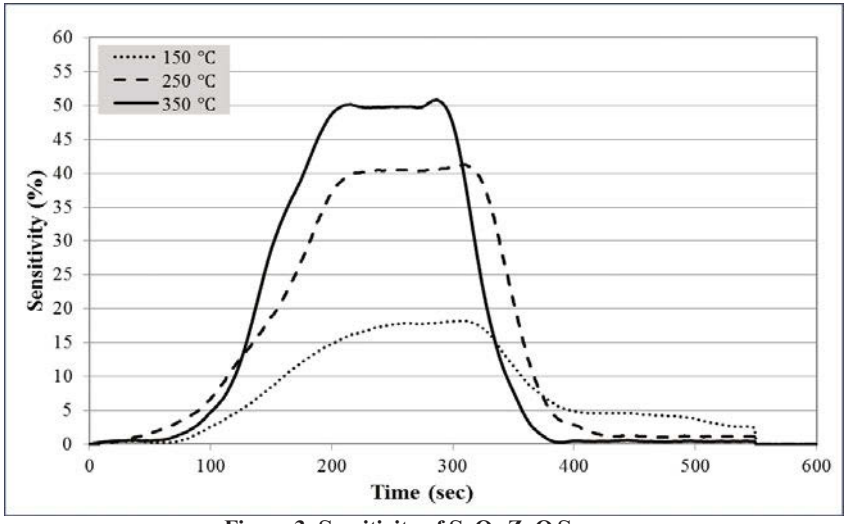

Figure 3: Sensitivity of SnO_2-ZnO Sensor

The sensitivity behaviour can be attributed to fact that there is an increase in photocatalytic activity on the surface of the metal oxide nanocomposite with increased temperature. The response time is also observed to be affected by the operating temperature. Comparing the response at different temperatures, at 350 °C, the sensitivity rises more rapidly than at 250 and 150 °C. Similarly, the observed behavior of the devices showed a rapid decline as the sensitivity returned to zero. This sensitivity behavior confirms that it is very easy for the nanocomposite sensor devices to overcome the activation energy of the device at increased temperature, and respond rapidly.

Conclusion

The response of the SnO_2-ZnO sensors to 200 ppm methanol was most sensitive at 350 °C, followed by 250 and 150 °C. The sensitivity behavior was supported by the morphology of the thin films. The results confirm that the nanoparticles of coupled SnO_2 and ZnO nanocomposites can promote the charge transportation, and be used to fine-tune the sensitivity of methanol and selectivity to a desired gas.

Acknowledgement

This research was supported by the Geoinformatics Research Centre and Engineering Research Innovation Cluster at Auckland University of Technology. We would like to acknowledge Prof Navakanta Bhat of Center for Nano Science and Engineering, Indian Institute of Science for facilitating the fabrication of the sensor devices.

References

1. N. Bârsan, M. Hübner, and U. Weimar, *Conduction mechanisms in SnO2 based polycrystalline thick film gas sensors exposed to CO and H2 in different oxygen backgrounds.* Sensors and Actuators B: Chemical, 157(2) (2011), 510-517.

2. E.E. Bassey, K. Prasad, and P. Sallis, "Analysis of SnO_2/ZnO Nanostructures Prepared for Gas Sensing" (Paper presented at the 15th International Symposium on Olfaction and Electronic Nose, EXCO, Daegu, Korea, 2-5 July 2013).

3. S. Sen, et al., *Growth of SnO2/W18O49 nanowire hierarchical heterostructure and their application as chemical sensor.* Sensors and Actuators B: Chemical, 147(2) (2010), 453-460.

4. E. Bassey, et al., "Wavelet transform smoothing filters for metal oxide gas sensor signal cleaning" (Paper presented at the 8th International Conference on Sensing Technology, ICST-2014, Liverpool John Moores University, United Kingdom, 2-4 September 2014), 5-10.

5. A.V.Shah, et al., *Basic efficiency limits, recent experimental results and novel light-trapping schemes in a-Si:H, c-Si:H and `micromorph tandem' solar cells.* Journal of Non-Crystalline Solids, 338–340 (2004), 639-645.

6. E.E. Bassey, K. Prasad, and P. Sallis, "Surface Structure and Particle Analysis of Combined SnO_2 and ZnO Nanoparticles Prepared for Gas Sensing" (Paper presented at the 8th Pacific Rim International Conference on Advanced Materials and Processing, PRICM-8, Waikoloa, Hawaii, USA, 4-9 August 2013), 2157-2162.

7. E. Çetinörgü, *Characteristics of filtered vacuum arc deposited ZnO–SnO2 thin films on room temperature substrates.* Optics Communications, . 280(1) (2007), 114-119.

8. G.T. Ang, et al., *High sensitivity and fast response SnO2 and La-SnO2 catalytic pellet sensors in detecting volatile organic compounds.* Process Safety and Environmental Protection, 89(3) (2011), 186-192.

Characterization of Minerals, Metals, and Materials 2016

Extraction

Session Chairs:
Li Qian
Mingming Zhang

Characterization of Minerals, Metals, and Materials 2016
Edited by: Shadia Jamil Ikhmayies, Bowen Li, John S. Carpenter, Jiann-Yang Hwang, Sergio Neves Monteiro, Jian Li, Donato Firrao, Mingming Zhang, Zhiwei Peng, Juan P. Escobedo-Diaz, and Chenguang Bai
TMS (The Minerals, Metals & Materials Society), 2016

EXPERIMENTAL STUDY ON QUALITY EVALUATION OF CALCIUM-BASED AGENTS FOR DESULFURIZATION OF SINTER GAS ON SDA

Lijun Lu[1], Jiann-Yang Hwang[2],Lingchen Kang[1],Likun Li[1],Honghui Fang[1],Ying Liu[1]

[1]Research and Development Center of Wuhan Iron and Steel (group) Corporation, Metallurgical Road NO.28, Wuhan, 430080, China, Email: 54310572@qq.com
[2]Michigan Technological University, Materials Science and Engineering, 1400 Townsend Dr. Houghton, MI 49931 USA

Keywords: Calcium-based agent, Reactivity, Desulfurization, SDA process, Sinter flue gas

Abstract

The evaluation method and quality index were established for calcium-based sorbents for desulfurizing sinter plant offgas. Two types of steelmaking by-products were tested and evaluated. An efficient desulfurization sorbent was selected for SDA desulfurization process.

Introduction

Traditional sintering process produces a large amount of gas containing SO_2, which has caused serious pollution to the atmospheric environment for a long time. To decrease this pollution, GB28662-2012 "Emission standard of air pollutants for sintering and pelletizing of iron and steel industry" stipulates that the sintering flue gas SO_2 emission shall be less than 200mg/m^3. Currently, desulfurization technology for sinter plant flue gas can be divided into dry, semi-dry and wet process, among which semi dry desulfurization process is preferred by most sinter plants [1]. SDA rotating spray method is one of semi-dry desulfurization processes, which is widely used in domestic and international electric power plants, iron-making and steel-making facilities. Because of its high desulfurization efficiency and low system resistance, the application quantity of SDA method, according to statistics, has reached hundreds of sets, which were far more than other semi dry process [2]. As the requirements for high quality atmospheric environment is increasing for decades, it is predictable that sintering flue gas SO_2 emission standards will be more stringent. Therefore, the research for improving the SDA process technology is in urgent need. The desulfurization agent employed in the SDA method is one of the key factors that affect the operation of desulfurization [3], which has an important influence on the desulfurization efficiency and the desulfurization cost of the system. This study explored the quality evaluation technology, studied a series of high quality and low price of desulfurization agents, and provided an economic new solution for the high desulfurization efficiency SDA process.

Experiments

Experimental apparatus

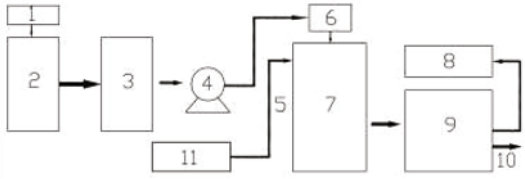

1. Temperature monitoring; 2. Digestion tank; 3.Slurry tank; 4.Slurry pump; 5.Air intake; 6.Atomizer; 7.Desulfurization tower; 8.Flue gas analyzer; 9.de-duster; 10. Air outlet; 11. Gas distribution system

Figure 1. Schematic diagram of experimental system

The test apparatus is shown in Figure 1, which mainly comprises a gas distribution system, a lime digesting system, a rotating spray reaction system, a dust removal system and a detection system. After entering the desulfurization tower, the sintering gas containing SO_2 is contacted with the lime slurry produced by the digestive system, and the desulfurization reaction occurs when the solid particles are dried in contact with the high temperature flue gas.

The temperature of the digestive system was monitored continuously by a multi parameter analyzer. The concentration of SO_2 in the inlet and outlet was recorded by Kaine KM9106 and the flue gas flow rate was 100m^3/h, the SO_2 concentration in the flue gas was 1000 mg/m^3, the flue gas temperature was 90~110℃.

Evaluation index and method

Lime digestion reaction is an exothermic reaction, in the premise of excess water, the higher the content of lime in the desulfurization agent, the more heat release, the higher of the temperature improving. By monitoring the slurry temperature, the content of lime in the agent can be quickly judged. Zhang et al.study the relationship of lime reactivity and oxidative calcium content[4]. He showed that the digestion temperature and lime content has a large association, pointed out that the digestive process temperature is higher, the higher the content of calcium oxide. In addition, the quality of desulfurization agent can be evaluated by desulphurization efficiency of calcium hydroxide after digestion, the desulfurization efficiency is higher, the quality of desulfurization agent is better. Therefore, the author intends to use "quick lime reactivity", "desulfurization effect" and "effective desulfurization time" as evaluation indexes when selection calcium based sorbent. The quick lime reactivity is measured by the time it takes to reach the maximum temperature as shown in the following equation (1):

$$A=（T_{max}-T_0）/t \qquad （1）$$

Where A is the reactivity of the quick lime(℃/s or ℃/min) ;T_{max} is the highest temperature reached during the test(℃);T_0 is the initial temperature(℃);t is the time required to reach the highest temperature(s or min).

The determination method and procedure refer to DLT 323-2011 Measurement method for reactivity of quicklime used in dry flue gas desulfurization.

The desulfurization efficiency refers to the ability of desulfurization agent for removing the SO_2 in the flue gas, the computational method is as equation (2):

$$\eta = (C_{inlet} - C_{outlet}) / C_{inlet} \times 100\% \quad (2)$$

Where η is the desulfurization efficiency; C_{inlet} is the SO_2 inlet concentration; C_{outlet} is the SO_2 outlet concentration; Effective desulfurization time refers to the time that takes to reach more than 90% desulfurization efficiency.

Materials

Four types of calcium-based desulfurizing agents (A-D) were used in this study. A and B were lime kiln refractory waste taken from a steelmaking plant, and C and D were taken from two SDA desulfurization systems in a sinter plant.

Comparison tests were conducted under the same conditions for these four desulfurizing agents. During the tests, SDA test device was kept at the same digestive parameters, pulping parameters and spray parameters. The performance of four types of calcium-based desulfurization agents were evaluated by two kinds of evaluation indices, in order to select high quality desulfurization agents to provide a new and economic solution for the high desulfurization efficiency SDA process.

Results and Discussion

Desulfurization mechanism

Quick lime and water prepared into slurry according to a certain proportion, the slurry temperature rise due to the reaction producing heat. The lime slurry sprayed mist shape into the SDA reactor by rotary atomizer to contact with SO_2 in flue gas, chemical reactions occur, generation of solid particles contact with high temperature flue gas and drying, the particles collected to set down by fan suction pumped into the dust collector, and return desulfurization tower recycling. The main chemical reactions of SDA process are as (3) ~ (5):

$$CaO + H_2O = Ca(OH)_2 \quad (3)$$

$$SO_2 + H_2O = H_2SO_3 \quad (4)$$

$$Ca(OH)_2 + H_2SO_3 = CaSO_3 + 2H_2O \quad (5)$$

Effects of lime particle size on lime reactivity

In order to make the four kinds of desulfurization agent in the same particle size range of the digestive reaction, in first, the range of size of lime was optimized. Respectively with three sieve whose aperture is 0.9mm, 1.25 mm and 2mm screening one kind of desulfurization agent, and get three kinds of particle size range of lime, we study the influence of particle diameter on the reactivity of lime digestion. As shown in Figure 2, the calculated results are shown in Table I.

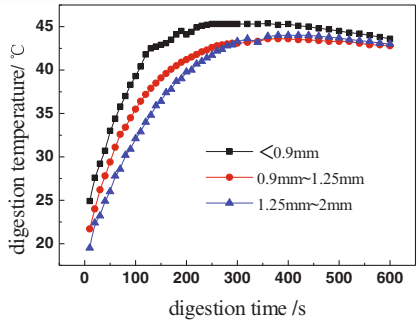

Figure 2. Effect of different lime particle size on digestive reactivity

Table I. Reactivity of lime with different granularity

Particle size range /mm	T_0 /℃	T_{max} /℃	t /S	A ℃/S
<0.9	20	45.4	360	0.071
0.9~1.25	20	44	380	0.063
1.25~2	20	43.6	390	0.061

With the increase of the particle size range, the maximum digestion temperature decreases gradually. As shown in Table I, when particle size is less than 0.9mm,it takes 360 seconds to reach the maximum temperature of 45.4℃.The calculated reactivity is 0.071℃ /S. When particle size is in the range of 0.9~1.25mm, it takes 380 seconds to reach the maximum temperature of 44℃. The calculated reactivity is 0.063℃ /S; When particle size is in the range of 1.25~2mm, it takes 390 seconds to reach the maximum temperature of 43.6℃.The calculated reactivity is 0.061℃ /S. Therefore, when the particle size is less than 0.9mm, the reactivity of the desulfurization agent is the highest.

Reactivity compared with the same size range of four kinds of calcium based sorbents

According to the above law, controlling the particle size of calcium based desulfurization agent in the range of 0.9mm by sieving.The reacvivity of four types of desulfurization agents was studied under the same digestion conditions, the results are shown in Figure 3.

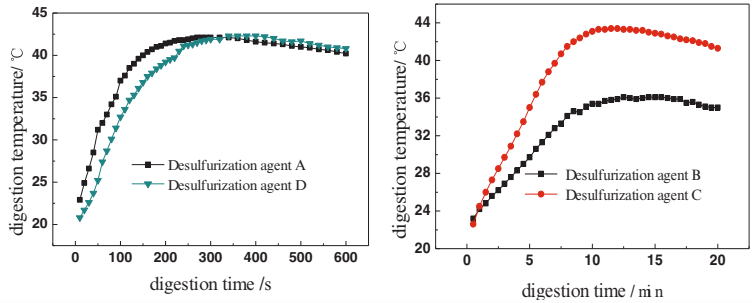

Figure 3. Digestion temperature as a function of time

By Figure 3, the digestion rate of A and D was faster, the time of reaching the highest temperature is 200~300S, while by comparison the digestion rate was lower of B and C, when the digestion time is over 10min, B and C had not yet reached the maximum temperature, the specific results were shown in Table II.

Table II. Comparison of reactivity of four types of desulfurization agents

Desulfurization agent	T_0 /℃	T_{max} /℃	t / min	A ℃/min
A	20	42.1	4.5	4.91
B	20	36.1	14.5	1.11
C	20	43.4	11.5	2.35
D	20	42.3	5.67	3.93

As shown in Table II, the reactivity of the four kinds of desulfurization agent were 4.91℃/min, 1.11℃/min, 2.35℃/min and 3.93℃/min, according to the size of the reactivity ,the result is: A >D > C > B , Because C and D were from SDA system of steel plant, which is used as desulfurization agent, and through the experiment found that the quality of B is not as good as C, indicating that B cannot be used as a substitute for desulfurization agent. The reactivity of A was higher than that of C and D, indicating that the reactivity of A can meet the requirements of the replacement of the desulfurization agent.

Evaluation of desulfurization performance for calcium based sorbent

Figure 4 shows the desulfurization effect curves for desulfurization agent A，C and D, which worked in the same condition. The effective desulfurization duration of three kinds of desulfurization agent when the desulfurization efficiency is higher than 90% is showed in Table III.

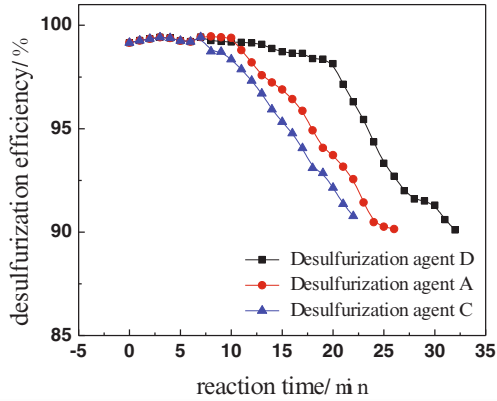

Figure 4. Desulfurization of efficiency of three types of agents

Table III. Effective desulfurization duration of three types of desulfurization agents

Desulfurization agent	Initial SO_2 concentration In flue gas /mg/m^3	Effective duration when the desulfurization efficiency is higher than 90% /min
A	436	28
B	535	11
C	464	24
D	482	32

It can be seen in Figure 4 and Table III that the three types of desulfurization agents, A, C and D can guarantee higher desulfurization efficiency and longer effective desulfurization duration. the effective desulfurization time of A, C and D reached 32min, 28min, 24 min, and the longest effective desulfurization time was A, which is about 1.33 times longer than D, it is showed that the performance of A was better. This because that A is granular lime, it compared to powder lime, the advantage is less affected by water vapor and carbon dioxide in the air, it can guarantee higher reactivity. C and D were powder lime. Although lime particles more fine, active degree is more higher, but at the same time ,the more larger of fine lime surface area, More susceptible impacted by water vapor and carbon dioxide in the air pollution and the deactivation[5].And the reactivity of C and D decline faster after experiencing a long-distance transportation to the desulfurization system.

Conclusions

In an integrated steelmaking facility, lime fines are generated as by-product during calcining of limestone in lime plant. This study showed that this lime fines can be used as raw materials for the preparation of calcium based sorbents for desulfurization. With simple screening and grading, it can be used in the SDA desulfurization system directly. The test results showed that the SDA desulfurization system using lime fines has higher efficiency and lower cost comparing to regular lime reagents. This new SDA desulfurization process is suitable for treating sinter plant offgas

and lime fines is the ideal desulfurization agent for this SDA sintering flue gas desulfurization process.

References

1. Y.-R. Li et al., “Summary and evaluation for the desulfurization technologies applied in iron-steel sintering flue gas”, *Environmental Engineering*, 32(11)(2014),34~52.
2. B. Gu et al., “Application of spray drying absorption (SDA) in desulfurization of sintering flue gas”,*Environmental Engineering*, 31(2)(2013),49~52.
3. J.-S. Li et al., “Experimental study on factors affecting efficiency of flue gas desulfurization by spray drying wet (semi-dry) process”, *Ciesc Jorunal*, 65(2) (2014),724~729.
4. D.-T. Zhang, “Study on desulfurization activity of calcium based sorbent during LIFAC process”, master thesis of Harbin Institute of Technology, *thermal energy engineering*, 2005.
5. L.-Z. Liu et al., “Study on comparability of three calcium-desulfurizing agents for desulfurization of sinter gas on CFBA”,*Environmental pollution & control*, 26(6) (2004) ,418~420.

Characterization of Minerals, Metals, and Materials 2016
Edited by: Shadia Jamil Ikhmayies, Bowen Li, John S. Carpenter, Jiann-Yang Hwang, Sergio Neves Monteiro, Jian Li, Donato Firrao, Mingming Zhang, Zhiwei Peng, Juan P. Escobedo-Diaz, and Chenguang Bai
TMS (The Minerals, Metals & Materials Society), 2016

KINETIC STUDIES FOR THE ABSORPTION OF ORGANIC MATTER FROM PURIFIED SOLUTION OF ZINC BY COCONUT SHELL ACTIVATED CARBON

Aiyuan Ma [1,2,3], Chenyu Sun [3,4], Guojiang Li [4], Yongguang Luo [1,2,3,4], Xuemei Zheng [1,2,3], Jinhui Peng [1,2,3], Hongying Xia [1,2,3], Libo Zhang [*1,2,3], Chao Liu [1,2,3]

[1]Yunnan Provincial Key Laboratory of Intensification Metallurgy, Kunming 650093, Yunnan, China;
[2]Key Laboratory of Unconventional Metallurgy, Ministry of Education, Kunming 650093, China;
[3]Faculty of Metallurgy and Energy Engineering, Kunming University of Science and Technology, Kunming 650093, China.
[4]Yunnan Chihong Zn & Ge Co., Ltd, Qujing 655011, China

Keywords: Organic matter, Coconut shell activated carbon, Adsorption kinetics, Adsorption mechanism

Abstract

In this study, the adsorption characteristics of organic matter from purified solution of zinc was investigated using coconut shell activated carbon, with the aim to remove the organic matter from the solution after zinc hydrometallurgy. The effects of adsorption time on organic matter removal rate were studied. According to the experimental result, the COD and removal rate of organic matter in purified solution of zinc were 33.04mg/L and 54.36%, respectively, under the condition of adsorption time of 160min, temperature of 75℃, sample weight of 0.75g/L. The kinetic results showed that the organic matter adsorption onto coconut shell activated carbon followed pseudo-second-order kinetics model well with a coefficient greater than 0.9916. Weber and Morris theory, Boyd dynamic equation analysis showed that external mass transfer is the primary control step.

Introduction

Zinc is an important base metal used in the production of alloys and chemical additives, and is a common metal used in the galvanizing and battery manufacturing industries [1, 2]. Zinc is mainly produced by the roasting–leaching–electrolysis route (RLE) which combines pyro- and hydrometallurgical operations [3]. However, various types of organic matters such as industrial bone glue [4], sodium ethylxanthate [5], alcohols organic matter [6], tannic acid [7], P_{204} [8], etc. are used in the zinc hydrometallurgical process. At the same time, these organic matters have some negative influence for the electrolytic zinc production in saving energy and reducing consumption and the improving quality [9-12]. Therefore, the removal of impurities in the purified solution of zinc is an important step for improving both zinc recovery and quality of the electrodeposited zinc.

Organic matter removal from purified solution of zinc has been traditionally carried out by

chemical precipitation, ion exchange, membrane processes [13, 14], which are expensive and inefficient, especially for low-strength wastewaters. However, adsorption has been shown to be an economically feasible alternative method for removing organic impurities from wastewaters [15]. These processes are usually based on the use of activated carbon. Activated carbon has a strong affinity for organic molecules and contains oxygenated functional groupings on the entire surface, which are capable for organic contaminants removal [7, 16].

This paper studied the effects of adsorption time on organic matter removal rate, and investigated the adsorption kinetics and mechanism. An adsorption model is proposed to predict the kinetic behavior for the sorption of organic matter based on the pseudo second-order kinetic equation, Weber and Morris theory and Boyd dynamic equation.

Materials and methods

Materials

Purified solution of zinc was obtained from a lead and zinc smelter in Yunnan province, China. Analytical grade reagents were used in this study. High quality coconut shell activated carbon was used to adsorb organic matter from purified solution of zinc. The coconut shell activated carbon used in this study was in the size of range of 10 - 24 mesh and supplied by Yunnan Chihong Zn & Ge CO, LTD, China. The BET surface area and iodine adsorption value of coconut shell activated carbon were measured to be 960.8 m^2/g and 890.61 mg/g, respectively. The coconut shell activated carbon was dried to a temperature of 80 ℃ for 2 h in a constant temperature drying oven. The initial concentration of organic matter in purified solution of zinc was 72.39 mg/L.

Experimental method

An amount of coconut shell activated carbon (0.375g, dry basis) was placed in 1000 mL closed glass reactor equipped with a magnetic stirrer, into which 500 mL of purified solution of zinc was added. The effect of different adsorption time on organic matter removal rate was studied, and the experiment was performed in a shaker bath for 200rpm and 75 ℃. After filtration with the quantitative filter, the content of organic compounds in the aqueous sample was analyzed with COD dichromate method (GB11914-89). The COD values were calculated by

$$COD\ (mg/L) = 8000C(V_1 - V_2)/V_0 \quad (1)$$

Where C is the concentration of ferrous ammonium sulfate standard solution, mol/L. V_1 and V_2 are the volumes of ferrous ammonium sulfate consumed in blank experiment and sample determination, respectively, mL. V_0 is the sample volume, mL.

Results and discussion

Effect of Adsorption time on organic matter removal rate

The organic matter removal rate under different adsorption times from the zinc purified

solution are displayed in Figure. 1. The results show that the organic matter removal rate increased with the rise of the adsorption time. The adsorption time showed the strong enhanced effect on the organic matter removal rate from the zinc purified solution. The organic matter removal rate was as high as 54.04 % while the adsorption time was 140 min, and the content of organic matter is 33.27 mg/L. On the other hand, the adsorption equilibrium is reached after 140 min.

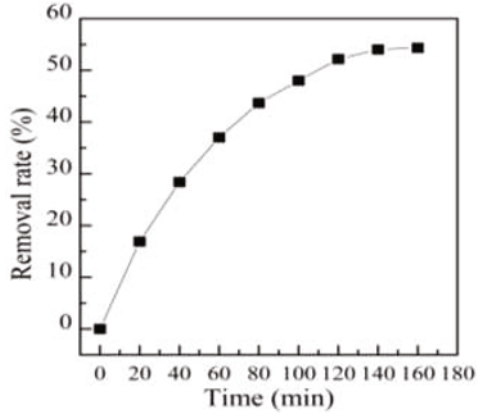

Figure 1 The effect of adsorption time on organic matter removal rate

Adsorption kinetics

Adsorption kinetics describes the rate of adsorbate uptake governing the contact time of adsorption reaction, which is an important characteristic defining the efficiency of adsorption. Adsorption kinetics provides understanding on adsorption mechanism. Based on the equilibrium data, the kinetics study was performed at 25℃. The adsorption kinetics data was evaluated using the pseudo second-order models [17, 18] as discussed below.

The experimental date in this paper have been analyzed using a pseudo second-order models according to Equation (2), which on integration becomes Equation (3),

$$\frac{dq_t}{d_t} = k\,(q_e - q_t)^2 \tag{2}$$

A linear equation can be shown as follows:

$$\frac{t}{q_t} = \frac{1}{h_0} + \frac{t}{q_e} \tag{3}$$

and as t=0, the initial sorption rate, h(mg/g•min) is:

$$h_0 = kq_e^2 \tag{4}$$

Where q_e is the amount of organic matter at equilibrium, mg/g, and k is the equilibrium rate constant for pseudo second-order sorption, g/mg•min. And the rate constant k, initial sorption rate h_0, and predicted q_e can be calculated from the plot of t/q versus time t using Eq. (3).

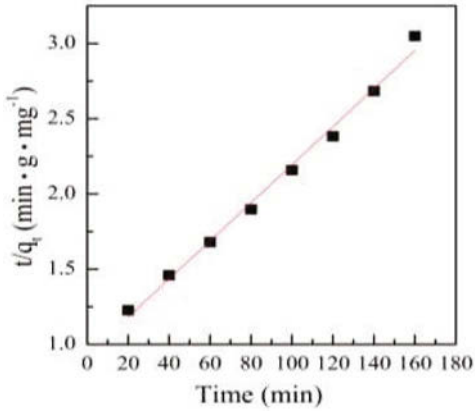

Figure. 2 pseudo second-order kinetic plot for the sorption of organic matter onto coconut shell activated carbon.

Table I. Kinetic parameters for organic matter onto coconut shell activated carbon.

Model	Equation	Constants		
		k ($g \cdot mg^{-1} \cdot min^{-1}$)	q_e ($mg \cdot g^{-1}$)	R^2
	$t/q_t = 0.0127t + 0.9283$	0.00017	79.05	0.9916

Figure 2 shows the plot between t/q versus time t. The initial sorption rate h_0, pseudo second-order rate constant k, amount of organic matter adsorbed at equilibrium q_e, the corresponding linear regression correlation coefficient R^2 values and Equation are given in Table 1. It can be seen that the correlation coefficient (R^2) of the pseudo second-order model is 0.9916. The higher R^2 values confirm that the sorption process follows a pseudo-second-order mechanism. Also this suggests the assumption behind the pseudo-second-order model that the organic matter uptake process is due to chemisorption [19].

Adsorption mechanisms

The Weber and Morris [20-23] intraparticle diffusion model was also used since most adsorption processes can be described with Eq. (5). This model considers intraparticle diffusion as a rate limiting step.

At the same time, a intraparticle diffusion parameter, ki, has been defined by Weber and Morris and is shown in Equation (5),

$$q_t = k_i t^{1/2} \quad (5)$$

Where k_i is the rate constant of intraparticle diffusion ($g \cdot kg^{-1} \cdot min^{-1/2}$) and is determined from the linear plot of q_t versus $t^{1/2}$ (Figure. 3). The rate constant k_i is shown in Table 2.

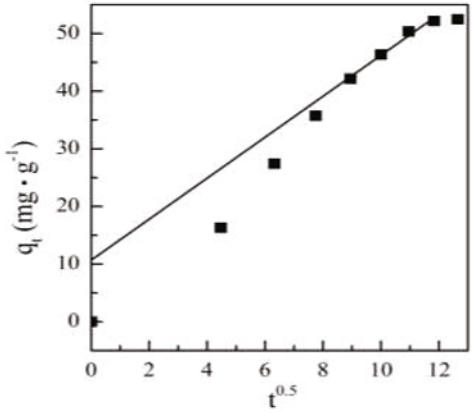

Figure 3. Intraparticle diffusion plot for organic matter onto coconut shell activated carbon.

In general the sorption process involves multisets mainly the surface diffusion followed by the intraparticle diffusion [24]. From Figure. 3, it was noted that the sorption process tends to be followed by two phases. It was found that the linear portion ended with a smooth curve followed by a linear portion. A similar type of pattern was reported previously by Vadivelan et al. [19] for methylene blue onto rice husk. The two phases in the intraparticle diffusion plot suggest that the sorption process proceeds by surface sorption and intraparticle diffusion. The initial curved portion of the plot indicates a boundary layer effect while the second linear portion is due to intraparticle or pore diffusion. The calculated intraparticle diffusion coefficient k_i value was 3.5527 $mg \cdot g^{-1} \cdot min^{-1/2}$.

Table II. The second linear parameter for intraparticle diffusion plot.

Model	Equation	Constants	
		k ($g \cdot mg^{-1} \cdot min^{-1}$)	R^2
	$q_t = 3.5527t^{1/2} + 10.6924$	3.5527	0.9749

In order to gain a better knowledge of the adsorption mechanism, the kinetic data were also analyzed by means of the Boyd model.

It was reported recently that Boyd's kinetic equation [21-23] was used for several solid liquid sorption systems including the sorption of malachite green onto jute fiber carbon [24], methylene blue onto fly ash [18] and methylene blue onto rice husk [19].

The Boyd's kinetic expression was given by the Eq. (6) as follows:

$$F = 1 - (6/\pi^2)\exp(-Bt) \tag{6}$$

And

$$F = q/\ q \tag{7}$$

Where q_0 is the amount of organic matter adsorbed at infinite time (mg/g) and q represents the amount of organic matter adsorbed at any time t (min), F represents the fraction of solute adsorbed at any time t, and Bt is a mathematical function of F.

Substituting Eq. (7) in (6), Eq. (6) simplifies to

$$Bt = -0.4977 - \ln(1 - F) \tag{8}$$

The Bt values at different contact times can be calculated using Eq. (8). The calculated Bt values were plotted against time t as shown in Figure. 3. Figure. 3 is used to identify whether external transport or intraparticle transport control the rate of sorption [19]. It was observed that the plots were linear but do not pass through the origin confirming that, for the studied initial organic matter concentration, external mass transport mainly governs the sorption process [19].

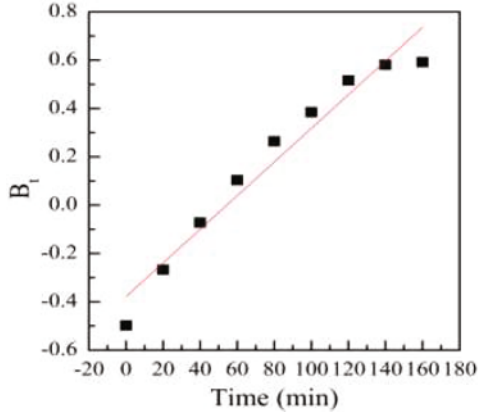

Figure 4. Plot of Bt versus t (Boyd plot).

Conclusions

The present study shows that the coconut shell activated carbon can be used as an adsorbent for the removal of organic matter from purified solution of zinc. The effect of adsorption time on organic matter removal rate was significant. The COD and removal rate of organic matter in purified solution of zinc were 33.04mg/L and 54.36%, respectively, under the condition of adsorption time of 160min, temperature of 75℃, sample weight of 0.75g/L.

The sorption data were found to follow pseudo-second order kinetics. The organic matter uptake process was found to be controlled by external mass transfer at earlier stages and by intraparticle diffusion at later stages. A Boyd plot confirms the external mass transfer as the slowest step involved in the sorption process.

Acknowledgements

The authors are grateful for the financial supports from the National Natural Science Foundation of China (51464024), the National Natural Science Foundation of China (51504119), the Yunnan Province Young Academic Technology Leader Reserve Talents (2012HB008), and the 2014 PhD Newcomer Award in Yunnan Province (1319880207). In addition, the authors would like to thank all those who helped during the writing of this paper, especially the corresponding author of this paper, Professor Libo Zhang.

References

[1] Z.Y. Liu et al., "Leaching of hemimorphite in NH_3–$(NH_4)_2SO_4$–H_2O system and its mechanism," Hydrometallurgy, 125(2012), 137-143.

[2] Q.X. Li et al., "Dissolution mechanism and solubility of hemimorphite in NH_3–$(NH_4)_2SO_4$–H_2O system at 298.15 K," Journal of Central South University, 21(2014), 884-890.

[3] H.S. Xu et al., "Sulfuric acid leaching of zinc silicate ore under pressure," Hydrometallurgy, 105(2010), 186-190.

[4] C.X. Xiong, "Study on effects of organic substance on zinc electrowinning," Yunnan Metallurgy (in Chinese), 38(2009), 78-81.

[5] X.L. He, "The effect and analysis of the organic and oil on zinc electrowinning," Hunan Nonferrous Metals (in Chinese), 26(2010), 30-33.

[6] I. Ivanov, "Increased current efficiency of zinc electrowinning in the presence of metal impurities by addition of organic inhibitors," Hydrometallurgy, 72(2004), 73-78.

[7] S.J. Pu and D.X. Yang, "Effect of tannin on zinc electrolysis current efficiency," Nonferrous Metals (Extractive Metallurgy) (in Chinese), (2004), 16-19.

[8] A.Y Tang, "The influence and removal of organic matter on electrodeposition process of zinc," Technology and Equipment (in Chinese), 2009, 35-37.

[9] D. Lidia, "Sorption of zinc ions from aqueous solutions on regenerated activated carbons," Journal of Hazardous Materials, 101(2003), 191−201.

[10] X.J. Hu et al., "Copper/activated carbon as catalyst for organic waster water treatment," Carbon, 37(1999), 631−637.

[11] W. Li et al., "Pilot-scale extraction of zinc from the spent catalyst of vinyl acetate synthesis by microwave irradiation," Hydrometallurgy, 92(2008), 79−85.

[12] A.J. Tsamba et al., "Pyrolysis characteristics and global kinetics of coconut and cashew nut shells," Fuel Processing Technology, 87(2006), 523−530.

[13] F. Pan et al., "Progress in research of adsorption of tannin acid from water," Technology of Water Treatment (in Chinese), 38(2012), 7-10.

[14] M. Campinas and M.J. Rosa, "The ionic strength effect on microcystin and natural organic matter surrogate adsorption onto PAC," Journal of Colloid and Interface Science, 299(2006), 520-529.

[15] S. Chegrouche, A. Mellah, and M. Barkat, “Removal of strontium from aqueous solutions by adsorption onto activated carbon: kinetic and thermodynamic studies,” Desalination. 235 (2009), 306–318.
[16] Y. Sun and B.X. Diao, “Performance of activated carbon adsorption for tannic acid removal,” Water Purification Technology (in Chinese), 21 (2012), 109-113.
[17] M. Do˘gan et al., “Kinetics and mechanism of removal of methylene blue by adsorption onto perlite,” Journal of Hazardous Materials, B109 (2004), 141–148.
[18] K. Vasanth Kumar et al., “Modeling the mechanism involved during the sorption of methylene blue onto fly ash,” Journal of Colloid and Interface Science, 284(2005) ,14–21.
[19] V. Vadivelan and K. Vasanth Kumar, “Equilibrium, kinetics, mechanism, and process design for the sorption of methylene blue onto rice husk,” Journal of Colloid and Interface Science, 286 (2005), 90–100.
[20] W.J. Weber and J.C. Morris, “Kinetics of adsorption on carbon from solution,” Journal of the Sanitary Engineering Division, 89(2) (1963), 31-60.
[21] G.E. Boyd, A.W. Adamson and L.S. Myers Jr, “The exchange adsorption of ions from aqueous solutions by organic zeolites. II. Kinetics1,” Journal of the American Chemical Society, 69(11) (1947), 2836-2848.
[22] M.R.R. Kooh et al., “Azolla pinnata: An Efficient Low Cost Material for Removal of Methyl Violet 2B by Using Adsorption Method,” Waste and Biomass Valorization, 6(2015),1-13.
[23] B. Acevedo et al., “Properties and performance of mesoporous activated carbons from scrap tires, bituminous wastes and coal,” Fuel, 151(2015), 83-90.
[24] K. Porkodi and K. Vasanth Kumar, “Equilibrium, kinetics and mechanism modeling and simulation of basic and acid dyes sorption onto jute fiber carbon: Eosin yellow, malachite green and crystal violet single component systems,” Journal of Hazardous Materials, 143 (2007), 311–327.

Characterization of Minerals, Metals, and Materials 2016
Edited by: Shadia Jamil Ikhmayies, Bowen Li, John S. Carpenter, Jiann-Yang Hwang, Sergio Neves Monteiro, Jian Li, Donato Firrao, Mingming Zhang, Zhiwei Peng, Juan P. Escobedo-Diaz, and Chenguang Bai
TMS (The Minerals, Metals & Materials Society), 2016

RECOVERY OF PALLADIUM FROM SPENT Pd/Al_2O_3 CATALYST BY HYDROCHLORIC ACID LEACHING

Yongbin Yang[1], Long Hu[1], Qian Li[*], Bin Xu[1], Xuefei Rao[1], Tao Jiang[1]

1School of Minerals Processing & Bioengineering, Central South University, Changsha, Hunan, China, 410083, *Corresponding author: Qian Li, csuliqian@ 126.com

Keywords: Palladium, Spent catalyst, Recovery, Hydrochloric acid leaching

Abstract

Spent Pd/Al_2O_3 catalyst is an important secondary resource of palladium metals. The highly efficient recovery of palladium was hard to implement due to the wrapping of catalyst carriers, accumulating carbon on surface and existing as stable palladium oxide. An effective process for recovery of palladium was investigated. Samples were initially roasted to eliminate carbon. Then, the roasted mass was reduced with reductive agent for the purpose of transferring palladium oxide to palladium. The reduced residue was further leached using hydrochloric acid with suitable oxidizing agent to recover palladium. The results showed that the palladium extraction only reached to16.24% by direct leaching process and 43.51% by roasting-leaching process. However, it achieved 98.71% by roasting-reduction-leaching process under the appropriate leaching conditions of HCl 5M, $NaClO_3$ 2.5g/L at 95° C for 2h.Additionally, the feasible conditions involved in roasting and reduction steps were also investigated.

Introduction

Palladium is an essential mineral resource in modern society due to the rapid increase in its demands in different fields of industry [1,2]. Because of its low natural abundance and high costs of production, it becomes a worldwide tendency to recover and refine palladium from different containing spent materials, particularly spent Pd/Al_2O_3 catalysts. Large quantities of these catalysts are used in the refining industry for the purification and upgrading of various petroleum streams and residues [1,3].

Therefore, hydrometallurgical processes are profitable for recovery and separation of precious metals from the catalysts containing precious metals such as platinum and palladium. Literature survey revealed that the support dissolution and noble metal dissolution have been generally reported [4,5].In the former case; the support is dissolved with a non-oxidizing acid while the noble metals are not dissolved and remained as residues. However, this process requires a large amount of reagents and causes high costs and environmental concerns. In the latter case; the noble metals are extracted from the support by an acidic solution of an oxidant, leaving the bulk

of the support. On the contrary, the process for direct dissolution of precious metals is environmentally friendly, lower corrosive and costly.

Due to the partly transformation of the acid soluble γ-alumina to the acid insoluble α-alumina and the γ-alumina partially dissolved and interfered with the precious metals, the latter process probably suffers from low recovery of the precious metals [6,7]. Unlike other precious metals, however, palladium can be more easily accessible into solution.

This paper aims to recover palladium from spent Pd/Al_2O_3 catalyst utilizing a clean and simple technique. A hydrochloric acid leaching process was investigated for achieving the appropriate recovery conditions of palladium.

Experimental

Materials

A representative sample of spent Pd/Al_2O_3 catalyst weighed 5 kg was obtained. The original catalyst was used for de-oxygenation during production of petrochemical industry. The spent catalyst was in the form of cylindrical pellets of alumina coated with a thin layer of palladium. The pellets have a diameter of 2~5 mm.

X-ray fluorescence, atomic absorption spectrometer and infrared C-S analyzer was used for chemical analysis of the spent catalyst. The composition of samples is shown in Table Ⅰ. The XRD pattern of the spent catalyst sample (see Figure 1.) showed that α-aluminum oxide (α-Al_2O_3) was the major components while palladium was the trace constituent. Palladium concentration in the solution was assayed by using atomic absorption spectroscopy. The palladium content in the spent catalyst sample was assayed to be 2120.0g/t while the main remainder was aluminum compounds.

Table Ⅰ. Main Components of Spent Catalyst/wt.%

Pd*	Pt*	Re*	Al_2O_3	SiO_2	C	S
2120.0	0.45	0.22	77.76	0.82	9.20	0.02

"*" units are g/t.

Chemicals

Hydrochloric acid (wt.37%), sodium chlorate ($NaClO_3$) (AR) and hydrogen peroxide (H_2O_2) (wt.30%) were used for the preparation of leaching solutions. Hydrazine hydrate ($N_2H_4 \cdot H_2O$) (wt.80%) and formic acid (HCOOH) (wt.88%) were used as a reductive agent for palladium. All used chemicals were of high grade for the laboratory usage. Doubly distilled water was used for dilutions.

Dissolution Procedures

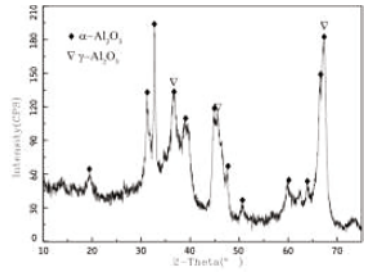

Figure 1. X-ray diffraction pattern of spent catalyst

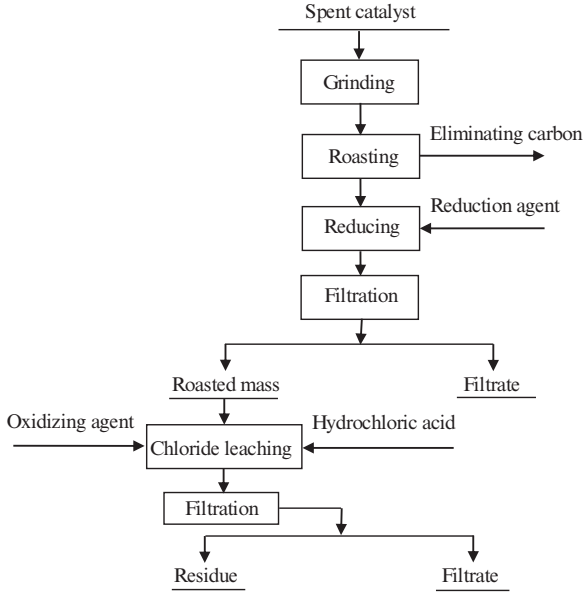

Figure 2. Process flow sheet for palladium recovery from spent catalyst

Preliminary exploratory experiments were conducted. The results figured out that the grinding of the spent catalyst is not a key controlling parameter in palladium recovery procedure. However, the grinding size is closely connective with homogenization of the sample [5]. Therefore, the sample of the spent catalyst was grounded using ball grinding mill, then, passed through a sieve of particle size 200 meshes. The minus sieve powder was used for follow-up experiments.
Samples were dried in a circulation oven at 75ºC more than 24h. After that, spent samples were

roasted in a muffle furnace at air atmosphere in order to eliminate the carbon. Then, the roasted mass is reduced with reductive agent for the purpose of transferring palladium oxide to palladium. Therefore, the reduced residue is further leached using hydrochloric acid with oxidizing agent as oxidant to recover palladium. The reducing and leaching experiments were conducted in a conical flask reactor along with an electronic agitation and a condenser pipe device. Figure 2. showed the procedures followed in this work for palladium recovery from the spent catalyst.

Results and Discussion

Theoretical Analysis of Palladium Leaching

Typically, dissolution of palladium from support materials by hydrometallurgical processes is controlled by the following reactions and the corresponding standard potentials measured in aqueous chloride media [8-11].

$$Pd + 4Cl^- = PdCl_4^{2-} + 2e^- \qquad E^o = 0.62V \qquad (1)$$

$$PdCl_4^{2-} + 2Cl^- = PdCl_6^{2-} + 2e^- \qquad E^o = 1.29V \qquad (2)$$

Meanwhile, it is listed the standard reduction potentials of some commonly used as oxidants.

$$ClO_3^- + 6H^+ + 6e^- = Cl^- + 3H_2O \qquad E^o = 1.34V \qquad (3)$$

$$H_2O_2 + 2H^+ + 2e^- = 2H_2O \qquad E^o = 1.77V \qquad (4)$$

According to Equations (1), Palladium can be oxidized with a standard electrode potential value of 0.62 V in the presence of chloride ions. Similarly, according to Equations (3) and (4), sodium chlorate or hydrogen peroxide as oxidant can be reduced in the acid media to water with a standard electrode potential value of 1.34 V or 1.77 V. Because of the highly enough potential of those reduction reactions, the oxidation reactions can be able to take place. Therefore, both of the two nonmetallic oxidizing agents should be capably dissolved palladium in chloride media.
Eventually, palladium leaching with oxidizing agent in hydrochloric acid was studied to optimize the different parameters that control the dissolution process. In the following sections the effect of hydrochloric acid concentration, oxidant type, roasting temperature will be discussed.

Direct Hydrochloride Acid Leaching

Based on the theoretical analysis of palladium leaching, it is known that recovery palladium with oxidizing agent in hydrochloric acid media was feasible process [8]. Samples from the minus sieve powder spent catalyst were used for direct hydrochloride acid leaching in the conditions 6M HCl and 2.0g/L $NaClO_3$ at 95°C for 1h with a l/s ratio of 5/1 under 500rpm.Under these conditions, only 16.24% palladium was extracted. Combined with the result, an analysis has

been given. On one hand, carbon content of the samples reach up to 9.20% and the carbonaceous matters are accumulated on surface of spent catalyst, which lead to difficulty in recovery of palladium. On the other hand, there is still part of palladium oxidized to palladium oxide in the use of the catalyst. The chemical properties of palladium oxide is so stable that it is not easy to extract effectively without reducing procedure

Roasting and Hydrochloride Acid Leaching

Because of the low extraction ratio, prior to the leaching process, a pretreatment roasting procedure was added to deprive the carbonaceous materials as well as other harmful elements. Samples were roasting at 600°C for 2h in air atmosphere and after cooling down, the carbon content was tested by infrared C-S analyzer in order to guarantee that carbon was totally deprived. Therefore, the roasted mass was used for hydrochloride acid leaching under the same conditions as direct leaching. Result suggested that the ratio of palladium extraction increased sharply from 16.24% to 43.51%.
Consequently, it is clearly indicated that roasting procedure contributes to recovery of palladium. In addition, palladium extraction is still inefficient and limited and palladium cannot leach into dissolution entirely without reduction process. Therefore, a reasonable process (see Figure 2) to reinforce the leaching procedure and increase the ratio of palladium extraction was presented in the following experiments.

Effects of Parameters of Palladium Recovery

Based on the results of exploratory experiments, it pointed out that palladium can relatively simply be dissolved in hydrochloric solution with an appropriate oxidant present under a suitable conditions. Importantly, the conditions must be considerably improved by adding a reduction procedure before leaching step. Several investigations have been studied for the various effects of palladium recovery from spent Pd/Al_2O_3 catalyst. However, there were so many parameters, only a few which considered to the major factors was investigated.
For instance, roasting temperature and time, types and concentration of reducing agent, types of oxidant, hydrochloride acid concentration, were studied in this section. The results emphasized the optimum flow conditions for palladium extraction. It is worth noting that the residue from the leaching experiment was filtered and washed with doubly distilled water several times and the results were depended upon residue analysis.

Roasting Temperature and Time The effect of roasting temperature on palladium extraction was shown in Figure 3(A). The palladium extraction increased with increasing temperature between 500ºC and 575ºC, reached a plateau at 575ºC and then decreased between 575ºC and 650ºC. The optimal roasting temperature was 575ºC.
The effect of roasting time on palladium extraction was shown in Figure 3(B). The palladium extraction increased with increasing time between 1h and 2.5h and decreased between 2.5h and

3h. In 2h and 2.5h, the palladium extraction was very nearly the same, whereas extending time consumed more energy, the optimal roasting temperature selected 2h. Furthermore, it confirmed that palladium was lie on the aluminum support as a thin metallic layer [12]. When roasting temperature was higher 575ºC and time was more than 2.5h, palladium may be infiltrated into the internal catalyst and caused the wrapping of the catalyst carriers. It seemed to be the main reason that palladium extraction was decreased.

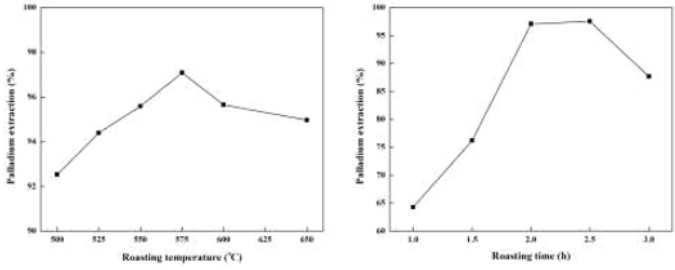

(A) (B)

Figure 3. Effects of roasting temperature and time on ratio of palladium extraction

Types and Concentration of Reducing Agent The effect of types of reducing agent on palladium extraction was shown in Table Ⅱ. Without reducing step, the ratio of palladium extraction was only 53.12%, while added reducing step it has been a considerable enhancement. Using HCOOH and $N_2H_4 \cdot H_2O$ as reducing agent, it was 91.04% and 91.10% and just little difference. Practically, HCOOH is acidic medium, which causes to filtrate difficultly. Therefore, choosing hydrazine hydrate($N_2H_4 \cdot H_2O$) as reducing agent is a better choice.

Table Ⅱ .Effect of Types of Reducing Agent on Ratio of Palladium Extraction

Types	None	HCOOH	HCOOH+HCl	$N_2H_4 \cdot H_2O$
Ratio/%	53.12	91.04	85.62	91.10

The effect of concentration of reducing agent on palladium extraction was shown in Figure 4(A).It can be seen that the palladium extraction was relatively high with a ratio up to 95%. The ratio of palladium extraction increased with increasing concentration of $N_2H_4 \cdot H_2O$, reaching a maximum value of 97.45% at the concentration of 4M, and then decreased between 4M and 4.67M. Hence, the optimal concentration of reducing agent selected 4M. Besides, to the mechanism of reducing process, we put forward to the further investigation.

Types of Oxidant and Concentration of Hydrochloride Acid The effect of types of oxidant on palladium extraction was shown in TableⅢ. Two groups of contrast experiments under different roasting temperature were in accord with the results, which the leaching efficiency of $NaClO_3$ as the oxidant was higher than H_2O_2 as the oxidant. Therefore, the ($HCl+NaClO_3$) system is

superior to the ($HCl+H_2O_2$) system for recovery of palladium.

The effect of concentration of hydrochloric acid (from 2M to 6M) on palladium extraction was studied and results were shown in Fig. 4(B). It showed that palladium extraction trended gradually to increase with increasing the concentration of hydrochloric acid reaching a constant maximum value of 96.21% at 5M HCl. However, palladium extraction decreased reaching a lower point at 6M HCl. The results indicated that better palladium extraction occurred when more concentrated hydrochloric acid was utilized. Hydrochloric acid concentration played an important role in palladium recovery [12]. However, when the concentration of HCl was higher than 6M, the properties of solution and the mechanism of oxidant may be changed, then attributing to the drop of palladium extraction sharply. Therefore, the optimal concentration of hydrochloric acid selected 5M.

TableⅢ. Effect of Types of Oxidant on Ratio of Palladium Extraction/%

Roasting temperature/°C	Types of oxidant	Conc. of oxidant/ mol/L	Palladium extraction
575	H_2O_2	1.5	97.09
575	$NaClO_3$	2.5*	98.71
600	H_2O_2	1.5	91.70
600	$NaClO_3$	2.5*	93.52

"*" units are g/L.

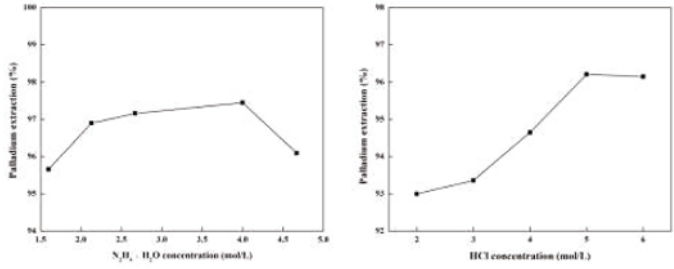

(A) (B)

Figure 4. Effects of the concentration of $N_2H_4{\cdot}H_2O$ and HCl on ratio of palladium extraction

Conclusions

Recovery of palladium from spent Pd/Al_2O_3 catalyst by hydrochloric acid leaching has been evaluated. The following conclusions can be drawn,

(1).Based on the exploratory experiments, roasting procedure deprived the carbonaceous materials and reduction procedure transferred palladium oxide into palladium. The two key steps devoted to reinforce the hydrochloric acid leaching process. Therefore, the complete and

reasonable flow sheet of roasting-reducing-leaching processes for recovery of palladium is presented.

(2).The major parameters affecting the palladium extraction was investigated. Through comparative study, hydrazine hydrate ($N_2H_4 \cdot H_2O$) and sodium chlorate ($NaClO_3$) were used as reductive agent in reducing step and oxidant in leaching step, respectively. Under the appropriate leaching conditions of HCl 5M, $NaClO_3$2.5g/L at 95ºC for 2h, the ratio of palladium extraction was up to 98.71%.

Acknowledgements

This work was financially supported by the National Natural Science Foundation of China (Grant No. 51574284), Science and Technology Program of Yunnan (No. 2013IB020).

References

[1].M.A. Barakat, M.H.H. Mahmoud and Y.S, Mahrous, "Recovery and Separation of Palladium from Spent Catalyst,"*Applied Catalysis A*, General 301(2006), 182-186.

[2].Deng Dexian, "Study on Recovery of Palladium from Pd-C Catalyst," *Chinese Journal of Rare Metals*, 23 (2) (1999), 104-107.

[3].M. Marafi and A. Stanislaus, "Options and Processes for Spent Catalyst Handling and Utilization," *Journal of Hazardous Materials*, B101(2003), 123-132.

[4].WangYunhua, WuXiaofeng and TongWeifeng, "Present Research Status and Developments on Recycling Technology of Renewable Resources of Platinum Group Metals," *Precious Metals*, 32(1) (2011), 76-79.

[5].Z. Xiao and A.R. Laplante, "Characterizing and Recovering the Platinum Group Minerals——a Review," *Minerals Engineering*, 17 (2004), 961-979.

[6].Liu Shijie, *Metallurgy of Platinum Group Metals* (ChangSha, CS: Central South University Press, 2013), 426-427, 446-449.

[7]. B. Ramachandra Reddy, B. Raju and Jin Young Lee et.al., "Process for the Separation and Recovery of Palladium and Platinum from Spent Automobile Catalyst Leach Liquor Using LIX 84I and Alamine 336,"*Journal of Hazardous Materials*, 180(2010), 253-258.

[8].Wu Kuo-Ying Amanda, "Recovery of Precious Metals from Automatic Catalytic Converters" (Ph.D.thesis, the University of Tulsa, 1993), 8-14.

[9].Shuai Chen, ShaoboShen and Yao Cheng et.al., "Effect of O2 and CO Pretreatment on Leaching Rh from Spent Auto-catalysts with Acidic Sodium Chlorate Solution," *Hydrometallurgy*, 144-145(2014), 69-76.

[10].Chu Jianhua, "Metallurgical Thermodynamics Analysis of Palladium Extraction," *Precious Metals*, 5(4) (1984), 9-15.

[11].Chen Jing, "Some Rules on Redox Reaction of Platinum Group Metals," *Precious Metals*, 1(1) (1991), 7-15.

[12].K. Shams and F. Goodarzi, "Improved and Selective Platinum Recovery from Spent α-aluminum Supported Catalysts Using Pretreated Anionic Ion Exchange Resin," *Journal of Hazardous Materials*, B131(2006), 229-237.

Characterization of Minerals, Metals, and Materials 2016
Edited by: Shadia Jamil Ikhmayies, Bowen Li, John S. Carpenter, Jiann-Yang Hwang, Sergio Neves Monteiro, Jian Li, Donato Firrao, Mingming Zhang, Zhiwei Peng, Juan P. Escobedo-Diaz, and Chenguang Bai
TMS (The Minerals, Metals & Materials Society), 2016

PREVENTION OF AIRBORNE DUST FROM PETROLEUM COKE STOCKPILES

Robert Kozicki[1], George Wrightson[1]

[1]Andrew S. McCreath & Son, Inc.; 1649 Bobali Drive, Harrisburg, PA 17104

Keywords: Silt, Moisture, Stockpile

Abstract

To prevent airborne dust from Petroleum Coke stockpiles, there must be an understanding of all the variables. The first variable is the particle size of the material in the stockpile. The USDA has defined silt as material with a particle size smaller than 200 mesh. The US EPA has adopted this definition in their regulations (EPA Appendix C.2). The second variable is moisture. It is common for stockpiles of petroleum coke to have water or some other dust suppressant applied to them to prevent airborne dust. This technique is only effective if the suppressant can impact the moisture of the -200 mesh material. This study will provide data on the relationship between moisture and particle size as it applies to the prevention of airborne dust from petroleum coke stockpiles.

Introduction

In the last several years, the movement of nascent dust from petroleum coke stockpiles has become a hot political topic in places such as Detroit and Chicago. Dust or silt, defined by the EPA as material < 200 mesh in size, is regulated to ensure good air quality for all people living in the United States. For years the process of minimizing dust from petroleum coke stockpiles was to add a dust suppressant to the material usually in the form of water. The water is applied by water cannon or rain bird directed at the top of the stockpile. The top of the stockpile is most susceptible to the effect of wind on the pile hence the application of dust suppression in this area.

How much dust suppression is needed to keep the dust from becoming airborne or what moisture does the -200 mesh material need to be to keep it from going airborne? What happens to the water that is applied?

The primary mechanism when looking at the effects of applying water to silt material is that it causes the silt to adhere to itself and larger particles through a surface attraction. When the silt pieces have attached themselves to other particles, including other silt particles, they appear to be larger in size and thus will not pass the -200 mesh sieve. At this point the natural state that will not pass 200 mesh is not silt and will not be airborne particles.

Anatomy of a Stockpile

A stockpile contains a heterogeneous combination of particle sizes. During normal handling of the material breakage occurs and the proportion of undersize material increases. The hardness of the material is the key variable in how much undersize material is generated during this normal handling. To the inexperienced eye, many stockpiles appear to have no fines associated with them, but the fines are there. Fines tend to hang in the middle of the pile and the lumpy material will roll down the sides. The picture below illustrates this phenomenon.

Figure 1: Typical Stockpile

The next picture illustrates how fines will hang in the middle of the pile.

Figure 2: Same stockpile with fines showing

So what is the typical size distribution in a stockpile of petroleum coke? It depends on whether any processing of the material was done at the refinery and how many times it was handled. A typical stockpile from a Midwestern refinery shows the following size distribution.

Table I. Typical Stockpile Sizing in Natural State

	%
+1/4	55.6
+16M	37.3
+30M	7.1
+60M	0.0
+200M	0.0
-200M	0.0

The data shows that no silt is present in the stockpile since no material passes 200 mesh sieve. However, the sizing of the stockpile materials shifts toward the smaller sieves when performing an Air Dry Loss moisture analysis as shown in the following table.

Table II. Sizing after Air Dry Loss and Completely Dry

			After ADL			Completely Dry	
	%	ADL %	Resize	%	Residual %	Resize	%
+1/4	55.6	6.62	+1/4	51.2	2.34	+1/4	50.6
+16M	37.3	9.71	+16M	24.2	0.95	+16M	24.6
+30M	7.1	11.95	+30M	6.8	0	+30M	7.1
+60M	0.0	0	+60M	7.8	0.56	+60M	7.8
+200M	0.0	0	+200M	6.5	0.47	+200M	6.3
-200M	0.0	0	-200M	3.5	0.42	-200M	3.6

In this example, each sieve size was individually put through the Air Dry Loss moisture procedure. Now silt is present after 1.40% moisture is removed from the material due to the smaller particles releasing from the larger size petroleum coke. To continue the process and put the material through the 105ºC moisture process the data shows even more silt present. Fully dried material shows silt content of 3.6% of the stockpile. In the case of very large stockpiles, this is a significant amount of silt that can become airborne.

Properties of Petroleum Coke

Petroleum coke is produced in many forms. One common form is shot coke. Shot coke is spherical in shape at its base unit but can agglomerate into large balls of these spheres. It is also non-porous so any water applied as dust suppression will cling to the surface only. The following table illustrates the available surface area at different sieve sizes represented in a typical stockpile.

The surface area to volume ratio is a direct correlation of the amount of surface area that can be wetted for impervious solids relative to the mass of that size fraction. It has long been known that finer materials have more surface area than larger ones. Assuming a consistent density, a given dry weight of silt material will be able to hold more moisture than an equal weight of a larger particle size.

Table III. Surface area of different particle sizes in a typical shot coke stockpile

Sieve size	Diameter of sphere (inches)	Surface area to volume SA/V (1/inches)		Ratio of SA/V to 3/8"
Plus 3/8"	0.0095	631.57		1
8 mesh	0.00236	2542.37		4.02
30 mesh	0.0006	10,000		15.83
100 Mesh	0.00015	40,000		63.33
-200 mesh	0.000075	80,000		126.66

Note: If the density across each size is constant, the volume is directly proportional to the weight retained on the sieve.

Experimental 1

Experiments were done to verify that relationship using petroleum coke. Dried and sized particles were combined along with water, well mixed and then sieved using a Rotap. A Rotap is a machine that shakes in addition to tapping, in an aggressive way to perform sizing. Each fraction of particles sizes were dried and then re-sieved again using a Rotap.

Based on the weights and particle size ratios, the amount of water on each sieve was proportional, both overall and within each set of sieves, to weighted amounts of surface area. Each size fraction has a different moisture level consistent with the wetted surface area to weight ratio.

Experimental 2

This experiment was designed to determine at what moisture a sample of petroleum coke prepared to -200 mesh would no longer pass through a 200 mesh sieve. A known quantity of dried -200 mesh petroleum coke had water added to it by weight. It was then mixed in a Spex 8000D mixer/mill and sieved on a 60 mesh, 200 mesh and pan in a Tyler Rotap for 2 minutes. Eight different weights of moisture were added and sieved. Data table is shown below.

Table IV. Data from -200 mesh experiment as moisture was added

Run	Dry Sample Weight (g)	Weight Water (g)	Theoretical Moisture (%)	+60 mesh retained weight (g)	+200 mesh retained weight (g)	-200 mesh retained weight (g)	% passing 200 mesh
0	34	0	0	0	0	34	100
1	34.34	2.46	6.68	0.3	29.68	5.11	14.6

2	34.32	3.68	9.68	0.94	32.63	1.27	3.65
3	33.03	4.5	11.99	0.5	33.35	1.4	3.97
4	49.26	6.82	12.16	0.84	50.82	2.28	4.23
5	32.05	4.68	12.74	0.83	33.71	0.55	1.57
6	46.86	9.08	16.23	1.75	51.42	0.24	0.45
7	50.45	10.49	17.21	2.64	55.83	0.95	1.60
8	51.04	13.7	21.16	49.38	13.84	0.04	0.06

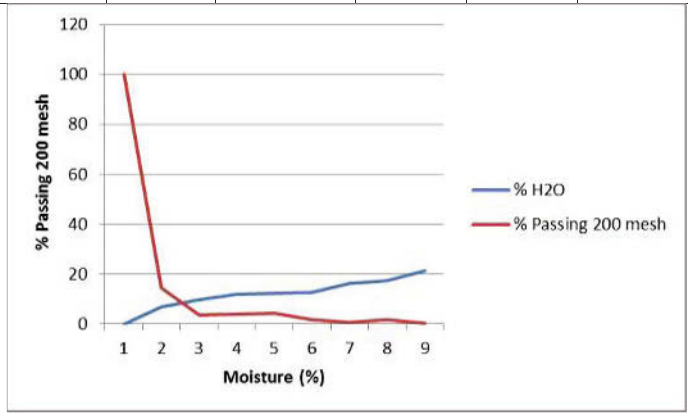

Figure 3: Moisture content vs Silt

Both the data and chart illustrate that as the moisture increases the -200 mesh (silt) material will not pass a 200 mesh sieve. This is critical information for the storage of the petroleum coke. The data shows that as little as 7% moisture content in the -200 mesh material will reduce the mobility of silt material by nearly 85%.

Conclusions

Stockpiles of petroleum coke can be a dust producer if the silt content of the pile is not understood by the storage party. By raising the moisture content of the silt to as little as 7%, the mobility of the dust can be reduced by 85%. It is beneficial for the community, the owners of petroleum coke and the stockpile handlers to understand what forces are at work on the stockpiles. Stockpile handlers have in many cases installed complex and expensive dust suppression systems in an attempt to control the silt. Hundreds or thousands of tons of water are applied to stockpiles everyday as part of silt control programs. The runoff from this application needs to be captured, treated and stored to reuse in the fight to control wind-blown silt. All this results in a very expensive endeavor that ultimately gets passed on to the consumer. By understanding the dynamics of the petroleum coke stockpile, the costs can be better controlled and still achieve the goal of the regulatory agencies. Using the knowledge that the water is held by the particle sizes based on the surface area to volume ratios several useful items come to light.

Once the particle size distribution of a stockpile is known, the overall moisture level needed to keep the natural state silt to a low percentage can be calculated and monitored. Checks should be made on a regular basis for both the sizing and moisture levels.

A stockpile without any dried -200 mesh material doesn't need any water to control the dust, while a stockpile that is 100% -200 mesh will need at least 25%. Most piles will be in between.

Table V: Hypothetical Stockpile Calculation

Hypothetical pile

	Dry sieve percentage	Surface area	% of surface area	Ratio of SA/V to 3/8"
Plus 3/8"	5.00%	0.05	0.12%	1
8 Mesh	20.00%	0.81	1.95%	4.02542
30 Mesh	35.00%	5.54	13.44%	15.8333
100 Mesh	25.00%	15.83	38.40%	63.3333
-100 Mesh	15.00%	19.00	46.08%	126.667
	100.00%	41.23	100.00%	

	From previous test		-100 mesh value	Minimum H2O in stockpile	Moisture Value
Minimum needed to keep dust to zero	25%	X	46.08%	11.52%	10.33%

References

Appendix C.2, Procedures for Laboratory Analysis of Surface/Bulk Dust Loading Samples; US Environmental Protection Agency; 7/93 (Reformatted 1/95)

Characterization of Minerals, Metals, and Materials 2016
Edited by: Shadia Jamil Ikhmayies, Bowen Li, John S. Carpenter, Jiann-Yang Hwang, Sergio Neves Monteiro, Jian Li, Donato Firrao, Mingming Zhang, Zhiwei Peng, Juan P. Escobedo-Diaz, and Chenguang Bai
TMS (The Minerals, Metals & Materials Society), 2016

LIGAND SELECTION MODEL FOR LEACHING OF LOW GRADE ZINC OXIDE ORES

Tianzu Yang, Shuai Rao, Duchao Zhang*, Lin Chen, Weifeng Liu
School of Metallurgy and Environment, Central South University, Changsha 410083, China
* Corresponding Author, Tel: +86 13787003744, Email: zdc015@sina.com
Keywords: Ligand selection, Formation constant, Zinc complexes, Leaching process.

Abstract

A new ligand selection model is proposed for leaching of low grade zinc oxide ores. The model demonstrates that the formation constant between ligand and zinc ions plays a significant role in the leaching process. A series of leaching experiments with different ligand concentration are conducted to assess the selection model. The results show that when nitrilotriacetic acid is used as the leaching agent, the highest zinc extraction is obtained. The zinc leaching rate is 84.33% in the presence of 0.4 mol/L nitrilotriacetic acid and liquid-solid ratio of 10 mL/g.

Introduction

Zinc is an important base metal in the galvanizing and battery manufacturing industries [1]. At present, zinc is produced from zinc sulfide minerals which are the primary source of zinc, and it is easy to separate the sulfide minerals from the gangue using conventional flotation techniques [2]. As sulfide ores become depleted with the passage of time, the treatment of oxidized zinc has assumed great importance in recent years. Currently, more than 10% of the zinc production in the world comes from oxidized ores. Using the leach/ solvent extraction/ electrowinning process route is the most common method of extraction of zinc from zinc oxide deposits [3]. At the present time, sulfuric acid leaching is viewed as the most viable and versatile of the available processes, and many of the commercial zinc plants that are currently in operation using this process [4]. However, for the low grade zinc oxide ores, especially those containing high contents of iron, calcium and silicon, excessive acid consumption and complex impurity metal removal process are factors that cause significant concern. In addition, the formation of silica gel makes it difficult to separate the zinc sulfate from the slurry. For these kinds of ores, alkaline leaching is generally more selective. Due to the relatively high pH of the medium, impurities such as Fe_2O_3, CaO and MgO are not soluble in the resulting solution and the following purification of the leaching solution is very simple [5]. The main leaching agents used in alkaline process are sodium hydroxide solutions and ammoniacal solutions [6-8]. In sodium hydroxide solutions, OH^- is viewed as a leaching ligand to coordinate Zn^{2+} to form soluble $[Zn(OH)_i]^{2-i}$ (i=1~4) complexes. In ammoniacal solutions, NH_3 is used as a leaching ligand to coordinate Zn^{2+} to form soluble $[Zn(NH_3)_i]^{2+}$ complexes [9]. However, because the 4^{th} zinc complexes are the most stable, the relatively high leaching rate only can be obtained under the large

liquid-solid ratio and high leaching agent concentration condition. Therefore, it is urgent to find out new ligands or leaching agents to treat the low grade zinc oxide ores.

In this research, a new ligand selection model for leaching of low grade zinc oxide ores is proposed. This ligand selection model provides a theoretical knowledge for selecting new and suitable leaching agent to treat the low grade zinc oxide ores. A series of leaching experiments with different ligand concentration also are conducted to assess the model.

Model development

Thermodynamic equilibrium

In this work, the insoluble compounds are symbolized as M_mA_n, the ligand is symbolized as L. In aqueous solutions, the insoluble compounds have the solubility equilibrium and the corresponding reaction is listed as follows:

$$M_mA_n \rightleftharpoons mM + nA \tag{1}$$

Its solubility product constant can be written as

$$k_{sp} = [M]^m \times [A]^n \tag{2}$$

When L is used as the leaching agent, the complex reaction of M with L occurs and the corresponding reaction can be described as follows:

$$M + iL \rightleftharpoons ML_i (i = 1, 2, 3, \cdots, x) \tag{3}$$

The formation constant of ML_i complex can be written as:

$$\beta_{ML_i} = \frac{[ML_i]}{[M][L]^i} (i = 1, 2, 3, \cdots, x) \tag{4}$$

The formation of ML_i complex decreases the concentration of free metal ions and shifts the solubility equilibrium to the right, facilitating further dissociation. Therefore, the solubility equilibrium of M_mA_n dissolved by ligand in aqueous solution can be expressed as:

$$M_mA_n + miL \rightleftharpoons mML_i + nA (i = 1, 2, 3, \cdots, x) \tag{5}$$

The equilibrium constant can be written as:

$$K = \frac{[ML_i]^m [A]^n}{[L]^{mi}} (i = 1, 2, 3, \cdots, x) \tag{6}$$

According to equation (2) and equation (4), the equation (6) can be simplified as:

$$K = k_{sp} \times \beta_{ML_i}{}^m (i = 1, 2, 3, \cdots, x) \tag{7}$$

It can be seen from equation (7), the dissolution ability of insoluble compounds M_mA_n mainly depends on the formation constant of metals complexes and the solubility product constant. Therefore, the most stable metal complexes with the largest formation constant should be formed to obtain the largest equilibrium constant. Base on the perspective, some assumptions have to be made. The assumptions of the

model are as follows:

(1) The protonation of L is not considered, so L can be used as a ligand to coordinate metal ions fully.

(2) The complex reaction of M with OH^- is not considered. In aqueous solutions, all metal ions exist in the form of metal complexes with the largest formation constant.

(3) The protonation of A should be neglected.

Based on the first assumption, the total concentration of L can be expressed as:

$$[\mathrm{L}]_T = [\mathrm{L}] + i[\mathrm{ML}_i] \tag{8}$$

Based on the second assumption, the total concentration of M can be expressed as:

$$[\mathrm{M}]_T = [\mathrm{ML}_i] = (\beta_{\mathrm{ML}_i})_{\max}[\mathrm{M}][\mathrm{L}]^i \tag{9}$$

Based on the third assumption, the total concentration of A can be expressed as:

$$[\mathrm{A}] = [\mathrm{A}]_T = \frac{n}{m}[M]_T \tag{10}$$

Selection model

It is well known to that a low total ligand concentration should be chosen in the leaching process. Therefore, the required total ligand concentration is the crucial factor to assess the ligand suitability. It is necessary to find out the relationship between the total ligand concentration and the largest formation constant of metal complexes.

According to equation (8) and equation (9), the largest formation constant of metal complexes can be described as:

$$(\beta_{\mathrm{ML}_i})_{\max} = \frac{[\mathrm{M}]_T}{[\mathrm{M}]\{[\mathrm{L}]_T - i[\mathrm{M}]_T\}^i} \tag{11}$$

According to equation (2) and equation (10), the free metal ions concentration can be described as:

$$[\mathrm{M}] = \frac{k_{sp}^{\frac{1}{mi}} m^{\frac{n}{m}}}{n^{\frac{n}{m}}[\mathrm{M}]_T^{\frac{n}{m}}} \tag{12}$$

Inserting equation (12) into equation (11), the total ligand concentration can be simplified as:

$$[\mathrm{L}]_T = \frac{1}{k_{sp}^{\frac{1}{mi}}}\left(\frac{n[\mathrm{M}]_T}{m}\right)^{\frac{n}{mi}}\left(\frac{[\mathrm{M}]_T}{(\beta_{\mathrm{ML}_i})_{\max}}\right)^{\frac{1}{i}} + i[\mathrm{M}]_T \tag{13}$$

As shown in equation (13), the solubility product constant, the largest formation constant of metal complex and the total metal concentration all affect the required total ligand concentration obviously. From the view of mathematics, the lowest total ligand concentration can be obtained under following conditions:

$$k_{sp}^{\frac{1}{m}} \cdot (\beta_{\mathrm{ML}_i})_{\max} >> 1 \tag{14}$$

The lowest total ligand concentration can be expressed as:

$$([\mathrm{L}]_T)_{\min} = i[\mathrm{M}]_T \tag{15}$$

Model supplement

Based on above discussion, the ligand selection model is proposed according to equation (14). However, the aforementioned analysis mainly depends on the complexation reaction of M with L, the protonation of A is neglected to simplify the calculation process. In fact, when A is defined as strong acid anions, the assumption about the protonation of A is reasonable. If A is weak acid anions, the protonation should be considered adequately. The concentration of free A is decreased due to the effect of protonation, facilitating the solubility equilibrium to the right and promoting the dissolution of insoluble compounds. Under these conditions, the total concentration of A can be modified as follows:

$$[\mathrm{A}]_T = [\mathrm{A}] + [\mathrm{HA}] \tag{16}$$

The protonation constant can be described as:

$$\beta_{\mathrm{HA}} = \frac{[\mathrm{HA}]}{[\mathrm{A}][\mathrm{H}^+]} \tag{17}$$

According to the solubility equilibrium, the total concentration of A can be described as:

$$[\mathrm{A}]_T = \frac{n}{m}[\mathrm{M}]_T \tag{18}$$

Inserting equation (18) into equation (16), the free concentration of A can be expressed as:

$$[\mathrm{A}] = \frac{n}{m}\frac{[\mathrm{M}]_T}{1+\beta_{\mathrm{HA}}[\mathrm{H}^+]} \tag{19}$$

Inserting equation (19) into equation (2), the free concentration of M can be expressed as:

$$[\mathrm{M}] = [\frac{k_{sp}}{[\mathrm{A}]^n}]^{\frac{1}{m}} \tag{20}$$

According to equation (11), (19) and (20), the total ligand concentration can be expressed as:

$$[\mathrm{L}]_T = \frac{1}{k_{sp}^{\frac{1}{mi}}}(\frac{n[\mathrm{M}]_T}{m})^{\frac{n}{mi}}(\frac{[\mathrm{M}]_T}{(\beta_{\mathrm{ML}_i})_{\max}})^{\frac{1}{i}}(\frac{1}{1+\beta_{\mathrm{HA}}[\mathrm{H}^+]})^{\frac{n}{mi}} + i[\mathrm{M}]_T \tag{21}$$

Based on equation (21), the lowest total ligand concentration can be obtained under following conditions:

$$k_{sp}^{\frac{1}{m}} \cdot (\beta_{\mathrm{ML}_i})_{\max} \cdot (\frac{1}{1+\beta_{\mathrm{HA}}[\mathrm{H}^+]})^{\frac{n}{m}} >> 1 \tag{22}$$

When the insoluble compounds are symbolized as $M_mA_nB_t$, considering the protonation of A and B, the lowest ligand concentration can be expressed as:

$$[L]_T = \frac{1}{k_{sp}^{\frac{1}{mi}}}[M]_T^{\frac{n+t}{mi}} \frac{n}{m}^{\frac{n}{mi}} \frac{t}{m}^{\frac{t}{mi}} (\frac{[M]_T}{(\beta_{ML_i})_{max}})^{\frac{1}{i}} (\frac{1}{1+\beta_{HA}[H^+]})^{\frac{n}{mi}} (\frac{1}{1+\beta_{HB}[H^+]})^{\frac{t}{mi}} + i[M]_T \quad (23)$$

Based on the equation (23), the lowest total ligand concentration can be obtained under following conditions:

$$k_{sp}^{\frac{1}{m}} \cdot (\beta_{ML_i})_{max} \cdot (\frac{1}{1+\beta_{HA}[H^+]})^{\frac{n}{m}} \cdot (\frac{1}{1+\beta_{HB}[H^+]})^{\frac{t}{m}} >> 1 \quad (24)$$

Ligand selection for various zinc minerals

The main sources of zinc metal production are zinc sulfide ore and zinc oxide ore. The main phase of Zn in zinc sulfide ore is sphalerite (ZnS). Oxidized ores contain zinc in various carbonate and silicate minerals, such as zincite (ZnO), smithsonite ($ZnCO_3$), hydrozincite ($Zn_5(OH)_6(CO_3)_2$), willemite (Zn_2SiO_4) and hemimorphite ($Zn_4Si_2O_7(OH)_2 \cdot H_2O$) [10]. All these zinc minerals are insoluble in aqueous solution and their solubility equilibrium can be listed in Table I. The protonation constants of different weak acid anions are listed in Table II. According to equation (21) and (23), the relationship between $[L]_T$ and $lg(\beta_{MLi})_{max}$ for different zinc minerals is shown in Fig.1. According to equation (22) and (24), the required formation constants for the dissolution of various zinc minerals are listed in Table 3. It can be seen from figure 1 and table III that the required formation constant for the dissolution of sphalerite is the largest. It is very difficult to find a suitable to dissolve sphalerite. For zinc carbonate minerals, the formation constant of $[Zn(NH_3)^4]^{2+}$ complex is close to the required value, so ammonia can be used as leaching ligand to dissolve zinc carbonate minerals by increasing ammonia concentration moderately. For willemite and hemimorphite, the formation constant of $[Zn(OH)_4]^{2-}$ complex is large enough to promote the dissolution of willemite and hemimorphite. However, the main gangue composition-silica also can be dissolved into the solutions, which causes the huge consumption of OH^-. Another alternative inorganic ligand is CN^-, but it is abandoned due to huge toxicity. Therefore, organic ligand can be considered as an alternative method. According to Table IV, the selected ligand contains NTA and EDTA. EDTA is well known as chelating agent, and it has been used in analytical chemistry industry. During the leaching process of hemimorphite and willemite, the mass concentration of leaching agent should be as low as possible. Therefore, compared with EDTA, it is more suitable to select NTA as leaching agent due to relatively lower molecular weight.

Table I Equilibrium equations of main insoluble zinc species and their solubility products [11]

Insoluble species	Equilibrium equation	Solubility products
ZnO	$ZnO + H_2O \rightleftharpoons Zn^{2+} + 2OH^-$	$k_{sp} = [Zn^{2+}][OH^-]^2 = 10^{-16.84}$
$ZnCO_3$	$ZnCO_3 \rightleftharpoons Zn^{2+} + CO_3^{2-}$	$k_{sp} = [Zn^{2+}][CO_3^{2-}] = 10^{-10}$
$Zn_5(OH)_6(CO_3)_2$	$Zn_5(OH)_6(CO_3)_2 \rightleftharpoons 5Zn^{2+} + 6OH^- + 2CO_3^{2-}$	$k_{sp} = [Zn^{2+}]^5[OH^-]^6[CO_3^{2-}]^2 = 10^{-75.27}$
Zn_2SiO_4	$Zn_2SiO_4 + 2H_2O = 2Zn^{2+} + 2OH^- + H_2SiO_4^{2-}$	$k_{sp} = [Zn^{2+}]^2[OH^-]^2[H_2SiO_4^{2-}] = 10^{-36.66}$

$Zn_4Si_2O_7(OH)_2 \cdot H_2O$ ZnS	$Zn_4Si_2O_7(OH)_2 \cdot H_2O+2H_2O=4Zn^{2+}+4OH^- + 2H_2SiO_4^{2-}$ $ZnS \rightleftharpoons Zn^{2+}+S^{2-}$	$k_{sp}=[Zn^{2+}]^2[OH^-]^2[H_2SiO_4^{2-}]=10^{-36.66}$ $k_{sp}=[Zn^{2+}][S^{2-}]=10^{-23.8}$

Table II. Protonation constants of different weak acid anions [11]

Equilibrium equation	Protonation constant	Equilibrium equation	Protonation constant
$H^+ + OH^- \rightleftharpoons H_2O$	lgK=14	$H^+ + S^{2-} \rightleftharpoons HS^-$	lgK=12.9
$H^+ + CO_3^{2-} \rightleftharpoons HCO_3^-$	lgK=10.33	$H_2SiO_4^{2-} + H^+ \rightleftharpoons H_3SiO_4^-$	lgK=11.8

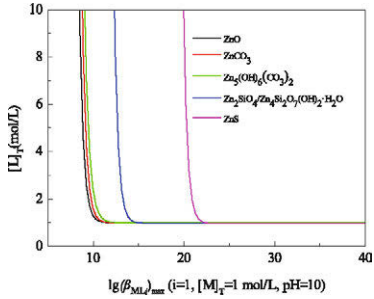

Fig.1 The relationship between $[L]_T$ and $lg(\beta_{MLi})_{max}$ for different zinc minerals

Table III. Required formation constants for the dissolution of various zinc minerals

Insoluble species	Required formation constants	Insoluble species	Required formation constants
ZnO	$lg(\beta_{MLi})_{max}$ >8.84	$ZnCO_3$	$lg(\beta_{MLi})_{max}$ >9.75
$Zn_5(OH)_6(CO_3)_2$	$lg(\beta_{MLi})_{max}$ >10.15	Zn_2SiO_4	$lg(\beta_{MLi})_{max}$ >13.43
$Zn_4Si_2O_7(OH)_2 \cdot H_2O$	$lg(\beta_{MLi})_{max}$ >13.43	ZnS	$lg(\beta_{MLi})_{max}$ >20.9

Table IV. The maximum formation constants for various zinc complexes [11]

L	i	$lg(\beta_{MLi})_{max}$	L	i	$lg(\beta_{MLi})_{max}$
OH^-	4	17.66	Cit^{3-}	1	11.4
NH_3	4	9.46	Gly^-	2	9.96
CN^-	4	16.7	Ida^{2-}	2	12.52
SCN^-	1	1.62	NTA^{3-}	2	13.45
CH_3COO^-	1	1.5	EDTA	1	16.26

Experimental verification

In order to verify the ligand selection model, a series of leaching experiments with different ligand are conducted. The low grade zinc oxide ore investigated in the present study was from Lanping town in Yunnan province of China. The phases of low grade zinc oxide ores samples were detected by X-ray diffraction analysis (Rigau, TTR-III) in 2θ scale using Cu Kα radiation (λ=1.5406 Å, 50 kV and 100 mA) at the scanning rate of 10°/min from 10° to 80°. The result indicates that hemimorphite ($Zn_4Si_2O_7(OH)_2 \cdot H_2O$) and cerussite ($PbCO_3$) were main mineral phase, while quartz (SiO_2) and calcite ($CaCO_3$) were main gangue components. The main chemical composition of samples were characterized by X-ray fluorescence (XRF, Rigaku, model ZSX Primus II) and the results were listed in Table V, showing that the main contents in the low grade zinc oxide ore samples were Zn-4.48%, Fe-7.63%, Pb-7.32%, Ca-24.9% and Si-15.2%.

The leaching agents used in this study were glycine, iminodiacetic acid and nitrilortiacetic acid. The formula and formation constants of zinc complexes are listed in Table VI. It can be seen from Table 6 that glycine, iminodiacetic acid and nitrilortiacetic acid have analogues chemical structure. The only difference derives from the number of substituent group. During leaching process, the concentration was varied from 0.05 mol/L to 0.4 mol/L. The other leaching conditions were held constant at liquid-solid ratio of 10 mL/g, leaching temperature of 313 K and stirring speed of 400 r/min.

Table V. Chemical composition of low grade zinc oxide ore samples by XRF (mass fraction, %)

Elements	Content	Elements	Content	Elements	Content
O	35.09	Ca	24.90	Fe	7.63
Pb	7.32	Zn	4.48	Si	15.20

Table VI. Formation constant of zinc complexes

Organic ligand	Formula	Formation constant (i=1)	Formation constant (i=2)
glycine	H_2NCH_2COOH	5.52	9.96
iminodiacetic	$HN(CH_2COOH)_2$	7.24	12.52
nitrilortiacetic	$N(CH_2COOH)_3$	10.45	13.45

The effect of various leaching agent concentration on (a) zinc leaching ratio and the XRD pattern of leaching residue is shown in Fig.2. It can be seen from Fig. 2(a) that the increasing organic ligand concentration enhances zinc leaching ratio significantly. The highest zinc leaching ratio is obtained in the presence of 0.4 mol/L NTA solutions. The zinc leaching ratio is extremely low when glycine is used as leaching agent. The results indicate that the zinc leaching ratio mainly depends on the formation constant of zinc complexes composed of zinc ions and ligand.

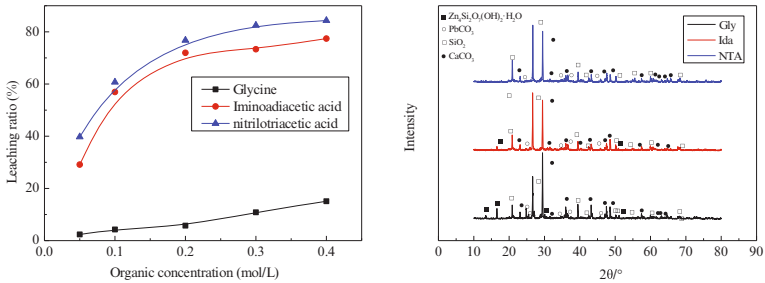

Fig.2 Effect of organic ligand on (a)-zinc leaching ratio (b)-leaching residue by the XRD analysis

The leaching residues, obtained in the presence of 0.4 mol/L Gly, Ida and NTA solutions, were analyzed by XRD and the results were shown in Fig. 2(b). It can be seen clearly in Fig. 2(b) that the characteristics peaks of hemimorphite still appear in the presence of 0.4 mol/L Gly solutions whereas the peaks disappear absolutely in the presence of 0.4 mol/L NTA solutions. The main phases of zinc leaching residue in the presence of 0.4 mol/L NTA solutions are calcite and quartz, showing an effective and selective leaching process in NTA solutions.

Conclusions

(1) The key factor for ligand selection is the formation constant of zinc complexes composed of ligand and zinc ions.

(2) The ligand selection model is an effective tool to select leaching agent for leaching of zinc oxide ores. However, this model is not suitable for selecting leaching agent for zinc sulfide ores

(3) Experimental verification of the model indicated that NTA can be used as a complex agent for leaching of zinc oxide ores. Zinc leaching ratio reached 84.33% in the presence of 0.4 mol/L NTA and at a liquid-solid ratio of 10 mL/g.

References

[1] E. Abkhoshk et al., "Review of the hydrometallurgical processing of non-sulfide zinc ores,"hydrometallurgy,149 (2014), 153-167.

[2] M. Ejtemaei, M. Gharabaghi, and M. Irannajad, "A review of zinc oxide mineral beneficiation using flotation method," advances in Colloid and Interface Science, 206 (2014), 68-78.

[3] V.Safari et al., "A shrinking particle-shrinking core model for leaching of a zinc ore containing silica," International Journal of Mineral Processing, 93 (1) (2009), 79-83.

[4] H.S.Xu et al., "Sulfuric acid leaching of zinc silicate ore under pressure," Hydrometallurgy, 105 (1-2) (2010), 186-190.

[5] F.M. Santos et al., "The kinetics of zinc silicate leaching in sodium hydroxide," Hydrometallurgy, 102 (1-4) (2010), 43-49.

[6] Z.L.Yin et al., "Dissolution of zinc silicate (hemimorphite) with

ammonia-ammonium chloride solution," Hydrometallurgy, 103 (1-4) (2010), 215-220.
[7] Z.Y.Ding et al., "Dissolution kinetics of zinc silicate (hemimorphite) in ammoniacal solution," Hydrometallurgy, 104 (2) (2010), 201-206.
[8] A.L.Chen et al., "Alkaline leaching Zn and its concomitant metals from refractory hemimorphite zinc oxide ore," Hydrometallurgy, 97 (3-4) (2009), 229-232.
[9] T.Z.Yang et al., "Ligand selection for complex-leaching valuable metals in hydrometallurgy", Transactions of Nonferrous Metals Society of China, 20 (6) (2010), 1148-1153.
[10] S. Espiari, F. Rashchi and S.K. Sadrnezhaad, "Hydrometallurgical treatment of tailings with high zinc content," 82 (1-2) (2006), 54-62.
[11] J. A. Dean. *Lange's handbook of chemistry (15 edition) Simplified Chinese Translation Edition* (Beijing, BJ: Science Press, 2003).

Characterization of Minerals, Metals, and Materials 2016
Edited by: Shadia Jamil Ikhmayies, Bowen Li, John S. Carpenter, Jiann-Yang Hwang, Sergio Neves Monteiro, Jian Li, Donato Firrao, Mingming Zhang, Zhiwei Peng, Juan P. Escobedo-Diaz, and Chenguang Bai
TMS (The Minerals, Metals & Materials Society), 2016

STUDIES ON LEACHING OF OXIDIZED COPPER ORE FROM SOUTH AMERICA

Deqing Zhu, Tengjiao Wu, Zhenqi Guo, Jian Pan and Ziyun Li

School of Minerals Processing & Bioengineering, Central South University, Changsha, Hunan 410083, China

Keywords: Oxidized copper ore, Acid leaching, Parameters optimization

Abstract

A leaching study was conducted on South America oxidized copper ore assaying 3.10% Cu, and the process parameters were optimized, including leaching temperature, leaching time, acid consumption, liquid-solid ratio and stirring rate. The results show that copper leaching rate of 92.02% were achieved under the optimized conditions as follows: raw ore crushed to 100% passing 1mm, leaching by sulfuric acid at 70ºC for 1.5h with a sulfuric acid consumption of 150kg/t, liquid-solid ratio of 2:1, stirring rate of 300r/min. The leaching solution is a good feed for the subsequent extraction-electrowinning processes due to its high copper concentration and low contents of impurities like calcium and iron ions.

Introduction

Copper continues to be a highly demanded commodity because it is widely used in a variety of industries including electronics, electrical, pipeline, and infrastructure [1]. The survey indicates that more than 3 billion tons of copper ores are widely distributed in more than 150 countries on six continents. Chile has the most abundant copper resource in the world; Peru, Australia, Mexico, USA, China, Russia and Indonesia follow closely. There are about 200 kinds of copper ores in nature, which can be briefly divided into two categories: copper sulfide ores and copper oxide ores, according to their different chemical composition [2-4].

The copper commonly produced from sulfide and oxide copper ores is extracted through pyrometallurgical and hydrometallurgical processes, respectively [5]. Recently, many researchers have focused on the extract of copper using hydrometallurgical processes in order to replace the traditional pyrometallurgical processes. Currently, more than 20% of world copper production is produced by hydrometallurgical processes, particularly by acid leaching–extraction–electrowinning processes [6-8]. Due to its effectiveness, less investment, low operational cost and less environmental impacts, hydrometallurgical processes have wide

development prospects [9]. In this paper, a hydrometallurgical process was conducted to obtain copper from the South America copper ore using acid leaching. Effect Factors of the copper leaching rate, such as the leaching time, leaching temperature, particle size and consumption of sulfuric acid, were investigated.

Materials and methods

Materials

The copper oxide ore used in this study was obtained from South America. The ores present a color of emerald, sky blue, brown and black. According to the process mineralogical investigation, the textures of ores are mainly in blocky, granule xenomorphic, interstitial, metasomatic relict and disseminated structures, and the main mineral bearing copper are malachite and chrysocolla. The X-ray diffraction result (Fig. 1.) shows that the main gangue minerals are quartz, kaolinite and fayalite. The copper oxide ore samples were pulverized to 100% passing 1 mm and representative samples were taken for chemical and phase analysis. Table I and II shows the chemical composition and mineral phase of the sample.

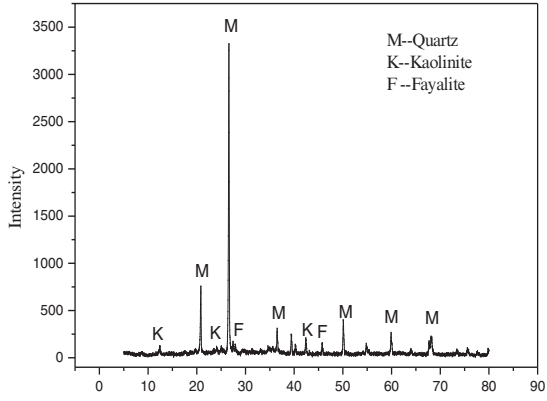

Fig. 1. X-ray diffraction pattern of original ore sample

Table I. Chemical composition of oxidized copper ore

Composition	Cu	Fe	SiO_2	MgO	CaO	Al_2O_3	Zn
wt %	3.10	6.89	64.64	0.88	1.36	8.71	0.23
Composition	$Au/g \cdot t^{-1}$	$Ag/g \cdot t^{-1}$	Pb	C	As	S	LOI*
wt %	0.78	52.18	0.11	0.31	0.002	0.10	5.29

* LOI (loss on ignition).

As shown in Table I, the ore has relatively high grade of copper, which reaches 3.1%. Contents of harmful impurities like sulfur and arsenic are very low. Sliver grade reaches 52.18g/t, it's worthy of reclaim. Silica is a kind of acid gangue, whose content is as high as 64.64%.

Table II. Phase analysis of the copper ore sample

Phase	Free copper oxide	Combined copper oxide	Secondary sulfide copper	Primary copper sulfide	Cu_{total}
wt %	2.64	0.18	0.26	0.02	3.10
Fraction	85.16	5.81	8.39	0.65	100

The phase analysis of copper is shown in Table II. 85% of copper is determined as free copper oxide, 8.39% and 5.81% of copper are in the form of secondary sulfide copper and combined copper oxide, respectively. Only 0.65% copper is hosted in primary copper sulfide，which is difficult to leach. The ore is a typical oxidized copper ore, and the total oxygenation efficiency is as high as 90.97%. In the case that free copper oxide and secondary sulfide copper are leached completely, the maximum leaching rate in theory is 93.55 %.

Methods

First the ore samples were crushed down to 100 percent passing 1 mm using a jaw crusher, then mixed and dried. Weigh accurately 40g of the prepared sample in a 400-ml beaker within a certain amount of distilled water and concentrated sulphuric acid (98.53 wt %). The beaker was placed in an electro-thermostatic water bath with a stirrer stirring at 300r/min. Leach the samples at a selected temperature and for a specified time. Filtrate immediately after leaching, collect the leaching solution and dry the residue in the oven at 105°C for 3h. The copper content in the leaching solution and residue was determined by atomic spectroscopy or elemental analysis using iodometry. The leaching rate of copper is taken as evaluation index and calculated by Eq. (1):

$$H = \left(1 - \frac{m_1 \times r_1}{m_0 \times r_0}\right) \times 100\% \quad (1)$$

where H is the copper leaching rate, wt %; m_1 is the mass of leaching residue, g; m_0 is the mass of sample, g; r_1 is the copper grade of leaching residue, wt %; r_0 is the copper grade of sample, wt %.

Results and discussion

Effect of Sulfuric Acid Consumption

Acid leaching is a suitable way to process the copper oxide ore. In this study, we chose sulfuric acid as leaching agent for its efficient and available on market. Trials were conducted at constant pressure, leaching the prepared sample (-1mm) by sulfuric acid at 20ºC for 1.5h with liquid-solid ratio of 3:1, stirring rate of 300r/min. Effects of sulfuric acid consumption on copper leaching rate is shown in Fig. 2.

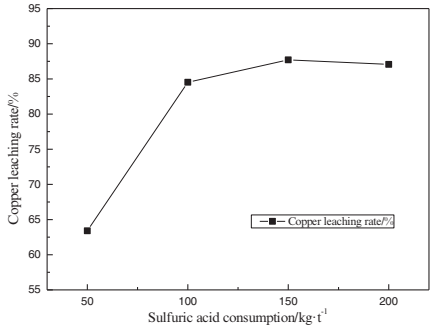

Fig. 2. Effect of sulfuric acid consumption on copper leaching rate
(Leaching time: 90min, temperature: 20 ºC, liquid-solid ratio: 3:1.)

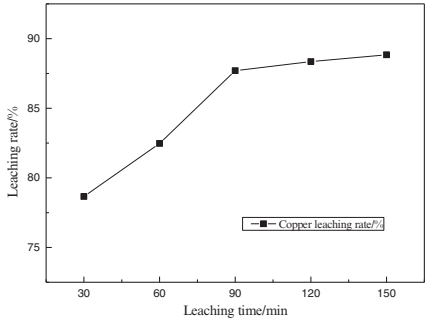

Fig. 3. Effect of leaching time on copper leaching rate
(Temperature: 20ºC, liquid-solid ratio: 3:1, sulfuric acid consumption: 150kg/t.)

As shown in Fig. 2. With increasing sulfuric acid consumption from 50kg/t to 150kg/t, copper leaching rate increased gradually from 63.41% to 87.07%, the copper grade of leaching residue dropped from 1.21% to 0.42%. Within certain realms, high acid concentration could accelerate the reaction rate, the copper leaching rate was increased as well. Continue increasing sulfuric acid consumption to 200kg/t, the copper leaching rate has no significant change, acid concentration is not a limit for leaching process. Considering both production cost and copper leaching rate, the optimal sulfuric acid consumption should be 150kg/t.

Effect of Leaching Time

The results of copper leaching rate by leaching versus time are presented in Fig. 3. It can be seen from Fig. 3, as the leaching time increased from 30min to 90min, the copper leaching rate increased from 78.66% to 87.70%, and the copper grade of residue decreased from 0.72% to 0.42%. Continue to extend the leaching time, the copper leaching rate didn't change significantly. Reaction between ores and acid took place in solution, enough leaching time

could ensure ores thoroughly exposed to sulfuric acid. Within certain range, extending leaching time, the copper leaching rate continues increaseing until a balance is achieved. Thus, the most appropriate leaching time is 90min.

Effect of Liquid to Solid Ratio

Fig. 4 gives the effect of liquid to solid ratio on copper leaching rate. As shown in Fig. 4, with the increase of liquid-solid ratio, copper leaching rate increased first and then decreased slightly. Copper leaching rate reached a maximum at a liquid-solid ratio of 2:1. A higher liquid-solid ratio is favorable for the extraction of copper since increasing the volume of leaching solution could increase the efficiency of mass transfer, thus accelerating the copper recovery. However, an over ligh liquid-solid ratio is not conducive to the extraction of copper. It can be concluded that the proper liquid-solid ratio is 2:1.

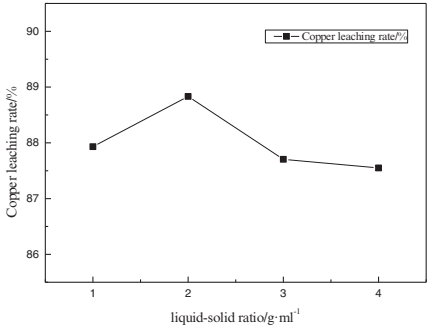

Fig. 4. Effect of liquid-solid ratio on copper leaching rate
(Leaching temperature: 20°C, leaching time: 90min, sulfuric acid consumption: 150kg/t.)

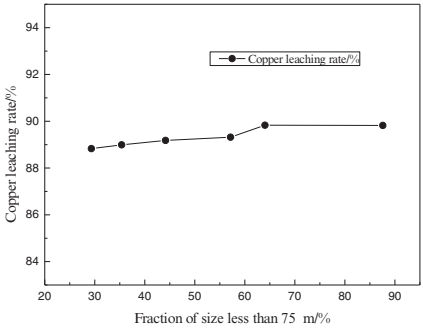

Fig. 5. Effect of particle size on copper leaching rate
(Leaching temperature: 20°C, leaching time: 90min, sulfuric acid consumption: 150kg/t, liquid-solid ratio: 2:1.)

Effect of particle size

In order to study the effect of particle size on copper leaching rate, further grinded the copper ore (-1mm) by rod mill. The particle sizes of copper ores at different grinding time are listed in Table III. Conducted the experiment under the same conditions as before, only the particle size was changed, results are shown in Fig. 5. As it can be seen in Fig. 5, when the fraction of -75 m particle size of the ground ore increased from 29.33% to 87.58%, the copper leaching rate only increased by 1%. Under the same conditions, particle size plays an insignificant role in the

leaching process of copper. For the sake of lower cost, we choose -1mm ore without further grinding as materials in this study, considering the expensive cost of grinding.

Table III. The particle size of copper ore at different grinding time

Grinding time/min	0	0.5	1	2	3	4
Fraction of -75 m/%	29.33	35.37	44.15	57.15	64.03	87.58

Effect of temperature

Effect of the leaching temperature on copper leaching rate is plotted in Fig. 6. The copper leaching rate increased gradually and the copper grade of residues decreased as the increase of leaching temperature. Copper leaching rate increased from 88.83% to 92.02% when leaching temperature was increased from 20ºC to 70ºC. Consecutively increasing temperature from 70ºC to 90ºC, the copper leaching rate increased only by 0.6%. Besides, the solution evaporate intensely at 90ºC, which is not beneficial to practical production. Therefore, the optimal temperature should be 70ºC.

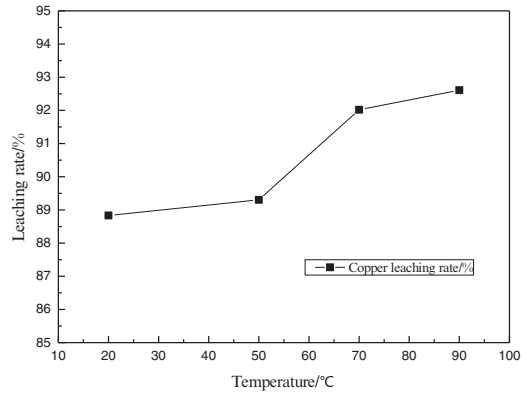

Fig. 6. Effect of leaching temperature on copper leaching rate.
(Sulfuric acid consumption: 150kg/t, leaching time: 90min, liquid-solid ratio: 2:1.)

Products analysis

Based on the above experimental results, the optimal leaching condition were determined to be, raw ore crushed to 100% passing 1mm, leaching by sulfuric acid at 70ºC for 1.5h with a sulfuric acid consumption of 150kg/t, liquid-solid ratio of 2:1, stirring rate of 300r/min.

Repeat the trial under the optimized conditions, 150ml leaching solution and 35.12g residue were obtained. The copper leaching rate reached 92.92% and the copper grade of residue was 0.25%. This method is feasible with good reproducibility. The concentration of major ion in the leaching solution is given in Table IV.

Table IV Chemical analysis of leaching solution

Ion concentration	Cu^{2+}	$Fe^{2+,3+}$	Si^{2+}	Ca^{2+}	Al^{3+}	Mg^{2+}	pH
g/L	7.52	2.92	0.44	0.74	1.38	0.41	1.63

The concentration of cupric ion is the most important quality index, which, as shown in Table IV, reaches a target of 7.52g/L. The concentration of iron ion is 2.92 g/L, concentration of other ions such as silicon, calcium, aluminum and magnesium is dilute. High copper concentration and low contents of impurities make the leaching solution a good raw material for the subsequent extraction-electrowinning processes[10]. The leaching solution has a pH of 1.63.

Conclusions

1. The copper oxide ore used in this study was obtained from South America. The ore is characterized by high copper grade (3.10 wt %), high silica content (64.64 wt %) and low harmful impurities (sulfur, arsenic). The phase analysis shows that 85% of copper is hosted in free copper oxide, 8.39% and 5.81% of copper are in the form of secondary sulfide copper and combined copper oxide, respectively.
2. In this study, we demonstrated that the South America oxidized copper ore can be successfully leached out by sulfuric acid. A 92.02%~92.92% of copper leaching rate was achieved under the optimized conditions as follows: raw ore crushed to 100% passing 1mm, leaching by sulfuric acid at 70ºC for 1.5h with a sulfuric acid consumption of 150kg/t, liquid-solid ratio of 2:1, stirring rate of 300r/min. The leaching solution is a good raw material for the subsequent extraction-electrowinning processes due to its high copper concentration (7.52g/L) and low contents of impurities like calcium and iron ions.

Acknowledgements

This work was financially supported by Co-Innovation Center for Clean and Efficient Utilization of Strategic Metal Mineral Resources of Hunan Province.

References

1. S. Northeya, et al. “Modelling future copper ore grade decline based on a detailed assessment of copper resources and mining,” *Resources, Conservation and Recycling*, 83(2014),

190–201.

2. C. H. Yuan, et al. “Analysis of the global copper resource potential,” *China Mining Magazine*, 11(21) (2012), 1–6. (In Chinese)

3. Zh. X. Liu, “The prospect of China's major non-ferrous metals – copper mine,” *Northwestern Geology*, 1(40) (2007), 83–91. (In Chinese)

4. H. K. Haghighi, et al. “Production of copper cathode from oxidized copper ores by acidic leaching and two-step precipitation followed by electrowinning,” *Hydrometallurgy*, 133(2013), 111–117.

5. D. Cui, “A New Copper Hydrometallurgical Process,” *Hydrometallurgy of China*, 1(15) (2005), 56. (In Chinese)

6. E.A. Oraby, J.J. Eksteen, “The selective leaching of copper from a gold–copper concentrate in glycine solutions,” *Hydrometallurgy*, 150(2014), 14–19.

7. S. C. Wang, et al. “The advances on processing of oxidized copper,” Multipurpose *Utilization of Mineral Resources*, (2) (2006), 37-42. (In Chinese)

8. “World mineral statistics archive,” *British Geological Survey (BGS) Centre for Sustainable Mineral Development*, 2012.

9. Crowson P. “Some observations on copper yields and ore grades,” *Resources Policy*, 37(2012), 59–72.

10. M. L. Zhu, et al. “Status and development of copper electrowinning,” *Nonferrous Metals (Extractive Metallurgy)*, 8(2014), 9-14.

Characterization of Minerals, Metals, and Materials 2016
Edited by: Shadia Jamil Ikhmayies, Bowen Li, John S. Carpenter, Jiann-Yang Hwang, Sergio Neves Monteiro, Jian Li, Donato Firrao, Mingming Zhang, Zhiwei Peng, Juan P. Escobedo-Diaz, and Chenguang Bai
TMS (The Minerals, Metals & Materials Society), 2016

EFFECT OF FERRIC IONS ON BIOLEACHING OF PENTLANDITE CONCENTRATE

Qian Li[1], Huimin Lai[1], Yongbin Yang[1], Bin Xu[1], Tao Jiang[1], Yaping Zhang[2]
1 School of Minerals Processing and Bioengineering, Central South University, Changsha, Hunan, PR China, 410083;
2 College of Food and Biological Engineering, Jimei University, Xiamen, Fujian, PR China, 361021

Keywords: Pentlandite concentrate, Ferric phosphate, Bioleaching, Intensification

Abstract

The intensified effects of ferric phosphate and ferric sulfate as nutrient and oxidant on the bioleaching of pentlandite concentrate with *Acidithiobacillus ferrooxidans* and *Sulfobacillus thermosulfidooxidans* were studied. The results showed that the nickel leaching rate was enhanced continuously with $FePO_4$ or $Fe_2(SO_4)_3$ added in certain extent, but declined at excess. For *A. ferrooxidans*, the optimum additive amount of $Fe_2(SO_4)_3$ was 6.63mM/L and the nickel leaching rate reached 71.76%. Compared with $Fe_2(SO_4)_3$, the optimum additive amount of $FePO_4$ was 26.52mM/L for both strains. For *A. ferrooxidans* and *S. thermosulfidooxidans*, the nickel leaching rate could increase to 98.06% and 98.11% which was 1.83 times and 1.55 times of the leachig rate of blank test, respectively.

Introduction

Nickel metal plays a significant role on the steel industry and has broad application scope, including stainless steel, alloy steel, special steel, magnetic materials, battery material and so on [1]. Driven by the stainless market, demands for nickel have been rapidly improved in global scope. At present, most of nickel metal is extracted from sulfide ores and almost occupies 2/3 of the total output. Poor, thin and low grade nickel ores have been becoming the main nickel resources gradually, which makes it increasingly difficult to utilize by conventional methods including pyrometallurgical and hydrometallurgical processes [2]. However, one of the most important forms of nickel in these resources is sulfide and it can be easily etched by a variety of microorganisms used for bioleaching. Furthermore, bioleaching is an environmentally friendly method, which has a moderate capital investment, low operation costs and simple operation procedures. It becomes increasingly popular in the field of utilization of low grade sulfide ores [3]. Besides, there are still some problems in bioleaching processes, including time inefficiency and lacking effective bioleaching bacteria. A variety of measures had been taken to boost the development of bioleaching process.
Corrans and Scholtz observed that the nickel leaching rate was approximately proportional to ferric ion concentration in the research of the leaching kinetic of pentlandite in acidic ferric sulfate solutions [4]. However, an excess of ferric ion

would be connected with some ions (e.g., sodium, potassium ion, ammonium ion and so on) to form jarosite which hinder the leaching of pentlandite concentrate although the sulfide ores can be oxidized by the ferric ion[5]. The effect of inorganic phosphate (P) on the bioleaching of tannery sludge was investigated and it was revealed that the growth of *A. ferrooxidans* and its oxidization ability of S^0 were both influenced under the deficiency of inorganic phosphate [6].

In this study, *A. ferrooxidans* and *S. thermosulfidooxidans* were used as the bioleaching bacteria and effects of adding $Fe_2(SO_4)_3$ and $FePO_4$ on bioleaching of pentlandite concentrate were studied systematically.

Experimental

Chemical analysis of the pentlandite concentrate contained 2.68% Ni, 42.21% Fe, 1.51% Cu, 0.07% Co, 0.45% Mg and 33.51% S. Combined with the X-ray diffraction analysis of the sample (see Figure 1), it can be seen that the concentrate was mainly composed of pentlandite (9.5%), pyrite (52.6%), pyrrhotite (29.5%) and chalcopyrite (8.3%). The proportion of -75 m particles accounted for over 85%.

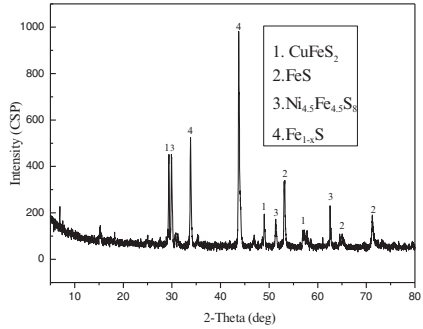

Figure 1. X-ray diffraction pattern of pentlandite concentrate sample

The strains of *A. ferrooxidans* and *S. thermosulfidooxidans* were provided by the Bioleaching Laboratory, Central South University in China. Both strains were cultured in the 9 K medium which contained 3g/L $(NH_4)_2SO_4$, 0.1g/L KCl, 0.5g/L K_2HPO_4, 0.5g/L $MgSO_4 \cdot 7H_2O$, 0.01g/L $Ca(NO_3)_2$, 44.7g/L $FeSO_4$. Yeast extract (0.2g/L) was added to the medium to support the growth of *S. thermosulfidooxidans*. The optimum initial pH and temperature for *A. ferrooxidans* and *S. thermosulfidooxidans* were 1.8, 30°Cand 1.6, 50°C, respectively. In addition, the rotation speed was 160rpm for both strains. *A. ferrooxidans* had been cultivated by ferrous salts and inorganic sulfur compounds as energy source [7].

S. thermosulfidooxidans is able to oxidize ferrous ion, pyrite and elemental sulfur autotrophically and mixotrophically in the presence of yeast extract. Autotrophic oxidation of elemental sulfur was relatively weak [8]. The medium, without $FeSO_4$, was autoclaved at 121°C for 20min. Thereafter, 1.0g pentlandite concentrate was

autoclaved at 115℃ for 15min and then put separately into flask. The $FeSO_4$ medium was separately sterilized through a 0.2 m filter and was added to the leaching flasks. All chemicals used in this work were analytical grade reagents. Water was purified using a water MilliQ system.

To ensure that the iron in the original medium did not affect the results, cells were harvested in the stationary phase by filtration onto a Millipore filter (pore size 0.22 m) and re-suspended in the sterilized 9K medium before leaching experiments started. The initial density of cells in the solution was approximately 1×10^7cells/ml when 10%(v/v) bacteria was inoculated into 250ml flasks.

Leaching experiments were carried out in 250ml conical flasks containing 100ml 9K solution with 1%(w/v) pulp density. Additionally, different amounts of ferric phosphate were added into the 250ml conical flask to prepare a series of $FePO_4$ dosage including 0mM/L, 13.26mM/L, 19.90mM/L, 26.52mM/L and 33.16mM/L respectively, and then were put into an orbital shaker at 160rpm. In order to investigate the effect of ferric ion and PO_4^{3-} respectively, the accretion of ferric sulfate was studied as control group to inspect the single action of ferric ion. The control group of 0mM/L, 6.63mM/L, 9.45mM/L, 13.26mM/L and 16.58mM/L ferric sulfate were also prepared to add into 250ml conical flask respectively. Bioleaching with *A. ferrooxidans* was carried out at 30℃, pH 1.8 (adjusted with 1:1 sulfuric acid) and *S. thermosulfidooxidans* at 50℃, pH 1.6 (adjusted with 1:1 sulfuric acid). Each experiment with *A. ferrooxidans* lasted for 18 days and *S. thermosulfidooxidans* lasted for 8 days. The pH value was measured at each sampling instant first. Periodically, samples were taken and the sterilized 9 K medium was added into the flasks to compensate for the loss nutrition.

The concentration of dissolved nickel in lixivium was determined by inductively coupled plasma atomic absorption spectrometer (AAS). The concentrations of ferrous ions was measured by potassium dichromate titration[9]. The pH value and redox potential (Eh) in the leaching solution were, respectively, measured by using a Mettler Toledo PE20K pH/Eh process controller.

Results and Discussion

Effect of $Fe_2(SO_4)_3$ on Bioleaching of Pentlandite by *A. ferrooxidans*

As shown in Figure 2, after being leached for 18 days, when there was no $Fe_2(SO_4)_3$ the nickel leaching rate reached 53.47%. When the additive amount of $Fe_2(SO_4)_3$ was 6.63mM/L, the nickel leaching rate increased to 71.76%, but with the amount of $Fe_2(SO_4)_3$ increasing to 9.45mM/L, it began to decrease to 58.78% which was still higher than blank test. Although no improvement could be achieved for nickel leaching with additive amount increased, the leaching velocity with additive added was rising faster than nothing added from the 13th days. Therefore, from the overall trend, the leaching effect of adding 0mM/L~16.58mM/L $Fe_2(SO_4)_3$ was better than nothing added. The mineral was oxidized by ferric ions indirectly. This phenomenon can be explained by Equation (1), (2) and (3) simultaneously. However, the excess ferric would be hydrolyzed to jarosite and covered on the surface of mineral so as to

hinder the bacteria and ferric ion contacting on the mineral. For this result, the nickel leaching rate will be accelerated and the leaching time will be reduced by adding appropriate amount of ferric sulfate.

$$Fe_{1-x}S + (2-2x)Fe^{3+} \rightarrow (3-3x)Fe^{2+} + S^0 \quad (1)$$

$$(Ni, Fe)_9S_8 + 36Fe^{3+} \longrightarrow 9Ni^{2+} + 45Fe^{2+} + 8S^0 \quad (2)$$

$$2Fe^{2+} + 1/2O_2 + 2H^+ \xrightarrow{\text{Bacteria}} 2Fe^{3+} + H_2O \quad (3)$$

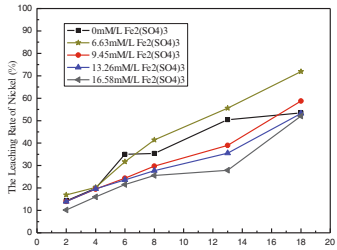

Figure 2. Nickel leaching rate of adding different $Fe_2(SO_4)_3$ concentration on the bioleaching of pentlandite concentrate

Effect of Adding Ferric Phosphate on the Bioleaching of Pentlandite Concentrate by *A. ferrooxidans* and *S. thermosulfidooxidans*

The leaching effect of adding $Fe_2(SO_4)_3$ and $FePO_4$ was compared in the Figure 3. When bioleaching bacteria were *A. ferrooxidans*, the nickel leaching rate of adding ferric phosphate was 1.36 times of the ferric sulfate in 18 days when ferric ions were commensurate. Furthermore, the nickel leaching rate of adding 26.52mM/L $FePO_4$ was 1.36 times of the $Fe_2(SO_4)_3$ at the optimum additive amount.

As shown in Figure 4, the tendency of the curves was similar. The XRD graph (see Figure 1.) showed that 29.5% pyrrhotite was contained in the pentlandite concentrate. The ferrous ion or ferric ion of pyrrhotite was usually replaced by nickel ion in nickel sulfide. The nickel will be dissolved into solution with the pyrrhotite dissolved. As shown in Equation (3), (4) and (5), the H^+ was consumed when the ferric ion, pyrrhotite and pentlandite were oxidized in the presence of bacteria. In addition, some acid soluble substance (carbonate) was also easily dissolved by H^+. Therefore, the pH was higher than the initial pH which was 1.8 shown in Figure 4(b). The pH declined when the elemental sulfur was oxidized to vitriol and the generated ferric ion was hydrolyzed to jarosite in the bioleaching process (shown in Equation (6) and (7)). The pH was elevatory with the reaction of the Equation (3), (4) and (5) which proceeded in 8 days. It can be concluded that the consumed acid rate was faster than the generated acid rate. As shown in Figure 4(c), the concentration of ferrous ion was descended and the ratio of Fe^{3+}/Fe^{2+} was ascending when the ferrous ion was oxidized to ferric ion in the first 8 days. However, the ferrous was oxidized to ferric ion to accelerate the sulfide oxidation process by oxidizing S^{2-} to S^0[8]. Some researchers

[10-12] reported that the redox potential in the bioleaching solution had a great impact on the leaching of sulfide ores. Mariekie Gericke reported that the optimum redox levels in the bioleaching of nickel-copper sulfide concentrate ensured that a maximum nickel extraction could be achieved while it was true for a reduction in nickel extraction rates observed at redox potential levels below 460mV [12]. Appropriate redox potential levels was a restrict factor for the effective leaching of nickel sulfide even if the bioleaching microorganisms exists. From Figure 4(a) and 4(b), it can be observed that the Eh values of the best nickel extraction were maintained in the range of 495mV～505mV. The nickel leaching rate was lower at higher or lower Eh levels.

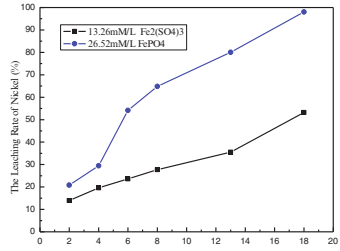

Figure 3. Nickel leaching rate of adding $Fe_2(SO4)_3$ and $FePO_4$ when the ferric ion was equal on volume and the bacteria were *A. ferrooxidans*

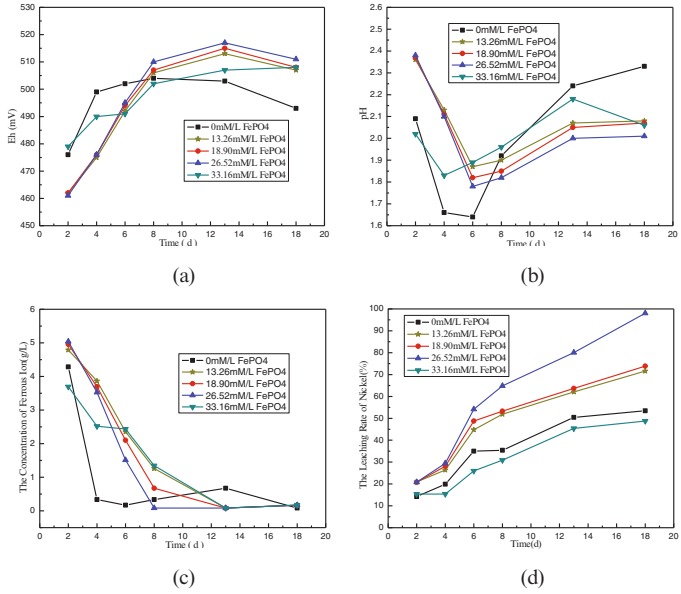

Figure 4. Effect of $FePO_4$ on bioleaching of pentlandite concentrate by *A. ferrooxidans*

As shown in Equation (8), the redox potential levels were mainly decided on the ratio of Fe^{3+}/Fe^{2+}. The Eh was increased with the ratio of Fe^{3+}/Fe^{2+} increased (shown in

Equation (6)) and influenced by pH. As shown in Figure 4(a), 4(b) and 4(c), the Eh increased greatly in the first 8 days whilst the concentration of ferrous and the pH declined dramatically. The value of Eh was ascending when the ratio of Fe^{3+}/Fe^{2+} was rising, the ferric ion was readily hydrolyzed to jarosite (showed in Equation (5)) when the ferric ions were superabundant and the pH was between at 2.0～3.0.

$$Fe_{1-\chi}S + 1/2(1-\chi)O_2 + 2(1-\chi)H^+ \xrightarrow{\text{Bacteria}} (1-\chi)Fe^{2+} + S^0 + (1-\chi)H_2O \quad (4)$$

$$(Ni,Fe)_9S_8 + 23\frac{1}{4}O_2 + 29H^+ \xrightarrow{\text{Bacteria}} 9Ni^{2+} + 9Fe^{3+} + 14\frac{1}{2}H_2O + 8SO_4^{2-} \quad (5)$$

$$S^0 + 3/2O_2 + H_2O \xrightarrow{\text{Bacteria}} 2H^+ + SO_4{}^{2-} \quad (6)$$

$$3Fe^{3+} + 2SO_4^{2-} + 6H_2O + K^+ \longrightarrow KFe_3(SO_4)_2(OH)_6 + 6H^+ \quad (7)$$

$$\varphi_{Fe^{3+}} = 0.78 + 0.0591\lg\frac{[Fe^{3+}]}{[Fe^{2+}]} \quad (8)$$

The ferric phosphate difficult to decompose in the neutrality condition can be decomposed by the multiple organic acid (citric acid) which can integrate with Ca^{2+}, Fe^{3+}, Mg^{2+} and so on or inorganic acid (nitric acid, sulfuric acid). Furthermore, the ferric phosphate can be reverted to ferrite (ferrous phosphate), which react with sulfuretted hydrogen produced in the bioleaching of sulfide ores and produce ferrous sulfide in order to release phosphate group in the solution [13].

The nickel leaching rate of sulfide ores was in direct proportion to the activity of bacteria. Therefore, the activity of bacteria must keep good in order to achieve high metal leaching rate. Phosphate is indispensable for the growth of microorganism due to phosphate is one portion of enzyme, energy metabolism, nucleotide and its ramification. Carbon dioxide fixation, growth of bacteria and oxidation of all kinds of resource will be restricted when the phosphate nutrients are in shortage.

The ferric phosphate contains only PO_4^{3-} but also ferric ion which can elevate the redox potential levels when ferric ions released into the solution. Figure 4(a) showed that the Eh (redox potential) levels with ferric phosphate added increased faster than 0mM/L $FePO_4$ and kept at 505~520mV from the eighth day. In addition, the nickel leaching rate was concerned with the change of Eh and leaching effect was better when the Eh values was bigger except that the ferric phosphate additive amount was 33.16mM/L. The Eh values of adding 26.52mM/L ferric phosphate was greater than others. Figure 4(d) showed that the nickel leaching rate with 26.52mM/L ferric phosphate added was higher than others and the nickel leaching rate reached to 98.06% in 18 days. The nickel leaching rate was 53.47%, 71.62%, 73.86% and 48.76% when the additive amount of $Fe_2(SO4)_3$ was 0mM/L 13.26mM/L, 18.90mM/Land 33.16mM/L, respectively. It can be concluded that the nickel leaching rate was not improved with the additive increased and it can decline when the additive was superfluous. The nickel leaching rate with 26.52mM/L ferric phosphate added was 1.83 times of the blank test in 18 days. However, compared Figure 2 and Figure 4(d), the global leaching effect of adding ferric phosphate was obviously better than

ferric sulfate. At the optimum addition, the nickel leaching rate of adding ferric phosphate was 1.36 times of ferric sulfate. As indicated by the results, it is probably that the release of phosphate radicals could facilitate the growth of bacteria and thus have a great impact on the bioleaching of the nickel concentrate. As shown in Table I, the best nickel leaching rate reached to 98.11% when the additive amount of $FePO_4$ was 26.52mM/L for *S. thermosulfidooxidans* in 8 days. For *S. thermosulfidooxidans*, the optimum additive amount of ferric phosphate was 26.52mM/L and the nickel leaching rate was 1.55 folds of nothing added. Furthermore, the nickel leaching rate fell when the additive amount was excess. As shown in Figure 4(d) and Table I, for *S. thermosulfidooxidans* and *A. ferrooxidans*, the best additive amount of $FePO_4$ was both 26.52mM/L. However, the leaching efficiency of *S. thermosulfidooxidans* was better in the mass. On the one hand, the growth of S. thermosulfidooxidans was very good when the pH and temperature of the leaching system was 1.6 and 50℃, respectively. On the other hand, the higher temperature and lower pH will accelerate the dissolution of pentlandite concentrate. As shown in Figure 3, Figure 4(d) and Table I, the nickel leaching effect with ferric phosphate added was better than the effect of ferric sulfate at the optimum additive amount. By analyzing the above results, ferric ion and phosphate groups could be favorable to the bioleaching of penlandite concentrate at proper additive amount.

Table I. Effect of $FePO_4$ on Bioleaching of Pentlandite Concentrate by *S. thermosulfidooxidans*/%

Time (d)	0mM/L Ferric phosphate	13.26 mM/L Ferric phosphate	18.90 mM/L Ferric phosphate	26.52 mM/L Ferric phosphate	33.16 mM/L Ferric phosphate
3	22.58	25.15	25.55	39.51	27.29
6	50.47	51.26	55.86	83.80	51.90
8	63.37	66.09	66.38	98.11	69.61

Conclusions

In the bioleaching of pentlandite concentrate by adding different amount of ferric phosphate or ferric sulfate, experimental results showed that an appropriate additive amount was needed to strengthen the bioleaching of pentlandite concentrate. For *A. ferrooxidans*, the best additive amount of $Fe_2(SO_4)_3$ was 6.63mM/L and the nickel leaching rate was 71.87%. Furthermore, the nickel leaching rate with 26.52mM/L ferric phosphate added was reached to 98.06%. In addition, the nickel leaching rate with 26.52mM/L ferric phosphate added was 1.83 times of the 0mM/L ferric phosphate and 1.36 times of $Fe_2(SO_4)_3$ of which the additive amount was the best in 18 days. For *S. thermosulfidooxidans*, the optimum additive amount of ferric phosphate was 26.52mM/L and the nickel leaching rate reached to 98.11% in 8 days. At proper additive amount, the leaching effect of adding $Fe_2(SO_4)_3$ or $FePO_4$ was superior to that of without addition. The nickel leaching efficiency of *S. thermosulfidooxidans* was better than *A. ferrooxidans*. Although the ferric ion has an

oxidation for bioleaching of pentlandite concentrate, the nickel leaching rate could be further strengthened when phosphate radicals which is indispensable for the growth of bioleaching bacteria, were dissolved into the lixivium to promote the growth of the bacteria.

Acknowledgments

This work was financially supported by National Natural Science Foundation of China (Grant No. 51574384), Science Technology Program of Yunnan (No.2013IB020) and Southern Ocean Research Center of Xiamen.

References

[1].J. R. Davis, ASM Specialty Handbook, Nickel, Cobalt, and Their Alloys (Ohio, O: ASM International, 2000), 7-13.

[2].Xing F L, Xiao B Q, Wang Z M, "Research Progress on Copper-nickel Separation Technology in Copper-nickel Ore," *Mining and Metallurgy*, 19 (1) (2010), 25.

[3].Watling, H.R, "The Bioleaching of Nickel-copper Sulfides," *Hydrometallurgy*, 91(1–4) 2008 , 70–88.

[4].Corrans, I.J., Scholtz, M.T., "A Kinetic Study of the Leaching of Pentlandite in Acidic Ferric Sulphate Solutions," *J. S. Afr. Inst. Min. Metal*, 76 (10)1976, 403–411.

[5].Leahy, M.J., Schwarz, M.P., "Modeling Jarosite Precipitation in Isothermal Chalcopyrite Bioleaching Columns," *Hydrometallurgy*, 98 (2009), 181–191.

[6].Zhen G-Y, L.-X Zhou, "Supplementation of Inorganic Phosphate Enhancing the Removal Efficiency of Tannery Sludge-borne Cr through Bioleaching," *Water search,* 45 (16) (2011), 5295-5301.

[7].Nakasono, S., Matsumoto, N., Saiki, H., "Electrochemical Cultivation of Thiobacillus ferrooxidans by Potential Control," *Bioelectrochemistry and Bioenergetics*, 43 (1) (1997), 61–66.

[8].Suting Wang, Guangji Zhanga, Qiuhong Yuan, "Comparative Study of External Addition of Ferrous and Inoculum on Bioleaching of Marmatite Flotation Concentrate Using Mesophilic and Moderatethermophilic Bacteria," *Hydrometallurgy*, 93 (2008), 51–56.

[9].Breed, A.W., Hansford, G.S., "Effect of PH on Ferrous Ion Oxidation Kinetics of *Leptospirillum ferrooxidans* in Continuous Culture," *Biochemical Engineering Journal*, 3(3)(1999) , 193–201.

[10].A. Ahmadi, M. Schaffie, Z. Manafi, "Electrochemical Bioleaching of High Grade Chalcopyrite Flotation Concentrates in a Stirred Bioreactor," *Hydrometallurgy*, 1(104) 2010, 99–105.

[11].Ali Ahmadi, Mahin Schaffie, Jochen Petersen, "Conventional and Electro-chemical Bioleaching of Chalcopyrite Concentrates by Moderately Thermophilic Bacteria at High Pulp Density," *Hydrometallurgy*, 1-2(106)2011, 84–92.

[12].M. Gericke, Y. Govender, A. Pinches, "Tank Bioleaching of Low-grade Chalcopyrite Concentrates Using Redox Control," *Hydrometallurgy*, 3-4(104) (2010), 414–419.

[13].Ahonen, L., Tuovinen, O.H., “Solid-phase Alteration and Iron Transformation in Column Leaching of a Complex Sulphide Ore,” *American Chemical Society,* Washington, DC, pp,1994, 79–89.

Characterization of Minerals, Metals, and Materials 2016
Edited by: Shadia Jamil Ikhmayies, Bowen Li, John S. Carpenter, Jiann-Yang Hwang, Sergio Neves Monteiro, Jian Li, Donato Firrao, Mingming Zhang, Zhiwei Peng, Juan P. Escobedo-Diaz, and Chenguang Bai
TMS (The Minerals, Metals & Materials Society), 2016

CHARACTERIZATION AND STOICHIOMETRY OF THE CYANIDATION REACTION IN NaOH OF ARGENTIAN WASTE TAILINGS OF PACHUCA, HIDALGO, MÉXICO

Francisco Patiño[1], Juan Hernández[1], Mizraim U. Flores[2], Iván A. Reyes[3], Martín Reyes[1], Julio C. Juárez[1]

[1]Área Académica de Ciencias de la Tierra y Materiales, Universidad Autónoma del Estado de Hidalgo, carretera Pachuca-Tulancingo km. 4.5, C.P. 42184, Mineral de La Reforma, Hidalgo, México, Email: uri_fg@hotmail.com
[2]Área de Electromecánica Industrial, Universidad Tecnológica de Tulancingo, Camino a Ahuehuetitla #301 Col. Las Presas, C.P. 43642, Tulancingo, Hidalgo, México
[3]Instituto de Metalurgia, Universidad Autónoma de San Luis Potosí, Av. Sierra Leona No. 550, Lomas 2da Sección C.P. 78210, San Luis Potosí S.L.P. México

Abstract

The argentian resources of Pachuca, Hidalgo, México have suffered an extensive exploitation, resulting in more than 100 million tons of waste tailings located in several sites around the city of Pachuca and surrounding municipalities. Chemical, mineralogical and granulometric characterization of the waste tailings of Pachuca, Hidalgo, México, was carried out in this work. Characterization results indicate that these argentian wastes contain 56 g Ag ton^{-1}, and the silver is present in the forms of metal, argentite and argentian jarosite in a quartz matrix. Stoichiometry of the cyanidation reaction in NaOH media was analyzed, and the following conclusions were obtained: 1) both metal silver and silver present in the form of argentite can be quickly cyanidation, 2) Alkaline decomposition of argentian jarosite is the rate-control step in the cyanidation reaction.

Keywords: Characterization, Stoichiometry, Cyanidation reaction, Argentian waste tailings, Pachuca-Hidalgo-Mexico

Introduction

The mining district comprising Pachuca and Real del Monte in the State of Hidalgo, México, has been providing the world with silver for 470 years. This mining region has also been a pioneer in several technologies on the processing of argentian ores, such as the patio process and the Pachuca tanks. However, the argentian resources of this region have suffered an extensive exploitation, resulting in more than 100 million tons of waste tailings [1]. These tailings or *mine dumps* are becoming an environmental issue for the city of Pachuca and the Municipality of Mineral de La Reforma. There are mainly two causes for this: first, because, in periods of strong winds, dust clouds are formed which seriously affect the inhabitants' health; a second point is that these residues take up 1200 hectares, obstructing the city's proper and sustainable growth. Since the value of this precious metal is 15.21 dollars per troy ounce and these tailings contain 56 g

Ag ton^{-1}, it renders them appealing from an economic perspective (Monex Precious Metals, 2015) [2].

For these reasons, this piece of work presents an extensive reprocessing study of the Dos Carlos waste tailings of the city of Pachuca with the aim of: 1) recovering the silver contained in those residues through different silver leaching methods; 2) and using these residues as alternative construction material and in the glass industry. This paper presents only the results of the granulometric, mineralogical and chemical characterization, as well as the stoichiometry of the cyanidation reaction in NaOH of the Dos Carlos tailings located in the northeast area of the city of Pachuca. In spite of the toxic nature of the cyanidation, this process remains one of the most used processes in the extraction of silver and gold, either from natural deposits or mining wastes; and this process has undergone numerous improvements with the aim of improving efficiency, including the use of oxidizing and reducing agents such as ferricyanide and pyrite, cyanidation at high pressures, membrane processes and electrochemical processes [3-7]. Of the mining metallurgical district of the company Real del Monte y Pachuca, these tailings are the second richest in silver. It is found in different forms: quartz matrix, distributed as metal silver, as argentite and as argentian jarosite. This last ore is also called argentian potassium jarosite when it is synthesized in laboratories [8, 9]. This compound is also obtained in the metallurgical industry, where the precipitation of jarosite has been widely used in the hydrometallurgical circuits of zinc as a means to control the impurities of the solutions containing it, generating millions of tons of this jarosite type compound that has a high silver content [10].

Methods and materials

It is known that, for obvious reasons, the cyanidation of ores is practiced at alkaline pH levels between 9 and 12. The experiments were conducted in a conventional glass kettle coupled to a mechanical stirring system provided with an RPM meter, a thermometer and a pH meter to control the concentration of alkaline reagent. The kettle was also coupled to an electric heater that allows to dial temperature variations of ± 0.5 °C. The argentian tailings' cyanidation was conducted in a 500 cm^3 kettle under the following experimental conditions: 40 g argentian tailings sample, 25 °C, 1×10^{-2} mol L^{-1} [NaOH], 2.04×10^{-2} mol L^{-1} [NaCN], and a stirring rate of 750 min^{-1} in order to keep the solids suspended and to avoid the liquid film diffusion effect.

Since this study on the stoichiometry of alkaline cyanidation shows that silver ions are removed from the solids and diffuse towards the solution, the reaction was followed by analysis of silver ions in the liquid. The x fraction of cyanided silver was calculated with the following:

$$x = [Ag]_t / [Ag]_\infty \quad (1)$$

where $[Ag]_t$ is the concentration of silver at a time t, and $[Ag]_\infty$ is the concentration of Ag after the solids have been completely leached. The kinetic

models selected for the experimental data on the cyanidation in NaOH, were the following [11-13]:

$$1-(1-x)^{1/3} = k_{exp}t \quad (2)$$

$$1-3(1-x)^{2/3}+2(1-x) = k_{exp}t \quad (3)$$

Where k_{exp} is the experimental rate constant, x is the reacted fraction, and t is the reaction time.

Results and discussion

Figure 1 presents the X-ray Diffraction (XRD) spectrum, showing the presence of jarosite ($KFe_3(SO_4)_2(OH)_6$) in a quartz (SiO_2) matrix with other main species, such as orthoclase, albite ($NaAlSi_3O_8$) and berlinite ($AlPO_4$). Geyne reported this compound as argentian jarosite; it is original from the Paricutin mine in the mining district of Pachuca and Real del Monte [14].

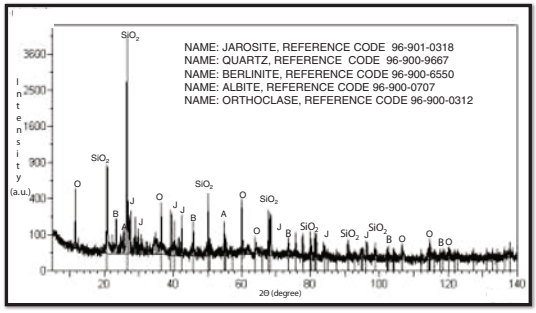

Fig. 1. X-ray diffractogram of the tailings sample (major phases: Quartz (SiO_2), O-Orthoclase ($KAlSiO_3$), A-Albite ($NaAlSi_3O_8$), B-Berlinite ($AlPO_4$), and J-Jarosite ($KFe_3(SO_4)_2(OH)_6$))

Table I summarizes the atomic absorption spectrophotometer (AAS) and inductively coupled plasma (ICP) chemical analysis data, where it can be observed that the gold and silver content is 56 g ton^{-1} and 0.60 g ton^{-1}, respectively. It can also be noted that the major elements are silicon, sulfur and aluminium, whereas the minor elements are iron, potassium, strontium, calcium, sodium, phosphorus and barium. The rest are considered trace elements. The problem is to explain how silver is distributed in the Dos Carlos waste tailings. In this respect SEM-EDS images show that the silver is distributed as follows: a) In metal form, as shown in Fig. 2a, where an 8 µm particle can be observed. Fig. 2b shows the same particle's X-ray microanalysis (EDS), showing the typical intensity peaks of metal silver. b) In the form of argentite, as observed on Fig. 3a, where argentite particles of up to 2 µm were obtained; Fig. 3b displays the EDS analysis of these particles, showing the typical intensity peaks of argentite. c) In

the form of argentian jarosite. Fig. 4a shows argentian jarosite particles finally scattered in the quartz matrix, and Fig. 4b presents the EDS analysis of the argentian jarosite particles, where the typical intensity peaks of this ore can be observed, with elements such as sulfur, iron, potassium and silver. This confirms that the peaks correspond to those of argentian jarosite, also known as silver potassium jarosite when it is obtained in the laboratory [8, 9].

Table I. Chemical composition of the waste tailings.

Elements	Wt %	Elements	Wt %
Au	0.60 g ton^{-1}	Ca	0.200
Ag	56 g ton^{-1}	Si	56.00
Cu	0.011	K	2.32
Bi	0.0002	Na	0.30
Ni	0.005	Al	6.095
Mn	0.046	Ti	0.278
Fe	2.69	P	0.14
Sn	0.0002	Mg	0.005

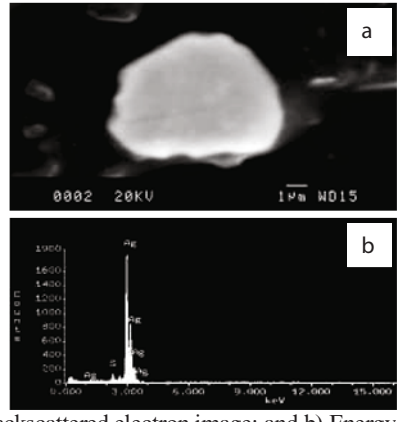

Fig. 2. a) SEM-backscattered electron image; and b) Energy dispersive X-ray microanalysis of a silver particle

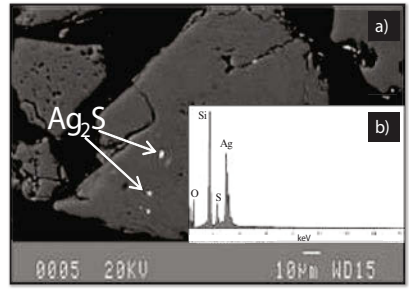

Fig. 3. a) SEM-backscattered electron image; and b) Energy dispersive X-ray microanalysis of argentite particles

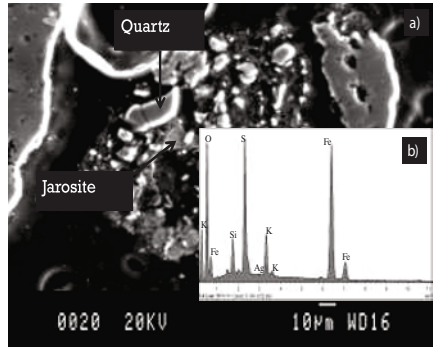

Fig. 4. a) SEM-backscattered electron image; and .b) Energy dispersive X-ray microanalysis of argentian potassium jarosite.

The results of the nature of the alkaline cyanidation reaction are summarized in Table II. The decomposition products of this ore are quickly cyanided; therefore, this second process consists of two consecutive phases, as previously observed in other studies on synthesized argentian jarosite-type compounds [9]. The reaction stoichiometry of the previously mentioned processes is described as follows:

Process 1- quick cyanidation of silver and argentite:

$$2Ag_{(S)} + 4NaCN_{(aq)} + \tfrac{1}{2}O_{2\,(g)} + H_2O_{(l)} \rightarrow 2Na[Ag(CN)_2]_{(aq)} + 2NaOH_{(aq)} \quad (4)$$

$$2AgS_{(S)} + 4NaCN_{(aq)} \rightarrow 2Na[Ag(CN)_2]_{(aq)} + NaS_{(s)} \quad (5)$$

Process 2- slow alkalination:

$$(K_xAg_{1-x})Fe_3(SO4)_2(OH)_{6\,(s)} + [3 + (1 - x)]OH^-_{(aq)} \rightarrow xK^+_{(aq)} + (1 - x)Ag(OH)_{(s)} + 3Fe(OH)_3 + 2SO^{2-}_{(aq)} \quad (6)$$

Process 3 – quick cynaidation of argentian jarosite:

$$(1-x)Ag(OH)_{(s)} + 2CN^-_{(aq)} \rightarrow (1-x)[Ag(CN)_2]^{2-}_{(aq)} + (1-x)OH^-_{(aq)} \qquad (7)$$

The chemical-control and diffusive-control kinetic models were then tested in order to determine the rate control steps of alkaline cyanidation. It was found that once the quick cyanidation (process 1) of metal silver and argentite takes place, the experimental results corresponding to process 2 adapt to both models with a similar regression coefficient, as shown in Figure 5. Therefore, it can be concluded that the global decomposition and cyanidation process of argentian jarosite is controlled in a mixed manner. The cyanidation rate constant obtained in this study for the naturally formed jarosite is calculated to be 0.007 min^{-1}, which is very similar to that of the synthetic jarosite obtained in previous studies [9].

Table II. Silver cyanidation at different time intervals: 40 g L^{-1}waste tailings, 2.04×10^{-2} mol L^{-1} [NaCN], 1×10^{-2} mol L^{-1} [NaOH], pH 11.71 and 298 K.

Time(min)	$X_{[Ag]}$	$1-(1-X_{Ag})^{1/3}$	$1-3(1-X)^{2/3}+2(1-X_{Ag})$
0	0.000	0.000	0.000
1	0.380	0.150	0.059
2.5	0.400	0.160	0.066
5	0.400	0.160	0.066
7.5	0.460	0.180	0.091
10	0.520	0.220	0.121
20	0.640	0.290	0.202
30	0.740	0.330	0.298
40	0.780	0.390	0.347
80	0.840	0.390	0.436
100	0.860	0.440	0.471
120	0.890	0.520	0.531
180	0.990	0.780	0.881
200	1.000	1.000	1.000

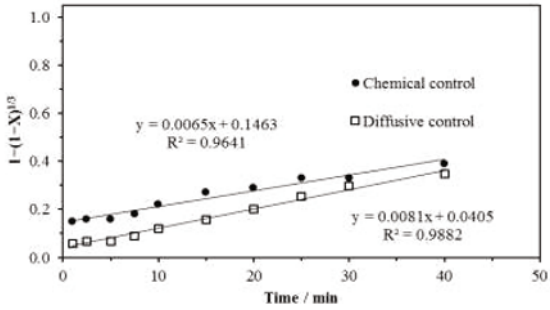

Fig. 5. Fitting of experimental data with chemical and diffusive control models

Conclusions

The Dos Carlos waste tailings located in Pachuca, Hidalgo, Mexico, are made of a quartz matrix that contains silver in the forms of metal, argentite and argentian jarosite. The silver content of these mining wastes is about 56 g Ag ton^{-1}. The stoichiometry of the alkaline cyanidation consists of: 1) quick cyanidation of both metal silver and silver present in the form of argentite, and 2) slow decomposition of the argentian jarosite and quick cyanidation of the silver contained in the decomposition products. The cyanidation rate constant of the naturally formed argentian jarosite is similar to that of the synthesized silver potassium jarosite.

References

[1] J. Hernández, F. Patiño, I. Rivera, et al., E. Salinas, E. Cerecedo, M. Reyes, and M. Pérez, (2009) *Silver dissolution from the waste mounds of Pachuca, Hidalgo State, México - Effect of Cyanide concentration on dissolution rate*, Edited by EMC, Innsbruck, Austria, 2009, p.1037.

[2] Monex Precious Metals, (2015), http://www.monex.com/liveprices/

[3] A. Azizi, C.F. Petre, C. Olsen, and F. Larachi, Untangling galvanic and passivation phenomena induced by sulfide minerals on precious metal leaching using a new packed-bed electrochemical cyanidation reactor, *Hydrometallurgy,* 107(2011), p.101.

[4] P. Karimi, H. Abdollahi, A. Amini, M. Noaparast, S.Z. Shafaei, and F. Habashi, Cyanidation of gold ores containing copper, silver, lead, arsenic and antimony, *Int. J. Miner. Process.,* 95(2010), p.68.

[5] H. Koseoglu, and M. Kitis, (2009) The recovery of silver from mining wastewaters using hybrid cyanidation and high-pressure membrane process, *Miner. Eng.,* 22(2009), p.440.

[6] X. Qiu, Z. Hu, B. Song, H. Li, and J. Zou, A novel process for silver recovery from a refractory Au–Ag ore in cyanidation by pretreatment with sulfating leaching using pyrite as reductant, *Hydrometallurgy,* 144(2014), p. 34.

[7] F. Xie, D. Dreisinger, and J. Lu, The novel application of ferricyanide as an oxidant in the cyanidation of gold and silver, *Miner. Eng.,* 21(2008), p. 1109.
[8] J.E. Dutrizac, and S. Kaiman, Synthesis and properties of jarosite-type compounds, *Can. Mineral*, 14(1976), p.151.
[9] M. Cruells, A. Roca, F. Patiño, E. Salinas, and I. Rivera, Cyanidation kinetics of argentian jarosite in alkaline media, *Hydrometallurgy*, 55(2000), p.153.
[10] B. Arregui, A.R. Gordon, and G. Steintvelt, *The jarosite process-Past, Present and Future,* Edited by TMS-AIME, New York, USA 1979, p. 97.
[11] O. Levenspiel, *Ingeniería de las reacciones químicas. Edited by Reverté*, Barcelona, Spai 2005, p. 393.
[12] A. Ballester, L.F. Verdeja, and J. Sancho, *Metalurgia Extractiva, Vol. 1, Fundamentos,* Edited by. *Síntesis*, Madrid, Spain, 2001, p.170.
[13] H.Y. Sohn, and M.E. Wadsworth, *Cinética de los procesos de metalurgia extractiva,* Edited by Trillas, Mexico City, Mexico, 1986, p.158.
[14] A.R. Geyne, C. Fries, C. Segerstrom, R.F. Black, and I.F. Wilson, *Geología y yacimientos minerales del distrito minero de Pachuca-Real del Monte, estado de Hidalgo, México,* Edited by. Consejo de Recursos Naturales no Renovables, Mexico City., Mexico, 1963.

Characterization of Minerals, Metals, and Materials 2016

Soft Materials

Session Chairs:
Sergio Monteiro
Zhiwei Peng

Characterization of Minerals, Metals, and Materials 2016
Edited by: Shadia Jamil Ikhmayies, Bowen Li, John S. Carpenter, Jiann-Yang Hwang, Sergio Neves Monteiro, Jian Li, Donato Firrao, Mingming Zhang, Zhiwei Peng, Juan P. Escobedo-Diaz, and Chenguang Bai
TMS (The Minerals, Metals & Materials Society), 2016

TENSILE STRENGTH OF POLYESTER COMPOSITES REINFORCED WITH THINNER RAMIE FIBERS

Sergio Neves Monteiro[1], Lucas de Almeida Pontes[2], Frederico Muylaert Margem[2], Jordana Ferreira[2], Pedro Amoy Netto[2], Jean Igor Margem[3]

1- IME - Military Institute of Engineering, Department of Materials Science, Praça General Tibúrcio, 80, 22290-270, Rio de Janeiro, Brazil.
2- UENF - State University of the Northern Rio de Janeiro, UENF, Advanced Materials Laboratory, LAMAV; Av. Alberto Lamego, 2000, 28013-602, Campos dos Goytacazes, Brazil.
3- Isecensa - Instituto Superior de Ensino Centro Educacional Nossa Senhora Auxiliadora, Rua Salvador Corrêa, 139 - Centro, Campos dos Goytacazes, Brazil.
Keywords: Ramie Fiber, Polyester Composite, Tensile Test.

Abstract

This study evaluated the tensile properties of polyester composites reinforced with ramie fibers with thinner diameters. Specimens with different ramie fibers percentages (0,10,20 and 30%) in continuous and aligned ramie stalk fibers volume , were tensile tested at room temperature to evaluate the ultimate strength, elastic modulus and total strain. The results indicated that the tensile properties tend to improve with increasing volume fraction of ramie fibers. The role played by the fiber/matrix interaction was analyzed by scanning electron microscopy.

Introduction

Nowadays, composites are the most popular materials with engineered combinations of properties that cannot be achieved by a conventional monolithic material [1,2]. This is particularly the case of components with special requirements for aerospace, underwater and transportation applications [3].

Modern aircrafts demand lighter, stronger, tougher and stiffer structural parts that can only be made with carbon fiber reinforced composites. The space shuttle is a high-tech example of a vehicle using different types of expensive composites including carbon fiber reinforcing pyrolized graphite matrix composites. Less expensive glass fiber composites are also used as interior components of aircrafts in addition to an extensive application in many other products, from packaging to automobile components [3].

All synthetic composites like the aforementioned ones reinforced with carbon and glass fibers are, however, associated with environmental drawbacks. Their production is energy-intensive and they cannot be easily recycled. Moreover, glass fiber is related to health problems [4].

Several natural fibers are increasingly being considered as viable alternatives to replace glass fiber in polymer composites reinforcement. Lignocellulosic fibers extracted from plants have shown a real potential for this substitution [5-10]. Their comparative

advantages are lower density and cost as well as renewability, biodegradability, recyclability and neutrality with respect to CO2 emission, which is one of the gases responsible for global warming. Less known natural fibers like piassava, sponge gourd, caroa, curaua [11] and ramie [12] are currently being investigated for their potential as composite reinforcement, even review works on the application of natural fibers in composites [12-21] fail to report on Ramie fibers (Figure 1 shows the plant and fibers of ramie). Since the heterogeneous characteristics of lignocellulosic fibers indicates that the strength varies inversely with the fiber diameter [22], the present work carried out a mechanical behavior analysis on the tensile strength of polyester composites reinforced with thinner ramie fibers.

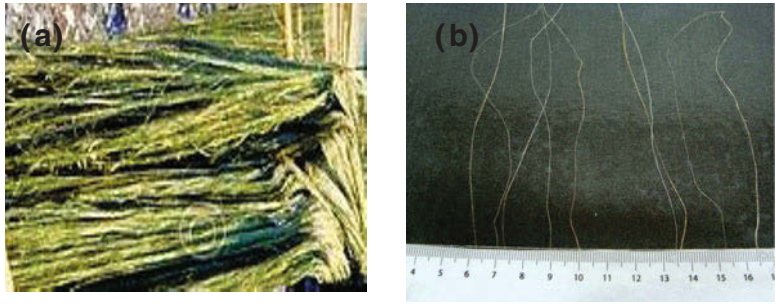

Figure1 (a) Ramie Fibers and (b) individually separated fibers

Experimental Procedure

Ramie fibers extracted from *Boehmeria Nivea*, as illustrated in Figure 1, were obtained from a Brazilian firm SisalSul. The petiole was cleaned with water and dried for one hour at 60°C. Then, with a razor blade, the fibers were extracted from the petiole. No treatment was applied to the fibers. Thinner fibers with diameter between 0.1 and 0.4 mm were manually separated and considered for polyester composites reinforcement. A commercially supplied unsaturated orthophtalic polyester resin hardened with 0.5% of methyl-ethyl-ketone was used as the composite matrix.

Figure 2. Specimens of 0, 10, 20 and 30% of ramie fibers in volume fraction.

Figure 2 illustrates the macro aspect of tensile ruptured specimens corresponding to the different volume fraction of ramie fibers. In this figure, the fracture of neat polyester specimens tends to be transversal to the tensile axis but with the increase of ramie amount the evidence of ramie fiber participation could be detected.

Composite specimens were individually prepared with continuous and aligned ramie fibers placed inside dog-bone shape silicone molds. The thinner fibers in amounts of up to 30% in volume were aligned along the specimens corresponding tensile axis. Still fluid polyester resin was poured onto the thinner ramie fibers, and cured for 24 hours. These specimens were subjected to tensile tests in a model 5582 Instron machine at room temperature and 0.5 mm/min. For each volume fraction of ramie fiber, from 0 to 30% in volume, six samples were tested and the results statistically analyzed. The specimens were gold sputtered and observed by scanning electron microscopy (SEM) in a model SSX 550 Shimadzu microscope.

Results and Discussion

From the data acquisition system of the Instron machine, were obtained results that revealed that ramie fibers does not act as effective reinforcement, and decrease the plastic deformation of the composites. The data of these tests also were recorded and used to find the values of tensile strength at break.

The Table I shown the results of tensile strength for the composites incorporate with the corresponding volume of fiber incorporated.

Table I. Tensile properties of polyester composites reinforced with ramie fibers

Volume Fraction of Ramie Fiber [%]	Tensile Strength [MPa]	Elasticity Modulus [GPa]
0	29.27 ± 3.42	0.42 ± 0.26
10	17.02 ± 5.72	0.32 ± 0.09
20	16.50T ± 5.23	0.19 ± 0.12
30	25.52 ± 5.21	0.45 ± 0.13

Table I shown that occur a decrease in the tensile strength when the volume fraction of fiber is increased. It can be seen especially when compared the results of pure polyester (0% of volume fraction of fiber) and the higher volume of fiber incorporated (30%). Comparing both is observed an decrease about 15%.

The mean values of the tensile stress and elasticity modulus, listed in Table I for the polyester composites, are plotted in Figure 3 as a function of volume fraction of ramie thin fibers. In this figure it can be noteworthy that the introduction of ramie fibers does

not represent an increase neither strength, Figure 3(a), nor the elastic modulus, Figure 3(b), to the polyester matrix composites. The cause of this can be an error in the cure of the specimens or the during the tensile strength test.

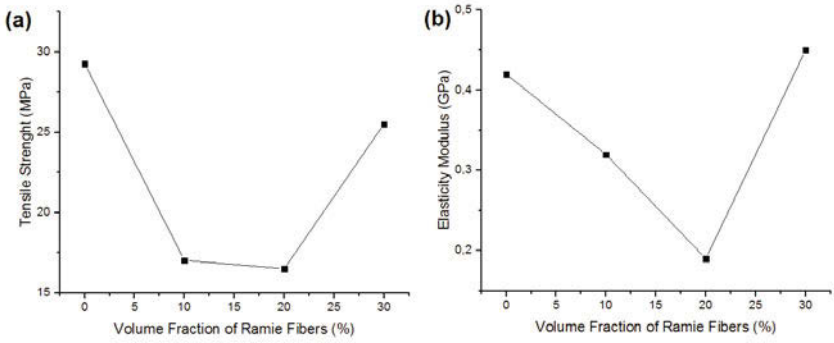

Figure 3. Variation of tensile strength (a) and elastic modulus (b) with the volume fraction of
thinner ramie fibers

The macro aspect of tensile ruptured specimens showed in figure 2 can indicate that the fracture mechanism for the pure polyester matrix was mainly associated with the propagation of transversal cracks although for the composites the non transversal cracks indicate a low interface relation between the ramie fiber and the polyester matrix.

However is wise to notice that the deviations of some of these results are significant. It can be explained by the difficult of prepare samples uniformly. Also it can be explained by the irregular surface of the natural fibers which causes irregularities on the interface between the fiber and polymer.

Another explanation of the weak interface is because of the natural fibers are hydrophilic and the polymer matrix is hydrophobic. Therefore, even after drying in the oven, these fibers always have residual surface moisture which difficult the adhesion between fiber and matrix.

This kind of deficiency can be solved improving the techniques of preparation of the samples by taking extra care with the process of putting fibers and resin on the mold. Also the pressure it the system was submitted improve the interface between fiber and matrix which leads to superior materials.

Figure 4 shows a typical SEM fractograph of a tensile rupture specimen for a polyester composite reinforced with 30% of ramie fiber. In this figure, one can see a few broken fibers well adhered to the polyester matrix. By contrast, an empty space corresponding to a fiber that was detached from the matrix can also be seen. A crack associated with

this empty space suggests that the fiber had initially acted as a barrier for the rupture process, in agreement with the macroscopic rupture in Figure 2.

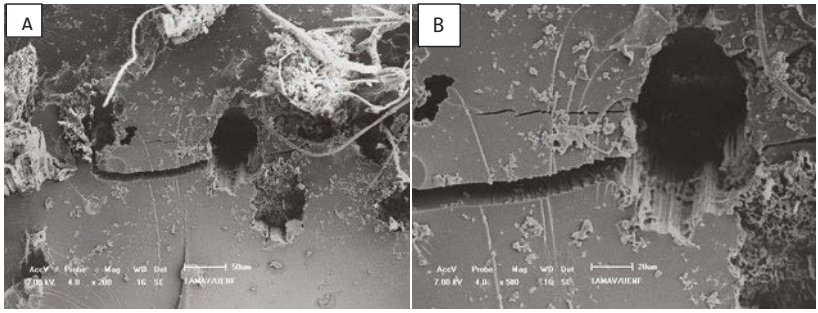

Figure 4. Composite with 30% in vol. of ramie fiber, with different magnifications: (a) 200x and (b) 500x.

Conclusions

The ramie fibers may not be strong enough to provide reinforcement of polyester matrix composites, but the bad result in the reinforcement test can be also attributed to a problem with the resin cure time or other trouble in the manufacture procedure. In fact, polyester composites reinforced with aligned ramie fibers, significantly improve the mechanical performance in literature, what can indicate some problem in the manufacture or test procedure. This decrease can be attributed to ramie fibers not acting as a barrier for the crack propagation throughout the brittle polyester matrix. The resistance decreased in the samples tensile energy can be attributed to the fiber hydrophilic characteristic and the resin hydrophobic property, which would compromise a tougher interface. In the literature lignocellulosic fibers inclusion into polymer matrix normally increase the tensile strength, but for the ramie/polyester composite it does not occur, ramie fibers are not acting as a barrier for the crack propagation throughout the brittle matrix.

Acknowledgements

The authors thank for the support provided by the Brazilian agencies: CNPq, CAPES, and FAPERJ.

References

1. B.D. Agarwal and L.J. Broutman: *Analysis and Performance of Fiber Composites.* (New York, NY: John Wiley & Sons, 1990).
2. K.H.G. Ashbee: *Fundamental Principles of Fiber Reinforced Composites.* (Lancaster: Technomic Pub. Co. Inc., 1993).

3. W.D. Callister Jr.: Materials *Science and Engineering – An Introduction*. (5 ed. New York, NY: John Wiley & Sons, 2000).
4. P. Wambua, I. Ivens and I.Verpoest*: Composites Science and Technology* Vol. 63 (2003), 1259.
5. A.K. Bledzki and J. Gassan: Prog. Polym. Sci. Vol. 4 (1999), 201.
6. D. Nabi Sahed and J.P. Jog: Advances in Polymer Technol. Vol. 18 (1999), 221.
7. A.K. Mohanty, M. Misra and G.Hinrichsen: Macromolecular Mat. and Engineering Vol. 276/277 (2000), 1.
8. M.J. John and S. Thomas: *Carbohydrate Polymers* Vol. 71 (2008), 343.
9. J. Crocker: *Materials Technology* Vol. 2-3 (3) (2008), 174.
10. S.N. Monteiro et al.: JOM Vol. 61(1) (2009), 17.
11. A.L.F.S. d'Almeida et al., *Thermal Analysis and Calorimetry* Vol. 91 (2008), 405.
12. S.N. Monteiro et al,.*Polymer Testing* Vol. 23 (2) (2004), 131.
13. R.S. Santos, E.L.C. Silveira and C.M.L. Souza: 30th Annual Meeting of the Brazilian Chemistry Society (SBQ). Águas de Lindóia, May 31 to June 3 2007. Proceeding Águas de Lindóia 2007. (SP). 1.
14. N.S.S. Santos et al., paper presented in 18° Congresso Brasileiro de Ciência dos Materiais (CBECIMAT). Porto de Galinhas, 24 - 28 November 2008. Procceding...Porto de Galinhas 2008. (PE). 3565.
15. S.N. Monteiro et al., paper presented in 64º Congresso Anual da Associação Brasileira de Metalurgia, Materiais e Mineração (ABM). Belo Horizonte 13 - 17 July 2009. Proceeding...Belo Horizonte (2009). (MG). 1.
16. S.N. Monteiro, F.P.D. Lopes, L.C. Motta, L.S. Marques, T.G.R. Portela, paper presented in Annual Meeting & Exhibition Conference: Characterization of Minerals, Metals, and Materials (TMS). San Francisco 15 to 19 February 2009. Proceeding San Francisco 2009. California (USA). 1.
17. T.G.R. Portela, L.L. Costa, F.P.D. Lopes and S.N. Monteiro, paper presented in Annual Meeting & Exhibition Conference: Characterization of Minerals, Metals, and Materials (TMS). Seattle 14 to 18 February 2010. Proceeding Seattle 2010. Washington (USA). 1.
18. S.N. Monteiro et al., Rev. Mater. Vol. 15 (2) (2010), 216.
19. R.S. Santos, A.A. Souza, M.-A. de Paoli and C.M.L. Souza: Composites Part A. Vol 41 (2010), p. 1123. Materials Science Forum Vols. 775-776, 187
20. A.P. Barbosa, "Structural Characteristics and Properties of Polymeric Composites Reinforced with Buriti Fibers." (Doctoral thesis, Campos dos Goytacazes, 2009. Universidade Estadual do Norte Fluminense (UENF). (RJ) (In Portuguese)
21. S.N. Monteiro et al., paper presented in Annual Meeting & Exhibition Conference: Characterization of Minerals, Metals, and Materials (TMS). San Diego February 27 to March 3 2011. Proceeding San Diego 2011. California (USA). 1.
22. S. N. Monteiro et al., Met. Mat. Trans. A. Vol. 42 (2011), 2963.

Characterization of Minerals, Metals, and Materials 2016
Edited by: Shadia Jamil Ikhmayies, Bowen Li, John S. Carpenter, Jiann-Yang Hwang, Sergio Neves Monteiro, Jian Li, Donato Firrao, Mingming Zhang, Zhiwei Peng, Juan P. Escobedo-Diaz, and Chenguang Bai
TMS (The Minerals, Metals & Materials Society), 2016

CHARPY IMPACT TESTS OF POLYESTER COMPOSITES REINFORCED WITH PALF FIBERS

Gabriel O. Glória [1], Giulio R. Altoé[1], Maycon A. Gomes[1], Carlos Maurício F. Vieira[1], Maria Carolina A. Teles[1], Frederico M. Margem[1], Glênio Daniel[2], Sergio N. Monteiro[3]

1 State University of the Northern Rio de Janeiro, UENF, LAMAV; Av. Alberto Lamego, 2000, 28013-602, Campos dos Goytacazes, Brazil.

2 Faculdade Redentor, FAC, Rodovia BR 356, nº 25. Bairro Cidade Nova. CEP 28300-000, Itaperuna, Brasil

3 Instituto Militar de Engenharia , IME, Praça Gen. Tibúrcio, nº80 Urca, Rio de Janeiro - RJ, 22290-270

Keywords: PALF fiber, Polyester composite, Charpy test.

Abstract

With the society's demand for new environmentally friendly materials, new alternatives, such as the PALF fiber, are being developed to replace synthetic fibers which are harmful to the environment. However, there is limited information about the impact resistance of polyester composites incorporated with PALF fibers. Therefore, the aim of this work was to analyze the absorbed impact energy of these composites. Impact specimens with up 30% in volume of PALF fibers were fabricated. The fibers were press molded with a orthophtalic polyester resin mixed with the proper hardener and set to cure for 24 hours at room temperature and pressured in the mold up to 5 tons. Specimens were test in a charpy pendulum. The results showed increase in the absorbed impact energy with higher amount of incorporated fiber. This performance can be explained by the difficult of rupture imposed the type of cracks resulting from fiber/matrix interaction.

Introduction

Today the society is demanding materials that have low costs as well as benefits for the environment. In this context, lignocellulosic fibers become a promising solution. The application of these natural fibers is also motivated by advantages like good toughness and less wear of equipment used in the processing of composites. Nowadays, they are being considered as a substitute for synthetic fibers, used by the industry on a large scale [1-5]. In addition, such composites are environmentally friendly because they are renewable, biodegradable and neutral with respect to CO_2 emissions, the main responsible for global warming and climate changes [5,6].

Lignocellulosic fibers also have some disadvantages in relation to synthetic fibers such as the difficulty of coupling with polymer matrices, due to the hydrophilic character of fiber and the hydrophobic nature of the matrix, as well as dimensional heterogeneity [4,5]. This last one is characteristic of the nature of this material and constitutes an obstacle to the use of these fibers in certain projects, especially those aiming at obtaining high performance. The above mentioned disadvantages are worrisome reasons for the occurrence of reduction in the strengthening capacity, as indicated by the rule of mixtures for composites [6-8].

The most important problem for the composite strength according to Wambua et al. [9], is the adhesion of polymeric matrix and fiber. Since the matrix has to transfer an applied load to the reinforcing fibers through interfacial shear stress, a good bond between the matrix and the fiber is required.

Polyester is relatively a strong polymer used as composite matrix [10-12]. Therefore, the objective of the present work was to obtain the mechanical toughness by impact test, for polyester composites reinforced with different amounts of PALF fibers.

Experimental Procedure

100 PALF fibers shown in Figure 1 are randomly selected from the bundle. The equivalent diameter corresponding to the average between the larger and smaller (90º rotation) cross section dimensions at five locations for each fiber was measured in a profile projector Nikon 6C.

Figure 1. A small bundle of PALF fibers

Figure 2 presents histogram corresponding to the distribution of diameter of the as-received PALF fibers. The equivalent diameter of each fiber was actually the average value obtained by 10 different measurements performed in a profile projector at five distinct locations (two with 90° rotation at each location).

The histogram in Figure 2 reveals a relatively large variation in the diameter, which is a consequence of the non-uniform physical characteristics of a lignocellulosic fiber, common in natural fibers [1,2,7-9]. It should be noticed that the diameter range was 0.10-0.28 mm with an average of 0.20 mm.

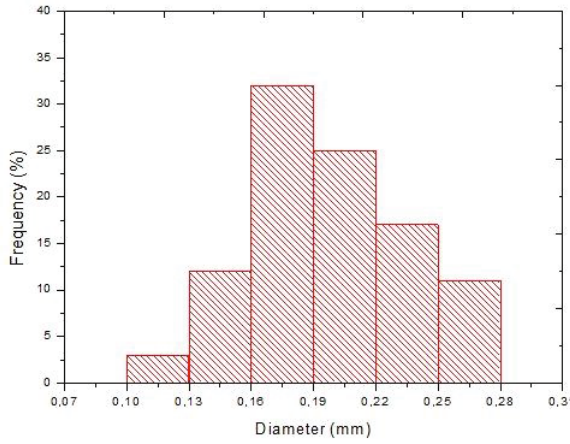

Figure 2. Histogram for the distribution of diameter of the as-received PALF fibers.

Composites with up to 30% in volume of PALF fibers were fabricated by placing the fibers longitudinally aligned inside a steel mold and then pouring the still fluid orthophtalic polyester resin mixed with a methyl-ethyl-ketone hardener into the mold. Standard specimens for Charpy impact test, with 125 x 12.7 x 10 mm, were prepared according to the ASTM D256 [12,13] with aligned Fibers along its length. Figure 3 illustrates the Charpy impact pendulum and the schematic specimen with standard dimensions. The notch with 2.54 mm in depth, angle of 45° and a tip curvature radius of 0.25mm was machined with a DIN 847 milling tool. For each volume fraction of fiber, 10 specimens were impact tested in a PANTEC hammer pendulum to ensure a statistical validation.

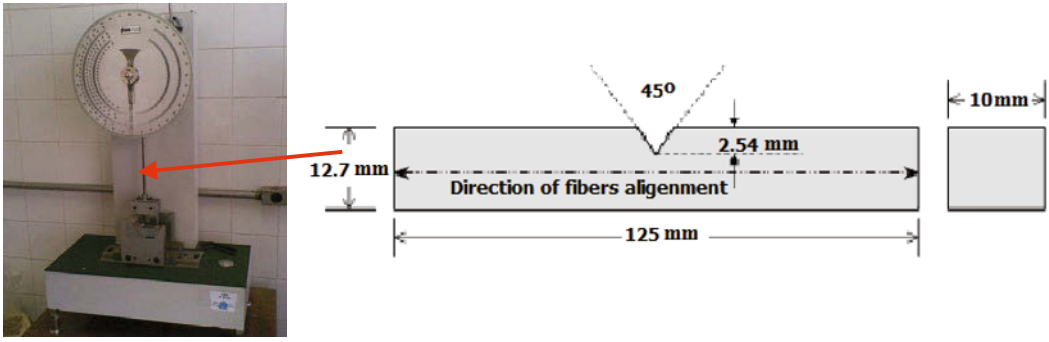

Figure 3. Charpy equipment and standard specimen schematic.

The impact fracture surface of the specimens was gold sputtered and analyzed by scanning electron microscopy, SEM, in a model SSX-500 Shimadzu microscope with secondary electrons imaging at an accelerating voltage of 15 kV.

Results and Discussion

Table I presents the results of Charpy Impact Tests of polyester matrix composites reinforced with different volume fractions of PALF fibers.

Table I. Charpy Impact Energy for polyester composites reinforced with PALF fibers.

Amount of PALF Fiber (wt.%)	*Energy (J/m)*
0	39.28 ± 2.77
10	325.00 ± 86.84
20	749.16 ± 100.94
30	1213.33 ±149.74

Based on the results shown in Table 1, the variation of the Charpy Impact Energy with the amount of PALF fibers in the polyester matrix is shown in Figure 4.

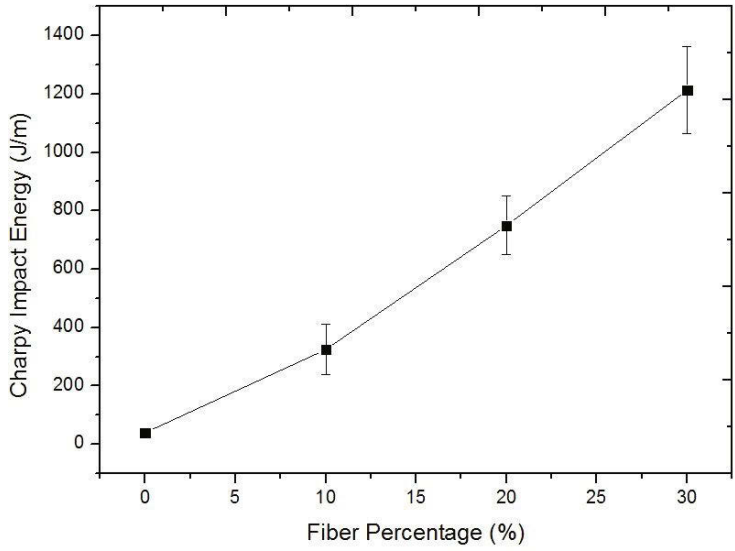

Figure 4. Charpy Impact Energy as a function of amount PALF fibers

In this figure it should be noticed that the PALF fibers incorporation into the polyester matrix significantly improves the impact toughness of the composite. Within the standard deviation, this improvement can be considered as a linear function with respect to the amount fiber until 30%. The values shown in this figure are consistent with results of the literature. The reinforcement of a polymeric matrix with natural [11,13] fibers increases the impact toughness of the composite.

The relatively low interface strength between a hydrophilic natural fiber and a hydrophobic polymeric matrix gives a weak load transfer from the matrix to a longer fiber. This results in relatively greater fracture surface and higher impact energy is spent for the rupture [14].

The specimen with PALF fibers was not completely broken upon impact. This is due to the relatively high tensile strength characteristic of the PALF fiber, which prevents a total collapse. For these larger fiber fractions, the impacted specimen is bent enough to allow the hammer to continue its trajectory, while the two parts of the folded specimen remained attached. The non-occurrence of rupture upon impact indicates a high toughness of the composite. Was assumed that if the rupture had occurred, the absorbed energy would be even higher.

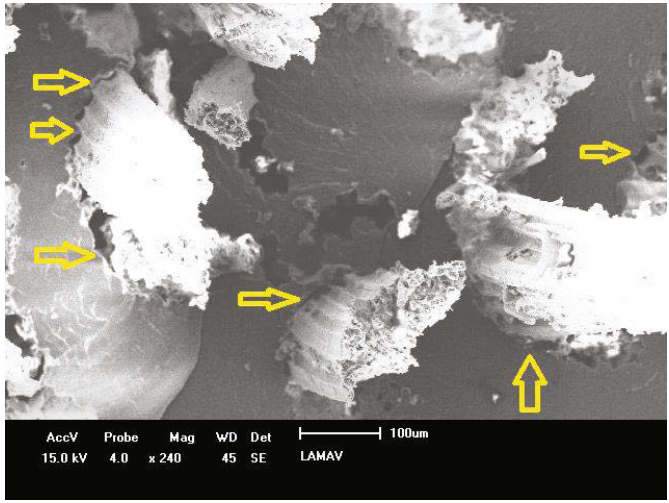

Figure 5. Impact fractured surface of the composite with 30% in volume of PALF fibers.

The SEM analysis of the microstructure of the fractured region resulting from Charpy impact support a better understanding of the mechanisms responsible for the toughness of PALF fiber reinforced composites as compared to the pure resin. The general SEM aspect shows an effective low adhesion between the fibers and the epoxy matrix, where cracks preferentially propagate. This behavior results in a greater fracture area. Some fibers were broken and others were pulled out from the matrix. This greater fracture area correlated with the PALF fibers acting as reinforcement for the composite, justify the higher absorbed impact energy with increasing amount of PALF fiber.

Conclusions

Composites made of continuous and aligned PALF fibers used as reinforcement of polyester matrix showed an almost linear increase in notch toughness, measured by Charpy impact tests, as compared to the pure polyester resin. The incorporation of 30% of PALF fiber in the polyester matrix significantly improves the toughness of the composite, 1213.33 J/m, as compared to pure polyester resin, with 39.28 J/m. Most of this increase in toughness is apparently due to the low PALF fiber/polyester matrix interfacial shear stress. This results in a higher absorbed energy as a consequence of a longitudinal propagation of the cracks throughout the interface, which generates larger ruptures areas, as compared to a transversal fracture.

Acknowledgements

The authors thank the support to this investigation by the Brazilian agencies: CNPq, CAPES, FAPERJ and TECNORTE/FENORTE.

References

1. Bledzki, A.K., Gassan, J. Composites reinforced with cellulose-based fibres. Program Polymer Science, 24 (1999), 221-274.
2. Nabi Sahed, D., Jog J.P. Natural fiber polymer composites: a review. Advances in Polymer Technology, 18 (1999), 221-274.
3. Mohanty, A.K.; Misra, M.; Hinrichsen, G. Biofibres, biodegradable polymers and biocomposites: An overview. Macromolecular Matererials and Engineering, 276 (2000), 1-24.
4. Crocker, J. Natural materials innovative natural composites. Materials technology, 2-3 (2008), 174-178.
5. Monteiro S.N.; Lopes, F.P.D.; Ferreira, A.S.; Nascimento, D.C.O. Natural fiber polymer matrix composites: cheaper, tougher and environmentally friendly. JOM, 61 (2009), 17-22.
6. W.D. Callister Jr., Materials Science and Engineering – An Introduction, 5 ed., (New York, NY: John Wiley & Sons, 2000).
7. C.Y. Yue, H.C. Looi and M.Y. Quek, "Assessment of Fibre-Matrix Adhesion and Interfacial Properties Using the Pullout Test". Int. J. of Adhesion and Adhesives, 15 (1995), 73-80.
8. S.Y. Fu, B. Lauke, E. Mäder, X. Hu, C.Y. Yue, "Fracture resistance of short-glass-fiber-reinforced and short-carbon-fiber-reinforced poly-propylene under charpy impact load and dependence on processing", *J. Mater. Process. Technol*., 89-90 (1999), 501-507.
9. P. Wambua, I. Ivens, I.Verpoest, "Natural fibers: can they repalce glass and fibre reinforced plastics?", *Composites Science and Technology*, 63 (2003) 1259-1264.
10. Monteiro, S.N., Margem, F.M., Santos JR., L.F.L., "Izod Impact energy in polymeric composites reinforced with ramie fiber.", (Paper presented at *18th Brazilian Congress on Materials Science and Engineering - CBECIMAT* (Porto de Galinhas, PE, Brazil, November, 2008), 1-12.
11. Monteiro, S.N., Ferreira, A.S., Lopes, F.P.D. "Izod impact energy of polyester matrix composites reinforced with aligned curaua fibers.", (Paper presented at Characterization of Minerals, Metals & Materials Characterization Symposium – TMS Conference, San Francisco, EUA, March 2009) 1-8.
12. Monteiro, S.N.; Costa, L.L.; Lopes, F.P.D.; Terrones, L.A.H. "Characterization of the impact resistance of coir fiber reinforced polyester composites.", (Paper presented at Characterization of Minerals, Metals & Materials Characterization Symposium – TMS Conference, New Orleans, LA, USA, March, 2008), 1-6.
13. Monteiro, S.N., Margem, F.M., Santos JR., L.F.L. "Ensaios de impacto Izod em compósitos poliméricos reforçados com fibras de rami.", (Paper presented at 18° Congresso Brasileiro de Engenharia e Ciencia dos Materiais, CBECIMAT 2008, Porto de Galinhas, PE, Novembro, 2008), 1-12.
14. C.Y. Yue, H.C. Looi and M.Y. Quek, "Assessment of Fiber-Matrix Adhesion and Interfacial Properties Using the Pullout Test". *Int. J. of Adhesion and Adhesives*, 15 (1995), 73-80.

Characterization of Minerals, Metals, and Materials 2016
Edited by: Shadia Jamil Ikhmayies, Bowen Li, John S. Carpenter, Jiann-Yang Hwang, Sergio Neves Monteiro, Jian Li, Donato Firrao, Mingming Zhang, Zhiwei Peng, Juan P. Escobedo-Diaz, and Chenguang Bai
TMS (The Minerals, Metals & Materials Society), 2016

DYNAMIC-MECHANICAL CHARACTERIZATION OF POLYESTER MATRIX COMPOSITES REINFORCED WITH EUCALYPTUS FIBERS

Caroline G. de Oliveira[1], Anna C. C. Neves[1], Noan T. Simonassi[2], Artur C. Pereira[1], Frederico M. Margem[1], Anderson Barbosa[1], Sergio N. Monteiro[2]

[1] State University of the Northern Rio de Janeiro, UENF, LAMAV; Av. Alberto Lamego, 2000, 28013-602, Campos dos Goytacazes, Brazil.
[2] Instituto Militar de Engenharia , IME, Praça Gen. Tibúrcio, nº80 Urca, Rio de Janeiro - RJ, 22290-270
sergio.neves@ig.com.br

Keywords: EucalyptusFibers, PolyesterComposite, Dynamic-MechanicalCharacterization.

Abstract

Recently, the eucalyptus fibers have been investigated as a potential option in composites application, due to some advantages in comparison with synthetic fibers. It is largely cultivated in all Brazilian territory. The present work has as objective to characterize the dynamic-mechanical behavior of eucalyptus fiber composites subjected to thermal and mechanical constraints. In this work, the temperature variation and the dynamic-mechanical parameters of polyester composites incorporated with up to 30% in volume of eucalyptus fibers were investigated by Dynamic Mechanical Analysis (DMA) experiments. The results showed that the incorporation of eucalyptus fibers tends to increase the viscoelastic stiffness of the polyester matrix. It was also observed changes in the glass transition temperature (Tg) and the structure dumping capacity of the composites with increasing fraction of fibers.

Introduction

Nowadays, the environmental issues are not only an important concern of many projects and researches, but they are frequently the focus. The use of synthetic materials and non-renewable energy resources contributes to the air pollution, to the non-sustainable exploitation of natural reserves and to the accumulation of non-biodegradable waste [1-4].

New processes and products have been developed based on their environmental advantages. In this matter, the natural lignocellullosic fibers should be highlighted as an environmentally friendly material. They are recyclable, renewable and biodegradable. In addition, they provide a balance between CO_2 absorption during cultivation and its industrial processing emission, which is an attractive characteristic with the concern of green house effect . Moreover, natural fibers have lower cost when compared to

synthetic fibers. They cause a reduced process of equipment wear and have lower density, which allows the manufacture of lighter materials [5-7].

Applications of natural lignocellulosic fibers, obtained from cellulose-based plants, are receiving increased attention as an alternative to replace some synthetic materials, such as glass fibers. These applications can vary, but currently it has been increasing in the construction and automotive fields. Ramie, Jute, Curaua and Sisal fibers are just some examples of natural fibers that have been investigated as potential reinforcements and presented a relevant set of mechanical properties [8-10].

It is worth noting that the cultivation of natural fibers can also have a positive social impact. It contributes for the non-food agriculture, working as a source of income, especially in developing countries [6]. The Eucalyptus plant is cultivated extensively in all Brazilian territory.

In this work, the dynamical-mechanical behavior of polyester matrix composites reinforced with eucalyptus fibers has been investigated in order to determine the reaction of the material to thermal and mechanical constraints.

Experimental Procedure

Rectangular specimens with nominal dimensions 35 x 13 x 3 mm were used in DMA testing. The manufacture of these specimens was initiated by placing separately, 10, 20 and 30% by volume of fibers aligned along the length of a silicone mold. The liquid polyester resin, plus 0.5% of catalyst based on methyl ethyl ketone as indicated by the manufacturer, was poured into the eucalyptus fibers within the mold. The specimens were cured at room temperature, about 25 ° C, for at least 24 hours. Figure 1 shows the appearance of the eucalyptus fibers.

Figure 1. Eucalyptus fibers.

Each sample, including pure polyester resin, i.e., 0% fiber, was subjected to DMA testing in three point flexural test in a machine of TA Instruments Model Q800, operating at a frequency of 1 Hz at a heating rate of 3 ° C / min under nitrogen flow. Curves of variation of E ', E" and tan δ with temperature were simultaneously recorded between 20 and 180 ° C.

Results and Discussion

Figure 2 shows curves associated with mechanical-dynamic parameters E ', E" and tan δ as a function of temperature for the test specimen with 0% fiber that i. e. pure resin. These curves correspond to the first run of tests DMA. Figure 5 shows similar curves for the composite with 30% eucalyptus fibers. Comparing the curves of Figures 2 and 5 as well as the other curves for compounds of 10 and 20% eucalyptus fibers, the effect was caused by the introduction of these fibers in the dynamic viscoelastic behavior of the materials investigated.

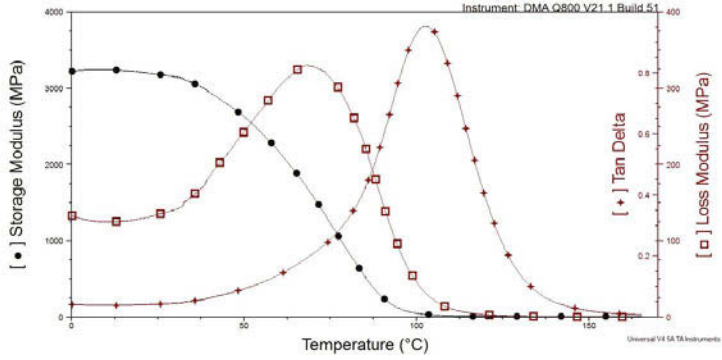

Figure 2. DMA curves corresponding to the specimen of pure polyester resin, 0% fiber.

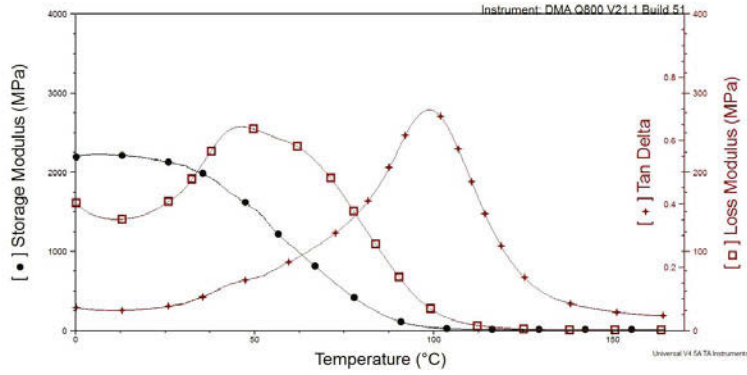

Figure 3. DMA curves corresponding to the specimen with 10% fiber.

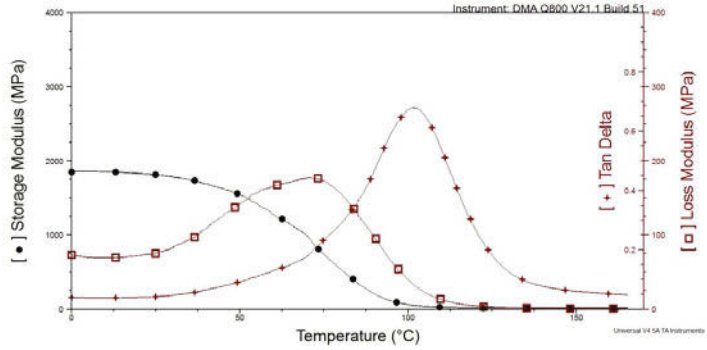

Figure 4. DMA curves corresponding to the specimen with 20% fiber.

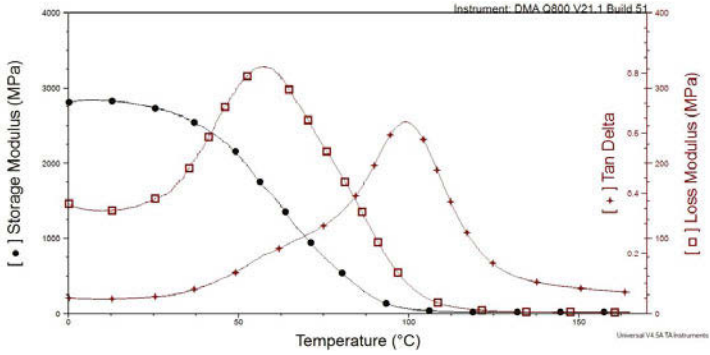

Figure 5. DMA curves corresponding to the specimen with 30% fiber.

Initially, the positions of various peaks in the DMA curves are close to each other, as shown in Figures 2-5. These peaks correspond to changes in the material structure, especially the transition from one crystalline structure to the glass one, characterized by its Tg. Experimentally, the value of the temperatures of different peaks, indicated in each curve, are visual estimates for comparing the evolution of structural transitions that occur with the incorporation of eucalyptus fibers in polyester matrix composites. Among the peaks found in the DMA curves, one associated with higher temperature is the tan δ, considered the upper limit for Tg. Comparing this peak in the various composites, there is a tendency of displacement of Tg to lower temperatures with the increase of eucalyptus fiber fraction. In principle this means that the interaction between the eucalyptus fibers and the polymer chains of the matrix reduces the polyester ability to crystallize to higher temperatures, as suggested by Rana et al. [11] for composite polypropylene reinforced with jute fibers.

Comparing the values of the loss modulus shown in the Figures 2 to 5 , E", all E" curves of these figures go through a well defined maximum value that can be associated with δ peak relaxation. According Mohanty et al. [12] this relaxation is attributed to the

mobility of the chains in the crystalline polymer phase in the case of this work, the polyester matrix. For composites with eucalyptus fibers, the δ peaks in curves E" are displaced at about 20°C for lower temperatures, excepting the composite with 20% of fibers. This is possibly due to the increase in flexibility of the composite matrix [13] caused by the introduction of the eucalyptus fibers, that have low adhesion to the matrix. This can also be an effect of incomplete or inefficient polymerization process.

Figure 6 compares the variation of storage modulus, E' with temperature for various composites studied. The curves in this figure show that the E' value is relatively higher at 20 ° C, between 3 and 4 GPa, which means rigid structure for polymer materials, although the pure resin shows lower values of storage modulus compared with the literature [12]. Moreover, for all temperature levels, the value of E' for composites with eucalyptus fibers is worse than pure polyester resin, i.e. 0% fiber. In fact, the E' value is directly related to the material's ability to withstand mechanical loads recoverable viscoelastic deformation. In the case of DMA test this work, E' is analogous to the flexural modulus [13]. With increasing temperature, Figure 6, there is a rapid decrease in the value of E 'from 25 ° C to achieve a level of less than 1 GPa.

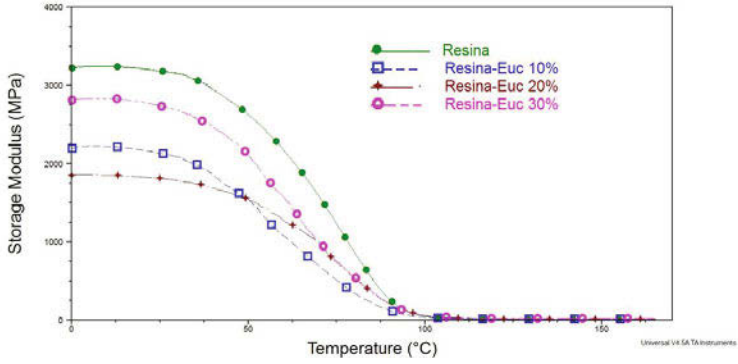

Figure 6. Storage modulus curves as a function of temperature for pure polyester and reinforced composites with different fractions eucalyptus fibers.

To the pure polyester resin, i.e., 0% fiber, this level of thermal softening starts at about 95 - 100°C as observed in other publications [14, 15]. It can be observed that the incorporation of the eucalyptus fibers doesn't have a significant influence on the onset. This means that the lignocellulosic fibers do not have a reinforcement characteristic. Furthermore, from the results of quasi-static bending [13], other lignocellulosic fiber shows no ability to reinforce the polyester matrix. Thus, for the dynamic conditions of this work, eucalyptus fiber apparently does not effectively transfer the viscoelastic efforts from the matrix to the fibers.

The variation of tan δ with temperature for the pure polyester resin and composites reinforced with eucalyptus fibers is shown in Fig. 7. In this figure it can be seen that both the composites and the polyester resin have characteristic peaks of the upper value

for the glass transition temperature. It is important to bear in mind that the tan δ is associated with the damping capacity of the material [15]. This damping is maximized in the balance between amorphous and crystalline structures, characterizing the Tg. It is observed in Fig. 7 that the composites exhibit lower amplitude peaks decreasing to lower temperatures compared to the pure polyester resin. This suggests that the eucalyptus fibers does not interact so efficiently with the chains of the polyester matrix. There is no significant hindering of mobility nor reducing of structural damping capacity. Instead, the higher mobility of the chains reduces the crystallinity of the matrix, ie, the value of Tg to lower temperatures. Due to introduction of 30% eucalyptus fiber, Tg is decreased by 7 ºC.

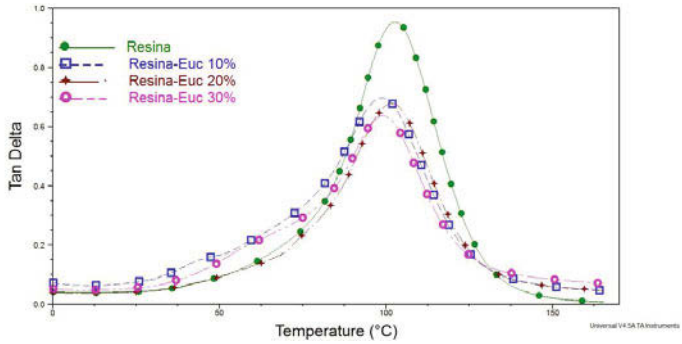

Figure 7. Curves δ tangent versus temperature for pure polyester and reinforced composites with different fractions ramie fibers.

As a final note, it is worth mentioning that the eucalyptus fibers incorporated into the polyester matrix do not form good interfacial fiber/matrix bonding due to natural incompatibility of lignocellulosic hydrophilic fiber with a hydrophobic polymer [6]. Moreover, dynamic-mechanical stress, just as the quasi-static applications, witness the poor interaction between the eucalyptus fibers and the chains of polyester resin. An advance in the thermal softening of the composite and a decrease in its glass transition temperature are observed.

Conclusions

DMA tests in composites with up to 30% volume eucalyptus fibers incorporated into the polyester matrix lead to slight changes in dynamic-mechanical parameters. The introduction of eucalyptus fiber decreases the level of rigidity and viscoelasticity tends to displace the curves of storage modulus, E', to lower temperatures. This causes an advance in the start of the heat softening of the composite. Moreover, the δ peak of loss modulus, E'', is also decreased to lower temperatures, indicating no major mobility constraints caused by the interaction eucalyptus fibers. Finally, the maximum in the

curve of tan δ suffers not only reduction in its amplitude, but also a reduction in temperature with the introduction of eucalyptus fibers. It is suggested that the interaction of these fibers with polyester chains reduces the crystallinity of the matrix, decreasing the value of the glass transition temperature and the difficulty in damping composites.

Acknowledgements

The authors thank the support to this investigation by the Brazilian agencies: CNPq, CAPES, FAPERJ and TECNORTE/FENORTE.

References

1. S.N. Monteiro, F.P.D. Lopes, A.S. Ferreira, D.C.O. Nascimento, "Natural fiber polymer matrix composites: cheaper, tougher and environmentally friendly" *JOM*, 61 (2009) 17-22.
2. P, Wambua, I. Ivens, I. Verpoest, Natural fibers: can they replace glass and fibre reinforced plastics?, Composites Science and Technology, 63 (2003) 1259-1264.
3. A.K. Mohanty, M. Misra, L.T. Drzal, Sustainable biocomposites from renewable resources: opportunities and challenges in the green material world J. Polym. Environ, 10 (2002) 19-26.
4. A.N. Netravali, S. Chabba, Composites get greener, Material Today, 6 (2003) 22-29.
5. Crocker, Natural materials innovative natural composites, Materials Technology, 2008, no 2-3: 174-178.
6. S.N. Monteiro, F.P.D. Lopes, A.S. Ferreira, Nascimento, D.C.O. Natural fiber polymer matrix composites: cheaper, tougher and environmentally friendly, JOM, 61, (2009) 17-22.
7. B.D. Agarwal and L.J. Broutman: Analysis and Performance of Fiber Composites. (New York,NY: John Wiley & Sons, 1990).
8. S. Hill; Cars that grow on trees. New Scientists, v. 153(2067), p. 36-39, 1997.
9. G. Marsh. Next step for automotive materials. Mater. Today, v. 6(4), p.36-43, 2003.
10., R. Zah; R. Hischier; A.L. Leão; I. Brown. Curaua fibers in automobile industry – A sustainability assessment. J. Cleaner Production, v. 15, p. 1032-1040, 2007.
11. A.K. Rana, B.C. Mitra, A.N. Banerjee, "Short jute fibre-reinforced polypropylene composites: dynamic mechanical study". *J. Appl. Polym. Sci.* 71 (1999) 5331-539.
12. S. Mohanty, S.K Verma, S.K. Nayak, "Dynamic mechanical and thermal properties of MAPE treated jute/HDPE composites", *Compos. Sci. Technol*. (66) (2006) 538-547.
13. F.M. Margem, S.N. Monteiro, J. Bravo Neto, R.J.S. Rodriguez, B.G. Soares, " The dynamic-mechanical behavior of epoxy matrix composites reinforced with ramie fibers". Revista Mater, 15(2) (2010) 167–175.
14. K.C.M. Nair; S. Thomas; G. Groeninckx; Thermal and dynamic mechanical analysis of polystyrene composites reinforced with short sisal fibres. Compos. Sci. Technol., v. 61, p. 2519-2529, 2001.
15. S. Cassu, F. Navarro; Dynamic-mechanical behavior and relaxations in polymers and polymer blends. Quím. Nova, São Paulo, v. 28, n. 2, Mar. 2005.

Characterization of Minerals, Metals, and Materials 2016
Edited by: Shadia Jamil Ikhmayies, Bowen Li, John S. Carpenter, Jiann-Yang Hwang, Sergio Neves Monteiro, Jian Li, Donato Firrao, Mingming Zhang, Zhiwei Peng, Juan P. Escobedo-Diaz, and Chenguang Bai
TMS (The Minerals, Metals & Materials Society), 2016

FLEXURAL MECHANICAL CHARACTERIZATION OF POLYESTER COMPOSITES REINFORCED WITH RAMIE FIBERS

Lucas de Almeida Pontes[1], Pedro Amoy Netto[1], Jordana B. Ferreira[1], Frederico Muylaert Margem[1], Sergio N. Monteiro[2].

1- State University of the Northern Rio de Janeiro, UENF, Advanced Materials Laboratory, LAMAV; Av. Alberto Lamego, 2000, 28013-602, Campos dos Goytacazes, Brazil.
2- Military Institute of Engineer, Praça Gen. Tibúrcio, 80 - Urca, Rio de Janeiro - RJ, 22290-270, Brazil.
sergio.neves@ig.com.br

Keywords: Ramie Fiber, Polyester Composite, Flexural Properties, Fracture Analyses.

Abstract

Ramie fibers have in the past decades being investigated as possible reinforcement of polymer composites. However, information is still needed on the fiber interaction with a polymeric matrix for a complete evaluation of the capacity of load transference inside the composite. The present work investigated the interaction of ramie fibers with polyester matrix through tests of strength. Separate sets containing 0, 10, 20 and 30% by volume of ramie fibers were aligned along the entire length of a mold and plates of these composites were obtained with polyester matrix. The fractured specimens were analyzed by SEM and the results showed an improvement in some properties of flexion with the incorporation of ramie fiber.

Introduction

Synthetic fiber has been gradually replaced by natural fiber, such as lignocellulosic fiber. In comparison with synthetic fiber, natural fiber has shown economic and environmental advantages, such as replacing particularly the common glass fiber, as the reinforced phase of polymeric composites in many engineering applications such auto mobile and construction industries, and as environmental solution. Composites reinforced with long and aligned fibers present the best mechanical performance in comparison with other types of reinforcements like particles as well as short or randomly oriented fibers. Natural ramie fiber lignocellulosic has been extensively investigated in several studies, such as polymer composites reinforced by ramie. In addition to not cause problems to the environment, the composites reinforced with such fiber can replace synthetic products. Then, in order to have a sufficiently rigid composite to compete with conventional products such as synthetic fibers, only a limited percentage of ramie fiber can be incorporated into the polymeric matrix. This means that the final cost of the composite would more depending on its processing and polymer resin used as matrix. Therefore the objective of this work was to evaluate the flexural properties of polyester composites incorporated with ramie stalk fibers.

Experimental Procedure

The material used in this work was untreated ramie fiber extracted from the stalk of the ramie plant *Boehmeria Nivea* plant, as can be seen in the Fig 1, and polyester resin, the material was obtained from the Brazilian firm SISALSUL, which commercializes natural fibers.

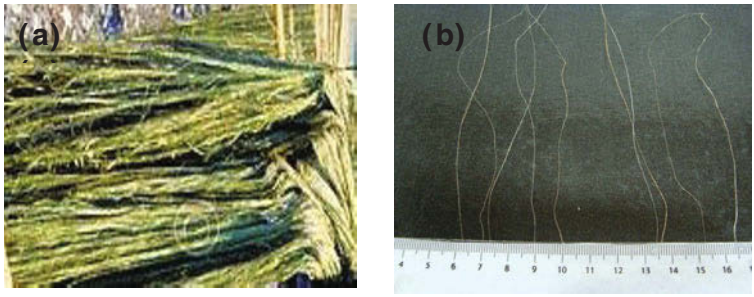

Figure 1. (a) Ramie Fibers and (b) individually separated fibers

The composites of 0, 10, 20 and 30% in volume of aligned and continuous ramie fibers were prepared in a rectangular mold of 152 x 122 x 10 mm and with the polyester matrix. Still fluid unsaturated orthophtalic polyester resin with 0.5wtof methyl – ethyl – ketone catalyst/hardener was then poured onto the mold. Each specimen was set to cure at room temperature for 24 hours inside the mold before taking out for testing.

After cure, the specimen were cut into six samples, each consisting of 20 mm width. All specimens were three points bend tested in a model DL10.000 EMIC machine with 10 kN of capacity at room temperature and a speed of 1mm/min. The span-to-depth ratio was set at 9.

Isolated ramie fibers and ruptured composite specimens were analyzed by scanning electron microscopy, SEM, in a model SSX – 550 Shimadzu microscope operating with secondary electrons accelerated at 15 kV and the relationship of distance between support points for the thickness was maintained at 120mm and the speed of 1mm / minute assay.

The flexural resistance, σ_f and Elastic modulus, E_f, were calculated by the Eq 1, below:

$$\sigma_m = \frac{3F_m L}{2bd^2} \qquad E_m = \frac{L^3 F_m}{4bd^3 e} \tag{1}$$

Results and Discussion

Table I. Flexural results for the polyester composites reinforced with ramie fibers.

Volume fraction of ramie fibers (%)	Flexural strength (MPa)	Flexural Modulus (GPa)
0	22.75 ± 2.14	0.22± 0.03
10	27.49 ± 1.33	0,60 ± 0.22
20	39.87 ± 2.79	0.54± 0.08
30	42.17 ± 3.83	1.08 ± 0.26

From the results in Table I, curves of the variation of both flexural strength and Elastic modulus with the volume fraction of ramie fibers are presented in Fig 2(a, b). From these curves, some relevant comments should be made regarding the flexural behavior of ramie fiber reinforced polyester composites. Within the error bars, Fig 2a, the flexural strength display a slight tendency to increase with volume fraction of ramie fibers. A significant increase, almost linear, can be observed, Fig 2b, in the elastic modulus.

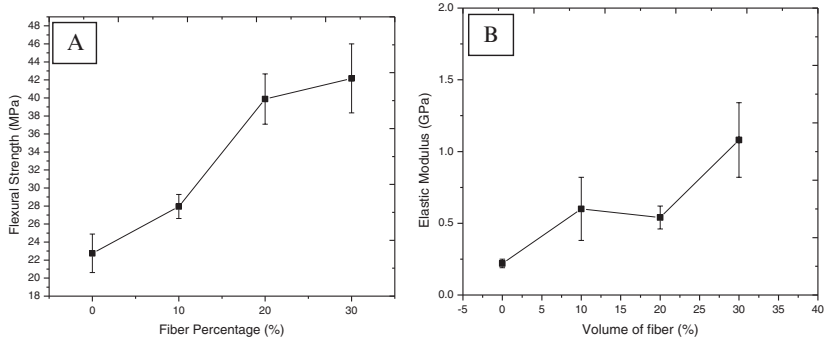

Figure 2. Variation of the Flexural strength (a) and the Elastic modulus with the amount of fiber incorporation.

Figure 3 shows the typical SEM of a neat polyester crack with the river patters in simple transversal rupture. Figure 4 shows aspect of representative ruptured composite specimens with volume inclusion of ramie fibers. This fracture is associated with propagation of cracks through the polyester matrix. An important aspect occurs with the incorporation of ramie fibers. Above 10% in volume fraction the result shows evidence of fiber participation in the fracture exists. The fact that individual fibers are sticking out of the fracture surface for specimens with 30% in Fig. 4, indicates that a separation process between the fiber and the matrix is occurring. This is known as delamination and is a consequence of the relatively weak interface of the ramie fiber with respect to the polyester matrix.

Delamination with a final rupture of the fiber is also an indication that transversal cracks are being arrested while other longitudinal cracks propagate through the weak fiber/matrix interface. During the flexural test, this longitudinal mode of rupture allows the specimen to bend until the flexible ramie fibers being delaminated are broken. For the 10, 20 and 30% specimens in Fig 4, the fracture is not perfectly transversal as compared to the 0% specimens. Moreover, the many individual fibers seen at the fracture attest their effective participation in the 10, 20 and 30% composites. Therefore, since the ramie stalk fiber are stronger than the polyester, one should expect a reinforcement effect for the 10 to 30% volume fraction as actually shown in Fig. 2.

Figure 3 shows by SEM the typical fracture surface of a 0% (pure polyester) specimen. With lower magnification, Fig. 3(a), the facetted surface of the polyester can be related to its brittle characteristics with marks of the transversal propagation of the crack responsible for the fracture. With higher magnification, Fig. 3(b), the "river patterns" and wavy marks are evidences of crack propagation through a polymeric brittle material.

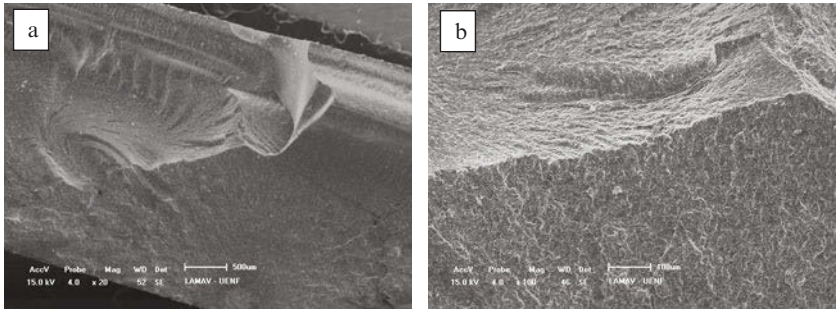

Figure 3. SEM fractographs of a 0% fiber (pure polyester) specimen with different magnifications: (a) 20X and (b) 100X.

Figure 4 shows by SEM the typical fracture surface of a specimen with 30% of volume fraction of ramie fiber. In this figure, with lower magnification, Fig. 4(a), one may notice the fracture surface of the polyester matrix with many ramie fibers pointing out. Some relatively long fibers indicate that delamination had occurred. With higher magnification, Fig. 4(b), there is evidence of fiber/matrix decohesion (white arrow), which can nucleate the longitudinal cracks that propagate through the weak fiber/matrix interface. Furthermore, Fig. 4(b) also displays evidence of marks associated with transversal crack arrest of at the ramie fiber.

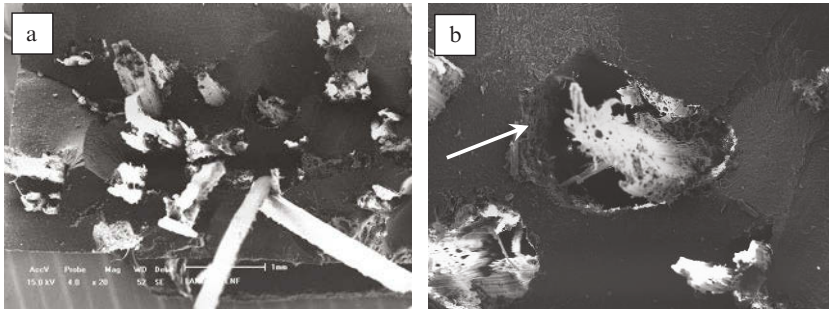

Figure 4. SEM fractographs of a 30% of ramie fiber volume fraction reinforced polyester composite: (a) 20X and (b) 100X.

As final comments, it is relevant to emphasized that continuous and aligned ramie stalk fibers improve the strength of polyester matrix composites above 20% of volume fraction. With lower amounts of fibers, cracks propagate transversally through the brittle polyester matrix with limited interference of the relatively fewer ramie fibers. On the other hand, at 20 and 30% volume fractions, cracks are effectively arrested by the ramie fiber and delamination causes the participation of the stronger fibers in the rupture mechanism, which contributes to a higher strength of the composites.

Conclusions

Polyester matrix composites reinforced with continuous and aligned ramie stalk fibers show an improvement in both the strength and the elastic modulus as compared to the pure polyester matrix. The flexural strength is increased for fiber incorporation above 10% of volume fraction owing to the effective participation of the ramie fibers. The flexural modulus is significantly increased for any incorporation of ramie fibers. The visual observation and SEM fractographs revealed that above 10%, transversal cracks are effectively arrested by the fibers. As a consequence, longitudinal propagation through the weak fiber/matrix interface causes delamination and results in an efficient contribution to the relatively stronger ramie fiber to the final rupture of the composite, which then occurred at higher strength.

References

1. D. Hull, T.W. Clyne, *An Introduction to Composite Materials*, (Cambridge: Cambridge Univers. Press, 1981).
2. B.D. Agarwal and L.J. Broutman, *Analysis and Performance of Fiber Composites* (New York, NY: John Wiley & Sons, 1990).
3. K.H.G. Ashbee, *Fundamental Principles of Fiber Reinforced Composites*, (Lancaster: Technomic Pub. Co. Inc., 1993).
4. K.K. Chawla, *Composite Materials*, (New York: Springer–Verlag, 1993).
5. W.D. Callister Jr., *Materials Science and Engineering – An Introduction*, 5 ed., (New York, NY: John Wiley & Sons, 2000).
6. A. Kelly, W.R. Tyson, *High Strength Materials* (New York: Wiley, 1965).

7. S.N. Monteiro, J.R.M. d'Almeida, "Pullout Test in Lignocellulosic Fibers – A Methodology of Analysis" (in Portuguese). *Rev. Mater.,* 11(3) (2006) 189-196.
8. C.Y. Yue, W.L. Cheung, "Interfacial Properties of Fibrous Composites: Part I. Model for the Debonding and Pullout Processes". *Journal of Materials Science*, 27 (1992) 3173-3180.
9. C.Y. Yue, H.C. Looi and M.Y. Quek, "Assessment of Fibre-Matrix Adhesion and Interfacial Properties Using the Pullout Test". *Int. J. of Adhesion and Adhesives*, 15 (1995), 73-80.
10. K. Tanaka, K. Minoshima, W. Grela, K. Komai, "Characterization of the Aramid/eEpoxy Interfacial Properties by Means of Pullout Test and Influence of Water Absorption". *Composites Science Technology*, 62 (2002) 2169-2177.
11. R.C.M.P. Aquino, S.N. Monteiro and J.R.M. d'Almeida, "Evaluation of the Critical Fiber Length of Piassava (*Attalea funifera*) Fibers using the Pullout Test", *J. Mater. Sci. Letters*, 22 (2003), 1495-1497.
12. S.N. Monteiro, J.R.M. d'Almeida, J.F. de Deus, "Pullout Tests to Evaluate the Critical Length of Natural Fibers (in Portuguese) *Proceedings of the 60th International Congress of the Brazilian Association for Metallurgy and Materials.,* (Belo Horizonte, Brazil, July 2005) 1-10.
13. S.N. Monteiro et al., "Pullout Tests of Coir Fiber to Evaluate the Interface Strength in Polyester Composites", *Proceedings of the TMS 137th Annual Meeting & Exhibition,* (San Antonio, USA, February 2006) 1-8.
14. S.N. Monteiro et al., "Analysis of the Impact Strength of Epoxy Composites Reinforced with Aligned Curaua Fibers (in Portuguese) *Proceedings of the 63rd International Congress of the Brazilian Association for Metallurgy and Materials*. (Santos, Brazil, July 2008) 805-813.
15. S.N. Monteiro, R.C.M.P. Aquino, F.P.D. Lopes, "Performance of Curaua Fibers in Pullout Tests*". J. Materials Science*, 43, (2008) 489-493.
16. P. Wambua, I. Ivens, I.Verpoest, "Natural Fibers: Can They Repalce Glass and Fibre Reinforced Plastics?", *Composites Science and Technology*, 63 (2003) 1259-1264.
17. K.G. Satyanarayana, J.L. Guimarães, F. Wypych, "Studies on Lignocellulosic Fibers of Brazil. Part I: Source, Production, Morphology, Properties and Applications". *Composites: Part A*, 38, (2007) 1694-1709.
18. S.N. Monteiro et al., "Pullout Tests of Coir Fibers Embedded in Epoxy Matrix" (in Portuguese). *Proceedings of the 63rd International Congress of the Brazilian Association for Metallurgy and Materials*. (Santos, Brazil, July 2008) 618-625.
19. S.N. Monteiro, et al., "Photoacoustic Thermal Characterization Tests of Malva Fiber", *Proceedings of the TMS 144th Annual Meeting & Exhibition,* (Orlando, Flórida USA, March 2015) 215-216.

Characterization of Minerals, Metals, and Materials 2016
Edited by: Shadia Jamil Ikhmayies, Bowen Li, John S. Carpenter, Jiann-Yang Hwang, Sergio Neves Monteiro, Jian Li, Donato Firrao, Mingming Zhang, Zhiwei Peng, Juan P. Escobedo-Diaz, and Chenguang Bai
TMS (The Minerals, Metals & Materials Society), 2016

TENSILE STRENGTH OF EPOXY COMPOSITES REINFORCED WITH FIQUE FIBERS

Giulio Rodrigues Altoé, Pedro Amoy Netto[1], Maria Carolina Andrade Teles[1], Luiz Gustavo Xavier Borges[1], Frederico Muylaert Margem[1], Sergio Neves Monteiro[2]

1 State University of the Northern Rio de Janeiro, UENF, Advanced Materials Laboratory, LAMAV; Av. Alberto Lamego, 2000, 28013-602, Campos dos Goytacazes, Brazil
2 Instituto Militar de Engenharia , IME, Praça Gen. Tibúrcio, nº80 Urca, Rio de Janeiro - RJ, 22290-270
mariacarolinateles@live.com

Keywords: Fique Fiber, Epoxy, Tensile Test

Abstract

Environmentally friendly composites, made from natural fibers, are among the most investigated and applied today. Natural fibers have showed advantages, such as, flexibility and toughness, if compared with synthetic fibers. This work investigates the tensile strength of epoxy composites reinforced with Fique fibers. The Fique fiber was extracted from Fique leaf presents some significant characteristic, but until now only few studies on Fique fiber were performed. Composites reinforced with up to 30% in volume of long, continuous and aligned Fique fibers were tested in an Instron machine at room temperature. The incorporation of Fique fibers increases the tensile strength of the composite. After fracture the specimens were analyzed by a SEM (scanning electron microscope).

Introduction

Natural fibers with high cellulose content, known as lignocellulosic fibers, become firmly established as a potential substitute for synthetic fibers, particularly glass fiber [1-5]. The use of natural fibers to replace the existing synthetic ones, especially in aircraft and cars, is motivated by several advantages. Among these, the low cost and weight as well as good toughness and less abrasion equipment used in processing composite[3-5]. In fact, unlike the glass fibers[6] lignocellulosic fibers are relatively soft and the processing procedures produce less wear on equipment. The environmental issue is another point in favor of natural fibers, which are renewable, recyclable, biodegradable and neutral with regard to CO_2 emissions [7-8] .

The incorporation of Fique fibers in polymeric matrices of composite was investigated[9-11] and found to be associated with significant properties. These properties are directly related to the microstructure of the fiber as well as the physical and chemical characteristics present in any lignocellulosic fiber[12-14].Then, in order to have a composite rigid enough to compete with conventional products such as sheets of wood, only a limited percentage of Fique fiber can be incorporated in the polymeric matrix [15-17]. This means that the final cost of the composite will depend on its processing and polymer resin used as matrix. Therefore, the aim of this work was to study the mechanical properties of polyester matrix composites reinforced with continuous fibers and lined with Fique.

Experimental Procedure

The basic material used in this work was the fiber extracted from the leaf of Fique plant (*Furcraea Andina),* Figure 1(a), supplied by a producer in Colombia. No treatment was applied on Fique fibers, Figure 1(b).

Figure 1. Fique plant(a) and Fique fibers(b)

Composites with amounts of 0, 10, 20 and 30 % in volume of Fique fibers were fabricated by mixing the proper percentage of fibers with a still fluid epoxy resin diglycidyl ether of bisphenol A (DGEBA) with triethylene tetramina (TETA) as hardener. Tensile specimens for each composite were fabricated by laying down the Fique fibers in a flat and open dog-bone shaped silicone mold with 5.8 × 4.5 mm of reduced cross section and 35 mm of gage length of the specimen, which corresponds to the tensile axis.

A total of seven composite specimens were prepared for a given volume fraction of Fique fiber. Each specimen was tensile tested in a model 5582 universal Instron machine at an acclimatized 25º C and a strain rate of 1.0 mm/s

Results and Discussion

Examples of tensile load vs. elongation curves for distinct volume fraction composite specimens are shown in Figure 2.

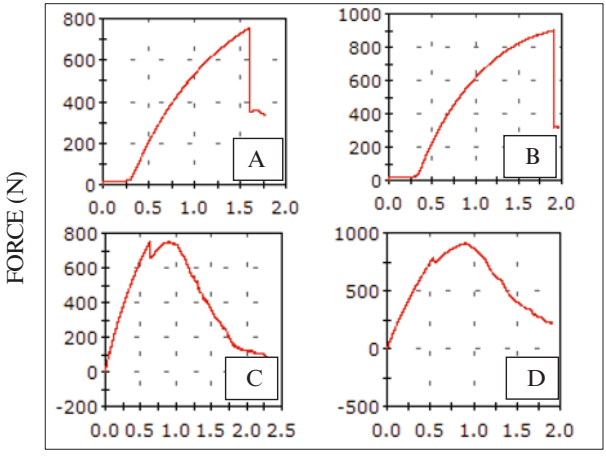

Figure 2: Tensile Load versus Extension of traction for a sample with (a) 10%, (b) 20% and (c) 40% and (d) 50% of Fique fiber incorporated.

Based on results of Instron machine, the Table I presents the average value of these tensile properties for the distinct volume fraction incorporated into epoxy composite

Table I. Tensile properties of the epoxy composites incorporated with continuous and aligned Fique fibers.

Volume fraction of Fique fiber (%)	Tensile Strength(MPa)	Elastic Modulus (GPa)	Total Deformation (%)
0	34.92 ±10.97	1.04 ± 0.17	3.33 ± 1.80
10	19.88 ± 5.32	0.91 ± 0.20	2.90 ± 0.69
20	24.03 ± 6.36	0.99 ± 0.15	4.19 ± 0.73
30	34.35 ± 7.65	1.10 ± 0.26	5.14 ± 0.73

According to Table I, Figure 3 plots the variation elastic modulus, tensile strength and total deformation for epoxy composites, with the volume fraction of Fique fibers.

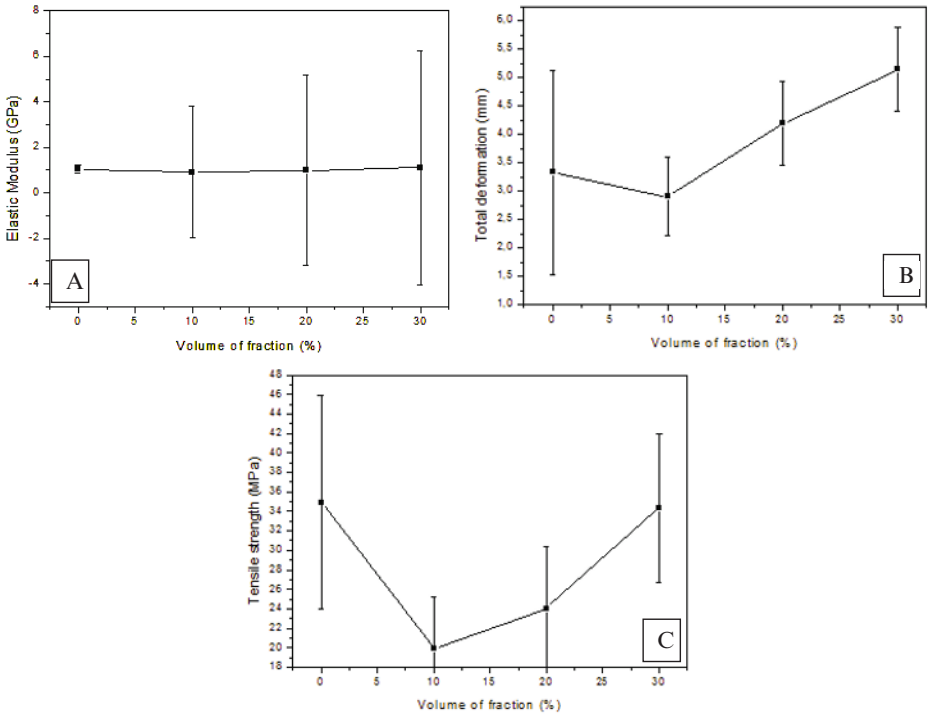

Figure 3.Variation of elastic modulus (a) total deformation (b) and tensile strength (c) with the volume fraction of Fique fibers in epoxy composites.

Figure 4**.** Samples with 0, 10, 20 and 30 % in volume of Fique fiber.

Based on the results of the Table I and Figure 3 shown above, the composite reinforced by Fique fiber shows atypical tensile strength and elastic modulus. Therefore, the reduction it was seen initially, may be attributed to low adhesion between the matrix and the fiber, considering that the fiber taken off almost entirely of the matrix, occurring a fragile fracture in the matrix. The fact shows the fiber not only serves as a potential reinforcement, but may induce concentration of stress in the material. The poor result can also be related to possible errors made in the manufacturing process. However, if look up a no great responsibility material, the composite with 30 % volume may be a solution since it has a lower weight (fiber density is lower than that of the matrix) and greater deformation, becoming one more flexible material for high volumes of fiber.

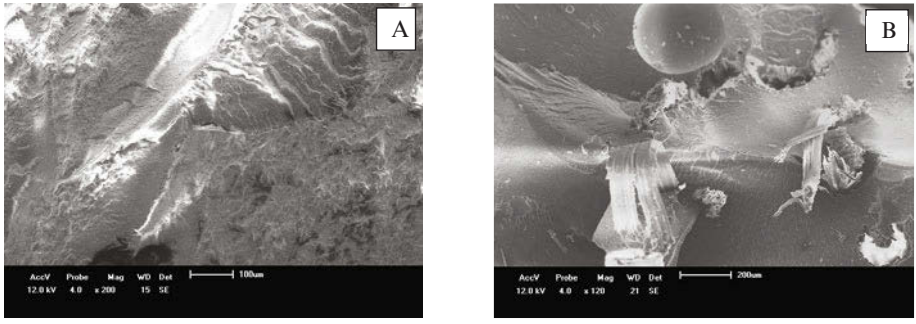

Figure 5. SEM fractgraphs of epoxy composite. (a) 0% of volume fraction (b) 30% of volume fraction

The fracture analysis of representative tensile ruptured specimens was performed by microscopic (SEM) observations. Figure 5(a) and Figure 5(b) shows typical SEM fractographs respectively of 0% and 30 % volume fraction of Fique fiber reinforced epoxy composite. The Figure 5(a), reports neat epoxy typically behavior, which is seen a fragile crack propagation into to the matrix. Figure (b) presents the composite and indicates that the fiber has a weak adhesion to the matrix, which means the fiber, besides acting as a matrix reinforcement, works as a stress concentrator.

Conclusions

The Fique fibers may not be strong enough to provide reinforcement of epoxy matrix composites, but the bad result in the reinforcement test can be also attributed to a problem with the resin cure time or other trouble in the manufacture procedure. In fact, epoxy composites reinforced with aligned lignocellulosic fibers displays significantly improvement in mechanical performance on literature, what can indicate some problem in the manufacture or test procedure. This decrease can be attributed to Fique fibers not acting as a barrier for the crack propagation throughout the brittle polyester matrix.

References

1. Bledzki, A.K.; Gassan, J. *Composites reinforced with cellulose-based fibers*. Prog. Polym. Sci, 24 (1999), 221-274.
2. NABI SAHED, D.; JOG J.P. *Natural fiber polymer composites: a review, Advances in Polymer Technol*. 18 (1999), 221-274.
3. Mohanty, A.K.; Misra, M.; Hinrichsen, G. Biofibres, biodegradable polymers and biocomposites: An overview. *Macromolecular Mater. and Eng*. 276 (2000), 1-24.
4. Crocker, J. Natural materials innovative natural composites. *Materials technology*, 2-3 (3) (2008), 174-178.
5. Monteiro S.N.; Lopes, F.P.D.; Ferreira, A.S.; Nascimento, D.C.O. Natural fiber polymer matrix composites: cheaper, tougher and environmentally friendly. *JOM*, 61 (1) (2009), 17-22.
6. Peijs, T. Natural Fibers Based Composites. *Mater. Technol*. 15 (2000), 281-285.
7. Wambua P.; Ivens. I.; Verpoest, I. "Natural fibers: can they replace glass and fiber reinforced plastic?" *Composites Science and Technology*, 63 (2003), 1259-1264.
8. Mohanty, A q.K.; Misra, M.; Drzal, L.T. Sustainable biocomposites from renewable resources: Opportunities and challenges in the green materials world. *J. Polym. Environ*. 10 (2002), 19-26.
9. Paul, S.A.; Boudenne, A.; Ibos, L.; Candau, Y.; Joseph, K.; Thomas, S. Effect of fiber loading and chemical treatments on thermo physical properties of banana fiber polypropylene commingled composite materials. *Composites: Part A,* 39 (2008), 1582-1588.
10. Zainudin, E.S.; Sapuan, S.M.; Abdan, K.; Mohamad, M.T.M. Thermal degradation of banana pseudo-stem filled unplasticized polyvinyl chloride (UPVC) composites. *Mater. Design*, 30 (2009), 557-582.
11. Ibrahim, M.M.; Dufresne, A.; El-Zawawy, W.K.; Agblevor, F.A; Banana fibers and microfibrils as lignocellulosic reinforcement in polymer composites. *Carbohydrate Polym.* 81 (2010), 811-819.
12. Satyanarayana, K.G.; Sukumaran, K.; Kulkarni, A.G.; Pillai, S.G.K.; 14 – Rohatgi, P.K. Fabrication and properties of natural fibre-reinforced polyester composites. *Composites.* 17 (1999), 329-274.
13. Callister Jr., W.D. *Materials Science and Engineering – An Introduction*, 5ª Edição, (Nova York : John Wiley & Sons, 2000).

15. S.Y. FU, B. Lauke, E. Mäder, X. HU and C.Y. Yue, "Fracture resistance of short-glass-fiber-reinforced and short-carbon-fiber-reinforced poly-propylene under charpy impact load and dependence on processing", *J. Mater. Process. Technol*., 89-90 (1999), 501-507.
16. S.N. Monteiro, F.P.D. Lopes, A.S. Ferreira, D.C.O. Nascimento, "Natural fiber polymer matrix composites: cheaper, tougher and environmentally friendly", *JOM*, 61 (1) (2009), 17-22.

17. A.K. Mohanty, M.A. Khan, G. Hinrichsen, "Influence of Chemical Surface Modification on the Properties of Biodegradable Jute Fabrics-Polyester Amide Composites", *Composites: Part A*, 31 (2000), 143-150.
18. S. Mohanty, S.K. Verma, S.K. Nayak, "Dynamic Mechanical and Thermal Properties of MAPE Treated Jute/HDPE Composites", *Composites Science and Technology*, 66 (2006), 538-547.

Characterization of Minerals, Metals, and Materials 2016
Edited by: Shadia Jamil Ikhmayies, Bowen Li, John S. Carpenter, Jiann-Yang Hwang, Sergio Neves Monteiro, Jian Li, Donato Firrao, Mingming Zhang, Zhiwei Peng, Juan P. Escobedo-Diaz, and Chenguang Bai
TMS (The Minerals, Metals & Materials Society), 2016

THERMAL ANALYSIS OF CURAUA FIBER REINFORCED EPOXY MATRIX COMPOSITES

Mariana A. Barcelos, Carolina Gomes D. Ribeiro, Jordana Ferreira, Janaina da S. Vieira, Frederico M. Margem, Sergio N. Monteiro

State University of the Northern Rio de Janeiro, UENF, Advanced Materials Laboratory, LAMAV; Av. Alberto Lamego, 2000, 28013-602, Campos dos Goytacazes, Brazil

marianaabarcelos@yahoo.com.br

Keywords: curaua fiber, epoxy composites, thermogravimetric analysis, fiber/matrix interaction

Abstract

Thermoset polymers, like the epoxy, become harder with increasing temperature owing to molecular crosslink formation, which is a thermal benefit for composite matrix applications. Natural lignocellulosic fibers, however, have low thermal resistance and tend to degrade with increasing temperature. Therefore, the combination of a lignocellulosic fiber, as reinforcement, with a thermoset polymer, as the matrix, results in a composite material with complex thermal behavior. In the present work, a thermal analysis was conducted on epoxy composites with different amounts of curaua fibers. Both TGA and DTG curves were analyzed to determine the effect of the curaua fiber on the thermal resistance of the composites. It was found that the curaua fiber sensibly affects the thermal behavior of the epoxy matrix for fiber amounts above 10% in volume. This effect is associated with an increase in thermal degradation.

Introduction

In recent years, there has been an increase application of natural fibers as reinforcement of polymer matrix composites in several industrial sectors, with special participation in automobile components [1-3]. Figure 1 illustrates the different components of a modern BMW sedan that are fabricated with lignocellulosic reinforced polymer composites.

Figure 1. BMW sedan and its different parts made of polymer composites reinforced with lignocellulosic fibers. (www.bmwgroup.com)

In fact, both environmental benefits and technical, economic and social advantages are motivating the substitution of natural fibers for glass fiber in polymer composites [5,6]. A number of reasons favor the use of natural fibers, mainly those obtained from cellulose-based vegetables, also known as lignocellulosic fibers such as cotton, flax, sisal, jute, hemp, wood, pineapple, to mention a few. Actually, it is estimated that more than 500 lignocellulosic fibers are known and have potential to be used in engineering applications. Most of these fibers are native of tropical regions in Africa, South Asia, Central and South Americas. The plant cultivation, extraction and processing of lignocellulosic fibers represent an important source of income for people and countries in these regions.

In the Amazonian region, for instance, lignocellulosic fibers such as curaua, piassava, buriti, guarumã, tucumã and many others that have been for long time used in simple products like ropes, baskets, brooms and carpets, are recently being investigated as possible reinforcement for composites [7-9]. In particular, the curaua, Figure 2, one of the strongest lignocellulosic fibers, is at the present time extensively investigated for this purpose [10]. As any lignocellulosic fiber, however, the curaua fiber is subjected to thermal degradation at temperatures around 280°C [22], which would impair the performance of a polymer composite subjected to such higher temperature.

Araujo [22], working on curaua fiber up to a fraction of 20% reinforcing both polyurethane and polypropylene composites, found by thermogravimetric analysis (TGA) and by its derivative thermogravimetry (DTG), two stages of composite decomposition between 300-380°C and 400-440°C. Since a thermal analysis of curaua fiber composites has not been performed thus far on thermoset polymer matrix, the objective of this work was to investigate the effect caused by different amounts of curaua fibers on the thermal behavior of epoxy matrix composites.

Figure 2. Plantation (a), manual processing (b) and bundle (c) of curaua fibers.

Experimental Procedure

A lot of processed curaua fibers were purchased from a Brazilian firm, "Amazon Paper", which commercializes lignocellulosic fibers cultivated in the Amazonian region. From the as-received lot, one hundred fibers were separated for a statistic analysis of length and diameter as shown in Figure 2. This figure reveals that the dimensions of the curaua fibers as any other lignocellulosic fiber [4-6], are heterogeneous with a significant dispersion in values.

Another relevant information from the histograms in Figure 3 is that the average length of 846 mm is more than 15 times its critical length of 3 mm, obtained in epoxy pullout tests [20]. This is considered a condition for long and continuous fiber [23] and assures the most effective strengthening of the matrix. Here it is important to mention that the statistical distribution in Figure 2 is similar to others recently reported on curaua fibers [16,17]

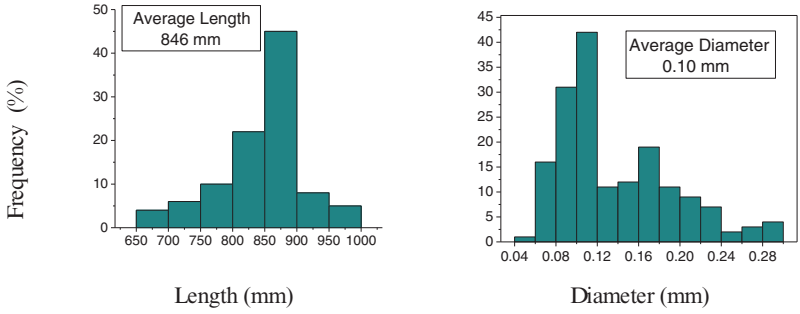

Figure 3. Histogram of the statistical distribution: (a) length and (b) diameter of curaua fibers.

Composites were fabricated by placing, separately, amounts of 0, 10, 20 and 30% in volume of continuous and aligned curaua fibers inside a small cylindrical mold with 5.5 mm in diameter and 20 mm in length. Still fluid commercial orthophtalic epoxy resin added with Dgeba Teta hardener was poured into the mold to serve as the composite matrix. The composites were allowed to cure at 25ºC for 24 hours. After removing each composite from its cylindrical mold, thin-cut discs with 2 mg in weight, corresponding to approximately 1 mm in thickness, were used as samples for thermal analysis. TGA and DTG analyses were conducted in a model 2910 TA instrument equipment.

Results and Discussion

Figure 4 shows both the TGA and DTG curves for the curaua fiber reinforced epoxy composites as well as the corresponding curves for the pure (0% fiber) epoxy resin.

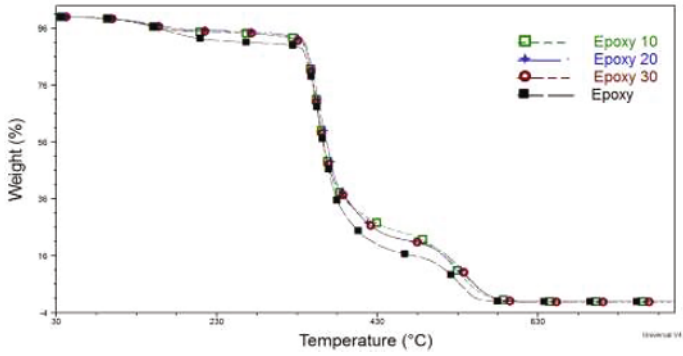

Figure 4. TGA and DTG curves for the pure epoxy and the epoxy composites reinforced with different volume fractions of curaua fibers.

The TGA and DTG curves shown in Figure 4 reveal the thermal stability of the composites in terms of weight loss. In this figure, it is important to notice that the epoxy used as matrix, corresponding to 0% fiber, begin to decompose around 330ºC and finishes around 380ºC. This is expected for this type of thermoset polymer in which thermal degradation starts with the evolution of volatile compounds followed by breaking and depolymerization of molecular chains [24]. It should also be noticed in Figure 4 that, for both types of curves TGA and DTG, there is an apparent superposition of all investigated composites with respect to the pure epoxy curves. In principle, this would indicate that, at least up to a volume fraction of 30%, no effect on the thermal behavior of the epoxy composite could be attributed to the curaua fibers. Such result is difficult to be explained since the curaua fiber deteriorates at temperatures lower [22] than those, 300-500ºC, associated with the epoxy matrix decomposition.
A careful observation of the DTG curve, which is amplified in Figure 5, reveals a sensible effect caused by the curaua fiber.

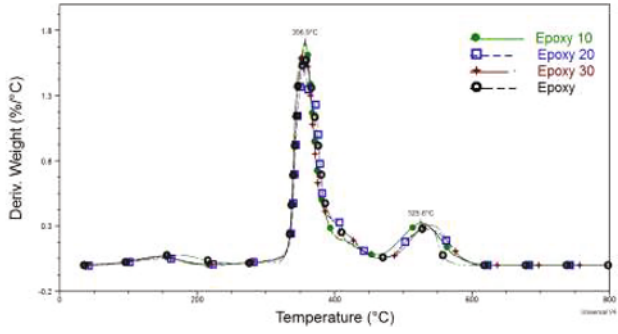

Figure 5. Amplified DTG curves for the pure epoxy and the epoxy composites reinforced with different volume fractions of curaua fibers.

The effect of the curaua fibers on the thermal behavior of the epoxy composites can be detected by distortions caused in the DTG curve as compared to the pure epoxy curve (0% fiber) around

370 and 390ºC. These distortions are more pronounced the greater the volume fraction of curaua fiber.

A possible interpretation for this behavior can be apprehended if one considers that the actual curves for the composites are formed by three peaks. One peak is that corresponding to the pure epoxy with a maximum around 410ºC. The two other peaks around 370 and 390ºC would correspond to the influence of the curaua fiber degradation.

The possibility of the curaua fiber to contribute to two thermal degradation peaks was also reported by Araujo [22] in thermoplastic matrix composites. In that work, a better definition of the two peaks was facilitated by the decomposition of the matrix, which occurs through two thermal peaks. The reason for the two decomposition peaks in the curaua fiber could be apparently related to the decomposition of cellulose and lignin as found in other natural lignocellulosic fibers [25]. For the particular case of curaua fibers, it was concluded [14] that in oxidative atmosphere it is not possible to separate the different degradation processes of the fiber components such as hemicellulose, cellulose and lignin. Degradation reactions in the curaua fiber are complex and overlap in the range of 220 to 350ºC [14]. This temperature range is lower than the peaks around 370 and 290ºC, Figure 6, suggested in the present work. However, the protection of the epoxy matrix could be responsible for allowing the degradation of the curaua fiber to begin at higher temperatures.

Conclusions

A thermal analysis based on TGA and DTG curves revealed the effect of curaua fibers incorporated up to a volume fraction of 30% into an epoxy matrix composite. The TGA curves of the composites fail to show any sensible difference to the pure epoxy curve. By contrast, the DTG curves were able to reveal a noticeable effect caused by the curaua fiber, as evidenced by distortions towards lower temperatures in comparison to the pure epoxy curve. It is suggested that these distortions are due to peaks around 370 and 390ºC superimposed with the main epoxy peak at 410ºC. These curaua fiber related peaks can be possibly attributed to the separate decomposition of cellulose and lignin in the fiber.

Acknowledgements

The authors thank the support to this investigation by the Brazilian agencies: CNPq, CAPES, FAPERJ and TECNORTE/FENORTE.

References

1. S. Hill, “Cars that grow on trees”. *New Scientists*, 153(2067) (1997) 36-39.
2. G. Marsh, “Next step for automotive materials”. *Mater. Today*, 6(4) (2003) 36-43
3. R. Zah, R. Hischier, A.L. Leão, I. Brown, “Curaua fibers in automobile industry – A sustainability assessment”. *J. Cleaner Production*, 15, (2007) 1032-1040.
4. P. Wambua, I. Ivens and I.Verpoest, “Natural fibers: can they replace glass and fibre reinforced plastics?”, *Composites Science and Technology*, 63 (2003) 1259-1264.
5. Crocker, J., “Natural materials innovative natural composites”. *Materials Technology*, 2-3 (2008) 174-178.
6. S.N. Monteiro, F.P.D. Lopes, A.S. Ferreira and D.C.O. Nascimento, “Natural fiber polymer matrix composites: cheaper, tougher and environmentally friendly”. JOM, 61(1) (2009) 17-22.

7. K.G. Satyanarayana, J.L. Guimarães, F. Wypych, "Studies on lignocellulosic fibers of Brazil. Part I: Source, production, morphology, properties and applications". *Composites: Part A*, 38, (2007) 1694-1709.
8. S.N. Monteiro, F.P.D. Lopes, L.C. Motta, L.S. Marques and T.G.R. Portela, "Statistical analysis to characterize the uniformity of mechanical properties of buriti fibers". *Proceedings of Characterization of Materials Symposium, TMS 2009* (San Francisco, CA, USA, March 2009) 1-6.
9. N.S.S. Santos, C.G.B.T. Dias, "Mechanical properties of plant braided fabrics/post-consumer polypropylene composites", *Proceedings of the 41st International Symposium on Macromolucules – MACRO 2006* (Rio de Janeiro, Brazil, July 2006) 1-2.
10. A.L. Leão, I.H. Tan and J.C. Caraschi, "Curaua Fiber – A tropical natural fibre from Amazon – Potential and applications in composites", *Proceedings of the International Conference on Advanced Composites*, (Hurghada, Egypt, May, 1998) 557-564.
11. S.N. Monteiro, R.C.M.P. Aquino, F.P.D. Lopes, E.A. Carvalho and J.R.M. d'Almeida, "Mechanical behavior and structural characteristics of polymeric composites reinforced with continuous and aligned curaua fibers". *Rev. Mater*, 11(3) (2006) 197-203.
12. S.N. Monteiro, J.F. de Deus and J.R.M. d'Almeida, "Mechanical and structural characterization of curaua fibers", *Proceedings of Characterization of Minerals, Metals & Materials - TMS Conference*, (San Antonio, USA, March, 2006) 1-8.
13. F. Tomczak, K.G. Satyanarayana, T.H.D. Sydenstricker, "Studies on lignocellulosic fibers of Brazil. Part III: Morphology and properties of Brazilian curaua fibers". *Composites: Part A*, 38, (2007) 2227-2236.
14. S.N. Monteiro, R.C.M.P. Aquino, and F.P.D. Lopes, "Performance of curaua fibers in pullout tests". *J. Mater. Sci.* 43 (2008) 489-493.
15. S.N. Monteiro, A.S. Ferreira and F.P.D. Lopes, "Rupture mechanisms in composites reinforced with curaua fibers", *Proceedings of Characterization of Minerals, Metals & Materials - TMS Conference*, (New Orleans, USA, March, 2008) 1-8.
16. R.V. Silva, E.M.F. Aquino, L.P.S. Rodrigues and A.R.F. Barros, "Curaua/Glass Hybrid Composite: The Effect of Water Aging on the Mechanical Properties", *J. Reinforced Plast. & Comp.*, 28 (2009) 1857-1868.
17. S.N. Monteiro, A.S. Ferreira and F.P.D. Lopes, "A comparative study of curaua fiber reinforced epoxy matrix composites as building materials", *Proceedings of the Global Symposium on Recycling, Waste Treatment and Clean Technology – REWAS2008,* (Cancun, Mexico, October 2008) 1653-1658.

Characterization of Minerals, Metals, and Materials 2016
Edited by: Shadia Jamil Ikhmayies, Bowen Li, John S. Carpenter, Jiann-Yang Hwang, Sergio Neves Monteiro, Jian Li, Donato Firrao, Mingming Zhang, Zhiwei Peng, Juan P. Escobedo-Diaz, and Chenguang Bai
TMS (The Minerals, Metals & Materials Society), 2016

CHARACTERIZATION OF THERMAL BEHAVIOR OF EPOXY COMPOSITES REINFORCED WITH CURAUA FIBERS BY DIFFERENTIAL SCANNING CALORIMETRY

Mariana A. Barcelos, Carolina Gomes D. Ribeiro, Jordana Ferreira, Janaina da S. Vieira, Frederico M. Margem, Sergio N. Monteiro

State University of the Northern Rio de Janeiro, UENF, Advanced Materials Laboratory, LAMAV; Av. Alberto Lamego, 2000, 28013-602, Campos dos Goytacazes, Brazil
marianaabarcelos@yahoo.com.br

Keywords: Curaua Fiber, Epoxy Composite, Thermal Behavior, DSC.

Abstract

Epoxy composites reinforced with natural lignocellulosic fibers have, in recent times, been gaining attention in engineering areas as lighter and cheaper alternatives for traditional composites such as the “fiberglass”. The curaua fiber is the one strongest today being considered as reinforcement of composites for automobile interior parts. In fact, several studies are currently being dedicated to curaua fiber composites since physical and mechanical properties are required for practical uses. In this work, the thermal behavior of epoxy composites reinforced with up to 30 % in volume of curaua fibers was investigated by differential scanning calorimetry, DSC. The results showed endothermic and exothermic events associated with water release and possible molecular chain amorphous transformation. Comparison with similar composites permitted to propose mechanism that explains this DSC thermal behavior.

Introduction

The modern composite materials, especially those reinforced with synthetic fibers such as glass and carbon, have been used since last century to satisfy the demands required by most technological fields, from home appliances to aerospace. In fact, fiber composites offer significant advantages over monolitic materials, such as common metallic alloys, plastic and ceramics. One of the most important properties is the ratio between the ultimate stress and the density, known as the specific strength. For example, in common glass fiber polymer composites, the so called “fiberglass”, the specific strength of around 400 MPa.cm3/g is higher than any conventional monolitic material. However, drawbacks exist. The energy required to fabricate “fiberglass” generates large emissions of CO2, which are responsible for global warming. Moreover, “fiberglass” is not recyclable and cannot be incinerated. As a result, most synthetic fiber composites end up in landfills or contribute to rivers and oceans pollution.

Natural fibers composites with biodegradable polymer matrices are considered environmentally friendly materials and currently accepted as possible substitutes for synthetic composites. These green composites can be safely discarded or composted at the end of their life without harm to the environment. Using soy concentrate resin as matrix reinforced with 65 % volume fraction of ramie fiber, Nam and Netravali found a specific strength of 194 MPa.cm3/g, which is far below that of “fiberglass”. More importantly, the fully biodegradable resins are considerably more expensive than the conventional polyester or epoxy.

Another alternative for synthetic composites is to apply natural lignocellulosic fibers as reinforcement of conventional polymer matrices. This has been the subject of many published papers and already used in the automobile industry. In addition to the environmental and societal advantages of the green composites, the lignocellulosic fiber reinforced conventional polymer composite also has economical and technical advantages. In the case of a fiber collected as a waste, the price of the composite can be considerably lower than "fiberglass". Furthermore, with high strength lignocellulosic fibers such as sisal, ramie and curaua the specific strength of a composite may approach that of "fiberglass".

In order to develop a composite, the properties of the fibers should be well known. As above-mentioned, curaua (Ananas erectifolius) is a promising lignocellulosic fiber with high strength and an inverse relation with its diameter. Thermal properties of curaua fiber reinforced polymer composites have been investigated in terms of thermogravimetric analysis. Investigation on differential scanning calorimetry, DSC, for epoxy composites reinforced with curaua fibers, revealed the glass transition temperature, Tg, and other parameters. To complement that work, the present paper investigated the thermal behavior by DSC of epoxy composites reinforced with different volume fractions of curaua fibers.

Experimental Procedure

The materials used in this work were curaua fibers, supplied by the Brazilian firm Amazon Paper that commercializes natural fibers cultivated in the Amazonian region, and an epoxy resin supplied by the Dow Chemical Co. Figure 1 illustrates the curaua plant and the as-received bundle of fibers.

Figure 1. Curaua plant (a) and fibers extracted from the leaves (b).

A statistical analysis of the fibers from the as-received bundle revealed that the diameters were dispersed in the interval from 0.04 to 0.3 mm, with an average of 0.10 mm. These equivalent diameters were measured at 5 positions along the fiber length with two measurements performed at the same position with a 90° rotation. General characteristics and properties of curaua fibers are shown in table I.

Table I – General characteristics and properties of the curaua fiber.

Density (g/cm^3)	Diameter (μm)	Cellulose (%)	Hemi-cellulose (%)	Lignin (%)	Micro-Fibril Angle (degree)	Tensile Strength (MPa)	Elastic Modulus (GPa)
0.92	40-300	71-74	21	8-11	18.8	200-1400	30-80

Composite samples for DSC analysis were prepared by laying down, separately, different volume fractions of 0, 10, 20 and 30 % of curaua fibers inside a small cylindrical mold with 5.5 mm in diameter and 20 mm in length. The still fluid commercial epoxy resin already mixed with an Dgeba Teta, was then added to the mold. After removing each composite (same volume fraction of fibers) from the mold, thin-cut discs with 2 mg in weight, corresponding to approximately 1 mm in thickness were sectioned. These disc shaped DSC samples were analyzed in a model 2010 TA Instruments, operating from -20 to 250°C.

Results and Discussion

Figure 2 shows the DSC curves for the epoxy matrix composites with 0 % (pure epoxy), 10, 20 and 30 % volume fraction of curaua fibers. In this figure one sees the typical aspects of DSC curves for polymer-based materials. Starting from an almost similar heat flow values at 0°C, there is a fall on the heat flow , which displays an endothermic peak around 50°C. In polymer-based materials, this DSC peak is associated with the heat absorbed in macromolecular structural transformation such as the thermal amorphization.

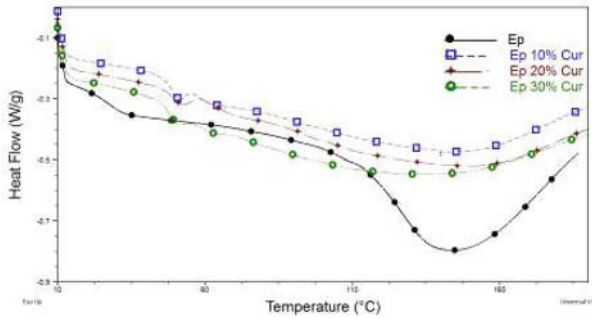

Figure 2. DSC curve for the pure epoxy, 0 % fiber as well as 10, 20 and 30% volume fraction of curaua fibers.

First, one should notice that the amplitude of the endothermic peaks varies for the different composites. However, no apparent correlation exists since the sequence of heat flow levels starts from the bottom with the 0% curaua fiber composite and then goes up with the 30%, the 20% (pure epoxy) and the 10% as the top curve.

A second subtle change occurs at the temperature position of the endothermic peak in Figure 2 around 138°C. This could be attributed to an interference of the curaua fibers on the transition from partial crystallized to amorphous structure of the epoxy matrix. In fact, another relevant aspect of this DSC curves in Figure 2 is inexistence the peaks exothermic because the crystallization temperature was not reached. This peak in other lignocellulosic fiber composites was associated with a small variation in the heat capacity owing to the glass transition temperature.

Conclusions

The thermal behavior, investigated by differential scanning calorimetry, of epoxy composites reinforced with curaua fibers revealed both endothermic events associated with corresponding heat flow peaks.

Acknowledgements

The authors thank the support to this investigation by the Brazilian agencies: CNPq, CAPES, FAPERJ and TECNORTE/FENORTE.

References

1. K.K. Chawla *Composite Materials Science and Engineering*, 2nd edition, Springer-Verlag, New York, 1998.
2. P. Wambua, I. Ivens and I.Verpoest, "Natural fibers: can they replace glass and fibre reinforced plastics?", *Composites Science and Technology*, 63 (2003) 1259-1264.
3. S. Nam, A.N. Netravali "Green Composites II. Environment-friendly, biodegradable composites using ramie fibers and soy protein concentrate (SPC) resin", *Fibers and Polym.* 7(4) (2006), pp. 380-388.
4. A .K. Bledzki, and J. Gassan, "Composites Reinforced With Cellulose-Based Fibers". *Prog. Polym. Sci*, 4 (1999) 221-274
5. D. Nabi Sahed and J.P. Jog, "Natural fiber polymer composites: a review", *Advances in Polymer Technol.,* 18 (1999), 221-274
6. A.K. Mohanty, M. Misra and G. Hinrichsen, "Biofibers, biodegradable polymers and biocomposites: an overview", *Macromolecular Mat. And Engineering*, 276/277 (2000), 1-24
7. S.J. Eichhorn, C.A. Baillie, N. Zafeiropoulos, L.Y. Mwakambo, M.P. Ansell, A. Dufresne, "Review of current international research into cellulosic fibres and composites", *J. Mater. Science*, 36 (2001) 2107-2113
8. A.K. Mohanty, M. Misra and L.T. Drzal, "Sustainable biocomposites from renewable resources: opportunities and challenges in the green material world", *J. Polym. Environ*., 10 (2002), 19-26
9. S.N. Monteiro, F.P.D. Lopes, A.S. Ferreira and D.C.O. Nascimento, "Natural fiber polymer matrix composites: cheaper, tougher and environmentally friendly". *JOM*, 61(1) (2009) 17-22.
10. S. Hill, "Cars that grow on trees". *New Scientists*, 153(2067) (1997) 36-39.
11. G. Marsh, "Next step for automotive materials". *Mater. Today*, 6(4) (2003) 36-43.
12. R. Zah, R. Hischier, A.L. Leão and I. Brown, "Curaua fibers in automobile industry – A sustainability assessment". *J. Cleaner Production*, 15, (2007) 1032-1040.
13. S.N. Monteiro, A.S. Ferreira and F.P.D. Lopes, "A comparative study of curaua fiber reinforced epoxy matrix composites as building materials", *Proceedings of the Global*

Symposium on Recycling, Waste Treatment and Clean Technology – REWAS2008, (Cancun, Mexico, October 2008) 1653-1658.
14. S.N. Monteiro, K.G. Satyanarayana, F.P.D. Lopes. "High strength natural fibers for improved polymer matrix", *Mat. Sci. Forum* 638-642, 2010, 961-966.
15. C.R. Araujo, "Kinetics of thermal decomposition of polymeric composites with curaua fibers" (in Portuguese) D.Sc. Dissertation, School of Chemistry, Federal University of Rio de Janeiro – UFRJ (Rio de Janeiro, Brazil, 2003).
16. K.G. Satyanarayana, J.L. Guimarães, F. Wypych, "Studies on lignocellulosic fibers of Brazil. Part I: Source, production, morphology, properties and applications". *Composites: Part A*, 38, (2007) 1694-1709.

Characterization of Minerals, Metals, and Materials 2016
Edited by: Shadia Jamil Ikhmayies, Bowen Li, John S. Carpenter, Jiann-Yang Hwang, Sergio Neves Monteiro, Jian Li, Donato Firrao, Mingming Zhang, Zhiwei Peng, Juan P. Escobedo-Diaz, and Chenguang Bai
TMS (The Minerals, Metals & Materials Society), 2016

COMPARATIVE STUDY OF THE EFFECTS OF CELLULOSE NANOWHISKERS AND MICROCRYSTALLINE CELLULOSE ADDITION AS REINFORCEMENT IN FLEXIBLE FILMS BASED ON BIOPOLYMER BLENDS

Douglas A. Paiva[1]; Rene R. Oliveira[1]; Wilson da Silva Maia[2]; Maria L. Auad[3]; Vijaya K. Rangari[4]; Esperidiana A. B. Moura[1]

[1]Nuclear and Energy Research Institute, IPEN-CNEN/SP;
2242 Prof. L. Prestes Av., São Paulo, SP, 05508-000, Brazil

[2]Metallurgical and Materials Engineering Department, Polytechnic School, University of São Paulo; 2463 Av. Prof. Mello de Morais, São Paulo, SP, 05508-900, Brazil

[3]Director, Engineering Center for Polymers and Advanced Composites (CPAC), Associate Professor, Department of Chemical Engineering, Auburn University, AL 36849-5327

[4]Department of Materials Science and Engineering; Tuskegee University, Tuskegee, AL 36088, USA

Keywords: nanowhiskers, biodegradable polymer, flexible films, mechanical properties, SEM.

Abstract

The objective of this study is to compare the effects of the addition of cellulose nanowhiskers and microcrystalline cellulose on properties of flexible films based on biodegradable polymer blends. Composite films containing 1 wt. % of microcrystalline cellulose and 1-2 wt. % of cellulose nanowhiskers were prepared by melt extrusion, using a twin screw extruder machine and blown extrusion process. The effects of the addition of cellulose nanowhiskers and microcrystalline cellulose on mechanical and thermal properties of biocomposite films were investigated by tensile tests, XRD, TG, DSC and FE-SEM analysis and the correlation between properties was discussed.

Introduction

Since the advent of the food can in the 19th century, protection, hygiene, product quality and convenience have been major drivers of food technology and packaging innovation. In recent years, there has been a rising demand for packaging that offers both ease of use and high quality food to consumers with busy lifestyles. Currently, the materials used for food packaging consist of a variety of petroleum-derived plastic polymers, metal, glass, paper, and board, or combinations thereof. These materials and polymer used in various combinations to prepare materials with unique properties which efficiently ensure safety and quality of food products from processing and manufacturing through handling and storage and, finally, to consumer use [1- 3]. The use of plastics in packaging has increased worldwide. The packaging industry is the largest user of plastics; more than 90 % of flexible packaging is made of plastics and only 17 % of rigid packaging [4]. Flexible packaging is widely used instead of rigid and semi-rigid packaging because of its flexible characteristics like low weight, durability, cost effectiveness,

attractiveness and its easiness to be shaped [3-5]. Flexible packaging is in general not recyclable, practically non-degradable, consequently not selectively collected and as such, it ends up in the main stream of municipal household waste to be dumped into a landfill, representing a serious global environmental problem. Therefore, the use of bio-based materials to develop biodegradable films can be an important alternative to minimize the quantities of plastic waste material disposed of to landfill throughout the world. The recent preoccupation with environment makes the using of biodegradables material instead the commons polymers in the production of flexible and other packaging for food or agro products a sustainable perfect choice. Its renewable nature and natural origin are capable to transform the packaging industry and society habits.

Among commercial biodegradable plastics, poly(lactic acid) (PLA), a class of crystalline biodegradable thermoplastic polymer with relatively high melting point and excellent mechanical properties, and poly (butylene adipate-co-terepthalate) (PBAT), an aliphatic-aromatic copolyester are among the most promising materials to be considered as environmentally friendly high performance biodegradable plastics. Recently PLA has been highlighted because of its availability from renewable resources such as corn and sugar beets [6-8]. PLA is a biodegradable polyester with good biocompatibility and physical properties, such as high mechanical strength, and shows a number of interesting properties including biodegradability, high strength and high modulus [9, 10]. PLA is considered a relatively brittle material, thus it needs to be plasticized to produce flexible packaging films by cast film extrusion or blown film extrusion [10, 11]. PBAT has gained research and industry attention due to good processability in extrusion lines LDPE; besides PBAT begins to degrade after only few days in soil and enzymatic environments in contrast to petroleum derived polymers, such as polypropylene, polyethylene, that takes hundreds or even thousands of years to degrade [9,10]. The PBAT is considered a good candidate for the toughening of PLA due to its high toughness and biodegradability and no indication of environmental risk (ecotoxicity) when are introduced into composting processes [12, 13]. The combination of these two materials in a blend (PBAT/PLA), aims to bring the best characteristics for a biodegradable material, therefore aliphatic polyesters are the most promising biodegradable materials because they are readily susceptible to biological attack [12, 13]. Unfortunately, PBAT/PLA blends yet have poor properties for application in flexible food packaging field, related to performance, such as its limited mechanical properties and cost. Several composites have been developed by adding reinforcing compounds to polymers to enhance the thermal, mechanical and barrier properties. The use of fillers from natural resources at nanoscale and microscale level as reinforcements to biodegradable polymer and polymer blends may open new possibilities for improving not only the properties but also the cost-price-efficiency [5, 14, 15].

The incorporation of cellulose nanowhiskers and microcrystalline cellulose is being large studied because its abundance in nature, low density, relative high strength and stiffness, renewable nature and biodegradability [15-17]. The incorporation of nanoparticles as a filler in a polymeric matrix can produce a composite with better properties than a compound made with micro particles instead. The great differential of nanoparticles are their higher surface/volume ratio, the smaller the particle is greater the ratio. This technology can even change the visual properties of some material, like the color of gold [15-17].The target of this study was to produce flexible film composites based on biodegradable PBAT/PLA blends reinforced with cellulose nanowhiskers

and microcrystalline cellulose and to compare the properties of reinforced PBAT/PLA flexible film with neat PLA/PBAT blend flexible film.

Experimental

Materials

The materials used in this study to prepare the polymeric matrix were Poly Lactic Acid (PLA), Poly Butylene Adipate Terephtalate (PBAT) and as fillers commercial Microcrystalline Cellulose (MCC, Avicel PH- 101, FMC BioPolymer, USA) and Cellulose Nanowhiskers.

Preparation of Cellulose Nanowhiskers

Cellulose nanocrystals were produced from commercial microcrystalline cellulose (MCC, Avicel PH- 101, FMC BioPolymer, USA). The MCC was treated by acid hydrolysis in a concentrated sulfuric acid solution (64 wt% sulfuric acid in water). The ratio of MCC to acid solution was 1-8.75 g/ml. The treatment was performed at 45 °C and under strong stirring. The selection of the initial conditions was based on the work of Dong [16] and subsequently optimized for this system [17].After treatment, the hydrolyzed cellulose (HC) was washed 4–5 times, separating the crystals from the solution by centrifuge (12,000 rpm, 10 min) after each washing. The final aqueous suspension was freeze-dried (lyophilized) to avoid re-agglomeration of the cellulose crystals.

Preparation of blend and composite

PLA and PBAT pellets and the nanoclay were dried at 60 ± 2 ºC for 4 h to reduce its moisture content to less than 2 %. The PBAT/PLA blend (80 %/ 30% based on wt. %) and PBAT/PLA reinforced with 1 % (wt. %) of cellulose microcrystalline (PBAT/PLA/ Micro) and 1-2 % (wt. %) of cellulose nanowhiskers (PBAT/PLA/Nano1 and PBAT/PLA/Nano2, respectively) were processed by extrusion using a twin screw extruder Haake Rheomix with 16 mm and L/D = 25 rate from Thermo Scientific. The temperature profile was 95/ 118/ 125/ 135/ 135/ 135 ºC. Screw speed was 50 rpm. The extrudates coming out of the extruder were cooled down for a better dimensional stability, pelletized by a pelletizer, dried again at 60 ± 2 ºC for 4 h and fed into extrusion blown film, single screw machine with 25 mm diameter, Carnevalli, and specimens test samples were obtained.

Analyses

Tensile tests: Tensile specimens were obtained in the way of process and in longitudinal way from the films samples in order to evaluate the mechanical behavior and tested using an INSTRON Universal Testing Machine, model 5564 according to ASTM D 882-91 standard at 25ºC and a loading rate of 10mm/min. Six replicates were made of each sample and the average values were reported.

X Rays Diffraction (XRD): XRD patterns were recorded on a Simens - D5000 diffractometer operated at 40 kV and 40 mA, with CuKα radiation (λ= 15.4 Å).

Thermogravimetric analysis (TG): In this study the tests were made in a Mettler Toledo TGA module "TGA/SDTA851e".

Differential Scanning Calorimetry (DSC): (DSC) analyses were carried out using a Mettler Toledo DSC 822e from 25 to 250°C at a heating rate of 10 °C/min under nitrogen atmosphere (50 ml/min).

Field Emission Scanning Electron Microscopy (FE-SEM): FE-SEM of cryofractured samples under liquid nitrogen were carried out using a JEOL-JSM-6701 F, microscope with an accelerating voltage of 1-30 kV, using EDS Thermo-Scientific mod. Noran System Six software, in carbon sputtered samples.

Results and Discussion

Tensile tests results:

Figure 1 shows the diagram stress (MPa) X strain (mm/mm) for PBAT/PLA blend and its composites, PBAT/PLA/Micro 1%, PBAT/PLA/Nano 1% and PBAT/PLA/Nano 2 %,. From of this Figure it is possible observe that the stress increases linearly with strain, due to cellulose Nanowhiskers addition. The addition of Microcrystalline Cellulose in PBAT/PLA blend initially causes an increase in strength followed by a pronounced reduction, as well as a reduction in strain properties.

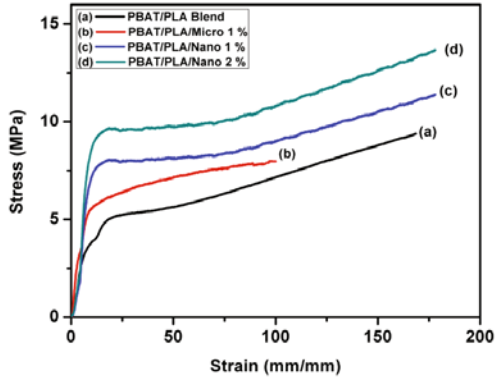

Figure 1. Diagram stress (MPa) X strain (mm/mm) for PBAT/PLA blend and its composites.

Table I presents the results of tensile tests of PBAT/PLA blend and its composites. The results presented shows the average values calculated from the data obtained in tests for five test specimens. From Table I it can be seen increase of the tensile strength at break, elongation at break and Young modulus properties of blend due to nanowhiskers addition. The addition of microcrystalline cellulose in PBAT/PLA blend led to a reduction of its tensile properties.

Table 1. Tensile test results of PBAT/PLA blend and its composites.

Sample	Tensile strength at break (MPa)	Elongation at break (%)	Young's modulus (MPa)
PBAT/PLA Blend	9.6 ± 0.4	370 ± 27	45 ± 3.6
PBAT/PLA/Micro 1 %	7.9 ± 0.3	279 ± 23	38 ± 2.8
PBAT/PLA/Nano 1 %	12.1 ± 0.3	460 ± 32	73 ± 4.2
PBAT/PLA/Nano 2 %	14.5 ± 0.2	478 ± 39	98 ± 7.3

X Rays Diffraction (XRD) analysis results:

The XRD patterns of PBAT/PLA blend and its composites are shown in Figure 2. As can be seen in Figure 2, the XRD spectrum of PBAT/PLA blend showed three prominents 2θ peak at around 9.5º; 28.5º and 29.5º, which has reduced of intensity due to nanowhiskers addition, and practically disappears upon microcrystalline cellulose addition.

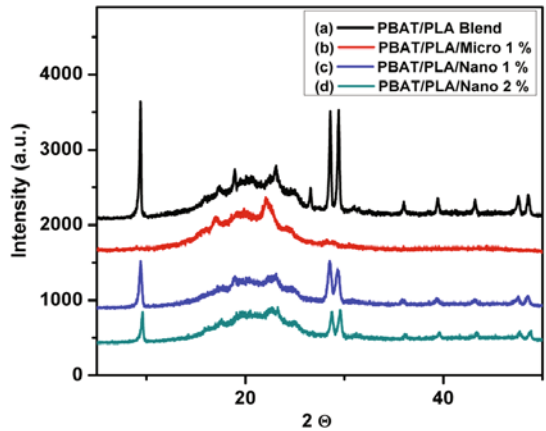

Figure 2. XRD diffraction patterns for the PBAT/PLA blend and its composites.

Thermogravimetric analysis (TG) results:

Figure 3 shows the TG (Figure 3a) and DTG (Figure 3b) thermograms of PBAT/PLA blend and its composites. TG of the composites showed a great difference in weight loss and in the onset temperature when compared with the neat blend. As can be seen in Table I the onset temperature of PBAT/PLA blend increased due to microcrystalline cellulose and nanowhiskers addition.

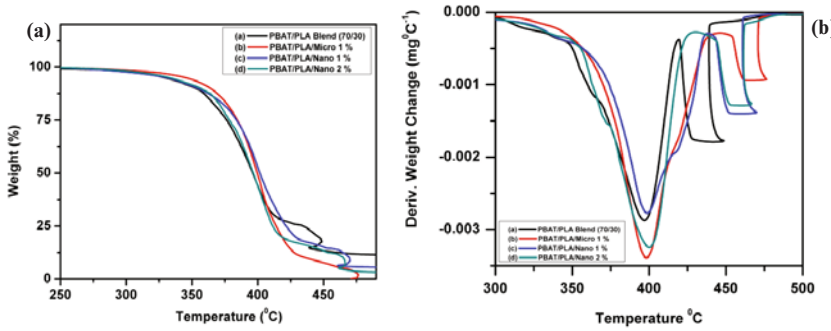

Figure 3. TG (3a) and DTG (3b) thermograms of PBAT/PLA blend and its composites.

Table II. Decomposition temperature and weight loss of PBAT/PLA Blend and its composites

Flexible Films	T_{onset} (°C)	T_{max} (°C)	Weight Loss (%)
PBAT/PLA Blend	341.1	405.9	87.4
PBAT/PLA/Micro [(a)]	365.7	410.3	99.1
PBAT/PLA/Nano 1[(b)]	346.8	415.7	93.7
PBAT/PLA/Nano 2 [(c)]	367.8	409.6	95.5

[(a)] PBAT/PLA/Microcrystalline cellulose; [(b)] PBAT/PLA/Nanowhiskers 1 %; [(c)] PBAT/PLA/Nanowhiskers 2 %

Differential Scanning Calorimetry (DSC) analysis results:

The results of DSC are exposed in Table II and they show no difference in the melting temperature of the neat blend when compared to the nanocomposites films but when compared to its composites. From Table II, it could be inferred that compared with the PBAT/PLA blend the endothermic melting enthalpy of PBAT/PLA blend increased considerably due to microcrystalline cellulose and nanowhiskers addition. The increases in the melting enthalpy can be attributed to the increase in crystallinity of PBAT/PLA composite.

Table II. DSC analysis results of PBAT/PLA Blend and PBAT/PLA Composite Flexible Films

Flexible Films	Melting Temperature (T_m, °C)	Melting Enthalpy (ΔH_m,Jg^{-1})
PBAT/PLA Blend	154.78	4.5
PBAT/PLA/Micro 1[(a)]	153.83	5.6
PBAT/PLA/Nano 1[(b)]	154.34	7.6
PBAT/PLA/Nano 2[(c)]	154.98	9.5

[(a)] PBAT/PLA/Microcrystalline cellulose 1 %; [(b)] PBAT/PLA/Nanowhiskers 1 %; [(c)] PBAT/PLA/Nanowhiskers 2 %

Field Emission Scanning Electron Microscopy (FE-SEM) analysis results:

FE-SEM micrographs of cryofractured surfaces of the PBAT/PLA blend and composite specimens were studied to understand the failure mechanisms and also study possible interaction between different components. FE-SEM micrographs of PBAT/PLA blend and its composites in

different magnifications are showed in Figure 4. Figure (4a) is an overview of PBAT/PLA blend showing a uniform dispersion of in the PBAT matrix. Micrographs surface of PBAT/PLA/Micro with 3.000 X and 6.000 X of magnifications are showed in Figures (4b) and (4c), respectively. It can be seen in these figures a homogeneous distribution of microcrystalline particles, but with several large aggregates of the particles in the surface of the blend. Further in Figures (4b) and (4b) large number of holes in the PBAT/PLA blend are visible where microcrystalline particles have been located before the fracture.

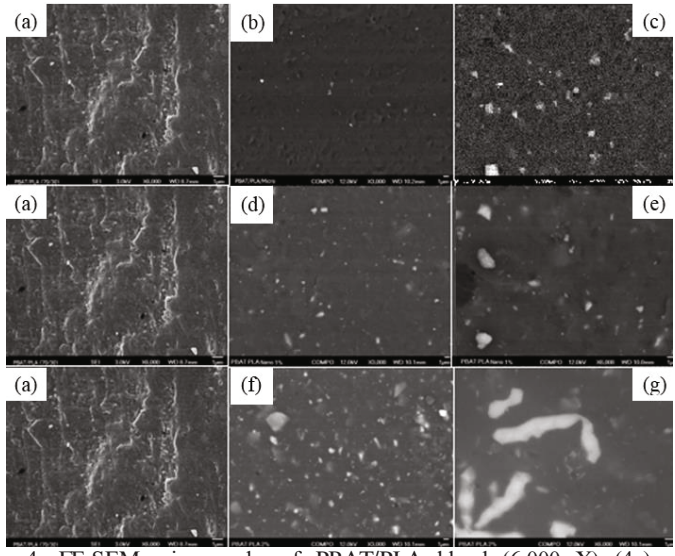

Figure 4. FE-SEM micrographs of PBAT/PLA blend (6.000 X) (4a), and its composites: PBAT/PLA/Micro (3.000 X) (4b), (6.000 X) (4c); PBAT/PLA/Nano 1 % (3.000 X) (4d), (6.000 X) (4e); PBAT/PLA/Nano 2 % (3.000 X) (4f), (6.000 X) (4g).

Cellulose nanowhiskers addition in blend led to a homogeneous distribution of nanoparticles, and reduced occurrence of the large aggregates and holes in the PBAT/PLA blend, Figures (4d-4g). These result suggests good adhesion between nanowhiskers cellulose and PBAT/PLA blend matrix, when compared with cellulose microcrystalline addition, which could play an important role in improving the mechanical performance of the resulting nanocomposite.

Conclusion

Results showed gains in tensile strength at break, elongation at break and Young modulus properties of blend due to nanowhiskers addition. The addition of microcrystalline cellulose in PBAT/PLA blend led to a reduction of its tensile properties. These result suggests good adhesion between nanowhiskers cellulose and PBAT/PLA blend matrix, when compared with cellulose microcrystalline addition, which may have played an important role in improving the mechanical performance of the resulting nanocomposite.

References

1. Coles, R.; McDowell, D.; Kirwan, M. J. Food Packaging Technology, 2003, Blackwell Publishing Ltd., Oxford, UK. ISBN 1-84127-221-3.
2. Robertson, G. L. Food Packaging – Principles and Practice, 1993, New York, Marcel Dekker, Inc.,
3. Soroka, W. Fundamentals of Packaging Technology, Second Edition, 2000, published by Institute of Packaging Professionals.
4. Raheem, D. Application of plastics and paper as food packaging materials? An overview. Emir. J. Food Agric. 2013; 25(3): 177-188, doi: 10.9755/ejfa.v25i3.11509
5. Duncan, T.V. Applications of nanotechnology in food packaging and food safety: Barrier materials, antimicrobials and sensors. Journal of Colloid and Interface Science 363 (2011) 1–24.
6. Alidedeoglu HA, Kannan G. Evaluation of biodegradable copolyester resins with increase green content. Antec. 2011.
7. Kirvan MJ, Strawbridge JW. Plastics in food packaging. Food Packaging Technology. 2003. 174-240.
8. Yamamoto M, Witt U, Skupin G, Beimborn D, Müller RJ. Biodegradable aliphatic-aromatic polyesters: "Ecoflex®". BASF.
9. Ljungberg N, Wesslen B. "Tributyl citrate oligomers as plasticizers for poly (lactic acid): thermo-mechanical film properties and aging". Polymer. 2003; Vol. 44, 7679-7688.
10. Teamsinsungvon A, Ruksakulpiwat Y, Jarukumjorn K. Mechanical and morphological properties of poly (lactic acid)/ poly (butylenes adipate-co-terephtalate)/ calcium carbonate composite. International conference on composite materials. 18th Internacional conference on composite materiails. 2011.
11. Pillin I, Montrelay N, Grohens Y. Polymer. 2006; Vol. 47: 4676.
12. Jiang L, Wolcott MP, Zhang J. "Study of biodegradable poly (lactide)/poly (butylene adipate-co-terephthalate) blends". Biomacromolecules. 2005; Vol.7: 199-207.
13. Witt U, Einig T, Yamamoto M, Kleeberg I, Deckwer W-D, Muller R-J. Biodegradation of aliphatic-aromatic copolyesters: evaluation of the final biodegradability and ecotoxicological impact of degradation intermediates. Chemosphere. 2001; Vol. 44(2):289 – 299.
14. Reddy, M. M.; Vivekanandhan, S.; Misra, M.; Bhatia, S. K.; A.K. Mohanty. Biobased plastics and bionanocomposites: Current status and future opportunities. Progress in Polymer Science 38 (2013) 1653– 1689.
15. Faruk O, Bledzki AK, Fink HP, Mohini S. Biocomposites reinforced with natural fibers: 2000–2010. Progress in Polymer Science. 2012; Vol. 37: 1552– 1596.
16. Dong, X.M.; Revol, J.F.; Gray, D. G. Effect of Microcrystallite preparation conditions on the formation of colloid crystals of cellulose. Cellulose. 5, 1998, Vol. 19.
17. Marcovich, N. E.; Auad, M.L.; Bellesi, N.E. Nutt, S.R.; Aranguren, M. I. Cellulose micro/nanocrystals reinforced poyurethane. Cambridge Journals. 1, 2006, Vol. 21, 4, pp. 870-881.

Characterization of Minerals, Metals, and Materials 2016
Edited by: Shadia Jamil Ikhmayies, Bowen Li, John S. Carpenter, Jiann-Yang Hwang, Sergio Neves Monteiro, Jian Li, Donato Firrao, Mingming Zhang, Zhiwei Peng, Juan P. Escobedo-Diaz, and Chenguang Bai
TMS (The Minerals, Metals & Materials Society), 2016

FLEXURAL TEST IN EPOXY MATRIX COMPOSITES REINFORCED WITH HEMP FIBER

Anna Carolina C. Neves[1], Lázaro A. Rohen[1], Frederico M. Margem[1], Carlos Maurício F. Vieira[1], Sergio N. Monteiro[2]

[1] State University of the Northern Rio de Janeiro, UENF, LAMAV; Av. Alberto Lamego, 2000, 28013-602, Campos dos Goytacazes, Brazil.
[2] Instituto Militar de Engenharia , IME, Praça Gen. Tibúrcio, nº80 Urca, Rio de Janeiro - RJ, 22290-270

Keywords: HempFiber, Epoxy Composite, Flexural Properties.

Abstract

Synthetic fiber has been gradually replaced by natural fiber, such as lignocellulosic fiber. In comparison with synthetic fiber, natural fiber has shown economic and environmental advantages. The natural fiber presents interfacial characteristics with polymeric matrices that favor a high impact energy absorption by the composite structure. However, until now, little information has been released about the hemp fiber incorporated in polymeric matrices. Specimens containing 0, 10, 20 and 30% in volume of hemp fibers were aligned along the entire length of a mold to create plates of these composites. Those plates were cut following the ASTM standard to obtain specimens for bending tests and the results showed the increase in the flexural strength with the increase of fiber amount.

Introduction

Natural fibers are steadily substituting synthetic fibers, particularly the common glass fiber, as the reinforced phase of polymeric composites in many engineering applications such as automobile interior components, cyclist helmets, housing panelsand windmill fins [1-4]. Then, from the engineering point of view, lignocellulosic fibers present today important environmental, economical, societal and technological advantages [5-7]. Moreover, several lignocellulosic fibers are known since the beginning of our civilization and still cultivated or naturally extracted all over temperate and tropical regions of the world. According to Kalia et al [8], these fibers can be classified by their origin, as shown in Table I.

Table I. Classification of lignocelluloses fibers according to their origin [8].

ORIGIN	LIGNOCELLULOSIC FIBERS
leaf	abaca, cantala, curaua, date, palm, henequen, pineapple, sisal
seed	Cotton
bast/stem	hemp, flax, jute, ramie
fruit	coir, kapok, palm oil
grass	alfalfa, sugarcane bagasse, bamboo
stalk	banana, straw

The lignocellulosic fiber for this work was extracted from the stem of the hemp plant (*Cannabis sativa*). Hemp is one the lignocellulosic fiber with least knowledge as far as mechanical properties are concerned. Characterizations of these composites are being carried out for different polymer matrices and mechanical tests [9-14] Science expect that hemp fibers can be more useful than glass fiber. The dimensional heterogeneity and the large dispersion of the values of the diameter of lignocellulosic fibers are limitations to its use in composites [4,15].

However, no tensile characterization was done so far for polymer composites reinforced with hemp fibers. Therefore, the objective of this work was to conduct the flexural tests of epoxy matrix composites reinforced with hemp fibers.

Experimental Procedure

The material used in this work was untreated hemp fiber extracted from the stem hemp plant and epoxy resin. Statistical analysis was performed on one hundred fibers randomly removed from the as-received the lot. Figure 1 shows the characteristic hemp plant and the extracted hemp fibers.

Figure 1. (a) Typical hemp plant and (b) the extracted fibers.

Initially, one hundred fibers were randomly taken out from the bundle for a statistical evaluation of diameter as shown in the histograms in Figure 2. From the histogram an average diameter of 0.065 mm was obtained.

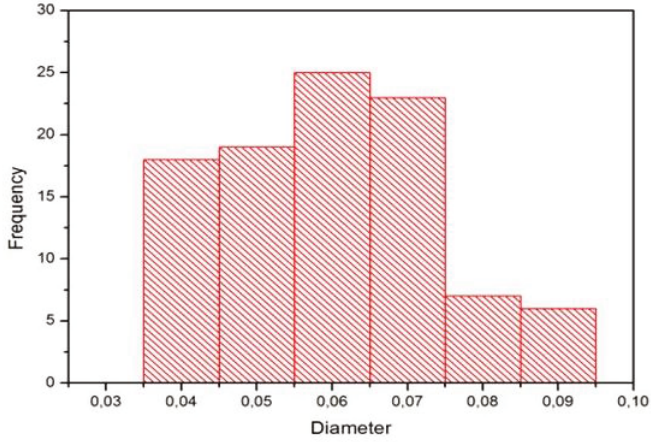

Figure 2. Distribution histogram for six diameter intervals.

Composites with amounts of 0, 10, 20 and 30 % in volume of hemp fibers were fabricated by mixing the proper percentage of fibers with a still fluid epoxy resin type commercial diglycidyl ether of bisphenol (DGEBA) wich were cured with triethylene tetramine (TETA) in stoichiometric proportion of 13 parts of hardener to 100 parts of still liquid resin. The samples were prepared by laying down the hemp fibers into the rectangular mold (152x122x10 mm) under pressure. The samples were cured at room temperature for 24 hours.

After the samples were unmolded, they were cut following the ASTM D790 (2007) standard. The hemp fibers were aligned along the 122 mm width of the mold, which corresponds to the length of seven specimens cut from the composite plate, extracted from the mold after curing. These specimens, for each different amount of hemp fibers were three points bend tested in a model 5582 Instron machine with 100 kN of capacity at a strain rate of $1.6 \times 10^{-2}\ s^{-1}$.

Results and Discussion

Figure 3 shows the macrostructural appearance after flexural test in specimens with different amounts of hemp fibers, from 0 to 30% in volume. In this figure, it is important to note that the pure polyester and the specimen with 10% of hemp fibers were completely separated in two parts. This indicates that the polyester matrix with less than 10% the addition of hemp fiber is brittle and the crack propagates without

being arrested until the specimen separates. However, for more than 20% of hemp fiber the initial propagating crack is blocked and the rupture migrates to the fiber/matrix interface.

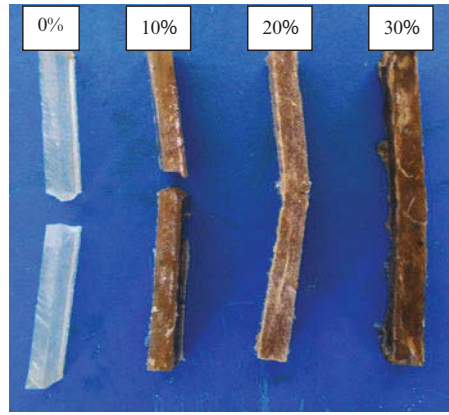

Figure 3. Typical flexural specimens tested of polyester matrix composites with different volume fractions of hemp fiber.

Typical flexural force *vs*. deflection curves were directly obtained from the machine acquisition data program. The flexural curve for the pure epoxy (0% fiber) specimens but also for the hemp fiber reinforced composite specimens display limited plastic deformation [12,16]. Indeed, after the first linear elastic part of the curves, a sudden drop associated with the rupture occurs. This indicates a brittle behavior. From curves the flexural strength (maximum bend stress) was calculated. Table II presents these values for composites with different volume fraction of hemp fibers.

Table II. flexural results for the epoxy composites reinforced with hemp fibers.

Amount of Hemp Fiber (%)	Flexural Strength (Mpa)
0	40.30 ± 5.00
10	39.24 ± 6.32
20	50.75 ± 8.33
30	76.69 ± 5.96

From the results in Table II, the variation curve of flexural strength with the volume fraction of hemp fibers is shown in Figure 4.

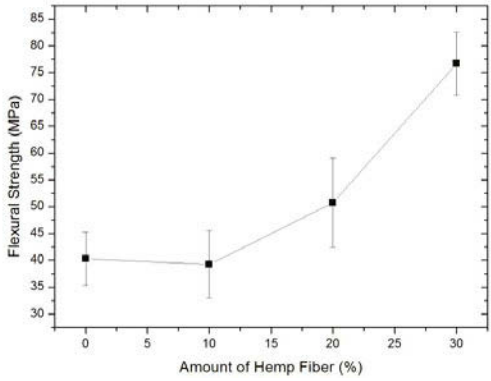

Figure 4. Variation of the flexural rupture with the amounts of hemp fibers in the composites.

It is also relevant to discuss the implication of the rupture mode to the mechanical response of the composites. The rupture that initiates inside the epoxy matrix and propagates transversally to the fibers alignment provides a longer path to the rupture what consume more energy to complete the material rupture. This effect provides the increase in the flexural strength showed in the figure [17,18].

Conclusions

Epoxy matrix composites reinforced with aligned hemp fibers show an improvement in the strength as compared to the pure epoxy matrix. The incorporation up to 10% hemp fibers in epoxy matrix causes an increased resistance to flexural strength of the composite. However, the incorporation of 10% hemp fiber in composites with epoxy matrix causes a small decrease in this value, weakening the matrix by internal defects and low adhesion between matrix and fiber. Better results can be achieved with higher volume of hemp fiber added in matrix, e.g., 30% hemp fiber. The longitudinal propagation through the weak fiber/matrix interface causes delimitation and results in an efficient contribution to the relatively stronger hemp fiber to the final rupture of the composite, which occurs at higher strength.

Acknowledgements

The authors thank the support to this investigation by the Brazilian agencies: CNPq, CAPES, FAPERJ and TECNORTE/FENORTE.

References

1- Aquino, R. C. M. P.; Almeida, J. R. M; Monteiro, S.N, "Análise do Compósito de Piaçava/Resina poliéster, como substituto da Madeira". (Paper presented at 60º Congresso Anual da Associação Brasileira de Metalurgia e Materiais – ABM, Belo Horizonte, MG, Brazil 24-27 de July de 2006)

2- Hull, D.; Clyne, T. W. (1996) "An Introduction to Composite Materials", 2ª ed.,Cambridge: Cambridge Univ. Press.

3- Monteiro, S.N, Costa, L.L., Santafé, H.P. G, "Tenacidade ao impacto Charpy de compósito epoxídico reforçado com fibras de coco" (Paper presented at Congresso Brasileiro de Engenharia e Ciência dos Materiais CBECIMAT , Porto de Galinha, Pernanbuco, Brazil, October, 2008) 12.

4- Bledzki, A.K.; Gassan, J. Composites reinforced with cellulose-based fibres. Prog.Polym. Sco, v. 24, (1999) p. 221-274.

5- A.K. Mohanty, M. Misra and G. Hinrichsen, "Biofibers, biodegradable polymers and biocomposites: an overview", Macromolecular Mat. And Engineering, 276/277 (2000), 1-24.

6- P. Wambua, I. Ivens and I.Verpoest, "Natural fibers: can they replace glass and fibre reinforced plastics?" Composites Science and Technology, 63 (2003) 1259-1264.

7- A. Netravali, S. Chabba, "Composites get greener", Material Today 6 (2003) 22-29.

8- S. Kalia, B. S. Kaith, I. Kaur "Pretreatment of natural fibers and then application as reinforcing material in polymer composites – A review" Polym. Eng. Sci. 49(7) (2009) 1253-1272.

9- S.N. Monteiro, J.F. de Deus and J.R.M. d'Almeida, "Interfacial Strength of Sisal Fiber Reinforced Polyester Composites", (Paper presented at SAM-CONAMET, Mar del Plata, Argentina, 2005) 6.

10- S.N. Monteiro, R.C.M.P. Aquino, F.P.D. Lopes, E.A. Carvalho and J.R.M. d'Almeida, "Mechanical behavior and structural characteristics of polymeric composites reinforced with continuous and aligned curaua fibers". Rev. Mater, 11(3) (2006) 197-203.

11- S.N. Monteiro, J.F. de Deus and J.R.M. d'Almeida, "Mechanical and structural characterization of curaua fibers", (Paper presented at Characterization of Minerals, Metals & Materials - TMS Conference, San Antonio, USA, March, 2006) 8.

12- K.G. Satyanarayana, J.L. Guimarães, F. Wypych, "Studies on lignocellulosic fibers of Brazil. Part I: Source, production, morphology, properties and applications". Composites: Part A, 38, (2007) 1694-1709.

13- S.N. Monteiro, A.S. Ferreira and F.P.D. Lopes, "Rupture mechanisms in composites reinforced with sisal fibers", (Paper presented at Characterization of Minerals, Metals & Materials - TMS Conference, New Orleans, USA, March, 2008) 8.

14- S.N. Monteiro, A.S. Ferreira and F.P.D. Lopes, "A comparative study of sisal fiber reinforced epoxy matrix composites as building materials", (Paper presented at

Global Symposium on Recycling, Waste Treatment and Clean Technology, REWAS2008, Cancun, Mexico, October 2008) 1653-1658.
15- NABI SAHEB, D.; JOG, J.P, "Natural fiber polymer composites: A review. Advances in Polymer Technology", v. 18, p. 351-363, 1999.
16- S.N. Monteiro, F.P.D. Lopes, A.S. Ferreira and D.C.O. Nascimento, "Natural fiber polymer matrix composites: cheaper, tougher and environmentally friendly". JOM, 61(1) (2009) 17-22.
17- T.G.R. Portela, L.L. da Costa, N.S.S. Santos, F.P.D. Lopes, S.N. Monteiro "Tensile behavior of lignocellulosic fiber reinforced polymer composites: Part II buriti petiole/polyester" Rev. Mater., 15(2) (2010) 216-222.
18- W.D. Callister Jr., Materials Science and Engineering – An Introduction, 5 ed., (New York, NY: John Wiley & Sons, 2000).

Characterization of Minerals, Metals, and Materials 2016

Electronic, Magnetic, Environmental, and Advanced Materials

Session Chairs:

Shadia Jamil Ikhmayies

Eren Yunus Kalay

Characterization of Minerals, Metals, and Materials 2016
Edited by: Shadia Jamil Ikhmayies, Bowen Li, John S. Carpenter, Jiann-Yang Hwang, Sergio Neves Monteiro, Jian Li, Donato Firrao, Mingming Zhang, Zhiwei Peng, Juan P. Escobedo-Diaz, and Chenguang Bai
TMS (The Minerals, Metals & Materials Society), 2016

THE INFLUENCE OF HEAT TREATMENT ON THE OPTICAL PARAMETERS OF SPRAY-DEPOSITED CdS:In THIN FILMS

Shadia J. Ikhmayies

Al Isra University, Faculty of Science, Physics Department, Amman 11622, Jordan.

Keywords: Cadmium sulfide, thin films, spray pyrolysis, optical parameters, annealing.

Abstract

Cadmium sulfide is an important material for solar cells and optoelectronic devices. For the development of these technologies, there is a need for comprehensive optical characterization of this material. Doping with indium improves the bandgap energy and other optical parameters of CdS. In this study, polycrystalline indium doped cadmium sulfide thin films (CdS:In) are produced by the spray pyrolysis technique on glass substrates. The films were annealed in nitrogen atmosphere, and the influence of heat treatment on the optical parameters was investigated. Transmittance was measured at room temperature and used to deduce absorption coefficient, bandgap energy, extinction coefficient, and refractive index before and after annealing in nitrogen atmosphere. It is found that all of these parameters are influenced by such heat treatment.

Introduction

Cadmium sulfide (CdS) is a II-VI compound semiconductor of a wide bandgap of about 2.42 eV at room temperature. CdS has reasonable conversion efficiency, stability and availability of low-cost deposition technique. In addition, it has high electron affinity, and it is easy to make ohmic contact. CdS thin films have potential use in optoelectronic device fabrication and in photovoltaic applications as a window layer in CdTe based and $CuInS_2$ solar cells**.** For the use as window layers in thin film solar cells CdS must have n-type electrical conductivity. There are different dopants that can be used to get n-type CdS, such as In [1-4], Ag [1], Al [1,5], Cl [6], etc. In this work indium was used as the dopant to improve the n-type conductivity of CdS films. There are different techniques to produce CdS thin films such as chemical bath deposition (CBD) [1,7-9], thermal evaporation [10], and spray pyrolysis (SP) technique [10-12]. The SP technique is a simple, and low cost method, which enables intentional doping, and the production of large area films. The study of the optical properties and optimizing the optical parameters of CdS is important for the use of this material in solar cells and optoelectronic devices. The aim of the present work is to pay more attention to study the influence of annealing on the optical parameters of indium doped cadmium sulfide (CdS:In) thin films prepared by the spray pyrolysis technique.

Experimental Procedure

Indium doped cadmium sulfide (CdS:In) thin films were prepared by spraying an aqueous solution of approximately stoichiometric ratios of the hydrated cadmium chloride ($CdCl_2.H_2O$) and thiourea [$(NH_2)_2CS$] on glass substrates kept at 490°C. Indium chloride ($InCl_3$) was used as a

dopant source in the starting solution. The produced films were annealed in nitrogen atmosphere for 30 minutes at 400°C. Transmission spectra of the prepared films were measured at room temperature by normal incidence of light, using a double beam UV-1601 PC Shimadzu spectrophotometer, in the wavelength range 400–1100 nm. The structure of the films was explored using X-ray diffraction (XRD) with Cu K_α radiation (λ = 1.5405 Å) in the range of Bragg angles $2 \leq 2\theta \leq 60°$ in steps of 0.04°.

Results and Discussion

XRD diffractograms of an as-deposited and annealed CdS:In thin films are shown in Figure 1. The figure reveals that the films are polycrystalline and they have a mixed phase (cubic and hexagonal). All the prominent peaks are indexed with Millar indices which are shown in the figure. The lines C(1 1 1), C(2 2 0), and C(3 1 1) belong to the cubic phase. However, the peaks

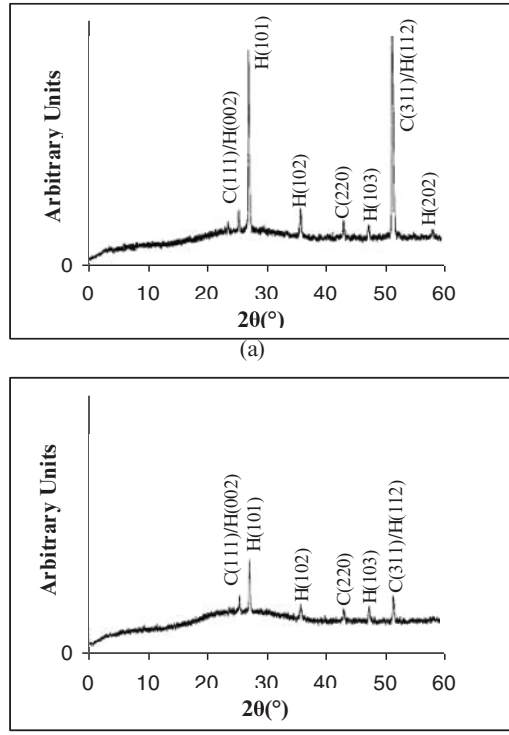

Figure 1. XRD diffractograms of two CdS:In thin films; as-deposited with thickness = 400 nm (a), and annealed with thickness = 230 nm (b).

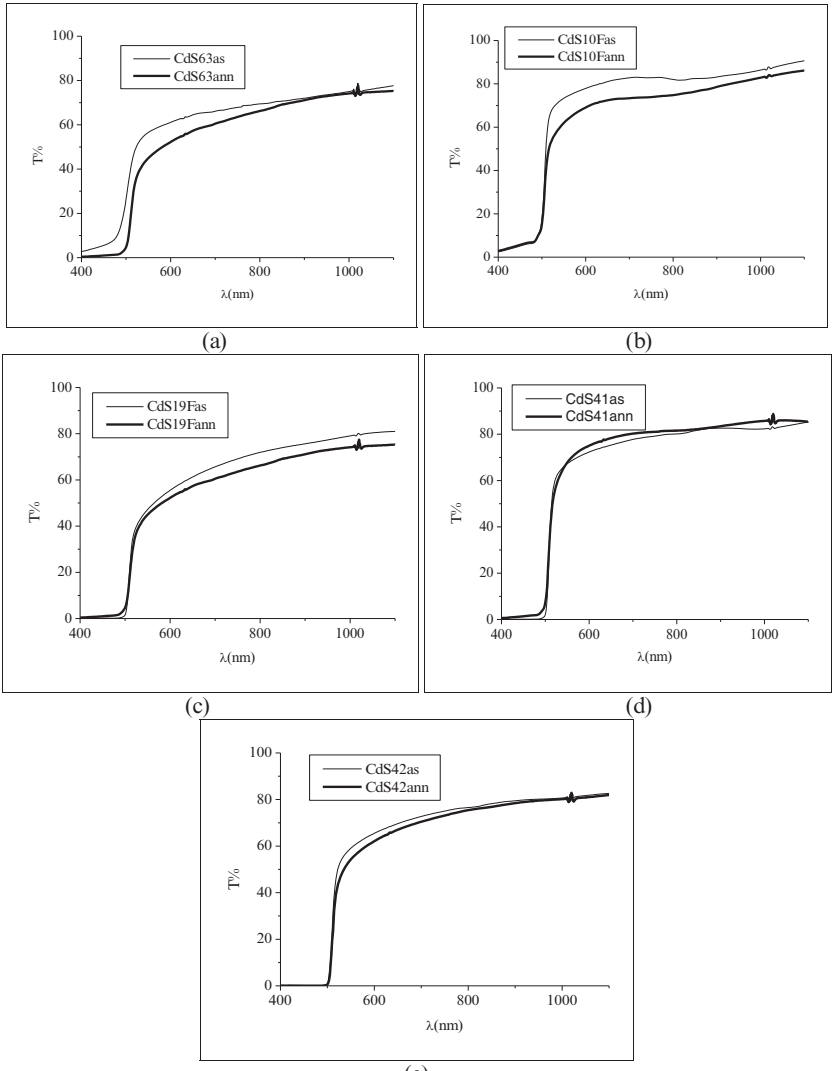

Figure 2. Transmittance spectra of as-deposited and annealed CdS:In thin films with different thickness t. a) t = 335 nm. b) t = 400 nm. c) t = 730 nm. d) t = 740 nm. e) t = 800 nm. Note: The legend contains the names of the samples.

H(0 0 2), H(1 0 1), H(1 0 2), H(1 0 3), H(1 1 2), and H(2 0 2) belong to the hexagonal phase. The as-deposited and annealed CdS:In films were preferentially oriented along the H(1 0 1), and the C(3 1 1)/ H(1 1 2) planes, where the positions of the C(3 1 1) line of the cubic phase and that of the H(1 1 2) line of the hexagonal phase approximately coincide.

Figure 2 displays the transmittance of films of different thickness which are annealed in nitrogen atmosphere at 400°C. The transmittance decreased with annealing, and the absorption edge was shifted towards the longer wavelengths, which refers to the decrease in the optical bandgap energy. The decrease in transmittance is related to the improvement in crystallinity and the increase of the number of free charge carriers after annealing.

To estimate the value of the bandgap energy, a plots of $(\alpha hv)^2$ versus hv is displayed in Figure 3, where the transition is assumed to be a direct one. Linear fits were made in the linear regions of the curves, and optical bandgap energy E_g was estimated from the intercepts with the energy axis. The obtained values of E_g are shown in Figure 3, and they are in the ranges 2.440-2.448 eV

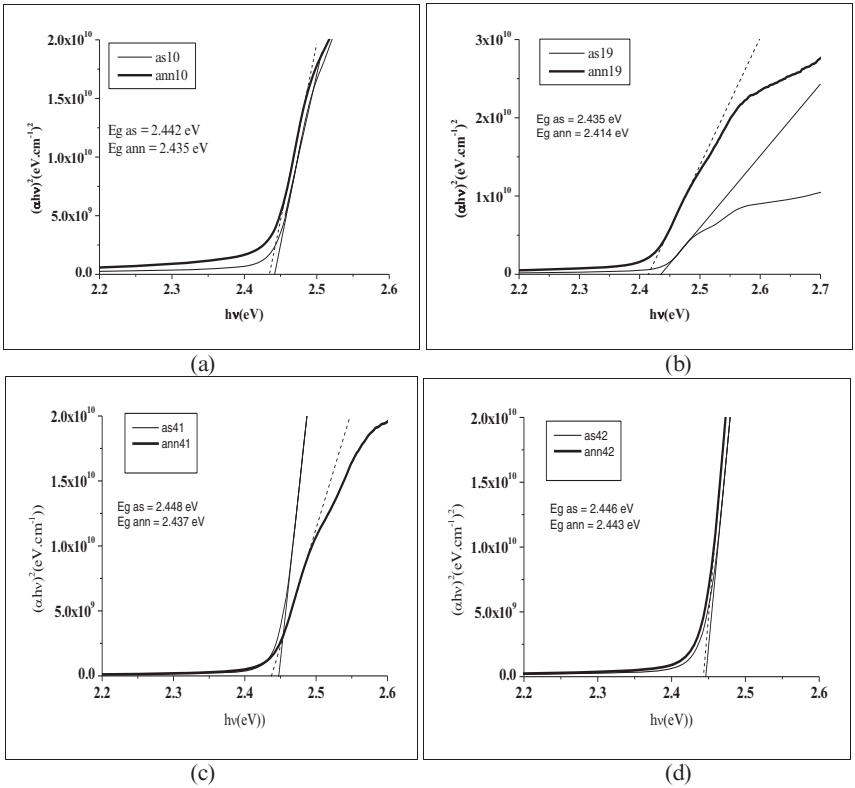

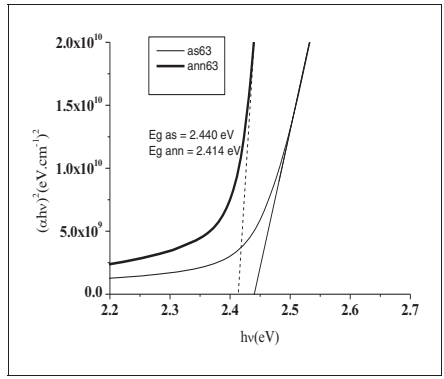

(e)

Figure 3. The plot and linear fit of $(\alpha h\nu)^2$ against the photon's energy $h\nu$ for CdS:In films before and after annealing.

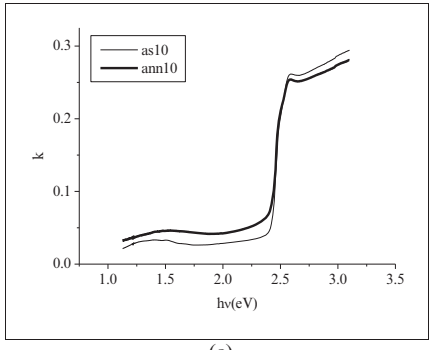

(a)

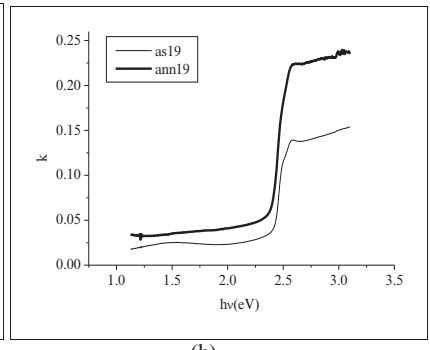

(b)

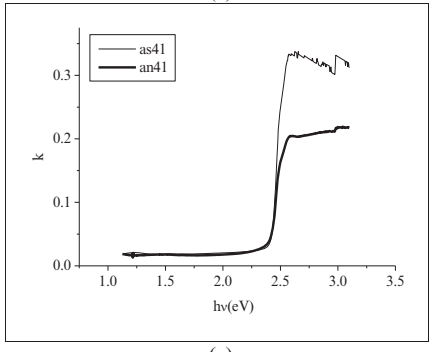

(c)

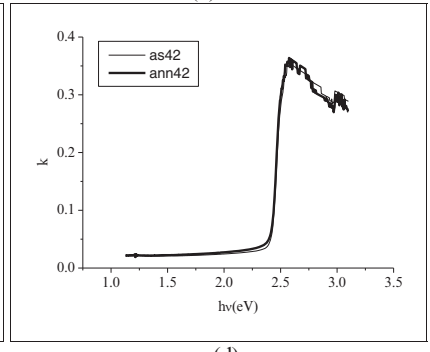

(d)

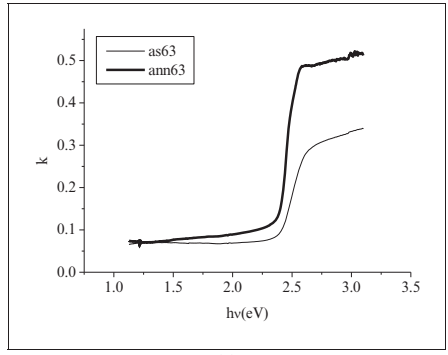

(e)

Figure 4. A plot of the extinction coefficient k against the photon's energy hv for CdS:In films before and after annealing.

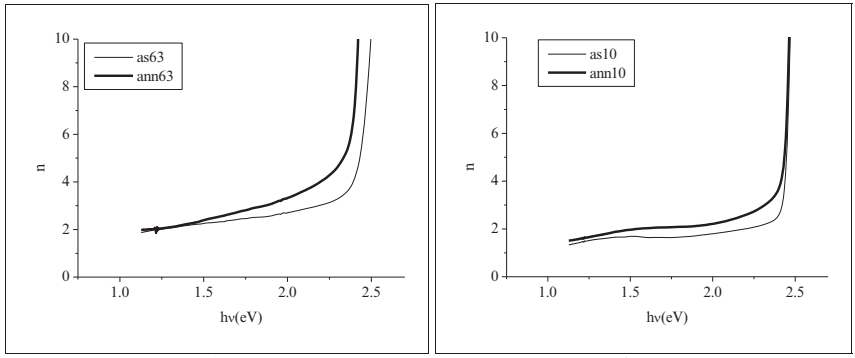

(a) (b)

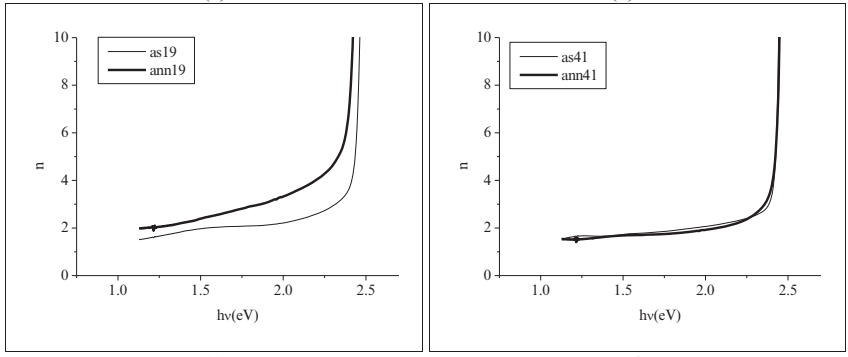

(c) (d)

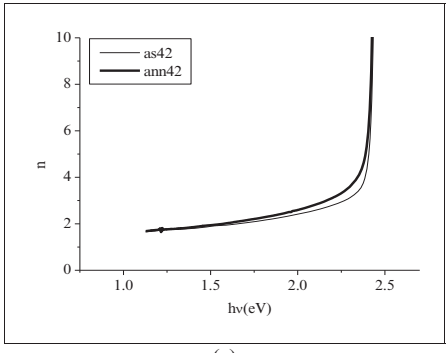

(e)

Figure 5. A plot of the refractive index n against the photon's energy hv for CdS:In films before and after annealing.

and 2.414-2.443 eV before and after annealing respectively .So, the annealed films have reduced bandgap values than the as-deposited ones.

To find the refractive index and the extinction coefficient, the definition of the reflectance of a film for a light wave incident normally from air, with refractive index $n_0 = 1$, on a medium of complex refractive index $n^* = n + ik$ is used [13].

$$R = \frac{(n^* - 1)^2}{(n^* + 1)^2} = \frac{(n-1)^2 + k^2}{(n+1)^2 + k^2} \tag{1}$$

where n is the refractive index and k is the extinction coefficient of the film. Knowing the value of the absorption coefficient α from the transmittance, the extinction coefficient can be calculated using the relation $k = \frac{\lambda\alpha}{4\pi}$, where λ is the wavelength in free space. Solving Eq.1 for the refractive index n gives;

$$n = \frac{(1+R) + \left[(1+R)^2 - (1-R)^2(1+k^2)\right]^{1/2}}{1-R} \tag{2}$$

Figure 4 shows the dependence of extinction coefficient of the films on hv. It is restricted for all the films in the ranges 0.018-0.077 and 0.019-0.110 before and after annealing respectively. It is also fairly constant in the regions before the absorption edge. A sharp increase of k occurs at the absorption edge, then it becomes approximately constant or decreases slowly with hv. Refractive index n values for all films were calculated using Eq.2 and plotted against the photon's energy hv in Figure 5. The figure implies that the refractive index increases with hv, slowly before the absorption edge, then strongly after it. Annealing increases the refractive index for all films. For $hv \leq 2.3$ eV, the refractive index of all as-deposited films lies in the range 1.33-3.29, and of all

annealed films in the range 1.51-4.64. The increase of the refractive index with annealing is an indicative of the improvement of the crystallinity of the films.

Conclusions

Polycrystalline CdS:In thin films were prepared by the SP technique, and the influence of heat treatment on the optical parameters of the films was studied. In general, it is found that transmittance and optical bandgap energy decrease with annealing, which is related to the improvement of crystallinity. On the other hand, the extinction coefficient and refractive index, increased with annealing. These results are important for the use of CdS:In films in optoelectronic devices and thin film solar cells.

References

1. Biswajit Ghosh et al., "Growth of CdS thin films on indium coated glass substrates via chemical bath deposition and subsequent air annealing", *Applied Surface Science* 320 (2014), 309–314.
2. N.M. Megahid et al., "Microstructure and electrical conductivity of In-doped CdS thin films", *Physica B* 353 (2004), 150–163.
3. T.D. Dzhafarov, F. Ongul, and S. Aydin Yuksel, "Effect of indium diffusion on characteristics of CdS films and nCdS/pSi Heterojunctions", *Vacuum* 84 (2010), 310–314.
4. G. Perna et al., "Structural and optical characterization of undoped and indium-doped CdS films grown by pulsed laser deposition", *Thin Solid Films* 453 –454 (2004), 187–194.
5. C.D.Lokhande and S.H.Pawar, "Optical and transport properties of chemical bath deposited CdS:Al films, *Solid State Communications*, 44 (8) (1982), 1137-1139.
6. Amanullah Fatehmulla et al., "Structural, electrical and optical properties of chlorine doped CdS thin films", *World Applied Sciences Journal* 31 (12) (2014), 2073-2078.
7. G. Sasikala, P. Thilakan, and C. Subramanian, "Modification in the chemical bath deposition apparatus, growth and characterization of CdS semiconducting thin films for photovoltaic applications", *Solar Energy Materials & Solar Cells* 62 (2000), 275–293.
8. P.K. Nair, M.T.S. Nair and J. Campos, "Photocurrent response in chemically deposited CdS thin films", *Solar Energy Materials* 15 (1987), 441-452.
9. Deshani Fernando, Mughees Khan, and Yolanda Vasquez, "Control of the crystalline phase and morphology of CdS deposited on microstructured surfaces by chemical bath deposition", *Materials Science in Semiconductor Processing*, 30 (2015),174–180.
10. P. P. Sahay, R. K. Nath, and S. Tewari, "Optical properties of thermally evaporated CdS thin films", *Cryst. Res. Technol.*, 42 (3) (2007), 275 – 280.
11. Shadia J. Ikhmayies and Riyad N. Ahmad-Bitar, "Effect of film thickness on the electrical and structural properties of CdS:In thin films", *American Journal of Applied Sciences* 5 (9) (2008), 1141-1143.
12. Shadia. J. Ikhmayies and Riyad N. Ahmad-Bitar, "The influence of the substrate temperature on the photovoltaic properties of spray-deposited CdS:In thin films", *Applied Surface Science* 256 (2010), 3541–3545.
13. Saeed Salem Babkair, Najat Mohammad Al-Twarqi, and Azhar Ahmad Ansari, "Optical characterization of CdTe films for solar cell applications", *Karachi University Journal of Science* 39 (2011), 1-5.

Characterization of Minerals, Metals, and Materials 2016
Edited by: Shadia Jamil Ikhmayies, Bowen Li, John S. Carpenter, Jiann-Yang Hwang, Sergio Neves Monteiro, Jian Li, Donato Firrao, Mingming Zhang, Zhiwei Peng, Juan P. Escobedo-Diaz, and Chenguang Bai
TMS (The Minerals, Metals & Materials Society), 2016

DETERMINATION OF THE STABILITY CONSTANTS OF MIXED-LIGAND COORDINATION COMPOUNDS IN THE Zn(II)-NITRILOTRIACETIC ACID-AMMONIA SYSTEM

Lin Chen, Zhandong Hao, Tianzu Yang*, Duchao Zhang, Weifeng Liu

School of Metallurgy and Environment, Central South University,
Changsha 410083, China
* Corresponding Author, Tel: +86 13508482570, Email: tianzuyang@163.com

Keywords：Mixed-ligand coordination compounds, Zinc complex, Stability constants, pH Potentiometric method

Abstract

By means of the pH potentiometric method, this work investigates the stability constants $K^{ZnL}_{ZnL(NH_3)_i}$ (i=1,2) of the mixed-ligand coordination compounds in the Zn(II)-nitrilotriacetic acid (H_3L)-ammonia system at the temperature of 25±0.1℃,40±0.1℃, 55±0.1℃, 70±0.1℃ and ionic strengths of 1.0, 2.0, 3.0, 4.0 (NaCl). The precise value for the stability constants are calculated with a continuously approximating method subsequent to the obtainment of their approximations via the half-integer strategy. The results indicate that the stability constants $K^{ZnL}_{ZnL(NH_3)_i}$ (i=1,2) increase with the decrease of temperature and decrease with the increase of ionic strength. The stability of the system is good, therefore the system can be applied to the leaching of zinc oxide.

Introduction

The mixed ligand complexes are widely used in hydrometallurgy, plating process, biochemical effects, analytical chemistry and other fields. In this paper, complexes reaction of nitrilotriacetic acid [$N(CH_2COOH)_3$, below, to H_3L represent] ions as the first ligand and ammonia (NH_3) as the second ligand and Zn(II) were studied by pH potentiometric method. Stability constants of mixed reactions were determined at the temperature of 25±0.1℃,40±0.1℃, 55±0.1℃, 70±0.1℃ and ionic strengths of 1.0, 2.0, 3.0, 4.0 (NaCl).

Theoretical Basis and Calculation Method

Nitrilotriacetic acid ions and Zn(II) can form stable complexes, however its coordination is not saturated, in which condition, ZnL could continue to react with ammonia (NH_3) forming mixed ligand coordination. Within a certain pH range, it can be considered to have

been carried out completely that complex reaction of nitrilotriacetic acid ions and Zn(II) (1:1), therefore, ammonia and Zn(II) could be considered as the binary system. In this context, probable electrical charges of each species have been ignored.

For the first ligand and metal ion concentration is 1:1, the existing literature [1] had reported that the coordination could be considered to be complete at a certain pH. In this paper, by identifying the exact parameters [ZnL]/[Zn] = σ, the pH value can be obtained when L with Zn(II) complexes completely. Stability constant formula of ZnL and plus proton constants formula of L are respectively:

$$Zn + L \rightleftarrows ZnL \qquad K_1 = \frac{[ZnL]}{[Zn][L]} \tag{1}$$

$$ZnL + L \rightleftarrows ZnL_2 \qquad K_2 = \frac{[ZnL_2]}{[ZnL][L]} \tag{2}$$

$$L + qH \rightleftarrows H_qL \qquad \beta_q^H = \frac{[H_qL]}{[L][H]^q} \tag{3}$$

q=1,2,3,4

$$T_{Zn} = [Zn] + [ZnL] + [ZnL_2] \tag{4}$$

For Zn(II)-L system, because $K_2 << K_1$ [2], when $T_L = T_{Zn}$, ZnL_2 was negligible. Therefore:

$$T_{Zn} = [Zn] + [ZnL] \tag{5}$$

Then

$$T_L = [L] + [HL] + [H_2L] + [H_3L] + [H_4L] + [ZnL] \tag{6}$$

On the basis of (3), (4) ,(5) can be obtained:

$$[Zn] = [L](1 + \beta_1^H[H] + \beta_2^H[H]^2 + \beta_3^H[H]^3 + \beta_4^H[H]^4) \tag{7}$$

when [ZnL]/[Zn] = σ, the reaction forming ZnL of Zn and L was completed, then you can get:

$$[L] = \frac{\sigma}{K_1} \tag{8}$$

According to formula (3) and [ZnL]/[Zn] = σ, so:

$$[Zn] = \frac{1}{\sigma + 1} T_{Zn} \tag{9}$$

Taking (8) and (9) into (7), we have:

$$\frac{1}{\sigma + 1} T_{Zn} = \frac{\sigma}{K_1}(1 + \beta_1^H[H] + \beta_2^H[H]^2 + \beta_3^H[H]^3 + \beta_4^H[H]^4) \tag{10}$$

Within the arrange of pH , the Zn-L is completely coordinated by ratio of 1: 1, [L]，[H_2L]，[H_3L]，[H_4L] of formula (6) can be ignored, and equation (9) becomes,

$$\frac{1}{\sigma+1}T_{Zn}=\frac{\sigma}{K_1}\beta_1^H[H] \quad (11)$$

That,

$$[H]=\frac{K_1}{\sigma(\sigma+1)\beta_1^H}T_{Zn} \quad (12)$$

Through (12) can be obtained the [H] when the reaction of ZnL1:1 completed fully.

Data Processing

In the Zn(II)-H_3L-NH_3-H_2O system, when Zn-L1:1 complex reaction was completed, there exist the following equilibrium:

$$ZnL+NH_3 \rightleftarrows ZnL(NH_3) \qquad K_{Zn(L\ 1)H}=\frac{[Zn(L\ N_3)H]}{[Zn(L)][N_3H]} \quad (13)$$

$$ZnL(NH_3)+NH_3 \rightleftarrows ZnL(NH_3)_2 \qquad K_{ZnL(NH_3)_2}=\frac{[ZnL(NH_3)_2]}{[ZnL(NH_3)][NH_3]} \quad (14)$$

$$NH_3+H \rightleftarrows NH_4 \qquad K_1^H=\frac{[NH_4]}{[NH_3][H]} \quad (15)$$

The $\log K_{ZnL(NH_3)}$ and $\log K_{ZnL(NH_3)_2}$ can be used to generate a half-integer function and be obtained.

The approximations for the $\log K_{ZnL(NH_3)}$ and $\log K_{ZnL(NH_3)_2}$ are calculated via the half-integer strategy.

To this end, we can think the ZnL as a whole look, and try to calculate the free ligand concentration of NH_3 and a series of corresponding values of generating functions according to the experimental data.

It has been reported that in the determination of a single ligand stability constants mononuclear complexes, the concept of total acidity could be used to calculate the concentration of free ligand[3]. The method also applies to the mixed ligand complex systems studied in this paper. Since the formation of mixed ligand complex Zn with L has been completed, the protonation effect of each species of L is negligible.

The total acidity can be written as:

$$T_H=[H]+[NH_4]-[OH] \quad (16)$$

Taking (13) into (14),

$$[NH_3]=\frac{T_H-[H]+[OH]}{K_1^H[H]} \quad (17)$$

The algorithm of $\overline{n_{NH_3}}$ is as follows:

$$\overline{n_{NH_3}} = \frac{\left[ZnL(NH_3)\right] + 2\left[ZnL(NH_3)_2\right]}{T_{Zn}} = \frac{\left[ZnL(NH_3)\right] + 2\left[ZnL(NH_3)_2\right]}{[ZnL] + \left[ZnL(NH_3)\right] + \left[ZnL(NH_3)_2\right]} \quad (18)$$

Where, $\left[ZnL(NH_3)\right] + 2\left[ZnL(NH_3)_2\right]$ can be calculated on the basic of the total concentration of the second ligand and [NH_3]

$$T_{NH_3} = [NH_3] + [NH_4] + \left[ZnL(NH_3)\right] + 2\left[ZnL(NH_3)_2\right] \quad (19)$$

$$\left[ZnL(NH_3)\right] + 2\left[ZnL(NH_3)_2\right] = T_{NH_3} - [NH_3]\left(1 + K_1^H[H]\right) \quad (20)$$

Making plots of $\overline{n_{NH_3}}$ against -log[NH_3], where $\log K_{ZnL(NH_3)}$ can be obtained at $\overline{n_{NH_3}} = \frac{1}{2}$, and $\log K_{ZnL(NH_3)_2}$ can be obtained at $\overline{n_{NH_3}} = \frac{3}{2}$.

Experimental Procedure

1. Materials and Solutions

Solutions.-Nitrilotriacetic acid (Sinopharm Chemical Reagent Co., Ltd, China) was purified by double recrystallization from distilled water, washed with absolute ethanol, and dried in vacuum drying oven [4]. It was pure within the limits of acidimetric titration. A 0.024591 M solution of its disodium salt was obtained by preparing an acid solution, adding sodium hydroxide to the potentiometric end-point[5], diluting appropriately, and analysised with the method of the literature[6]. A carbonate-free sodium hydroxide solution was prepared by dissolving Analar pellets in ultrapure water, and standardized potentiometrically with potassium hydrogen phthalate (Tianjin Institute of Chemical Reagents, China). A hydrochloric acid (Sinopharm Chemical Reagent Co., Ltd, China) solution (≈0.3mol·dm^{-3}) was prepared and used after being standardized. Zinc dichloride ($ZnCl_2$) and ammonia chloride (NH_4Cl) were supplied by Tianjin Guangfu Science and Technology Development Co., Ltd, China. Sodium chloride (NaCl) were obtained from Sinopharm Chemical Reagent Co., Ltd, China.

All solutions used throughout the experiments were prepared freshly in ultrapure water obtained from a NANO pure-Ultrapure water system (Lead R&D Hi-end Water Treat Equipment Co., Ltd) that was distilled and deionized with a resistance of 18.2 M ·cm^{-1}.

2. Apparatus and Equilibrium Titration Procedures.

The pH-potentiometric titrations were performed using a Mettler MT320-S type pH meter with a LE438 electrode, a 728 magnetic stirrer, coupled with a dosino buret（BOMEX, 5mL）. The electrode response can be read to the second decimal place in terms of pH units with a precision of ±0.01 and the potential with a precision of 1 mV. The pH titrations were

carried out in a 100 cm^3 commercial glass vessel. The ionic strength of the solutions was maintained at a constant level by using the desired concentration of NaCl solution as supporting electrolyte. The pH meter was calibrated with standard buffer solutions (pH 4.00, 6.86 and 9.18) before and after each series of pH measurements. For the protonation constants estimation of NTA and NH_3, the following solutions were prepared (total volume 50 cm^3) and titrated potentiometrically against a standard carbonate-free NaOH (0.33938 $mol \cdot dm^{-3}$) solution:

For the determination of the binary metal complexes, solutions containing NTA or NH_3 and metal ions were titrated at 1:3 metal ion to ligand mole ratios to fulfill the maximum coordination number of the metal ion, and for ternary systems, a 1:1:100 metal ion/NTA/NH_3 ratio was used.

All experiments were carried out at the atmosphere of purified high purity nitrogen. Each solution was thermostatted at 25±0.1℃、40±0.1℃、55±0.1℃、70±0.1℃, where the solutions were left to stand for several minutes before titration. A magnetic stirrer was used during all titrations. Each titration was repeated at least three times under carefully controlled experimental conditions. Typically, more than 20 pH readings (points of potentiometric measurements) were collected and taken into account for each titration. All metering containers have been corrected.

The measured stability constant is concentration equilibrium constant. In order to calculate the concentration of H^+ and OH^- under different conditions, the standard solution of hydrochloric acid and sodium hydroxide solution were used to correct the relationship between the activity and the concentration of H^+, OH^- at different temperatures, different ionic strength ,obtaining a series of correction factor.

Results and Discussion

1. Experimental Results

Protonation constants of ammonia and nitrilotriacetic acid were remeasured under the above conditions.

According to equation (10), the value of pH on the condition that Zn and L coordinate completely is as follows: $\log K_1 = 10.66$, $\log \beta_1^H = 9.65$. σ in (12) is taken to be 50, $T_{Zn} = 1\times10^{-3}$. The pH value is 5.40 when the reaction that Zn react with L forming ZnL is carried out completely. The reaction occurs above this pH is mixed reaction, as shown in equation (13) and (14).

According to the measured proton constants, the volume of sodium hydroxide added into mixed system and pH of the solution system, generating functions $\bar{n}$ of Zn^{2+}-Nta^{3-}-NH_3-H_2O system and negative logarithm -log[NH_3] of free ligand [NH_3] are calculated under appropriate conditions. Draw the diagram, in which -log [NH_3] as the horizontal axis, $\bar{n}$ as the vertical axis, then directly read out stepwise stability constants of complex ions with half-integer method. Since using half-integer law requires $K_1 > 500K_2$,

while K_1, K_2 relatively are close in the Zn^{2+}-Nta^{3-}-NH_3-H_2O mixed system, there are some errors with half-integer method. So the precise value for the stability constants Kn are obtained[7] by manipulating the approximations via the half-integer strategy with a continuously approximating method.

Continuously approximating method：It is easy to draw the following relationship between the generating function and K_1, K_2.

$$K_1 = \frac{1}{[L]} \cdot \frac{\bar{n}}{(1-\bar{n}) + (2-\bar{n}) K_2 [L]} \tag{21}$$

$$K_2 = \frac{1}{[L]} \cdot \frac{\bar{n} + (\bar{n}-1) K_1 [L]}{(2-\bar{n}) K_1 [L]} \tag{22}$$

Press the value of pL with $\bar{n} = 0.5$ and 1.5 (determined by the resulting curve) as a first approximation of K_1 and K_2. Put them into (21) and (22) respectively, and calculate the second approximation of K_1 and K_2. Then put the second approximation of K_1 and K_2 into equation (11) and (12) to seek a third-generation approximation. So continue.

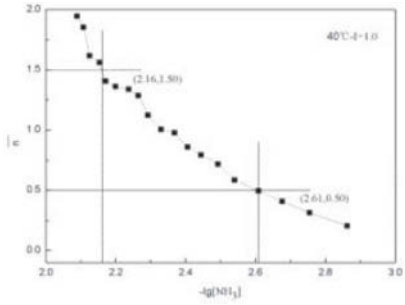

Fig. 1 Plot of $\overline{n_{NH_3}}$ against -log[NH_3] in the system Zn(II)-nitrilotriacetic acid-ammonia

Figure 1 shows the relationship of $\overline{n_{NH_3}}$ against -log[NH_3] in the system of Zn(II)-nitrilotriacetic acid-ammonia.

The concentration of OH^- increases with adding of NaOH, and pH gradually increased. At the same time, the concentration of free ligand and the number of ligand binding zinc ion increase, forming mixed ligand complexes continuously. As shown in Fig.1, it is known that $\log K_1 = 2.61$, $\log K_2 = 2.16$ by half-integer method, then the precise value for the stability constants that $\log K_1 = 2.60$, $\log K_2 = 2.15$ are calculated with a continuously approximating method.

2. Effects of temperature and ionic strength on a mixed ligand complex stability constants

The corrected data list is summarized as follows:

Table I. The first stage stability constants of Zn^{2+}-Nta^{3-}-NH_3-H_2O system under different ionic strength at different temperatures

$\log K_1$	I=1.0	I=2.0	I=3.0	I=4.0
25℃	2.65	2.62	2.60	2.44
40℃	2.60	2.45	2.38	2.30
55℃	2.49	2.38	2.23	2.17
70℃	2.41	2.35	2.20	2.14

Table II. The second stage stability constants of Zn^{2+}-Nta^{3-}-NH_3-H_2O system under different ionic strength at different temperatures

$\log K_2$	I=1.0	I=2.0	I=3.0	I=4.0
25℃	2.20	2.16	2.13	1.89
40℃	2.15	2.06	1.89	1.86
55℃	2.14	2.03	1.93	1.82
70℃	2.10	1.99	1.90	1.78

Table I. and Table II. indicate that the stability constants (i=1,2) decrease with the increase of temperature and the increase of ionic strength.

3. Discussion

Considering the equilibrium constant of the following reactions:

$$ZnL_2 + Zn(NH_3)_2 \rightleftarrows 2ZnL(NH_3) \qquad (23)$$

$$x = \frac{[ZnL(NH_3)]^2}{[ZnL_2][Zn(NH_3)_2]} = \left(\beta^{Zn}_{ZnL(NH_3)}\right)^2 / (\beta_{ZnL_2} \cdot \beta_{Zn(NH_3)_2})$$

($\beta^{Zn}_{ZnL(NH_3)}$ is theequilibrium constant of the reactions $Zn+L+NH_3 \rightleftarrows ZnL(NH_3)$) (24)

$$\log x = 2\log \beta^{Zn}_{ZnL(NH_3)} - \left(\log \beta_{ZnL_2} + \log \beta_{Zn(NH_3)_2}\right) \qquad (25)$$

The $\log x_{theoreical}$=0.6 are obtained according to the equation[8] that is $\log x = 2\log \beta^{Zn}_{ZnL(NH_3)} - \left(\log \beta_{ZnL_2} + \log \beta_{Zn(NH_3)_2}\right)$, whilst the logx value of 6.44 can be worked out with the stability constants the mixed ligand complex[9] and binary complexes of $\log \beta_{ZnL_2}$ [2] and $\log \beta_{Zn(NH_3)_2}$ [10]. And the latter value turns out to be greater than former one, which illustrates that the stability of the formed mixed ligand complex is greater than the stability that estimated according to statistics effect. The stability of the system is good,

making it possible that the system can be applied to the leaching of zinc oxide.

Acknowledgment

The financial supports from National Basic Research Program of China (No. 2014CB643404) are gratefully acknowledged.

Conclusions

1. The article makes a deduction of a new method to calculate the stability constants of the mixed ligand complex, as described in "Data Processing"

2. This work investigates the stability constants $K^{ZnL}_{ZnL(NH_3)_i}$ (i=1,2) of the mixed-ligand coordination compounds in the Zn(II)-nitrilotriacetic acid (H_3L)-ammonia system. The results indicate that the stability constants $K^{ZnL}_{ZnL(NH_3)_i}$ (i=1,2) increase with the decrease of temperature and decrease with the increase of ionic strength.

3. The stability of the the Zn(II)-nitrilotriacetic acid (H_3L)-ammonia system is good, therefore the system can be applied to the leaching of zinc oxide.

References

1. T. Yang, C. Chen, and X. Zhang, "A study of mixed-ligand coordination compounds in the systems of Cu(II)-n-alkyl iminodiacetic acids-amino acids," *Journal of Central-south Institute of Mining and Metallurgy* , 18 (3) (1987), 331-354

2. R.M. Smith et al., eds., Critical stability constants, vol.2 (New York, NY: Plenum Press·New York and London, 1974), 142.

3. X. Zhang, "On the calculation of free ligand concentrations in course of the determination of the stability constants of mononuclear complexes," *Journal of Central-south Institute of Mining and Metallurgy*, 1982, no.31:121-126.

4. T. Moeller, and R. Ferrus, "Observations on the Rare Earths. LXXIV. The enthalpy and entropy of formation of the 1:1 and 1:2 chelates of nitrilotriacetic acid with tripositive cations," *Inorganic Chemistry*, 1(1) (1962), 49-55.

5. G. Schwarzenbach, E. Kampitsch, and R. Steiner, Helv. Chim. Acta, 1945, no.28:828-832.

6. G. Hong, "Determination of nitrilotriacetic acid by complexometric titration. *Chemistry Reagents*," 6 (3) (1984), 189-190

7. K. Wang, and X. Chen, "Determination of the complex stability constants by the potential method (III-1)," *Analysis Laboratory*, 4 (5) (1985), 48-53

8. C. Su, and B. Liao, "Mixed ligand complex compounds and their biological significance," *Molecular Science and Chemical Research*, 3 (2) (1983), 153-162.

9. А .Я. Фридман, идр., Ж. Неорз. Хцм, 15 (3) (1970), 701-705

10.R.M. Smith et al., eds., Critical stability constants, vol.4 (New York, NY: Plenum Press·New York and London, 1974), 41.

Characterization of Minerals, Metals, and Materials 2016
Edited by: Shadia Jamil Ikhmayies, Bowen Li, John S. Carpenter, Jiann-Yang Hwang, Sergio Neves Monteiro, Jian Li, Donato Firrao, Mingming Zhang, Zhiwei Peng, Juan P. Escobedo-Diaz, and Chenguang Bai
TMS (The Minerals, Metals & Materials Society), 2016

RESONANCES OF MICROWAVE POWER ABSORPTION IN ALUMINA AND SILICON CARBIDE

Zhiwei Peng[1], Xiaolong Lin[1], Jiann-Yang Hwang[2], Yuzhe Zhang[2], Yuanbo Zhang[1], Guanghui Li[1], Tao Jiang[1]

[1]School of Minerals Processing and Bioengineering, Central South University, Changsha, Hunan 410202, China
[2]Department of Materials Science and Engineering, Michigan Technological University, Houghton, MI 49931, USA

Keywords: Microwave, Power Distribution, Resonance Peak, Attenuation, Thickness

Abstract

Power absorption resonances in microwave irradiated low-loss Al_2O_3 and high-loss SiC have been investigated by determining the normalized average power distribution in the sample slabs. For Al_2O_3, multiple resonance peaks initially occur at the position following a "half-wavelength ($0.5\lambda_m$) rule". As temperature increases, this rule becomes invalid due to the attenuation of microwaves with increased dielectric loss. For SiC, however, only one strong resonance peak is observed at the sample thickness of $0.33\lambda_m$. This indicates that only the sample having the size corresponding to resonance can obtain the maximum power absorption, considerably increasing the microwave heating efficiency.

Introduction

Microwave energy has been extensively applied in the field of materials processing [1-3]. The heating efficiency directly depends upon the power absorption in microwave absorbers [4]. While a substantial amount of experimental/empirical work has been conducted to improve microwave power absorption by optimizing various heating factors (e.g., thermal conditions, microwave frequency, applicator geometry, etc.), surprisingly little theoretical research was devoted to the characterization of power absorption in materials [5]. Previous theoretical studies primarily focused on the effects of sample geometry and size on the power absorption [6-10]. It is found that power absorption resonance, represented by the local maximum power absorption, may occur within materials having a finite size. The resonance phenomenon is closely associated with the sample dimension L and microwave wavelength within the substance λ_m. For material slabs exposed to microwaves at one face, power resonances occur at $L/\lambda_m = 0.5n$, where n is an integer [6]. This is known as the "half-wavelength rule" which has been confirmed by the observations in some typical microwave absorbers (e.g., water and Al_2O_3) [6,7,10]. However, a literature review revealed that the temperature dependence of power resonance has not received sufficient attention. It is highly necessary to carry out such investigations since microwave power absorption in substances strongly relies on the temperature-dependent dielectric properties [11,12]. On the other hand, it is well known that selective heating is one of the most distinguished characteristics of microwave processing of materials. This indicates that microwave power absorption may show apparent discrepancies between different absorbers. Since microwaves have found widespread application in the heating of both low- and high-loss

materials, it is beneficial to make a comparative study on the power absorption in different absorbers. Thus, it can be expected that a quantitative analysis of the resonance would contribute to the enhancement of power absorption in materials and thus to an effective design and control of microwave-related process with high energy efficiency.

The present work mainly attempts to investigate the effect of temperature on the power resonance in microwave irradiated absorbers. A quantitative analysis of the resonances in two representative materials, including low-loss Al_2O_3 and high-loss SiC, was performed and the validity of the "half-wavelength rule" in microwave heating was examined. The finding obtained by this study may shed new light on the optimization of sample dimension in microwave heating, leading to a maximum microwave power absorption and high heating efficiency.

Theory

Microwave power absorption in a dielectric medium during microwave heating can be attributed to the dielectric loss of the material, which depends on the distribution of microwave electric field. Assuming that the microwaves are uniform plane waves incident from air to a dielectric medium of thickness L propagating in the z direction (one face incidence), the contribution of dielectric loss Q_E to the power absorption per unit volume (W m^{-3}) can be determined by Poynting vector. It is simplified as [13]

$$Q_E(z)=\frac{1}{2}\omega\varepsilon_0\varepsilon_r''\left|E_0\right|^2\left|T\right|^2\frac{e^{-2\alpha z}-2\left|R\right|e^{-2\alpha L}cos\left(2\beta L-2\beta z-\delta\right)+\left|R\right|^2e^{-2\alpha L}e^{-2\alpha(L-z)}}{1-2\left|R\right|^2e^{-2\alpha L}cos\left(2\beta L-2\delta\right)+\left|R\right|^4e^{-4\alpha L}} \quad (1)$$

where ω is the angular frequency, ε_0 is the permeability of free space (8.854×10^{-12} F m^{-1}), ε_r'' is the imaginary part of complex relative permittivity of the medium (relative dielectric loss factor), E_0 is the incident microwave electric field strength, T and R are the transmission and reflection coefficients at the interface between free space and the magnetic dielectric medium, respectively, δ is the phase angle for reflection coefficient (rad), with α and β as the field attenuation factor (Np m^{-1}) and phase constant (rad m^{-1}), respectively.

For nonmagnetic dielectrics (assuming the relative permeability $_r$=1), α and β can be determined using the following equations:

$$\alpha=\frac{\sqrt{2}\pi}{\lambda_0}\left\{-\varepsilon_r'+\left[\left(\varepsilon_r'\right)^2+\left(\varepsilon_r''\right)^2\right]^{1/2}\right\}^{1/2} \quad (2)$$

$$\beta=\frac{\sqrt{2}\pi}{\lambda_0}\left\{\varepsilon_r'+\left[\left(\varepsilon_r'\right)^2+\left(\varepsilon_r''\right)^2\right]^{1/2}\right\}^{1/2} \quad (3)$$

where λ_0 is the microwave wavelength in free space (m) and ε_r' is the real part of complex relative permittivity of the medium (relative dielectric constant). In principle, the values of α and β can be used to determine λ_m and the microwave penetration depth D_p [14,15] which indicate the behaviors of microwave propagation and dissipation in the targeted materials. The relevant equations are as follows.

$$\lambda_m=\frac{1}{2\beta}=\sqrt{2}\lambda_0\left\{\varepsilon_r'+\left[\left(\varepsilon_r'\right)^2+\left(\varepsilon_r''\right)^2\right]^{1/2}\right\}^{-1/2} \quad (4)$$

$$D_p = \frac{1}{2\alpha} = \frac{\lambda_0}{2\sqrt{2}\pi}\left\{-\varepsilon_r' + \left[\left(\varepsilon_r'\right)^2 + \left(\varepsilon_r''\right)^2\right]^{1/2}\right\}^{-1/2} \quad (5)$$

As indicated by eq. (1), microwave power absorption in dielectrics relies on the sample thickness (L) and shows a spatial variation in the medium (indicated by z). The thickness dependence of overall power absorption in materials can be indicated by the calculation of an average power absorption [7,16]. It is defined as the term ($Q_{E,ave}$) by integrating the power distribution throughout the sample slab:

$$Q_{E,ave}(L) = \frac{1}{L}\int_0^L Q_E(z)dz \quad (6)$$

Based on this definition, the average power absorption in the dielectric slab of thickness L can then be expressed as

$$Q_{E,ave}(L) = \frac{1}{2L}\omega\varepsilon_0\varepsilon_r''\left|E_0\right|^2\left|T\right|^2 \frac{\frac{\left|R\right|^2-1}{2\alpha}e^{-2\alpha L} - \frac{\left|R\right|}{\beta}e^{-2\alpha L}sin(\delta) - \frac{\left|R\right|}{\beta}e^{-2\alpha L}sin(2\beta L-\delta) - \frac{\left|R\right|^2}{2\alpha}e^{-4\alpha L} + \frac{1}{2\alpha}}{1-2\left|R\right|^2 e^{-2\alpha L}cos(2\beta L-2\delta)+\left|R\right|^4 e^{-4\alpha L}} \quad (7)$$

As mentioned before, power absorption resonance shows the dependence of L/λ_m. Thus, to further simply the calculation, one may use the normalized value of average power absorption, which is defined as

$$Q_{E,ave,n} = \frac{Q_{E,ave}}{\omega\varepsilon_0\varepsilon_r''\left|E_0\right|^2} \quad (8)$$

.The validity of the "half-wavelength rule" for materials during microwave heating can then be examined by plotting $Q_{E,ave,n}$ against L/λ_m at various temperatures.

Results and Discussion

Resonance of Microwave Power Absorption in Al_2O_3

The dielectric parameters of Al_2O_3 (from 22 to 1379 °C) used for the calculations are given in Table I [8,17,18]. The corresponding power absorption resonance patterns of Al_2O_3 are presented in Figure 1.

Table I. Microwave Absorption Properties of Al_2O_3 and SiC at 2.45 GHz

Parameters	Al_2O_3							SiC
	22 °C	491 °C	683 °C	871 °C	1050 °C	1221 °C	1379 °C	
ε_r'*	8.9	9.82	10.15	10.4	10.81	11.18	11.77	26.66
ε_r''*	0.004	0.025	0.055	0.093	0.158	0.241	0.476	27.99
λ_m (m)	0.041	0.039	0.038	0.038	0.037	0.037	0.036	0.021
D_p (m)	14.535	2.443	1.129	0.676	0.406	0.270	0.140	0.004

*Data taken from [8,17,18]

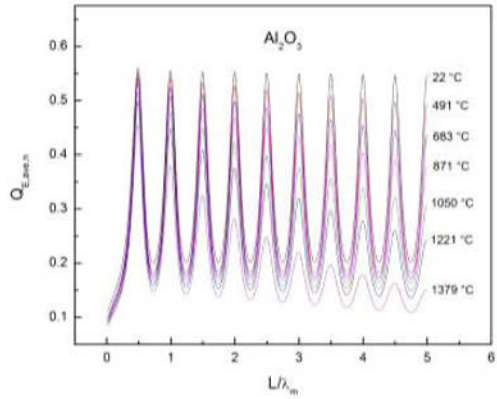

Figure 1. Temperature dependence of microwave power absorption resonance in Al_2O_3.

As shown in Figure 1, there are multiple resonance peaks for Al_2O_3 slabs. The peak positions can be determined from the patterns and the position values corresponding to different temperatures are summarized in Table II. It is identified that the power resonances for Al_2O_3 at low temperatures (e.g., 22 °C) essentially occur at integer multiples of 0.5 L/λ_m, indicating the validity of the "half-wavelength rule". However, as the temperature increases, the corresponding resonance peaks shift to a smaller L/λ_m. This tendency becomes more pronounced above 871 °C. It suggests that the "half-wavelength rule" is imprecise at high temperatures and thus not valid for the entire microwave heating process. Simultaneously, it is seen that the peak intensity decreases with increasing temperature. At 22 °C, negligible decrease in peak intensity can be observed in the tested sample dimension range. Continuous increase in temperature leads to a significant decline in the peak amplitude. This phenomenon can be attributed to the temperature dependence of dielectric property of Al_2O_3, as listed in Table I. The increased dielectric loss at higher temperatures gives rise to lower average power absorption as the sample dimension increases.

Table II. Resonance Peak Positions for Al_2O_3 in the Examined Temperature Range

Peak No.	L/λ_m						
	22 °C	491 °C	683 °C	871 °C	1050 °C	1221 °C	1379 °C
1	0.490	0.490	0.490	0.490	0.490	0.485	0.485
2	0.995	0.995	0.995	0.995	0.995	0.990	0.990
3	1.495	1.495	1.495	1.495	1.495	1.495	1.490
4	1.995	1.995	1.995	1.995	1.995	1.995	1.990
5	2.500	2.495	2.495	2.495	2.495	2.495	2.490
6	3.000	3.000	2.995	2.995	2.995	2.995	2.990
7	3.500	3.500	3.500	3.495	3.495	3.495	3.490
8	4.000	4.000	4.000	3.995	3.995	3.995	3.990
9	4.500	4.500	4.500	4.495	4.495	4.495	4.490
10	5.000	5.000	5.000	4.995	4.995	4.995	4.990

Resonance of Microwave Power Absorption in SiC

In comparison with poor absorbers like Al_2O_3, high-loss materials such as SiC have gained more widespread popularity in recent years [1,5]. These materials exhibit high dielectric losses under microwave irradiation. They are often used as microwave susceptors to promote microwave processing efficiency. For this reason, it is important to characterize the power absorption in these materials.

Figure 2(a) presents the power absorption pattern of SiC at room temperature, in which the values of $Q_{E,ave,n}$ for SiC were determined based on the dielectric data given in Table I. It is found that there is only one strong peak in the entire dimension range. The power absorption peak locates at 0.33 L/λ_m, which is much less than the value (0.50 L/λ_m) predicted by the "half-wavelength rule". It can be assumed that the original resonance peak was "shifted" by the significant attenuation of microwaves resulting from high dielectric loss, which agrees well with the small penetration depth (D_p=0.004 m) in Table I. In other words, the microwave loss dominates the power distribution in SiC. Furthermore, the sharp peak indicates that microwave heating of SiC with the dimension of 0.33λ_m (~0.007 m) would give rise to the highest heating rate. SiC samples of other thicknesses may exhibit much lower power absorption. For instance, when L=0.5λ_m, 2.5λ_m, and 5.0λ_m, the values of $Q_{E,ave,n}$ are only 0.030, 0.006, and 0.003, respectively. Thus, we may conclude that an appropriate sample size is particularly important for strong microwave absorbers like SiC since only one resonance peak may be present in these materials. An analysis of power absorption resonance in materials is essential for design of an efficient microwave heating process.

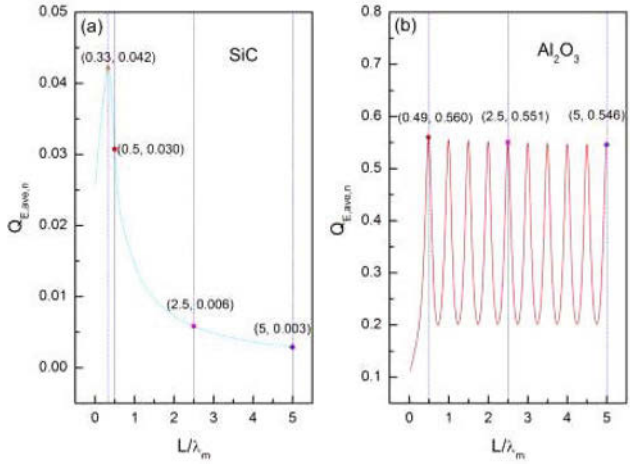

Figure 2. Power absorption patterns of SiC and Al_2O_3 at room temperature.

Further analysis also shows that the peak intensity of SiC ($Q_{E,ave,n}$=0.042) is much lower than that of Al_2O_3 (0.546≤$Q_{E,ave,n}$≤0.560), as shown in Figure 2(b). This is primarily caused by the low transmission coefficient (T) and high attenuation factor (α) of SiC. For example, the values of T and α for SiC are 0.28 and 125.663 Np m^{-1} while the respective values for Al_2O_3 at 22 °C are 0.50 and 0.034 Np m^{-1}. It shows that although high-loss absorbers usually possess larger attenuation factors which indicates a rapid heating process, their microwave transmission coefficients may be considerably lower than those of low-loss materials. Therefore, efficient microwave heating for high-loss materials can only be achieved in an applicator where repeated heating by reflected waves occurs. This explains that a microwave cavity with the metal wall is essential for most microwave heating cases. Conversely, these results also imply that unidirectional microwave heating which commonly takes place in waveguide may be inefficient from the perspective of energy conservation.

Conclusions

In summary, the power absorption characteristics of low- and high-loss materials including Al_2O_3 and SiC were investigated in this work. Multiple microwave power resonance peaks are identified in the Al_2O_3 slab. The peak positions initially follow the "half-wavelength rule", and then shift to smaller L/λ_m with increasing temperature. It suggests that the rule is not valid throughout the heating process. Simultaneously, an increase in temperature leads to a decline in peak intensity due to the increased dielectric loss. These results are compared with those of SiC, in which only one power absorption peak is found to locate at the dimension of $0.33\lambda_m$. The sharp peak is formed mainly due to the strong attenuation of microwaves. It is shown that the influence of dimension-dependent resonance tends to be weaker in a strong microwave absorber and the microwave loss exerts a dominant effect on the power distribution in the sample. Thus, for high-loss absorbers, only the sample with the size corresponding to resonance could obtain the maximum power absorption and the ones of other dimensions may give rise to a substantially lower heating rate. The comparison further demonstrates a relatively lower microwave transmission of SiC. It is expected that repeated heating by the reflected waves between the microwave cavity metal wall and the sample is important for the enhancement of heating efficiency. An analysis of the power absorption resonances would contribute to the optimization of sample size in microwave heating with which a high-efficiency process could be easily achieved.

Acknowledgements

This work was supported by the National Natural Science Foundation of China under Grant 51504297 and the Shenghua Lieying Program of Central South University under Grant 502035016.

References

1. S. Das, A. K. Mukhopadhyay, S. Datta, and D. Basu, "Prospects of Microwave Processing: An Overview," *Bulletin of Materials Science*, 32 (2009), 1-13.
2. Z. Peng and J. Y. Hwang, "Microwave-Assisted Metallurgy," *International Materials Reviews*, 60 (2015), 30-63.

3. S. W. Kingman, “Recent Developments in Microwave Processing of Minerals,” *International Materials Reviews*, 51 (2006), 1-12.
4. Z. Peng, J. Y. Hwang, and M. Andriese, “Absorber Impedance Matching in Microwave Heating,” *Applied Physics Express*, 5 (2012), 077301-077301-3.
5. S. Chandrasekaran, S. Ramanathan, and T. Basak, “Microwave Material Processing–A Review,” *AIChE Journal*, 58 (2012), 330-363.
6. K. G. Ayappa, H. T. Davis, S. A. Barringer, and E. A. Davis, “Resonant Microwave Power Absorption in Slabs and Cylinders,” *AIChE Journal*, 43 (1997), 615-624.
7. K. G. Ayappa, “Resonant Microwave Power Absorption in Slabs,” *Journal of Microwave Power and Electromagnetic Energy*, 34 (1999), 33-41.
8. A. Chatterjee, T. Basak, and K. G. Ayappa, “Analysis of Microwave Sintering of Ceramics,” *AIChE Journal*, 44 (1998), 2302-2311.
9. T. Basak and S. S. Kumaran, “A Generalized Analysis on Material Invariant Characteristics for Microwave Heating of Slabs,” *Chemical Engineering Science*, 60 (2005), 5480-5498.
10. T. Basak and A. S. Priya, “Role of Ceramic Supports on Microwave Heating of Materials,” *Journal of Applied Physics*, 97 (2005), 083537-083537-12.
11. Z. Peng, J. Y. Hwang, M. Andriese, W. Bell, X. Huang, and X. Wang, “Numerical Simulation of Heat Transfer during Microwave Heating of Magnetite,” *ISIJ International*, 51 (2011), 884-888.
12. Z. Peng, J. Y. Hwang, “Numerical Analysis of Heat Transfer Characteristics in Microwave Heating of Magnetic Dielectrics,” *Metallurgical and Materials Transactions A*, 43A (2012), 1070-1078.
13. Z. Peng, J. Y. Hwang, and M. Andriese, “Magnetic Loss in Microwave Heating,” *Applied Physics Express*, 5 (2012), 027304-027304-3.
14. Z. Peng, J. Y. Hwang, J. Mouris, R. Hutcheon, and X. Huang, “Microwave Penetration Depth in Materials with Non-Zero Magnetic Susceptibility,” *ISIJ International*, 50 (2010), 1590-1596.
15. Z. Peng, J. Y. Hwang, J. Mouris, R. Hutcheon, and X. Sun, “Microwave Absorption Characteristics of Conventionally Heated Nonstoichiometric Ferrous Oxide,” *Metallurgical and Materials Transactions A*, 42A (2011), 2259-2263.
16. Z. Peng, J. Y. Hwang, and M. Andriese, “Microwave Power Absorption Characteristics of Ferrites,” *IEEE Transactions on Magnetics*, 49 (2013), 1163-1166.
17. Z. Peng, J. Y. Hwang, and M. Andriese, “Design of Double-Layer Ceramic Absorbers for Microwave Heating,” *Ceramics International*, 39 (2013), 6721-6725.
18. R. M. Hutcheon, M. S. De Jong, F. P. Adams, P. G. Lucuta, J. E. McGregor, and L. Bahen, “RF and Microwave Dielectric Measurements to 1400°C and Dielectric Loss Mechanisms,” *MRS Proceedings*, 269 (1992), 541-551.

Characterization of Minerals, Metals, and Materials 2016
Edited by: Shadia Jamil Ikhmayies, Bowen Li, John S. Carpenter, Jiann-Yang Hwang, Sergio Neves Monteiro, Jian Li, Donato Firrao, Mingming Zhang, Zhiwei Peng, Juan P. Escobedo-Diaz, and Chenguang Bai
TMS (The Minerals, Metals & Materials Society), 2016

PHYSICAL AND CHEMICAL PROPERTIES OF MSWI FLY ASH

He Xinghua[1], Zhu Shujing[2,*], Jiann-Yang Hwang[3]

[1]School of Civil Engineering and Architecture, Wuhan Polytechnic University, 430023 Wuhan, China
[2]Department of Resource and Environment, Wisco R and D Center, 430080 Wuhan, China
[3]Department of Materials Science and Engineering, Michigan Technological University Houghton, Michigan 49931-1295

Keywords: MSWI fly ash; physical and chemical property; heavy metal; microscopic morphology

Abstract

This paper presents a study of the properties of municipal solid waste incineration (MSWI) fly ash, including their size distribution, pH value, microscopic morphology, mineral components, heavy metal content, and leaching toxicity. It is found that: over 80% of fly ash particles have diameters between 0.105~0.154mm, and the mass ratios of particles smaller than 0.063mm and larger than 0.154mm are both lower than 5%; the fly ash particles tend to be strongly alkaline (pH≥11); their main elements are Cl, Ca, K, Na, Si, Al, O and S, and their main heavy metal elements are Zn, Pb, Cr and Cu. The material generally exists as irregularly shaped amorphous solids and polycrystalline aggregates. Their leaching toxicity has exceeded the criteria for hazardous wastes.

Introduction

Incineration is a widely used method of municipal solid waste (MSW) disposal due to its obvious effect in reducing the volume and mass of solid wastes. Municipal solid waste incineration fly ash (MSWI fly ash) refers to the solid matter generated from the incineration process and collected by the heat recovery and flue gas purification systems. The amount of fly ash is dependent on types of wastes, conditions of incineration, types of incinerator, and flue gas treatment methods, generally amounting to 3%~5% of the waste before incineration. Analysis has shown that incineration fly ashes are not chemically inert, but rather contain a high amount of water-leachable toxic heavy metals and their salts including Cd, Pb, Zn, Cr, etc., making them a type of hazardous waste. [1]

Inappropriate treatment during the storage and reuse of MSWI fly ash may allow these high-concentration heavy metal contaminants to re-enter the environment and cause groundwater pollution. The physical and chemical properties of MSWI fly ash has significant impact on the adaptability, effects and economic property of treatment methods, and some in-depth work has been done in this area, including the research on MSWI fly ash granularity by Richer U et al.[2] and Le Forestier et al.[3], and Tay et al.'s study[4] focusing on MSWI fly ash's engineering characteristics. This paper presents a systematic study of MSWI fly ash's basic properties, including morphology, distribution of particle diameters, chemical compositions, and leaching toxicity, which can serve as reliable data for the hazard-free treatment and possible utilization of MSWI fly ash.

Materials and Methods

The Origin of Samples

Municipal solid waste incineration fly ash from Pudong New District Incineration Power Plant, Shanghai, was used. The plant employs a semi-dry flue gas purification system (workflow shown in Fig.1), in which a lime water solution (10% mass ratio) is sprayed by a rotary atomizer; the lime water droplets come into contact with hot flue gas inside a reaction tower, reacting with the acidic gases, as the moisture vaporizes to reduce the temperature of the flue gas. In addition, a powdered activated carbon (PAC) injection system can be found before the dust catcher, useful for removing volatile heavy metals such as Hg from the flue gas. The fly ash from the reaction tower and the dust catcher is combined, and discharged from an incineration fly ash outlet.

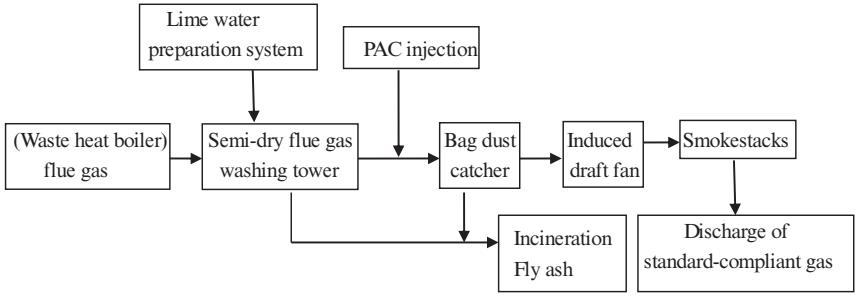

Fig.1 Flue gas purification system of the incineration plant

Testing Method

Diameters: The MSWI fly ash samples were screened manually by passing them through standard sieves. The mass ratios of particles at different diameters were measured, and their size distributions (including cumulative distribution) were calculated.

Leach liquor pH: The method for measuring pH value of the samples is based on SW-846 Method 9045C of U.S. Environmental Protection Agency: 5g of incineration fly ash samples were placed in a 150mL beaker; 100mL of deionized water was added into the beaker; the beaker was capped, then the liquid was stirred once every 5 minutes; after the stirring, the liquid was left to stand for about 15 minutes, allowing the suspended particles to sediment. The pH value of the liquid was measured using a PHC-3S acidity meter.

Toxicity test: The toxicity of samples was determined using the China leachability toxicity standard method as described below: for 100 g of the samples, 900 ml of water was added, the pH was adjusted using NaOH or HCl to a range of 5.8–6.3, and then the solution was diluted to 1000 ml. The pH value in the leaching solution must be kept in this range. If the pH deviates outside this range, NaOH or HCl solutions should be added during the leaching operation. The sample was leached by rotating in a mechanical shaker with an oscillating frequency of 110 ± 10 min^{-1} for 8 h at 25°C. The sample was allowed to settle for 16 h and filtered. The supernatant was analyzed by ICP-ES or AAS.

Chemical composition and morphology test: The contents of the main oxides in the fly ash were analyzed by X-Ray Fluoresence (XRF). The mineralogical constituents were analyzed by X-Ray Diffraction (XRD) and the morphology of the fly ash was observed by scanning electron microscopy (SEM).

In order to test the content of heavy metals in the fly ash, 2.0g fly ash samples were firstly dissolved in concentrated nitric acid solution while heating. When most of the samples were dissolved in the acid solution and then some distilled water were added into the container to fix the dimension with 100ml. The concentration of heavy metals in the filtrate was analyzed with atomic absorption spectrometry (AAS) or Inductively Coupled Plasma Emission Spectroscopy (ICP-ES), and thus the contents of heavy metals in fly ash was calculated.

Results and Analysis

Particle Size Distribution

The samples were mechanically screened using nylon sieves with varying opening sizes (54 m, 63 m, 90 m, 105 m, 125 m, 154 m and 600 m). The size distribution was calculated using the weights of residues on sieves (see Fig. 2).

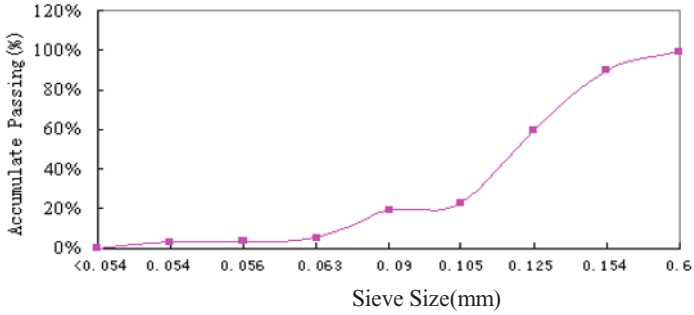

Fig. 2 Particle size distribution curve

Fig. 2 shows that particles smaller than 0.063mm and 0.154mm in diameter each have a mass ratio below 5%, while particles between 0.105~0.154mm have the highest mass ratio at around 80%. When the fly ash particle size is less than 0.09 mm, mass fraction with the decrease of the particle size decreases. When the fly ash particle size is greater than 0.105 mm, mass fraction decreases gradually with the increase of particle size. The low ratio of particles below 0.063mm is caused by the smaller particles aggregating into larger particles through collision and homogeneous nucleation, helped by the heterogeneous condensation of some smaller particles on larger particles.[5] The coarse particles in MSWI fly ash are primarily unburned mineral particles that had been carried off by air draft into dust catchers. The majority of such particles tend to be retained by incinerator bottom ash, which explains their low ratio in MSWI fly ash.

PH Value of MSWI Fly Ash Leach Liquor

Studies have shown that MSWI fly ash contains a high amount of calcium oxide, making it strongly alkaline with a pH of 10 to 12 or higher.[6,7] The samples in this test had a pH value of 11.2. The high alkalinity of MSWI fly ash may be caused by the dust collection equipment and chemical reactions during the incineration process. The purification system

in this facility has introduced a large amount of $Ca(OH)_2$ (via the lime water) as a stabilizer of heavy metals in fly ash. The carbonate salts and metal oxides would also contribute to the alkalinity of the samples. The high alkalinity makes the fly ash more resistant to variations in environmental pH. Considering that hydroxides of heavy metals tend to be highly unsoluble, the high pH should help suppress the leaching of heavy metals. However, this may not necessarily be the case with amphoteric hydroxides.

Cemical Composition and Morphology

Table 1 shows that the chemical composition of MSWI fly ash is similar to pulverized fuel ash and other soil minerals, with Si, Al, Ca, Cl, Na, K, Mg, Fe and S as its main elements, which is consistent with existing research.[8,9] The high CaO content came from excessive lime water injected by the purification system, used to ensure the acidic gases from the incineration can be completely neutralized. The high chlorine content originated from the high amount of kitchen waste and plastics in MSW. The fly ash also contains a notable amount of sulfur, which is due to sulfur having a dry basis mass ratio of 0.1%~0.24% in Shanghai's municipal solid waste. Allowing the sulfur to escape in the form of SO_x after incineration would accelerate the corrosion of the flue gas pipeline and add to the workload of the purification system. Instead, most sulfur has been retained in MSWI fly ash.

It can be seen from the X-ray diffraction (XRD) spectrum of theMSWI fly ash (Fig. 3) that the samples' main mineral components are $CaSO_4$, $Al_2O_3 \cdot SiO_2$, KCl, NaCl, SiO_2, Al_2O_3, $CaCO_3$ and $CaO \cdot Al_2O_3 \cdot 2SiO_2$. The heavy metal content is low enough, in addition to largely being contained in silicon aluminate or silicate crystals, or existing as complex compounds or amorphous solids, that even if the MSWI fly ash contains any heavy metal crystals, their structures would be so fine as to be below the XRD detection limit.

Table 1. Oxide content in MSWI Fly ash (%)

Sample	SiO_2	Al_2O_3	CaO	Fe_2O_3	MgO	SO_3	(Na or K)Cl
MSWI Fly Ash	23.0	7.3	36.9	2.1	3.3	14.8	12.6

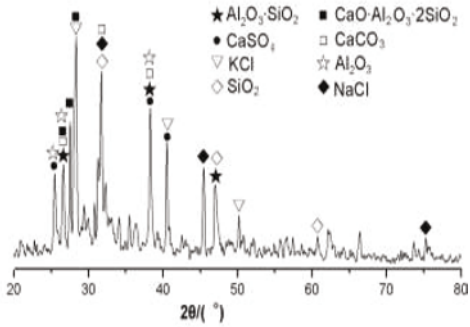

Fig.3 XRD Pattern of MSWI fly ash

Fig.4 depicts scanning electronic microscopic (SEM) images. It can be seen that the particle sizes of MSWI fly ash are non-uniform, as they are irregular solids combined from fine grains, products of incineration reactions, unreacted substances, and condensed products. Their rough and irregularly angular surfaces are full of porosities, which significantly increases their actual surface areas, and enables the condensation and aggregation of volatile metals on their surfaces.

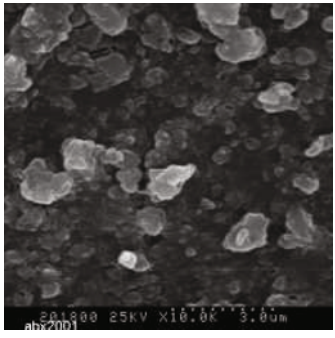

Fig.4 SEM photograph of fly ash

Heavy Metal Content in MSW IFA Samples

Table 2 shows that the concentrations of different heavy metals vary greatly in the fly ash. Cu, Pb, Zn and Cr are higher, with Pb at 3720mg/kg, followed by Zn, then by Cu. The

amount of Hg is the lowest. This may reflect the efficacy of the purification system, the content of the source MSW, or the different migration characteristics of heavy metals during the incineration. Katsunori's [10] study showed that during the incineration process, 33% of Pb in the wastes migrated into the fly ash, 1% was discharged with the flue gas, and the remaining 66% was retained in the bottom ash. 92% of Cd migrated into the fly ash, 2% was discharged with the flue gas, and 6% remained in the bottom ash. The research by Vogger et al.[11] showed that the migration and distribution of heavy metals in MSW incineration are dependent not only on the types of metals, but also on temperature and the wastes' non-metal content.

Table 2 Heavy metal content in MSWI fly ash (mg/kg)

Zn	Pb	Cu	Cd	Cr	Hg
3112	3720	422	20.6	232	18.8

In the case of the test samples, their relatively high Zn, Pb, Cr and Cu and smaller amounts of Cd and Hg may be explained by the temperature of incineration and the evaporation points of heavy metals. The majority of heavy metals which evaporation points are lower than the incinerator temperature would be evaporated and enter the flue gas. The heavy metals in the flue gas would condense into uniform grains on the ash particles, while some other heavy metals that would not condense can also be adsorbed by the particles, which would be captured by the dust collection system as incineration fly ash. The high Zn content may come from primarily zinc-manganese batteries, and the Pb may come primarily from plastics.

Leaching Toxicity of Heavy Metals in MSWI Fly Ash

Table 3 Leaching toxicity of heavy metals in MSWI fly ash

Heavy Metal	percent of heavy metal leached (%)	leaching concentration of MSWI fly ash(mg/L)	leaching toxicity discriminate standard of solid waste[12](mg/L)
Pb	42.7	159	≤3
Cr	20	4.64	≤1.5
Zn	4.6	14.3	≤50
Cu	0.9	0.394	≤50
Cd	4.0	0.082	≤0.3
Hg	—	not detected	≤0.05

Table 3 shows the results of the heavy metal leaching test. The Pb and Cr contents in the leached solution are both higher than the standard limits. For this reason, incinerator fly ash is commonly considered a hazardous waste that requires additional stabilization.

Conclusions

1. The main element components of MSWI fly ash are Si, Al, Ca, Cl, Na, K, Mg, Fe, C and S. The main mineral components are SiO_2, Al_2O_3, CaO, Fe_2O_3, MgO and SO_3. The MSWI fly ash generally takes the form of amorphous solids and polycrystalline aggregates, with little fully-formed crystals. The samples contain no heavy metal crystals that can be detected by XRD.

2. The MSWI fly ash's heavy metal components and their amounts are dependent on the composition of solid wastes and conditions in the incineration. Among the heavy metals, the MSWI fly ash contains the highest amounts of zinc and lead, followed by copper, chromium and cadmium, and the lowest amount of mercury.

3. Leaching test was performed on the MSWI fly ash samples using the horizontal vibration method, and the leached zinc and chromium exceed the relevant standard limits for toxicity. The leaching toxicity of MSWI fly ash depends not only on the initial mass ratios of heavy metals, but also on the forms of heavy metals in the fly ash.

References

[1] Anne J P. Evaluation of assisting agents for electrodialytic removal of Cd，Pb，Zn，Cu and Cr from MSWI fly ash. Journal of Hazard Materials B，2002,95：185-198
[2] Richer L, Birnbaum L. Detailed investigations of filter ash from municipal solid waste incineration [J]. Waste Management Res, 1998,16(2):190- 197.
[3] Le Forestier, Libourel G. Characterization of flue gas residues from municipal solid waste combustors [J]. Environ Sci Technol 1998, 32(15):2250- 2256.
[4] Tay J H, Goh ATC. Engineering properties of incinerator residues [J]. J Environ Eng ASCU, 1991, 117(2):224-235.
[5] Chang M B，Huang C K，Wu H T，et a1. Characteristics of heavy metals on particles with different sizes from municipal solid waste incineration. Journal of Hazardous Materials A，2000，79：229-239.
[6] Hansen H K, Pedersen A J, Ottosen L M，et a1. Speciation and mobility of cadmium in straw and wood combustion fly ash. Chemosphere，2001，45：123-128.
[7] Chandler A G，Eighmy T T，Harden J，et a1. Municipal solid waste incinerator residues. Studies in Environmental Science，Elsevier，Amsterdam，1997, 67: 974.
[8] Evans J，Williams P. T. Heavy metaI adsorption onto fly—ash in waste incineration flue gases [J] Process safety and Environmental Protection： Transactions of the

Institution of Chemical Engineers. Part B，2000，78(1)：40-46.
[9] Min Li，Jun Xiang，Song Hu，Characterization of S0lid residues from municipal so1id waste incinerator [J]. Fuel，2004，83(10)：1397-1405.
[10] Katsunori N, Yoshikazu N, Hitoshi O. Melting and stone production using MSW incinerated ash [J].Waste Management,2001,21(5):443~449
[11] Vogger H, Braun H. The specific role of cadmium and mercury in municipal solid waste incineration [J]. Waste Management & Research, 1985, 4(1):65~74.
[12] The second publishing campany for standard in China : GB5085.3-1996 , Dangerous waste discriminate criterion [S]. Beijing：Publishing company for standard in China，1997.

Characterization of Minerals, Metals, and Materials 2016

Welding and Solidification

Session Chairs:
Yuanbo Zhang
Ece Canan Koşmaz

Characterization of Minerals, Metals, and Materials 2016
Edited by: Shadia Jamil Ikhmayies, Bowen Li, John S. Carpenter, Jiann-Yang Hwang, Sergio Neves Monteiro, Jian Li, Donato Firrao, Mingming Zhang, Zhiwei Peng, Juan P. Escobedo-Diaz, and Chenguang Bai
TMS (The Minerals, Metals & Materials Society), 2016

INFLUENCE OF Al AND C ON MECHANICAL PROPERTIES OF SUB-RAPIDLY SOLIDIFIED Fe–20Mn–xAl–yC LOW-DENSITY STEELS

Libing Liu, Zhengyan Shen, Yang Yang, Changjiang Song*, Qijie Zhai

Shanghai Key Laboratory of Modern Metallurgy & Materials Processing, Shanghai University; 149 Yanchang Rd, Zhabei district; Shanghai, 200072, China; Email: riversxiao@163.com

Keywords: Low-density steels, mechanical properties, $D0_3$ phase, sub-rapid solidification.

Abstract

Fe-Mn-Al-C low density steels with high manganese and high aluminum content have received much attention recently because their potential of more than 10wt.% reduction of density, excellent mechanical properties and multiphase microstructures. For present study, sub-rapidly solidified Fe–20Mn–xAl–yC low-density steels with different Al (5, 9,12wt.%) and C(0.4, 0.6, 0.8, 1.0,wt.%) have been produced to understand the influence of Al and C on phases content and mechanical properties. These near-net shaped Fe–20Mn–xAl–yC steels all revealed duplex phases (δ+γ) during sub-rapid solidification, and some ordered DO_3 phases formed in δ-ferrite. The changes of aluminum and carbon content lead to the volume fractions changes of δ-ferrite, and the dissolved aluminum content have a vital influence on tensile properties, but there is no clear relationship between phase proportions and tensile properties. The yield strength, ultimate tensile strength and total elongation of 9Al-0.8C steel are 593MPa, 952 MPa, and 46%, respectively, which shows the best comprehensive performance of these sub-rapidly solidified Fe–20Mn–xAl–yC steels.

Introduction

Recently, Fe-Mn-Al-C alloys become a hot research subject for their great potential application in automobile industry with low density and superior mechanical properties[1]. Aluminum addition in steel can markedly reduce the density, promote the formation of ferrite, and increase the stacking fault energy (SFE) in austenite[2-4]. Furthermore, the too high Al content will result in the formation of intermetallic compounds Fe_3Al (DO_3 type), FeAl (B_2 type)[5]. Mn and C are strong austenite former, C can also markedly increase the SFE, hence, Fe-Mn-Al-C alloys can be ferritic, austenitic, duplex, or triplex phases depending on the Mn, Al and C content as well as the manufacturing process[6].

Researches on high manganese and high aluminum Fe–Mn–Al–C low-density steels[4, 7-10] have shown their potential of 15wt.% reduction of density, excellent mechanical properties and multiphase microstructures. It is a perfect combination of mechanical properties, safety and low fuel consumption for automotive industry[11, 12]. But, as an engineering structural material, it needs to take into account the mass production for industrial applications and low-density steels could not be produced by the conventional continuous casting because of the high Mn and Al content bring in the cracking during casting and hot strip rolling of slabs[1, 13]. So it is worth to develop the new process considering its potential as the advanced vehicle body and commercially viable materials.

In the present work, a new attempt to produce low density steels was conducted. The near-net shape Fe-20Mn-xAl-yC (nominal composition, hereafter in wt.%) low-density steels have been prepared by sub-rapid solidification to study the influence of Al and C content on phase content and mechanical properties.

Experimental

Fe-20Mn-xAl-yC alloy ingots were prepared by using high purity iron (99.99 wt.%), manganese (99.99 wt.%), aluminum(99.99 wt.%) and Fe-4wt.% C master alloy via the electric arc melting under argon protective atmosphere. The melts were homogenized by using electromagnetic stirring for several times. After homogenization, the ingots were re-melted in a quartz tube then injected into copper mold. The 2 mm thickness strips were obtained, which solidified at sub-rapidly cooling rate[14]. The width of the strip is 15mm, the length is 55mm. The density of 5Al-yC density is 7.17 g/cm^3, 9Al-yC is 6.73 g/cm^3, and 12Al-yC is 6.42 g /cm3 measured by the AccuPyc II 1340 Gas Displacement Density Analyzer, which are 8.1%, 13.7%, 17.7% lower than conventional steels, respectively.
Phases of the strips were analyzed by X-ray diffraction (XRD, Rigaku D/max-2200 X, Cu Ka target operated at 40 kV and 60 mA) and transmission electron microscopy (TEM, Tecnai G^2 F20 S-Twin). TEM samples were electrolytically thinned by double-jet polishing in a solution of 10 vol.% perchloric acid and 90 vol.% ethanol at the temperature range of -25℃ to -35℃ under a potential of 30V. Macrostructure of samples were observed by OM (optical microscope (Zeiss AXIO IMAGER A2M)) after mechanical polishing and chemical etching. Tensile tests were performed at a strain rate of 2.5×10^{-4}/s (the gage dimensions of 24mm×4mm×0.7 mm) by MTS Criterion Model 44 with a 12mm gauge extensometer at room temperature. The tensile tests were repeated at least 3 times to verify the reliability of the samples. Ferrite volume fraction was measured by Fischerscope Ferrit.

Results and discussion

Phase constitution

As shown in Fig. 1, the detected phases of sub-rapidly solidified Fe-20Mn-xAl-yC steels were all marked nearby the associated peaks of the x-ray diffraction patterns. XRD patterns were all normalized to the max intensity in order to qualitative analysis of the changes. All these sub-rapidly solidified Fe-20Mn-xAl-yC steels reveals duplex phases (δ-ferrite and γ-austenite), δ-ferrite and γ-austenite directly formed from the liquid metal, and retained to the room temperature. The marked DO_3[$(Fe/Mn)_3Al$][15] phase is actually the ordered ferrite[16].
Fig. 1a shows the XRD patterns of 20Mn-5Al-0.4/0.6C steels, it can be seen that the Fe-20Mn-5Al-0.6C steel almost exclusively contained austenite phase, the diffraction peaks intensity of δ-ferrite was very weak. When the carbon content reduced to 0.4wt.%, δ-ferrite diffraction peaks intensity enhanced, which revealed that the volume fraction of ferrite increased, and DO_3 can be detected. Because the substitutional Al atoms in δ-ferrite caused lattice distortion, the weak $(400)_{DO3}$ peak had a slightly offset value to the $(200)_\delta$ peak, it means that the formation of DO_3 could not be suppressed in sub rapid solidification.
Increasing the Al content in Fe-20Mn-xAl-yC made austenite diffraction peaks intensity weaken and ferrite diffraction peaks intensity enhanced, and the effect of carbon is just the opposite,

which were shown in Fig. 1b and (c). When the aluminum content increased to 12wt.%, the $(200)_{DO_3}$ diffraction peak appears, indicating that the supersaturated aluminum will promote the ordered DO_3 formation in the sub-rapidly solidified low-density steels.

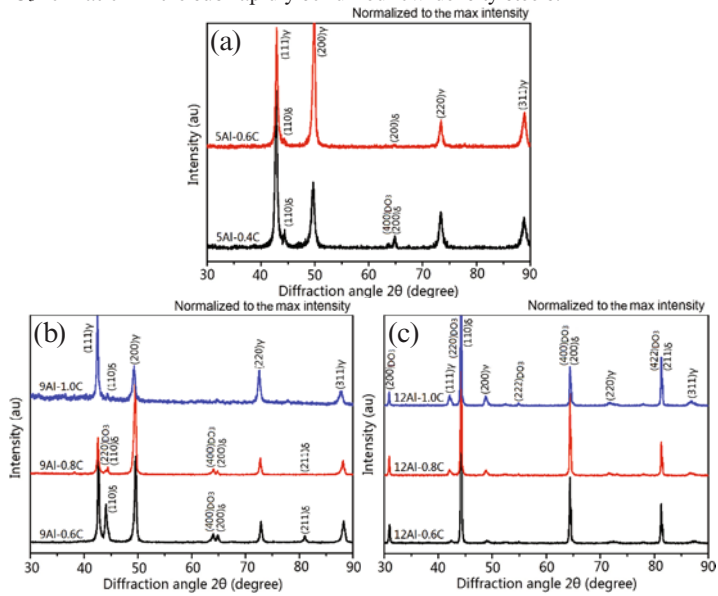

Figure 1. X-ray patterns of the Fe-20Mn-xAl-yC low-density steels: (a) 5Al-yC; (b) 9Al-yC; (c) 12Al-yC.

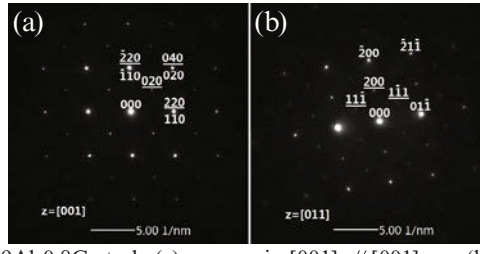

Figure 2. SADP of 9Al-0.8C steel: (a) zone axis $[001]_{\delta} // [001]_{DO_3}$; (b) zone axis $[011]_{\delta} // [011]_{DO_3}$, (hkl denotes DO_3 phase; hkl denotes δ phase)

TEM was conducted to further identify the ordered DO_3 phase. The typical selected area electron diffraction (SADP) zone axis $[001]_{\delta} // [001]_{DO_3}$ of 9Al-0.8C steel was shown in Fig 2a, it can be seen that DO_3 superlattice was superimposed on the ferrite fundamental reflections, which means that the ordered DO_3 phase coexist with ferrite, and the supersaturated aluminum in ferrite promote the disorder to order transformation. Another zone axis $[011]_{\delta} // [011]_{DO_3}$ was given in Fig 2b, it also reveals that coexistence relationship of ordered DO_3 and ferrite. (hkl denotes DO_3 phase; hkl denotes δ phase)

Macrostructure

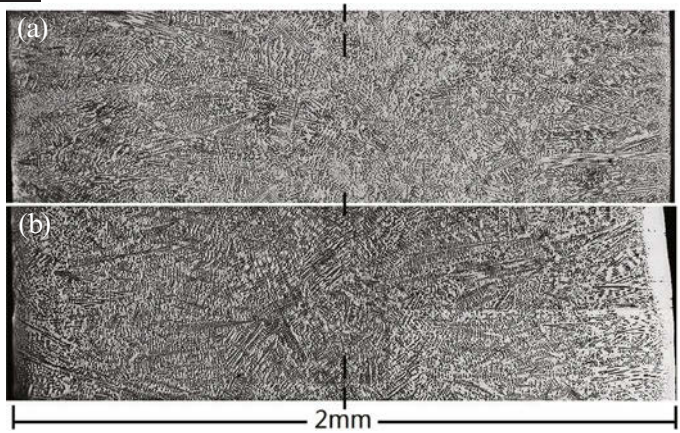

Figure 3. OM macrostructure on thickness direction: (a) 9Al-0.6C; (b) 9Al-0.8C.

Fig. 3 shows the sectional macrostructure on thickness direction of 9Al-0.6C and 9Al-0.8C steels, which could represent these sub-rapidly solidified steels in present work. There were three typical solidification zones in the section for 9Al-0.6C and 9Al-0.8C steels: (1) an indistinguishable morphology of fine grains area is distributed near the strip surface; (2) relatively coarse columnar grains extend from the edge of the fine grains area, the columnar grains are almost parallel to the direction of the heat flow; (3) a large number of messy dendrites and central equiaxed grains zone concentrate near the section central area.

Sectional macrostructure in Fig 3 clearly shows the beginning of solidification to the end from copper mold surface to strip center. It exactly verified the FA mode (liquid→L+δ→L+δ+γ→δ+γ) according to classification of solidification modes for stainless steels[17], especially in columnar grains area and central equiaxed grains area, where δ and γ dendrites are interleaved with each other, growth together. Macroscopically saying, the solidification microstructure of 9Al-0.6C and 9Al-0.8C steels had no significant difference with each other, but it can be seen that the dendrite in 9Al-0.6C steel slightly finer than 9Al-0.8C steel.

Tensile properties

Phase constitution and macrostructure on strip section of the sub-rapidly solidified Fe-20Mn-xAl-yC low-density steels have been studied in the preceding analyses, and they were closely related to the mechanical properties.

Engineering stress-strain curves of all these Fe-20Mn-xAl-yC steels were shown in Fig. 4. The phase proportions and tensile properties for present study were given in table 1. For the all these steels, the engineering stress-strain curves could be divided to three levels according to the three Al content, namely, the dissolved aluminum content had a vital influence on tensile properties. The 5Al-yC steels reveals low yield strength (YS) and low ultimate tensile strength (UTS), and general total elongation (TE). Just the opposite, the 12Al-yC steels reveals very high YS and UTS, but extremely low TE. Mechanical properties of 9Al-yC steels exactly in the middle of the 5Al-yC and 12Al-yC steels, show up the excellent comprehensive performance which have high

strength and high elongation. The YS, UTS and TE of 9Al-0.8C steel were 593MPa, 952 MPa, and 46%, respectively, which is the best comprehensive performance in present work. The specific strength (SS= UTS/density) exhibits the continuous increasing with raising the aluminum and carbon content, there is no clear relationship phase proportions and tensile properties, the dissolved aluminum content had a vital influence on tensile properties.

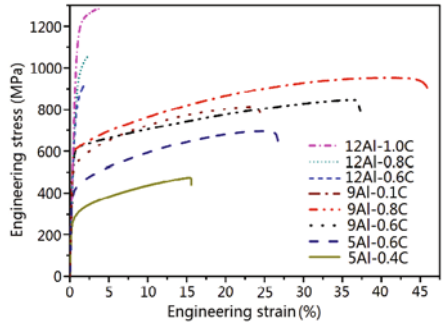

Figure 4. Engineering-strain curves of sub-rapidly Fe-20Mn-xAl-yC low-density steels.

Table I. Tensile properties and phase proportions.

Steel (wt.%)	Density (g/cm^3)	YS (MPa)	UTS (MPa)	TE (%)	SS (MPa • cm^3/g)	Ferrite (vol)
5Al-0.4C	7.17	270	475	16	66.2	10.3
5Al-0.6C		399	696	27	97.1	0.2
9Al-0.6C	6.73	519	814	25	121.0	36.7
9Al-0.8C		593	951	46	141.3	18.8
9Al-1.0C		605	846	37	125.7	8.37
12Al-0.6C	6.42	696	930	2	144.9	74.9
12Al-0.8C		921	1055	2	164.3	67.8
12Al-1.0C		1078	1285	4	200.2	47.5

Summary

The Fe–20Mn–xAl–yC steels reveals duplex phases (δ+γ) during sub-rapid solidification, and some ordered DO_3 phases formed in δ-ferrite. The aluminum and carbon content changes lead to the volume fractions of δ-ferrite changes, and the dissolved aluminum content have a vital influence on tensile properties, but there is no clear relationship of phase proportions and tensile properties. 9Al-yC shows the excellent comprehensive performance which have high strength and high elongation. The YS, UTS and TE of 9Al-0.8C steel are 593MPa, 952 MPa, and 46%, respectively, which shows the best comprehensive performance in present work.

Acknowledgments

This work was financially supported by the National Natural Science Foundation of China (No. 51574162). XRD and TEM were made in the Instrumental Analysis & Research Center at Shanghai University. The authors would like to express sincere thanks for their support.

References

1. D.-W. Suh and N. J. Kim, "Low-density steels," *Scripta Materialia*, 68(2013), 337-338.
2. K.-T. Park, "Tensile deformation of low-density Fe–Mn–Al–C austenitic steels at ambient temperature," *Scripta Materialia*, 68(2013), 375-379.
3. K.-T. Park, et al., "Stacking fault energy and plastic deformation of fully austenitic high manganese steels: Effect of Al addition," *Materials Science and Engineering: A*, 527(2010), 3651-3661.
4. M. C. Ha, et al., "Tensile deformation of a low density Fe–27Mn–12Al–0.8C duplex steel in association with ordered phases at ambient temperature," *Materials Science and Engineering: A*, 586(2013), 276-283.
5. R. Rana, C. Liu and R. K. Ray, "Low-density low-carbon Fe–Al ferritic steels," *Scripta Materialia*, 68(2013), 354-359.
6. R. Rana, "Low-Density Steels," *Jom*, 66(2014), 1730-1733.
7. S. H. Kim, H. Kim and N. J. Kim, "Brittle intermetallic compound makes ultrastrong low-density steel with large ductility," *Nature*, 518(2015), 77-9.
8. Y. Sutou, et al., "High-strength Fe–20Mn–Al–C-based Alloys with Low Density," *ISIJ International*, 50(2010), 893-899.
9. I. Gutierrez-Urrutia and D. Raabe, "Multistage strain hardening through dislocation substructure and twinning in a high strength and ductile weight-reduced Fe–Mn–Al–C steel," *Acta Materialia*, 60(2012), 5791-5802.
10. S. W. Hwang, et al., "Tensile deformation of a duplex Fe–20Mn–9Al–0.6C steel having the reduced specific weight," *Materials Science and Engineering: A*, 528(2011), 5196-5203.
11. I. Gutierrez-Urrutia and D. Raabe, "Influence of Al content and precipitation state on the mechanical behavior of austenitic high-Mn low-density steels," *Scripta Materialia*, 68(2013), 343-347.
12. I. Zuazo, et al., "Low-Density Steels: Complex Metallurgy for Automotive Applications," *Jom*, 66(2014), 1747-1758.
13. S. H. Wang, et al., "Microstructure and Mechanical Property of Strip in Fe–23Mn–3Si–3Al TWIP Steel by Twin Roll Casting," *ISIJ International*, 49(2009), 1340-1346.
14. L. B. Liu, et al., "Structure evolution of Fe–15wt-%Mn sub-rapidly solidified strips under different cooling rates," *Materials Research Innovations*, 19(2015), S199-S204.
15. A. S. Ilyushin and W. E. Wallace, "Structural and magnetic properties of the Fe3−xMnxAl system," *JOURNAL OF SOLID STATE CHEMISTRY*, 17(1976), 385-387.
16. A. Etienne, et al., "Ferrite Effects in Fe-Mn-Al-C Triplex Steels," *Metallurgical and Materials Transactions A*, 45(2013), 324-334.
17. K. Rajasekhar, et al., "Microstructural evolution during solidification of austenitic stainless steel weld metals: A color metallographic and electron microprobe analysis study," *MATERIALS CHARACTERIZATION*, 38(1997), 53-65.

Characterization of Minerals, Metals, and Materials 2016
Edited by: Shadia Jamil Ikhmayies, Bowen Li, John S. Carpenter, Jiann-Yang Hwang, Sergio Neves Monteiro, Jian Li, Donato Firrao, Mingming Zhang, Zhiwei Peng, Juan P. Escobedo-Diaz, and Chenguang Bai
TMS (The Minerals, Metals & Materials Society), 2016

DYNAMIC DEEP ETCHING AND PARTICLE EXTRACTION FOR HIGH-STRENGTH ALUMINUM ALLOYS

Tonica Boncina, Franc Zupanic

University of Maribor, Faculty of Mechanical Engineering, Smetanova 17, SI-2000, Maribor, Slovenia

Keywords: Aluminum alloys, Quasicrystals, Metallography, Deep etching, Particle Extraction

Abstract

Aluminum alloys contain many phases that can form during different processing steps. Their type, size, and morphology have a significant influence on various properties of the alloys. Thus, the determination of all their geometrical features is very important. Knowing the 3D particle shapes is essential not only for choosing the best processing routes for conventional alloys but also for designing new alloys.
A patented procedure of dynamic deep etching and extraction of particles was used for analyzing particles in quasicrystalline aluminum alloys and several high-strength aluminum alloys.
The mode and sequence of individual stages of the procedure enabled the uniform dissolution of aluminum matrix throughout the entire volume of a specimen. An ultrasonic treatment facilitated the penetration of the electrolyte into the specimen. The results were deep-etch and powder samples that enabled thorough characterization of particles using different techniques.

Introduction

Aluminum alloys have more heterogeneous microstructures than other alloys. Such microstructures usually originate from many alloy additions and impurities, which combine to produce a lot of phases with wide ranges of chemical compositions. While the microstructures of basic aluminum alloys are well known, the microstructures of novel aluminum alloys may consist of several new hard intermetallic phases (hardness even higher than 1000 HV) in a soft aluminum matrix (hardness around 70 HV). These phases need to be characterized in greater detail. The abundance of phases partly arises from different manufacturing processing methods, in which the conditions are more or less far from the thermodynamic equilibrium. In such cases, many complex intermetallic phases and even aperiodic phases (e.g. quasicrystals) may form.
Precise knowledge of the microstructure is crucial for the development of new alloys. Classical metallographic preparation by grinding, polishing and etching, which give the 2D cross-sections of phases, is not sufficient in many cases.
In this work, we describe a method of dynamic deep etching and particle extraction from aluminum alloys. The method has been developed especially for understanding the aluminum alloys with quasicrystalline phases, but has also been applied for phase identification in novel high-strength aluminum alloys with addition of Zr or Ce. The quasicrystals normally have 5-, 8-, 10- or 12-fold rotational symmetries which also dictates the morphology of the quasicrystalline

phases. Consequently, this method enables the distinction of quasicrystalline phases from crystalline phases based on their morphology.

Experimental work

Within the experimental work, we tested a number of etchants, which are described in the open literature. Descriptions and the main characteristics of the etching process are available in the monographs and handbooks in the field of metallography [1, 2]. One of the most important sources is an overview article of Gupta et al. [3], who collected the most useful methods and solutions used for different aluminum alloys.
We used etchants with the same composition as in the literature data and etchants with modified compositions, containing acidic or basic components. The best results were achieved with a solution containing the iodine and the tartaric acid in methanol. The effectiveness of etching was conveniently influenced by the application of the so-called "dynamic etching", by setting the beaker with an etchant into an ultrasonic bath.
The procedure incorporates several steps. Firstly, an aluminum sample was rinsed into a solution containing from 3 to 10 g of iodine and from 10 to 17 g of tartaric acid in 100 ml of methanol. The beaker with the solution and the sample was placed into an ultrasonic bath. The sequential periods of etching exposed to ultrasonic vibrations from 1 to 15 minutes and periods of resting from 10 min to 24 hours, when ultrasonic vibrations were not applied. The sequence of rinsing and dissolving, followed by exposure to ultrasonic action was alternately repeated 10 to 50 times. After deep etching, the sample was finally treated in the ultrasonic bath to remove the final particles, washing with alcohol and drying by using warm air. The result was a clean fracture surface with partly removed aluminum matrix and undissolved particles.
By particles extraction, the solution was filtered using a glass filter, which was connected to a vacuum pump, and was able to retain particles even smaller than 500 nm. The water-soluble iodides were dissolved by washing the sediment by alcohol and water and then filtered and dried in the air. The possible presence of iodides was checked by performing XRD.
The samples were investigated employing scanning electron microscopy – SEM (Sirion, FEI), energy dispersive X-ray spectroscopy – EDS (Oxford), and X-ray diffraction – XRD (Sincrotrone Elletra, Trieste, Italy).

Results and discussion

Examination of the polished surface prepared with the classical metallographic preparation was necessary to obtain a general overview of the microstructural constituents and enables reliable EDS analysis. However, it is very difficult to determine the 3D-shapes of microstructural constituents based on 2D metallographic sections. Several methods have been described in the open literature that enable obtaining 3D-shapes of microstructural constituents. Kral et al. [4] obtained 3D-shapes of phases in a steel by using a computer-aided visualization of 3D-reconstructions from serial section images. The material was gradually removed in steps of approximately 0.2 mm, and the photos of the section were taken after each step. The sequential cross-sectioning was also done by using focused ion beam (FIB), usually dual beam SEM/FIB systems. When a system is equipped with EDS, then the 3D-elemental distribution can be obtained along with the particle shapes [5]. Such approach is feasible but is very time-consuming and difficult to use for routine investigations.

Chemical etching of aluminum alloys is based on selective dissolution of the samples in a multi-component etching solution. Microstructural constituents in a material possess different electrode potentials; some act as cathodes, whereas other as anodes, the latter constituents dissolves during etching. The etchant is usually composed of three types of ingredients: corrosive, modifying and oxidative components. The most significant etching parameters are types of components and their concentrations in an etchant, rinsing duration, temperatures of the electrolyte and a sample. According to the intensity of a process or the mode of execution, etching method can be divided to:

1. Deep etching. By using this procedure, a considerable amount of an aluminum matrix is dissolved, whereas other microstructural constituents remain intact and stay at the same positions in a material as before etching.
2. Extraction of microstructural constituents by controlled corrosion. During extraction, the aluminum matrix is completely dissolved, and an extracted powder sample is obtained. In this case, it is not possible to determine from which part of the sample an individual particle arises. On the other hand, we can determine geometrical features, structure and chemical composition of the particles.

The extraction of particles in aluminum alloys is rather difficult because the main types of particles, such as inclusions, dispersoids and precipitates can dissolve in the solution faster than the aluminum matrix.

The method is based on the total (extracted particles) or partial (deep-etched surface) removal of the aluminum matrix without damaging or dissolution of other phases [6]. A term “dynamic” is used because of the application of ultrasonic vibrations that makes the movement of an electrolyte more vigorous and accelerates the process dynamics. The combination of the etchant and vibrations enable dissolution of the aluminum matrix throughout the whole volume of the sample, whereas the remaining phases remain chemically and geometrically unchanged. It also prevents the presence of the reaction products in the sample. Ultrasonic vibrations caused the damage of the oxide layer, producing small pinholes in it, which later widened and formed craters. The additional role of ultrasonic vibrations is to accelerate the removal of the extracted particles from the surface and the sample interior into the solution. Selected components of an etchant (I_2, tartaric acid ($C_4H_6O_6$) and methanol) caused that phases in alloys acted as cathodes, and aluminum matrix as the anode. This enabled complete dissolution of the aluminum matrix, whereas other phases remain unchanged, and that they can be removed out of the etching solution by filtering. A very influential component was iodine. Iodine is the least reactive among the halogens. It namely possesses the largest ionic diameter (0.22 nm), the smallest electronegativity (2.5) and the slowest diffusivity through the passivation layer, and the best ability to adsorption into the oxide layer. In the selected solution, it acts as an oxidant that accelerates dissolution. Its stability enables controlled dissolution. The main drawback is that the dissolution processes are long-lasting, they require even several days. The task of the tartaric acid was to prevent hydrolysis of aluminum ions during dissolution. The gelation of an aluminum hydroxide would take place without tartaric acid, which may ultimately stop the dissolution process. Figure 1 shows a schematic presentation of the chemical dissolution.

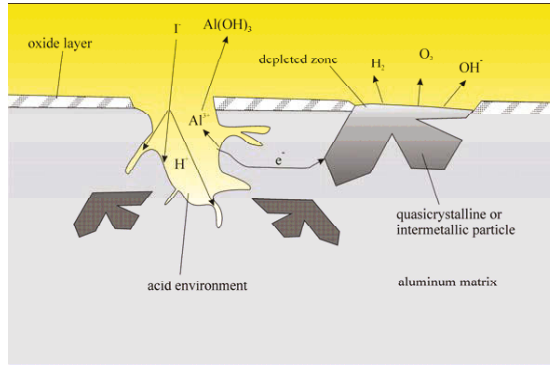

Figure 1: The schematic presentation of deep etching of an aluminum alloy, which contains an intermetallic phase

Under the action of the solution and ultrasonic vibrations, the etchant enters into a sample through surface pinholes and cracks and penetrates through the whole volume of the sample (Figures 2a and b). Reactions take place throughout the entire volume of the sample. The sample becomes very brittle, and can be easily fractured.

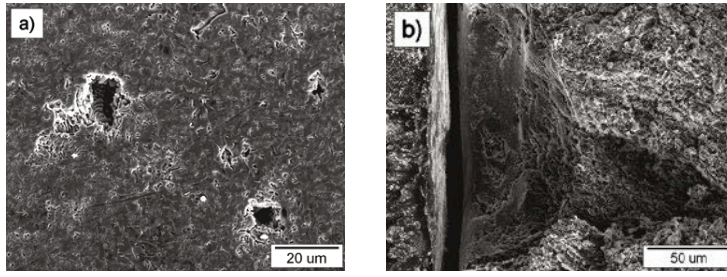

Figure 2: The backscattered electron micrographs of a) pinholes on the surface of an aluminum alloy and b) the transverse fracture at the site of a crater, through which the solution migrate into the sample

The result of the investigated procedure is a fractured surface or a powder sample (Figure 3). The fractured surface of the sample with partly removed aluminum is suitable for the microscopic analysis and microchemical analysis. The extracted powder samples are used for TEM (transmission electron microscopy) and XRD analysis. The figure 4 shows a comparison of the microstructure metallographic prepared sample alloys or 2D-section and the extracted phases of the same alloy and 3D-image.

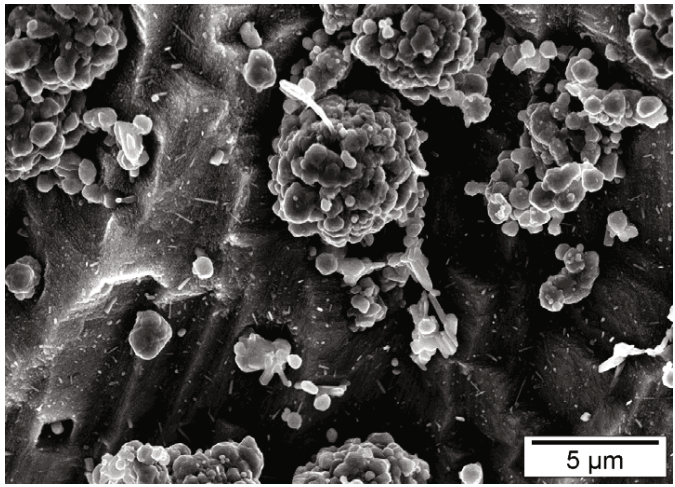

Figure 3: The backscattered electron micrograph (SEM) of a deep-etched microstructure of a heat treated alloy Al-Mn-Be-Cu, with readily visible morphology of the quasicrystalline particles and small rodlike precipitates in the matrix

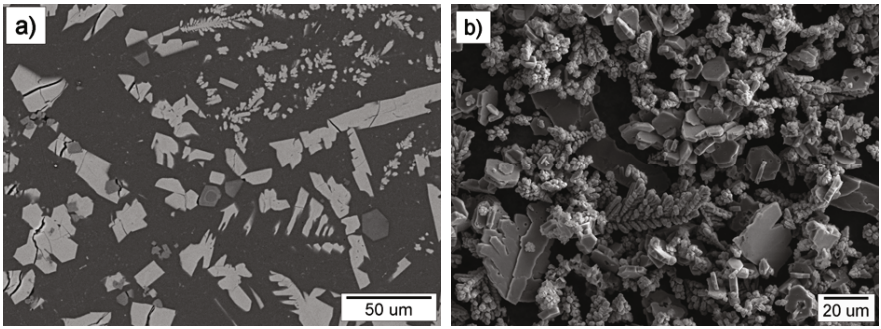

Figure 4: The backscattered electron micrographs (SEM) of a) the microstructure of the metallographically prepared sample of the alloy Al-Mn-Be (2D-section) and b) the extracted phases of the same sample and their 3D-shapes.

Conclusions

The combination of different methods of sample preparation, as the classic metallographic preparation, deep etching and extracting the particles allows the successful characterization of aluminum alloys containing a large number of different phases. We have developed a method of chemical dynamic deep etching and extracting the particles, which enables successful

preparation of deep-etched surfaces and extracted powder samples without dissolving intermetallic phases present in the alloys.

References

[1] George, F., Vander, Voort. Metallography Principles and Practice, McGraw-Hill, 1984.
[2] ASM Handbook, Volume 9, Metallography and Microstructures. Volume Editor George, F., Vander Voort, ASM International, Materials Park 2004.
[3] Gupta, A., K., Marois, P., H., Lloyd, D., J. Review of the Techniques for the Extraction of Second-Phase Particles from Aluminum Alloys, Materials Characterization, 1996, vol. 37, str. 61-80.
[4] Kral, M. V.; Mangan, M. A.; Spanos, G.; Rosenberg, R. O.: Three-dimensional analysis of microstructures. Materials Characterization 45 (2000) 17–23.
[5] Lasagni, F.; Lasagni, A.; Marks, E.; Holzapfel, C.; Mucklich, F.;Degischer, H. P.: Three-dimensional characterization of 'as-cast' and solution-treated AlSi12(Sr) alloys by high-resolution FIB tomography. Acta Materialia 55 (2007) 3875–3882.
[6] Bončina, T., Zupanič, F., Markoli, B. Procedure of dynamic deep etching and particle extraction from aluminium alloys : European patent EP2458033, granted 6.9.2013 ; published on 9.10.2013; application no. 11468004.4-2122, 4. October 2011. Munich: Europäisches Patentamt: = European Patent Office: = Office européen des brevets, 2013.

Characterization of Minerals, Metals, and Materials 2016
Edited by: Shadia Jamil Ikhmayies, Bowen Li, John S. Carpenter, Jiann-Yang Hwang, Sergio Neves Monteiro, Jian Li, Donato Firrao, Mingming Zhang, Zhiwei Peng, Juan P. Escobedo-Diaz, and Chenguang Bai
TMS (The Minerals, Metals & Materials Society), 2016

OPTIMIZATION OF TiN_P/Ti CONTENT FOR Si_3N_4/42CrMo JOINTS BRAZED WITH Ag-Cu-Ti+TiN_P COMPOSITE FILLER

Tianpeng Wang, Jie Zhang, Chunfeng Liu

School of Materials Science and Engineering,
Harbin Institute of Technology, Harbin 150001, PR China

Keywords: Si_3N_4 ceramic, brazing, composite filler, 42CrMo steel

Abstract

The Si_3N_4 ceramic was brazed to 42CrMo steel by using TiN particles modified braze, and the proportion of TiNp reinforcement and active element Ti was optimized to improve the joint strength. The brazed joints were examined by means of SEM and EDS investigations. Microstructural examination showed that TiN+Ti_5Si_3 reaction layer was adjacent to Si_3N_4, whereas TiC was formed in 42CrMo/filler reaction layer. The Ag-Cu-Ti brazing alloy showed intimate bonding with TiNp and Cu-Ti intermetallics precipitated in the joint. The strength tests demonstrated that the mechanical properties of joints increased and then decreased by increasing the TiNp content when a low Ti content (6wt.%) was supplied. When the Ti content (>6wt.%) was offered sufficiently, the joint strength decreased firstly and then stayed stable with increasing the TiNp content. The maximum four-point bending strength (221MPa) was obtained when the contents of TiNp and Ti were 10vol.% and 6wt.%, respectively.

Introduction

Si_3N_4 ceramic is a kind of hard, lightweight material capable of withstanding severe abrasion and maintaining chemical inertness at elevated temperatures [1]. However, because of its brittle nature, it is difficult to produce ceramic components with large size or complex shape. So the joining of Si_3N_4 ceramic is frequently required, especially to metals. However, because of ceramic's strong covalent bonding and its low self-diffusivity of the constituent atoms, the joining of Si_3N_4 ceramic, even to itself, is not an easy problem to solve. Joining to metals is then even more difficult. Active metal brazing is a well-established technique for joining ceramics both to themselves and to metals [2, 3]. The main difference between active metal brazing as opposed to conventional brazing, is that the active brazing alloys consist of a certain quantity of active elements, such as titanium or zirconium. The active element is characterized as having sufficient thermodynamic driving force to destabilize the covalent bonding of the ceramic, and then reacts with one or more of the ceramic elements to form a reaction layer [4]. For joining Si_3N_4 to itself or metals, Ag/Cu eutectic brazing alloy with Ti active component has been most frequently adopted.

The second issue is that of the mismatch in coefficient of thermal expansion (CTE) between the ceramic and the metal to which it is joined, especially for the joining of ceramic to metal [5]. It is well known that the ceramic with intrinsic brittleness cannot relieve the residual stress through plastic deformation like most metals, tensile stresses will be induced in the ceramic at the free surfaces of joined components. These stresses can cause the propagation of flaws into the ceramic and the formation of characteristic 'dome-shaped' crack profiles, detaching the

ceramic from the metal. So the reduction of residual stress is a big issue in the ceramic-metal joining. It is well known that the thermal expansion of the filler materials will be reduced through the addition of low CTE materials (e.g. carbon fiber, W, Al_2O_3 or SiC) in the filler, which contributes to relieving some stresses caused by the thermal mismatch between the filler materials and the substrates. So the joining with composite filler has attracted extensive attention in these years. Reinforced particles, such as SiC or Mo, have been successfully incorporated into Ag-Cu-Ti brazing alloy for acquiring high quality brazed joints [6, 7]. However, the active element Ti in the brazing alloy can react with all of these reinforcing particles at the bonding temperatures [8], thereby making their interfaces scavenge the available titanium and negatively influencing the reaction between Ag-Cu-Ti and the ceramic substrates. TiN is one of the reaction products of Si_3N_4 and Ti. Thus the TiNp (p=particle) was adopted as the reinforcing particles to limit the interaction with active Ti component in the joint. In addition, the thermal expansion coefficient of TiN (9.35×10^{-6}/K) is significantly lower than that of Ag-Cu-Ti (20.0×10^{-6}/K) [9, 10]. Therefore, the thermal expansion of the filler materials is reduced through the addition of TiNp.

However, TiN includes the nonstoichiometric composition of a broad range extending from $TiN_{0.37}$ to $TiN_{1.2}$ [11], and the Ti-contained alloys produce a strong denitridation of TiN at the interface between metal and TiN according to the Ref. [12]. Even the improvement of the mechanical properties and relatively small amount of Cu-Ti intermetallics in the Si_3N_4/42CrMo brazed joint have been obtained in our previous study [13], the interaction between the TiN and Ti still needs to be investigated. In this paper, a commercial Ag-Cu eutectic brazing alloy accompanying with different contents of TiNp and Ti was evaluated for the joining Si_3N_4 ceramic to 42CrMo steel. The effect of TiNp and Ti content on microstructure and mechanical properties of the joints was investigated. The interface structure and microstructure evolution mechanism were comprehensively investigated by using scanning electron microscopy (SEM) and Energy-dispersive X-ray spectroscopy (EDS).

Materials and Experimental Procedures

The ceramic material used in the research was commercially polycrystalline Si_3N_4 and they were sliced into small pieces with dimensions of 3mm×4mm×18mm. The metal partner was 42CrMo steel whose chemical composition was Fe- 0.42C- 1.0Cr- 0.7Mn- 0.3Si- 0.5Mo (mass fraction, %). The raw 42CrMo steel was also cut into specimens with sizes of $3.0\times4.0\times18.0mm^3$ by performing wire electrical discharge machining. Then coarse grinding and fine grinding were performed on the bonding surface ($3.0\times4.0mm^2$) with SiC paper, down to a grit size of 1200. Then the diamond suspension with an average grain size of 1μm was used in the last preparation step. Prior to brazing, the specimens were degreased and cleaned with acetone in an ultrasonic bath for 15 min.

Ag-28Cu (wt.%) alloy powder, whose mean particle size is 50μm, Ti powders with an average size of 50μm and TiN particles with a mean particle size of 10μm were milled for 2h in vacuum using a planetary ball mill to prepare the new composite filler. The overall weight percent of the Ti particles in the composite filler varied from 4% to 10%, whereas the volume fractions of the TiN particles in the composite filler were 5%, 8%, 10%, 15%, respectively. The overall weight of the composite filler for each brazed joint was fixed to be 20mg. The as-milled Ag-Cu-Ti+TiNp composite filler was mixed with a small amount of high viscosity cellulose nitrate binder for preparing a composite brazing paste. Then the composite paste was placed

between Si_3N_4 and 42CrMo steel and the assembly was put in a graphite jig. In addition, a normal load of 0.015MPa was applied on the top of the assembly in case of unfavorable destabilization. Brazing experiments were carried out at 1173K for 5 min. The heating rate was 10K/min and cooling rate was 5K/min. The vacuum in the furnace was kept at $(1.3\text{-}1.7)\times10^{-3}$Pa during brazing.

The strength of the brazed joint was measured by a four-point bending test with a cross-head speed of 0.5mm/min. The configuration for the joint strength testing was the same as the one drawn in Ref.[13]. At least five samples were used to determine the bending strength of joint for each joining condition. The cross-sections of the Si_3N_4 ceramic/steel joints were cut perpendicularly to the bonded interface and the samples for microstructure analysis were prepared by standard polishing techniques. The joint microstructure, chemistry and morphology were investigated using SEM coupled with EDS.

Results and discussions

Fig.1 displays the microstructure of a Si_3N_4/42CrMo joint brazed with Ag-Cu-Ti4+8vol.% TiNp composite filler at 1173K for 5min. Good wettability of the filler alloy and its intimate contact with the substrates are detected in the brazed joint, and continuous and sound interfacial reaction layers are formed at the interfaces between the brazing alloy and the substrates. The microstructural details of the both interfaces are magnified in Fig.1 (b) and (d). As shown in Fig.1, the Si_3N_4/42CrMo joint can be divided into three characteristic zones: (I) interfacial reaction layer with an average thickness of 3 m adjacent to the Si_3N_4; (II) solid solution in the center of the joint where some TiNp and intermetallics exist; (III) a thin reaction layer with an average thickness of only 1 m at the filler/42CrMo steel interface.

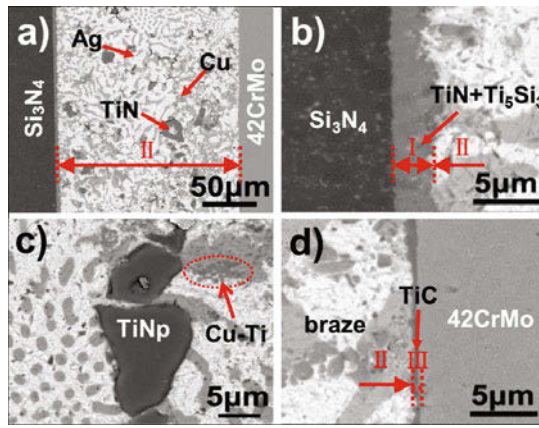

Fig. 1. Microstructure of the Si_3N_4/ 42CrMo joint brazed with Ag-Cu-Ti4+8vol.%TiNp composite filler at 1173K for 5min: (a) integral joint, (b) reaction layer at Si_3N_4 side, (c) the morphology around TiNp and (d) filler/ steel interface.

The interfacial microstructures of the Si_3N_4/Si_3N_4 or Si_3N_4/metal joints brazed with Ag-Cu-Ti braze alloy have been extensively studied. The formation of a thin TiN layer next to Si_3N_4 as well as granular Ti_5Si_3 beside the inner alloy has been reported [14, 15]. The reaction phases at the interface of 42CrMo/ braze were determined to be randomly oriented TiC with the grain size ranging from 50 to 100 nm in our previous study [13]. The central part of the joint is mainly composed of bright Ag-based solid solution, grey Cu-based solid solution and black TiN particles. If we magnify the TiNp reinforcement in the filler part, as shown in Fig. 1(c), a well-contacted interface between Ag-Cu-Ti brazing alloy and TiNp can be observed. Besides, a small amount of fine intermetallics can also be detected in the vicinity of the TiNp, as shown by the red dotted line in Fig. (c). The EDS results show that these intermetallics are mainly composed of Cu and Ti elements. According to the Cu-Ti binary phase diagram [16], Cu can easily react with Ti thermodynamically to form Cu-Ti intermetallics owing to their strong mutual affinity, indicating that the displayed intermetallics are Cu-Ti compounds.

In summary, the typical microstructure of Si_3N_4/42CrMo joint brazed at 1173K for 5 min is: Si_3N_4 ceramic/ TiN+Ti_5Si_3 reaction layer/ Ag(s.s) + Cu(s.s) + TiNp +Cu-Ti intermetallics/ TiC reaction layer/ 42CrMo steel (s.s: solid solution).

Fig. 2 shows the effects of TiNp content in the composite filler on the microstructure of Si_3N_4/42CrMo joint when the content of Ti in the composite filler is fixed at 6wt.%. A similar interfacial structure is observed regardless of the variation of TiNp content. However, the microstructure observations reveal a noticeable difference in the thickness of the interfacial reaction layers at Si_3N_4 ceramic and 42CrMo steel side. The thickness of the reaction layer at the Si_3N_4 ceramic side (I) decreased with increasing TiNp content, whereas the thickness of the reaction layer at steel side also decreases a little, but not vary too much. Furthermore, Ag(s.s) and Cu(s.s) phases are uniformized and refined on account of those undissolved TiNp, which act as nucleation sites for Ag(s.s) and Cu(s.s). In this perspective, a higher TiNp content provides more nucleation sites, which is advantageous for grain refinement in the joint.

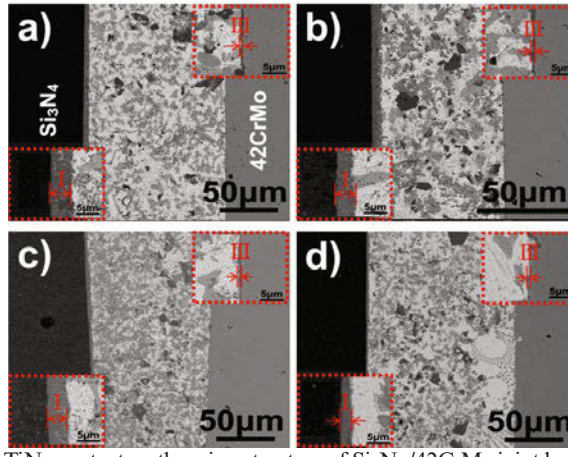

Fig.2. Effect of TiNp content on the microstructure of Si_3N_4 /42CrMo joint brazed with Ag-Cu-Ti6 (wt.%)+x vol.%TiNp composite (x=): (a) 5, (b) 8, (c) 10 and (d) 15 (vol.%).

SEM micrograph at higher magnification around the TiNp is shown in Fig. 3. It is interesting to note that only a small amount of fine Cu-Ti intermetallics can be detected when the content of TiNp in the composite filler is less than 8vol.%, which is shown in Fig.3a-b). As the content of TiNp raises to 10vol.%, fine Cu-Ti intermetallic compounds occurred a lot. When the TiNp content further climbs to 15vol.%, more Cu-Ti intermetallic compounds appear in the brazed joint, especially around the TiNp, as indicated in Fig. 3 (d). So we know that even TiN is one of the reaction products between Si_3N_4 and Ti, there are still some interactions between TiN and Ti. According to the Ref. [17], the activity of titanium in the Ag-Cu-Ti molten filler at the brazing temperature (1173K) is estimated to be 0.2. At the same time, the Ref. [18] suggests that the activity of Ti in TiN is around minus three orders of magnitude. Then we know that the activity of Ti in the Ag-Cu-Ti molten filler is much larger than that in TiN. If titanium nitride is considered to be a solution of nitrogen in titanium, the difference of titanium chemical potentials in the liquid filler and TiN can be written as:

$$\Delta\mu_{Ti} = \mu_{Ti}^{l} - \mu_{Ti}^{TiNp} = \mu_{Ti}^{0}(\mathrm{l}) - \mu_{Ti}^{0}(TiNp) + RT\ln a_{Ti}^{l} / a_{Ti}^{TiNp} \tag{1}$$

where μ_{Ti}^{0} is the chemical potential of component in the standard state, and a_{Ti}^{l}, a_{Ti}^{TiNp} are the activities of titanium in the molten filler alloy and TiNp, respectively. R is the gas constant and T is the absolute temperature. In the Eq. (1), the change of chemical potential of titanium associated with different standard states is: [19]

$$\mu_{Ti}^{0}(\mathrm{l}) - \mu_{Ti}^{0}(s) = -16218 + 8.36T \tag{2}$$

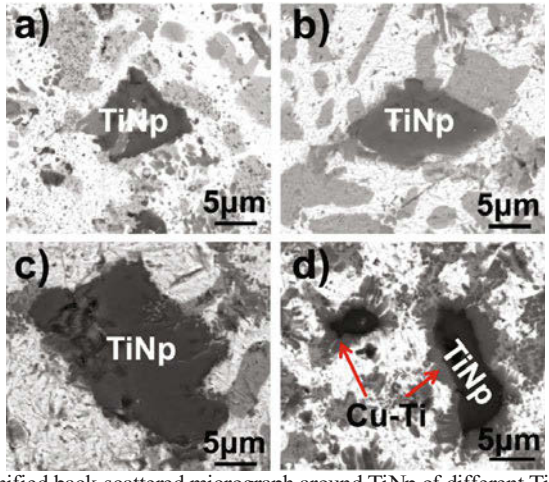

Fig.3. Magnified back-scattered micrograph around TiNp of different TiNp content: (a) 5%, (b) 8%, (c) 10% and (d) 15% (vol.%).

Combining the Eq. (1), Eq. (2), it is easy to know that the Eq(1) >>0 at 1173K, indicating that the chemical potential of titanium in the liquid alloy is much higher than that in the nitride.

Once some TiN particles are added into molten Ag-Cu-Ti alloy, Ti will diffuse towards and enrich in the vicinity of the TiNp. Besides, Cu can easily react with Ti thermodynamically to form Cu-Ti intermetallics, so we can easily understand that Cu-Ti intermetallics prefer to precipitate around the TiNp, which is more noticeable in the joints with the high TiNp content, e.g. 15vol.%.

Fig. 4(a) indicates the dependence of four-point bending strength of the Si_3N_4/42CrMo joints with different TiNp content when the content of Ti in the composite filler is still 6wt.%. It can be observed that the joint strength firstly increases and then drops with increasing TiNp content from 5 to 15 vol.%. The highest bending strength of 221MPa is obtained with 10 vol.% TiNp, which is 156.98% higher than that for the case with 8vol.% TiNp (86MPa). However, the bending strength decreases sharply after TiNp content exceeded 10vol.%. When the TiNp content increases to 15 vol.%, the bending strength decreases below 50MPa. The fracture surfaces were further examined after bending tests in order to study the fracture characteristics. Two distinct failure modes can be observed. When the joints were brazed with Ag-Cu-Ti6+(5, 8, 15)vol.% TiNp composite filler, as displayed in Fig. 6(b), (c) and (e), fracture occurred in the ceramic and appeared as bowed fracture pattern, providing an evidence of considerable thermal residual stresses near the interface [20]. In the case of the joint brazed with Ag-Cu-Ti6+ 10vol.%TiNp composite filler, the fracture mode (Fig. 6(b Ⅱ)) implies that the crack also initiated from the ceramic near the joint interface, propagated into the ceramic and then fractured far away from the interface, leaving a sharp edge at the ceramic side.

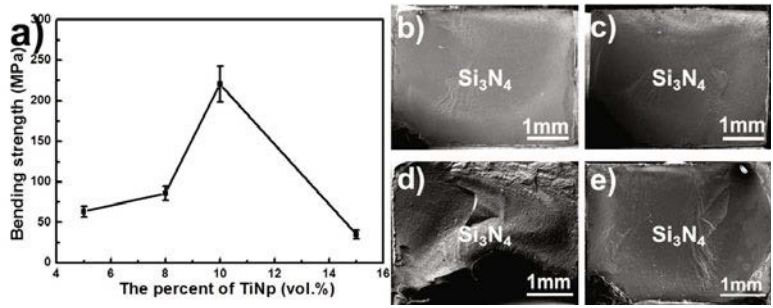

Fig.4. Bending strength versus TiNp content in the joint (a) and fractography of the joints brazed with different TiNp incorporations: (b) 5%, (c) 8%, (d) 10% and (e) 15%TiNp (vol.%).

Then we increase the Ti content to 8wt.%, or even to 10wt.%, whereas the TiNp content still varies from 5 to 15vol.%. The four-point bending strength of different TiNp and Ti contents is shown in Fig.5. When the content of Ti is fixed at 8wt.%, the joint strength decreased by 31.5% when increasing the TiNp from 5vol.% to 8vol.%. Then the joint strength stays stable with increasing the content of TiNp, around 50MPa. Further increasing the content of Ti to 10wt.%, the bending strength decreases from 55MPa to 25MPa when increasing the TiNp content from 5 to 8vol.%. Then the increasing of the TiNp content has no influence on the joint strength, which is stable around 25MPa.

In summary, the content of TiNp and Ti has crucial impacts on the thickness of the reaction layers at the Si_3N_4 and 42CrMo side, Ag(s.s.) and Cu(s.s.) refinement and the precipitation of Cu-Ti intermetallics, and finally influences the final joint strength. Reliable joints can be

achieved by using composite filler with optimum TiNp and Ti content. In this study, the soundest joint was obtained by incorporating 10vol.% TiNp and 6wt.% Ti in the joint.

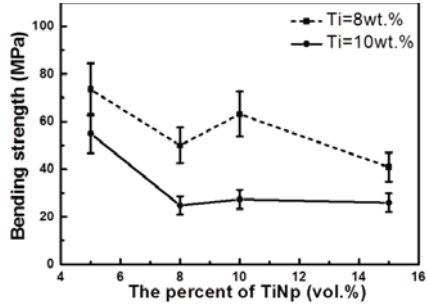

Fig.5. Effect of the content of Ti and TiNp in the composite filler on the four-point bending strength of the Si_3N_4 /42CrMo joint.

Conclusions

The Si_3N_4 ceramic was successfully brazed to 42CrMo steel using Ag-Cu-Ti+TiNp composite filler. TiN+Ti_5Si_3 reaction layer was formed adjacent to Si_3N_4, whereas TiC was formed in 42CrMo/filler reaction layer. With increasing TiNp content, the thickness of the interfacial reaction layers on both sides gradually decreased, and the Ag- and Cu-based solid solution became more uniform. In addition, more Cu-Ti intermetallics precipitated in the joint with higher TiNp content. The bending strength increased and then decreased by increasing the TiNp content when no more than 6wt.% Ti content was provided. Further increasing the content of Ti to 8wt.% and 10wt.%, the joint strengths decreased firstly and then stayed stable with increasing the TiNp content. The optimum TiNp and Ti contents for achieving the highest bending strength (221MPa) were 10vol.% and 6wt.%, respectively.

Acknowledgements

This work was financially supported by the National Nature Science Foundation of China under Grant No. 50975064, 51321061 and 51372049. The first author acknowledges support from the China Scholarship Council for a visiting scholar position in the Laboratory for Joining Technologies and Corrosion, Empa-Swiss Federal Laboratories for Materials Science and Technology.

References

1. S.D. Peteves, "Joining Nitride Ceramics," *Ceramics International,* 22 (6) (1996), 527-533.
2. G. Elssner and G. Petzow, "Metal/Ceramic Joining," *Isij International,* 30 (12) (1990), 1011-1032.
3. M. Galli, J. Janczak-Rusch, and M. Szankowska, "Influence of Ti on the Mechanical Properties of AgCuInTi Active Brazing Fillers," *Advanced Engineering Materials,* 11 (1-2) (2009), 71-74.

4. C. Iwamoto et al., "In Situ HRTEM Observations of the Formation of Reaction Phases from Liquid Ag–Cu–Ti Alloy and SiC, Si and C Substrates," *Nanotechnology,* 15 (6) (2004), S398-S401.
5. M. Galli, J. Botsis, and J. Janczak-Rusch, "Relief of the Residual Stresses in Ceramic-Metal Joints by A Layered Braze Structure," *Advanced Engineering Materials,* 8 (3) (2006), 197-201.
6. G. Blugan et al., "Brazing of Silicon Nitride Ceramic Composite to Steel Using SiC-Particle-Reinforced Active Brazing Alloy," *Ceramics International,* 33 (6) (2007), 1033-1039.
7. Y.M. He et al., "Uncovering the Critical Factor in Determining the Residual Stresses Level in Si_3N_4-GM Filler Alloy-42CrMo Joints by FEM Analysis and Experiments," *Ceramics International,* 39 (1) (2013), 709-718.
8. Y.M. He et al., "Effect of Brazing Temperature on Microstructure and Mechanical Properties of Si_3N_4/Si_3N_4 Joints Brazed with Ag-Cu-Ti+Mo Composite Filler," *Journal Of Materials Science,* 46 (2011), 2796-2804.
9. J. Kim and S. Kang, "Elastic and Thermo-physical Properties of TiC, TiN, and Their Intermediate Composition Alloys Using Ab Initio Calculations," *Journal Of Alloys And Compounds,* 528 (2012), 20-27.
10. J. Malzbender, W. Fischer, and R.W. Steinbrech, "Studies of Residual Stresses in Planar Solid Oxide Fuel Cells," *Journal Of Power Sources,* 182 (2) (2008), 594-598.
11. H.A. Wriedt and J.L. Murray, "The N-Ti (Nitrogen-Titanium) System," *Bulletin of Alloy Phase Diagrams,* 8 (4) (1987), 378-388.
12. S. Lequeux et al., "Wetting and Interfacial Reactions of Cu and Cu Alloys on TiN" (Paper presented at the Proc. 2nd Int. Conf. High Temp. Capillarity, Cracow, Poland, 29 June-2 July 1997), 112-117.
13. T.P. Wang et al., "Microstructure and Mechanical Properties of Si_3N_4/42CrMo Joints Brazed with TiNp Modified Active Filler," *Ceramics International,* 40 (5) (2014), 6881-6890.
14. C. Iwamoto and S.-I. Tanaka, "Interface Nanostructure of Brazed Silicon Nitride," *Journal Of The American Ceramic Society,* 81 (2) (1998), 363-368.
15. M. Nomura, C. Iwamoto, and S.I. Tanaka, "Nanostructure of Wetting Triple Line in A Ag-Cu-Ti/Si_3N_4 Reactive System," *Acta Materialia,* 47 (2) (1999), 407–413.
16. M. Turchanin, P. Agraval, and A. Abdulov, "Thermodynamic Assessment of the Cu-Ti-Zr system. I. Cu-Ti System," *Powder Metallurgy And Metal Ceramics,* 47 (5) (2008), 344-360.
17. O. Dezellus., R. Arroyave., and S.G. Fries, "Thermodynamic Modelling of the Ag-Cu-Ti Ternary System," *International Journal Of Materials Research,* 102 (3) (2011), 286-297.
18. P. Xiao and B. Derby, "Wetting of Titanium Nitride and Titanium Carbide by Liquid Metals," *Acta Materialia,* 44 (1) (1996), 307-314.
19. N. Frage et al., "Iron-Titanium-Carbon System. I. Equilibrium between Titanium Carbide (TiCx) of Various Stoichiometries and Iron-Carbon Alloys," *Scripta Materialia,* 35 (7) (1996), 791-797.
20. J.-W. Park, P.F. Mendez, and T.W. Eagar, "Strain Energy Distribution in Ceramic-to-Metal Joints," *Acta Materialia,* 50 (5) (2002), 883-899.

Characterization of Minerals, Metals, and Materials 2016

Poster Session

Characterization of Minerals, Metals, and Materials 2016
Edited by: Shadia Jamil Ikhmayies, Bowen Li, John S. Carpenter, Jiann-Yang Hwang, Sergio Neves Monteiro, Jian Li, Donato Firrao, Mingming Zhang, Zhiwei Peng, Juan P. Escobedo-Diaz, and Chenguang Bai
TMS (The Minerals, Metals & Materials Society), 2016

TRIBOLOGICAL TESTING, ANALYSIS AND CHARACTERIZATION OF D.C. MAGNETRON SPUTTERED Ti-Nb-N THIN FILM COATINGS ON STAINLESS STEEL

Prathmesh Joshi[1]
[1]Metallurgical and materials engineering, Visvesvaraya national Institute of technology, Nagpur-440010, India.

Keywords: Coatings, Sputtering, Characterization, Tribology, Interferometer, Adhesion

Abstract

To enhance the surface properties of stainless steel, the substrate was coated with a 1µm thick coating of Ti-Nb-N by reactive DC magnetron sputtering at different N_2 flow rates, substrate biasing and Nb-Ti ratio. The characterization of the coated samples was performed by the following techniques: hardness by Knoop micro-hardness tester, phase analysis by X-ray Diffraction (XRD), compositional analysis by Energy Dispersive X-ray Spectroscopy (EDS) and adhesion by scratch test. The tribology testing was performed on linearly reciprocating ball-on-plate wear testing machine and wear depth and wear volume were evaluated by white light interferometer. The micro-hardness test yielded appreciable enhancement in the surface hardness with the highest value being 1450 HK. Presence of three prominent phases namely NbN, Nb_2N_3 and TiN resulted from the XRD analysis. EDS analysis revealed the presence of Ti, Nb and Nitrogen. Adhesion was evaluated on the basis of critical loads for cohesive (Lc_1) and adhesive (Lc_2) failures with values varying between 7–12 N and 16–25 N respectively, during scratch test for coatings on SS substrates.

Introduction

Functional properties of a material can be enhanced by protective coatings. Protective layer impart corrosion resistance, oxidation resistance, wear resistance, low friction coefficient and high surface hardness. Protective layer modifies the surface properties and maintains its stability in severe service conditions thereby increasing the life of the components [1-3].

Two protective coatings namely TiN and NbN are widely used because of their favorable mechanical properties and high corrosion resistance [4]. TiN coated component combines high load bearing capacity, high wear resistance and good fatigue strength [5]. Ti-based hard nitride coatings are being used for various applications [6]. NbN exhibit good mechanical properties coupled with high wear resistance, high temperature stability, chemical inertness, high melting point and good electrical conductivity [7, 8] and therefore used for field emission cathode [9], protective surface coating [10] and diffusion barrier in microelectronic devices [11]. In the reactive DC magnetron sputtering target metal is sputtered in the presence of a gas or mixture of gases that will react with the sputtered metal to form a protective layer [12-14]. Application of magnetron sputtering is increasing in the areas including hard, wear-resistant coatings, low friction coatings, corrosion-resistant coatings, decorative coatings and coatings with specific optical or electrical properties [15].

Few studies have been performed on the ternary Ti-Nb-N ceramic coating deposited by reactive magnetron sputtering on various aspects such as texture, structure, properties [16-18]. The objective of this paper is to report the results of characterization of these coatings on SS substrate and compare them with the results from previous studies so as to provide the conditions for a founded choice of their applications. In the present study, hard ceramic Ti-Nb-N coatings were deposited on stainless steel (SS) substrates using reactive DC magnetron sputtering by varying the process parameters. Thin film coatings formed on the surface of SS have been characterized by its micro-hardness using Knoop micro-hardness tester [19], scratch-adhesion, phase identification by X-ray diffraction (XRD) [20] and composition using Scanning Electron microscope(SEM) [21] and Energy Dispersive X-Ray Spectroscopy (EDS) [22].

Experimental Procedure

AISI SS-304 substrate was used for the deposition of Ti-Nb-N ceramic coatings. The substrate of dimensions 40 mm ×25 mm ×2 mm and 100 mm ×100 mm ×0.2 mm were used. Deposition of Ti-Nb-N film was carried out by reactive DC magnetron sputtering using Ti-Nb (with varying surface area ratio of Nb-Ti mentioned in Table I) target of 160 mm diameter and 4 mm thickness. The distance between target and substrate was kept constant at 60 mm. Chamber was evacuated to a base pressure of 2×10^{-6} mbar. Pressure during deposition was kept at 5×10^{-3} mbar by admitting high purity argon (Ar) and nitrogen (N_2) gases into the chamber. Flow of Ar gas was kept constant at 20 cc/min and N_2 flow was varied between 7.0-16.5 cc/min. Power to the target was supplied through a stabilized D.C. power supply of 0-1000V (6A maximum). Substrate bias was kept at 100V for four samples (A,B,C,D) and 50V for one sample (E) (keeping the N_2/Ar flow ratio constant at 25%) by means of a stabilized D.C. power supply of variable voltage (0-300V) and current (0-700mA). Each sample was coated with a 1 µm thick Ti-Nb-N coating. The samples prepared with their process parameters can be viewed in Table I.

Table I. Samples prepared at different process parameters.

Sample	Target Nb-Ti ratio	Surface Biasing Volts(V)	Nitrogen flow cc/min	Current mA
A	50:50	-100	7	700
B	40:60	-100	10.5	350
C	40:60	-100	14	350
D	40:60	-100	16.5	400
E	40:60	-50	16	350

Knoop Micro-hardness tester (Future Tech FM-7 model) was used to evaluate the surface hardness of the coating. Knoop-diamond indenter was used with a load of 25gm for a dwell time of 5 seconds as per ASTM standard. The hardness measurements were performed on both the coated and the non-coated substrate. The readings were reported in HK (Knoop hardness number). Five readings on each sample were taken and the mean of these values was used. The compositional analysis of the coating was performed using scanning electron microscopy (SEM - AIS 2100 Seron Tech) at 20kV in conjugation with EDS Analysis (INCA E350). For effective analysis of the coating, the samples were cut into small dimensions (10mm×10mm) and the cross sections were cold mounted in a direction such that the coating and the substrate were distinctly

visible. The mounted samples were polished. XRD analysis was performed on the surface of the coated substrates to observe and analyze the phases present. XRD (make-Diano) was carried out at 20 mA and 35 kV in combination with Cuk_{α} radiations in routine Bragg–Brentano θ–2θ geometry. Scratch-adhesion tester (CSEM, Revetest) was used to evaluate the adhesive strength of the coatings. The scratch test was performed on the surface of the coated substrate. The scratch was carried out in a progressive mode with linearly increasing load from 0.9 N to 30 N with a loading rate of 30 N/min. The scratch indenter used was a Rockwell diamond indenter with a spherical tip of radius of 200µm.The coating was scratched for a length of 3 mm with a scratch speed of 3.09 mm/min. Wear tests were performed on a wear and friction machine (TE-70, Phoneix Tribology Ltd., UK) with reciprocating ball-on plate configuration. The specimens were cleaned before and after the tests by immersing in acetone in an ultrasonic bath. The ball was made to slide on the plate sample with three frequencies (5, 10 and 15 Hz) keeping the sliding amplitude of 1 mm constant for different time durations. The tests were performed at different load conditions (3, 5, 7, 9 and 11 N). Each test was repeated three times to verify the repeatability of the results. 3-D profilometry using Hommelwerke make white light interferometer T2000 was carried out to calculate the dimensions of wear grooves.

Results and Discussions

Microhardness

Table II. Hardness results obtained along with the process parameters

Sample	Nitrogen flow Cc/min	Hardness (HK)
A	7	920 ±2
B	10.5	1125 ±3
C	14	1280 ±1
D	16.5	1450 ±2
E	16	1406 ±1

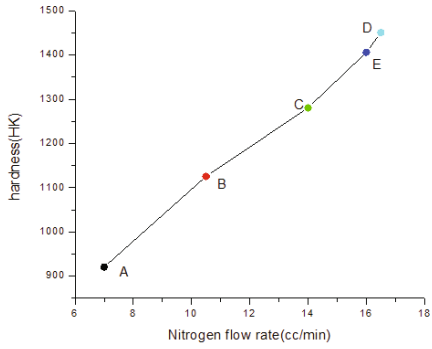

Figure 1. Variation of hardness with the increasing nitrogen flow

The hardness for the non-coated stainless steel substrate was 290 HK. The average value of the HK for each of the samples is seen from the table II. It was observed that the hardness increased with increase in the nitrogen flow as can be seen in the figure 1. The maximum hardness observed was 1450HK at a N_2 flow rate of 16.5cc/min. The changes in hardness values are attributed to changes in grain size, phase, stoichiometry, residual stress or appearance of texture [23]. In the previous works on hardness evaluation of Magnetron Sputtered NbN Films with Nb Interlayer on SS as well as mild steel, there was an appreciable increase in hardness with NbN films with Nb interlayer [24] which broadens the scope of research in Ti-Nb-N coatings with a metal interlayer.

SEM-EDS (compositional analysis)

Line scan of the laterally cold mounted samples was performed individually. The line scan shown in the figure 2 and figure 3 are of sample (C). The scans were carried out at 1000X and 1500X magnification respectively. There is a significant rise in the composition of Ti and Nb as the coating is scanned which is clearly depicted in the SEM micrographs in the figure 2 and figure 3. At the same time it can be observed that the iron content decreases steeply from the substrate end at the interface of the substrate and coating. The qualitative analysis of elemental composition showed the presence of Ti, Nb and N for all the samples irrespective of the variation in nitrogen flow rate, as can be seen from the two micrographs.

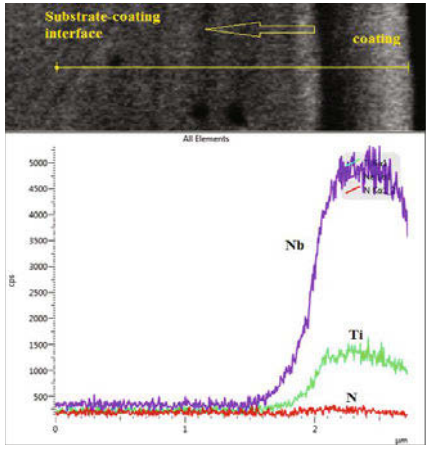

Figure 2. SEM micrographs at 1000X

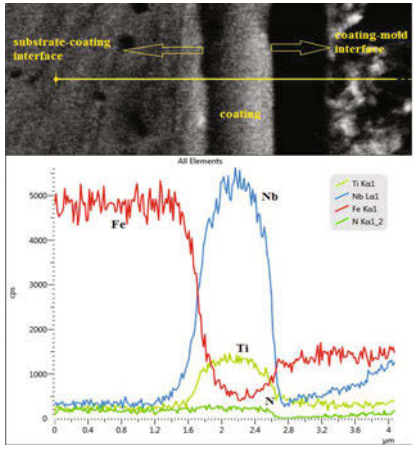

Figure 3. SEM micrographs at 1500X

XRD

X-ray diffraction was carried out on the surface of the coated SS substrates to find the phases present in the coating. Mainly three phases were found in significant amount: NbN, Nb_2N_3 and TiN. A representative analysis is depicted in figure 4 for samples A and C. Previous studies on

Ti-Nb-N coatings have mentioned significant presence of NbN and TiN in the XRD evaluation which is coherent with the results obtained in this study [25].

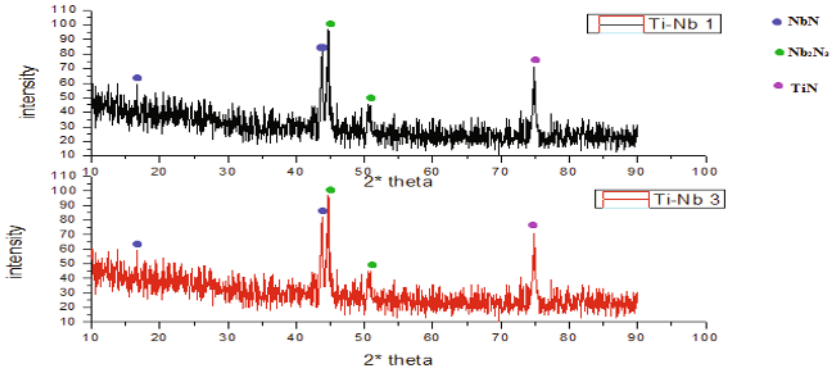

Figure 4. The XRD pattern for samples depicting phases present

Scratch-adhesion testing

Friction force and depth of indentation for all the scratch tests were recorded online along with the indenter movement to check the critical loads for cracks, chipping, delamination, coating failure, and any other phenomena. Tests performed at different loading rates were observed to give almost similar results, and variation in loading rate had little impact, therefore loading rate for scratch tests was kept at 30 N/min. The above mentioned observations were revealed as the scratch progressed, such as upper layer removal, pile-up on the sides, visibility of small cracks to long wide cracks within the coatings, pores, chipping, and partial or complete delamination of the coating. Figure 5 exhibits the scratch patterns for Ti-Nb-N coating on SS (sample **C**) taken at various loads. Start of the scratch is shown at 1N load; at 10.5 N load, segregation, cracks within coating and pores were visible though coating was still intact; at 19 N load, delamination at few places was observed along with pores, chipping and pile up; at 29.3 N load, coating delamination was observed at many places.

There are two critical loads stated for the failure of the coatings namely, Lc_1 and Lc_2. The first critical load i.e. Lc_1 signifies initial cohesive failure of the coating which can be attributed to the appearance of initial small cracks within the coating. At this point of time the coating remains intact without any delamination. The second critical load Lc_2, corresponds to primary adhesive failure of the coating, which can be attributed to the first observation of adhesive failure such as chipping, partial delamination, pores, or some phenomena, where substrate beneath coating is exposed. For coatings deposited on SS substrates Lc_1 varied between 7–12 N and Lc_2 between 16–25 N.

Coefficient of friction ( ) was observed to increase with the increase in scratch load. represents the value for the combination of coatings and substrate. This increase in is attributed to the increasing contribution from the substrate. For the coated substrates, the value was found to vary

within a narrow range of 0.23–0.26 at 30 N (as can be seen from the figure 6 for sample **C**) load irrespective of deposition at different N_2 flow rates.

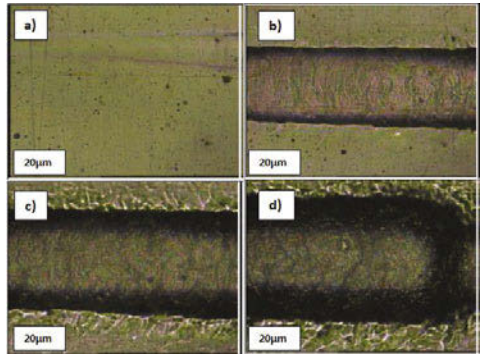

Figure 5. Scratch test for Ti-Nb-N coating on SS (sample C) at (a) 1N showing initiation of scratch, (b)at 10.5N depicting segregation, cracks and pores, (c) 19N revealing chipping, cracks, pores, pile-up, and (d) 29.3N, showing chipping, cracks, pores, pile-up, and delamination

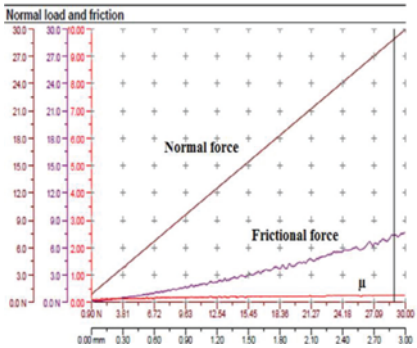

Figure 6. Coefficient of friction ( ) vs. load, normal force vs. load, and frictional force vs. load for sample C.

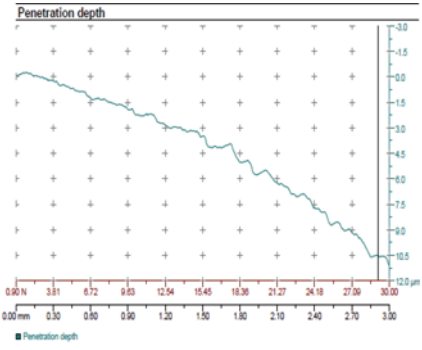

Figure 7. Variation in depth of penetration with increase in load (scratch length) for sample C.

Depth of penetration increased with the increase in applied load as can be seen from figure 7 (Sample C). At 30 N load, on an average, the coated SS samples had 10-12 m depth of penetration for different nitrogen flow rates. The change in nitrogen flow rates had no significant effect on the penetration depth. These results can be compared with the results obtained for SS substrates coated with NbN so as to know the relatively better coating in terms of abrasion

resistance. The variation in depth of penetration is much less in Ti-Nb-N coating as compared to NbN coating with Nb interlayer which was found to be 12-25 m [24]. However, the scope of error in such testing may rise from factors such as natural slopes of the samples (thickness variation in sample) and mounting errors.

Acoustic emission signals depicted small peaks wherever cracks occurred and big peaks where coating delaminated. For brittle coatings the height of the peaks increased. Acoustic emission signals (shown in figure 8) confirmed the critical loads for various failure events as observed in the scratch micrographs in figure 5.

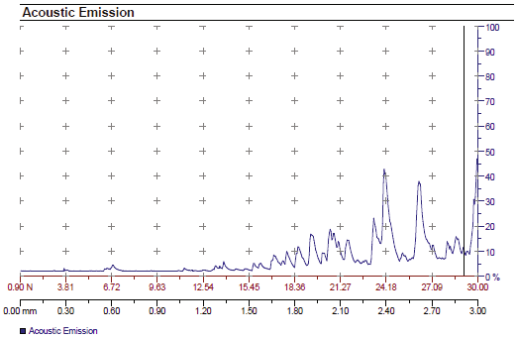

Figure 8. Acoustic emission graph for the scratch test of sample C**.**

Conclusion

Ti-Nb-N coatings were deposited on SS substrates by reactive DC magnetron sputtering. Nitrogen flow rate was varied from 7 cc/min to 16.5 cc/min.. Effect of Ti-Nb-N coating on SS substrate was studied for the improvements in surface hardness by various characterization techniques. The following results were inferred:

Surface hardness for the coated substrates increased with increase in nitrogen flow. Surface hardness on SS reached a maximum of 1450HK25 at a N_2 flow rate of 16.5cc/min. SEM-EDS analysis shows the presence of Ti, Nb and Nitrogen in the coating in a uniformly distributed fashion over a range of 1 m. XRD analysis reveals the presence of three prominent phases namely NbN, Nb_2N_3 and TiN. Critical loads for cohesive (Lc_1) and adhesive (Lc_2) failures during scratch test for coatings on SS substrates were between 7–12N and 16– 25 N, respectively. Coefficient of friction ( ) during scratch test was 0.23–0.26 at 30 N load for coatings deposited on SS samples. Increase in loading rate had little impact on critical loads. Further Tribological study is being done to measure the wear rate and wear volume. There is a scope for high temperature testing of such coatings on SS.

References

1. A. Kavaleiro and D. de Hossona, *Nanostructured coatings* (Technosphere, 2011, 792.)
2. E.V. Berlin, L.A. Seydman, *Ion-plasma processes in thin film technology* (Technosphere, 2010), 528.

3. N.A. Azarenkov et al., *Material Science of non-equilibrium state of the modified surface* (Sumy State University, 2012), 683.
4. G.V. Samsonov, I.M. Vinnitskiy, *Refractory compounds* (Metallurgy, 1976), 530.
5. Bell T, Dong H, Sun Y. *Tribology Int* (1998), 31(1-3):127-37.
6. Nakamura, D. Matsui, M. Sasaki, I. Takano, Y. Sawada, "Surface modification of TiN films by nitrogen ion beam irradiation in ethylene gas atmosphere", *Vacuum* 74 (2004) 659–663.
7. Ezirmik, K. V.; Rouhi, S.; "Influence of Cu additions on the mechanical and wear properties of NbN coatings", *Surface and Coatings Technology*, 260, (15), (2014), 179-185.
8. Stone, D. S.; Migas, J.; Martini, A.; Smith, T.; Muratore, C.; Voevodin, A. A.; Aouadi, S. M.; "Adaptive NbN/Ag coatings for high temperature tribological applications", *Surface and Coatings Technology*, 206, (25), (2012), 4316-4321.
9. Y. Gotoh, M. Nagao, T. Ura, H. Tsuji, and J. Ishikawa, "Ion beam assisted deposition of niobium nitride thin films for vacuum microelectronics devices," *Nuclear Instruments and Methods in Physics Research B*, 148, (1-4), (1999), 925–929.
10. M. Benkahoul, E. Martinez, A. Karimi, R. Sanjin´es, and F. L´evy, "Structural and mechanical properties of sputtered cubic and hexagonal NbNx thin films," *Surface and Coatings Technology*, 180, (2004), 178–183.
11. P. Al´en, M. Ritala, K. Arstila, J. Keinonen, and M. Leskel¨a, "The growth and diffusion barrier properties of atomic layer deposited NbNx thin films," *Thin Solid Films*, 491, (1-2), (2005) 235–241.
12. Hollands, E., Campbell, D.S. "The mechanism of reactive sputtering" *Journal of Materials Science*, 3, (1968), 544-552.
13. M. Ohring, *The Material Science of Thin Films* (Academic Press, 1992).
14. I.Safi, *Surface and Coatings Technology* (127, 2000) 203-219.
15. Rossnagel, Sproul WD, Legg KO, Sputter Deposition, *Opportunities for Innovation: Advanced Surface Engineering* (Switzerland: Technomic Publishing Co., 1995).
16. N. N. Iosad, N. M. van der Pers, S. Grachev, M. Zuiddam, B. D. Jackson, P. N. Dmitriev, and T. M. Klapwijk, "Texture-Related Roughness of (Nb,Ti)N Sputter-Deposited Films", *IEEE Transactions on applied superconductivity*, 13, (2), (2003), 3301-3304.
17. K. Vasu, M. Ghanshyam Krishna, K.Padmanabhan, "Effect of Nb concentration on the structure, mechanical, optical and electrical properties of nano-crystalline $Ti_{1-x}Nb_xN$ thin films", *J Mater. Sci.*, 47, (2012), 3522-3528.
18. Kamlesh V. Chauhan and Sushant K. Rawal, "A review paper on tribological and mechanical properties of ternary nitride based coatings", *Procedia Technology* 14 (2014), 430 – 437.
19. Mott, B. W, *Micro-indentation hardness testing* (Butterworth & Co. Ltd., London, 1956).
20. M. Birkholz, *Thin Film Analysis by X-Ray Scattering* (WILEY-VCH Verlag GmbH &Co. KGaA Publishing, Weinheim, 2006).
21. David Brandon and Wayne D. Kaplan, *Microstructural Characterization of Materials* (2nd edition, pp. 261-286).
22. B.D. Cullity, *Elements of X-ray diffraction* (2nd edition, Addison-Wesley Publishing Company, Inc., 1978) 439-442.
23. Bernoulli, Müller, Schwarzenberger, Hauert, Spolenak, "Magnetron sputter deposited tantalum and tantalum nitride thin films: An analysis of phase, hardness and composition", *Thin Solid Films*, 548, (2), (2013), 157–161.
24. Kulwant Singh, A. C. Bidaye, and A. K. Suri, "Magnetron Sputtered NbN Films with Nb Interlayer on Mild Steel", *International Journal of Corrosion* (2011), Article ID 748168, 11 pages doi:10.1155/2011/748168.
25. C. Benvenuti, P. Chiggiato, L. Parrini, R. Russo, "Production of niobium-titanium nitride coatings by reactive diffusion for superconducting cavity applications", *Nuclear Instruments and Methods in Physics Research*, 124 (1997), 106-111.

Characterization of Minerals, Metals, and Materials 2016
Edited by: Shadia Jamil Ikhmayies, Bowen Li, John S. Carpenter, Jiann-Yang Hwang, Sergio Neves Monteiro, Jian Li, Donato Firrao, Mingming Zhang, Zhiwei Peng, Juan P. Escobedo-Diaz, and Chenguang Bai
TMS (The Minerals, Metals & Materials Society), 2016

ASSIMILATION REACTION CHARACTERISTIC NUMBER FOR EVALUATING THE ASSIMILATION OF IRON ORE IN SINTERING

Yong Zhao, Keng Wu*, Ruiling Du, Wei Shen, Xiaodong Du, Chunen Zhu

State Key Laboratory of Advanced Metallurgy, University of Science and Technology Beijing
Beijing, 100083, China
*Email: 541348637@qq.com

Keywords: iron ore, sintering, assimilation reaction characteristic number, assimilation process.

Abstract

The assimilation properties of iron ores are important during sintering. The amount of formed calcium ferrite was firstly used to evaluate the assimilation. Then, temperature and time of assimilation were proposed rather than the former one, which simplify the process and improve the operability of experiments. However, the factors affecting the temperature were always neglected and using several indexes to evaluate the assimilation was inconvenient. In this paper, the assimilation reaction characteristic number taking the actual sintering temperature as the reference temperature was put forward to evaluate the assimilation of iron ores. This assimilation reaction characteristic number was a dimensionless number including kinds of important information during the assimilation reaction process. Results showed that the assimilation characteristic number can reflect the overall process of assimilation reaction between ores and CaO, which could help further analyze the assimilation difference of ores.

Introduction

In the sintering process, the phenomenon that iron ore reacts with CaO to create liquid phase is called assimilation [1]. The assimilation characteristic has been extensively studied to evaluate the reactivity between iron oxide of ores and CaO in flux [2-5]. Appropriate assimilation characteristic of iron ores could help produce binding phase with good property, needed for high quality sinters. The sintering process is a complex physical and chemical process. Assimilation between nuclear particles and adhering fines occurs in the high temperature zone called combustion zone of sintering bed, and it lasts for just a few minutes. To investigate the assimilation characteristic, previous researchers tried to simulate the actual sintering process, and analyzed the sintered sample. It's very complicated to carry out in lab. Current method is measuring the lowest assimilation temperature of iron ores proposed by Prof. Wu [6]. Previous researches on assimilation characteristic of ores are listed as follows.

Previous Research on Assimilation Characteristic of Iron Ores

Loo has come up with two simple model systems to study the assimilation process between ores and flux. This method required the samples more strictly in the particular size between 0.71 and 1.0 mm [7]. Noda put forward a simple and direct method to evaluate assimilation characteristic of iron ores by measuring the volume shrinkage during sintering [8]. Noda believed that the volume shrinkage of the sample can reflect the amount of calcium ferrite liquid phase to a certain extent. This method was very brief but fuzzy. Hida [9] also defined an assimilation ratio. In Hida's paper, the iron ore made into cube was put on the CaO sample of cylinder. The sintered sample was cut out from the middle. The cross sectional area unassimilated (S cm^2) was measured. Then the assimilation ratio can be obtained by comparing to

the cross sectional area before sintering (S0 cm^2).

Based on the previous researches, Wu proposed a method by measuring the lowest assimilation temperature to characterize the assimilation of iron ores. He proposed to search a lowest target temperature of the reaction on the interface between ore and CaO. When the reaction was observed, the target temperature was then considered to be the lowest assimilation temperature. This method greatly simplified the experimental process. But factors such as time and heating, affecting the temperature, were ignored. Wu's method results are given in table 1 [10].

Table 1. The results of experiments on the lowest assimilation temperatures K

Ore	Assimilation temperature(K)	Test 1	Test 2	Test 3	Test 4	Test 5	Test 6
A	1488	1250 M	1200 U	1230 M	1215 O		
B	1468	1200 M	1170 U	1185 U	1195 O		
C	1641	1250 U	1300 U	1350 U	1360 U	1370 M	1380 M
D	1446	1200 M	1170 U	1180 M	1175 M		
E	1505	1200 U	1250 M	1225 U	1235 M	1230 U	

Where, M: reaction between ore and CaO has overreacted; U: reaction between ore and CaO hasn't occurred; O: reaction between iron and CaO has just begun

Using WU'S method to characterize the assimilation of iron ores may greatly simplify the measuring method. But it could ignore some important information during the assimilation process.

Therefore, Northeastern University used visual high temperature furnace to observe the process of assimilation reaction between ores and CaO [11]. And the assimilation characteristic of iron ore was described by two parameters: assimilation temperature and assimilation time [12]. Shougang Research Institute of Technology added a high temperature microscope to the infrared heating furnace. The assimilation process was described by four characteristic temperatures [13]. Although the assimilation characteristic of iron ore associates with assimilation reaction temperature and rate, it would be inconvenient to use two or more parameters to describe it. For example, the assimilation characteristic was considered as one of the parameters in the model of evaluation system for iron ore powder [10].

The heating rate of sintering bed is very fast as a whole. But in different stages, the heating rate is different. For example, the dry zone has a very fast heating rate with maximum of 1700~2000 K/s and minimum of 450~650 K/s. When it comes to the preheating zone, the heating rate has fallen a lot. The maximum is 500 K/s and the minimum can be 100 K/s (anhydrous dry materials). In other words, the heating rate will fall dramatically around the peak of the temperature curve, which is exactly the section for iron ores to finish the sintering. The assimilation reaction between ores and CaO should occur in this zone. And previous study [14] also shows that no calcium ferrite formed before the iron ore melted no matter the heating rate was fast or slow.

In this paper, the assimilation reaction characteristic number was proposed based on previous measures. The information, such as the assimilation starting temperature, assimilation finishing temperature, the amount of assimilation and assimilation lasting time, can be obtained through a camera set beside the high temperature furnace. In order to reduce the influence of thermal hysteresis, a lower heating rate was applied. Then the assimilation properties of five ores were evaluated by this new index.

Experimental Procedure

Apparatus and Procedure

In this paper, a high temperature furnace, shown as Fig.1, was applied to observe assimilation reaction by a camera set beside the furnace. This apparatus is consisted of a heating section, a data recording section and a gas supply section. The length of constant temperature zone in the furnace was 30 mm with a margin error of 2 K. There was a sliding guide beneath the furnace shaft. The thermocouple measuring the temperature of samples was fixed on the corundum support. The data recording system consisted of a camera and a computer. The time and temperature were recorded by self-making software every 3 seconds. The temperature profile used as follows——heating to 1073 K by 10 s, to 1473 K from 1073 K by 5 s and 1473 K above at 5 K/min, and cooling at 100 K/min after assimilation reaction finished.

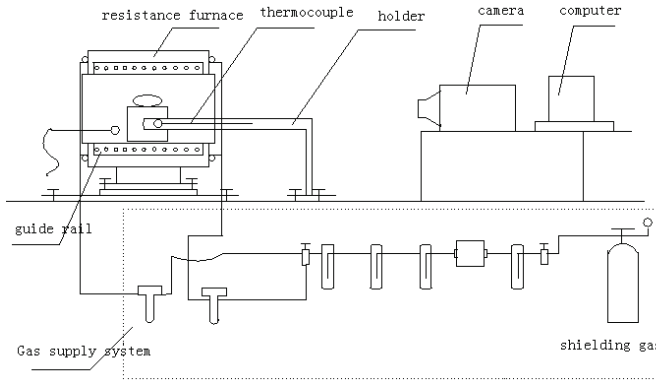

Fig. 1. The schematic plot of assimilation's experiments

Preparation of Samples

Table 2 shows chemical composition of five ores (mass fraction) %. The ores and analytically pure CaO, dried in oven, were both ground to less than 147 μm. Then 0.8 g ore powder was pressed into Φ8 mm×5~6mm cylinders. And 2.0 g CaO was pressed into Φ25 mm×6mm shims.

Table 2. Chemical composition of iron ore (mass fraction)%

Ore	TFe	FeO	SiO_2	Al_2O_3	CaO	MgO	LOI
New Zealand	55.87	27.29	6.60	3.76	2.25	3.60	-2.45
Malaysia	64.15	17.73	3.93	1.86	1.08	0.44	0.65
FMG	57.54	1.06	5.58	2.77	0.46	0.14	10.27
Caolou	69.15	30.20	2.67	0.28	0.20	0.20	-3.15
Russia	64.09	24.68	0.50	1.59	0.49	4.93	-1.62

Experimental Results

Assimilation Phenomenon of Ores

Fig. 2 shows the initial state of the sample. Fig.3 shows the beginning state of assimilation reaction between ore and CaO, which can be determined by wetting phenomenon appearing on the interface. As shown in Fig.3, the wetting angle of the interface between ore and CaO is less than 90°. It suggests that wetting phenomenon has happened on the phases interface. Previous work has proved that there is calcium ferrite occurred by XRD [14]. Thus, the time and temperature in Fig.3 are considered as assimilation starting dates. The height scale in the left of the picture can help judging the beginning state of assimilation reaction. The finishing state of assimilation reaction between ore and CaO is shown in Fig.4. The finishing date of assimilation reaction was obtained when the shape of the sample did not change any more. The temperature and time when the sample firstly transfers to the unchanged shape are considered as the finishing date. The experimental temperature won't be higher than 1673 K. The experiment would end when it comes to 1673 K. Then the assimilation volume was recorded for the subsequent comparison of assimilation characteristic, as shown in Fig.5. Actually, without comparison, we can tell that the assimilation characteristic of these ores won't be better than those assimilate with CaO entirely under 1673 K.

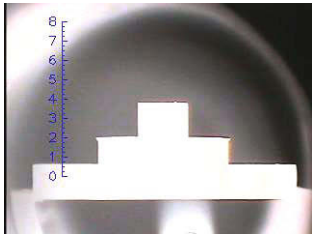

Fig. 2. Initial state of the sample

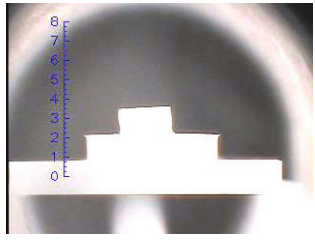

Fig. 3. Beginning state of assimilation reaction

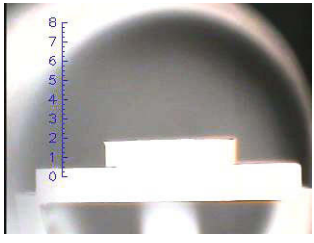

Fig. 4. Finishing state of assimilation reaction (a)

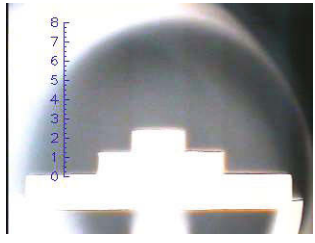

Fig. 5. Finishing state of assimilation reaction (b)

Assimilation Characteristic Reaction Number of Ores

The assimilation reaction time and temperature are both important indexes for assimilation reaction

characteristic. The assimilation reaction between ore and CaO needs a certain time to complete. And the amount of calcium ferrite is increasing during the reaction. Obviously, it's not comprehensive to use single outcome index such as the assimilation starting temperature or assimilation finishing temperature to characterize the assimilation temperature of ores. In this article, the average temperature of the starting and finishing temperature was uesd as the reaction temperature of assimilation between ore and CaO. The basic statistics of the five ores in assimilation reaction process are given in table 3.

Table 3. Basic statistics of iron ore in assimilation reaction process

Ore	Starting		Ending		Assimilation time, t/s	Assimilation volume, V/%	Average assimilation temperature, T/K	Assimilation velocity, υ_z/s
	T_0/K	t_0/s	T_f/K	t_f/s				
New Zealand	1605	3690	1620	5064	1374	100	1613	0.07
Malaysia	1538	1620	1547	1815	195	100	1543	0.51
FMG	1520	1299	1534	1605	306	100	1527	0.33
Caolou	1609	3297	1613	3402	105	100	1611	0.95
Russia	1608	3252	1652	4401	1149	100	1630	0.09

In Table 3, t: assimilation reaction time, the difference value of assimilation starting time and assimilation finishing time; T: average assimilation reaction temperature; V: assimilation volume; υz: self assimilation reaction velocity of ore, the ratio of assimilation volume to assimilation reaction time (V/t).

The heating rate represents the heat load of the furnace per unit time. It would affect the assimilation time and temperature in the assimilation reaction process although it has no effect on the calcium ferrite forming. So it should be one of the factors affecting the assimilation of ores. Because the average assimilation reaction temperature of ores are different, and temperatures have a great influence on the assimilation reaction velocity, so analyzing the influence of temperature on the assimilation reaction velocity must be under the same standard. Then the relationship between temperature and velocity was settled by Van't Hoff's law: when the temperature increases by 10 K, the reaction rate increases by 2~4 times. The Van't Hoff's law suits for the reactions that temperature difference changes a little. As the assimilation reaction occurs at a relatively low temperature, the change value caused by temperature change was confirmed as 2 times in Van't Hoff's law. The temperature in actual sinter thought to be 1563K. The assimilation reaction temperature of ores is different with it. Compared to the actual temperature, the self assimilation reaction velocity of ores was modified. And the definition formula of assimilation reaction characteristic number is given as formula (1):

$$TH = \frac{\upsilon_R(\frac{T}{1000})}{\beta} \tag{1}$$

where, *TH*: assimilation reaction characteristic number, it's a dimensionless number.

υ_R: the modified assimilation reaction velocity, modified as $\upsilon_Z \times 2^n$. The modified factor n was get by comparing average assimilation temperature and sintering temperature. It added one every 10K above. When the average assimilation temperature was less than sintering temperature, n was a positive value. Otherwise, n was a negative value.

T: average assimilation temperature, K.

β: the heating rate above 1473 K, K/s.

The assimilation reaction characteristic numbers of the five ores can be obtained by formula (1). The sintering temperature may be different because of different carbon addition, thermal efficiency of sintering equipments and operation levels. Table 4. shows that assimilation reaction characteristic numbers of five ores at 1553K, 1563K and 1573K.

Table 4. Assimilation characteristics number of iron ore TH at different sintering temperature

Ore	TH		
	1553K	1563K	1573K
New Zealand	0.02	0.04	0.08
Malaysia	18.89	37.77	75.54
FMG	36.66	73.32	146.65
Caolou	0.33	0.66	1.32
Russia	0.01	0.02	0.03

Discussion

From the assimilation process of ores, the faster the assimilation reaction velocity is, the lower the assimilation reaction temperature it will be. It can be proved that the assimilation reaction characteristic number increases with the increase of assimilation reaction velocity and decreases with the increase of assimilation reaction temperature. Based on the assimilation reaction characteristic number, the order of the five ores' assimilation should be FMG>Malaysia>Caolou>New Zealand>Russia. It's similar with the result of the previous got by the lowest assimilation temperature[10], as shown in table 5.

Table 5. Result comparison of using different methods to represent assimilation

Order	The lowest assimilation temperature	Order	TH (1563K)
1	FMG (1509K)	1	FMG (73.32)
2	Russia (1588K)	2	Malaysia(37.77)
3	Malaysia (1596K)	3	Caolou(0.66)
4	New Zealand (1623K)	4	New Zealand (0.04)
5	Caolou (1651K)	5	Russia(0.02)

Fig.6 shows the assimilation of five ores characterized by two measuring methods. The two results show consistency as a whole. Therefore, the assimilation reaction characteristic number considering the assimilation process can reflect the overall process of assimilation reaction between ores and CaO.

The results of the five ores' assimilation can also be explained by their composition. The content of FeO of Caolou, New Zealand and Russia are very high (>20%). Their LOI are negative. They belong to magnetite and have compact structure [15]. The Fe_3O_4 must first be oxidized to Fe_2O_3 and then react with CaO. Thus, the assimilation temperatures of the three ores are higher than 1573K. And their assimilation characteristics are worse. Because of the high content of MgO in New Zealand and Russia,

the assimilation reaction times are longer than the others. MgO has a very high melting point. According to Wang's study[16], MgO inhibit the formation of calcium ferrite. The LOI of FMG is 10.27%. It belongs to limonite. The crystal water in limonite decomposed in high temperature. And a lot of pores were produced which can increase reaction contact area, accelerate the diffusion of iron ion and Ca^{2+} ion, and favor the formation of low melting point compounds [15]. So the assimilation characteristic of FMG is the best of the five ores. The LOI of Malaysia is low. It belongs to hematite whose assimilation characteristic is between limonite and magnetite.

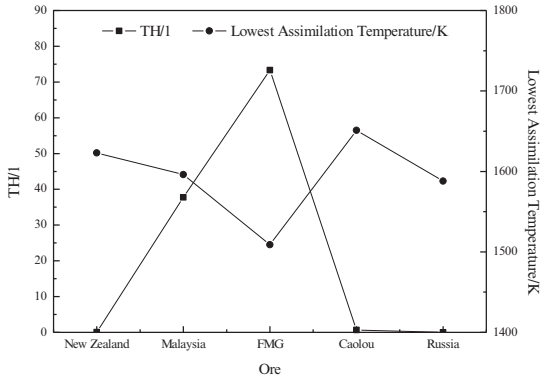

Fig. 6. Assimilation of five ores characterized by two measuring methods

Conclusions

Although parameters of assimilation process, such as assimilation temperature and velocity are very important for the research of assimilation characteristic of ores, the current method mainly focuses on the lowest assimilation temperature ignoring other vital information.

The assimilation reaction characteristic number was put forward to characterize the assimilation characteristic of ores. It can reflect the overall process of assimilation reaction between ores and CaO, which could help analyze further the assimilation difference of ores.

The assimilation reaction characteristic numbers of the five ores have been measured and their different assimilation behaviors have been analyzed through their assimilation process statistics. Results are consistent with that measured by current method on the whole. Considering the assimilation temperature only, the assimilation of ore from Russia is better than from Caolou by current method. However, the result shows the opposite tendency using the assimilation reaction characteristic number by taking the assimilation temperature and assimilation velocity into account.

Acknowledgements

The authors are grateful for support from the National Science Foundation China (Grant No. 51474022), the Independent Research Project of State Key Laboratory of Advanced Metallurgy (Grant No. 41603003), University of Science and Technology Beijing (USTB), China. Correspondence author: Keng WU, E-mail: 541348637@QQ.com.

References

1. L. X. Wang, *Ferrous Metallurgy,* (Beijing: Metallurgical Industry Press, 2000), 40-45.
2. L. X. Yang and L. Davis, "Assimilation and Mineral Formation during Sintering for Blends Containing Magnetite Concentrate and Hematite/Pisolite Sintering Fines," *ISIJ International*, 39(1999), 239-245.
3. T. Otomo, Y. Takasaki and T. Kawaguchi, "Properties of core in quasi-particle required for large amounts usage of limonitic ores in iron ore sintering process," *ISIJ International*, 92(2006), 763-768.
4. C. E. Loo, and J. Heikkinen, "Heikkinen. Structural Transformation of Beds during Iron Ore Sintering," *ISIJ International*, 52(2012), 2158-2167.
5. C. Shang, M. S. Zhou, L. W. Zhai, and F. M. Shen, "Study on basic sintering properties of iron ores in ansteel,"*Journal of Northeastern University*, 30(2009), 1139-1142.
6. S. L. Wu, Y. Liu, J. X. Du, K. Mi and H. Lin, "New Concept of Iron Ore Sintering Basic Characteristics," *Journal of University of Science and Technology Beijing*, 24(2002), 254-257.
7. C. E. Loo, R. P. Williams, and L. T. Matthews, "Assimilation of large ore and flux particles in iron ore sintering" *Transactions of the Institution of Mining and Metallurgy, Section C,* 101(1992), 7-10.
8. H. Noda, H. Yanaka, and R. Yamamoto, H. Kawata, and Y. Yamaoka, "Assimilative characteristics of iron ores and their influence on sinter qualities," *Transactions ISIJ*, 25(1985), 1103-1110.
9. Y. Hida, J. Okazaki, K. Ito, and S. Hirakawa, "Effect of Mineralogical Properties of Iron Ore on Its Assimilation with Lime," *Tetsu-to-Hagane* ,78(1992), 1013-1020.
10. C. M. Wang, K. Wu, Y. Zhao, W. L. Zhan, T. F. Shao, and J. J. Qu, "Research on Establishing an Evaluation System of Iron Ore Fines by Fuzzy Mathematics," *Sintering and Pelletizing*, 37(2012), 1-5.
11. S. G. Li, M. F. Jin, G. Wei, X. G. Li and F. M. Shen, "On Wettability of Binding Phase in Flnorine-Bearing Sinte," *Iron and Steel*, 42(2007), 12-15.
12. M. F. Jin, G. S. Li, X. Jiang, X. M. Wang, and F. M. Shen, "Influence factors on the formation of initial melt during sintering," *Energy conservation*,4(2008), 7-9.
13. Z. X. Zhao, Y. D. Pei, and W, "Pan Influencing Factors on High Temperature Properties of Iron Ore in Shougang," *Iron and Steel*, 45(2010), 208-213.
14. K. Wu, M. Wang, Y. Zhao, and C. M. Wang, "A New Method for the Mearsuration of Assimilation Characteristics of Iron Ore Powder," *Journal of Northeastern University*, 34(2013), 961-965.
15. J. L. Zhang, B. X. Su, and X. M. Che, " Experimental Study of Assimilation Characteristics of Some Iron Ore Powder," *The Chinese Journal of Process Engineering*, 11(2011), 97-102.
16. Z. Q. Wang, J. M. Pang and Z. Yu, "Effect of MgO on Composition of the Sinter Mineral Phase," *Journal of Anhui University of Technology*, 22(2005), 450-452.

Characterization of Minerals, Metals, and Materials 2016
Edited by: Shadia Jamil Ikhmayies, Bowen Li, John S. Carpenter, Jiann-Yang Hwang, Sergio Neves Monteiro, Jian Li, Donato Firrao, Mingming Zhang, Zhiwei Peng, Juan P. Escobedo-Diaz, and Chenguang Bai
TMS (The Minerals, Metals & Materials Society), 2016

EXPERIMENTAL STUDY OF ADVANCED TREATMENT OF COKING WASTEWATER USING MBR-RO COMBINED PROCESS

Lei ZHANG[1], Jiannyang HWANG[2], Ting LENG[3], Gaifeng XUE[1], Hongbing CHANG[1]

[1] R&D center of WISCO, Wuhan, 430080, China;
[2] Michigan Technological University, Michigan, MI 49931, USA
[3] Manufacturing department of WISCO, Wuhan, 430050, China

Keywords: coking wastewater; membrane bioreactor(MBR); reverse osmosis(RO); advanced treatment

Abstract

A membrane bioreactor-reverse osmosis（MBR-RO）combined process was used for advanced treatment of coking wastewater from secondary biological treatment. MBR and RO units' treatment efficiency for the pollution removal were conducted, and effects of raw water conductivity and trans-membrane pressure on water yield and desalination rate in RO unit were investigated in detail. The experimental results proved that MBR-RO combined process ran steadily with good treatment effect, which could obtain stable effluent water quality and met the requirement of "Design Criterion of the Industrial Circulating Cooling Water Treatment" (GB 50050-2007).

Introduction

Coking wastewater is considered as the most toxic one to be treated before being discharged into the environment, which is mostly generated from coal gas purification and recovery of production process, and contains various toxic compounds such as ammonia, thiocyanate, phenols and cyanides, etc[1-3]. The conventional treatment process of coking wastewater includes steam stripping of ammonia, followed by different forms of A/O biological nitrogen removal process. However, these processes are not sufficient to meet the strict requirements of the National Discharge Standard of China(GB16171-2012). Therefore, advanced technologies need to be developed to treat coking wastewater and reutilize the product as industrial cooling water, which would be one of the best choices to achieve zero discharge of wastewater. Membrane bioreactor (MBR) and Reverse osmosis(RO) membrane have been widely used in wastewater treatment and desalination processes [4-6]. In this study, we explored membrane bioreactor-reverse osmosis (MBR-RO) combined process for coking wastewater advanced treatment and reuse, which provided data support for industrial application.

Experimental

Materials

The wastewater was treated by the traditional O/A/O biological treatment processes and coagulation treatment. The effluent quality was shown in Table 1.

Table 1 Characteristics of raw wastewater used in the experiments

Item	pH	COD ($mg.L^{-1}$)	NH_3-N ($mg.L^{-1}$)	Turbidity NTU	TFe mg/L	Cl^- mg/L	Conductivity ms/cm
Raw water	7.0±0.2	101±10	5.3±0.5	16.4	4.55	308.9	5.9
Reuse standard[1]	6.0～9.0	30	5	5	0.5	250	-

[1] Industrial circulating cooling water treatment design specifications in China (GB50050-2007)

NaOH, HCl, $K_2Cr_2O_7$, NaCl, $HgSO_4$, Ag_2SO_4, AR, all chemicals were obtained from Sinopharm Chemical Reagent Co., Ltd (China). All the chemicals were used as received.

Experimental setup

The experimental setup was shown in figure 1. Aerobic treatment was carried out in the MBR process. MBR membrane was made of tubular hollow fiber membrane module. The effective membrane area and filter pore size was 2.0 m^2, 0.1 m, respectively. The flux was 15L/(m^2.h). RO membrane material was polyamide composite membrane, and the effective area was 0.3m^2. MBR first separate suspended solids from water in the form of membrane filtration, then the product water was piped into the middle water tank, and then the high quality of water produced by the reverse osmosis membrane under the pressure of the booster pump, the high salinity wastewater was discharged. Activated sludge was inoculated from the coking plant, and the aerobic sludge concentration (MLSS) and sludge ageing were 5600mg/L and 15d, respectively. The air blower provides dissolved oxygen, and dissolved oxygen concentration was 5 ~ 6mg/L. At the same time, air also increased the turbulence intensity and surface shear effect of the membrane, which decreased membrane pollution.

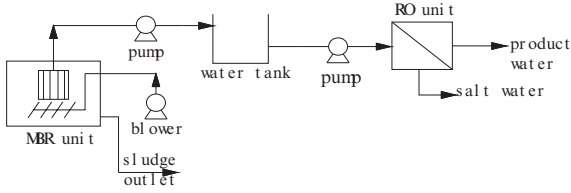

Figure. 1 Schematic diagram of experimental setup

Analytical method

Analytic items and methods is shown in Table 2.

Table 2. Analytic Item and Methods

Item	Analytical method & instrument
COD	Potassium dichromate oxidation method/COD-571analyzer
NH_3-N	Nessler's agent/5B-6DHanalyzer
Conductivity	Selective electrode/EC215analyzer
pH	PHS-3B pH meter
Tubrity	Portable turbidity meter /HACH2100P

Results and Discussion

MBR unit treatment effect

MBR can effectively retain the sludge, and maintain a high sludge concentration. Due to the rich microbial species in sludge and longer hydraulic retention time, MBR showed superior performances in COD removal. In MBR process, COD removal rate was affected by the influent organic concentration, MBR membrane fouling, sludge activity, sludge concentration and sludge growth cycle and so on. In this experiment, the MBR activated sludge was collected from the biochemical aerobic tank of coking plant. The hydraulic retention time was 5h, the MLSS concentration, pH value and COD were 5600mg/L, 7.2 85mg/L, respectively. 7 days' operating results is shown in Figure 2. From the operating data, the COD removal rate fluctuation range was between 15 ~ 40%, this can be explained that MBR had high efficiency of COD removal. Because small amount of sludge in MBR unit was discharged, the sludge concentration increased distinctly from initial 5600mg/L to 7615mg/L, and realized high sludge concentration operation, which is benefit for COD removal.

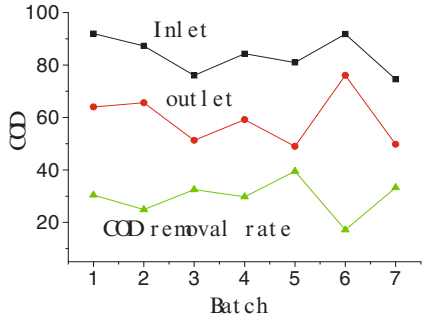

Figure .2 COD removal of MBR unit

RO unit processing effect

In order to investigate the COD removal in RO unit, the water inlet was mixed with coking wastewater and tap water. Effects of electrical conductivity, transmembrane pressure difference on water production rate and desalination rate were considered.RO effluent turbidity was less than 0.2, and COD concentration range was 5～25mg/L. Effects of transmembrane pressure on water production rate of the RO unit was shown in the Figure 3. The yield rate of product water increased with the increase of transmembrane pressure, while the desalination rate decreased from the figure 3. This can be explained that the transmembrane pressure difference was transfer driving force, and The yield rate of product water increased with the driving force increasing [7]. However, the greater the transmembrane pressure difference across the membrane, the greater flux of the membrane, and the higher probability of the solute molecules along with the solvent through the membrane, and resulting higher conductivity of the product water. It was also proved

that higher conductivity water, such as coking wastewater had lower yield rate of product water than that of tap water. Therefore, clean the membrane pollutants were very important to extend the membrane life and to improve water production rate, desalination rate, etc[8].

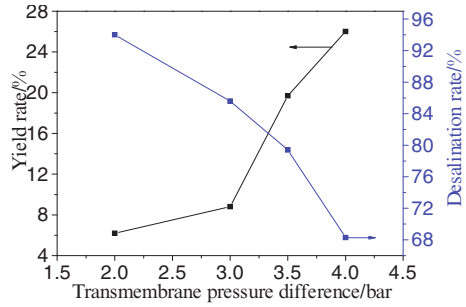

Fig. 3 Effects of transmembrane pressure difference on the yield rate and desalination rate

Effects of different electric conductivities of water on yield rate of product water and desalination rate under the pressure of 2.0bar in RO unit was investigated. The yield rate of product water and desalination rate decreased with the increase of the electric conductivity of water. This can be explained that with the increase of conductivity of the solution, greater resistance were formed, and less solvent and solute permeated, thus, the flux of the membrane decreased. The yield rate of production water decreased, and the desalination rate decreased accordingly[9].

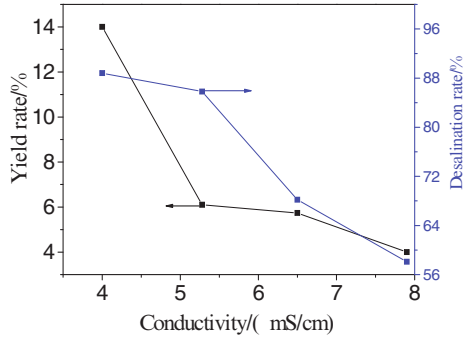

Figure. 4 Effect of conductivity on the yield rate and desalination rate

As can be seen in table 3, MBR-RO combined process had superior separation performances for coking wastewater advanced treatment and reuse. Most of organic pollutants, such as COD and NH3-N can be removed, the product water can meet the water quality index (GB50020-2007).

Table 3 Results of water quality before and after treatment of wastewater

Item	COD (mg/L)	NH_3-N (mg/L)	turbidity (NTU)	conductivity (ms/cm)	TFe (mg/L)	Cl^- (mg/L)
Raw water	85	5.0	16.4	5.9	4.55	308.9
RO water	≤6.1	≤0.3	≤0.2	≤1.0	0.023	36.7
Reuse standard[1]	30	5	5	-	≤0.5	≤250

[1] Industrial circulating cooling water treatment design specifications in China (GB50050-2007)

Conclusion

MBR-RO combined process is very promising for advanced treatment of coking wastewater. In the investigated conditions, the average removal rate of COD, NH_3-N and turbidity were 92.8%, 8.8% and 94%, respectively and the effluent water quality can meet the " Industrial circulating cooling water treatment design specifications in China (GB50050-2007). Due to the higher conductivity of coking wastewater (≥ 5.0ms/cm), the yield rate of production water was low, and the reverse osmosis membrane maybe existed serious pollution. Therefore, how to prevent and control membrane fouling, how to choose appropriate chemical cleaning agent and cleaning method will be the key factors for MBR-RO combined process in engineering application aspects.

References

[1]Zhu X. et al., "Optimization of Fenton and electro-Fenton oxidation of biologically treated coking wastewater using response surface methodology," *Separation and Purification Technology*, 81(3)(2011),444-450.

[2]Zhang L. et al.,"Advanced treatment of coking wastewater using three-dimensional fluid bed electrode reactor", *Ecology and environmental sciences,* 21(2)(2012) ,370-374(in Chinese).

[3] Zhang M. et al., "Adsorption of organic pollutants from coking wastewater by activated coke," *Colloids and Surfaces A: Physicochemical and Engineering Aspects*, 362(1-3)(2010),140-146.

[4]Kang X. et al., "Engineering application of membrane bioreactor for wastewater treatment in China: Current state and future prospect," *Frontiers of Environmental Science & Engineering in China,* 8(6) (2014),805-819.

[5] Zhong W., et al., "Application of RO technology to the project of steel plant wastewater reuse," *Industrial Water Treatment,* 33 (3)(2013), 83-85. (in Chinese)

[6]Li Q., et al., "Pilot test on the reclaimed water by a ultrafiltration/reverse osmosis process," *Membrane Science and Technology*,33(3)(2013),88-91. (in Chinese)

[7]N.O.Y, et al., “Membrane fouling in a pilot-scale submerged membrane bioreactor operated under various conditions,”*Desalination,*231(1)(2008),124-132.

[8]Xing K., et al., “Effect of Periodical Cleaning on Reduction of RO Membrane Fouling in Combined MBR/RO Process,” *China Water & Wastewater*,26(11)(2010),56-59. . (in Chinese)

[9] Yang X., et al., “Analysis of organic, inorganic and complex pollution in long process RO system”, *Membrane Science and Technology*,32(4)(2012), 50-53. (in Chinese)

Characterization of Minerals, Metals, and Materials 2016
Edited by: Shadia Jamil Ikhmayies, Bowen Li, John S. Carpenter, Jiann-Yang Hwang, Sergio Neves Monteiro, Jian Li, Donato Firrao, Mingming Zhang, Zhiwei Peng, Juan P. Escobedo-Diaz, and Chenguang Bai
TMS (The Minerals, Metals & Materials Society), 2016

SMALL PUNCH CREEP TEST IN A 316 AUSTENITIC STAINLESS STEEL

Maribel L. Saucedo-Muñoz[1], Ken-Ichi Komazaki[2], Arturo Ortiz-Mariscal[1], Victor M. Lopez-Hirata[1]

[1]Instituto Politecnico Nacional (ESIQIE);
Apartado Postal 118-556, Mexico, D.F., 07730, Mexico
[2]Kagoshima University, Kagoshima, Japan

Keywords: Small punch creep test, Creep properties, Austenitic stainless steel.

Abstract

The small punch creep test was used to evaluate the creep behavior of a 316 type austenitic stainless steel at temperatures of 650, 675 and 700 °C and loads from 199 to 512 N using a creep tester with a specimen size of 10 x 10 x 0.3 mm under an argon atmosphere. The small punch creep curves shows the three stages found in the creep curves of the conventional uniaxial test. The time to rupture decreases as the testing temperature and load increase. The secondary stage is also reduced with the increase in test load. An intergranular ductile fracture mode was observed at a testing temperature of 700 °C, while intergranular brittle mode at 650 °C which is associated with the absence of abundant precipitation at 650 °C.

Introduction

Austenitic stainless steels are widely used in industrial applications at high temperatures because of their high corrosion resistance and creep strength. The evaluation of creep characteristics are usually carried out by the conventional uniaxial creep test at selected values of temperature and stresses. The results of this test are used to determine design parameters such as the rupture life [1]. However, the application of the conventional test has some disadvantages because of its specimen size, which cannot be extracted from in-service components. Thus, the use of miniaturized mechanical testing has become a necessity to manage the evaluation of properties in materials. The Small Punch (SP) test is a miniaturized mechanical testing method which employs a specimen size of about 10 mm x 10 mm x 0.3 mm. This specimen is clamped in a fixture and punched, up to several millimeters, with a spherical indenter [2]. The evaluation of the microstructural condition of high temperature components is often carried out non-destructively by indirect methods such as metallurgical replication or hardness testing. These procedures may provide useful guidance regarding the damage state, but there is frequently a need for direct measurement of creep and other mechanical properties. The required testing then necessitates the removal of material from specific component locations. Nevertheless, the removal of a sample large enough to produce a typical uniaxial test specimen has the drawback that weld repair must normally be carried out. The repair may adversely affect the structure integrity of the remaining structure. For this reason, the use of small specimens in the evaluation of the creep behavior is worthy. Several [3-5] studies with small punch creep test have been carried out to evaluate successfully the creep properties in different steels. This work has the purpose to show the application of the small punch creep test on the evaluation of creep behavior of a 316 austenitic stainless steel at temperatures between 650 and 700 °C.

Experimental Procedure

Specimens of 316 austenitic stainless steel were used to study the creep behavior and its chemical composition is shown in Table I. This steel is in the condition of as-received, solution treated and quenched. The small punch creep test was carried out using a creep tester [4]. This consists of a striker bar, alumina puncher, alumina ball of 2.4 mm diameter, specimen holder, with associated instrumentation for loading, oxidation-proofing and data acquisition. Specimens of 10 x 10 x 0.3 mm±0.002mm were spark cut. The specimen surface was ground from both sides using abrasive papers up to grade1000 grit. The test load was kept constant by hanging a weight through a lever. Tests were conducted at 650, 675 and 700 °C using loads from 199 to 512 N under an argon atmosphere. The deflection of specimen was monitored by measuring the displacement of a quartz rod using a linear variable differential transducer. The tested specimens and fracture surfaces were observed with a SEM at 15 kV. The microstructural characterization of these samples was carried out by metallographic preparation, etching with Villela´s reagent and then observation in a SEM at 15 kV. Precipitates were extracted by electrochemical dissolution of the austenite matrix using a solution of 10 vol.% HCl in methanol at 6 V (d.c.). Residues were analyzed in an X-ray diffractometer with a monochromated Cu Kα radiation.

Table I. Chemical composition of steel

Element	C	Si	Mn	Ni	Cr	Mo
Wt. %	0.08	0.45	1.50	12.90	16.50	2.10

Results and Discussion

Creep behavior

The typical plots of central deflection δ versus time for the 316 austenitic stainless steel, after SP creep testing at 650, 675 and 700 °C, are shown in Figs. 1 (a-c), respectively. The SP creep test curves are very similar to those of the conventional uniaxial creep test. Three stages can be clearly observed in curves for all the tested specimens. That is, the primary creep which is recognized by the decreasing slope of the creep curve; the secondary-stage creep with a nearly constant creep rate; and the accelerating tertiary-stage creep that marks the final fracture at rupture time t_r It is evident from these figures that the SP creep test curves change its shape as a function of testing load in a similar manner as in the uniaxial creep tests. Figures 1 (a-c) show clearly that the width of secondary-creep stage and rupture time t_r decrease as the testing load increases. These also decrease with testing temperature for the same testing load. With decreasing loads, the two first stages become clearly defined, usually at the expenses of the tertiary stage [6].

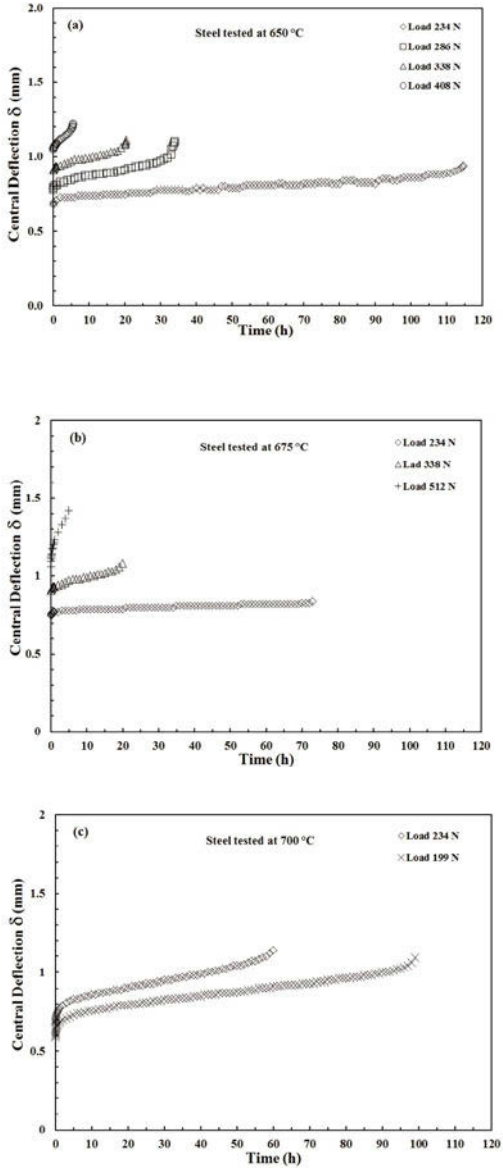

Figure 1. Curves of SP creep test for steel tested at (a) 650, (b) 675 and (c) 700 °C.

Figures 2 (a-c) show the plots of the creep deflection δ_c as a function of the creep life fraction *t/tr* for the steel tested at 650, 675 and 700 °C, respectively, corresponding to curves shown in Figs. 1 (a-c), respectively. The creep deflection was defined by the following equation:

$$\delta_c = \delta - \delta_i \qquad (1)$$

Where δ is the central deflection and δ_i the instantaneous deflection, which corresponds to the elastic and plastic strain immediately after loading. The creep deflection is practically independent of testing load at 650 °C. In contrast, the creep deflection increases with the test load at testing temperatures of 675 and 700 °C, being the latter one which has the highest central deflection.

Morphology and deformation of specimens

The morphology of small punch is shown in Figs. 3 (a and b) for the specimens tested at 650 °C and 700 °C with a load of 234 N. In general, all of the SP-C specimens showed a hemispherical specimen surface and the fracture occurred along the circumference, where the equivalent strain was largest. The deformation process takes place first by the bending of specimen, where a rapid increase in the contact area between ball and specimen surface occurs and then the stretching of contact area, where the increase in central deflection is predominant. The fracture appearances for the tested steel, corresponding to Figs. 3 (a and b), are shown in Figs. 4 (a and b), respectively. These photographs were taken using the cross-section of the SP creep test ruptured specimens. An intergranular fracture was observed for this specimen with a small decrease in thickness, Fig. 4 (a). This brittle intergranular fracture is responsible for the lower ductility this steel during small creep testing at 650 °C. On the other hand, the creep fracture for the specimen tested at 700 °C with a load of 234 N occurred in a ductile intergranular manner, Fig. 4 (b). This specimen shows a great reduction in thickness. This type of fracture was observed to occur in specimen tested at 675 and 700 °C independent of the testing load level.

Microstructural Characterization of Small Punch Creep Specimens

The microstructure of the as-received steel is shown in Fig. 5 (a) which shows the presence of the austenite matrix without any trace of precipitation. In contrast, the SEM micrographs of small punch creep specimens tested at 650 and 700 °C with a load of 234 N show mainly precipitation on grain boundaries; however, a few precipitates are also observed within the austenite grains. The grain boundary precipitation is more abundant for the specimen tested at 700 °C. The X-ray diffraction pattern of the residues extracted from steel aged at 650 °c for 40 h shows that all the diffraction peaks correspond to a $Cr_{23}C_6$ carbide which is in agreement with the Time-Temperature-Precipitation (TTP) reported in the literature [7]. This diagram predicts first the grain boundary precipitation of $Cr_{23}C_6$ carbide followed by the precipitation of the η (Fe_2Mo) phase in steel specimen aged at temperatures between 650 and 750 °C for times of 1 to 1000 h.

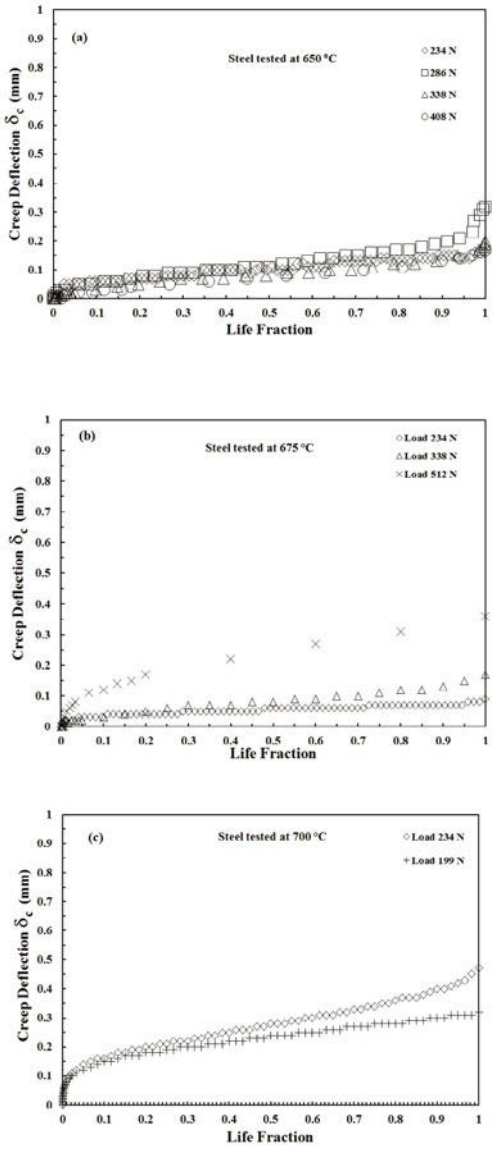

Figure 2. Creep deflection curves versus creep life fraction for steel tested at (a) 650, (b) 675 and (c) 700 °C.

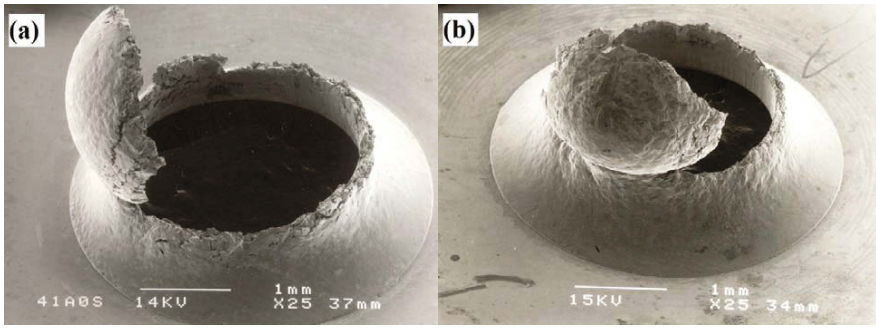

Figure 3. SEM photographs of small punch creep test specimens after testing at (a) 650 and (b) 700 °C with a load of 234 N.

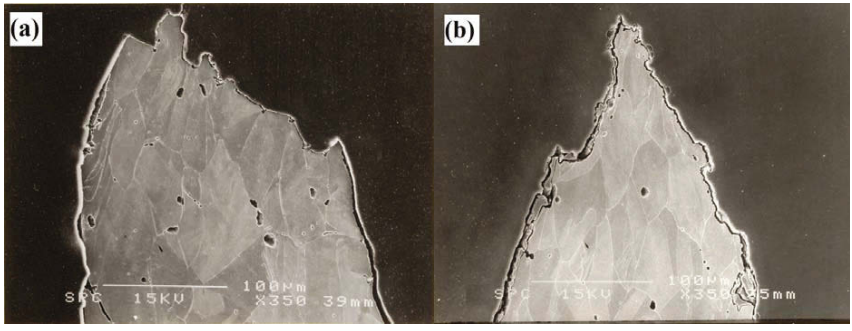

Figure 4. SEM photographs of the fracture appearance of small punch creep after testing at (a) 650 and (b) 700 °C with a load of 234 N.

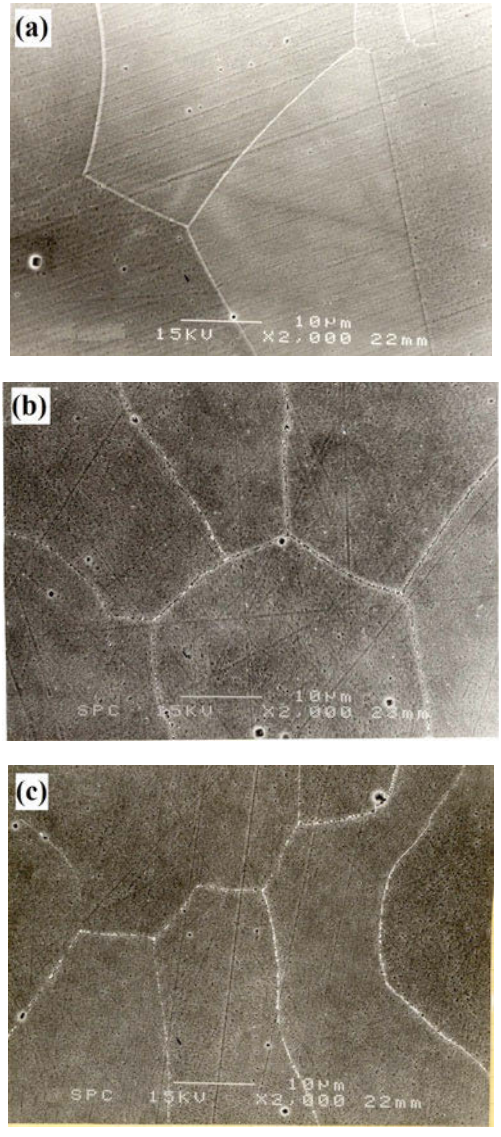

Figure 5. SEM micrographs of (a) the as-received steel, the specimens after testing at (b) 650 and (c) 700 °C with a load of 234 N.

Conclusions

The small punch creep test enables us to reproduce the main characteristics observed in the creep curve of the conventional uniaxial test. The time to rupture decreases as the testing temperature and load increase. A ductile fracture behavior was observed to occur in specimens tested at 700 °C, while a brittle behavior in specimens tested at 650 °C which seems to be associated with the absence of abundant precipitation at 650 °C.

Acknowledgements

The authors wish to thank the financial support from SIP-COFAA-IPN and CONACYT.

References

1. P. Marshal, Austenitic stainless Steels Microstructure and Properties (Elsevier, London, 1984) p. 125.
2. M.L. Saucedo-Muñoz, S. Komazaki, T. Hashida, T. Shoji and V.M. Lopez-Hirata, Revista de Metalurgia de Madrid, **39** (2003) 378.
3. M.L. Saucedo-Muñoz, S. Komazaki, T. Takahashi and T. Shoji, J. Mater. Res. **17** (2002) 1945.
4. S. Komazaki, S., Hashida, T., Shoji, T., Suzuki, K., 2000. Development of small punch tests for creep property measurement of tungsten-alloyed 9%Cr ferritic steels Journal of Testing and Evaluation **28**, 249-256.
5. K. Komazaki, T. Kato, Y. Kohno and H. Tanigawa, Mater Sci. Eng. **511A** (2009) 229.
6. Dieter, G.E., 1988. *Mechanical Metalurgy*, Mc Graw-hill, New York.
7. NRIM, Metallographic Atlas of Long-term Crept Materials No. M-2 (National Research Institute for Metals, Tokyo, Japan, 2003)

Characterization of Minerals, Metals, and Materials 2016
Edited by: Shadia Jamil Ikhmayies, Bowen Li, John S. Carpenter, Jiann-Yang Hwang, Sergio Neves Monteiro, Jian Li, Donato Firrao, Mingming Zhang, Zhiwei Peng, Juan P. Escobedo-Diaz, and Chenguang Bai
TMS (The Minerals, Metals & Materials Society), 2016

EFFECT OF PHASE TRANSFORMATIONS ON HARDNESS IN Zn-Al-Cu ALLOYS

Jose D. Villegas-Cardenas[1,2], Victor M. Lopez-Hirata[1], Maribel L- Saucedo-Muñoz[1], Jorge L. Gonzalez-Velazquez[1], Erika O. Avila-Davila[3]

[1]Instituto Politecnico Nacional (ESIQIE);
Apartado Postal 118-556, Mexico, D.F., 07730, Mexico
[2]Universidad Politecnica del Valle de Mexico
[3]Instituto Tecnologico de Pachuca, Pachuca de Soto, Hidalgo

Keywords: Phase transformations, Zn-Al-Cu alloys, Hardness.

Abstract

Zn-Al-Cu alloys were prepared by melting of pure elements. The as-cast alloys were homogenized at 350 °C for 180 h. Both the as-cast and homogenized alloys were analyzed with X-ray diffraction and scanning electron microscope with Energy Dispersive X-Ray analysis. The hardness of alloys was determined using Rockwell "B" hardness. The X-ray diffractograms and scanning electron micrographs indicated the presence of several phases in the as-cast alloys. Some of them do not correspond to those shown in the equilibrium Zn-Al-Cu phase diagram. On the other hand, the homogenized alloys showed most of the phases present in the equilibrium diagram. The hardness of alloys increases with the increase in Cu content because of the presence of Cu-containing phases such as, the θ and τ' phases.

Introduction

Zinc–rich aluminum alloys with copper additions have been of engineering interest over recent years because the addition of this alloying element enhances the wear resistance, elastic modulus, yield strength and corrosion resistance under the service conditions of stress and temperature without having a significant detrimental effect on the superplastic behavior during production of components [1–4]. The properties of this type of alloys change with the increase in copper content; however, this alloying element also causes the formation of intermetallic compounds which can affect the phase reactions in the solid-state. Besides, the presence of copper enhances the resistance to the creep and corrosion. However, the Cu addition may also decrease certain physical properties such as, ductility [5]. Recent works [6-8] related to the Zn–Al–Cu alloys are focused to alloy compositions close to the eutectic composition, Nevertheless, it is also important to know the phase transformations and mechanical properties of Al-rich and Zn-rich Zn-Al-Cu alloys.
Thus, the purpose of present work is to investigate the effect of chemical composition on the microstructure and mechanical properties, hardness, in order to establish relationships among them to determine the hardness in the as-cast and homogenized Zn-Al-Cu alloys.

Experimental Procedure

Eight compositions of Zn–Al–Cu alloys were prepared by melting of pure elements at 750 °C under an argon atmosphere and then cooled slowly. These compositions were designated as M1 to M8 and they are shown in Table I. All the as-cast alloys were homogenized at 350 °C for 180 h in order to eliminate the dendritic structure. The as–cast and homogenized alloy specimens were prepared metallographically using the standard techniques and subsequently etched in a solution composed of 0.5 ml hydrofluoric acid and 99.5 ethylic alcohol. Metallographic specimens were examined using both optical light (OLM) and scanning electron microscopy (SEM) equipped with an (Energy Dispersive X-Ray) EDX analysis and X-ray diffraction (XRD) analysis with copper K_α radiation. The Rockwell "B" hardness of specimens was determined according to the standard procedure [9].

Table I. Chemical composition of the M1 to M8 alloys

Alloy	Cu		Zn		Al	
	% wt.	% at.	% wt.	% at.	% wt.	% at.
M1	5.00	3.54	63.18	43.44	31.82	53.02
M2	10.00	6.87	55.31	36.96	34.70	56.17
M3	15.00	10.03	47.43	30.82	37.57	59.15
M4	20.00	13.01	39.56	25.02	40.44	61.97
M5	25.00	15.84	31.69	19.52	43.31	64.64
M6	30.00	18.53	23.82	14.30	46.19	67.17
M7	35.00	21.08	15.94	9.33	49.06	69.59
M8	40.00	23.51	8.07	4.61	51.93	71.88.

Results and Discussion

Microstructural characterizations of alloys

The X-ray diffractograms of the as–cast M1–M8 alloys are shown in Fig. 1. It can be seen that the α, η, ε and τ' phases are present in almost all the as–cast alloys. The α, η and ε phases are present in the case of M8 alloy. Besides, the θ and β phases are present in almost all the specimens.. The equilibrium phases are α, η and τ' phases for these alloy compositions at room temperature, according to the equilibrium Al–Cu–Zn [8]. The cooling rate during the casting process does not follow the equilibrium conditions, slow cooling rate, thus the phases formed in the as-cast alloys do not correspond to the equilibrium phases. However, the homogenizing treatment is expected to cause the formation of the equilibrium phases in these alloys. The increase in Cu content was observed to be related to the increase in the intensity of X–ray diffraction peaks corresponding to the θ phase. In contrast, the peak intensity of the η phase also increases with the increase in Zn content. This fact suggests the increase in the volume fraction of both phases. The amount of the α and ε phases showed no clear tendency for increasing or decreasing with the contents of either Al or Zn. The β phase is present in a small fraction in the samples M1 to M7 alloys. The τ´ phase is, in general, more stable as the Cu content increases.

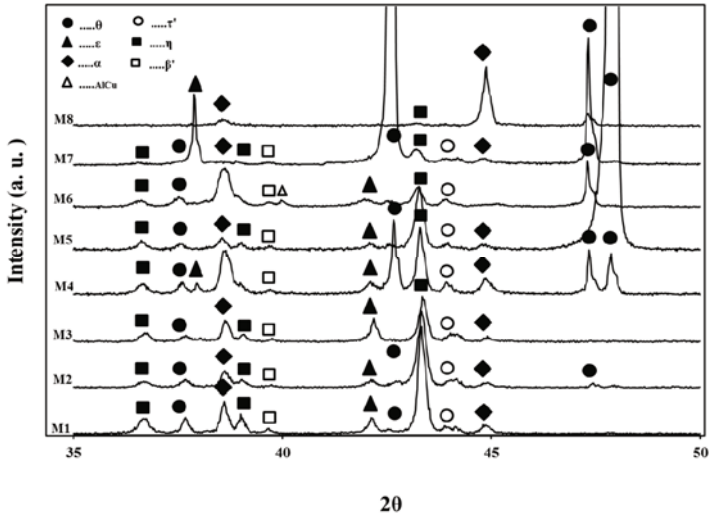

Figure 1. X-ray diffractograms of the as–cast M1–M8 alloys.

Figure 2 shows the X-ray diffractograms of the homogenized M1–M8 alloys. These indicated that the α, η and τ' phases are present in all samples. These phases are in agreement with the equilibrium ones. The increase in the intensity of X-ray diffraction peaks corresponding to the α phase is related to the increase in the Al content, whereas the presence of phase η decreases with the increase in Al and Cu contents. The presence of phase τ' increases, in general, as the Cu content increases. The ε phase was still present in the M1 to M3 alloys. The θ phase was detected in the M4 to M8 alloys. The presence of the expected equilibrium α, η and τ' phase mixture was not observed in any composition. This fact suggests that the homogenizing time should be longer than 180 h in order to obtain the equilibrium phases.

The β phase is presented after homogenizing only in the alloys with high contents of Cu and Al, the M8 alloy. This means that the Cu and Al alloying elements can retain the β phase at room temperature. In the case of the other alloys, the β phase is transformed into a mixture of α and η phases according to the following phase reaction: $\beta \rightarrow \alpha + \eta$ [4]. The presence of the τ' phase is usually associated with the four-phase reaction $\alpha + \varepsilon \rightarrow \eta + \tau'$ [4]. The formation of the equilibrium τ' phase is expected to occur in a more favorable way during the homogenizing process of these alloys.

The optical observation of the as–cast alloys shows the presence dendritic structure. SEM micrographs of the as–cast and homogenized M1, M3, M5 and M7 alloys are shown in Figs. 3 (a –d) and (e-h), respectively. There are several microconstituents in these SEM micrographs. They correspond to the phases shown in the X-ray diffractograms shown in Figs. 1 and 2. The identified microconstituents are indicated in these figures. The increase in volume fraction of the θ and the α phases is more evident with the increase in the content of Cu and Al, respectively. Figures 3 (i-l) show the secondary electron imaging SEM micrograph, for instance, in the case of the as–cast M4 alloy and their corresponding Energy Dispersive X-Ray elemental mapping images for Zn, Al and Cu. These SEM micrographs verify the identification of microconstituents shown in Figs. 3 (a-h).

Figure 2. X-ray diffractograms of the homogenized M1–M8 alloys.

These microconstituents correspond to those detected in the X-ray diffactograms of these alloys, shown in Figs. 3 (a-h). The volume fraction of the θ and ε phases, and the α phase increases with the increase in the content of Cu and Al, respectively.

Hardness estimation of the as–cast and homogenized alloys

Figure 4 shows the average Rockwell "B" hardness, HRB, of the as–cast and homogenized M1 – M8 alloys as a function of the copper content. The hardness of the as–cast alloys is higher than that corresponding to the homogenized alloys. This behavior is mainly associated with the disappearance of dendritic structure and the θ phase. In general, there is an increase in hardness with the increase in the Cu and Al contents. This can be attributed to the presence of θ phase which is the phase with the highest hardness [4].
The linear regression analyses were conducted in order to determine the correlation between the hardness and chemical composition of the as–cast and homogenized alloys. The regression equations for the as–cast alloys were as follows:

$$HRB = 93.28 + 5.32\ln(X_{Cu}) - 4.74\ln(X_{Zn}) \quad (1)$$

In contrast, the equations corresponding to the homogenized ones were the following:

$$HRB = 103.55 + 13.7\ln(X_{Cu}) - 4.88\ln(X_{Zn}) \quad (2)$$

It is interesting to notice that the regression coefficients are positive for the Cu composition and negative for the Zn composition. These coefficients suggest that the increase in volume fraction of the Cu-containing phases, ε, θ and τ' phases, are mainly responsible for the increase in hardness. This type of equations might be useful for the alloy design. These can be used to determine the hardness of a given as-cast or homogenized Zn-Al-Cu alloy based on its chemical

composition. It can be also used to establish the chemical composition of a new alloy with a given hardness.

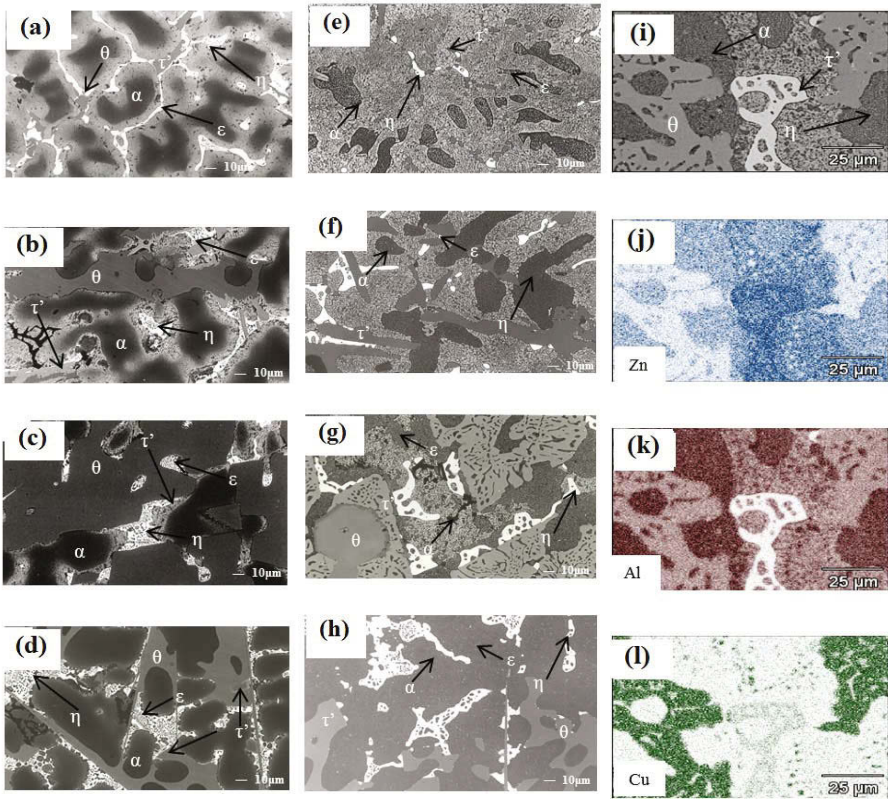

Figure 3. SEM micrographs of the as–cast (a) M1, (b) M3, (c) M5 and (d) M7 alloys, homogenized (e) M1, (f) M3, (g) M5 and (h) M7 alloys, and SEI–SEM images of the (i) as–cast M4 alloy, and EDS elemental mapping images of (j) Zn, (k) Al and (l) Cu.

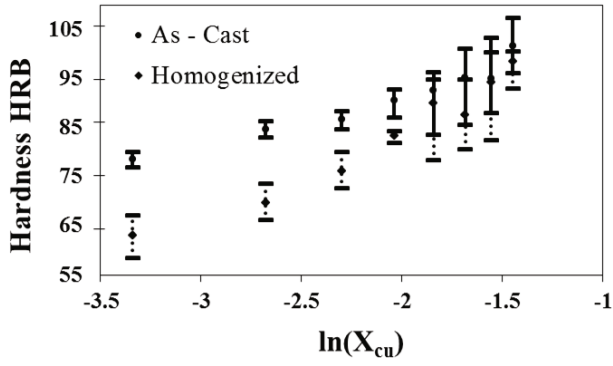

Figure 4. Plot of hardness vs. composition for the as–cast and homogenized alloys.

Conclusions

The hardness for both the as-cast and homogenized alloys increased with the increase in volume fraction of the Cu and Al due to the increase in volume fraction of the θ phase in both the as-cast and homogenized Zn-Al-Cu alloys. Likewise, the Cu addition kept the β phase stable at room temperature even after the homogenizing process. A multiple linear regression analysis permitted to obtain two equations to determine the hardness in the as-cast and homogenized Zn–Al–Cu alloys.

Acknowledgements

The authors wish to thank the financial support from SIP-COFAA-IPN and CONACYT.

References

1. H. Duong and F.A. Mohamed, Metall. Mater. Trans. **32** (2001) 48.
2. F.A. Mohamed, Mater Sci Forum. **83** (2001) 357.
3. A. Mendoza A, E. Orozco E and J. Montemayor Aldrete, J. Mater. Sci. Letter. **11** (1992) 1285.
4. J. Negrete, A. Torres and G. Torres Villaseñor , J. Mater. Sci. Lett. **14** (1995) 1092.
5. E. Gervais, H. Levert and M. Bess, AFS Transactions. **88** (1980) 183.
6. Y. Zhu, Mater. Trans. **45** (2004)3083.
7. Y. Shuqing , X. Jingpei , L. Zhongxia , W. Wenyan, W. Aiquin and L. Jiwen, Mater. Sci. Technol. **26** (2010) 648.
8. L. Börnstein L. In: Ternary alloy system phase diagrams, crystallographic and thermodynamic data. Vol. 11 (Springer, Germany; 2005) p. 71.
9. ASTM, Standard test methods for Rockwell hardness and Rockwell superficial hardness of metallic materials. Designation E 18. 2008.

Characterization of Minerals, Metals, and Materials 2016
Edited by: Shadia Jamil Ikhmayies, Bowen Li, John S. Carpenter, Jiann-Yang Hwang, Sergio Neves Monteiro, Jian Li, Donato Firrao, Mingming Zhang, Zhiwei Peng, Juan P. Escobedo-Diaz, and Chenguang Bai
TMS (The Minerals, Metals & Materials Society), 2016

RECOVERY OF PALLADIUM AND ALUMINUM FROM SPENT CATALYSTS BY ROASTING-LEACHING

Qian Li, Xuefei Rao, Yongbin Yang, Bin Xu, Long Hu , Tao Jiang
School of Minerals Processing & Bioengineering, Central South University,
Changsha, Hunan 410083, China

Keywords: Palladium, Aluminum, Dissolution percentage, Enrichment ratio

Abstract

The spent catalysts containing platinum group metals (PGMs) is one of the precious secondary resources. Recovery of PGMs from spent catalysts by an economic and effective method is a significant subject. The spent Pd/Al_2O_3 catalysts used in this study contains more than 2120g/t Pd, 9% C and 76% Al_2O_3, it was treated by roasting-water leaching method in order to dissolve the alumina in spent catalysts. Aluminum could be recovered from the lixivium and palladium was then enriched in the residues for further recovery. The result showed that the decoking ratio of the spent catalysts was almost 100% after roasting at 550ºC for 80min. The calcine was roasted with 54.5% (wt. %) of sodium hydroxide at 800ºC for 2h, then leached at 95ºCfor 0.5 h. The dissolution percentage of alumina was over 98% and meanwhile the palladium content was over 48000g/t in the residues.

Introduction

Platinum group metals (PGMs), known as industrial vitamin [1], has been widely used in modern industry because of the special physical and chemical properties like high melting point, high thermal stability, high resistance to corrosion, good catalytic activity, and so on [2]. Among these properties, the most extensive application in industry was the good catalytic activity. PGMs catalysts were used in petroleum refinery industry, chemical industry, automobile industry and some other industries [1, 3]. Therefore, a lot of precious metals, non-ferrous metals or oxides are needed to manufacture these catalysts as the rapid development of these industries. However, PGMs in the earth crust is rare, with the continuous exploitation of mineral resources in the world, high-grade ore increasingly exhausted, the cost of PGMs beneficiation from lean ore is getting higher and higher, the supply of platinum group metals in China is far from meeting the demand of domestic consumption [4]. At the same time, the increasingly serious environmental problems have also been valued all over the world. As the spent catalysts are rich in resources, PGMs content much higher than that of PGMs deposit, price expensive and has a very high recovery value, to realize the comprehensive utilization

of these kind of secondly resources is imminent [5, 6].

The main step of recover PGMs from spent catalysts is to achieve the effective separation of the active components and carriers [7]. At present, the main methods of recovering PGMs from spent catalysts are pyrometallurgical and hydrometallurgical processes [3, 5]. Pyrometallurgical commonly used including the plasma melting method, the high temperature chlorination volatilization method and the metal trapping method. Hydrometallurgical can be mainly divided into noble metal dissolution, carrier dissolution and total dissolution method [1, 7-8]. All of these methods have their advantages, disadvantages and special adaptability. In this study, the spent catalysts was consisted by palladium as the active component and Al_2O_3 as the carrier. In course of using, the catalysts absorbed carbon in the surface and the carrier transformed from γ-Al_2O_3 to α-Al_2O_3 which is a kind of hard dissolved crystal form and make palladium hard to be dissolved for being wrapped up in the process of crystal transformation. At the same time, the active component palladium will also be oxidized to inert palladium oxide which is difficult to be leached and then lead to the low leaching rate. Therefore, roasting water-leaching method had been proposed to recover palladium and aluminum according to these properties of this kind of spent catalysts.

Experimental

Materials

The spent Pd/Al_2O_3 catalysts used in this research were taken from a company about precious metal recycling in Yunnan, China. The material is black spherical (diameter 3 mm), small amount of powder (about 10%) and gray particles. Chemical compositions of the spent Pd/Al_2O_3 catalysts are given in Table I.

Table I. Chemical Compositions of the Spent Catalysts

Component	Pd*	Al_2O_3	C	Fe_2O_3	SiO_2
Content/%	2120	76.76	9.20	1.22	0.816

"*" unit is g/t.

From the above analysis results, the content of alumina and carbon in the spent catalyst was 76.76% and 9.20%, respectively. The palladium content is relatively low, only 2120g/t, followed by a small amount of other elements.

Methods

The main experimental principle is based on the reaction of sodium hydroxide with alumina under the condition of high temperature roasting, then calcine leached by water to dissolve the sodium aluminate to achieve the separation of active component and carriers of the spent catalyst. Reaction equations as below:

$$2NaOH + Al_2O_3 = Na_2O \cdot Al_2O_3 + H_2O \quad (1)$$

$$Na_2O \cdot Al_2O_3 + aq = 2NaAl(OH)_4 + aq \quad (2)$$

The experimental flow sheet is shown in Figure 1. The raw materials were fine grinded to an appropriate particle size. Take amount of the spent catalyst heating in the muffle furnace with the setting temperature, weighing after roasting some time, then calculated weight loss rate and analyzed the carbon content. Calcine roasted with proper amount of sodium hydroxide then leached to dissolve sodium aluminate and obtained the palladium residue. The filtrate was set to volumetric flask, weighted the filter residue after stoving. The contents of Pd and Al in the filter residue and filtrate were analyzed by chemical analysis method.

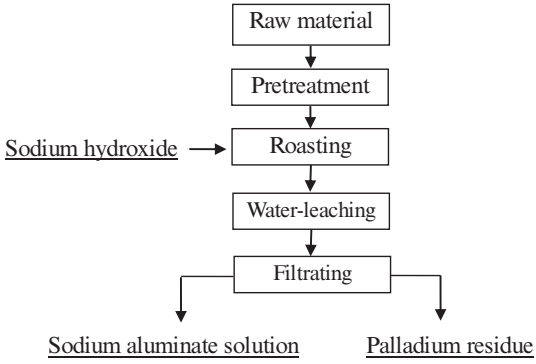

Figure 1.The experimental flow sheet

Results and Discussion

Pretreatment

The Carbon in the spent catalysts has a high content with a percentage of 9.20% and it will be harmful to the leaching process for polluting the solution and its adsorption preventing the dissolving of the carriers. In order to improve the decarbonization rate and decreased the negative effects, grinding and decarbonization processes are necessary before the roasting-leaching process.

Experimental results showed that the decarbonization rate of the raw material was only 75.94% without grinding, however, adding grinding process the decarbonization rate was improved and reached almost 100% when grinding fineness was more than 80% could pass through a 200 mesh screen (<0.074 mm).

Before decarbonization experiments, a TG-DTA of the raw material has been done and the result showed in Figure 2. It can be concluded that the DTA curve has an endothermic peak and an exothermic peak. Endothermic peak occurred from the beginning to 89.79 ºC to reach the peak, it corresponding to the removal of the attached water; exothermic peak occurred in 504.91ºC and it corresponding to the oxidation of carbon. At the end of the test the whole weight loss rate was 16.61%.

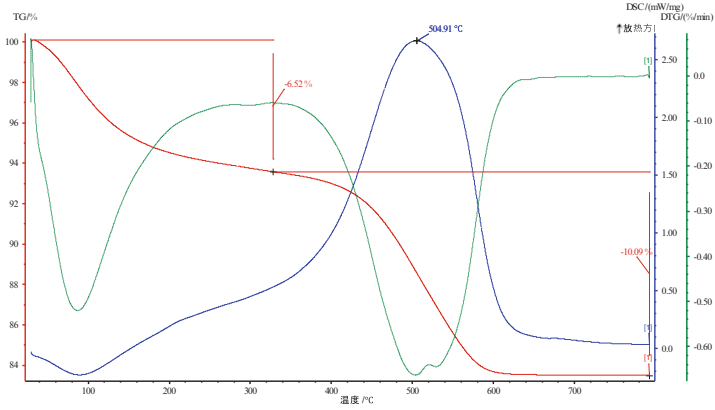

Figure 2. TG-DTA of the raw material (heating rate: 10ºC /min，air atmosphere)

According to the TG-DTA, approximate heating conditional range can be known, in order to determine the optimum conditions, the single factor experiments were carried out to investigate the effect of heating temperature and time on the decarbonization percentage. Results were shown in Figure 3 and Figure 4.

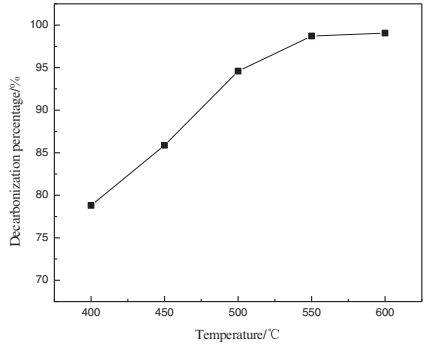

Figure 3. Effect of roasting temperature on decarbonization percentage (air atmosphere，roasting time: 1 h)

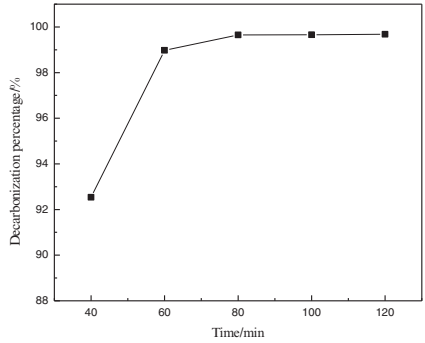

Figure 4. Effect of roasting time on decarbonization percentage
(air atmosphere，roasting temperature: 550ºC)

As it shown in Figure 3, when roasting temperature is lower than 550ºC, the decarbonization percentage increased significantly with the temperature rising. When the temperature reached 550ºC, the decarbonization percentage was almost 100%. And in Figure 4, the decarbonization percentage is relatively flat and almost reached 100% when the roasting time is exceed 60 min. Taking the economic costs into account, the final determination of pretreatment process condition was raw materials which grinding fineness was more than 80% could pass through a 200 mesh screen roasted in 550ºC for 80 min.

Roasting with Sodium Hydroxide

Roasting was the most important step in the whole process, the control of the roasting conditions can not only affect the quality of the calcine, also have a close relationship with residue ratio. If the roasting effect was not satisfactory, the dissolution rate of alumina would significantly decreased, residue ratio would be higher and palladium could not be well enriched. For the purpose of finding most suitable roasting conditions, three main factors, namely, the roasting temperature, the roasting time and dosage of sodium hydrate, were investigated.

The effect of roasting temperature on dissolution percentage of alumina and enrichment ratio of palladium was shown in Figure 5. It can be seen that the leaching rate increased with the roasting temperature rising at the beginning but reduced when the temperature was higher than 800ºC. If the temperature was not high enough, the calcine would not reacted completely, while if the temperature was too high the calcine would be too hard to penetrate through solution, both of these two cases could cause the leaching rate reduced. In contrast, when roasting temperature was 800ºC, residue ratio was the lowest (8.73%), dissolution percentage of alumina was the most efficient (94.37%) and enrichment ratio of palladium was the highest (11.42 times). Therefore, the follow-up

experiments are carried out at 800ºC.

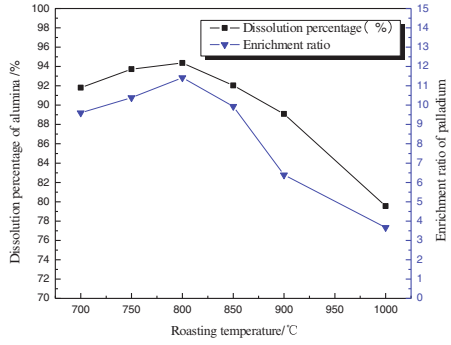

Figure 5. Dissolution percentage of alumina and enrichment ratio of palladium versus roasting temperature (dosage of sodium hydrate:50%(wt%)，roasting time: 100min)

The effect of roasting time on dissolution percentage of alumina and enrichment ratio of palladium was shown in Figure 6. When the roasting time was not long enough, the material was not reacted completely, and residue ratio was relatively high. Therefore, with the roasting time prolonging, experimental results gradually become better. When the roasting time reached 2h, the residue ratio was 8.73%, and both of the dissolution percentage of alumina and enrichment ratio of palladium were highest which was approaching to 97.82% and 19.43 times, respectively. However, when roasting time was over 2h, results were deteriorated. Accordingly, the follow-up experiments are carried out at 800ºC for 2h.

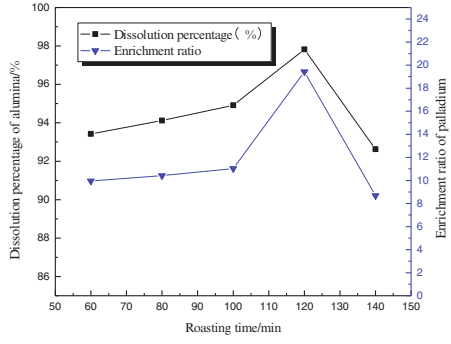

Figure 6. Dissolution percentage of alumina and enrichment ratio of palladium versus roasting time (dosage of sodium hydrate:50%(wt%)，roasting temperature: 800ºC)

Figure 7 showed that the final results became better and better with the increase of the sodium hydroxide dosage. Compared with dosage 37.5%, the results were much better when the dosage was more than 50%, especially the dosage reached 58%. Then the residue ratio down to 4.58% and the dissolution percentage of alumina increased to 98.46%, meanwhile, palladium content was almost 46000g/t in the residues and enrichment ratio reached 21.77 times. Considering saving production costs, choosing 54.5% as the most suitable sodium hydrate dosage for the experimental effect of the dosage of 54.5% was closed to dosage of 58%.

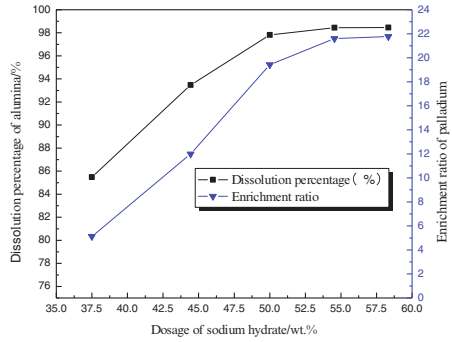

Figure 7. Dissolution percentage of alumina and enrichment ratio of palladium versus dosage of sodium hydrate (roasting temperature: 800°C, roasting time: 2h)

Water-leaching

The purpose of water-leaching was dissolving the solid sodium aluminate into solution. In this process, the effects of leaching time and liquid-solid ratio on the results was mainly considered. In order to improve production efficiency and save resources under the condition of ensuring the dissolution percentage, some leaching experiments which were on the basis of roasting with 54.55% of sodium hydrate in 800°C for 2h had been done to find the most suitable leaching time and liquid-solid ratio. The results showed that, at 95°C for 0.5h with liquid-solid ratio of 3 under 300r/min, water-leaching attained the satisfactory results with residue ratio 4.42%, leaching rate of aluminum 98.52% and Pd in the residue more than 48000g/t.

Conclusions

Recovering the spent Pd/Al_2O_3 catalysts by roasting-water leaching method is efficient for both aluminum and palladium can be retrieved efficiently. The process has advantages of strong adaptability to raw materials, simple operation, low reagent consumption, low residue ratio, high enrichment of palladium, and comprehensive

recovery of aluminum. Thus it is suitable for industrial production.

The results showed that the optimum pretreatment conditions for the spent catalysts are grinding fineness more than 80% could pass through a 200 mesh screen and roasting carbon in 550ºC for 80min. The optimum roasting condition was roast with 54.55% of sodium hydrate in 800ºC for 2h. Under the leaching condition of 95ºC for 0.5h with liquid-solid ratio of 3 at 300r/min, experiment attained the results of residue ratio 4.42%, leaching rate of aluminum reached 98.52%, palladium in the residue enriched more than 48000g/t.

Acknowledgement

Financial supports from the National Natural Science Foundation of China (Grant No. 51574284) and Science and Technology Program of Yunnan (No. 2013IB020) are gratefully acknowledged.

References

[1] Y.H. Wang, X.F. Wu, and W.F. Tong, "Recovery Technology and Development Trends of Platinum Group Metal Catalysts," *Precious Metals*, 32 (1) (2011), 76-81.
[2] M.F. Wang, "Research Status and Prospect of Platinum Group Elements Analysis," *Rare Metal Materials and Engineering*, 39 (12) (2010), 2255-2261.
[3] C. Masuda et al., "Recovery of Platinum from Spent Reforming Catalyst by Acid Leaching and Coprecipitation," *Procedia Earth and Planetary Science*, 6 (2013), 435-440.
[4] M.A. Barakat, M.H.H. Mahmoud, Y.S. Mahrous, "Recovery and Separation of Palladium from Spent Catalyst," *Applied Catalysis*, A: General 301 (2006), 182-186.
[5] A.A. Pinheiro et al., "Recovery of Platinum from Spent Catalysts in a Fluoride-Containing Medium," *Hydrometallurgy*, 74 (2004), 77-84.
[6] M.A. Barakat, M.H.H. Mahmoud, "Recovery of Platinum from Spent Catalyst," *Hydrometallurgy*, 72 (2004), 179-184.
[7] M.K. Jha et al., "Hydrometallurgical Recovery/Recycling of Platinum by the Leaching of Spent Catalysts: A Review," *Hydrometallurgy*, 133 (2013), 23-32.
[8] M. Marafi, A. Stanislaus, "Spent catalyst waste management: A Review," *Resources, Conservation and Recycling*, 52 (2008), 859-873.

Characterization of Minerals, Metals, and Materials 2016
Edited by: Shadia Jamil Ikhmayies, Bowen Li, John S. Carpenter, Jiann-Yang Hwang, Sergio Neves Monteiro, Jian Li, Donato Firrao, Mingming Zhang, Zhiwei Peng, Juan P. Escobedo-Diaz, and Chenguang Bai
TMS (The Minerals, Metals & Materials Society), 2016

PREPARATION OF POLYMERIC PHOSPHATE FERRIC SULFATE FLOCCULANT AND APPLICATION ON COKING WASTEWATER TREATMENT

Lina WANG[1], Jiannyang HWANG[2], Gaifeng XUE[1], Lei ZHANG[1]
[1] R&D center of WISCO, Wuhan, 430080, China;
[2] Michigan Technology University, Michigan, MI 49931, USA

Keywords: Polymeric Phosphate Ferric Sulfate；coking wastewater; flocculation

Abstract

Na_2HPO_4 and Polymeric ferric sulfate (PFS) were used as raw materials to synthesize the polymeric phosphorus ferric sulfate (PPFS) in the laboratory, which was used for the treatment of coking wastewater. Effects of nPO_4^{3-}/ nFe^{3+}, preparation temperature, preparation time, and dosage on flocculation influence were discussed by single factor experiment. The results indicated that PPFS had superior flocculation effect for coking wastewater. Total organic carbon (TOC) minimum concentration can be reduced to 23.88mg/L, and the removal rate of TOC was above 60% when nPO43-/ nFe3+ is 0.3, preparation temperature 80℃，preparation time 60min，and the dosage 0.8ml/L. In addition, the structure of PPFS was characterized by SEM, and mechanism of flocculation was discussed.

Introduction

Coking wastewater is a kind of typical refractory, metallurgical wastewater with high concentration of organics, mainly containing ammonia, phenols, mono-and polycyclic nitrogen-containing aromatics, oxygen- and sulfur-containing heterocyclic compounds and polycyclic aromatic hydrocarbons etc. Currently, coking wastewater is usually treated by biological methods combined with coagulation. Polymeric ferric sulfate (PFS) coagulant were often used during coagulation stage, however, due to low molecular weight, poor bridging ability and hydrolysis instability of PFS, PFS complex was favorable.

Polyphosphate Ferric Sulfate (PPFS) is a multi - nuclear intermediate complex which was introduced in an appropriate amount of phosphate in PFS under certain conditions. Compared to PFS, it has the advantages of rapid formation of floc, large particle density and good flocculation effect. Currently, the development and application of PPFS has been studied, which is mainly used in municipal sewage, industrial water, drinking water

purification and other aspects [5-6]. In view of its excellent properties, experiments of coagulation treatment of coking wastewater were carried out using lab-made PPFS. The synthetic conditions and influencing factors were explored, and the microstructure was characterized, which provided technical support for the promotion and application of PPFS in the treatment of coking wastewater.

Materials and Methods

Water quality indicators, reagent and Instrument

Experimental samples were taken from a coking company in Central China. After O/A/O biological treatment, the wastewater flowed to the secondary settling tank for sludge separation .The determination of TOC was 80-150mg/L, pH value7~8, electrical conductivity ~ 5000 μs/cm and turbidity 30NTU.

Reagents: polymeric ferric sulfate (industrial products, liquid, total iron content:11.0% ~ 11.5%, basicity:10.5% ~ 11.5%, pH:1.0 ~ 2.0), Na2HPO4, NaOH, HCl, in addition to the polymeric ferric sulfate, all reagents are analytical grade.

Instruments: MultiN/C2100TOC/TN tester (Jena, Germany). UV-vis2450 ultraviolet (UV) visible spectrophotometer (Shimadzu, Japan). 2100P nephelometer (HACH), PHS-3B pH value measuring instrument (Shanghai Jingke), Quanta 400 FEI scanning electron microscope (FEI company, the Netherlands). SH23-2 thermostat magnetic stirrer (Shanghai Chijiu), Guohua JJ-4 type mixer and other conventional experiment instrument etc.

Preparation of Polymeric Phosphate Ferric Sulfate

A certain amount of Na2HPO4 solid weighed was added into 100mL PFS liquid in a conical flask, then the flask was placed in a constant temperature water bath at a certain temperature for a period of stirring reaction. After the reaction, 0.1mol/L solution of NaOH was used to adjust the pH value, and the solution was cooled to room temperature, placed after a certain standby time.

Experimental method

Flocculation method: 250 mL coking wastewater was measured and poured in a 500 mL conical flask and the pH value of wastewater need not be corrected; After that prepared PPFS solution was added to wastewater stirring for a certain time; At last the supernatant was measured after standing.

Analytical method: TOC, infrared combustion method (MultiN/C2100TOC/TN meter); PH, glass electrode method (PHS-3B type precision pH meter); Turbidity, colorimetric method (2100P HaCH type turbidity analyzer); UV-254, ultraviolet visible spectrophotometry (UV-vis2450 UV visible spectrometer), UV-254, as a substitute for the content of aromatic hydrocarbons, double bonds or carbonyl groups in water, is a substitute for the characterization of organic pollutants in water [7].

Result and discussion

Influence of different P / Fe ratio on the flocculation effects

Under the temperature 80 degrees and reaction time 60min, PPFS flocculant with P/Fe 0.1, 0.3 and 0.5 (molar ratio) were prepared in accordance with the method of 1 2. Then flocculation experiments were carried out in accordance with the 1.3 flocculation method, with the given flocculant dosage 1.2ml/L, and the pH value of the wastewater was not changed during the experiment. The effects of different P/Fe ratio on the flocculation effect were studied and the results were shown in Figure 1.The figure1 showed that when P / Fe ratio was 0.3, the treatment effect was better, and the removal rate of TOC was 64%. In a certain range, with increasing amount of PO_4^{3-}, bridging bond of Fe^{3+}~PO_4^{3-}~Fe^{3+} enhanced, Therefore, the netting capability ability and adsorption bridging of flocculants were enhanced too[8].However, when amount of PO_4^{3-} was excessive, negative charge carried by the flocculant could be influenced by the negative charge of PO_4^{3-}, thus the charge neutralization capability of flocculant was effected. Therefore, combining the treatment effect and economic reasons, P/Fe ratio of 0.3 was the best choose.

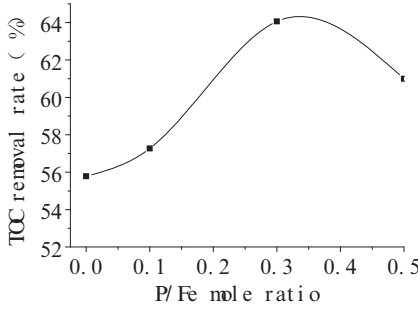

Figure. 1 Influence of different P / Fe ratio on the flocculation effects

Influence of different temperature on flocculation effects

Given P/Fe ratio 0.3, complex reactions of flocculant were carried out at 20℃, 40℃,60 ℃ and 80℃. Then flocculation experiments were carried out in accordance with the 1.3 flocculation method, with the given flocculant dosage 1.2ml/L. The effects of different composite temperature of PPFS on the flocculation effect were studied and the results were shown in Figure 2. The results showed that the higher the temperature was, the better the treatment effect. A new type of multi-core intermediate complex was produced when appropriate amount of phosphate was added into Polymeric ferric sulfate liquid[9]. Therefore, the treatment effect of flocculants had been enhanced. However, when the temperature increased from 60℃ to 80℃, the removal rate of organic matter increased slowly. So 80℃ was the best optimal temperature for the synthesis of PPFS.

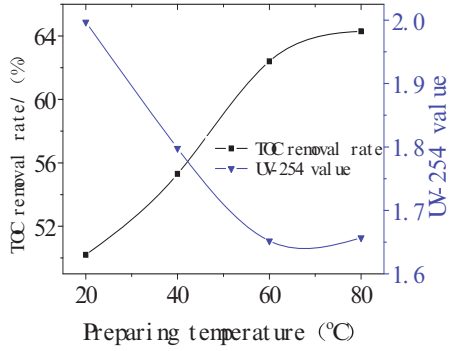

Fig.2 Influence of different temperature on flocculation effects

Influence of different preparation time on flocculation effects

Given P/Fe ratio 0.3 and temperature 80℃ , complex reactions of flocculant were carried out for 30min, 60min and 90min respectively. Then flocculation experiments were completed in accordance with the 1.3 flocculation method, with the given flocculant dosage 1.2ml/L. The effects of different preparation time of PPFS on the flocculation effect were studied and the results were shown in Figure 3. It was found that the residual TOC concentration of the supernatant was lowest when the preparation time was 60min, and TOC concentration of 90min was equivalent to 60min. The reaction of phosphate and polymeric ferric sulfate was a very complex process, which needs a certain reaction time. The reaction was insufficient when preparation time was 30min, but when preparation time was extended to 60min, the reaction had been fully completed.

Therefore, the most appropriate preparation time of PPFS was 60min.

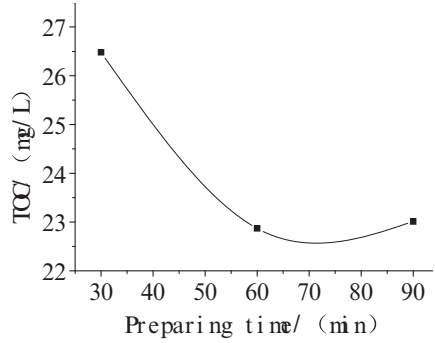

Fig. 3 Effect of different preparation time on flocculation effects

Influence of different dosage on flocculation effects

PPFS was prepared under the conditions of given P/Fe ratio 0.3, reaction temperature 80 ℃ and preparation time 60 min, then flocculation experiments were carried out in accordance with the 1.3 flocculation method. The Influence of different dosages of PPFS on the flocculation effect were studied and the results were shown in Figure 4.The results showed that when the dosage was 0.8ml/L, the residual concentration of TOC and the turbidity of the supernatant were the lowest in the same coagulation condition, and in a certain range, with the increase of dosage the flocculation effect gradually became better and then gradually became worse. That can be explained that when the coagulant dosage increased in certain range, the charge neutralization and adsorption bridging enhancement, charge neutralization and adsorption bridging of PPFS had been enhanced, but when the dosage was more than the optimum dosage, the colloid could be stabilized again [10]. So the concentration of residual organic matter and turbidity in the supernatant after flocculation increased. Finally, the optimal dosage was 0.8ml/L.

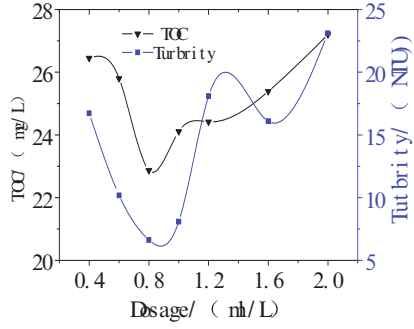

Fig. 4 Influence of different dosage on flocculation effect

SEM analysis

Figure 5 and Figure 6 are microscopic morphologies of PPFS prepared under optimal conditions and PFS sold on the market. It can be seen that under the condition of same magnification, the surface of PPFS was relatively flat and smooth, while the surface of PFS was rough and the shape was irregular. Figure 7 is micro graph of the surface branched chains of PPFS. The figure 7 showed that there were some irregular branched chains on surface of PPFS which increased the specific surface area of the particles, therefore, the adsorption capacity and bridging effect were also enhanced compared with PFS. In the process of hydrolysis, the colloidal particles with a large amount of positive charge could be generated, which could effectively reduce the surface charge of organic matter and make it stable and agglomerate. With the enhanced adsorption and bridging action of PPFS, the coagulation performance had been further strengthened [11].

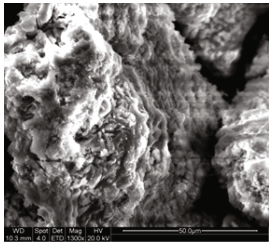

Figure 5.SEM image of lab-made PPFS

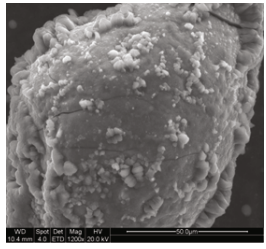

Figure 6.SEM image of PFS sold on the market

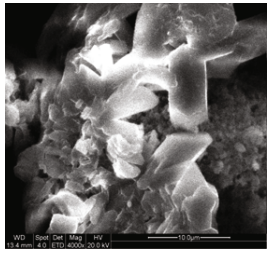

Figure 7. SEM image of branched chains of PPFS

Conclusion

Coagulation process was investigated for treatment of coking wastewater using the lab-made polymeric phosphorus ferric sulfate, and the results indicated that PPFS had

suerior flocculation effect for coking wastewater. The removal rate of TOC could reach above 60% when P/Fe ratio was 0.3, preparation temperature 80℃, preparation time 60min, and the dosage 0.8ml/L. The SEM analysis showed that a new type of Polymeric Phosphate Ferric Sulfate was produced by the combination of Polymeric ferric sulfate and phosphate.

References

[1] Du X. et al., "Denitrification dynamics of treating analog coking wastewater in upflow blanket filter,"*Journal of Chemical Engineering*, 64(7)(2013),2650-2655.(in Chinese)

[2] Hu X. et al., "Advanced treatment of biologically pretreated coking wastewater by electrochemical oxidation using boron-doped diamond electrodes". *Water research,*43(17)(2009),4347-4355.

[3]Ren Y. et al., "Environmental and biological characteristics of coking wastewater". *Acta Scientiae Circumstantiae.* 27(7)(2007),1094-1100.(in Chinese)

[4]Tian B.Z. et al.,"The hydrolyzed and other chemical characters of ferric chloride solution containing phosphate". *Environmental Chemistry.* 14(4)(1995),329-336.(in Chinese)

[5]Zheng Y.J. et al., "Treating municipal living sewage with new type coagulant PPFS". *Journal of Central South University of Technology.* 33(2)(2002),141-144.(in Chinese)

[6]Zheng H.L. et al., "Coagulation removal of phthalic acid esters environmental hormones by polymeric phosphate ferric sulfate". *Journal of civil, Architectural & Environmental Engineering*. 34(3)(2012),129-132.(in Chinese)

[7]Bao X.J, et al., "Application of UV_{254} in coking wastewater treatment". *Fuel & Chemical Process.* 42 (6)(2011),42-44.(in Chinese)

[8]Han X.Y, et al., "Preparation and application of a novel flocculent polyferric phosphate sulfate". *Petrochemical Technology & application*. 27(4)(2009),322-324.(in Chinese)

[9]Shi T.H, et al., "Studies on new production method and flocculation properties of PPFS flocculants". *China Environmental Science*. 21(2)(2001),161-164.(in Chinese)

[10] Zhang Z, et al., "Experimental study on advanced treatment of coking wastewater by

magnetic flocculation technology". *Industrial Water and Wastewater*. 43(2)(2012),25-29.(in Chinese)

[11] Zheng H.L, et al., " Topography structure and flocculation mechanism of polymeric phosphate ferric sulfate(PPFS)". *Spectroscopy and Spectral Analysis,* 31(5) (2011), 1410-1413.(in Chinese)

Characterization of Minerals, Metals, and Materials 2016
Edited by: Shadia Jamil Ikhmayies, Bowen Li, John S. Carpenter, Jiann-Yang Hwang, Sergio Neves Monteiro, Jian Li, Donato Firrao, Mingming Zhang, Zhiwei Peng, Juan P. Escobedo-Diaz, and Chenguang Bai
TMS (The Minerals, Metals & Materials Society), 2016

CHARACTERIZATION OF INCORPORATION THE GLASS WASTE IN ADHESIVE MORTAR

Santos, D.P. [1], Azevedo, A.R.G.[1], Hespanhol, R.L.[1], Alexandre, J.[1],

[1]UENF - State University of the Northern Rio de Janeiro, LECIV – Civil Engineering Laboratory; Av. Alberto Lamego, 2000, Campos dos Goytacazes, Rio De Janeiro, 28013-602, Brazil.

Keywords: Mortar, glass waste and civil construction.

Abstract

The search for reuse generated waste in urban centers, intending to preserve natural resources, has remained fairly constant, both in context of preventing exploitation of resources as the emplacement of waste on the environment. Glass waste glass created a serious environmental problem, mainly because of inconsistency of its flows. The use of this product as a mineral additive, finely ground, cement replacement and aggregate is a promising direction for recycling. This work aims to study the influence of glass waste from cutting process in adhesive mortar, replacing part of cement. The glass powder is used replacing Portland cement at 10, 15 and 20% by mass. The produced mortars will be evaluated its performance in fresh and hardened states through tests performed in laboratory. The selected feature is indicated by producers of additive and researchers to present good results when used as adhesive mortar.

Introduction

A great technological development significantly increased the production of industrial goods and volume of explored mineral resources. Associated with this large productive expansion there was a huge increase in amount of waste produced, generating millions of tons of waste every day around the world. These wastes are defined as products not used for human, social and industrial activity.

Among all types of waste, solid waste (RS) are worth mentioning, as they represent a significant part of all waste generated and, when poorly managed, they become a health, environmental and social problem.

Recently, several studies were carried out replacing part of conventional waste materials by different industrial wastes. This fact has prompted industry to develop alternative technologies, level of processing and even the consumption of raw materials in order to save resources for future generations and preserve the environment. In some cases, the opportunity arose to develop new materials and products with similar physical and mechanical characteristics, or sometimes even higher when compared to conventional materials and products [1].

In the process of manufacture glass articles during lapping is produced a solid residue consisting essentially of glass powder. This research deals with application of crushed glass powder as pozzolanic material.

Materials and Methods

The used residue was collected at ETE installed in Viminas, processing glass industry located in CIVIT II, municipality of Serra, Vitória's metropolitan region (Figure 1), state of Espirito Santo, Brazil.

Figure 2 – Localization of the Serra municipality.

To implement this study, the residue slurry was dried and clods were broken (Figure 2).

Figure 2 – Stone waste.

After collecting the residue, it was crushed and then passed through a sieve ABNT No. 200 (# 0,074mm) to be performed chemical and physical analysis for residue characterization.

Is not deemed necessary subjecting the residue to be used in this research at milling procedures, once it is already a result from a process that generates very fine polishing particles.

Chemical analysis was performed using the method of analytical X-ray fluorescence, in which sample was in powder form. The sample was ground using a ball

mill in Civil Engineering Laboratory until the material was screened (200 mesh sieve, ABNT 0.074 mm), making it more uniform, and facilitating the analysis.

It was determined the specific mass according to NBR NM 23 (ABNT, 2001) [2]. Also the determination of bulk density in loose state was performed in accordance with NBR 12127 (ABNT, 1991) [3] and the specific surface was determined by the method of Blaine, regulated by NBR 16372 (2015) [4].

Among the different techniques for studying the pozzolan, it was held tests of electrical conductivity in the residue, a method that measures the evolution of pozzolanic activity [5]. The method monitors variation in electrical conductivity within 2 minutes after addition of residue to the mixture.

For specimens and production of standard substrate was used Portland cement CP V ARI. Table 1 shows the chemical and physical characteristics of Portland cement CPV - ARI, provided by the manufacturer.

Table 1 – Cement characterization Portland CPV – ARI

Physical assays	
Blaine (cm^2/g)	≥ 3000
Handle starting time (h; min)	≥ 1
End of handle time (h; min)	≤ 10
Fineness in the sieve #200 (%)	≤ 6,0
Fineness in the sieve #325 (%)	-
Expandability hot (mm)	≤ 5,0
Chemical assays	
Loss on Ignition (%)	≤ 4,5
Waste insoluble (%)	≤ 1,0
Sulfur trioxide – SO_3 (%)	≤ 3,5
Magnesium oxide CaO Livre (%)	-
Calcium Oxide – MgO (%)	≤ 6,5

Once identified, the mortar was prepared for consistency test according to the NBR 13276 (ABNT, 2005) [5], using a mixture 1: 2 with glass waste partials substitution, in percentage 10% 15% and 20%, and also one mortar was produced without replacement as a reference.

The consistency test was performed according to NBR 13276 (ABNT, 2005) [5]. Several attempts with different quantities of water were realized until it was found the diameter required by the standard, 260 ± 5 mm. The consistency test was conducted only for a composition to be referenced (Figure 3).

Figure 3 – The consistency test – flow table.

In order to evaluate the effect of adhesive mortar incorporated with glass waste, tests will be performed for mechanical properties characterization. The mortars will be evaluated after curing period of 28 days.

After 28 days of curing, metal inserts with same dimension of ceramic plate were bonded with epoxy resin on top of each ceramic plate, and proceeds to determination of tensile adhesion in the plates fixed on the substrate surface, using a dynamometer with capacity of 5 kN and a speed of 250 50 N / s to do the mentioned test. (Figure 4).

Figure 4 – Grip strength test.

Results

The density parameter obtained, according to NBR NM 23, was the value of 2.488 g / cm³. Also the determination of bulk density in the loose state resulted the value of 0.627 kg / dm³. The specific surface area determined by the Blaine method, presented 3685.70 cm² / g, a little thicker than used cement, which has a specific surface of 3000 cm² / g.

Table II shows the proportions of each material forming the mortar mass studied, always by volume.

Table 1 - The composition and its consistency

Composition	Cement	Sand	Waste	Water/cement	Consistence
Reference	1	2	0	0,48	257 mm

Figure 5 shows particle size curve distribution of glass residue. The particle size distribution showed that the residue particles have dimensional uniformity, where 70% with a particle size of approximately 40 micrometers.

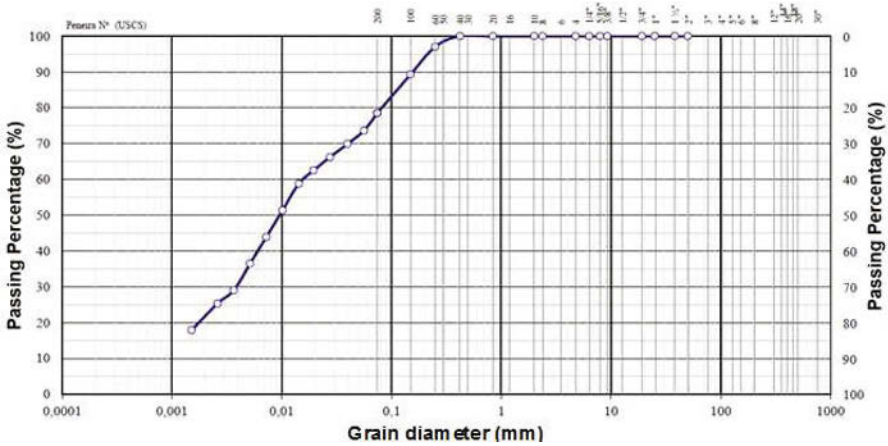

Figure 5 - Particle size distribution of the raw material.

The results of chemical composition performed by X-ray fluorescence is shown in Table 3. In this analysis, was found that glass consists mainly of silica (67.9%), as expected; sodium, appearing as a second component, thus presenting, a high amount of alkalis.

Table 2- Characterization of the studied glass waste.

Oxides	%
SiO_2	67.90
Na_2O	13.60
CaO	8.40
MgO	2.40
Al_2O_3	2.30
Fe_2O_3	1.30
K_2O	0.30
SO_3	0.30
TiO_2	0.20
NiO	0.10
ZrO_2	0.10
Cr_2O_3	0.10
P_2O_5	0.06
CuO	0.04
Lol	2.80
Total	99.90

Table 4 shows the results of electrical conductivity of powdered glass residue measured during 20 min to classify the residue as a pozzolan.

Table 3- Result of the electrical conductivity of glass waste

Pozzolanicity			
Sample	Conductivity (mS/cm)		Difference Conductivity
	Initial	End	
1	8.12	6.88	1.24
2	8.82	7.26	1.56

The tested residue showed a conductivity variation of two minutes, which classifies a good pozzolanic activity waste, according to classification proposed by Luxán et al. (1989).

Table 4 - Leaderboard pozzolanicity the material proposed by Luxan et al. (1989).

Material classification	Variation conductivity (C)
Not pozzolanic	C < 0.40
Moderate pozzolanicity	0.40 < C < 1.20
Good pozzolanic	C > 1.20

Currently, we are mounting the substrates to make different tests as adhesion, resistance, slip, open time, retraction of paste that characterize the adhesive mortar.

Conclusion

In analyzing the results achieved so far, it can be seen:

- Can be concluded that glass is a pozzolanic waste material according to all analysed samples, which attended the standard requirements.
- In the test pattern of mortar consistency index, was obtained a necessary quantity of water to acquire both resistance and good workability, extremely important factors for proper dosing.
- The mortars produced with glass residue showed characteristics within the Brazilian technical standards, podenso be used following some proportions.

Acknowledgements

The authors thank the Brazilian agencies: CNPq, CAPES and FAPERJ for the support provided to this investigation.

References

1. Pereira F.R. Industrial waste recovery as mineral alternative source: ceramics and cimenticeas composition. Thesis (PhD in Materials Science and Engineering)– Universidade de Aveiro Departamento de Engenharia Cerâmica e do vidro, 2006
2. Brazilian Association of Technical Norms –ABNT NBR NM 23:2001,Portland cement and other powdered material - Determination of density

3. Brazilian Association of Technical Norms –ABNT NBR 12127:1991, Gypsum for civil construction - Determination of physical properties of powder - Test method
4. Brazilian Association of Technical Norms –ABNT NBR 16372:2015, Portland cement and other powdered materials — Determination of fineness by the air permeability method (Blaine method)
5. LÚXAN M. P., MADRUGA F., SAAVEDRA J. "Rapid evaluation of pozzolanic activity of natural products by conductivity measurement". Cement and Concrete Research, v. 19, pp. 63-68. 1989.
6. Gao JM, Qian CX, Wang B, Morino K. Experimental study on properties of polymer-modified cement mortars with silica fume. *Cement and Concrete Research*. 2002; 32:41-45.

Characterization of Minerals, Metals, and Materials 2016
Edited by: Shadia Jamil Ikhmayies, Bowen Li, John S. Carpenter, Jiann-Yang Hwang, Sergio Neves Monteiro, Jian Li, Donato Firrao, Mingming Zhang, Zhiwei Peng, Juan P. Escobedo-Diaz, and Chenguang Bai
TMS (The Minerals, Metals & Materials Society), 2016

CHARACTERIZATION OF A MINERAL OF THE DISTRICT OF ZIMAPAN, MINA CONCORDIA, HIDALGO, FOR THE VIABILITY OF THE RECOVERY OF TUNGSTEN

Martín Reyes P.[1], Miguel Perez L.[1], Julio Cesar Juárez T.[1], Aislinn Michelle Teja R.[1], Francisco Patiño C.[2], Mizraim Uriel Flores G.[3], Iván A. Reyes D.[4]

[1] Universidad Autónoma del Estado de Hidalgo, Área Académica de Ciencias de la Tierra y Materiales. Abasolo No. 600 Col. Centro, Pachuca, 42184, Hidalgo, México.
ice9791@gmail.com

2 Ingeniería en energía. Universidad Politécnica Metropolitana de Hidalgo. Boulevard Acceso a Tolcayuca No. 1009, Ex Hacienda San Javier, Tolcayuca, 43860, Hidalgo, México.

3 Área de Electromecánica Industrial, Universidad Tecnológica de Tulancingo, Camino a Ahuehuetitla 301 Col. Las Presas, Tulancingo, 43642, Hidalgo, México.

4 Instituto de Metalurgia, Universidad Autónoma de San Luis Potosí, Av. Sierra Leona No. 550, Lomas 2da Sección, San Luis Potosí, 78210, San Luis Potosí, México.

Keywords: Tungsten, silver, characterization, mineral

Abstract

A sulfide-type mineral of the district of Zimapan, Hidalgo, Mexico, was chemically and mineralogically analyzed with the aim of detecting minor species with added value for their subsequent beneficiation. Apart from the usual species of the site, the X-ray diffraction analysis (XRD) detected the presence of tungsten sulfate (WS_2) and the mineral species typical of a base-metal sulfide site, as well as impurities such as: orthoclase, quartz, magnesium-silicon oxide, magnesioferrite, monticellite, andradite, magnetite and calcite, the latter being the mineral matrix. The Scanning Electron Microscopy (SEM) mapping confirmed the presence of the typical elements of the mineral: W, Si, O, Mg, Ca, C, Al, K, Fe, S, Zn and Cu. The Inductively Coupled Plasma Spectroscopy (ICP) analysis indicates an average concentration of 380 g W ton^{-1}, as well as 1.81% Zn, 3.41% S, 0.15% Cu, 2.36% Fe, 0.78% Pb, 0.04% Mn, Sb 0.05% and 0.01% Ag. This mineral is a potential source for the extraction of tungsten .

Introduction

The main economic ores of tungsten are wolframite [(Fe, Mn) WO_4] and scheelite ($CaWO_4$), and approximately two thirds of the world's reserves consist of scheelite deposits [1]. Tungsten is one of the most important refractory metals used in several industrial applications due to its robust performance and resistance to heat in the form of tungsten carbide. Most of the tungsten ores contain less than 1% WO_3 [2]. The main sources of tungsten are the high grade concentrates of wolframite and scheelite ores, with concentrations of 60-70% WO_3 [3]. These ores are crushed, ground and subject to separation processes, such as flotation, magnetic separation, gravity, and electrostatic separation.

One of the conventional methods to process scheelite concentrates is the route based on hydrochloric acid used in some companies in the last century [4]. In this leaching process, the

formed solid layer of tungstic acid makes it very difficult for the HCl to penetrate into the ore's core, which leads to a very low leaching yield [5, 6, 7]. In order to improve the leaching process and obtain a high tungsten yield, the HCl concentrations were increased and high temperatures were used. However, HCl is extremely corrosive and highly volatile, thus causing difficulties in the operation; as a consequence this process is rarely adopted today by the tungsten metallurgical companies [8]. Nowadays, the scheelite digestion with sodium hydroxide through an autoclaving process is mainly applied in western countries [1,9]. A good yield can be achieved through this method by using a large amount of Na_2CO_3, high temperatures and high pressures, reaching tungsten recoveries of 98% in 1,5 to 4,0 h, at typical digestion conditions of 190-225 C, a corresponding pressure of 12- 26 bar, and a Na_2CO_3 concentration of 10.18% [10]. A thermo-grinding process especially designed for the digestion of a scheelite concentrate through sodium hydroxide has had a successful commercial application [11,12]. The thermo-grinding process makes a good use of mechanical activation to kinetically improve the leaching process. Since operating at low liquid/ solid proportion conditions is necessary for the grinding process, an involuntarily higher concentration of sodium hydroxide is obtained inside the thermo-grinding reactor with a dose of sodium hydroxide, which makes the operation difficult [13]. In normal operating circumstances, medium grade tungsten concentrates have seen their commercial value reduced, making them difficult to place in the market [5].

The value of tungsten exports in Mexico has drastically dropped since 2006, with a 78% loss by 2011 [14]. A production of 287 tons of tungsten was reported in 1995, while there was no production of this metal in 2013 [15]. Although the minerals coming from mining districts in the state of Hidalgo have high tungsten concentrations, the lack of knowledge of new technologies for the extraction of this metal at industrial levels limits their use.

This piece of work presents the chemical and mineralogical characterization of a mineral coming from the mine *Mina Concordia* in the mining district of Zimapan, Hidalgo, Mexico, with the purpose of knowing the aspects of its composition that could affect its subsequent processing for the extraction of tungsten.

Experimentation

We collected a mineral sample from the mining district of Zimapan, Hidalgo. It was totally dried, homogenized and repeatedly chopped up to obtain a representative 500 g sample. The mineral dusts were mounted in epoxy to know their morphology and to identify the mineral species present in the ore by using Scanning electron microscopy-Energy-dispersive X-ray spectroscopy (SEM-EDS). The dust in the sample was also mineralogically analyzed through the X-ray diffraction technique (XRD). The chemical analysis was performed in triplicate using 1 g of mineral digested with aqua regia (3 parts HCl for 1 part HNO_3) and heated until dry. A smaller volume of aqua regia was then added, the insoluble was filtered and the remaining solution was gauged at 0.1 L.

Experimental methods

The identification and quantification of the elements present in the mineral sample was conducted by Inductively Coupled Plasma Spectroscopy (ICP) using a Perkin Elmer 8300 spectrometer. The equipment used for the mineralogical study was the following: INEL EQUINOX 2000 X-ray diffractometer, with a Cu-Ka1 radiation of 1.540598 Å, operation at 30 mA and 20 KV, 220V and a resolution of 0.095 FWHM. JEOL JSM 6701F scanning

electron microscope, with a voltage of 25 KV and a depth of field of 16.5 mm at different magnifications with secondary electrons.

Results and discussion

Table 1 shows the chemical analysis, performed by Inductively Coupled Plasma Spectroscopy (ICP), of copper (Cu), zinc (Zn), sulfur (S), iron (Fe), molybdenum (Mo), antimony (Sb), tungsten (W), silver (Ag), lead (Pb), and manganese (Mn) for different mesh sizes.

Table 1. Chemical analysis of the mineral by mesh size

Element Percentage (%)	Mesh Size 100 149 µm	150 90 µm	200 74 µm	270 53 µm	325 44 µm	400 37 µm	500 25 µm	-500 -25 µm	Average Percentage (%)
Cu	0.110	0.137	0.139	0.148	0.164	0.152	0.166	0.180	0.15
Zn	1.811	1.896	1.958	2.005	1.926	1.747	1.703	1.444	1.81
S	4.099	3.856	3.392	3.260	3.806	3.230	3.176	2.438	3.41
Fe	3.005	2.763	2.530	2.446	2.312	2.015	2.076	1.722	2.36
Mo	0.008	0.008	0.005	0.005	0.008	0.006	0.005	0.007	0.01
Sb	0.092	0.093	0.088	0.099	0.999	0.098	0.114	0.127	0.05
W (g ton^{-1})	355.50	384.22	402.88	374.00	325.70	352.02	381.04	356.06	0.038
Ag (g ton^{-1})	133.76	136.32	137.50	158.03	117.51	142.58	163.68	155.36	0.01
Pb	0.674	0.718	0.749	0.852	0.784	0.746	0.875	0.838	0.78
Mn	0.030	0.032	0.034	0.035	0.038	0.042	0.046	0.067	0.04

In average, S is the most abundant element, with 3.41%, followed by Fe and Zn, with 2.36% and 1.81% respectively. Pb, Cu, Sb, Mn and Mo are among the minor elements. The concentration of both the major and minor elements is shown in a homogeneous fashion regarding the mesh sizes, as observed in figure 1.

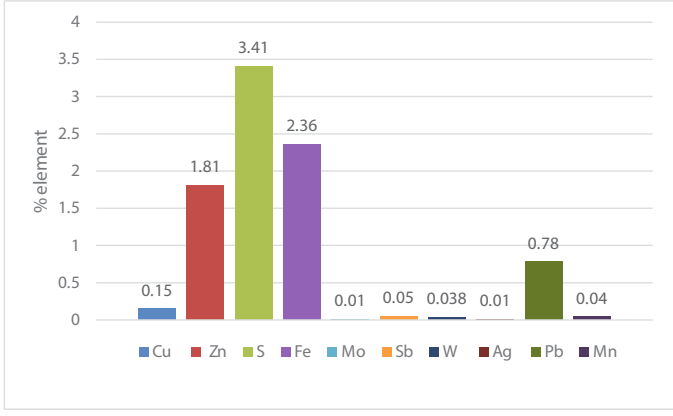

Figure 1. Average elemental composition of the mineral sample.

The highest concentration of tungsten appears in the mesh size measuring 74 µm, with 402.88 g ton^{-1} of mineral (see Figure 2a). On the other hand, the highest concentration of silver was found in the 25 µm mesh size, with 163.68 g/ton of mineral (see Figure 2b), so it could be considered as a metal of interest for its extraction. Both elements are evenly present in the sample in the range between 325.7 and 402.88 g/ton for tungsten, and between 117.51 and 163.68 g/ton for silver. The lowest concentrations of both metals were reported in the mesh size measuring 44 µm.

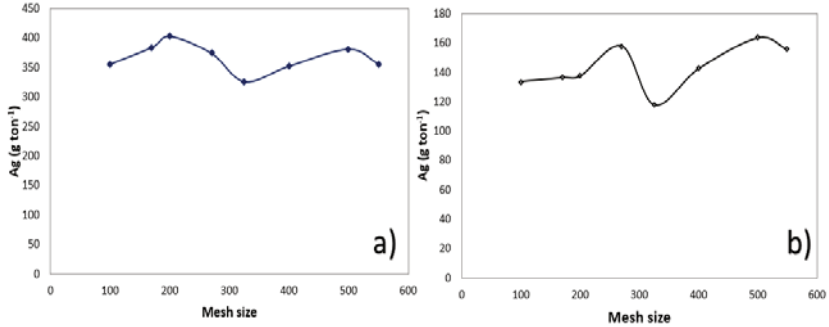

Figure 2. a) Tungsten distribution (g ton^{-1}) by mesh size. b) Silver distribution (g ton^{-1}) by mesh size.

Calcite ($CaCO_3$) was identified as the matrix of the mineral in the diffractogram obtained from the dust sample of the pull size ore. Other species that are present in the sample are quartz (SiO_2), franklinite ($Zn_{0.98}Fe_{2.02}O_4$), Bornite ($Cu_{1.25}Fe_{0.25}S$) and tungstenite (WS_2); the latter is the species where the tungsten content was identified, as is the case with the analysis performed for white and whitish particles (see Figure 3).

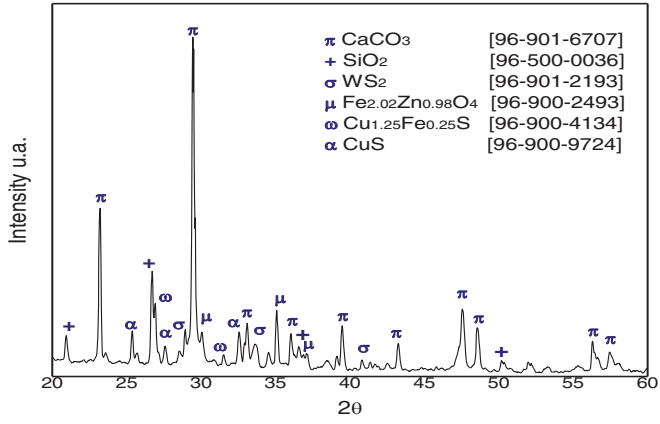

Figure3. X-ray diffractogram of the dusts of pull size ore.

We performed a handpicked separation of the run-of-mine by color. It included black, gray, white and dark gray particles (magnetic particles); they were pulverized and characterized by XRD. The mineralogical analysis performed through this technique allowed us to determine calcite ($CaCO_3$) as the matrix of the mineral in all of the particles except for the gray and grayish particles, whose mineralogical matrix was identified as orthoclase ($AlKSi_3O_8$). Some minor mineral phases were also found, whose reflection numbers are shown in table 2 for particles with different colors.

Table 2. Mineral species present in particles with different colors.

Particle Colors	No. PDF	Composition	Mineral Shases
Dark gray (Magnetic particle)	[96-900-6904]	Fe_2O_4Zn	Franklinite
	[96-900-1077]	$CaMgO_4Si$	Monticellite
	[96-901-1801]	FeS	Mackinawite
	[96-900-6284]	$Ca_{1.08}Fe_{3.92}O_{12}Si_3$	Andradite
	[96-101-0929]	$CCaO_3$	Calcite
	[96-900-9724]	$Ca_{0.63}Fe_{4.37}O_{12}Si_3$	Almandine
White particles	[96-900-5841]	Fe_3O_4	Magnetite
	[96-901-1453]	$CaCO_3$	Calcite (Wallastonite-2M)
	[96-710-3015]	SiO_2	Quartz
	[96-900-9146]	WS_2	Tungstenite
Black particles	[96-901-5843]	FeS_2	Pyrite
	[96-901-6707]	$CaCO_3$	Calcitae
	[96-900-8219]	$AlKSi_3O_8$	Sanidine
	[96-901-3322]	SiO_2	Quartz
Gray particles	[96-900-0163]	$AlKSi_3O_8$	Orthoclase
	[96-901-6707]	$MgSiO_3$	Magnesium-silicon oxide
	[96-900-7274]	Fe_2MgO_4	Magnesioferrite
	[96-901-3322]	SiO_2	Quartz

By using grayscale contrast, an SEM-EDS micrograph, which is shown in figure 4 was obtained. An irregular, varied morphology can be observed in the mineral dusts. For the mapping performed on mineral particles sieved with sizes of 25 microns, the micrograph was first obtained by second electrons. The elements identified in the mapping were Si, K, Mg, Ca, Al, S, O and Fe, of which a strong relation between S and Fe can be observed. This confirms the presence of pyrite and mackinawite in the sample. The presence of large

amounts of Si, Mg, Ca and O evenly distributed in the mineral indicate that calcite is the mineral's matrix.

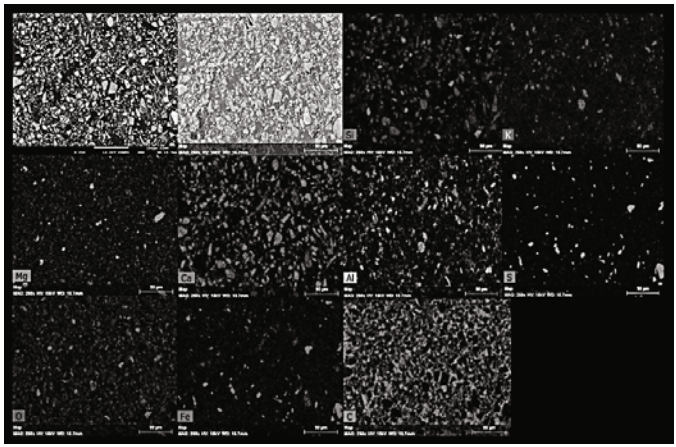

Figure 4. Mapping of polished particles sieved at a mesh size of 25 µm

The punctual analysis performed on a light colored particle reports a metal composition associated to iron sulfides. The energy dispersive analysis performed on the dark particle indicates the presence of Ca, Al, Si, Fe and O, which suggests the existence of andradite and calcite in the mineral, as with the particles smaller than 25 microns.

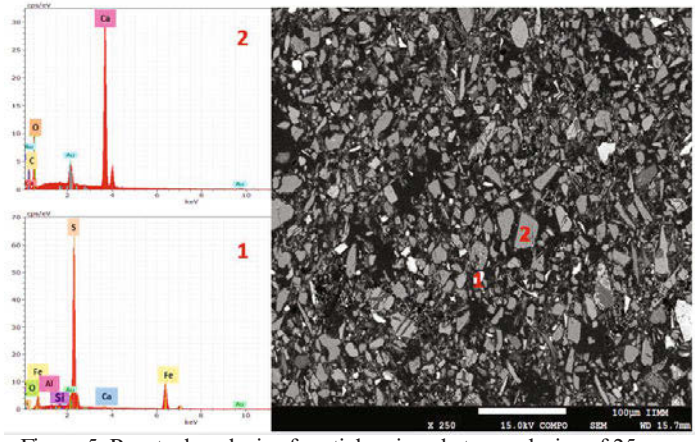

Figure 5. Punctual analysis of particles sieved at a mesh size of 25 µm.

Figure 9 shows the mapping performed on particles sieved at a mesh size of 37 µm, where Si, K, Mg, Ca, Al, S, C, O and Fe were identified, as well as an important concentration of W evenly distributed in the mineral. The relation between Fe and S is present in the same manner as the previous samples, and it was confirmed by the energy dispersive microanalysis performed on the particle seen in the bottom micrograph in figure 6.

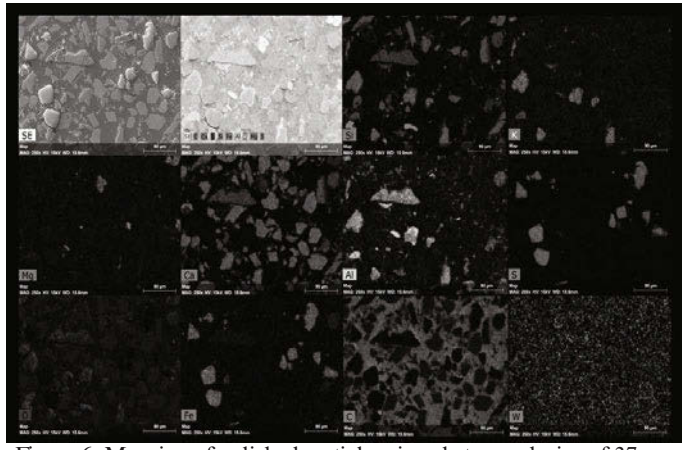

Figure 6. Mapping of polished particles sieved at a mesh size of 37 µm

The element O was observed to be evenly distributed; however, in this case, Ca is concentrated in larger particles, and it is associated to Si and Al. The punctual analysis performed on the particle shown in the top micrograph of figure 7 reveals the presence of S, Fe, and Mg, which suggests the existence of magnesioferrite.

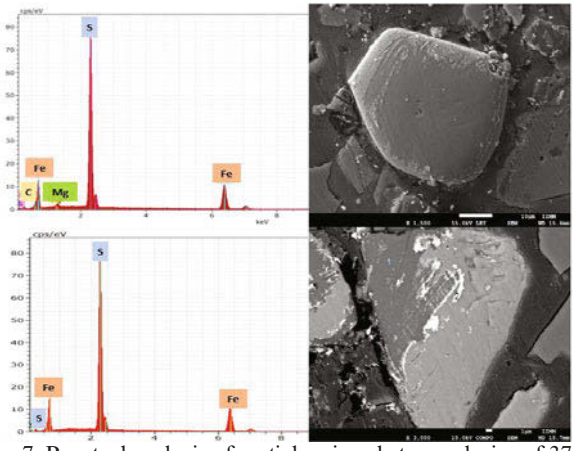

Figure 7. Punctual analysis of particles sieved at a mesh size of 37 µm.

Conclusions

By means of the XRD technique, tungstenite (WS_2) was identified as the mineral species that contains tungsten; this element was confirmed by the mapping performed through the SEM-EDS technique on particles sieved at 37 microns, as well as the elemental chemical analysis by ICP. This suggests that the mineral from the *mina Concordia* mine is a viable source for the extraction of tungsten, with the highest concentration of 402.88 g ton^{-1} identified in particles sieved at 74 microns. However, tungsten is likewise present in the pull size ore sample. Elements typical to the ore, such as S, Fe, and Zn, confirm the presence of abundant

metal sulfides that were identified through XRD and SEM-EDS; they are contained in the mineral sample, whose matrix is mainly composed of calcite and quartz. Among the minor elements, important concentrations of silver can be observed which coincide with the even presence of tungsten at the different mesh sizes at which the sample was sieved.

References

1. Lassner E. and Schubert W. *Tungsten: Properties, Chemistry, Technology of the Element, Alloys, and Chemical Compounds.* (Berlin, GER: Kluwer Academic, Plenum, 1999), 73–80.
2. L. Luo, T. Miyazaki, A. Shibayama, W. Yen and T. Fujita. "A novel process for recovery of tungsten and vanadium from a leach solution of tungsten alloy scrap." *Minerals Engineering.* 16 (2003), 665–670.
3. K. Srinivas, T. Sreenivas, R. Natarajan and N.P.H. Padmanabhan. "Studies on the recovery of tungsten from a composite wolframite–scheelite concentrate". *Hydrometallurgy*. 58 (2000), 43–50.
4. P. Borchers. "Processing of tungsten. Proceedings of the 1st International Tungsten Symposium." *Mining Journal Books Ltd*. 1(1979), 64–77.
5. J.I. Martins, A. Moreira and S.C. Costa. "Leaching of synthetic scheelite by hydrochloric acid without the formation of tungstic acid." *Hydrometallurgy*. 70 (2003), 131–141.
6. H.Q. Gao and Y.F. Su. "Kinetics of the decomposition of scheelite concentrate by leachex process." *Journal of Chemical Industry and Engineering*. 6(1991), 70–78.
7. C.Q. Zheng, Z.Q. Li and Z.Y. Zhang. "Kinetic study of decomposition scheelite with HCl." *Chinese Journal of Rare Metals*. 6 (1980), 11–16.
8. Z. Zhongwei, L. Jiangtao, W. Shibo, L. Honggui, L. Maosheng, S. Peimei and L. Yunjiao. "Extracting tungsten from scheelite concentrate with caustic soda by autoclaving process." *Hydrometallurgy*. 108(2011), 152–156.
9. M. Shamsuddin and H.Y. Sohn. "Extractive metallurgy of tungsten." *Proceedings TMS AIME Symposium. TMS, Warrendale, Chicago.* 1 (1981), 205–230.
10. E. Lassner. "From tungsten concentrates and scrap to highly pure ammonium paratungstate(APT)." *Journal of Refractory Metals and Hard Materials*. 13 (1995), 36–44.
11. H.G. Li , M.S. Liu, P.M. Sun and Y.J. Li. "Caustic decomposition of scheelite and scheelite–wolframite concentrates through mechanical activation." *Journal Central South University of Technology*. 2(1995), 816–20.
12. Y.J. Li, H.G. Li, M.S. Liu and P.M. Sun. "Mechanical activation of alkaline leaching of scheelite concentrate." *Chinese Journal of Rare Metals*. 17(1998), 308–311.
13. Z.W. Zhao and H.G. "Thermodynamics for leaching of scheelite-pseudo-ternarysystem phase diagram and its application." *Metallurgical and Materials Transactions*. 39(2008), 519–523.
14. INEGI."La minería en México." *Series estadísticas sectoriales,* 7(2013), 29-36.
15. DGPM con cifras del IMSS, CAMIMEX. "Participación de México en la Producción minera mundial". 02(2014), 26-42.

Characterization of Minerals, Metals, and Materials 2016
Edited by: Shadia Jamil Ikhmayies, Bowen Li, John S. Carpenter, Jiann-Yang Hwang, Sergio Neves Monteiro, Jian Li, Donato Firrao, Mingming Zhang, Zhiwei Peng, Juan P. Escobedo-Diaz, and Chenguang Bai
TMS (The Minerals, Metals & Materials Society), 2016

MECHANICAL PROPERTIES AND MICROSTRUCTURE OF K418 USING MASTER ALLOY TECHNIQUE AND MECHANICAL ALLOY

Xiaowei Chen, Lin Zhang, Chi Chen, Xuanhui Qu

Institute of Advanced Materials and Technology, University of Science and Technology Beijing; Haidian District Xueyuan Road 30; Beijing, 100083, China

Keywords: Powder metallurgy, Ni-based superalloy, Master alloy, K418.

Abstract

The master alloy technique is a significantly cost-benefit process, in which the master alloy powders and the carbonyl nickel powder are blended together and sintered to form the alloy with homogenous composition. The mechanical properties and microstructures of the K418 superalloy with blending ratio 3:2 (Master alloy: Ni) were mainly discussed in this paper. The master alloy powder was prepared by mechanical alloying. The specimens are near total densification after hot isostatic pressing, and the ultimate tensile strength of the specimens reaches 1118 MPa after solution treatment at 1200^{o}C for 2h, which exceeds that of cast specimens by far.

Introduction

The chemical compositions of the K418 alloy are similar to IN 713C. It is without cobalt and has low density, which has great advantage in civilian high temperature components. Due to its excellent high temperature strength and high oxidation resistance at elevated temperature, it has been widely used in high temperature applications like blade material in aero engines and turbine wheel in automotive industry [1]. The properties of the K418 alloy can reach, or even exceed that of IN713C.

The Ni-based superalloy prepared by pre-alloyed powders has homogeneous microstructure and excellent mechanical properties [2]. However, the high cost of the pre-alloy powder limits the application of Ni-based superalloys in civilian high temperature components. Master alloy method is to blend the master alloy powders, which usually contain oxygen sensitive elements, with carbonyl Fe or carbonyl Ni and then to sinter the mixed powders to homogenous components. Due to the highly alloyed contents of up to several times that of the standard pre-alloyed material [3], the master alloy method can reduce the use of pre-alloyed powders. Moreover, the melting of master alloy particles during sintering process was proved to enhance sintering and promote the homogeneous distribution of the alloying elements [4]. The master alloy method has been widely used in stainless steel for metal injection molding and has extensive market prospects [5]. Therefore, the application of the master alloy method in Ni-based superalloy can effectively reduce the manufacture cost and improve the market competitiveness.

The design of the master alloy component is significant because the proper master alloy powder can produce proper transient liquid phase to homogeneously distribute the alloying elements and promote their diffusion during sintering [6]. The mechanical alloying method has been proved as an effective technique for the synthesis of powders with compositions that cannot be obtained by conventional methods, especially when there is not enough time for more lengthy

methods [7]. Therefore, we chose the mechanical alloying method to produce the master alloy powder with the blending ratio 3:2 (Master alloy: Ni), and explored the microstructure and mechanical properties of the K418 alloy prepared by master alloy method.

Experiment Procedure

The chemical components of the master alloy powders of K418 are presented in Table 1. According to the weight percentage of the carbonyl Ni when blending with the master alloy powder, we named the master alloy powders and specimens as K418 40Ni. The mixtures of elemental powders as shown in Table 1 were milled under argon in a stainless vial. The ball-to-powder weight ratio was 5:1. The mechanical alloying process was then carried out at room temperature using a planetary ball mill with a rotational speed of 400 rpm for 48 hours. The master alloy powder was blended with 0.5 μm carbonyl Ni powder. The mixed powders were spark plasma sintered at 1050°C for 3 minutes under the pressure 40 MPa. Density of sintered specimens was measured by Archimedes method. Then the sintered specimens were homogenization treated at 1200°C for varied periods and then cooled in air. The sintered specimens were heat isostatic pressed at 1210°C for 2 hours under the pressure 160 MPa and then furnace cooled. The HIPed specimens were carried out the tensile test at room temperature after different heat treatments. Their fracture appearance and microstructure were observed by hot field emission scanning electron microscope.

Table Ⅰ. The Designed Chemical Components of Master Alloy Powder of K418 (wt.%)

	Ni	Cr	Al	Ti	Mo	Nb	C	Zr	B
K418 super-alloy	Base	12.5	5.95	0.75	4.3	2.15	0.12	0.105	0.014
40Ni master alloy	Base	20.83	9.92	1.25	7.17	3.58	0.20	-	-

Results

The master alloy powder prepared by mechanical alloying is shown in Figure 1. The average particle size of the master alloy is about 5 μm, whereas a large amount of particles with the size of 2~3 μm exist. For the long milling time (48h), the particles appear polyhedral because of the fracture after the initial stage of cold welding [8]. The XRD pattern (Fig.2) shows that the main peaks of Ni, Cr, Al, Ti, Nb are combined to one peak, which indicates that the elements have gotten into the Ni lattice and been fully alloyed. However, the element Mo is not alloyed because of its large atomic size, which will lead to larger lattice defects and increase the Gibbs free energy violently if it gets into the Ni lattice.

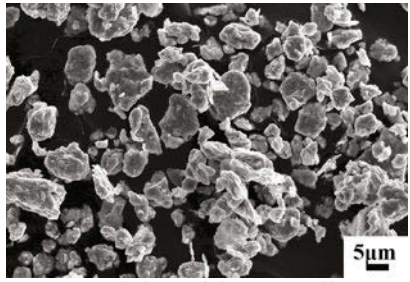

Figure 1. Morphology of the master alloy powder

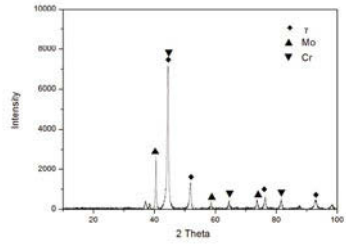

Figure 2. XRD spectrum of the master alloy powder

Figure 3 shows backscattered electron image of the K418 alloy sintered at 1050°C. Alloying elements diffuse homogenously during sintering because there is not significant distinction in the backscattered electron image. However, around the grain boundary, the γ′ phase and the carbide is coarse. Because the elements are easier to diffusion along the grain boundary rather than the bulk, the chemical concentration around the grain boundary is a little higher. Meanwhile, the slow cooling rate (furnace cooling) leads to the desolution of the γ′ phase out from the supersaturated solid solution and growing severely. The nonuniform size of γ′ phase is the origin of the low mechanical properties. Therefore, suitable homogenization treatment is necessary in order to improve the microstructure.

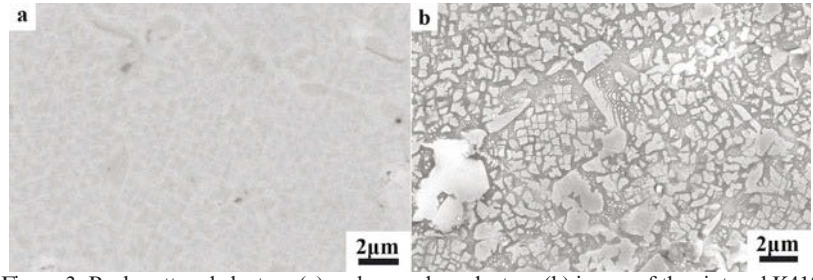

Figure 3. Backscattered electron (a) and secondary electron (b) image of the sintered K418 40Ni specimens

Homogenization of alloying element is prerequisite in order to achieve high mechanical properties. The sintered specimens were homogenized at 1200°C for varied periods in order to dissolve the primary γ′ phase into the matrix and cooled them in air to prevent the severe growing of precipitate phases. As shown in Figure 4, the primary γ′ phase dissolves in γ matrix after homogenized for 1h (Fig.4b) when comparing to the untreated specimen (Fig.4a). The square primary γ′ phase disappears and the sphere secondary γ′ phase separates out uniformly. Compared between Figure 4c and Figure 4d, the γ′ phase becomes smaller with the size less than 0.1 μm from 2h to 4h, so the treatment time of 4h is suitable for the specimens to get homogenous microstructure.

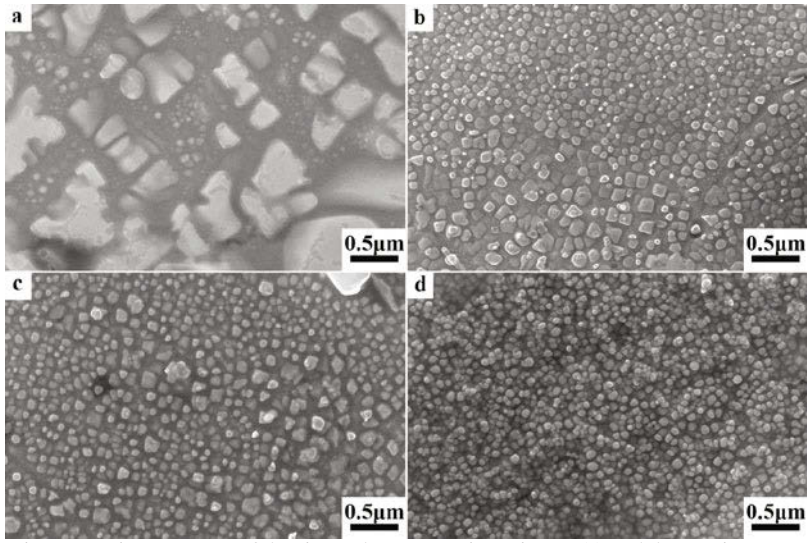

Figure 4. Microstructure of the sintered K418 40Ni specimens (a) and the specimens homogenized at 1200°C for varied periods of time: (b) 1h; (c) 2h; (d) 4h

The microstructure of HIPed and further heat treated specimens is shown in Figure 5. After HIPing, the pores in the specimens almost disappear and the relative density is higher than 99.5%. Furthermore, the precipitated phases turn fine and distribute more uniformly than that of sintering. Thus, the ultimate tensile strength of the HIPed specimens reaches 734 MPa, which approaches to that of cast K418 specimens (755 MPa). However, because of the slow cooling rate of furnace cooling, the γ′ phase is a little coarser (0.35 μm) than that of air cooling (about 0.1 μm). Therefore, the solution treatment condition of 1200°C×2h was taken to improve the microstructure and the mechanical properties. After solution treatment, the size of the γ′ phase changes from 0.35 μm to 0.11 μm, and the shape changes from square to sphere. Hence,

mechanical property of the solution treated samples is improved significantly and the ultimate tensile strength reaches 1118 MPa, which exceeds that of cast K418 by far. Nevertheless, after aging at 750°C for 24h, the film-like γ′ phase forms along grain boundary, and pores appear at the grain boundary, which reduces the mechanical properties sharply. Meanwhile, the size of the γ′ phase increases to 0.18 μm. Consequently, the ultimate tensile strength of the aged sample is only 684 MPa, even worse than that of the cast specimens.

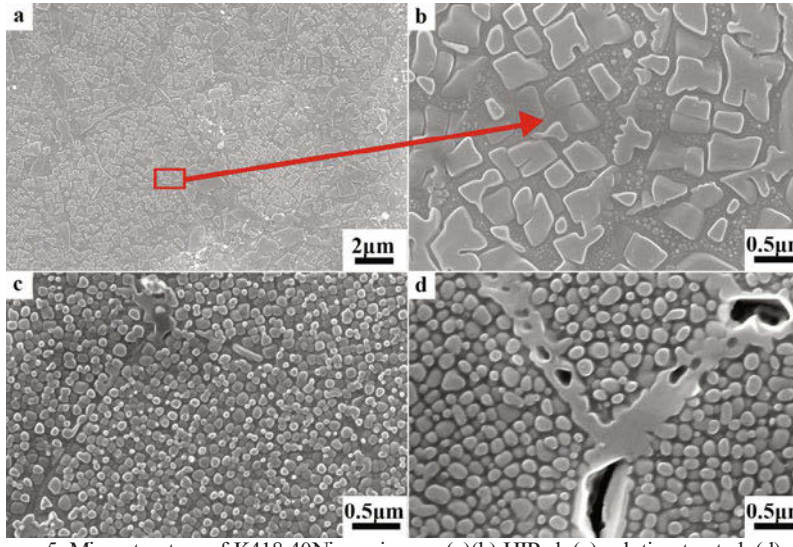

Figure 5. Microstructure of K418 40Ni specimens: (a)(b) HIPed; (c) solution treated; (d) aged

Table Ⅱ. The Ultimate Tensile Strength of K418 by Master Alloy Method

Heat treatment conditions	Ultimate tensile strength/MPa
HIPed	734
Solution treated	1118
Aged	684

The fracture morphology of the HIPed specimens is shown in Figure 6. For HIPed specimens, brittle fracture appears on most of the fracture surface and some dimple fracture exists in the grains. In case of the solution treated specimens, the dimple fracture is in the major, which indicates that the high ultimate tensile strength results from the improvement of ductility. As for the aged specimens, there is much ravine-like texture in the fracture, which illustrates that the pores along the grain boundary is the source of cracks and the intergranular fracture is the dominant factor.

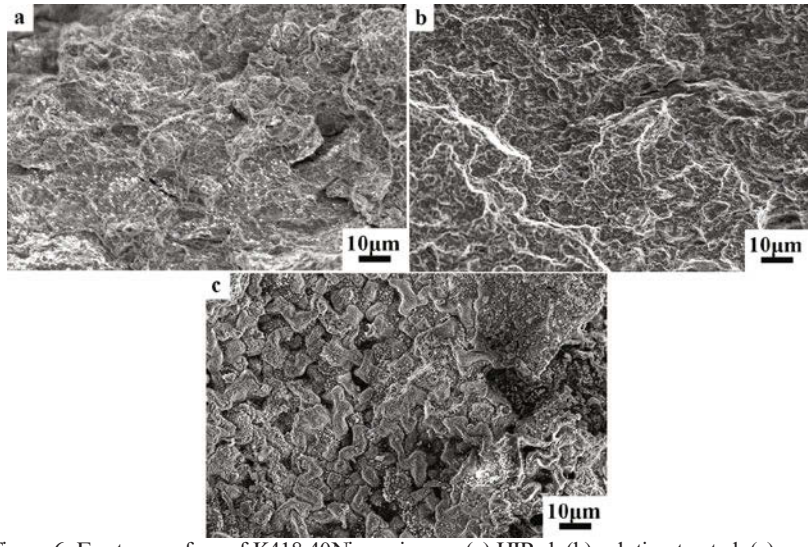

Figure 6. Fracture surface of K418 40Ni specimens: (a) HIPed; (b) solution treated; (c) aged

Conclusion

The K418 alloy using master alloy method was prepared with the blending ratio 3:2 (Master alloy: Ni) and the master alloy powder was prepared by mechanical alloying. The master alloy powder is alloyed well with the average size of 5 μm. And it is found that keeping the specimens at the temperature 1200°C for varied period can improve the microstructure and the suitable time is 4h. After HIPed, the relative density of the specimens exceeds 99.5% and then the ultimate tensile strength of the specimens reaches 1118 MPa after solution treatment at 1200°C for 2h, which exceeds that of cast specimens by far. However, the aged treatment at 750°C for 24h reduces the mechanical property of K418 40Ni specimens by the appearance of the pores along the grain boundary.

Acknowledgements

This work was financially supported by the National Natural Science Foundation of China under Grant No. 51374027 and 51574029.

References

1. Zhaoxia Shi et al., "Solidification Characteristics and Segregation Behavior of Ni-based Superalloy K418 for Auto Turbocharger Turbine," *Journal of Alloys and Compounds*, 571(2013), 168-177.
2. Salk N, "Metal Injection Moulding of Inconel 713C for Turbocharger Applications," *PIM Int*, 5(3)(2011), 61-64.

3. P. A. Davies et al., "Development of Master Alloy Powders, Including Nickel-Based Superalloys, for Metal Injection Molding (MIM)," *Advances in Powder Metallurgy and Particulate Materials*, 8(2003), 8-1.
4. R. Oro et al., "Lean Alloys in PM: From Design to Sintering Performance," *Powder Metallurgy*, 55(4)(2012), 294-301.
5. D. F. Heaney, T. W. Mueller, P. A. Davies, "Mechanical Properties of Metal Injection Moulded 316L Stainless Steel Using Both Prealloy and Master Alloy Techniques," *Powder Metallurgy*, 47(4)(2004), 367-373.
6. R. Oro, M. Campos, J. M. Torralba, "Study of High Temperature Wetting and Infiltration for Optimising Liquid Phase Sintering in Low Alloy Steels," *Powder Metallurgy*, 55(3)(2012), 180-190.
7. José Sicre-Artalejo et al., "Quantification of Hardening in Fe–Mn Master Alloys Prepared by a Mechanical Alloying Process Via Nanoindentation Experiments," *Journal of Materials Research*, 26(14)(2011), 1726-1733.
8. R. Besson et al., "Mechanisms of Formation of Al4Cu9 During Mechanical Alloying: An Experimental Study," *Acta Materialia*, 87(2015), 216-224.

Characterization of Minerals, Metals, and Materials 2016
Edited by: Shadia Jamil Ikhmayies, Bowen Li, John S. Carpenter, Jiann-Yang Hwang, Sergio Neves Monteiro, Jian Li, Donato Firrao, Mingming Zhang, Zhiwei Peng, Juan P. Escobedo-Diaz, and Chenguang Bai
TMS (The Minerals, Metals & Materials Society), 2016

PASSIVE FILMS FORMED ON STAINLESS STEELS IN PHOSPHATE BUFFER SOLUTION

Claudia Marcela Méndez[1], Rodrigo Elvio Burgos[1], Florencia Bruera, Alicia Esther Ares[1,2]

[1] Materials Institute of Misiones, IMAM (CONICET-UNaM), University of Misiones; 1552 Azara Street, Posadas, Misiones, 3300 Argentina.
[2] Member of CIC of the National Research Council (CONICET) of Argentina.

Keywords: stainless steels, corrosion, impedance.

Abstract

The behaviour of passive films formed on directionally solidified stainless steels, 18Cr10Ni2Mo0.08C, 18Cr14Ni8Mo0.03C and 18Cr10Ni8Mo0.08C, in different areas that were formed during solidification (columnar, columnar-to-equiaxed transition (CET) and equiaxed) was studied using electrochemical testing in Na_2HPO_4 with / without NaCl. The behavior of stainless steel in the presence of phosphate chlorides is the best compared to non-chloride phosphate.

Introduction

Pitting corrosion is one of the most common mechanisms of failure that occurs in the chemical, petroleum and petrochemical industry. In general, resistance to localized corrosion is strongly dependent on the protective capacity of the oxide film formed on the material, and alloy composition and the aggressive environment are responsible for the protective characteristics of the oxide layer [1-4]. Thus, although 316 and 316L austenitic stainless steel are more resistant to general corrosion and pitting corrosion than conventional austenitic stainless steels such as alloy 304, they are still susceptible to pitting corrosion in severe operating environments. Furthermore it is known that the composition of stainless steels influences the macro and microstructure of the material, in terms of inclusions and secondary phases formation, which in turn can give special characteristics to the passive film that forms on them [5-8].
During unidirectional solidification process three types of structures are obtained: Columnar (C), equiaxed (E), and the zone of columnar-to-equiaxed transition (CET), comprising the final macrostructure. Also, dendritic growth being the most common structure in solidification obtained by process in steels [9]. In previous works [10] was found that zones of samples with equiaxed structure showed the highest values of secondary dendritic spacing within the same cylinder, and a good ability to repassivation after pitting in chloride media. Also, it was also noted that the Fe-14Ni-18Cr-8Mo-0,03C (sample C) stainless steel in medium with chlorides, the oxide layer formed was of the less porous and greater resistance to charge transfer, while the Fe-18Cr-10Ni-2Mo-0,08C (sample A), alloy with columnar structure, formed a protective film but with low resistance to charge transfer, and high porosity passive film, making it susceptible against localized corrosion. The steel sample of composition Fe-18Cr-10Ni- 8Mo-0,08C (Sample F) had the best performance against localized corrosion.
The addition of sodium hydrogen phosphate to media significantly reduces the aggressive nature of the chloride ion improving corrosion resistance of the material [11]. The practical procedures

for preventing the corrosion of metallic material by phosphate anions usually involve redox processes where precipitation reactions occur on the surface of the material, forming highly insoluble salts such products acting as protective barrier [12-13].
Several investigators have evaluated its effectiveness as an inhibitor for different materials in acidic and neutral media [14-20], iron in alkaline medium [21-22], 304 stainless steel in neutral medium with added chlorides [23], 13CrNiMo soft martensitic steel [24-29].
This paper aims to study by voltammetry technique and electrochemical impedance spectroscopy (EIS) the effect of Na_2HPO_4 as a corrosion inhibitor of stainless steels, with different microstructures, in the presence and absence of 0.5 M NaCl, at room temperature.

Experimental Procedure

Stainless steels used in this study were solidified in a vertical directional solidification device, and their compositions are shown in Table 1.

Table 1: Composition of the samples (wt%).

SAMPLE	C	Si	Mn	P	S	Cr	Ni	Mo	Fe
A	0.08	1.00	2.00	0.045	0.030	18.00	10.00	2.00	Balance
C	0.03	1.00	2.00	0.045	0.030	18.00	14.00	8.00	Balance
F	0.08	1.00	2.00	0.045	0.030	18.00	10.00	8.00	Balance

Each specimen has three grain structures: columnar, equiaxed, and columnar-to-equiaxed transition (CET).
The samples were grounded using SiC papers until #1500 granulometry, washed with demineralized water and dried by compressed air.
Electrochemical measurements were performed in a three electrode cell, saturated calomel electrode (SCE) was used as reference electrode. The tests were performed in solutions of 0.5 M Na_2HPO_4 (pH = 9.2) and 0.5M Na_2HPO_4 plus 0.5 M NaCl, and temperature of 25 ± 1 ° C, using a potentiostat / galvanostat Gamry Reference 300.
The cyclic voltammetry measurements were developed at a rate of 100 mV/s, sweeping a potential from -1.2 V to 1 V vs SCE.
Electrochemical impedance spectroscopy (EIS) tests were performed prior to precatodized, -1 V during 3 minutes, then left open circuit for 1 hour, with a potential amplitude: 10 mV / s in a frequency range of 100 kHz -1 mHz. Measurements were performed at open circuit potential. For setting method of results, the nonlinear least squares method designed by Bouckamp was used.

Results and Discussion

The voltammograms obtained for A, C and F samples appear in Figures 1 to 3. The evolution of the current density is similar for both materials and as potential at which the current increases, and can be assigned different processes occurring during the film formation.
In all samples were observed two peaks in the anodic sweep and two in the cathodic direction.
The first peak, A_I, is at -0.45V and corresponds to the oxidation of magnetite, according to Eq (1 and 2):

$$Fe_3O_4 + OH^- + H_2O \rightarrow 3FeOOH + e^- \quad (1)$$

$$3Fe_3O_4 \rightarrow 4\gamma - Fe_2O_3 + Fe^{2+}_{(ads)} + 2e^- \quad (2)$$

Magnetite is of prime importance in the passive layer, as it plays an important role protecting steel against corrosion [30].
It may also be the balance in the presence of phosphate,

$$Fe_3(PO_4)_2 + 4H_2O \rightarrow Fe_3O_4 + 2HPO_4^{2-} + 6H^+ + 2e^- \quad (3)$$

where E = -0.520V, the pH variation and concentration of HPO_4^{-2} affects the equilibrium potential [22] according to

$$E(V/SCE) = 1.094 - 0.178pH + 0.0296\log\left[HPO_4^{2-}\right]$$

And the oxidation of Fe^{+2}

$$Fe(OH)_2 \rightarrow \gamma - FeOOH + 2H_2O + H^+ + e^- \quad (4)$$

where E= -0.521V/SCE,
The last anodic peak, A_{II}, at 0.6 V describes the reaction of oxidation of chromium,

$$Cr_2O_3 + 5H_2O \rightarrow 2HCrO_4^- + 8H^+ + 6e^- \quad (5)$$

It is associated with an internal oxidation film of Cr^{+3} to Cr^{+6} species, either an oxide or in solution [31]. Discarded here that this maximum is related to the species of Mo since as shown in Pourbaix diagram containing superimposed contributions of Fe, Cr and Mo, the pH of the electrolyte used, Mo does not oxidize at a valence state higher in the range of potential [32].
The traces of the curves end at the end of the anode potential, with the occurrence of the reaction of oxygen evolution that follows the general trend of higher Ni content to lower the potential [33].
Lower current in the curves may be interpreted as a result of a thinner oxide, having a different conductivity attributed to two factors, a different distribution of nickel in the passive film [34], and another possibility is probably related to the existence of molybdenum in the passive film in the samples C and F further, can change the structure of the passive film and the dielectric properties thereof [35].
Sample C shows the columnar structure in the higher current values, followed by equiaxed.
In cathodic turn, C_I and C_{II} peaks are observed, which representing the reverse reactions present in the anodic peaks A_I y A_{II} [34].

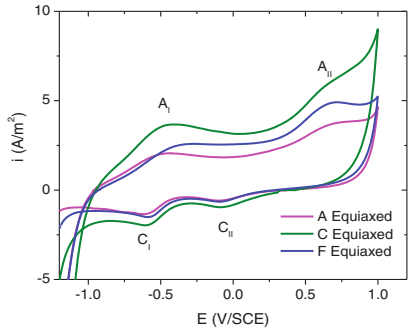

Figure 1.Cyclic voltammograms of equiaxed sample in Na_2HPO_4.

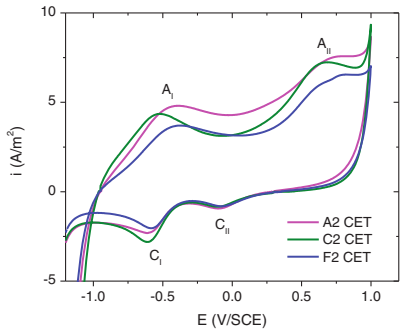

Figure 2. Cyclic voltammograms of CET sample in Na_2HPO_4.

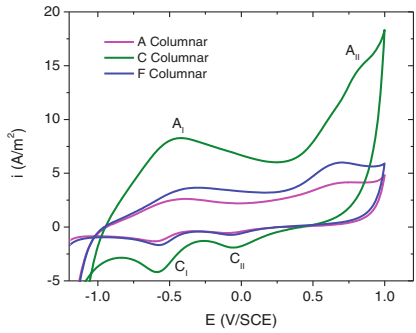

Figure 3. Cyclic voltammograms of columnar sample in Na_2HPO_4.

.

The results obtained with the addition of 0.5 M NaCl (Figure 4) have not significantly affected the electrochemical behavior of the materials; the only place where there has been an increase in

current only about the presence of phosphate is in the sample F (columnar zone) and the sample A (equiaxed zone). This increased current may be due to adsorption of chlorides.

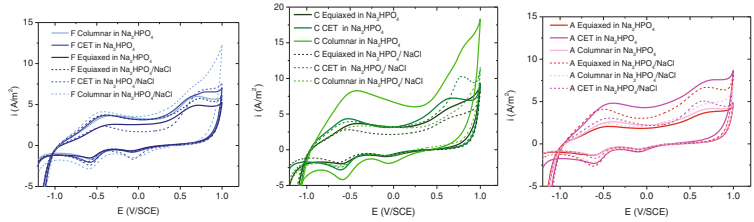

Figure 4.Cyclic voltammogram in 0.5 M Na_2HPO_4 and 0.5 M NaCl/0.5M Na_2HPO_4.

Electrochemical Impedance Spectroscopy (EIS) is used to explain the behavior of the electrolyte/solution interfaces, and generally the data are adjusted to an equivalent circuit models for interpretation.

Impedance responses obtained for the three alloys in solution were simulated using the equivalent circuits shown in Figure 5.

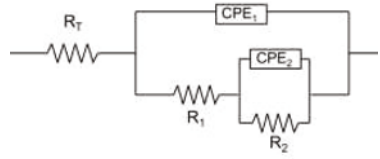

Figure 5. Proposed equivalent circuit.

Where R_T, corresponds to the resistance of the electrolyte, R_1 corresponds to the resistance to charge transfer accompanying the double layer and R_2 refers to the resistance of the oxide layer; constant phase elements CPE_1 corresponds to the ability of the double layer and CPE_2 are attributed to capabilities porous oxides.

The adjustment results are seen in Figures 6 and 7. With regard to values of CPE_1 and CPE_2, they remain similar for all three samples in the three zones of structures; there is no clear trend in Figure 6. As regards of overall resistance values, the resistors R_1 and R_2 tend to increase when the phosphate is combined with the presence of chlorides, except for sample F (equiaxed zone) and the sample C (CET zone). The presence of Na_2HPO_4 allows to form a protective layer because the mechanisms of formation of thereof are different to those seen in the absence of inhibitors [22] intervening part of the same intermediates as quickly generate Fe oxides.

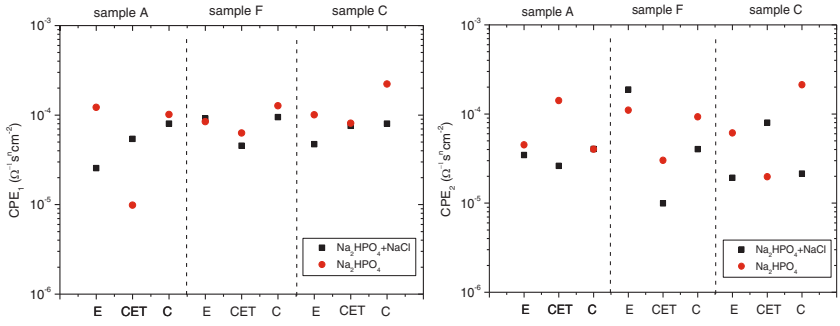

Figure 6. Constant phase elements (CPE) obtained from fits of the electric equivalent circuit.

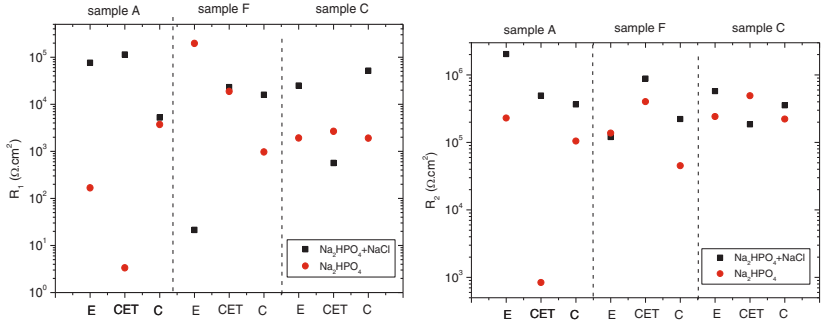

Figure 7. Polarization resistance obtained from fits of the electric equivalent circuit model.

Conclusions

The passive films formed on stainless steels in Na_2HPO_4 solution, with and without addition of NaCl, differ from each other according to the steel composition and structure.

Cyclic voltammetry analysis shows that stainless steels clearly exhibit two peaks corresponding to the oxidation/reduction of Fe^{+2}/Fe^{+3} and Cr^{+3}/Cr^{+6}, as well as a passive region.

The 18Cr14Ni8Mo0.03C sample, in its columnar structure, shown higher current values when operating in phosphate medium in the absence of chloride, however, the 18Cr10Ni2Mo0.08C sample, in its columnar and equiaxed structures, is that having better performance.

The stainless steels studied in the present research respond and properly matched to an equivalent circuit of the $R_I(CPE_1(R_1(CPE_2\ R_2)))$ type.

The 18Cr10Ni2Mo0.08C sample has the higher strength values in the oxide layer, according to the impedance measurements, when NaCl has been added to the Na_2HPO_4 solution.

In general, the resistance of the oxide layer formed on stainless steels has been greatest in Na_2HPO_4 media in the presence of chlorides than in the absence of them.

References

[1] G.S. Frankel, L. Stcckert, F. Hunkeler and H. Boehni, Corrosion NACE. 1987:43, 429.
[2] L. Stockert and H. Bohni, Materials Science Forum. 1989:313 44-45.
[3] K. E. Heusler, Corrosion Science 31. 1990:597.
[4] C. Boulleret. D. Gorse and B. Baroux. Eurocorr. 1996: 199 24-26.
[5] P. Schmuki, H. Böhni, Electrochimica Acta 40 (1995) 775–783.
[6] C.A. Gervasi, P.D. Bilmes, C.L. Llorente, Metallurgical factors affecting localized corrosion of low-C 13CrNiMo martensitic stainless steels, (Chapter 1).in: I.S. Wang (Ed.), Corrosion Research Trends, Nova Science Publishers, NY, (2007).
[7] P.D. Bilmes, C.L. Llorente, C.M.Méndez, C.A. Gervasi, Corrosion Science 51 (2009) 876–881.
[8] C.A. Gervasi, C.M. Méndez, P.D. Bilmes, C.L. Llorente, Materials Chemistry and Physics. 126 (2011) 178–182.
[9] M.C. Flemings, Solidification Processing, (p. 148), McGraw Hill Book Co., New York, NY, (1947).
[10] M.M. Covinich, C.M. Mendez, A.E. Ares, SAM-CONAMET 2013, Iguazú, Argentina, 2013, paper T6C.45.
[11] R. Burgos, F. Bruera, L. Santa Cruz, A. Ares, C. Méndez. Pasividad en Solución de Fosfato de Aceros Inoxidables Solidificados Unidireccionalmente. Matéria. 2013.
[12] L.,Fedrizzi, F. Deflorian, S.,Rossi, L. Fambri, P.L. and Bonora, (2001), "Studyof the corrosion behaviour of phosphatized and painted industrial water heaters", Progress in Organic Coatings, Vol. 42 Nos 1/2, pp. 65-74.
[13] E. Klusmann, and J.W. Schultze, (2003), "pH-microscopy: technical application in phosphating solutions", Electrochimica Acta, Vol. 48 Nos 20/22, pp. 3325-32.
[14] G. Kilincceker, B. Yazici, M. Erbil, and H. Galip, (1999), "The effect of phosphate ions (PO32 4) on the corrosion of iron in sulphate solutions", Turkish Journal of Chemistry, Vol. 23 No. 1, pp. 41-50.
[15] C.A., Borra´s, R. Romagnoli, and R.O. Lezna, (2000), "In-situ spectroelectrochemistry (UV-visible and infrared) of anodic films on iron in neutral phosphate solutions", Electrochimica Acta, Vol. 45 No. 11, pp. 1717-25.
[16] L.S. McNeill, M. and Edwards (2002), "Phosphate inhibitor use at US utilities", Journal American Water Works Associations, Vol. 94 No. 7, pp. 57-63.
[17] H., Amar, J. Benzakour, A., Derja, D.Villemim, B. and Moreau, (2003), "A corrosion inhibition study of iron by phosphonic acids in sodium chloride solution", Journal of Electroanalytical Chemistry, Vol. 558, pp. 131-9.
[18]. M. Kurosaki, and M. Seo, (2003), "Corrosion behavior of iron thin in deaerated phosphate solutions by an electrochemical quartz crystal microbalance", Corrosion Science, Vol. 45 No. 11, pp. 2597-607.
[19] O. Benali, M. Abdemmoula, P. Refait and J.M.R. Genin (2002), "The behaviour of phosphate ions as corrosion inhibitor for Fe(II)-Fe(III) hydroxycarbonate green rust" Hyperfine Interactions, Vol. 139 Nos 1/4, pp. 223-30.
[20] E.M.A., Martini, S.T. Amaral, and I.L Müller,. (2004), "Electrochemical behaviour of invar in phosphate solutions at pH ¼ 6.0", Corrosion Science, Vol. 46 No. 9, pp. 2097-115.
[21] C. Giacomelli, F.C. Giacomelli, R.L. Bortolluzzi, A. Spinelli, Properties of potentiostatic passive films grown on iron electrodes immersed in weak-alkaline phosphate solutions, Anti-Corrosion Methods and Materials. 53 (2006) 232-239.
[22] C. Giacomelli, and A. Spinelli, (2004), "A potentiodynamic and SEM study of the behaviour of iron in pH 8.9-11.0 phosphate solutions", Anti-Corrosion Methods and Materials, Vol. 51 No. 3, pp. 189-99.
[23] M., Lakatos-Varsányi, F. Falkenberg, I. Olefjord, "The influence of phosphate on repassivation of 304 stainless stees in neutral chloride solution", Electrochimica Acta, Vol.43, N1-2, pp 187-197. 1998.
[24] C.A. Gervasi, C.M. Méndez, P.D. Bilmes, C.L. Llorente, "Analysis of the impact of alloy microstructural properties on passive films formed on low-C 13CrNiMo martensitic stainless steels", Materials Chemistry and Physics 126 (2011) 178–182, ISSN 0254-0584. March 2011.

[25] P.D. Bilmes, C.L. Llorente, C. M. Méndez, E.R. Ruiz, C.A. Gervasi. “Comportamiento pasivo y susceptibilidad al picado de aceros inoxidables soft martensíticos” 9° Congreso Internacional de Metalurgia y Materiales SAM-CONAMET 2009: Primeras Jornadas Internacionales de Materiales Nuclares, compilado por José Ovejero García, 1a ed., Buenos Aires, Comisión Nacional de Energía Atómica-CNEA, 2009. CD-ROM. Págs 908-913. ISBN 978-987-1323-13-5.
[26] C.A. Gervasi, C.M. Méndez, P.D. Bilmes, C.L. Llorente XI Congreso Binacional de Metalurgia y Materiales, Conamet/SAM 2011, Rosario, Argentina, del 18 al 21 de octubre del 2011. “Propiedades semiconductoras de las películas pasivas formadas sobre aceros inoxidables softmartensíticos”
[27] C.A. Gervasi, C.M. Méndez, P.D. Bilmes, C.L. Llorente “Propiedades de las películas pasivas formadas sobre aceros inoxidables soft martensíticos”. XVII Congreso Argentino de Fisicoquímica, 3 al 6 de mayo de 2011, Córdoba, Argentina.
[28] C. M. Méndez, C.A. Gervasi, P. Palacios, P.D. Bilmes, C.L. Llorente, “Pasividad de acero inoxidables soft martensíticos en solución buffer de fosfato ácido disódico”.VII Latincorr de la NACE, Quito, Ecuador, 31 de agosto al 3 de setiembre del 2010.
[29] C.A. Gervasi, C.M. Méndez, P.D. Bilmes, C.L. Llorente. "Estructura y propiedades electrónicas de la película pasiva de aceros inoxidables softmartensíticos en solución buffer de fosfato”, XX Congreso de la Sociedad Iberoamericana de Electroquímica, SIBAE 2012, Fortaleza, Brasil, 25-30 de marzo de 2012.
[30] L. Freire, M.A. Catarino, M.I. Godinho, M.J. Ferreira, M.G.S. Ferreira, A.M.P. Simões, M.F. Montemor, Electrochemical and analytical investigation of passive films formed on stainless steels in alkaline media, Cement & Concrete Composites 34 (2012) 1075–1081
[31] H. Kaesche, “Metallic Corrosion”, 2nd Edition; 1985, NACE, Houston TX .
[32] S. Chun-Che, S. Chun-Ming, S. Yea-Yang, Lin Hui Julie Su, Mau-Song Chang and Shing-Jong Lin, “Effect of surface oxide properties on corrosion resistance of 316L stainless steel for biomedical
[33] Abreu CM, Cristobal MJ, Novoa XR, Pena G, Perez MC. The effect of Ni in the electrochemical properties of oxide layers grown on stainless steels. Electrochim Acta 2006;51:2991–3000.
[34] R.F.A. Jargelius- Petterson, B.G. Pound. Examination of the role of Molybdenum in passivation of stainless steels using AC impedance spectroscopy. J Electrochem Soc 1998;145(5):1462–9.
[35] Q. W. Knapp, J. C. Wren, Film formation on type-316L stainless steel as a function of potential: Probing the role of gamma-radiation, Electrochimica Acta 80 (2012) 90– 99.

Characterization of Minerals, Metals, and Materials 2016
Edited by: Shadia Jamil Ikhmayies, Bowen Li, John S. Carpenter, Jiann-Yang Hwang, Sergio Neves Monteiro, Jian Li, Donato Firrao, Mingming Zhang, Zhiwei Peng, Juan P. Escobedo-Diaz, and Chenguang Bai
TMS (The Minerals, Metals & Materials Society), 2016

EFFECT OF THE PAPER INDUSTRY RESIDUE ON PROPERTIES IN THE FRESH MORTAR

Azevedo, A.R.G.[1], Alexandre, J.[1], Vieira, C. M. F.[2], Xavier, C.G.[1], Zanelato, E.B.[1], Oliveira, L.I.V.[3]

[1]UENF - State University of the Northern Rio de Janeiro, LECIV – Civil Engineering Laboratory; Av. Alberto Lamego, 2000, Campos dos Goytacazes, Rio De Janeiro, 28013-602, Brazil.

[2]UENF - State University of the Northern Rio de Janeiro, LAMAV – Laboratory of Advanced Materials; Av. Alberto Lamego, 2000, Campos dos Goytacazes, Rio De Janeiro, 28013-602, Brazil.

[3]UENF - State University of the Northern Rio de Janeiro, LENEP – Laboratory of Exploration and Production of Oil; Av. Alberto Lamego, 2000, Campos dos Goytacazes, Rio De Janeiro, 28013-602, Brazil.

Keywords: Mortar, waste and paper

Abstract

The problem of solid waste generation not only restricts construction, the industrial sector in general is a major contributor in this regard. Solid waste can be of domestic or industrial origin, hence arises a major problem, which are the quantitative generated. The objective of this study is the evaluation and characterization of the incorporation of waste from paper industry in mortars at different levels (0% 5%, 10%, 15%, 20%, 25% and 30%), according properties in the fresh state as consistency index, entrained air content and water retention. It can be said that levels from 20% incorporation in lime, mortar produce very workability.

Introduction

A major concern of the world's productive sector is the issue of management of solid waste, various organizations around the world realize the production reduction campaigns and a correct management of these materials. In Brazil the establishment of the National Plan for Solid Waste has made great strides were achieved, such as the requirement of generating waste industry as a proper disposal.

In this context emerged a great demand for economically viable possibilities to allocate this material, disposal in landfills despite being the most usual is not ideal, as well as an impact (less than disposal in the open) generate costs for industry, which ultimately affects the profitability of their production. An economically viable and environmentally acceptable solution is the embodiment of this waste in other productive activities, either in the process or in the constitution of materials [1].

Although there are several studies involving the recycling of waste for construction purposes, many studies still need to be developed to obtain information about the behavior and properties of materials over time. This understanding will enable to establish the actual relationship between recycling, technological performance and ecology, contributing to the pursuit of sustainable development, supporting him on scientific grounds [2].

Among the various building materials can highlight the mortar as one of the most used, whether to finish or to Masonry settlement. The study of new application techniques and new mixtures preparation is extremely important for large construction companies and developers in the country, they can financially impact their activities, generating resource savings which is essential to survival of these companies.

The objective of this study is the evaluation and characterization (real density testing of grains, physical characterization of sand and residue of chemical analysis) of the incorporation of waste from paper industry in mortars at different levels (0% 5%, 10%, 15%, 20%, 25% and 30%), according properties in the fresh state as consistency index, entrained air content and water retention.

Materials and Methods

The residue used in this work was collected in one of the points of discard from the molding process.

After collecting the residue the Chemical Analysis and Density Real grain were performed for material characterization. The particle size test was done with sand using the standard sieves and then the sedimentation test with the passing material sieve (sieve mesh 200, ABNT, 0.075mm) [3].

Chemical analysis was performed using the technique of X-ray spectroscopy by energy dispersive (EDX) using a Shimadzu EDX-700. The sample was ground using a ball mill at the Laboratory of Civil Engineering until the material was sieved (sieve mesh 325, ABNT, 0.045 mm), making it more uniform, which facilitates analysis.

The Density Real grain was performed using calibrated pyknometers in the Laboratory of Soil Mechanics.

Once characterized, the mortars were prepared for consistency test. The mortars were prepared according to NBR 13276 (ABNT, 2005) [4] using the 1:1:6 (cement: lime :sand) ratio, making the replacement of lime for paper residuo (waste), in percentages of 0% 5%, 10%, 15%, 20%, 25% and 30% beyond the reference composition without replacement.

The consistency test was performed according to NBR 13276 (ABNT, 2005)[4]. Several attempts with different additions of water masses were held until it was found the diameter required by standard, 260 ± 5 mm. The consistency test was conducted for the three different compositions, and discovered the water/cement ratio for each of them (Figure 1).

Figure 1. The consistency test - flow table.

The calculation of the entrained air content should follow NBR 13278/2005 [5]. Before starting the test should be done calibration of the drum.

The test water retention will be held according to the NBR 13277/2005 [6]. To carry out the test must be used in fresh mortar prepared according to the NBR 13276/2005 [4].

Results

Figure 2 shows the particle size distribution curve of the sand. In this figure one sees that the so-called "silt fraction" ($2 < d < 20$ m) is 18.90%, the "sand fraction" ($d > 20$ m) is 54.20% and "boulder" is 28.80%.

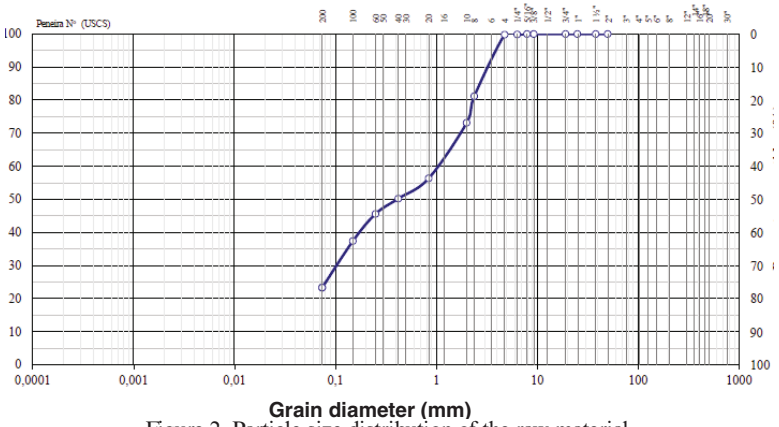

Figure 2. Particle size distribution of the raw material.

The chemical composition of the waste obtained by XRF, is presented in Table 1.

Table 1 – Chemical composition by XRF of the raw material given in terms of oxides (%).

Fe_2O_3	Al_2O_3	CaO	SiO_2	MgO	TiO_2
1.00	22.07	46.18	27.48	2.50	0.68

The density materials used in this work (cement, sand, lime and waste) , are presented in Table 2.

Table 2 – The density materials used in this work.

Materials	*Density (g/cm^3)*
Cement (CPII E32)	2.97
Sand	2.69
Lime (CH_3)	2.31
Waste (Paper reside)	1.71

The mortar was made following the Brazilian rules and immediately after we performed the consistency test. Table 3 shows the results obtained for all the studied traits and their respective water / cement ratio.

Table 3 – The density materials used in this work

Composition	*Consistency Average*	*Water/cement*
Reference	263mm	0.69
5%	256mm	0.69
10%	255mm	0.78
15%	260mm	0.79
20%	261mm	0.85
25%	260mm	0.86
30%	258mm	0.91

In accordance with the obtained density for each material was possible entrapped air content test, whose results are shown in Table 4 below.

Table 4 – The compositions and their consistencies (%).

Composition	*Entrained air content (%)*
Reference	23.00%
5%	23.80%
10%	23.50%
15%	25.10%
20%	26.10%
25%	28.90%
30%	29.50%

The results of water retention in each trace are shown in Figure 3.

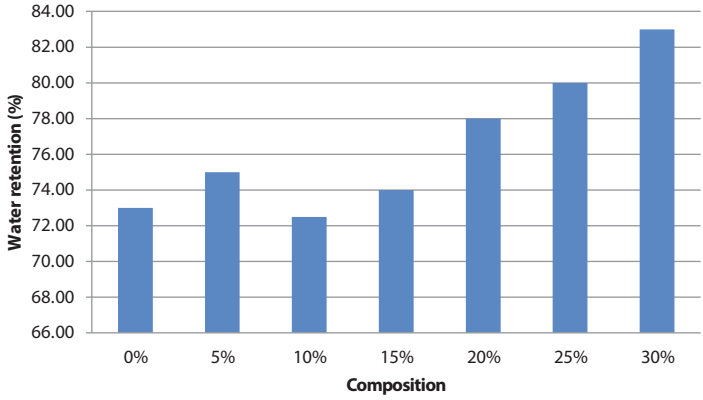

Figure 3. Water retention in diferentes composition (%).

Conclusion

With the findings of this study, the different levels of incorporation, one can check for feasibility in the incorporation of waste from the paper industry in the production of multiple-use mortars, however it was found that some incorporation levels, although meet the specifications in the standards, do not exhibit appropriate characteristics for its use.

We can say that levels from 20% incorporation in lime, mortar produce with great workability, which makes its use and difficult to manufacture, and present properties that can influence the durability of the composite.

Acknowledgements

The authors thank the Brazilian agencies: CNPq, CAPES and FAPERJ for the support provided to this investigation.

References

1. KATZ, A. Properties of Concrete Made With Recycled Aggregate from Partially Hydrated Old Concrete. Cement and Concrete Research, New York, v. 33, n. 5, p. 703-711, 2003.
2. DE AZEVEDO, AFONSO RANGEL GARCEZ; ALEXANDRE, JONAS; DE CASTRO XAVIER, GUSTAVO; CESAR COELHO FRANÇA, FERNANDO; DE ANDRADE SILVA, FLAVIO; MONTEIRO, SERGIO NEVES. Addition of Paper Sludge Waste into Lime for Mortar Production. Materials Science Forum (Online), v. 820, p. 609-614, 2015.

3. Brazilian Association of Technical Norms –ABNT NBR NM 248, Aggregates - Sieve analysis of fine and coarse aggregates (in Portuguese), Rio de Janeiro, Brazil, 2003.
4. Brazilian Association for Technical Norms – ABNT NBR-13276, Mortars applied on walls and ceilings - Preparation of mortar for unit masonry and rendering with standard consistence index (in Portuguese), Rio de Janeiro, Brazil, 2005.
5. Brazilian Association of Technical Norms –ABNT NBR-13278, Mortars applied on walls and ceilings - Determination of the specific gravity and the air entrained content in the fresh stage (in Portuguese), Rio de Janeiro, Brazil, 2005.
6. Brazilian Association of Technical Norms –ABNT NBR-13277, Mortars applied on walls and ceilings - Determination of the water retentivity (in Portuguese), Rio de Janeiro, Brazil, 2005.
7. Brazilian Association of Technical Norms –ABNT NBR-13277, Mortars applied on walls and ceilings - Requirements (in Portuguese), Rio de Janeiro, Brazil, 2005.

Characterization of Minerals, Metals, and Materials 2016
Edited by: Shadia Jamil Ikhmayies, Bowen Li, John S. Carpenter, Jiann-Yang Hwang, Sergio Neves Monteiro, Jian Li, Donato Firrao, Mingming Zhang, Zhiwei Peng, Juan P. Escobedo-Diaz, and Chenguang Bai
TMS (The Minerals, Metals & Materials Society), 2016

Brillouin Scattering Spectroscopy on Mg-Nd Alloy in Different Aging Time

Xinyi He, Wenjian Meng and Yongquan Wu*

State Key Laboratory of Advanced Special Steels, Shanghai University, Shanghai 200072, P. R. China

Keywords: Brillouin Scattering, Mg-Nd alloy, aging treatment

Abstract

Brillouin scattering is a nondestructive optical measurement that can be used to test the elastic properties of materials precisely, i.e. elastic constant, viscosity, and etc. In this paper, we report a backscattering configuration to measure the elastic constants of a series of opaque Mg-Nd alloys in different aging time. The elastic constants, C_{11} and C_{12}, increase sharply with the increase of aging time, while after 16 hours, C_{11} and C_{12} tend to be stable. It indicates that aging time can improve elastic properties of Mg-Nd alloy, which explains the change of texture, in a certain time range.

Introduction

Magnesium alloys are important engineering structure materials used widely to produce 3C (computer, communication and consumption) and automobile products[1-3]. Compared with other traditional metal materials, magnesium alloys have their unique characteristics such as low density, light weight, high specific strength and high elastic modulus; Meanwhile, they perform well in heat dissipation, vibration elimination, impact resistance and corrosion resistance[4, 5]. All of these advantages aroused many researchers' interest in magnesium alloys. As we all know, for the structure materials, we care about their deformability which is determined by elastic modulus directly. Thus, obtaining the elastic modulus of magnesium alloys precisely is significant.

Up to now, there are lots of ways to investigate elastic properties, such as Mechanical stress method[6-8], Ultrasonic pulse and Ultrasonic resonance[9-11]. The limitations of these techniques are the requirement of material size, and can't be used to test multi-layered films and superlatives. As an optical method, Brillouin scattering can detect elastic properties and viscosity of materials precisely[12-15]. It can be carried on under higher temperature and pressure as well. Brillouin scattering requires no mechanical contact and it can be applied to samples as small as one micron on edge, as well as to reactive samples. Therefore, Brillouin scattering has proved to be one of the most powerful means to study elastic properties of materials.

In this study, we report a backscattering configuration to measure the elastic constants of a series of opaque Mg-Nd alloys in different aging time, and then we obtain the influence of the aging time to the alloys' elastic properties.

Experiment

Materials

The materials we measured are pure magnesium and NZ30K alloys in sand casting whose components are showed in table 1. All the samples are φ20× 10mm size cylindrical specimen treated in different aging time showed in table 2. At the same time, we tested the density of the samples via densitometer.

Table 1 Components of NZ30K alloy

Element	Nd	Zn	Zr	Mg
Percentage（wt%）	2.89	0.19	0.41	Bal.

Table 2 The NZ30K alloys in Brillouin scattering experiments

Alloy	Treatment	Density(g/cm^3)
Mg	anneal at 300℃ for 12h	1.737
NZ30K	cast state（F）	1.786
NZ30K	T4[a]（T6-0h）	1.785
NZ30K	T6[b]-1h	1.784
NZ30K	T6-5h	1.782
NZ30K	T6-10h	1.782
NZ30K	T6-16h	1.785
NZ30K	T6-120h	1.785

[a] represents solid solution treatment at 540℃ for 12h;

[b] represents solid solution treatment at 540℃ for 12h, then aging at 200℃.

Method

Brillouin scattering measurements are performed using a Diode-Pumped laser (λ_0=532nm, 1.2w) as a light source and a 180° symmetric scattering geometry for collection. Since the Mg-Nd alloy is opaque material, the laser cannot incident into the inner part of the material, we report a backscattering configuration like the Figure 1 shows to measure. The frequency of the scattered light is analyzed with a six-pass Fabry-Pérot interferometer of Sandercock type[16], then the scattered light is detected by solid-state photon detector. Further details of the experimental setup can be found elsewhere[17]. The mirror distance is 5mm and the scan amplitude is 600nm.

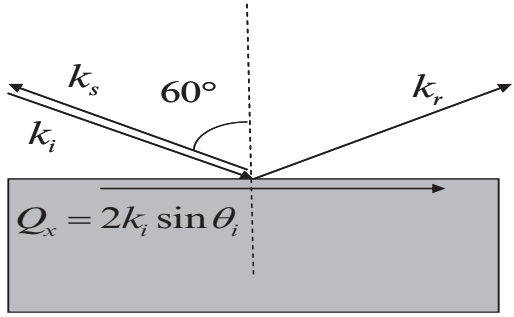

Figure 1 Schematic diagram of general backscattering geometry

As we can see in the Figure 1, the angle θ between incident light and normal of surface plane is 60°, however, during the experiment, we change the angle θ to 30°, 45° and 60°. With the changing of θ, the frequency shift of scattered light would change correspondingly. The relationship between the velocity of wave and frequency shift of wave is:

$$\omega = qv = 2 * k_i * v \sin\theta \quad (1)$$

and can be changed as:

$$f = qv = \frac{2\sin\theta}{\lambda} v \quad (2)$$

ω for angle frequency shift, q for wave vector of phonon, k_i for wave vector of incident light, θ for angle between incident light and normal of surface plane, f for line frequency shift.

Results and Discussion

Brillouin scattering spectroscopy on Mg-Nd alloy

Brillouin scattering spectroscopy of Mg-Nd alloy on F state, with the 30° angle is exhibited in Figure 2(a). We can see there are high intensity peaks in both the Stokes and Anti-Stokes sides of elastic peak called Rayleigh surface acoustic wave (RSW), and near the RSW is Lamb shoulder, at the tail of the Lamb shoulder is a dip called longitudinal wave (LW). We find a new scattering signal peak on the Lamb shoulder, its frequency is between the RSW and LW, and its intensity is much lower than RSW. G Carlotti[18] has found such wave on GaAs crystal, they named it Pseudo Surface Acoustic Wave (PSAW). However, NZ30K is polycrystalline but not crystal, it is uncertain whether the peak in Figure 2(a) is PSAW. At the same time, X. Zhang[19] has found peaks between RSW and LW on pure silicon coating via Brillouin Scattering, and named it Sezawa Wave. Nevertheless, our sample is too thick to be penetrated by laser, it should be regarded as bulk material but not thin film. Therefore, the peak between the RSW and LW is still unknown.

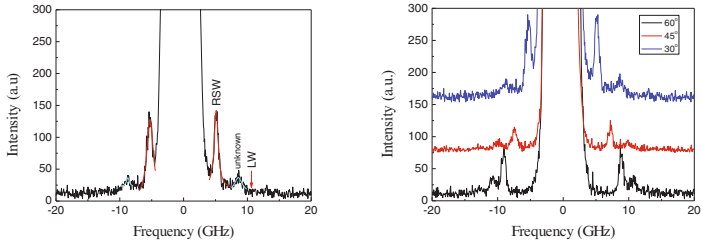

(a) (b)

Figure 2 Brillouin scattering spectrum of NZ30K alloy in cast state when (a) θ is 30°; (b) θ are 30°, 45°, 60° separately.

We can see from the Figure 2(b) that with the increase of angle θ, the frequency shift of both RSW and LW increased. According to the equation (1), when the angle is θ_a, the frequency of the wave is $\omega_a=2*k_i\ sin\theta_a*v$; when the angle is θ_b, the frequency is $\omega_b=2*k_i\ sin\theta_b*v$. The velocity of waves is unchanged for the same material, thus, we can get the relationship as follow, which explains the frequency shift in Figure 2(b).

$$\frac{\omega_a}{\omega_b}=\frac{\sin\theta_a}{\sin\theta_b} \tag{3}$$

Calculation of elastic constants

Spectrums of all the samples in three kinds of angles have been collected, and the signal peaks of RSW and LW were all captured. The observed Brillouin spectrums were fitted by a Lorenz function to determine the Brillouin shift and width accurately. First of all, through equation (1) we obtained the velocity of RSW and LW of NZ30K Alloys on different states separately. Second, via the equation below, we calculated the velocity of Transverse Wave (TW) as well.

$$4v_T^{\,3}\left(v_L^{\,2}-v_R^{\,2}\right)^{1/2}\left(v_T^{\,2}-v_R^{\,2}\right)^{1/2}=v_L\left(2v_T^{\,2}-v_R^{\,2}\right)^2 \tag{4}$$

In polycrystalline materials, the elastic constants and the velocity of the waves have the following relationship:

$$v_L=\sqrt{\frac{c_{11}}{\rho}} \tag{5}$$

$$v_T=\sqrt{\frac{c_{44}}{\rho}}=\sqrt{\frac{c_{11}-c_{12}}{2\rho}} \tag{6}$$

ρ for density of NZ30K Alloys, the dates were listed in table 2.

Third, we calculated the elastic constants of NZ30K Alloys and pure Mg annealed in 300℃ on different states separately, the dates showed in table 3.

Table 3 Elastic constants of polycrystalline NZ30K alloys in different states and pure Mg annealed in 300℃

	Status	Elastic constant (GPa)		
		C_{11}	C_{12}	C_{44}
Mg	anneal at 300℃ for 12h	52.66	22.62	15.02
NZ30K	cast state（F）	59.07	27.77	15.65
NZ30K	T4（T6-0h）	54.01	20.73	16.64
NZ30K	T6-1h	54.61	21.17	16.72
NZ30K	T6-5h	57.53	24.17	16.68
NZ30K	T6-10h	58.53	26.31	16.11
NZ30K	T6-16h	60.90	28.18	16.36
NZ30K	T6-120h	62.47	29.79	16.34

From the table we can see that the C_{11} and C_{44} of NZ30K are bigger than that of Mg which is annealed in 300℃. Comparing the cast state of NZ30K with Mg annealed in 300℃, the elastic properties of F state are better than pure Mg's obviously. It indicates that adding alloy elements to the pure Mg would strength the material and improve the elastic properties. Comparing the NZ30K on F state and T states we find that at the beginning of aging, the strength of T state is lower than F's. It is because that treatment T6-0h is a solution treatment to the alloy, which can be regarded as tempering process, it would eliminate the defects and segregation in alloys, and turn metastable phase to stable phase. While with the aging time extended, there would be precipitated phase nucleate and grow up continuously, and the strength and hardness would surpass F state alloy gradually.

Figure 3 shows the elastic constant as a function of aging time for NZ30K alloys, the dashed line from up to down is the elastic constant C_{11}, C_{12}, C_{44} of NZ30K on cast state. we found that C_{44} is hardly affected by aging time, while C_{11} and C_{12} increase gradually with the extended of aging time, and then remain stable until 16h. This is because of the release of precipitation phase during the aging time, the solid solubility of parent phase decreases step by step. Therefore, during the beginning 16h, the elastic constants increase rapidly, until the supersaturated solid solution turn to saturated solid after 16h, there would not be any precipitation, and the whole system stays stable.

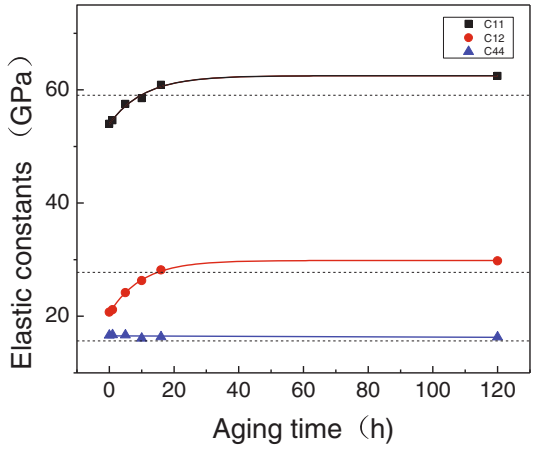

Figure 3 Elastic constant as a function of aging time for NZ30K alloys

Conclusion

In this work, we report a backscattering configuration to obtain the Brillouin scattering spectrum of a series of opaque Mg-Nd alloys and pure Mg. We calculate the elastic constants of NZ30K alloys in different aging time via the frequency shift from the scattering light as well.

Comparing the elastic constants of NZ30K alloys treated by aging with not treated one, we get several findings as follow:

At 0h, due to the solution treatment, the defects and segregation in alloys are eliminated. Thus, the treatment can be regarded as a softening effect, which makes the C_{11} of this state lower than C_{11} of F state. Under the aging treatment, there are more and more new phases precipitate from the supersaturated solid solution. Because of the nucleation and growth of precipitation phases, the elastic properties of alloys changed.

After 10h, the elastic constants C_{11} and C_{12} of T state NZ30K alloys exceed the constants of F state, while C_{44} keeps unchanged. Meanwhile, with the increase of aging time, the constants of NZ30K alloys would not keep on growing. At 16h, the solubility of parent phase decrease, and the dispersed precipitation phases decreases, as a result, the constants turn to steady status gradually.

Acknowledgements

This work is supported by National Natural Science Foundation of China (Nos. 50504010, 50974083, 51174131, 51374141), Joint Funds of the National Natural Science Foundation of China (No. 50774112), National Basic Research Program of China (No. 2012CB722805).

References

1. F.A. Mirza, et al., "Low cycle fatigue of an extruded Mg–3Nd–0.2Zn–0.5Zr magnesium alloy," *Materials & Design*, 2014. **64**: p. 63-73.
2. X. Cao, et al., "A review of laser welding techniques for magnesium alloys," *Journal of Materials Processing Technology*, 2006. **171**(2): p. 188-204.
3. B.L. Mordike and T. Ebert, "Magnesium: Properties — applications — potential," *Materials Science and Engineering: A*, 2001. **302**(1): p. 37-45.
4. M. Pastor, H. Zhao, and T. DebRoy, "Continuous wave-Nd: yttrium–aluminum–garnet laser welding of AM60B magnesium alloy," *Journal of Laser Applications*, 2000. **12**(3): p. 91-100.
5. F.H. Froes, D. Eliezer, and E. Aghion, "The science, technology, and applications of magnesium," *JOM*, 1998. **50**(9): p. 30-34.
6. J. Sundqvist, et al., "Identifying residual stresses in laser welds by fatigue crack growth acceleration measurement," *Journal of Laser Applications*, 2015. **27**(4): p. 042002.
7. B. Taskonak, et al., "Analysis of subcritical crack growth in dental ceramics using fracture mechanics and fractography," *Dental Materials*, 2008. **24**(5): p. 700-707.
8. D. Shakhvorostov, K. Pöhlmann, and M. Scherge, "Structure and mechanical properties of tribologically induced nanolayers," *Wear*, 2006. **260**(4–5): p. 433-437.
9. R.I. Cottam and G.A. Saunders, "An investigation of the validity of ultrasonic pulse-superposition velocity measurements using thin-film transducers," *Journal of Physics D: Applied Physics*, 1974. **7**(2): p. 216.
10. A. Iwaki, et al., "Development of Multiple-Frequency Ultrasonic Imaging System Using Multiple Resonance Piezoelectric Transducer," *Japanese Journal of Applied Physics*, 2012. **51**(7S): p. 07GF02.
11. B.M. Wrobel and R.W. Time, "Improved pulsed broadband ultrasonic spectroscopy for analysis of liquid-particle flow," *Applied Acoustics*, 2011. **72**(6): p. 324-335.
12. J.C. Crowhurst, et al., "Surface Brillouin scattering at high pressure: Application to a thin supported gold film," *Physical Review B*, 1999. **60**(22): p. R14990-R14993.
13. J.D. Comins, et al., "Surface Brillouin scattering of opaque solids and thin supported films," *Ultrasonics*, 2000. **38**(1–8): p. 450-458.
14. A.G. Every, L.M. Kotane, and J.D. Comins, "Characteristic wave speeds in the surface Brillouin scattering measurement of elastic constants of crystals," *Physical Review B*, 2010. **81**(22): p. 224303.
15. L.M. Kotane, et al., "Surface Brillouin scattering measurement of the elastic constants of single crystal InAs 0.91 Sb 0.09," *Journal of Physics: Conference Series*, 2011. **278**(1): p. 012001.
16. J.R. Sandercock, "Trends in Brillouin scattering. Studies of opaque materials, supported films, and central modes," *Light scattering in solids III. Recent results*, ed. M. Cardona and G. Guntherodt. 1982. 173-206.
17. S.V. Sinogeikin, T. Katsura, and J.D. Bass, "Sound velocities and elastic properties of Fe-bearing wadsleyite and ringwoodite," *Journal of Geophysical Research*, 1998. **103**(B9): p. 20819.
18. G. Carlotti, et al., "Brillouin scattering by pseudosurface acoustic modes on (11(mean)1)

GaAs," *Journal of Physics: Condensed Matter*, 1992. **4**(1): p. 257.
19. X. Zhang, et al., "Surface Brillouin scattering study of the surface excitations in amorphous silicon layers produced by ion bombardment," *Physical Review B*, 1998. **58**(20): p. 13677-13685.

Characterization of Minerals, Metals, and Materials 2016
Edited by: Shadia Jamil Ikhmayies, Bowen Li, John S. Carpenter, Jiann-Yang Hwang, Sergio Neves Monteiro, Jian Li, Donato Firrao, Mingming Zhang, Zhiwei Peng, Juan P. Escobedo-Diaz, and Chenguang Bai
TMS (The Minerals, Metals & Materials Society), 2016

THE CHARACTERIZATION OF THE DESULFURIZATION POWDER IN THE SEMI-DRY DE-SO_2 PROCESS OF THE SINTERING PLANT EXHAUST GAS AND ITS INTERACTION WITH THE SOIL PARTICLES

Ling-Chen Kang[1], Li-jun Lu[1], Gai-feng Xue[1], Jiann-Yang Hwang[2]

[1]R&D Center of Wuhan Iron and Steel (Group) Corporation;
28# Yejing Road, Qingshan District; Wuhan, Hubei Province, 430080, P.R. China
[2]Michigan Technological University;
1400 Townsend Dr.; Houghton, Michigan, 49931, USA

Keywords: desulfurization powder, sintering, exhaust gas, soil

Abstract

The desulfurization (de-SO_2) powders are a solid waste obtained from the sintering plants of the iron and steel industries. It is mostly landfilled due to its massive quantities and complicate compositions. A new utilization was developed in this study as a de-soil reagent for the treatment of tailings in the open-pit mines. In this paper, the de-SO_2 powders were collected from a sintering plant using the semi-dry de-SO_2 process. The chemical compositions of the de-SO_2 powders were analyzed by titrations and the chemical phases were determined with a X-ray diffractometer (XRD). The size distribution was measured by a laser particle size analyzer. The micro-morphology was observed by a scanning electron microscopy (SEM). Furthermore, the interaction between the de-SO_2 powder and the soil particle was studied.

Introduction

Air pollutions such as the haze and PM 2.5 have been serious in China in recent years. SO_2 emission is a typical source of the air pollutants, which makes great contribution to the PM 2.5 index. The Chinese government has issued many national standards to restrict the SO_2 emissions from almost every industry. For the iron and steel industry, every sintering machine must have desulfurization (de-SO_2) equipment installed to deal with SO_2 emissions in the exhaust gas. The regulation sets SO_2 concentration at 200 mg/m^3 [1]. Otherwise, the sintering machine would not be permitted to operate.

With the benefits of high efficiency, low installation and operation costs, the semi-dry de-SO_2 process has been adopted by most sintering plants in China. A typical de-SO_2 process

includes the circulating fluidized bed (CFB), spin drying atomizing (SDA), and novel integration design (NID) operations. In the process, CaO powders are transformed to $Ca(OH)_2$ and are then blown into the exhaust gas ducts to capture the SO_2. After the reaction, the de-SO_2 powders are discharged from the dust collecting unit as a by-product,. The de-SO_2 powders contain mainly $Ca(OH)_2$, $CaCO_3$, $CaSO_3$, $CaSO_4$ and $CaCl_2$. The use of the byproduct in many applications such as gypsum replacements has been greatly limited due to the presence of $CaSO_3$. Hence, the de-SO_2 powders became a new solid waste for the iron and steel companies in China. Many stidies have been carried out to solve the waste utilization problem [2-4]. However, it is still a challenge due to various issues including massive amounts, cost/benefit ratio, operation difficulty, transportation, safety and market interests.

During the open-pit mining, the soil layer and the lean ore should always be peeled off, yielding the tailings. These tailings are a mixture of the soil and rocks. The rocks could be separated after crushing and meshing procedure. Then, the separated rocks would be washed with water to clean the remaining soil content, which is also called the de-soil procedure. Finally, the rocks became the qualified macadam or gravels in the construction field.

Recently, a new de-soil method has been developed by our department. The de-soil reagent is mixed with the tailings before crushing. After crushing and meshing, the soil contents in the macadam or gravels could qualify the requirement for the market without water washing procedure. Usually, most soil particles/layers attached on the surface of the rocks were crushed to small fragments during the crushing procedure. However, there were still some small fragments bonded to the rock surface and cause the high soil content in the macadam or gravels. The effect of the de-soil reagent is to solidify the soil particles/layer to a relatively integral solid. Then, in the crushing process, the soil layer could be separated as a whole, and the soil content remaining in the products would be significantly decreased. This new technique could replace the traditional water washing de-soil procedure and was applied in the treatment of the tailings of the Wulongquan lime mine of Wuhan Iron and Steel Corporation (WISCO).

Considering the potential similarity in the chemical composition and the physical morphology between the first generation de-soil reagent and the de-SO_2 powder, the de-SO_2 powder was studied to be used as the second generation de-soil reagent, which may possibly lower the cost. The characterization of the de-SO_2 powder is an important part of the research, which justifies the accommodation of the de-SO_2 powder to the new technique. In this paper, the de-SO_2 powder was characterized by chemistry titration, particle size analysis, powder X-ray diffraction (XRD) and scanning electron microscope (SEM) observation. Furthermore, a brief study on the interactions between the soil particle and the de-SO_2 powder was conducted. The results provided here offer a versatile access to the potential massive scale application of the de-SO_2 powder in the dry de-soil process of the tailings.

Experiment Section

General description.

The de-SO_2 powder was collected from the SDA exhaust gas of the de-SO_2 system in the 2nd branch of the sintering plant of WISCO. The soil samples were collected from random positions. All other chemicals in the experiment are reagent grade and commercial available.

The particle size distribution was measured by the BT-9300H laser particle size analyzer with the anhydrous ethanol as the dispersing reagent. XRD patterns were obtained on D_{max}-2500c X-ray diffractometer with Mo as the X-ray resource. The microscopic observations were captured on a FEI-Quanta 400 scanning electron microscope.

The chemical composition titration experiments.

The $Ca(OH)_2$ content was measured by the acid-base titration method using HCl standard solution with the phenolphthalein as the indicator. The $CaSO_3$ content was measured by the standard iodometry method using the KI-I_2 solution and the $Na_2S_2O_3$ solution with the amylum as the indicator. The $CaSO_4$ content was calculated by subtracting the sulfate content of $CaSO_3$ from the total SO_4^{2-} content. The de-SO_2 sample was pre-oxidized by the Na_2O_2, and the total SO_4^{2-} was measured by the standard gravimetric method using the $BaCl_2$ solution as the precipitant. The $CaCl_2$ content was determined by Ag/AgCl potentiometric titration. The $CaCO_3$ content was calculated by subtracting the CaO content of $Ca(OH)_2$, $CaSO_3$, $CaSO_4$ and $CaCl_2$ from the total CaO content. The total CaO content was determined by the EDTA complexometry method using triethanolamine as the masking reagent and the Chrome blue-naphthol green (K-B) as the indicator.

Pre-treatment of the soil sample.

The as-prepared soil sample was randomly collected. And, it was sieved with 3 mm soil mesh griddle to separate the big-size cobblestone, plate root and so on. The sieve residue was collected for the experiment.

Preparations for the comparison samples.

Two portions of the soil sample (100 g/portion) were loaded in a metal box. One portion was for the experimental portion and the other was the comparison portion. 20 g de-SO_2 powder was added to the experimental portion and uniformly mixed. Afterwards, these two portions were sealed, and stayed in dark. After 7 days, the experimental portion and the comparison portion were sieved with 0.9 mm mesh griddle, then the oversize parts were obtained.

The free dropping impact experiment.

In each portion, 20 individual particles were picked out for dropping test. In the test, the particles fall freely from 0.8 m height. The dropping times were recorded until the particle crushing. Once the particles would not crush after 10 times free falling dropping, the dropping time was record as more than 10 times.

Result and Discussion

Chemical composition of the de-SO_2 powder.

The chemical composition of the de-SO_2 powder was determined by the titration experiments. And the experiment results were listed in Table 1. The de-SO_2 powder was mainly a mixture of the calcium salts. The lime powder (CaO) was converted to $Ca(OH)_2$ slurry and used as the de-SO_2 reagent. Usually, not all $Ca(OH)_2$ could react with the SO_2 gas in the semi-dry de-SO_2 process, and the unreacted $Ca(OH)_2$ and the generated $CaSO_3$ would be the main content of the de-SO_2 powder. The amount of the $Ca(OH)_2$ and $CaSO_3$ depended on the operating conditions and the de-SO_2 efficiency of the de-SO_2 process. The higher $Ca(OH)_2/CaSO_3$ ratio, the lower usage of the de-SO_2 lime. The CaO and $Ca(OH)_2$ are not stable in air because they are able to react with the CO_2 gas, then yielding the $CaCO_3$. Consequently $CaCO_3$ exist in the de-SO_2 powder, and the amount of the $CaCO_3$ depended on the exposure time in the air. $CaSO_3$ is mainly stable, however it could be partly oxidized to $CaSO_4$ by O_2 when exposure to the air. Experimentally, about 10%–20% of the total $CaSO_3$ would be oxidized. Beside the SO_2 gas, some other acid gas, such as SO_3 and HCl, would also appear in the exhaust gas of the sintering machine. It resulted in an increased in the amount of $CaSO_4$ and the existence of $CaCl_2$ in the de-SO_2 powder. Generally, the chemical composition of the de-SO_2 powder is not constant which varies as the status of the de-SO_2 system and the storage conditions of the powder. This is a great challenge for the utilization development of the material.

Table 1 the chemical composition of the de-SO_2 powder

Item	T_{CaO}	$Ca(OH)_2$	$CaSO_3$	$CaCl_2$	$CaSO_4$	$CaCO_3$
Percent	59.1 %	41.9 %	30.3 %	2.2 %	6.1 %	17.2 %

The particle size distribution of the de-SO_2 powder.

The particle size distribution of the de-SO_2 sample measured by a laser analyzer was shown in Figure 1. The median particle diameter D_{50} was 7.29 m, and the diameter of 90% particles was smaller than 21.18 m. The specific surface area based on the size measurement was 531.68 m^2/kg.

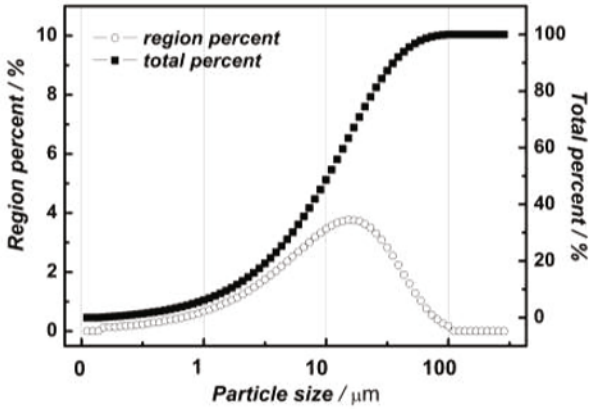

Figure 1. The particle size distribution of the de-SO_2 powder

X-ray diffraction analysis of the de-SO_2 powder.

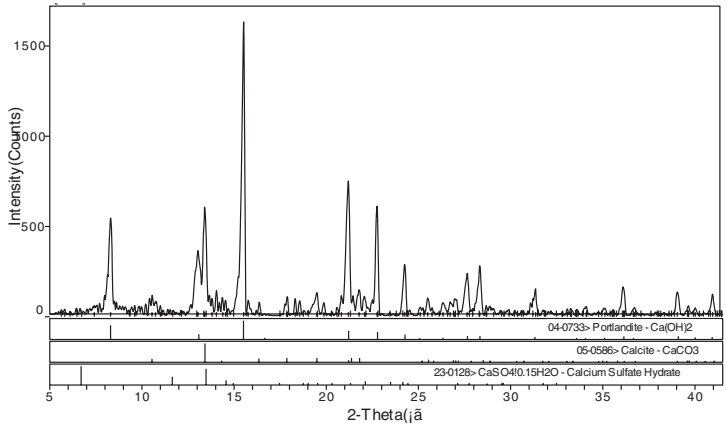

Figure 2. The XRD pattern of the de-SO_2 powder

The XRD pattern of the de-SO_2 powder was shown in Figure 2. The main phase of the mixture was $Ca(OH)_2$, and the 2θ angle of the strongest line laid at 15.5° , 8.3° and 21.2° . The minor phase was $CaCO_3$, and the 2θ angle of the strongest line laid at 13.4° , 21.8° and 10.5° . The phases for the $CaSO_3$ and $CaSO_4$ were not clearly observed and assigned in the XRD pattern; hence they were served as the trace phase for the XRD analysis. The XRD method could only

give a qualitative judgment of the sample, and was difficult to give a quantitative determination of the sample. Based on the chemical titration result, the amount of the $CaSO_3$ and $CaSO_4$ content took a certain part in the sample. Since the de-SO_2 powder is a complicated mixture, the XRD signals of the $CaSO_3$ and $CaSO_4$ related phases would be too weak to be observed due to the poor crystallization status of the related phases, or the signals were masked by the strong signals of the other phases.

The SEM observation and micro area composition analysis of the de-SO_2 powder.

a)

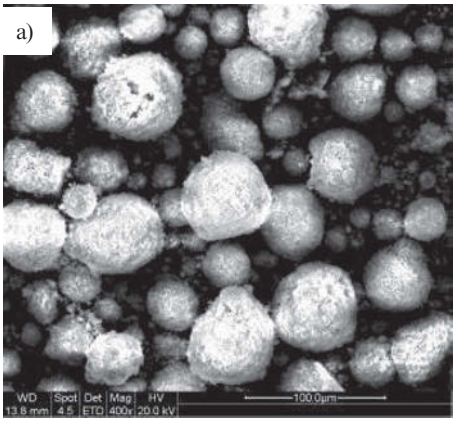

b)

Element	Weight%
S	13.50
Cl	2.32
Ca	45.72
O	38.46
Totals	100.00

c)

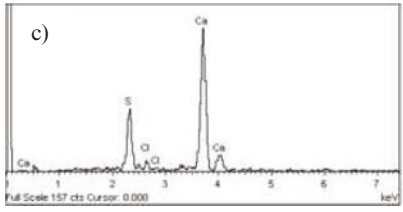

Figure 3. The SEM observation (a) and the micro area composition analysis

The micro-morphology of the de-SO_2 powder was shown in Figure 3a. The Calcium salts aggregated together to give a sphere-like appearance. This morphology might be ascribed to the spray drying atomizer process. And, the chemicals in the slurry aggregated and dried in high spin condition, which finally formed the de-SO_2 powder. The micro area composition analysis (Figure 3b and 3c) revealed that the particles contained Ca, S, and Cl elements. The O element in Figure 3b was calculated based on the chemical stoichiometry since the light atoms O and C were not obviously detected by the energy dispersal X-ray spectrum.

The interaction between the de-SO_2 powder and the soil particle.

In order to study the interaction between the de-SO_2 powder and the soil sample, 5 parts of the soil was mixed with 1 part of the de-SO_2 powder, then the mixture was placed in dark for 7 days.

Another portion of the soil sample without mixing with the de-SO_2 powder was similarly treated for comparison. They were compared in the appearance and the mechanic strengths.

As shown in Figure 4a, the close-up of a typical soil particle in the comparison portion was brown with a relatively rough surface. In Figure 4b, a typical soil particle mixed with de-SO_2 powder was gray with relatively smooth surface. It indicated that there should be some underlying chemistry reactions happened between the surface of the soil particles and the de-SO_2 powder.

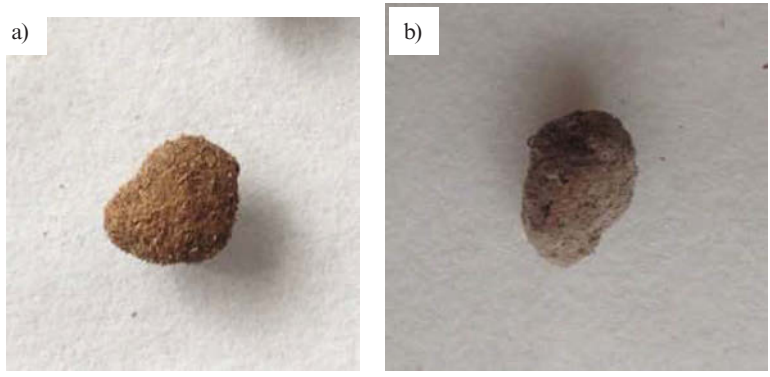

Figure 4. The appearance of the soil particle sample (a) and the mixture particle sample (b).

20 individual particles were picked out from each of the comparison portion and the experiment portion. And the free-dropping impact experiment results were shown in Figure 5. For the comparison portion, only 1 individual particle did not crush after 10 dropping, and 16 individual particles crushed after 3 droppings. For the experiment portion, 11 individual particles did not crush after 10 droppings, and only 7 individual particles crushed after 3 droppings. The mechanical strength of the soil particles significantly increased.

Based on the chemical composition of the de-SO_2 powder, it is possible that the basic Calcium content, such as $Ca(OH)_2$, could react with the acidic SiO_2 or Al_2O_3 content in the soil, yielding the calcium silicate or calcium aluminate phase. Moreover, the $CaSO_4$ or $CaSO_3$ contents might also join the reaction to yield the calcium sulfoaluminate phase. These reactions could generate some new binder phase on the surface of the soil particles and formed a solid and hard integral shell, which changed the appearance and enhanced the mechanical strength of the soil particles. This strengthen effect made the potential application for the de-SO_2 powder in the de-soil process.

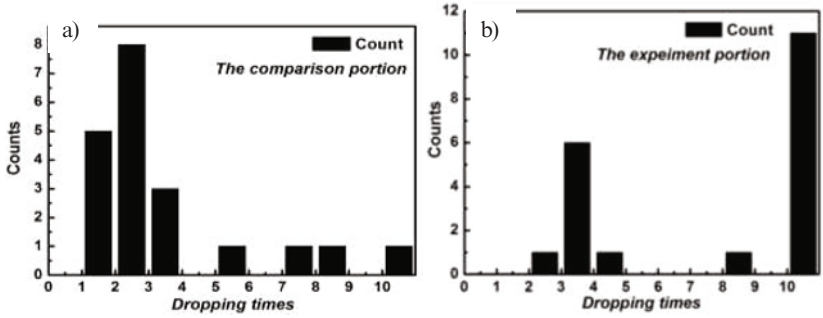

Figure 5. The free dropping impact result of the comparison portion (a) and the experiment portion (b).

Conclusions

The de-SO_2 powder sample was collected from the sintering plant of WISCO. The chemical titration revealed that the de-SO_2 powder contained 41.9% $Ca(OH)_2$, 30.3% $CaSO_3$, 2.2% $CaCl_2$, 6.1% $CaSO_4$ and 17.2% $CaCO_3$. The $Ca(OH)_2$ and $CaCO_3$ phases were confirmed by XRD. The de-SO_2 powder exhibited a sphere-like morphology under SEM observation, and the median particle diameter D50 was 7.29 m. The interaction between the de-SO_2 powder and the soil particle resulted in changes in appearance and mechanic strength. The results show that the de-SO_2 powder is a good candidate for the second generation de-soil reagent.

References

1. *The air pollutant disposal standard for the sintering and pelletizing industry* (Beijing, BJ: Ministry of environment protection of the people's republic of China, 2012), GB28772-2012.
2. J.C. Huang, "The influence of the semi-dry de-SO_2 powder to the concrete," *China concrete and cement product*, 2014, no.8: 19-22.
3. X.L. Yang, "The study on the utilization of the de-SO_2 powder in the roadbed," *Shanghai hiways*, 2014, no. 1: 52-55.
4. Y.L. Fu, et al., "The modifying and application of the semi-dry de-SO_2 powder," *Environmental Science & Technology*, 36 (2) (2013), 155-158.

Characterization of Minerals, Metals, and Materials 2016
Edited by: Shadia Jamil Ikhmayies, Bowen Li, John S. Carpenter, Jiann-Yang Hwang, Sergio Neves Monteiro, Jian Li, Donato Firrao, Mingming Zhang, Zhiwei Peng, Juan P. Escobedo-Diaz, and Chenguang Bai
TMS (The Minerals, Metals & Materials Society), 2016

DIRECT SYNTHESIS OF CARBON NANOTUBES AT LOW TEMPERATURE BY THE REACTION OF CCl_4 AND FERROCENE

Wei Luo[1], Yan Tang[2], Mingsheng He[1], Degang Ouyang[1], Cuijiao Ding[1], Bin Han[1], Shanhe Zhu[1], Minghui Li[1]

[1]Research and Develpoment Center of Wuhan Iron and Steel Company; No.28, Yejin Road, Qingshan District, Wuhan City; Wuhan, Hubei Province, 430080, China
[2]Wuhan University of Science and Technology; No. 947, Heping Road, Qingshan District, Wuhan City; Wuhan, Hubei Province, 430081,China

Keywords: Carbon nanotubes, Ferrocene, Specific surface area

Abstract

Islands-like amorphous carbon nanotubes (a-CNTs) and multi-wall carbon nanotubes (MWCNTs) have been synthesized by the reaction of CCl_4 and ferrocene without or with Co/Ni alloy as growth catalyst at 160 and 350 ºC, respectively. The as-obtained products are characterized by FESEM, TEM, HRTEM, Raman spectroscopy, and nitrogen adsorption-desorption analysis. The results show that a-CNTs have an outer diameter around 450 nm and a length of up to 5 μm, whereas MWCNTs are 20 nm in diameter and 1.5 μm in length. The specific surface area of a-CNTs and MWCNTs are determined to be 1092 and 364 $m^2 \cdot g^{-1}$, respectively. Dichlorocarbene and cyclopentadienyl groups are proved to be the reaction intermediates by GC-MS measurements. A possible growth mechanism of the a-CNTs and MWCNTs has been proposed.

Introduction

Since the discovery of carbon nanotubes (CNTs) in 1991 by Iijima [1], there has been great interest in developing new methods for the synthesis of CNTs due to their potential applications in various technologies [2]. Previous synthesis of crystalline CNTs often involved the transformation of sp^2-hybridized alkene, aromatic hydrocarbons and their derivations to graphite-like structures, in which ferrocene with typical pentagon structure used to act as catalyst and carbon resource [3–5]. New researches indicate that sp^3-hybridized carbon tetrachloride can be also used to synthesize CNT, although its structure is far from graphitic. In the previous research of our group, Xiong et al. [6] had designed a catalytic reduction route using carbon tetrachloride and amide as feeding block and prepared bucky-carbon materials from sp^3-carbon stock at low temperature (230 ºC) for the first time.

Recently, abundant carbon nanostructures were successfully obtained by treating ferrocene in Cl_2 atmosphere at different conditions [7], which provided a promising way to produce carbon nanostructures at relative low temperature. However these carbon materials are almost amorphous. In this paper, we developed a low temperature chlorination approach between sp^3-hybridized carbon tetrachloride and ferrocene to synthesize different morphologic CNTs with good quality by controlling the temperature and catalysts.

Experimental Procedure

All chemicals were of analytical grade and were used without further purification. In our study, 0.3 g ferrocene was added into a 50 mL stainless steel autoclave lined with glass, which was then filled with carbon tetrachloride to 90% of the total volume. The autoclave was sealed and maintained at 160 ºC for 6 h, and then cooled to room temperature naturally. The black precipitate was filtered off, washed with absolute ethanol, carbon tetrachloride, diluted HCl solution and distilled water for several times, and then dried in vacuum at 60 ºC for 4 h. Another experiment was carried out with 1.0 g Co/Ni alloy (Co: Ni molar ratio of 1: 1) at 350 ºC for 8 h. FESEM images were recorded on a JEOL JSM-6700F SEM. TEM images were taken with a Hitachi H-800 transmission electron microscope with an accelerating voltage of 200 kV. HRTEM images and ED pattern were obtained from a JEOL-2010 transmission electron microscope. Raman spectra were recorded at room temperature with a LABRAM-HR Confocal Laser MicroRaman Spectrometer. GC–MS were recorded on a Finnigan GC–MS spectrometer. BET surface areas were measured on a Micromeritics ASAP-2000.

Results and discussion

Field emission scanning electron microscopy (FESEM) images of the products prepared under different conditions are shown in Figure 1. Figure 1a displays a panoramic image of islands-like amorphous CNTs (a-CNTs) prepared at 160 ºC and exhibits tube-like morphology, in which most nanotubes have sealed ends and interlace with one another to form island structures. The inset of Figure 1a is the enlargement of the boxed region, in which some broken nanotubes are shown revealing the character of hollow nature. The FESEM image of multi-wall CNTs (MWCNTs) prepared at 350 ºC with the existence of catalyst is shown in Figure 1b, demonstrating the diameters of 10–40 nm and lengths of up to several micrometers. Some catalyst particles also can be distinguished at the ends of MWCNTs since their diameters are larger than outer diameters of MWCNTs.

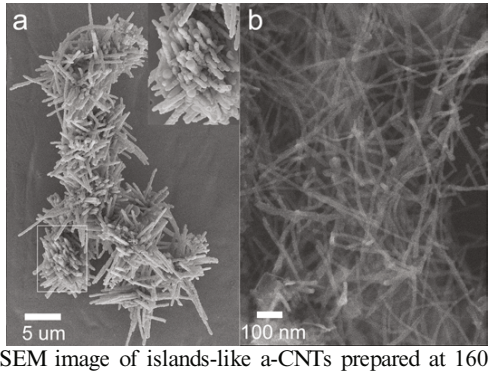

Figure 1 (a) The FESEM image of islands-like a-CNTs prepared at 160 ºC; (b) The FESEM image of MWCNTs prepared at 350 ºC.

Transmission electron microscopy (TEM) and high-resolution TEM (HRTEM) were used to further characterize the microstructures of the as-obtained products. Figure 2a and 2b show the typical TEM images of the product prepared at 160 ºC. The island structure composed of nanotubes can be clearly seen from Figure 2a, consistent with the FESEM results. In general, the nanotubes have an outer diameter around 450 nm and a length of up to 5 μm. The thickness of the wall is 80 nm. The inset of Figure 2b is the selected area electron diffraction (SAED) of the product that indicates the product is amorphous. The TEM images (Fig. 2c, 2d) of the product prepared at 350 ºC show that CNTs are dominant with average length of 1.5 μm. CNTs embedded catalyst particles at their tips (Fig. 2d) indicate that the particles promote nanotube formation in the reactor [8, 9]. Figure 2e shows the tow typical straight coordinate lined nanotubes, with the thickness of walls of about 8 nm. Some irregular particles were also observed within the scope. The content of carbon nanotube is over 70% in the as-synthesized product. Figure 2f shows the HRTEM image of one wall of an individual MWCNT, indicating the high crystallinity of the walls. The walls are composed of graphite sheets aligned parallel to the tube axis. The inter-space between two adjacent layers is around 0.35 nm, which coincides with the c/2 lattice parameter of graphite, that is, d (0002). The inset of Figure 2e is SAED pattern, which also proved the good crystallinity of CNTs.

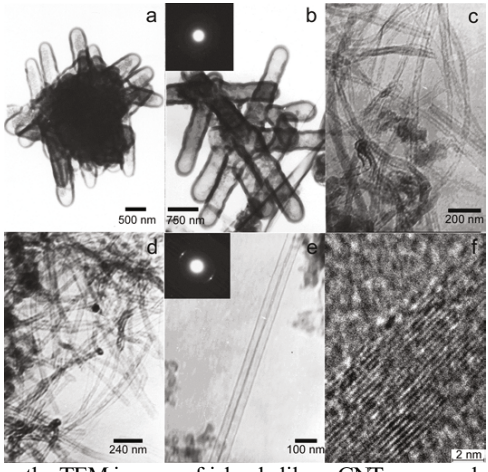

Figure 2 (a) and (b) are the TEM images of islands-like a-CNTs prepared at 160 ºC ; (c) and (d) are the TEM images of MWCNTs prepared at 350 ºC; (e) is the image of typical two straight coordinate lined nanotubes ; (f) is the HRTEM image of one wall of MWCNT.

More convincing evidence of carbon materials is provided by the Raman spectra (Fig. 3). Figure 3a shows wide G and D bands at around 1590 cm^{-1} and 1360 cm^{-1}, which move to higher positions compared to the G and D bands of graphite. It is consistent with the Raman spectrum of amorpous carbon or disorderd graphite in reference [10]. The Raman spectrum of the as-obtained product prepared at 350 ºC (Fig. 3b) is clearly a sharp doublet at 1574 cm^{-1} (G band) and 1346 cm^{-1} (D band) with a ratio of about 0.6, which is characteristic for a disordered sp^2-bonded carbon and similar to the case of multiwall carbon nanotubes [3].

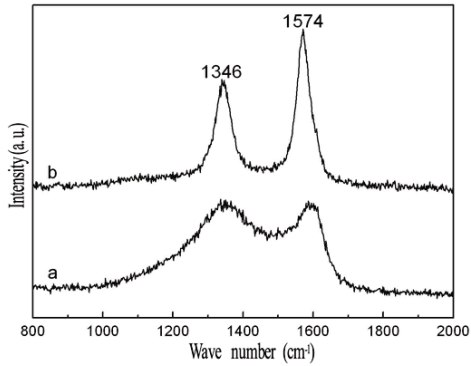

Figure 3 (a) and (b) are Raman spectra of islands-like a-CNTs and MWCNTs.

It was reported by Elsner et al. [11] that dichlorocarbene may occur in the forms of decomposition of carbon tetrachloride, which subsequently forms MWCNTs with the cooperation of Fe@dendrimer catalyst in supercritical CO_2 [12]. However their work on trapping dichlorocarbene by electron-rich alkenes in the reactor is still in progress. In our experiments, fuming hydrochloric acid and $FeCl_2$ are easily detected in the raw products. To further investigate the reaction process, we collected 1 mL of filtered solution after reaction, taking the formation of a-CNTs as the example. After removing inorganic compounds, the solution was then determined by gas chromatography–mass spectrometry (GC–MS). From the gas chromatogram (ESI) corresponding to the mass spectrum, it is found that the filtered solution includes the produced CH_2–CCl_2, CCl_3–CCl_3, dichlorobenzene, CCl_3–CCl=CCl_2, unreacted CCl_4 and ferrocene, and other compounds with higher molecular weight. The existence of byproduct dichlorobenzene indicates that dichlorocarbene and cyclopentadienyl group occurred in the reaction process. Thus it is proposed that dichlorocarbene and cyclopentadienyl groups are most probably the reaction intermediates in the formation of a-CNTs and MWCNTs. It is worth noting that catalyst particles can be found at the ends of MWCNTs in the FESEM and TEM images and their diameters are larger than the diameters of MWCNTs, which indicates the growth mechanism is rather "root growth mode" than "folded growth mode" [8, 9]. The whole formation path of islands-like a-CNTs and MWCNTs is described as seen in Figure 4.

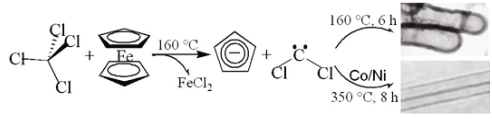

Figure 4 Schematic formation illustration for the chlorination reaction of CCl_4 and ferrocene to produce islands-like a-CNTs and MWCNTs.

To further ascertain the effect of the catalyst and temperature on the morphologies and crystallinity of CNTs, a series of parallel experiments were performed. In the absence of Co/Ni

alloy catalyst, when the temperature changed in the range of 160–220 ºC, the morphology of a-CNTs vary within narrow limits. While the reaction temperature is higher than 240 ºC, some irregular lamellas begin to exist in the final product, and eventually become the leading morphology at 320 ºC. With the cooperation of the catalyst, MWCNTs were obtained at 350 ºC, whose diameters are much thinner than the amorphous ones. It indicates that the reaction temperature and catalyst are vital for the control of the crystallinity and nanostructures of final products.

The BET surface areas of as-obtained islands-like a-CNTs and MWCNTs determined by the adsorption of N_2 at 78 K are 1092 and 364 $m^2 \cdot g^{-1}$. By controlling the reaction rates, carbon nanoantennae and CNT networks (ESI) have also been synthesized. The CNT network shows a specific high BET area value (Sg = 1280 $m^2 \cdot g^{-1}$). The novel islands-like and network structures and their high BET surface areas may produce unique physical properties and potential applications.

Conclusions

In summary, islands-like CNTs (450 nm × 5 μm) and MWCNTs (20 nm × 1.5 μm) have been synthesized from sp^3-CCl_4 and ferrocene without or with Co/Ni alloy as growth catalyst at 160 and 350 °C, respectively. Dichlorocarbene and cyclopentadienyl groups are proved to be the reaction intermediates by GC-MS measurements. The possible mechanism has also been proposed.

References

1. S. Iijima, "Helical Microtubules of Graphitic Carbon," *Nature*, 354 (6348) (1991), 56.
2. M. S. Dresselhaus, G. Dresselhaus, and P. Avouris, *Carbon Nanotubes: Synthesis, Structure, Properties, and Applications* (New York, Springer, 2002)
3. Y. Jiang et al., "A Catalytic-Assembly Solvothermal Route to Multiwall Carbon Nanotubes at a Moderate Temperature," *J. Am Chem. Soc.*, 122 (49) (2000), 12383-12384.
4. Z. J. Zhang et al., "Substrate-site Selective Growth of Aligned Carbon Nanotubes," *Appl. Phys. Lett.*, 77 (23) (2000), 3764.
5. X. Wang et al., "A Novel Route to Multiwalled Carbon Nanotubes and Carbon Nanorods at Low Temperature," *J. Phys. Chem. B*, 106 (5) (2002), 933-937.
6. Y. Xiong et al., "A Novel Approach to Carbon Hollow Spheres and Vessels from CCl_4 at Low Temperatures," *Chem. Commun.*, (7) (2003), 904-905.
7. E. Urones-Garrote et al., "Amorphous Carbon Nanostructures from Chlorination of Ferrocene," *Carbon*, 43 (5) (2005), 978-985.
8. O. A. Louchev and J. R. Hester, "Kinetic Pathways of Carbon Nanotube Nucleation from Graphitic Nanofragments," *J. Appl. Phys.*, 94 (3) (2003), 2002.
9. D. C. Lee, F. V. Mikulec, and B. A. Korgel, "Carbon Nanotube Synthesis in Supercritical Toluene," *J. Am. Chem. Soc.*, 126 (15) (2004), 4951-4957.
10. M. de la Chapelle et al., "Raman Studies on Single Walled Carbon Nanotubes Produced by the Electric Arc Technique," *Carbon*, 36 (5-6) (1998), 705-708.

11. M. Elsner et al., “Mechanisms and Products of Surface-Mediated Reductive Dehalogenation of Carbon Tetrachloride by Fe (II) on Goethite,” *Environ. Sci. Technol.*, 38 (7) (2004), 2058-2066.
12. J. K. Vohs, et al., “Low-temperature Growth of Carbon Nanotubes from the Catalytic Decomposition of Carbon Tetrachloride,” *J. Am. Chem. Soc.*, 126 (32) (2004), 9936-9937.

Characterization of Minerals, Metals, and Materials 2016
Edited by: Shadia Jamil Ikhmayies, Bowen Li, John S. Carpenter, Jiann-Yang Hwang, Sergio Neves Monteiro, Jian Li, Donato Firrao, Mingming Zhang, Zhiwei Peng, Juan P. Escobedo-Diaz, and Chenguang Bai
TMS (The Minerals, Metals & Materials Society), 2016

EFFECT OF MAGNESIUM ALUMINATE SPINEL CONTENT ON PROPERTIES OF BN BASED COMPOSITES

Meng Liu[1,2], Yijie Song[1,2], Xiaohong Xu[3], Guotao Xu[1], Gaifeng Xue[1], Jixiong Liu[2]
[1] Research and Development center of Wuhan Iron and Steel (group) Corporation, Wuhan 430080, China
[2]Advanced materials R&D Center of Wuhan Iron and Steel (group) Corporation, Beijing 102211,China
[3]State Key Laboratory of Silicate Materials for Architectures, Wuhan University of Technology, Wuhan 430070, China

Keywords: Hot-pressing; h-BN; magnesium aluminate spinel; mechanical properties; microstructure; thermal properties

Abstract

BN based composites were prepared by hot-pressing using h-BN as main material in ceramic preparation process. The bulk density, bending strength, vickers' hardness, thermal expansion coefficient, phase composition and microstructure were tested and analyzed by using modern testing technology. The results indicate that the best formula is H1, the bulk density is 2.77 g.cm^{-3}, the bending strength is 231.7MPa, the hardness is HV5 182.73 and the thermal expansion coefficient is 6.75×10-6℃$^{-1}$ at 1400℃. XRD phase composition analysis showed that the main crystal phase of the sample is magnesium aluminium spinel and boron nitride. SEM and EPMA microstructure and element analysis showed that the porosity apertures diameters are under 3 m, the phase distribution are uniformly as well.

Introduction

Twin roller continuous casting, a sort of near-net-shape technology, presents numerous advantages on economical production of thin strips, such as low energy consumption, low equipment and operating costs, and rapid solidification [1-3].The twin roll strip steel casting process, developed by the Usinor company under a project called Myosotis[2-4]. In the process of twin roller continuous casting, the side dams in contact with the rollers act as un-replaceable roles on keeping molten metal from leakage in whole casting process. For more than twenty years, continuous casting process has been actively developed and improved by several major steel companies [5-7]. During casting process, molten metal is frequently dumped into pool region surrounded by rollers and dams, along with rolls rotate to drag metal strips [5, 6]. So, basic properties such as heat resistance to withstand a molten steel temperature of about 1600℃, thermal shock resistance to withstand a temperature difference of about 400℃, less thermal deformation, less wettability with molten steel and excellent wear resistance are required of a material used for side dams which interpose cooling

drums from the both sides and form a moltern steel pool[3-8]. So far, research on materials for side dams is seldom reported. And in the earlier working, other researchers have experimented tens of stuffs such as high temperature ceramics and refractory materials for side dams, unfortunately no solo commercial material was successfully found out. Therefore, it is imperative to develop an appropriate ceramic material to match the using condition in strip casting operations. Generally, each of the monolithic phases ceramic exhibits only a single physical and chemical property, which highly hinders its applications. Accordingly, to develop the multiphase ceramics has been attracting more and more attention because it can combine with the exceptional properties of each ceramic. The object of the present work is to prepare a ceramic material for side dams having excellent properties sufficient for the ceramic plate material to be used continuously casting for a long time. a sort of new composite of BN based ceramics were successfully fabricated by hot pressing method. The properties, such as the mechanical properties and thermal properties as well as phase and microstructure were tested and discussed detailedly.

Experimental Methods

Materials preparation

Commercial available raw materials were used in this study. The h-BN (1 m, Zhongpu Co., Ltd., He Bei, China), $MgAl_2O_4$ (20 m, Almatis, Beijing, China), AlN (0.5 m, Hefei Moke Co., Ltd., An Hui, China), Al_2O_3 (2 m, Luoda Co., Ltd., Shan Dong, China) and Y_2O_3(3 m, Shangyuan new material Co., Ltd., Jiang Xi, China) were used to prepare the BN based composites. The batch formula of series H is designed and show in table 1. These powder mixtures were ball-milled for 12 h in an aluminum bottle using aluminum balls as milling media and alcohol as carrier fluid. The mixed slurry was then dried in a rotary evaporator and sieved through an 80-mesh screen. The composites were fabricated by hot-pressing at 1800 °C for 60 min under a uniaxial load of 25 MPa in N_2 protection.

Table 1 The batch formula composition of series H

Specimen	BN	$MgAl_2O_4$	AlN	Additives	Total
H1	30	30	30	10	100
H2	40	20	30	10	100
H3	50	10	30	10	100

Characterization

Bulk density of the composites was measured by the Archimedes method. Bending strength was tested in a three-point configuration (3 mm×4 mm×36 mm), with a span of 30 mm and a crosshead speed of 0.5 mm/min. Hardness was determined by a Vickers indentation tester(Model FV-700, Wuhan, China)using a diamond indenter with a load of 5 kg for 20 s. Thermal expansion coefficient was tested by the thermal

expansion coefficient instrument (Model RPZ-03, Wuhan, China). The phase constituents of sintered specimens were identified by X–ray diffraction (XRD) (Model D/MAX–Ⅲ, Rigaku., Japan) using Cu Kα radiation source. The observations of microstructures were performed by scanning electron microscope (SEM) (Model JSM–5610LV, Jeol., Japan) and electron probe micro-analyzer(EPMA)(Model JXA-8800R, Jeol., Japan).

Results and discussion

Bulk density and bending strength

The results of the bulk density of specimen H1, H2 and H3 are 2.77g·cm^{-3}, 2.45 g·cm^{-3} and 2.23 g·cm^{-3} respectively. Fig. 1 is the relationship of bending strength and hardness with different specimens. As can be seen from fig. 1, the bending strength of specimen H1, H2 and H3 are 231.7 MPa, 185.6 MPa and 154.25 MPa. What's more, the hardness of specimen H1, H2 and H3 are 182.73 kg/mm^2, 84.95 kg/mm^2 and 53.03 kg/mm^2 as well. The results of the properties of specimen H1, H2 and H3 reflect that with the decrease of magnesium aluminate spinel cotent, the bulk density, bending strength and hardness all declined. The material of magnesium aluminate spinel is kinds of oxide and is beneficial to enhance density behavior and indirectly increase the bending strength and hardness of BN composite as sintering additive due to formation of liquid phase during the sintering process. While in the sintering process, the formation of new phases filled in the pores between different grains in the sintering process, which can increase the force of grain boundary phases and make the increase of relative density and bending strength.

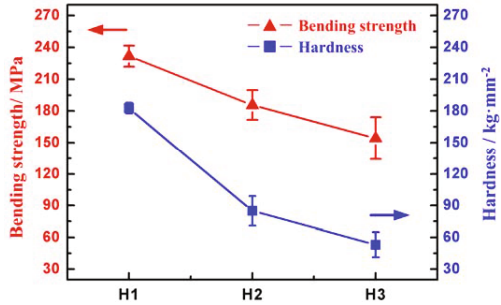

Fig. 1 Bending strength and hardness of BN based composite ceramics

Thermal expansion coefficient

In the process of twin roller continuous casting process, it need the side dam material have good thermal shock resistance to resistant the shock of melt metal. The thermal shock resistance performance of ceramic materials are mainly depends on its thermal expansion properties, low expansion material has excellent performance in thermal

shock resistance. Fig. 2 shows the thermal expansion coefficient from room temperature to 1450°C. The figure shows that with the magnesium aluminate spinel content increase, the thermal expansion coefficient of specimen H1, H2 and H3 all have increased. What's more, with the increase of the temperature, each of the thermal expansion coefficients reveals a tendency of parabola increase. When the temperature is 1400℃, the thermal expansion coefficient of specimen H1, H2 and H3 are 6.75×10^{-6} °C^{-1}, 6.15×10^{-6} °C^{-1} and 5.37×10^{-6} °C^{-1}. Usually, the thermal expansion coefficient of multiphase ceramics can meet a criterion of additive law, while the thermal expansion coefficient of magnesium aluminate spinel is bigger than BN, resulting that with the increase of the content of magnesium aluminate spinel, the thermal expansion coefficient will increase as well. All in all, compact from the result of relative density, bending strength and hardness, the specimen H1 can be choosed as the best batch formula.

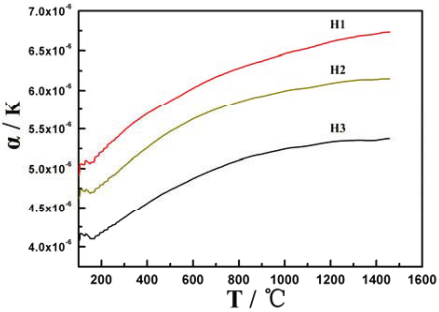

Fig.2 The thermal expansion coefficient of series H

Phase composition and microstructure

In order to understand the internal phase distribution of the optimum specimen H1, XRD, SEM and EPMA analyses were applied to investigate the morphological formation after sintered.Fig. 3 shows the XRD patterns of the optimized specimen H1. As can be seen from the figure, the main phases of specimen H1 while sintered at 1800 °C are h-BN, $MgAl_2O_4$ and $(Al_2O_3)_{10}\cdot(B_2O_3)_2$. Fig. 4 reveals the typical SEM micrographs showing the fracture features of the specimen H1 sintered at 1800 °C. Fig. 4 shows the elements distribution analyzed by EPMA. Figure 4 reveals that there are little pores among the microstructure, and the diameter is about 1~5 m. Also, some big grains exist among the micrograph as well, while the diameter is about 10~20 m. By contact the analysis of XRD patterns and element distribution of EPMA, in the area of the big grains, there both exist the element of Mg and Al, and the element of O can be detected as well which reflect the grains are $MgAl_2O_4$ phase. Meanwhile, among the bases, the accelerate elements of B and N were detected, which detected that is the phase of BN.What's more, among the grain boundary, the elements of Al, O and B can be detected while reveal the phase is $(Al_2O_3)_{10}\cdot(B_2O_3)_2$ which act as binding phases. The phases of $MgAl_2O_4$ and BN distribute evenly among

the specimen thus offer high bulk density and good mechanical properties.To summarize the analysis of the bulk density, mechanical properties, thermal expansion coefficient, XRD patterns, microstructure and element distribution, the addition of $MgAl_2O_4$ phase among the specimen is useful for the improvement of the performance of bulk density and bending strength while low thermal expansion coefficient severely helps to improve thermal shock resistance of the sintered specimen. So, it is acceptable that the multiphase BN based composite ceramic with a good thermal shock resistance, can be prepared completely by hot-pressing sintering technique, thus being suitable to use as the side dam materials in twin roller continuous casting.

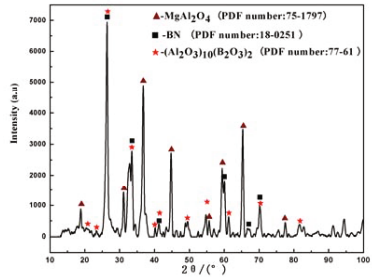

Fig. 3 XRD patterns of the hot-pressed specimen H1

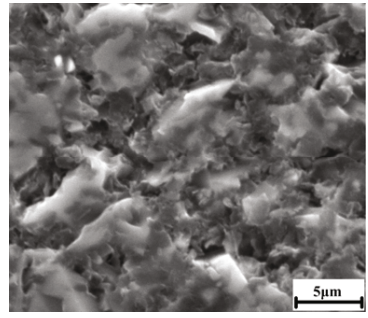

Fig. 4 SEM images of polished fractured surface of hot-pressed specimen H1

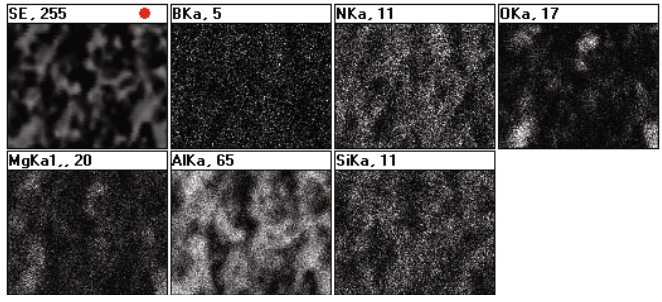

Fig. 5 The element distribution of the specimen H1 tested by EPMA

Conclusions

Results from the present work show that the prepared BN based composite ceramic by adding magnesium aluminate spinel as the main additives is suitable for use as side dam material in twin roller continuous casting. The optimum specimen is H1 which consists by using h-BN as the main material. The hot-pressing temperature of specimen H1 is 1800 °C with the bulk density of 2.77 $g.cm^{-3}$, the bending strength is 231.7MPa, the hardness is HV5 182.73 kg/mm^2, the thermal expansion coefficient is 6.75×10^{-6} $°C^{-1}$. Analysis of XRD indicates that the main phases after hot-pressing are h-BN, $MgAl_2O_4$ and $(Al_2O_3)_{10}\cdot(B_2O_3)_2$. SEM morphology and EPMA element distribution observation shows that the specimen of H1 with a evenly phases distribution of h-BN and $MgAl_2O_4$, while the phase of $(Al_2O_3)_{10}\cdot(B_2O_3)_2$ act as binding phases which helps to improve the mechanical properties. The prepared multiphase BN based composite ceramic with a good mechanical property, thermal property and microstructure can be prepared completely by the hot-pressing sintering technique, which is suitable for use as side dam material in twin roller continuous casting.

Acknowledgements

The financial support of Beijing Science and Technology Commission (No. Z131100002413002) is gratefully acknowledged. Also, the authors gratefully acknowledge the collaboration of several of their colleagues for materials synthesis and processing for their many useful discussions in the present work.

References

1. H. Toshio et al., “Twin roll casting of aluminum alloy strips,” *Journal of Materials Processing Technology,* 153(2004), 42–47.
2. R. Wechsler, “The status of twin roll casting technology,” *Scandinavian Journal of Metallurgy*, 32(2003), 56–62.
3. H.L. Wang et al., “Study on side containment technology of twin-roll thin strip continuous casting,” *Ironmaking & Steelmaking*, 23(2007), 54–58.
4. P. Fournier and F. Platon, “Wear of refractory ceramics against nickel,” *Wear*, 244(2000), 118–125.
5. Zehua Zhou et al., “Novel side dams including advanced laminated ceramic for twin roller continuous casting,” *Ceramics International*, 38(2012), 1779-1783.
6. Z.H. Zhou et al., “A thermal shock resistance model for laminated ceramics and its validation,” *Journal of European Ceramic Society*, 30(2010), 1543-1547.
7. R. Bermejo et al., “Optimal strength and toughness of Al_2O_3-ZrO_2 laminates designed with external or internal compressive layers,” *Journal of European Ceramic Society*, 28(2008), 1575-1583.
8. T. Lube et al., “Effective fracture toughness in Al_2O_3-Al_2O_3/ZrO_2 laminates,” *Journal of European Ceramic Society*, 27(2007), 1449-1453.

Characterization of Minerals, Metals, and Materials 2016
Edited by: Shadia Jamil Ikhmayies, Bowen Li, John S. Carpenter, Jiann-Yang Hwang, Sergio Neves Monteiro, Jian Li, Donato Firrao, Mingming Zhang, Zhiwei Peng, Juan P. Escobedo-Diaz, and Chenguang Bai
TMS (The Minerals, Metals & Materials Society), 2016

SILVER CEMENTATION WITH ZINC FROM RESIDUAL X RAY FIXER, EXPERIMENTAL AND THERMOCHEMICAL STUDY

M. Pérez Labra[1], M. Reyes Pérez[1], J. A. Romero Serrano[2], E. O. Ávila Dávila[3], F. R. Barrientos Hernández[1], Pandiyan Thangarasu[4]

1 Academic Area of Earth Sciences and Materials. Autonomous University of Hidalgo State. Road Pachuca- Tulancingo Km 4.5 Mineral de la Reforma Zip Code 42184, Hidalgo México.
2 Metallurgy and Materials Department, ESIQIE-IPN. UPALM, Zacatenco, Zip Code 07738, México D.F.
3 Mechanical Engineering Department, Technological Institute of Pachuca, Road México-Pachuca km. 87.5 Pachuca de Soto Zip Code 42080, Hidalgo, México.
4 Circuito interior s/n Facultad de Química Edif. F Lab. 114 Ciudad Universitaria UNAM México D. F. Tel/Fax 56223499 ext. 114

Abstract

Silver cementation with zinc from residual X ray fixers (XRF) was studied. The chemical analysis of XRF showed 5.16 g/l (Ag), 0.56 g/l (Al), 5.24 g/L (K), 7.02 g/L (Na) and 172.56 g/L (S). The cementation process in terms of solution pH was thermodynamically modeled using FactSage by constructing the potential-pH diagram at 298.15 K. This diagram showed that the cementation process leads to metallic silver together with residual unreacted zinc. The parameters experimentally evaluated were: pH (ranged from 3.0 to 7.0, temperature (ranged from 298.15 to 318.15 K) and the Ag:Zn weight ratio (1:1, 1:2, 1:3, 1:4 and 1:5). The maxim silver cementation (99.99 % Ag) was obtained at 90 s of reaction, pH 6.0, 318 K and Ag:Zn equal to 1:3. Silver cementation increases whit the Ag:Zn weight ratio, pH and temperature increases. The X-Ray and SEM-EDS results showed that the cementation product is formed by Ag and Zn.

Keywords: Cementation, Silver, X ray fixer, Zn Powder, thermochemical

Introduction

Silver is unique in its ability to react to light and produce images in applications such as photography and radiography (X -rays). This is released from the photographic film during the developing and printing processes and can be successfully recovered from the effluent resulting for reuse. Residual X ray fixer used in the developing process of x-ray films may contain from 5 to 12 g / L silver in solution [1]. The treatment of spent solutions from fixing process is presented as a technical problem due to the large volume generated; however, the cementation process may overcome this problem. Cementation involves the precipitation of an electropositive metal from solution by a metal more electronegative. This is one of the oldest, efficient and economical hydrometallurgical processes for the recovery of metal values in solution, and for the purification of leach liquors. This process has been widely used for removing Cu, Cd and Ta from leach liquor of zinc sulfate [2]. The cementation processes have been constantly used and researched [3-6], some of them are batch agitated processes, other use reactors with disc rotating cylinder [3]. Silver is the most studied metal using zinc as a cementing medium [6]; however, researches to recover Au, Co, Cd, Cu and Ni have also been reported [6-12]. It has been reported that the process has a first-order reaction, wherein the reaction is controlled by diffusion, together with the activation energy (Ea) [6, 13, and 14]. The present work aims to determine the optimal conditions for the cementation process of silver from residual zinc X ray fixers, and propose an effective and feasible method to treat this effluents.

Materials and experimental procedure

Residual X ray fixers were used, chemically pure zinc powder, sodium hydroxide and sulfuric acid to adjust the pH of the solution. Previously the X ray fixers were characterized with the ICP method to determine their chemical composition. The cementation process was carried out using 1 liter of solution in a glass reactor of 2 L. A hot plate (Barnstead/ Thermolyne Super-nova) equipped with temperature control and a mechanical stirring system with six-blade propeller type axial at 250 rpm was also used. The initial pH of the solution was measured and kept constant throughout the process. Zn powder was added and the progress

of cementation was studied at different times during the reaction by obtaining successive samples of 10 mL and filtering with Whatman No. 42 filter paper. The reaction progress was monitored by determining the Ag concentration with the ICP method.

The following Ag cementation with Zn trials were tested:

(a) At 298 K (25°C) with the following Ag:Zn weight ratios: 1:1, 1:2, 1:3, 1:4, y 1:4. The required stoichiometric amount of zinc was calculated by the following reaction.

$$2Ag(S_2O_3)_2^{[3-]} + Zn^o = 2Ag^o + Zn^{[2+]} + 4(S_2O_3)^{[2-]} \quad (1)$$

(b) At 298 K (25°C), Ag:Zn weight ratio constant and with the following pH values: 3, 4, 5, 6 y 7. The [OH^-] concentration was calculated taking into account the solubility product constant of NaOH in water [16] and the pH of the alkaline solution according to the experimental temperatures.

(c) At Ag:Zn ratio and pH constants and with the following temperatures 303K (30°C), 308(35°C) K, 313K (45°C) and 318K (45°C).

After the reaction the solution was filtered and the solid was dried and analyzed by scanning electron microscopy (SEM), and the solids were characterized by X-ray diffraction (XRD).

Results and discussion

Residual X ray fixers Chemical composition

The chemical analysis of residual X ray fixers is shown in **Table 1**. The chemical analysis of each element was carried out four times; the obtained standard deviation was about σ=0.1422. All elements were determined by ICP method.

Element	Content (mg/L)
Al	556.98
Cu	0.18
Pb	0.20
K	5,244.19
Ag	5,165.21
Na	7,023.26
S	172,558.14

Table 1. Chemical composition of Residual X ray fixers

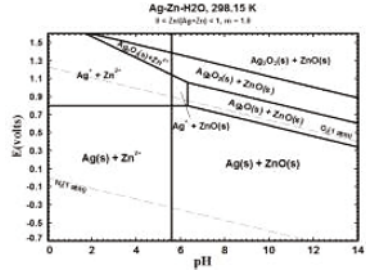

Figure 1. Potential-pH diagram for the Ag-Zn-H_2O system at 298 K (25°C).

Potential-pH diagram

Pourbaix diagrams can be used to identify the conditions required to dissolve a solid compound in an aqueous solution at a given temperature and pressure as well as estimate the solid and aqueous products of the dissolving reaction. **Figure 1** shows the potential-pH diagram at 298.15 K (25°C) for the Ag-Zn-H_2O system calculated with the FACTSage thermodynamic software [17]. The molality of all the aqueous species in this system has been fixed at m = 1. Water is only stable in the region bounded by the dashed lines. The equilibrium conditions that can be utilized for the leaching of minerals or any solid compound in aqueous solutions at ambient temperature are constrained to those defined by the region of water stability. **Figure 1** shows that Ag(s) is stable when pH of the liquid solution is between 0 and 14 and almost all the E values where water is stable. Zn^{2+} ion is stable when pH is less than 5.65, whereas ZnO(s) is stable at pH higher than 5.65.

Cementation Kinetic

Effect of zinc concentration

In most cases, the cementation reactions follows first order reaction kinetics and generally are limited by diffusion of the noble metal ion through the mass-transfer boundary layer. Most of the cementation reactions are found to be first-order diffusion process [18] with respect to the noble metal ion, and the reaction velocity constant, km, for such a reaction may be computed from the general first-order rate equation:

$$\frac{dc}{dt} = \frac{-kmAC}{V} \tag{2}$$

If km in not concentration dependent and the area in unchanging, equation (2) is integrated resulting in the integrated fisrt-order reaction.

$$log\,\frac{C}{C_0} = -\frac{-kmAC}{2.3V} \tag{3}$$

Where *Km* is the reaction velocity constant (cm/s), which, among others factors, is the function of the activity coefficient of silver. *A* is the surface area of cementing metal (cm^2), *V* is the solution volume (cm^3), *t* is time (s) and C and C_0 are the noble metal concentrations at time *t* and the initial concentration at time = 0 respectively. The required amount of zinc was calculated by the reaction (1), and it is shown in **Table 2** together with different Ag:Zn weight ratios. **Table 2** also shows the calculated surface area values for each studied weight

ratio such was measured using the BET technique (quatasorb Model 0S10, Quantachrome Corporation).

Weight ratio (Ag:Zn)	Mass Zn (g/L)	Surface area Zn (cm^2/g)
1:1	1.38	1161
1:2	2.76	2324
1:3	4.54	3484
1:4	5.88	4942
1:5	7.56	6371

Table 2. Weight ratios, weights and surface area of Zn powder.

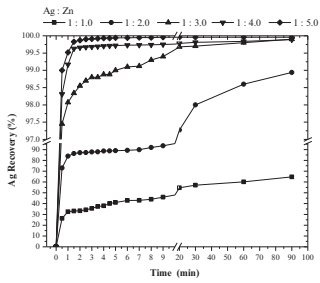

Figure 2. Ag recovery (%) vs Time (min.). Effect of zinc concentration. pH 5.0, 1 L solution and 2.13 sec^{-1} agitation.

Figure 2 shows the results obtained for cementing Ag using the amounts of Zn powder shown in **Table 2**. It is observed that using the Ag:Zn weight ratios 1:1 and 1:2 produce less than 95% of silver cemented in 10 minutes of process, while is higher than 96% using Ag:Zn weight ratios of 1:3, 1:4 and 1:5 in less than 1 minute. This is due to the high surface area of the zinc powder added. The silver ions are readily reduced by zinc due to the difference in standard reduction potentials:

$$Ag^{2+} + e^- = Ag^+ \qquad E^o = 1.77\ V \tag{4}$$

$$Zn^{2+} + 2e^- = Zn \qquad E^o = -0.763\ V \tag{5}$$

Under standard conditions the cementation reaction is the shown in reaction (1) with E° = 0.1923 V. It is worth to note that if the electrochemical potential of the cell is greater than zero (positive), then the change in Gibbs free energy (ΔG) is negative, and the reaction may proceed spontaneously as written. **Figure 3** shows the values obtained from the logarithm of the fraction of Ag cemented (calculated with equation (3)) vs cementation time. According to the equation (3) the plot is been to be linear in the first 15 minutes, indicating that this reaction is firs order, which has been verified by others authors [6]. Where the process is tightly controlled by hydrodynamic conditions within the reactor, so it is confirmed that the process is controlled by mass transfer solution to the surface film of the zinc particles.

It can be seen that there is a slight increase in the rate constant with increasing amount of Zn. However have been reported [2] that in some cases the structure and morphology of the

reaction product can have a significant effect on passivating the surface. The **Figure 4** shows a micrograph of the cemented silver obtained by SEM-EDS. The effect of the mechanical propeller separates the Ag that forms around the Zn particle, and comes off easily, therefore, for each reaction time a new Zn surface area is exposed.

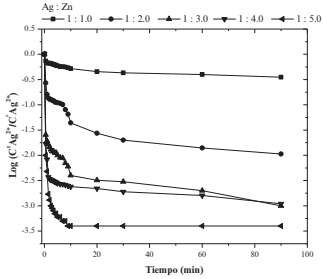

Figure 3. Effect of zinc concentration on the rate of cementation.

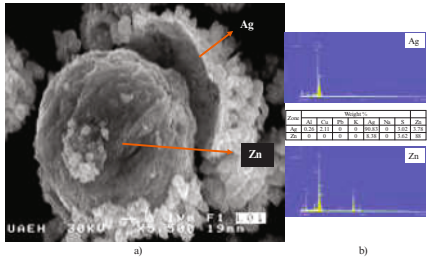

Figure 4. a) SEM micrograph of a Ag cementation with Zn, Ag/Zn 1:3, pH 6.0, 303K (30 ° C), b) EDS analysis of the reaction.

Analysis by X-ray diffraction carried out to cementation products, confirms two phases product corresponding to Ag (JCPD file 4-783) and Zn (JCPD file 4-831) this is repeated for all the products obtained (**Figure 5**).

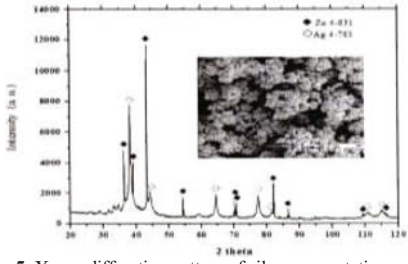

Figure 5. X -ray diffraction pattern of silver cementation products.

pH effect

Figure 6 shows the results for the pH effect on silver cementation with zinc powder. Is observed that by acidic pH the Ag recovery decreases. This is due to the increased competition between Ag ions and hydrogen ions for discharge sites on the metal surface at higher concentrations of hydrogen ions:

$$Zn + 2H^{2+} = Zn^{2+} + H_2 \quad (6)$$

Which can proceed to higher extent at low pH, the surface area available for the cementation reaction is decreased. The hydrogen so produced is likely to block the metal surface because of it slow desorption step [2]

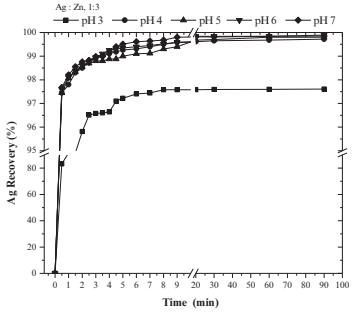

Figure 6. % silver recovery vs. time. Effect of pH, Ag:Zn ratio 1: 3, 1 liter of solution and 2.13 sec $^{-1}$ stirring.

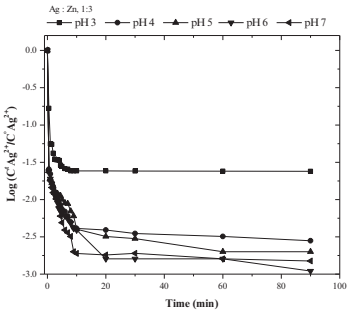

Figure 7. Effect of solution acidity on the rate of cementation.

Figure 7 shows the effect of solution acidity on the rate of cementation with Zn powder, it shows that speed cementation decreases when the pH decreases. The decrease of the rate constant with increasing acidity of the solution can be attributed mainly to the effect of hydrogen ions mentioned above.

Temperature effect

Figure 7 shows the effect of temperature solution on the kinetics of Ag cementation. It can be seen that the silver recovery increases whit the temperature increases. Experimental investigations [2, 6] indicate that most cementation reactions are controlled by a mass transfer process. For almost all the cementation process systems the apparent activation energy is in the range 2 – 6 kcal/mol which suggest that the cementation reactions are limited by mass transfer in the aqueous phase. **Figure 8** shows the effect of temperature on the rate of cementation. This results are consistent with those reported by others authors [2], also the reaction is strongly dependent on the hydrodynamic conditions of the bath. This also confirm that the rate cementation is controlled by mass transport through the boundary film.

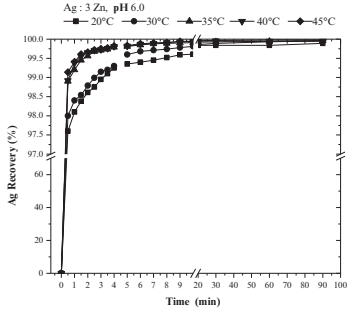

Figure 8. Ag recovery vs time (min.). Effect of reaction temperature. Ag:Zn 1:3 ratio , pH 6 and 2.13 s^{-1} agitation.

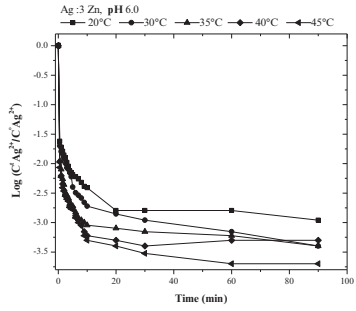

Figure 9. Effect of temperature on the rate of cementation.

Conclusions

The effect of some factors influencing the rate of Ag cementation with Zn of residual X ray fixers was studied. The X ray fixers has a silver concentration of 4.55 g/L. The maxim silver cementation (99.99 % Ag) was obtained at 90 s of reaction, pH 6.0, 318 K and Ag:Zn equal to 1:3. Silver cementation increases whit the Ag:Zn weight ratio, pH and temperature increases. The potential-pH diagram showed that the cementation process leads to metallic silver together with residual unreacted zinc.

References

1. Rivera I. L., A. Roca, M.Cruells, F. Patiño and E. Salinas. "Study of silver precipitation in thiosulfate solutions using sodium dithionite. Application to an industrial effluent" *Hydrometalurgy*. Vol. 89, 2007, pp. 89-98.

2. Agrawal, R. D. "Theoretical considerations of the cementation of copper with iron". *Journal of the South African institute of mining and metallurgy*. 1982, pp. 106-111

3. Amin, N.K.: Rate of cadmium ions removal from dilute solutions by cementation on zinc using a rotating fixed bed reactor. *Hydrometallurgy*. Vol.89, 2007, pp. 224-232.

4. Mohammad sadegh safarzadeh davood moradkhani and mehdi ojaghi ilkhchi, "Determination of the optimum conditions for the cementation of cadmium with zinc powder in sulphate medium". *Chemical Engineering and, Processing: Process Intensification*. Vol. 46, No.12, 2007, pp.1332-1340

5. Zhike Wang, Donghui Chen, Liang Chen. "Gold cementation from thiocyanate solutions by iron powder." *Minerals Engineering*, Vol.20, No. 6, 2007, pp.581-590

6. Gabriela V. Figueroa Martínez, José R. Parga Torres, Jesús L. Valenzuela García, Guillermo C. Tiburcio Munive, Gregorio González Zamarripa. *"Kinetic Aspects of Gold and Silver Recovery in*

Cementation with Zinc Power and Electrocoagulation Iron Process" Advances in Chemical Engineering and Science. Vol. 2, 2012, pp. 342-349

7. Lamya, R. M. and Lorenzen, L.: "A study of factors influencing the kinetics of copper cementation during atmospheric leaching of converter matte". *The Journal of the South African Institute of Mining and Metallurgy*. 2005, pp.21-28

8. Dib, A., Makhloufi, L. "Mass transfer correlation of simultaneous removal by cementation of nickel and cobalt from sulphate industrial solution containing copper: Part I: Onto rotating zinc electrode disc". *Chemical Engineering Journal*, Vol.130, No.1, 2007, pp. 39-44

9. G. Viramontes Gamboa, M. Medina Noyola, A. López Valdivieso. "The effect of cyanide and lead ions on the cementation rate, stoichiometry and morphology of silver in cementation from cyanide solutions with zinc powder." *Hydrometallurgy*. Vol. 76, No.3-4, 2005, pp.193-205

10. Nizamettin Demirkıran, Ahmet Ekmekyapar, Asım Künkül, Ahmet Baysar. "A kinetic study of copper cementation with zinc in aqueous solutions." *International Journal of Mineral Processing*. Vol. 82, No 2, 2007, pp.80-85

11. Boyan, S. Boyanov, Victoria, V. Konareva, Nikolai, K. Kolev. "Purification of zinc sulfate solutions from cobalt and nickel through activated cementation." *Hydrometallurgy*, Vol. 73, 2004, pp. 163-168.

12. J. Brent Hiskey, Jaeheon Lee. "Kinetics of gold cementation on copper in ammoniacal thiosulfate solutions." *Hydrometallurgy*. Vol. 69, No.1-3, 2003, pp.45-56

13. Trina M. Dreher, Amy Nelson, George P. Demopoulos, Dimitrios Filippou. "The kinetics of cobalt removal by cementation from an industrial zinc electrolyte in the presence of Cu, Cd, Pb, Sb and Sn additives." *Hydrometallurgy*. Vol. 60, No. 2, 2001, pp. 105-116

14. Karavasteva M. "The effect of certain surfactants on the cementation of nickel from zinc sulphate solutions by suspended zinc particles in the presence of copper." *Canadian Metallurgical Quarterly*. Vol. 38, No. 3, 1999, pp.207-210

15. E. Guerra, Dreisinger, D. B. "A study of the factors affecting copper cementation of gold from ammoniacal thiosulphate solution." Hydrometallurgy. Vol. 51, No. 2,1999, pp.155-172

16. D.R. Lide: CRC Handbook of Chemistry and Physics. 71st ed., CRC Press, Boca Raton, FL, 1990-1991, 8–38.

17. W.T. Thompson, C.W. Bale, and A.D. Pelton: Facility for the Analysis of Chemical Thermodynamics (FACTSage), Ecole Polytechnique, Montreal, 2010, http://www.crct.polymtl.ca.

18. S. Gamini, "The Cyanidation of Silver Metal: Review of Kinetics and Reaction Mechanism," *Hydrometallurgy*, Vol. 81, No. 2, 2006, pp. 75-85.

Characterization of Minerals, Metals, and Materials 2016
Edited by: Shadia Jamil Ikhmayies, Bowen Li, John S. Carpenter, Jiann-Yang Hwang, Sergio Neves Monteiro, Jian Li, Donato Firrao, Mingming Zhang, Zhiwei Peng, Juan P. Escobedo-Diaz, and Chenguang Bai
TMS (The Minerals, Metals & Materials Society), 2016

CHARACTERIZATION OF WASTE MOLDING SANDS, FOR THEIR POSSIBLE USE AS BUILDING MATERIAL

Mauricio Guerrero R.[1], Juan Hernández A.[2], Javier Flores B.[2], Eleazar Salinas R. [2], Isauro Rivera L.[2], Ma. Isabel Reyes V.[2], Eduardo Cerecedo S.[2], Víctor E. Reyes C.[2], Carmen Cortés L.[2],

[1] Universidad Autónoma del Estado de Hidalgo, Área Académica de Ingeniería y Arquitectura. Carretera Pachuca-Tulancingo Km. 4.5, C.P. 42184 Pachuca, Hidalgo, México. mgr@uaeh.edu.mx

[2] Universidad Autónoma del Estado de Hidalgo, Área Académica de Ciencias de la Tierra y Materiales. Carretera Pachuca-Tulancingo Km. 4.5, C.P. 42184 Pachuca, Hidalgo, México. wik_1000@hotmail.com y herjuan@uaeh.edu.mx

Abstract

It was done a physicochemical and mineralogical characterization of the molding sand wastes of the iron casting process, being these sands the main residue of the process, representing 65 to 85 % of the total waste. According with the obtained results, the chemical composition of the material (expressed in weight percentages) is the following: 77.9 SiO_2, 6.6 Al_2O_3, 8.56 Fe_2O_3, 0.14 TiO_2, 2.48 MgO, 0.34 K_2O, 1.52 CaO and 1.03 Na_2O. The major mineral phases found were: Albite, Orthoclase, Quartz (anorthic) and Laihunite, and as minority phases were present both the Berlinite and the Montmorillonite. Furthermore the material presented a thick granulometry, around 60% corresponds to a particle size of 53µm. According to this characterization, these residues could be used in the manufacture of construction materials such as bricks, blocks, or as a cementing material.

Keywords

Molding sand waste, sustainability, steel industry.

Introduction

The technological development of recent decades has caused collaterally various environmental problems that have cost too much for society, as many ecosystems are reaching the limits of their capacity to assimilate wastes, resulting from the consumption of the population. It is in this way, that the functionality and comfort of the advancement of technology, based on the consumption of renewable and non-renewable natural resources, has put humanity at a crossroads: continue the culture of consumerism and disposability, thus forgetting the preservation of life on planet Earth, or commit to stop and reverse the effects caused to the environment due to technological "maturity".

The magnitude of the metallurgical industry worldwide, particularly in the steel industry, involves the problem of waste disposal of different processes that is of great importance, given the large number of them and due also to heavy mineral contents with differences in their composition [1].

Therefore, any waste disposal process that seeks its inerting involves considerable expense, so that strategies for treating these materials have experienced an evolution that seeks its transformation or reuse, to help reduce the costs of processing, compensating or in the best cases, to produce a benefit, that is, to reuse them in a new industrial process [2].

The main waste generated by the steel making activity, is the molding sand used in casting of ferrous and nonferrous metals. These are solid wastes with very low moisture content; the generation of this type of waste has increased in recent years in direct proportion to the advancement of technology in industrial production, and coupled with this, we can mention other factors such as increased consumption by the population, obsolescence of production equipment and improvements in technology, more and better productivity, and low cost of landfills in developing countries [2].

Currently the foundries located in the municipality of "Tepeapulco, Hidalgo" operate with about 3500 tons of recycled sand which is mixed daily with 20 tons of new sand, that is 99.94% of the used sand is recycled to same process and only 0.06% is discarded. These wastes (burnt silica sand) correspond to the portion of sand that was exposed to stresses and thermal effects, due it was in contact with the molten metal into molds and was reused an average of seven cycles, therefore it presents grains fractured, some debris (chips and scrap), burnt materials, and slag binders burnt. The above represents a total of 600 tons per month of wastes of molding sand.

In a study conducted in the UAEH [2], was obtained the characterization of the wastes of molding sand from the iron smelting process, in the zone of "Ciudad Sahágun"; the material characterized presented the following chemical composition expressed in percentages by weight of 70.1 % of SiO_2, 14.7 % of Al_2O_3, 4.4 % of Fe, 0.20 % of MnO, 4.30 % of MgO, 0.40 % of K_2O, 0.6 % of CaO and 5.26 % of Na_2O. The above data show a type-bentonite composition, similar to that used in the original process, which let note that these residues could be used to manufacture building material such as blocks or bricks.

Therefore, treatment and reuse of these kind of wastes is proposed to allow a major contribution to mitigating environmental impact, generated due to the method of disposal of such waste, which basically consists of open dumps [3].

From the metallurgical point of view, are essential the corresponding characterization and leaching studies, to determine the feasibility of a revaluation of these wastes because they can be an alternative of use like raw material in other industrial processes, mainly for its adequate content of oxides of silicon, iron, aluminium, sodium and potassium, and their mineralogy as well as the distribution of chemical elements in their primary and secondary phases [4,5].

Also, it is important to have in account the possibility of that this residue could be a potentially pozzolanic material, because according to Montaño Cisneros *et al.*, it is necessary to have a percentage in the sum of SiO_2 and Al_2O_3 of at least 70% [6]. According to the standard ASTM C618, a pozzolanic material needs a percentage in sum of SiO_2, Al_2O_3 and $Fe_2O_3$of at least 70%, and a maximum percentage of SO_3 of 5%, for being considered as a material with high pozzolanic potential [7].

Experimental procedure

For sampling, was necessary to consider the mineralogical and physical characteristics of the residual sand, so this was carried out systematically on different mounds of the sand bank, to cover the three dimensions of the mound where sampling was conducted (x, y, z), and was a type channel sampling, with a weight of 5 kilos each sample. Taking in account a length of 2 m by 0.30 cm. of wide, taking a total of 20 representative samples.

For characterization, the quartering of samples to know the material properties was performed, and was made a composite taking into account the similarity of the samples of each mound of sand, and the study was done by the following methods: X-ray diffraction, with an INEL diffractometer, model EQUINOX 2000, and for this analysis was necessary to prepare the sample to a -200 +270 mesh size (74-53 microns) then indexing of the results was done using the MATCH software version 1.10 [8]

The characterization by scanning electron microscopy, in conjunction with the microanalysis of energy dispersive spectrometry of x-rays (SEM-EDS) was used for the study of morphology of the particles, and microanalysis study was in order to determine the nature of the material studied. A SEM, brand JEOL, Model JSM 6300 equipped with a EDS detector of the brand Noran was used. The sieve analysis was performed on wet and this analysis was conducted with standard sieves (TYLER® series), No. 80, 100, 140, 200, 270, 400. Was sieved a sample of 100 g where the fractions obtained were dried at room temperature and then were subsequently weighed for its statistical analysis.

The residual molding sand from "Ciudad Sahágun" also was characterized through X-ray fluorescence, using a spectrometer Venus brand, model 200 MINILAB and the samples were prepared according to the following process:

Calcination of the material was performed previously, putting the sample into a porcelain crucible then heated in an oven at 800 ° C for 20 minutes, holding heating at this temperature, and then the sample was removed from the oven and was cooled up to 25 °C. Subsequently was prepared a pill for its use by FRX, for which 9 grams of LiB4 as flux and 0.9 grams of residual molding sand were used in a crucible of Au-Pt heated during 10 minutes in a Fluxy, until melting of the sample and its subsequently solidification at 25 °C, then it was characterized in the XRF spectrometer using a mixture of cooling gases with a composition of 90% Ar and 10% CH4, within the spectrometer.

Results and discussion

The average chemical composition of residual sand from "Tepeapulco, Hidalgo", that was found by XRF, is shown in Table 1, where it is seen as major compounds to the silica, alumina and the iron oxide. The above, it allows us to say that this material basically is composed by silica sand with clay and slag, as impurities. The presence of ZrO_2 may be due to that this compound was used for internal coating of the sand mold, before being filling with molten metal.

Table 1. Average chemical composition of the waste of sand, obtained by XRF.

Element	Na_2O	MgO	Al_2O_3	SiO_2	K_2O	CaO	TiO_2	Fe_2O_3	ZrO_2
%	0.00	0.43	2.32	92.83	0.27	0.36	0.25	3.14	0.43

The results of the average particle size analysis of the wastes, are shown in Figure 1 wherein it can be seen that the particle size is predominantly in the mesh 80 (177 microns) and has an average size of mesh 200 (74 microns), also showing that the greater weight is retained on the mesh 100 with a 19.18%, thereafter presenting, a very sharp drop to the mesh 400 (37 microns), where the minimum weight retained is of 4.50%. According to sieve analysis, it was determined that the material has a size that is within the specifications for its direct use in the manufacture of building materials and ceramic industry. The wastes of molding sand, can substitute to the fine and medium size sand for concrete building materials. In ceramic industry, the wastes of molding sand can be used with a small grinding, to achieve a particle size nearly of the mesh 200 (74 microns), or even lower sizes.

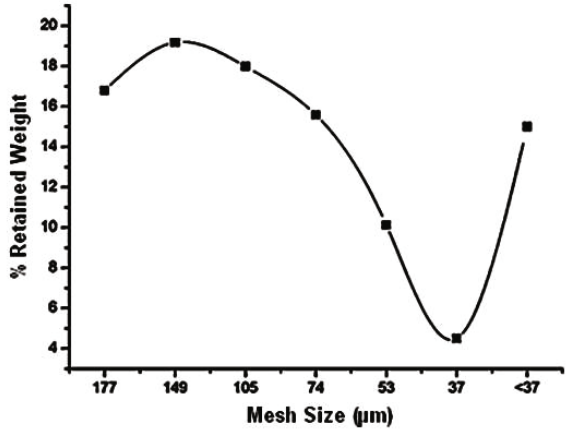

Figure 1. Particle size distribution of the wastes of molding sand

According to the phases obtained by X-ray diffraction (Figure 2), the major mineral phases were: Orthoclase,

Albite, Quartz Anorthic, Laihunite and Berlinite; these phases come from the same silica sand, as in the case of quartz, in addition to residual slag or the clay, that were formed by the weathering; like in the case of the majority of the rest of the phases present. As minor phase is present the Berlinite, and the residual phase is the Montmorillonite. The Berlinite was formed within the slag and also it was found a residual amount of Montmorillonite that was used to unite silica sand in the production of casting molds, during the green sand process. The total amount of Montmorillonite stops being of importance, because this phase is present in a lower concentration for a correct use in the green molding process, and it has a particle size less than to the mesh 200 (74 microns).

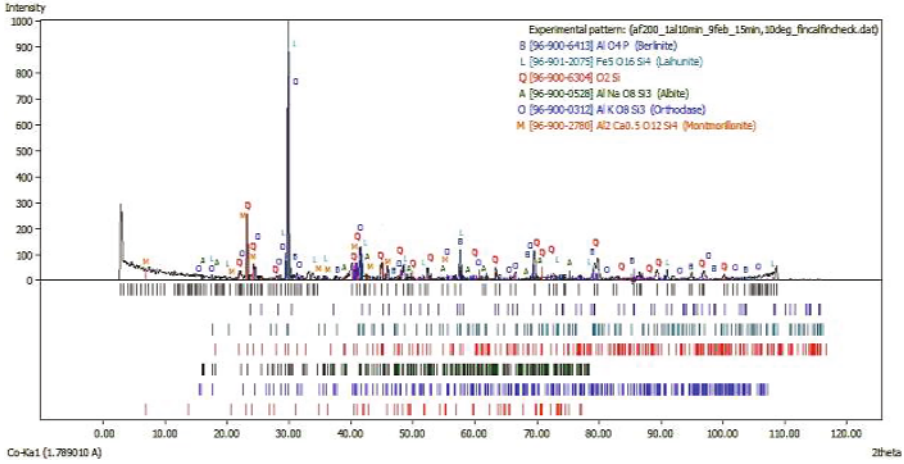

Figure 2**.** X-ray diffractogram of the wastes of molding sand, the main mineral species are: Orthoclase (O), Albite (A), Quartz (Q) and Laihunite (L). Berlinite (B) and Montmorillonite (M) are the minority and residual phases, respectively.

Table 2 shows the amount found for each phase in the wastes of the molding sand. According the quantity of phases in the wastes of the molding sand, it was determined that the material has an adequate composition to be used in the manufacture of building materials, and in the ceramic industry, because these wastes of the molding sands, can be feldspar substitutes, because the high quantity of feldspar and other silicates phases like Laihunite and Montmorillonite. Furthermore, quartz content is very high and the wastes of the molding sands, also these can be used for production of silica refractories and building materials.

Table 2. Phases found in the residual sand, obtained by XRD

Entry Number	Phase	Formula	Quantity in Weight Percent
96-900-0528	Albite	$(Al, Na)Si_3O_8$	33.7
96-900-0312	Orthoclase	$(Al, K)Si_3O_8$	30.8
96-900-6304	Quartz (Anorthic)	SiO_2	21.9
96-901-2075	Laihunite	$Fe_5Si_4O_{16}$	7.6
96-900-6413	Berlinite	$AlPO_4$	4.8
96-900-2780	Montmorillonite	$(Al_2,Ca_{0.5})\ Si_4O_{12}$	1.2

In Figure 3, can be seen images of residual sand particles, obtained by SEM-EDS, which notes that have a

fairly homogeneous distribution in size, showing compact particles with rounded edges without the presence of edges or sharp angles. Can be also observed in small amounts, the presence of different grain-like molten phases, which were characterized by EDS (Figure 4 and Table 3.) which proved that the material is constituted by Si, Ca and O, in form of calcium silicate; along with a substantial proportion of aluminosilicate, and iron oxide formed during the weathering of these residual sands, and before the formation of the slag.

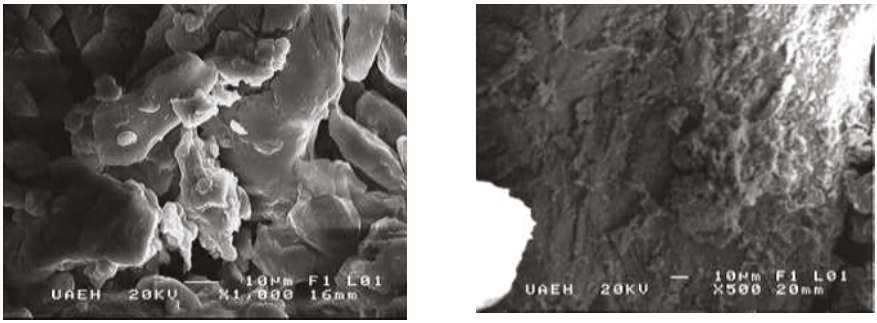

a) b)

Figure 3. Micrographs of the residual molding sands, obtained in a JEOL JSM-6300 SEM, taken at an accelerating voltage of 20 kV; a) Micrograph of the residual sand obtained at 1000 X and a distance of the detector of 16mm. b) Micrograph of residual sand obtained at 500X and a distance of the detector of 20mm.

According the composition of the wastes of molding sand, obtained by EDS (Figure 4 and Table 3), this material can be a substitute of feldspar, due to its similar composition, mainly by the silica and alumina amount that is near to that for oxides of the I and IIA groups. So it was determined that the material has a composition that can be used in the manufacture of building materials, the ceramic industry, because these wastes of molding sand, had a composition mainly based in silica, with alumina and iron oxide (6.6% wt. and 8.56% wt., respectively). Furthermore, with the sum of these two species in the chemical composition of the wastes of molding sand, have a high potential like pozzolanic material, which can be used to prepare blocks and concrete in the form of a fine aggregate. For its use in ceramics, the iron oxide removal is needed, to avoid rejection of the ceramic pieces that will be produced.

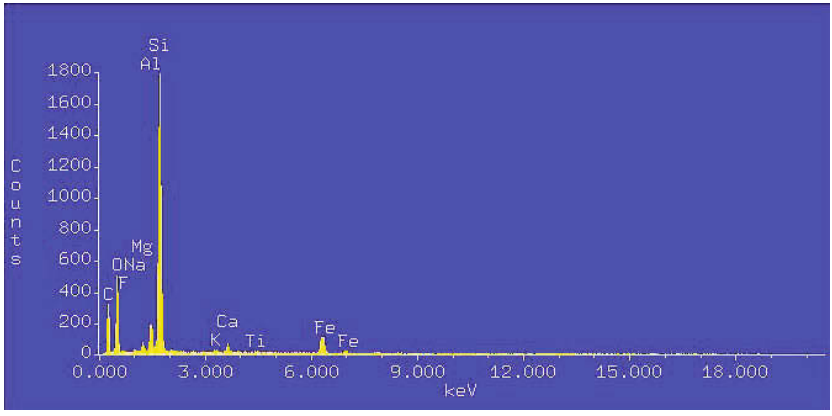

Figure 4. Spectrum obtained by SEM-EDS of the residual molding sand, using an accelerating voltage of 20 kV

Table 3. Chemical composition of the wastes of sand, obtained by SEM-EDS

Compound	Weight Percentage
SiO_2	77.9
Al_2O_3	6.6
Fe_2O_3	8.56
Na_2O	1.03
K_2O	0.34
CaO	1.52
MgO	2.48
TiO_2	0.14

Conclusions

The major compounds determined by XRF, are silica, alumina and iron oxide, which can help us to deduce that this is mainly clay and silica sand with slag as impurity. Furthermore, the presence of small quantities of ZrO_2 could be due to that this compound was used for the internal coating of the sand mold, before being filling with molten metal.

According to sieve analysis, it was determined that residual molding sand has a grain size that is within technical specifications for direct use in the manufacture of building materials, and ceramic industry, because this wastes of molding sands can substitute fine, and also sands of medium size for concrete building materials and for ceramic industry, the wastes of molding sand can be used only with a soft grinding, to achieve a particle size near to the mesh 200 (74 microns) or lower sizes.

The controlled particle size conforms to ASTM C331 [9] and C33 [10] standards, since residual foundry sand has a fine grain size, which is within the specifications. Also, the results comply well with the Mexican standard SCT N-CMT-2-02-002/02 [11], which relates to a fine particle size.

On the basis of the analysis by SEM-EDS, it is observed that the sample of wastes of molding sand, has a fairly even distribution in size, with compact particles having rounded edges, without the presence of edges or sharp angles.

Based on this research, it was determined that the residual sand, by their chemical and mineralogical composition is potentially usable as an alternative industrial material for the manufacture of various products (brick, block, tile, refractory bricks, etc.), as well as a feldspar substitute for production of dark or reddish burnt compounds. The high amount of silica, alumina and iron oxide, that form the felsic and silicate phases inside the wastes of molding sands, have similar quantities as to be a feldspar substitute. Also the high amount of silica, alumina and iron oxide can provide a high pozzolanic potential.

A pilot testing is recommended for the production of building materials, as well as the implementation of a previous step of magnetic separation, due to the possibility of finding metal parts contained in the residual molding sand.

References

1. Empleo de residuos industriales siderúrgicos como materiales aglomerantes en construcción. Mymrin, V. (Mayo de 1998). Revista de Metalurgia, 441-447.

2. Caracterización y reúso de arenas residuales de moldeo Juan Hernández A.1, Eleazar Salinas R., Isauro Rivera L., Alberto Blanco P., Ister Mireles G., Javier Flores B. Eduardo Cerecedo, Miguel Pérez L., Julio C. Juárez T. Boletín de la Sociedad Química de México, 2014, Vol.8. ISSN 1870-1809.

3. US EPA, Industrial Material Recycling, Guide for Industrial Waste Management, web page.http://www.epa.gov/epaoswer/non-hw/industd/guide/index.htm

4. E. A. Domínguez, R. Uhlmann, Ecological bricks made with clays and steel dust pollutants, Appl. Clay. Sci., 1996, Vol 11 pp 237-249

5. Juan Hernández A., Eleazar Salinas R., Francisco Patiño C., Isauro Rivera L., Javier Flores B., Norma Trapala P., Miguel Pérez L., Mizraim U. Flores G., Ivan A, Reyes. G., Title Production Using Wastes From Minimg Industry Of The Mining District Pachuca Real del Monte, TMS (The Minerals, Metals & Materials Society), 2012, Pp 203-209, US

6. E. Montaño Cisneros, J. Robles Camacho, P. Corona Chávez, M. Martínez Medina y Y. R. Ramos Arroyo, "Caracterización mineral y geoquímica de los jales del Distrito Minero El Oro-Tlalpujahua. Reutilización potencial de los desechos mineros," *Memorias del 3er. foro de Ingeniería e Investigación en Materiales*, 3, Morelia, Michoacán: (Universidad Michoacana de San Nicolás de Hidalgo, 2006), pp. 198-203.

7. ASTM C618-05, " Standard Specification for coal Fly Ash or Calcined Natural Pozzolan for Use in Concrete" Annual book of ASTM Standards Volume 4.02, ASTM International.

8. Software Match! Version 1.10

9. ASTM C331-05, "Standard Specification for Light Weight Aggregates for Concrete Masonry Units" Annual book of ASTM Standards Volume 4.01, ASTM International.

10. ASTM C33-07, "Standard Specification for Concrete Aggregates" Annual book of ASTM Standards Volume 4.01, ASTM International.

11. SCT N-CMT-2-02-002/02. "Calidad de Agregados Pétreos para Concreto Hidráulico" Características de los Materiales, Título 2 "Materiales para Concreto Hidráulico". SCT, México.

Characterization of Minerals, Metals, and Materials 2016
Edited by: Shadia Jamil Ikhmayies, Bowen Li, John S. Carpenter, Jiann-Yang Hwang, Sergio Neves Monteiro, Jian Li, Donato Firrao, Mingming Zhang, Zhiwei Peng, Juan P. Escobedo-Diaz, and Chenguang Bai
TMS (The Minerals, Metals & Materials Society), 2016

IMPROVEMENT OF MECHANICAL PROPERTIES IN NATURAL RUBBER WITH ORGANIC FILLERS

GONZALES-FERNANDES, M. [1, 2, 3], BASTOS ANDRADE, C.G.[1], ESPER, F. J. [4], VALENZUELA-DIAZ, F. R. [1], WIEBECK, H. [1]

[1] PMT (Metallurgical and Materials Engineering Department of Polytechnic School); Av. Prof. Mello Moraes, 2463; São Paulo, SP, 05508-000, Brazil

[2] IFES (Federal Institute of Education, Science and Technology of São Paulo); Rua Pedro Vicente, 625; São Paulo, SP, 01109-010, Brazil

[3] FMU/FISP (United Metropolitan Colleges); Av. Brigadeiro Luís Antônio, 1089; São Paulo, SP, 01324-010, Brazil

[4] Centro Universitário Estácio Radial de São Paulo; Av. dos Remédios, 810; São Paulo, SP, 05107-001, Brazil

Keywords: elastomers, natural rubber, nanocomposites, organophilic clays.

Abstract

When added to polymeric matrices, organophilic clay transforms the performance of the resulting composites. A natural rubber matrix with different loads was prepared as bentonite chocolate B modified by sodification and treated with ammonium quaternary salt with cellulose charge, cardboard and palm fiber. After the mixture of natural rubber in a roller mill with the additives and subsequent addition of loads individually, plates were vulcanized for fabricating specimens. We measured the mechanical properties of traction and the interlayer distances analyzed by XRD. The aim of the paper is to show that the composite obtained improved in mechanical properties as compared to plates without the addition of loads.

Introduction

The volume and diversity of materials that are incorporated into polymer nanocomposites have been growing yearly. The interaction of charges in polymer matrices depends on the chemical nature and on the dispersion of the components [1]. The thermoplastic addition of organophilic clay and other fillers in minor amounts leads to a significant improvement in the limits of tensile strength and toughness. A study of the effects of adding loads on the mechanical behavior of natural rubber composite / organoclay obtained by vulcanized mechanical mixing is presented herein [2].

Experimental

The materials used are natural rubber as a matrix and loads of organophilic clay, paper, cardboard and palm fiber, crushed and sieved, opening 0.074 mm. Used as vulcanization additives, zinc oxide (ZnO) and stearine (stearic acid and glycerol (glycerin tristearate) ($C_{57}H_{110}O_6$) and thiazoles accelerators, disulfide dibenzotiazol (MBTS), moderate cure speed tiurans, tetramethylthiuram disulphide (TMTD), fast cure speed and sulfur (S), crosslinking agent, any standard commercial grade materials [3].

NR nanocomposites preparation

The natural rubber gum is passed through the opening of 1 mm of the two rollers of a roller mill at room temperature until reaching sufficient plasticity for gradually adding clay in powder form; after homogenization are added to organic fillers individually for each mixture, followed by homogenizing and gradual addition of the vulcanization reagents in a total time of 10 minutes [4]. The recipe of the compound is described in Table 1.

Table 1. Recipes of the rubber compounds

	NR	NR CHO10	NR CHO10 PIA1	NR CHO10 CEL1	NR CHO10 PAP1
Natural rubber	100	100	100	100	100
Zinc oxide	5	5	5	5	5
Stearin	1	1	1	1	1
MBTS[1]	1	1	1	1	1
TMTD[2]	0.5	0.5	0.5	0.5	0.5
Sulfur	1	1	1	1	1
Organoclay		10	10	10	10
Palm fiber			1		
Cellulose				1	
Cardboard					1

[1] benzothiazyl disulfite
[2] tetramethylthiuram disulfide

The material was vulcanized in an electrically heated press at 170 ±2 °C and 20 MPa for the optimum cure time (t_{90}), previously determined from an oscillating disc rheometer (TEAM-ODR 2000), ASTM D-2084. Specimens were mechanically cut out from the cured plaques, abiding by ASTM D 412.

Results and discussion

The X-ray diffraction patterns of the natural rubber (NR), natural rubber with organoclay (NR CHO10), natural rubber with organoclay and cardboard (NR CHO10 PAP1), natural rubber with organoclay and palm fiber (NR CHO10 PIA1) and natural rubber with organoclay and cellulose (NR CHO10 CEL1), Figure 1.

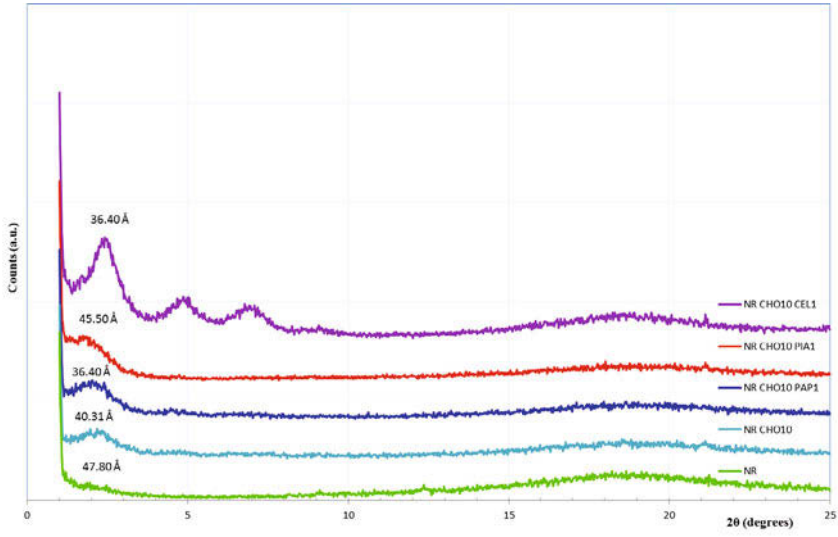

Figure 1. XRD patterns of the various systems.

Mechanical properties

The conventional tensile test is one of the most important methods of polymer testing. Also for elastomers, it is one of the basic tests for determining the quantitative characterization of strength and deformability. In this sense, the effects of organoclay and organic fibers content on the mechanical properties of the NR nanocomposites were studied.
Tensile tests performed at room temperature and at a cross-head speed of 500 mm/min on the composite materials are reported in Figure 2.

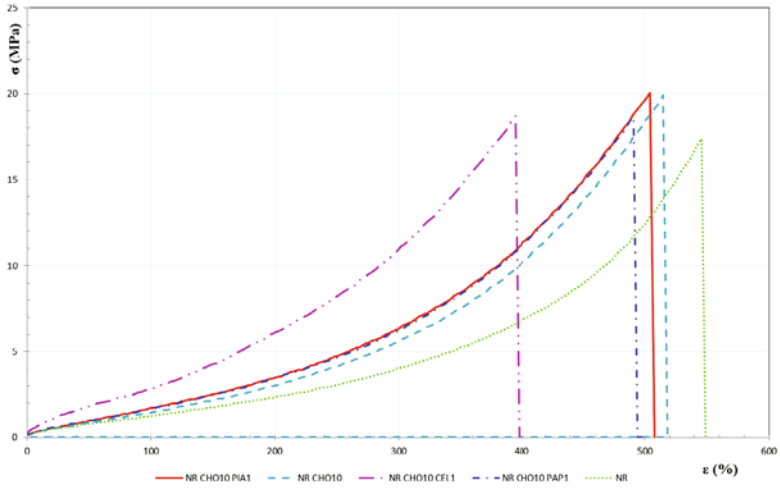

Figure 2. Stress-strain curves obtained from tensile tests.

The maximum strength, elongation at break and moduli at different elongations (100, 200 and 300%) of the elastomeric compounds studied are compiled in Table 2. The results allow deducing that the incorporation of small amounts of organophilic clays, 10 parts per hundred parts of rubber (phr), gives rise to an important increase in tensile strength.

Table 2. Mechanical properties of the compounds

Compounds	**σ** **(N/mm^2)** (MPa)	**T $_{90}$** (s)	**Toque** (lbf.in)	**Elongation at break** (%)	**Modulus 100%** (Mpa)	**Modulus 200%** (Mpa)	**Modulus 300%** (Mpa)
NR CHO10 PIA1	20.12	101	20.1	834.1	3.83	5.65	8.13
NR CHO10	19.41	99	12.9	758.6	2.91	4.64	7.13
NR CHO10 CEL1	18.81	97	17.7	561.5	4.88	6.90	9.50
NR CHO10 PAP1	18.77	98	18.1	685.2	3.29	5.40	8.45
NR	17.49	139	14.8	803.9	3.13	4.33	5.81

NR	Natural Rubber
CEL	Cellulose
PIA	Palm fiber
CHO	Organoclay
PAP	Cardboard

Conclusions

The mechanical reinforcement produced by the presence of organoclay in vulcanized natural rubber with organic fillers was demonstrated by tensile tests with an increase by about 15% in the tensile stress in compound NR CHO10 PIA1. In fact, the mix of organoclay and palm fiber behaves as an effective reinforcing agent for natural rubber matrix.

Acknowledgements

The authors thank the IFSP-SP for the qualifying license.

References

1. **Okamoto, Masami.** Polymer/Clay Nanocomposites. *Encyclopedia of nanosciencie and nanotechnology.* s.l. : www.aspbs.com/enn.
2. **Galimberti., Maurizio, [ed.].** Rubber-Clay Nanocomposites: Science, Technology, and Applications, First Edition. s.l. : John Wiley & Sons, Inc., 2011.
3. **L. B. de Paiva, A. R. Morales, F. R. V. Díaz.** Organophilic clays: characteristics, preparation methods, intercalation compounds and characterization techniques. *Ceramica.* 54, 2008, 54, pp. 213-226.
4. **Ciesielski, Andrew.** *An introduction to rubber technology.* s.l. : Rapra technology limited, 1999.

Characterization of Minerals, Metals, and Materials 2016
Edited by: Shadia Jamil Ikhmayies, Bowen Li, John S. Carpenter, Jiann-Yang Hwang, Sergio Neves Monteiro, Jian Li, Donato Firrao, Mingming Zhang, Zhiwei Peng, Juan P. Escobedo-Diaz, and Chenguang Bai
TMS (The Minerals, Metals & Materials Society), 2016

SPECIATION AND CHARACTERIZATION OF E-WASTE, USING ANALYTICAL TECHNIQUES

C. Cortés López [1], V. E. Reyes Cruz[1], M. A. Veloz Rodríguez[1], J. Hernández Ávila[1], J. Flores Badillo[1], J.A. Cobos Murcia[1, 2]

[1] Universidad Autónoma del Estado de Hidalgo, Área Académica de Ciencias de la Tierra y Materiales, Carr. Pachuca-Tulancingo km 4.5 C.P.42184
[2]Consejo Nacional de Ciencia y Tecnología, Depto. de Cátedras, Av. Insurgentes Sur 1582, Col. Crédito Constructor, Delegación Benito Juárez, México D.F., C.P. 03940.

Abstract

Electronic waste (e-waste), have a high potential as a source of precious metals, since they can contain metals like silver, gold, platinum, copper, zinc, nickel, tin and others. In this paper some e-waste were characterized using several analytical techniques as Scanning Electron Microscopy (SEM), X-ray diffraction (XRD) and inductively coupled plasma (ICP) in addition to the thermodynamic study by Pourbaix diagrams of silver (Ag), gold (Au), platinum (Pt), copper (Cu), nickel (Ni), tin (Sn) and zinc (Zn); considering an average low concentration of HNO_3 (10% v/v). With results of the characterization was determined that the e-waste is an ideal source for the recovery of valuable metals. Similarly, the thermodynamic studies showed that it is possible to obtain all metallic species except Pt, in a potential window of 1.45V to 2.0V vs SCE.

Keywords: e-waste, Pourbaix, thermodynamic, x-ray diffraction, electron microscopy.

Introduction

Metals in the electronic industry are intended to be used for connecting cables, soldering, printed circuit boards, switches and touch screens. Among the most commonly used metals are copper, barium, nickel, zinc, tantalum, iridium, vanadium, silver, gold, beryllium, manganese, antimony, bismuth, mercury and selenium. This is due to its conductive and corrosion resistance characteristics. The metals contained in electronic waste (e-waste) make them a potential source for the recovery of high economic value metals such as: Ag, Au, Pt, Cu, Ni, Zn and Sn. The lack of technologies for a selective recovery in many countries, have promoted the illegal removal of these residues. In this paper, trying to contribute to the development of some alternatives, a general view is established for the electrochemical leaching of Ag, Au, Pt, Cu, Ni, Zn and Sn, derived from e-waste. First, a characterization study by SEM-EDS, XRD and ICP techniques, is performed. Then, Pourbaix diagrams of Ag, Au, Pt, Cu, Ni, Zn and Sn were constructed considering a low concentration electrolyte of HNO_3 (10% v/v).

Experimental

Sample characterization

The Characterization of the metal sample material of e-waste that was provided by the company "Corporación de Valores Reciclados SA de C.V.", was performed by the SEM-EDS, XRD and ICP techniques to determine the content values of the metals (Ag, Au, Pt, Cu, Ni, Zn and Sn).

The SEM-EDS characterization of the metal powder from the e-waste was carried out using an electronic microscope JEOL JSM-6300, with high vacuum, energy dispersive MORAN detector and using a magnification of 20X, with a 20kV acceleration voltage. In addition, the EDS analysis was made using different regions of the e-waste sample, to obtain an average concentration.
The XRD analysis of the e-waste sample was performed using a NEM Equinox 2000 diffractometer, with a cobalt Co-Kα1 source at 20 kV and 30 mA.
A spectrophotometer Perkin Elmer Optima 8300 was used for the study of e-waste sample by ICP. 1g of the sample was digested using concentrated HCl and HNO_3 2: 1 and heating for 15 min.

Thermodynamic study

For the Pourbaix diagrams construction of the Ag, Au, Pt, Cu, Ni, Zn and Sn species the free software *HSC Chemistry 5* was used. Simulation was performed considering a nitric acid concentration of 10% v/v (2.4 M), at room temperature and the Ag, Au, Pt, Cu, Ni, Zn and Sn concentrations of 9.1×10^{-5}M, 4.2×10^{-5}M, 4.1×10^{-6}M, $2.88 \times 10^{-}$M, 2.86×10^{-3}M, 2.4×10^{-3}M, 8.39×10^{-4}M , obtained by ICP, respectively.

Results

Sample characterization

Figure 1 shows a micrograph from the e-waste powder sample with a 20X magnification. It can be observed a regular morphology of the metallic particles and a size nearby to 1 mm and white areas, which are due to the presence of plastic components from the electronic circuitry of the e-waste.

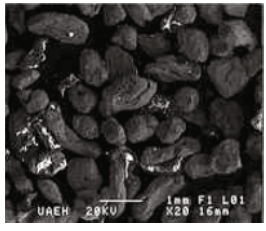

Figure 1 E-waste powder micrograph at 20X using 20 kV.

Table 1 shows the results of average weight percentages of the metals contained in the two regions under study of the sample obtained by EDS analysis.

Table 1 Percentages of the metals found in e-waste powder by SEM-EDS

Element	average weight / %
Cu	58.4 ± 2.1
Ni	25.0 ± 2.8
Zn	0
Ag	0.04 ± 0.06
Au	10.01 ± 0.1
Sn	6.6 ± 4.8
Pt	0

This table shows that the most economically valuable metals, Au and Ag, have 10.01% and 0.04% weight percentage respectively. Also it is observed that the metals with the highest concentration are Cu with a concentration of 58.4 % and Ni with 25.0%. It is noteworthy to point out that the SEM-EDS technique is semi-quantitative, so it is not possible to properly ascertain the content of Ag and Pt. Therefore it was necessary to use more precise techniques, such as XRD and ICP, for studying the e-waste sample.

Figure 2 shows the XRD pattern obtained for the contained metals in the e-waste sample. The most intense peaks correspond to the interest phases of Pt, Ag and Au, in addition to Cu, Zn, Ni and Sn. From this XRD pattern the concentrations of all metallic phases were obtained and they are shown in Table 2. The weight percentage concentrations of Ag, Au and Pt are 11.1%, 6.6% and 6.8%, respectively. Besides, concentrations of Cu, Ni, Zn and Sn with 18%, 19%, 19.7% and 18.8% respectively, were found.

Table 2 Metal e-waste estimated concentrations by DRX

Pattern	Phase	Weight Percentage %
96-901-3053	Ag	11.1
96-210-4030	Pt	6.8
96-901-3036	Au	6.6
96-900-8571	Sn	18.8
96-901-3016	Cu	18
96-901-1600	Zn	19.7
96-901-8571	Ni	19

The differences between SEM and DRX in the mass percentage of Cu, can be attributed, the technique nature. SEM is a semicuantitative analysis, just a scanning of the sample. While DRX, takes a view of the phases angles contained in the sample. So that it is necessary, to use a more precise technique like ICP, that reveals, all phases content.

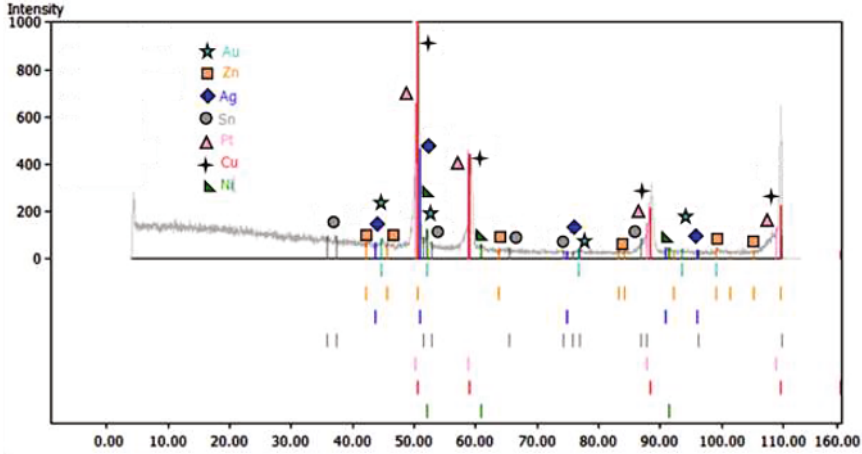

Figure 2 E-waste sample diffract pattern obtained by DRX.

Table 3 shows concentrations obtained by the ICP technique, where the weight percentage content of Ag is 0.05%, Au is 0.04 % and Pt is 0.0043%. It is important to mention, that most metals contained in e-waste, are present as solders or recovered metal parts. Differences between these results and those presented in Table 1 and 2, can be attributed; to the sample pretreatment. While ICP can reveal all metals, because the acid digestion, X-Ray diffraction and SEM-EDS don´t. These results (table 3) demonstrate that the e-waste are a potential source of precious metals, because of the amount in the sample in comparison to the mining usual concentration, which usually have a smaller percentage of Au, Ag and Pt of 0.000567, 0.01 and 0.0004% respectively.

Table 3 E-waste sample concentrations obtained by ICP.

Element	ppm	Weight percentage %
Cu	18324.00	97.64
Ni	168.82	0.90
Zn	155.52	0.83
Ag	9.82	0.05
Au	8.40	0.04
Sn	99.66	0.53
Pt	0.80	0.0043
Total		100

The results of XRD and ICP verify the presence of significant amounts of Ag, Au, Pt, Cu, Ni, Zn and Sn metals.

To carry out the selective electrochemical leaching of a multielemental metallic sample it is necessary to know the potential ranges in which metals are leached. It is therefore compulsory to carry out a thermodynamic study by constructing Pourbaix diagrams that provide information on

the potential of the oxidation processes of each metal. However, it is essential to consider this study as an approximation to the real system, because it does not take into account the nature of electrodes and interactions between all metallic elements present.

Thermodynamic study

Figure 4 (a, b, c, d, e, f, g) shows the Pourbaix diagrams obtained for Ag, Au, Pt, Cu, Ni, Zn and Sn with $9.1x10^{-5}$M, $4.2x10^{-5}$M, $4.1x10^{-6}$M, $2.88x10^{-1}$M, $2.86x10^{-3}$M, $2.4x10^{-4}$M, and $8.39x10^{-3}$M concentrations respectively, whereas a concentration of 10% HNO_3 and pH 1.03 electrolyte is used.

Figure 4a, shows that the formation of Ag^{+} ionic species and AgO_2 oxides is favored in the conditions tested. The Ag^{+} ion species is favored in a range of electrochemical potential imposed between 0.55V to 1.5V vs SCE at pH 1.03. Moreover, it is observed that the leaching of the ionic species of Ag^{+} can be affected by the oxygen evolution reaction from the electrochemical potential of 1.17V.

Figure 4b shows that Gold produces only one ionic specie, Au^{+3}, which predominates in a range of electrochemical potential imposed between 1.45V and 2.0V vs SCE at pH 1.03. Furthermore, it is noted that production of Au^{+3} is always coupled with oxygen evolution; because it is presented to less anodic potentials (1.17V) respect to the working pH.

Figure 4c shows that the production of oxidized Pt species is favored; PtO, PtO_2, throughout the pH range, without the production of platinum ionic species.

In Figure 4d the presence of ionic species, Cu^{+2} and oxidized copper, Cu_2O and CuO, are observed. The production of the ionic species Cu^{+2} is favored in the range of electrochemical imposed potential between 0.4V and 2.0V vs SCE at pH 1.03 and whose production is carried out, coupled to the oxygen evolution reaction from 1.17 V vs SCE.

In Figure 4e, the ionic species of Nickel, Ni^{+2}, oxidized, NiO, and hydroxylated, $Ni(OH)_3$, are observed. The production of the ionic species, Ni^{+2}, is favored in the range of electrochemical potential from -0.3V to 2.0V vs SCE. In addition there is the coupled reaction of oxygen evolution from 1.17V during leaching of nickel.

In Figure 4f, the ionic species of Zinc, Zn^{+2}, and oxidized ZnO, are observed. Production of the ionic species Zn^{+2} is carried out at electrochemical potentials between -0.7V to 2.0V vs SCE. In addition, the oxygen evolution reaction, observed from 1.17V, affects leaching process of zinc Zn^{+2} species.

Figure 4g shows that the production of ionic species Sn^{+2} and oxide SnO_2 is possible; however, the ionic species Sn^{+2} are favored in a small range of electrochemical potential of -0.1V to -0.25V vs SCE.

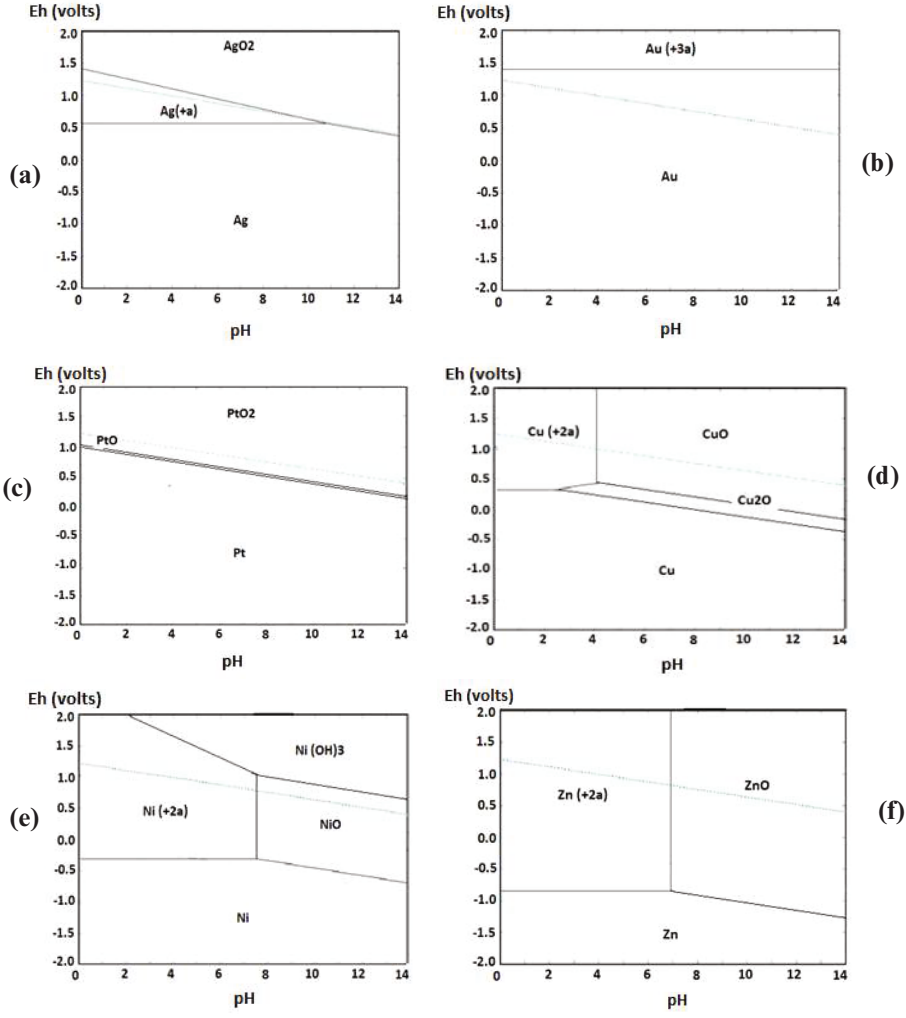
(a)
Eh (volts)
AgO2
Ag(+a)
Ag
pH
(b)
Eh (volts)
Au (+3a)
Au
pH
(c)
Eh (volts)
PtO2
PtO
Pt
pH
(d)
Eh (volts)
Cu (+2a)
CuO
Cu2O
Cu
pH
(e)
Eh (volts)
Ni (OH)3
Ni (+2a)
NiO
Ni
pH
(f)
Eh (volts)
Zn (+2a)
ZnO
Zn
pH

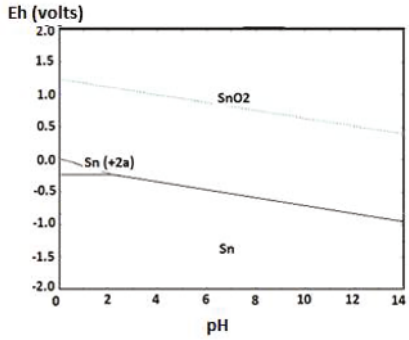

(g)

Figure 4 Pourbaix diagrams for a) Ag , b) Au, c) Pt, d) Cu , e) Ni, f) Zn and g) Sn considering pH 1.03 nitric acid concentration.

Taking into account the above, redox reactions under standard conditions for ionic metal species, which are expected to carry out under the conditions of this work are:

$$Cu^{2+} + 2e^- \leftrightarrow Cu^o \quad E^o = 0.34 \tag{1}$$

$$Ni^{2+} + 2e^- \leftrightarrow Ni^o \quad E^o = -0.250 \tag{2}$$

$$Zn^{2+} + 2e^- \leftrightarrow Zn^o \quad E^o = -0.73 \tag{3}$$

$$Sn^{2+} + 2e^- \leftrightarrow Sn^o \quad E^o = -0.36 \tag{4}$$

$$Au^{3+} + 3e^- \leftrightarrow Au^o \quad E^o = 1.49 \tag{5}$$

$$Ag^{+} + e^- \leftrightarrow Ag^o \quad E^o = 0.799 \tag{6}$$

$$Pt^{2+} + 2e^- \leftrightarrow Pt^o \quad E^o = 1.2 \tag{7}$$

It is worth mentioning that these equilibriums are affected by the specific conditions of the real system, and there can be deviations in the values of potential to which the leaching process is held.

Therefore, the thermodynamic results indicate that it is possible the Ag^+ and Au^{+3}ionic species existence, without platinum; under working conditions. However, these results do not take into account other important factors such as the electrodes nature or interferences in the equilibrium state due to the rest metals interactions.

Conclusions

The characteristics of the metal sample evaluated were determined by verifying the amount of each metal, showing that the e-waste are a viable source for the recovery of Ag, Au, Pt, Cu, Ni, Zn and Sn.

The thermodynamic study indicated that it is possible to obtain the ionic species of Ag, Au, Cu, Ni and Zn metal at an interval of electrochemical potentials of 1.45V to 2V at a pH of 1.03. It is also noted that the tin ion species are produced in an interval of electrochemical potential of -0.1V to -0.25V vs. SCE. Conversely, the formation of platinum ionic species in this potential range and in this medium is not favored. So also it can be concluded that the HNO_3 is a suitable medium for the leaching of most metals in e-waste.

References

1. Jadhov, U. (2012). Recovery of precious metals from industrial waste. *Journal of achievements in materials and manufacturing engineering , 4* (2), 159-167.
2. Escutia, L. (2003). Lixiviación de Ag a partir de concentrados sulfurados con thiourea electrodo-oxidada. *Tesis para obtener el grado de Maestro en Ciencias* . Ciudad de México: UAM Iztapalapa.
3. Newton, J. (2002). *An introduction to Metallurgy* (Segunda edición ed.).

Characterization of Minerals, Metals, and Materials 2016
Edited by: Shadia Jamil Ikhmayies, Bowen Li, John S. Carpenter, Jiann-Yang Hwang, Sergio Neves Monteiro, Jian Li, Donato Firrao, Mingming Zhang, Zhiwei Peng, Juan P. Escobedo-Diaz, and Chenguang Bai
TMS (The Minerals, Metals & Materials Society), 2016

DEVELOPMENT OF BIO-BASED FOAMS PREPARED FROM PBAT/PLA REINFORCED WITH BIO-CALCIUM CARBONATE COMPATIBILIZED BY ELECTRON-BEAM RADIATION

Elizabeth Carvalho L. Cardoso[1]; Marcus Vinicius S. Seixas[2]; Helio Wiebeck[2], René R. Oliveira[1]; Glauson Aparecido F. Machado[1]; Esperidiana A. B. Moura[1]

[1]Instituto de Pesquisas Energéticas e Nucleares- IPEN/CNEN-SP – Av. Lineu Prestes 2242 – CEP 05508-900 – Cidade Universitária, São Paulo/SP- Brasil.
[2]Universidade de São Paulo, Escola Politécnica, Dep. de Eng. Metalúrgica e de Materiais. Av. Prof. Mello de Moraes 2463, São Paulo, SP, 05508-030 – Brasil

Keywords: Bio-based foams; Electron-beam radiation; PBAT; PLA; Eggshell

Abstract

In Brazil, the food industry generates every year huge amounts of avian eggshell waste, an industrial byproduct containing 95% of calcium carbonate, and its disposal constitutes a serious environmental hazard. This study aims to the development of bio-foams from PBAT/PLA blends reinforced with bio-calcium carbonate from eggshells. Composites were obtained by melting extrusion process, blending PBAT/PLA (50/50) with 25% of bio-calcium carbonate, PBAT/PLA (50/45) with 25% of bio-calcium carbonate and 5 % of pre-irradiated PLA and PBAT/PLA (50/40) with 25% of bio-calcium carbonate and 10 % of pre-irradiated PLA. PLA was previously e-beam irradiated at 150kGy in air and used as compatibilizer agent. The composites were then extruded in a Rheomex 332p single special screw for foaming. Samples were submitted to Tensile and Compression tests, MFI, DSC, TGA, XRD and FEG/SEM, analyses.

Introduction

Polymers are vastly employed for numerous purposes in different industrial segments [1, 2], generating enormous quantities of discarding in the environment. Amongst the various components of waste in landfills, polymeric materials composites account for an estimated from 20 to 30% of total volume of solid waste disposed. Much endeavor has been committed to developing biodegradable and renewable resource–derived polymers because of worldwide environmental concerns and sustainability problems resulting from petroleum-based polymers. As the world moves toward the production of sustainable environmentally friendly plastics (bio-plastics), the production of biodegradable polymers has become an area of significant scientific interest [3, 4]. The bio-plastic market is estimated to increase from approximately 1.4 million tons in 2012 to around 6.2 million tons in 2017 and is being used for a variety of different applications, including automotive, agricultural, pharmaceutical and packaging industries [5, 6].

Bio-based feedstock is one option to reduce environmental impacts related to fossil polymer production; they will have to satisfy future material demand and simultaneously reduce negative environmental impacts besides providing income to the agricultural sector [7, 8].
Polylactide or poly(lactic acid) (PLA) is the front runner in the emerging bio-plastics market with the best availability and the most attractive cost structure. PLA is linear, aliphatic thermoplastic polyester with rigidity and clarity similar to polystyrene (PS) and poly ethylene

terephthalate (PET). It is used for different applications ranging from medical to packaging, resorbable and biodegradable under industrial composting conditions. Despite all its advantages, some properties of PLA such as inherent brittleness, poor melt strength, narrow processing window and low thermal stability pose considerable scientific challenges and limit their large scale-applications (film blowing or injection molding) [9].

Blending PLA with another flexible polymer was the way to solve problems depicted: PBAT, a petroleum-based but fully biocompostable copolymer with high ductility was choosen. Due to its high toughness and biodegradability, PBAT is considered as a good candidate for the toughness of PLA. This paper examines the use of PBAT blended with PLA due to its high impact strength and low stiffness. In order to decrease interfacial tension exhibited by PLA/PBAT blend, compatibilization is essential: herein it was used as compatibilizing agent PLA previously irradiated, at 150 kGy, e-beam source, dose ratio 11.22 kGy/s, Dynamitron II electrons accelerator, 1.5 MeV energy, 25 mA current, 37.5 kw power, in CTR-IPEN/CNEN-SP. Güven and collaborators[10] have proposed the use of ionizing radiation, in replacing chemical compatibilizing agents for thermoplastic materials with enhanced properties.

Eggshell is an important waste material by-product of poultry industries and domestic kitchen waste. Currently, egg production throughout the world is 65.5 million metric tons per year, with Asia as a key contributor to global egg output growth [11]. By taking 11% of the weight, nearly 7.2 million tons of eggshell waste is created every year; these residue materials, if unutilized, create a potential pollution problem. Therefore, resourceful utilization of this waste is of great importance not only for reducing the environmental impact, but also for gaining higher profits. Eggshell is a natural bio-ceramic composite with a unique chemical composition of high inorganic (95% of calcium carbonate in the form of calcite) and 5% of organic (type X collagen, sulfated polysaccharides) components; this eggshell characteristic structure combined with substantial availability makes eggshells a potential source of bio-fillers that can be efficiently used for polymer composites [12].

A significant element of sustainability is the recognition that Earth´s resources are finite. As the global human population continues to grow exponentially, the strain on our finite resources will be ever increasing, creating the need for innovative and sustainable solutions; bio-based foams from agro-industrial residues will be able to replace petroleum-based foams.

The proposal of present work is the development of biodegradable foams from PLA/PBAT blends reinforced with avian eggshell and compatibilized with ionizing radiation, further assessed for Tensile and Compression tests, MFI, DSC and TGA, XRD and FEG-SEM.

Materials and Methods

Materials

PLA: Ingeo Biopolymer 3251 D, from Nature Works LLC, dried at 70℃for 12 hours before processing.
PBAT: Ecoflex – FS, Basf, dried at 70℃for 12 hours before processing.
PLA e-beam irradiated at 150 kGy*:* compatibilizing agent, from PLA e-beam irradiated at 150 kGy, dose ratio 11.22 kGy/s, Dynamitron II electrons accelerator, 1.5 MeV energy, 25 mA current, 37.5 kw power, in CTR-IPEN/CNEN-SP

ENDEX 2650™: Endothermic Chemical Foaming Agent and Process Aid, used in all extruded samples, at 0.5% level.
Avian eggshell: White chicken eggshells were subjected to a thorough cleaning using tap water for removing of internal membranes. Afterwards, clean eggshells were kept for 4 hours in a water bath kept at 100ºC and finally dried at 100º± 2ºC for 2 h in an air-circulating oven. Eggshells were size reduced to fine powder, particle size equal or lower than 125 m by using ball mills and granulometric sieve, respectively. Then they were dried again at 100 ± 2 ºC, for 24 h, in order to reduce its moisture content to less than 2 %.
Irgafos 168 and Irganox 1010, Basf: A synergistic blend, 0.1% each one used and acting to provide a processing and long-term thermal stabilizer system.

Blends preparation

The composite materials were prepared according to Table I; they were first homogeneized by melting extrusion process, using a co-rotating twin-screw extruder (HAAKE Rheomex 332p, 3.1 L/D, 19/33 compression ratio), by using a 120 to 145ºC temperature profile and 50 rpm.

Table I. Compositions prepared in extruder.

	PLA	PBAT	$CaCO_3$(*)	PLA eb-irradiated at150 kGy
%, wt/wt	50	50	--	--
	50	50	15	-
	45	50	15	5
	40	50	15	10

(*) $CaCO_3$ added in phr (parts per hundred parts of resin).

Foaming

Composite materials prepared according to Table I were extruded foamed within a 120 to 145ºC temperature range, special mono-screw for foaming, using 0.5% of Endex 2650™ as expansion agent. Samples were collected directly from die to be further investigated.

Characterization

Mechanical tests

Tensile and Compression tests: Samples were analyzed in a texturometer (TA-Hdi Stable Micro Systems Texture Analyser texturometer) 5 kg load cell, 0.5 $m.s^{-1}$ deformation rate, 2 $mm.s^{-1}$ speed), under room temperature. The specimen dimension was 80×10 mm^2 denoting respectively the length and breadth for tensile and 2 mm diameter for compression evaluations. Both tensile and compression evaluations were performed in accordance with ASTM D 638-08.

MFI (Melt Flow Index)

Analyses were accomplished in a CEAST apparatus, *modular line,* 170º C, 2.16 kg load, 240 seconds pre-heating time, according to ASTM D1238-13.

Differential Scanning Calorimetric Analysis (DSC)

Thermal behavior was examined in a DSC Mettler Toledo apparatus, according to ASTM D3418-08. A set of heating/cooling ramps was carried out following a three step process; the samples were firstly heated to 200°C and kept in the molten state for 10 min to erase the thermal history of the material. They were then cooled down to 30°C at 10°C.min^{-1} to evaluate the ability of PLA component to crystallize upon cooling. After cooling treatment, the samples were heated back to 200°C at 10°C.min^{-1}. The percent crystallinity was calculated upon the second heating by using Eq.1 based on Hermans and Weidinger equation [13]:

$$X_c(\%) = 100 * \frac{\Delta H_m - \Delta H_{cc}}{f * \Delta H_{m\infty}} \quad (1)$$

Where "ΔHm" is the measured heat of fusion, ΔHcc the cold crystallization enthalpy (J.g^{-1}) , "f" is the weight fraction of PLA or PBAT in the blend and "ΔH∞m "is the enthalpy of fusion for a crystal having infinite crystal thickness (93J.g-1 for PLA and 114 J.g-1 for PBAT).

Thermogravimetric analyses (TG)

Thermogravimetric analyses provides complimentary and supplementary characterization information to DSC, by measuring the amount and rate (velocity) of change in the mass of a sample as a function of temperature or time in a controlled atmosphere. Measurements are used primarily to determine the thermal and/or oxidative stabilities of materials as well as their compositional properties. The technique can analyze materials that exhibit either mass loss or gain due to decomposition, oxidation or loss of volatiles (such as moisture). TGA were performed using a DSC Mettler Toledo apparatus, according to ASTM E1641-07, by using 5 – 9 mg of foam sample, within a 25 to 600ºC program, at a 10ºC.min^{-1}, in a nitrogen flow of 50ml.min^{-1}.

XRD (X-Ray Diffraction Analysis)

It was used a X-Ray diffractometer, Rigaku Multiflex, 40 kV, 20 mA, scanning 5 t0 60º.2 θ, step 0.02º. 2 θ, 1ºC.min^{-1}, continuous analysis. It provides, among other, information on samples crystallinity, via diffractograms.

Field Emission Scanning Electron Microscopy (FE-SEM)

Investigations were accomplished in a JEOL-JSM-6701 F microscope with an accelerating voltage of 1-30 kV, EDS Thermo-Scientific mod. Noran System Six software, carbon sputtered samples, for an investigation of morphology, in various magnification micrographs.

Results and discussion

Mechanical Test Results

Tensile Tests Results: Figure 1 shows the diagram Stress (MPa) against Strain (mm/mm) for PBAT/PLA blend foams and its composites:

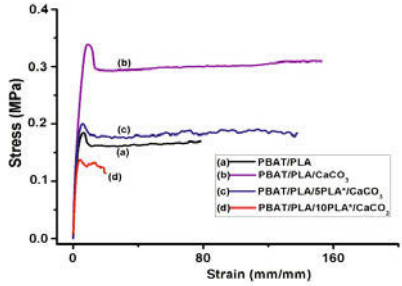

Figure 1.Diagram Stress (MPa) x Strain (mm/mm) for PBAT/PLA blend foams and its composites.

Results obtained for tensile test showed that addition of 15% of calcium carbonate improved mechanical behavior; values for both force and strain practically doubled.
Compatibilizing agent PLA previously e-beam irradiated, added to a 5% level wt in PBAT/PLA/$CaCO_3$ reduced in approximately 70% tensile at break and 14% strain; when PLA e-beam irradiated was added to a 10% level in PBAT/PLA/$CaCO_3$, there was a drastic reduction around 40% in tensile at break and 90% in strain.

Compression Test Results: Figure 2 shows the diagram compression stress (MPa) x Strain (%) for PBAT/PLA blend foams and its composites:

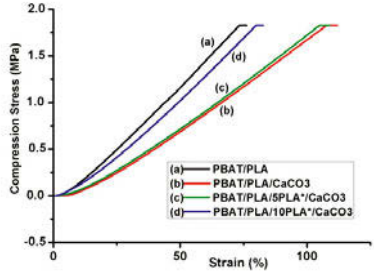

Figure 2.Compression force for PBAT/PLA foams compositions.

As can be seen in Figure 2, all assessed samples presented a compression force about 1.75 MPa. A higher strain (100%) was shown for PBAT/PLA + 15% $CaCO_3$ and PBAT/PLA + 15% $CaCO_3$ + 5% PLA i. samples; Both PBAT/PLA and PBAT/PLA + 15% $CaCO_3$ + 10% PLAi. samples showed values about 80% for strain.

Melt Flow Index (MFI) Measurement Results

MFI results are shown in Table II. In PBAT/PLA blend, addition of 15 % of CaCO3 lowered melt index from 8.7 to 4.8 dg.min-1, providing consequently a straighter standard deviation and a higher molar mass. 5 % and 10 % addition of PLA irradiated, melt index about 14.4 dg.min-1, in PBAT/PLA/CaCO3, increased melt index from 4.8 to approximately 10.1 and 12.6 dg.min-1, respectively, pointing toward a decrease in molar mass.

Table II: MFI evaluation for PBAT/PLA compositions

	1	2	3	4	5	6	7
MFI ($dg.min^{-1}$)	9.1	13.2	14.4	8.7	4.8	10.1	12.6

1 = PLA; 2 = PBAT; 3 = PLA*; 4 = PBAT/PLA; 5 = PBAT/PLA + 15% $CaCO_3$; 6 = PBAT/PLA + 15% $CaCO_3$ + 5% PLA*; 7 = PBAT/PLA + 15% $CaCO_3$ + 10% PLA*; PLA* = PLA eb-irradiated at 150 kGy.

Differential Scanning Calorimetry Analysis (DSC) Results

In Table III is shown thermal behavior of PLA, PBAT, PLA* and its compositions, from the second heating cycle and corresponding crystallization cycle. Crystallinity assessments were accomplished based on Hermans and Weidinger equation. Individually, both PLA and PBAT have a very low crystallinity; nevertheless, its blend proved to achieve a workable crystallinity value for going on with further experiments.

Table III: Thermal properties and crystallinity evolution for PBAT/PLA compositions

	1	2	3	4	5	6	7
Tcc (ºC)	33.5	51.2	39.8	71.7	69.7	69.8	70.0
Enthalpy Tcc($J.g^{-1}$)	36.8	20.5	43.5	7.2	7.1	7.3	7.5
Tm (ºC)	87.8	120.0	86.9	86.9	87.4	87.8	87.2
Enthalpy Tm ($j.g^{-1}$)	43.5	16.8	41.6	22.5	21.2	17.2	10.7
X	7.2	3.2	2.1	33.0	33.0	33.0	33.0

1 = PLA; 2 = PBAT; 3 = PLA*; 4 = PBAT/PLA; 5 = PBAT/PLA + 15% $CaCO_3$; 6 = PBAT/PLA + 15% $CaCO_3$ + 5% PLA*; 7 = PBAT/PLA + 15% $CaCO_3$ + 10% PLA*; Tcc = cold crystallization temperature; Tm = melt temperature; X = crystallinity.

Thermogravimetric Analyses (TG) Results

Values obtained for thermogravimetric analyses are presented in Table IV. All PBAT/PLA blends presented close values for T_{onset} and T_{endset}; consequently, it is impossible to establish a given value for the maximum degradation temperature.

Table IV: Thermogravimetric analyses for PBAT/PLA compositions:

	1	2	3	4	5	6	7
T_{onset} (ºC)	377.3	376.7	366.2	370.7	361.8	360.4	370.0
T_{enset} (ºC)	410.1	412.1	410.1	418.1	412.2	410.1	410.1

X-rays Diffraction (XRD) Analysis Results

Diffractogram presented in Figure 3 confirmed values obtained for DSC and TG evaluations.

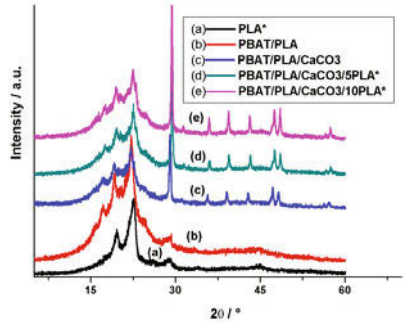

Fig. 3. XRD patterns of PBAT/PLA blend and its composites.

PBAT/PLA composites presented complete interaction according to XRD pattern, indicating the feasibility of future essays.

Field Emission Scanning Electron Microscopy (FE-SEM)

FE-SEM micrographs of cryo-fracturated surfaces of PBAT/PLA blend foams and its composites are shown in Figure 4:

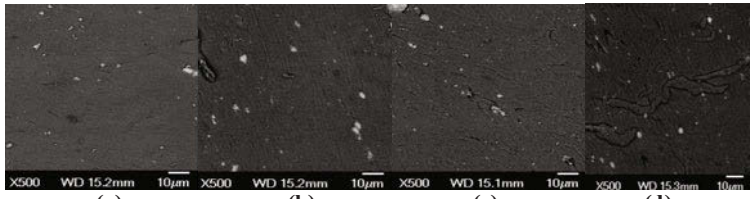

(a) **(b)** **(c)** **(d)**

Figure 4.FE-SEM micrographs of cryo-fracturated surfaces, 500 x magnification: PBAT/PLA (a), PBAT/PLA + 15% $CaCO_3$ (b); PBAT/PLA + 15% $CaCO_3$+ 5% PLA irradiated (c); PBAT/PLA + 15% $CaCO_3$ + 10% PLA irradiated (d).

Micrograph related to PBAT/PLA blend (a) shows the immiscibility between both components. The addition of $CaCO_3$ as well PLA irradiated compatibilizer did not improve the overall dispersion in PBAT/PLA matrix.

Conclusions

The addition of calcium carbonate from avian eggshells proved to be an effective reinforcement for PBAT/PLA matrix, according to tensile and compression tests. MFI assessments confirmed a lower value for PBAT/PLA matrix, after insertion of calcium carbonate, indicating a lower molecular weight distribution and consequently a higher molar mass. A much higher crystallinity (from around 5 to 33%) was observed after blending PBAT and PLA. Thermal behavior was ineffective to indicate a maximum degradation temperature due to very close results. DRX confirmed previous DSC crystallinity results for PBAT/PLA and composites. FE-SEM micrographs pointed toward a required improvement in dispersion of all blends.

Acknowledgements

The authors acknowledge Basf, Endex and IPEN, fundamental for work development.

References

1. H.G. Elias, *An Introduction to Polymer Science*, (1st Ed., VCH Publishers Inc., New York, NY, 1997), p.413.

2. R.B Lieberman and P.C. Barbe, *Propylene Polymers*. In: H. F. Mark, N.M. Bikales, C.G. Overberg, G. Menges (Encyclopaedia of Polymer Science and Engineering 1st ed. New York: John Wiley and Sons Inc, vol.13 1988), p.464.

3. N. Miskolczi, L. Bartha and A. Angyal, "High energy containing fractions from plastic wastes by their chemical recycling", *Macromolecular Symposia*, vol. 245-246, (2006), pp. 599–606.

4. S.M.M. Franchetti et al, "Uma solução para diminuir a quantidade dos resíduos plásticos", *Quimica Nova*, 29, (N. 4), (2006), 811-816.

5. K. S. Anderson, K. M. Schreck, and M. A. Hillmyer, "Toughening polylactide", *Polymer Reviews*, 48, (2008), 85–108.

6. B. Gupta, N. Revagade and J. Hilborn, "Poly(lactic acid) fiber: an overview", *Progress in Polymer*, 32(4), (2007), pp 455-482.

7. A.P. Gupta, V. Kumar, "New Emerging Trends in Synthetic Biodegradable Polymers – Polylactide: A Critique," European Polymer Journal, 43, (2007), 4053-4074.

8. R. Al-Itry, K. Lamnawar and A. Maazouz, "Improvement of thermal stability, rheological and mechanical properties of PLA, PBAT and their blends by reactive extrusion with functionalized epoxy", *Pol. Deg. Stab.*, 97¸ (2012), 1898-1914.

9. Yun-Yuan Weng et al, "Biodegradation behavior of PBAT, PLA and their blend under soil conditions", *Pol. Test.*, v.32, (issue 5), (August 2013), pp. 918-926.

10. O. Guven et al, "Polymer recycling: potential application of radiation technology", *Radiation Physics and Chemistry*, 64, (2002), 41–51.

11. Global poultry trends: "Asia is a key to global egg output growth". 2013. The Global Poultry Site. http://www. thepoultrysite.com/articles/2735/global-poultry-trends-asia-is-key-to-global-egg-output-growth.

12. S. B., Hassan, V. S. Aigbodion and S. N. Patrick, "Development of polyester egg shell particulate composites", *Tribol. Ind.* 34(4), (2012), 217–225.

13. P. H. Hermans, and Weidinger, "Estimation of crystallinity of some polymers from X-ray intensity measurements", *J. Polym Sci.,* v.4, (1949), p.709-723.

Characterization of Minerals, Metals, and Materials 2016
Edited by: Shadia Jamil Ikhmayies, Bowen Li, John S. Carpenter, Jiann-Yang Hwang, Sergio Neves Monteiro, Jian Li, Donato Firrao, Mingming Zhang, Zhiwei Peng, Juan P. Escobedo-Diaz, and Chenguang Bai
TMS (The Minerals, Metals & Materials Society), 2016

MICROSTRUCTURE ANALYSIS OF BUILDUPS EMBEDDED IN CARBON SLEEVE IN CONTINUOUS ANNEALING FURNACE FOR NON-ORIENTED SILICON STEEL

Mingsheng He[1], Gaifeng Xue[1], Shoujun Peng[2], Meng Liu[1], Wangzhi Zhou[1], Huasheng Chen[1], Jing Zhang[2]

[1]R&D Center of WISCO, Wuhan 430080, China;
[2]Silicon Steel Division of WISCO, Wuhan 430080, China

Keywords: Non-oriented silicon steel, buildup, microstructure, continuous annealing, carbon sleeve

Abstract

Based on the investigation and study of the microstructure, topography and composition of the low-temperature and high-temperature buildups which form in the surface of carbon sleeve in continuous annealing furnace for non-oriented silicon steel strip, combined with production process of non-oriented silicon steel, the mechanism and major causes for forming buildups of carbon sleeve are discussed. Meanwhile, some countermeasures to reduce the formation of the buildups are put forward.

Introduction

Non-oriented silicon steel strips are used in the core of a generator, a motor, a small size transformer and the like. The electromagnetic properties demanded to the silicon steel strips are high magnetic induction and low iron loss. Recently, from the standpoint of saving natural sources and energy, small sizes and high efficiency electromagnetic or electronic parts have been demanded, and soft magnetic properties, especially in silicon steel strips having excellent iron loss properties, have been also required. Generally, non-oriented silicon steel strip by cold or hot rolling process is decarburized, re-crystallized and annealed in continuous roller-hearth annealing furnace. Annealing furnace is the center of continuous annealing production line for non-oriented silicon steel strip and key equipment in heat processing for silicon steel. The carbon sleeve is usually used to support and convey steel strip in continuous annealing furnace. Under the condition of H_2-N_2-H_2O weak oxidation or H_2-N_2 strong reducing atmosphere and the high temperature, buildups form in the surface of carbon sleeve after using for a period of time, especially during the production of the high-grade non-oriented silicon steel and some low- and medium-grade non-oriented silicon steel containing low melting point metal, embedded buildups are much easier to form. Once embedded buildups come into being in carbon sleeve surface, they will

easily indent, bruise and scratch the surface of steel strip, which seriously affects the quality of steel strip surface and even causes degraded or waste products. The service life of carbon sleeve is shortened due to the shutdown caused by frequently grinding or changing rollers during the normal production, which not only severely influences the production efficiency, but also causes huge economic losses[1-4]. The quality and life time of carbon sleeve have been troubling the production of continuous annealing line for non-oriented silicon steel for both domestic and overseas iron and steel enterprises. The buildup formation of carbon sleeve is even more severe in continuous annealing furnace at high-temperature zone in the production of some high-grade non-oriented silicon steel.

Topography, Composition and Microstructure Analysis of Buildups

Topography of Buildups

Fig. 1 shows the embedded buildups forming in the surface of carbon sleeve during the decarburizing and annealing for non-oriented silicon steel strips. Fig. 1(a) is the photo of buildup embedded in the surface of carbon sleeve in low temperature zone (abbreviated as LTZ) of the annealing furnace. Fig. 1(b) is the photo of buildup embedded in the surface of carbon sleeve in high temperature zone (abbreviated as HTZ) of the annealing furnace. Fig. 1(c) is the photo of buildups in different shapes and sizes taken out from the surface of carbon sleeve. Most of the buildups are in cylinder shape, 0.5-6mm in length, 0.3-4mm in diameter, and the axial direction of buildups parallels that of carbon sleeve, but a small number of buildups are in irregular shape. Usually, the LTZ buildups are bigger than HTZ buildups. According to the observation and analysis of visible buildups taken out from the surface of the replaced and discarded carbon sleeve, most buildups are hollow cylinder in shape[1].

Fig. 1 Photos of buildups embedded in the surface of carbon sleevein low temperature zone (a) and high temperature zone (b) of annealing furnace; (c) buildups in different shapes and sizes.

Composition Analysis of Buildups

In order to figure out the inner structure and compositions of embedded buildups, the buildups are sectioned along radial or axial direction, inlaid, ground, and polished. And then the as-prepared samples were observed and analyzed by a scanning electron

microscope (SEM) (Quanta 400, FEI Co., Netherland) equipped with energy-dispersive X-ray spectroscopy (EDS).

Fig. 2(a) is the cross-section SEM micrographs of the LTZ buildup along radial direction; Fig. 2(b) is the cross-section partially enlarged SEM micrographs of the buildup. As shown in Fig. 2(a), it can be seen that the buildup is with the diameter of about 3.1mm and composed of light and deep color belts in alternately dark and bright annular concentric circles. In the center of the buildup is about 1mm hollow cavern in column shape[1].

Fig. 2(c) and Fig. 2(d) are respectively EDS spectrums of the light and deep color belts of the buildup cross-section. EDS composition analysis of the buildup sees Table 1. According to Fig. 2(c) and Table 1, the results show that the main chemical compositions of the light color belts are Fe, C and O, and the mass percent of composition are 79.95%, 9.08%, 6.34% respectively with a small amount of Si and Al. According to Fig. 2(d) and Table 1, the results show that the main chemical compositions of the deep color belts are Fe, O, Al, and Si, and the mass percent of composition are 44.98%, 23.14%, 18.67% and 8.32% respectively with a small amount of Na, Mg and P. The deep color belts contain the larger percent of oxide, which reveals that the atmosphere and dew point in annealing furnace are not controlled unsteadily and the majority of time is reducing atmosphere, but sometimes oxidizing atmosphere occurs.

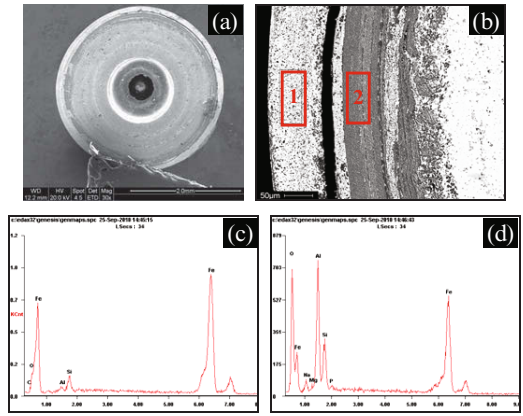

Fig. 2 Cross-section SEM micrographs of LTZ buildup: (a) general view, (b) partially enlarged; EDS spectrum of the buildup: (c) light color belt 1, (d) deep color belt 2.

Table 1 EDS composition analysis of the LTZ buildup (%)

Analysis section	C	O	Na	Mg	Al	Si	P	Fe
Light color 1	9.08	6.34	---	---	1.36	3.27	---	79.95
Deep color 2	---	23.14	2.93	1.17	18.67	8.32	0.79	44.98

Fig. 3(a) is the longitudinal section SEM micrographs of the HTZ buildup along the axial direction of the carbon sleeve; Fig. 3(b) and Fig. 3(c) is the longitudinal section partially enlarged SEM micrographs of the buildup. As shown in Fig. 3(a), it can be seen that the buildup is with the diameter of about 1mm. Fig. 3(e) and Fig. 3(f) are respectively EDS spectrums of the deep color and light color positions of the HTZ buildup. EDS composition analysis of the buildup sees Table 2. According to Fig. 3(e) and Table 2, the results show that the main chemical compositions of the deep color position are Fe, Si, O and C, and the mass percent of compositions are 33.69%, 19.37%, 26.68%, and 10.69% respectively with a small amount of Mn, Al and Ca. According to Fig. 3(f) and Table 2, the results show that the main chemical compositions of the light color position are Fe, and the mass percent of compositions is 98.48% with a small amount of Si. The deep color position contains the larger percent of oxides, but almost no oxide at light color position. Compared with the LTZ buildup, there are much more C and less oxides at deep color position and much more iron because the dew point is lower, the reducing atmosphere is stronger, and the temperature is higher in HTZ of the annealing furnace.

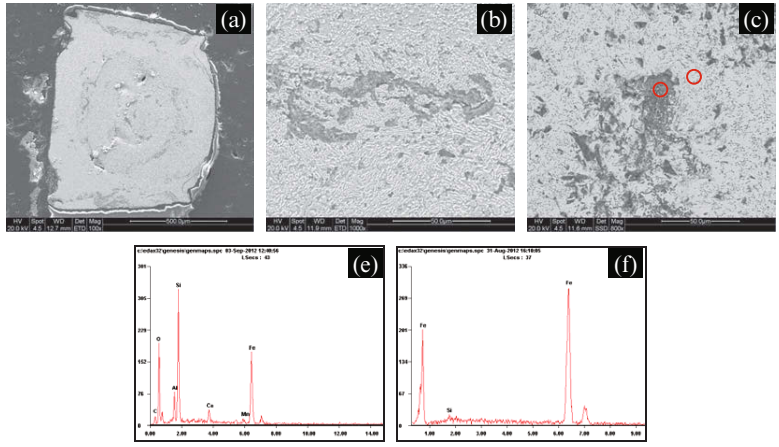

Fig. 3 Longitudinal section SEM micrographs of HTZ buildup: (a) general view, (b-c) partially enlarged; EDS spectrum of the buildup: (e) deep color position, (f) light color position.

Table 2 EDS composition analysis of the HTZ buildup (%)

Analysis section	C	O	Ca	Mn	Al	Si	Fe
Deep color position	10.69	26.68	2.67	2.51	4.39	19.37	33.69
Light color position	---	---	---	---	---	1.52	98.48

The results show that buildups experience the process from nucleating to growing-up. Iron powder, iron oxide powder, graphite powder, dust in the furnace, oil and grease and other oxide accumulate to form core in the pores of carbon sleeve

surface[1,5]. With the relative movement of steel strip and carbon sleeve, oxides constantly adhere to the surface, accumulate, sinter and grow up, and even take a solid phase reaction with each other and eventually form buildups in different shapes and sizes embedded in the surface of the carbon sleeve. Both in the LTZ and HTZ of the annealing furnace, the shapes, sizes and forming time of the buildup embedded in the surface of the carbon sleeve depend on the pore size and shape, and the amount of material sources.

Microstructure

The microstructures of the LTZ (a-c) and HTZ (d) buildups are shown in Fig. 4. As can be seen from Fig 4(a), the LTZ buildup is with the diameter of about 3.1mm and composed of light and deep color belts in alternately dark and bright annular concentric circles. In the center of the buildup is about 1mm hollow cavern. Fig. 4(b) exhibits one of the typical deep color belts with 15-20 micron in width. The light color belts composed of 10-50 micro ferrite grains (in Fig. 4(c)), and there are some deep color inclusions at grain boundary of the ferrite. As can be seen from Fig 4(d), the HTZ buildup is mainly composed of lamellar pearlite in the microstructure which comes into being due to high content of carbon. The carbon results from the constant friction and wear of carbon sleeve because the dew point is lower, the reducing atmosphere is stronger, and the temperature is higher in HTZ of the annealing furnace.

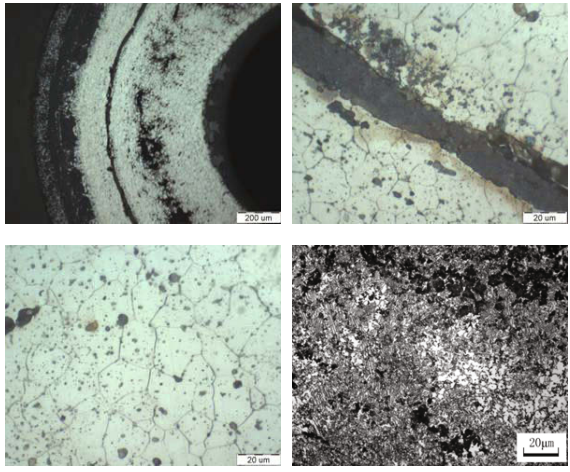

Fig. 4 Microstructure of the LTZ (a-c) and HTZ (d) buildups.

Causes for Buildup Formation of Carbon Sleeve

According to the results of the analysis above, it can be seen that the embedded buildups experience the “nucleation-growing up” process, and the main components

are iron, a small amount of iron oxide, and oxides of Al, Si, Mn, Na, Mg, Ca and so on. Obviously, the two necessary conditions for buildup formation are: (1) there exist pores or gaps in the surface of carbon sleeve; (2) rich material sources such as iron scale, iron rust, greasy dirt, dust on the surface of steel strip constantly accumulate and grow up in the pores, gaps in the surface of carbon sleeve[1,5].

Quality of Carbon Sleeve

Graphite is chemically inert in non-oxygen media. At normal temperature and pressure, graphite does not make any chemical reactions except the long-term immersion in nitric acid, hydrofluoric acid or in fluorine, bromine and other strong oxidizing atmosphere leads to form intercalation compounds slowly. However, due to complex procedures and processes of producing carbon sleeves together with porous material itself, it is inevitable to form larger holes in the surface during production and processing. Although the surface of carbon sleeve is smooth after soaking of various chemical substances and processing, graphite begin to react with water vapor over 700℃. One of the important purposes of the annealing to the finished product of non-oriented silicon steel is decarburization, therefore, holes inevitably appear due to oxidation during the use of carbon sleeves in continuous annealing furnace for silicon steel. As a result, these holes provide the necessary conditions for stubborn embedded buildups to form. When there are larger holes together with rich iron scale, iron rust, greasy dirt, dust, and other material sources, the stubborn embedded buildups could form.

Other Factors

According to the above study on the topography, composition and formation of buildups, the mechanism of forming buildups embedded in carbon sleeve as well as the actual production technology and process for non-oriented silicon steel, many other factors influence buildup formation embedded in carbon sleeves, such as furnace atmosphere, dew point, uncleanness of alkali wash, outer-sync of the actual speed of carbon sleeves and the running line speed of steel strip, uncleanness of inside furnace, and so on. Any increase in the oxidation of carbon and material sources such as iron scale, iron rust, greasy dirt, dust may lead to forming buildups embedded in carbon sleeve during the production of the non-oriented silicon steel.

Measures to Control and Reduce Buildups Formation

According to the present production technology, equipment and conditions, it is impossible to completely eliminate buildups, but it is possible to take some process control in technology or preventive measures to reduce buildups embedded in carbon sleeve in continuous annealing furnace for non-oriented silicon steel. The smaller pores in the surface of carbon sleeve are, and the less material sources for forming buildups such as iron scale, iron rust, greasy dirt on the surface of silicon steel strip

are, the less the possibility of buildup formation is. In order to control and reduce buildup formation, extend the service life of carbon sleeve, the following methods and measures are put forward [1]:

(1) Further improve the surface quality of carbon sleeve and enhance its oxidation resistance, wear resistance, and buildup formation resistance;

(2) Improve descaling equipment and process, strengthen the pickling, and reduce iron scale;

(3) Under the condition of guaranteeing rolling temperature, strictly control the heating temperature and soaking time, and avoid producing a large amount of iron scale due to the local overheating of steel plate surface;

(4) Strictly monitor atmosphere and dew point to prevent steel strip oxidation;

(5) Strengthen the cleanness of steel strip and alkaline wash to reduce iron rust, greasy dirt.

References

1. M.S. He, S.J. Peng, G.F. Xue, et al. "Cause analysis about buildup formation of carbon sleeve in continuous annealing furnace for silicon steel," *Advanced Materials Research*, 2011, 317-319: 1954-1959.
2. T. Yamada, I. Tanokuchi and Y. Uchiyama, "Carbon material for hearth roll, hearth roll and application of hearth roll," J.P. Patent 2006232660. (2006).
3. S. Midorikawa and S. Katoh, "Cermet powder for sprayed coating excellent in build-up resistance and roll having sprayed coating thereon," U.S. Patent 6,572,518B1. (2003)
4. T. Zhu, Y.J. Wang, X. Zhai, et al. "Development of full-processed non-oriented electrical steel in a CSP line," *Journal of University of Science and Technology Beijing*, 2009, 31(7): 862-866.
5. M.S. He, S.J. Peng, G.F Xue, et al. "Cause analysis about breakage of carbon sleeve in continuous annealing furnace for silicon steel," *Iron and Steel Research*，2012，40 (supplement): 24-27.

Characterization of Minerals, Metals, and Materials 2016
Edited by: Shadia Jamil Ikhmayies, Bowen Li, John S. Carpenter, Jiann-Yang Hwang, Sergio Neves Monteiro, Jian Li, Donato Firrao, Mingming Zhang, Zhiwei Peng, Juan P. Escobedo-Diaz, and Chenguang Bai
TMS (The Minerals, Metals & Materials Society), 2016

PROPERTIES OF CLAY FOR CERAMICS WITH ROCK WASTE FOR PRODUCTION STRUCTURAL BLOCK BY PRESSING AND FIRING

Cerqueira, N. A.[1]; Choe, D.[1], Alexandre, J.[1]; Azevedo, A.R.G.[1]; Xavier, C.G.[1], Souza, V. B.[2]

[1]UENF - State University of the Northern Rio de Janeiro, LECIV – Civil Engineering Laboratory; Av. Alberto Lamego, 2000, Campos dos Goytacazes, Rio de Janeiro, 28013-602, Brazil
[2]UFF – Federal Fluminense University – Mechanical Engineering Laboratory; Rua Passo da Pátria, 156 - Sala 213 Bloco E, Niterói, Rio de Janeiro, 24210-240, Brazil.

Keywords: rock waste; block pressing and firing; clay

Abstract

Building work requires optimization of materials and labor, so that the execution of its subsystems contribute to the quality, reduce costs, decrease waste in buildings, productivity, practicality and especially agility. Thus, the fitting blocks can contribute in this direction. This work therefore consists of physical characterization (determination of fitness levels, grain size and bulk density), chemical (EDX) and thermal (DTA and TGA) sample clay Campos dos Goytacazes-RJ and waste rock ornamental Cachoeiro de Itapemirim-ES, to verify potential for producing red ceramic blocks, pressed and burned, male and female type. The output of block will be with different percentages of incorporation of residues of ornamental rocks (0%, 5% and 10%). With the results obtained, it was found that the raw materials under consideration has the potential for application in the production of ceramic articles.

Introduction

The construction industry has gone through a major period of expansion, development, much driven by the economic situation of recent years in Brazil. Thus, it is of paramount importance mastery of techniques and products that enable greater speed in construction processes, lower costs and at the same time, a high standard of quality. It is important to, at the present stage of development, companies prezem for efficiency, aiming at profitability, customer satisfaction and, consequently, ensure their permanence in the market.

The art of building requires optimization of materials and labor, so that the execution of its subsystems contribute to the achievement of quality, reduce costs, decrease waste in buildings, productivity, practicality and especially agility. Thus, the use of Structural Masonry regained ground as an alternative to the use of reinforced concrete, by allowing a number of advantages, such as higher material savings, lower generation of waste, improvement in the finishing stage, etc. (Sanches, 2013) [1]. Another relevant factor is that such a building method performs both the sealing function and structure.

The production of plug-in blocks is usually associated with soil cement and lower value-added products. In order to contribute to the generation of a new product which combines the features of rationalization of the engaging blocks with a more valuable product, from the standpoint of strength and durability, Pedroti [2] proposed to replace the extrusion process in parts manufacturing ceramic brick, by pressing blocks in ceramic, process similar to what is done with the soil-cement bricks. The block type "male and female" are then pressed and burned, allowing a gain resistance.

In addition to strength, the bricks and blocks must have other characteristics which attest to the good quality material for use in masonry. Thus, Pedroti [3] proposed the inclusion of

granite residue in the ceramic material for the production of pressed blocks and burned in order to reduce porosity and therefore the water absorption, because it is a flux material.

The city of Campos dos Goytacazes, northern state of Rio de Janeiro, stands out on the national scene as a reputable pole of the clay industry. In 2012, according DRM-RJ [4], of 222 Rio de Janeiro ceramics, 113 were located in Campos, a total of 51% of ceramic production units.

In the Brazilian market, the Holy Spirit has emerged as a major benefactor producer of ornamental rocks, and currently accounts for about 50% of Brazilian production of rock and 60% of the installed capacity of processing [5]. The processing of ornamental rocks, there is a loss of up to 30% by volume, which creates a very large environmental liabilities. Several studies have been implemented with use of this residue incorporated into the ceramic body, for being such a great way to promote recycling of waste noblest form. Xavier [6] proposed the use of granite and marble residue in ceramic paste, adding value to waste and improving ceramic properties. According to Xavier a the use of 5% of granite cutting in red residue ceramic body molded by pressing, produced burning temperature of 900 °C produced ceramic parts of low water absorption, less variation of the linear dimensions and less weight.

Vieira et al. [7] studied the use of granite in red ceramic residue from a plant located in St. Anthony de Padua-RJ, indicate characteristics favorable for addition in red ceramic, because the facilities for the stages of drying and decreased porosity
This research deals with the characterization of the raw material (clay and waste): physical, chemical, mineralogical and thermal analysis for the production of pressed and burned blocks of ceramic with different percentages of incorporation of waste ornamental stones (0%, 5% and 10%).

Materials and Methods

In implementing this research, tests were conducted to determine the characteristics of raw materials (clay mass and ornamental rock waste). 15 kg of clay samples were collected in Campos - RJ Ceramics, and 15 kg of waste from a quarry in Itapemirim-ES, for characterization in the laboratory. The material was bagged to maintain humidity characteristics thereof. In the laboratory the samples dried out in the open, homogenized and separate for use in trials, as prescribed by NBR 6457:1986 [8].

With the prepared samples, assays for the characterization of the raw material using equipment available on LECIV-UENF and other laboratories UENF were performed to define key parameters for the production of blocks.

Physical Characteristics

They were performed in LECIV-UENF the Soil Laboratory to characterize clay and waste. The tests were performed according to the willing in the technical standards of the NBR 7181: 1984 [9] (grain size), NBR 7180: 1984 [10] and NBR 6459: 1984 [11] (Atterberg limits), NBR 6508: 1984 [12] and NBR 6457: 1986 [8] (density).

Chemical Analysis

The determination of the chemical composition of raw materials was held at Microanalysis Workshop of Civil Engineering Laboratory (LECIV-UENF) with Shimadzu EDX-700 equipment, with through material in the sieve #200.

Thermal Analysis

The differential thermal analysis (DTA) and thermogravimetric (TGA) of the samples

were performed on equipment Universal, Model V2.6D of TA Instruments SDT 2960 model operating at 10 °C/min in the Polymer Laboratory on LAMAV, with through material in the sieve #325.

Results and discussion

In Clay, the analysis of physical parameters, the particle size distribution of the sample is determined that displays 60% of clay fraction a liquid limit of 68% Plasticity index 37% and the real density of grains of 2.75 g/cm^3. The EDX showed that the clay has 44.6% SiO_2, 38.1% Al_2O_3 and 10.8% Fe_2O_3.

The results indicate that the clay exhibits good characteristics for the manufacture of ceramic articles.

To the residue the analysis of physical parameters, the particle size distribution of the sample is determined that displays 50% of clay fraction a liquid limit of 43% Plasticity index 20% and the real density of grains of 2.75 g/cm^3. The EDX showed that the clay has 51.8% SiO_2, 17.6% Al_2O_3, 10.45% CaO, 10.33% Fe_2O_3 and 5.2% K_2O.

The results indicate that the residue might be employed in the ceramic paste for manufacturing ceramic articles.

In Figures 1, 2, 3, 4, 5 and 6 show the charts with thermal analysis (TG and DTA).

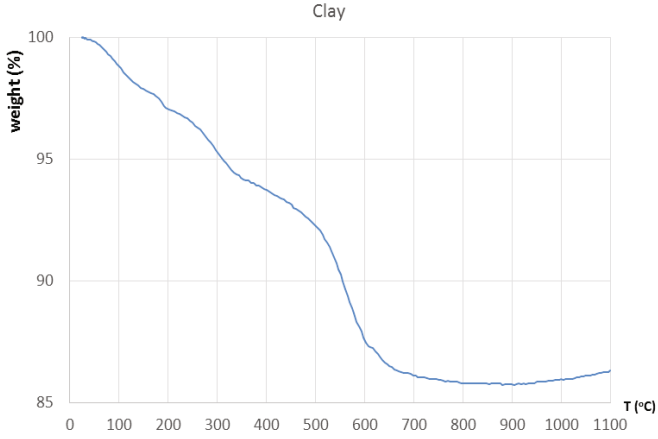

Figure 1 - TG - Clay

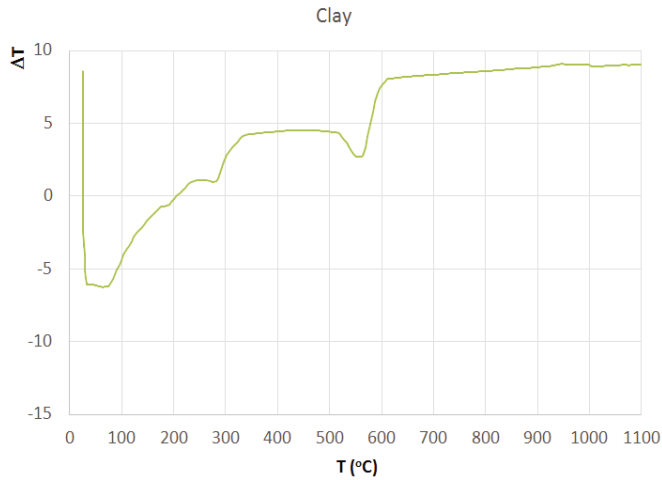

Figure 2 - DTA – Clay

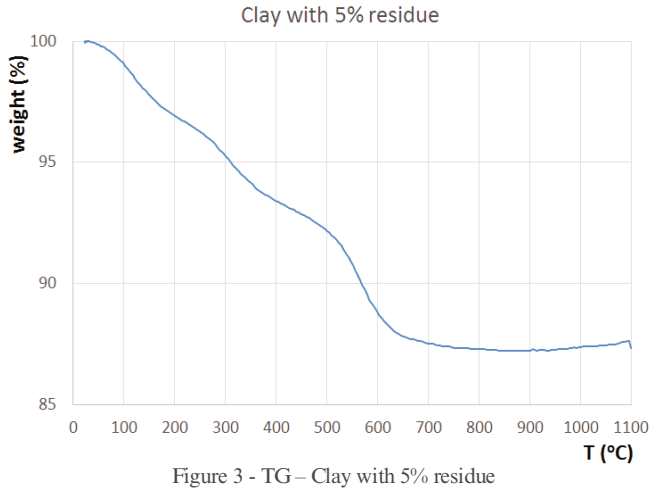

Figure 3 - TG – Clay with 5% residue

Figure 4 - DTA – Clay with 5% residue

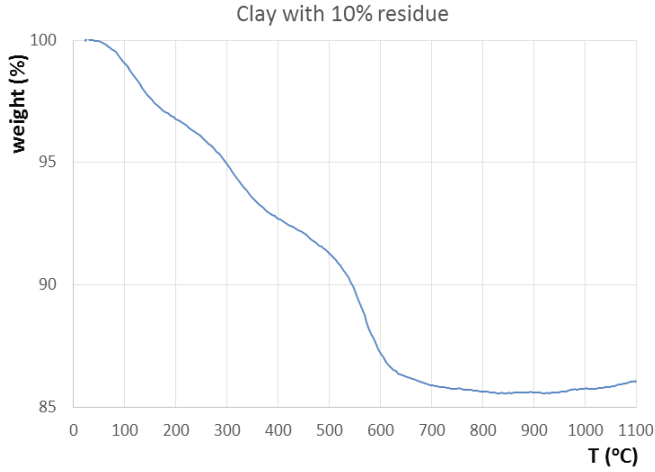

Figure 5 - TG – Clay with 10% residue

Figure 6 - ATD – Clay with 10% residue

The results of thermal analysis indicates that there is no change in the material between 800 and 900 °C, firing temperature ceramics used in polo of Campos-RJ.

Conclusion

From the results, it can be concluded that the clay exhibits good characteristics for the manufacture of ceramic articles.

The plasticity of clay and the chemical characteristics of both the clay as the granite residue indicate a strong possibility of use of the same.

The next stage of work, the pressed and burned blocks, which should be analyzed for mechanical strength will be made, water absorption, failure modes, among other features for its use as structural masonry.

Acknowledgements

The authors thank the Brazilian agencies: CAPES for the support provided to this investigation.

References

1. SÁNCHES, E. *Nova Normalização Brasileira para a Alvenaria Estrutural*. Rio de Janeiro: Interciência, 2013.
2. PEDROTI, L. G. *Compliance Study in Relation to ABNT of Ceramic blocks Pressed and Burnley*. / Dissertation in Civil Engineering - Northern State University Fluminense Darcy Ribeiro. Centre for Science and Technology. Civil Engineering Laboratory. Campos dos Goytacazes, 2007.
3. PEDROTI, L. G. *Mass development ceramics with use of granite residue to obtain ceramic blocks of pressed clay matrix fit*. Doctoral Thesis in Engineering and Materials

Science - State University of Norte Fluminense. Centre for Science and Technology. Advanced Materials Laboratory. Campos dos Goytacazes, 2011.
4. DRM – RJ. *Mineral overview of the state of Rio de Janeiro 2012*. Department of Mineral Resources of the State of Rio de Janeiro: Rio de Janeiro, 2012. 259f.
5. CASTRO, N. F.; VIDAL, F. W. H. (Org). *Proceedings of the VI Symposium of Northeast Natural Stone*. Rio de Janeiro: CETEM/MCT, 2008.
6. XAVIER, G. C. *Resistance, changeability and Parts Durability Red Ceramics Incorporated with Granite residue*. Doctoral Thesis in Civil Engineering - University of North Fluminense, UENF. Campos dos Goytacazes, 2006.
7. VIEIRA, C. M. F.; SOARES, T. M.; SÁNCHEZ. R.; MONTEIRO, S. N. (2004). *Incorporation of granite in red ceramic*. Materials Science and Engineering: A. Volume 373, Issues 1–2, 25 May 2004, Pages 115–121.
8. Brazilian Association of Technical Norms - ABNT NBR 6457: Soil samples - Preparation for compression testing and characterization tests. Rio de Janeiro Brazil, 1986.
9. Brazilian Association of Technical Norms - ABNT NBR 7181: Determination of Sieve Analysis of Soil. Rio de Janeiro, Brazil, 1984.
10. Brazilian Association of Technical Norms - ABNT NBR 7180: Soil - Determination of plastic limit. Rio de Janeiro, Brazil, 1984.
11. Brazilian Association of Technical Norms - ABNT NBR 6459: Soil - Determination of liquid limit. Rio de Janeiro, Brazil, 1984.
12. Brazilian Association of Technical Norms - ABNT NBR 6508: Soil grains passing the 4.8 mm sieve - Determination of density. Rio de Janeiro, Brazil, 1984.

Characterization of Minerals, Metals, and Materials 2016
Edited by: Shadia Jamil Ikhmayies, Bowen Li, John S. Carpenter, Jiann-Yang Hwang, Sergio Neves Monteiro, Jian Li, Donato Firrao, Mingming Zhang, Zhiwei Peng, Juan P. Escobedo-Diaz, and Chenguang Bai
TMS (The Minerals, Metals & Materials Society), 2016

PROPERTIES OF MORTARS WITH PARTIAL AND TOTAL REPLACEMENT OF CONVENTIONAL AGGREGATE BY WASTE CONSTRUCTION

Cerqueira, N. A.[1]; Choe, D.[1], Alexandre, J.[1]; Azevedo, A.R.G.[1]; Xavier, C.G.[1], Souza, V. B.[2]

[1]UENF - State University of the Northern Rio de Janeiro, LECIV – Civil Engineering Laboratory; Av. Alberto Lamego, 2000, Campos dos Goytacazes, Rio de Janeiro, 28013-602, Brazil

[2]UFF – Federal Fluminense University – Mechanical Engineering Laboratory; Rua Passo da Pátria, 156 - Sala 213 Bloco E, Niterói, Rio de Janeiro, 24210-240, Brazil.

Keywords: Mortar, waste construction, civil construction.

Abstract

Environmental problems related to waste construction (RCC) permeate from the extraction of raw materials to its final disposal. The use of RCC in masses ceramics, concrete and mortar has been appointed as an important contribution. This work you assess the physical and mechanical properties of mortars with partial replacements (25% and 50%) of conventional aggregate for construction waste (RCC) come from a building of reinforced concrete structure and walls ceramic blocks. The mortars were tested to study their behavior fresh (consistency index and entrained air content) and solid (tensile strength in bending, compression strength and water absorption). The results approve of the use of the RCC, being limited to the grinding capacity of the same to a particle size that is interesting to the substitution of natural aggregates.

1 - Introduction

The construction industry is one of the oldest activities which are known, generating as a byproduct lot of debris, called Waste Construction (RCC). The first significant application of RCC was only registered after the second world war, the reconstruction of European cities, which had their buildings completely demolished and the rubble or the resulting rubble were crushed for aggregate production order to meet demands at the time. Thus, it can be said that from 1946 was started the development of RCC recycling technology. Several waste from works in the stages of construction, renovation or demolition can be recycled, providing materials for new structures with quality equal or superior to those of primary sources [1]

The reuse appears to be still widespread because of misinformation about the process of recycling and environmental damage caused by the traditional method, the lack of effective collection measures, sorting and recycling of its end [2]. This research deals with the manufacturing and testing of mortar properties with the incorporation of construction waste (RCC) come from cities in the North and Northwest Fluminense regions. The emphasis in this project is to characterize the fresh and hardened mortar produced with RCC reuse of sand replacement.

The objective of this study is to characterize the physical and mechanical properties of mortars with partial replacements (25% and 50%) of conventional aggregate for construction waste (RCC). The mortars were tested to study their behavior in the fresh state (consistency index and entrained air content) and hardened (tensile strength in bending, compression strength and water absorption).

2 - Materials and Methods

The sample of the RCC was ground in ball mill to search a finer grain size. The same was physically characterized Laboratory. The tests were performed according to the willing in the technical standards of the NBR 7181:1984 [3] (grain size), NBR 7180:1984 [4] and NBR 6459:1984 [5] (Atterberg limits), NBR 6508:1984 [6] and NBR 6457:1986 [7] (density).

After characterizing, some tests were made with the mortars without (reference) and RCC. The line was set at 1:2:8 (cement: quicklime:sand/RCC) , and the mortars produced according to NBR 13276:2005 [8]

The incorporation of the RCC was given to replace sand in different proportions, as follows below: 0R - Reference (with 0% addition of waste and sand 100% proportion); 25R (with addition of 25% waste and 75 % sand ratio); 50R and (with addition of 50% waste and 50 % sand ratio).

The consistency tests were performed on mortar in the fresh state according to NBR 13276:2005 [8] , which recommends the consistency index (260 ± 5) mm and the calculation of entrained air content followed the NBR 13278:2005 [9] .

For the tests were made in hardened specimens of 4 cm x 4 cm x 16 cm, according to the NBR 13279:2005 [10] . The molds were placed on a level with controlled temperature to cure the air. The samples was taken in minimum time of 72 hours after being molded.

Tensile strength tests in bending and axial compressive strength were performed according to NBR 13279:2005 [10]. Nevertheless, the test for determining the capillarity coefficient was performed according to NBR 15259:2005 [10].

3 - Results and Discussion

3.1 - Particle size

The particle size analysis allows particles to be certain that the size of the sample. The particle size distribution was studied using sieve analysis and sedimentation assay. Figure 1 shows the curves of granulometric size distribution of the dried particles by sieving.

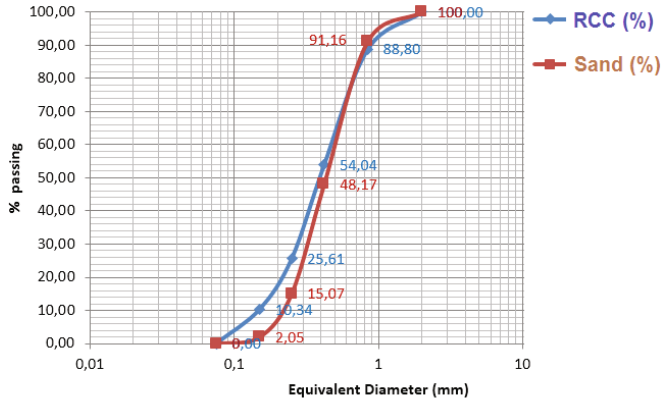

Figure 1 - Particle size distribution curve of the RCC

As can be seen, the particle size of the sand used in the tests and triturated RCC are very similar, and the real density of the grains obtained for the RCC of 2.59 g/cm³ and sand of 2.60 g/cm³.

3.2 - Consistency

Table 1 shows the amount of water used and the consistency index of the reference mortar and replacing 25 and 50 % of the sand for construction waste.

Table 1 - Consistency index, water content and binder

% Replacement for RCC	Consistency index (mm)	Water Content (g)	Relationship water/binder
0%	260	238	0,79
25%	263	290	1,11
50%	265	334	1,31

The values found consistency index were obtained from the mean of the measurements of orthogonal diameters in the consistency table in each trait studied. To achieve these values , various attempts have been made so that the consistency was determined as corresponding to a diameter of 260 mm ± 5 mm (between 255 mm and 265 mm). This value was defined in order to practice using the mortar, depending on their applicability.

It can be seen that the amount of water in traces, as well as the water / binder increased the extent of increasing the incorporation workability and to maintain a consistency that allows its application.

3.3 - Content of Corporate Air

Figure 2 shows the results of the air content embedded in all studied mortars.

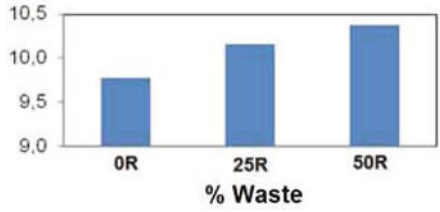

Figure 2 - Air content of the various incorporated features.

The mortar produced with hydrated lime and no residue introduced air content lower embedded the residue with produced mortars in all analyzed proportions in accordance with Figure 2, however, are all within the reference standards used within the limits proposed by the Association Brazilian Portland Cement [11], which is 8 % to 17 %.

3.4 - Traction in flexion

The tests to determine the tensile strength in bending were conducted on prismatic specimens with dimensions 16cm x 4cm x 4cm, at ages 7, 14 and 28 days.

The results were obtained by averaging efforts into three test samples for each residue percentage and time tested.

Table 2 shows the results of tensile strengths obtained in flexion.

Table 2 - Tensile strength (bending)

% Waste	Age	Compression strength (MPa)
0	7	0,66
	14	0,83
	28	1,02
25	7	0,69
	14	0,85
	28	1,04
50	7	0,71
	14	0,88
	28	1,10

According to Table 2, it can be said that there is a small gain strength with the incorporation of residue (RCC) to replace the sand, which enables the use of the same.

3.5 - Coefficient of capillarity

Figure 3 shows the results for the different levels of incorporation of the capillary coefficient.

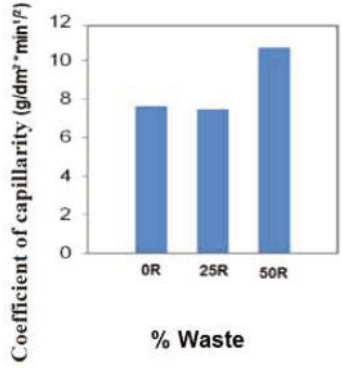

Figure 3 - Coefficient of capillarity of mortars.

Figure 3 shows the coefficient of capillary 25R mortar had the lowest value, this indicates that there was a better packing of sand particles at this residue by substitution when compared with other mortar.

3.6 - Resistance to Axial Compression

The test to determine the compressive strength was carried out with the parts generated in the bending tests, forming cubes with dimensions 4,0 cm x 4,0 cm x 4,0 cm, being evaluated at the ages of 7, 14 and 28 days.

In Figure 4 presents the values compared to each test age.

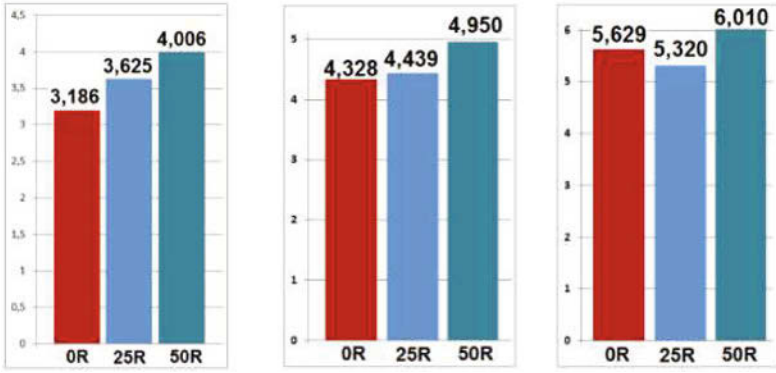

7 days 14 days 28 days

Figure 4 - Compressive Strength (MPa)

Again, there is a small gain strength with the incorporation of residue (RCC) to replace the sand.

4 - Conclusion

From the results, it can be concluded that:

- Addition of waste by replacing 50% of the amount of sand produced a higher water consumption (due to residual component fineness);
- For future work is feasible using mortar characterization of different doses and testing purposes as absorbing water, voids , water retention and air content embedded;
- The mortar 0R showed less entrained air content than the waste produced with mortars in all analyzed proportions, however, observe the order of magnitude of values, 25R and 50R mortar can also be used;
- With respect to mechanical strength (bending and compression), a small gain value but it does not imply that statistical gain can be used either traits.

Acknowledgements

The authors thank the Brazilian agencies: CAPES and FAPERJ for the support provided to this investigation.

References

1- CARNEIRO, A. P.; BRUM, I. A. S.; COSTA, D. B.; ALBERTE, E. P. V.; SAMPAIO, T. S. *Reciclagem de entulho da região metropolitana de Salvador para a produção de materiais de construção de baixo custo*. In IX Simpósio Luso-Brasileiro de Engenharia Sanitária e Ambiental. Porto Seguro, 2000.

2- PINTO, T. P. 2001. *Gestão de resíduos de demolição e construção em áreas urbanas – da ineficácia a um modelo de gestão sustentável*. In Cassa, J.V.S.; Carneiro, A.P.; Brum, I.A.S.(Orgs). Reciclagem de entulhos para a produção de materiais para construção. EDUFBA/ Caixa Econômica Federal, Salvador, BA. 2001. pp.77-113.

3- Brazilian Association of Technical Norms - ABNT NBR 7181: Determination of Sieve Analysis of Soil. Rio de Janeiro, Brazil, 1984.

4- Brazilian Association of Technical Norms - ABNT NBR 7180: Soil - Determination of plastic limit. Rio de Janeiro, Brazil, 1984.

5- Brazilian Association of Technical Norms - ABNT NBR 6459: Soil - Determination of liquid limit. Rio de Janeiro, Brazil, 1984.

6- Brazilian Association of Technical Norms - ABNT NBR 6508: Soil grains passing the 4.8 mm sieve - Determination of density. Rio de Janeiro, Brazil, 1984.

7- Brazilian Association of Technical Norms - ABNT NBR 6457: Soil samples - Preparation for compression testing and characterization tests. Rio de Janeiro Brazil, 1986.

8- Brazilian Association of Technical Norms - ABNT NBR 13276: Mortars applied on walls and ceilings - Preparation of mortar for unit masonry and rendering with standard consistence index (in Portuguese), Rio de Janeiro, Brazil, 2005.

9- Brazilian Association of Technical Norms - ABNT NBR 13278. Mortars for laying and coating walls and ceilings - Determination of bulk density and entrained air content. Rio de Janeiro, Brazil, 2005.

10- Brazilian Association of Technical Norms - ABNT NBR 13279. Mortars applied on walls and ceilings - Determination of the flexural and the compressive strength in the hardened stage (in Portuguese), Rio de Janeiro, Brazil, 2005.

11- Brazilian Portland Cement Association (ABCP). Available in http://www.abcp.org.br.

Characterization of Minerals, Metals, and Materials 2016
Edited by: Shadia Jamil Ikhmayies, Bowen Li, John S. Carpenter, Jiann-Yang Hwang, Sergio Neves Monteiro, Jian Li, Donato Firrao, Mingming Zhang, Zhiwei Peng, Juan P. Escobedo-Diaz, and Chenguang Bai
TMS (The Minerals, Metals & Materials Society), 2016

EFFECTS OF GRAPHENE OXIDE ADDITION ON MECHANICAL AND THERMAL PROPERTIES OF EVOH FILMS

Jesús González-Ruiz[1,2], Lourdes Yataco-Lazaro[3], Sueli Virginio[4], Maria das Graças da Silva-Valenzuela[5,6], Esperidiana Moura[4], Francisco Valenzuela-Díaz[5]

[1]Biomaterials Center, University of Havana, Av. Universidad / G y Ronda, PA 10400, Havana, Cuba
[2]High Polytechnic Institute "José Antonio Echeverría", Street 114 / 119 and 127, PA 10800, Havana, Cuba
[3] University of São Paulo, Faculty of Pharmaceutical Sciences, Av. Professor Lineu Prestes, 580, São Paulo, PA 05508-000 – Brazil
[4]Nuclear and Energy Research Institute – IPEN-CNEN/SP Av. Prof. L. Prestes, 2242 São Paulo, PA 05508-000, Brazil
[5]Metallurgical and Materials Engineering Department, Polytechnic School, University of São Paulo, Av. Prof. Mello de Moraes, 2463, São Paulo, PA 05508-030, Brazil
[6]Federal University of ABC, Santo André, São Paulo, PA 09210-580, Brazil

Keywords: Composites, ethylene vinyl alcohol, graphene oxide, flexible films, mechanical properties, thermal properties

Abstract

Currently, ethylene vinyl alcohol (EVOH) is one of the oxygen barrier materials most used for food packaging. The addition of graphene oxide nanosheets to the EVOH matrix is employed to improve their mechanical and barrier properties. In this work, films of EVOH-based composites reinforced with graphene oxide were prepared by melt extrusion, using a twin screw extruder machine and blown extrusion process. The graphene oxide was prepared via chemical oxidation of natural graphite and then was exfoliated into nanosheets using the sonochemical method. The composite films samples were characterized using FTIR and DSC analysis. In addition, their mechanical properties were also determined.

Introduction

In recent years there has been increased interest in improving food packaging. For this have been used new polymeric materials and polymer matrix composites, because they can increase its shelf life. Among the polymers used for this purpose is the Ethylene-Vinyl-Alcohol (thermoplastic polymer) [1-3]. Ethylene vinyl alcohol (EVOH) are copolymers of ethylene and vinyl alcohol that are widely used in the food packaging industry due to their high transparency, excellent chemical resistance, as well as very good gas barrier properties to oxygen, organic solvents, and food aromas [2].

Currently, the graphene-based nanocomposites are under intense research because they allow significantly improvement of the properties of the composites [1, 2]. The polymer composites with graphene or graphene oxide (GO) as filler, have shown improvements in properties such as elasticity modulus, tensile strength, electric conductivity, and thermal stability [1, 3-6]. Moreover,

these improvements are often observed using low filler contents, behavior related to the surface area of these materials [4, 7]. For example, it is reported that with a 0.7 wt. % graphene oxide loading on a PVA nanocomposite, were observed a 76% increase in tensile strength and 62% increase in Young's modulus [8]. Furthermore, nanocomposites of graphene oxide (0.9 wt. %) in a PS matrix showed significant improvements in the mechanical properties (57% increase in elastic modulus and 70% in strength) [9]. Also, recent work has shown that the use of nanocomposites of graphene or graphene oxide with EVOH polymeric matrix can improve the mechanical properties and oxygen permeability of EVOH films [6, 10-12]. However, to achieve significant improvements in the properties of nanocomposites, the graphene oxide should be exfoliated and well dispersed in the polymer matrix [13].

Chemical oxidation of graphite is the most used method for the preparation of graphene [14]. The graphene oxide (GO) is obtained employing concentrated acids (sulfuric acid, nitric acid, and phosphoric acid) and highly oxidizing agents (potassium permanganate or potassium perchlorate) [14, 15]. This method was developed by Hummers et al. [16] and was modified by different researchers to improve their efficiency. The GO syntheses using an improved variant of the method of Hummer was reported by Marcano et al. [17]. The advantages of this variant are the employ of a relatively simple protocol, with temperature controlled at 50 °C and no toxic gas evolution during the preparation, this make it attractive for preparing GO on a large scale. However, the method has the disadvantage that the conversion rate of graphite to GO is not 100%.

Recently, Huang et al. reported a new variant that simplify the process of synthesis of GO [14, 18]. This method has the advantages of obtaining a nearly 100% conversion of graphite to GO and further enables obtaining GO nanosheets. However, for use in composite materials, it has the disadvantage that the nanosheets have micron-scale dimensions. On the other hand, exfoliation of graphene oxide (GO) can be performed by stirring and most commonly by sonication in solvents [14, 19, 20].

In this work, GO was prepared via a simplified Hummer's method. In addition, the obtained particles were used in the manufacture of EVOH/GO composite flexible films.

Materials and methods

Materials

Graphite flakes from Quimesp Química Ltda (Sao Paulo, Brazil) were used. Sulfuric acid (H_2SO_4, 98%), phosphoric acid (H_3PO_4, 85%), potassium permanganate ($KMnO_4$, 99.9%), Hydrogen chloride (HCl, 37%) and hydrogen peroxide (H_2O_2, 30%), were purchased from Casa Americana de Artigos para Laboratórios Ltda (São Paulo, Brazil). The polymeric material used in this study was the Ethylene vinyl alcohol copolymer (EVOH) with 32% mol/ethylene (EVAL™ manufactured by Kuraray Co. Ltd.).

Preparation of GO particles

GO was obtained from purified conventional flake graphite employing the method used by Huang et al. (simplified Hummer's method) [14]. Synthesis of GO was carried out by mixing

H_2SO_4:H_3PO_4 (320:80 mL), graphite flakes and $KMnO_4$ (18 g) in a magnetic stirrer. All reagents were added slowly and then stirred for 3 days to allow the oxidation of graphite. After this process, the synthesis product was poured into a H_2O_2 solution (400 ml of distilled water and 20 ml of H_2O_2). The graphite oxide obtained was washed with a 1 M HCl aqueous solution and repeatedly with deionized water until a pH of 4–5 was achieved. The decantation of supernatant was realized via a centrifugation technique at 3900 rpm for 5 – 10 min. Then the GO (in water solution) was strongly sonicated at room temperature for 10 minutes (using a power of 450 W) and centrifuged at 3900 rpm for 5 minutes. The GO gel was dried at 90 ºC for 24 h in air atmosphere. Finally, the product was grind and sieved using a sieve with a 90 μm mesh size.

Preparation of EVOH/GO composite films

The EVOH/GO composites were prepared by melting extrusion process, using a twin-screw extruder Haake Rheomex P332 operating in the L/D 3:1.33 rate. The extrudates coming out of the extruder were cooled down for a better dimensional stability, pelletized by a pelletizer, dried again and fed into blow extrusion to obtain the film samples. The temperature profile used in the blow extrusion process of the EVOH films was 190/ 195/ 197/197/ 205/ 205 ºC and the screw speed was 30 rpm. The manufacture of EVOH/GO films (0.1% wt. of GO) was done using in the blow extrusion process a temperature profile of 182/ 192/ 197/197/ 205/ 205 ºC and a screw speed of 30 rpm; while, was used in the blow extrusion of EVOH/GO films (0.5% wt. of GO) a temperature profile of 177/ 179/ 184/184/ 187/ 187 ºC and a screw speed of 40 rpm.

Characterization methods

Fourier Transform Infrared Spectroscopy (FTIR): The functional groups were characterized for the as prepared GO powders and EVOH/GO films by a FTIR spectrometer, IR Prestige-21 (Shimadzu corporation, Japan).

Differential Scanning Calorimetry (DSC): Thermal characteristics such as the Tg and Tc of the composites were determined using differential scanning calorimetry (DSC). Analyses were carried out using a DSC 822e (Mettler Toledo Inc.) from 25 to 250°C at a heating rate of 10 °C/min under nitrogen atmosphere (50 ml/min).

Mechanical Tests: Tensile tests were performed using an INSTRON Testing Machine, model 5564 (Norwood, MA) according to ASTM D 882-91), in order to evaluate the mechanical behavior of the materials studied. Each value obtained represented the average of eight samples.

Results and Discussion

Functional groups

The spectral analyses (FTIR) were performed to identify the functional groups on the surface of the graphite, GO and in the EVOH/GO composite films. In the Figure 1A are shown the characteristic bands of the graphite. The spectra of GO (Figure 1B), show a broad peak between 2500–3600 cm^{-1} and two sharp peaks at 1726 and 1052 cm^{-1} , indicating the presence of hydroxyl (–OH), carboxyl (–COOH), and epoxy groups (–O–), respectively [6]. Also, the spectra of the GO

(Figure 1B) show new bands (at 529, 622, 999 cm^{-1}), demonstrating the modification of graphite to GO. Additionally, the greatest relative intensity is observed in the band corresponding to 999 cm^{-1}, which also confirms the formation of graphene oxide.

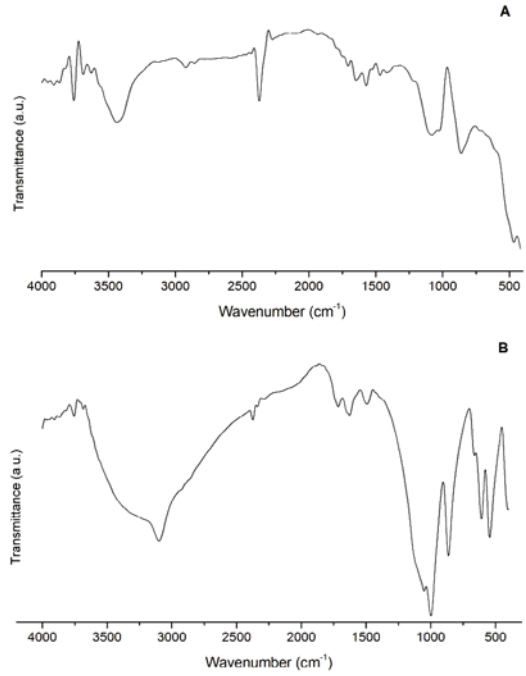

Figure 1. FTIR spectra of (A) graphite and (B) GO.

In the FTIR spectra of EVOH/GO composite films were not observed variations in comparison with spectra of EVOH films. These results are similar to the reported by Kim et al. in EVOH/EFG nanocomposite films [2]. On the other hand, this behavior can be related to the GO low content in the studied composites.

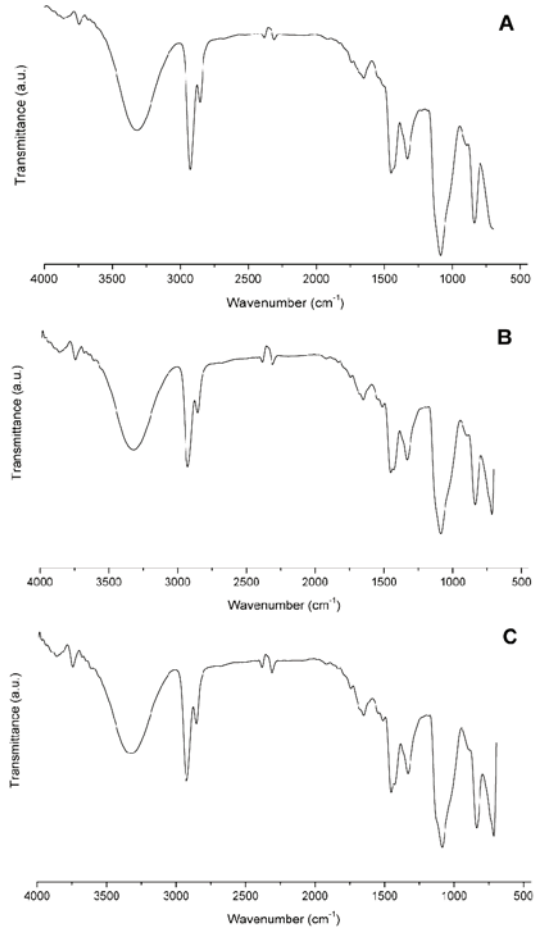

Figure 2. FTIR spectra of EVOH/GO composite films. A- EVOH film, B – EVOH/GO film (0.1 wt. % GO), C - EVOH/GO film (0.5 wt. % GO).

Thermal stability

In some industrial processes such as food packaging, it is required polymeric materials with thermal stability due to the heat treatments they are subjected to, such as pasteurization and sterilization [2]. In this work, the effect GO contents on the thermal stability of EVOH/GO composite films, was studied by DSC analysis. Figure 3 shows that the composite films have the same pattern that pure EVOH films; the GO addition did not change the Tg and Tm of the

composite films. Tg and Tm are strongly dependent on the polymer chains mobility and of the filler which can increase the Tg and Tm of polymeric films. However, also this behavior should be related to the low content of GO in the composite films.

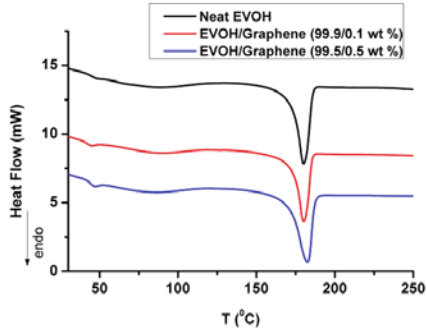

Figure 3. DSC thermograms of EVOH films and EVOH/GO composite films.

Mechanical properties

In order to evaluate the effect on the mechanical properties of the incorporation of graphene oxide particles in EVOH films, tensile tests were performed. The mechanical tests of pure EVOH and EVOH/GO composite flexible films were carried out in the longitudinal direction. Pure EVOH presented a tensile strength of 6,0 MPa. Figure 4 shows the tensile stress–strain curves of the EVOH/GO composite films, with a mean tensile strength of 36 MPa. The incorporation of only 0.1 wt. % of GO particles to the EVOH films caused a significant and important increase in the tensile strength. In addition, the elongation was not significantly affected after the GO incorporation. Such behavior may be due to the easily deformable nature of graphene oxide itself, relative to other fillers such as nanoclays.

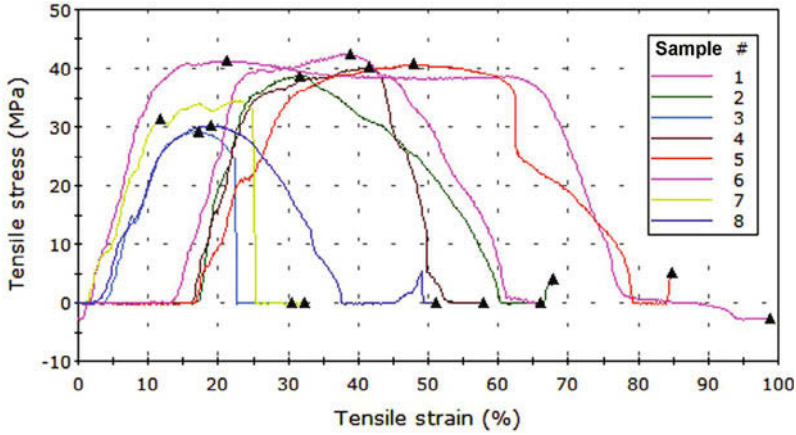

Figure 4. Tensile stress–strain curves of the EVOH/GO (0.1 wt. % GO) composite films.

Conclusions

We successfully prepared GO particles using a simplified Hummer's method. The new bands in the FTIR spectra, demonstrate the modification of graphite to GO during the chemical synthesis. In addition, we obtained EVOH/GO composite films. These films showed a significant and important improvement in their tension strength without affecting their elongation and thermal stability.

Acknowledgments

This work was supported by the project CAPES/MES Cuba № 041/2011. The authors thank the Nuclear and Energy Research Institute (Brazil) for their assistance in conducting some of the tests.

References

1. S.W. Kim and H.M. Choi, "Enhancement of thermal, mechanical, and barrier properties of ethylene vinyl alcohol copolymer by incorporation of graphene nanosheets: effect of functionalization of graphene oxide," *High Performance Polymers*, 27 (6) (2014), 694-704.
2. D. Kim, H. Kwon and J. Seo, "EVOH nanocomposite films with enhanced barrier properties under high humidity conditions," *Polymer Composites*, 35 (4) (2014), 644-654.
3. H.M. Kim and H.S. Lee, "Water and oxygen permeation through transparent ethylene vinyl alcohol/(graphene oxide) membranes," *Carbon Letters*, 15 (1) (2014), 50-56.
4. T.K. Das and S. Prusty, "Graphene-based polymer composites and their applications," *Polymer-Plastics Technology and Engineering*, 52 (4) (2013), 319-331.
5. J.R. Potts et al., "Graphene-based polymer nanocomposites," Polymer, 52 (1) (2011), 5-25.
6. W. Alkarmo et al., "Preparation of graphene oxide-poly (methyl methacrylate) nanocomposites by a precipitation polymerization process and their dielectric and rheological characterization"

(Paper presented at the Belgian Polymer Group (BPG) Annual Meeting, Houffalize, Belgium, 18 May 2015).
7. O.M. Istrate and J.N. Coleman, "Reinforcement in melt-processed polymer–graphene composites at extremely low graphene loading level," *Carbon*, 78 (2014), 243-249.
8. D.E. Kranbuehl and H.C. Schniepp, "Polyamide composites containing graphene oxide sheets," US Patent 20150114472, 2014.
9. T. Ramanathan et al., "Functionalized graphene sheets for polymer nanocomposites," *Nature nanotechnology*, 3 (6) (2008), 327-331.
10. J. Liang et al., "Molecular-level dispersion of graphene into poly (vinyl alcohol) and effective reinforcement of their nanocomposites," *Advanced Functional Materials*, 19 (14) (2009), 2297-2302.
11. B.Z. Jang, A. Zhamu, "Processing of nanographene platelets (NGPs) and NGP nanocomposites: a review," Journal of Materials Science, 43 (15) (2008), 5092-50101.
12. J. Yang et al., "Thermal reduced graphene based poly (ethylene vinyl alcohol) nanocomposites: enhanced mechanical properties, gas barrier, water resistance, and thermal stability," *Industrial & Engineering Chemistry Research*, 52 (47) (2013), 16745-16754.
13. E.T. Thostenson, C. Li and T.W Chou, "Nanocomposites in context," *Composites Science and Technology*, 65 (3) (2005), 491-516.
14. N. Huang et al., "Simple room-temperature preparation of high-yield large-area graphene oxide," *International Journal of Nanomedicine*, 6 (2011) 3443-3448.
15. Y. Zhu et al., "Graphene and graphene oxide: synthesis, properties and applications," *Advanced Materials*, 22 (35) (2010), 3906-3924.
16. J.W.S. Hummers, "Preparation of graphitic acid," US Patent 2798878, 1957.
17. D.C. Marcano et al., "Improved synthesis of graphene oxide," *ACS Nano*, 4 (8) (2010), 4806-4814.
18. X. Huang et al., "Graphene-based composites," *Chemical Society Reviews*, 41 (2) (2012), 666-686.
19. K. Krishnamoorthy, G.S Kim, S.J Kim, "Graphene nanosheets: Ultrasound assisted synthesis and characterization," *Ultrasonics Sonochemistry*, 20 (2) (2013), 644-649.
20. X. Qi et al., "Size-specified graphene oxide sheets: ultrasonication assisted preparation and characterization," *Journal of Materials Science*, 49 (4) (2014), 1785-1793.

Characterization of Minerals, Metals, and Materials 2016
Edited by: Shadia Jamil Ikhmayies, Bowen Li, John S. Carpenter, Jiann-Yang Hwang, Sergio Neves Monteiro, Jian Li, Donato Firrao, Mingming Zhang, Zhiwei Peng, Juan P. Escobedo-Diaz, and Chenguang Bai
TMS (The Minerals, Metals & Materials Society), 2016

EVALUATION OF PHYSICO-CHEMICAL PROPERTIES WHEN ADDING BOILER ASHES TO MORTAR

M.A. Caetano[1]; R.O.G. Martins[1]; G.E.S. de Lima[1]; A. I. Araújo[1]; L.G. Pedroti[1]; A.A.P. Rezende[1]; R.C.S.S. Alvarenga[1]

[1]UFV – Federal University of Viçosa, DEC – Civil Engineering Department; Av. PH Rolfs, Viçosa, Minas Gerais, 36570-900, Brazil.

Keywords: mortar, residue, composite material.

Abstract

Over the past few years, environmental concern is on focus, it is the case of the continuous reuse of residues from several areas. This work aimed to reuse ashes from a boiler, which temperature reaches 600ºC, from a textile factory fueled by wood splinter. It is notorious the amount of generated residue, around 15 tons a month. The material was chemically analyzed with high contents of CaO, this element is ordinarily found in the main binders used in this research. In order to reuse the residue in the mortar mix, several experiments were made, such as SEM, EDX, XRD, pozzolan content, bending and compression trials, adherence and consistency, to characterize the material. The samples analyzed showed progress regarding resistance characteristics, revealing that the residue can be a viable alternative when it comes to contributing to the reduction of Environmental Issues in textile industries.

Introduction

In most industrial processes, there is generation of residue, which has brought concern to businessman from several sectors. In the past few years, environmental concern is in focus, because the residue generated from factories are hard to dispose and can bring several environmental issues.

The ashes are a sub product of the combustion of wood splinter in a boiler from several fabric factories. This residue becomes an issue for the generating companies concerning the final disposal in the industrial process.

Incorporating this residue to mortar, the objectives would be to reduce the cost and, mainly, the decrease or even the extinction of environmental impacts caused by the elimination of these ashes.

According to Petrucci (1980), mortar is composed of a mixture of one or more binders, small aggregate and water. Besides these components, special products and aggregates can be added. In this study ashes were added in different proportions seeking the improvement of mortar properties in comparison with the proportion 1:3:12 (cement: lime: sand) of a brick settlement mortar, dosed by volume.

These ashes are generated during the process of making and colouring fabric, which heats up to 600º C. In a medium size factory, this process generates around 15 tons of ashes monthly, which is a relevant amount for the study and application of the residue as an aggregate. This residue is basic composed of calcium carbonate, which helps the physical properties of the mixture.

Ashes have little or none commercial value so producing mortar using this material improves material savings, besides it reduces storage of this material (Siqueira *et.al.,* 2012)

Alternative materials, just like the ashes, when used in construction show ecological advantages and can diminish the cost in construction processes. However for the reuse of this residue become feasible, there must be attention to the facts like the cost of transportation of this product, the volume of residue generated and the amount of residue needed to the mortar making process and the possible stocking of the product (PEDROTI *et al.,* 2015).

Several studies analysed are showing success in the reuse of inorganic residues for mortar production, evidencing it is suitability as an alternative material in civil construction. Therefore, this article objective is to study the suitability of ashes use in mortar production.

Materials and Methods

In order to characterize the residue used in this research, initially were collected samples in the generating plant and after taken to the Construction Materials Lab in the Universidade Federal de Viçosa. Several tests were conducted with the intention to characterize the material and determine its best application way in mortar, among them: SEM, EDX, XRD (Figure 1), pozzolan content, bending and compression trials and consistency.

Figure 1. Ashes sample and tablet used in the XDR test.

The proportion by volume used was determined by 1:3:12 (cement: lime: sand), due to its use in brick settlement. The trails conducted to determine the consistency index were conducted for each of the research proportions to assure the desired consistency according to the ABNT NBR 13276/2005 of 260 ±5mm. For comparison effects, a reference mortar was made, without any ashes added, which would be compared to others mortars with ashes content.

The residue was strained through 200 mesh and then added to the mixture. This addition was calculated in weight proportion to the used aggregate, sand. Table I shows the percentages of ashes added to the research proportions.

Table I. Experimental Mortar Dosage (by volume)

Proportion	Cement	Lime	Sand	Ashes
T00	1	3	12	0%
T05	1	3	12	05% sand weight
T10	1	3	12	10% sand weight
T15	1	3	12	15% sand weight

After being prepared, the mixtures were moulded in prismatic cast of 40x40x160mm for confection of specimens according to the ABNT NBR 13279/2005. For each proportion were casted nine specimens, to be tested 3 for each age (3, 7 and 28 days old).

Tests were conducted to determine pozzolan content through Luxan Method, residue's EDX and XRF, MEV of the specimen fractured surfaces (at 28 days old) and the studied residue, besides bending and compression trials (Figure 2).

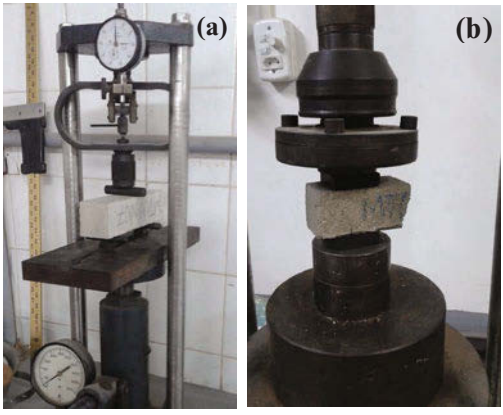

Figure 2. Tests with 3 days: (a) bending test; (b) compression test.

Results

The Pozzolan Content Trial was conducted through Luxan Method and the residue had no pozzolan activity.

Table II shows chemical composition of the ashes, obtained through EDX. It is noted that the material has a high content of calcium oxide, which favoured the enhancement of physical properties of the grout, increasing its consistency in 5,51% when comparing T15 with T00.

Table II. Chemical composition by XRF of the raw material given in terms of elements (%).

Composition	CaO	SiO_2	K_2O	P_2O_5	Al_2O_3	Fe_2O_3	OTHER
Percentage	52,14%	10,47%	9,92%	7,04%	5,57%	3,19%	11,67%

For a better material characterization, XRD trial was conducted, which results are in Figure 3. It was observed the presence of $CaCO_3$, $CaSO_4$ and $NaNO_3$, using crystal based structure ICSD – Inorganic Crystal Structure Database (2015).

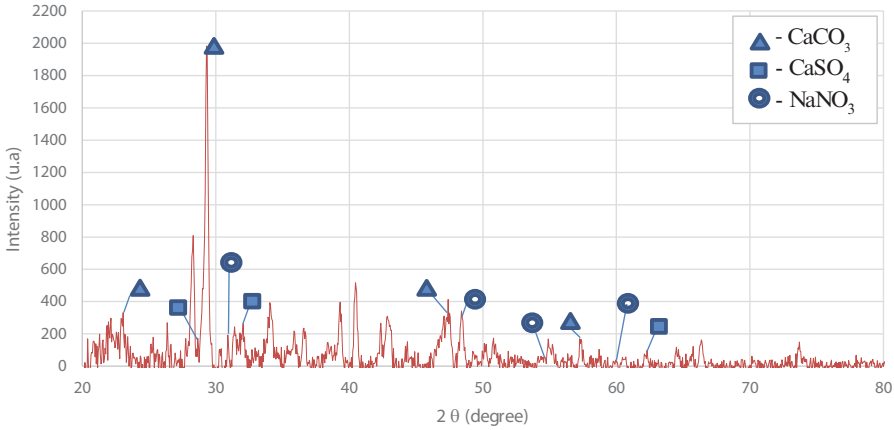

Figure 3. Ash residue DRX trial.

The crystallographic characterization of the residue was made through SEM trial (Figure 4). The ashes have some particles with spherical shape and homogeneous distribution, that can explain the plasticity improvement observed in the mortar when increasing ashes content.

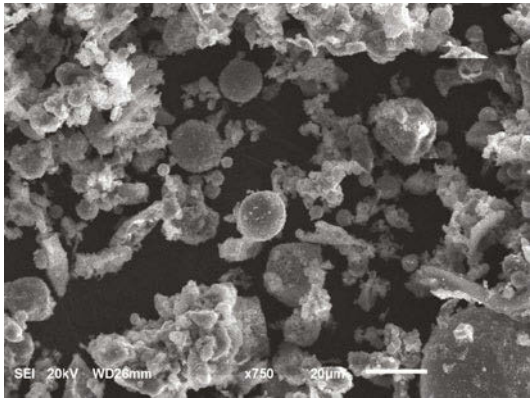

Figure 4. Particle shape obtained through SEM.

In the figure below of the fractured surfaces obtained through SEM, it was verified that the addition of ashes influenced positively in the mortar microstructure, seen that porosity decreased. The figures are in decreasing order of porosity, considering that the mortar with no addition of ashes obtained the highest porosity and the one with 15% of ash addition obtained the lowest porosity.

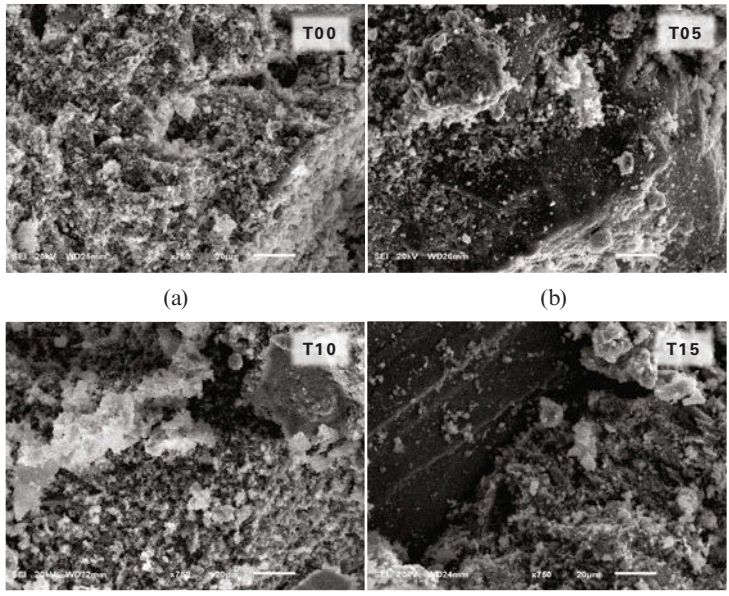

Figura 5. Ash scanning electron microscopy. (a) T00: Reference proportion; (b) T05: Proportion with 5% addition; (c) T10: Proportion with 10% addition; (d) T15: Proportion with 15% addition.

The resistance of the mortars T05, T10 and T15 was superior to reference mortar T00. The results from Graph 1 and 2 represent the trials conducted with prismatic specimens 3, 7 and 28 days old, for compression and bending resistance respectively.

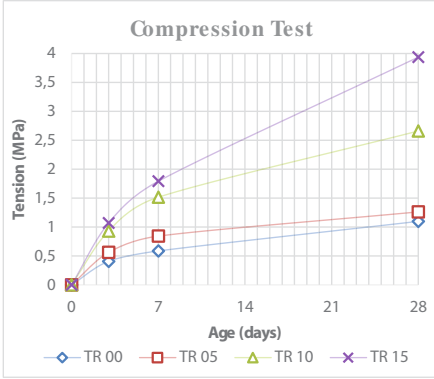

Graph 1. Compression trial results with defined 4 proportions at 3, 7 and 28 days of age.

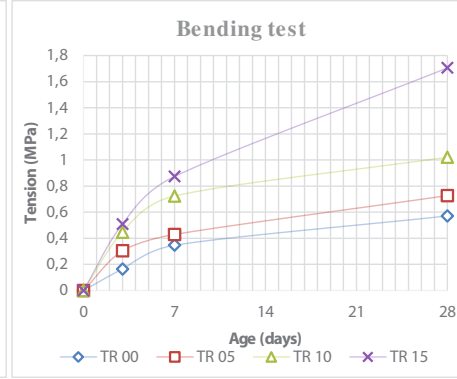

Graph 2. Bending trial results with defined 4 proportions at 3, 7 and 28 days of age.

Conclusion

The chemical and physical tests in the four proportions showed that the addition of ashes increases the values of bending and compression resistance, relating to the presence of calcium oxide in the residue that is object of this study. Bending and compression resistances since early ages showed elevated values compared to the reference proportion.

The proportion with 15% of ashes content, with 28 days of age, showed in Bending Trial a resistance of 1,7 MPa, while the reference proportion showed 0,6MPa, a increase of 198% in bending resistance. In the Compression Trials, the results were 1,1 MPa for the reference proportion and 3,9 MPa for the proportion with 15% of ashes content, at 28 days of age.

Through SEM characterization it was possible to observe that the ashes displayed good mixture dispersion, favouring the fill of the mortar pores and decreasing porosity, as showed in Figure 5. Mortar resistance increase can be related with the concentration of inactive ashes and with the homogeneous dispersion of the residue in it.

The results demonstrate high potential in using ashes in the production of Civil Construction materials, relating to its mechanical performance, which is interesting and feasible to develop mortars with industrial residues addition, proven that the material has similar chemical attributes to the materials used in cement industry. Contributing in a promising way to the environment, since today there are great difficulties faced when disposing industrial residues.

Acknowledgements

The authors thank the Brazilian agencies: CNPq, CAPES and FAPEMIG for the support provided to this investigation.

References

1. BRAZILIAN ASSOCIATION OF TECHNICAL NORMS. *NBR 13279:* Mortars applied on walls and ceilings - Determination of the flexural and the compressive strength in the hardened stage. Rio de Janeiro, 2005. 9 p.

2. BRAZILIAN ASSOCIATION OF TECHNICAL NORMS. *NBR 13276:* Mortars applied on walls and ceilings - Preparation of mortar for unit masonry and rendering with standard consistence index. Rio de Janeiro, 2005. 3 p.
3. BRAZILIAN ASSOCIATION OF TECHNICAL NORMS. *NBR 13281:* Mortars applied on walls and ceilings - Requirements. Rio de Janeiro, 2005. 7 p.
4. Eládio G. R. Petrucci, *Concreto de Cimento Portland.* (14. ed. Porto Alegre: Globo, 1980).
5. Eládio G. R. Petrucci, *Materiais de Construção.* (14. ed. Porto Alegre: Globo, 1980).
6. J. S. Siqueira; C. A. G. Souza; J. A. S. Souza. "Reuse of ash coal in the formulation of mortars" (Cerâmica, São Paulo, v. 58, p.275-279, 2012).
7. Povindar K. Metha; Paulo J. M. Monteiro. *Concreto: Estrutura, Propriedades e Materiais.* (2. ed. São Paulo: Pini, 1994).
8. ICSD FIZ KARLSRUHE (Germany). *Inorganic Crystal Structure Database.* 2015. Available in: <https://icsd.fiz-karlsruhe.de/search/basic.xhtml>. Accessed in: 02 out. 2015.

Characterization of Minerals, Metals, and Materials 2016
Edited by: Shadia Jamil Ikhmayies, Bowen Li, John S. Carpenter, Jiann-Yang Hwang, Sergio Neves Monteiro, Jian Li, Donato Firrao, Mingming Zhang, Zhiwei Peng, Juan P. Escobedo-Diaz, and Chenguang Bai
TMS (The Minerals, Metals & Materials Society), 2016

SIGNIFICANCE OF GRAPHITIC SURFACES IN AURODICYANIDE ADSORPTION BY ACTIVATED CARBON: EXPERIMENTAL AND COMPUTATIONAL APPROACH

Dhiman Bhattacharyya, Tolga Depci, Keith Prisbrey, Jan D. Miller

Department of Metallurgical Engineering, University of Utah;
135 S. 1460 E. WBB 412, Salt Lake City, UT 84112, USA

Keywords: Aurodicyanide, Activated carbon, Graphitic edge, Slit pore, Simulations

Abstract

Despite tremendous developments in industrial use of activated carbon (AC) for gold adsorption, specific aurodicyanide [$Au(CN)_2^-$] adsorption sites on the carbon have intrigued researchers. The graphitic structure of AC has been well established. Previously radiochemical and now, XPS and Raman characterizations have demonstrated higher site-specific gold adsorption on graphitic edges. Morphological characterizations have revealed the presence of slit-pores (5-10 Å). Molecular-dynamics-simulation (MDS) performed on graphitic slit-pores illustrated gold-cyanide ion-pair preferentially adsorbs on edges. Ab-initio simulations predicted lower barrier for electron sharing in pores with aurodicyanide, indicating tighter bonding than graphitic surface and was well supported by Gibbs energy calculations too. Interaction energy as function of the separation distance indicated tighter bonding of gold cyanide to the graphite edges than water molecules. Selective adsorption of aurodicyanide ion-pair seems to be related to low polarity of gold complex and its accommodation at graphitic edges.

Introduction

Activated carbon (AC) has been an indispensable component in the extractive metallurgy of gold. In the gold industry, AC is most often used to adsorb low levels of gold from alkaline cyanide solutions. The gold dissolved as an ion pair complex, is recovered from the solutions by carbon-in-pulp (CIP) or carbon-in-leach (CIL) processes. Extensive research has been carried out to understand the mechanism of gold adsorption by AC. The most accepted theories include adsorption of ion pairs $M^{n+} - \left[Au(CN)_2^-\right]$ onto active sites of AC [1]. This ion pair adsorption process is somewhat selective due to the structure of aurodicyanide anion. It is believed that adsorption of the gold cyanide anion occurs through electrostatic interaction at highly active sites of the AC that have appropriate polarity [2]. Sibrell and Miller [3] claimed the site specific adsorption as a predominant gold adsorption mechanism on graphitic carbons (including AC, carbon black and graphite). AC is characterized by their cryptocrystalline graphitic structure [4]. They have a disordered microcrystalline structure quite similar to graphite, though less ordered (Fig. 1a). Previous studies have revealed that AC comprised small regions of elementary crystallites, composed of roughly parallel layers of hexagonally ordered atoms; or disordered cross-linked, space lattice of carbon hexagons. Fig.1b shows a typical schematic representation of activated carbon comprising distorted graphitic sheets with exposed face and edge surfaces

[5]. Hence, studies have been accomplished to facilitate better understanding of gold adsorption on the graphite face and edge surface. A TEM micrograph of activated carbon has also been presented in Fig. 1c. This figure illustrates the abundant presence of typical slit-shaped micropores around a cylindrical mesopore. Further studies encompassing the discussion of gold adsorption in slit pores have also been presented in this paper.

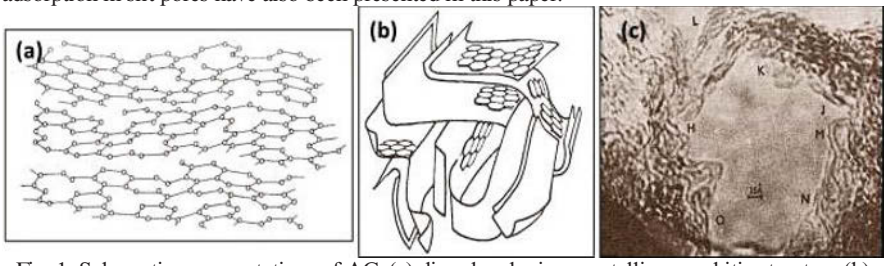

Fig. 1. Schematic representations of AC. (a) disordered microcrystalline graphitic structure (b) distorted graphitic sheets (5). (c) TEM micrograph of AC, with typical 0.5nm slit-shaped micropores (source unknown).

Having established a preface that various morphological aspects of AC (viz. face and edge surfaces, slit pores) might affect gold adsorption, this paper illustrates recent evidences of the same through experimentation and with the aid of computational chemistry tools.

Experimental

Raman and X-ray Photoelectron Spectroscopy (XPS)

Raman spectroscopy of gold loaded AC was carried out. Further, highly oriented pyrolytic graphite (HOPG) was used as a model surface for fundamental studies of gold cyanide adsorption characteristics on face and edge surfaces. HOPG is a highly anisotropic material, exhibiting different properties on its face and edge surfaces. Raman measurements were carried out using a Renishaw inVia Reflex Raman spectrometer, with 514 nm laser excitation at 50% power (approx 6 mW at sample) and X50 objective. Extended scan was carried out with 10 second peak integration time.

To further confirm the presence of gold and to determine its oxidation states, XPS (Kratos Axis Ultra DLD model) was used. A monochromatic X-ray excitation source of Al Kα radiation was used under ultra-high vacuum. CasaXPS software was used for peak fitting. Charging effects were corrected using the C1s line at 284.6 eV as an internal reference. Shirley-type background was subtracted from the spectra.

Simulations

A free molecular structure simulation program Avogadro [6] was used to build the graphite crystal and the gold cyanide anion and their geometry was optimized using universal force fields (UFF) until energy had converged. These molecules were constructed using lattice parameters obtained from the American Mineralogist Crystal Structure Database. Quantum chemistry-based ab initio simulation was performed using a Gaussian09 simulation package at

the PM6 level employing 3-21G basis sets for creating molecular orbitals for C and N, and SDD (Stuttgart/Dresden) basis sets were used for Au metal atoms. Also, the Mulliken atomic charges of each atom were obtained from ab initio simulation and used for MDS. To observe the behavior of the aurodicyanide ion at graphitic surfaces and slit pores, MOPAC was used to yield the Gibbs free energy values as a function of temperature, indicating the relative stability. A plot of the interaction energy versus distance compared the reactivity of the gold cyanide and the water molecule at the graphite surface and complemented the results from the ab-initio calculations.

A MDS program DL_POLY_214 [7] was used for the analysis of gold cyanide at graphite surfaces. In the simulations, to examine interactions of the gold cyanide complexes at graphite surfaces, simple cubic cells containing graphitic orientations (face and edge), 1000 SPC water molecules, 8 gold cyanide anions, and potassium counter ions (to maintain charge neutrality) were constructed with periodic boundary conditions. Similar simulations were also performed on face pores and edge pores with a pore width of 25 Å to ensure complete wetting of the pores. In the initial configuration, water molecules and cyanide complexes were randomly distributed in the simulation cell. The system was simulated for 2 ns, including an equilibration time of 1 ns under NPT (isothermal/isobaric) ensemble with pressure fixed at 0.1 MPa and the temperature fixed at 298 K. The Leap-frog method with a time step of 1fs was used to integrate the particle motion. The Ewald sum was used to account for the electrostatic interactions.

Results and Discussion

Researchers have previously used almost defect-free face and edge surfaces of HOPG to determine that adsorption of gold cyanide complex by graphitic carbonaceous material is much greater at the edges of the graphitic planes than on the planes themselves, through autoradiography and counting of radiolabelled samples, leading to site-specific adsorption concept [3]. Further, they believed that for the ion pair adsorption, van-der-Walls forces were involved and unsymmetrical distribution of charge at the edge defects also played an important role. To gain further insight, characterizations and simulations of gold cyanide on graphitic surfaces were carried out.

Raman Characterization

AC, as other graphitic carbons, exhibit two sharp Raman peaks, namely G (graphite) and D (disorder) bands, and they explicitly appear at about 1580 and 1360 cm^{-1} respectively [8] (Fig. 2). The G band is ascribed to the Raman-active *E2g* in-plane vibration mode, while the D band to the *A1g* mode similar to an in-plane breathing vibration type. Since gold is also Raman-active, variation in gold concentration illustrates an apparent change in Raman peak intensities of D and G bands along with drastically variation in the depth of the valley between the G and D band. For comparison, gold adsorbed on HOPG face and edge surfaces have also been characterized by Raman. For the edge surface, the spectra reveals increase in peak intensities for both G and D bands as the concentration is increased from 25 – 200 ppm. In addition, a small shoulder near 1620 cm^{-1}, labelled D' band, is also observed [8]. The relatively small variation in peak intensity of D band is due to the fact that in a large single crystal like HOPG, the *A1g* mode is Raman inactive caused by the relaxation of the symmetry rule for Raman scattering due to presence of disorder parts like grain edges. On the contrary for the face surface, as expected, results indicate

the absence of D band and negligible variation in peak height of the G band. The slight variation caused may be attributed to the steps on the face surface which present edge like sites and act as preferential gold adsorption sites. This indicates that inside AC, predominant gold adsorption is taking place on the graphitic edge surfaces.

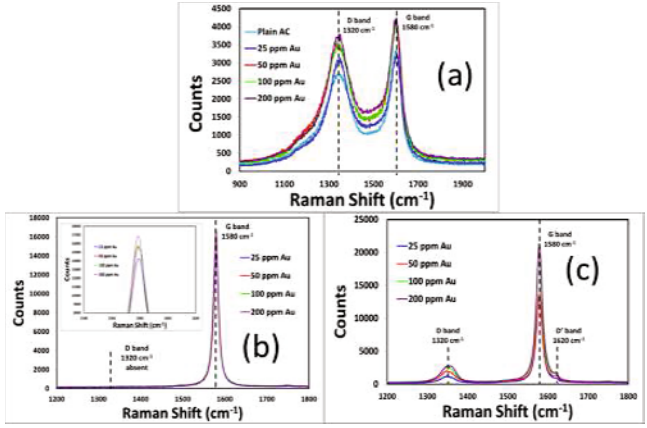

Fig. 2. Raman spectra of (a) plain and Au loaded AC, (b) Au loaded HOPG face surface, and (c) Au loaded HOPG edge surface.

XPS Characterization

XPS has enabled us to throw some more light on the aurodicyanide adsorption mechanism by studying the $Au4f_{7/2}$ and $Au4f_{5/2}$ spectra for gold adsorbed on the HOPG face and edge surface. The Au-4f binding energy for the edge surface of HOPG samples was resolved into several peaks corresponding to Au 4f7/2 (84.15 eV) and 4f5/2 (87.91 eV) (Fig. 3). At the edge sites, the binding energy of Au 4f is found to be shifted towards higher values compared to pure gold ($4f_{7/2}$ ~84.00 eV and $4f_{5/2}$ ~87.71 eV). This shift is due to the Au(+1) oxidation state and is indicative of the $Au(CN)_2^-$ ion. The HOPG face surface does not exhibit appreciable intensity of either Au4f peaks. These results provide further confirmation of the greater adsorption density of gold at the HOPG edge planes than on the basal planes. The spectrum is presented in Fig. 3 for HOPG samples contacted with 200 ppm alkaline gold cyanide solution. The HOPG edge sample clearly shows the presence of gold, by the Au 4f doublet which is caused by spin- orbit coupling arising out of two possible spin states of electrons in p, d and f orbitals [3].

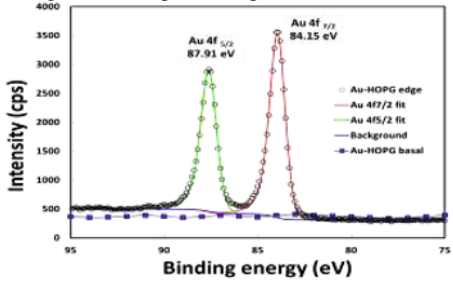

Fig. 3. Au4f XPS spectra for HOPG face and edge surface equilibrated with 200ppm Au

Simulations

Quantum chemistry provides that a Schrodinger's equation can be solved at different levels of complexity. One simpler method by Huckel [9] can be applied to gold cyanide and carbon surfaces as the two reactants of the adsorption scenario. Huckel energy calculations include the repulsion of closed-shell occupied orbitals, the attraction of positive and negative charges, and the interaction of unoccupied orbitals (especially the lowest unoccupied molecular orbital, LUMO) with the occupied orbitals (especially the highest occupied molecular orbital, HOMO) (Fig.4). Huckel computations can associate the frontier orbitals (HOMO and LUMO) with traditional Lewis-acid like 'hardness' and 'softness' concepts developed from experimental observations, wherein hard reacts better with hard, and soft reacts better with soft. In summary, soft nucleophiles have a high-energy HOMO and soft electrophiles have a low-energy LUMO. A hard-hard reaction is favorable because of large Coulombic attractions, and a soft-soft reaction is favorable because of a large interaction between the HOMO of the nucleophile and the LUMO of the electrophile. The higher the HOMO energy of the nucleophile, the softer it is. In this case we are dealing with soft-soft reactions, with the gold cyanide complex acting as a nucleophile with respect to activated carbon. During adsorption, the HOMO electrons of the gold cyanide seek to occupy the 'real estate' provided by the LUMO levels of activated carbon. The key point is that small pores tend to change these LUMO levels in activated carbon by raising them when compared to planar activated carbon. Therefore, the pore's LUMO more readily occupies gold cyanide's HOMO, creating a stronger bond. In frontier orbital theory this concept of reactivity is defined by the absolute value of HOMO – LUMO, with a lower value indicating greater reactivity (Table I and II).

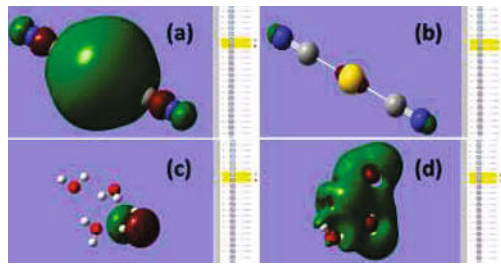

Fig 4: (a) HOMO of gold cyanide. (b) LUMO of gold cyanide. (c) HOMO of water molecule (only 1 molecule is shown; other molecules have similar HOMO). (d) LUMO of water molecule.

Table I: Frontier orbitals show higher reactivity of gold cyanide over water towards graphite edge.

HOMO(gold cyanide) - LUMO(graphite edge)	1.4002 eV
HOMO(water) - LUMO(graphite edge)	3.3128 eV

Table II: Frontier orbitals show lower barrier for electron sharing in pores, indicating tighter bonding than edge surface.

HOMO(gold cyanide + water) - LUMO (graphite edge + water)	3.095 eV
HOMO(gold cyanide + water) - LUMO (graphite edge pore + water)	2.601 eV

The interaction energy (Fig. 5) complements the quantum chemical HOMO-LUMO calculations and gives an approximate estimate of the reactivity of gold cyanide and water at the graphite edge surface. In other words, it gives an approximate estimate of how tightly the gold cyanide or the water molecules are bound to the graphite edge surface. In each case, the molecule was fixed at an initial position away from the graphite edge surface and given an initial velocity of 50Å/sec towards the surface and the system was allowed to evolve and equilibrate according to the imposed force field. The potential energy was plotted as a function of the separation distance. It is evident from the plot that at a distance of around 3.5Å from the surface of graphite edge, gold cyanide is more tightly bound to the surface of graphite (7.65 kcal/mol) than water molecule (2.9 kcal/mol) by a factor of almost 2.5. An interesting point to note here is that coincidentally, the width of the exclusion zone between the surface of graphite and the layer of water molecules is also around 3.52Å. This indicates that the region of closest approach at the graphite surface for adsorption or any chemical reaction is at a distance of 3.5Å from the surface.

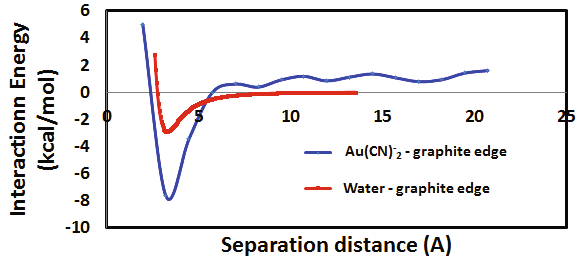

Fig. 5: Plot of the interaction energy as a function of the separation energy indicating gold cyanide more tightly bound to the graphite surface than water molecule.

Gibbs energy is the chemical potential that is minimized when a system reaches equilibrium under constant pressure and temperature. It is a convenient criterion to assess the spontaneity of the process with constant temperature and pressure. With respect to STP, as a general rule of thumb, every system seeks to achieve a minimum free energy. As it turned out from semi-empirical simulations using the MOPAC software package at the PM6 level, the gold cyanide has a more favorable tendency to bond with the narrow slit pore (13Å) than a wide slit pore (26Å) or the graphite surfaces. The Gibbs energy calculations (Fig. 6) further reinforces the results from the quantum chemical ab-initio calculations.

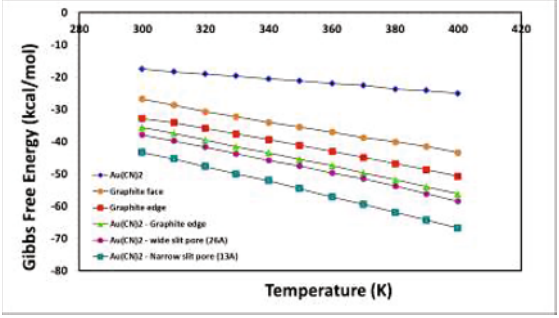

Fig. 6: The plot of the Gibbs energy as a function of temperature giving evidence that gold cyanide has a more favorable tendency to bond with a narrow slit pore (13Å) than a wide slit pore (26Å) or the graphite surface

Molecular dynamics simulations (MDS) of gold cyanide with potassium counter ions at graphite face and edge surface have been performed. After equilibration, snapshots are presented in Figure 7. It is clearly evident from the simulation results that gold cyanide has a favorable tendency to get accommodated at the graphite edge surface. In Figure 7(a) the aurodicyanide ions tend to form clusters, as has been observed before by other researchers [10], but do not get oriented along the graphite face surface. On the contrary, the aurodicyanide anions exhibit favorable tendency to adsorb on the graphite edge surface in clusters. These MD simulation results of gold cyanide at graphite surfaces support the evidences presented earlier that gold cyanide is adsorbed at the graphite edge surface with almost negligible or no adsorption at the face surface. One of the theories of activated carbon adsorption is based upon ionic size and hydration. It is assumed that aurodicyanide ions are larger and have a smaller hydration shell than other metal-cyanide ions and thus, are selectively adsorbed by activated carbon. Moreover, the strong tendency of $Au(CN)_2^-$ to form stable clusters may increase the possibility of adsorption. The hydrophobic tendency of aurodicyanide anions and their corresponding cluster formation probably contribute to the selectivity exhibited in ion pair adsorption by activated carbon. The phenomenon of aggregation may be of importance in the adsorption reaction and cluster formation may account for stabilization in the activated carbon pores.

TEM analysis of activated carbon had revealed the presence of slit pores, which are responsible for gold adsorption. To simulate such slit pores, molecular dynamics simulations were performed in 25 Å graphite slit pores, i.e., face pore and edge pore. Snapshots of the equilibrium positions are illustrated in Figure 7(c) and (d). The simulation results again clearly show that gold cyanide tend to form clusters, as seen in previous simulations too, and are well accommodated at the edge surface of a graphite edge pore. There is no favorable adsorption of the gold cyanide at the graphite face surface of the face pore although the tendency to form clusters is still evident. These simulation results help us to provide a plausible explanation to determine the sites of gold cyanide adsorption in activated carbon.

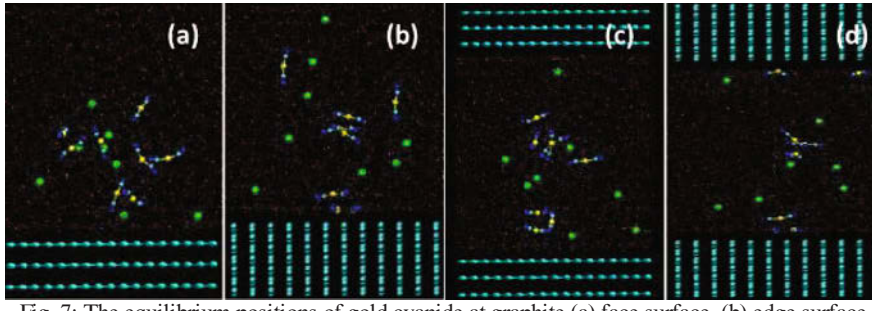

Fig. 7: The equilibrium positions of gold cyanide at graphite (a) face surface, (b) edge surface, (c) face pore, and (d) edge pore as revealed from MDS.

Conclusions

Experimental characterizations and simulations have established that the graphitic structure of AC contributes significantly to the adsorption of gold from alkaline cyanide solutions. Raman and XPS characterizations demonstrated the favorable tendency of gold

cyanide adsorption on the HOPG edge surface, which further reinforced previous hypotheses. The interaction of water with graphite surfaces and its inclusion in structural cavities or pores and interlayer spaces of graphite is an important phenomenon. Many aspects of the structure, dynamics and energetics of the water-graphite interaction have been elucidated here. In this regard, computational chemistry analysis, involving ab-initio quantum chemical calculations and molecular dynamics simulations of the adsorption of aurodicyanide cyanoanions at graphite surfaces was performed to understand the nature of gold loading in AC. The selective adsorption of the aurodicyanide ion pair seems to be related to the low polarity of the gold complex and its accommodation at the graphitic edge surface. Ab-initio calculations based on frontier orbital theory and Gibbs free energy plot indicated that gold cyanide has a greater affinity to be adsorbed in a pore than on the surface and were well supported by MDS. Visual examination of some equilibrium configurations from MD simulations allowed for the understanding of the adsorption phenomena at a microscopic level.

References

1. M.D. Adams, C.A. Fleming, "The Mechanism of Gold Adsorption of Aurocyanide onto Activated Carbon," *Metallurgical Transactions,* 208 (1989), 315-325.

2. S. Lagerge et al., "Adsorption of cyanide gold complexes inferred from various experimental studies," *Langmuir,* 13 (1997), 4683–4692.

3. P.L. Sibrell, J.D. Miller, "The significance of graphitic structural features in gold adsorption by carbon," *Minerals and Metallurgical Processing,* 9 (1992), 189-195.

4. M.D. Adams, "The chemistry of the carbon-in-pulp process" (Ph.D. thesis, University of Witwatersrand, Johannesburg, 1989), 53-189.

5. F. Rodriguez-Reinoso, Molina M. Sabio, "Textural and chemical characterization of microporous carbons," *Advances in Colloid and Interface Science,* 76-77 (1998), 271-294.

6. M.D. Hanwell et al., "Avogadro: an advanced semantic chemical editor, visualization, and analysis platform," *Journal of Cheminformatics*, 4 (2012), 1-17.

7. W. Smith, T.R. Forester, "DL_POLY_2.0: A general-purpose parallel molecular dynamics simulation package," *Journal of Molecular Graphics,* 14(3) (1996), 136-141.

8. N. Shimodaira, and A. Masui, "Raman spectroscopic investigations of activated carbon materials," *Journal of Applied Physics*, 92 (2002), 902-909

9. R. Hoffmann, "An Extended Hückel Theory: I. Hydrocarbons," *Journal of Chemical Physics*, 39 (1963), 1397-1412

10. X. Yin et al., "Molecular dynamics simulations of metal–cyanide complexes: Fundamental considerations in gold hydrometallurgy," *Hydrometallurgy*, 106(1–2) (2011), 64-70.

Characterization of Minerals, Metals, and Materials 2016
Edited by: Shadia Jamil Ikhmayies, Bowen Li, John S. Carpenter, Jiann-Yang Hwang, Sergio Neves Monteiro, Jian Li, Donato Firrao, Mingming Zhang, Zhiwei Peng, Juan P. Escobedo-Diaz, and Chenguang Bai
TMS (The Minerals, Metals & Materials Society), 2016

CLINKER PRODUCTION FROM WASTES OF CELLULOSE AND GRANITE INDUSTRIES

Délio Porto Fassoni[1], Rita de Cássia Alvarenga[1], Leonardo Pedrotti[1], Beatryz Mendes[1]

[1]UFV – Federal University of Viçosa, DEC – Civil Engineering Departament; Av. PH Rolfs, Viçosa, Minas Gerais, 36570-900, Brazil.

Keywords: Cement, Clinker, Waste.

Abstract

This work presents a belite cement based made from two industrial waste types. Binary mixtures were prepared using waste from rock cutting and polishing industries and waste from cellulose industry (named grits), in diferente proportions. The mixed raw materials were burned at a temperature of 950 °C in an electric oven for 30 minutes and then cooled at a rate of 70 °C per minute. The mineralogical composition of the material obtained was studied by means of XRD techniques, confirming the dominance of dicalcium silicate. Mixed mortars produced with the new material, in full replacement of Portland cement, showed satisfactory performance for use in construction works. This research shows that it is possible to obtain hydraulic binders from industrial waste, at lower temperatures than the required for the Portland cement production, with significant positive environmental impact by reducing the consumption of non-renewable resources and energy.

Introduction

Industries have been increasingly concerned with environmental issues, and in relation to cement this is not different. The production of cement involves the release of a high content of CO_2 in the atmosphere and the use of large quantities of fuel. One way to minimize these effects would be decreasing the tricalcium silicate - C_3S which is the predominant phase in Portland cements, offset by the increase of dicalcium silicate - C_2S - in the cement formulation [1].

Cements in which predominate dicalcium silicates are called belite cements. Those can be sintered at lower temperatures, because according Raupp [2], the formation of belite is between 900 ° C and 1200 ° C, from the combination of silica with the remaining free lime crystals. This leads to a reduction in energy consumption in relation to the manufacture of Portland cement.

In recent years, many experimental studies have been conducted in order to obtain belite clinker at laboratorial level. Studies such as those performed by Pimraksa et al and Pereira et al show that it is possible to obtain belite binders using waste materials as additives to the clinker [1].

In Brazil, there is a lot of granite processing industries, responsible for releasing tons of waste per year in the environment [3]. The residue granite processing, also known as mud is generally composed of rock dust, with high contents of SiO_2, Al_2O_3, Fe_2O_3 and CaO_4.

Other waste generated in large quantities is the grits, coming from the pulp production process by kraft5. According to Cenibra (2010), the production of 1.0 ton of pulp produces 268 kg of waste, encouraging the search for a suitable destination for the pulp [4]. One solution, both environmentally and financially, would be the application of this waste in construction, specifically in the production of mortars or binders.

The manufacture of belite cements from industrial waste is an alternative that contributes to sustainable development, saving non-renewable raw materials and energy, reducing environmental impacts. It is noteworthy that the performance of the product depends on factors related to the means of production, as the sintering time and control the cooling rate, so that the formed belite phase has hydraulic and reactive properties.

Materials and Methods

For the characterization of waste used in this research were first collected samples of generating industries and then transported to the Building Materials Laboratory of the Federal University of Viçosa. One of the tests carried out to identify the composition of these materials was EDX, Espectrophotometry by X-ray Energy Dispersive.

The waste is crushed and then mixed by wet at the rate 60% of grits and 40% of granite waste. This ratio provides a rate CaO/SiO = 2 and it favors the almost complete transformation of raw mixture in dicalcium silicate.

The mixture was formed into prismatic blocks and subjected to drying. Subsequently, they were brought to the oven for sintering at 950 ° C, where they remained for 30 minutes. The cooling occurred at a rate of 70 ° C per minute, through the injection of compressed air in freshly burned material.

The clinker obtained was ground and sieved in the sieve #200. Samples were removed for the mineralogical characterization using the Diffraction Test X-ray (XRD) in order to prove the formation of belite after firing. The pozzolanicity test according to the Luxan method was realized too.

Confirmed the presence of C_2S in the material, started the production of mortars composed by a belite produced and washed, sifted and wet sand (fine aggregate).

Compressive strength tests were made on mortar cylindrical specimens with 5 cm in diameter and 10 cm high, with two specimens for each age of rupture (7, 14, 21, 28 and 42 days). It was still added in the serie of mortar the additive Muraplast (Sika) to obtain water/cement factor lowered and evaluation of the new cement behavior and the use of additives (Figure 1).

Figure 1. Mortar and additive blend.

Results

The results for the EDX analysis of the granite cutting waste composition and grits are shown in Table I.

Table I. Waste composition analysis by EDX.

Compound	Granite Waste	Grits
CaO (%)	3.784	94.396
SiO_2 (%)	68.828	2.138
Al_2O_3 (%)	15.82	0
Fe_2O_3 (%)	2.052	0.36
SO_3 (%)	1.843	0.286

The plot obtained by the sintered clinker analysis through XRD indicates the presence of dicalcium silicate, as seen in Figure 2.

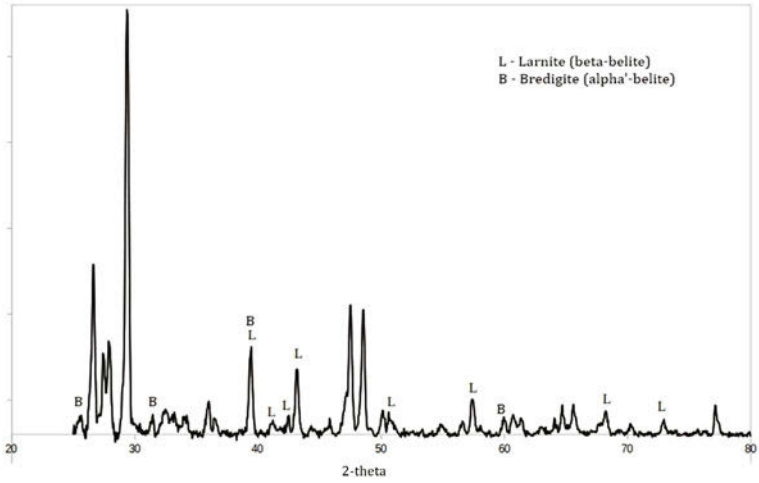

Figure 2. XDR analysis of the sintered clinker.

As expected, the pozzolanicity test according to the Luxan method indicated that the material does not present pozzolanic activity, possessing pozzolanicity index of -0.03 mS / cm. The results of the pozzolanic test are shown in Table 2.

Table 2. Results of the pozzolanicity test according to the Luxan method.

Pozzolanicity			
Amostra	Conductivity (mS/cm)		Conductivity Difference
	Initial	Final	
Belite Clinker	8.92	8.95	-0.03

The mortars produced with the sintered material have a 1: 1.5 trace (by size) of binder and fine aggregate. It was adopted a water/binder factor equal to 0.32, adding the additive.

The results of the compressive strength test of the specimens are shown in Table 3. The test was done at 7, 14, 21, 28 and 42 days old.

Table 3. Results of the mortar compressive strength tests.

Nº.	Age (days)	Belite Clinker Consumption (kg/m^3)	A/C Factor	Max Stress by Age
1	7	316.4	0.32	0.8 MPa
2	14			2.8 MPa
3	21			4.7 MPa
4	28			6.6 MPa
5	42			8.5 MPa

Figure 3. Specimens broken at 7 days old.

As expected, the results of maximum stress by age show that the mechanical strength of the mortar produced with belite material grows with the age of the specimens. This fact is best illustrated in the chart below.

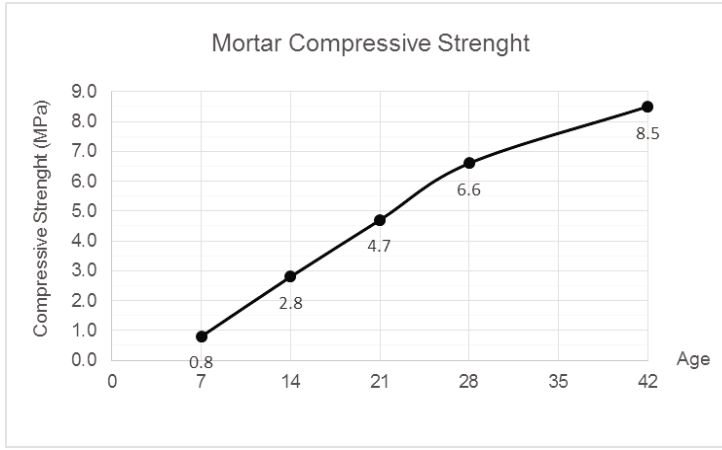

Figure 4. Graphic of compressive strength of specimens *versus* age.

Conclusions

The already performed analyzes of the belite cement produced indicate that it have the same binder characteristics, which can enable its use in mortars for laying and coating.

The absence of pozzolanic activity shows that the resistance gain of the prepared mortars is due to the presence of calcium silicate in the clinker, and not the action of silica present in the mixture.

There are still some material properties to be evaluated, in addition to perform compressive resistance tests in mortars at older ages. However, the obtained results so far are enough to show that obtaining a cement produced from industrial residues with similar chemical characteristics of the raw materials used in the cement industry is possible.

The research has shown that the developed product has a great sustainable potential, since the firing at 950 ° C is sufficient for the formation of dicalcium silicate. One can have in the future, an economically more viable cement that meets the necessary criteria for use in buildings, especially of a social nature.

Acknowledgements

The authors thank the Brazilian agencies: CNPq, CAPES and FAPEMIG for the support provided to this investigation.

References

1. BAESSO, J. et al. “Obtenção de Clínquer Belítico a Partir de Resíduos”. *Cerâmica Industrial*, 17 (2012), 38-41.

2. PEREIRA, R. F. Valorização de resíduos industriais como fonte alternativa mineral: composições cerâmicas e cimentíceas (Ph. D. thesis, Universidade de Aveiro, 2006), 49-53.

3. FILHO, J. Estudo da durabilidade de argamassas alternativas produzidas de resíduos de construção e granito (Ph. D. thesis, Universidade Federal de Campina Grande, 2007), 13-15.

4. MARQUES, M. et al. “Potencialidades do uso de resíduos de celulose (dregs/grits) como agregado em argamassas”**.** *Revista Brasileira de Produtos Agroindustriais*, 16 (2014), 423-431.

5. MENEZES, R. et al. “Reciclagem de resíduos da construção civil para a produção de argamassas”. *Cerâmica*, 55 (2009), 263-270.

6. ZAWAWI, R. “Artificial hydraulic lime mortar obtained by calcining limestone and siliceous waste materials” (Ph. D. thesis, Heriot Watt University, 2010), 51-82.

Characterization of Minerals, Metals, and Materials 2016
Edited by: Shadia Jamil Ikhmayies, Bowen Li, John S. Carpenter, Jiann-Yang Hwang, Sergio Neves Monteiro, Jian Li, Donato Firrao, Mingming Zhang, Zhiwei Peng, Juan P. Escobedo-Diaz, and Chenguang Bai
TMS (The Minerals, Metals & Materials Society), 2016

EFFECTS OF CARBON BLACK INCORPORATION ON MORPHOLOGICAL, MECHANICAL AND THERMAL PROPERTIES OF BIODEGRADABLE FILMS

Julio Harada[1,2]; José Ricardo N. Macedo[1]; Glauson Aparecido F. Machado[2]; Francisco Valenzuela-Díaz[3]; Esperidiana A. B. Moura[2]; Derval S. Rosa[1]

[1]Universidade Federal do ABC – UFABC, Av. dos Estados, 5001, São Paulo, SP, 09210-580, Brasil
[2]Instituto de Pesquisas Energéticas e Nucleares – IPEN-CNEN/SP
Av. Prof. L. Prestes, 2242 São Paulo, SP, 05508-000, Brasil
[3]Universidade de São Paulo, Escola Politécnica, Dep. de Eng. Metalúrgica e de Materiais. Av. Prof. Mello de Moraes, 2463, São Paulo, SP, 05508-030 – Brasil

Keywords: Biodegradable Films, Carbon Black, Mechanical Properties, FE-SEM

Abstract

This work evaluates the effects of carbon black incorporation on morphological, mechanical and thermal properties of biodegradable films. The biodegradable composite films based on PBAT/PLA blend and PBAT/PLA blend containing 2 wt. % of carbon black were prepared by melt extrusion, using a twin screw extruder machine and blown extrusion process. The properties of biodegradable film samples were investigated by tensile tests, XRD, MFI, TGA, DSC and FE-SEM analysis and the correlation between properties was discussed.

Introduction

Increasing interest in new materials based on blends of two or more polymers has been observed during the last decades. Conventional thermoplastic polymers have good mechanical properties and thermal stability, much better than the biodegradable ones. Biopolymers have advantages over the conventional polymers; biopolymers are from renewable materials and can be biodegradable. There is also a limitation in the performance and application of biopolymers in comparison to conventional thermoplastics. Therefore, the extensive application of these biopolymers is still challenged by one or more of their possible inherent limitations, such as poor processability, brittleness, hydrophilicity, poor moisture and gas barrier, inferior compatibility, poor electrical, thermal and mechanical properties [1, 2]. Blends of conventional plastics (petroleum-derived polymers) and biopolymer can form a new class of materials with improved mechanical properties compared with those of single components. Polymer blending offers possibility of adjusting the cost-performance balance and tailoring the technology to make products for specific end-use applications; extends engineering resins' performance; improves specific properties or solvent resistance; and provides means for industrial and consumer plastics waste recycling [3].

Combination of polymer blends with micro or nanofillers appears quite promising based on balanced performance of biopolymer, to compare better thermal and mechanical properties, improve service temperature, moisture resistance, gas barrier, and in some cases reduce the cost of biodegradable thermoplastic polymers. Incorporation of nanoparticles into polymer materials

has attracted a great deal of attention due to its ability to enhance polymer properties such as thermal, mechanical, and gas barrier [1]. Inorganic materials due to their ability in harsh process conditions, such as metal or metal oxides have attracted a great deal of attraction recently. Carbon Black among the inorganic materials have particular interesting due to both safe material for animals and human and stability under harsh condition processes [4, 5].

The synthesis of inorganic-biopolymer nanocomposites has been intensely studied due to their unique combination of properties and widespread potential applications. These generations of biocomposites have more desirable functional properties, such as good mechanical strength, and low water vapor permeability. Lately, researchers have reported the improvements of biopolymer properties by incorporation of nanoparticles, such as clay, silica, layered silicate nanoparticles, calcium carbonate, zinc oxide and titanium dioxide. In general, these researchers have reported that the incorporation of nanoparticles improve mechanical properties, as well as barrier and antimicrobial properties of biopolymers [6,7].

The aim of this study was to process and investigate the changes in the mechanical, morphological and environmental UV protection of the biodegradable PBAT/PLA blend due to the incorporation of Carbon Black nanoparticle.

Materials and Methods

Materials:

The materials used in this work were biodegradable aliphatic-aromatic copolyester (PBAT); biodegradable poly(lactic acid) (PLA), and Carbon Black nanoparticles.

Preparation of blend and composite:

PLA, PBAT, and the Carbon Black nanoparticle were dried at 60 ± 2 ºC for 4 h to reduce its moisture content to less than 2 %. The PBAT/PLA blend (59 %/ 39 %, based on wt. %) with 2 wt. % of Carbon Black addition were prepared by melting extrusion process, using a co-rotating twin-screw, with 20 mm of diameter, Haake Rheomex P 332 extruder. The temperature profile was 135/145/148/150/150/150 ºC. Screw speed was 180 rpm. The extrudates coming out of the extruder were cooled down in air for a better dimensional stability, pelletized by a pelletizer, dried again at 60 ± 2 ºC for 4 h and fed into extrusion blown film, single screw machine with 25 mm diameter, Carnevalli, and specimens test samples were obtained.

Characterization

Mechanical tests:

Tensile tests: tensile tests were performed using an INSTRON 5900 with 500 kg load cell and 50mm.min^{-1}, according to ASTM D 638, in order to evaluate the mechanical behavior of the materials studied.

X-rays diffraction (XRD) tests:

X-rays diffraction (XRD) were recorded on a BRUKER, Focus-D8 diffractometer operated at 40 kV and 40 mA, with CuKα radiation (λ= 1.54 Å).

Melt Flow Index (MFI) measurements:

Melt Flow Rate (ASTM D1238) were carried out using CEAST Melt Flow modular line at 190°C / 2.16 kg. MFI measurements were determined work in order to evaluate the Carbon Black addition on blow film extrusion process.

Thermogravimetric analysis (TG):

Thermogravimetric analysis was performed using an appliance STA 449 F3 Jupiter of Netzch with analysis from 25 to 500°C under a rate of 10°C.min^{-1} in an atmosphere of N_2.

Differential scanning calorimetry analysis (DSC):

DSC analyses were carried out using a Mettler Toledo DSC 822 from 25 to 250°C at a heating rate of 10 °C/min under oxygen atmosphere.

Field Emission Scanning Electron Microscopy (FE-SEM):

FE-SEM were carried out using a JEOL-JSM-6701 F, microscope with an accelerating voltage of 1-30 kV, using EDS Thermo-Scientific mod. Noran System Six software, in carbon sputtered samples.

Results and Discussion

Mechanical tests results:

Tensile test results: The Table I presents the results of tensile tests of PBAT/PLA blend and PBAT/PLA/Carbon Black nanocomposite. These results shown the average values calculated from the data obtained in tests for five test specimens. As can be seen in this table, the addition of Carbon Black in PBAT/PLA blend improved the tensile strength at break (of around 100 %), elongation at break and modulus properties of blend. The improve of tensile properties in PLA due to Carbon Black has been reported in the literature by Chivrac, et al. [8] and Luduena, et al. [9]. These authors suggested that Carbon Black could be acting as nucleating agent improving the crystallinity of PLA.

Table I. Tensile test results of PBAT/PLAblend and PBAT/PLA/Carbon Blacknanocomposite.

Sample	Young's modulus (MPa)	Tensile strength at break (MPa)	Elongation at break (%)
PBAT/PLA Blend	41 ± 19	6 ± 3	326 ± 94
PBAT/PLA+2%CB	78 ± 9	12 ± 1	430 ± 27

Figure 1 shows the diagram stress against strain for PBAT/PLA blend and PBAT/PLA/Carbon Black nanocomposite. From this Figure it is possible to observe that the behavior of nanocomposites perfectly elastic, the stress increases linearly with strain. However, Carbon Black addition caused a significant increase on tensile strength and elongation of blend.

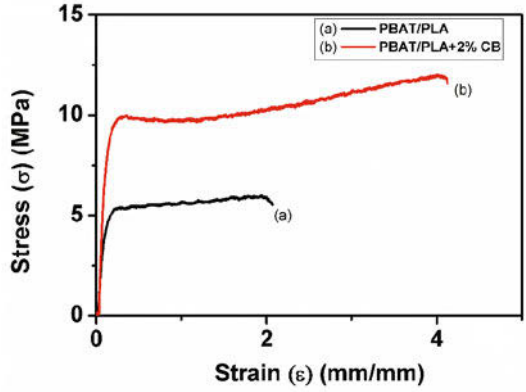

Figure 1. Diagram stress (MPa) against strain (mm/mm) for PBAT/PLA blend and PBAT/PLA/Carbon Black nanocomposite.

X-ray diffraction (XRD) analysis results:

The XRD patterns of PBAT/PLA blend and PBAT/PLA/Carbon Black nanocomposite are shown in Figure 2.

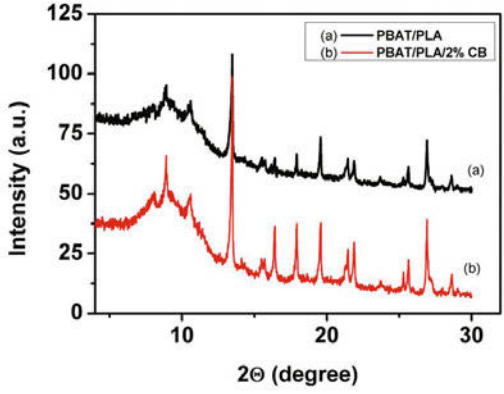

Figure 2. XRD diffraction patterns for the PBAT/PLA blend and PBAT/PLA/Carbon Black nanocomposite in the range of 2θ between 4° to 30°.

It can be seen in Figure 2, the XRD pattern of PBAT/PLA blend showed a prominent 2θ peak at around 16.4°, which has increased intensity due to Carbon Black nanoparticle addition. From this figure, it can be observed that two new 2θ peaks at around 8.1° and 8.9° that may be related to the Carbon Black structure.

Melt flow index (MFI) measurements:

The MFI values of PBAT/PLA blend and PBAT/PLA/Carbon Black nanocomposite are presented in Table II. The MFI value of PBAT/PLA presented reduction due to Carbon Black addition. These results suggest that Carbon Black incorporation may have caused a reduction of the mobility of the PBAT/PLA blend chains.

Table II. MFI results for the PBAT/PLA blend and PBAT/PLA/Carbon Black nanocomposite.

Sample	MFI ($g.10min^{-1}$)
PBAT/PLA Blend	27 ± 3
PBAT/PLA+2%CB	23 ± 3

Thermogravimetric analysis (TG) results:

Figure 3 shows the TG thermograms of PBAT/PLA blend and PBAT/PLA/Carbon Black nanocomposite. The decomposition temperature and weight loss of PBAT/PLA/Carbon Black nanocomposite are presented in Table III. It can be seen in Figure 3 and Table III that Carbon Black nanoparticle addition reduced the degradation temperature of PBAT/PLA blend.

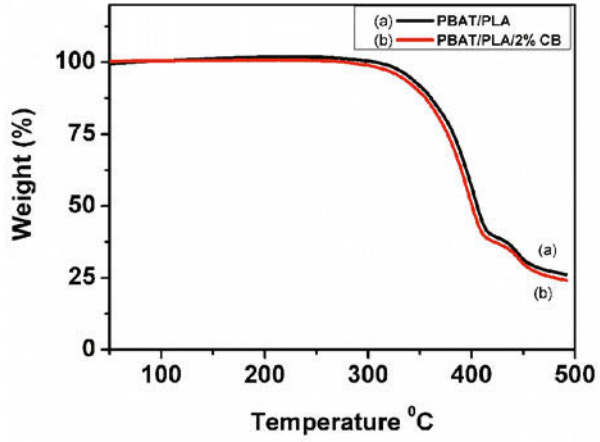

Figure 3. TG thermograms of PBAT/PLA blend and PBAT/PLA/Carbon Black nanocomposite.

Table III. Decomposition temperature and weight loss of PBAT/PLA blend and PBAT/PLA/Carbon Black nanocomposite.

Sample	T_{onset} (°C)	T_{max} (°C)	Weight Loss (%)
PBAT/PLA Blend	347.54	410.44	74.08
PBAT/PLA+2%CB	343.78	407.23	76.01

Differential Scanning Calorimetry (DSC) analysis results:

DSC curves for the PBAT/PLA blend and PBAT/PLA/Carbon Black nanocomposite can be seen in Figure 4. From Figure 4, it could be inferred that compared with the PBAT/PLA blend the endothermic melting enthalpy of PBAT/PLA blend increased considerably due to Carbon Black nanoparticle addition. The increases in the melting enthalpy can be attributed to the increase in crystallinity of PBAT/PLA composite.

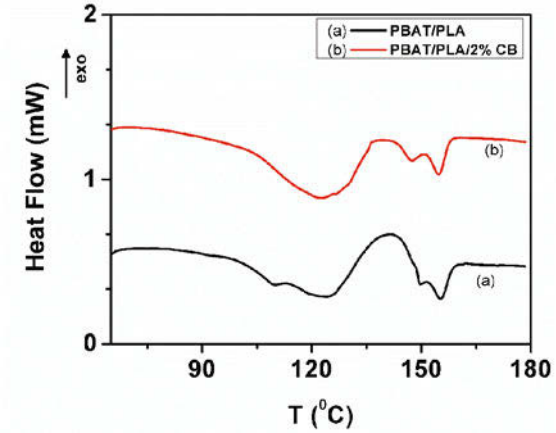

Figure 4. DSC analysis for the PBAT/PLA blend and PBAT/PLA/Carbon Black nanocomposite.

Table IV show the average values of melting temperature (Tm) and melting enthalpy (ΔHm) of the PBAT/PLA blend and PBAT/PLA/Carbon Black nanocomposite.

Table IV. The average values of Melting temperature (Tm) and melting enthalpy (ΔHm) of the PBAT/PLA blend and PBAT/PLA/Carbon Black nanocomposite.

Sample	Tm^1 (°C)	Tm^2 (°C)	ΔHm ($J.g^{-1}$)
PBAT/PLA Blend	124	155	4.4
PBAT/PLA+2%CB	123	154	7.2

From Figure 4 and Table IV, it can be observed two melting temperatures (Tm^1 and Tm^2), which are near of the melting temperatures of PBAT and PLA respectively [10, 11]. It means that blend processing and Carbon Black nanoparticle addition had a capability to reorient the polymeric molecules present in crystal form in order to obtain a composite material with high melting enthalpy and, consequently, high crystallinity percentage.

Field Emission Scanning Electron Microscopy (FE-SEM) analysis results:

FE-SEM micrographs of PBAT/PLA blend and PBAT/PLA/Carbon Black nanocomposite in different magnifications are showed in Figure 5. As can be seen in Figure 5a, the PBAT/PLA blend with 6.000 X of magnification appeared to have a clear, phase-separated morphology with PLA dispersed in the PBAT matrix. Figure 5b and 5c shows micrographs of PBAT/PLA/Carbon Black with 6.000 X and 10.000 X of magnifications, respectively. It can be seen that there are several Carbon Black nanoparticle agglomerates in the surface of the blend. This result suggests that part of nanoparticles were not dispersed in the PBAT/PLA blend.

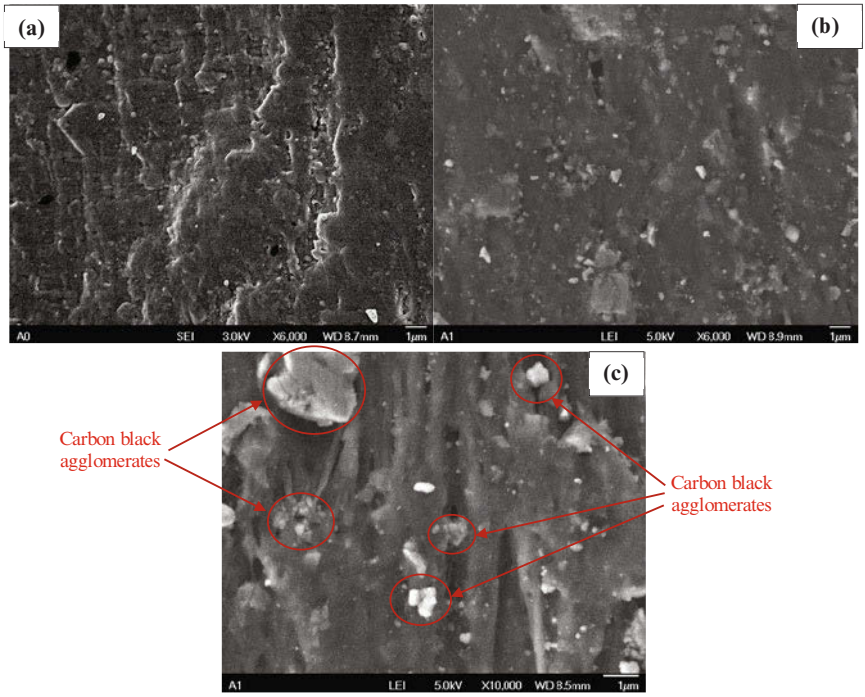

Figure 5. FE-SEM micrographs of PBAT/PLA blend and PBAT/PLA/Carbon Black nanocomposite: (a) PBAT/PLA Blend (6.000 X); (b) PBAT/PLA/Carbon Black (6.000 X); (c) PBAT/PLA/Carbon Black (10.000 X).

Conclusions

Results showed that incorporation of (2 wt. %) of Carbon Black nanoparticle in the PBAT/PLA blend matrix led to significant gain of mechanical properties of the blend. The DSC analysis results indicated that blending PBAT with PLA, followed by of Carbon Black nanoparticle addition increased considerably the melting enthalpy of PBAT/PLA blend, and consequently, increased the crystallinity percentage. Although gains in mechanical properties of the blend due to the Carbon Black addition were observed, the FE-SEM micrographs results showed that there were several Carbon Black nanoparticle agglomerates in the surface of the blend. These results indicates that Carbon Black nanoparticle addition in the PBAT/PLA matrix, despite the presence of agglomerates, improved the biodegradable blend and led to the obtaining of composite materials with superior properties suitable for several industrial application

Acknowledgements

The authors wish to thank IPEN, UFABC and MAMAPLAST for the support for this work.

References

1. R. Nassiri, A. MohammadiNafchi, "Antimicrobial and Barrier Properties of Bovine Gelatin Films Reinforced by Nano TiO_2," *Journal of Chemical Health Risks*, 3 (3) (2013), 12-28.
2. M. Kurian et al., "A Novel Route to Inducing Disorder in Model Polymer-Layered Silicate Nanocomposites," *Macromolecules*, 39 (2006), 1864-1871.
3. L.A. Utracki (ed.), Polymer Blends Handbook, vol. 1 (Kluwer Academic Publishers, Dordrecht, Chapter 1, 2003).
4. P. K. Stoimenov et al., "Metal Oxide Nanoparticles as Bactericidal Agents," *Langmuir*, 18 (2002), 6679-6686.
5. W. Lin, et al., "Toxicity of nano and micro-sized ZnO particles in human lung epithelial cells. *Journal of Nanoparticle Research*, 11 (2009), 25-39.
6. C. Chawengkijwanich, Y. Hayata, "Development of TiO2 powder-coated food packaging film and its ability to inactivate Escherichia coli in vitro and in actual tests," *International Journal of Food Microbiology*, 123 (2008), 288-292.
7. C. Bastioli (ed.), Handbook of Biodegradable Polymers (Rapra Technology, 2005).
8. F. Chivrac et al., "Aromatic Copolyester-based Nano-biocomposites: Elaboration, Structural Characterization and Properties," *J. Polym. Environ*. 14 (2006), 393-401.
9. L.N. Luduena, et al., "Extraction of Cellulose Nanowhiskers from Natural Fibers and Agricultural Byproducts," *Fibers and Polymers*, 14 (7) (2013), 1118-1127.
10. F.P. Carrasco et al., "Processing of poly(lactic acid):Characterization of chemical structure, thermal stability and mechanical properties," *Polymer Degradation and Stability*, 95 (2) (2010), 116-125.
11. P. Georgiopoulos, E. Kontou, and M. Niaounakis, "Thermomechanical Properties and Rheological Behavior of Biodegradable Composites," *Polymer Composites*, 35 (6) (2014), 1140-1149.

Characterization of Minerals, Metals, and Materials 2016
Edited by: Shadia Jamil Ikhmayies, Bowen Li, John S. Carpenter, Jiann-Yang Hwang, Sergio Neves Monteiro, Jian Li, Donato Firrao, Mingming Zhang, Zhiwei Peng, Juan P. Escobedo-Diaz, and Chenguang Bai
TMS (The Minerals, Metals & Materials Society), 2016

INFLUENCE OF INOCULATION ON STRUCTURE OF CHROMIUM CAST IRON

Dariusz Kopyciński[1], Sylwester Piasny[2]

[1]AGH University of Science and Technology; 23 Reymont Str.; Krakow, 30-059, Poland
[2]Technical Company - HARDKOP; 125 Harcerska Str, 32-540, Trzebinia, Poland

Keywords: Inoculation, Chromium White Cast Iron, Titanium Carbide, Chromium Carbide, Primary Austenite

Abstract

It has been proved that the addition of Fe-Ti inoculant to chromium cast iron changes the structure of castings. The said operation increases the number of crystallization nuclei for the dendrites of primary austenite. In this case, due to a similar behaviour of crystal lattice, titanium carbides act as substrates for the nucleation of primary austenite. The more numerous are the dendrites of primary austenite, the more refined is the structure, and the higher are the mechanical properties. Fractures of castings after Fe-Ti inoculation show different fine-grained structures.

Introduction

Chromium cast iron belongs to the group of white cast irons. Its main characteristic is structure containing chromium carbide precipitates of the M_7C_3 type. For this reason, the inoculants effective in the technology of grey cast iron manufacture, in the case of white cast iron are far from giving the expected spectacular results of structure refinement and hence the improvement of mechanical properties.
It seems therefore that in the case of chromium cast iron technology, one should think of a method for the modification of primary structure, that is, the structure related with the grains of primary austenite dendrites. In terms of morphology, the grains of primary austenite dendrites formed in white cast iron can be divided into two types:

- long columnar dendrites with well defined crystal orientation and position parallel to each other. These dendrites form large and coarse grains of primary austenite during exogenous crystallization;
- equiaxed dendrites that grow in random directions without the defined crystal orientation. These dendrites form fine grains of primary austenite during endogenous crystallization.

This division is directly related to the type of crystallization (exogenous directional crystallization [2] or endogenous bulk crystallization) that occurs in casting, especially when it is made of white cast iron. In the structure of white cast iron, the columnar grains of primary austenite nucleate on the surface of foundry mould. Based on the results of studies of the white cast iron crystallization, several basic types of microstructure present in this cast iron were distinguished [1], specifying the four main types of crystallization and six typical cases shown in Figure 1. It is generally known that the most convenient form of control of the crystallization process of the grains of austenite dendrites is when the liquid metal changes its physical and

chemical state. For example, when the carbon content is increasing in cast iron, or when the pouring temperature is increasing, or when the temperature of overheating is increasing and the melt holding time is decreasing, there is a growing tendency to endogenous crystallization yielding structures V and VI [1]. At this point, a general rule can be formulated that white cast iron produced under industrial conditions has the microstructure composed mainly of morphology I and II (Fig. 1), while grey cast iron has the microstructure composed mainly of morphology V and VI. Hence the conclusion follows that chromium cast iron should be subjected to some sort of modification (inoculation) that will lead to the formation of microstructure V or VI with the increased number of chromium carbide precipitates.

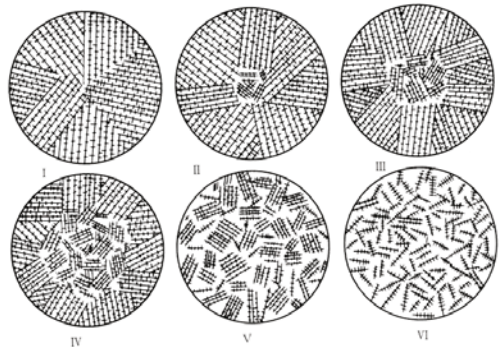

Figure 1. Different types of the dendritic crystallization of primary austenite grains in white cast iron [1]. Designations: I - exogenous (directional) crystallization, during which the precipitates of dendrites extend to the axis of the sample; II, III, IV – exogenous/endogenous crystallization, during which the precipitates of dendrites are distant from the sample axis; V - endogenous (bulk) crystallization during which the precipitates of dendrites grow in the cross-section; VI - endogenous crystallization during which individual dendrites grow in the entire cross-section

Knowing some basic aspects of the crystallization process, the conclusion is as follows: the impact of austenite grain morphology on the mechanical properties of white cast iron is important, although it has to be remembered that of some relevance is in this case also the number of the grains of austenite dendrites. Another important issue when the mechanical properties of white cast iron are tested and the occurrence of casting defects is detected is establishing a link between the number of austenite grains and grains of the eutectic precipitates of chromium carbides.

Thus, the crucial problem in planning of the inoculation treatment is to define the type of crystal lattice in the reagent selected as an inoculant. The crystal lattice of the inoculant should bear a high degree of similarity to the crystal lattice of the grains for which it will act as a substrate for nucleation. In [3], a coefficient of the inoculant - crystal matching was defined, assuming the form of the following equation:

$$\xi_d = \left(1 - \frac{x_p - x_k}{x_k}\right) \cdot 100\% \qquad (1)$$

where: x_p and x_k - lattice parameters of the substrate for nucleation and crystal, respectively.

The crystallographic data of selected substrates for nucleation with the calculated coefficients of substrate-iron dendrite matching are summarized in Table 1. From the results given in this table it follows that when the matching coefficient (1) reaches 90% and more it means that the effect of inoculation in the form of increased particle density is satisfactory and the degree of supercooling ΔT reaches its lowest value, and vice versa when the matching coefficient is unsatisfactory, the degree of supercooling ΔT reaches high values.

Table 1. Examples of substrates for nucleation present in molten iron and values of respective matching coefficients [3].

Substrate	Crystal lattice	ΔT	Matching coefficient
TiN	cubic - (B1)	3.1ºC	96.1%
TiC	cubic - (B1)	3.3ºC	94.1%
SiC	cubic - (B3)	7.5ºC	94.0%
ZrN	cubic - (B1)	12,6ºC	88,8%
WC	hexagonal - (Bh)	29.0ºC	87.3%
ZrC	cubic - (B1)	24.5ºC	85.6%

An example of the crystal lattice matching determined for titanium carbide TiC, which acts as a substrate for the austenite nucleation in cast iron is shown in reference [4]. In contrast, Fig. 2b shows the microstructure of high-aluminium white cast iron with the addition of titanium [5]. The precipitates of TiC are located inside the grains of primary austenite. Nevertheless, this does not necessarily imply the substrate-forming power of titanium inoculation, but may also indicate possible "sucking in" of TiC precipitates by the crystallization front of austenite dendrites or "closing" of TiC precipitates in the interdendritic spaces. However, one can not exclude the idea that it is the surface of titanium carbide on which the crystallization of alloyed austenite occurs. These doubts lead in many scientific works to rejection of the theory of crystal matching of the substrate for grain nucleation. Yet, if we consider the above theory as negligible, then in the discussion of inoculation treatment, inoculants will have to be evaluated in terms of their ability to reduce the nucleus-substrate contact angle, or in terms of their ability to reduce surface tension at the liquid metal - nucleus interface.

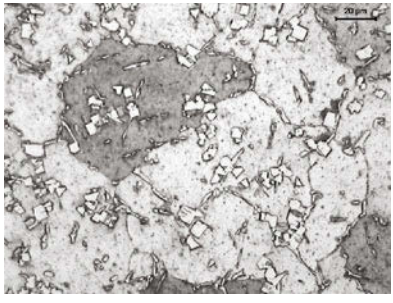

Figure 2. Microstructure of high-aluminium cast iron showing the presence of titanium carbide (TiC) precipitates in the interior of alloyed austenite grains [5]

Thus, in this case, it is the topography of the nucleation substrate and difference in the substrate-crystal electrostatic potential that, together with the similarity of chemical bonds, play an important role in this specific case. In contrast, the role of inoculation treatment is to produce, as a result of reactions of different types, substrates for the heterogeneous nucleation immediately upon the introduction of inoculating reagents into the liquid metal [6-10]. In this case, in the steel metallurgy and casting, the following inoculants are proposed for use: Nb, Ti, V, Ti + N, V + N, Zr + N, and as a result, the following substrates for nucleation are obtained: NbC, TiC, VC, VN, TiN ZrC, ZrN. In the iron metallurgy and casting, the inoculant used most frequently is ferrosilicon (FeSi) doped with simple inoculants like Ca, Ba, Sr, Zr, Bi, Al, rare earth metals, and other elements. When this type of inoculant is introduced into the liquid metal, the obtained substrates for the nucleation of graphite eutectic include CaC_2, BaC_2, SrC_2, BiC_2 and the like ones, and the end result is higher density of graphite eutectic grains. In the next part of the study, the effect of Fe-Ti addition on the structure of chromium cast iron was investigated.

Methodology

Studies of the effect of inoculation treatment carried out with the addition of Fe-Ti on the structure, and in particular on the number of primary austenite grains in eutectic chromium cast iron, were carried out in a "Balzers" VSG – 02 vacuum furnace with crucible of 1.2 kg capacity. The liquid metal after suitable degassing (pressure in a vacuum chamber of 0,113 Pa) and holding for approx. 5 minutes was cast at a temperature 1500°C into special metal moulds producing ϕ 20 mm diameter rods. Chemical composition of the tested chromium cast iron was as follows: 3.45% C, 24.5% Cr, 0.5% Si, 0.5% Mn, 0.03% S, 0.03% P, and it was established in the previous melting operation carried out in a medium frequency induction furnace with crucible of 15 kg capacity.

Effect of inoculation treatment

Titanium belongs to the group of carbide forming elements. Therefore it can be assumed that even prior to the crystallization of primary austenite, in high-chromium cast iron this element will combine with carbon to form MC type carbides. This is confirmed by calculations carried out in a Thermo CALC program. The operation of Thermo CALC program is based on a CALPHAD method. CALPHAD method is used to predict the thermodynamic parameters of selected phases and for modelling of processes that occur in multiphase systems. For the eutectic chemical composition of high-chromium cast iron, part of the equilibrium phase diagram of Fe-C-Cr alloys was calculated by this method, as shown in Figure 3a. Figure 3b shows the sequence of formation of various phases in the base high-chromium cast iron for further inoculation. Calculations show that the first one to nucleate is M_7C_3 carbide, followed by austenite; the last one to nucleate is manganese sulphide MnS, and it appears just before the decay of the liquid phase. After the introduction of titanium into high-chromium cast iron, the phase which nucleates as the first one is $Ti_4C_2S_2$ (see Figure 3c).
The occurrence of TiC carbide precipitates in the structure of high-chromium cast iron is confirmed in Figure 4, which shows a SEM microstructure with marked positions of the titanium carbides. Figure 4 also confirms the ability to create first the crystals of TiC ($Ti_4C_2S_2$ – strictly speaking).

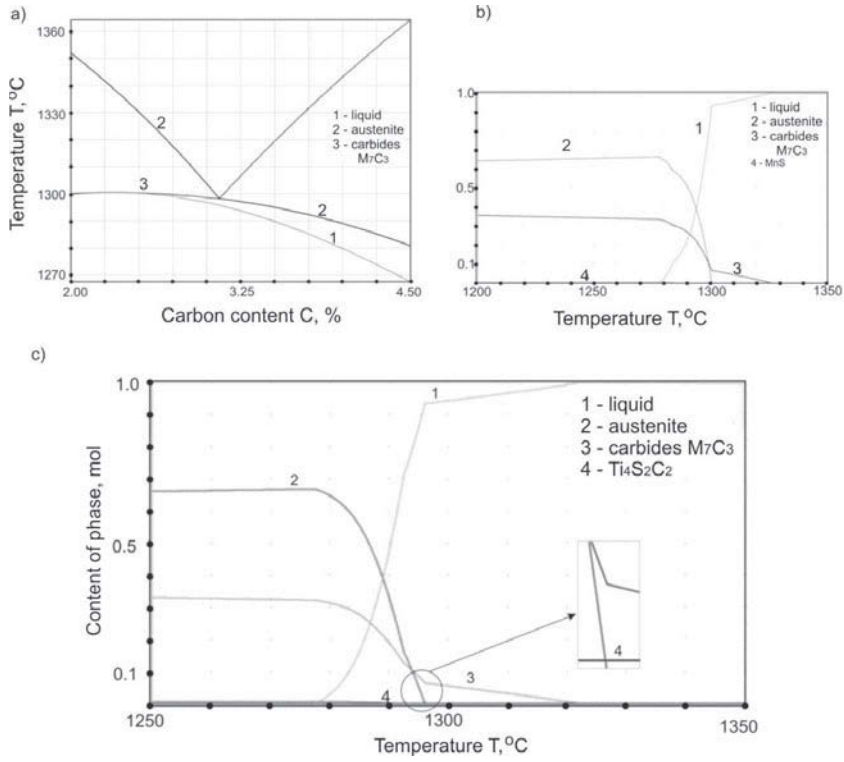

Figure 3. Part of the phase equilibrium diagram of Fe-C-Cr alloys calculated for high-chromium eutectic cast iron (a), and the content and sequence of phase formation during the crystallization of base eutectic high-chromium cast iron for further inoculation (b), and the sequence of phase formation during the crystallization of eutectic chromium cast iron with 0.4% Ti

It can be expected that the precipitates will form crystallization centres for the grains of primary austenite and, as demonstrated, also for the chromium carbide crystals. This is consistent with the theory according to which the similarity of one of the parameters of the crystal lattice of titanium carbide is the driving force for the crystallization of other phases. Table 2 shows the calculated values of the equilibrium crystallization temperature for individual phases of the base high-chromium cast iron and for the same cast iron after the inoculation treatment with FeTi. From the calculations it follows that titanium carbide can crystallize very early, i.e. at a temperature of 2170°C, which proves the appearance of this phase as the first one in metal bath.

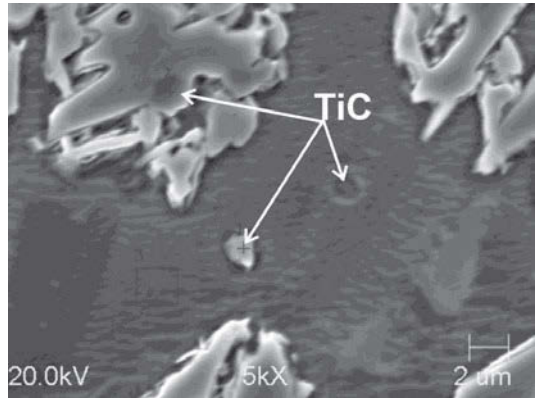

Figure 4. SEM microstructure of chromium cast iron with marked places of the occurrence of titanium carbides

Table 2. The calculated values of equilibrium crystallization temperature of different phases in base high-chromium cast iron and in the same cast iron after the inoculation treatment with FeTi

Eutectic chromium cast iron	Primary M_7C_3	Eutectic		$Ti_4C_2S_2$	MnS
		M_7C_3	Austenite		
base composition	1326	1301		none	1284
with the addition of 0.2%Ti	1324	1298		1739	none
with the addition of 0.4%Ti	1320	1296		2170	none

Major additions of Ti increase the ductility of alloyed white cast iron, while the addition of 0.2% titanium introduced to molten metal increases the bending strength of chromium cast iron to more than 1100 MPa and produces a refined structure in the samples of inoculated cast iron. Moreover, castings inoculated with Fe-Ti show increase in both hardness and abrasive wear resistance combined with improved resistance to cracking.

Figure 5 compares the macrostructure of base high-chromium cast iron (Fig. 5a) with the cast iron after inoculation treatment using minor amounts of Fe-Ti and maintaining the same process conditions for crystallization and casting. Studies of the macrostructure produced in test samples lead to the conclusion that in some of them titanium has enhanced the endogenous crystallization of high-chromium cast iron, resulting in the formation of equiaxed grains and subsequent structure refinement.

Next, applying special heat treatment, the number of primary austenite grains was estimated in the eutectic high-chromium cast iron before and after the inoculation treatment with FeTi, as shown in Table 3. The results listed in Table 3 also prove that the inoculation effect is enhanced by the increasing degree of supercooling ΔT and, consequently, the decreasing rod diameter.

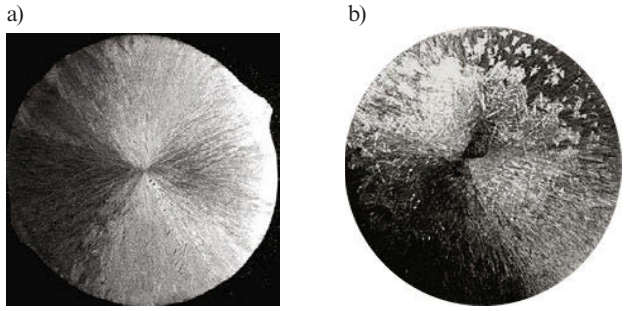

Figure 5. Macrostructure of high-chromium cast iron before (a) and after (b) the inoculation treatment with FeTi

Table 3. Austenite grains number and supercooling degree ΔT as a function of casting modulus

Rod diameter ϕ, mm	Cast iron before inoculation	Cast iron after inoculation
	Austenite grains number N, [N/cm^2]	
30	12	13
25	19	20
20	31	34

Figure 6 shows the macrostructure of eutectic chromium cast iron (Fig. 6a) and also the macrostructure of hypoeutectic cast iron (Fig. 6b), which contains the precipitates of the equiaxed grains of primary austenite demonstrating the properly conducted inoculation treatment.

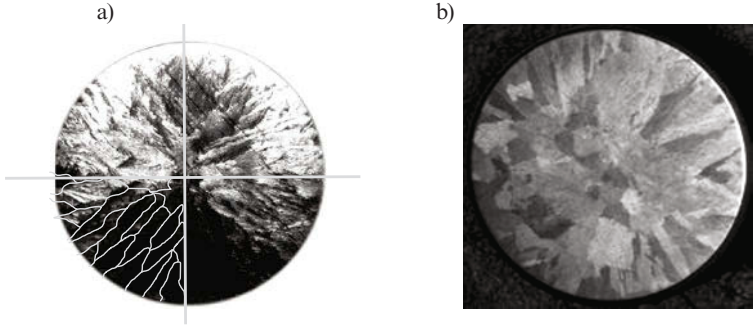

Figure 6. Disclosed as an example is the metallographic section of eutectic chromium cast iron showing the macrostructure of primary austenite grains obtained by special heat treatment with marked boundaries of columnar grains (a) and equiaxed grains of primary austenite visible in chromium cast iron sample (b)

Conclusions

From the obtained results it follows that it is possible to reveal the grains of primary austenite in chromium cast iron. Moreover, with the established correlation between the number of grains N and the estimated degree of supercooling ΔT, an equation can be derived which will allow predicting the effect of supercooling degree ΔT on the number N of primary austenite grains in chromium cast iron before and after the inoculation with Fe-Ti. Mechanical tests linked with the N = f (ΔT) equation will lead in the next stage of research to the development of a formula, which will account for the bending strength of base chromium cast iron and chromium cast iron inoculated with Fe-Ti.

Studies presented in this work allow predicting that the Fe-Ti inoculant introduced to molten metal will increase the abrasive wear resistance of high-chromium cast iron and the resistance of this cast iron to cracking. This is due to the refinement of cast iron microstructure, i.e. increasing the number of primary austenite grains and / or the number of the grains of carbide eutectic and / or reducing the interfacial (inter-carbide) distance. It is also worth noting that higher degree of structure refinement will be obtained in chromium iron castings with reduced wall thickness.

Acknowledgements

This work was supported by Polish NCBiR project.

References

1. R. Döpp, "Solidification and graphite formation in white cast iron", The Metallurgy of Cast Iron. Proceedings of the Second International Symposium on the Metallurgy of Cast Iron, Georg. Publ. Co. Geneva, Switzerland (1974).
2. E. Guzik, D. Kopyciński, "Modeling structure parameters of irregular eutectic growth modification of Magnin-Kurtz theory", *Metal. and Mat. Trans. A*, 37 (2006), 3057-3068.
3. E. Fraś, *The solidification of metals*, (WNT Warsaw 2003), 1-465.
4. J. Zhou, "Colour Metallography of Cast Iron" *China Foundry* 8 (2011), 447-462.
5. E. Fraś, D. Kopyciński, H. Lopez, "Processing and properties of high aluminium Fe-Al-C alloys". *Int. J. of Cast Met.*, 15 (2002), 9-14.
6. D. Kopyciński, M. Kawalec, A. Szczęsny, R. Gilewski, S. Piasny, "Analysis of the structure and abrasive wear resistance of white cast iron with precipitates of carbides", *Archives of Metal. and Mat.*, 58 (2013), 973-976.
7. D. Kopyciński, "The inoculation of white cast iron". *TMS 2013 (The Minerals, Metals & Materials Society). Published by John Wiley&Sons, Inc., Hoboken, New Jersey. Supplemental Proceedings* (2013), 601-608.
8. D. Kopyciński, E. Guzik, A. Szczęsny, "Equiaxed and oriented microstructure in high chromium cast iron", *Archives of Metal. and Mat.* 59 (2014), 723-727.
9. X.Wu, J.Xing, H.Fu, X.Zhi, "Effect of titanium on the morphology of primary M_7C_3 carbides in hypereutectic high chromium white iron", *Mat. Sci. and Engn. A,* 457 (2007), 180-185.
10. A. Studnicki, "Transmission electron microscope studies of the chromium cast iron modified at use of B_4C addition", *Archives of Foundry Engn.,* 10 (2010) 209-216.

Characterization of Minerals, Metals, and Materials 2016
Edited by: Shadia Jamil Ikhmayies, Bowen Li, John S. Carpenter, Jiann-Yang Hwang, Sergio Neves Monteiro, Jian Li, Donato Firrao, Mingming Zhang, Zhiwei Peng, Juan P. Escobedo-Diaz, and Chenguang Bai
TMS (The Minerals, Metals & Materials Society), 2016

CHARACTERIZATION OF IRRADIATED AND NON-IRRADIATED RUBBER FROM AUTOMOTIVE SCRAP TIRES

Clécia Moura Souza[1a], Leonardo G. Silva[2b]

[1]Instituto de Pesquisas Energéticas e Nucleares (IPEN/CNEN-SP)
Av. Professor Lineu Prestes 2242
05508-000, São Paulo SP, Brazil
[a]cleciamsouza@ymail.com
[b]lgasilva@ipen.br

Keywords: Rubber, Electron Accelerator, Irradiation, Scrap Tires

Abstract

The aim of this work was to characterize the samples of irradiated and non-irradiated rubber from automotive scrap tires. Rubber samples from scrap tires were irradiated at irradiation doses of 200, 400 and 600kGy in an electron beam accelerator. Subsequently, both the irradiated and non-irradiated samples were characterized by thermogravimetry (TG), differential scanning calorimetry (DSC), tensile strength mechanical test, and Fourier transform infrared (FTIR) spectrophotometry.

Introduction

Recycling process has become important to preserve natural resources, to avoid waste and prevent pollution of the rivers it would be harmful to the health, safety or welfare of the population. Recycling is the recovery of waste through a series of operations that allow processed material to be reused or to reduce the amount of virgin material used [1, 2].

Tires are one of the main components of the automotive to be considered by recycling process because they are the combination of raw materials, such as petroleum derivatives, natural rubber, steel and chemicals. The concentrations of natural rubber (BN), butadiene rubber (BR), styrene-butadiene rubber (SBR), vary according to the manufacturer and the end use. Several methods have been developed to solve the tires problem in Brazil. For example, they have been reused in various ways, as an alternative fuel for cement industry, the manufacture of shoes soles, rubber seal, rainwater pipes, for blocks courts, industrial floors, asphalt and rubber mats for automotive [3].

One of the most widely used elastomers in the manufacture of tires is SBR (styrene-butadiene copolymer) containing 25% by weight of styrene. Other kinds of rubbers used in the manufacture of tires are poly (cis-isoprene), which is natural rubber, and synthetic poly (cis-butadiene) [4].

Current legislation establishes that improperly disposed tires are environmental liabilities that may result in serious risk to the environment and public health. Also in accordance with this resolution, for each new tire sold to the aftermarket, the manufacturers or importers should dispose properly the waste tire.

The main problem faced by preserving environment is the management of waste polymeric materials before and after consumption such as production remains and used artifacts. Generally food packaging, bags, bottles and tires are the most materials founded in dumps, landfills, rivers, lakes every day without any control [5]. The rubber from automotive scrap tires tire is the subject of investigation of this current work.

Material and Methods

This current work was used granules and rubber powder from automotive scrap tires, density of 0.907g/cm^3 supplied by Reciclanip which is an institution responsible for the collection and disposal of scrap tires in Brazil. Rubber granules samples were prepared with2 mm for TG and DSC analysis. The mechanical tests were used powder of rubber from automotive scrap tires of 250 m and natural rubber matrix not vulcanized. Additives and accelerators were used for rubber samples vulcanization. The samples compositions were: zinc oxide, stearic acid, sulphur, MBTS: mercapto benzothiazol sulfenamide, TMTD: tetramethyl tiuran disulfides.

Thermogravimetry

The TG curves were obtained using the thermo balance model TGA-51 (Shimadzu) with the temperature range 25°C to 600°C, dynamic air atmosphere (50 mL/min), heating rate 10°C min^{-1} and Pt crucible containing approximately 5mg of sample. The TGA-51 equipment was calibrated according to ASTM (1582-04) and conducted by the measures conditions evaluation where it was used a standard of calcium oxalate monohydrate with 99.99% purity, origin Merck.

Differential Scanning Calorimetry (DSC)

DSC curves were obtained using the DSC cell model DSC-50 (Shimadzu), with dynamic N_2 atmosphere (50 mL/min) in the temperature range 25ºC to 550°C, heating rate 10°C min^{-1}. Al partially enclosed crucible containing approximately 2 mg of the sample. In additional, it was necessary to obtain blank curves in these experiments to evaluate the baseline system with the same conditions of the measures. However, it was not necessary to use the reference capsules sample. Because the cell DCS was calibrated using standard substances indium (T_m = 156.6°C; H_m = 28.7J/g) and zinc (T_m = 419.5°C) metal purity 99.99%.

Fourier Transform Infrared (FTIR) Spectrophotometry

Infrared spectra with Fourier transform infrared (FTIR) were registered in the Perkin Elmer, spectrometer, Spectrum model One, coupled with Universal device ATR ("Sampling Accessory"), employing solid samples and wavelength spectral range from 500 to 4000cm^{-1}. The equipment has a comparison program that allows correlate the spectral differences occurred between the samples analyzed.

Irradiation of samples

The samples were irradiated in air at room temperature with electron beam using an electron accelerator Dynamitron JOB 188 power 0,5 to 1,5MeV and 0,3 to 25mA current, and subjected to irradiation dose of 200kGy to 600kGy, at 22.39kGy/s dose rate.

Results and Discussion

Thermogravimetry

The results for non-irradiated and irradiated samples at doses of 200, 400 and 600kGy heated in air atmosphere showed different mass losses with temperature increase and the occurrence of several events (see Figure 1).

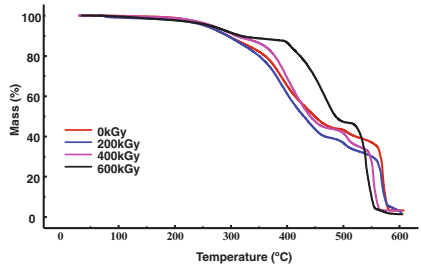

Figure 1. Thermogravimetric curves obtained in a dynamic atmosphere in air for automotive scrap tires samples at different doses.

Table I shows obvious changes of weight loss in the temperature ranges at varying irradiation doses.

Table I. Comparison in the percentage (%) of the weight losses of samples with temperature increase to 600ºC at different doses.

Dose (kGy)	Range of temperature (ºC)	Higher weight loss (%)	Total weight loss (%)	Residue (%)
0	530 – 599	36	96.9	3.0
200	518 – 599	36	97.1	2.8
400	471 – 599	41	97.8	2.1
600	382 – 599	86	99.6	1.3

Figure 2 and Table II present the TGA results for non-irradiated and irradiated samples under nitrogen atmosphere. The results showed the weight loss as a function of irradiation dose, with temperature increase.

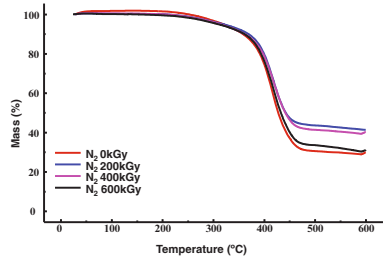

Figure 2. Thermogravimetric curves obtained in a dynamic atmosphere of N_2 for automotive scrap tires samples at different doses.

Table II. Comparison of percentage (%) of the weight losses of samples with temperature increase to 600ºC of the samples at different doses.

Dose (kGy)	Range of temperature (ºC)	Higher weight loss (%)	Total weight loss (%)	Resídue (%)
0	300 – 499	66	70.5	29.4
200	211 – 485	56	58.7	41.2
400	179 – 489	58	60.0	39.9
600	162 – 490	66	69.1	30.8

Differential Scanning Calorimetry

DSC curves show the thermal behavior of the rubber samples from automotive scrap tires. The component of the sample chemically reacts due to heat energy. It was observed that the peaks area it is proportional to the enthalpy involved in the reactions.

In the case of exothermic events, it is judged in the DSC heat flow. In general the difference TA (sample temperature) – TR (reference temperature) serves as the basis for heat calculation absorbed or released by the sample, and the result is positive ($\Delta T>0$) for exothermic events.

DSC curves obtained in dynamic N_2 atmosphere for automotive scrap tires samples non-irradiated, irradiated at dose of 200kGy, 400kGy, 600kGy show a peak at approximately 393ºC, 395ºC, 383ºC, 381ºC and another peak at approximately 435ºC, 439ºC, 437ºC, 435ºC, respectively.

It is revealed that the peaks observed in the DSC curves are exothermic because the energy produced in the process can be regarded as materials decomposition. The enthalpy was calculated from peak area in the temperature range.

Tensile Strenght Mechanical Test

Figure 3 shows the results of the percentage of maximum elongation at break for the samples without tire powder and with different percentages of 10, 30 and 50% of tires powder non-irradiated and irradiated with 200, 400 and 600kGy. Figure 3 shows a reduction in maximum elongation at break with irradiation dose increase. These results are shown in Table III.

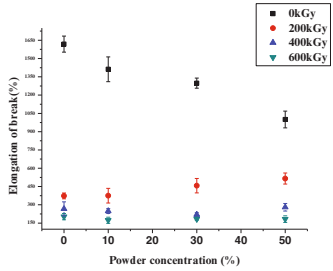

Figure 3. Variation of the maximum elongation at break of the non-irradiated and irradiated at doses of 200kGy, 400kGy and 600kGy with increasing concentration of tire rubber powder.

As shown in Figure 3, when comparing the samples without powder and samples with powder non-irradiated, sample without powder has a 1618% order behavior in maximum elongation at break while all other samples 10, 30 and 50% of powder had a loss at maximum elongation at break, 1411%, 1298% and 999% respectively. However for the samples non-irradiated can be possible to add 10 to 30% of rubber powder from automotive scrap tires for residue recovery purposes.

Table III. Maximum elongation at break (%) for samples without powder and with 10%, 30% and 50% of tire rubber powder irradiated and non-irradiated

Doses	0kGy	200kGy	400kGy	600kGy
Samples without powder	1618	372	267	202
Samples 10% powder	1411	374	248	173
Samples 30% powder	1298	456	219	183
Samples 50% powder	999	515	279	182

FTIR

Figures 4-6 show the FTIR spectra for beads samples automotive scrap tires non-irradiated and irradiated at doses of 200, 400 and 600kGy respectively.

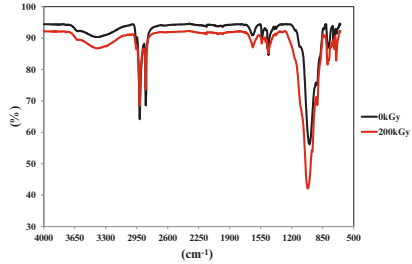

Figure 4. Absorption spectra in the infrared region for samples of automotive scrap tires non-irradiated and irradiated at a dose of 200kGy.

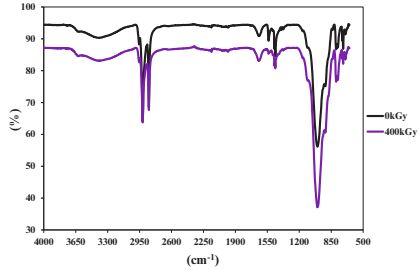

Figure 5. Absorption spectra in the infrared region for samples of automotive scrap tires non-irradiated and irradiated at a dose of 400kGy.

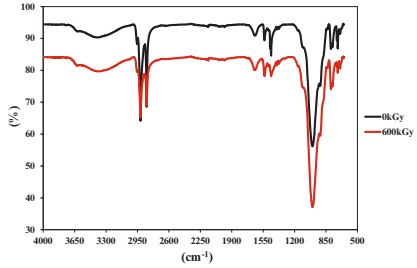

Figure 6. Absorption spectra in the infrared region for samples automotive scrap tires non-irradiated and irradiated at a dose of 600kGy.

These spectra show no changes and shifts of the peaks due to irradiation and it was not possible detect changes caused by irradiation for beads samples automotive scrap tires.

Conclusion

This study showed different weight losses with temperature increase for non-irradiated and the irradiated samples. From the results of the thermogravimetric curves obtained in the presence of air it can be concluded that in the non-irradiated and irradiated samples at different irradiation doses, there was a probable oxidation of the components of the rubber from automotive scrap tires in relation to the temperature increase. The thermogravimetric curves showed that various events occurred. These events occurred at different temperatures. It can be observed that there was a possible degradation when the samples were irradiated and the thermal behavior of the samples remained unchanged at each irradiation dose.

The granules rubber samples from automotive scrap tires when subjected and characterized by thermogravimetric analysis in nitrogen (N_2) have demonstrated a single event. It has not oxidation because it is an inert atmosphere, possibly with increasing radiation dose may have occurred changes in thermal behavior of the sample, but the thermal stability did not change with increasing irradiation dose.

Through the thermal evaluation of these samples, it can be seen that the thermal behavior varies according to each irradiation dose. The thermal behavior of the sample is a sum of the thermal degradation curves. However, increased temperature promotes not only the chemical reactions but also the fractions of volatilization of components. Besides, the differential scanning calorimetry, DSC, was adequate to determine the degradation behavior, and this degradation is different as irradiation doses.

In the mechanical tests maximum elongation at break was observed degradation with respect to all the irradiated samples when compared to non-irradiated. Therefore, for non-irradiated samples it is possible to add 10 to 30% of rubber powder from automotive scrap tires for residue recovery purposes.

Regarding FTIR spectra, it can be concluded that there was not changes and shifts of the peaks due to irradiation, that is, the technique lacks sensitivity to detect changes caused by the irradiation rubber samples from automotive scrap tires.

References

1. Eloisa B. Mano, *Meio Ambiente, Poluição e Reciclagem* (São Paulo, SP: Edgard Blücher, 2005), 101-111.

2. H. Wiebeck, W.M. Risso, and A.M. Piva, "Reciclagem de Plástico: Necessidade de Maior Incentivo," *Limpeza Pública,* 1(51) (1999), 20-24.

3. T.C. Billiter, "The Characterization of asphalt – rubber binder" (Ph.D. thesis, Texas University, 1996).

4. N.C. SEGRE, "Reutilização de borracha de pneus usados como adição em pasta de cimento" (Ph.D. thesis, Universidade Estadual de Campinas- São Paulo, 1999), 9-14.

5. Hélio Wiebeck, Fábio Esper, and Antônio Carlos Feijó, *Tecnologia da Borracha* (São Paulo, SP: Apostila da FUSP, Cooperação Universidade Empresa CECAE/USP, 2002).

Characterization of Minerals, Metals, and Materials 2016
Edited by: Shadia Jamil Ikhmayies, Bowen Li, John S. Carpenter, Jiann-Yang Hwang, Sergio Neves Monteiro, Jian Li, Donato Firrao, Mingming Zhang, Zhiwei Peng, Juan P. Escobedo-Diaz, and Chenguang Bai
TMS (The Minerals, Metals & Materials Society), 2016

PROPERTIES OF CERAMIC PIGMENT $Zn_{0.5}Cu_{0.5}Cr_2O_4$ SYNTHESIZED BY SOLUTION COMBUSTION METHOD

Edgar Andrés Chavarriaga Miranda[1], Juan Fernando Montoya Carvajal[1], Alex Arbey Lopera Sepúlveda[1], Juan Camilo Restrepo Gutierrez[1], Oscar Jaime Restrepo Baena[1]

[1]National University of Colombia. Faculty of Mines.
Street 59 A Number 63-20, Medellín, Colombia

Keywords: Ceramic pigment, spinel, solution combustion synthesis, color

Abstract

The present study reports the effect of the fuels: glycine, urea, and citric acid on the optical properties of ceramic pigment $Zn_{0.5}Cu_{0.5}Cr_2O_4$, synthesized by solution combustion. The powders were characterized by X-ray diffraction, which showed the formation of the expected phases. Scanning electron microscopy (SEM) was also used, and the images showed the formation of agglomerates and porous samples. Finally, VIS-spectroscopy, and CIEL*a*b* color-measurements showed the powders are black. The results demonstrated that the synthesis by the combustion reaction was very fast and safe, and that the heat released in the combustion reaction is a function of fuel, releasing more heat with glycine, and less with citric acid. It was observed that the powder is more black with urea and citric acid that with glycine. The optical properties showed that the powders could be used as ceramic pigments.

Introduction

Ceramic pigments are inorganic compounds, which are used in the ceramic industry in color decoration in ceramic bodies and ceramic glazes. The reason of using inorganic pigments is due to their present high thermal stability and are chemically stable in the melt with the compounds of the compositions of the ceramic products, such as tiles, porcelain enamel, pottery glazes. For this reason in the USA, the Color Pigments Manufacturers Association (CPMA) [1] have classified the structures used in the ceramic industry as pigments [2], in this classification the spinel structures present many color, such as red, blue, brown, yellow, and black.

Spinels are structures with chemical formula AB_2O_4, which has 64 tetrahedral sites and 32 octahedral sites, of which 8 tetrahedral sites and 16 octahedral sites are occupied by the cations A^{2+} and B^{3+}, respectively in spinels 2-3 [3]. Nowadays, there is a great interest to find a decrease in the concentrations of heavy metals chromophores of inorganic pigments, such as Co^{2+}, Ni^{2+}, Pb^{2+}, Sb^{2+}, Cr^{3+}, also to find new solid solutions with the same coloration [4], as well as to use routes of chemical synthesis that allow to obtain inorganic pigments with particle size between 10 and 500 nm [5], such as polymer precursor [6], solvothermal synthesis [7], aerosol pyrolisis [8] and solution combustion [9]. Among the above, the combustion solution synthesis is characterized by a simple experimental equipment [10] and for its short process times [11].

The aim of this research is to synthesize the ceramic pigment with spinel structure $Zn_{0.5}Cu_{0.5}Cr_2O_4$ using the method of solution combustion synthesis glycine-nitrate, urea-nitrate

and citrate-nitrate. The results show the possibility of using these powders for ceramic decoration.

Material and Methods

The ceramic pigment with spinel structure $Zn_{0.5}Cu_{0.5}Cr_2O_4$ was synthesized by solution combustion using glycine, urea, and citric acid as fuels. The stoichiometric composition of the metal nitrates, and the fuels is calculated based on the total oxidizing and reducing valences of the oxidizer (O) and fuel (F) which serve as numerical coefficients for stoichiometric balance so that the equivalence ratio (φ_e) is unity, O/F = 1, therefore, the energy released is at a maximum [12]. According to the concepts used in propellant chemistry, the elements C, H, Zn, Cu, Cr, or any other metal are considered as reducing elements with the corresponding valencies +4, +1, +2, +2 and +3 (or valency of the metal ion in that compound), respectively. The element oxygen is considered as an oxidizing element with the valency -2. The valency of nitrogen is considered to be zero. Accordingly, the oxidizing and reducing valencies of the compounds used in the combustion mixtures can be calculated [13]. In figure 1 is showed the flowchart of the solution combustion synthesis.

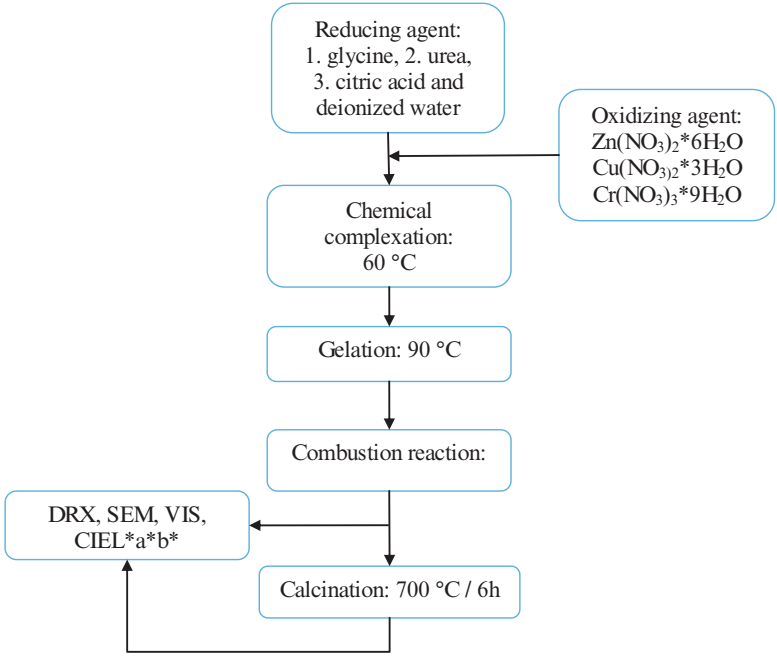

Figure 1. Flowchart of the solution combustion synthesis (SCS).

The amounts used in the synthesis for the three samples were as different fuels 5.73 g of NH_2CH_2COOH (Panreac, 99% of purity), 6.82 g of $(NH_2)_2CO$ (Carlo Erba, 98% of purity) and 7.93 g of $C_6H_8O_7*H_2O$ (Panreac, 99% of purity), in the case of oxidants the amounts were the same for the three samples 2.58 g of $Zn(NO_3)_2*6H_2O$ (Panreac, 98% of purity), 2.07 of $Cu(NO_3)_2*3H_2O$ (R-A Chemicals, 99% of purity) and 13.88 g of $Cr(NO_3)_3*9H_2O$ (Panreac, 98% of purity).

X-Ray Diffraction (XRD) studies of the samples as-prepared and calcined were carried out using a PANanalytical X'Spert Pro X-ray diffractometer, using Cu Kα radiation (0.15406 nm). The X-ray generator voltage was 45 kV and the tube current was of 45 mA, with scan step size 0.013° and step time of 1.0 s. The scanning was between 17° and 69° (2θ). The experimental diffractograms were interpreted with the help of High Score X'Spert program and were compared with the database of PDF (Powder Diffraction File) of ICDD (International Center of Diffraction Data).

The surface morphology of polycrystalline samples of the ceramic pigments $Zn_{0.5}Cu_{0.5}Cr_2O_4$ were analyzed by scanning electron microscopy (SEM) using a SEM - JEOL JSM 6701F. The operational voltages were 12 kV and 15 kV, and electricity current of 10 μA for generating images. The samples were subjected to high vacuum, and coated with a layer of gold to improve its electrical conductivity.

Analysis of visible diffuse reflectance and colorimetric coordinates CIEL*a*b* of the pigments were performed on a UV-VIS spectrophotometer Glacier™ X with spectral range 200-1050 nm. Colorimetric data were measured by combining object spectral data with data representing a CIE standard observer of 10° and a CIE standard illuminant D65 (day light). In this method, L* is the lightness axis [black (0) - white (100)], b* is the blue (-) and yellow (+) axis, a* is the green (-) and red (+) axis.

Results and Discussion

Figure 2 shows the XRD patterns of the polycrystalline powders as-prepared and calcined in air at 700 °C for 6 h. The powders as-prepared using glycine as fuel do not show the formation of pure phase $Zn_{0.5}Cu_{0.5}Cr_2O_4$, due to the presence of the characteristic peaks in 23.9° and 33.5° of the Cr_2O_3 (JCPDS 038-1479), which indicate that the temperature of combustion in less than the necessary for the formation of spinel structure, for this reason the samples were calcined at 700 °C for 6 h, the samples after show only the peaks of $Zn_{0.5}Cu_{0.5}Cr_2O_4$ (JCDPS 01-076-1566), which is a cubic crystal system with space group Fd3m, also increased the crystallization of the structure.

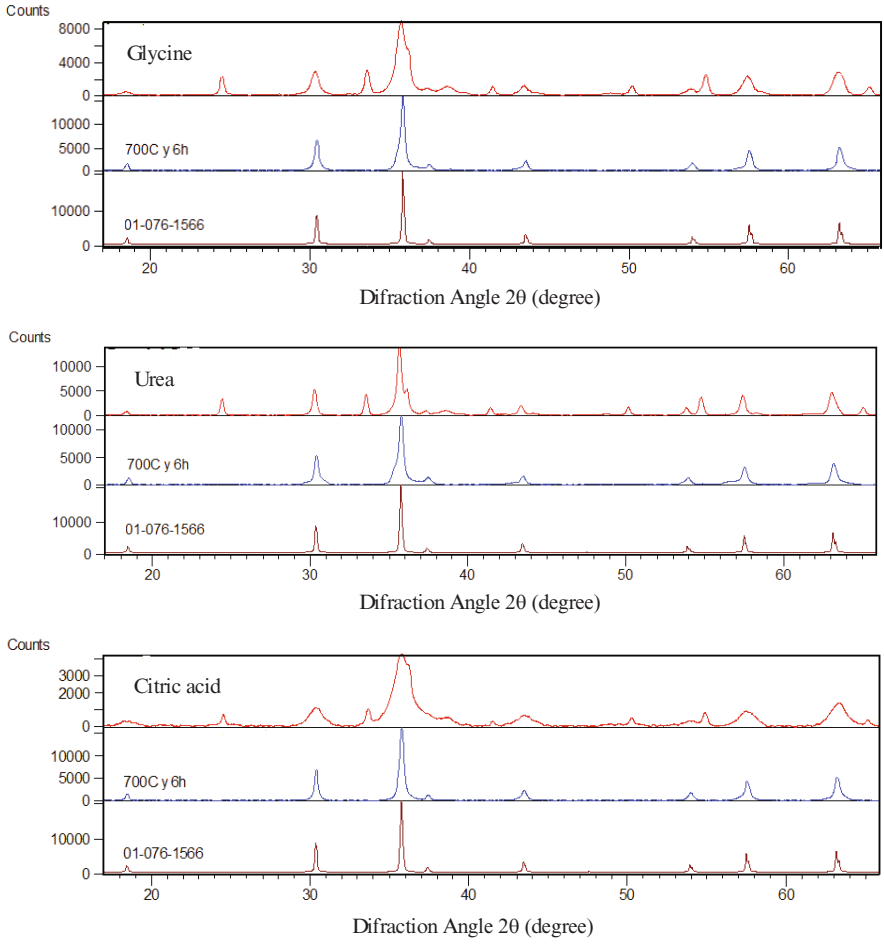

Figure 2. X-ray diffraction patterns for $Zn_{0.5}Cu_{0.5}Cr_2O_4$ obtained by glycine-nitrate, urea-nitrate and citrate-nitrate.

Figure 3 presents the SEM micrographs of the $Zn_{0.5}Cu_{0.5}Cr_2O_4$ obtained by solution combustion with the fuels glycine, urea, and citric acid, which reveal porous, and sponge-like morphologies of the samples, these characteristics are reported in the scientific literature for the solution combustion synthesis [14], this is due to evolution of the large amount of gaseous products during combustion, which produces highly porous voluminous powders, and these parameters dependent of fuel used in the synthesis. The glycine shows higher porous than urea

and citric acid. Therefore, these results indicate that a change in the fuel used in the synthesis lead to significant changes in the microstructure of the powders.

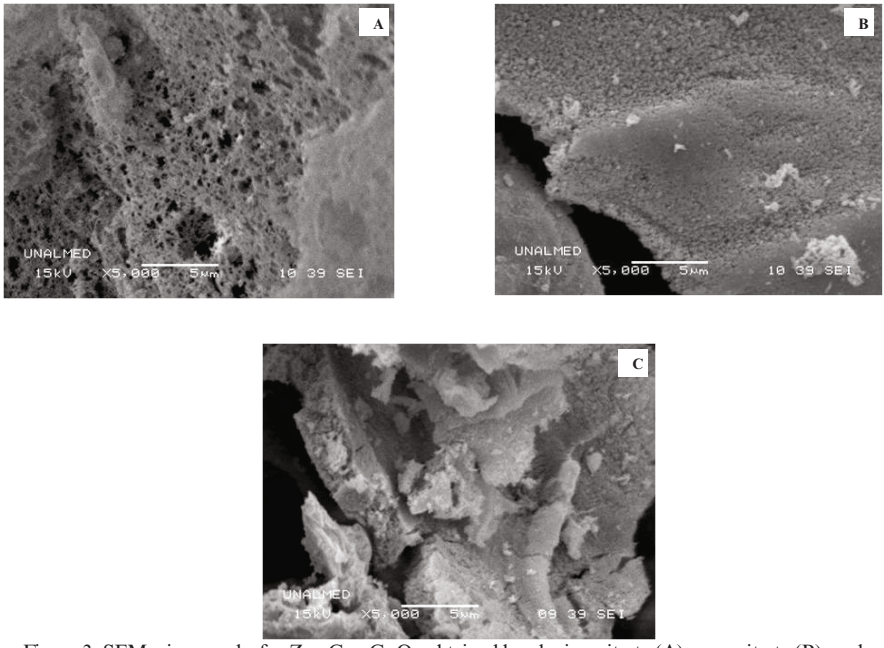

Figure 3. SEM micrographs for $Zn_{0.5}Cu_{0.5}Cr_2O_4$ obtained by glycine-nitrate (A), urea-nitrate (B), and citric acid-nitrate (C).

Figure 4 shows the diffuse reflectance factor spectra in the range of 400-700 nm of the powders $Zn_{0.5}Cu_{0.5}Cr_2O_4$ synthesized by solution combustion which were annealed at 700°C for 2h. The minima reflectance peaks between 420-430 nm and 580-600 nm can be assigned to $^4A_{2g} \rightarrow {}^4T_{2g}$ and $^4A_{2g} \rightarrow {}^4T_{1g}$ transitions of octahedral Cr(III) (d^3) ion, respectively, and the Cu(II) present absorption in the bands of 400-420 nm, 430-580 nm and 600-700nm, which indicate that samples are black because the energy absorbed is converted to heat through a mechanism of phonons.

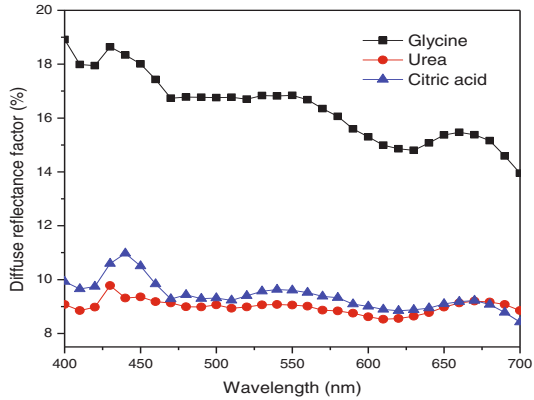

Figure 4. Visible spectrum of $Zn_{0.5}Cu_{0.5}Cr_2O_4$ powders calcined at 700 °C for 6 h for glycine-nitrate (A), urea-nitrate (B), and citric acid-nitrate (C).

Table I shows the colorimetric coordinates CIEL*a*b* of $Zn_{0.5}Cu_{0.5}Cr_2O_4$ obtained by solution combustion synthesis, the colorimetric coordinate L* shows a higher value when is used glycine as fuel, because the scattering of the light increases due to porosity of the powder, in another way the slower value when is used citric acid as fuel, the samples have low values in the colorimetric coordinates a* and b*, which indicate that samples are not chromatics.

Tabla I. Colorimetric coordinates CIEL*a*b* of the powders calcined at 700 °C and 6 h.

	Glycine	***Urea***	***Citric acid***
L*	47.470	35.844	36.706
a*	-0.939	-0.236	-0.030
b*	-3.511	-1.236	-2.110

The coordinates colorimetric for the three samples correspond with the results obtained with diffuse spectroscopy in the visible region.

Conclusions

The ceramic pigment $Zn_{0.5}Cu_{0.5}Cr_2O_4$ with spinel structure was synthesized by solution combustion synthesis using three different fuels: glycine, urea and citric acid. The color obtained was black, but the optical properties of the samples depend of the microstructure, which also depend of the type of fuel used, because the gases of the reaction were the responsible of porosity in the samples. The ceramic pigment could be used in the ceramic decoration.

References

1. M. Llusar et al., "Synthesis and coloring performance of Ni-geikielite (Ni,Mg)TiO_3 yellow pigments: Effect of temperature, Ni-doping and synthesis method," Journal of the European Ceramic Society, 35 (13) (2015), 3721–3734.
2. C. Provisions, "Classification and chemical descriptions of the complex inorganic color pigments" (Report CPMA/Color Pigments Manufacturers Association, 2013).
3. L. Desouza et al., "Blue pigments based on $Co_xZn_{1-x}Al_2O_4$ spinels synthesized by the polymeric precursor method," Dyes and Pigments, 81 (3) (2009), 187–192.
4. M. Llusar et al., "Stability and coloring properties of Ni-qandilite green spinels $(Ni,Mg)_2TiO_4$: the „half color wheel' of Ni-doped magnesium titanates," Dyes and Pigments, 122 (2015), 368–381.
5. M. Blosi et al., "Au–Ag nanoparticles as red pigment in ceramic inks for digital decoration," Dyes and Pigments, 94 (2) (2012), 355–362.
6. H.E. Sadek et al., "Nano $Mg_{1-x}Ni_xAl_2O_4$ spinel pigments for advanced applications," Spectrochimica Acta Part A: Molecular and Biomolecular Spectroscopy, 125 (2014), 353–358.
7. M. Jovaní et al., "Pigments based on Cr and Sb doped TiO_2 prepared by microemulsion-mediated solvothermal synthesis for inkjet printing on ceramics," *Dyes and Pigments*, 116 (2015), 106–113.
8. T.S. Lyubenova, J.B. Carda, and M. Ocaña, "Synthesis by pyrolysis of aerosols and ceramic application of Cr-doped $CaYAlO_4$ red–orange pigments," *Journal of the European Ceramic Society*, 29 (11) (2009), 2193–2198.
9. I. Mindru et al., "Copper aluminate spinel by soft chemical routes," *Ceramics International*, In press (2015).
10. S. Mestre, M.D. Palacios, and P. Agut, "Solution Combustion Synthesis of (Co,Fe)Cr_2O_4 pigments," *Journal of the European Ceramic Society*, 32 (9) (2012), 1995–1999.
11. Y. Zhang et al., "Preparation and characterization of pyrochlore oxide $Y_2Ti_2O_7$ nanocrystals via gel-combustion route," *Ceramics International*, 40 (4) (2014), 5223–5230.
12. Annelise Alves, Carlos Bergmann, and Felipe Berutti, *Novel Synthesis and Characterization of Nanostructured Materials* (Berlin: Springer-Verlag Berlin Heidelberg, 2013), 78.
13. K.C. Patil et al., *Chemistry of nanocrystalline oxide materials combustion synthesis, properties and applications* (Singapore: World Scientific Publishing Co. Pte. Ltd, 2008), 337.
14. M.C. Merino et al., "Combustion Syntheses of $CoAl_2O_4$ Powders Using Different Fuels," *Procedia Materials Science*, 8 (2015). 519–525.

Characterization of Minerals, Metals, and Materials 2016
Edited by: Shadia Jamil Ikhmayies, Bowen Li, John S. Carpenter, Jiann-Yang Hwang, Sergio Neves Monteiro, Jian Li, Donato Firrao, Mingming Zhang, Zhiwei Peng, Juan P. Escobedo-Diaz, and Chenguang Bai
TMS (The Minerals, Metals & Materials Society), 2016

EVALUATION OF ENVIRONMENTAL AGING OF POLYPROPYLENE IRRADIATED VERSUS PRISTINE

Rebeca S. Grecco Romano[1], Washington Luiz Oliani[1], Duclerc Fernandes Parra[1], Ademar Benevolo Lugao[1]

[1]Nuclear and Energy Research Institute, IPEN-CNEN/SP, Av. Prof. Lineu Prestes, 2242 – Cidade Universitária – CEP 05508-000, São Paulo – SP – Brazil

Keywords: Polypropylene, Gamma Irradiation, Environmental Aging

Abstract

Polypropylene (PP) is the most common thermoplastic resin of the plastic market due to its very interesting physical, chemical and processing properties at very low market price, however after its use the resin does not degrade in the environment or it degrades at very low rate. This study has the objective of comparing the environmental exposure of PP irradiated with 20 kGy and pristine PP. Dumbbell samples were manufactured by injection molding and exposed to the environment during 90 days; another one set was subjected to gamma irradiation at 20 kGy total dose and exposed at the same conditions too. The samples were characterized by mechanical testing, visual inspection, infrared spectroscopy (IR), scanning electron microscopy (SEM) and differential scanning calorimetry (DSC). The irradiated samples, after environmental aging, showed oxidation and presence of cracks in samples of the PP 20 kGy.

Introduction

Polypropylene is a thermoplastic polyolefin obtained by polymerization of propylene monomer. PP is of great importance to the market due to its versatility, easy processing, and good mechanical properties, at very low market price and up to 20% lighter than other polymers [1]. The structural changes, typically chain scission and crosslinking, induced by ionizing radiation cause changes in the physical properties of irradiated polymers. Although the degradation reactions of the type crosslinking or chain scission occur simultaneously during irradiation of the polymer, one of these processes is generally dominant, depending on the chemical structure of the polymer, dose, dose rate, type of radiation and the conditions of the environment (pressure and temperature) in which the material is irradiated. The primary process due to irradiation of the polymer is the generation of excited species and free radicals resulting from the breakage of chemical bonds [2, 3]. Environmental aging is widely used in research and industrial assessment and strictly depends on geographical variables and atmospheric exposure conditions. Reasons for degradation may result from the combination of these variables such as heat, ultraviolet light, moisture, oxygen and pollutants. PP is a sensitive polymer due to the presence of tertiary carbon in their structure and suffers the effects of degradation and alteration of mechanical and aesthetic properties [4-7]. The energy to break the tertiary carbon may also be provided by gamma irradiation, which will modify the chemical structure of the polypropylene by increasing the content of carbonyl and hydroxyl groups suggesting the occurrence of oxidative degradation [8].

Disruptions in tertiary carbon may form macroradicals by P•. From that macroradicals, oxygen will interact with it and will form peroxide which is represented by POO•. Still

in the macromolecule there is the presence of macroradicals because there might be other points where that may have occurred formation of peroxides. At first, the oxygen interacts with the methyl radical, and in a second moment it can interact with hydrogen forming a hydroperoxide represented by POOH. The energy of the O-O bond hydroperoxide is very low and hydroperoxides may decompose at room temperature. Thermolysis at room temperature may break this bond quite easily. The termination or interruption of autocatalytic cycle may occur by recombination of two free radicals [9].

When the polymer is irradiated in an environment with oxygen like air, oxidation takes place promoting chain scission with formation of free radicals [10]. The irradiation dose will determine the initial content of free radicals formed, oxidation will follow and will be a function of time and temperature, influencing the occurrence of chain scission or crosslinking. The greater or lesser mobility of macro radicals formed will hinder or promote recombination. The association of radiation with warming will increase the mobility of free radicals and reduce the recombination [11]. The effects of ultraviolet radiation in the PP mechanical behavior have been reported by several authors. It is noted in general, a drastic reduction in the mechanical properties, attributed to the fact that oxidative reactions that lead to chain scission especially in the region of the molecules that participate in more than one crystalline lamellae which together with the formation of surface cracks causes great deterioration in strength [12]. Previous studies on the photodegradation of polyolefins showed that the tensile strength starts to fall drastically from 42 days of natural exposure [13]. In the case of PP 30 kGy and then exposed to the environment the study showed that the tensile strength decreases with time during the exposure period of 60 days, so the study showed that the PP exposed to environmental degradation is accelerated by irradiation [14]. The PP degradation and its variations showed that with the natural aging PP increases the crystalline fraction during the exhibition and the High Melt Strength Polypropylene (HMSPP) 20 kGy seems to be more stable to the chain scission reactions despite the irregularity of appearance during exhibition as it relates to UV radiation. Regarding the mechanical tests the samples HMSPP 20 kGy, initially showed maximum tensile values at breakage compared to the PP, but at the end of the natural aging it was found values lower than the PP, so there was loss of maximum stress at breakage in HMSPP samples that differed in PP at the beginning [15,16].

Study on the effects of accelerated thermal aging on polypropylene modified by irradiation process showed that aging on PP and HMSPP causes the intense cracks formation. Chain scission and oxygen diffusion were more evident in the PP as concluded by Oliani et al. [17]. Surface cracks propagation showed increases with the aging time. The results indicated that PP suffered greater thermooxidative degradation and chain scission than HMSPP 12 kGy and HMSPP 20 kGy. During the process of irradiation, the ionizing radiation permits the formation of reactive sites which may modify chains of the polypropylene [18].

The main objective of this paper was to study the degradation of polypropylene irradiated at 20 kGy using gamma radiation and compares the effect of environmental aging with pristine PP.

Materials and Methods

Materials

The isotactic polypropylene (iPP) pellets that were used are supplied by Braskem, suitable for injection with Melt Flow Index of 3.5 dg min^{-1}, density of 0.905 g cm^{-3}, M*w* = 300,000 g mol^{-1}, and pristine (without factory additives) polypropylene.

Methods

The PP dumbbell samples that were used in this study were manufactured by injection molding process. The Injection Molding Machine model used for manufacturing samples ROMI PRIMATE 65-R. The PP were irradiated by gamma rays at dose of 20 kGy, in an irradiator with ^{60}Co source, at dose rate of 5 kGy h^{-1}.

Scanning Electron Microscopy

Specimens were coated with gold in a sputter coater prior to examination to avoid charging. The EDAX Philips XL30 SEM was used for collecting secondary electron images from the samples.

Fourier Transform Infrared Spectroscopy

The FTIR was carried out with a Thermo Nicolet 6700 FTIR spectrometer with a Smart Orbit accessory, in the wavelength range 4000 to 400 cm^{-1}. In order to ensure satisfactory contact between the ATR diamond crystal and the sample, three or more FTIR spectra were recorded at various locations on the sample.

Differential Scanning Calorimetry

Assays were performed in equipment Mettler Toledo 822 DSC in a nitrogen atmosphere. The program was used: heating 50-280 ºC for 10 ºC min^{-1}, keeping at 280 ºC for 5 minutes, cooling from 280 to -50 ºC at a rate of -5 ºC min^{-1} and reheating -50 to 280 ºC at a rate of rewarming 10 ºC min^{-1}. The samples were weighed and placed in crucibles with aluminum caps ASTM D 3418-08 [19].

Tensile strength at breakage

Tensile strength at breakage analyses were accomplished according to ASTM D-638-14 [20], by using type I specimen, in an essay universal Instron machine-model 5567-of 300 kN maximum capacity and 500 mm min^{-1} grips speed, under a strain rate of 0.17 s^{-1} at room temperature.

Results

The samples were exposed in an environmental aging device in which a North position 45º, according to ASTM D 1435-05. Geographical position: Latitude (23º 33º South) Longitude (46º 44º West) and Altitude (750 meters) [21]. Figure 1 shows how this was done.

Figure 1. Device with dumbbell samples for environmental ageing exposed outside at the polymer processing laboratory IPEN/CQMA.

Scanning Electron Microscopy

Figure 2 shows SEM results for the PP and irradiated PP to 20 kGy over 30, 60 and 90 days of environmental aging.

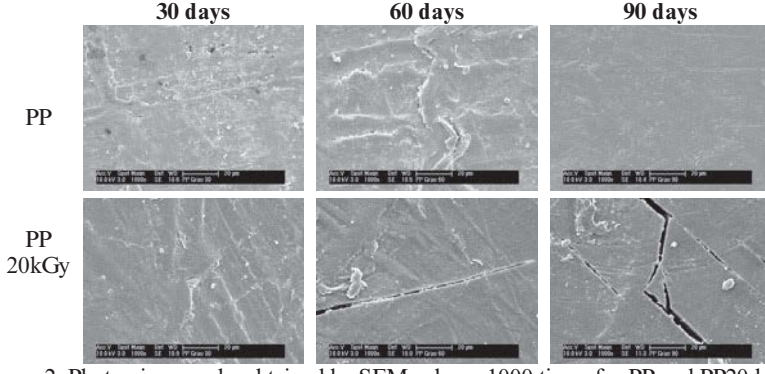

Figure 2. Photomicrographs obtained by SEM enlarge 1000 times for PP and PP20 kGy.

The effect of UV radiation (chain scission), in the irradiated PP 20 kGy, was more intense and the pictures showed cracks formation. Surface cracks increased with the aging time. The figures showed the appearance of cracks and fissures in the samples of 60 and 90 days environmental aging. The SEM analysis, Figure 2 shows interesting aspects of the fractured surface of the materials as a result of the process of chain scission. The cracks are more pronounced in the irradiated PP 20 kGy, than PP. A possible explanation for this fact is the gamma irradiation accelerated the degradation due to the appearance of free radicals. However in the PP with stabilizers at the end of the end 90 days was not noted cracks or fissures [22].

Fourier Transform Infrared Spectroscopy

FTIR spectra of the samples exposed in the environmental aging, Figure 3.

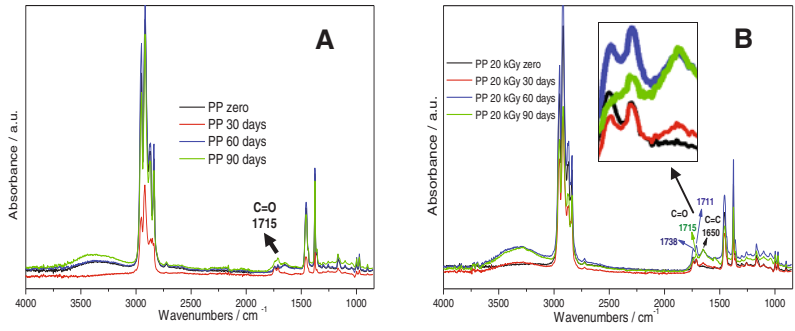

Figure 3. Infrared spectra: (A) PP and (B) PP 20 kGy.

When PP is exposed to UV radiation in air, the energy absorbed by the polymer results in free radicals formation followed by oxidation. Radical reactions with the oxygen generated oxidative and decomposition products specially carbonyl groups (C=O). In Figure 3, it was observed an absorption peaks attributed to stretching of carbonyl group at 1715 cm^{-1} and deformation of C=C from unsaturated groups at 1650 cm^{-1}. In Figure 3, these groups are of relative low intensity. In Figure 3B the absorption bands at around 1715cm^{-1}, indicating the presence of carbonyl unsaturated groups of higher intensity. It was observed relative higher intensity in those irradiated PP samples that characterized the oxidative degradation of the material. Peaks attributed to C=C absorption at 1650 cm^{-1} of the double bonds are common of early periods of the degradation as indicated in the literature [23-25].

Differential Scanning Calorimetry

DSC technique was applied to evaluate the temperatures of second melting (Tm_2) and the degree of crystallinity (X_c). Table I and Figure 4 show the values.

Table I. Melting temperature of samples and the degree of crystanillity.

	T_{m2} /°C (±0.1%)				X_C/% (±0.5%)			
Time / Samples	zero	30 days	60 days	90 days	zero	30 days	60 days	90 days
iPP	162.2	161.9	161.7	161.7	50.2	49.8	49.6	45.1
PP 20kGy	160.3	159.5	151.3	159.1	48.5	44.4	47.7	52.7

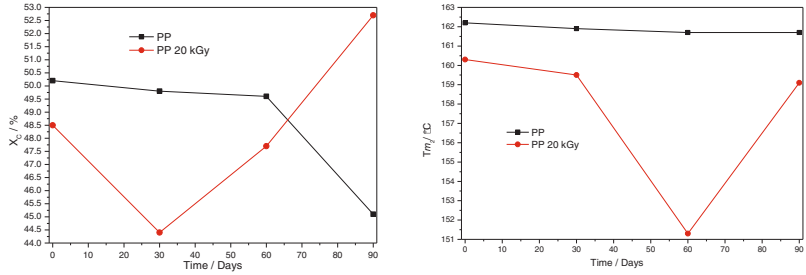

Figure 4. Polypropylene crystallinity (A), and Melting temperature (B) of samples PP and PP 20 kGy.

The DSC results showed small changes in crystallinity and melting temperature, while the polymer morphology had not undergone significant changes. It is known that when the PP exposed to UV radiation, there is a decrease of its molecular weight, due to presence of carbonyl groups (identified in Figure 3), indicating a probable increase in the number of chain scission events, especially in the cases of short-term exposure, wherein the chain scission effect dominates on morphological irregularities, thus justifying the increase of crystallinity and the melting temperature decreasing [26].

More prolonged exposure, 90 days of the PP plates, decreased the crystallinity. This can be attributed to defects in macro chains derived from photooxidation such as the carbonyls, and hydroperoxides compounds, Figure 3A. Chemical reactions that occur during the PP photodegradation can lead to chain scissions and carbonyl group formation, observed in sample of the PP 20 kGy in 90 days. The oxidation reactions occur predominantly in the amorphous phase where oxygen can be accessed easily. During the photodegradation process new imperfect crystals are formed due to the chemicrystallization in the crystal phase. The increased crystallinity in the sample PP 20 kGy at 90 days, could be attributed to the recombinations of the radicals in the more ordered forms, and to chemicrystallization.

Tensile Strength

The mechanical testing is an important method to evaluate the changes in properties and correlate them with structural modifications from degradation such as crosslinking and chain scission. Each result of Tensile strength at break was an average of eight measurements. Figure 5A shows the results of tensile strength at break results from zero to 90 days and figure 5B shows tensile strength at break versus strain at break.

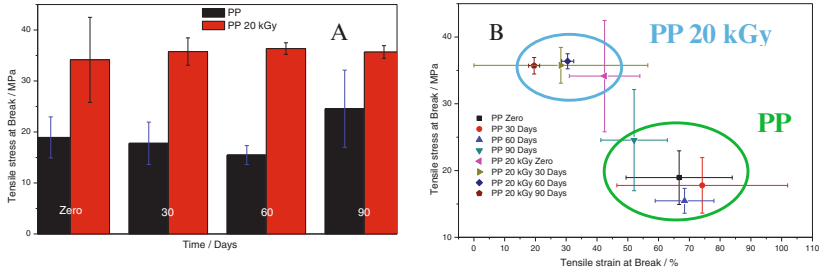

Figure 5. Results of tensile strength at break (A), and tensile strength at break versus strain break (B) of samples PP and PP 20 kGy.

Polyolefins rapidly lost most of their mechanical properties after severe exposure to heat and light. The irradiated samples showed higher tensile stress at break as presented in Figure 5B. This result can be explained by the crosslinking formation caused by irradiation but also by induced crystallization by chain scission.

Conclusion

The appearance of cracks and fissures as well as the presence of carbonyl groups were explained as results of oxidative reactions after environmental aging. Mechanism of chain scission are competitive and identified as displacement on melting temperature and chemicrystallization. Moreover, SEM results showed clearly that PP 20 kGy suffered more intense degradation than PP.

Acknowledgments

The authors acknowledge CAPES for supported the project, and Centre of Science and Technology of Materials – CCTM-IPEN, for microscopy analysis (SEM), the technician Eleosmar Gasparin for technical support and multipurpose gamma irradiation facility at the CTR-IPEN.

References

[1] A. P. Cavalcante, L. B Canto, *"*Uso de resíduo industrial a base de resina fenólica como carga para o polipropileno," *Polímeros*, 22(2012), 3, 245-252.

[2] Z. Stojanovic, Z. Kacarevic-Popovic, S. Galovix, D. Milicevic, E. Suljovrujic, "iPP changes crystallinity and the melting behavior of uniaxially oriented exposed to high doses of gamma radiation," *Polymer Degradation and Stability,* 87(2005), 279-286.

[3] A. G. Osinkolu. "The gamma irradiation, modification induced property of polypropylene," *International Journal Physics Science*, 5(2010), 7, 960-967.

[4] F. Gugumus, "Effect of temperature, on the lifetime of stabilized and unstabilized polypropylene films,*" Polymer Degradation and Stability*, 63(1999), 40-53.

[5] P. A. Santos, "Avaliação do Efeito Pró-Oxidante no PP, em Blendas com PHB,". *Polímeros*, 23(2013), 3, 432-439.

[6] M. A. De-Paoli, "Degradação e estabilização de polímeros," (São Paulo, Artliber Editora, 2008), 43-68.

[7] D. M. Wiles, G. Scott, "Polyolefins with controlled environmental degradability," *Polymer Degradation and Stability*, 91(2006), 1581-1592.

[8] B. Keene, M. Bourham, V. Viswanath, H. Avci, R. Kotek, "Characterization of degradation of polypropylene nonwovens irradiated by gamma rays," *Journal of Applied Polymer Science,* 131, 4(2014), 39917, 1-10.

[9] Hans Zweifel, *"Stabilization of Polymeric Materials,"* (Berlin, Springer-Verlag, 1998), 1-156.

[10] H. Otaguro , L. F. C. P. Lima, D. F. Parra, A. B. Lugao, M. A. Chinelatto, S.V Canevarolo, "High-energy radiation forming chain scission and branching in polypropylene," *Radiation Physics and Chemistry*, 79(2010), 318-324.

[11] W. K. Busfield, T. Morley-Buchanan, P. J. Pomery, "Post-gamma-irradiation grafting of polypropylene. Part II. Butadiene: ESR Experiments," *Journal of Polymer Science. Part A-1. Polymer Chemistry,* 24(1986) 3089-3099.

[12] A. V. Shyichuck, D. Y. Stavychna, J. R. White, "Effect of tensile stress on chain scission and crosslinking, during photo-oxidation of polypropylene," *Polymer Degradation and Stability",* 72(2001), 85-279.

[13] J. M. F. Guilhermino, J. A. B dos Santos, M. S. Rabello, "Avaliação da fotodegradação de poliolefinas através da exposição natural e artificial," *Química Nova*, 29(2006), 674-680.

[14] F. Yoshi, G. Meligi, T. Sasaki, K. Makuiuchi, A. M. Rabie, "Effect of irradiation on the degradability of polypropylene in the natural environment," *Polymer Degradation and Stability,* 49(1995), 315-321.

[15] W. L. Oliani, D. F. Parra, A. B. Lugao, "UV stability of HMS-PP (high melt strength polypropylene) obtained by radiation process," *Journal Radiation Physics and Chemistry,* 79(2010), 383-387.

[16] L. G. H. Komatsu, W. L. Oliani, D. F. Parra, A. B. Lugao, "Environmental ageing of irradiated polypropylene/montmorillonite nanocomposites obtained in molten state," *Journal Radiation Physics and Chemistry,* 97(2014), 233-238.

[17] W. L. Oliani*,* A. B. Lugao, D. F. Parra, "Effects of accelerated thermal aging on polypropylene modified by irradiation process,*" 2015 - TMS - Characterization of Minerals, and Materials*, (2015), 651-658.

[18] A. B. Lugao, "Estudos da Síntese por Irradiação, da Estrutura e do Mecanismo de Formação de Polipropileno com Alta resistência do Fundido," (PhD thesis, São Paulo University, 2004), 95-147.

[19] ASTM D 3418-2008 – Standard Test Method for Transition Temperatures of Polymers by Differential Scanning Calorimetry (DSC).

[20] ASTM D 638-2014 – Standard Test Method for Tensile Properties of Plastics.

[21] ASTM D 1435-05 – Standard Practice for Outdoor Weathering of Plastics.

[22] A. Yoshiga, D. F. Parra, H. Otaguro, L. F. C. P. Lima, A. B. Lugao, "Controlled degradation and crosslinking of polypropylene induced by gamma radiation and acetylene," *Polymer Bulletin*, 63(2009), 397-409.

[23] A. Rivaton, D. Lalande, J. L. Gardette, "Influence if the structure on the gamma irradiation of polypropylene and on the post-irradiation effects," *Nuclear Instruments and Methods in Physics Research B*, 222(2004), 187-200.

[24] M. Sclavons, M. Laurent, J. Devaux, V. Carlier, "Maleic anhydride-grafted polypropylene: FTIR study of a model polymer grafted by ene-reaction," *Polymer* 46 (2005), 8062-8067.

[25] J. R. Silvano, S. A. Rodrigues, J. Marini, R. E. S. Bretas, S. V. Canevarolo, B. M. Carvalho, L. A. Pinheiro, "Effect of reprocessing and clay concentration on the degradation of polypropylene/montmorillonite nanocomposites during twin screw extrusion," *Polymer Degradation and Stability*, 98 (2013) 801-808.

[26] M. S. Rabello, J. R. White, "Crystallization and melting behavior of photodegraded polypropylene – I. Chemi – crystallization," *Polymer* 48(1997), 6379-6387.

Characterization of Minerals, Metals, and Materials 2016
Edited by: Shadia Jamil Ikhmayies, Bowen Li, John S. Carpenter, Jiann-Yang Hwang, Sergio Neves Monteiro, Jian Li, Donato Firrao, Mingming Zhang, Zhiwei Peng, Juan P. Escobedo-Diaz, and Chenguang Bai
TMS (The Minerals, Metals & Materials Society), 2016

INTERFACE REACTION BETWEEN Y_2O_3 DOPED $BaZrO_3$ AND TiNi MELT

Cheng Zhiwei[1], Meng Fanlong[1], Chen Guangyao[1], Li Zheng[1], Lu Xionggang[1,2] and Li Chonghe[1,2]
1. State Key Laboratory of Advanced Special Steel, Shanghai 200072, China
2. Shanghai Special Casting engineering technology research centre, Shanghai
Email: chli@staff.shu.edu.cn

Keywords: Titanium alloy; isostatic pressing; melt; interface reaction

Abstract

Using the solid reaction method, the Y_2O_3 4mol%-doped $BaZrO_3$ powder was prepared by $BaCO_3$, ZrO_2 and Y_2O_3 as raw materials, the effect of sintering temperature on the property and microstructure of Y_2O_3-doped $BaZrO_3$ pellets was investigated, the crucible made of this Y_2O_3-doped $BaZrO_3$ was utilized to melting the TiNi alloy by the vacuum induction method. The phase constitution of doped powder and the interface reaction between the crucible and the melt were studied by XRD and SEM. The results showed that this Y_2O_3-doped $BaZrO_3$ consists of two phase ($BaZrO_3$ and Ba_2YZrO_6), the pellets sintered at 1750℃ for 6h reached the maximum relative density of 98.0%. Besides, there was no obvious interaction layer and element diffusion between the crucible and the melt, which may imply that the Y_2O_3-doped $BaZrO_3$ refractory is a promising candidate for melting titanium alloys.

Introduction

Titanium alloys were widely applied in various industrial fields, such as weaponry, aviation, aerospace, chemical, medical .etc, because of their excellent performance, such as low density, high specific strength, non-magnetic and high temperature mechanical properties[1,2]. However, as titanium and titanium alloys can react chemically with almost all of the refractory in the molten state, they should be melted with the inert protective gas atmosphere, resulting in the increasing of difficulty and cost with melting titanium and titanium alloys. With the development of technology, preparation of titanium was also in constant development and improvement stage.

Currently, water-cooled copper crucible melting process was widely used in titanium alloy melting. But it had high energy consumption and increased the production costs. At the same time, this process made titanium organization serious segregation and affected the performance of titanium alloy because of the non-uniform thermal field. The researchers found that vacuum induction melting technology can reduce the cost of production, and vacuum induction furnace

had a strong electromagnetic stirring, keeping the alloy melt a high degree of superheat, which was conducive to the elimination of segregation to obtain uniform composition of titanium[3]. With the proviso, there must be a material that had no interfacial reaction with titanium melt[4]. Crucible materials used for melting titanium alloys were mainly of graphite, oxides[5], BN[6] and so on currently. In addition, according to the research of Zhang Zhao[7], the stability of refractory still needed to be improved.

The structure of $BaZrO_3$ is cubic perovskite, the melting temperature and lattice constant are 2700℃ and 0.4193nm, respectively. It was an ideal crucible material for the preparation of high-quality single-crystal YBCO superconducting because of its low thermal conductivity, excellent mechanical properties and structural stability[8]. The Y_2O_3 belongs to the cubic crystal system, and it was a good transparent ceramic material and infrared material due to its excellent heat resistance, corrosion resistance and high temperature stability [9,10]. In present, Y_2O_3 as doping agent, such as Y_2O_3-doped ZrO_2, was also widely used, which is remarkable to the researchers due to its high chemical thermal stability, high strength, etc [11]. Meanwhile, the Y_2O_3-doped $BaZrO_3$ was also widely utilized as proton conductor in the electrolyte material with solid fuel cell [12-14]. However, using the Y_2O_3-doped $BaZrO_3$ for melting titanium alloys, as the refractory, was reported rarely.

In this paper, the powder of Y_2O_3-doped $BaZrO_3$ was prepared by solid phase synthesis, and then its constituent was analyzed by X Ray Diffraction (XRD). The crucible made of this Y_2O_3-doped $BaZrO_3$ was utilized for melting the TiNi alloy by the vacuum induction method. The interface reaction between the crucible and the melt were studied by scanning electron microscope (SEM) and point scanning technology (EDS).

Experimental

Preparation of Powder

The powder was prepared by industrial-grade $BaCO_3$ (purity> 99.0%), ZrO_2 (purity> 99.2%) and Y_2O_3 (purity> 99.0%) with a molar ratio of n ($BaCO_3$): n (ZrO_2): n (Y_2O_3) = 1: 1: 0.04, and the TiO_2 (0.5%) was added into the powder as a sintering aid. Then the powder was sintered at 1400℃ for 12 hours.

Preparation of pellets

The powder was pressed into pellets, and then sintered at 1550℃, 1650℃ and 1750℃ for 6h respectively.

Preparation of crucible

The crucible mold compacted with the powder was placed inside cold isostatic press at 140MPa for 3min, and the green body of crucible was prepared. Then the green body was pre-sintered at 900℃ for 3h to remove the organic compounds and to achieve bisques with much higher mechanical strength. Finally, the sintering process was carried out at 1750℃ for 6h.

Melting experiment

The TiNi alloy (50g) was placed into the homemade crucible and was melted in a WZG-2 type vacuum induction melting furnace. Before the melting process, the alloy bar was polished, cleaned and dried, and then it was melted in the homemade crucible with a certain proportion under a dry argon atmosphere at 0.06Mpa. Before the heating cycle, vacuum degree within the furnance was evacuated up to less than 10^{-2} pa, and then the furnance was backfilled with argon 3 times in order to reduce the oxygen content to a minimum level. When the alloy bar was completely melted, the melted-alloy was held at the superheating temperature of 1400℃ for 60s to get chemical homogenization. Sample was prepared after cold set, cutting, rough grinding, fine grinding and polishing. The scanning electron microscopy (SEM) was used for evaluating the surface topography and microstructure of the sample, and the energy dispersive spectroscopy (EDS) was used for analyzing the chemical composition of the sample.

Characterization

The powder, after solid phase synthesis reaction, was analyzed by D/Max - 2200-type X-ray diffraction. The density of pellets after sintering was measured by the AccupycII1340 density tester. The morphology of ceramic surface and interfacial reaction layer was observed by JSM-6700F scanning electron microscope with the energy spectrum analysis.

Result and discussion

Phase analysis of powder

The XRD spectra of the synthesized powder (1400℃，12h). As shown in Figure 1.

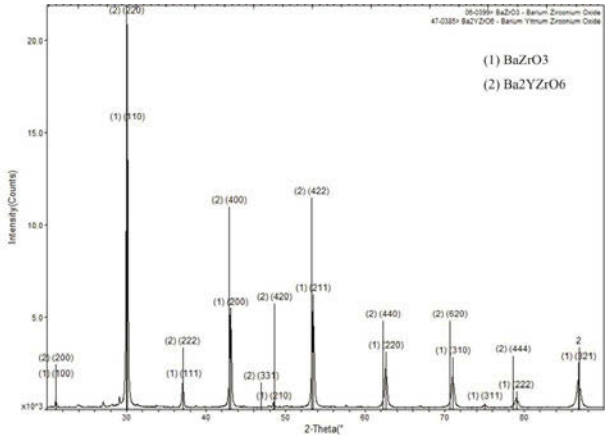

Fig. 1 XRD patterns of Y_2O_3-BaO-ZrO_2 composite powder synthesized at 1400℃

Figure 1 showed the phase composition of the synthesized powder, mainly Ba_2YZrO_6 and $BaZrO_3$ phases, and no diffraction peak of Y_2O_3 existed, which indicated that the Y_2O_3 doped had been reacted with $BaZrO_3$, and Ba_2YZrO_6 was synthesized.

Pellets analysis

It was pointed out that the relative density of the ceramic had a great influence on the quality of the melt [15]. In this experiment, pellets were divided into three groups (sample a, sample b and sample c) and were sintered at 1550℃, 1650℃, 1750℃ for 6h respectively. Then their densities were measured. As shown in table 1. The relative density of the sample 3 was up to 98%, and this sintering process can be used in the preparation of crucible.

Table 1 Density of pellets prepared under different temperatures

Sample No.	Temperature/ ℃	Density /(g·cm^{-3})	Relative density/%
a	1550	5.950	95.5
b	1650	6.074	97.3
c	1750	6.105	98.0

Figure 2 shows the SEM photo of the pellet sintered at 1750℃ for 6h.

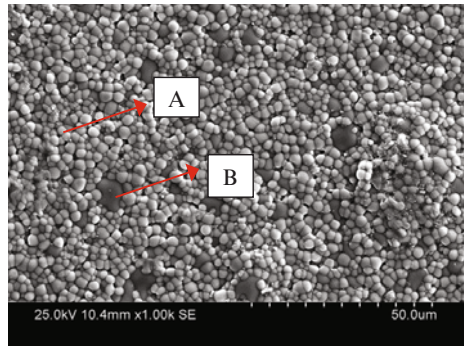

Fig. 2 SEM photograph of the pellet sintered at 1750℃ for 6h.

Figure 2 showed that the pellet was composed of two areas, point A and B. The color of grain B was darker than that of A, and the grain size of B was bigger than that of A. It also showed that the grain B was surrounded by grain A. At the same time, the composition of point A(white grain) and B(black grain) were obtained by EDS analysis, as shown in Table 2. The atom ratio of Ba:Zr:Y for grain A was about 1:1:0, the value for grain B was about 2:1:1, this fact may imply that they were $BaZrO_3$ and Ba_2YZrO_6, respectively, which was consistent with the XRD results in Figure 1.

Table 2 EDAX result of the different positions

Position	Elements		
	Ba(at%)	Zr(at%)	Y(at%)
A	47	53	0
B	48	28	24

Interface analysis between crucible and melt

Macro analysis The crucible after sintering at 1750℃ for 6h was used for melting TiNi alloy. The sample obtained from the end of melting was shown in Figure 4, and it was very easy to peel off between metal ingot and crucible, and no reaction layer existed. It was a sign of reaction between the metal and the crucible if they were madefacted each other and the roughness of the surface was the most intuitive reflect to wettability[16]. The ingot had a smooth surface by using the crucible, claiming that the wettability between crucible material and titanium alloy melt was poor, meaning that the refractory was resistant to the titanium melt.

Fig. 4 External appearance of crucible after melting

Microstructure analysis The sample after melting was cooled by a curing agent, and the reaction layer of the metal - crucible was obtained by mechanical method. The sample was analyzed by SEM and EDS, and the results were shown in figure 5. In Figure 5, the area A is a refractory material and the area B is the melt. The results from EDS line scan showed that the contents of Ba, Zr and Y in the area B decreased significantly, while the contents of Ti and Ni in the refractory materials were almost equal to zero. The gaps in area A was due to the cracks of the crucible, caused by the mechanical cutting. The boundary between area A and area B was clear, and no transition layer existed. This phenomenon was rare in other research about melting of titanium alloy[17-19].

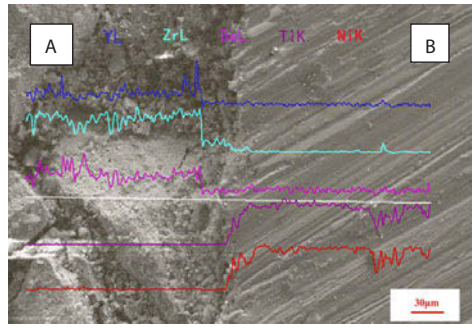

Fig. 5 SEM/EDS photograph of interfacial reaction layer

Conclusion

(1) Using Y_2O_3, $BaCO_3$ and ZrO_2 as raw materials, the powder of Y_2O_3 doped $BaZrO_3$ prepared by solid-phase synthesis at 1400℃ for 12h was composed of $BaZrO_3$ and Ba_2YZrO_6.

(2) This powder was shaped by cold isostatic pressing at 120MPa for 3min as well as sintered at 1750℃ for 6h, which density reached 98.0%

(3) The TiNi alloy was melted by the crucible prepared using mentioned-above condition, there was no obvious interaction layer and element diffusion between the crucible and the metal, so the Y_2O_3-doped $BaZrO_3$ refractory is a promising candidate for melting titanium alloys.

References

[1] R. R. Boyer, "An overview on the use of titanium in the aerospace industry," *Materials Science and Engineering*, 213 (1-2) (1996), 103–114.

[2]S. Miyazaki et al., *Medical and Dental Applications of Shape Memory Alloys* (*Cambridge: Cambridge University Press*, 1999), 267–274.

[3] H.Q. Dong et al., "Development of low energy consumption titanium and titanium alloy melting technology," *Mater Rev (in Chinese)*, 22 (5) (2008), 68–72.

[4] J. Frenzel et al., "High quality vacuum induction melting of small quantities of TiNi shape memory alloys in graphite crucibles," *Journal of Alloys Compounds*, 385 (1–2) (2004), 214–223.

[5]T. Tetsui et al., "Evaluation of yttria applicability as a crucible for induction melting of TiAl alloy," *Materials Transactions*, 51 (9) (2010), 1656–1662.

[6] F. Gomes, et al., "Effect of melting pressure and superheating on chemical composition and contamination of yttria-coated ceramic crucible induction melted titanium alloys," *Journal of Materials Science*, 46 (14) (2011), 4922–4936.

[7] Z. Zhang et al., "Preparation of BaZrO3 crucible and interfacial reaction with titanium alloy melt," *Journal of silicate*, 41(9) (2013), 1277–1283.

[8]Hans G. Bohn and Tilman Schober, "Electrical conductivity of the high–temperature proton conductor $BaZr_{0.90}Y_{0.10}O_{2.95}$," *Journal of the American Ceramic Society*, 83 (4) (2000), 768–772.

[9] J.Q. Wang et al., "Fabricating transparent yttria ceramics at low temperature," *Journal of inorganic materials*, 18 (6) (2003), 1222–1228.

[10] Takayuki Hirai, Yusuke Kawamura, and Isao Komasawa, "Preparation of Y_2O_3 nanoparticulate thin films using an emulsion liquid membrane system," *Journal of Colloid and Interface Science*, 275 (3) (2004), 508–513.

[11] H.Y. Du et al., "Effect of adding method on structure and properties of materials," *Journal of silicate*, 28 (6) (2000), 553 –556.

[12] Z.Z. Peng et al., "$BaZr_{0.9}Y_{0.1}O_{2.95}$ composite with enhanced protonic conductivity," *Journal of WuHan University of Technology-Materials Science Edition*, 24 (2) (2009), 269–272.

[13] S. Ricote, Nikolaos Bonanos, and G. Caboche, "Water vapor solubility and conductivity study of the proton conductor $BaCe_{(0.9-x)}Zr_xY_{0.1}O_{(3-\delta)}$," *Solid State Ionics*, 180 (14–16) (2009), 990–997.

[14] Ikwhang Chang, Pilwon Heo, and Suk-Won Cha, "Thin film solid oxide fuel cell using a pinhole-free and dense Y-doped $BaZrO_3$," *Thin Solid Films*, 534 (2013), 286–290.

[15] A. Erb, E.Walker, and R. Flukiger, "The use of BaZrO3 crucibles in crystal growth of the high-Tc superconductors progress in crystal growth as well as in sample quality," *Phys Rev C*, 258 (1) (1996), 9–20.

[16] B. C. Weber et al., "Observations on stabilization of zirconia," *Journal of the American Ceramic Society*, 39 (6) (1956), 197–206.

[17] S. K. Sadrnezhad and Sadegh Badakhshan Raz, "Interaction between refractory crucible materials and the

melted NiTi shape memory alloy," *Metallurgical and Materials Transactions B*, 36 (3) (2005), 395–403.
[18]A.V. Kartavykh, V. V. Tcherdyntsev, and J. Zollinger, "TiAl-Nb melt interaction with AlN refractory crucibles," *Materials Chemistry and Physics*, 116 (1) (2009), 300–304.
[19] Q. Jia, Y.Y. Cui, and R. Yang, "Intensified interfacial reactions between gamma titanium aluminide and CaO stabilized ZrO_2," *International Journal of Cast Metals Research*, 426 (2) (2003), 1643–1648.

Characterization of Minerals, Metals, and Materials 2016
Edited by: Shadia Jamil Ikhmayies, Bowen Li, John S. Carpenter, Jiann-Yang Hwang, Sergio Neves Monteiro, Jian Li, Donato Firrao, Mingming Zhang, Zhiwei Peng, Juan P. Escobedo-Diaz, and Chenguang Bai
TMS (The Minerals, Metals & Materials Society), 2016

HYDRATION RESISTANCE OF Y_2O_3 DOPED CaO AND ITS APPLICATION TO MELTING TITANIUM ALLOYS

Meng Fanlong[1],Cheng Zhiwei[1], Chen Guangyao[1], Lu Xionggang[1,2] and Li Chonghe[1,2]
1. State Key Laboratory of Advanced Special Steel, Shanghai 200072, China
2. Shanghai Special Casting engineering technology research centre, Shanghai
Email: chli@staff.shu.edu.cn

Keywords: CaO refractory, Y_2O_3, Hydration resistance, Titanium and titanium alloy

Abstract

Various amount Y_2O_3(1-8 mol%) doped CaO powder was synthesized by the solid state reaction method, the pellete and crucible were fabricated by the cold isostatic pressing and were sintered at 1750℃ for 4h.The microstructural characterization was revealed by X-ray diffraction(XRD) and scanning electron microscopy(SEM).The XRD results showed that when Y_2O_3 doped 2 mol%, metastable CaY_2O_4 phase existed in CaO grain boundary, when Y_2O_3 doped 3 mol%-8 mol%, in addition to the above structure, Y_2O_3 phase also be found in CaO grain boundary. Hydration experiment results showed when Y_2O_3 doped 0 mol%-4 mol%, CaO had excellent hydration resistance performance, Y_2O_3 doped 2 mol% had the best hydration resistance, its weight addition stored after 7 weeks (49 days) was only about 0.2 wt%. Melting experiment results showed that it was no reaction between crucible and alloy layer. Oxygen, calcium, titanium, nickle and yttrium element not diffusion between the CaO crucible and TiNi alloy, it was no oxygen content increase after melting.

1 Introduction

Titanium and titanium alloy, which possess the high specific strength, the good corrosion resistance and the good performance at elevated temperature, are widely used in various areas, such as: aerospace industry, biomedical engineering, military industry and so on[1,2]. However, titanium and its alloys possess the high chemical activity of metals in the molten state, can not be melted in the atmosphere, furthermore they almost can react with all kinds of refractory, such as MgO, Al_2O_3, etc., to generate brittle compounds. Nowadays, most of titanium alloys are melted and cast by vacuum arc remelting (VAR) and induction skull melting[3-4].these complicated melting processes increase the production cost, therefore limit their industrial application[3-4].

Calcium oxide refractory attracts the attention due to its high melting point, good thermodynamic properties and stability, otherwise, there is no pollution of the titanium melt when CaO is used as the crucible material for melting TiNi alloys[5], TiNi alloy is the most widely used shape memory materials due to its excellent shape memory and super-elastic properties, corrosion resistance and biocompatibility. CaO seems a potential candidate of

refractory for melting titanium alloys[6-8]. However, CaO crucible is easy to hydrate in the air and difficult to sinter, both disadvantages limit its industrial application as the refractory for melting the titanium alloys. Recently, lots of interests are focus on the improvement of the hydration resistance of CaO, the methods for improving the hydration resistance of calcium oxide are concentrated two areas: adding additives method and surface treating method.

In this paper, according to CaO-Y_2O_3 Binary phase diagram, a small amount of additives of Y_2O_3 was used to modify the the hydration resistance of calcium oxide. A series of CaO samples were synthesized by adding 1 to 8 mol% Y_2O_3, the influence of the quantity of Y_2O_3 addition on the hydration property was investigated. The home-made crucible was used to melt TiNi alloy by vacuum induction melting, the interface reaction between the refractory and TiNi alloy was discussed. All efforts were contributed to the development of refractory for melting titanium alloys with the good hydration resistance.

2 Experimental procedures

The raw materials: analytically pure CaO,purity≥99%, the average particle size 4.5 m; industrial Y_2O_3, purity≥99%, the average particle size 4.8 m;

The mixture of powder (the mole percentage of 1-8 % Y_2O_3 and CaO) were ball milled for 8 hours . Afterwards, the mixture of powder was shaped into the chip samples with the size of Φ25×5mm by the cold isostatic pressing method. Finally, all samples were pre-sintered at 800℃ for 2 hours and sintered at 1750℃ for 3 hours. The phases of samples were determined by X-ray diffraction (XRD) with D/Max-2200 XRD instrument.

The hydration resistance of the samples are evaluated by measuring the mass gain kept at atmosphere at 25-30℃and 65-75% relative humidity. The mass of the samples is measured after they are stored for the given periods (from one week to nine weeks), the hydration resistance is evaluated by its addition of mass, expressed by the following equation:

$$\text{Mass gain rate}=(m_1-m_2)/m_2\times100\% \quad (1)$$

where, m_1 is the total mass of sample after hydration, m_2 is the original mass. Mass gain rate of hydration was shown in Fig.3.

Scanning electron microscope was used to evaluate the microstructure of the different samples (Fig.4) and the energy dispersive X-ray spectroscopy (EDS).

The equal atomic ratio of TiNi alloys are used as the melting alloy. The temperature was measured by the marathon two-color infrared thermometer. About 20g TiNi alloy was melted by using the home-made crucible in the inducting furnace under vacuum and argon atmosphere. At the beginning of the melting, the furnace chamber was evacuated up to less than 5Pa by rotary pump and backfilled with argon several times, in order to reduce the oxygen content to a minimum level. The temperature of the crucible was gradually raised up to 1500°C and kept at this temperature for 5min. Finally, the crucible with the melted titanium alloy was taken out

from furnace at room temperature. The ingot were mounted in the epoxy resin and sectioned longitudinally to a suitable size using a water-cooled wheel, and then the samples were ground using silicon carbon paper, polished on alumina paste impregnated cloth. The interfacial reaction between the melts of alloys and CaO refractory was revealed by scanning electron microscope (SEM) and energy dispersive X-ray spectroscopy (EDS).

3 Results and discussion

3.1 XRD and hydration test analysis

XRD patterns of samples of different ratios of Y_2O_3 doped into CaO and sintering into ceramic chip can be seen in Fig.1. It can be seen when Y_2O_3 doped 1 mol%, only CaO diffraction peak can be found, when Y_2O_3 doped 2 mol%, CaO diffraction peak and CaY_2O_4 diffraction peak can be found, when Y_2O_3 doped 3 mol%-8 mol%, CaO diffraction peak CaY_2O_4 diffraction peak and Y_2O_3 diffraction peak can be found. Fig.2 was CaO-Y_2O_3 Binary phase diagram[9]. It shows that CaO can react with Y_2O_3 and production CaY_2O_4 phase at about 2100k, when Y_2O_3 doped was little(1 mol%), the limit solubility of Y_2O_3 in CaO was not reached, so there would be no CaY_2O_4 phase generated, Y_2O_3 solid solution in matrix CaO, when Y_2O_3 doped 2 mol%, the limit solubility of Y_2O_3 in CaO was reached, so there would be CaY_2O_4 phase generated, CaY_2O_4 phase as a metastable phase at room temperature, so CaO phase and CaY_2O_4 phase were existed, when Y_2O_3 doped further increased(3 mol%-8 mol%), in addition to CaY_2O_4 metastable phase, CaO phase and Y_2O_3 phase were also existed, the concrete existence form of the phase will be expounded in the next.

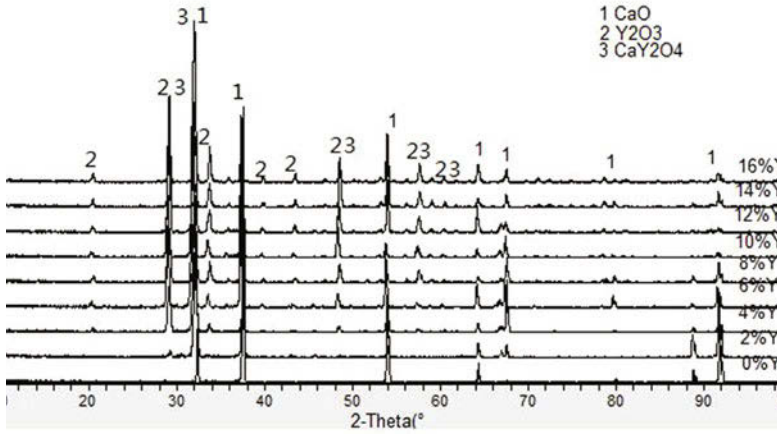

Fig.1. XRD patterns of samples (sintering at 1750°C 3h)

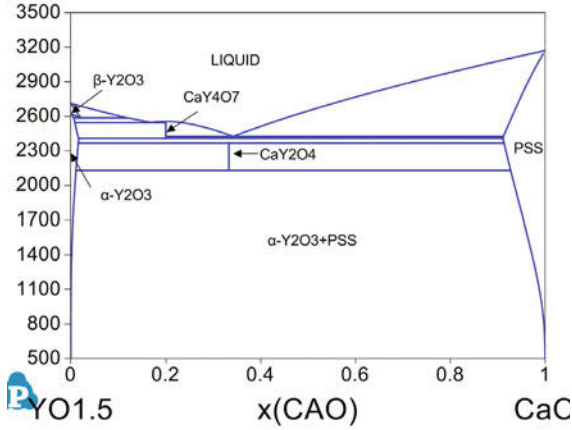

Fig.2 CaO-Y_2O_3 Binary phase diagram

The hydration experiment results of different ratios of Y_2O_3 doped into CaO and sintering into ceramic chip can be seen in Fig.3a. Experiment in 25 to 30℃ temperature, air relative humidity was 50-70%. Measuring changes in the quality of every 7 days. It can be seen when Y_2O_3 doped 0 mol%-4 mol%, CaO had excellent hydration resistance performance, when Y_2O_3 doped 5 mol%-8 mol%, the hydration resistance of CaO fell sharply. In order to find out the best doped Y_2O_3 content, the partial enlarged drawing of Y_2O_3 doped 0 mol%-4 mol% in Fig.3a was shown in Fig.3b. It can be seen with the increase of Y2O3 content, the hydration resistance of CaO was increases at first and then decreases, Y_2O_3 doped 2 mol% had the best hydration resistance, its weight addition stored after 7 weeks (49 days) was only about 0.2 wt% . In addition the CaO of no Y_2O_3 doped had good hydration resistance too, the studies of Stephen C et al had shown that CaO is easily hydrated material[10], this hydration experiment result seems to be conflict with the studies of Stephen C et al, it will be expounded in the next.

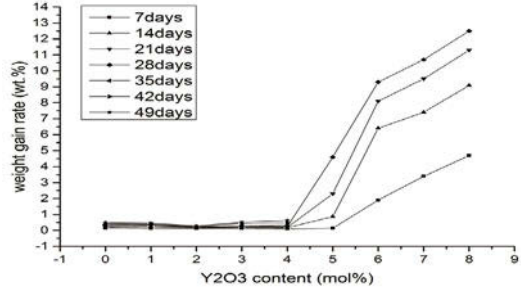

Fig.3a. The results of hydration resistance of samples
(Temperature: 25-30℃ relative humidity: 50-70%)

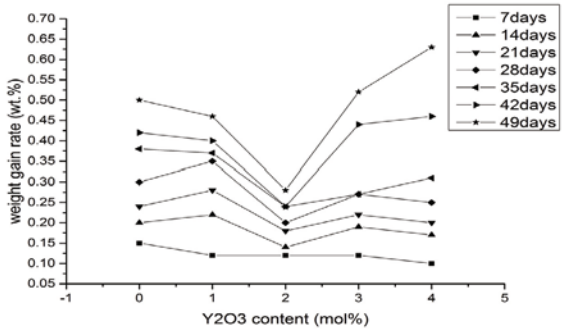

Fig.3b. The results of hydration resistance of samples
(Temperature: 25-30℃ relative humidity: 50-70%)

3.2 SEM and EDS analysis

The SEM micrographs of different ratios of Y_2O_3 doped into CaO and sintering into ceramic chip can be seen in Fig.4. According to Fig.4a, it shows that no Y_2O_3 additive CaO had very big grain, the grain size was about 100 m. The studies of Bhattacharya T had shown that the larger size of CaO grain, the better performance of hydration resistance[11]. This was the reason that pure calcium oxide has very good hydration resistance in this experience. According to Fig.4b-Fig.4f, it shows that it was different between the grain phase and the grain boundary phase, according to the point in Fig.4b-Fig.4e EDS results(Table I.) can be concluded that grain boundary phase was Y_2O_3 phase CaY_2O_4 phase. The SEM micrographs of 2 mol% Y_2O_3 additive was shown in Fig.4b, it shows that CaO grain was covered by CaY_2O_4 phase, the grain size was about 150 m, bigger than no Y_2O_3 additive, it was as moderate amount of Y_2O_3 doped promoted the sintering of CaO, made grain size bigger and good for hydration resistance[11]. In addition the CaY_2O_4 phase in grain boundary covered CaO grain, CaY_2O_4 phase prevent CaO grain contact with the outside world and good for hydration resistance too. The SEM micrographs of 3 mol% Y_2O_3 additive was shown in Fig.4c, it shows that CaO grain was covered by CaY_2O_4 phase and Y_2O_3 phase, the grain size was about 100 m, the grain size smaller than 2 mol% Y_2O_3 additive and had larger porosity. The SEM micrographs of 4 mol% Y_2O_3 additive was shown in Fig.4d, it shows that CaO grain was covered by CaY_2O_4 phase and Y_2O_3 phase, the grain size was about 80 m. The SEM micrographs of 5 mol% Y_2O_3 additive was shown in Fig.4e, it shows that CaO grain was covered by CaY_2O_4 phase and Y_2O_3 phase, the grain size was about 80 m and began to appear the discontinuous of CaO grain. The SEM micrographs of 7 mol% Y_2O_3 additive was shown in Fig.4e, it shows that CaO grain was covered by CaY_2O_4 phase and Y_2O_3 phase, the grain size was about 80 m and began to appear the discontinuous of CaO grain. According to Fig.4c-Fig.4f, it shows that the grain size was smaller than Fig.4b, it was as too much Y_2O_3 doped restraint of the sintering of CaO and made the grain size decrease. So 2 mol% Y_2O_3 additive had the best hydration resistance.

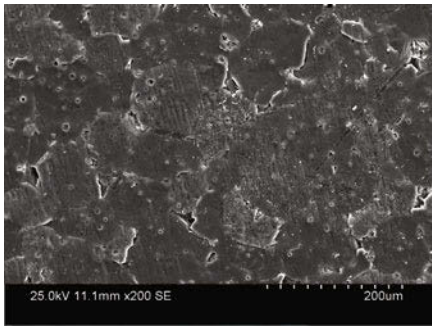

a. No Y_2O_3 additive

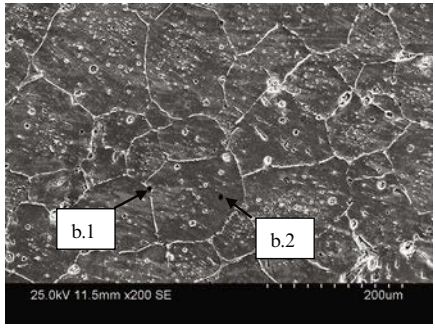

b. 2 mol% Y_2O_3 additive

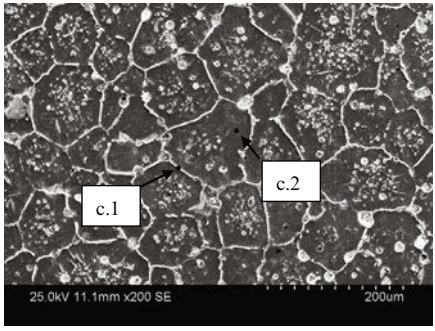

c. 3 mol% Y_2O_3 additive

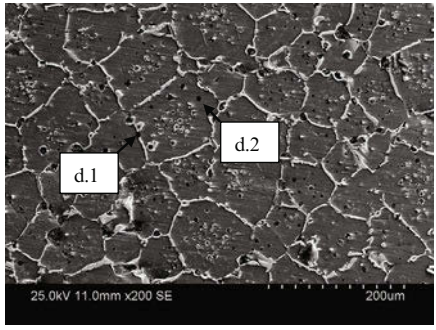

d. 4 mol% Y_2O_3 additive

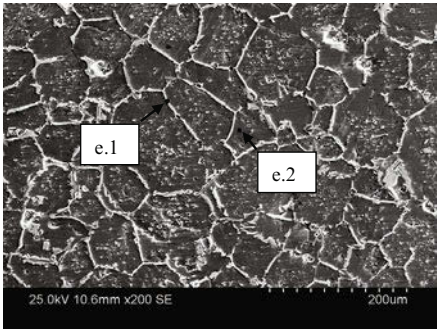

e. 5 mol% Y_2O_3 additive

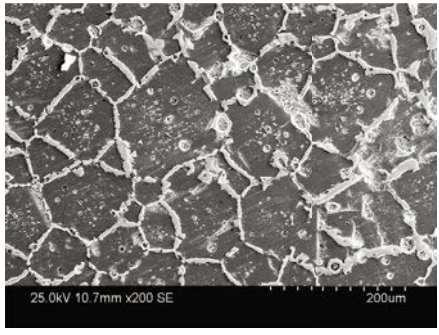

f. 7 mol% Y_2O_3 additive

Fig.4. SEM of different samples

Table I. EDS results of points

Position	Mole fraction, x/%			phase
	Ca	Y	O	
b.1	16.81	33.26	49.92	CaY_2O_4
b.2	76.21	01.96	22.31	CaO
c.1	17.98	29.60	52.42	CaY_2O_4
c.2	70.98	02.69	26.33	CaO
d.1	01.84	42.72	55.45	CaY_2O_4,Y_2O_3
d.2	74.62	01.65	23.72	CaO
e.1	06.74	43.93	49.33	CaY_2O_4,Y_2O_3
e.2	73.62	02.04	24.34	CaO

Y_2O_3 doped 2 mol% in CaO was made in crucible with the same process.The crucible was used to melting TiNi alloy by the vacuum induction method. Fig.4 shows the SEM micrograph of interface reaction layer of TiNi with CaO refractory crucible. Left was CaO, Right was TiNi alloy. It shows after melting this interface layer between TiNi and the crucible was very uniform and compact. It was no reaction between crucible and alloy layer. According to line EDS result in Fig.5the interface reaction was not apparent and no significant element diffusion. Oxygen, calcium and yttrium element sharply decrease and no element diffusion in interface. Titanium and nickle element sharply increase and no element diffusion in interface. It probably means that the TiNi melts did not react with the refractory, and the CaO modified with Y_2O_3 additive may be a promising candidate of the refractory for melting the TiNi alloys.

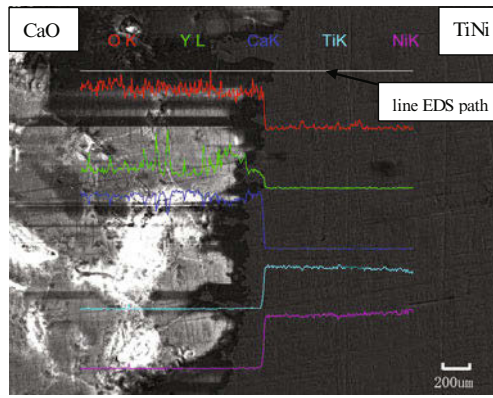

Fig.5. SEM micrograph of interface reaction layer of TiNi with CaO refractory

The oxygen content shows that: before melting TiNi oxygen content is 0.060 wt %, after melting, TiNi oxygen content is 0.059 wt %. The crucible did not add oxygen content in TiNi alloy.

4 Conclusion

Y_2O_3 doped in CaO power synthesized by solid phase sintering, phase composition was measured by XRD, made in circle chip by sintering the power 3 hours at 1750℃.The microstructure observed by SEM and did the hydration experiment. Made the CaO power into crucible for TiNi alloy melting. Combined the results of experiment can draw the following conclusions:

(1) when Y_2O_3 doped 2 mol%, metastable CaY_2O_4 phase and Y_2O_3 phase existed in CaO grain boundary, when Y_2O_3 doped 3 mol%-8 mol%, in addition to the above structure, Y_2O_3 phase also be found in CaO grain boundary.

(2) In hydration experiment, when Y_2O_3 doped 0 mol%-4 mol%, CaO had excellent hydration resistance performance, Y_2O_3 doped 2 mol% had the best hydration resistance, its weight addition stored after 7 weeks (49 days) was only about 0.2 wt%.

(3) Made 2 mol% Y_2O_3 additive CaO into crucible, the crucible was used to melting TiNi alloy, it was no reaction between crucible and alloy layer. Oxygen, calcium, titanium, nickle and yttrium element not diffusion between the crucible and TiNi alloy, it was no oxygen content increase after melting.

References

[1] Cai W, Meng X L, and Zhao L C, "Recent development of TiNi-based shape memory alloys," *Current Opinion in Solid State and Materials Science*, 9(2005), 296-302.

[2] Wu S K, Lin H C,"Recent development of TiNi-based shape memory alloys in Taiwan," *Materials Chemistry and physics*, 64(2000), 81-92.

[3] Mitchell A, "Melting, casting and forging problems in titanium alloys," *Materials science and Engingeering*, A258(1-2)(1998), 229-235.

[4] Sikka V K et al., "Melting and casting of FeAl-based cast alloy," *Materials Science and Engineering*, A258(1-2)(1998), 229-235.

[5] X.Y. Zhang, Y.Q. Zhao, and C.G. Bai, *Titanium Alloy and Its Applications*(Beijing: Chemical Industry Press, 2005), 21-24.

[6] Harkki J, Palander M. "Theoretical considerations about reoxidation of the steel metal by refractory materials," *Interceram*, 40(5)(1991), 284-289.

[7] Kuchar L, Harrki J, "Refractory material source of reoxidation in tundish" (Proceedings of Unitecr'93 congress, 1993), 1389-1410.

[8] Bannenberg N, "Demands on refractory materials for clean steel production" (Proceedings of Unitecr'95 congress, 1995(1)), 36-59.

[9] Z.P.Jin, Y.Du, "Thermodynamic calculation of the ZrO_2-$YO_{1.5}$-CaO phase diagram," *Calphad*, 16(1992), 355-362.

[10] Stephen C, Gordon L, *Handbook of industrial refractories technology*(First Edition, New Jersey, Noyes Publications, 1992)98-101.

[11] Bhattacharya T, Ghosh A, "DasA. Densification of reactive lime from limestone" *Ceramics International*, 7(4)(2001), 455-499.

Characterization of Minerals, Metals, and Materials 2016
Edited by: Shadia Jamil Ikhmayies, Bowen Li, John S. Carpenter, Jiann-Yang Hwang, Sergio Neves Monteiro, Jian Li, Donato Firrao, Mingming Zhang, Zhiwei Peng, Juan P. Escobedo-Diaz, and Chenguang Bai
TMS (The Minerals, Metals & Materials Society), 2016

SHEAR DISPLACEMENT AND ACTUAL STRAIN DURING CHIP SEGMENTATION WHEN CUTTING AEROSPACE ALLOY Ti-5553

D. P. Yan[1], T. Hilditch[2], H. A. Kishawy[3], G. Littlefair[2]
[1]Department of Natural and Applied Sciences, University of Wisconsin-Green Bay, Green Bay, WI 54311
[2]School of Engineering, Deakin University, Geelong, VI 3217, Australia
[3]Machining Research Laboratory, University of Ontario Institute of Technology, Oshawa, ON, Canada, L1H 7K4

Keywords: Ti-5553, metal cutting, chip segmentation, shear displacement, shear strain

Abstract

Ti-5553 (Ti–5Al–5Mo–5V–3Cr–0.5Fe) is a recently developed near-β Ti alloy with potential application in structural components of aircrafts. However, Ti-5553 has shown poorer machinability than other Ti alloys. The objectives of the present study are to understand the chip formation mechanism, calculate the actual strain within the segments of chip and its narrow shear bands, and to evaluate the effect of cutting condition on the shear strain. Cutting tests were conducted under three levels of cutting speeds and feeds, and the chips micrographs were collected and analyzed. It was found that the cutting conditions have a significant impact on the shear strain.

Introduction

Titanium (Ti) alloys have received considerable interest due to their excellent corrosion resistance, high strength-to-weight ratio and high strength at elevated temperatures. Ti alloys have wide demands in the aerospace industry due to excellent strength-to-weight ratio. However, Ti alloys are difficult to machine owing to their high strength, high chemical reactivity, relatively low modulus of elasticity, and low thermal conductivity [1]. Ti-5553 was publicly introduced in 1997 as an improved version of Russian near-β Ti alloy VT-22. As reported by Nag et al. [2], its application niche is for thick-section aerospace components such as landing gear due to its high-strength (1,250 MPa) and deep-hardenability (over 150 mm). In spite of these superior mechanical properties, its usage is limited due to processing difficulties, e.g. poor machinability as mentioned by Fanning [3]. In fact, Arrazola et al. [4] have reported that Ti-5553 causes more severe tool wear than other common titanium alloys such as Ti-6-4. Ugarte et al. [5] employed an analytical model to determine the plastic shear strain in the shear bands during orthogonal milling of Ti-5553, and reported that Ti-5553 has remarkably higher strain (21.1) than the Ti-6-4 (6.2).

The poor machinability of Ti alloys is often related to the low tool life and high forces required for machining. Also of importance is the surface integrity, as it significantly affects the performance of machined parts subjected to dynamic loading and aggressive environments such as landing gear components. Surface integrity includes the surface topography, sub-surface microstructural changes and residual stress. As reported by Guo et al. [6], surface integrity is

determined by the deformation state, which is characterized by strain, strain rate and temperature, and complex loading histories and microstructural evolution during machining. Thus understanding the impact of cutting conditions on the shear displacement and shear strain during chip segmentation is an important consideration for the machinability improvement.

In metal cutting processes, a large stress is generated as the tool cuts into the workpiece. Initially, elastic deformation occurs as the stress reaches the yield limit of the workpiece, then plastic deformation starts and is followed by the formation of a chip. As reported by Shivpuri et al. [7] and Davies [8], a serrated (saw-toothed) type of chip is commonly found in machining of Ti alloys. This type of chip is the result of the cyclic formation of adiabatic narrow shear bands in the workpiece. According to Komanduri [9], the deformation within the chips is heterogeneous, and an intense shear is concentrated in the narrow shear bands that divides the chip into discrete segments.

Figure 1 was constructed to illustrate a serrated Ti chip and assist with the calculation of shear strains in chip formation. Turley et al. [10] reviewed the model of Ti chip formation and reported that a discrete Ti chip is formed in two steps: (1) indentation of workpiece by cutting tool results in a homogeneous shear (ε_h) in the segments of chip. (2) Catastrophic shear (ε_c) concentrates within the shear band which separates each segment of chip.

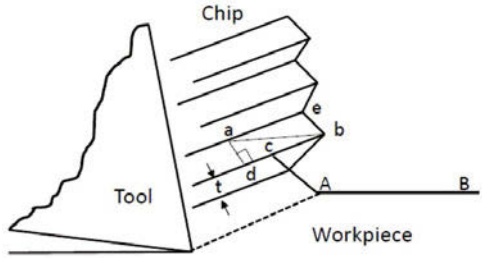

Figure 1: Graphic representation of a serrated Ti chip showing critical parameters used in shear strains calculation.

As illustrated in Figure 1, Turley et al. [10] suggested that line 'eb' would be parallel to the unmachined surface i.e. line 'AB' if no deformation occurred. Thus, ε_h=ae/ad. They also suggested that 'cb' is the shear displacement within shear band, and 't' is the thickness of the shear band. Thus, ε_c=cb/t. Total shear strain in the shear band $\varepsilon_t = \varepsilon_h + \varepsilon_c$ [10]. Interestingly enough, the principle to determine the shear displacement within the shear band of the segment is still lacking and needed to be developed for facilitating the shear strain calculation. Therefore, the motive of the present study is to calculate the shear displacement and actual shear strain via chip metallographic examination, and to evaluate the effect of cutting conditions on the shear strain during machining of Ti-5553.

Experimental Setup

A billet of Ti-5553 (non-heat treated) was machined to a diameter of 25mm and the turning tests were carried out on a CNC lathe where an explosive 'quick-stop' device was mounted on to the lathe. As illustrated in Figure 2 (a), the quick-stop device comprises of a tool holder held in position by a pivoting rod and shearing pin. The impact on the tool holder is provided by a release bolt after activating a captive bolt stunner gun. The impact force shatters the shearing pin while accelerating the tool away from the workpiece during cutting. To effectively freeze the cutting action and obtain the chip roots, care was taken to ensure that the dropping velocity of the tool is greater than the cutting velocity. Figure 2 (b) shows the 'quick-stop' tests experimental setup. WNMG carbide inserts, with zero degree clearance angle and comprised with chip breaker were utilized. Cutting tests were conducted under dry condition with combination of 3 cutting speeds and feeds of 37, 49 and 66m/min and 0.05, 0.1 and 0.2mm/rev respectively. The depth of cut was kept constantly at 2mm for all tests.

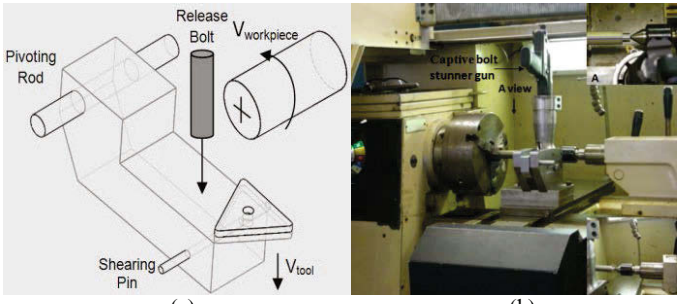

(a) (b)

Figure 2: (a) Schematic illustration of 'quick-stop' device; (b) Photo of experimental setup.

After each cutting test, the produced frozen chip was sectioned away from the workpiece. Subsequently, the specimen was cold mounted and then wet grinded until the sectioned chip layer was reached. Muller's three-step Ti metallographic preparations were utilized, and Kroll's etchant (2ml HF and 6ml HNO_3 in 100ml H_2O) was used for revealing the microstructure. Etched samples were observed using optical microscopy to obtain the shear band structure for shear displacement and shear strain calculation.

Results and Discussion

Determination of Shear Displacement in Chip Segmentation

Figure 3 was constructed to illustrate the shear band within the segment of serrated chip and shows how the different types of shear displacements takes place within the segment. It is apparent from the figure that, if no deformation or shear occurred within the segments, the free surface of the segment of chip, i.e. line 'eF' would be parallel to the unmachined surface, i.e. line 'AB'. Thus, the shear displacement (i.e. line 'ae') within the segment can be determined by drawing a line (i.e. line 'ab') parallel to the line 'AB' through a transitional point (i.e. point 'b')

along the free surface of the segment. Accordingly, the segment of chip is formed as a result of the point 'a' shearing to point 'e' due to the tool indentation and consists of the constructed lines 'ae', 'eF' and 'Fg'.

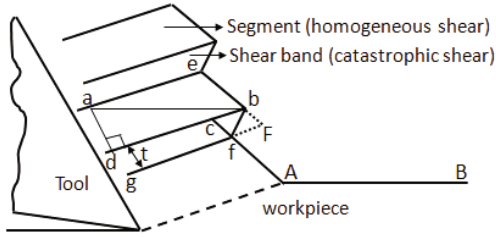

Figure 3 Illustration of a serrated chip, showing homogeneous and catastrophic shares within the segment of chip and shear band of the segment, and indicating critical parameters and shear displacements used in shear strain calculation.

Regarding the shear displacement within the shear band, it is obvious from Figure 3 that if no further deformation or catastrophic shear occurred within the shear bands, i.e. no further tool advancement, the free surface of the segment of chip, i.e. line 'eF' would not be sheared away, torn apart and bent down into two lines, i.e. lines 'eb' and 'bf'. Therefore, the shear displacement (i.e. line 'cb') within the shear band can be determined by drawing a line (i.e. line 'cA') parallel to the line 'eb' through a lower edge point (i.e. point 'f') of the shear band. It should be noted from the figure that the shear band within the segment is formed as a result of the point 'F' shearing to point 'f' due to the further tool advancement and consists of the constructed lines 'db', 'bf' and 'fg'.

Measurement of Shear Displacement and Calculation of Shear Strain in Chip Formation

Figure 4 show the optical micrographs of the midsection of chips produced from samples Q21, Q24 and Q27, obtained under a constant feed rate of 0.08mm/rev and varying cutting speeds of 27, 39 and 55m/min respectively. These micrographs also illustrate the segment of chip, shear band within the segment of chip (i.e. bottom portion of the segment), and critical parameters (i.e. shear displacements) used in shear strain calculation.

During construction of the segment of chip and shear band within the segment in samples Q21, Q24 and Q27 micrographs, care was taken to ensure that the line 'ab' was parallel to line 'AB', the line 'ae' was parallel to line 'db' and the line 'eb' was parallel to line 'cf'.

Table 1 lists the measured shear displacements (i.e. lines 'ae', 'ad', 'cb', and 't') in forming the segment of chip and its shear band for samples Q21, Q24 and Q27. The method introduced by Turley et al. [10] was used to calculate the shear strain, and Table 2 lists the comparisons of the calculated total shear strains for samples Q21 (6.69), Q24 (5.04) and Q27 (8.19).

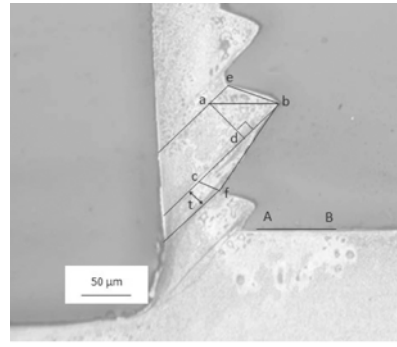

Q21, v=27m/min and f=0.08mm/rev

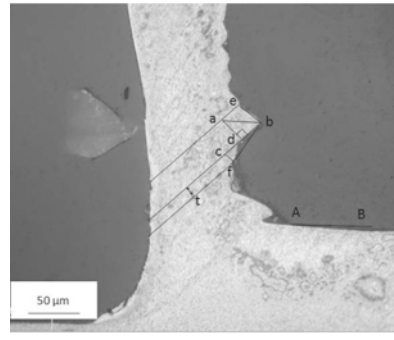

Q24, v=39m/min and f=0.08mm/rev

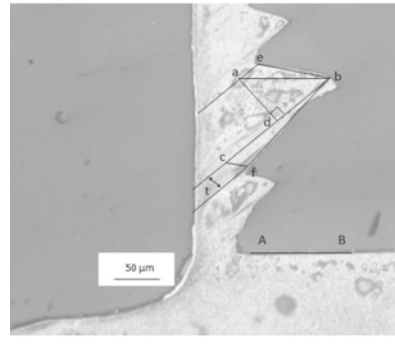

Q27, v=55m/min and f=0.08mm/rev

Figure 4 Optical micrographs of midsection of serrated chip obtained from samples Q21, Q24 and Q27; illustrating the segment of chip, shear band within its segment and critical parameters (i.e. shear displacements) used in shear strain calculation.

Table 1 Measured shear displacement in forming the segment of chip and its shear band for samples Q21, Q24 and Q27.

Shear displacement (μm)	Sample No.		
	Q21	Q24	Q27
ae	26.30	23.67	28.93
ad	49.97	28.93	63.12
cb	118.35	49.97	152.54
t	18.41	11.84	19.73

Table 2 Calculated shear strain in segment of chip and its shear band for samples Q21, Q24 and Q27.

Shear strain	Sample No. Cutting conditions (v/f)		
	Q21 (27/0.08)	Q24 (39/0.08)	Q27 (55/0.08)
ε_h	0.53	0.82	0.46
ε_c	6.43	4.22	7.73
ε_t	6.96	5.04	8.19

Effect of Cutting Speed on Shear Strain

Table 2 shows that the total shear strain in samples Q21, Q24 and Q27 increased with increasing cutting speed. The plot of cutting speed versus shear strain in Figure 5 below shows these trends, in particular, when increasing the cutting speeds from 27 to 55m/min, the calculated total shear strain increased 22.4%.

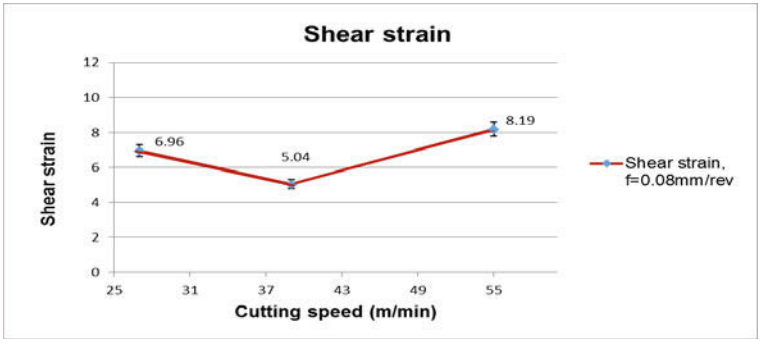

Figure 5 Graph of total shear strain vs. machining conditions for samples Q21, Q24 and Q27 obtained at constant feed rate of 0.08mm/rev and cutting speed of 27, 39 and 55mm/min respectively; showing the effect of cutting speed on the total shear strains (including errors).

By comparing the average actual shear strain with predicted shear strain (ε_t =21.1) reported by Ugarte et al. [5], it can be found that the predicted values are 3 times higher than the average measured values obtained thought this experimental study. It is not clear as to the origin of these differences, however, the results of Ugarte highlight that there is potential for a significant difference in determined shear strain value depending on the method of determination, and potentially as a result of cutting conditions and/or initial material condition/properties.

It should be noted that when calculating the total shear strain for sample Q24, an unexpected lower shear strain value was obtained. This was believed to be due to the thermoplastic instability of catastrophic shear concentration within the Q24 shear band resulting in formation of an abnormal free surface in the shear band (i.e. line 'bf' shown in Q24 micrograph in Figure 4).

Concluding Remarks

An approach to determine the shear displacement within the shear band of the segment in Ti chip formation was developed. The actual shear strain in relation to cutting conditions during Ti-5553 chip segmentations were experimentally investigated. The followings are observed:

- The maximum total shear strain within the shear bands (8.19) was much greater than in the segments (0.46) obtained at cutting speed and feed rate of 55m/min and 0.08mm/rev.
- The total shear strain increased 22.4% when raising the cutting speeds from 27 to 55m/min.
- The measured shear strain value is lower than what was predicted in previous studies.

Acknowledgement

The authors acknowledge funding of Australian Postgraduate Awards and National Science and Engineering Research Council, Canada. They also acknowledge Allegheny Technologies Incorporated (ATI) for supplying the material and Drs. L. Xu, and J. Cotton of Boeing, US, for their useful discussions.

References

[1] Ezugwu, E.O., Bonney, J. and Yamane, Y., 2003, An Overview of the Machinability of Aeroengine Alloys, Journal of Materials Processing Technology, pp. 233-253.

[2] Nag, S., Banerjee, R., Srinivasan, R., Hwang, J.Y. and Fraser, H.L., 2009, ω-Assisted Nucleation and Growth of α Precipitates in the Ti-5Al-5Mo-5V-3Cr-0.5Fe β Titanium Alloy, Acta Materialia, Vol. 57, No. 7, pp.2136–2147.

[3] Fanning, J.C., 2005, Properties of TIMETAL 555 (Ti-5Al-5Mo-5V-3Cr-0.6Fe), Journal of Materials Engineering and Performance, Vol. 14, No. 6, pp.788–791.

[4] Arrazola, P.J., Garay, A., Iriarte, L.M., Armendia, M. and Marya, S., 2009, Machinability of Titanium Alloys (Ti6Al4V and Ti555.3), Journal of Materials Processing Technology, Vol. 209, No. 5, pp.2223–2230.

[5] Ugarte, A., M'Saoubi, R., Garay, A., and Arrazola, P.J., 2012, Machining Behaviour of Ti-6Al-4V and Ti-5553 Alloys in Interrupted Cutting with PVD Coated Cemented Carbide, Procedia CIRP, Vol. 1, pp. 202-207.

[6] Guo, Y.B., Wen, Q., and Horstemeyer, M.F., 2005, An Internal State Variable Plasticity-based Approach to Determine Dynamic Loading History Effects on Material Property in Manufacturing Processes, International Journal of Mechanical Sciences, Vol. 47, pp. 1423-1441.

[7] Shivpuri, R., Hua, J., Mittal, P., Srivastava, A.K., and Lahoti, G.D., 2002, Microstructure Mechanics Interactions in Modeling Chip Segmentation during Ti Machining, Annals of CIRP, Vol. 51, No. 1, pp. 71-74.

[8] Davies, M.A., 1997, On the Dynamics of Chip Formation in Machining Hard Metals, Annals of CIRP, Vol. 46, pp. 25-30.

[9] Komanduri, R., 1982, Some Clarifications on the Mechanics of Chip Formation when Machining Titanium Alloys, Wear, pp.15–34.

[10] Turley, D.M., and Doyle, E.D., 1982, Calculation of Shear Strains in Chip Formation in Titanium, Materials Science and Engineering, pp.45-48.

Characterization of Minerals, Metals, and Materials 2016
Edited by: Shadia Jamil Ikhmayies, Bowen Li, John S. Carpenter, Jiann-Yang Hwang, Sergio Neves Monteiro, Jian Li, Donato Firrao, Mingming Zhang, Zhiwei Peng, Juan P. Escobedo-Diaz, and Chenguang Bai
TMS (The Minerals, Metals & Materials Society), 2016

Surface Behavior of Iron Sulfide Ore during Grinding with Alumina Media

Martín Reyes P.[1], Elia Palácios B.[2], Francisco Patiño C.[3], Ramiro Escudero G.[4], Mizraim Uriel Flores G[5], Iván A. Reyes D.[6] Laura Angeles Palazuelos[1]

[1] Universidad Autónoma del Estado de Hidalgo, Área Académica de Ciencias de la Tierra y Materiales. Abasolo 600 Col. Centro, Pachuca, Hidalgo, México.
[2] Escuela Superior de Ingeniería Química e Industrias Extractivas, Instituto Politécnico Nacional, Unidad profesional, Adolfo López Mateos. C.P. 07738, México, D.F. Tel-Fax. 57296000, ext. 55270 y 55269
[3] Ingeniería en energía de la Universidad Politécnica Metropolitana de Hidalgo. Boulevard acceso a Tolcayuca 1009, Ex-Hacienda San Javier, 43860, Tolcayuca, Hgo.
[4] Universidad Michoacana de San Nicolás de Hidalgo. Instituto de Investigaciones Metalúrgicas. Santiago Tapia 403, Morelia, Michoacán, México.
[5] Universidad Tecnológica de Tulancingo. Área de Electromecánica Industrial. Camino a Ahuehuetitla #301 Col. Las Presas, Tulancingo, Hidalgo, México 43642.
[6] Universidad Autónoma de San Luis Potosí, Instituto de Metalurgia, Av. Sierra Leona 550, Lomas 2ª. Sección 78210 San Luis Potosí, S.L.P., México.

Abstract

This research was conducted to study the oxidation and surface modification of pyrite in an inert mill and alumina grinding media at different pH values. The extent and progress of the oxidation function of milling time, by measuring some physicochemical variables, zeta potential (ZP), infrared analysis and monitoring. The results indicate pyrite oxidation during grinding, releasing iron and sulfur ions to the solution increasing its concentration with the initial pH and the milling time, the ORP and DO decrease the grinding time, on the other hand presents negative values ZP pH of 9, 11 and 12, whereas at pH 5, 7 and 13, the ZP is positive, FTIR generally detect the presence of free sulfate ion molecule 1084 cm^{-1}, goethite with the absorption band at about 794 cm^{-1}, also occurs in a band assigned to 470 cm^{-1} lepidocrocite oxy iron hydroxide γ- FeOOH, nucleated species or formed during milling.

Keywords: surface, Pyrite, grinding, oxidation, alumina,

Introduction

Has been studied extensively, the surface reactivity of pyrite during media grinding steel. [1-3]. previously it is shown that surface modification of pyrite occurs due to the adsorption of hydroxide type iron species from the surface decomposition of pyrite mineral itself and the means of steel grinding present during mineral processing [4-6]. However the oxidation of pyrite and surface modification during grinding with alumina media is a topic scarcely studied.

The presence of solid and aqueous ferric and ferrous iron in mineral slurries also comes species, other carriers iron sulfides and wear of steel grinding media. During the oxidation of the mineral, it is mainly oxidised to sulfur and not to Fe^{2+} pyrite; however, due to the oxidizing conditions of the aqueous medium Fe^{2+} is oxidized to Fe^{3+}, the ferric ion is hydrolyzed and allows the appearance of solid species of ferric (oxy hydroxides, hydroxides and hydroxy iron sulfates III) [6].

The energy involved during the grinding process is another important factor that significantly alters the surface of sulphide minerals, has recently been shown altering the physicochemical properties of the pyrite ore pulp during milling, that, due to a process mechanical activation [4, 7, 8], caused by the fracture mechanisms, impact, friction and abrasion between the mineral particles, the mill and grinding media steel.

It is known that the presence of iron, aqueous and solid during the milling media and steel species is inevitable release due to oxidation of iron atoms and sulfur and iron ore Fe^{2+} of the grinding media; however, there is no knowledge about the surface condition of the particles of mineral pyrite obtained from a media milling alumina in inert mill and its electrokinetic behavior and chemical nature structural stable solid phases iron goal is also unknown and non-stoichiometric, formed on the pyrite surface.

For this reason, in this research the chemistry of mineral pyrite surface nature is studied by analysis in infrared and electrokinetic (zeta potential) of the particles obtained during grinding in inert mill and media of alumina, held in a wide range of pH and grinding times.

Experimentation

Pyrite grinding mill with alumina media, was performed on a cylinder nylamid 1 liter volume, using 0.45 kg of grinding media, alumina 1.27 cm in diameter and 50 grams of iron sulfide ore size + 0.16 cm. – 0.43 cm, classified as a series of Tyler sieves. The pH values and time tested were 5, 7, 9, 11, 12 and 13. It is noteworthy that the alumina grinding media itself is not intended to simulate the milling process. The objective is to analyze the oxidation and modification of pyrite particles in a wide range of chemical environments, without contact with steel surfaces during the crushing process.

The inert media mill containing alumina ore pyrite and 0.25 liters of solution pH study was rotated in a series of rollers in order to make the pyrite grinding process upon completion of

the proposed time withdrew from mill the total volume of the pulp generated, which along with the solids obtained were characterized.

Subsequently, the media mill and alumina were washed with deionized water, to proceed to the next grinding time, loading the mill with 0250 L of fresh pH study and pyrite mineral untreated (fresh) solution, this procedure it was repeated successively for all times and pH pyrite grinding mill with inert alumina media.To characterize the mineral pyrite before and after oxidation, analytical techniques were used as quantitative chemical analysis in a spectrometer by inductively coupled plasma (ICP) and instrumental; X-ray diffraction (XRD), scanning electron microscopy (SEM) spectroscopy, Fourier transform infrared (FTIR) and zeta potential (PTZ).

Generally, deionized water was used for all tests of pyrite oxidation in aqueous media, and J.T. Baker analytical grade reagents. Table I shows the chemical composition of the mineral. Oxidation and surface modification of pyrite grinding was evaluated in a wide pH range, this solution was titrated with NaOH 1 molal, and four different milling times were used: 5, 15, 30 and 45 minutes, allowing the variation pH during the course of milling.

Table I Chemical composition of the mineral pyrite.

Ore	**Element (% w/w)**							
Pyrite	**Fe**	**S**	**Cu**	**Pb**	**Zn**	**Ca**	**Na**	**Si**
	43.71	54.12	0.138	0.010	0.004	0.003	0.001	0.371
without characterize 1.64 (% w/w)								

The ore pulp obtained in each grinding test was analyzed by measuring physicochemical variables involved during the oxidation reaction and surface modification such as pyrite; pH, oxide reduction potential ORP (mV) and dissolved oxygen concentration OD ($mg \cdot L^{-1}$). The concentration of iron and sulfur are further analyzed in the solution after milling via spectrometry by inductively coupled plasma (ICP).

The dispersion of pyrite contained in the ore pulp obtained in each grinding time and for each pH value, was analyzed for its value zeta potential (mV), while the solids obtained were examined by XRD, FTIR and SEM in conjunction with EDS.

Results and discussion

Previous research has established that the surfaces of the mineral sulfides are oxidized by effect of galvanic contact with steel media and superficially contaminated with oxidation products of iron from the grinding media [6, 7, 8], altering the physicochemical properties of mineral.

However, previous work does not consider self mineral surface modification, the effect of adsorption, nucleation and growth of the oxidation of iron ore on the surface itself, due to oxidation / release of iron atoms and sulfur the last atomic layer of pyrite during grinding; for this reason, to clarify this phenomenon were conducted a series of tests grinding using media inert grinding (alumina) and a mill made of a polymeric material, this in order to avoid galvanic contact ore with balls steel.

With regard to the measurement of pH of the pulp, it was found that, generally tends to decrease with increasing grinding time (at pH 7, 9 11 and 12), whereas the initial pH 5.0 the potential ion hydrogen pulp increases with milling time, while at pH 13 it remains practically constant throughout the milling. The decrease in pH over time of milling at pH 7, 9, 11 and 12 is due in part to the use of ion OH^{-1} effect of surface hydroxylation of pyrite and the acidity generated by the oxidized to sulfate ion resulting from the surface modification of pyrite, where however the continuous production of OH^{-1} ions produced by the cathodic reduction process of the oxygen concentration, the pH of the pulp decreases throughout the milling time sulfur studied.

Fig. 1 shows the dissolved oxygen concentration versus time $mM{\cdot}L^{-1}$ grinding initial values for milling pH 5 to 13. It is noted that the decrease in the OD is greater comminution tests strongly alkaline pH values; However no greater reduction in the dissolved oxygen content, pH of the pulp decreases as described above, this means that the hydroxyl ions produced by the cathodic reaction is not sufficient to neutralize the acid produced by the oxidation of pyrite during milling with alumina media.

In fact, chemical analysis of the sulfur ion obtained by plasma spectrometry by inductively coupled (ICP) showed that the concentration of sulfur "S" in testing grinding pyrite means alumina at pH 11 to 13 and 45 minutes grinding, they are on average about 5.8 times higher than those obtained during milling performed at initial pH 5 to pH 9, as shown in Fig. 2

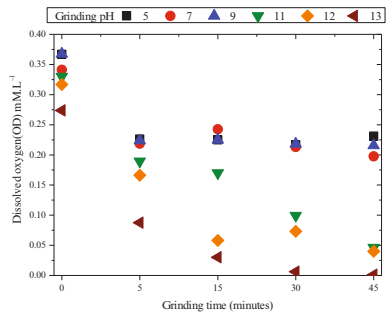

Fig. 1 Dissolved oxygen concentration ($mM{\cdot}L^{-1}$) versus time (minutes) with inert grinding means pH 5 to 13.

While the concentration of ferrous iron Fe^{2+} in test media milling alumina initial pH of 11-13 and 45 minutes of grinding, is on average about 6 times higher than that obtained at initial pH of 5 to pH 9 fig. 3. That is, a higher pyrite oxidation occurs at highly alkaline pH values, due to the availability of OH^{-1} ions which attack the pyrite surface liberating iron and sulfur ions to the solution.

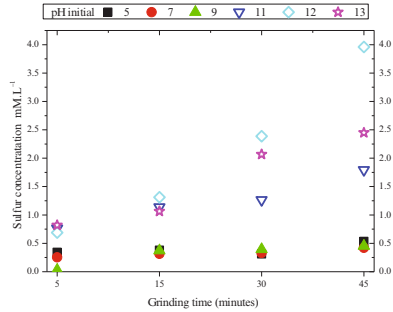

Fig. 2 Sulfur concentration ($mM \cdot L^{-1}$) as a function of grinding time (minutes) with alumina media of pH 5 to 13.

In regard to potential oxide - reduction OR, the results show that generally have potential oxidizing during grinding media made of alumina. Fig. 4 shows the potential variation OR function of time with inert grinding at an initial pH of 5 and 13 means including OR potential after the first 5 minutes of grinding and initial pH between 5 and 9, tend to stabilizing at approximately 0.44 V, this indicates that the electron transfer between the solid and aqueous species remains significant changes throughout the milling time studied.

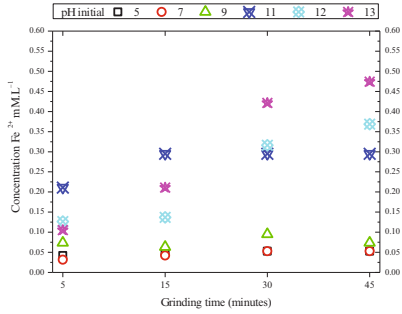

Fig. 3 Iron Fe^{2+}concentration ($mM \cdot L^{-1}$) of as a function of grinding time (min) initial inert media with pH 5 and 13

While grinding pyrite means alumina made to initial pH of 11 to 13, there are potential values OR less positive result of a higher concentration of ions Na^+ and OH^- used to titrate the desired pH (11 to 13). Fig. 4 also shows that the potential ORP to pH 11 virtually unchanged, while at pH 12 and 13 ORP decreases with increasing grinding time even at pH 13 and 30 minutes on ORP pulp is negative.

That is, it behaves as a reducing system, the continuous decrease of ORP shows involving electrochemical reactions throughout the grinding, as discussed earlier values strongly alkaline pH pyrite oxidation is greater extent, therefore greater transfer of electrons between the solid and aqueous species present in the pulp.

Pyrite particles obtained during the media grinding alumina have no magnetic susceptibility, qualitatively proven by approximating a magnet mineral particles. While analysis by XRD of pyrite obtained during milling with inert media, showed pyrite as the only majority phase present, however it is the change in intensity of the diffraction peaks most representative of pyrite, this is due to formation of secondary phases on the surface of pyrite altering its crystallinity not shown herein.

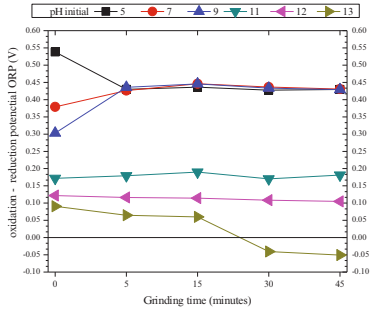

Fig. 4 Redox potential (ORP) versus grinding time (minutes) with inert media initial pH of 5 and 13.

Moreover, the oxidation of pyrite particles obtained during the media milling alumina was monitored by determining the zeta potential value. Figure 5 shows the values of zeta potential pyrite, for different initial pH values and reaction times studied. It is noted that the pyrite obtained during grinding to initial pH of 5.0 and 7.0, and usually has a magnitude value of positive zeta potential, 5 and 15 minutes of grinding, respectively, this is attributed to the surface chemical nature of pyrite and conditions chemical pulp.

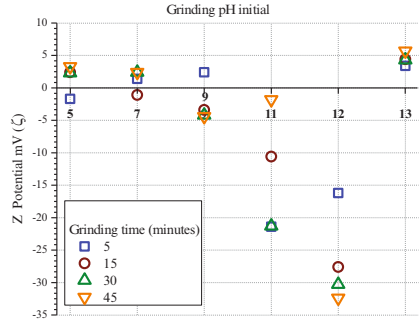

Fig. 5 Zeta potential mV vs. pH. Grinding times 5, 15, 30 and 45 minutes.

Moreover, Fig. 6 shows the FTIR spectra obtained pyrite initial pH 7 and different grinding times in the range of 15 minutes grinding, unlike the rest of the spectra occurs mainly dissolving the absorption band mode vibration S = O group at around 1383 cm^{-1} quimia assigned to molecular oxygen absorption of the sulfur atoms of the di - sulfide that has suffered a break in one of its sulfur covalent bonds S – S, dissolving this absorption band with the factors of chemical pulp vire influence the magnitude and zeta potential value previously presented in Fig. 5 for the initial pH 7.0 and 15 minutes of milling.

Fig. 6 shows that despite the absence of oxidation products iron produced steel media mill and the mill itself, the pyrite surface consists of a variety of secondary phases decomposition products and auto surface modification that pyrite undergoes during grinding with inert media.

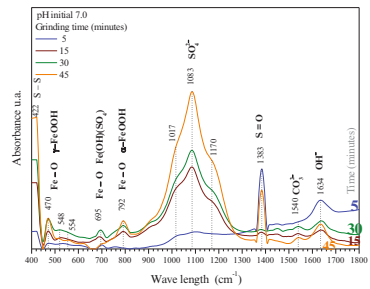

Fig. 6 Infrared (FTIR) of the milled pyrite initial pH 7.0 with inert media.

Furthermore, fig.7 shows the FTIR spectra of pyrite obtained during milling to an initial pH 12. The presence of a wide variety of secondary phases formed on the pyrite particles is

observed. In the spectral range sulphates has a sharp peak at 1083 cm^{-1} absorption with increasing grinding time, even with long grinding times, 45 minutes, the presence of the start of the formation of sulfate compound is observed, iron coordinated with three absorption bands

In the area of oxy hydroxides of iron, the absorption band at 475 cm^{-1} is assigned to the vibration mode bond Fe –O of lepidocrocite γ–FeOOH. The band at 699 cm^{-1} is attributed to the group of Fe – O a link or iron sulfate oxy hydroxy previously identified by other authors [8]. While band 795 cm^{-1} indicates the presence of goethite phase. For grinding times of 30 and 45 minutes, the presence of a weak absorption band at 620 cm^{-1} occurs, this band is associated with the presence of akaganeite β–FeOOH.

The weak absorption band in 1377 cm^{-1} is assigned to the vibration mode of the links S = O, while the weak bands at 1446 $cm^{-1}$and 1542 cm^{-1}, are associated with the presence of carbonate species coordinated with the iron. The presence of the band vibration mode Fe – OH 1639 cm^{-1} is assigned to the absorption of water molecules on the surface of mineral pyrite.

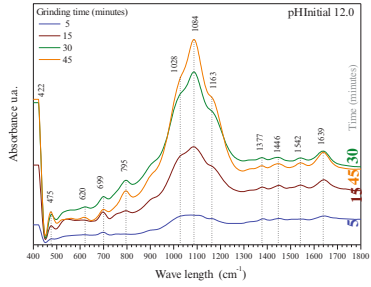

Fig. 7 Infrared (FTIR) of the grinding pyrite initial pH 12.0 with inert media.

Conclusions

However takes place pyrite grinding, free surfaces iron with inert grinding means, the pyrite particles superficially contaminated mainly by the nucleation and growth of the oxidation of iron or oxidized active sites, where the breaking of surface bonds Fe–S and S –S occurs promoting growth oxy - iron hydroxides as γ–FeOOH, lepidocrocite, hydroxy oxy iron sulfates Fe(OH)SO4 and iron complexes coordinated with sulphate as monodentate species identified by infrared spectroscopy, Fourier transform.

References

1. Murphy, R. and D.R. Strongin, Surface reactivity of pyrite and related sulfides. Surface Science Reports, (2009). 64(1): p. 1-45.
2. Schaufuß, A.G., et al., Reactivity of surface chemical states on fractured pyrite. Surface Science, (1998). 411(3): p. 321-328.
3. Adam, K., K.A. Natarajan, and I. Iwasaki, Grinding media wear and its effect on the flotation of sulfide minerals. International Journal of Mineral Processing, (1984). 12(1–3): p. 39-54.
4. Woods, Y.R.D.F.K.a.R., The interaction of iron species with pyrite surfaces. Journal of Applied electrochemistry, (1991). 21: p. 531 - 536.
5. Huang, G. and S. Grano, Galvanic interaction of grinding media with pyrite and its effect on floatation. Minerals Engineering, (2005). 18(12): p. 1152-1163.
6. Peng, Y. and S. Grano, Inferring the distribution of iron oxidation species on mineral surfaces during grinding of base metal sulphides. Electrochimica Acta, (2010). 55(19): p. 5470-5477.
7. Michael Descostes, C., Beaucaire, Florence Mercie, Sebastien Savaoy, Joachim Sow and Pierpaolo Zuddas, Effect of carbonate ions on pyrite (FeS2) dissolution. Bull. Soc. géol. France, (2002). 173(3): p. 265 - 270.
8. Peng, Y. and S. Grano, Effect of grinding media on the activation of pyrite flotation. Minerals Engineering, (2010). 23(8): p. 600-605.

Characterization of Minerals, Metals, and Materials 2016
Edited by: Shadia Jamil Ikhmayies, Bowen Li, John S. Carpenter, Jiann-Yang Hwang, Sergio Neves Monteiro, Jian Li, Donato Firrao, Mingming Zhang, Zhiwei Peng, Juan P. Escobedo-Diaz, and Chenguang Bai
TMS (The Minerals, Metals & Materials Society), 2016

ZINC CHLORIDE INFLUENCE ON THE RESINS FURAN POLYMERIZATION TO FOUNDRY MOULDS

Leila Figueiredo de Miranda[1], Marcus Vale[1], Antonio Hortêncio Munhoz Júnior[1],Terezinha Jocelen Masson[1], Leonardo Gondin de Andrade e Silva [2]

[1]Mackenzie Presbyterian University – Materials Engineering
Rua da Consolação, 930 – Consolação – São Paulo –Brazil- CEP 01302-907

[1]Instituto de Pesquisas Energéticas e Nucleares – CTR
Avenida Lineu Prestes, 2242 – Cidade Universitária - São Paulo –Brazil- CEP 05508-000
Keywords: Foundry, Furan resin, Polymerization, Mixed sand, Productivity.

Abstract

The resins used in foundry molds developed for the automotive market has led to major changes in the manufacturing method of foundry molds. The polymerization of these resins and a subsequent curing are used to connect to the foundry sand in a rigid structure capable of receiving and holding liquid metal. It is essential to know the process of polymerization of these resins and their impact on the final properties of the obtained molds, especially in the mechanical characteristics. In this work it was studied the influence of the addition of zinc chloride (in solution) in the sand-furan resin mixture, with the aim of reducing the relation between the extraction time intervals and time bench life. The results showed that addition of percentages of the order of 5.0wt% to 7.5wt% zinc chloride solution reduces this ratio between 10% and 17%; this means that the casting model may be extracted from the sand mass in a smaller time interval increasing the productivity of manufacturing molds. It was also observed that there was also an increase of 9% to 18% in bench life intervals.

Introduction

With the globalization of the economy, companies have been forced to modernize more and have more lean and productive processes. Several methodologies supported this change, among them the Honda system, the Toyota system and lean manufacturing. The basis of these methods is the reduction of waste, improvement of layout and reduction of manufacturing times and costs [9;10].

In the specific case of this study, its base is sustained in the fact that the foundry industries are struggling to meet the demands within the required deadlines that are increasingly tight [8]. Some general problems are detected, but there were manufacturing processes that required a very great deal of time to materialize. The largest manufacturing times were recorded in the molding industry, where the manufactured mold stay awaiting the model extraction time for a minimum of 5 hours after casting, and the workpiece stay awaiting its cooling for a minimum of 90 hours after the end time of filling the mold cavity with liquid metal.

In the case of cooling the piece, alternative to accelerate the cooling speed while keeping the metallurgical properties as specified are few. But in the case of molding sand and specifically the synthetic resin, the model extraction time is basically set in function of two parameters: the time

required bench life (gelling time of the molding sand), and the mechanical strength of the mold at the moment of extraction of the casting model.
Within this context, the variables related to molding sand generate no direct impact on the metallurgical quality of the product itself, unlike the variable cooling after casting mold. Variables related to molding sand are associated with the manufacturing process and whose change can raise productivity and optimize the resources required to fabricate the molds; either through increased availability of the casting model or the reduction in the total space required to store the templates that are waiting for the time of extraction of the model. The critical factor is that changes in these parameters in order to reduce processing time may become friable mold, i.e., easy fragmentation, due to the shorter bench life or decrease the mechanical strength due to the rapid polymerization of the synthetic resin [6]. This can result in even higher process time due to the rework resulting from the low mechanical strength of the sand mold .
Since the furan resin has been introduced in castings industry in 1958, catalysts such as acids were used in its cure system [5], and in 1985 Krawiec and Menting studied the use of the acid salts systems as accelerators for this resin [8].
Brazil is a country that has the ideal conditions for the implementation of a wind farm, whose implementation depends on the foundry industry to produce the components of wind turbines. On the other hand, experts of one of the most respected consulting to the global wind market, the *MAKE Consulting*, drew up a report on the supply chain for major manufacturers of wind turbines installed around the world and which was entitled *Global Wind Turbine Supply Chain* [11], pointed to the specific case of Brazil, as a critical point for the wind turbine manufacturers, the supply chain of critical components and, among these, are the cast. Only three companies were identified in Brazil specialized in this type of component, with a high cost of cast components and in some cases, with delays in the delivery of the same.
In Brazil the lines of credit from the government establish strict rules of nationalization, preventing the import of most cast components, in addition to electricity generated by wind farms is cheap the pressing more and more manufacturers reduce the cost of manufacturing of wind turbines [14]. Therefore, work aiming at reduction in cast components manufacturing costs for the wind sector are highly valued by wind turbine manufacturers.
The objective of this study was to investigate the influence of the addition of zinc chloride in solution in the polymerization speed of furan resin curing acid used as a binder for sand cold cure molding, evaluate the influence of this solution in the bench life interval, the model extraction time and the molding sand strength cold cure and evaluate the influence of zinc chloride solution in the morphology of the furan resin as a binder used for cold cure molding sand.

Materials and Methods

Materials

Silica base sand particle: size between 45 and 50 AFS, provided by Jundu Mining Company Ltd; Resin acid curing furan (Furotek NG®240): provided by the Foseco Industrial e Comercial Ltda; p-toluene sulfonic acid (catalyst acid type) with a concentration of 65% (65% APTS), supplied by the company Foseco Industrial e Comercial Ltda; zinc chloride solution (conc. 50w%), provided by the company Produquímica Indústria e Comércio S.A.

Method

The preparation of the composite material molding sand cold cure was conducted by adding 2.0kg of the silica sand base, new, in the planetary type laboratory mixer, followed by addition of the acid catalyst. The base sand and the acid catalyst was then mixed for a period of one and half minutes. After this time, the zinc chloride 50% was added and mixed for another minute and a half. Subsequently, he added to the furan resin and mixed for another minute and a half. This method was defined as recommended by the ABIFA CEMP number 182 (method used in most Brazilian foundries) [3].
Five experiments were carried out with different molding sand compositions cure at low temperature (Table 1). The percentage of furan resin were calculated on the mass of silica base sand and the percentage in APTS acid catalyst and zinc chloride were calculated on the mass of furan resin.

Table 1: Composition of molding sand mixtures cure cold

EXPERIMENT	COMPOSITION OF MOLDING SAND MIXTURES CURE COLD			
	Mixture	% Furan Resin	% $ZnCl_2$ in the mixture	%APTS in the Mixture
1	Ref.	1,0	0,0	30,0
	2		10,0	30,0
2	Ref.	1,0	0,0	30,0
	2		2,5	30,0
	3		5,0	30,0
	4		7,5	30,0
3	Ref.	1,0	0,0	30,0
	2		10,0	30,0
	3		10,0	25,0
	4		10,0	20,0
4	Ref.	1,0	0,0	30,0
	2		10,0	20,0
	3		20,0	10,0
	4		30,0	0,0
5	Ref.	1,0	0,0	30,0
	2		2,5	27,5
	3		5,0	25,0
	4		7,5	22,5
	5		10,0	20,0
	6		12,5	18,5

The bench life was measured by visual evaluation of the flow ability of cold cure furan sand molding when grains were moved over each other. With 250g of the sand molding cure cold, there was the movement of sand grains and visually evaluated the moment the grains failed to move freely. This is the method practiced by the laboratory of the Foseco Industrial e Comercial Ltda. and by most foundries working with furan sand molding with cure the cold.
The extraction time intervals was also determined from the time the mixing time interval ended. The extraction time interval was measured by evaluating the penetration resistance offered by a mass of 150g duly compacted molding sand in a mold with a minimum of 40mm diameter.
The extraction time interval is reached when a non-pointed shank diameter of 5mm cannot penetrate more than 10mm in mass of sand, without plucking grains of sand that have adhered

to each other. This method too is practiced by the laboratory of the Foseco Industrial e Comercial Ltda. and by most foundries working with cold cure furan sand molding.
Parallel sample preparation to determine the intervals bench life and extraction time was held compaction of the specimens used to determine the tensile strength (according to ABIFA CEMP number 162 recommendation [2], specimen strangled Dietert type, Figure 1).

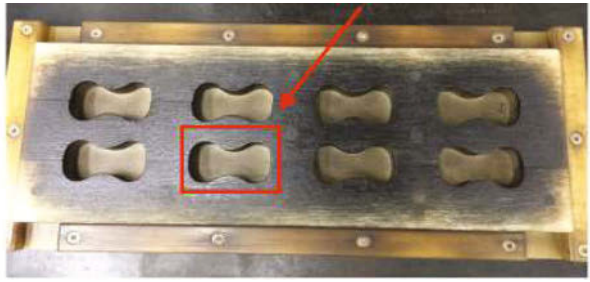

Figure 1 - Molding of the test specimens for tensile strength test.

The tensile strength tests were performed at defined time intervals from the end of the mixing time, and the minimum values must comply with the specifications of the ABIFA CEMP, Nº E- 09 [4]. The time intervals after mixing the molding sand and the respective minimum values for tensile strength are shown in Table 2.

Table 2: Minimum values of tensile strength after mixing (ABIFA CEMP, Nº E-09).

TENSILE STRENGTH AFTER MIXING (N/ cm²)			
2 hours	4 hours	6 hours	24 hours
62	96	110	138

Results

Sand Molding Cure Cold

The Table 3 shows the results obtained to the bench time, cure time and the cure time/bench life ratio of the different compositions of sand molding studied.

Table 3: Results obtained to the bench time, cure time and the cure time/bench life ratio of the different compositions of sand molding studied.

MOLDING SAND COMPOSITION			ENVIRONMENTAL CONDITIONS		POLYMERIZATION TIMES OF MIXTURE		
Mixture	[$ZnCl_2$](w%)	[APTS] (w%)	Temperature (°C)	Relative humidity (%)	Bench time (min)	Cure time(min)	Cure time/bench time
Ref.	0,0	30,0	25,6	48,0	5,5	39,0	7,1
2	2,5	27,5			5,5	40,0	7,3
3	5,0	25,0			6,0	38,0	6,3
4	7,5	22,5			6,5	38,0	5,8
5	10,0	20,0			6,5	45,0	6,9
6	12,5	18,5			7,0	50,0	7,1

Table 3 shows that:
- The bench life intervals and extraction time obtained for blends 3 and 4 attend the polymerization times objectives proposed for this work [1], so, to obtain a sand molding composition for molding cold cure that has a range bench life over the same interval from the reference mixture, combined with a reduced extraction time interval when also compared to the same time interval obtained for the reference mixture;
-There was an increase in the bench life range of 9.1% to 18.2% for blends 3 and 4 respectively; allies with a decrease of 2.6% in extraction time range for both compounds as compared to the values obtained for the reference mixture. These results are showed in Table 4.

Table 4 – Results obtained of the variation in polymerization times of the mixtures studied in the fifth experiment.

MOLDING SAND COMPOSITION			ENVIRONMENTAL CONDITIONS		POLYMERIZATION TIMES OF MIXTURE		
Mixture	[$ZnCl_2$](w%)	[APTS] (w%)	Mixture	[$ZnCl_2$](w%)	[APTS] (w%)	Mixture	[$ZnCl_2$](w%)
Ref.	0,0	30,0	25,6	48,0	100,0	100,0	100,0
2	2,5	27,5			0,0	2,6	2,6
3	5,0	25,0			9,1	-2,6	-10,7
4	7,5	22,5			18,2	-2,6	-17,6
5	10,0	20,0			18,2	15,4	-2,4
6	12,5	18,5			27,3	28,2	0,7

Table 4 shows that:
- The results of bench life intervals for blends 5 and 6 suffered an increase of 18.2% and 27.3% respectively, compared to the time interval obtained with the reference mixture. However, there was an increase in extraction time range of 15.4% and 28.2% respectively. The relationship between the ranges of bench life and extraction time of the mixture 5 decreased by 2.4% and the mixture 6 an increase of 0.7%, both with respect to the values obtained for the reference mixture; - The mixture 2 had the same result as bench life compared to the reference mixture interval however there was an increase of 2.6% in the result of extraction time interval compared to the

value obtained for the reference mixture. Consequently, the mixing 2 showed a value relationship between the extraction time interval, and 2.6% bench life higher when compared to the value obtained with the reference mixture.
Figure 2 shows the results obtained for the tensile strength of the blends of the experiment 5.

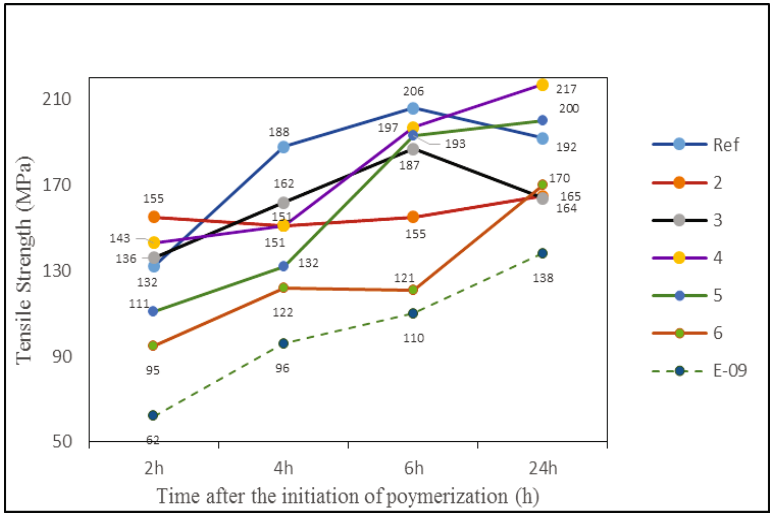

Figure 2: Results obtained for the tensile strength of the blends of the experiment 5.

Figure 2 shows that:
- For mixtures 2, 3 and 4, the tensile strength results for the time interval of 2 hours after mixing were higher than found for the reference mix. For the other time intervals, there was not the same behavior. The percentage change in tensile strength values obtained for mixtures with addition of zinc carried out during the fifth chloride experiment are presented in Table 5.

Table 5: Results obtained to the loss of the tensile strength of the mixtures studied in the fifth experiment

MIXTURE	DECREASE OF THE TENSILE STRENGTH IN RELATION TO REFERENCE MIXTURE (%)			
	2 hours	4 hours	6 hours	24 hours
Ref.	100	100	100	100
2	17,0	-19,7	-24,8	-14,1
3	2,6	-13,8	-9,2	-14,6
4	7,9	-19,7	-4,4	13,0
5	-16,2	-29,8	-6,3	4,2
6	-28,3	-35,1	-41,3	-11,5

Table 5 shows that mixtures 3 and 4 show reduction in tensile strength in all time intervals after mixing, except for the 24-hour time interval (decrease of 4.4% and 19.7%) in bora meet the specifications of ABIFA CEMP E-09 [4]. The result of the increase in 24-hour time interval of the mixture 3 was 13.0%.
The mixture 5 has a tensile strength results for the 24-hour interval after mixing higher than the result obtained with the reference mixture to the same period considered.
The mixture of 6 was the mixture which had the lowest tensile strength results for two time intervals, 4 and 6 hours after mixing. As for time intervals of 24 hours, the obtained result with this mixture was higher than the results obtained with the mixtures 2 and 3.

Morphological analysis of the polymer in the Sand Molding Cure Cold

The morphology of the polymer adhered on the surface of the base sand grains was evaluated by SEM in the region of the contact points between sand grains basis. The chemical composition in the contact region between the base grains of sand was determined by detection of characteristic X-rays made by energy dispersive spectrometer (EDS) coupled to SEM. Figure 3 shows micrographs for molding sands containing 0%, 2.5%, 5%, 7.7%, 12.5% 2 10% $ZnCl_2$. The images show the change in morphology of the polymer as the zinc chloride concentration increased.

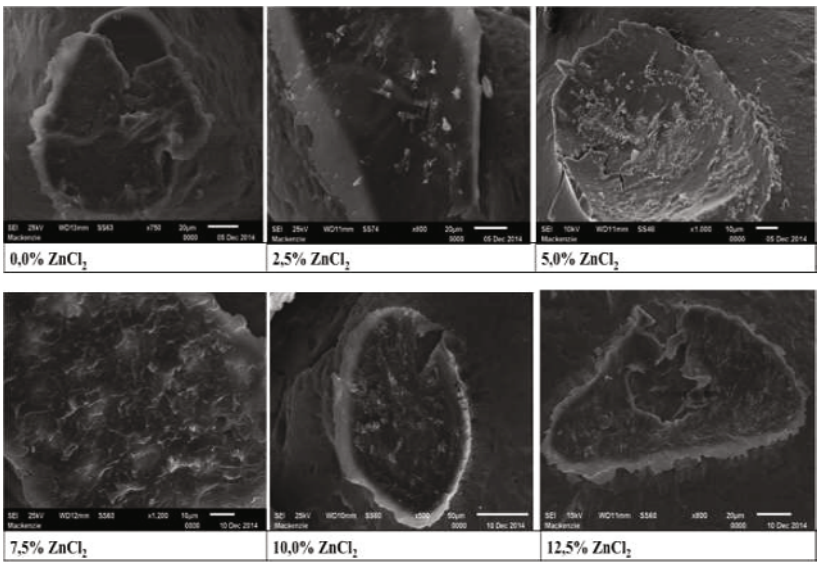

Figure 3: Molding sands obtained with resins containing various concentrations of zinc chloride.

According to Figure 3 the polymer no longer porous and has become compact, but had a compound in the shape of plates rich in iron and zinc, in accordance the EDS results.

Conclusions

From the results we conclude that the concentration between 5 and 7,5wt% of zinc chloride solution (50 wt%),calculated in relation to the furan resin can be used with 22,5 and 25wt% of the catalyst APTS (65 wt%) calculated also in relation to furan resin. This composition with silica makes good molds for foundry.

This conclusion is based in the results of the bench life. The results proved that there would be a reduction in the processing time resulting in a higher productivity.

The addition of 50wt% zinc chloride solution resulted in the reduction of the strength for all range of time.

References

[1] ABIFA CEMP. Comissão de Estudos de Matérias Primas. *Determinação da reatividade* - Resinas e catalisadores cura a frio para fundição. CEMP-149, Março 2003.

[2] ABIFA CEMP. Comissão de Estudos de Matérias Primas. *Determinação da resistência à tração da mistura padrão.* CEMP-162, Fevereiro 2003.

[3] ABIFA CEMP. Comissão de Estudos de Matérias Primas. *Preparação da mistura padrão utilizando batedeira planetária para o ensaio de resina cura a frio para fundição.* CEMP-182, Março 2003.

[4] ABIFA CEMP. Comissão de Estudos de Matérias Primas. *Resina para processo cura a frio para fundição*. CEMP E-09, Março 2003.

[5] CAREY P. R.; LOTT M. A aplicação da resina furânica no-bake como sistema aglomerante de areia. *Revista Fundição e Serviços*, nº 72, 1998.

[6] DZIAKOVÁ, M.; VASKOVÁ, I.; FECKO, D. *Influence of Operating Factors on Properties of Furan Mixtures.* Technical University of Kosice, Slovakia, 2010.

[7] FERNANDES, D. L. *Areias de fundição aglomeradas com ligantes furânicos.* SENAI-DR.MG. ISBN: 85-7466-057-4, 2001.

[8] KRAWIEC R., MENTING J. E., Qo Chemicals, Inc. *Fast curing furan foundry binder system containing a metal salt accelerator.* USA Patent number US4543373 A, September 1985. [9] KUKLA S. *Production System Rationalisation on the Example of Iron Foundry.* Archives of Foundry Engineering. ISSN (1897-3310), Volume 10, Issue 2, 2010.

[10] KUKLA S. *Evaluation and Verification of Time and Costs of Production Activities in Foundry Industry.* Archives of Foundry Engineering. ISSN (1897-3310), Volume 7, Issue 3, 2007.

[11] MAKE CONSULTING. *Global Wind Turbine Supply Chain Conference:* Relatory. Hamburg, Germany, 2010.

[12] MANIOWSKI, Z.; MLYNSKI, M.; SIERANT, Z.; ZÓLKIEWICZ, Z. *Selected Aspects of the Piece Production of Iron Alloy Casting in Terms of Their Environmental Impact.* Archives of Foundry Engineering. ISSN (1897-3310), Volume 10, Issue 3, 2010.

[13] MODERN CASTING. Census of world casting production: steady growth in global output.(A Modern Casting Staff Report). *Modern Casting*. V.104, n.12, p 17-21, 2014.

[14] SHREVE D., LEWANDOWSKI L., GAYLORD B., SACHDEVA B. Make Consulting. *Global Wind Turbine Supply Chain.* Make report, 2012.

Characterization of Minerals, Metals, and Materials 2016
Edited by: Shadia Jamil Ikhmayies, Bowen Li, John S. Carpenter, Jiann-Yang Hwang, Sergio Neves Monteiro, Jian Li, Donato Firrao, Mingming Zhang, Zhiwei Peng, Juan P. Escobedo-Diaz, and Chenguang Bai
TMS (The Minerals, Metals & Materials Society), 2016

CHARACTERIZATION OF GAMMA-ALUMINA OBTAINED FROM AGED PSEUDOBOEHMITES

Antonio Hortencio Munhoz Jr[1], Leonardo Gondin de Andrade e Silva[2], Leila Figueiredo de Miranda[1], Raphael Cons Andrades[1]

[1]Universidade Presbiteriana Mackenzie, R. Consolação, 930 – ZIP CODE 01302-907 -São Paulo – SP – Brazil
[2]IPEN – São Paulo – SP - Brazil

Keywords: gamma-alumina, pseudoboehmite, ceramics

Abstract

Gamma-alumina is a very important material industrially due to their use in adsorption and catalysis. The nanoparticles of aged pseudoboehmites materials with high specific surface area are being recently studied for the controlled release of drugs. Pseudoboehmites was synthesized by the sol-gel process and gamma-alumina with high purity was obtained from pseudoboehmite aiming their use in controlled release of drugs. The gamma-alumina was characterized by several techniques such as X-ray diffraction, scanning electron microscopy, differential thermal analysis, thermogravimetric analysis and nitrogen isotherm adsorption.

Introduction

Alumina (compound) and corundum (mineral) is one of the most important ceramic compounds. In chemical formula Al_2O_3, it can be found in nature as aluminum metal oxidation product, being mainly present as the major constituent of the ore used in obtaining primary aluminum, bauxite. In the laboratory, among other possible routes, the alumina can be synthesized by calcining a synthetic aluminum compound, the pseudoboehmite, which in turn can be produced in the laboratory by the sol-gel process. Pseudoboehmite is an aluminum compound that has been studied for the controlled release of drugs [1,2]. This material can be obtained by the sol-gel process, which allows the obtaining of highly pure inorganic oxides with excellent properties, since all steps of synthesis from molecular precursors to the final product can be controlled. This process permits a good control of the stoichiometry, porosity, crystalline structure and particle size of the desired products, which influence their morphology and surface area [3]. The structure of pseudoboehmite is considered to be similar to the structure of boehmite due similarity in the peak positions on their diffraction patterns. The calcination of pseudoboehmite follows the stage of processing sequence of aluminum hydroxide, resulting in the polymorphic structures of alumina, -Al_2O_3, -Al_2O_3, -Al_2O_3 and -Al_2O_3 [3], following the order processing stages with increasing temperature in accordance with equation 1.

$$\text{Pseudoboemita} \rightarrow \gamma Al_2O_3 \rightarrow \delta Al_2O_3 \rightarrow \theta Al_2O_3 \rightarrow \alpha Al_2O_3 \qquad (1)$$

The polymorphic alumina have different structure and properties. The gamma-alumina, for example, differed from eta alumina, not only in its pore-size distribution, but also in the fact that the water content of gamma-alumina was much greater than that of eta alumina. This "excess" water associated with gamma alumina was regarded as consisting of molecular water strongly adsorbed on the surface of the alumina.

Gamma alumina is an important support for catalysts. It is used, for example, in synthesis of long chain hydrocarbon from natural gas [4], preferential oxidation of carbon monoxide from a hydrogen-rich gas stream [5]. The gamma-alumina can be produced by calcination of boehmite at 500º C [6,7,8,9,10].

Experimental

The pseudoboehmite was prepared by the sol-gel process according to the methodology described by Munhoz et al [3]. This method was used because it do not use sodium hydroxide. It is important in the production of gamma-alumina that the product has no sodium as contaminant.

Characterization of the samples:

The pseudoboehmite samples were characterized by several techniques. Thermal analyses: thermogravimetric analysis (TG) and differential thermal analysis (DTA) were performed in a Netzsch-Jupiter STA449F3 equipment heating from room temperature to 1300°C at 20°C min^{-1} and 50cm^3/ min N_2 flow.

X-ray powder diffraction: the samples were dried at 70º C and analyzed by X-ray diffraction. The samples were analyzed by a Rigaku MultiFlex diffractometer with a fixed monochromatic radiation. The experimental conditions were: 40kV, 20mA, 20º < 2θ < 90°, Δ2θ = 0.02°, λCuKα, divergence slit = 0.5°, reception slit = 0.3 mm and step time = 2s.

Scanning electron microscopy: the SEM images were taken with Jeol equipment JSM 6510, using secondary electron detector and EDS detector. The powders were placed upon SEM stubs covered with double-face tape. After that, the powders were covered with gold in an Edwards Sputter Coater model S150B for the SEM analysis using secondary electron detector. The images were registered under several magnifications.

To obtain nitrogen adsorption data for characterisation of the alumina porous structure, it was used a Bell equipment (Belsorp MAX). The nitrogen isotherm were carefully measured at −196 °C and the specific surface area was determined by BET (Brunauer-Emmet-Teller) method [11].

Results and discussion

The differential thermal analysis and the thermogravimetric analysis (Figure 1), shows the characteristic behavior of pseudoboehmite.

The differential thermal analysis (DTA) of pseudoboehmite showed at approximately 100º C a endothermic peak due to water loss. At 220-450°C the mass loss associated with the phase transformation of pseudoboehmite (AlOOH)n to γ- Al2O3 was observed.

The very fast transformation of pseudoboehmite to γ- Al2O3 is an indication of the high specific surface area of this material. Powders with high specific surface area, containing nanoparticles, promotes faster heat transfer, and influences the rate of transformation of pseudoboehmite to γ- Al_2O_3.

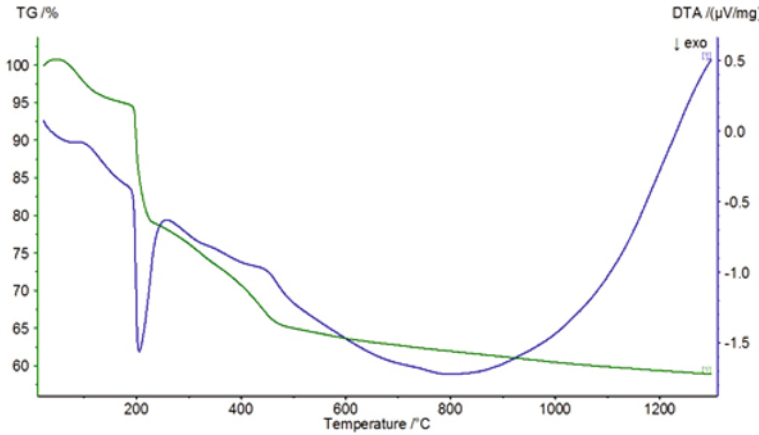

Fig. 1. DTA and TG analyses of pseudoboehmite.

The results of X-ray diffraction of the sol-gel product sample are shown in Figure 2. It was observed that this sample displayed an XRD pattern similar to the pseudoboehmite described in the literature [12]. The samples shows also the characteristics patterns of boehmite (ICDD card 01-073-9093)[13].

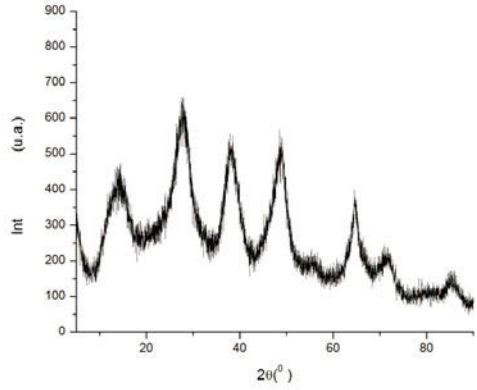

Figure 2. X-ray diffraction synthetized sample showing the characteristics XRD patterns of the sol-gel product [12].

The X-ray diffraction data of the sol-gel product calcined at 500° C are shown in Figure 3. It should be considered that this material was obtained from calcination of nanoparticles of the

sol-gel product. Comparing the results of the calcined sample with the files of International Centre for Diffraction Data-ICDD, the results shows the characteristics patterns of the alumina gamma (ICDD card 01-074-4629) [14].

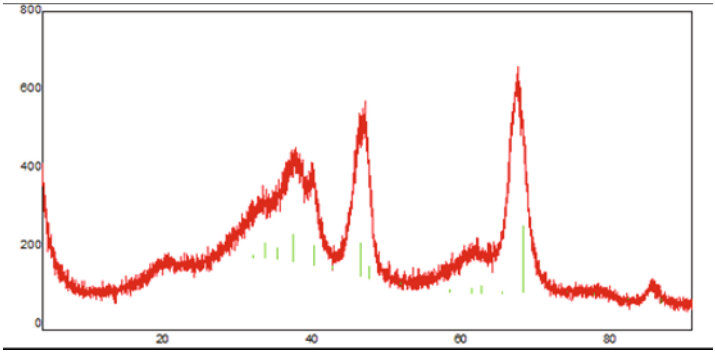

Figure 3. X-ray diffraction pattern of the calcined sample showing characteristics XRD patterns of gamma-alumina [14].

The scanning electron micrograph of sol-gel product (shown in Figure 4), obtained using secondary electron detector and a magnification of 2000 shows that the sample (agglomerated of particles) is a porous material. The EDS detector, in scanning electron micrograph, indicated that aluminum and oxygens is homogeneously distributed in the sample. Considering that the chemical formula of pseudoboehmite is $(AlOOH)_n$, the result of EDS is coherent. According to Yan porous pseudoboehmite is very promising for use in drug delivery system, including treatment of cancer disease [15].

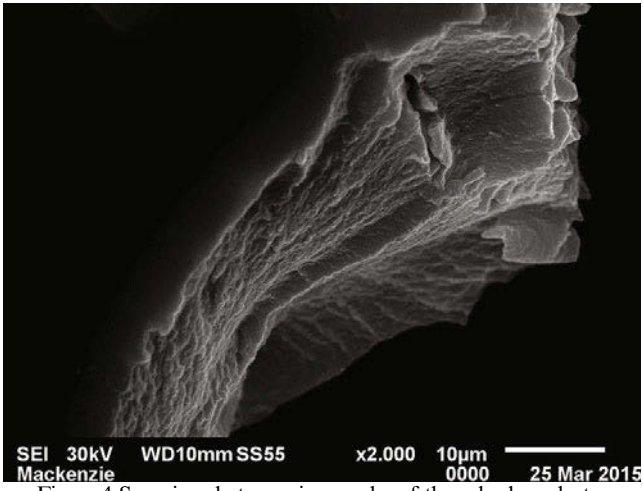

Figure 4 Scanning electron micrography of the sol-gel product.

Figure 5 shows the nitrogen adsorption analysis of the calcined sample, sol-gel product calcined at 500° C. The results shows a Type IV isotherm. The isotherm adsorption data shows the presence of macropores and mesoporous material. There is a hysteresis in the adsorption/desorption isotherm. The specific surface area obtained by B.E.T. method was 215 m ^{2}/g.

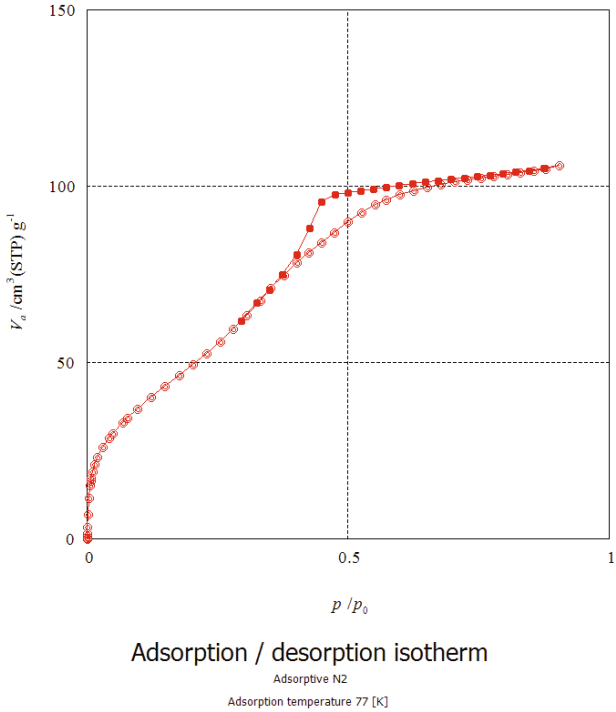

Figure 5 Nitrogen adsorption/desorption isotherm of calcined sample.

Conclusion

The synthesis route adopted in this work proved to be highly effective to produce gamma-alumina from pseudoboehmite.

The X-ray diffraction data and other analyses together with the literature review confirm that the obtained material by the sol-gel process has the pseudoboehmite structure.

Also the X-ray diffraction data shows that the product obtained from the calcination of the sol-gel product produced a material that has the characteristic XRD pattern of gamma-alumina.

It was observed in the electron scanning microscopy that the material is porous and aluminum and oxygen was homogeneously distributed in the analyzed samples.

Thus, the results presented in this study indicate that pseudoboehmite was produced by sol-gel process and the potential use of pseudoboehmite in the production of pure gamma-alumina.

Acknowledgment: The authors are grateful for the supoport given by MackPesquisa, Universidade Presbiteriana Mackenzie and São Paulo Research Foundation (FAPESP, grant 2010/19157-9).

References

[1] RIBEIRO, R. R. ; JR, A. ; MUNHOZ JR, A. H. ; R.W.NOVICKIS, ; MARTINS, M. V. S. ; SILAV, L. . Development of nanosystems to release atenolol. **Advances in Science and Technology** (Online), v. 86, p. 102-107, 2013

[2] NOVICKIS, RICHARD. W. ; MARTINS, MARCOS V. SURMANI ; DE MIRANDA, LEILA F. ; RIBEIRO, ROBERTO R. ; SILVA, LAUREANO ; MUNHOZ JR., ANTONIO H. . Development of Nanosystems to Release Atenolol. **Advances in Science and Technology** (Online), v. 86, p. 102-107, 2012.

[3] MUNHOZ JR, A. H. ; MIRANDA, L. F. ; UEHARA, G. N. . Study of pseudoboehmite by sol-gel synthesis. **Advances in Science and Technology**, v. 45, p. 260-265, 2006

[4] Oyvind Borg, Sigrid Eri, Edd A. Blekkan, Solvi Storsaeter, Hanne Wigum, Erling Rytter, Anders Holmen. 2007. "Fischer-Tropsch synthesis over gama-alumina-supported cobalt catalysts: Effect of support variables." **Journal of Catalysis** 248 (2007) 89-100

[5] Chan Kwak, Tae-Jin Park, Dong Jin Suh. 2004. "Effects of sodium addition on the perdormance of PtCo/Al2O3 catalysts for preferential oxidation of carbon monoxide from hydrogen-rich fuels." **Applied Catalysis A: General** 278 (2005) 181-186,

[6] ZHANG, Z.; PINNAVAIA T.J.; Mesoporous gamma-alumina formed through the surfactant-mediated scaffolding of peptized pseudoboehmite nanoparticles. **Langmuir.** 2010 Jun 15;26(12):10063-7

[7] K.M.PARIDA, AMARESH C. PRADHAN, J. DAS, NRUPARAJ SAHU, **Materials Chemistry and physics** 113 (2009) 244-248.

[8] CHUAH, G.K.; JAENICKE, S.; XU, T.H.; The effect of digestion on the surface area and porosity of alumina. **Microporous and Mesoporous Materials** 37, p. 345–353, 2000

[9] HIRASHIMA, H.; KOJIMA, C.; IMAI, H.; Application of Alumina Aerogels as Catalysts. **Journal of Sol-Gel Science and Technology** 8, p. 843-846. 1997

[10] RAO, P.K.; SIVARAJ, C.; REDDY, B.P.; RAO, B.R.; Preparation of catalytically active y-al203 from a basic aluminium succinate precursor precipitated from homogeneous solution. **Applied Catalysis, E.** 24 p 25-35, 1986

[11] S. Brunauer, P. H. Emmett and E. Teller, **J. Am. Chem. Soc.**, 1938, 60, 309.

[12] Ella M. Moroz, Kristina I. Shefer, Dmitry, A. Zyuzin, Aleksandra S. Ivanova, Eugenia V, Kulko, Vasily V. Goidin, Viktor V. Molchanov. 2006. "Local Structure of pseudoboehmites." **React.Kinet.Catal.Lett**, Vol. 87, No. 2, 367-375.

[13] BOKHIMI, X., SANCHEZ-VALENTE, J., PEDRAZA, F.J. **Solid State Chem**, 166 (2002) 182

[14] PAGLIA, G.; BUCKLEY, C.E.; ROHL, A.L., HUNTER, B.A., HART, R.D., HANNA, J.V., BYRNE, L.T., Phys. Rev. B68,144110 (2003).

[15] Yan Chen, Kelong Ai, Yanlan Liu, Lehui Lu. 2013. "Tailor-Made Charge-Conversional Nanocomposite for pH-Responsive Drug Delivery and Cell Imaging." **Applied Materials & Interfaces**, 5 de dezembro.

Characterization of Minerals, Metals, and Materials 2016
Edited by: Shadia Jamil Ikhmayies, Bowen Li, John S. Carpenter, Jiann-Yang Hwang, Sergio Neves Monteiro, Jian Li, Donato Firrao, Mingming Zhang, Zhiwei Peng, Juan P. Escobedo-Diaz, and Chenguang Bai
TMS (The Minerals, Metals & Materials Society), 2016

MICROSTRUCTURE, MECHANICAL AND OXIDATION BEHAVIOR OF NIOBIUM MODIFIED 9% CHROMIUM STEEL

Anup Mandal[1], Tapas Kumar Bandyopadhay
Department of Metallurgical & Materials Engineering, Indian Institute of Technology, Kharagpur-721302, India.
[1]Corresponding Author: Email:anupmetal@gmail.com, Phone No: 08101338702, Fax: 03222282238

Keywords: Microstructure; 9Cr steel, Niobium; Tensile property; Cyclic oxidation

Abstract

Microstructure, mechanical and oxidation behavior of niobium modified 9Cr steel has been reported in this work. Cast microstructure consists of martensite along with retained austenite and undissolved carbide phases. Martensite and Carbide phase changes are observed with increasing temperature during high temperature x-ray diffraction. Tensile properties of the steel are dependent on hot working and subsequent heat treatment parameters. The best combination of strength and elongation is achieved for 80% hot rolling, followed by normalizing at 1100˚C and tempering at 700˚C. Creep curve consists of primary, secondary and tertiary regions. Cyclic oxidation curve follows near parabolic rate regime.

1. Introduction

Ferritic/martensitic 9Cr steels are used as materials for high temperature applications. These classes of steels have properties like high thermal conductivity, low thermal expansion, adequate creep strength, and resistance towards oxidation and stress corrosion cracking. 9Cr steel has extensive single phase austenite region between 800 and 1200˚C and narrow two phase region between austenite and ferrite. Therefore, austenitization of the steel is easier and upon cooling to room temperature, the steel converts to fully martensitic structure. Also, delta ferrite formation which is detrimental for high temperature application can be avoided [1–3]. High temperature property of the steel has been further improved by solid solution strengthening and precipitation strengthening through addition of Mo, W, Cu, Mn, Co, V, Nb [4–6] etc. The development 9Cr steel like P91, P92 contains numerous alloying elements that lead to increase in cost. Hence, producing high temperature material at low cost is the priority of our study. Heat treated microstructure of 9% Cr steel consists of ferrite sub grains with a high dislocation density and very fine stable precipitates, evenly distributed around the lath and grain boundary. These precipitates help to block the movement of dislocations along grain boundary region. To achieve sufficient creep strength, relatively large amount of different types of stable finely dispersed precipitates (such as MC, $M_{23}C_6$, Laves phase etc.) having different kind of nucleation and growth kinetics are required [7–9]. Increasing carbon as the primary alloy for higher strength and hardness of steels is usually the most economical approach to improve performance. However some of the adverse effects of high carbon levels are reduced weldability, ductility and impact toughness. When these reduced properties can be tolerated the increased strength and hardness of the high carbon steels can be used to a significant advantage. Common applications of high carbon steels include forging grades, rail steels, spring steels, wear resistance steels and high

strength bars. When there is a need to improve the performance of the steels with additional strength or hardness other strengthening mechanism like precipitation strengthening using a micro alloy addition is useful [10]. The available choices for micro-alloying elements include niobium, titanium and vanadium. Vanadium is primarily used as carbide former in 9Cr steel [2–9]. However, niobium can also be used as principal carbide forming alloying element. The effect of niobium in 9Cr steel is not reported. Therefore, the objective of this work is to study microstructure, mechanical and oxidation properties of niobium modified 9Cr steel.

2. Experimental Procedure

The investigated steel was produced in an induction furnace with a batch size of 3 kg. The steel ingot was homogenized at 1200˚C for four hours in a programmable muffle furnace and subsequently forged to 40% thickness reduction. Another two samples were subjected to hot rolling with 40% and 80% thickness reductions in the same heating conditions. The hot worked samples were normalized at 1100˚C for 1 hour followed by tempering at 700˚C for 1 hour. The chemical composition of the steel was analyzed by X-Ray Flourescence (BRUKER, Model-S8 Tiger). Table-1 shows the compositions of the steel in wt%. Small cubic samples of cast, forged and tempered steels were polished and etched using 2% Nital (Nitric Acid+Ethanol) or Vilella's reagent (Picric acid + Hydrochloric Acid + Ethanol) to observe the microstructures by Optical Microscopy (LEICA, Model-DM2500M). High resolution FESEM (FEI, Model-QUANTA FEG 250) was used to observe the detailed microstructural features. X-Ray diffraction studies (BRUKER, Model-D8 Advance) were carried out using Co K radiation at the diffraction angle (2) from 20 to 120˚. Differential Scanning Calorimetry study of the steel was conducted using a Netzsch STA 409PC calorimeter. Non isothermal DSC measurement was done by heating the sample of around 40 mg from 25˚C to 900˚C and then cooling to room temperature at a rate of 15˚C/min. Tensile tests were carried out using sub size specimen with 25 mm gauge length in tensile testing machine (SHIMADZU: AG 5000G) at a displacement rate of 1mm/minute. Creep tests were performed at 600˚C (873 K) and 120 MPa using an Applied Test Systems (ATS) lever arm (20:1) creep tester. The changes in the specimen's length (uni-axial creep tests) were measured using an inductive transducer with a high measuring accuracy (repeatability approximately 1 μm) and were recorded continuously by a computer. The cyclic oxidation tests were carried out with cubic samples of dimension 10 mm × 10 mm × 5 mm. The samples were polished down to 1 m surface finish and washed in acetone. The thermal cycle consisted of 1 hour heating and then 1 hour cooling. The oxidation test was performed in a muffle furnace working in air at a desired temperature of 600, 650 and 700˚C. The sample was directly put in a horizontal muffle furnace which is kept at a specified temperature of 600, 650 and 700˚C for 1 hour holding. After one hour holding, the test was ended by immediately removing the sample from the furnace and cooling in air to room temperature. The weight of the sample was measured after each cycle in a standard balance (Sartorious CP124S microbalance with a resolution of 10^{-5} g). The specific weight gain of the sample after each cycle was plotted against total number of cycles at a desired oxidation temperature.

Table 1: Composition of the steel in wt. %

C	Cr	Mn	Si	S	P	Nb	Fe
0.9	8.84	1.17	0.5	0.06	0.09	0.41	Bal.

3. Results and discussion

3.1 Differential Scanning Calorimetry: Phase transformation of the steel was studied using DSC. The phase transformation and reactions associated with heating and cooling of the alloy is shown in figure1. The transformation of martensite to ferrite starts at 572˚C and the Curie temperature (T_c) signifying the change of ferromagnetic property is found at 750˚C. The austenite phase transformation (Ac_1) starts at 780˚C, peaks (Ac_p) at 800˚C and completes (Ac_3) at 830˚C. The enthalpy associated with ferrite to martensite transformations, Curie transformation and ferrite to austenite transformation are 8.913 J/G, 3.291 J/g and 16.18 J/g respectively. The enthalpy values are closer to the reported values of Grade 91 steel [11]. The observed T_c, value is similar but, Ac_1, Ac_p, Ac_3 temperatures are around 20˚C lower than the reported values of Grade 91 steel [12]. This may be due to higher carbon content of the investigated steel compare to Grade 91 steel. During cooling austenite to ferrite transformation starts at 700˚C and finishes at 630˚C. Martensitic transformation is not observed at the cooling rate 15 K/min.

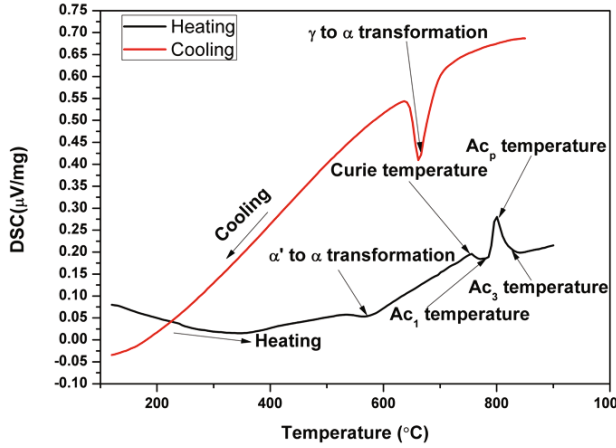

Figure 1: Critical temperatures during heating and cooling at 15 K/min in DSC

3.2 Microstructure: Figure2a, 2b shows optical micrograph of cast and forged steel respectively. Cast and forged microstructure consists of martensite/ferrite along with small amount of retained austenite. The martensites are lath type due to high carbon content of the steel. The larger grain size of cast structure has been reduced after forging. The grain structure of cast and forged steel is shown in figure 2c and 2d respectively.

3.3 High temperature phase analysis: The evolution of different phases at high temperature was conducted with high temperature XRD analysis. Figure 3 shows the high temperature XRD plot for different phases of the steel at 25˚C, 500˚C, 700˚C and 900˚C. At room temperature martensite/ferrite, iron carbide (Fe-C), chromium carbide (Cr_3C_2) phases are present. With increase in temperature the intensity of the carbide phases increases at 500˚C. With further

increase in temperature, chromium carbide changes its structure and forms $Cr_{23}C_6$ and iron carbide (FeC) changes to Fe_5C_2 at 700˚C. Austenite phase appears at 900˚C temperature.

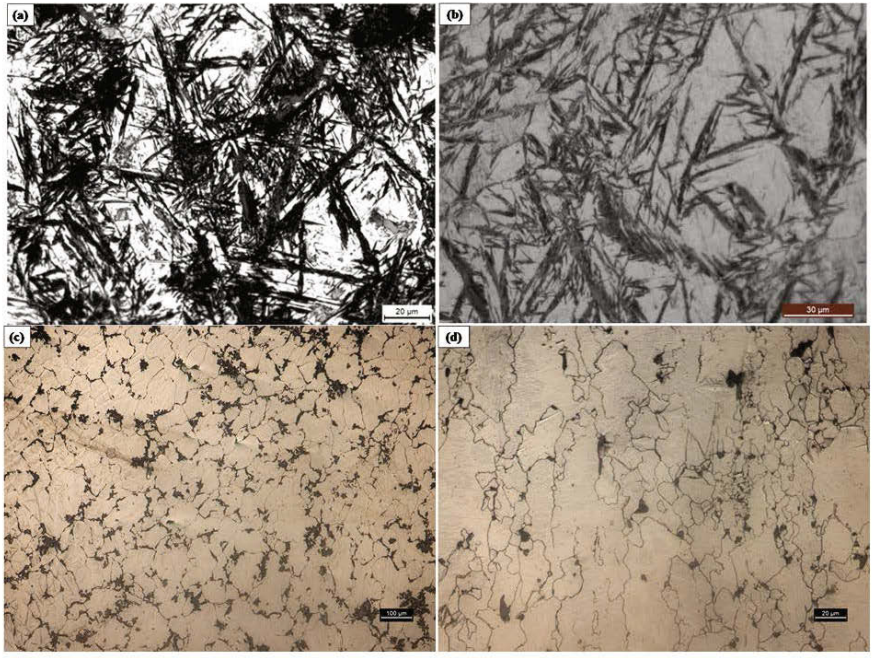

Figure 2: Optical micrograph of (a) cast steel, (b) forged steel; grain structure of (c) cast steel, (d) forged steel

3.4 Effect of tempering on microstructure: As the steel is cooled from austenizing temperature to room temperature the microstructure is transformed from austenite to martensite with lot of internal stresses. Wang *et al*. [1] have reported that to improve the plasticity, relieve the normalizing stress and microstructural stability high temperature tempering should be employed. Moreover, the tempering temperature should not be higher than 800˚C; otherwise Z phase which is injurious to creep properties will form [13]. It is reported that dissolution of MX and $M_{23}C_6$ type precipitates begin at about 780˚C and 900˚C and finish at about 940 and 1200˚C, respectively [7]. The steel after hot working is subjected to normalizing at 1100˚C for 1 hour followed by tempering at 700˚C for 1 hour. Figure 4a shows the SEM micrograph of the sample tempered at 700˚C. Carbide precipitates are observed with various shape and sizes. Two types of precipitates are observed namely MX (M=Nb/Fe) type and $M_{23}C_6$ (M=Cr/Fe) type carbides. Precipitates are having different shape and sizes. The EDS spectrum from Nb rich MX precipitate and chromium rich $M_{23}C_6$ precipitates are shown in figure 4b and 4c respectively.

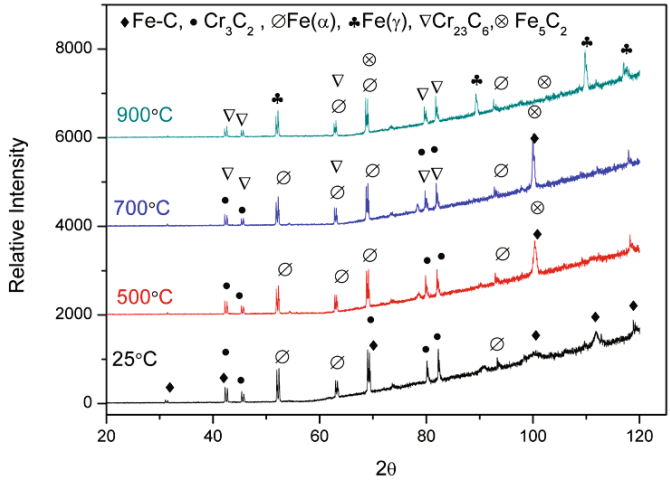

Figure 3: High temperature XRD plot

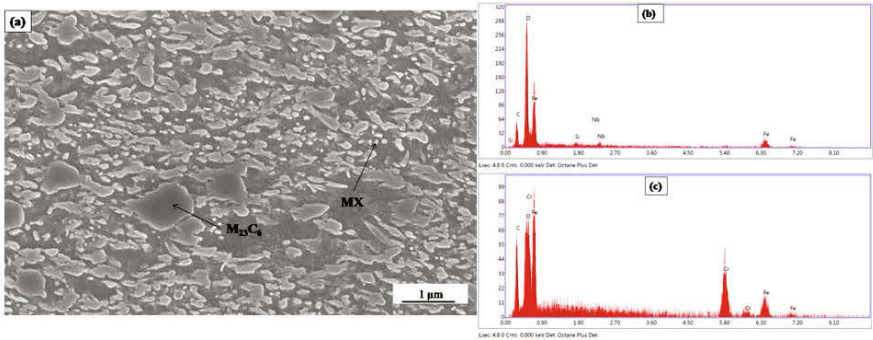

Figure 4: (a) SEM micro graph of tempered steel, (b) EDS results from Nb-MX precipitate, and (c) EDS results from Cr rich $M_{23}C_6$ precipitate

3.5 Effect of hot working on tensile properties: Homogeneous, single phase austenitic microstructure with appropriate grain size should be obtained firstly as a starting point of heat treatment. It has been reported that the upper limit of normalizing temperature for 9-12% Cr steel should be around 1100˚C to avoid coarsening of microstructure [1]. It is well known that the tensile properties like strength and elongation depends on the mechanical working and heat treatment temperature. Figure5a shows the engineering stress-strain diagram for different conditions of the steel. Yield strength and tensile strength are better for rolling than forging. In case of rolling, ultimate tensile strength and ductility increases with increasing thickness reduction. The best mechanical properties are achieved at hot rolling with 80% reduction

followed by normalizing at 1100˚C and tempering at 700˚C for 1 hour. The tensile properties are comparable with the reported values of P91 steel [1].

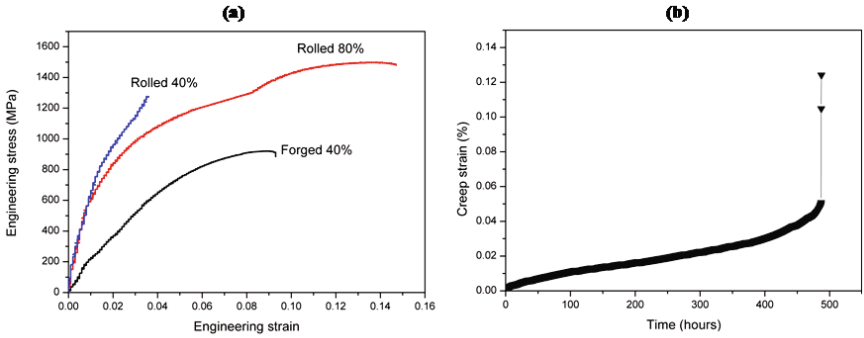

Figure 5: (a) Tensile properties with different hot working conditions, (b) Creep rupture curve at 600˚C and 120 MPa

Table2: Tensile properties of the steel at different working condition

Hot Working Condition	Y S (MPa)	U T S (MPa)	Elongation (%)
Forged 40%	245	920	9.6
Rolled 40%	871	1275	3.6
Rolled 80%	618	1500	14.7

3.6 Creep properties: The creep rupture curve at 600˚C and 120 MPa load is shown in figure 5b. The creep curve consists of: a) a short primary creep corresponding to a decrease in the creep strain rate, b) a secondary creep with a characteristic steady strain rate and c) a tertiary creep where the strain rate increases and failure occurs. It is observed that the primary creep region is around 100 hours whereas the secondary creep region extends up to around 300 hours and the final tertiary stage exists around 75 hours. In secondary region, the rate of strain hardening and thermal recovery get into equilibrium over period of time during deformation. From this region creep rate was estimated to determine the creep parameter of the steel. Steady state creep rate for the steel at 600˚C and 120 MPa load is $5.082 \times 10^{-2} h^{-1}$.

3.7 Cyclic Oxidation Properties:

3.7.1 Oxidation Kinetics: A set of cyclic oxidation tests is performed in the temperature range between 600 and 700˚C up to 50 cycles. Each thermal cycle consists of 1 hour heating and 1 hour cooling. The specific weight gain by the specimen is used to determine the oxidation kinetics. Figure 6a shows a plot of specific weight gain vs. time plot at 600, 650 and 700˚C. It is evident that oxidation rate increases with temperature. The mass gain at 600˚C are extremely small and it increases at 650 and 700˚C. The oxidation kinetics follows the near parabolic rate regime. The nature of the curves is similar with previous observations during isothermal oxidation of P91 steel [14, 15]. The parabolic rate indicates that the reaction is a diffusion controlled character at all temperatures. The high temperature oxidation kinetics of metals or

alloys is generally controlled by the diffusion of ionic species through the oxide scale [16]. The experimental data points corresponding to every temperature can be reasonably fitted by a parabolic curve through the origin of the coordinate system as:

$$(\Delta m/s)^2 = A + K_p \times t \quad (1)$$

where $\Delta m/s$ is the specific weight gain per unit area and t is the oxidation time and A is a constant. The relationship between the parabolic rate constant (K_p) and temperature (T) in an Arrhenius type of equation, is given by

$$K_p = K_0 \exp(-Q/RT) \quad (2)$$

where Q is the activation energy of the process, R is the gas constant and T is the absolute temperature. A logarithmic plot of the equation (2) allows the determination of the activation energy of the oxidation process. The scattering of the data may be associated with the experimental factors leading to the difficulties in the precise determination of the area exposed to oxidation due to the concave surface, as well as, slight damage of the oxide scale during weighing. Figure 6b shows the K_p vs 1/T plot for the steel. The calculated activation energy for the oxidation process is 53.2 kJ mol^{-1}. The activation energy corresponds to the overall process involving a combination of mechanisms like the outward migration of metallic cations as well as the inward diffusion of oxygen ions [17].

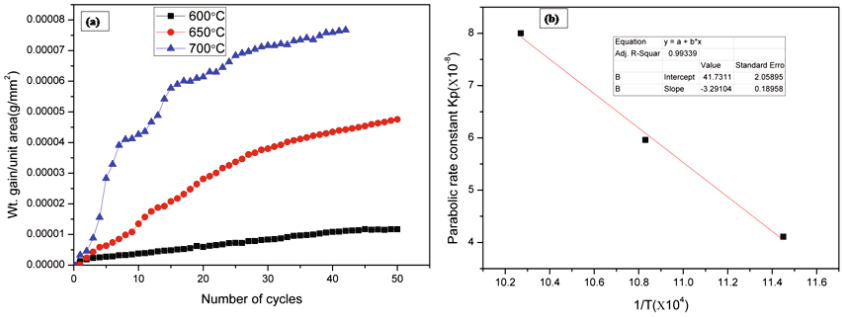

Figure 6: (a) specific weight gain vs. time plot, (b) K_p vs 1/T plot at 600, 650 and 700°C.

3.7.2 Surface morphology after oxidation: Figure 7a shows the morphology of the oxide surfaces after oxidation at 600°C for 50 cycles. The surface has irregular morphology due to selective growth of oxide scale. Due to high oxidation resistance of the carbide a selective oxidation in the matrix occurs. This results in irregular morphology of oxide scale [18]. Hence, the growth of the oxide scale is not uniform and maintains irregular morphology. A lot of microporosity is observed after oxidation of 50 cycles. The cross section of oxide scale is shown in figure 7b. The thickness of oxide scale increases with increasing oxidation time. The oxide scale after oxidation of 50 cycles is very thick and usually consists of three layers: (1) a thin Fe_2O_3 outer layer, (2) a thick and porous Fe_3O_4 (Fe_2O_3+FeO) intermediate layer, and the (3) inner spinel M_3O_4 (M=Fe,Cr,V) produced by the internal oxidation.

3.7.3 Phase characterization of oxide scale: To find out the reaction mechanism and growth behavior of oxide layer, XRD has been carried out for samples oxidized for 50 cycles. As the depth of penetration of XRD amounts to only a few micrometers, the patterns are representative of the constitution of outer part of the oxide scale [18]. Figure 7c shows the XRD patterns of the oxide specimens after oxidation of 50 cycles at 700˚C. Fe (matrix) and hematite (Fe_2O_3), spinel [$(Fe,Cr)_3O_4$] peaks are observed after oxidation of 50 cycle at 700˚C. The intensity of Fe peaks decreases whereas the intensity of hematite and magnetite peaks increases with increasing oxidation time and temperature. This may be due to the increase in oxide layer thickness.

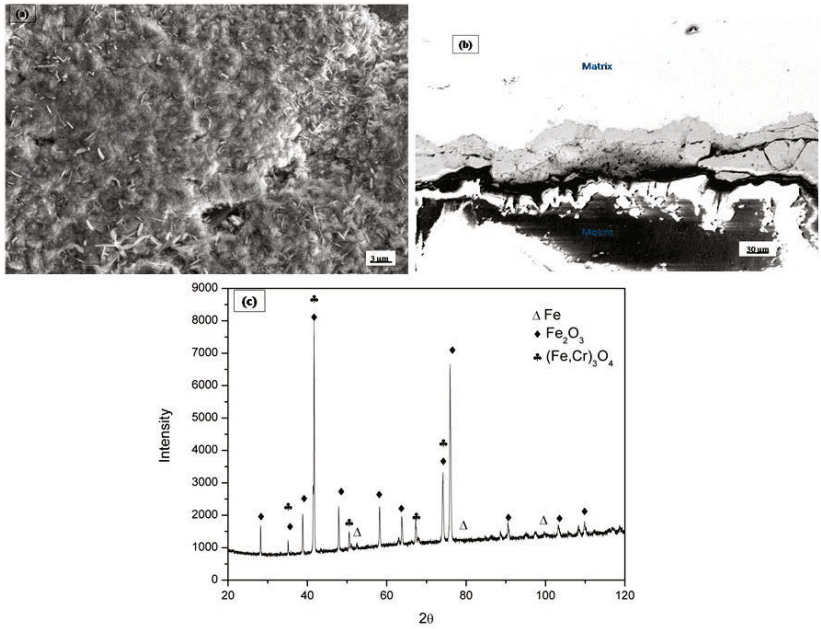

Figure 7: (a) cross section of oxide scale (b) SEM micrograph of oxide scale and (c) XRD plot of oxide scale after 50 cycles at 700˚C

4. Conclusions

Cast microstructure consists of martensite along with retained austenite and complex carbide phases. Martensite and Carbide phase change are observed with increasing temperature during high temperature x-ray diffraction. Tensile properties of the steel are dependent on hot working and subsequent heat treatment parameters. The best combination of strength and elongation is achieved for 80% hot rolling, followed by normalizing at 1100˚C and tempering at 700˚C conditions. Creep curve consists of primary, secondary and tertiary regions. Cyclic oxidation curve follows near parabolic rate regime.

5. References

[1] S. S. Wang, D. L. Peng, L. Chang, and X. D. Hui, Enhenced mechanical properties induced by refined heat treatment for 9Cr-0.5Mo-1.8W martensitic heat resistant steel, Materials and design, 50 (2013), 174–180.

[2] D. Rojas, J. Garcia, O. Prat, C. Carrasco, G. Sauthoff, and A. R. Kaysser-Pyzalla, Design and characterization of microstructure evolution during creep of 12% Cr heat resistant steels; Material Science and Engineering A , 257(2010), 3864–3876.

[3] P.J. Ennis and A. Czyrska-Filemonowicz, Recent advances in creep resistant steels for power plant applications, Operation Maintainance and Materials Issue, 1(1)2002, 1–28.

[4] R. Agamennone , W. Blum, C. Gupta, and J. K. Chakravartty, Evolution of microstructure and deformation resistance in creep of tempered martensitic 9-12%Cr-2%W-5%Co steels ; Acta Materialia 54 (2006), 3003–3014.

[5]M. Hattestrand, H. O. Andren, Microstructural development during ageing of an 11% chromium steel alloyed with copper; Materials Science and Engineering A, 318 (2001), 94–101. [6] H. Magnusson, R. Sandstrom, Influence of aluminium on creep strength of 9-12% Cr steels, Material Science and Engineering A, 527(2009), 118–125.

[7] V. Knezevic, J. Balun, G. Sauthoff, G. Inden, and A. Schneider, Design of martensitic/ferritic heat resistance steels for application at 650˚C with supporting thermodynamic modelling, Materials Science and Engineering A, 477 (2008), 334–343.

[8] U. E. Klotz , C. Solenthaler , P. Ernst , P. J. Uggowitzer , and M. O. Speidel, Alloy compositions and mechanical properties of 9-12% chromium steels with martensitic-austenitic microstructure; Materials Science and Engineering A, 272 (1999), 292–299.

[9] George E. Dieter, Mechanical Metallurgy; SI Metric Edition, London,1928, P. 203–205.

[10]Robert J Glodowski; Vanadium in medium and high carbon steels; http://vanitec.org/wp-content/uploads/2011/09/Vanadium-in-Medium-and-High-Carbon-Steels.pdf visited on 1.9.2015

[11]B. J. Ganesh, S. Raju, A. K. Rai, E. Mohandas, M. Vijayalakshmi, K. B. S. Rao, and B. Raj; Differential scanning calorimetry study of diffusional and martensitic phase transformations in some 9 wt-%Cr low carbon ferritic steels, Material Science and Technology, 27(2011), 500–512.

[12]T. Shrestha, S.F. Alsagabi, I. Charit, G.P.Potirniche and M.V. Glazoff; Effect of heat treatment on microstructure and hardness of grade91 stee, Metals, 5(2015),131–149.

[13] Z. Lu, R.G. Faukner, and N. Riddle, Effect of heat treatment on microstructure and hardness of Eurofer 97, Eurofer ODS and T92 steels, Journal of Nuclear Materials, 386–388(2009), 448–.

[14] B.J. Downey, J.C. Bermel, P.J .Zimmer, Kinetics of the nickel-chlorine reaction at temperatures between 350 and 600˚C, Corrosion, 25/12 (1969), 502–508.

[15] J.P.T. Vossen, P.Gawenda, K.Raths, M.Schorr, M.Schutze, Limits of the oxidation resistance of several heat resistance steel under isothermal and cyclic oxidation as well as under creep in air at 650˚C, Materials at high temperature, 14/4 (1997), 387–401.

[16] A. M. Huntz, Parabolic laws during high temperature oxidation: relations with the grain size and thickness of oxide scale, Journal of Material Science Letters, 18(1999), 1981–1984.

[17] D. Laverde, T.G.Acebo, and F. Castro, Continuous and cyclic oxidation of T91 ferritic steel under steam, Corrosion Science, 46 (2004), 613–631.

[18] A. Molinari, G. Straffelini, A.Tomasi,A. Biggi, and G.Corbo, oxidation behavior of ledeburitic steels for hot rolls, Material Science Engineering A, 280 (2000), 255–262.

AUTHOR INDEX

Characterization of Minerals, Metals, and Materials 2016

D

E

F

G

H

I

J

K

L

M

N

O

P

Q

R

S

T

V

SUBJECT INDEX

Characterization of Minerals, Metals, and Materials 2016

D

E

F

G

H

I

K

L

M

N

O

P

Q

V

W

X

Y

Z